Comportement mécanique des roches et dynamique de la lithosphère: Des données de terrain aux modèles numériques

Philippe Yamato

Mémoire d'Habilitation à Diriger des Recherches

Université de Rennes 1

Comportement mécanique des roches et dynamique de la lithosphère: Des données de terrain aux modèles numériques

Philippe YAMATO

Maître de Conférences

Géosciences Rennes, UMR UR1/CNRS 6118

SOUTENANCE PREVUE LE 27 NOVEMBRE 2014 DEVANT LE JURY COMPOSE DE :

Anne DAVAILLE	*Université de Paris Sud, Paris*
Luce FLEITOUT	*Ecole Normale Supérieure, Paris*
Denis GAPAIS	*Géosciences Rennes, Rennes*
Taras GERYA	*ETH, Zürich*
Claudio ROSENBERG	*Université Pierre et Marie Curie, Paris*
Jeroen VAN HUNEN	*Durham University, Durham*

AVANT-PROPOS

Ce mémoire dresse le bilan de mes activités de recherche depuis ma thèse de 3ème cycle. Il s'agit là d'une tentative de synthèse des travaux effectués à Rennes pendant 2 ans de post-doctorat (2007-2008), à Zürich durant 1 an (en 2008-2009), puis à Rennes depuis mon recrutement en septembre 2009 en tant que maître de conférences.

Ce qui me frappe au moment d'écrire ces quelques lignes c'est l'importance des rencontres et du partage d'idées et de point du vue que j'ai pu avoir avec les personnes que j'ai rencontrées lors de ces dernières années. Celles-ci ont, en effet, façonné à la fois mon cheminement scientifique et la façon dont je vois les choses aujourd'hui. Ma *« philosophie de recherche »* qui en découle peut brièvement se résumer à la compréhension des processus qui régissent la dynamique de la lithosphère et à leur quantification grâce à un outil qui est la modélisation numérique. Ce travail ne peut être réalisé, cependant, que si les modèles se trouvent suffisamment bien contraints. Une telle approche ne peut donc se faire sans un aller retour constant entre les observables de terrain et les modèles, travail que je m'efforce de faire et que je vais tâcher d'illustrer dans ce mémoire.

Ce manuscrit présente tout d'abord un curriculum vitae qui résume mon parcours et dresse un bilan synthétique de mes activités de recherche, d'enseignement et d'encadrement, complété par une liste de mes publications et communications. Mon approche scientifique et mes activités de recherche sont ensuite détaillées, autour du thème principal de la compréhension du comportement mécanique des roches et des processus qui régissent la dynamique de la lithosphère. Les développements futurs de l'activité de recherche que je souhaite mener sont ensuite décrits succinctement.

Une sélection des publications récentes auxquelles j'ai participé et qui sont utilisées pour illustrer mes propos dans ce manuscrit est présentée au sein d'un volume annexe.

Ma façon de voir le travail de recherche est née à l'Université Paris 6 au cours de ma thèse. Je voudrais profiter de cette occasion pour remercier encore Philippe Agard, Génia Burov, Laetitia Le Pourhiet et Laurent Jolivet avec qui j'ai pu faire mes premiers pas dans le monde de la recherche sans encombres. Mes années de post-doctorat, à Rennes puis Zürich, ont constitué une étape importante dans le développement de mes travaux. Je tiens à remercier tout particulièrement Laurent Husson pour toutes nos inlassables discussions, mais également Jean Braun et Michel Ballèvre pour leur positivisme constant qui m'ont permis de grandir un peu plus, de prendre du recul, de regarder les choses différemment, et d'explorer de nouveaux horizons. A cet épanouissement s'ajoute la mise en confiance sur mes capacités à devenir indépendant. Pour cela, je tiens particulièrement à remercier Sébastien Castelltort, Boris Kaus mais aussi les personnes sans qui je ne pourrais certainement pas écrire ces quelques lignes aujourd'hui : Thibault Duretz, Dave May, Benjamin Huet, ou encore Samuel Angiboust… Un grand merci à vous ! Enfin, je remercie ceux grâce à qui je me suis immédiatement senti *à la maison* à Géosciences Rennes (Pavel, Denis, Philippe, Marc, Marc, Jean-Pierre, Jean, Pierre et Ben)… et les étudiants de Géosciences, partis ou encore présents (Romain, Stephen, Sylvia, Bryan et Solenn) qui constituent de vrais produits dopant pour la réflexion scientifique mais aussi personnelle.

Enfin, je ne peux finir cet avant-propos sans remercier Marie, toujours présente à chaque étape de ce fabuleux (mais parfois dur) parcours et dont le soutien incommensurable ne faiblit jamais.

… À Jean et Minoru

TABLE DES MATIÈRES

Volume principal

Volume Annexe : Sélection d'articles

1. CURRICULUM VITAE

YAMATO PHILIPPE 33 ans
Maître de conférences en Géologie né le 23 octobre 1980 à Maisons-Alfort (94)
Section CNU 35

Géosciences Rennes – UMR CNRS 6118,
Université de Rennes1, Campus de Beaulieu
Bat. 14B, E1, Bureau 111
35042 Rennes Cedex, France

☎ : +33 2 23 23 60 95
✉ : philippe.yamato@univ-rennes1.fr
🌍 : http://sites.google.com/site/philippeyamato/

THEMES DE RECHERCHE

- **Dynamique des zones de convergence** (subduction, obduction, collision, plissement, chevauchement)
- **Rhéologie des roches**
- Processus d'**exhumation des roches métamorphiques**
- Dynamique des **dykes magmatiques**
- **Interaction** entre **processus tectoniques** et **érosion**

Spécialités : Tectonique · Géodynamique · Pétrologie métamorphique · Modélisation numérique

EXPERIENCE PROFESSIONELLE

2008 - 2009 ▸ **Chercheur post-doctoral**, ETH - Zürich – Suisse (~ 1 an)
Position entre le groupe E.S.D. (S. Willett) et G.F.D. (P. Tackley)
Thèmes : - Modélisation à l'échelle crustale de la déformation des chaînes plissées
- Interactions Tectonique - Erosion

2007 - 2008 ▸ **Chercheur post-doctoral**, Université de Rennes 1 (~ 2 ans)
Thèmes : - Modélisation 3D des zones de subduction
- Etude pétrologique des éclogites du massif du Grand Paradis

2006 - 2007 ▸ **A.T.E.R.**, Université Pierre & Marie Curie, Paris VI

FORMATION

2003 - 2006 ▸ **Doctorat en Sciences de la Terre**, Université Pierre & Marie Curie, Paris VI
▸ **Moniteur**, Université Pierre & Marie Curie, Paris VI

2002 - 2003 ▸ **Master** en Sciences de la Terre, Université Pierre & Marie Curie, Paris VI et IFP.

THESE DE 3ème CYCLE

Titre ▸ Des contraintes pour les zones de convergence : Confrontation des données du métamorphisme et des modélisations numériques thermomécaniques – Application aux Alpes et à l'Oman

Version pdf disponible à : http://tel.archives-ouvertes.fr/tel-00134728

Directeurs ▸ P. Agard, E. Burov et L. Jolivet
Soutenance ▸ 8 Décembre 2006
Distinction ▸ Prix de thèse Van Straelen de la Société Géologique de France (2007)

COMPÉTENCES ET OUTILS

Modélisation numérique

- Mise en œuvre d'un code personnel thermomécanique 2D (cf. Yamato et al., 2012; 2013; 2014)

- Code Thermomécanique PARA(O)VOZ (cf. Doctorat avec E. Burov). Large contributions à l'implémentation des changements progressifs de densité (via THERIAK), à l'intégration de particules et à l'amélioration de la procédure de remaillage.
- Bonne connaissance du code Thermomécanique 3D DOUAR (cf. post-doctorat avec J. Braun)
- Utilisateur de MILAMIN_VEP et LAMEM (cf. post-doctorat avec B. Kaus)

- Langages de programmation: MATLAB, Fortran 90, C, Fortran 77
- Logiciels: suite Office, suite Adobe, Gimp, GMT, LATEX, Keynote, …

Géologie de terrain

- Géologie structurale et analyse de la déformation (cassante et ductile)
- Terrain de recherche: Alpes occidentales, Oman, et massif Armoricain
- Terrain pour l'enseignement (niveau Licence et Master): massif Armoricain, Alpes occidentales, Pyrénées, Bétiques

Pétrologie métamorphique

- Analyse des textures métamorphiques (de l'échelle du terrain à celle de la lame mince)
- Utilisateur de programmes d'estimations thermo-barométriques (TWEEQU, THERMOCALC).
- Calcul de diagrammes de phases (THERMOCALC, PerpleX, Theriak-Domino).
- Développement d'outils numériques pour la décomposition des minéraux, les estimations P-T et les pseudo-sections automatiques utilisant THERMOCALC.

COLLABORATIONS PRINCIPALES

- Philippe Agard (Paris) – Etude de l'obduction (Oman)
- Samuel Angiboust (Potsdam) – Etude de l'interface de subduction (Alpes)
- Thibault Duretz (Lausanne) – Modélisation numérique
- Benjamin Huet (Vienne) – Rhéologie des roches, Modélisation thermodynamique
- Laurent Husson (Grenoble) – Tectonique et Géodynamique
- Dave May (Zürich) – Modélisation numérique
- Pavel Pitra (Rennes) – Modélisation thermodynamique, Zones de cisaillement

RESPONSABILTÉS ET ACTIVITÉ ÉDITORIALE

Nationales et Internationales

- Rapporteur (Reviewer) pour des journaux internationaux (e.g., EPSL, GJI, G-cubed, JAES, Tectonophysics, Terra Nova, Lithos)

- Rapporteur de projets pour l'Institut National des Sciences de l'Univers (INSU)

- Opposant (Rapporteur) au sein du jury de thèse de Reza Khabbaz Ghazian (Université d'Oslo, 2014)

- Examinateur au sein du jury de thèse de Jonathan Mercier (Université de Grenoble, 2014)

- Participation aux programmes de recherche :

2009-2010 : - ANR blanche O:NLAP (P. Agard)
Obduction : la fin d'une énigme géodynamique ?

2010-2011 : - ANR blanche INVERVAR (M. Ballèvre) – non financé
Mécanisme de transfert de chaleur dans une croûte épaissie : le métamorphisme inverse dans la chaîne varisque.

- ANR JC ALBORAN (F. Gueydan) – non financé
Déformation lithosphérique d'Alboran contrôlée par un roll-back extrême du slab.

- INSU SYSTER (P. Yamato) – non financé
Métamorphisme inverse : genèse, mise en place et préservation.

2011-2012 : - A.O. OSUR (P. Yamato)
Rhéologie des zones de cisaillement

- INSU SYSTER (P. Yamato) – non financé
Métamorphisme inverse : genèse, mise en place et préservation.

2012-2013 : - ANR blanche RhεReS (J.P. Brun) – non financé
Rheology and deformation of Retreating Slab

- INSU SYSTER (P. Yamato)
Rhéologie des zones de cisaillement : Effets combinés du métamorphisme et de la déformation (AO2013-786508).

2013-2014 : - ANR blanche RhεReS (J.P. Brun) – non financé
Rheology and deformation of Retreating Slab

- A.O. OSUR (P. Yamato) – non financé
Modélisation numérique des milieux polyphasés

- ANR JC EROQUAKE (P. Steer)
Erosion and Earthquakes

2014-2015 : - INSU SYSTER (P. Yamato) – demande en cours
Déformation des roches à l'interface de subduction

Au sein du laboratoire (Géosciences Rennes et de l'Université de Rennes 1 depuis 2009)

En cours…

- En charge de la Licence 3 Sciences de la Terre (depuis 2012)
- En charge de l'équipe "Systèmes Tectoniques" de Géosciences Rennes (depuis 2012)
- Membre du jury de la Licence Sciences de la Terre (depuis 2010)

… et passé

- Représentant des doctorants de l'école doctorale Géosciences and Ressources naturelles (2003-2006)
- Représentant des doctorants du laboratoire de Tectonique de l'UPMC (2003-2006)
- Membre actif de la société Géologique de France – section "jeunes" (2004-2006)
- Membre de la commission de recrutement MCF (Concours 2012 pour Géosciences)
- Membre du jury du Master "Modélisation and Calcul Scientifique" – Univ. Rennes 1 (2009-2012)

DIVERS… parce que c'est important aussi!

Sport	▸ floorball, jorkyball, course, natation, escalade, salsa, voile, tennis…
Musique	▸ Flute, djing
Autre	▸ BAFA

2. PUBLICATIONS

Google Scholar: h-index: 13; Number of citations: 640
ISI counts: h-index: 12; Number of citations: 491

Articles

En préparation **:**

- Cochelin B., **Yamato P.**, Pitra P. & Gapais D., " Continuous activity of the South Armorican Shear Zone: from migmatization to late brittle deformation (Baie des Trépassés, Brittany, France)".

Soumis **:**

- Duprat-Oualid S., **Yamato P.** & Schmalholz S.M., "A dimensional analysis to quantify the thermal budget around lithospheric-scale shear zones", *Terra Nova*.

- Ballouard C., Boulvais P., Poujol M., Gapais D., **Yamato P.**, Tartèse R. & Cuney M., “Tectonic record, magmatic history and hydrothermal alteration in the Hercynian Guérande leucogranite, Armorican Massif, France”, *Lithos*.

- **Yamato P.**, Duretz T., May D.A. & Tartèse R., “Quantifying magma segregation in dykes”, *Earth and Planetary Science Letters*.

Publiés :

2014 **[25]** Burov E., Francois T., Agard P., Le Pourhiet L., Meyer B., Tirel C., Lebedev S., **Yamato P.**, & Brun J.-P., "Rheological and geodynamic controls on the mechanisms of subduction and HP/UHP exhumation of crustal rocks during continental collision: Insights from numerical models", *Tectonophysics*, 2014.

[24] Burov E., Francois T., **Yamato P.** & Wolf S., "Advances and challenges in geotectonic modeling", *Bulletin de la Société Géologique de France*, v.185, p.147-168, doi:10.2113/gssgfbull.185.3.147

[23] Huet B., **Yamato P.** & Grasemann B., "The Minimized Power Geometric model: an analytical mixing model for calculating polyphase rock viscosities consistent with experimental data", *J. Geophys. Res. Solid Earth,* v.119*,* doi:10.1002/2013JB010453

[22] Burov E., Francois T., **Yamato P.** & Wolf S., "Mechanisms of continental subduction and exhumation of HP and UHP rocks", *Gondwana Research*, v.25, p.464-493, doi:10.1016/j.gr.2012.09.010

[21] Fauconnier J., Labrousse L., Andersen T.B., Beyssac O., Duprat-Oualid S. & **Yamato P.**, "Thermal structure of a major crustal shear zone, the basal thrust in the Scandinavian Caledonides", *Earth and Planetary Science Letters*, v.385, p.162-171, doi:10.1016/j.epsl.2013.10.038

2013 **[20]** **Yamato P.**, Husson L., Becker T.W. & Pedoja K., "Passive margins getting squeezed in the mantle convection vice", *Tectonics*, v.32, p.1559-1570, doi:10.1002/2013TC003375

[19] Duprat-Oualid S., **Yamato P.** & Pitra P., "Major role of shear heating in intracontinental inverted metamorphism: Inference from a thermo-kinematic parametric study", *Tectonophysics*, v.608, p.812-831, doi:10.1016/j.tecto.2013.07.037

[18] Castelltort S. & **Yamato P.**, "The influence of surface slope on the shape of river basins: Comparison between nature and numerical landscape simulations", *Geomorphology*, v.191, p.71-79, doi: 10.1016/j.geomorph.2013.03.022

2012 **[17]** Angiboust S., Wolf S., Burov E., Agard P. & **Yamato P.**, "Effect of Fluid Circulation on Subduction Interface Tectonic Processes: Insights from Thermo-mechanical Numerical Modelling", *Earth and Planetary Science Letters*, v.357-358, p.238-248, doi:10.1016/j.epsl.2012.09.012

[16] Angiboust S., Agard P., **Yamato P.** & Raimbourg H. "Eclogite breccias in a subducted ophiolite: a record of intermediate-depth earthquakes?", *Geology*, v.40, p. 707-710, doi:10.1130/G32925.1

[15] **Yamato P.**, Tartèse R., Duretz T. & May D.A., "Numerical modelling of magma transport in dykes", *Tectonophysics*, 526-529, p. 97-109, doi:10.1016/j.tecto.2011.05.015

2011 **[14]** Angiboust S., Agard P., Raimbourg H., **Yamato P.** & Huet B., "Subduction interface processes recorded by eclogite-facies shear zones (Monviso, W. Alps)", Lithos, v.127, p.222-238, doi:10.1016/j.lithos.2011.09.004

[13] Tartèse R., Poujol M., Ruffet G., Boulvais P., **Yamato P.** & Košler J., "New U-Pb zircon and 40Ar/39Ar muscovite age constraints on the emplacement of the Lizio syn-tectonic granite (Armorican Massif, France)", *Comptes Rendus Géoscience*, v.343, p.443-453, doi:10.1016/j.crte.2011.07.005

[12] **Yamato P.**, Kaus B.J.P., Mouthereau F. & Castelltort S., "Dynamic constraints on the crustal-scale rheology of the Zagros fold belt, Iran", *Geology*, v.39, p. 815-818, doi:10.1130/G32136.1

2010 **[11]** Loiselet C., Braun J., Husson L., Le Carlier de Veslud C., Thieulot C., **Yamato P.** & Grujic D., "Subducting slabs: jellyfishes in the Earth's mantle", *Geochemistry Geophysical Geosystems*, 11, Q08016, doi:10.1029/2010GC003172

[10] Braun J. & **Yamato P.,** "Multi-scale couplings between surface processes and deformation of a three-dimensional orogenic wedge", *Tectonophysics*, 484, 1-4, p. 181-192, doi:10.1016/j.tecto.2009.08.032

2009 **[9]** Husson L., Brun J.P., **Yamato P.** & Faccenna C., "Episodic slab rollback fosters HP-UHP rocks exhumation", *Geophysical Journal International*, 179, p.1292-1300, doi:10.1111/j.1365-246X.2009.04372.x

[8] **Yamato P.**, Husson, L., Braun J., Loiselet C. & Thieulot C., "Influence of surrounding plates on 3D subduction dynamics", *Geophysical Research Letters*, 36, L07303, doi: 10.1029/2008GL036942

[7] **Yamato P.**, Mouthereau F. & Burov E., "Taiwan mountain building: insight from 2D thermomechanical modeling of a rheologically-stratified lithosphere", *Geophysical Journal International*, 176, 1, p. 307-326, doi: 10.1111/j.1365-246X.2008.03977.x

[6] Agard P., **Yamato P.**, Jolivet L. & Burov E. "Exhumation of oceanic blueschists and eclogites in subduction zones: timing and mechanisms", *Earth Science Reviews*, 92, p. 53-79, doi: 10.1016/j.earscirev.2008.11.02

2008 **[5]** **Yamato P.**, Burov E., Agard P., Le Pourhiet L. & Jolivet L., "HP-UHP exhumation during slow continental subduction: Self-consistent thermodynamically and thermomechanically coupled model with application to the Western Alps", *Earth and Planetary Science Letters*, 271, p. 63-74, doi: 10.1016/j.epsl.2008.03.049

[4] Burov E. & **Yamato P.** "Continental plate collision, P-T-t-z conditions and unstable vs.

stable plate dynamics: Insights from thermo-mechanical modelling", *Lithos*, 25, p. 178-204, doi: 10.1016/j.lithos.2007.09.014

2007 **[3]** **Yamato P.**, Agard P., Goffé B., De Andrade V., Vidal O. & Jolivet L., "New, high-precision P-T estimates for Oman blueschists: Implications for obduction, nappe stacking and exhumation processes", *Journal of Metamorphic Geology*, 25, p 657-682, doi: 10.1111/j.1525-1314.2007.00722.x

[2] **Yamato P.**, Agard P., Burov E., Le Pourhiet L., Jolivet L. & Tiberi C., "Burial and exhumation in a subduction wedge: Mutual constraints from thermomechanical modeling and natural P-T-t data (Sch. Lustrés, western Alps)", *Journal of Geophysical Research*, 112, B07410, doi: 10.1029/2006JB004441

2006 **[1]** Agard P., Monié P., Gerber W., Omrani J., Molinaro M., Meyer B., Labrousse L., Vrielynck B., Jolivet L. & **Yamato P.**, "Transient, synobduction exhumation of Zagros blueschists inferred from P-T, deformation, time, and kinematic constraints: Implications for Neotethyan wedge dynamics", *Journal of Geophysical Research*, 111, B11401, doi: 10.1029/2005JB004103

Communications Orales

2014
- **Yamato P.**, Husson L., Becker T.W. & Pedoja K., "Passive margins getting squeezed in the mantle convection vice" *E.G.U.*, Vienna, Austria.
- **Yamato P.**, Duretz T., Tartèse R. & May D.A. "Influence of crystalline load on magma behaviour in dykes: A numerical study" *E.G.U.*, Vienna, Austria.

2013
- Huet B.,**Yamato P.** & Grasemann B., "Influence of metamorphic reactions on rock strength: A new analytical model" *D.R.T.*, Leuven, Belgium.
- Huet B.,**Yamato P.** & Grasemann B., "A new analytical model to predict strength changes due to metamorphic reactions" *G.S.A.*, v. 45, 7, p.239, Denver, Colorado USA.

2011
- **Yamato P.**, Tartèse R., Duretz T. & May D. A., "Numerical modelling of magma transport in dykes" *E.G.U.*, Vienna, Austria
- **Yamato P.**, Agard P., Burov E., Le Pourhiet L. & Angiboust S., "Exhumation mechanisms in convergence zones: Insight from thermomechanical models" *I.L.P. Workshop*, Sampeyre, Italia

2010
- Kaus B., **Yamato P.**, Mouthereau F. & Castelltort S., "Dynamics constraints on crustal-scale rheology from the Zagros Mountains" *Swiss Geosciences Meeting*, Fribourg, Switzerland
- Mouthereau F., **Yamato P.**, Fillon C., Wang Y.J., Castelltort S., Nagel S., Lin A., Ma K.F., Chu H.T. & Shea K.S., "A new crustal-scale cross-section of the southern Taiwan orogenic wedge constrained by structural, geophysical, seismotetonic data and thermo-mechanical modelling", *E.G.U.*, Vienna, Austria
- Husson L., Brun J-P., **Yamato P.** & Faccenna C., "Episodic slab rollback fosters exhumation of HP-UHP rocks", *E.G.U.*, Vienna, Austria

2009
- Loiselet C., Grujic D., Braun J., Fullsack P., Thieulot C. & **Yamato P.**, "The temporal evolution of a subducting plate in the lower mantle", *E.G.U.*, Vienna, Austria

2008
- Braun, J. & **Yamato P.**, "Multi-scale couplings between surface processes and deformation of a three-dimensional orogenic wedge", *GeoMod*, Florence, Italia
- **Yamato P.**, Burov E., Agard P., Le Pourhiet L. & Jolivet L., "What controls the presence of HP-UHP continental rocks in convergent zones? Application to the Western Alps", *R.S.T.*, Nancy, France

2007
- **Yamato P.**, Burov E., Agard P., Le Pourhiet L. & Jolivet L., "What controls the presence of HP-UHP continental rocks in convergent zones? Application to the Western Alps", *E.G.U.*, Vienna, Austria

2006
- **Yamato P.**, Agard P., Burov E., Le Pourhiet L. & Jolivet L., "Burial and exhumation in a subduction wedge: Mutual constraints from thermo-mechanical modelling and natural P-T-t data (Schistes Lustrés, Western Alps)", *E.G.U.*, Vienna, Austria

2005
- Burov E. & **Yamato P.**, "Continent-continent collision styles and exhumation mechanisms as function of thermo-rheological profile and convergence rate", *E.G.U.*, Vienna, Austria

2004
- **Yamato P.**, Agard P., Burov E., Le Pourhiet L., Tibéri C. & Jolivet L., "Exhumation of HP-UHP metamorphic rocks during convergence: Constraints from thermomechanical models", *E.G.U.*, Nice, France
- **Yamato P.**, Agard P., Burov E., Le Pourhiet L., Tibéri C. & Jolivet L. "Les processus d'exhumation des roches métamorphiques de haute-pression et ultra-haute-pression en contexte de convergence : Des données de terrain vers la modélisation numérique, l'exemple des Alpes", *R.S.T.*, Strasbourg, France

Posters (1er ou second auteur seulement)

2013
- **Yamato P.**, Duretz T., Tartèse R. & May D.A., “Polycrystalline magma behaviour in dykes: Insights from high-resolution numerical models”, EGU2013-9802, EGU General Assembly 2013, Vienna, Austria
- Duprat-Oualid S. & **Yamato P., “**Inverted metamorphism and feedback between temperature and non-Newtonian viscosity in compressive shear zones: A 2D thermo-kinematic study”, EGU2013-803, EGU General Assembly 2013, Vienna, Austria
- Husson L., **Yamato P.**, Becker T.W. & Pedoja K., **“**Passive margins getting squeezed in the mantle convection vice”, EGU2013-5077, EGU General Assembly 2013, Vienna, Austria
- Duretz T., **Yamato P.** & Schmalholz S.M., **“**Deformation of two-phase aggregates using standard numerical methods”, EGU2013-9576, EGU General Assembly 2013, Vienna, Austria
- Agard P., **Yamato P.**, Francesca Piccoli, Mathieu Benoît, Benoît Dubacq, Stéphane Guillot, Patrick Monié, Alain Chauvet, Georges Ceuleneer, Christian Chopin & Cécile Prigent, **“**Petrological evolution of the metamorphic sole of Oman”, EGU2013-10051, EGU General Assembly 2013, Vienna, Austria

2012
- **Yamato P.**, Tartèse R., Duretz T. & May D.A., “Magma differentiation in dykes: from field evidence to numerical study”. GeoMod2012, Lausanne, Suisse.
- Duprat-Oualid S. & **Yamato P.**, “Syn-deformational inverted metamorphism: Insights from 2D thermo-kinematic numerical models”. GeoMod2012, Lausanne, Suisse.
- **Yamato P.**, Tartèse R., Duretz T. & May D.A., “Magma differentiation in dykes: from field evidence to numerical study”. Geophysical Research Abstracts, Vol. 14, EGU2012-913, 2012 EGU General Assembly 2012, Vienna, Austria
- Duprat-Oualid S. & **Yamato P.**, “Syn-deformational inverted metamorphism: Insights from 2D thermo-kinematic numerical models”. Geophysical Research Abstracts, Vol. 14, EGU2012-983, 2012 EGU General Assembly 2012, Vienna, Austria
- Huet B., **Yamato P.** & Grasemann B., “Physically consistent viscosity of polyphase rocks: a new method and its validation”. Geophysical Research Abstracts, Vol. 14, EGU2012-8732, 2012 EGU General Assembly 2012, Vienna, Austria

2011
- Mouthereau F. & **Yamato P.**, “Rheology of large-scale Zagros folding”.Geophysical Research Abstracts, Vol. 13, EGU2011-13838, 2011 EGU General Assembly 2011, Vienna, Austria

2010
- Kaus B., **Yamato P.**, Mouthereau F. & Castelltort S., “Dynamics constraints on crustal-scale rheology from the Zagros Mountains” *A.G.U.*, San Francisco, U.S.A
- **Yamato P.**, Tartèse R., Hallot E., Boulvais P., Poujol M. & Gallagher K., “Crystal-melt differential behaviours during magma ascent in dykes: insights from 2-d numerical modelling” *GeoMod2010*, Lisbon, Portugal
- **Yamato P.**, Kaus B., Mouthereau F. & Castelltort S., “Importance of multi-layering and rheology for crustal folding processes” *E.G.U.*, Vienna, Austria
- **Yamato P.**, Castelltort S. & Willett S., “Influence of surface slope and roughness on the shape of river basins: a comparison between nature and numerical experiments”, *E.G.U.*, Vienna, Austria

2009
- **Yamato P.**, Husson, L., Braun J., Loiselet C. & Thieulot C., “Influence of surrounding plates on 3D subduction dynamics, *11th International Workshop on Modeling of Mantle Convection and Lithosphere Dynamics.*, Braunwald, Switzerland

2008
- **Yamato P.**, Agard P. & Burov E., “Les mécanismes d'exhumation des roches de HP-UHP au niveau des zones de convergence: Des données de terrain aux modèles numériques (le cas des Alpes Occidentales)”, *R.S.T.*, Nancy, France
- **Yamato P.**, Mouthereau F. & Burov E., “Exhumation and Shortening during the Taiwan mountain building: insight from 2D thermomechanical modeling”, *E.G.U.*, Vienna, Austria
- **Yamato P.**, Burov E. & Agard P., “Exhumation mechanisms in convergence zones: Insight from thermomechanical models (The case of the Western Alps)”, *E.G.U.*, Vienna, Austria

2007
- **Yamato P.**, Agard P., Goffé B., De Andrade V., Vidal O. & Jolivet L., “New, high- precision P-T estimates for Oman blueschists: Implications for obduction, nappe stacking and exhumation processes”, *E.G.U.*, Vienna, Austria
- **Yamato P.**, Burov E., Agard P., Le Pourhiet L. & Jolivet, L., “What controls the presence of HP-UHP continental rocks in convergent zones? Application to the Western Alps”, *Subduction conference*, Montpellier, France
- **Yamato P.**, Agard P., Goffé B., De Andrade V., Vidal O. & Jolivet, L., “New, high-precision P-T estimates for Oman blueschists : Implication for obduction, nappe stacking and exhumation processes”, *Subduction conference*, Montpellier, France
- Agard P., **Yamato P.**, Jolivet, L. & Burov E.,“Discontinuous exhumation of oceanic crust: Insights from bueschists and eclogites into the subduction channel”, *Subduction conference*, Montpellier, France

2006
- **Yamato P.**, Burov E., Agard P., Le Pourhiet L. & Jolivet L., “Dynamics of accretionnary subduction wedges: Insights from thermo-mechanical modelling”, *E.G.U.*, Vienna, Austria

2005
- Le Pourhiet L., **Yamato P.**, Burov E. & Gurnis M. “Developing tools to test the thermomechanical models, examples at crustal and upper mantle scale”, *A.G.U.*, San Francisco, USA

Séminaires invité

2014
- Geosciences Rennes (University of Rennes1)

2013
- UNIL (University of Lausanne)
- Department of Geodynamics and Sedimentology (University of Vienna)

2012 ▸ UNIL (University of Lausanne)
2011 ▸ ETH (Zurich)
2009 ▸ ETH (Zurich)
2008 ▸ U.B.O (Brest)
▸ ETH (Zurich)
▸ Geosciences Rennes (University of Rennes1)
▸ ENS (Paris)
2007 ▸ LGCA/LGIT (Grenoble)
2006 ▸ VU University (Amsterdam)

3. ENCADREMENT

Le travail d'encadrement s'articule, selon moi, autour de deux axes majeurs : Il s'agit tout d'abord d'un travail de formation à la recherche mais aussi d'un travail d'encadrement en termes d'enseignement. En effet, de mon point de vue, même si le travail d'encadrement demeure en premier lieu un travail de formation à la recherche, il ne peut se résumer uniquement à la seule capacité à encadrer des travaux de recherche (Master et Thèse). L'encadrement des étudiants lors de leur formation en géologie, afin de les amener vers le monde de la recherche me paraît également être un aspect primordial.

3.1. ENCADREMENT EN LIEN AVEC LA FORMATION À LA RECHERCHE

Stages de Licence :

- 2011-2012, *Typhaine Rioual* (L2) *Étude des zones de cisaillement (Baie des trépassés, Finistère)*
- 2012-2013, *Remi Sarrazin* (L3) *Analyse structurale des veines et filons au sein du granite de Guérande*
- 2012-2013, *Marion Guinault* (L3) *Origine des micaschistes localises entre les deux branches du CSA*

Stages de M1 :

- 2009-2010, *Stephen Centrella*, *Structure et évolution métamorphique de l'île de Groix*
- 2011-2012, *Bryan Cochelin*, *Réactions métamorphiques et déformation en zone de cisaillement : Analyses structurales et pétrologiques de la Baie des Trépassés (Finistère, France)*
- 2012-2013, *Paul Lagautrière*, *Analyse structurale et cartographique de la pointe du Conquet aux gneiss de Brest (Léon, Finistère)*
- 2013-2014, *Solenn Hertgen*, *De la migmatisation à la mise en place des granites : le cas du massif migmatitique de Saint-Malo*

Stages de M2 :

- 2014-2015, *Solenn Hertgen*. *Genèse des éclogites rubannées : Une information clé pour la compréhension de la déformaion des roches au sein des zones de subduction?* [Co-encadrement : S. Angiboust, GFZ Potsdam]

- 2012-2013, *Bryan Cochelin*. *Zones de cisaillement et réactions métamorphiques : Approche thermodynamique et étude de terrain.* [Co-encadrement : P. Pitra, Rennes1]

Actuellement : En thèse à Toulouse

- 2010-2011, *Sylvia Duprat-Oualid*. *Modélisation numérique du métamorphisme inverse.*

Actuellement : En thèse à Géosciences Rennes

- 2010-2011, *Stephen Centrella*. *Structure et évolution métamorphique de l'île de Groix (Massif Armoricain, France)*. [Co-encadrement : M. Ballèvre et P. Pitra, Rennes1]

Actuellement : En thèse à l'Université de Münster, Allemagne.

Travaux de doctorat :

- *Sylvia Duprat-Oualid* (Sept. 2011-). Géosciences Rennes. Évolution thermique et mécanique des zones de cisaillement – approche analytique et numérique, et confrontation aux données de terrain [Co-encadrement avec P. Pitra].

- Au cours de ces dernières années, j'ai également été impliqué directement dans les travaux de

thèse de *Christelle Loiselet* (thèse soutenue en 2009 intitulée « Devenir d'une lithosphère en subduction dans le manteau terrestre » et encadrée officiellement par Jean Braun et Laurent Husson) ou encore *Samuel Angiboust* (thèse soutenue en 2011 intitulée « Couplages profonds et comportement de la lithosphère océanique dans les zones de subduction : approches pétrologiques et thermomécaniques » et encadrée officiellement par Philippe Agard et Evgueni Burov). J'ai également participé à des collaborations ponctuelles sur des projets spécifiques de modélisation ou de terrain avec des étudiants alors en thèse à Rennes (*Romain Tartèse*, *Christophe Ballouard*), à Zurich (*Thibault Duretz*) ou à Paris (*Julien Fauconnier*), comme en témoignent certaines publications auxquelles j'ai participé (Yamato et al., 2009a, Loiselet et al., 2010, Tartèse et al., 2011, Yamato et al., 2012, Fauconnier et al., 2014, Ballouard et al., soumis).

3.2. ENCADREMENT POUR CE QUI EST DE L'ENSEIGNEMENT

Contrairement à l'encadrement « classique » décrit précédemment, je me permets ici de distinguer, en deuxième lieu, l'encadrement en lien avec l'enseignement. En effet, dans le cas précédent il s'agit d'un encadrement bien souvent sollicité par les étudiants eux même et qui sont, par conséquent, déjà motivés et curieux de toucher de près au monde de la recherche. De mon point de vue, l'exercice est différent quand il s'agit d'amener les étudiants à susciter cet intérêt.

C'est en particulier l'une des raisons pour laquelle, en plus de ma curiosité de connaître le fonctionnement des rouages de l'organisation des enseignements, j'ai accepté de prendre la responsabilité de la licence de Sciences de la Terre en 2012. Je me suis alors rendu compte, au travers des discussions avec les étudiants concernant leurs orientations, leurs questions sur les choix de masters ou encore leurs questionnements sur le monde académique et professionnel, que cette responsabilité constitue un travail « d'encadrement » important qu'il ne faut pas prendre à la légère.

Ces discussions se trouvent, de plus, bien souvent dynamisées en contexte *hors salle*, et en particulier lors des stages de terrain. Il s'agit là d'un élément marquant lorsque l'on prend en charge l'organisation de ces derniers (L3, M1, Capes-Agreg), chose que j'avais déjà appréhendée en tant qu'encadrant « accompagnateur » mais qui se trouve renforcée lorsque l'on se retrouve en charge de l'organisation complète d'un stage de terrain.

4. ACTIVITÉS D'ENSEIGNEMENT

EN TANT QUE MAITRE DE CONFÉRENCES : (192h/an) – Université de Rennes 1, depuis 2009.

- ***Modélisation en Sciences de la Terre*** · Cours et TD (M2, ~40 h) : Pourquoi est-ce important? Equation de la chaleur, Equations de Stokes, Ecriture de codes sous MATLAB.
- ***Systèmes Tectoniques*** · Cours et TD (M1, 24 h) : Rhéologie de la lithosphère et Tectonique.
- ***Cartographie*** (L3, ~40 h) : Carte géologiques au 1/50.000 + travaux de synthèse à partir de cartes diverses (million, gravimétrie, métamorphisme, etc.)
- ***Géophysique*** (L2, ~12.5 h) : Diffusion et convection en Sciences de la Terre
- ***Stages de terrain*** : Alpes, Corse, Pyrénées, Bétiques, Massif Armoricain, Montagne Noire.

Tableau de Services

Année	Niveau Licence	Niveau Master	Total Eq. TD
2009-2010	61.5	126.0	187.5
2010-2011	48.0	169.5	217.5
2011-2012	54.5	166.5	221.0
2012-2013	62.5	127.5	190.0
2013-2014	101.5	127.5	229.0

Responsabilités

- Responsable du module ***Modélisation en Sciences de la Terre*** (M2) : Depuis 2009
- Co-Responsable du ***stage de terrain*** (Prepa. Capes/Agreg) : Depuis 2009
- Responsable du module de ***Cartographie Avancée 1*** (L3) : Depuis 2010
- Responsable du module de ***Cartographie Avancée 2*** (L3) : Depuis 2010
- Responsable de la ***Licence 3 ST*** : Depuis 2012
- Responsable du ***stage de terrain*** (L3) : Depuis 2013
- Responsable du module de ***Systèmes Tectoniques*** (M1) : Depuis 2014

EN TANT QUE MONITEUR PUIS ATER :

- Géologie générale (1ère année, ~ 207h, 2ème année, ~ 24h). TD de cartographie, paléontologie, pétrologie, sédimentologie et séismologie.
- Modélisation numérique (Master, ~ 10h). TD sur le flux de chaleur, rhéologie de la lithosphère.
- Métamorphisme et Tectonique (Master, ~ 70 h). Métamorphisme et déformation · Thermo barométrie · Radiochronologie · Chaîne alpine.
- Camp de terrain : Normandie (L2), Alpes (L3, M2).

5. ACTIVITÉS SCIENTIFIQUES

5.1. INTRODUCTION : Cheminement intellectuel et scientifique

Ce mémoire permet de faire le point sur le travail de recherche que j'ai effectué depuis ma thèse de 3ème cycle qui portait sur les processus d'exhumation des roches métamorphiques (2006). Au premier abord, les questions semblent simples : Que fais-je? Où vais-je? L'exercice de synthèse, cependant, peut s'avérer plus compliqué. En effet, si je dresse brutalement la liste des questions principales qui guident mes activités de recherche, elles peuvent se résumer ainsi:

- Quels sont les processus impliqués durant l'exhumation des roches, et en particulier, que se passe-t-il au niveau de l'interface de subduction en profondeur ?

- Comment fonctionnent les zones de cisaillement ? Quel est l'impact de la thermique et notamment du *shear heating*, des réactions métamorphiques, ou encore des fluides sur ces systèmes tectoniques ?

- Peut-on appréhender la rhéologie effective des roches en particulier lorsqu'elles ne sont plus considérées comme homogènes mais constituées de plusieurs minéraux?

- Comment se comportent les cristaux dans les dykes magmatiques ? Qu'est-ce qui contrôle leur ségrégation ?

- Quel est l'impact des rétroactions lithosphère/convection mantellique sur la tectonique grande échelle ?

- Les processus de surface jouent-ils un rôle important dans tout cela ?

Cette diversité s'explique par le fait que ces questions sont bien souvent le fruit de rencontres, de discussions, et de projets initiés avec des personnes issus de domaines différents (modélisateurs, tectoniciens, pétrologues, géochimistes). En rédigeant cette habilitation, je me rends compte que ces sujets, si différents soient-ils, m'intéressent tout particulièrement car, mis à part le fait qu'ils présentent tous intrinsèquement des aspects non résolus, ils se rejoignent en un point, fil conducteur de mon travail. En effet, à bien y réfléchir, un dénominateur commun évident se détache néanmoins de ces questions : **La compréhension de la déformation des roches à différentes échelles au cours du temps**. Au final, à chaque fois, la philosophie du travail de recherche est la même : **Quantifier les processus** avec un outil : **La modélisation**, pour lequel il faut apporter des contraintes, et donc nécessairement se tourner vers les observables.

Rétrospectivement, les cibles de terrain choisies ne sont pas si différentes non plus. Les objets sur lesquels se sont focalisés mes travaux correspondent peu ou prou aux zones en convergence : zones de cisaillement à différentes échelles (e.g., granodiorite du Zillertal (Autriche), Main Central Thrust (Himalaya), Cisaillement Sud Armoricain (France)), zones de subduction, marges passives (et oui !), ou encore chaînes plissées.

Par ailleurs, d'un point de vue méthode, l'évolution de mes travaux de recherche fut aussi marquée par le passage dans les années 2010-2011 de la fonction d'utilisateur averti de codes existants (PARA(O)VOZ, DOUAR, MILAMIN_VEP) à celui de modélisateur *sensus stricto*. Je me suis, en effet, mis à l'écriture de mon propre code thermomécanique afin d'en connaître tous les tenants et les aboutissants. Je me suis alors mis à avoir un regard différent sur ce qu'est, pour moi, le travail de modélisation : un moyen d'illustrer et de tester des idées mais aussi de comprendre la physique des processus au premier ordre en simplifiant au maximum le nombre de paramètres pris en compte dans un modèle et non plus de chercher à "coller" exactement aux données en jouant avec un nombre conséquent de paramètres, dont il est difficile, au final, d'en extraire le plus important.

C'est cette évolution en termes de thématiques mais également de méthodologie que je vais à présent tâcher d'illustrer.

5.2. DYNAMIQUE DES ZONES DE CONVERGENCE

5.2.1. L'exhumation des roches métamorphiques de HP-BT

Dans la continuité de mes travaux de thèse sur l'exhumation des roches métamorphiques de haute pression – basse température (HP-BT), plusieurs points se sont avérés important à traiter. Mes travaux de thèse, appliqués à l'exemple des Alpes et contraints par les données Pression-Température-temps (P-T-t) montraient comment il était possible d'expliquer l'enfouissement et l'exhumation lors de la structuration d'une chaîne de montagne et que les processus d'exhumation impliqués étaient différents (Fig.1) selon le matériel considéré (sédimentaire, océanique ou continental).

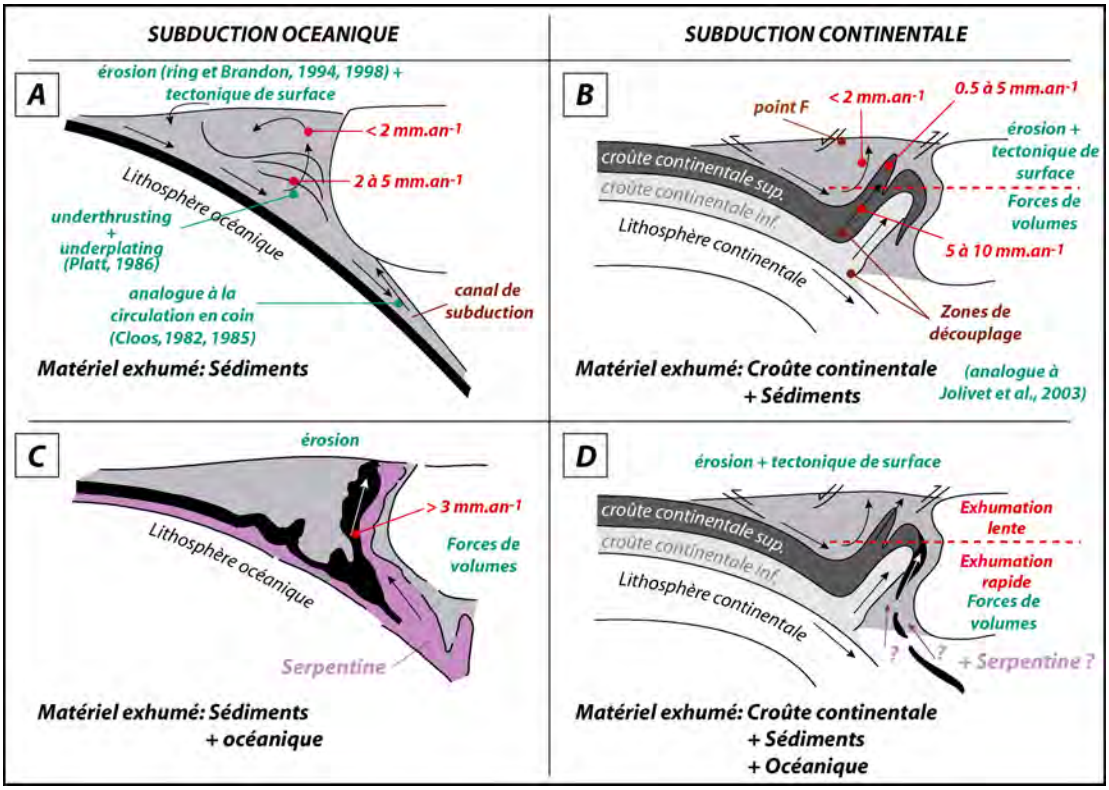

Figure 1 *: Mécanismes d'exhumations invoqués en fonction du type de subduction et du type de matériel mis en jeu. Les vitesses caractéristiques d'exhumation sont rappelées en rouge (Yamato, 2006).*

A partir de ce travail, nous avons continué avec Philippe Agard, Evgueni Burov et co-auteurs à travailler sur cette thématique en montrant que mes résultats pouvaient être généralisés. Ainsi, pour ce qui est du cas des unités d'affinités continentales, nous avons montré (Burov et al., 2014a,b) que l'exhumation de roches de (ultra) haute pression ((U)HP) ne peut pas se produire dans le cas de subductions impliquant des lithosphères froides et résistantes (T_{moho}<550 °C) et pour des vitesses de convergence rapides (> 3-5 cm.an^{-1}). L'exhumation d'unités continentales est un processus transitoire qui ne peut se produire qu'en cas de convergence lente. Dans ces conditions, les unités de (U)HP peuvent se découpler et leur exhumation, qui se fait par flottabilité, peut alors être rapide (Fig. 1). Nous avons également montré que les changements rhéologiques et les échanges de fluides à l'interface entre le panneau plongeant et la plaque supérieure, comme la serpentinisation, jouent un rôle majeur en produisant un affaiblissement de l'interface et l'hydratation du coin de manteau.

Dans le cas où le matériel impliqué est d'affinité océanique, nous avons montré, en compilant les données de toutes les zones des schistes bleus et éclogites océaniques (Agard et al., 2009), que les processus d'enfouissement/exhumation étaient différents (Fig. 2). Cette exhumation est plus lente (de l'ordre du mm.an^{-1}) contrairement aux cas des unités continentales (> cm.an^{-1}). Là encore, nous avons démontré l'importance des serpentinites et/ou d'une matrice faible qui se trouvent systématiquement

associées aux unités océaniques exhumées dans les zones internes des orogènes. Les roches océaniques exhumées enregistrent rarement des conditions de pression supérieures à 2-2.3 GPa, ce qui suggère l'existence d'une profondeur maximum pour l'échantillonnage de telles unités. Sous 70 km, il n'y a plus assez de serpentinites pour initier un découplage et la croûte océanique n'est plus assez légère pour être exhumée. Plus important, notre étude a montré le caractère rapide et discontinu (<15 Ma) de l'exhumation des roches océaniques. Dans ce contexte, l'exhumation se fait soit précocement, soit tardivement ou soit de manière accidentelle durant la subduction (Fig. 2). Ainsi, l'exhumation discontinue est permise soit par le régime thermique spécifique qui suit le début d'une subduction chaude (e.g., Franciscain, Chili), soit par le passage en subduction d'un continent (e.g., Alpes, nouvelle Calédonie) ou soit par une modification géodynamique (e.g., Zagros, Himalaya, Andes, Cuba).

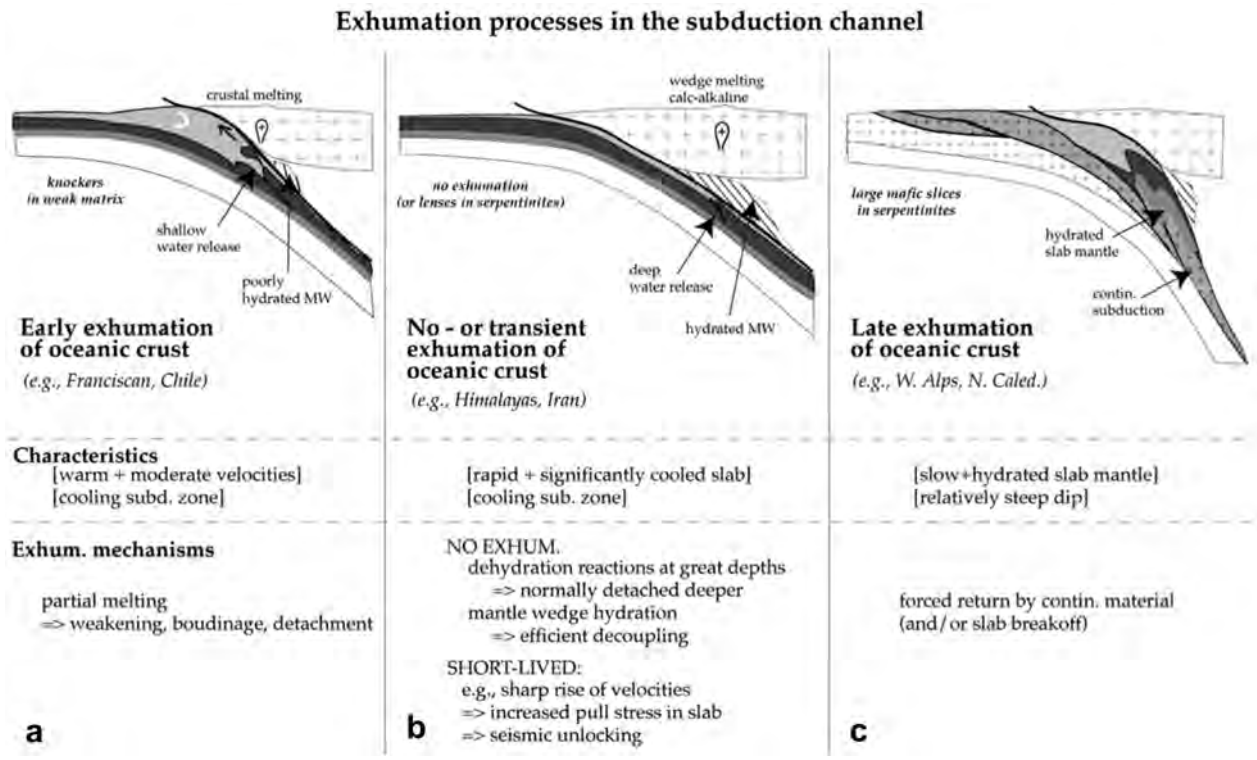

Figure 2 *: Exemples illustrant les différent processus contrôlant l'exhumation de matériel océanique au sein des zones de subduction (Agard et al., 2009).* ***(a)*** *Exhumation précoce,* ***(b)*** *Exhumation transitoire accidentelle,* ***(c)*** *Exhumation tardive.*

Partant de ce dernier constat, et arrivant à Rennes au moment où Brun et Faccenna (2008) publient un article montrant que le recul du panneau plongeant (slab *rollback*) permet de créer un espace suffisant pour exhumer les roches de HP-UHP, nous avons, avec Laurent Husson et co-auteurs, regardé plus attentivement cet effet du recul du slab et du flux mantellique associé sur l'exhumation des roches de (U)HP. Nous avons ainsi montré (Husson et al., 2009) que le cycle d'enfouissement/exhumation de matériel crustal dans les zones de subduction est contrôlé soit par sa flottabilité, soit par le flux environnant, soit par les deux. Si, comme dit précédemment, les roches de HP-UHP sont principalement exhumées où les zones de subduction montrent un caractère transitoire lié à une modification géodynamique (cf. Yamato et al., 2007, 2008, Agard et al., 2009, Guillot et al., 2009), cela conduit à un flux différent au niveau du coin de manteau. Nos résultats (Fig. 3a) montrent que l'enfouissement est favorisé dans le cas des fosses stationnaires (mode I). En revanche, lors du recul du slab (mode II), le flux ascendant induit contribue à l'exhumation. Ce régime est amplifié quand le pendage du panneau plongeant diminue (mode III). Le résultat principal est alors que les régimes épisodiques qui impliquent des unités lithosphériques différentes activent successivement ces modes (Fig. 3b) et favorisent grandement l'exhumation depuis les profondeurs mantelliques jusqu'à la surface sans avoir besoin d'invoquer d'autres paramètres comme l'érosion.

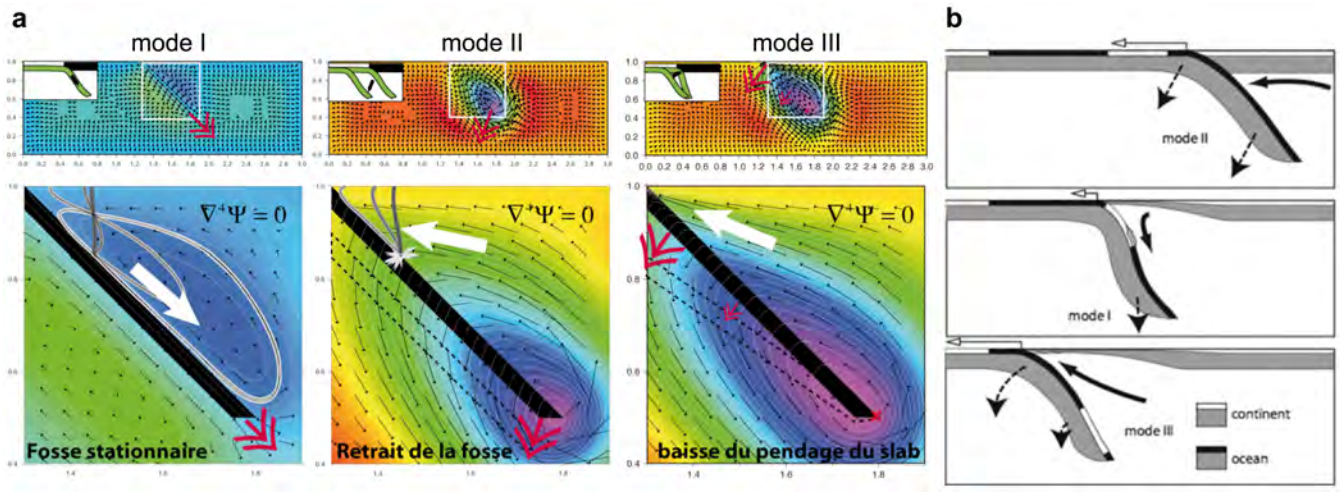

Figure 3 *: Influence du recul du slab sur les mécanismes d'enfouissement/exhumation des roches (Husson et al., 2009).* ***(a)*** *Champ de vitesse et lignes de courant dans le coin de manteau pour une fosse stationnaire (mode I), un slab en recul pur (mode II) et un slab en recul dont le pendage diminue (mode III).* ***(b)*** *Illustration de subduction épisodique montrant l'activation successive de ces différents modes en fonction de la migration de la fosse (flèches blanches), du mouvement du slab (flèches noires pointillées) et du flux mantellique associé (flèches noires).*

Avec ces études, nous avons progressé dans la compréhension des mécanismes permettant l'exhumation des unités enfouies à haute pression. Un point crucial, correspondant à la manière dont se détachent ces unités en profondeur, reste cependant à examiner attentivement. L'étude sur les mécanismes pouvant être à l'origine du découplage au niveau de l'interface de subduction émerge avec la thèse de Samuel Angiboust avec qui j'ai collaboré. Il s'agit d'un thème que j'évoquerai plus tard (paragraphe 5.2.2.) car il dépasse le simple cadre de l'exhumation des roches métamorphiques au sens strict.

5.2.2. La dynamique des zones de subduction

A mon arrivée à Rennes, j'ai pris du recul sur le *système subduction* que je ne voyais alors que du point de vue alpin et où je me limitais à regarder les unités de la plaque plongeante à l'échelle lithosphérique. La discussion précédente sur le rôle du slab *rollback* dans l'exhumation des roches de HP-UHP, et l'importance de regarder les systèmes à plus grande échelle, n'en était que les prémisses. En *dézoomant*, il apparaît évident que lorsque l'on étudie le système subduction il faut tenir compte de ce qui se passe autour. De nouveaux problèmes se posent alors si le manteau dans lequel évolue le panneau plongeant y est intégré ainsi que les plaques lithosphériques environnantes (plaque supérieure et latérale). Cela nécessite, dans un second temps, de s'intéresser aussi de plus près aux limites entre les plaques et notamment à l'interface entre la plaque plongeante et la plaque chevauchante.

Rôle des plaques adjacentes

En collaboration avec Laurent Husson, Jean Braun et Christelle Loiselet qui débutait alors sa thèse au laboratoire, nous avons exploré l'effet que pouvait engendrer la présence de plaques lithosphériques autour d'une zone de subduction. Il était d'autant plus facile de s'attaquer à ce problème puisque je bénéficiais alors d'un code tridimensionnel (DOUAR) développé par Jean Braun (Braun et al., 2008).

Les modèles 3D que nous avons réalisés (Yamato et al., 2009a) ont alors montré que la présence de plaques lithosphériques autour de la plaque en subduction influence significativement la dynamique de la subduction, en particulier le taux de retrait de la fosse, le pendage du slab, et le raccourcissement latéral du plan en subduction (Fig. 4). Les plaques lithosphériques voisines permettent alors de prévenir ce comportement non réaliste sans avoir besoin de faire intervenir des rhéologies

complexes (e.g., Moresi & Solomatov, 1998 ; Stegman et al., 2006). Pour autant, ce travail ne s'intéressait pas au problème de ce qui se passe au niveau des interfaces.

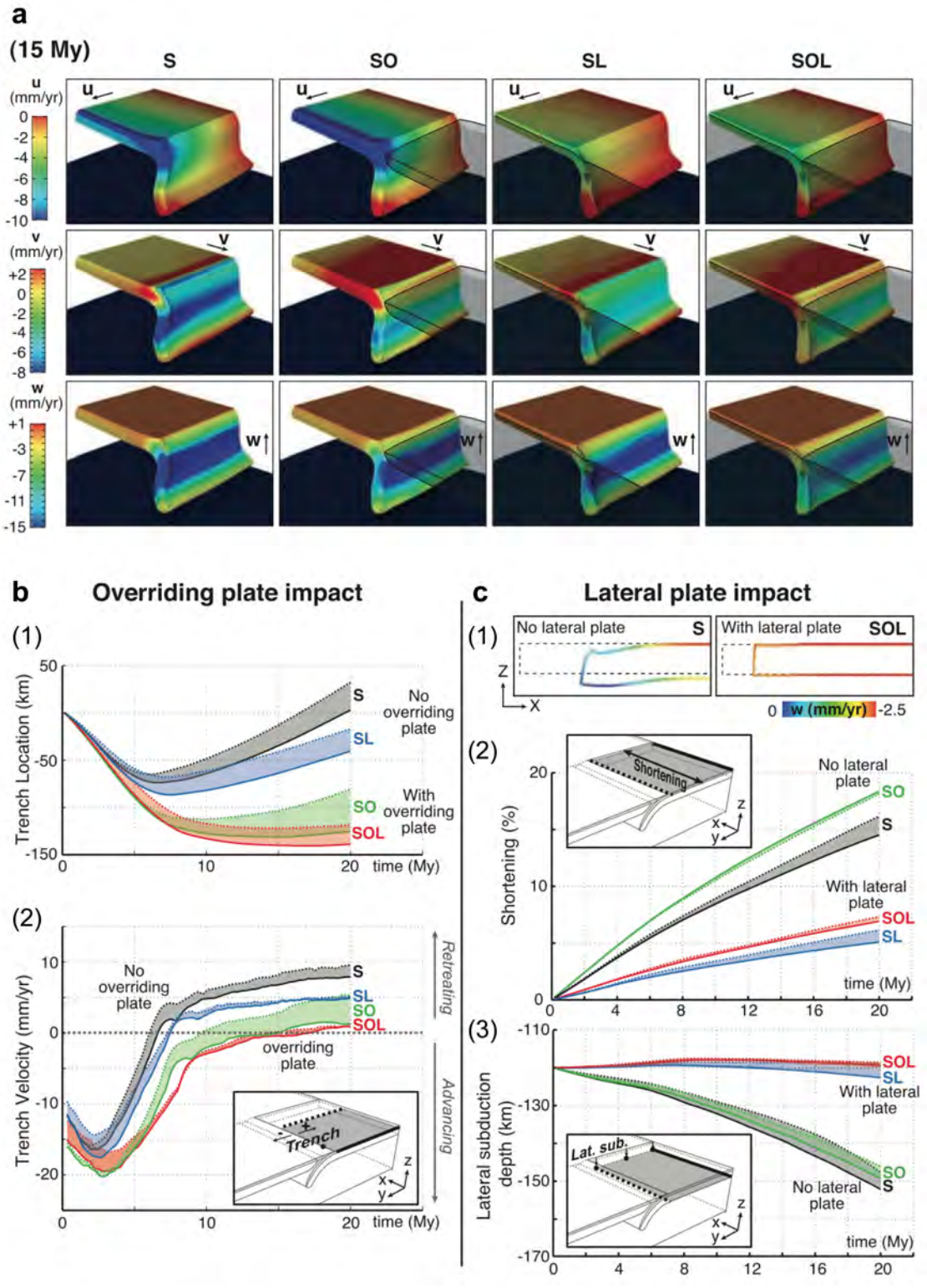

Figure 4 *: Influence des plaques lithosphériques environnantes sur le dynamique de subduction (Yamato et al. 2009).* ***(a)*** *Composantes du champ de vitesse pour la plaque en subduction après 15 Ma d'expérience. Les formes des lithosphères latérales et supérieures sont présentées en transparence.* ***(b)*** *La présence d'une plaque supérieure (1) limite le recul de la fosse et (2) diminue la vitesse de retrait.* ***(c)*** *La présence d'une plaque latérale limite le raccourcissement (1-2) ainsi que la subduction latérale (3) de la lithosphère en subduction sans avoir à introduire de rhéologies complexes permettant de contrecarrer ces effets.*

Déformation des plaques en subduction

Dans le même temps, nous avons exploré, dans le cadre de la thèse de Christelle Loiselet, le devenir des panneaux plongeants une fois que ceux-ci pénètrent au sein du manteau. Ce travail (Loiselet et al., 2010) est parti du constat que les données géophysiques et de tomographie sismique notamment montrent que les lithosphères ne conservent pas une épaisseur uniforme, une fois la subduction initiée (e.g., Bijwaard et al., 1998; Fukao et al., 2001 ; Li et al., 2008). Au contraire, elles se présentent généralement plutôt affinées dans le manteau supérieur et épaissies dans la zone de transition entre le manteau supérieur et inférieur (Fig. 5a). Cette observation était traditionnellement interprétée comme l'évidence d'un plissement et d'un empilement des slabs résultant du grand contraste de viscosité qui existe entre le manteau supérieur et inférieur qui cause alors une résistance à la pénétration du slab en profondeur dans le manteau inférieur (e.g., Griffiths & Turner, 1988 ; Ribe et al., 2007). Or, paradoxalement, la distribution et le type des séismes révèlent que les slabs subissent une extension verticale dans le manteau supérieur et de la compression proche de la zone de transition (e.g., Apperson & Frohlich, 1987; Isacks & Molnar, 1969; Vassiliou et al., 1984).

Dans cette étude, nous démontrons que ces observables peuvent s'expliquer par le fait que durant la subduction, la forme des slabs faiblement visqueux (1 à 100 fois plus visqueux que le manteau environnant) évolue vers une forme de panache inversée (méduse) dont la morphologie change afin de minimiser l'énergie (Fig. 5).

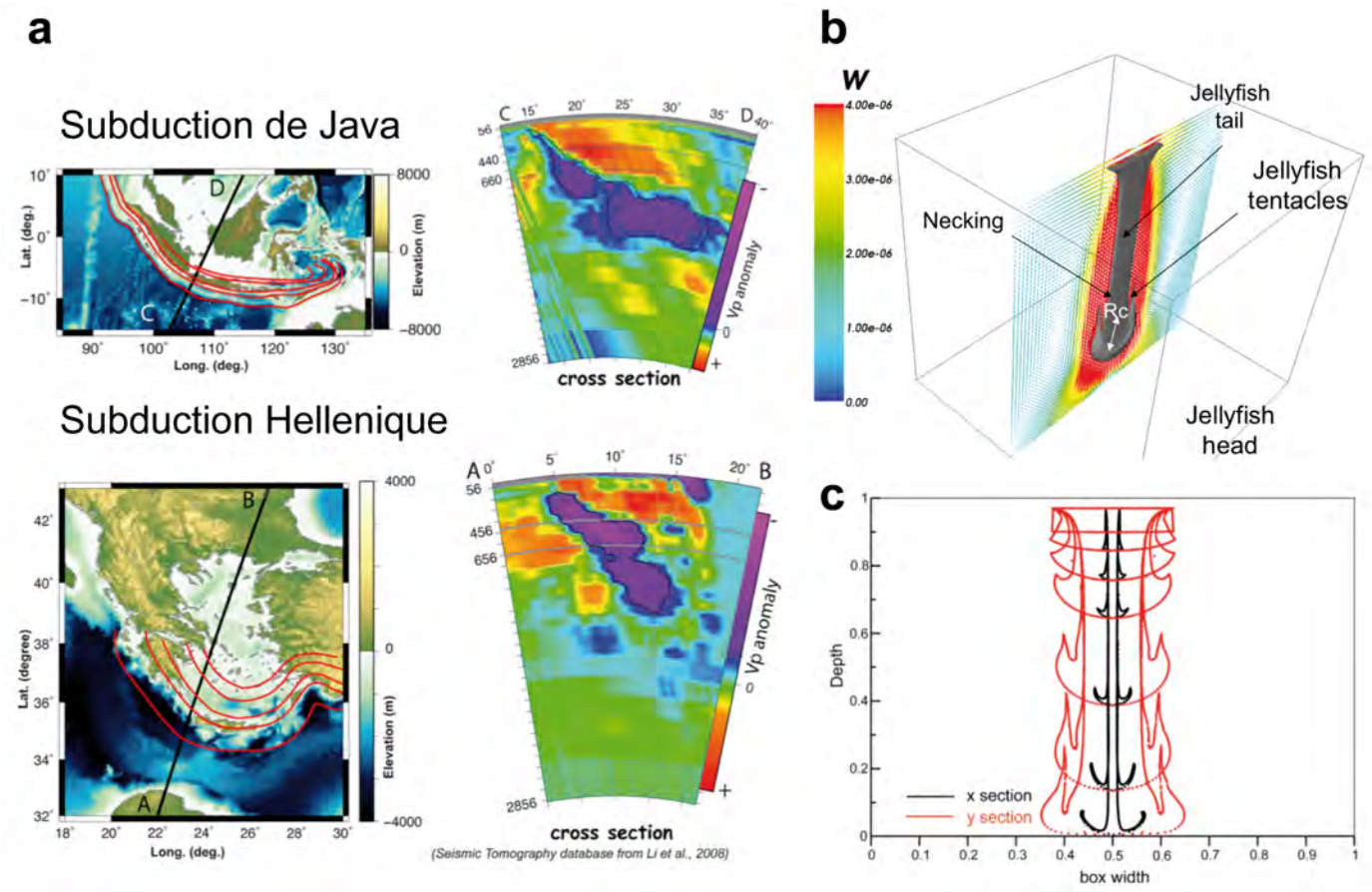

Figure 5 *: Evolution en panaches inversés des slabs dans le manteau (d'après Loiselet et al., 2009).* ***(a)*** *Données de tomographie sismique (modèles globaux en onde P) pour le cas de Java et Hellénique (d'après Li et al., 2008).* ***(b)*** *Exemple de modélisation 3D montrant l'évolution « en méduse » d'un panneau plongeant dans le manteau.* ***(c)*** *Evolution en coupe de la morphologie du slab au cours de sa pénétration dans le manteau.*

L'interface de subduction

Comprendre les processus qui agissent le long de l'interface est crucial pour estimer le couplage long terme (par exemple la façon dont se découplent les unités du panneau plongeant avant exhumation) et court terme (par exemple les mécanismes pouvant causer des séismes à des profondeurs intermédiaires) à l'échelle lithosphérique entre les plaques tectoniques. En effet, malgré de nombreuses études géophysiques visant à mieux caractériser l'interface de subduction (e.g., Oncken et al., 2003; Zhao et al., 2002 ; Abers et al., 2006), nous manquons encore de données contraignant les processus responsables de la sismicité au niveau des zones de subduction océaniques.

Les zones de cisaillement éclogitiques constituent alors une source d'information clé nous permettant de s'attaquer à ces problèmes car ces roches, désormais exhumées, sont les seuls vestiges accessibles ayant enregistrés les conditions P-T-t-déformation régnant à ces profondeurs.

Avec Samuel Angiboust, alors en thèse à Paris sur ce sujet sous la direction de Philippe Agard, nous avons spécifiquement focalisé notre attention sur ces points (Angiboust et al., 2011, 2012a), en prenant comme exemple le cas précis de l'unité du Lago Superiore de l'ophiolite du Monviso (Fig. 6). Cette unité correspond à un fragment quasi continu et intact de lithosphère océanique enfoui pendant la subduction alpine à ~ 80 km de profondeur. Cette ophiolite constitue donc un objet unique pour étudier les processus de couplage mécanique et les interactions fluides-roches à l'échelle du mètre se produisant aujourd'hui dans les zones de subduction à ces profondeurs.

Cette unité est constituée de 3 zones de cisaillement (Fig. 6a) où se localise la déformation : la première se situe au toit de l'unité (USZ), la seconde à la limite basaltes-gabbros (ISZ) et la troisième à la limite gabbros-serpentines (LSZ). Les résultats présentés par Samuel Angiboust et co-auteurs indiquent que, bien que la déformation ductile domine le long de ces zones de cisaillements, un comportement frictionnel cassant y est associé comme en témoigne l'existence de brèches d'éclogites de metagabbros ferro-titanés initialement situés le long de la ISZ (Fig. 6b et c). Ces brèches d'éclogites correspondent à des blocs de taille métrique composés de fragments d'éclogites mylonitiques cimentés, entre les clastes, par une matrice à omphacite-grenat-lawsonite et qui furent ensuite cisaillés et disséminés dans une zone de cisaillement serpentineuse de 30-150 m en faciès éclogitique.

A l'échelle des minéraux, les veines d'omphacites et la zonation des grenats indiquent l'existence d'évènements polyphasés de fracturation/cimentation (Fig. 6b). Nos observations suggèrent qu'une possible bréchification sismique se produit au milieu de la croûte océanique (Figure 6c et d), accompagnée par la circulation de fluides. Nous avons proposé que ces brèches marquent l'emplacement d'une ancienne faille associée à des séismes intra-slab de profondeur intermédiaire (~80 km).

A cet endroit, une circulation de fluide pervasive est, de plus, marquée par la présence d'une modification de la composition chimique, un affaiblissement des roches et de nombreuses cristallisations de paragenèses hydratées. En revanche le contact basaltes-gabbros (USZ) montre une évidence moindre de circulation de fluide. L'activité de ces zones de cisaillement cesse durant l'exhumation en facies éclogitique (marqué par la présence ubiquiste de lawsonite) quand la déformation se localise plus bas dans la sole serpentineuse, permettant le détachement de ce fragment éclogitique.

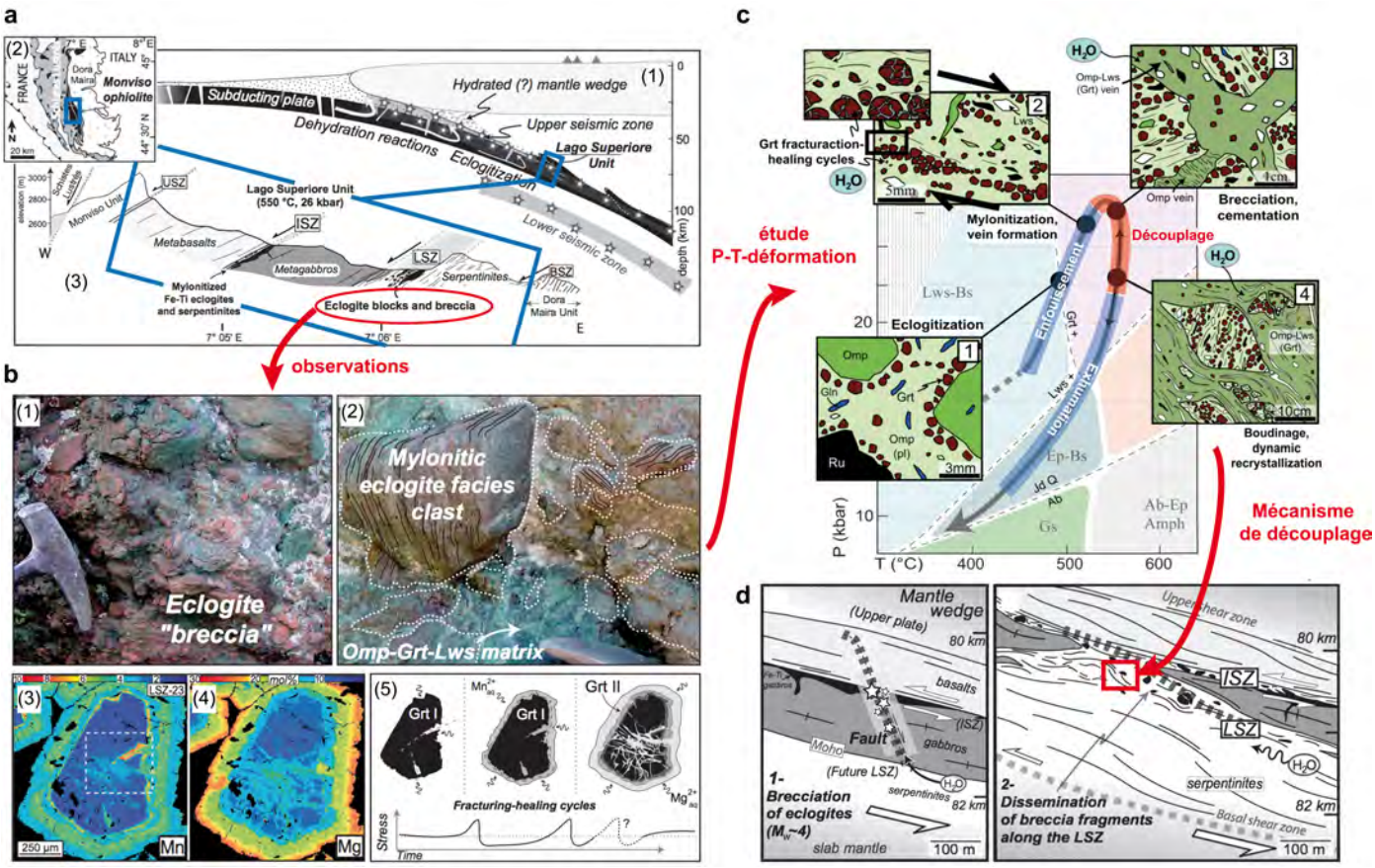

Figure 6 *: Mécanismes impliqués dans de découplage d'une écaille océanique de haute-pression – Exemple de l'unité du Lago Superiore (Monviso, d'après Angiboust et al., 2011, 2012a).* ***(a)*** *L'unité du Lago Superiore: proxy pour l'étude des processus impliqués à l'interface de subduction. 1 - Vue schématique (d'après Hacker et al., 2003) montrant la double zone sismique à l'intérieur du panneau plongeant et présentant la localisation de l'écaillage de l'unité du lac supérieur. 2 - Localisation de l'unité de l'ophiolite du Monviso dans la chaîne alpine occidentale. 3 - Coupe au travers de l'unité du Lago Superiore montrant les principale zones de cisaillement (USZ, upper shear zone ; ISZ, intermediate shear zone ; LSZ lower shear zone et BSZ, basal shear zone).* ***(b)*** *Fracturation multi-échelle enregistrée par les brèches d'éclogites. 1- Brèche d'éclogite issus de la LSZ. 2-clastes de mylonites cimentés par une matrice éclogitique (Lawsonite-Omphacite-Grenat), 3 et 4 : composition en Mn et Mg des grenats issus de la LSZ montrant un réseau de fractures cicatrisé par une nouvelle génération de grenat. 5 - Schéma interprétatif pour expliquer la présence de deux générations de grenat et la succession des évènements de fracturation, potentiellement liés à de la micro sismicité.* ***(c)*** *Chronologie des évènements associée aux conditions P-T : 1 - texture ignée progressivement effacée lors de l'enfouissement par la mylonitisation conduisant (2) à une forte réduction de la taille de grain, à la fracturation des grenats et à la ségrégation grenat-omphacite. (3) Fracturation conduisant à la bréchification en facies éclogitique cimentée par une paragenèse à omphacite-grenat-lawsonite. (4) Fragments de brèche que l'on retrouve ensuite disséminés sous forme de boudins dans la foliation tardive se faisant dans le facies des éclogites à lawsonite. (d) Scénario tectonique pour la formation et la dissémination des brèches éclogitiques le long de la zone de cisaillement permettant le découplage de cette unité avant son exhumation vers la surface.*

Cet exemple illustre qu'une large quantité de fluides est libérée au niveau des zones de subduction durant l'enfouissement de la lithosphère océanique via les réactions métamorphiques de déshydratation. Ces observations pétrologiques qui ne sont pas les seules (e.g., John & Schenk, 2006; Healy et al., 2009), sont par ailleurs corroborées par les données géophysiques (e.g., Green and Houston, 1995; Hacker et al., 2003; Yamasaki and Seno, 2003). Ces fluides sont généralement considérés comme responsables de l'hydratation du coin de manteau, de l'affaiblissement mécanique de l'interface et de la sismicité à l'interface (e.g., Hacker et al., 2003; Faccenda et al., 2012).

Afin de combler le manque entre la dynamique grande échelle de la subduction et les données issues du terrain et de la pétrologie (qui documentent une circulation à petite échelle), nous avons réalisé des modèles numériques 2D, dans lesquels la migration des fluides est régie par la concentration

en fluide de la roche, les gradients de pression non-lithostatiques et la déformation (Angiboust et al., 2012b). Des modèles de subduction océanique ont alors été réalisés dans la lignée de mes modèles de thèse (Yamato et al., 2007). Les résultats (Fig. 7) montrent que la déformation est accommodée le long de l'interface de subduction par une zone de cisaillement de faible résistance caractérisée par un front de serpentinisation étroit (<10km) et de faible résistance (10-25% de serpentinite). La déshydratation associée à l'éclogitisation de la croûte océanique (60-75km de prof) ainsi que la déstabilisation de la serpentinite (à 110-130 km) contribuent à une chute significative de la résistance du manteau à ces profondeurs, et donc favorisent le détachement de larges unités de croûte océanique le long de l'interface.

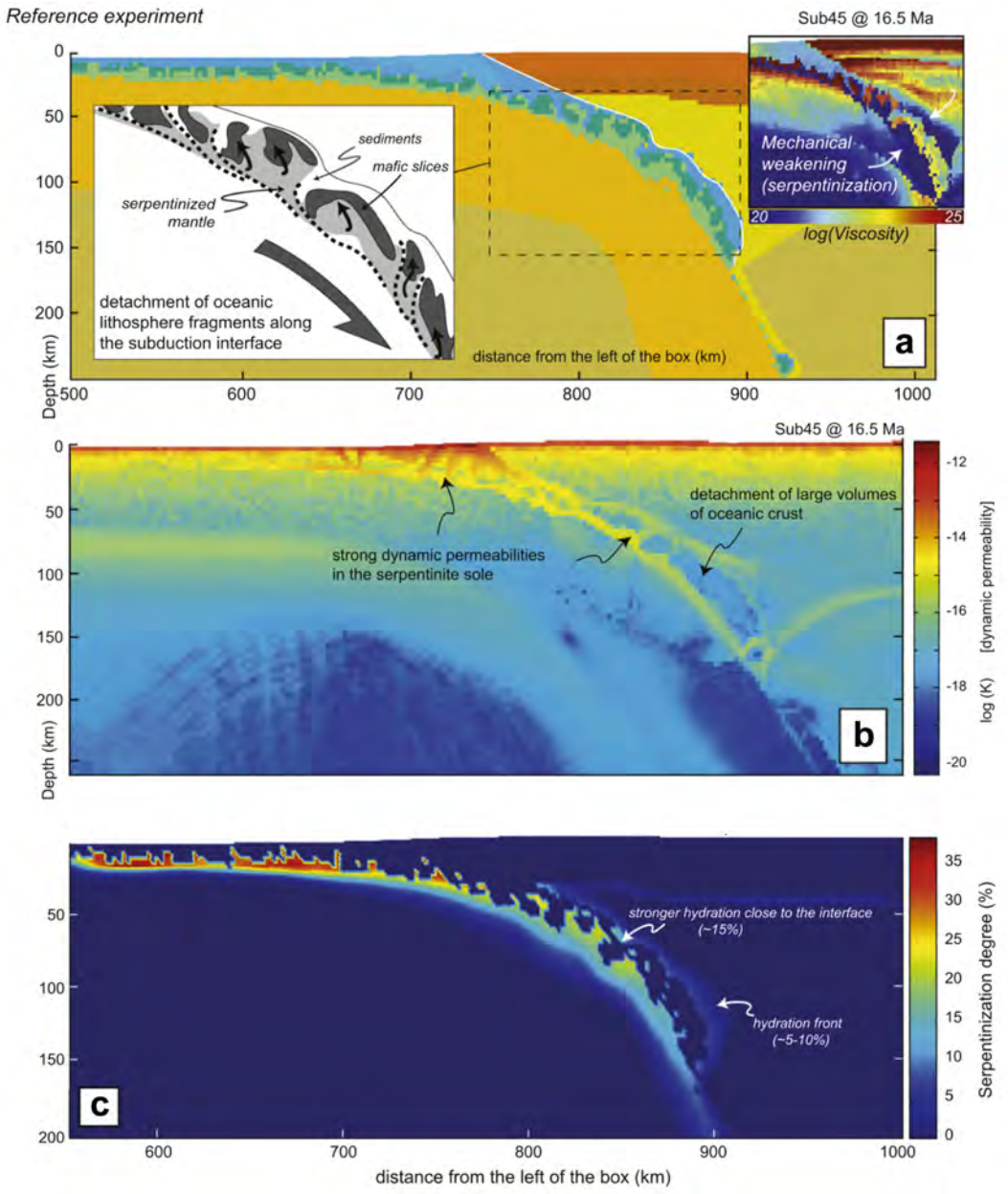

Figure 7 *: Rôle des fluides dans le détachement des écailles de croûte océanique (Angiboust et al., 2012b).* ***(a)*** *Morphologie et distribution effective de la viscosité au sein de la zone de subduction.* ***(b)*** *Structure de perméabilité dynamique montrant la présence de chenaux de forte perméabilité associés aux zones de localisation de la déformation qui entourent des domaines de plus faible perméabilité constituant les futures écailles découplées et exhumées.* ***(c)*** *Degré de serpentinisation associé illustrant la chute du degré de serpentinisation des péridotites avec l'enfouissement et la formation de front d'hydratation au niveau de l'interface de subduction à des profondeurs mantelliques.*

Les géométries obtenues sont en bon accord avec les reconstructions déduites des évidences de terrain pour les ophiolites alpines (e.g., Angiboust et al., 2009 ; Vitale-Brovarone et al., 2011). Par ailleurs, au travers d'une étude paramétrique, nous avons étudié le rôle de paramètres comme la circulation de fluides, la structure et la rhéologie de la croûte océanique sur la formation de ces écailles tectoniques. Nous en avons conclu que le détachement d'écailles de croûte océanique est largement permis par la circulation de fluides le long de l'interface et par la subduction d'une croûte mafique résistante et initialement discontinue (Fig. 7).

5.2.3. Les chaînes plissées

Les zones de convergence ne se résument pas à la compréhension des zones profondes. Durant mes années de post-doctorat, en m'intéressant de plus près au rôle des processus de surface et aux interactions qu'ils peuvent avoir avec la tectonique (volet que je ne détaillerai pas ici, cf. Braun et Yamato, 2010 ; Castelltort et Yamato, 2013), je me suis alors intéressé à des cibles n'ayant pas été enfouies en profondeur. En arrivant à Zürich, avec Boris Kaus et Sebastien Castelltort, nous avons considéré les interactions qu'il pouvait y avoir entre l'érosion et le plissement avec, pour exemple, le cas de la chaîne plissée du Zagros. Je me suis alors aperçu que, malgré de nombreuses études de terrain (e.g., Stocklin, 1968; Alavi, 2004; McQuarrie, 2004; Sherkati & Letouzey, 2004; Mouthereau et al., 2007) ou géophysiques (e.g., Jahani et al., 2009; Hatzfeld and Molnar, 2010; Nissen et al., 2010) sur cette chaîne, un problème fondamental persistait.

Les chaînes de plissement comme celle du Zagros sont généralement considérées comme le résultat de la déformation en compression d'une couche sédimentaire située au dessus d'un niveau de décollement (e.g., Colman-Sadd, 1978 ; Mouthereau et al., 2006). Le raccourcissement se traduit alors en surface par une succession d'anticlinaux et de synclinaux espacés de façon très régulière (Fig. 8).

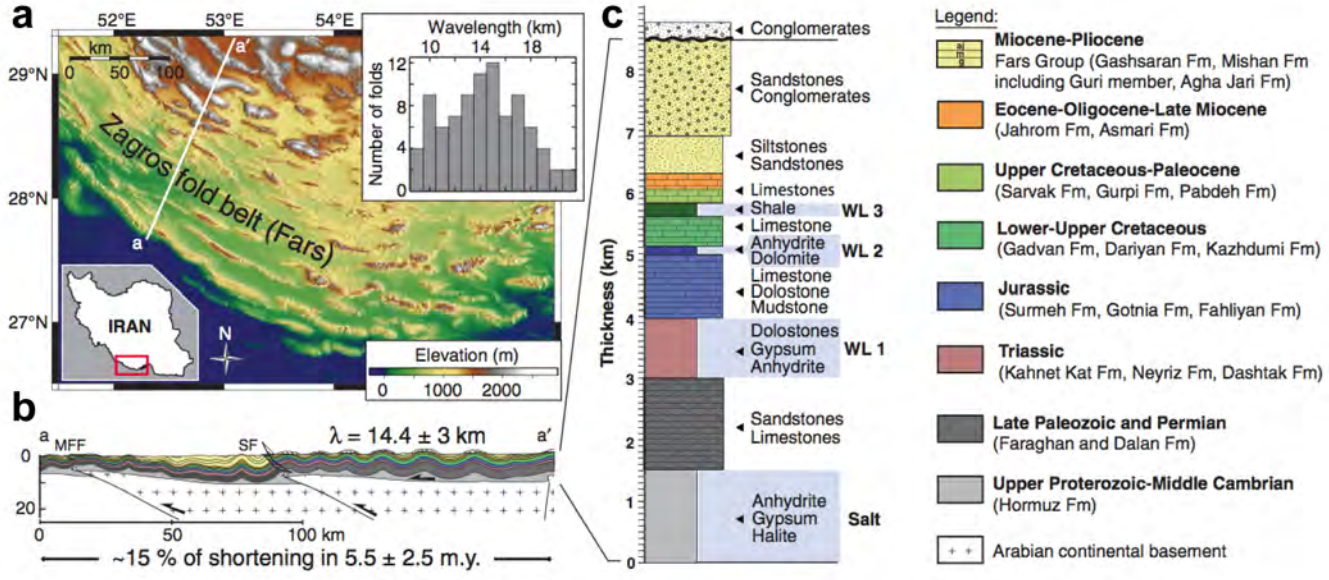

Figure 8 *: Contraintes de terrain pour la chaîne plissée du Zagros (Yamato et al., 2011).* ***(a)*** *Topographie illustrant l'espacement régulier des plis. L'encadré montre la distribution de la longueur d'onde des plis mesurés pour 88 anticlinaux de la chaîne du Zagros. (b) Coupe au travers de la chaîne (d'après Mouthereau et al., 2007). λ correspond à la moyenne des longueurs d'ondes des plis (MFF : Mountain front fault, SF : Surmeh fault) (c) Log stratigraphique synthétique où WL1, WL2, WL3 correspondent aux couches de faible résistance de la séquence sédimentaire (Fm : formation).*

Il est donc tentant d'utiliser cet observable afin d'en savoir plus sur la dynamique et la rhéologie de la croûte à l'échelle des temps géologiques. A l'aide d'une solution analytique et de modèles

numériques thermomécaniques, nous avons alors exploré ce qui pouvait contrôler l'espacement des plis et quelles étaient les conditions requises permettant d'expliquer l'accommodation du raccourcissement par plissement plutôt que par des failles.

Nos modèles ont alors montré (Fig. 9) que si l'on ne considère qu'un seul niveau de décollement à la base d'une pile sédimentaire cassante trop épaisse, la déformation est contrôlée par des failles, ce qui est inconsistant avec les observations et les données du Zagros. En revanche, si l'on considère des niveaux de décollement supplémentaires qui ont été documentés sur le terrain (Fig. 8c), le mode de déformation change. Des plis d'échelle crustale sont alors obtenus avec l'espacement correct pour un taux de raccourcissement en accord avec les données existantes pour le Zagros.

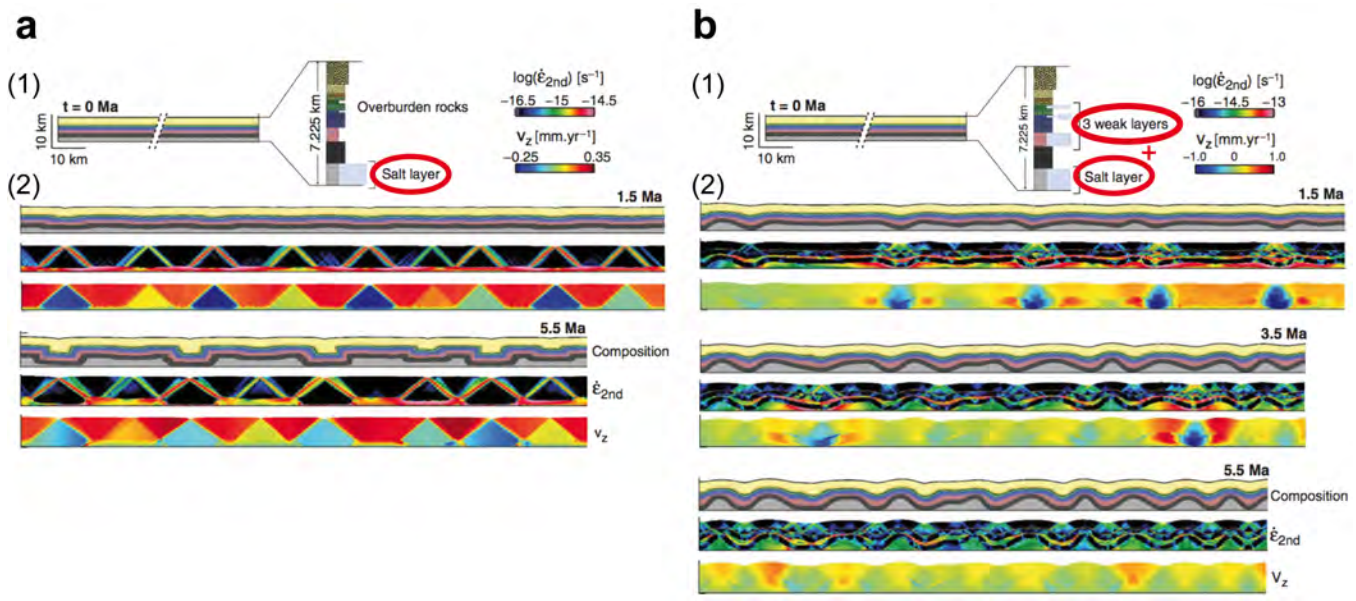

Figure 9 *: Influence de la stratigraphie sur le mode de déformation en raccourcissement (Yamato et al., 2011).* ***(a)*** *Simulation avec un niveau de décollement unique à la base. 1 - Configuration initiale. Toutes les roches situées au dessus de la couche de sel sont homogènes et ont un angle de friction de 5° et une cohésion de 20 MPa. La vitesse de déformation imposée est de 10^{-15} s^{-1}. 2 - Géométrie, vitesse de déformation et vitesses verticales (Vz) obtenues après 1.5 Ma et 5.5 Ma. La déformation est localisée le long de zones de cisaillement cassantes d'échelle crustale et le mode de déformation est dominé par des failles.* ***(b)*** *Simulation mettant en jeu des couches faibles intermédiaires. 1 - La configuration initiale et les conditions aux limites sont similaires à (a) mais 3 couches de faible viscosité (10^{18} Pa.s) ont été rajoutées. 2 - Evolution des géométries, de la vitesse de déformation et des vitesses verticales au cours du temps illustrant que la déformation est dominée par la formation de plis plutôt que par des failles cassantes.*

Le rôle important des niveaux plus faibles avait déjà été décrit mais sans vraiment avoir été quantifié (e.g., Sepehr et al., 2006 ; Sherkati et al., 2006). Dans notre étude, nous avons de plus utilisé cet espacement entre les plis pour contraindre l'angle de friction de la croûte, qui peut être estimé à ~5° pour le cas du Zagros (Fig. 10). Cela implique qu'à l'échelle des temps géologiques, la croûte supérieure peut potentiellement être plus faible que ce que l'on pense. Cela pouvant être du, notamment, à la présence de fluides (e.g., Huismans et al., 2005) ou à de la pré-fracturation (héritage structural).

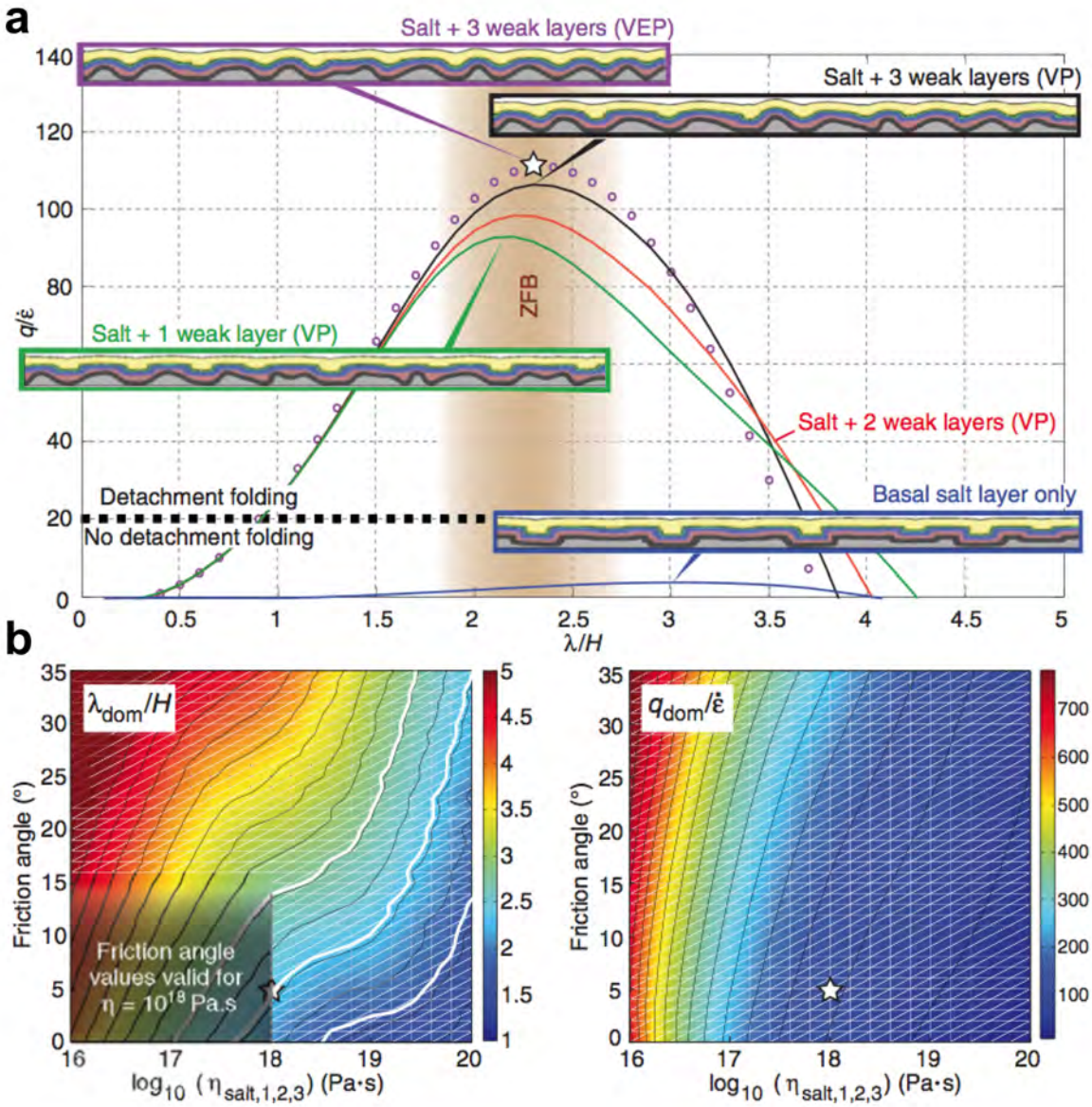

Figure 10 *: Influence de la présence de couches faibles (et de l'élasticité) sur le plissement. (voir Yamato et al., 2011 pour plus de détails). λ, H, q et $\dot{\varepsilon}$ correspondent respectivement à la longueur d'onde, à l'épaisseur totale, au taux de croissance des plis et à la vitesse de déformation (VP : Simulation visco-plastique, VEP : simulation visco-elasto-plastique).* ***(a)*** *Valeurs des taux de croissance obtenus pour des valeurs de λ/H pour 0, 1, 2 ou 3 couches faibles. Dans chacun des cas, la longueur d'onde caractéristique correspond à la plus haute valeur de taux de croissance (par ex., étoile blanche pour le cas avec 3 couches faibles). Les encadrés montrent les résultats obtenus via les simulations numériques. La présence d'un niveau de décollement unique produit un taux de croissance très faible et une déformation dominée par des failles. L'ajout d'au moins une couche faible conduit à une augmentation significative du taux de croissance et à une déformation dominée par des plis (ZFB : zone correspondant au rapport λ/H pour le cas du Zagros).* ***(b)*** *Digrammes présentant les longueurs d'ondes caractéristiques (à gauche) et les taux de croissance correspondants (à droite) en fonction de la viscosité effective des couches faibles et de l'angle de friction de la croûte. Les lignes blanches correspondent aux contraintes pour le Zagros. Si l'on contraint la valeur de la viscosité du sel (ici à 10^{18} Pa.s), on se rend compte que la meilleure valeur à utiliser pour l'angle de friction de la croûte est de ~5°.*

5.3. RHEOLOGIE DES ROCHES (De l'échelle du grain à l'échelle lithosphérique)

5.3.1. De l'importance de comprendre le comportement mécanique des roches

Déjà au cours de ma thèse de 3ème cycle, j'avais pris conscience de l'importance du comportement mécanique des roches et que l'impact sur la tectonique à grande échelle pouvait être

drastique (Fig. 11a). Mes travaux suivants, menés en collaboration avec Frédéric Mouthereau sur Taiwan ont conduit au même constat. Dans cette étude (Yamato et al., 2009b) où, là encore, les modèles étaient contraints par les données de thermochronologie, de déformation long terme/court terme, de flux de chaleur et de la distribution de l'érosion/sédimentation au travers de la chaîne, nous avons montré qu'un flux de matériel crustal profond de la croûte asiatique vers le prisme orogénique devait être invoqué pour expliquer l'exhumation et l'érosion dans la chaîne centrale. Nous avons alors montré qu'à l'opposé des précédents modèles thermo-cinématiques d'exhumation et de déformation qui suggéraient que le sous plaquage jouait un rôle significatif (e.g., Fuller et al., 2006 ; Simoes et al., 2007), l'exhumation et la déformation peuvent être interprétées par une accrétion frontale de la croûte asiatique stratifiée. Ces résultats, en accord avec le fait que la marge continentale chinoise est plus jeune (donc chaude et légère) et qu'elle a du mal à entrer en subduction sous la plaque océanique de la mer des Philippines plus vieille (froide et dense), montrent que la rhéologie crustale contrôle la structuration de la chaîne. Une étude paramétrique impliquant diverses rhéologies pour la croûte inférieure de la plaque en subduction (Figure 11b) montre, là encore, que les résultats obtenus pour la structuration de la chaîne sont très sensibles à la nature de la croûte inférieure considérée.

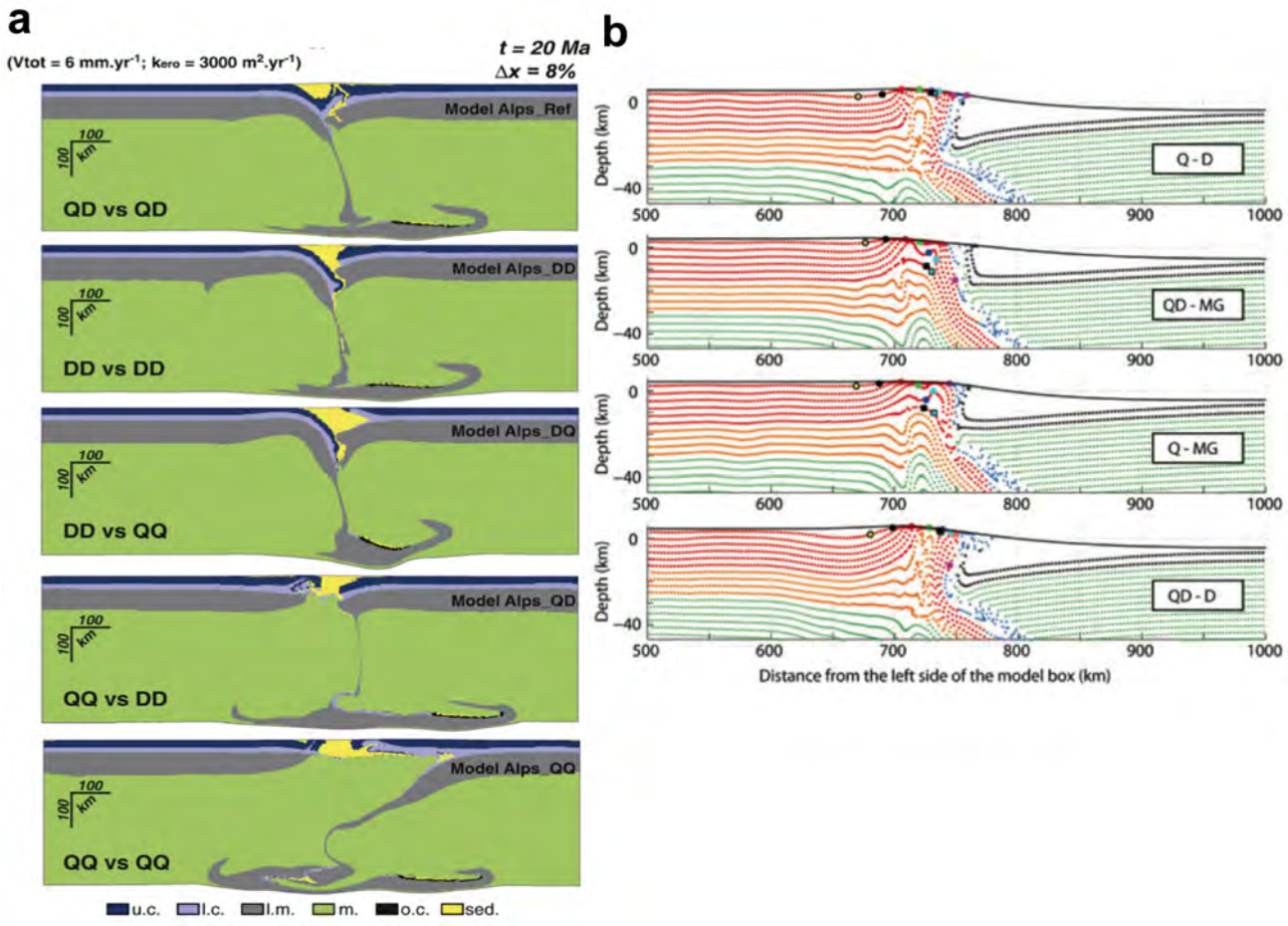

Figure 11 *: Influence de la rhéologie de la croûte sur la dynamique de subduction/collision. (a) Morphologies obtenues pour des modèles de subduction continent-continent (Cas des Alpes) après 20 Ma d'expérience pour différents profils de résistance de la* croûte *(Yamato et al., 2008). QD : structure bicouche Quartz-Diabase, QQ : structure monocouche faible simulée par du quartz, DD : structure monocouche résistante simulée par de la diabase. (clé de lecture : X vs Y signifie que la structure rhéologique X est utilisée pour le panneau subduction et la Y est utilisée pour la plaque supérieure).* ***(b)*** *Morphologies obtenues pour des modèles de subduction continent-ocean (Cas de Taiwan) Abréviations : Q, quartz ; QD : Quartz-Diorite ; D : Diabase ; MG : Granulite mafique. Une croûte inférieure résitante (MG) inhibe l'exhumation de la chaîne centrale. Les résultats qui impliquent une croûte inférieure faible sont en meilleur accord avec les vitesses de refroidissement observés (cf. Yamato et al., 2009b).*

Mon envie d'aller plus loin sur la réflexion concernant l'importance de la rhéologie des matériaux dans l'évolution des systèmes tectoniques s'est alors trouvée renforcée avec les travaux menés sur

l'interface de subduction au Viso et sur les plis du Zagros, présentés plus haut. Toutes ces études montrent que la compréhension de la déformation des roches demeure une question fondamentale des Sciences de la Terre. Ainsi, que l'on s'intéresse à la tectonique des plaques, à la formation des chaînes de montagnes ou encore au déclenchement des séismes, le système considéré répond toujours aux contraintes qui lui sont appliquées en se déformant. Le comportement rhéologique, qui caractérise la façon dont une roche se déforme en réponse à une contrainte, est défini par un certain nombre de paramètres. La viscosité est un de ces paramètres, de loin le plus important dès que l'on s'intéresse aux parties profondes de la Terre et aux échelles de temps géologiques. Les études de terrain et de laboratoire ont montré que la viscosité des roches dépend principalement de leur composition minéralogique, de la température et de la vitesse de déformation (ou de la contrainte appliquée). Afin d'approfondir notre connaissance sur le comportement rhéologique des roches, il faut donc pouvoir traiter ces dépendances, chose qu'il est possible de faire, en alliant données de terrain et modélisation.

D'un point de vue méthodologique, le travail présenté précédemment sur les plis du Zagros (Yamato et al., 2011) clôture parallèlement une étape de ma vie de modélisateur en tant qu'utilisateur de modèles thermomécaniques « tout-couplés ». La sortie de cet article coïncide, en effet, avec le moment où je me suis intéressé plus profondément à la technique de modélisation proprement dite et à l'écriture d'un code personnel (cf. Yamato et al., 2012). C'est avec cet outil, en particulier, que je me suis attaqué de plus près à ces problèmes de rhéologie des roches de manière autonome.

Les zones de cisaillement constituent une cible privilégiée pour une telle étude. En effet, tout comme nous l'avons vu précédemment dans le cas précis de l'interface de subduction, elles jouent un rôle clé dans la tectonique des plaques puisqu'elles sont le lieu où se localise la déformation. Elles permettent de s'intéresser précisément à ce problème car la rhéologie du matériel qui les constitue est encore mal connue, en partie parce que de nombreux paramètres interagissent (température, vitesse de déformation, nature des matériaux qui les constituent, circulation de fluides, etc...).

Afin de quantifier le rôle de ces différent paramètres il apparaît crucial de (i) simplifier au maximum les modèles afin de pouvoir en extraire précisément l'impact de chacun d'entre eux et (ii) de chercher s'il n'est pas possible d'utiliser les données de terrain, de pétrologie et de géochronologie afin de les contraindre au mieux. Si certains paramètres peuvent être issus des observations (e.g., vitesses de convergence, morphologie), il reste deux points majeurs que l'on peut résoudre par ce biais :

- Comment la température intervient dans ces systèmes tectoniques? Qu'est-ce qui la contrôle et quel est son impact ?

- Peut-on accéder à la rhéologie des matériaux qui sont impliqués dans les zones de cisaillement? Et de façon plus générale, puisque les roches ne sont pas des milieux homogènes, est-il possible d'accéder à la viscosité effective d'une roche constituée de différentes phases?

Les deux paragraphes suivants décrivent successivement les travaux que j'ai menés concernant ces deux volets. Le premier correspond, en grande partie, au travail de thèse de Sylvia Duprat-Oualid, que j'ai co-encadré avec Pavel Pitra, sur l'exemple précis des zones de cisaillement. Le second volet, présente les résultats de travaux réalisés avec Benjamin Huet à Vienne sur la rhéologie des agrégats. J'y décris également mes travaux sur le comportement des magmas dans les dykes où le problème est assez similaire puisque ces magmas sont également polyphasés (i.e., constitués à la fois d'une partie liquide et d'une partie cristalline).

5.3.2. Importance de la thermique

Le rôle important de la température sur le comportement des systèmes tectoniques, en particulier au niveau des zones de cisaillement, n'est plus à démontrer (e.g., Heard, 1976 ; Yuen et al., 1978 ; Fleitout & Froidevaux, 1980 ; Brun & Cobbold, 1980, Bürgmann & Dresen, 2008, Burov, 2011). L'évolution thermique autour des zones de cisaillement qu'elles soient chevauchantes, décrochantes ou normales est contrôlée par trois processus majeurs : La diffusion, l'advection et la production de chaleur (radiogénique ou par *shear heating*). D'un point de vue mécanique, de manière simple, lorsque la

température diminue, les roches sont plus résistantes, alors qu'elle deviennent de plus en plus ductiles quand la température augmente (c'est ce que prédisent d'ailleurs les lois de fluage).

Cependant, un problème se pose lorsque l'on considère les interactions possibles entre la thermique et la mécanique. En effet, lorsque la température diminue, si la résistance (viscosité effective) des matériaux augmente, un nouveau processus important entre en jeu. Il s'agit du *shear heating* qui correspond à la conversion de l'énergie mécanique en chaleur durant la déformation. Or, cette production de chaleur est d'autant plus grande que le matériel considéré est résistant. Ainsi, lorsque la viscosité augmente, la production de chaleur par *shear heating* est plus importante et la température augmente.

Cela alimente un débat important, qui n'est pas encore réglé, sur l'importance de ce *shear heating* (cf. discussion et références dans Duprat-Oualid et al., 2013) qui ne peut pourtant pas être ignoré, tout simplement parce qu'il correspond à une exigence de conservation d'énergie au sein des lois fondamentales de la mécanique. Il s'agit donc d'un processus qui est constamment présent durant la déformation mais la question est alors de savoir quelle est sa contribution réelle au budget thermique.

Pour cela, il me fallait des observables et des données suffisantes dans un contexte où ce problème est clairement exposé. C'est pour cette raison que je me suis intéressé, dans le cadre du master de Sylvia Duprat-Oualid puis de sa thèse (co-encadrée avec P. Pitra), au cas du métamorphisme inverse où ce débat, nourri par l'exemple himalayen du Main Central Thrust (MCT), est encore largement ouvert.

Le problème des séquences de métamorphisme inversées

Le métamorphisme inverse correspond à l'empilement d'une unité métamorphique de haute température structuralement au dessus d'une unité de plus basse température. Il est souvent observé le long des chevauchement principaux des orogènes majeures (e.g., Arita, 1983 ; Burg et al., 1984 ; Kohn, 2008 ; Pitra et al., 2010). Pourtant, en dépit des nombreux modèles existants (Jamieson et al., 1996 ; 2004 ; Henry et al., 1997 ; Bollinger et al., 2006), l'origine et la préservation d'inversions métamorphiques dans les chaînes de collision intracontinentales sont encore débattues. Dans cette étude nous avons utilisé un modèle thermocinématique 2D afin d'explorer les paramètres clés pouvant contrôler l'inversion du gradient géothermique à l'échelle crustale.

Nos résultats (cf. Duprat Oualid et al., 2013) confirment que les conditions cinématiques ont un impact fort sur l'évolution thermique autour des grands chevauchements (e.g. England & Molnar, 1993). Ils montrent, par ailleurs, que l'érosion et la conductivité thermique des roches sont deux paramètres qui contrôlent respectivement, la localisation spatiale de la perturbation thermique et l'intensité de l'inversion. Cependant, nous démontrons que même pour de fortes vitesses de convergence (> 3cm.an^{-1}) et de forts pendages, qui favorisent l'inversion thermique, celle-ci reste transitoire et la température au niveau du chevauchement ne peut pas atteindre des pics de température supérieurs à 600°, tels qu'ils sont observés dans la nature, si le *shear heating* n'est pas pris en compte (Fig. 12). La conversion de l'énergie mécanique en température représente donc une part importante du budget thermique le long de ces grandes zones de chevauchement à l'échelle crustale. Il conduit à des conditions de haute température dans la zone de chevauchement et constitue le seul processus qui permet la préservation au cours du temps d'une inversion thermique intense (Fig. 12c).

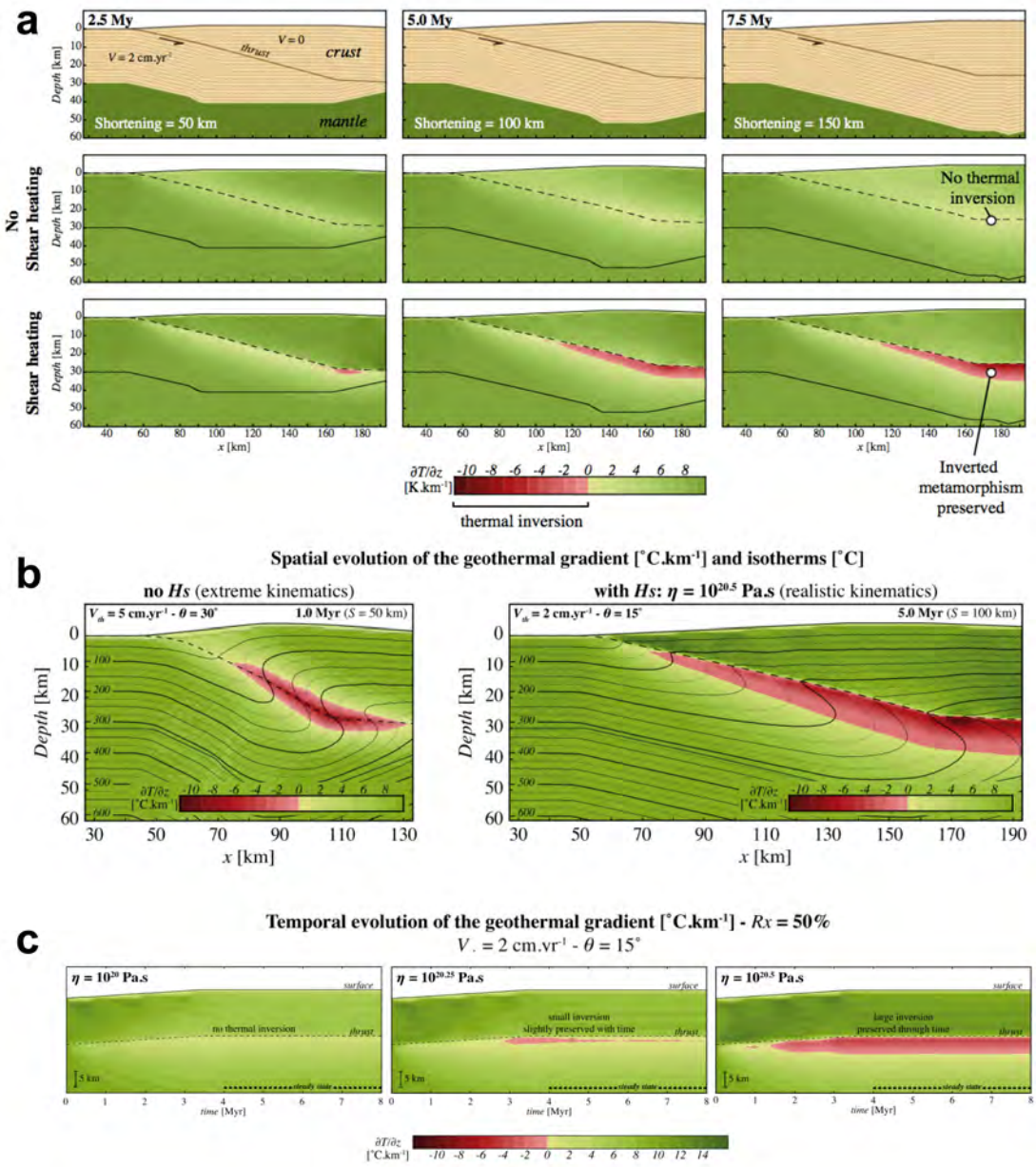

Figure 12 *: Rôle du shear heating sur le développement du métamorphisme inverse (cf. Duprat-Oualid et al., 2013).* ***(a)*** *Le shear heating permet l'inversion du gradient thermique et sa préservation au cours du temps.* ***(b)*** *L'inversion thermique est possible sans shear heating en conditions extrêmes mais elle reste transitoire et se localise à cheval sur la zone de cisaillement. En revanche, cette inversion se trouve uniquement sous le chevauchement en présence de shear heating.* ***(c)*** *Influence de la viscosité effective de la zone de chevauchement sur l'inversion thermique au cours du temps.*

Ce travail montre que le *shear heating* est bien plus efficace que les autres processus, tels que l'accrétion ou la dénudation en surface, et qu'il est compatible avec les observations de métamorphisme inverse en Himalaya ou dans la chaîne varisque par exemple. Cette comparaison avec les occurrences naturelles suggère que la formation et la préservation du métamorphisme inverse requiert des viscosités effectives à l'intérieur de la zone de cisaillement de l'ordre de 10^{20}-10^{21} Pa.s pour des vitesses de convergence entre 1 et 3 cm.an^{-1} (Fig. 12).

Suite à cette étude, il fallait donc aller plus loin en tentant de voir s'il n'était pas possible de généraliser ce travail (i) pour quantifier la part du *shear heating* dans le budget thermique pour n'importe quelle zone de cisaillement et (ii) pour tenter de résoudre les désaccords sur le cas himalayen et essayer de trouver, sans a priori, les paramètres permettant d'expliquer au mieux les données.

Pour cela, nous avons développé une analyse dimensionnelle afin de quantifier le budget thermique autour de n'importe quelle zone de cisaillement d'échelle lithosphérique (Duprat-Oualid et al., soumis). L'évolution thermique autour des zones de cisaillement, qu'elles soient chevauchantes, décrochantes ou normales, est contrôlée par trois processus majeurs : La diffusion, l'advection et la production de chaleur. Nous avons proposé (Fig. 12) une analyse dimensionnelle pour quantifier, au premier ordre, les contributions relatives de ces trois processus sur l'évolution thermique se produisant autour des zones de cisaillement d'échelle lithosphérique. Des 11 paramètres qui contrôlent la cinématique, la géométrie 3D, la structure thermique initiale et la résistance moyenne d'une zone de cisaillement (Fig. 12a), 3 paramètres sans dimension peuvent être extraits pour quantifier la contribution relative de ces 3 processus thermiques. L'application de cette analyse dimensionnelle pour différentes zones de cisaillement (chevauchement, détachement, décrochement) en fait alors un outil utile et complémentaire des étude numériques et analytiques précédentes (e.g., Yuen et al., 1978 ; Brun & Cobbold, 1980; Brewer, 1981; Molnar & England, 1990; England & Molnar, 1993).

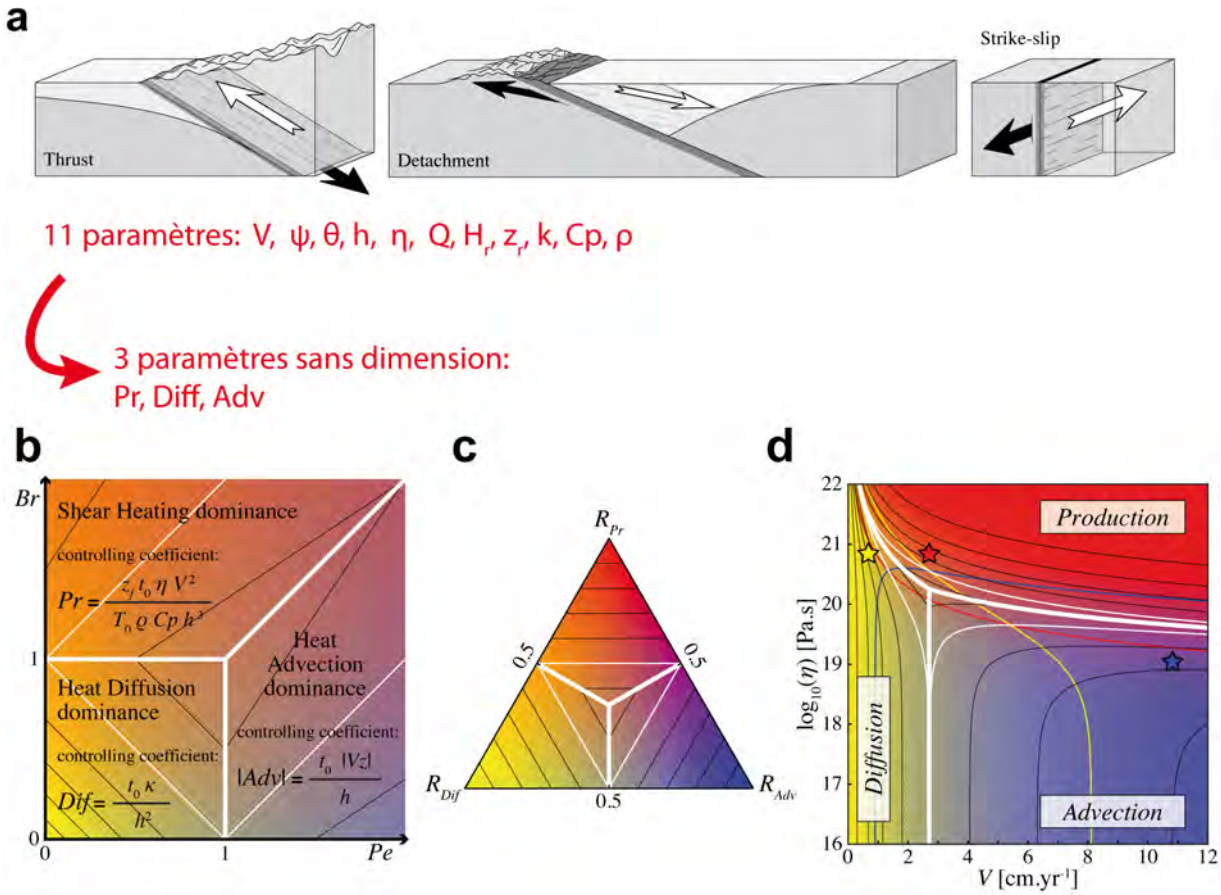

Figure 12 *: Budget thermique autour des zones de cisaillement (cf. Duprat-Oualid et al., soumis).* ***(a)*** *Schémas synthétiques 3D des différentes zones de cisaillement sur lesquelles notre analyse dimensionnelle peut être appliquée. Celles-ci sont définies par une vitesse de déplacement (V), un pitch (ψ), un angle de plongement (θ), une épaisseur (h), une viscosité effective (η), un flux de chaleur vertical (Q), une production de chaleur radiogénique (H_r et z_r), une conductivité thermique (k), une capacité thermique Cp et une densité (ρ).* ***(b)*** *Diagramme représentant les 3 champs où le budget thermique autour et à l'intérieur de la zone de cisaillement est dominé soit par de la diffusion, soit par de l'advection ou soit par shear heating en fonction du nombre de Peclet (Pe) et du nombre de Brinkman (Br) .* ***(c)*** *Diagramme ternaire représentant ces trois pôles de contribution thermique (autre visualisation possible).* ***(d)*** *Exemple d'application : contributions thermiques en fonction de V et η, pour une zone de chevauchement pur (ψ = 0) caractérisée par h = 2.5 km et θ = 30°. (cf. Duprat-Oualid et al., soumis pour plus de détails sur les paramètres utilisés). Les lignes jaune, bleue, et rouge représentent les lignes où la diffusion, l'advection et le shear heating correspondent respectivement à 25% du budget thermique.*

Cette étude est importante car elle permet, pour une zone bien caractérisée (dont nous connaissons les 11 paramètres, Fig. 12a), de quantifier au premier ordre la contribution du *shear heating* notamment au budget thermique. Dans une zone largement étudiée comme le MCT, il serait donc possible de trancher si l'on avait accès à ces paramètres, et plus particulièrement, à la viscosité effective du chevauchement. C'est ce que nous avons tenté de faire dans le cadre du travail de thèse de Sylvia Duprat-Oualid. L'idée est brièvement présentée ici (Fig. 13). Les résultats sont en cours et seront présentés en détail dans son manuscrit de thèse.

En utilisant les données disponibles dans la littérature sur le MCT (Fig. 13a, Duprat-Oualid, 2014), il est possible, en testant des paramètres via les modèles thermocinématiques que nous avons développés (Fig. 13b, Duprat-Oualid et al., 2013), de réaliser une étude statistique pour remonter aux paramètres qui permettent d'expliquer au mieux le pic de température et le gradient thermique. Cela nous permet, à rebours, non seulement de remonter à une estimation de la viscosité effective à l'intérieur du chevauchement, mais également, en utilisant notre analyse dimensionnelle, de quantifier réellement le rôle du *shear heating* au niveau du MCT.

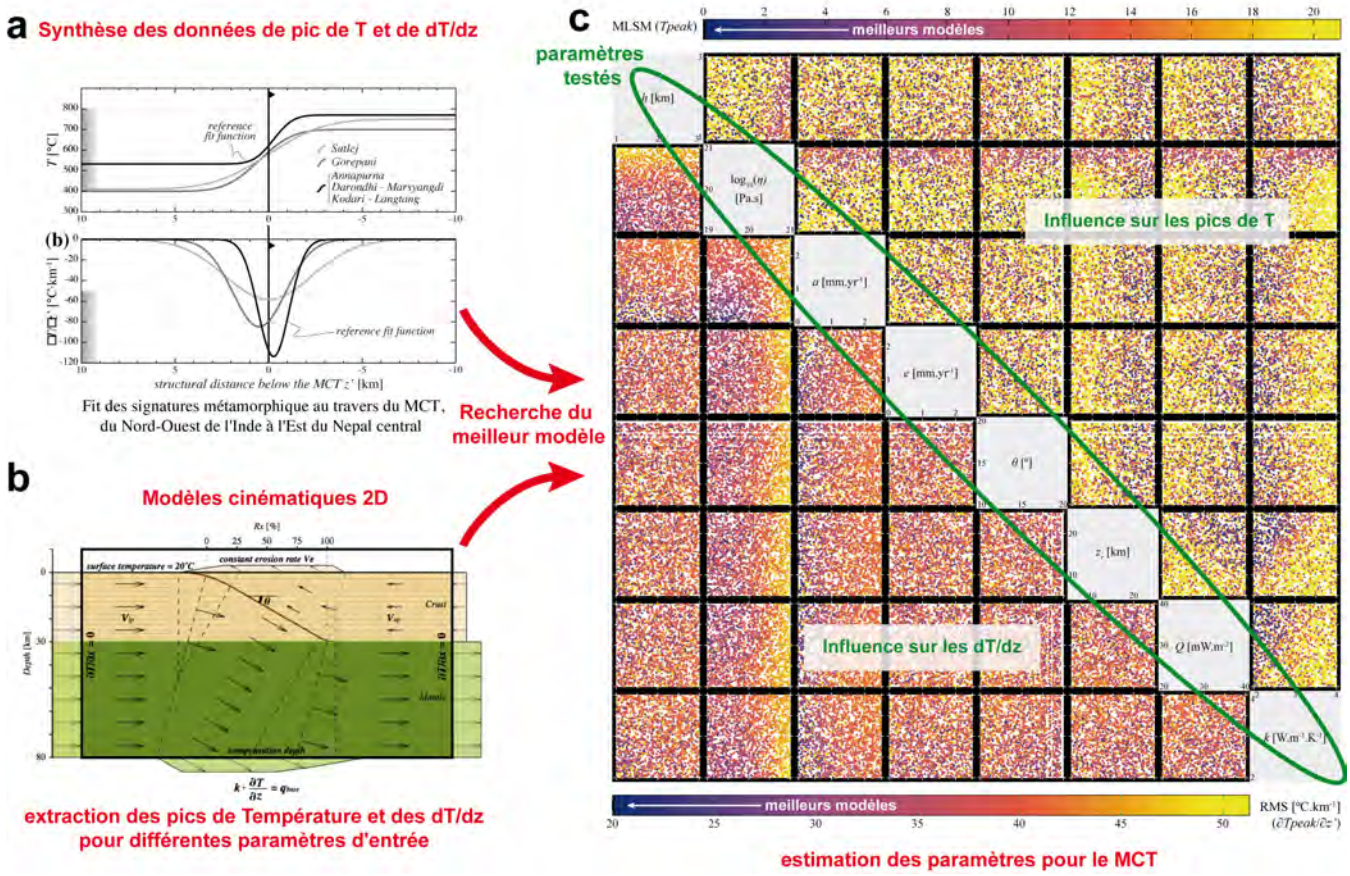

Figure 13 *: Etude statistique permettant, en couplant données de terrain et modèles thermocinétiques, de remonter aux paramètres expliquant au mieux le métamorphisme inverse pour le MCT (D'après Duprat-Oualid, 2014).* ***(a)*** *Fit correspondants à la synthèse des données de pic de température et de gradient de température au travers du MCT.* ***(b)*** *Configuration initiale du modèle thermocinématique 2D utilisé (Duprat-Oualid et al., 2013) et* ***(c)*** *Différences entre les résultats issus des modèles et les données (MLSM : Mean Last Square Misfit ; RMS : Root Mean Square) pour 8 paramètres testés. Les résultats montrent l'influence remarquable de la viscosité effective du chevauchement.*

Bien évidemment les résultats présentés ici restent de premier ordre (cinématique, morphologie fixée) et ne tiennent pas compte de toute la complexité du cas du MCT (notamment de la diversité des matériaux impliqués dans le chevauchement). Ils permettent, néanmoins, d'appréhender une viscosité effective moyenne. Le principal inconvénient reste que cela ne permet pas de résoudre le problème de l'évolution des zones de cisaillement au cours du temps et, en particulier, le fait que la viscosité va changer en fonction de la température. Pour accéder à cette information à ce stade, le cas du MCT est peut-être un peu trop complexe car (i) il met en jeu du matériel de différentes sources et (ii) nous avons

considéré un chevauchement unique, question qui reste discutée par certains auteurs (e.g., Huerta et al., 1998).

Si on veut étudier comment évolue la rhéologie des zones de cisaillement, il faut donc probablement rechercher des systèmes plus simples (i.e. constitués d'un seul type de roche) pour lesquels nous sommes sûr que la phase de déformation est unique. C'est en ce sens que, parallèlement à cette étude numérique, nous avons commencé un travail sur le terrain avec Sylvia Duprat-Oualid et Benjamin Huet (Université de Vienne) sur des zones de cisaillements du massif granodioritique du Zillertal (Autriche). En effet, ce massif, homogène initialement, présente des zones de cisaillement à différents stades d'évolution. L'idée est donc de pouvoir, *in fine*, par une méthode similaire à celle présentée précédemment, examiner comment évolue la viscosité effective au cours de la déformation, ce qu'il me semble possible de réaliser.

Les enjeux sont importants. En effet, les travaux quantitatifs sur la rhéologie des zones de cisaillement sont peu avancés. Les études de terrain permettent d'estimer le taux de déformation dans ces zones (Bürgmann & Dresen, 2008), et les études pétrologiques (Angiboust et al., 2011) et de laboratoire (Ji et al., 2001 ; Marques et al., 2011) montrent un lien clair entre changement de viscosité et changement de minéralogie. Malgré ces résultats, l'estimation de la viscosité effective des zones de cisaillement demeure problématique (Jessell et al., 2009) et ce, en partie, parce que les lois de mélange existantes qui permettent de calculer la viscosité de ces milieux polyphasés sont soit empiriques (Ji, 2004), soit peu précises (Zhou, 1995), soit trop complexes (Molinari et al., 1987) pour être introduites directement dans un code de calcul.

Avant de s'attaquer au problème des zones de cisaillement proprement dit, il apparait donc primordial, dans un premier temps, de trouver un moyen simple d'accéder à la viscosité effective des milieux polyphasés.

5.3.3. Comportement des milieux polyphasés

Le terme de « milieux polyphasés » est en fait un peu ambigu et nécessite avant tout d'être explicité afin de ne pas porter à confusion. En effet, il est bien souvent utilisé pour distinguer une phase liquide d'une phase solide. Ainsi, un magma constitué de liquide magmatique et de cristaux (considérés rigides) constitue un milieu polyphasé. Pour une roche constituée de plusieurs cristaux, le terme d'agrégat serait peut-être plus adéquat mais, puisque les différents minéraux d'une roche peuvent être assimilés à des phases minérales présentant des propriétés intrinsèques distinctes (densités, paramètres rhéologiques), je la considère ici également, par abus de langage, comme un système polyphasé. Etudier le comportement rhéologique des milieux polyphasés revient, cependant, à considérer ces deux cas et c'est pourquoi cette thématique de recherche s'articule ici autour de 2 volets : l'étude de la rhéologie d'une roche polycristalline et l'étude du comportement des cristaux au sein des dykes magmatiques.

Peut-on appréhender la viscosité effective d'une roche polycristalline ?

Dans la nature, les roches sont hétérogènes et sont constituées d'un assemblage de plusieurs minéraux qui ne possèdent pas les mêmes propriétés rhéologiques. En outre, pour une même roche, la composition minéralogique peut changer en fonction des conditions de température et de pression. Un granite, par exemple, est constitué de quartz, de feldspath, et de mica. Une zone de cisaillement qui se localise dans ce granite est constituée de chlorite, de mica et de quartz mais leurs proportions relatives varient en fonction du contexte métamorphique. La viscosité est alors plus faible que celle du granite original. Cet exemple classique est toujours largement étudié (e.g., Sassier et al., 2006 ; Oliot et al., 2010 ; Goncalves et al., 2012). Pourtant, on sait très mal quantifier l'évolution de la viscosité avec l'évolution de la minéralogie, car il s'agit d'un milieu polyphasé.

En effet, si la dépendance à la température et à la vitesse de déformation peut être quantifiée expérimentalement pour une roche monophasée ou un minéral seul, on ne sait pas rendre compte

mécaniquement de la diversité minéralogique des roches magmatiques et métamorphiques de manière réaliste. De ce fait, les études de modélisation numérique se retrouvent face à un paradoxe : malgré toutes les complexités introduites dans les codes de calculs modernes (comportement visco-élasto-plastique, changement de densité, érosion), les matériaux impliqués sont toujours considérés comme des roches simples, voire comme des phases uniques homogènes (cf. Fig. 11 par exemple).

Avec Benjamin Huet, nous avons développé un modèle qui permet de prédire la viscosité pour n'importe quelle roche polyphasée déformée en régime ductile. L'avantage de ce modèle (Huet et al., 2014) est qu'il nécessite uniquement de connaître les fractions volumétriques et les paramètres de loi de fluage des phases qui constituent la roche. Ce modèle est basé sur la minimisation de la puissance mécanique dissipée dans la roche durant la déformation (cf. Handy, 1990). A l'opposé des modèles de mélanges préexistants basés sur la minimisation qui utilisaient des itérations numériques (Zhou, 1995 ; Jiang et al., 2005), nous avons utilisé la méthode des multiplicateurs de Lagrange (e.g., Stewart, 2002) et contraint la vitesse de déformation (ou la contrainte) par une moyenne géométrique. Cela nous à permis (Fig. 14b) de déterminer des expressions analytiques pour la viscosité d'une roche polyphasée, ses paramètres de loi de fluage, ainsi que le partitionnement de la vitesse de déformation et de la contrainte entre les différentes phases.

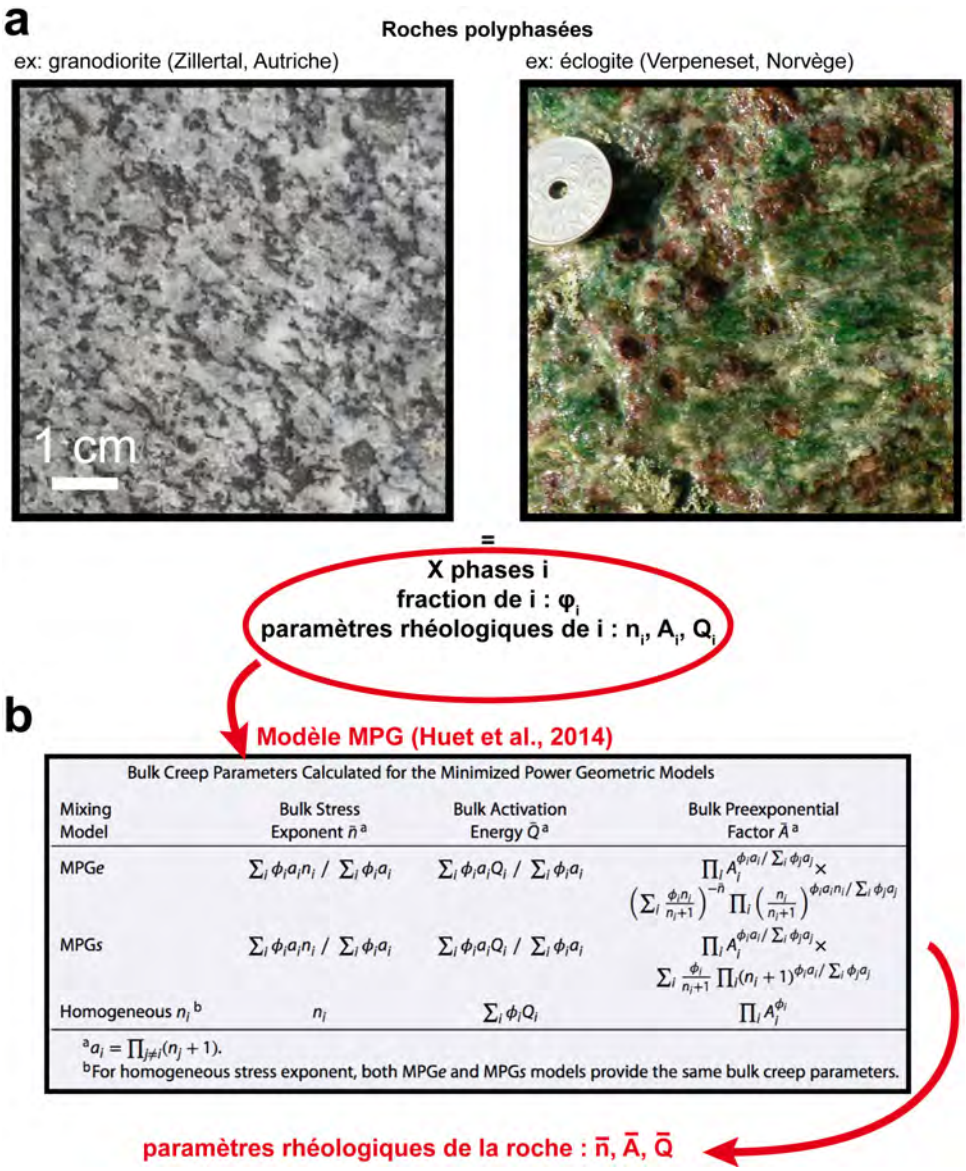

Bulk Creep Parameters Calculated for the Minimized Power Geometric Models

Mixing Model	Bulk Stress Exponent $\bar{n}$ [a]	Bulk Activation Energy $\bar{Q}$ [a]	Bulk Preexponential Factor $\bar{A}$ [a]
MPGe	$\sum_i \phi_i a_i n_i \,/\, \sum_i \phi_i a_i$	$\sum_i \phi_i a_i Q_i \,/\, \sum_i \phi_i a_i$	$\prod_i A_i^{\phi_i a_i / \sum_i \phi_j a_j} \times \left(\sum_i \frac{\phi_i n_i}{n_i+1}\right)^{-n} \prod_i \left(\frac{n_i}{n_i+1}\right)^{\phi_i a_i n_i / \sum_i \phi_j a_j}$
MPGs	$\sum_i \phi_i a_i n_i \,/\, \sum_i \phi_i a_i$	$\sum_i \phi_i a_i Q_i \,/\, \sum_i \phi_i a_i$	$\prod_i A_i^{\phi_i a_i / \sum_i \phi_j a_j} \times \sum_i \frac{\phi_i}{n_i+1} \prod_i (n_i+1)^{\phi_i a_i / \sum_i \phi_j a_j}$
Homogeneous n_i [b]	n_i	$\sum_i \phi_i Q_i$	$\prod_i A_i^{\phi_i}$

[a] $a_i = \prod_{j \neq i}(n_j + 1)$.
[b] For homogeneous stress exponent, both MPGe and MPGs models provide the same bulk creep parameters.

Figure 14 *: Viscosité effective d'un milieu polyphasé (cf. Huet et al., 2014).* ***(a)*** *Exemples de roches polyphasées. Granodiorite (à gauche) avec Quartz, Felspath, Plagioclase et Mica. Eclogite (à droite) à grenat, omphacite, mica, et épidote. Les roches sont donc constituées de i phases dont on peut connaître la fraction volumétrique (φ_i). Si l'on connaît les paramètres rhéologiques de chacune des phases, il est possible via* ***(b)*** *d'en estimer les paramètres rhéologiques moyens pour la roche.*

La comparaison des résultats de notre modèle (modèle MPG, cf. Huet et al., 2014) avec 15 jeux de données expérimentales publiés sur des agrégats à deux composants montre que notre méthode reproduit précisément, à la fois, les valeurs expérimentales de viscosité et les paramètres de fluage, même lorsque de grands contrastes de viscosité sont mis en jeu. Ce modèle présente bien sûr des limites (cf. Huet et al., 2014) mais il offre un potentiel énorme pour les applications en géologie structurale et en modélisation numérique. En effet, grâce à ce modèle analytique, il est à présent possible d'implémenter simplement dans les modèles numériques, des variations de viscosité pour n'importe quelle roche (connaissant sa composition chimique) en fonction des conditions P-T, de la même façon que sont implémentées, par exemple, les variations de densité (cf. Yamato et al., 2007).

Dykes magmatiques et comportement des cristaux

Cette étude constitue un de mes nouveaux champs d'intérêt. Il s'agit là d'un travail qui pourrait, au premier abord, paraître différent de celui proposé précédemment sur les zones de cisaillement. Il est, néanmoins, en lien direct avec mes développements méthodologiques en modélisation numérique (cf. Yamato et al., 2012), d'une part, et avec mon intérêt pour les granites qui a grandi depuis mon arrivée à Rennes, d'autre part (Yamato et al., 2012, soumis, Tartèse et al., 2011, Ballouard et al., soumis). Le but recherché est, là encore, de comprendre (i) comment se comportent les cristaux au sein des dykes lors de l'ascension de matériel magmatique, (ii) quelle peut être la conséquence de la présence de cristaux sur la ségrégation entre liquide et cristaux et (iii) quel est leur impact sur le comportement du matériel magmatique lors de sa remontée. Comme pour le cas des zones de cisaillement, il s'agit donc de comprendre comment se comporte une roche (polyphasée) au cours de sa déformation, la problématique de recherche en est donc extrêmement proche.

Les travaux d'observation, d'acquisition de données et d'expériences de laboratoire sur la rhéologie des magmas sont nombreux (e.g., Bagdassarov & Dorfman, 1998 ; Paterson, 2009). Par ailleurs, la rhéologie et la dynamique d'ascension de liquide magmatique dans un dyke a été intensivement étudiée dans le passé (e.g., Philpotts, 1990 ; Petford & Koenders, 1998). Néanmoins, les observations de terrain montrent que la plupart des dykes contiennent en réalité une charge cristalline. Si l'aspect qualitatif lié à l'effet des cristaux sur la rhéologie des magmas est de mieux en mieux connu, l'aspect quantitatif est encore peu étudié (par ex., Dingwell, 1996; Caricchi et al., 2007; Taisne & Jaupart, 2011). Ainsi, comme pour le cas de zones de cisaillement le problème réside dans la prédiction de la viscosité d'un magma constitué de plusieurs cristaux de taille, de densité et de propriétés rhéologiques différentes.

La présence de cristaux modifie la rhéologie effective du système et donc le comportement du flux (e.g., Arzi, 1978 ; Bagdassarov & Dorfman, 1998). En effet, le fait que les cristaux soient plus denses et rigides, comparé au liquide magmatique, entraine une baisse de la vitesse d'ascension et modifie la forme du profil de vitesse (d'un flux de poiseuille typique à un flux de type Bingham). D'autre part, une observation fréquente sur le terrain est que l'arrangement de ces cristaux se fait parallèlement (ou avec un très faible angle) à la bordure du dyke (e.g., Smith, 2002 ; Paterson, 2009 ; Chistyakova & Latypov, 2010). Un tel arrangement structural est souvent interprété comme le résultat du flux magmatique, qui entraine les cristaux en rotation et les aligne dans la direction du flux mais ce processus reste peu clair. Un autre problème, lié à l'introduction d'une charge cristalline, concerne la possibilité pour les cristaux de ségréguer de la phase liquide magmatique durant l'ascension dans les dykes. Enfin, les implications d'un tel processus sur la différentiation magmatique n'a jamais été considéré auparavant ni même investigué au travers de modèles numériques.

Dans une étude menée en collaboration avec Thibault Duretz, Roman Tartèse et Dave A. May, nous avons examiné le flux dynamique d'un magma granitique en ascension dans un dyke via des modèles numériques (Yamato et al., 2012). Le modèle est présenté en figure 15 et permet de simuler l'injection de matériel magmatique au travers d'un dyke représenté par un piston. Le gradient de pression permettant l'injection est alors assuré par la poussée de blocs rigides dans le mélange magmatique (Fig. 15).

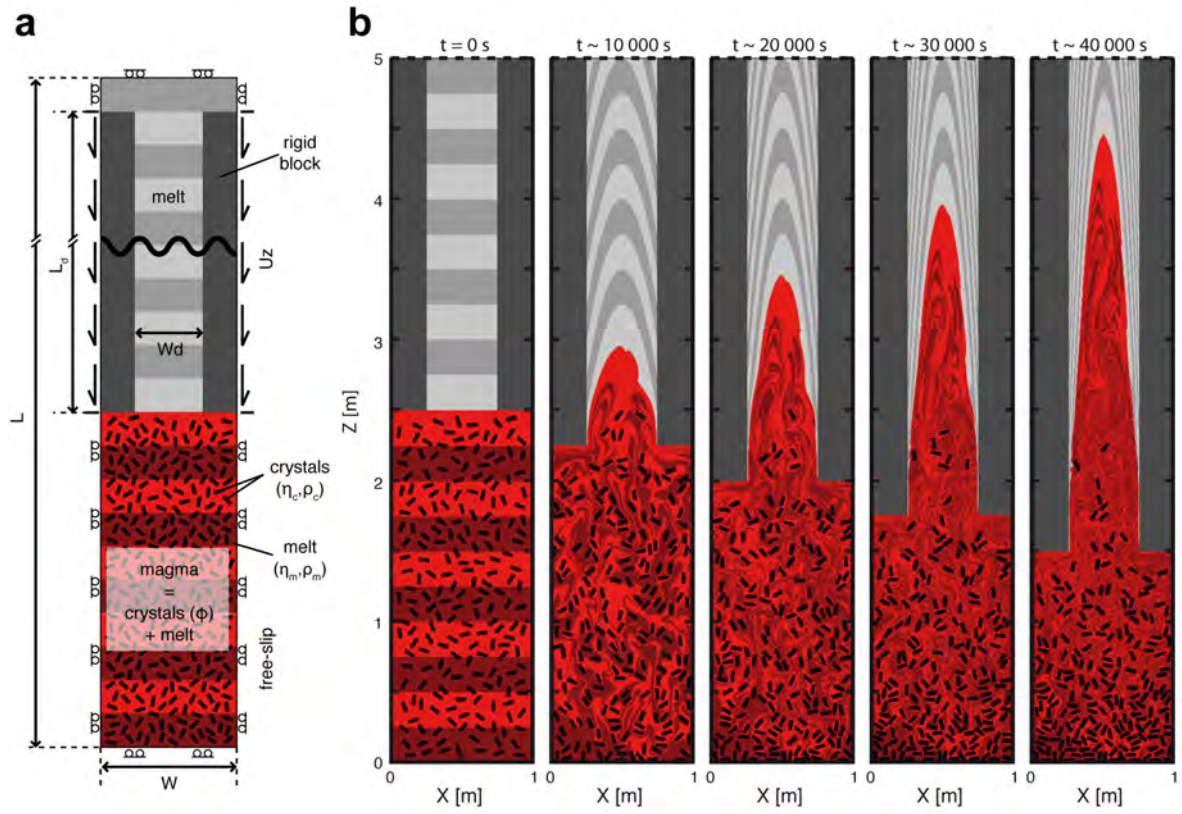

Figure 15 *: Modèle de piston utilisé pour étudier le comportement des magmas dans les dykes (Yamato et al., 2012; 2014).* ***(a)*** *Configuration initiale du modèle et conditions aux limites.* ***(b)*** *Exemple d'une simulation au cours du temps. Le magma constitué de liquide et de cristaux est injecté dans le dyke par l'intermédiaire d'un gradient de pression contrôlé par la poussée des deux blocs rigides latéraux dans le mélange magmatique initial.*

Dans nos modèles les cristaux sont représentés par des fluides hautement visqueux (considérés rigides) qui évoluent dans un liquide magmatique. Nos résultats révèlent que la présence de cristaux modifie drastiquement le profil de vitesse du magma au travers du dyke (Fig. 16a). De plus, nous avons montré que les cristaux tournent constamment dans le flux cisaillant mais que, sur une période de révolution, leur plus grand axe se trouve statistiquement aligné parallèlement à la direction du flux (Fig. 16b). Par ailleurs, certaines expériences montrent que la phase liquide peut effectivement être séparée du magma initial quand celui-ci est sujet à une gamme de gradient de pression précise (Fig. 16c). Cela démontre que la ségrégation liquide-cristaux dans les dykes pendant l'ascension des magmas granitiques constitue un mécanisme viable pour la différentiation magmatique.

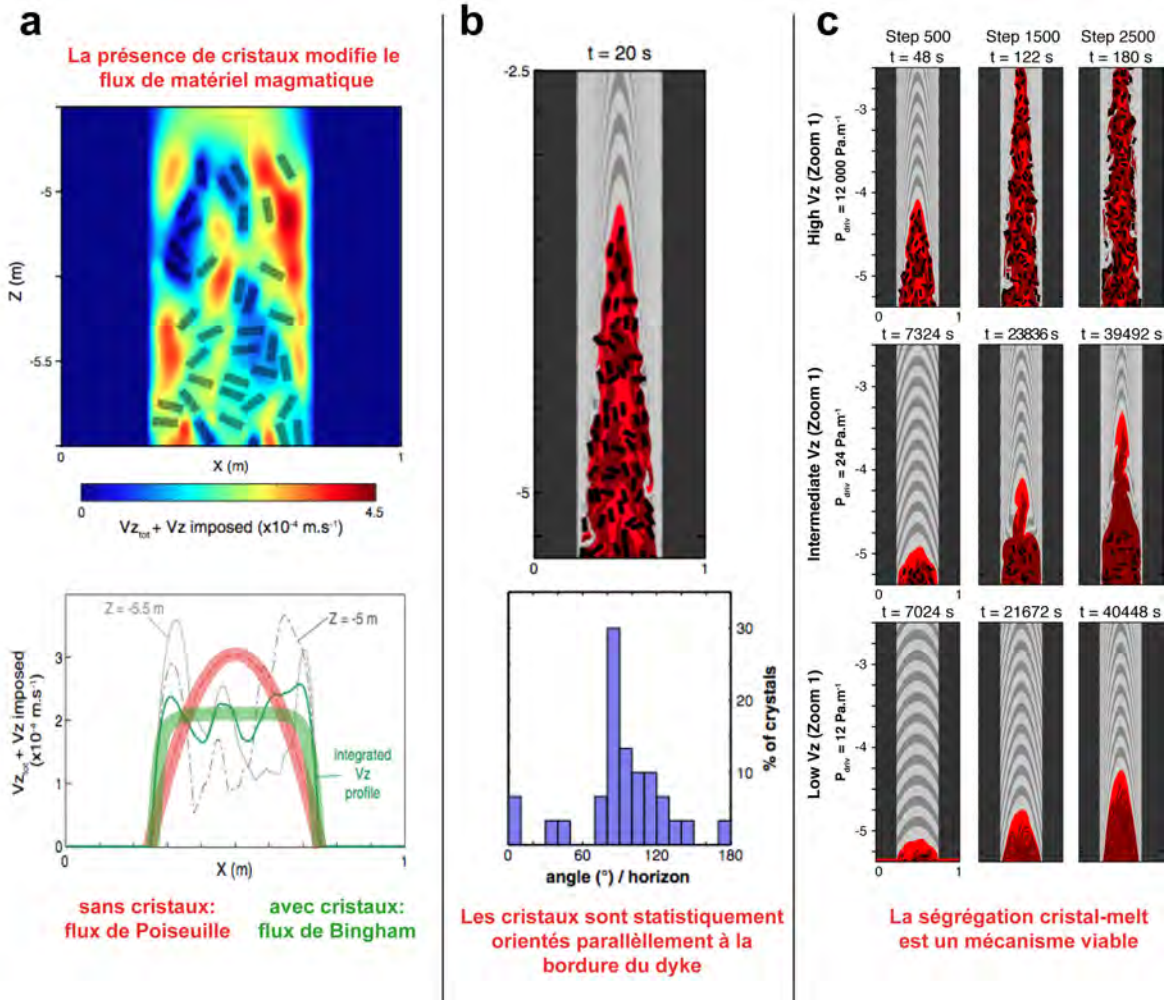

Figure 16 *: Comportement des cristaux dans les dykes (Yamato et al., 2012).* ***(a)*** *Modification du profil de vitesse lié à la présence d'une charge cristalline.* ***(b)*** *Orientation préférentielle des cristaux parallèlement à la bordure du dyke* ***(c)*** *La ségrégation cristal-liquide est un mécanisme viable contrôlé par le gradient de pression.*

Partant de ce constat, nous avons cherché à voir, dans un second temps, ce qui contrôle cette ségrégation cristal-liquide et s'il est possible de la quantifier en fonction du pourcentage de cristaux, de leur géométrie, de leur taille et de leur densité (Yamato et al., soumis). Afin de s'attaquer à ces problèmes nous avons réalisé une étude paramétrique en utilisant les même modèles direct 2D que ceux décrits précédemment (Fig. 15) qui modélisent l'ascension d'un magma constitué de cristaux dans un dyke vertical. A partir de ces modèles, nous avons caractérisé la quantité de ségrégation en fonction de différents paramètres incluant la fraction de cristaux, le contraste de densité entre liquide et cristaux, la taille des cristaux et leur rapport de forme. Nos résultats (cf. Etude paramétrique dans Yamato et al., soumis) montrent que le rapport de forme des cristaux n'affecte pas la ségrégation si ce rapport est suffisamment petit (axe long < 1/6 de la largeur du dyke). L'inertie au sein d'un tel système n'affecte pas, non plus, la ségrégation entre le cristal et le liquide. Le degré de ségrégation est cependant très dépendant des autres paramètres : la ségrégation est plus grande quand le contraste de densité cristaux-liquide est grand et/ou que ceux-ci sont de grande taille. En revanche, la ségrégation est plus faible pour de grands gradients de pression et/ou de grandes largeurs de dyke. Ces 4 paramètres peuvent être combinés en un seul, le nombre *S* (voir Yamato et al., soumis pour plus de détails), qui peut être utilisé pour quantifier la ségrégation. A l'aide d'une modélisation numérique systématique et d'une analyse dimensionnelle, nous avons alors pu fournir une loi d'échelle au premier ordre capable de quantifier la ségrégation pour un nombre *S* et une proportion de cristaux donnée, qui est valable pour de larges gammes de valeurs que l'on retrouve communément dans les systèmes magmatiques terrestres (Fig. 17).

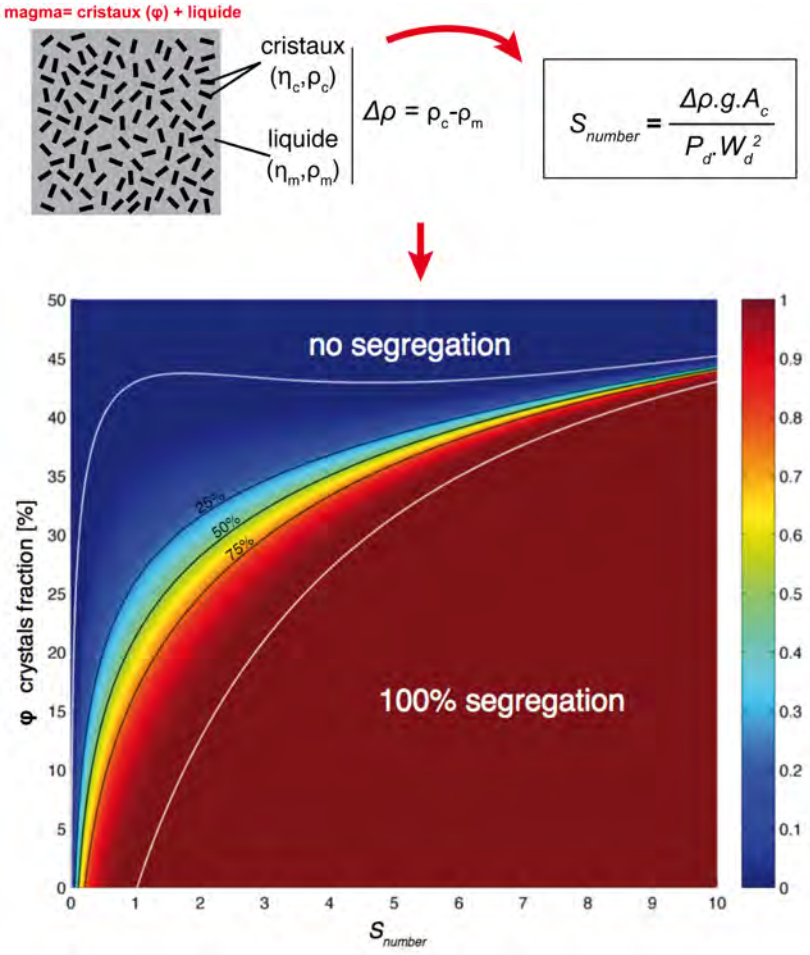

Figure 17 *: Estimation du pourcentage de ségrégation en fonction de la proportion initiale de cristaux (φ) dans le mélange magmatique et du nombre S (cf. Yamato et al., soumis). Abréviations : A_c, aire du cristal, g, accélération gravitationnelle, P_d, gradient de pression ; W_d, largeur du dyke; ρ_c , densité du cristal ; ρ_m , densité du liquide ; η_c , viscosité du cristal ; η_m , viscosité du liquide.*

5.4. LA RELATION LITHOSPHERE/MANTEAU CONVECTIF

Ce chapitre sur mes activités de recherche illustre un intérêt nouveau que j'ai depuis 2013 sur la tectonique à plus grande échelle. J'ai choisi de le placer en dernier car c'est ainsi qu'il apparaît dans l'évolution chronologique de ma recherche mais il aurait pu, d'un point du vue thématique, être interverti avec le chapitre précédent. En effet, comme je l'expliquais dans le chapitre 5.2., en commençant à prendre du recul sur les zones de subduction, je me suis mis à regarder les choses différemment en passant de l'échelle du prisme orogénique à l'échelle du manteau. Si l'on regarde d'encore plus loin, les zones de subduction ne correspondent qu'à une partie de la dynamique terrestre qui est régie au premier ordre par la convection mantellique. Ainsi, si l'on veut comprendre la dynamique de la lithosphère dans son ensemble, il apparaît nécessaire de s'intéresser aux interactions qu'elle peut avoir avec la dynamique du manteau.

Une vision simple mais classique du modèle de la tectonique des plaques présente souvent les choses de la manière suivante : la convection mantellique engendre des mouvements ascendants et descendants qui se traduisent en surface par des mouvements de la lithosphère. La lithosphère océanique est alors créée au niveau des rides et disparaît en subduction au niveau des fosses, ces zones de convergence donnant alors bien souvent naissance à des chaînes de montagnes. Cependant, dans un tel schéma, la lithosphère se déforme de manière passive en subissant le flux mantellique. Nous sommes alors en droit de nous demander si, en se déformant, la lithosphère ne peut pas à son tour avoir un impact fort sur la convection mantellique terrestre et en particulier lors de la formation des chaînes de montagnes qui bloquent les lithosphères les unes contre les autres.

Le premier exemple pour illustrer ce propos est celui du travail que nous avons mené avec Laurent Husson et co-auteurs afin de comprendre pourquoi les marges passives présentent bien souvent du soulèvement, de l'exhumation et de l'inversion tectonique. Le but était de voir si cela n'avait pas un lien direct avec la formation des chaînes de montagnes. En effet, depuis la fin du Crétacé, les observations montrent que les continents se contractent et forment des chaînes de montagnes (Fig. 18a). Si cette compression dans la lithosphère semble augmenter graduellement durant le Cénozoïque sur les marges actives, elle semble aussi affecter les marges passives durant cette même période (Fig. 18b, Yamato et al., 2013). Cependant, le lien entre ces observations n'était pas bien clair. Nous avons alors cherché à tester si la compression des marges passives correspond à une réponse au flux mantellique sous jacent qui résiste de plus en plus aux collision Cénozoïques (Fig. 18c).

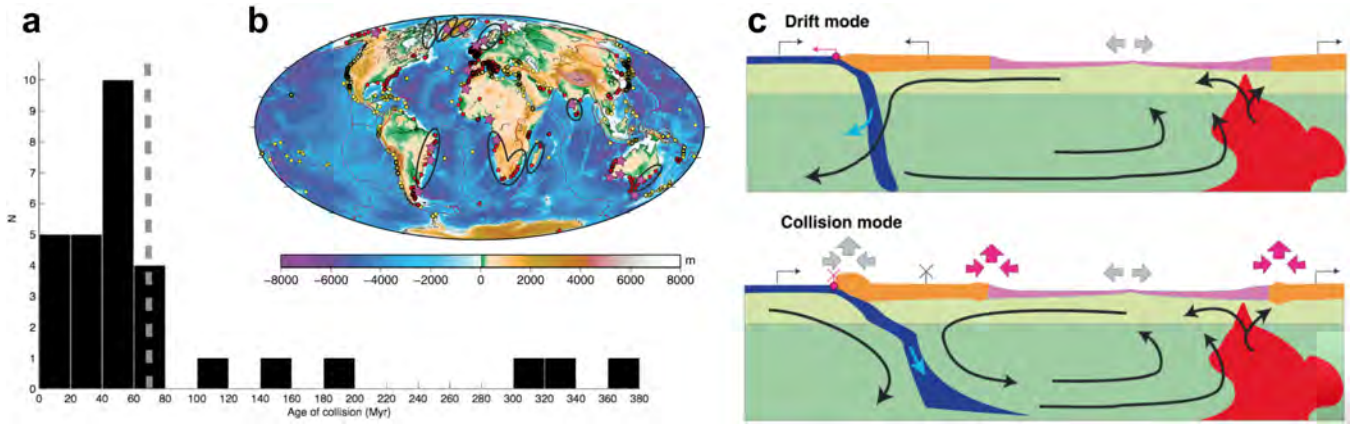

Figure 18 *: Influence des chaînes de montagnes sur la convection mantellique (cf. Yamato et al., 2013).* ***(a)*** *Graphique présentant le nombre des chaînes de collision en fonction de leur âges (d'après Mouthereau et al., 2013) et montrant que celles-ci sont de plus en plus nombreuses depuis la fin du Crétacé.* ***(b)*** *Carte synthétique montrant les marges passives anormalement élevées (ellipses noires, points rouges), exhumées et présentant une inversion tectonique (étoiles violettes) – voir Yamato et al., 2013 pour plus de détails.* ***(c)*** *Schéma présentant le flux de la cellule de convection mantellique lorsque la lithosphère est en libre expansion (drift mode, le slab en subduction recule et accommode la convergence de la lithosphère qui peut bouger librement) ou lorsque celle-ci est bloquée par une chaine de collision (collision mode, le slab en subduction ne recule plus, et la lithosphère se retrouve pris en étau dans la cellule de convection).*

Pour tester cette hypothèse, nous avons réalisé un modèle 2D visqueux où une plaque lithosphérique est placée au dessus du manteau. L'ensemble de ce système est alors soumis à une cellule de convection alternativement excitée par un *downwelling* d'un coté, un *upwelling* de l'autre, ou les deux simultanément (cf. Yamato et al., 2013 pour plus de détails). Afin de simuler les cas de convergence libre (mode Drift, i.e. dont le raccourcissement est accommodé par la subduction) et de collision, le bord gauche de la plaque lithosphérique a été soit laissé libre, soit fixé (Fig. 19a). Cette distinction modifie la condition limite supérieure des modèles, la circulation mantellique et donc le champ de contrainte. Entre ces deux régimes, la forme du flux évolue donc doucement depuis un mode de convection libre (Drift mode) vers une condition où le glissement de la lithosphère au dessus du manteau supérieur n'est plus permise (Collision mode). Dans ce second cas, la lithosphère subit de fortes contraintes horizontales et se déforme (Fig. 19b).

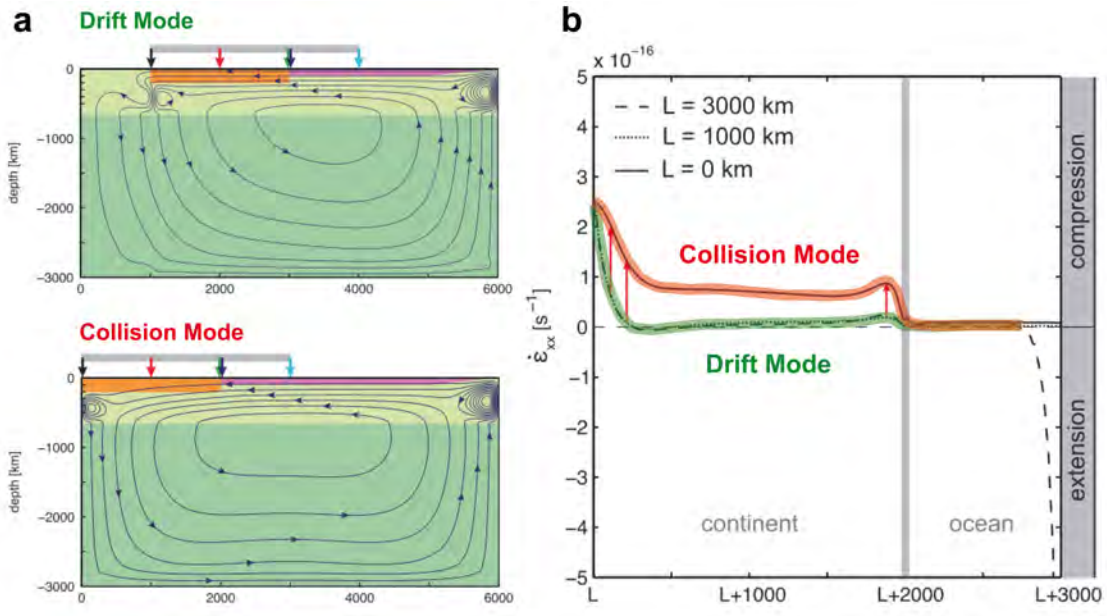

Figure 19 *: Modèles numériques montrant l'effet des chaines de collision sur la convection mantellique et les conséquences sur la compression de la lithosphère (cf. Yamato et al., 2013).* ***(a)*** *Configurations initiales des modèles en mode libre (haut) et en mode bloqué (bas).* ***(b)*** *vitesse de déformation dans la lithosphère continentale lors du passage du mode libre au mode bloqué.*

Nos résultats montrent que pour une force totale imposée donnée, la compression augmente drastiquement au niveau des marges passives si l'*upwelling* est actif. A l'inverse, si seul le *downwelling* est activé, la compression a lieu à courte distance de la fosse, et de l'extension domine partout ailleurs (cf. Yamato et al., 2013). Ils montrent également que la compression des marges passives peut correspondre à une réponse au flux mantellique sous jacent qui tente de résister à la collision qui se produit (Fig. 19). Ces résultats sont par ailleurs supportés par les modèles globaux qui montrent que les *upwellings* actifs sont nécessaires pour exciter la compression des marges passives.

Cet exemple illustre le fait que les chaînes de collision jouent un rôle crucial dans la perturbation de la convection terrestre. Il y a donc un champ d'exploration nouveau qui s'ouvre sur d'autres exemples possibles. En effet, il n'y a aucune raison pour que seules les marges passives se trouvent affectées. D'autres singularités, en limites de plaques, comme les rides ultra-lentes amagmatiques, l'obduction, ou l'initiation de la subduction pourraient être des cas où le rôle des chaînes de collision mériterait d'être examiné avec attention.

5.5. BILAN, PROJETS ET PERSPECTIVES

Le terme de bilan me paraît plus approprié que celui de conclusion. En effet, comme on a pu le voir au travers de la synthèse que je viens de dresser, bon nombre de points sont restés en suspens et il reste de nombreux problèmes dont les enjeux sur la compréhension de la tectonique des plaques peuvent être de premier ordre. Il convient donc, à présent, de résumer ici l'état de l'art de ces travaux, des implications qu'ils peuvent avoir et de s'intéresser aux perspectives et aux projets que je compte mener par la suite. Au final, je distingue trois principales directions de recherche qu'il est possible d'envisager et vers lesquelles je souhaite me tourner dans les années à venir. Certains de ces chantiers sont, d'ailleurs, déjà initiés (cf. articles en préparation, derniers congrès, ou demandes INSU/ANR auxquelles j'émarge).

5.5.1. Zones de cisaillement et limites de plaques

Depuis le début de la thèse de Sylvia Duprat-Oualid et avec les développements réalisés en collaboration avec Benjamin Huet et Pavel Pitra, nous avons progressé. Les résultats de ces travaux sont importants puisqu'il est désormais possible (i) de quantifier proprement le budget thermique des zones de cisaillement et (ii) d'estimer des viscosités effectives pour des roches polyphasées. Ces lois de mélange restent cependant à affiner (prise en compte de la connectivité entre les phases, et de l'agencement spatial des grains, cf. Handy, 1990). Pour cela, nous avons déjà réfléchi à la réalisation de « viscosimètres numériques » permettant de réaliser une étude systématique de ces paramètres. Une étude similaire à celle faite sur la ségrégation des cristaux nous permettrait alors, peut-être, de pouvoir en tenir compte. Avec l'ensemble de ces outils, nous pouvons envisager d'examiner de manière dynamique (en introduisant ces lois dans les modèles thermomécaniques) l'impact des transformations métamorphiques, ou encore de l'introduction de fluides, sur la viscosité effective des roches dans les zones de cisaillement au cours de leur évolution. Pour cela, l'idée est de commencer par s'intéresser à des cibles précises, simples, comme l'exhumation du manteau (dont la composition chimique reste assez simple) en contexte d'extension (travail en cours avec Benjamin Huet) ou encore le développement des zones de cisaillement dans les granites pour lequel nous disposons de données suffisantes pour contraindre les modèles (e.g., Oliot et al., 2010 ; thèse de Sylvia Duprat-Oualid).

Une fois ce travail fait, il sera possible d'envisager le même type d'étude sur des cas un peu plus complexes comme l'interface de subduction par exemple. Les enjeux sont importants en matière de compréhension des processus (de formation et de fonctionnement) aux limites des plaques tectoniques. Un tel projet (soumis à l'Insu avec Samuel Angiboust) permettrait par exemple de comprendre comment les textures brèchiques présentées précédemment (chapitre 5.2.2) se sont formées, quels sont les mécanismes impliqués et quelles en sont les conséquences pour ce qui est de la rhéologie court terme et long terme le long de l'interface de subduction. Ces questions nécessitent un aller-retour entre (i) observations de terrain (cartographie des structures), (ii) observations pétrologiques fines (étude des minéraux impliqués, des recristallisations et des relations microtexturales), (iii) étude de la déformation de l'échelle de l'affleurement à l'échelle microscopique et (iv) compréhension des processus à l'œuvre via la réalisation de modèles numériques. Un stage de M2 est d'ailleurs prévu sur ce sujet l'an prochain.

5.5.2. Transfert de matière dans la lithosphère

Les travaux auxquels j'ai participé ont permis d'avancer sur la compréhension des processus d'exhumation des roches métamorphiques et donc sur le transfert des unités de HP depuis les profondeurs mantelliques jusqu'à la surface. Ils ont permis notamment de différencier les mécanismes intervenant dans l'exhumation en fonction des matériaux impliqués (sédiments, croûte océanique, croûte continentale) et en fonction des contextes géodynamiques (subduction océanique ou continentale). Les implications sont fortes puisque ces résultats permettent d'expliquer la structuration des chaînes de montagnes en surface. Si des efforts ont été fait, en particulier sur le rôle des transferts de fluides, des problèmes résident dans la simplicité des rhéologies utilisées (qui ne prennent pas en compte notamment l'hétérogénéité des roches ou les réactions métamorphiques) ou encore dans la compréhension des processus de découplage de ces unités. Ces problèmes, puisqu'ils sont étroitement liés à la compréhension de la déformation des roches à l'interface de subduction, pourront cependant être étudiés à court terme avec les outils décrits précédemment.

Par ailleurs, mes travaux sur le comportement des cristaux dans les dykes ouvrent, eux aussi, de larges perspectives. Ils ont permis d'en savoir un peu plus sur la façon dont se comporte un magma présentant une charge cristalline et de montrer que le processus de ségrégation était un mécanisme viable (même pour des magmas granitiques) que l'on pouvait quantifier. Cependant, dans ces modèles à petite échelle, des points restent à éclaircir :

- contrairement à ce que des études précédentes ont montré (Bagnold, 1954 ; Bhattacharji & Smith, 1964 ; Barrière, 1976), nous n'observons pas de migration des cristaux depuis les bords du dyke vers le centre. Nous avons montré que cela ne pouvait pas être lié à l'inertie. Il reste donc un élément clé à étudier : le rôle de la température.

- nos modèles considèrent des cristaux qui sont tous de taille identique. Afin de pouvoir appliquer nos résultats à des cas concrets comme la ségrégation des granites (composés de quartz, feldspaths, biotites et plagioclases), une étude avec des cristaux de tailles multiples et de densités différentes mériterait d'être développée. Il serait alors possible de confronter ces modèles avec des données de géochimie qui existent déjà (e.g., Tartèse & Boulvais, 2010).

Le code que j'ai développé en collaboration avec Thibault Duretz permet à présent de prendre en compte la température. Il a été parallélisé afin de pouvoir aller à des résolutions bien plus grandes. Il est donc possible de s'attaquer à ces questions dès à présent. Il permettrait aussi de s'intéresser aux processus de croissance des cristaux au cours du temps, ce qui n'a pas encore été étudié numériquement.

Enfin, ces modèles restent limités à l'étude du magma injecté directement dans un dyke déjà ouvert et dont les bordures sont fixées latéralement. Si l'on veut aller plus loin et étudier le comportement à plus grande échelle, il faut à présent se pencher sur la dynamique d'ouverture des dykes. Cela nécessite de réaliser un saut d'échelle qui peuvent poser des problèmes techniques car de grand contrastes de viscosité sont alors mis en jeu. Cependant, les enjeux sont grands. Cela permettrait notamment d'étudier le transfert de matière au sein de la croûte depuis les processus de migmatitisation localisés à sa base jusqu'à la mise en place des granites ainsi que les causes/conséquences que cela peut avoir d'un point de vue tectonique (affaiblissement rhéologique lié à la présence de migmatites par exemple, e.g., Rosenberg et al., 2007 ; Handy et al., 2001). Ce travail n'en est, pour l'instant, qu'à ses premiers balbutiements (M1 de Solenn Hertgen sur les migmatites de Saint-Malo) mais devrait être développé rapidement.

5.5.3. Déformation lithosphérique et convection mantellique

A l'échelle de la lithosphère, deux points importants se dégagent de ce mémoire. Nous avons vu :

(1) que la rhéologie de la lithosphère (en particulier de la croûte) a un impact drastique sur la dynamique des zones de convergence. Ainsi, qu'il s'agisse des chaînes de montagnes anciennes (chaudes) ou récentes (froides), leur structuration est contrôlée au premier ordre par la rhéologie des lithosphères impliquées.

(2) que la présence des plaques autour de la lithosphère en subduction, notamment de la plaque supérieure, jouait un rôle majeur dans la dynamique des zones de convergence. Cette influence est de plus en plus mise en avant (e.g., Rodríguez-González et al., 2012 ; Butterworth et al., 2012) mais son influence (notamment l'impact de sa partie crustale) sur les systèmes orogéniques demeure largement énigmatique.

L'observation des chaînes de montagnes montre des différences en termes de taille des unités, de présence ou non de plateaux, ou encore en termes de métamorphisme. A chaque fois, la dynamique globale reste la subduction mais les chaînes formées (Alpes, Andes, Egée, Himalaya, etc…) sont uniques, en partie car le degré d'implication de la plaque chevauchante n'est pas le même. Cette influence de la rhéologie des croûtes impliquées dans la structuration des chaînes de montagnes, et en particulier, le rôle de la croûte de la plaque chevauchante reste donc une chose importante à préciser. Il est possible de s'y attaquer concrètement tout en s'appuyant sur des exemples de terrain (Alpes, Andes, Himalaya, Egée,…) où de nombreuses données existent et où une synthèse sur la composition et le degré d'implication de la croûte peut être réalisée.

A plus grande échelle, mes travaux sur la déformation des slabs ou encore sur la compression des marges passives montrent que la déformation de la lithosphère interagit fortement avec le manteau. En ce sens, le problème du déchirement des slabs (qui est en lien direct avec l'étude des zones de cisaillement) constitue un point important qui mériterait aussi maintenant d'être exploré. Nous avons proposé avec Benjamin Guillaume et Jean Pierre Brun, entre autres (cf. demandes ANR soumises), de s'attaquer à ce problème par le biais de modélisations analogiques et/ou numériques sur des cas précis comme le domaine Egéen ou les Bétiques pour lesquels les données de terrain, mais également de

tomographie, nous permettraient de contraindre à la fois les processus mis en jeu lors du cisaillement des slabs dans le manteau et leur comportement rhéologique en profondeur.

Par ailleurs, si les chaînes de montagnes modifient le flux mantellique et ont un impact fort sur la déformation de la lithosphère, il est fort probable que les marges passives ne soient pas les seules affectées. Mes derniers travaux en cours sur cette thématique, réalisés en collaboration avec Laurent Husson, montrent qu'elles pourraient également jouer un rôle important pour expliquer d'autres singularités comme l'obduction, l'initiation de la subduction, ou encore les rides ultra-lentes amagmatiques (cf. abstract EGU 2014).

5.6. S'IL FALLAIT CONCLURE…

Les différentes pistes de recherche que je souhaite mener sont donc étroitement liées et il est à mon avis possible de s'y attaquer avec la même démarche méthodologique et analytique qui est le couplage entre les observations de terrain (il ne faut pas oublier que beaucoup de questions se posent sur le terrain !) et les modèles. Avec les nouveaux développements du code numérique que je possède, réalisés en collaboration avec Thibault Duretz, il est possible de s'y attaquer.

Par ailleurs, toutes ces études montrent qu'il apparait difficile de prétendre comprendre le grand uniquement en regardant le petit. C'est pour cette raison que je suis convaincu qu'il ne faut pas uniquement s'attaquer aux problèmes dans un sens unique. En regardant l'ensemble de ces aspects à différentes échelles, il est probablement possible d'aller plus loin dans la compréhension de la dynamique de la lithosphère au premier ordre.

Comprendre *comment se déforment les roches dans le temps et dans l'espace?*, quelle qu'en soit l'échelle ou les cibles d'applications, cette même question subsiste… Elle est pourtant indispensable à la compréhension du système Terre. C'est donc peut-être ce qui définit le mieux le travail de recherche que je compte poursuivre.

6. BIBLIOGRAPHIE

Abers G.A., van Keken P.E., Kneller E.A., Ferris A., & Stachnik J.C., 2006. The thermal structure of subduction zones constrained by seismic imaging: implications for slab dehydration and wedge flow. *Earth and Planetary Science Letters,* v.241(3-4), p.387–397.

Agard P., Yamato P., Jolivet L. & Burov E., 2009. Exhumation of oceanic blueschists and eclogites in subduction zones: timing and mechanisms, *Earth Science Reviews*, v.92, p.53-79, doi: 10.1016/j.earscirev.2008.11.02

Alavi M., 2004. Regional stratigraphy of the Zagros fold-thrust belt of Iran and its proforeland evolution. *American Journal of Science*, v.304, p.1–20, doi:10.2475/ajs.304.1.1.

Angiboust S., Agard P., Jolivet L., & Beyssac O., 2009. The Zermatt-Saas ophiolite: the largest (60-km wide) and deepest (c. 70–80 km) continuous slice of oceanic lithosphere detached from a subduction zone? *Terra Nova,* v.21, p.171–180.

Angiboust S., Agard P., Raimbourg H., Yamato P., & Huet B., 2011. Subduction interface processes recorded by eclogite-facies shear zones (Monviso, W. Alps), *Lithos*, v.127, p.222-238, doi:10.1016/j.lithos.2011.09.004

Angiboust S., Agard P., Yamato P., & Raimbourg H., 2012a. Eclogite breccias in a subducted ophiolite: a record of intermediate-depth earthquakes?, *Geology*, v.40, p.707-710, doi:10.1130/G32925.1

Angiboust S., Wolf S., Burov E., Agard P., & Yamato P., 2012b. Effect of Fluid Circulation on Subduction Interface Tectonic Processes: Insights from Thermo-mechanical Numerical Modelling, *Earth and Planetary Science Letters*, v.357-358, p.238-248, doi:10.1016/j.epsl.2012.09.012

Apperson K. D., & Frohlich C., 1987. The relationship between Wadati-Benioff Zone geometry and P, T and B axes of intermediate and deep focus earthquakes, *J. Geophys. Res.*, v.92(B13), p.13821–13831, doi:10.1029/JB092iB13p13821.

Arita K., 1983. Origin of the inverted metamorphism of the lower Himalayas, Central Nepal. *Tectonophysics,* v.95(1–2), p.43–60.

Arzi A., 1978. Critical phenomena in the rheology of partially melted rocks. *Tectonophysics*, v.44, p.173–184.

Bagdassarov N., & Dorfman A., 1998. Granite rheology: magma flow and melt migration. *J. Geol. Soc.,* v.155, p.863–872.

Bagnold R.A., 1954. Experiments on a gravity-free dispersion of large solid spheres in a Newtonian fluid under shear. *R. Soc. Lond. Proc.,* v.225, p.49–63.

Ballouard C., Boulvais P., Poujol M., Gapais D., Yamato P., Tartèse R., & Cuney M., soumis. Tectonic record, magmatic history and hydrothermal alteration in the Hercynian Guérande leucogranite, Armorican Massif, France, *Lithos*.

Barrière M., 1976. Flowage differentiation: limitation of the “Bagnold effect” to the narrow intrusions. *Contrib. Mineral. Petrol.,* v.55, p.139–145.

Bhattacharji S., & Smith C.H., 1964. Flowage Differentiation, *Science*, v.145(3628), p.150-153.

Bijwaard H., Spakman W., & Engdahl E.R., 1998. Closing the gap between regional and global travel time tomography, *J. Geophys. Res.*, v.103(B12), p.30055–30078, doi:10.1029/98JB02467.

Bollinger L., Henry P., & Avouac J.P., 2006. Mountain building in the Nepal Himalaya: thermal and kinematic model. *Earth Planet. Sci. Lett.*, v.244, p.58–71.

Braun J., Thieulot C., Fullsack P., DeKool M., Beaumont C., & Huismans R., 2008. DOUAR: a new three-dimensional creeping flow model for the solution of geological problems, *Physics of the Earth and Planetary Interiors*, v.171, p.76-91.

Braun J., & Yamato P., 2010. Multi-scale couplings between surface processes and deformation of a three-dimensional orogenic wedge, *Tectonophysics*, v.484(1-4), p.181-192, doi:10.1016/j.tecto.2009.08.032.

Brewer J., 1981. Thermal effects of thrust faulting, *Earth and Planetary Science Letters*, v.56, p.233–244.

Brun J.P., & Cobbold P.R., 1980. Strain heating and thermal softening in continental shear zones: a review, *J. Struct. Geol.,* v.2(1,2), p.149–158.

Brun J.P., & Faccenna C., 2008. Exhumation of high-pressure rocks driven by slab rollback, *Earth planet. Sci. Lett.*, v.272, p.1-7, doi:10.1016/j.epsl.2008.02.038.

Burg J.P., Leyreloup A., Marchand J., & Matte P., 1984. Inverted metamorphic zonation and large-scale thrusting in the Variscan Belt: an example in the French Massif Central, *Geol. Soc. Lond. Spec. Publ.,* v.14(1), p. 47–61.

Bürgmann R., & Dresen G., 2008. Rheology of the Lower Crust and Upper Mantle: Evidence from Rock Mechanics, Geodesy, and Field Observations, *Annual Reviews in Earth and Planetary Sciences*, v.36, p.531-567.

Burov E., Francois T., Yamato P., & Wolf S., 2014a. Mechanisms of continental subduction and exhumation of HP and UHP rocks, *Gondwana Research*, v.25, p.464-493, doi:10.1016/j.gr.2012.09.010

Burov E., Francois T., Agard P., Le Pourhiet L., Meyer B., Tirel C., Lebedev S., Yamato P., & Brun J.-P., 2014b. Rheological and geodynamic controls on the mechanisms of subduction and HP/UHP exhumation of crustal rocks during continental collision: Insights from numerical models, *Tectonophysics*, sous presse.

Burov E.B., 2011. Rheology and strength of the lithosphere, *Marine and Petroleum Geology*, v.28, p.1402-1443

Butterworth N. P., Quevedo L., Morra G., & Müller R.D., 2012. Influence of overriding plate geometry and rheology on subduction, *Geochem. Geophys. Geosyst.*, v.13, Q06W15, doi:10.1029/2011GC003968.

Caricchi, L., Burlini, L., Ulmer, P., Gerya, T., Vassalli, M., & Papale, P., 2007. Non-Newtonian rheology of crystal-bearing magmas and implications for magma ascent dynamics, *Earth Planet. Sci. Lett.,* v.264, p.402–419.

Castelltort S., & Yamato P., 2013. The influence of surface slope on the shape of river basins: Comparison between nature and numerical landscape simulations", *Geomorphology*, v.191, p.71-79, doi: 10.1016/j.geomorph.2013.03.022.

Chistyakova, S., Latypov, R., 2010. On the development of internal chemical zonations in small mafic dykes, *Geol. Mag*., v.147, p.1–12.

Colman-Sadd S. P., 1978. Fold development in Zagros Simply Folded Belt, southwest Iran, *AAPG Bull.*, v.62, p.984–1003.

Dingwell, D.B., 1996. Volcanic dilemma: flow or blow?, *Science,* v.273, p.1054–1055.

Duprat-Oualid S., Yamato P., & Pitra P., 2013. Major role of shear heating in intracontinental inverted metamorphism: Inference from a thermo-kinematic parametric study, *Tectonophysics*, v.608, p.812-831, doi:10.1016/j.tecto.2013.07.037

Duprat-Oualid S., Yamato P., & Schmalholz S.M., soumis. A dimensional analysis to quantify the thermal budget around lithospheric-scale shear zones, *Terra Nova*.

England P., & Molnar P., 1993. The interpretation of inverted metamorphic isograds using simple physical calculations, *Tectonics,* v.12(1), p.145–157.

Faccenda M., Gerya T.V., Mancktelow N.S., Moresi L., 2012. Fluid flow during slab unbending and dehydration: implications for intermediate-depth seismicity, slab weakening and deep water recycling, *Geochem. Geophys. Geosyst.,* v.13, Q01010.

Fleitout L. & Froidevaux C. 1980. Thermal and mechanical evolution of shear zones, *J. Struct. Geol.*, v.2, p.159-164.

Fukao Y., Widiyantoro S., Obayashi M., 2001. Stagnant slabs in the upper and lower mantle transition region, *Rev. Geophys.*, v.39(3), p.291–323, doi:10.1029/1999RG000068.

Fuller C., Willett S.D., Fischer D., & Lu C.-Y., 2006. A thermomechanical wedge model of Taiwan constrained by fission-track thermochronometry, *Tectonophysics*, v.425, p.1–24.

Goncalves P., Oliot E., Marquer D., & Connolly J.A.D., 2012. Role of chemical processes on shear zone formation : an example from the Grimsel metagranodiorite (Aar massif, Central Alps), *Journal of Metamorphic Geology*, v.30, p.703-722.

Green H.W.I., & Houston H., 1995. The mechanics of deep earthquakes, *Annual Review of Earth and Planetary Sciences*, v.23, p.169–213, doi:10.1146/annurev.ea.23.050195.001125.

Griffiths R.W., & Turner J.S., 1988. Folding of viscous plumes impinging on a density or viscosity interface, *Geophysical Journal*, v.95(2), p.397-419.

Guillot S. Hattori K., Agard P., Schwartz S., & Vidal, O., 2009. Exhumation processes in oceanic and continental subduction contexts : a review. In S. Lallemand and F. Funiciello (eds.) Subduction Zone Dynamics, p.175-204, doi 10.1007/978-3-540-87974-9, Springer-Verlag Berlin Heidelberg.

Hacker B.R., Peacock S.M., Abers G.A., & Holloway S.D., 2003. Subduction factory 2. Are intermediate-depth earthquakes in subducting slabs linked to metamorphic dehydration reactions?, *Journal of Geophysical Research*, v.108, p.2030, doi:10.1029/2001JB001129.

Handy M.R., 1990. The solid-state flow of polymineralic rocks, *Journal of Geophysical Research*, v.95(B6), p. 8647-8661.

Handy M.R., Mulch A., Rosenau M., and Rosenberg C.L., 2001. A synthesis of the role of fault zones and melts as agents of weakening, hardening and differentiation of the continental crust. In : The nature and Tectonic Significance of Fault Zone Weakening, ed. R.E. Holdsworth et al., *Geol. Soc. of London Spec. Publ.*, v.*186*, p. 305-332.

Hatzfeld D., & Molnar P., 2010. Comparisons of the kinematics and deep structures of the Zagros and Himalaya and of the Iranian and Tibetan plateaus and geodynamic implications, *Review of Geophysics*, v.48, RG2005, doi:10.1029/2009RG000304.

Healy D., Reddy S.M., Timms N.E., Gray E.M., Brovarone A.V., 2009. Trench-parallel fast axes of seismic anisotropy due to fluid-filled cracks in subducting slabs, *Earth and Planetary Science Letters,* v.283(1–4), p.75–86.

Heard H.C., 1976. Comparison of the flow properties of rocks at crustal conditions, *Phil. Trans. R. Soc.,* v.A283, p.173-816.

Henry P., Le Pichon X., & Goffe B., 1997. Kinematic, thermal and petrological model of the Himalayas: constraints related to metamorphism within the underthrust Indian crust and topographic elevation, *Tectonophysics,* v.273(1–2), p.31–56.

Huerta A.D., Royden L.H., & Hodges K.V., 1998. The thermal structure of collisional orogens as a response to accretion, erosion, and radiogenic heating, *J. Geophys. Res. Solid Earth*, v.103, p.15287–15302.

Huet B., Yamato P., & Grasemann B., 2014. The Minimized Power Geometric model: an analytical mixing model for calculating polyphase rock viscosities consistent with experimental data, *J. Geophys. Res. Solid Earth*, v.119, doi:10.1002/2013JB010453

Husson L., Brun J.P., Yamato P., & Faccenna C., 2009. Episodic slab rollback fosters HP-UHP rocks exhumation, *Geophysical Journal International*, v.179, p.1292-1300, doi:10.1111/j.1365-246X.2009.04372.x

Huismans R.S., Buiter S.J.H., & Beaumont C., 2005. Effect of plastic-viscous layering and strain softening on mode selection during lithospheric extension, *Journal of Geophysical Research*, v.110, B02406, doi:10.1029/2004JB003114.

Isacks B., & Molnar P., 1969. Mantle earthquake mechanisms and the sinking of the lithosphere, *Nature*, v.223, p.1121–1124.

Jahani S., Callot J.P., Letouzey J., & Frizon de Lamotte D., 2009. The eastern termination of the Zagros Fold-and-Thrust Belt, Iran: Structures, evolution, and relationships between salt plugs, folding, and faulting, *Tectonics*, v.28, TC6004, doi:10.1029/2008TC002418.

Jamieson R.A., Beaumont C., Hamilton J., & Fullsack P., 1996. Tectonic assembly of inverted metamorphic sequences, *Geology*, v.24(9), p.839–842.

Jamieson R.A., Beaumont C., Medvedev S., Nguyen M.H., 2004. Crustal channel flows: 2. Numerical models with implications for metamorphism in the Himalayan–Tibetan orogen, *J. Geophys. Res.*, v.109, B06407.

Jessell, M.W., Bons, P.D., Griera, A., Evans, L.A., & Wilson, C.J.L, 2009. A tale of two viscosities, *Journal of Structural Geology*, v.31, p.719-736.

Ji, S. C., Wang, Z., & Wirth, R., 2001. Bulk flow strength of forsterite-enstatite composites as a function of forsterite content, *Tectonophysics*, v.341, p.69–93.

Ji, S., 2004. A generalized mixture rule for estimating the viscosity of solid-liquid suspensions and mechanical properties of polyphase rocks and composite materials, *Journal of Geophysical Research*, v.109, doi:10.1029/2004JB003124.

Jiang Y., Zang S., & Wei R., 2005. Decibel error test and flow law of multiphase rocks based on energy dissipation theory, *Earth Planet. Sci. Lett.*, v.235, p.200–210.

John T., & Schenk V., 2006. Interrelations between intermediate-depth earthquakes and fluid flow within subducting oceanic plates: constraints from eclogite facies pseudotachylytes, *Geology,* v.34(7), p.557–560.

Kohn M.J., 2008. P–T–t data from central Nepal support critical taper and repudiate large-scale channel flow of the Greater Himalayan sequence. *Geol. Soc. Am. Bull.,* v.120(3-4), p.259–273.

Li, C., van der Hilst R. D., Engdahl E. R., & Burdick S., 2008. A new global model for P wave speed variations in Earth's mantle, *Geochem. Geophys. Geosyst.*, v.9, Q05018, doi:10.1029/2007GC001806.

Loiselet C., Braun J., Husson L., Le Carlier de Veslud C., Thieulot C., Yamato P. & Grujic D., 2010. Subducting slabs: jellyfishes in the Earth's mantle, *Geochemistry Geophysical Geosystems*, v.11, Q08016, doi:10.1029/2010GC003172

Marques, F.O., Burlini L., & Burg J.P., 2011. Microstructural and mechanical effects of strong fine-grained muscovite in soft halite matrix: Shear strain localization in torsion, *Journal of Geophysical Research*, v.116, doi:10.1029/2010JB008080.

McQuarrie N., 2004, Crustal scale geometry of the Zagros fold-thrust belt, Iran. *Journal of Structural Geology*, v. 26, p. 519–535, doi:10.1016/ j.jsg.2003.08.009.

Molinari A., Canova G.R., & Ahzi S., 1987. A self-consistent approach of the large deformation polycrystal viscoplasticity, *Acta Metalurgica*, v.35, p.2983-2994.

Molnar P., & England P., 1990. Temperatures, heat flux, and frictional stress near major thrust faults, *Journal of Geophysical Research*, v.95(B4), p.4833–4856.

Moresi L., & Solomatov V., 1998. Mantle convection with a brittle lithosphere: Thoughts on the global tectonic styles of Earth and Venus, *Geophys. J. Int.*, v.133, p.669–682.

Mouthereau F., Lacombe O., & Meyer B., 2006. The Zagros folded belt (Fars, Iran): Constraints from topography and critical wedge modelling, *Geophysical Journal International*, v.165, p.336– 356, doi:10.1111/j.1365-246X.2006.02855.x.

Mouthereau F., Tensi J., Bellahsen N., Lacombe O., De Boisgrollier T., & Kargar S., 2007. Tertiary sequence of deformation in a thin skinned/thick skinned collision belt: The Zagros Folded Belt (Fars, Iran), *Tectonics*, v.26, TC5006, doi:10.1029/2007TC002098.

Mouthereau F., Watts A.B., & Burov E., 2013. Structure of orogenic belts contolled by lithosphere age, *Nature geoscience*, v.6(9), p.785-789, doi:10.1038/ngeo1902.

Nissen E., Yamini-Fard F., Tatar M., Gholamzadeh A., Bergman E., Elliott J.R., Jackson J.A., & Parsons, B., 2010. The vertical separation of mainshock rupture and microseismicity at Qeshm island in the Zagros fold-and-thrust belt, Iran, *Earth and Planetary Science Letters*, v.296, p.181–194, doi:10.1016/j.epsl.2010.04.049.

Oliot E., Goncalves P., & Marquer D., 2010. Role of plagioclase and reaction softening in a metagranite shear zone at mid-crustal conditions (Gotthard Massif, Swiss Central Alps), *Journal of Metamorphic Geology*, v.28, p.849–871.

Oncken, O., & ANCORP working group, 2003. Seismic imaging of a convergent continental margin and plateau in the central Andes (Andean Continental Research Project 1996 (ANCORP'96)), *Journal of Geophysical Research,* v.108(B7), p.2328.

Paterson, S.R., 2009. Magmatic tubes, pipes, troughs, diapirs, and plumes: late-stage convective instabilities resulting in compositional diversity and permeable networks in crystal-rich magmas of the Tuolumne batholith, Sierra Nevada, California, *Geosphere,* v.5, p.496–527.

Petford N., & Koenders MA, 1998. Granular flow and viscous fluctuations in low Bagnold number granitic magmas, *J. Geol. Soc. London,* v.155, p.873–881.

Philpotts A.R., 1990. Principles of Igneous and Metamorphic Petrology. New Jersey: Prentice Hall. 498 pp.

Pitra P., Ballèvre M., & Ruffet G., 2010. Inverted metamorphic field gradient towards a Variscan suture zone (Champtoceaux Complex, Armorican Massif, France), *J. Metamorph. Geol.*, v.28, p.183–208.

Ribe, N.M., Stutzmann E., Ren Y., & van der Hilst R., 2007. Buckling instabilities of subducted lithosphere beneath the transition zone, *Earth and Planetary Science Letters,* v.254, p.173–179.

Rodríguez-González, J., Negredo A. M., & Billen M. I., 2012. The role of the overriding plate thermal state on slab dip variability and on the occurrence of flat subduction, *Geochem. Geophys. Geosyst.*, v.13, Q01002, doi:10.1029/2011GC003859.

Rosenberg C., Medvedev S., & Handy M.R., 2007. On the effects of melting on continental deformation and faulting, in Tectonic faults : agents of change on a dynamic earth, edited by M.R. Handy et al., Dahlem workshop reports, MIT press.

Sassier C., Boulvais P., Gapais D., Capdevila R., & Diot H., 2006. From granitoid to kyanite-bearing micaschist during fluid-assisted shearing (Ile d'Yeu, France, *International Journal of Earth Sciences*, v.95, p.2-18.

Sepehr M., Cosgrove J., & Moieni M., 2006. The impact of cover rock rheology on the style of folding in the Zagros fold-thrust belt, *Tectonophysics*, v.427, p.265-281.

Sherkati S., & Letouzey J., 2004. Variation of structural style and basin evolution in the central Zagros (Izeh zone and Dezful embayment): Iran, *Marine and Petroleum Geology*, v.21, p.535-554, doi:10.1016/j.marpetgeo.2004.01.007.

Sherkati S., Letouzey J., & Frizon de Lamotte D., 2006. Central Zagros fold-thrust belt (Iran): New insights from seismic data, field observation, and sandbox modelling, *Tectonics*, v.25, TC4007, doi:10.1029/2004TC001766.

Simoes M., Avouac J.-P., Beyssac O., Goffe B., Farley K.A., & Chen Y.-G., 2007. Mountain building in Taiwan: a thermokinematic model, *J. Geophys. Res.*, v.112(B11405), doi:10.1029/2006JB004824.

Smith, J.V., 2002. Structural analysis of f low-related textures in lavas. *Earth Sci. Rev.,* v.57, p.279–297.

Stegman D. R., Freeman J., Schellart W. P., Moresi L., & May D., 2006. Influence of trench width on subduction hinge retreat rates in 3-D models of slab rollback, *Geochem. Geophys. Geosyst.*, v.7, Q03012, doi:10.1029/ 2005GC001056.

Stewart J., 2002. Calculus, 5th ed., Brooks Cole, Pacific Grove, Calif.

Stocklin J., 1968, Structural history and tectonics of Iran; a review, *American Association of Petroleum Geologists Bulletin*, v.52, p.1229–1258.

Taisne, B., & Jaupart, C., 2011. Magma expansion and fragmentation in a propagating dyke, *Earth Planet. Sci. Lett.,* v.301, p.146–152.

Tartèse, R., & Boulvais, P., 2010. Differentiation of peraluminous granites “en route” to the surface. *Lithos,* v.114, p.353–358.

Tartèse R., Poujol M., Ruffet G., Boulvais P., Yamato P., & Košler J., 2011. New U-Pb zircon and $^{40}Ar/^{39}Ar$ muscovite age constraints on the emplacement of the Lizio syn-tectonic granite (Armorican Massif, France), *Comptes Rendus Géoscience*, v.343, p.443-453, doi:10.1016/j.crte.2011.07.005

Vassiliou, M. S., Hager B. H., & Raefsky A., 1984. The distribution of earthquakes with depth and stress in subducting slabs, *J. Geodyn.*, v.1(1), p.11–28, doi:10.1016/0264-3707(84) 90004-8.

Vitale-Brovarone A., Beltrando M., Malavieille J., Giuntoli F., Tondella E., Groppo C., Beyssac O., & Compagnoni R., 2011. Inherited ocean–continent Transition zones in deeply subducted terranes: insights from Alpine Corsica, *Lithos,* v.124, p.273–290.

Yamasaki T., and Seno T., 2003, Double seismic zone and dehydration embrittlement of the subducting slab. *Journal of Geophysical Research*, v.108, p.2212, doi:10.1029/2002JB001918.

Yamato P., 2006. Des contraintes pour les zones de convergence : confrontation des données du métamorphisme et des modelisations numériques thermomécaniques – application aux Alpes et à l’Oman. Thèse de 3ème cycle. Académie de Paris, Université Pierre et Marie Curie.

Yamato P., Agard P., Burov E., Le Pourhiet L., Jolivet L., & Tiberi C., 2007. Burial and exhumation in a subduction wedge: Mutual constraints from thermomechanical modeling and natural P-T-t data (Sch. Lustrés, western Alps), *Journal of Geophysical Research*, v.112, B07410, doi: 10.1029/2006JB004441

Yamato P., Burov E., Agard P., Le Pourhiet L., & Jolivet L., 2008. HP-UHP exhumation during slow continental subduction: Self-consistent thermodynamically and thermomechanically coupled model with application to the Western Alps, *Earth and Planetary Science Letters*, v.271, p.63-74, doi: 10.1016/j.epsl.2008.03.049

Yamato P., Husson L., Braun J., Loiselet C. & Thieulot C., 2009a. Influence of surrounding plates on 3D subduction dynamics, *Geophysical Research Letters*, v.36, L07303, doi: 10.1029/2008GL036942

Yamato P., Mouthereau F., & Burov E., 2009b. Taiwan mountain building: insight from 2D thermomechanical modeling of a rheologically-stratified lithosphere, *Geophysical Journal International*, v.176(1), p.307-326, doi: 10.1111/j.1365-246X.2008.03977.x

Yamato P., Kaus B.J.P., Mouthereau F., & Castelltort S., 2011. Dynamic constraints on the crustal-scale rheology of the Zagros fold belt, Iran, *Geology*, v.39, p.815-818, doi:10.1130/G32136.1

Yamato P., Tartèse R., Duretz T., & May D.A., 2012. Numerical modelling of magma transport in dykes, *Tectonophysics*, v.526-529, p.97-109, doi:10.1016/j.tecto.2011.05.015

Yamato P., Husson L., Becker T.W., & Pedoja K., 2013. Passive margins getting squeezed in the mantle convection vice, *Tectonics*, v.32, p.1559-1570, doi:10.1002/2013TC003375

Yamato P., Duretz T., May D.A., & Tartèse R., soumis. Quantifying magma segregation in dykes, *Earth and Planetary Science Letters.*

Yuen D.A., Fleitout L., Schubert G., & Froidevaux C., 1978. Shear deformation zones along major transform faults and subducting slabs, *Geophys. J. R. astr. Soc.*, v.54, p.93-119.

Zhao D., Mishra O.P., Sanda R., 2002. Influence of fluids and magma on earthquakes: seismological evidence. *Physics of The Earth and Planetary Interiors,* v.132(4), p.249–267

Zhou S., 1995. Bounds on steady state flow strengths of multiphase rocks: theory and test with experimental data. *Journal of Geodynamics*, v.20, p.199-217.

Mémoire d'Habilitation à Diriger des Recherches

Université de Rennes 1

Comportement mécanique des roches et dynamique de la lithosphère: Des données de terrain aux modèles numériques

Philippe YAMATO

Maître de Conférences

Géosciences Rennes, UMR UR1/CNRS 6118

(VOLUME ANNEXE – Sélection d'articles)

SOUTENANCE PREVUE LE 27 NOVEMBRE 2014 DEVANT LE JURY COMPOSE DE :

Anne DAVAILLE	*Université de Paris Sud, Paris*
Luce FLEITOUT	*Ecole Normale Supérieure, Paris*
Denis GAPAIS	*Géosciences Rennes, Rennes*
Taras GERYA	*ETH, Zürich*
Claudio ROSENBERG	*Université Pierre et Marie Curie, Paris*
Jeroen VAN HUNEN	*Durham University, Durham*

SOMMAIRE

Sélection des publications auxquelles j'ai participé et qui sont mentionnés afin d'illustrer mes propos pour ce mémoire d'habilitation à diriger des recherches (cf. volume principal). Cette liste d'articles est ici classée par ordre chronologique :

Autres articles (depuis 2010):

Earth and Planetary Science Letters 271 (2008) 63–74

Contents lists available at ScienceDirect

Earth and Planetary Science Letters

journal homepage: www.elsevier.com/locate/epsl

HP-UHP exhumation during slow continental subduction: Self-consistent thermodynamically and thermomechanically coupled model with application to the Western Alps

P. Yamato [a,b,*], E. Burov [a], P. Agard [a], L. Le Pourhiet [a], L. Jolivet [a]

[a] Laboratoire de Tectonique, Université Pierre et Marie Curie-Paris 6, CNRS, UCP, Case 129-4 place Jussieu 75252 Paris, France
[b] Now at Geosciences Rennes, UMR 6118 CNRS, Université de Rennes 1, Rennes, France

ARTICLE INFO

Article history:
Received 18 June 2007
Received in revised form 20 March 2008
Accepted 23 March 2008
Available online 9 April 2008

Editor: R.D. van der Hilst

Keywords:
Western Alps
HP-UHP rocks
exhumation processes
thermomechanical modeling
exhumation rates
rheology

ABSTRACT

The exhumation of ultra-high pressure (UHP) crustal material often occurs at the rear of sedimentary accretion wedges (e.g., Alps, Himalaya, Norway). However, the mechanisms of deep (>100 km) burial in slow (<1–2 cm yr^{-1}) continental collision zones, where thermal diffusion competes with advection, resulting in weak slabs and Rayleigh-Taylor instabilities, may be different from those inferred from common kinematic models that are more applicable to fast convergence. In this study, we provide a thermodynamically and thermomechanically consistent numerical model explaining the mechanisms of exhumation of continental material in slow convergence zones such as the well-studied Western Alps. The results of the experiments are compatible with topographic and structural observations, and with pressure and temperature estimates from metamorphic petrology studies. The reported bimodal exhumation rate of HP rocks, fast at the initial (>10 mm yr^{-1}) and slow at the later stage (<4 mm yr^{-1}), is also well reproduced. The presence of a double-layered continental crust in the subducting plate leads to self-localization of non-predefined crustal splitting zones at the level of the brittle-ductile transition, from which the low-density continental material is exhumed. We conclude that syn-convergent exhumation at the rear of the accretionary wedge is a transient process (~10 Myr) largely controlled by buoyancy forces in the depth interval of 100–35 km, and by erosion at shallower depths, without significant impact from slab break-off.

1. Introduction

Most subduction-related HP-UHP metamorphic continental rocks (Liou et al., 2004; e.g., Alps, Dabie-Sulu, Himalaya, Norway) occur in zones of intracontinental collision. Although the transition from oceanic to continental subduction seems to be a continuous phenomenon (e.g., Lallemand et al., 2005), introduction of lighter continental material in the subduction zone is the source of strong buoyancy contrasts largely responsible for their exhumation, as shown by several analogue and numerical modeling studies (e.g., Burov et al., 2001; Burov and Yamato, 2007; Chemenda et al., 1995).

Interesting points about this type of metamorphism include the fact that: (1) exhumed continental material appears to be buried beyond lithospheric depths (>100–150 km; e.g., Liou et al., 2004; Chopin, 1984; Green, 2005). (2) Continental exhumation processes are short-lived, lasting ~10 Myr (e.g., Guillot et al., 2007; Hacker, 2007) and burial/exhumation processes for continental material are thus transient. (3) Such exhumation generally involves only a small quantity of material, as suggested by the small surface exposures of most UHP terrains (e.g. <2000 km^2 in the internal crystalline massifs of the Western Alps, Fig. 1). These areas are almost invariably exhumed as lenses of highly metamorphosed material included in less metamorphosed terrains (e.g., Guillot et al., 2007; Avigad et al., 2003; Jolivet et al., 2005), except for the Western Gneiss in Norway (Root et al., 2005) and the Dabie-Hong'an block (Hacker et al., 2000). (4) Exhumation rates for the continental material are higher than for metamorphosed oceanic crust and sediments (Agard et al., in press; Duchêne et al., 1997), at least during the first stages of exhumation. For slow convergence zones, these rates often largely exceed not only the denudation rates but also the rock uplift rates inferred from the convergence rates and common kinematical models of accretion and subduction. This definitely implies some additional mechanisms for this exhumation stage. For example, for the Dora Maira unit (Western Alps), exhumation rates reached 34 mm yr^{-1} (i.e., several times the convergence rate, Rubatto and Hermann, 2001) before later decreasing to 16 mm yr^{-1} and then to 5 mm yr^{-1}. A similar evolution of exhumation rates was found for Norway (~10–11 mm yr^{-1}, Carswell et al., 2003; Terry et al., 2000), Himalaya (30 to 80 mm yr^{-1}, Hermann et al., 2001; O'Brien et al., 2001; Parrish et al., 2006), Betic Cordillera

* Corresponding author. Laboratoire de Tectonique, Université Pierre et Marie Curie-Paris 6, CNRS, UCP, Case 129-4 place Jussieu 75252 Paris, France. Tel.: +33 2 23 23 60 95; fax: +33 2 23 23 67 80.
E-mail address: philippe.yamato.rennes1@gmail.com (P. Yamato).

0012-821X/$ – see front matter © 2008 Elsevier B.V. All rights reserved.
doi:10.1016/j.epsl.2008.03.049

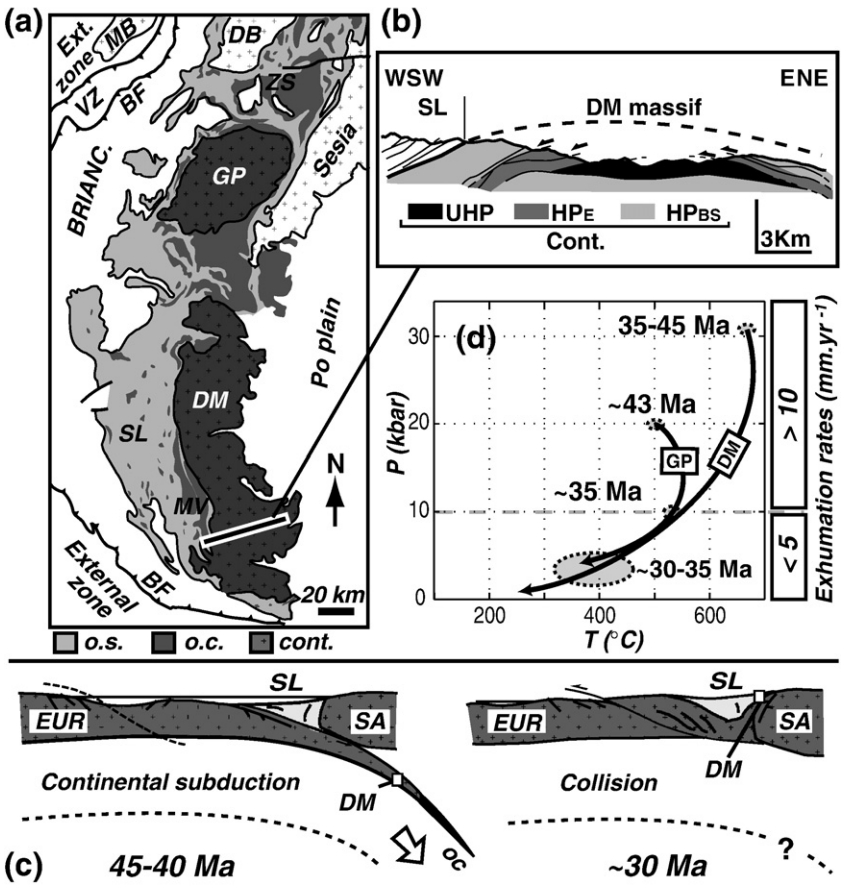

Fig. 1. Compiled data for the continental units from the western Alps. (a) Localisation of the continental (cont.), oceanic crust (o.c.) and sedimentary (sed.) units. (b) Schematic cross-section through the Dora Maira massif (after Henry et al., 1993) showing the lenses of UHP rocks within les metamorphosed units (HPE: high-pressure eclogites; HPBS: high-pressure blueschists). (c) Simplified evolution of the European passive margin continental subduction (Eocene) toward collision stage (Oligo–Miocene). Adapted from (Agard and Lemoine, 2005). (d) *P–T–t* path evolution for the continental units and exhumation rates estimates. Data are taken from (Duchêne et al., 1997; Le Bayon and Ballèvre, 2006; Henry et al., 1993). Abbreviations: Brianc., Briançonnais; DB, Dent Blanche; DM, Dora Maira; EUR, European margin; GP, Gran Paradiso; MB, Mont Blanc; MV, Monviso; SA, southern Alps; SL, Schistes Lustrés; VZ, Valais zone; ZS, Zermatt-Saas.

(22.5 mm yr^{-1}, De Jong, 2003) and Papua-New Guinea (>17 mm yr^{-1}, Baldwin et al., 2004). In all cases, the later rates decrease to values lower than 10 mm yr^{-1} (e.g., Terry et al., 2000; De Jong, 2003).

For these reasons, the first aim of this study is to build an unconstrained numerical thermomechanical (self-consistent) model explaining the most enigmatic first-order features of continental exhumation processes, with a particular focus on slow convergence zones. Indeed, these zones are expected to exhibit more complex behaviour and more deviations from the conceptual kinematic models of subduction since in the case of slow convergence, the system Peclet numbers (Pe, ratio of advection to diffusion time scale) may fall below 10 suggesting that continental subduction needed for burial of HP rocks is only marginally possible and may be associated with gravitational instabilities or should be highly short-lived (Toussaint et al., 2004).

The Western Alps were chosen because of the wealth of available data that can be used to constrain our models. The new experimental approach is needed to circumvent typical drawbacks of previous models of continental exhumation. For example, the analogue models (e.g., Chemenda et al., 1995) predict the exhumation of crustal-scale rock volumes, which is not generally observed in natural settings. These models are not thermally coupled and thus do not allow to account for important thermally controlled properties, such as slab strength and buoyancy, or for comparisons with *P–T* data. Numerical models reproducing some of the major characteristics of the Alpine belt structure were published by Pfiffner et al. (2000), but these models cannot be really used to test the mechanical viability of the models or for the comparison with *P–T* data because their results are preconditioned by a fixed internal "boundary" condition (subduction point, or "S-point") imposed inside the model area and maintained during the experiments. The models of Burov et al. (2001), Toussaint et al. (2004) and Burov and Yamato (2007) are free of such constraints but were not actually designed to compute synthetic thermodynamically consistent *P–T–t* (time) paths for continental domains, which makes it difficult to test their results against the petrologic data. Finally, Stöckhert and Gerya (2005) designed a thermodynamically coupled, yet still kinematically constrained, thermomechanical model and obtained *P–T–t* paths whose shapes are in a good agreement with the Alpine settings. However, in contrast with the available geological observations (Fig. 1), the exhumation of HP-UHP material implies only the overriding continental plate in their experiment.

We herein propose a new thermomechanical model that implies realistic visco-elasto-plastic rheologies, thermodynamically consistent progressive density changes, erosion-sedimentation processes and does not require any pre-imposed internal boundary conditions. The results of our best fitting experiments are then used to discuss the mechanisms of burial/exhumation.

2. Observational constraints on the continental subduction in the Western Alps

The large structural and petrological data sets available for the Western Alps were used to constrain our model. In the Western Alps, HP units also include oceanic material (e.g., Monviso, Zermatt-Saas). Exhumation of these mafic units was addressed in recent detailed

modeling study by Yamato et al. (2007), and therefore we focus here on continental material only. Fig. 1 summarizes the main points concerning the existing data for the internal crystalline (ICM) Dora Maira (UHP) and the Gran Paradiso (HP) massifs. These small metamorphic units of continental origin (e.g., Chopin, 2003; Le Bayon and Ballèvre, 2006) are located in the internal zones (to the east) of the Alpine belt structure (Fig. 1a and b).

Although the geodynamic context of the Alps is still discussed (e.g., Le Pichon et al., 1988; Marchant and Stampfli, 1997), the following points are widely accepted. According to the data, HP-UHP continental units of the Western Alps constitute the remnants of the European passive margin, which reached the subduction zone at ~45 Ma (e.g., Deville et al., 1992; Michard et al., 1996; Rosenbaum and Lister, 2005), after the subduction of the Liguro–Piemontese ocean (~100 to 40–45 Ma). Continental HP-UHP rocks were buried under the Schistes Lustrés complex before being exhumed to intermediate depths at ~35 Ma at the rear of the belt, when the collision began (Fig. 1c, Agard and Lemoine, 2005). Von Blanckenburg and Davies (1995) proposed that this exhumation, which coincided with a period of magmatic activity at around 40–35 Ma, was induced by a lithospheric slab break-off.

The current detailed knowledge of the Western Alpine geodynamics largely owes to the abundance of pressure-temperature-time data. A simplified compilation of these data for the main metamorphic units of the Western Alps can be found in Yamato et al. (2007). The *P–T–t* values for the main continental units are also summarized in Fig. 1d. The exhumation rates of these units, however, should be considered with caution because the age estimates of the UHP metamorphism are still debatable (Duchêne et al., 1997; Agard et al., 2002; Gebauer et al., 1997; Henry et al., 1993), although the majority of the recent ages fall in the interval between 35 and 45 Ma. Nevertheless, fast initial exhumation rates are additionally confirmed from observations in other continental convergent zones (e.g., Himalaya, Norway). Exhumation of continental material thus corresponds to a short event (<10 Myr) in the Alpine belt formation, with a first stage of exhumation at a very fast rate (>10 mm yr^{-1}) and the second stage at much lower rate (<4 mm yr^{-1}; see Agard et al., in press, 2002 for further details).

3. Numerical approach

We used the visco-elasto-plastic thermomechanical numerical code PARA(O)VOZ. This code incorporates the same mechanical solution kernel as the well-known F.L.A.C. (Fast Lagrangian Analysis of Continua) algorithm (Cundall, 1989) and particle-in-cell technique for particle tracing and interpolation of variables during dynamic remeshing. This code solves simultaneously the Newtonian motion equations and heat transfer equations in large-strain Lagrangian formulation:

$$\frac{\rho Dv_i}{Dt} - \frac{\partial \sigma_{ij}}{\partial x_j} - \rho g_i = 0, \tag{1}$$

$$\frac{D\sigma}{Dt} = F(\sigma, \mathbf{u}, \nabla \dot{\mathbf{u}}, \ldots T \ldots), \tag{2}$$

where $\mathbf{u}$ stands for displacement vector, $\boldsymbol{v}$ is velocity, ρ is density, t is time, g is acceleration due to gravity, D and overdot is material derivative and σ is the Lagrangian stress, T is temperature. F denotes functional relationship for visco-elasto-plastic constitutive law (we use Mohr–Coulomb criterion for plasticity and non-linear power law for viscous flow, Table 1, Ranally and Murphy, 1987; Goetze and Evans, 1979; Carter and Tsenn, 1987). The Eqs. (1)–(2) are coupled with the heat transfer Eq. (3). The Boussinesq approximation is used for thermal density variations in the experiments with no phase changes (Eq. (4), left expression), otherwise the density is updated as a function of P and T (Eq. (4), right expression) using the thermodynamic (free energy minimization) algorithm THERIAK (De Capitani, 1994). Finally, we account for surface processes using commonly inferred diffusion erosion/sedimentation (Eq. (5)):

$$k \cdot \mathrm{div}(\nabla T) - \rho C_p \frac{DT}{Dt} + H_r = \mathbf{v} \nabla T, \tag{3}$$

$$\rho = \rho_0 (1 - \alpha (T - T_0)) \quad \text{or} \quad \rho = f(P, T) \tag{4}$$

$$\frac{\partial^2 h}{\partial t^2} = k_{\mathrm{ero}} \mathrm{div}(\nabla h) \tag{5}$$

where v is the velocity vector, C_p is the specific heat, k is the thermal conductivity, H_r is the internal heat production per unit volume, α is the coefficient of thermal expansion, h is surface topography and k_{ero} is the coefficient of erosion (see Tables 1 and 2).

Apart from the abundant F.L.A.C. literature, this in-house geodynamic version of the algorithm was described in detail in (Burov et al., 2001; Yamato et al., 2007; Le Pourhiet et al., 2004). The particle-in-cell technique (9 particles, or markers, per cell) is used to minimize numerical diffusion due to remeshing (see Yamato et al., 2007 for details). In particular, the marker-based remeshing permits to model very slow-rate convergence processes (few mm yr^{-1}) typical of the

Table 1
Parameters used in our model

Physical parameters			
All rocks		$\rho = f(P,T)$ calculated using THERIAK (kg m^{-3})	
		Friction angle = 30°	
Upper continental crust		Material: quartz[a]	
		Thermal conductivity: 2.5 W m^{-1} $°C^{-1}$	
		Thermal diffusivity: 8.3×10^{-7} m^2 s^{-1}	
		Lamé constants: $\lambda = \mu = 3\times10^{10}$ Pa	
		Cohesion: 20×10^6 Pa	
Lower continental crust		Material: diabase[a]	
		Thermal conductivity: 2.5 W m^{-1} $°C^{-1}$	
		Thermal diffusivity: 6.7×10^{-7} $m^2.s^{-1}$	
		Lamé constants: $\lambda = \mu = 3\times10^{10}$ Pa	
		Cohesion: 20×10^6 Pa	
Sediments		Material: quartz	
		Thermal conductivity: 2 W m^{-1} $°C^{-1}$	
		Thermal diffusivity: 8.3×10^{-7} m^2 s^{-1}	
		Lamé constants: $\lambda = \mu = 1\times10^{10}$ Pa	
		Cohesion: 1×10^6 Pa	
Oceanic crust		Material: olivine	
		Thermal conductivity: 3.5 W m^{-1} $°C^{-1}$	
		Thermal diffusivity: 8.75×10^{-7} m^2 s^{-1}	
		Lamé constants: $\lambda = \mu = 3\times10^{10}$ Pa	
		Cohesion: 20×10^6 Pa	
Mantle		Material: olivine	
		Thermal conductivity: 3.5 W m^{-1} $°C^{-1}$	
		Thermal diffusivity: 8.75×10^{-7} m^2 s^{-1}	
		Lamé constants: $\lambda = \mu = 4\times10^{10}$ Pa	
		Cohesion: 300×10^6 Pa	
Material creep parameters[b]			
Quartz	$n=3$	$A = 6.8\times10^{-6}$ MPa^{-n} s^{-1}	$E = 1.56\times0^5$ J mol^{-1}
Diabase	$n=3.05$	$A = 6.3\times10^{-2}$ MPa^{-n} s^{-1}	$E = 2.76\times10^5$ J mol^{-1}
Olivine	$n=3$	$A = 7.0\times10^{3}$ MPa^{-n} s^{-1}	$E = 5.10\times10^5$ J mol^{-1}
Thermal parameters[c]			
T_0; T_{hl}		0 C; 1330 °C	
h_l; h_c; h_r		100 km; 40 km; 10 km	
H_s		1.10^{-9} W kg^{-1}	
ρ_c; ρ_m		2800 kg m^{-3}; 3300 kg m^{-3}	
k_c; k_m		2.5 W m^{-1} K^{-1}; 3.5 W m^{-1} K^{-1}	
C_m		10^3 J kg^{-1} K^{-1}	
T(age)		115 Ma	

[a] In the reference experiment.
[b] Creep parameters for Quartz, Diabase and Olivine are respectively taken from (Ranally and Murphy, 1987; Goetze and Evans, 1979; Carter and Tsenn, 1987).
[c] Significance of each term is given in Appendix A.

Table 2
Parametric study

Name of the experiment	Convergence rate (mm yr^{-1})	k^{a}_{eros} ($m^2.yr^{-1}$)	Material implied[b]				HP-UHP subducting continental crust exhumation?
			SPUC	SPLC	OPUC	OPLC	
Alps_Ref.	6	3000	Qtz	Diab	Qtz	Diab	Yes
Alps_03	3	–	–	–	–	–	Yes
Alps_09	9	–	–	–	–	–	Yes
Alps_12	12	–	–	–	–	–	Yes
Alps_30	30	–	–	–	–	–	No
Alps_ero500	–	500	–	–	–	–	No
Alps_ero1000	–	1000	–	–	–	–	No
Alps_ero1500	–	1500	–	–	–	–	No
Alps_ero2000	–	2000	–	–	–	–	No
Alps_ero4000	–	4000	–	–	–	–	Yes
Alps_ero5000	–	5000	–	–	–	–	Yes
Alps_ero6000	–	6000	–	–	–	–	Yes
Alps_QQ[c]	–	–	Qtz	Qtz	Qtz	Qtz	No
Alps_DD[c]	–	–	Diab	Diab	Diab	Diab	No
Alps_QD[c]	–	–	Qtz	Qtz	Diab	Diab	No
Alps_DQ[c]	–	–	Diab	Diab	Qtz	Qtz	No
Alps_QM[c]	–	–	Qtz	Qtz	Qtz	Diab	No
Alps_DM[c]	–	–	Diab	Diab	Qtz	Diab	No
Alps_MQ[c]	–	–	Qtz	Diab	Qtz	Qtz	No
Alps_MD[c]	–	–	Qtz	Diab	Diab	Diab	Yes

[a]Erosion coefficient. [b]Abbreviations: SPUC, subducting plate upper crust; SPLC, subducting plate lower crust; OPUC, overriding plate upper crust; OPLC, overriding plate lower crust; Qtz, quartz; Diab, diabase. [c]Reading key for the experiment testing rheology of the continental crust. After underscore symbol, the two letters correspond to the rheological property of respectively the subducting continental crust and the overriding continental crust. Q: quartz (single-layer crust), D: diabase (single-layer crust), M: mixed (double-layer crust composed by quartz and diabase respectively for the upper and the lower continental crust).

continental stage of Alpine collision. Passive markers are also needed to calculate synthetic *P–T–t* paths (Yamato et al., 2007).

4. Model setup

The model setup is based on the existing knowledge for the Western Alps (geometry, age of the lithosphere, convergence rates) and/or the results of earlier parametric study (erosion, rheology of the crust, convergence rates). Initial and boundaries conditions used in our experimental framework are described below and in Table 1.

4.1. Initial geometry

The initial dimensions of the model box are 399 km (height) by 1482 km (width) with spatial mesh resolution of 3×3 km (Fig. 2a). The initial geometry implies a continental plate that barely started to subduct and only reached the bottom of the oceanic accretionary wedge. This situation corresponds to that projected for the Western Alps at the beginning of the subduction of the thin continental margin (Dora Maira), at ~45–50 Ma (Fig. 1c). The dip of subduction is arbitrarily set to 30°, which is of minor importance, as the model is free to chose an optimal dip on further stages of evolution.

4.2. Thermal structure

The initial geotherm, presented in Fig. 2b, is based on plate cooling model modified from Parsons and Sclater (1977) assuming a multi-layer cooling half-space. This model, described in detail in Appendix A and Table 1, is unstationary and depends on the thermal age of the lithosphere (thermotectonic age) and on the radiogenic heat production of the crust. Considering thermal rejuvenation due to the spreading of the Tethyan Ocean at ~160 Ma (Lemoine et al., 1986), it is reasonable to suppose the initial thermotectonic age for the continental lithosphere of ~115 Ma (=160 Ma–45 Ma). This age is applied for both the subducting and the overriding plate.

4.3. Rheology and parameters

Commonly inferred parameters are used for establishing the lithosphere rheology (Ranally and Murphy, 1987; Goetze and Evans, 1979; Carter and Tsenn, 1987). The yield-strength envelope resulting from the assumed rheology (Table 1) and from the thermal profile chosen (Fig. 2c) is presented in Fig. 2d. The choice of these parameters was discussed in Yamato et al. (2007) and is therefore not recalled here. The rheological structure of the Alpine crust is still not well known. For this reason, an additional parametric study was carried out (see Section 5.3) in order to test the influence of a single- or a double-layer crustal rheology on the exhumation processes of the metamorphic rocks.

Quartz and diabase rheologies were used respectively for the upper and the lower continental crust in the experiments that tested double-layer crustal structure with two brittle-ductile transition zones (Fig. 2c). Quartz and diabase rheologies were also used for the entire crust (single layer crustal structure) for end-member cases of very weak and very strong (Fig. 2d) crust, respectively.

4.4. Boundary conditions

For lateral boundary conditions, we apply horizontal convergence at constant rate at both sides of the model (allowing free slip in the vertical direction). The upper surface is free and is affected by surface erosion and sedimentation. At the bottom of the model, we apply Winkler's pliable basement (i.e., hydrostatic equilibrium) with free horizontal slip condition. The Winkler's condition is such that the model overlies an infinite space filled with an inviscible fluid having a small density contrast (10 kg m^{-3}) with the lower part of the model.

5. Constraints from the parametric study

A preliminary parametric study was first carried out to test the model sensitivities to the implied convergence and erosion rates and rheological composition of the crust (Table 2). This study (see below) was necessary to justify our choice of the material parameters used in the reference experiment. For comparison, the general evolution of the reference experiment is presented on Fig. 3 and will be discussed later (Section 6.1).

5.1. Influence of the convergence rates

The entire range of relevant values of the convergence rate has been tested (see Table 2), from very slow (3 mm yr^{-1}) to moderate

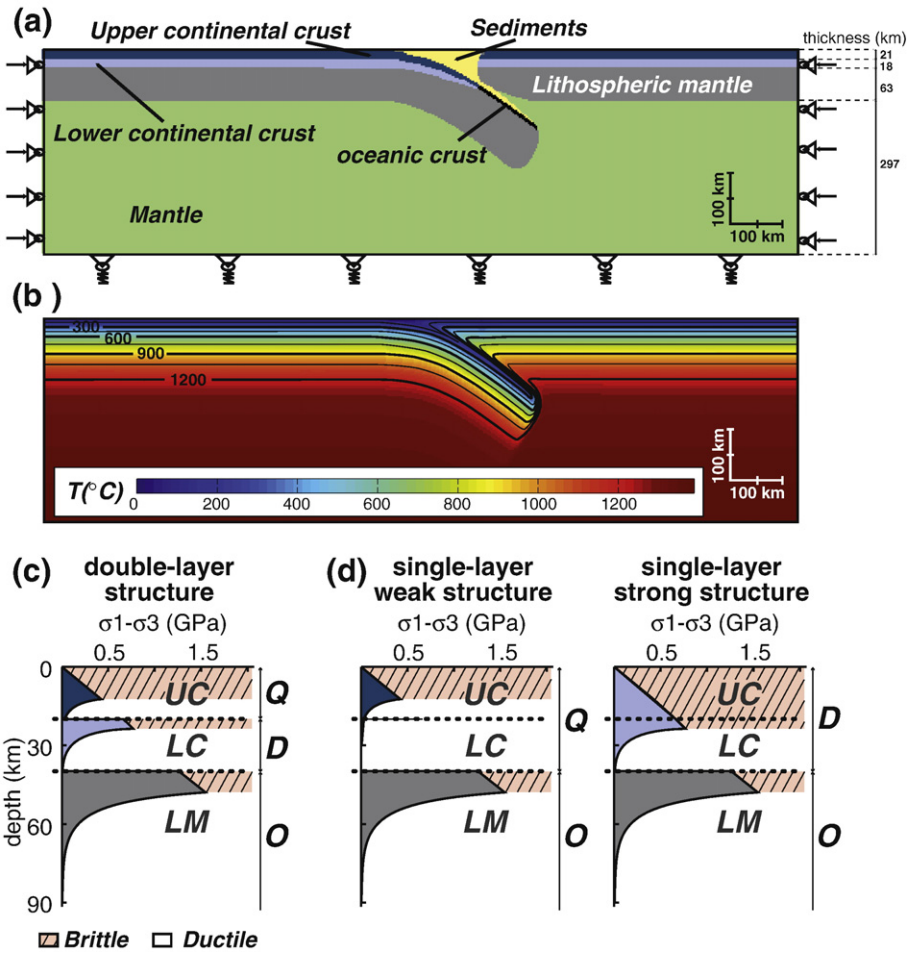

Fig. 2. Model setup. (a) Initial morphology and boundaries conditions. The horizontal arrows correspond to velocity boundary conditions imposed on the sides of the model. The basement is Winkler isostatic. The top is free (+ erosion/sedimentation). (b) Thermal structure used in the models (c) representative viscous-elastic-plastic yield strength profile for the continental lithosphere derived from the assumed rheological parameters (Table 1) for a double-layer structure of the continental crust and the initial thermal field assuming a constant strain rate of 10^{-14} s^{-1}. In the experiments, the strain rate is highly variable both vertically and laterally. (d) Same graphics for a single-layer structure using quartz (left) and diabase (right). Abbreviations: UC, upper crust; LC, lower crust; LM, lithospheric mantle.

(30 mm yr^{-1}). The obtained results show that exhumation of continental crustal material occurs in the experiments implying low convergence velocities (≤12 mm yr^{-1}). In contrast, for higher convergence rates (30 mm yr^{-1}), the continental material from the subducting plate was never exhumed to the surface (Fig. 4a). In these experiments, the imposed rapid collision does not allow for the creation of sufficient space between the upper and lower plates, inhibiting the possibility for deep material to come back to the surface (Fig. 4a). Moreover, in the cases where exhumation of continental crust occurs (convergence rates ≤12 mm yr^{-1}), the exhumation rate patterns are almost constant (with peak exhumation values of ~10 mm yr^{-1}; Fig. 4b), except for the experiment at 12 mm yr^{-1} that constitutes a threshold above which exhumation does not occur. The exhumation occurs in two stages, with the first-stage rates largely independent of the convergence rates. As suggested in Burov et al. (2001), these first-stage rates probably refer to Stokes velocity, that is conditioned by the viscosity and density contrast between the exhumed material (plus the matrix) and its environment.

5.2. Influence of the erosion rates

Fig. 5a shows selected examples of the experiments testing different erosion rates. These rates have been varied by changing the erosion coefficients (Table 2, Fig. 5b). After 20 Myr of convergence, the predicted surface topography is nearly the same for all the experiments. These results supports the existence of an efficient dynamic feedback between the erosion, isostasy and tectonic forcing that ensure stable morphology through time via re-adjustment of subsurface reaction to the changes in surface loading, and *vice versa* (Avouac and Burov, 1996; Burov and Toussaint, 2007). Moreover, the morphology at depths greater than ~50 km is largely independent of the surface erosion rate (Fig. 5a), a result which appears to be specific of slow convergence rate experiments (by comparison with the fast convergence rate experiments of (Avouac and Burov, 1996; Burov and Toussaint, 2007). In contrast, erosion strongly controls the latest stage of exhumation occurring near the surface. In particular, surface exhumation of continental crustal material is possible only for the values of erosion coefficient greater than 2000 m^2 yr^{-1} (Table 2, Fig. 5a). Thus, erosion rate plays a major role during the latest stages of exhumation but does not impact on the first deep stage, as also shown in other recent studies (e.g., Warren et al., 2008a). This result explains the two-stage evolution of the exhumation rate observed in the experiments: the first stage of rapid exhumation (>10 mm yr^{-1}) from great depth, which is mainly controlled by the buoyancy and viscous forces, and the slow second stage, which is controlled by the erosion rate yielding exhumation rates (<5 mm yr^{-1}) on the same order as the erosion rates (Fig. 5b).

5.3. Influence of the crustal rheology

We have carried out different experiments to test the influence of the crustal rheology on the burial/exhumation processes. Three types of rheological profile for the continental crust have been tested: (1) a

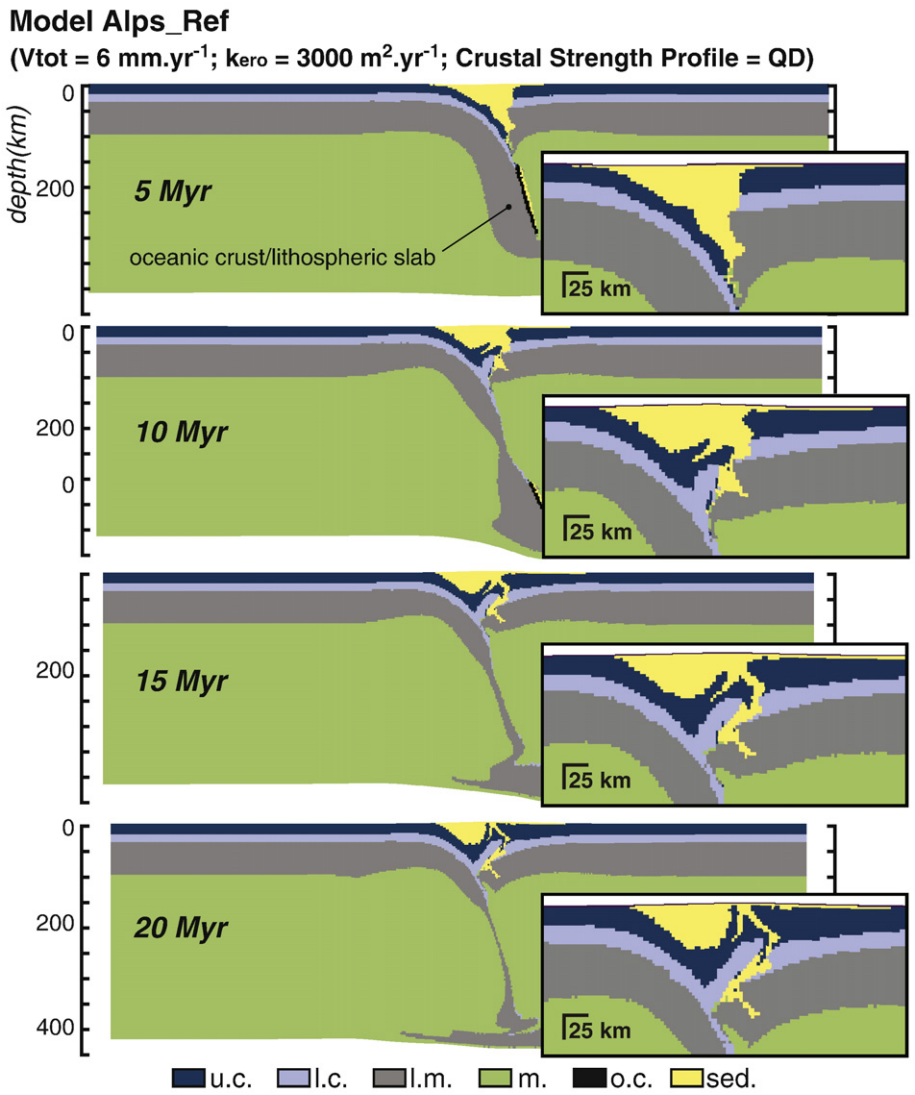

Fig. 3. Large scale evolution and zoom plots of the model during 20 Ma for the reference experiment. Abbreviations: u.c., upper crust; l.c., lower crust; l.m., lithospheric mantle; m., mantle; o.c., oceanic crust; sed., sediments; V_{tot}, convergence rate; k_{ero}, erosion coefficient; QD: Quartz-Diabase double layer structure (Fig. 2c).

double-layer structure (Fig. 2c) simulated by quartz and diabase for the upper and lower crust, respectively, (2) a weak single-layer structure (Fig. 2d) where quartz is used for the entire crust and (3) a strong single-layer structure where the entire crust has a diabase rheology (Fig. 2d). These experiments are described in Table 2 and representative predicted morphologies (after 20 Myr of experiment) are shown in Fig. 6. In the experiments with weak single-layer continental crust, the subduction does not persist, slab break-off occurs early, and neither burial nor exhumation is possible. In contrast, in the experiments implying strong single-layer continental crust, the continental crust is buried to very important depth (>100 km), yet, no exhumation occurs because the mechanical coupling between the upper and the lower continental crust is too strong. Both burial and exhumation of the continental material only took place in the models where a double-layer structure for the continental crust permitted the mechanical decoupling between the upper and the lower continental crust.

5.4. Summary and parameters choice for a reference experiment

This parametric study shows that exhumation of HP-UHP continental rocks from the subducting plate is most favoured for slow convergence rates (<1.5 cm yr^{-1}), high erosion/sedimentation rates (>2000 m^2 yr^{-1}) and occurs only in the cases implying a rheologically decoupled double-layer (quartz-diabase) continental crust. Under such conditions, the obtained results (predicted topography, structure, shapes of *P–T–t* paths, exhumation rates) are in a good agreement with the observational data for the Alps. The selected reference experiment described below thus implies convergence of two continental lithospheric plates with double-layer crustal structure (Fig. 2a and c). The total convergence rate is 6 mm yr^{-1} and the erosion/sedimentation coefficient is 3000 m^2 yr^{-1}.

6. Results

6.1. Large-scale evolution of the model

Fig. 3 shows the morphologies predicted by the reference model during the first 20 Myr of the reference experiment. During the first 5 Myr, the continental lithosphere is buried down to UHP depths and exhumation begins. At the same time, the subducted oceanic slab is progressively detached from the continental slab. 15 Myr are then needed for the deepest continental material (~100 km) to come back to the surface at the rear of the accretionary wedge. This exhumation is fast at the first stage: after ~10 Myr, the exhumed rocks already reach the bottom of the continental crust (~35–40 km), implying an exhumation

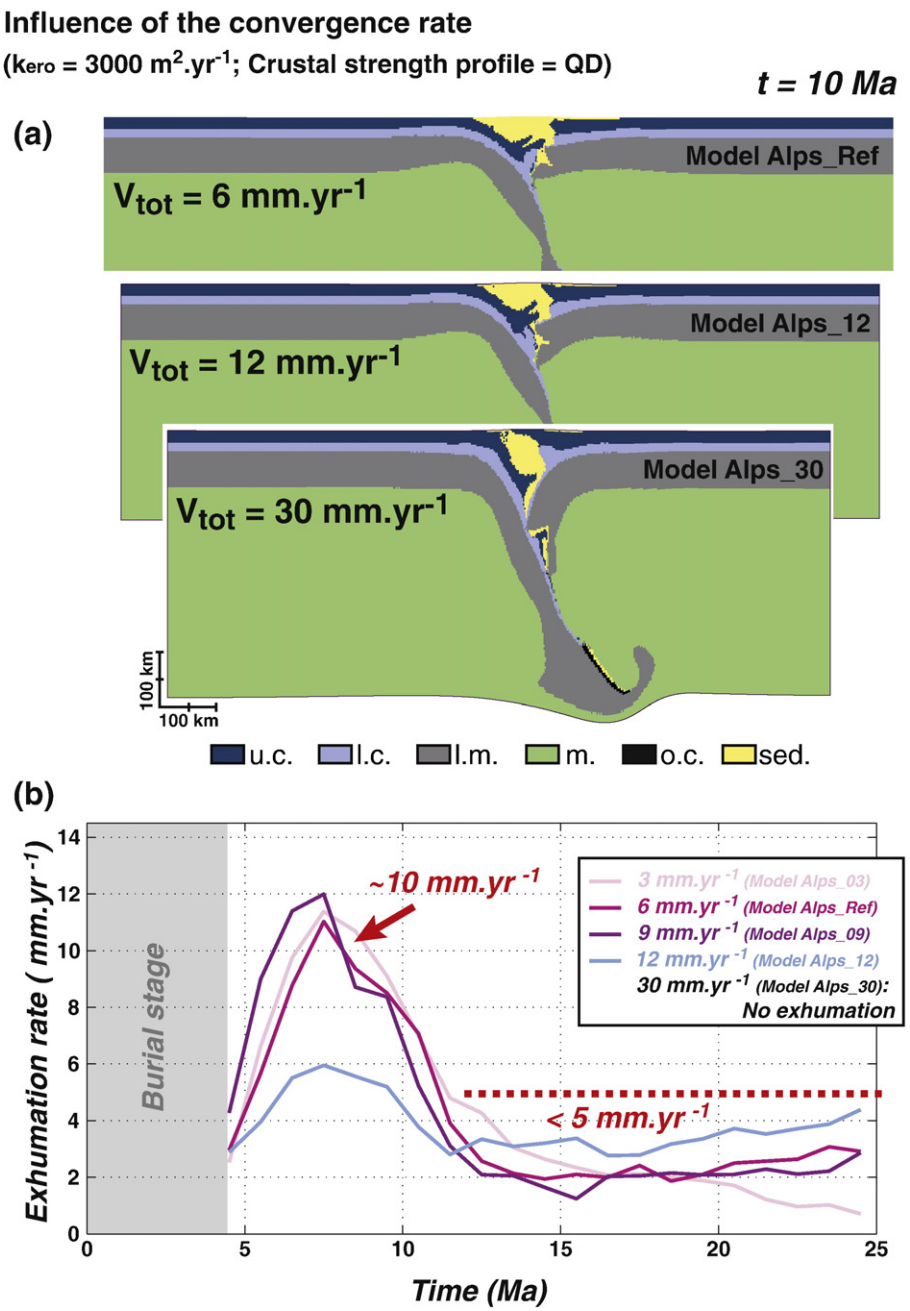

Fig. 4. Results from the parametric study (a) Morphologies of the models at 10 Myr for different convergence rates (other notations are as for Fig. 3). (b) Average of exhumation rates obtained in our models for all the markers in exhumation.

rate of > 10 mm yr^{-1}. It is also noteworthy that UHP exhumation occurs while the oceanic lithosphere is still attached to the subducting lithospheric plate, explaining the close association between oceanic eclogites and UHP rocks in the Western Alps (Agard et al., in press, 2002). Although only ~5 Myr are needed for the UHP rocks to travel vertically over 60–65 km, 10 Myr more are needed before they reach the surface during the second stage where the exhumation rates drop to ~4 mm yr^{-1}. The predicted topographic evolution, which represents one of the important validation criteria for our model, appears to be highly realistic during the entire experiment, with maximal topographic relief smaller than 4 km (Fig. 5b).

6.2. Predicted P–T–t paths

Fig. 7a shows the location of markers at the beginning and at the end of the numerical experiment. The *P–T–t* paths computed for all markers located in the continental crust are presented on Fig. 7b. A more detailed analysis of some of them is shown on Fig. 7c. The shape of the calculated *P–T* paths, as well as the maximum *P* values reached and the *P–T* gradients are very close to natural data. Burial/exhumation of the continental crust occurs during the first ~10 Myr, during the convergence process, with exhumation rates similar to those recorded in the Western Alps (Fig. 7c). The experiment also shows that when collision begins, erosion or near-surface tectonic processes can only exhume rocks from crustal depths but not from deeper levels.

We note, however, that although the predicted *P–T* trends are compatible with the data, the predicted temperatures are colder (100–150 °C) than those inferred from the observed *P–T* paths, as in the experiments of Stöckhert and Gerya (2005) or Warren et al. (2008a,b). This discrepancy may be due to the fact that, in our models, frictional heat production was set to zero (contrary to Burg and Gerya, 2005),

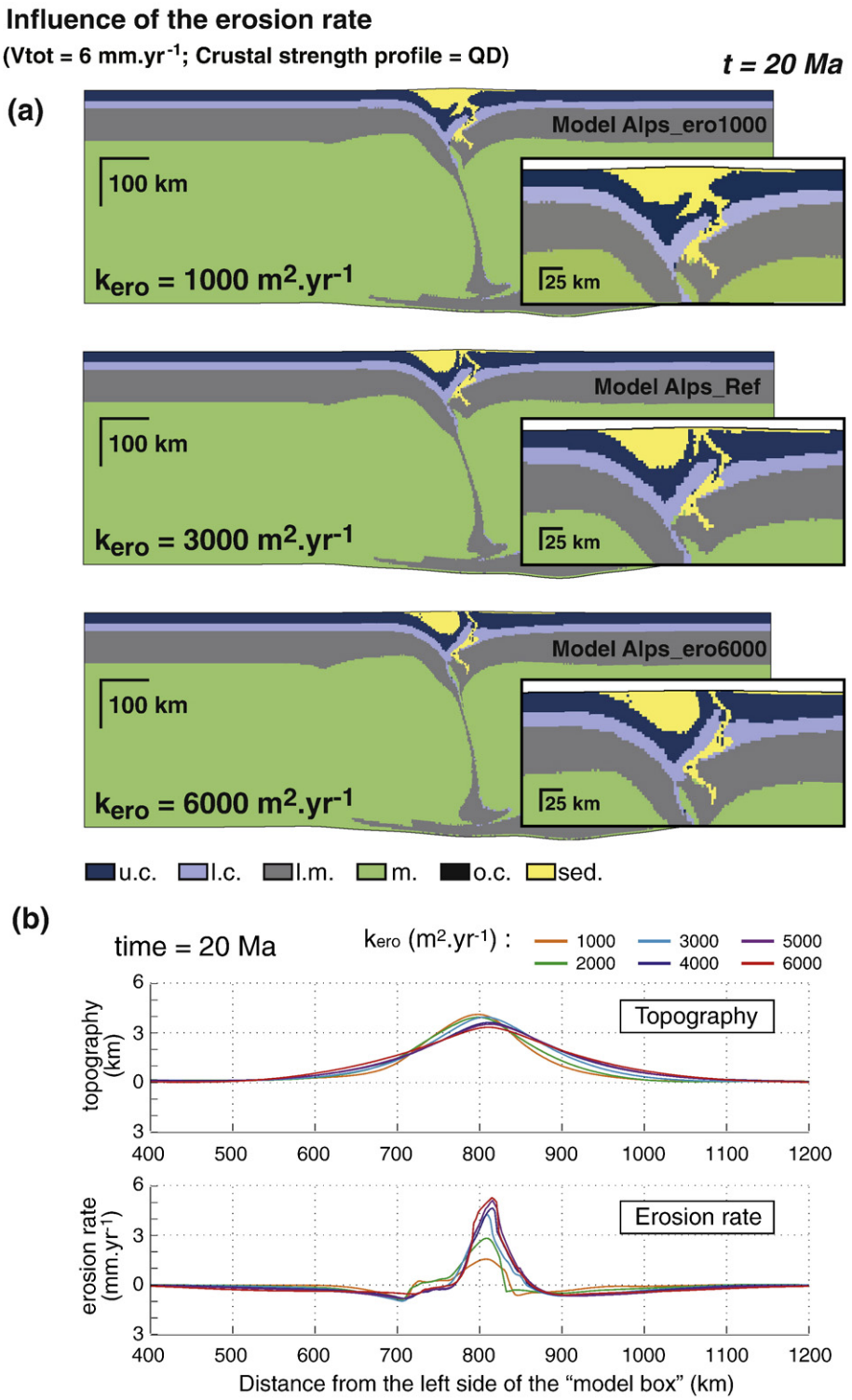

Fig. 5. (a) Morphologies of the models after 20 Myr of experiment for different erosion coefficients. Legend is as for Fig. 3. (b) Topography and erosion at 20 Myr obtained in different experiments testing the influence of the erosion coefficients.

and latent heat and partial melting are also neglected. The reason of doing so was to see how well the data can be fitted without additional heat sources or sinks, which allows one to isolate the amount of heat needed in addition to the heat diffusion-advection mechanisms. Accounting for heat production would increase the temperatures by ~100 °C (Turcotte and Schubert, 2002), bridging the gap with the data, as it was already done with success in some recent subduction models (Gerya et al., 2007; Faccenda et al., 2007). However, the actual parameters of the related mechanisms are difficult to constrain from any observational data available (see below): even if shear heating can be realistically accounted from conservation laws in a global sense, in case of delocalized deformation (convection models) there is much more uncertainty when one needs to treat localised temperature anomalies on shear bands, specifically in large-scale models. This uncetainty stems from scale-dependence of the predicted temperature variations associated with a number of reasons: (1) the local efficiency factor of conversion of the mechanical to thermal energy is unknown, and may be anything from 0.01 to 1; (2) the predicted

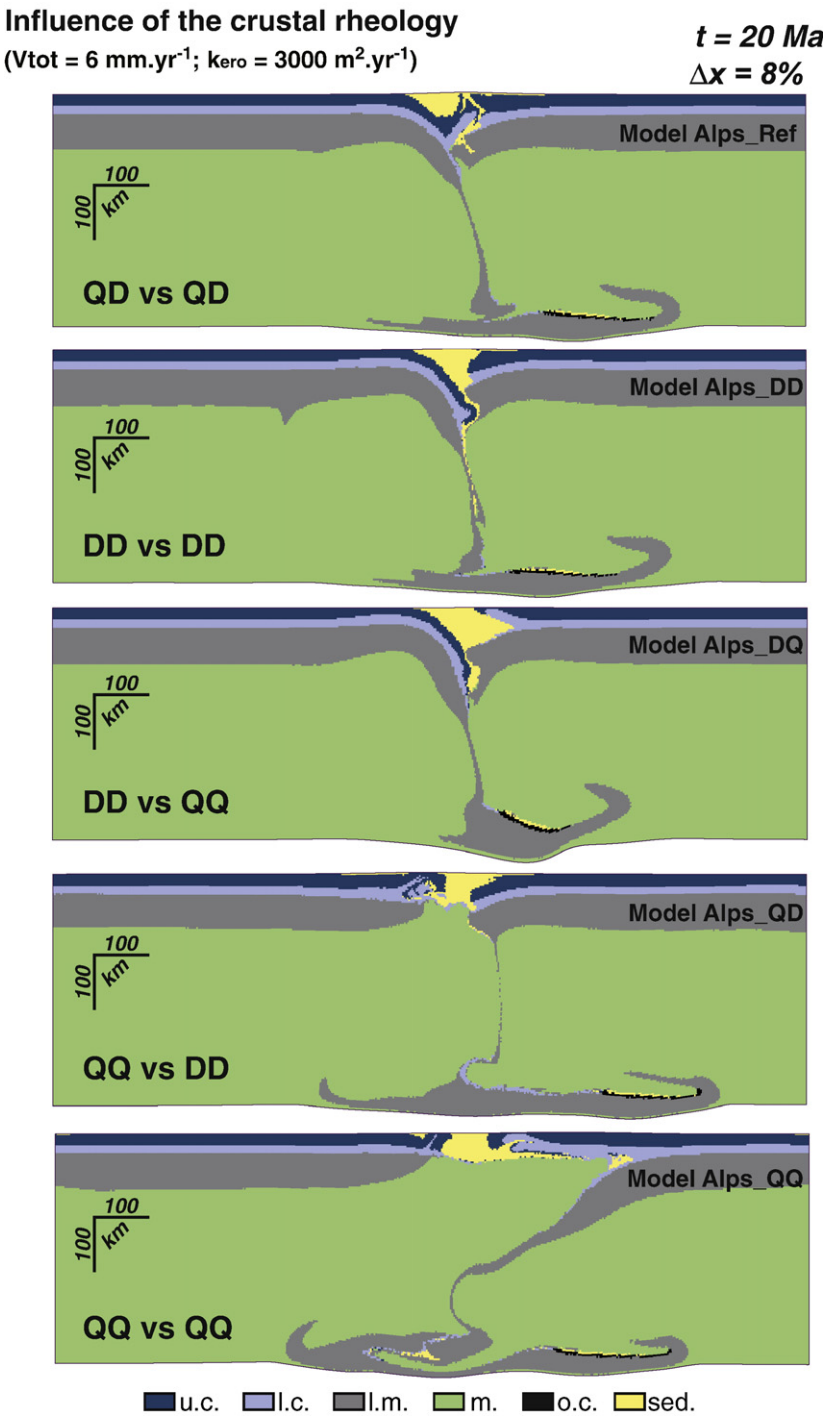

Fig. 6. Morphologies for the models at 20 Myr for different crustal strength profiles. Legend is as for Fig. 3. QD: quartz–diabase double-layer structure (Fig. 2c). QQ: weak single-layer structure simulated by quartz (Fig. 2d); DD: strong single-layer structure simulated by diabase (Fig. 2d). (Reading key: X vs Y means that rheological structure X is used for the subducting plate and Y rheological structure is used for the overriding plate).

temperature variations depend on local stress and strain rate and thus on the thickness of shear bands conditioned by numerical grid resolution; (3) the localized temperature highs are sensitive to the peculiarities of the assumed rheology laws, presence of fluids, thermal properties, variations in the subduction rate, etc.

6.3. Importance of crustal decoupling for exhumation mechanisms

We used passive markers to trace the *P–T–t* paths and trajectories of selected "rocks" in the model. The predicted thermal distributions combined with the predicted strain rate patterns (Fig. 8) also allow us to track the environment (ductile or brittle) in which each marker evolves. The experiments show that between 0 and 5 Myr (Fig. 8a), all of the subducting plate is buried, in particular, the marker "CC1" (Dora Maira equivalent, Fig. 7) reached a near 100 km depth. The marker "CC2" ("Gran Paradiso") was buried to nearly 50 km depth. The background deformation at these depths is ductile and intense (high strain rates ~10^{-14} s^{-1}).

Between 5 and 10 Myr (Fig. 8b), the direction of exhumation is at 90° from the slab dip. Exhumation proceeds from the zone of rheological decoupling between the lower crust and the lithosphere (hereafter noted LCDP — lower crustal decoupling point). The CC2

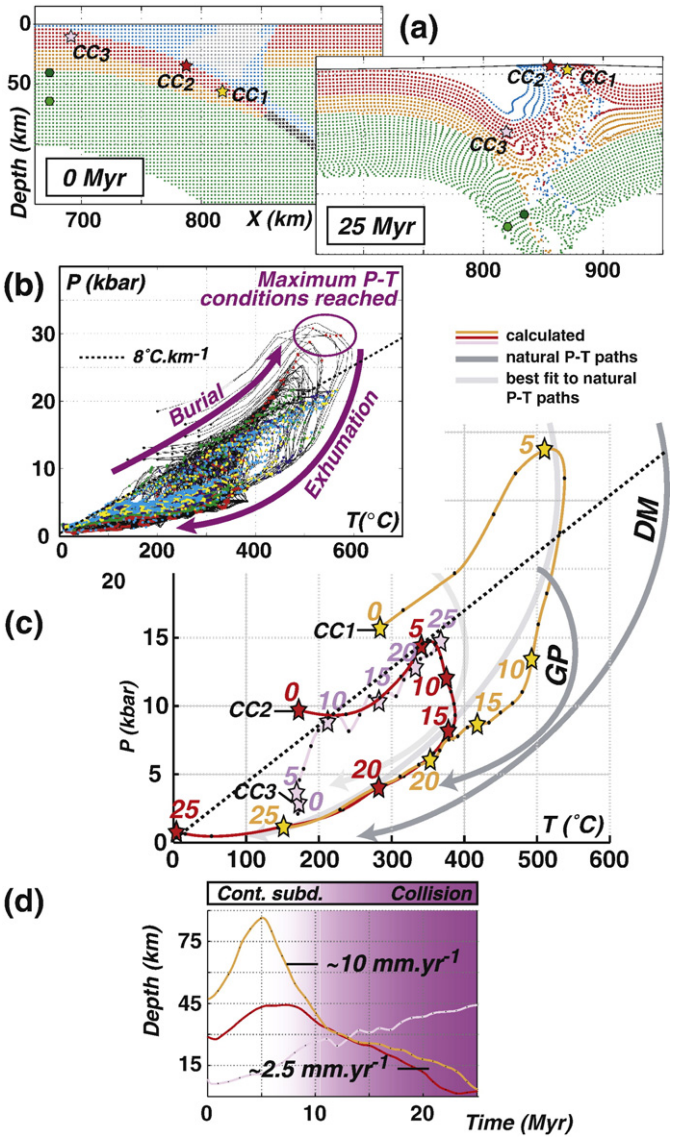

Fig. 7. (a) Location of passive markers at the beginning and at the end of the numerical experiments, showing also the position of points of specific importance discussed in the text. Markers of blue and grey colour correspond to initial sediments (Grey markers are those totally eroded after the 20 Myr of experiment. Red and orange markers correspond respectively to the upper crust and the lower crust. Green markers represent lithospheric mantle and black ones the oceanic crust. Abbreviations: CC, continental crust; SL, accretionary wedge sediments of the "Schistes Lustrés". (b) *P–T* evolution of all the pointers localized within the upper continental crust. (c) Example of *P–T–t* paths for pointers coming from the upper continental crust and comparison with the natural *P–T* path of the Western Alps. Color and symbols as for (a). GP: Gran Paradiso; DM: Dora Maira. (d) Evolution of pressure (and depth) for the selected markers through time. Switching heat dissipation "on" in the model would shift the predicted paths 100–150 °C along the *T* axis providing a perfect match with the petrology-based path.

marker follows a parallel exhumation trajectory, and the origin of this exhumation refers to the upper crustal decoupling point (UCDP), or zone of rheological decoupling between the upper and lower crust. The rheological decoupling zones at ~20 km depth for the upper crust (temperatures close to 350–400 °C) and at ~40 km depth for the lower crust (temperatures close to 600 °C), respectively, thus constitute privileged zones of intra-crustal decoupling controlling the exhumation of the UHP rocks. The fast first-stage exhumation occurs when the oceanic crust/lithosphere slab is not yet detached from the subducting plate (Figs. 3 and 8b). This indicates that slab break-off is not necessary to produce fast exhumation. These results and mechanisms are also in good agreement with the conclusions of some recent studies (e.g., Warren et al., 2008a,b). We note also that no surface exhumation occurs in the experiments implying only a single-layer crust (see Table 2, Fig. 6). In this case, subsurface exhumation actually takes place at the rear of the sedimentary wedge, but the exhumed material returns toward the overriding plate and never reaches the surface.

Between 10 and 15 Myr, a pure shear collision mechanism starts to dominate over the subduction mechanism of shortening. The exhumation of CC1 and CC2 still occurs in the same direction and originates from the LCDP and UCDP zones, but is much slower.

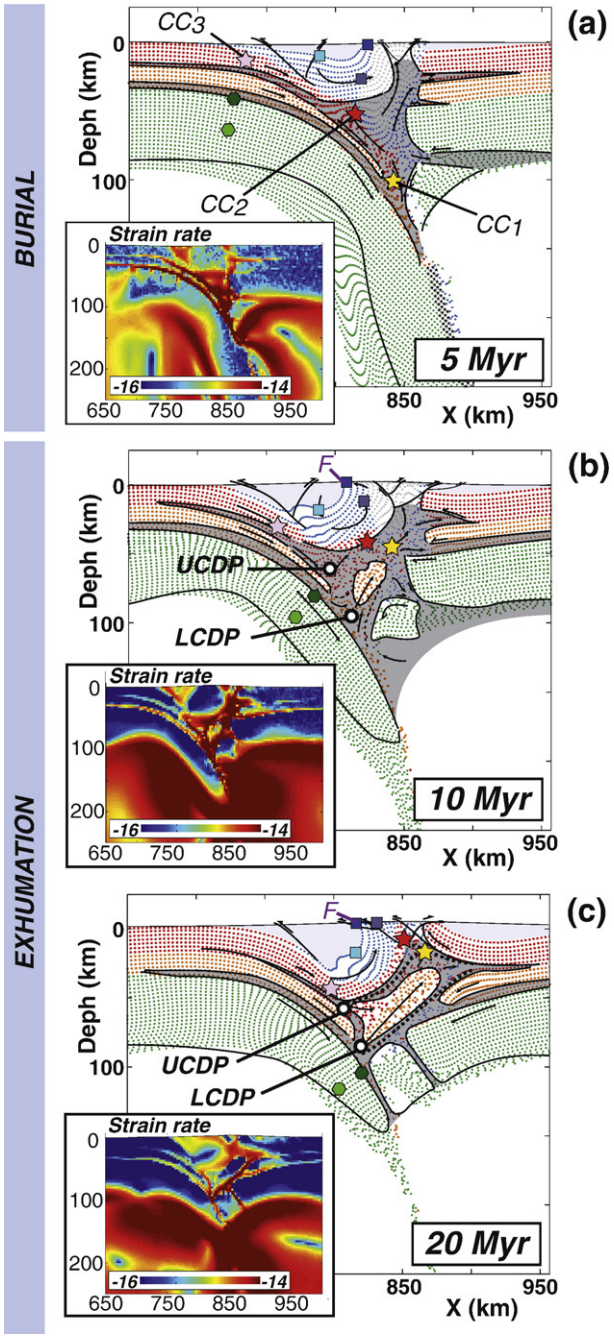

Fig. 8. Migration of markers and strain rate variations through time (see Fig. 7 for notations). Grey region corresponds to ductile domain between the subducting plate and the overriding plate. The position of the "*F* point" in the sedimentary accretionary wedge is virtually stable as well as that of two other characteristic points (UCDP and LCDP) (see text). Moreover, we note that within the pre-existing subjacent sedimentary accretionary wedge, sediments form a "rigid block", which stays non-deformed and moves, by rotation, around the stable point *F*. This mechanism would explain why "Schistes Lustrés" found at this place in the Western Alps are dated from the oceanic subduction.

Decoupling between the crust and the lithospheric mantle of the overriding plate now develops considerably, whereas the zone of point "CC3" continues to be buried. After 15 Myr (Fig. 8c), the exhumation of the areas of markers CC1 and CC2, which reach the brittle part of the crustal-scale accretionary wedge, is now very slow (~2.5 mm yr^{-1}, Fig. 7d), whereas the marker zone CC3 is still being buried (~40 km). This stage marks, in addition, a change of the vergence of the major faults at surface that now become synthetic with respect to the subduction plane. They are rooted in the great shear zone localized in the ductile part between the upper and the lower crust of the overriding plate.

7. Discussion and conclusion

Our model satisfactorily reproduces the overall geodynamics of the Western Alps (i.e., morphology (Fig. 3), topography (Fig. 5b), pressure peak (Fig. 7b), P/T gradient (dP/dT, Fig. 7c), exhumation rates (Fig. 7d), timing of the processes (Fig. 7c and d)), and provides important constraints on the mechanisms controlling exhumation in a slow continental subduction context:

(1) The exhumation of the continental material from the subducting plate (Chopin, 2003) occurs at the rear of the accretionary wedge, between the subducting and overriding plates, in agreement with the field observations for the Western Alps.
(2) Mechanical decoupling of two main ductile layers within the continental crust has a major role for deep exhumation. These critical layers mark the mechanical transition between the lithospheric mantle and the lower continental crust and the transition between the lower and the upper continental crust (LCDP and UCDP, respectively). They constitute the levels from which exhumation of the continental crust is initiated. The lower crust is not exhumed and is "underplated" below the upper continental crust of the overriding plate. Besides, one should note that only relatively small lenses of the continental material are exhumed, being inserted between less metamorphosed terrains.
(3) Lithospheric slab break-off occurs after the first stages of the exhumation. It is not needed for exhumation and does not impact on the exhumation rates.
(4) Continental subduction and the first fast stages of exhumation occur during the convergence as observed in many areas (e.g., Alps, Himalaya, Norway) and do not last more than ~10 Myr.
(5) In case of slow convergence rates (≤12 mm yr^{-1}), exhumation occurs in two stages at rates that are basically independent, at least at the first stage, of the convergence rate. The first "Stokes" stage results from the density contrast between the subducted crust and the surrounding mantle. Exhumation rates are fast (~10 mm yr^{-1}). The second stage originates from depths of 40–50 km, where the exhumed crustal material becomes more and more resistant (due to colder environment) and where the density contrast between the subducted and the surrounding rocks is reduced. Tectonic and surface processes control this second stage.
(6) Transition between the continental subduction and collision (i.e., when shortening is accommodated not only by subduction (simple shear) but also by pure shear thickening due to the accumulation of the exhumed/underplated continental material) corresponds to the moment when fast exhumation from great depth becomes impossible (Fig. 7d). During collision, only the second, slower exhumation stage persists.
(7) Although the discrepancies between the absolute values of temperature and those inferred from petrology data are on the order of 100–150 °C, the predicted trends dP/dT and P–T variations are very close to the data. This allows us to conclude that the main mechanisms of exhumation and burial are indeed reproduced in the model. The "missing" 100–150 °C, as in Stöckhert and Gerya experiments (Stöckhert and Gerya, 2005), most probably come from the absence of frictional heat sources in the model (Burg and Gerya, 2005). It is of trivial matter to estimate the amount of mechanical energy transferable to heat (Turcotte and Schubert, 2002), but the resulting temperature variations are much more uncertain because they depend on the effective thickness of shear bands in nature and in the model, as well as on many other unknown parameters that include material softening, fluid content, additional heating/cooling associated with concentration of radiogenic heat sources and thermal blanketing in the accretion prism, latent heat and partial melting, hydration-dehydration and so on. The real contribution of these sources at depth is unknown and one can be only confident in that ±100–150 °C maximal discrepancy with the data can be easily compensated in many ways (Gerya et al., 2007; Faccenda et al., 2007).
(8) In case of slow convergence and weak lower plate, surface processes have no significant impact on the deep (below 40 km depth) evolution of the collision zone. This is quite different from their role in the case of fast convergence zones involving strong subducting plates, where the erosion/sedimentation rate has a direct incidence on the amount of subduction and the geometry of the subduction channel (Burov and Toussaint, 2007).

Acknowledgements

Constructive reviews by C.J. Warren and T.V. Gerya are greatly appreciated. We also thank B. Goffé for fruitful discussions and G.W. Ernst for helping us to improve the earlier draft of the manuscript.

Appendix A. Initial thermal structure computation

To compute the initial continental geotherm T_{cont}, we use the Eq. (A1) taking into account, in T_{std}, the stationary part of the geotherm and contribution due to the radiogenic heat production H_s in the crust, and correction $T(\text{age})$ due to transient cooling of the lithosphere that depends on its age.

$$T_{cont}(z, \text{age}, H_s) = T_{std}(z, H_s) + T(\text{age}) \tag{A1}$$

Radiogenic contribution T_r in the crust depends of the thickness of the crust h_c, density ρ_c, radiogenic production H_s, radiogenic production decay depth h_r, and thermal conductivity coefficient k_c (Eq. (A2)):

$$T_r = \frac{\rho_c \cdot H_s \cdot h_r^2}{k_c} \cdot \left(1 - \exp^{-\frac{h_c}{h_r}}\right) \tag{A2}$$

Temperature T_m at Moho depth, h_c, is used for the calculation of the temperature for depths below the Moho and is given by:

$$T_m = T_0 + \frac{q_m}{k_c} \cdot h_c + T_r \tag{A3}$$

where T_0 and q_m correspond, respectively, to the temperature at the surface and the heat flux calculated at the Moho. This heat flux is given by:

$$q_m = \frac{T_{hl} - T_0 - T_r}{\frac{h_c}{k_c} + \frac{h_l - h_c}{k_m}} \tag{A4}$$

where T_{hl} is temperature at the thermal base of lithosphere (of a thickness h_l) and k_m is coefficient of thermal conductivity for the mantle.

Temperature at a depth z can thus be calculated as:

$$-If\ z \leq h_c: T_{std}(z) = T_0 + \frac{q_m}{k_c} \cdot z + T_r \tag{A5}$$

$$-If\ z > h_c: T_{std}(z) = T_m + q_m \cdot \frac{(z - h_c)}{k_m} \tag{A6}$$

This obtained temperature is then corrected for transient cooling that depends on thermotectonic age $T(\text{age})$ of the lithosphere using formulation from Parsons and Sclater (1977) adapted for the continental lithosphere.

$$T(\text{age}) = \frac{2}{\pi} \cdot (T_{h_l} - T_0) \cdot TT(\text{age}) \tag{A7}$$

where

$$TT(\text{age}) = \sum_{n=1}^{\infty} \frac{(-1)^{n+1}}{n} \cdot \exp\left(\frac{-k_m \cdot \pi^2 \cdot \text{age} \cdot n^2}{\rho_m \cdot C_m \cdot h_l^2}\right) \cdot \sin\left(\frac{n \cdot \pi \cdot z}{h_l}\right) \tag{A8}$$

with C_m and ρ_m are respectively the specific heat capacity and the density for the mantle. Values for the parameters used in our models for the initial geotherm are given in Table 1.

References

Agard, P., Lemoine, M., 2005. Faces of the Alps, Structure and Geodynamic Evolution, Comm. for the Geol. Map of the World, Paris. 48 pp.

Agard, P., Monié, P., Jolivet, L., Goffé, B., 2002. Exhumation of the Schistes Lustrés complex: in situ laser probe $^{40}Ar/^{39}Ar$ constraints and implications for the Western Alps. J. Metamorph. Geol. 20, 599–618.

Agard, P., Yamato, P., Jolivet, L., Burov, E., in press. Exhumation of oceanic blueschists and eclogites in subduction zones: timing and mechanisms, Earth Science Reviews.

Avigad, D., Chopin, C., Le Bayon, R., 2003. Thrusting and extension in the southern Dora-Maira ultra-high-pressure massif (Western Alps): view from below the coesite-bearing unit. J. Geol. 111, 57–70.

Avouac, J.P., Burov, E.B., 1996. Erosion as a driving mechanism of intracontinental mountain growth. J. Geophys. Res. 101 (8), 17747–17769.

Baldwin, S.L., Monteleone, B.D., Webb, L.E., Fitzgerald, P.G., Grove, M., Hill, E.J., 2004. Pliocene eclogite exhumation at plate tectonic rates in eastern Papua New Guinea. Nature 431, 263–267.

Burg, J.P., Gerya, T.V., 2005. The role of viscous heating in Barrovian metamorphism of collisional orogens: thermomechanical models and application to the Lepontine Dome in the Central Alps. J. Metamorph. Geol. 23, 75–95.

Burov, E., Toussaint, G., 2007. Surface processes and tectonics: forcing of continental subduction and deep processes. Glob. Planet. Change 58, 141–164.

Burov, E., Yamato, P., 2007. Continental plate collision, *P–T–t–z* conditions and unstable vs. stable plate dynamics: insights from thermo-mechanical modelling. Lithos. doi:10.1016/j.lithos.2007.09.014.

Burov, E., Jolivet, L., Le Pourhiet, L., Poliakov, A., 2001. A thermomechanical model of exhumation of high pressure (HP) and ultra-high pressure (UHP) metamorphic rocks in Alpine-type collision belts. Tectonophysics 342, 113–136.

Carswell, D.A., Brueckner, H.K., Cuthbert, S.J., Mehta, K., O'Brien, P.J., 2003. The timing of stabilisation and the exhumation rate for ultra-high pressure rocks in the Western Gneiss Region of Norway. J. Metamorph. Geol. 21, 601–612.

Carter, N.L., Tsenn, M.C., 1987. Flow properties of continental lithosphere. Tectonophysics 136, 27–63.

Chemenda, A.I., Mattauer, M., Malavieille, J., Bokun, A.N., 1995. A mechanism for syn-collisional rock exhumation and associated normal faulting: results from physical modelling. Earth Planet. Sci. Lett. 132, 225–232.

Chopin, C., 1984. Coesite and pure pyrope in high-grade blueschists of the Western Alps: a first record and some consequences. Contrib. Mineral. Petrol. 86, 107–118.

Chopin, C., 2003. Ultrahigh-pressure metamorphism: tracing continental crust into the mantle. Earth Planet. Sci. Lett. 212, 1–14.

Cundall, P.A., 1989. Numerical experiments on localization in frictional materials. Ingenieur-Archiv. 59, 148–159.

De Capitani, C., 1994. Gleichgewichts-Phasendiagramme: Theorie und Software, Beihefte zum European Journal of Mineralogy-Jahrestagung der Deutschen Mineralogischen Gesellschaft. 48 pp.

De Jong, K., 2003. Very fast exhumation of high-pressure metamorphic rocks with excess ^{40}Ar and inherited ^{87}Sr, Betic Cordilleras, southern Spain. Lithos 70, 91–110.

Deville, M., Fudral, S., Lagabrielle, Y., Marthaler, M., Sartori, M., 1992. From oceanic closure to continental collision: a synthesis of the 'Schistes Lustrés' metamorphic complex of the Western Alps. Geol. Soc. Amer. Bull. 104, 127–139.

Duchêne, S., Lardeaux, J.M., Albarède, F., 1997. Exhumation of eclogites: insights from depth-time path analysis. Tectonophysics 280, 125–140.

Faccenda, M., Gerya, T.V., Chakraborty, S., 2007. Styles of post-subduction collisional orogeny: influence of convergence velocity, crustal rheology and radiogenic heat production. Lithos. doi:10.1016/j.lithos.2007.09.009.

Gebauer, D., Schertl, H.P., Brix, M., Schreyer, W., 1997. 35 Ma old ultrahigh-pressure metamorphism and evidence for very rapid exhumation in the Dora Maira Massif, Western Alps. Lithos 41, 5–24.

Gerya, T.V., Perchuck, L.L., Burg, J.P., 2007. Transient hot channels: perpetrating and regurgitating ultrahigh-pressure, high-temperature crust-mantle associations in collision belts. Lithos. doi:10.1016/j.lithos.2007.09.017.

Goetze, C., Evans, B., 1979. Stress and temperature in the bending lithosphere as constrained by experimental rock mechanics. Geophys. J. R. Astron. Soc. 59, 463–478.

Green, H.W.I., 2005. Psychology of a changing paradigm: 40+ years of high-pressure metamorphism. International Geology Review 47, 439–456.

Guillot, S., Replumaz, A., Hattori, K.H., Strzerzynski, P., 2007. Initial geometry of Western Himalaya and ultra-high pressure metamorphic evolution. Journal of Asian Earth Sciences 30, 557–564.

Hacker, B.R., 2007. Ascent of the ultrahigh-pressure Western Gneiss Region, Norway. In: Cloos, M., Carlson, W.D., Gilbert, M.C., Liou, J.G., Sorensen, S.S. (Eds.), Convergent Margin Terranes and Associated Regions: A Tribute to W.G. Ernst. Geological Society of America Special Paper, vol. 419, pp. 171–184.

Hacker, B.R., Ratschbacher, L., Webb, L., McWilliams, M.O., 2000. Exhumation of ultrahigh-pressure continental crust in east central China: Late Triassic-Early Jurassic tectonic unroofing. J. Geophys. Res. 105, 13339–13364.

Henry, C., Michard, A., Chopin, C., 1993. Geometry and structural evolution of ultra-high pressure and high pressure rocks from the Dora Maira massif, Western Alps. J. Struct. Geol. 15, 965–981.

Hermann, J., Rubatto, D., Korsakov, A., Shatsky, V.S., 2001. Multiple zircon growth during fast exhumation of diamondiferous, deeply subducted continental crust (Kokchetav Massif, Kazakhstan). Contrib. Mineral. Petrol. 141, 66–82.

Jolivet, L., Raimbourg, H., Labrousse, L., Avigad, D., Leroy, Y., Austrheim, H., Andersen, T.B., 2005. Softening trigerred by eclogitization, the first step toward exhumation during continental subduction. Earth and Planetary Science Letters 237, 532–547.

Lallemand, S., Huchon, P., Jolivet, L., Prouteau, G., 2005. Convergence lithosphérique. 192 pp.

Le Bayon, B., Ballèvre, M., 2006. Deformation history of a subducted continental crust (Gran Paradiso, Western Alps): continuing crustal shortening during exhumation. J. Struct. Geol. 28, 793–815.

Lemoine, M., Bas, T., Arnaud-Vanneau, A., Arnaud, H., Dumont, T., Gidon, M., Bourbon, M., De Graciansky, P.C., Rudkiewicz, J.L., Megard-Galli, J., Tricart, P., 1986. The continental margin of the Mesozoic Tethys in the Western Alps. Mar. Pet. Geol. 3, 179–199.

Le Pichon, X., Bergerat, F., Roulet, M.J., 1988. Plate kinematics and tectonics leading to the Alpine belt formation: a new analysis. Geol. Soc. Amer. Special Papers 218, 111–131.

Le Pourhiet, L., Burov, E., Moretti, I., 2004. Rifting through a stack of inhomogeneous thrusts (the dipping pie concept). Tectonics 23, 1–14.

Liou, J.G., Tsujimori, T., Zhang, R.Y., Katayama, I., Maruyama, S., 2004. Global UHP metamorphism and continental subduction/collision: the Himalaya model. Int. Geol. Rev. 46, 1–27.

Marchant, R.H., Stampfli, G.M., 1997. Subduction of continental crust in the Western Alps. Tectonophysics 269, 217–235.

Michard, A., Goffé, B., Chopin, C., Henry, C., 1996. Did the Western Alps develop through an Oman-type stage? The geotectonic setting of high pressure metamorphism in two contrasting Thethyan transects. Eclogae geol. Helv. 89, 43–80.

O'Brien, P.J., Zotov, N., Law, R., Khan, M.A., Jan, M.Q., 2001. Coesite in Himalayan eclogite and implications for models of India–Asia collision. Geology 29, 435–438.

Parrish, R.R., Simon, J.G., Searle, M.P., Waters, D.J., 2006. Plate velocity exhumation of ultrahigh-pressure eclogites in the Pakistan Himalaya. Geology 34, 989–992.

Parsons, B., Sclater, T.G., 1977. An analysis of the variation of ocean floor bathymetry and heat flow with age. J. Geophys. Res. 82, 803–827.

Pfiffner, O.A., Ellis, S., Beaumont, C., 2000. Collision tectonics in the Swiss Alps: insight from geodynamic modeling. Tectonics 19, 1065–1094.

Ranally, G., Murphy, D.C., 1987. Rheological stratification of the lithosphere. Tectonophysics 132, 281–295.

Root, D.B., Hacker, B.R., Gans, P.B., Ducea, M.N., Eide, E.A., Mosenfelder, J.L., 2005. Discrete ultrahigh-pressure domains in the Western Gneiss Region, Norway: implications for formation and exhumation. J. Metamorph. Geol. 23, 45–61.

Rosenbaum, G., Lister, G.S., 2005. The Western Alps from the Jurassic to Oligocene: spatio-temporal constraints and evolutionary reconstructions. Earth-Sci. Rev. 69, 281–306.

Rubatto, D., Hermann, J., 2001. Exhumation as fast as subduction? Geology 29, 3–6.

Stöckhert, B., Gerya, T.V., 2005. Pre-collisional high pressure metamorphism and nappe tectonics at active continental margins: a numerical simulation. Terra Nova 17, 102–110.

Terry, M.P., Robinson, P., Hamilton, M.A., Jercinovic, M.J., 2000. Monazite geochronology of UHP and HP metamorphism, deformation, and exhumation, Nordøyane, Western Gneiss Region, Norway. Am. Mineral. 85, 1651–1664.

Toussaint, G., Burov, E., Jolivet, L., 2004. Continental plate collision: unstable versus stable dynamics. Geology 32, 33–36.

Turcotte, D.L., Schubert, G., 2002. Geodynamics. Cambridge University Press. 456 pp.

Von Blanckenburg, F., Davies, J.H., 1995. Slab breakoff: a model for syncollisional magmatism and tectonics in the Alps. Tectonics 14, 120–131.

Warren, C.J., Beaumont, C., Jamieson, R.A., 2008a. Modelling tectonic styles and ultra-high pressure (UHP) rock exhumation during the transition from oceanic subduction to continental collision. Earth Planet. Sci. Lett. doi:10.1016/j.epsl.2007.11.025.

Warren, C.J., Beaumont, C., Jamieson, R.A., 2008b. Formation and exhumation of ultra-high pressure rocks during continental collision: role of detachment in the subduction channel. Geochem. Geophys. Geosystems http://www.agu.org/journals/pip/gc/2007GC001839-pip.pdf.

Yamato, P., Agard, P., Burov, E., Le Pourhiet, L., Jolivet, L., Tiberi, C., 2007. Burial and exhumation in a subduction wedge: mutual constraints from thermomechanical modeling and natural *P–T–t* data (Sch. Lustrés, W. Alps). J. Geophys. Res. 112, B07410. doi:10.1029/2006JB004441.

Earth-Science Reviews 92 (2009) 53–79

Contents lists available at ScienceDirect

Earth-Science Reviews

journal homepage: www.elsevier.com/locate/earscirev

Exhumation of oceanic blueschists and eclogites in subduction zones: Timing and mechanisms

P. Agard *, P. Yamato, L. Jolivet, E. Burov

Laboratoire de Tectonique, UMR CNRS 7072, Université Pierre et Marie Curie-Paris 6, Case 129, Tour 46-0, 2E, 4 pl. Jussieu, 75252 Paris Cedex 05, France

ARTICLE INFO

Article history:
Received 14 November 2007
Accepted 5 November 2008
Available online 27 November 2008

Keywords:
blueschists
eclogites
HP–LT rocks
oceanic crust
subduction channel
exhumation mechanisms

ABSTRACT

High-pressure low-temperature (HP–LT) metamorphic rocks provide invaluable constraints on the evolution of convergent zones. Based on a worldwide compilation of key information pertaining to fossil subduction zones (shape of exhumation *P–T–t* paths, exhumation velocities, timing of exhumation with respect to the convergence process, convergence velocities, volume of exhumed rocks,…), this contribution reappraises the burial and exhumation of oceanic blueschists and eclogites, which have received much less attention than continental ones during the last two decades.

Whereas the buoyancy-driven exhumation of continental rocks proceeds at relatively fast rates at mantle depths (≥cm/yr), oceanic exhumation velocities for HP–LT oceanic rocks, whether sedimentary or crustal, are usually on the order of the mm/yr. For the sediments, characterized by the continuity of the *P–T* conditions and the importance of accretionary processes, the driving exhumation mechanisms are underthrusting, detachment faulting and erosion. In contrast, blueschist and eclogite mafic bodies are systematically associated with serpentinites and/or a mechanically weak matrix and crop out in an internal position in the orogen.

Oceanic crust rarely records *P* conditions >2.0–2.3 GPa, which suggests the existence of maximum depths for the sampling of slab-derived oceanic crust. On the basis of natural observations and calculations of the net buoyancy of the oceanic crust, we conclude that beyond depths around 70 km there are either not enough serpentinites and/or they are not light enough to compensate the negative buoyancy of the crust.

Most importantly, this survey demonstrates that short-lived (<~15 My), discontinuous exhumation is the rule for the oceanic crust and associated mantle rocks: exhumation takes place either early (group 1: Franciscan, Chile), late (group 2: New Caledonia, W. Alps) or incidentally (group 3: SE Zagros, Himalayas, Andes, N. Cuba) during the subduction history. This discontinuous exhumation is likely permitted by the specific thermal regime following the onset of a young, warm subduction (group 1), by continental subduction (group 2) or by a major, geodynamic modification of convergence across the subduction zone (group 3; change of kinematics, subduction of asperities, etc).

Understanding what controls this short-lived exhumation and the detachment and migration of oceanic crustal slices along the subduction channel will provide useful insights into the interplate mechanical coupling in subduction zones.

Contents

* Corresponding author.
E-mail address: agard@ccr.jussieu.fr (P. Agard).

0012-8252/$ – see front matter © 2008 Elsevier B.V. All rights reserved.
doi:10.1016/j.earscirev.2008.11.002

1. Introduction

Subduction zones are crucial areas to constrain interplate coupling (Hyndman et al., 1997; Conrad et al., 2004; Heuret and Lallemand, 2005), recycling processes to the mantle (Bebout, 1996; Schmidt and Poli, 1998; Bebout, 2007) and thermal structures of arc-magmatism (Iwamori, 1998; Peacock and Wang, 1999). They are also the distinctive locus of high-pressure low-temperature metamorphism (HP–LT; Ernst, 1970, 1972; Goffé and Chopin, 1986; Okay, 1989; Maruyama et al., 1996), as confirmed by deep drilling in active trenches (Maekawa et al., 1993; Fryer et al., 1999).

Over the past twenty years, many studies have dealt with exhumation processes of HP–LT rocks, chiefly because: (1) compared to subduction forces burying rocks at depth, processes that return rocks towards the surface are still poorly understood (for example Platt, 1993; Jolivet et al., 1998b; Ring et al., 1999; Jolivet et al., 2003), (2) the discovery that continental crust could be buried deeper than previously thought (>100 km; Chopin, 1984; Smith, 1984) challenged the research community, (3) exhumation velocities derived from *P*–*T*–*t* paths, though spanning a wide range from <mm/yr to a few cm/yr (Ernst, 1988; Rubatto and Hermann, 2001; Baldwin et al., 2004), are generally surprisingly lower than subduction plate velocities (except for Philippot et al., 2001), (4) the metamorphic evolution of HP–LT rocks brings invaluable insights into deep crustal processes (Green, 2005).

For the sake of clarity and terminology, the tectonic setting of exhumation in subduction zones is recalled in Fig. 1a. The prevalent view is that, during a period of oceanic subduction, the oceanic crust and the overlying sediments, part of which can be decoupled from the crust and accreted to form the accretionary wedge, are dragged at depth along the subduction plane into the so-called subduction channel (Fig. 1a; Shreve and Cloos, 1986; Cloos and Shreve, 1988). Exhumation of some of these rocks metamorphosed under HP–LT conditions may then take place in the wedge and/or in the channel (e.g. Jolivet et al., 2003). When a large continental piece (i.e., a passive margin or an isolated block) enters the subduction zone it may also be dragged by 'continental subduction', but generally only during a restricted period of time (c. 10 My; e.g. Ernst, 2001; Chopin, 2003), after which collision develops. The introduction of the low-density continental material is generally thought to be responsible for the choking of subduction, which then stops or jumps outboard of the continental block (e.g. Stern, 2004).

Research on the exhumation of HP–LT rocks mainly focused so far on continental high- to ultrahigh-pressure rocks (UHP; for example, Wain, 1997; Kurz and Froitzheim, 2002; Chopin, 2003; Hacker et al., 2003a), partly due to the diagnostic occurrence of the quartz polymorph, coesite (as noted by Bucher et al., 2005) and to the finding of UHP rocks from ever increasing depths (Fig. 1b). The new paradigm suggests that the buoyant UHP continental rocks return at plate velocities from mantle depths (1–5 cm/yr; Duchêne et al., 1997a;

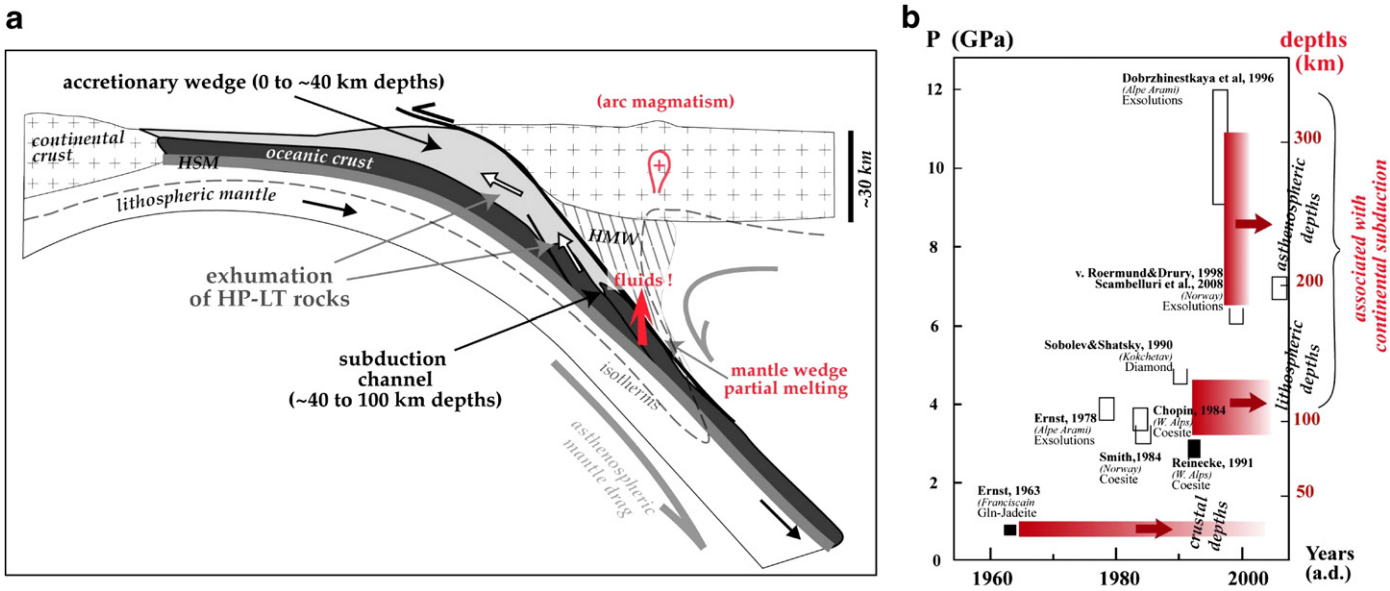

Fig. 1. (a) Sketch depicting the tectonic setting of the exhumation of high-pressure low-temperature (HP–LT) rocks in subduction zones. HMW: hydrated mantle wedge; HSM: hydrothermalized slab mantle. (b) Compilation of the main steps of discovery of HP–LT rocks illustrating the recovery of rock samples returned from increasing depths with time (Ernst, 1963, 1978; Chopin, 1984; Smith, 1984; Sobolev and Shatsky, 1990; Reinecke, 1991; Dobrzhinetskaya et al., 1996; van Roermund and Drury, 1998; Scambelluri et al., 2008). Empty boxes: continental material; black boxes: oceanic material. Note that no oceanic material has been documented from pressures >2.8 GPa so far (Reinecke, 1991, 1998).

Ernst et al., 1997; O'Brien, 2006), in some cases with the help of matrix serpentinites (Guillot et al., 2001), then decelerate in the crust, and that mechanisms driving exhumation vary with depth.

These conclusions pertain to continental subduction, however, that is to the late stages of subduction processes proper. The situation is somewhat different for the denser, oceanic HP–LT rocks, which have received much less attention, and for which exhumation velocities are still unresolved (Amato et al., 1999; Agard et al., 2002; Rubatto and Scambelluri, 2003; Federico et al., 2005). Some of them are demonstrably exhumed during oceanic convergence (for example Franciscan and Cuban rocks; Ernst, 1988, Baldwin, 1996; Schneider et al., 2004), but in other cases mainly during continental subduction, as we will later show (Western Alps, New Caledonia). Recent data for the Zagros (Agard et al., 2006) also showed that, during oceanic convergence, oceanic material was returned along the subduction plane (from depths ≥40–50 km back to depths ≤15–20 km) during short-lived time periods only, that is discontinuously with respect to the subduction duration.

In order to improve our understanding of the processes that take place at depth in subduction zones, we herein investigate the exhumation of oceanic HP–LT rocks worldwide. We more specifically address the following pending questions: (1) When are oceanic HP–LT rocks exhumed in the convergence history? Is exhumation steady or discontinuous and, in the latter case, what are the controlling processes (subduction of seamounts, obduction, etc)? (2) What are their exhumation velocities? (3) What are the driving forces? To what extent are sediments and oceanic lithosphere exhumed coevally and by the same process and/or how does the oceanic crust (+mantle) detach from the leading, sinking slab? (4) What does their exhumation tell us about the interplate mechanical coupling in subduction zones (e.g. Conrad et al., 2004) on the long-term (i.e., several My)?

For this purpose we compiled available data from various, generally young localities worldwide (<150 Ma for most of them), whose geodynamic context and oceanic origin are well-constrained (Fig. 2). For clarity, we will herein refer to two main types of oceanic material: oceanic sediments and oceanic 'crust', although in practice the latter may comprise a significant proportion of associated ultramafics derived from the lithospheric slab mantle and/or mantle wedge.

The example of the Western Alps is considered first, owing to the wealth of available data, both thermobarometric and radiometric, and for the insights it provides on key exhumation concepts and geodynamic processes. Other localities are considered next, focusing on the shape of exhumation *P–T–t* paths, on exhumation velocities, on the timing of exhumation with respect to the convergence process, and on other parameters listed in Table 1. The key constraints provided by subduction modelling are also reviewed and taken into account.

From this survey we conclude that each material (continental, sedimentary or oceanic) entering subduction zones has its own exhumation mode, and that for the latter category (the most poorly constrained, still), discontinuous exhumation appears to be the rule.

2. Insights from the Alpine case study

The Alpine case study has many advantages: it gives fruitful insights from a well-constrained geological setting, it offers the opportunity to evaluate the extent of lateral variations along a continuous subduction zone, and the lack of post-subduction collisional-related heating ensures a good record of subduction processes. It also serves as a reference frame for the comparison with other settings worldwide.

2.1. Overview of the geological context of the Western Alps

The Western Alps result from the closure of the approximately NS Valais and Liguro-Piemontese slow-spreading oceans from ~100 Ma onwards (for complete reviews of the Alpine geodynamic context: Lemoine et al., 1986; Coward and Dietrich, 1989; Polino et al., 1990; Lagabrielle and Lemoine, 1997; Stampfli et al., 1998; Dercourt et al., 2000; Dal Piaz, 2001; Agard et al., 2002; Oberhänsli et al., 2004; Rosenbaum and Lister, 2005; Ford et al., 2006), through an E-dipping subduction zone below Apulia/Africa at rates <20 mm/yr (Le Pichon et al., 1988; Lapen et al., 2003). During the Eocene (45–40 Ma), the thin, leading edge of the continental European margin reached the subduction zone and a short-lived (~10 My; Duchêne et al., 1997a; Rubatto and Hermann, 2001) period of continental subduction took place before the onset of collision between Eurasia and Apulia/Africa (at ~35–30 Ma; Sinclair and Allen, 1992). In the following, we refer to continental subduction as the period (40±5 Ma) during which continental crust material is (transiently, as recalled in the introduction) dragged to subduction depths and reequilibrates under HP–LT metamorphic conditions. During subsequent collision (~35–30 Ma

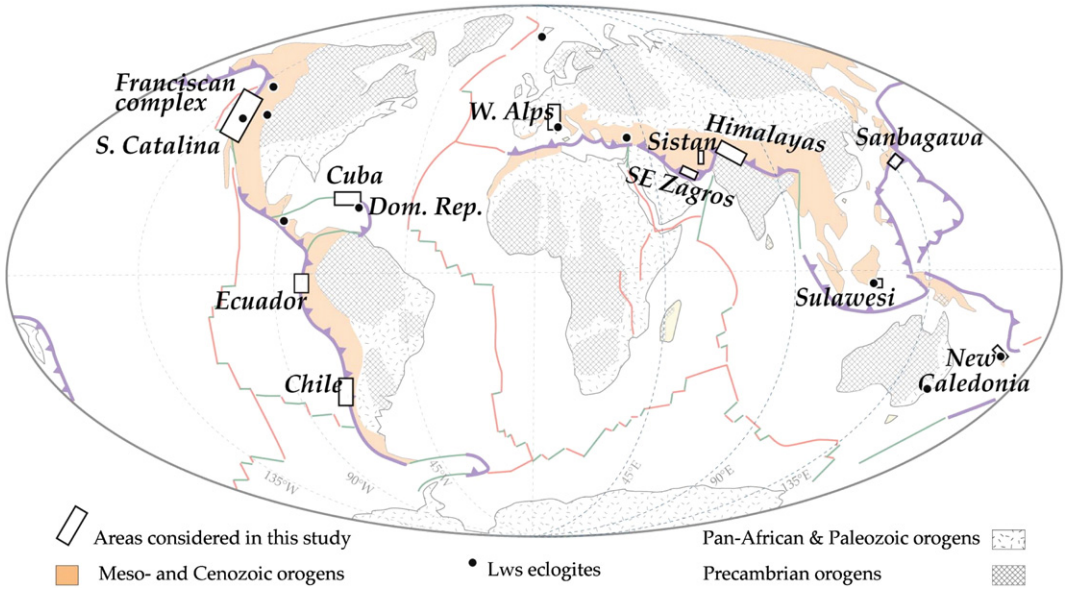

Fig. 2. Map showing the HP–LT areas considered here. Precambrian cratons and more recent orogens are also indicated. Lawsonite eclogite localities taken from Tsujimori et al. (in press).

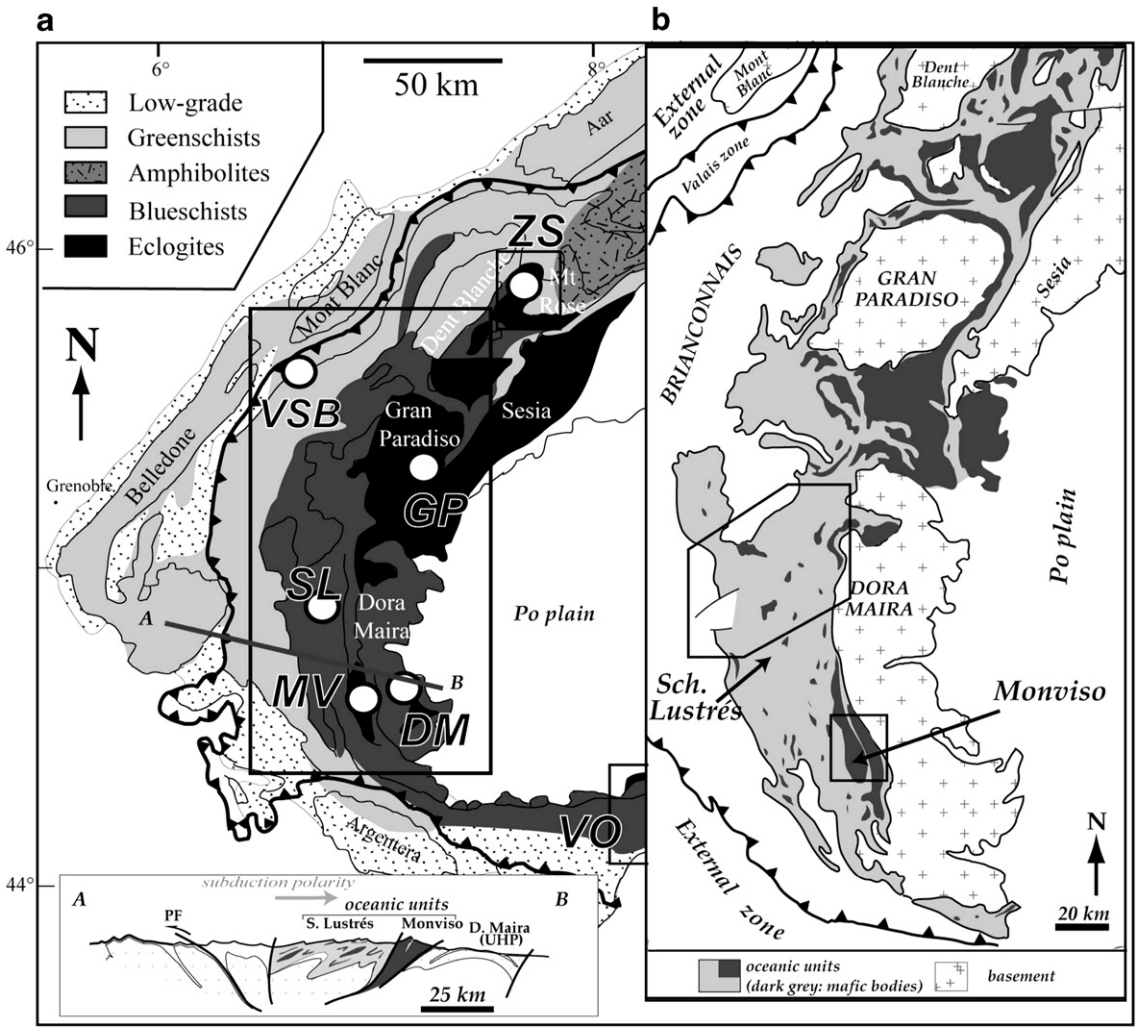

Fig. 3. (a) Metamorphic map of the Western Alps (simplified from Pognante, 1991; Oberhänsli et al., 2004; Agard and Lemoine, 2005). Inset: schematic cross-section along profile AB, showing the respective position of the ocean-derived units and the internal position of the mafic Monviso units with respect to the subuction polarity (same color scale as for panel b). Abbreviations: DM: Dora Maira; GP: Gran Paradiso; MV: Monviso; SL: Schistes Lustrés; VO: Voltri; VSB: Versoyen Grand St Bernard; ZS: Zermat-Saas. (b) Spatial distribution of oceanic sedimentary and crustal units, respectively, in the internal units. Note, again, the internal position of the mafic bodies and their close association with the internal crystalline massifs (Dora Maira, Gran Paradiso). Note the coincidence of eclogite facies conditions (panel a) with the distribution of mafic bodies (panel b).

onwards) the continental crust undergoes medium-pressure medium-temperature metamorphism (e.g., Central Alps: Todd and Engi, 1997).

Peak HP–LT metamorphic conditions grade eastward from high-pressure greenschist to blueschist facies in the Schistes Lustrés complex and in the Briançonnais (Fig. 3a; Goffé and Velde, 1984; Agard et al., 2001a,b; Oberhänsli et al., 2004) to eclogitic facies conditions in the oceanic Zermatt-Saas and Monviso units, and in the continental Dora Maira, Gran Paradiso, and Sesia massifs (Chopin, 1984; Philippot and Kienast, 1989; Pognante, 1991; Lardeaux and Spalla, 1991; Spalla et al., 1996; Van der Klauw et al., 1997; Reinecke, 1998; Fig. 3a). We focus in the following on the vanished, ~1000 km wide Liguro-Piemontese ocean. Metamorphic remnants of the Valais Ocean are very restricted and subordinate in the Western Alps (VSB, Fig. 3a; Bousquet et al., 2002) and not further considered here.

2.2. Oceanic sediments and oceanic crust (+mantle): two contrasting settings

Two contrasting settings are apparent in the geological map among ocean-derived units (Fig. 3b): dominantly blueschist facies sedimentary units with minor crustal lenses such as the Schistes Lustrés complex (SL complex; Lemoine and Tricart, 1986) are located to the west, whereas large, mainly eclogitic oceanic crust bodies (such as those found in Monviso and Zermat-Saas units) mainly crop out to the east (Pognante, 1991). Moreover, on the southern Western Alps transect, the metamorphic *P–T* conditions evolve progressively in the Schistes Lustrés (Fig. 4a; Agard et al., 2001a), whereas slices of units with contrasting *P–T* peaks characterize the Monviso area (Fig. 4b; Schwartz et al., 2000a). Besides, Monviso and Zermat-Saas units are closely associated in space with the continental Internal Crystalline Massifs (ICM, hereafter; Fig. 4a,b) and show similar exhumation-related tectonic patterns (for example eclogitic NS lineations and later, penetrative W-vergent shear senses; Philippot, 1990; Henry et al., 1993; Van der Klauw et al., 1997). These contrasts suggest that the fates of the subducted sediments and oceanic crust were different.

Another line of evidence comes from estimates of their respective volumes and from the ratio of the exhumed rock volumes over initial subducted volumes ($R_{e/s}$). Considering (1) that the ocean consisted of a ~400 m thick sedimentary cover (Michard et al., 1996; Lemoine et al., 2000) and a 2–6 km thick oceanic crust (including underlying serpentinites of this low-spreading ophiolite; Lagabrielle and Cannat, 1990) and (2) that a ~1000 km wide ocean (Lemoine et al., 1986; Stampfli et al., 1998) disappeared across the entire length of the Western Alps (~500 km along strike), it can be estimated that $\sim 2 \cdot 10^5$ km^3 of sediments and $\sim 1\text{–}3 \cdot 10^6$ km^3 of oceanic crust (+mantle) were subducted. Assuming that oceanic units can be extended at depth

Table 1a
Compilation of available data on exhumed ocecanic rocks worldwide (see also Fig. 7 and the Appendix) formed mainly from the Cretaceous onwards, whose geodynamic context and oceanic origin are reasonably well known. Some prominent blueschist and eclogite localities were discarded, such as those from Oman (not oceanic), Greece (partly continental) or Eastern Alps (geodynamic context insufficiently well-constrained)

Area		Subduction history					
		Locality	Ages (Ma) [Subd. period] (Onset collis.)	*P–T* grad (°C/km)… and time evolution	Conv. Velocities (mm/a)	Age of subd. plate	Slab dip
Chile	1	East. Series (Valdivia)	[310–210?] (no collis.)	15 to 10	~70	0–100	
Western USA Franciscan complex	2	California belts	[170–100] (no collis.)	15 to <8–9	50–100	10–60	M
and others	3	Santa Catalina	[~120–90] (no collis.)	16 to 9	~50–100?	10–40	M
	4	Cascades	[35–0] (no collis.)	12–15	30	<20	L
Iran	5	SE Zagros (Hajiabad)	[150–35] (30–25)	15 8	50–60	~100	L
	6	Sistan (Ratuk)	[~100–50] –50	7–10	–	30	?
New Caledonia	7	Pam Peninsula	[60–45] (no collis.) obd 40–35	~12	50	20–30	M?
Antilles	8a	S. Cuba (Escam bray)	[120–70?]	~10	–	30–40	–
	8b	N. Cuba (N. Serp. Melange)	[130–100?] subd flip	9–10	–	<50	–
	8c	E. Cuba	[80–60?]		–	?	–
	8d	Dominican Rep. (Samana Penins.)	[130–70?]	5 to 13	–	<50	–
Western Alps	9	Sch. Lustrés		8	5–20	50–100	M–S
	10	Voltri	[100–45] (35)	8	"	100	"
	11	Monviso		8	"	"	"
	12	Zermatt-Saas		8	"	"	"
	13	Alpine Corsica	[100–45] (no coil)	7–8	"	"	"
Himalaya	14a	Shancila	[110–55]	~12–13	100–180	~50?	M–S
	14b	Sapi-Shergol	(45)			"	M?
Japan	15	Sanbagawa (Beshi+Kotsu)	[140–60] (new wedge)	9–12	50–100	60–80	L–M
Others	16	Sulawesi (Bantimala)	[140–110?] (no collis.?)	8	?		?
	17	Ecuador (Raspas)	[>150–0]	8–10	~100	50–100	M

according to the available cross-sections (Roure et al., 1990; Schwartz et al., 2000a; Schmid and Kissling, 2000), approximately $5 \cdot 10^4$ km^3 of sediments and crust are preserved in the Western Alps today. Taking an average value for the erosion rate (0.5 mm/yr; Duchêne et al., 1997b) over the last 25 Ma, the volume of exhumed sediments and oceanic crust initially was ~10^5 km^3 each. These mass-balance calculations thus yield rough $R_{e/s}$ estimates of 0.5 and 0.03–0.1 for the sediments and the oceanic crust, respectively. Even if these values are somewhat crude, they nevertheless underline the fact that only a very small percentage of the subducted oceanic crust (+mantle) was preserved (<5 vol.%) compared to metasediments (~30–50 vol.%).

2.3. Oceanic sediments: the Schistes Lustrés paleoaccretionary complex

The Schistes Lustrés complex is mainly made of Upper Mesozoic pelagic metasediments (De Wever and Caby, 1981; Lemoine et al., 1984; Polino, 1984). Agard et al. (2001a) showed that the *P–T* conditions evolve rather continuously in the SL complex from 1.2–1.3 GPa–350 °C to 1.8–2.0 GPa–500 °C, as exemplified by the progressive eastward increase of the phengitic substitution in carpholite- or chloritoid-bearing assemblages (Fig. 4a). Subordinate, dm-sized mafic bodies found in the SL complex, particularly in the east of the complex, yielded comparable *P–T* values (Schwartz, 2002). The SL complex, as for the classical Franciscan complex (see below), therefore represents a fossil accretionary wedge, with metasediments scrapped off the underlying oceanic crust during subduction, whose tectonic and metamorphic architecture is roughly preserved (Agard et al., 2001a; Schwartz, 2002; Seno et al., 2005).

2.4. Oceanic crust (+mantle): slices and slabs

The main structural features and the *P–T* conditions of the three main oceanic crustal massifs of the Western Alps, together with northern Corsica, are recalled below.

Monviso: This elongate massif comprises several coherent slices of mafic and ultramafic material and insignificant amounts of metasediments. Two main slices (~20 km long), one of mafic material to the west, one dominated by serpentinites to the east, represent 90% of the massif (Fig. 4b). Contrasting peak *P–T* conditions were found in the different mafic slices (Fig. 4b; Messiga et al., 1999; Schwartz et al., 2000a), leading Schwartz et al. (2000a) and Guillot et al. (2004) to propose that this massif corresponds to a nappe of units sampled from various depths along the subduction channel as they returned to the surface. Maximum *P–T* conditions at 2.4 GPa–630 °C are found in Mg-rich metagabbros near the Lago Superiore (Messiga et al., 1999; star no. 2 in Fig. 4b). Serpentinites in Monviso may also display the prograde formation of olivine+Ti-clinohumite after previous antigorite assemblages (Lombardo et al., 1978).

Zermatt-Saas: This ophiolite fragment from the Liguro-Piemontese Ocean (Li et al., 2004; Fig. 4c) comprises a mixture of mafic bodies (glaucophane schists, eclogites, metagabbros) and ultramafic rocks containing antigorite–forsterite–diopside–chlorite–Ti-clinohumite, which are isofacial with the eclogites, and minor metasediments (Bearth, 1959; Ernst and Dal Piaz, 1978). Most *P–T* estimates of the litterature range from 1.8 GPa (Barnicoat and Fry, 1986; Cartwright and Barnicoat, 2002) to 2.8 GPa (in coesite-bearing metasediments; Reinecke, 1991, 1998) for temperatures around 600±30 °C. In the northern part of the Zermatt-Saas unit, however, Bucher et al. (2005) demonstrated that the same HP/UHP conditions, around 2.7 GPa/550–600 °C, prevailed at least 30 km along strike, as typified by the widespread garnet–omphacite–glaucophane–epidote–chloritoid ± talc ± chlorite asssemblage. These authors thus proposed that the oceanic crust detached from a 'return-point' depth of 100 km, which more or less coincides with antigorite breakdown depths (and water liberation; see discussion below). In the area south of the Aosta valley, recent *P–T* estimates point to somewhat lower, yet homogeneous pressure conditions over several tens of km (e.g., 2.1 GPa–550 °C, Martin et al., 2008; 2.3 GPa–540 °C, Agard et al., unpubl. data).

Table 1b

Area		Exhumation history								
		Sedim or crust	Exhum period (Ma)	Time lag (My) between exhum and onset of subduction (or area collision:*)	Nature of the material	Relation/ serpentinites	Rock volumes (metabas)	Re/s (vol.%)	Tect setting C/S	Contin. *P–T* in Accr wedge?
Chile	1	S	300–210	Continuous	Metagraywackes	–	hm	<<1		y
		C	305–295	<10–15	Mafic bodies	Wrapped/serp.			I	–
Franciscan	2	S	150–100	Continuous	Clastics	–				y
		C	165–150	<15	Mafic blocks	Wrapped/serp.	m–hm	<<1	NI	n
S. Catalina	3	S	110–95		Graywackes		hm			
		C		<10–15	Mafic+melange	Wrapped/serp.			I	
Cascades	4	S	14–0	Continuous	Graywackes	–	m	~80–90	–	y
		C								
SE Zagros	5	S	95–85		Clastics+rayw	–	m			n
		C	95–85	Short-lived	Mafic+volc	Wrapped/serp.	hm–km	<<1	I	
		C	110–85?		Blocks in melange	Serp dominated	hm–km		I	
Sistan	6	S								
		C	>70	Before coll.	Dism ophiolite	Wrapped/serp.			I	n
N. Caled.	7	S	45–35		Clastic+melange		hm–km	~10–20		y
		C	"	5 before*	Mafic	Wrapped/serp.		<1	I	
S. Cuba	8a	S	80–70	~10 before*	Carb micaschists	Various blocks	hm–km	–		
		C	"		Mafic	Wrapped/serp.			I	
N. Cuba	8b	S	105 (+80–70)	Continuous?	–			–		
		C	"		Melange	Serp dominated	>10 km			y
E. Cuba	8c	C	80–70?		Melange		hm–km	–		
D. Republ.	8d	S	80		Melange		hm	–		
		C	"	10 before*					–	
S. Lustrés	9	S	65–35	Continuous	Pelitic	Very few	m	~50	–	y
Voltri	10	C	49–40	Continuous?	Mafic lenses+calcsch	Some serp	hm–km		I	y?
Monviso	11	C	(50) 45–35	5–10 before*	hm to km mafic slices	Wrapped/serp.	>10 km	<3	I	n
Z. Saas	12	C	(50) 45–35	5–10 before*	hm to km mafic slices	Wrapped/serp.	>10 km	"?	I	y
Corsica	13	S	65–35?	Continuous?	Pelitic	Very few	hm–km	–	–	y
		C	?	?	Mafic	Some serp				
Shangla	14a	S	95–80	Short-lived	Volcanoclastics	–	hm	<<1		
S. Shergol	14b	C	100–90	"	Arc fragments?	Wrapped/serp.?	hm	<<1		
Sanbagawa	15	S	100–60?	Continuous	Metagraywackes	Few serp	hm–km	~10–50?	–	y
		C	95–75?	?	Mafic+volcanoclast	Some serp		<1	I	
Sulawesi	16	S	130–115		Volcanoclastics		hm–km			
		C			Mafic blocks	wrapped/serp.			I	
Andes	17	C	~130	Short-lived	Mafic+ultramafic		km	<<1		

Voltri: The Voltri massif comprises three main units (Fig. 4d; Hermann et al., 2000), from bottom to top: (1) the Voltri–Rossiglione unit, made of metasediments and metavolcanics, comprises blueschists and eclogites equilibrated at 1.3–1.8 GPa–500 °C (Federico et al., 2004); (2) the Beigua unit is made of serpentinites enclosing hm- to km-sized eclogite blocks (metabasalts and Fe–Ti metagabbros) equilibrated at 1.5 to 2±0.2 GPa/550 °C (Messiga and Scambelluri, 1991; Vignaroli et al., 2005) and comprises, in places, melange zones with blocks at 20/580 °C

Table 1b (*continued*)

Area		Exhumation history				References
		P–T max (GPa/°C)	Exhum. Velocities (mm/y)	Type**	Others (oblique conv., arc magm, evolution of subd zone gradients)	
Chile	1	1.2–1.4/400° 1.5/680°	0.6	B	Arc, cooling SZ Counterclock/blocks	Willner et al. (2004), Glodny et al. (2005)
Franciscan	2	1.0/400° 1.5/520° 2.2/550°	~1–2 ~1–2? 4–5	B	Cooling SZ Arc	Anczkiewicz et al. (2004), Baldwin (1996), Cloos (1982, 1984, 1985), Ernst (1965, 1971, 1993), Ernst and Liou (1995), Jayko et al. (1986), Kimura et al. (1996), Krogh et al. (1994), Moore and Blake (1989), Oh and Liou (1990), Sedlock (1996), Tagami and Dumitru (1996), Tsujimori et al. (2006), Wakabayashi (1990)
S. Catalina	3	1.2/660°	~1–2	B	Cooling SZ	Bebout (1991), Bebout and Barton (2002), Grove and Bebout (1995), Sorensen and Barton (1987), Sorensen (1988)
Cascades	4	–	~1	B	Arc	Batt et al. (2001), Brandon et al. (1998), Feehan and Brandon (1999), Orange et al. (1992), Ring and Brandon (1999)
SE Zagros	5	1.1/530° 1.1/530° 1.9/500°	~2–3 ~2–3 –	B	Cooling SZ? Arc, oblique Exhum in syntaxis	Agard et al. (2005b, 2006), Molinaro et al. (2005), Paul et al. (2006), Sabzehei (1974), Sabzehei et al. (1994)
Sistar	6	1.92.2/600°		?		Fotoohi Rad et al. (2005), Tirrul et al. (1983)
N. Caled.	7	1.2–1.6/550° 1.9/590°	~5? "	A?	Heating SZ? Arc?	Carson et al. (1999), Clarke et al. (1997), Cluzel et al. (2001), Fitzherbert et al. (2003, 2004, 2005), Marmo et al. (2002), Rawling and Lister (2002), Schellart et al. (2006), Spandler et al. (2005)
S. Cuba	8a	1.6–2.1/600°	2–4?	B	Arc	Kerr et al. (1999), Schneider et al. (2004), Stanek et al. (2006)
N. Cuba	8b	2.0/600°	?	A?	Arc Instab (oscill gt)	Kerr et al. (1999), Garcia-Casco et al. (2002, 2006)
E. Cuba	8c	1.5/660–750°	?	?		Cobiella-Reguera (2005), Garcia-Casco et al. (2006), Maresch et al. (2000)
D. Republ.	8d	0.7/320° 2.2/580	? 5–6	A?	Oblique, heating SZ?	Goncalves et al. (2000), Zack et al. (2004), Gorczyk et al. (2007), Krebs et al. (2008)
S. Lustrés	9	1.6–1.8/500°	~1–2	A	IsoT to cooling paths	S.Lustrés: Agard et al. (2001a,b, 2002), Goffé and Chopin (1986),
Voltri	10	1.8–2.5–600°	~3–4	A	Counterclock/blocks	Schwartz (2002); Voltri: Federico et al. (2004, 2005),
Monviso	11	2.4/630°	>5–10	A	No arc Near continental UHP	Hermann et al. (2000), Messiga et al. (1995), Rubatto and Hermann (2003), Vignaroli et al. (2005); Monviso: Guillot et al. (2004), Messiga et al. (1999), Schwartz et al. (2000a);
Z. Saas	12	2.8/600°	>5–10	A	UHP!	Z. Saas; Amato et al. (1999), Bucher et al. (2005),
Corsica	13	2.1/420° 2.4/480°	<5(?) <5(?)	A		Lapen et al. (2003), Li et al. (2004), Reinecke (1991, 1998), Rubatto et al. (1998); Corsica: Brunet et al. (2000), Caron and Pequignot (1986), Daniel et al. (1996), Fournier et al. (1991), Lahondére and Guerrot (1997), Ravna et al. (submitted for publication)
Shangla	14a	0.7/400°		B	Arc, partly oblique	Anczkiewicz et al. (2000), Guillot et al. (2007-in review), Honegger et al. (1989), Maluski and Matte (1984)
S. Shergol	14b	1.0/350–420°	?	B	Arc, syntaxis exhum.	Guillot et al. (1997, 1999), Mahéo et al. (2006), Searle et al. (1997), Tonarini et al. (1993)
Sanbagawa	15	1.8–2.1/610° 1.8–1.9/590°	– ~1	B	Arc	Banno (1986), Enami (1998), Inui and Toriumi (2002), Ko et al. (2005), Matsumoto et al. (2003), Takasu et al. (1994), Takeshita et al. (2005), Wallis (1998), Wallis and Aoya (2000), Wallis et al. (2004), Yagi and Takeshita (2002)
Sulawesi	16	1.8–2.4/620°	?	B	Arc Cooling SZ?	Miyazaki et al. (1996), Parkinson (1998)
Andes	17	~2.0/550°	?	B	Arc entrance oc. Plateau	Arculus et al. (1999), Feininger (1980), Gabriele et al. (2003), Kerr et al. (2002)

Abbreviations (by order of apparition in columns): Slab dips classified as low (L; <30°), moderate (M; 30°<.<50°), or steep (S; >50°). Sediments (S) or Crust (C). Rock volumes: typical size of rock-volumes of oceanic crust. Re/s: ratio of the exhumed rock volumes over initial subducted volumes (see text for details). Tectonic setting of crust with respect to sediments (C/S): I stands for internal, NI for non internal. Type ** refers to the classification of Maruyama et al. (1996) into type A or B protoliths. Others: SZ (subduction zone).

(Federico et al., 2007); (3) the Erro-Tobio unit, interpreted as a piece of sub-continental lithospheric mantle exhumed during the Alpine rifting and later subducted (Hoogerduijn Strating et al., 1993; Hermann et al., 2000), is made of variably serpentinized lherzolites hosting a number of mafic blocks (including Mg-rich metagabbros equilibrated at 1.8–2.5 GPa/600±30 °C; Messiga et al., 1995).

The Voltri massif therefore appears as intermediate between the Monviso/Zermatt-Saas massifs and the Schistes Lustrés complex:

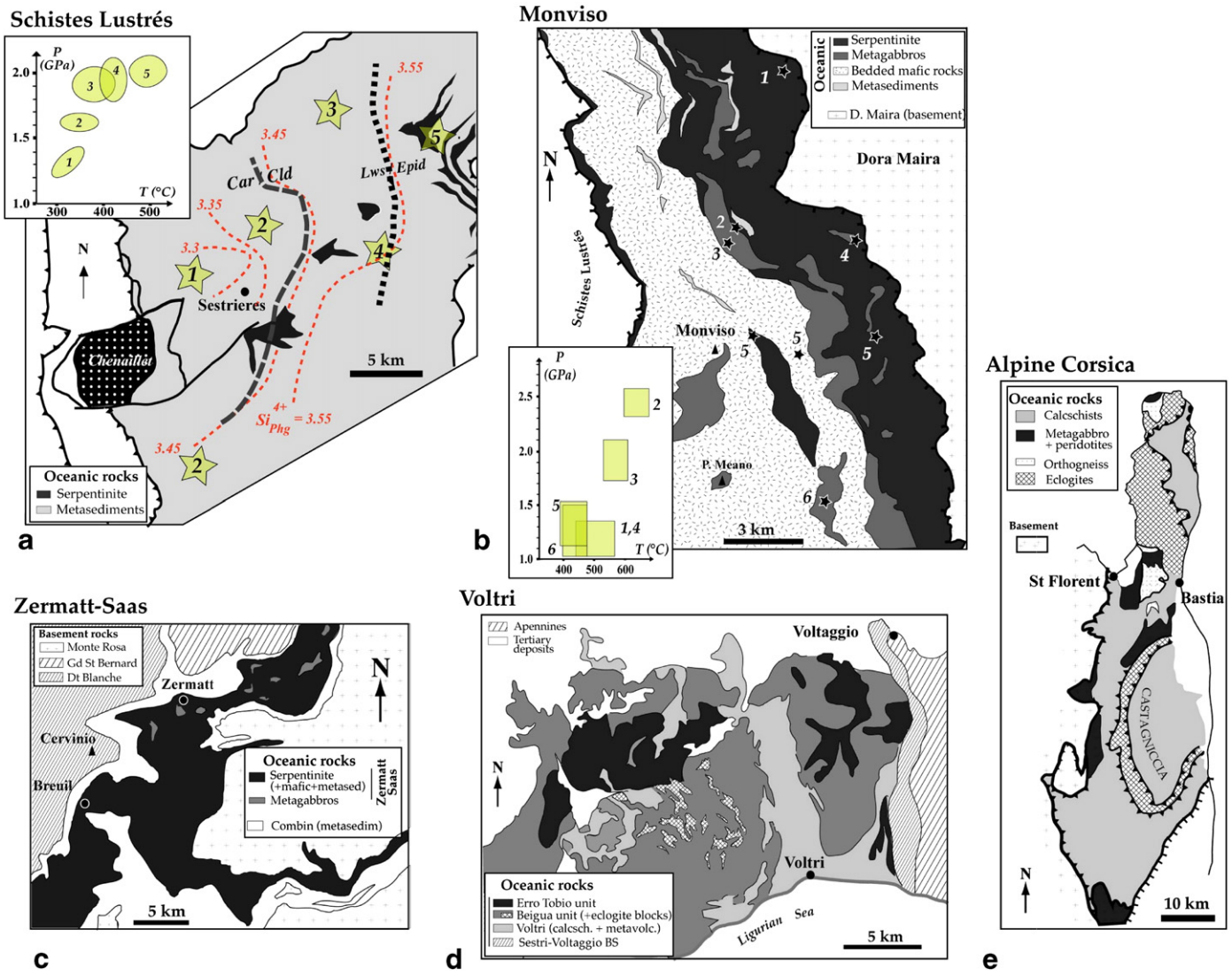

Fig. 4. Simplified geological maps of the four main metamorphosed oceanic units of the Western Alps (MV, SL, VO, ZS boxes in Fig. 3a,b) plus Corsica. Same abbreviations as for Fig. 3. (a) Map of the Schistes Lustrés area. Note the scarcity of serpentinites and the absence of large mafic units (m-sized blocks of metabasites are rare but can be found in places). Note the progressive eastward increase of both pressure (as shown by the increase of the Si content in phengite; doted lines) and temperature (as shown by the crossing of the carpholite/chloritoid and lawsonite/epidote isograds). *P–T* conditions after Agard et al. (2001a,b). (b) Map of the Monviso area (after Philippot, 1990; Schwartz, 2002). *P–T* conditions after Messiga et al. (1999) and Schwartz et al. (2000a). Note the contrasting *P–T* values a few hectometers or kilometers apart, and along strike. (c) Map of Zermatt-Saas area (after Bucher et al., 2005). (d) Map of Voltri massif (adapted from Hermann et al., 2000; Federico et al., 2005; Vignaroli et al., 2005). (e) Map of Alpine Corsica (after Jolivet et al., 1998a).

(1) calcschists and serpentinites wrapping gabbroic lenses are extensive and closely associated in the Voltri group (Fig. 4d; Federico et al., 2005 and references therein), (2) mafic bodies are smaller on average than for the Zermatt-Saas and Monviso units. Large mafic slabs, tens of km long and >km thick are not found, (3) *P–T* conditions either resemble those of the Schistes Lustrés (e.g., Voltri group) or of the Zermatt-Saas and Monviso units (Beigua and Erro-Tobio units). Some eclogitic blocks of the Beigua unit, however, provided evidence for a counter-clockwise *P–T* evolution (Vignaroli et al., 2005), (4) there is no internal crystalline massif nearby.

Corsica: HP–LT rocks from Corsica formed in the Alpine subduction zone. Corsica, however, evolved separately from the W. Alps after ~35 Ma, which marks the onset of widespread extension in the Mediterranean realm (Jolivet and Faccenna, 2000; Jolivet et al., 2003; Lacombe and Jolivet, 2005). Contrary to the W. Alps, Corsica thus escaped the later collisional deformation and provides useful insights into the fossil Alpine wedge (Fournier et al., 1991). Mafic bodies mainly crop out as nappes interleaved within dominantly blueschist facies metapelitic units analogous to those of the Schistes Lustrés (Fig. 4e). Lawsonite eclogites (Caron and Pequignot, 1986; Ravna et al., submitted for publication) and pseudotachylites in peridotites deformed under HP–LT conditions (Austrheim and Andersen, 2004) were reported. Blueschists and eclogites were finally exhumed in Oligo-Miocene extensional shear zones (Daniel et al., 1996; Jolivet et al., 1998b; Brunet et al., 2000).

2.5. Radiometric constraints: P–T–t paths and exhumation velocities

The shapes of the *P–T* paths of the five oceanic units are compared in Fig. 5a, as well as to those deduced for the neighbouring continental units. Radiometric constraints for the HP/UHP oceanic units of the Western Alps are somewhat scattered but mainly span the range 60–35 Ma (Fig. 5b).

Age constraints for the SL complex (Agard et al., 2002) support the idea of a steady state accretion between 60 and 45 Ma at least (Jolivet et al., 2003; Yamato et al., 2007). Exhumation velocities, calculated from age averages of the depth equilibrium steps (e.g. Fig. 5c), point to exhumation rates on the order of a few mm/yr (1–5 mm/yr at the most, assuming some minor excess argon; Yamato et al., 2007). A similar age range (49–40 Ma; Federico et al., 2005, 2007) and the same conclusions were drawn for the Voltri group, for which exhumation velocities are 3–4 mm/yr (Federico et al., 2005). Higher

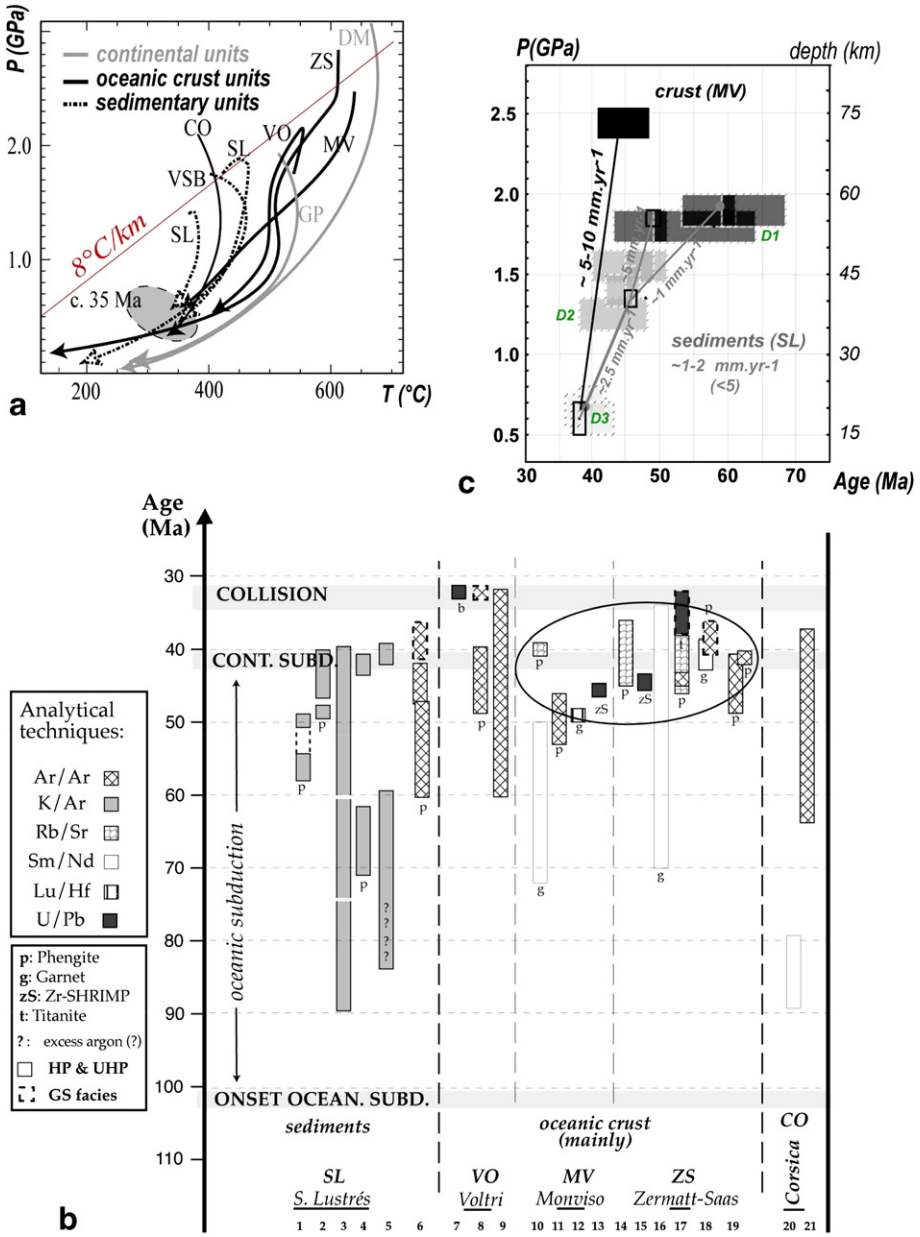

Fig. 5. (a) Compilation of *P–T* paths for the HP–LT areas outlined in Fig. 3a. Abbreviations: CO: Corsica; DM: Dora Maira; GP: Gran Paradiso; MV: Monviso; SL: Schistes Lustrés; VO: Voltri; VSB: Versoyen Grand St Bernard; ZS: Zermat-Saas. Data from Agard et al. (2001a,b), Bousquet et al. (2002), Bucher et al. (2005), Chopin et al. (1991), Federico et al. (2005), Jolivet et al. (1998a,b), Le Bayon et al. (2006), Messiga et al. (1995, 1999), Reinecke (1991, 1998), Skchwartz et al. (2000a), Vignaroli et al. (2005). (b) Compilation of recently published radiochronological data on the differents domains of the Western Alps and Alpine Corsica. Note, as outlined by the ellipse, the clustering of ages (apart from two Sm–Nd ages) during the period of continental subduction for Zermatt-Saas and Monviso. For each study, we give the method and minerals used (see legend box on the left hand side) and the overall domain of *P–T* conditions investigated (HP and UHP: high-pressure and ultrahigh-pressure conditions; GS: greenschist facies conditions). Studies are listed as follows: (1) Liewig et al. (1981), (2) Bonhomme et al. (1980), (3) Takeshita et al. (1994), (4) Delaloye and Desmons (1976), (5) Caby and Bonhomme (1982), (6) Agard et al. (2002), (7) Rubatto and Scambelluri (2003), (8) Federico et al. (2005), (9) Federico et al. (2004), (10) Cliff et al. (1998), (11) Monié and Philippot (1989), (12) Duchêne et al. (1997a,b), (13) Rubatto and Hermann (2003), (14) Reddy et al. (1999), (15) Rubatto et al. (1998), (16) Bowtell et al. (1994), (17) Barnicoat et al. (1995), (18) Amato et al. (1999), (19) Reddy et al. (2003), (20) Lahondère and Guerrot (1997), (21) Brunet et al. (2000). (c) Radiometric constraints for the Schistes Lustrés from Agard et al. (2002) and for Monviso from Monié and Philippot (1989), Duchêne et al. (1997a), Rubatto and Hermann (2003).

velocities were obtained for the Beigua unit (25 mm/yr; Rubatto and Scambelluri, 2003), based on U/Pb dating of baddeleyite from eclogite blocks, yet seem to conflict with sedimentary constraints from the nearby Early Oligocene basins (Federico et al., 2004).

Age constraints for the Monviso and Zermatt-Saas units cluster mostly between 45 and 35 Ma, apart from two poorly constrained Sm/Nd ages (Fig. 5b). Exhumation velocities deduced from these values are significantly higher than for the SL complex and range between 5–10 and 30 mm/yr (Fig. 5c; Amato et al., 1999; Rubatto and Hermann, 2003). We note that their exhumation is broadly coeval with the period of continental subduction (40±5 Ma; Fig. 5b).

Continental subduction necessarily developed after 45 Ma, given the presence of Mid-Eocene flysch deposits, later metamorphosed under HP–LT conditions, on the thin continental margin (Barfety et al., 1995), but may have been slightly diachronous along strike. Most recently published radiometric age constraints for this HP to UHP continental metamorphism suggest that peak burial conditions were reached between 40 and 35 Ma (see Agard et al., 2002 for a review).

Radiometric constraints for Alpine Corsica do not support fast exhumation (Lahondère and Guerrot, 1997), but data pertaining to the subduction stages are still too few to conclude.

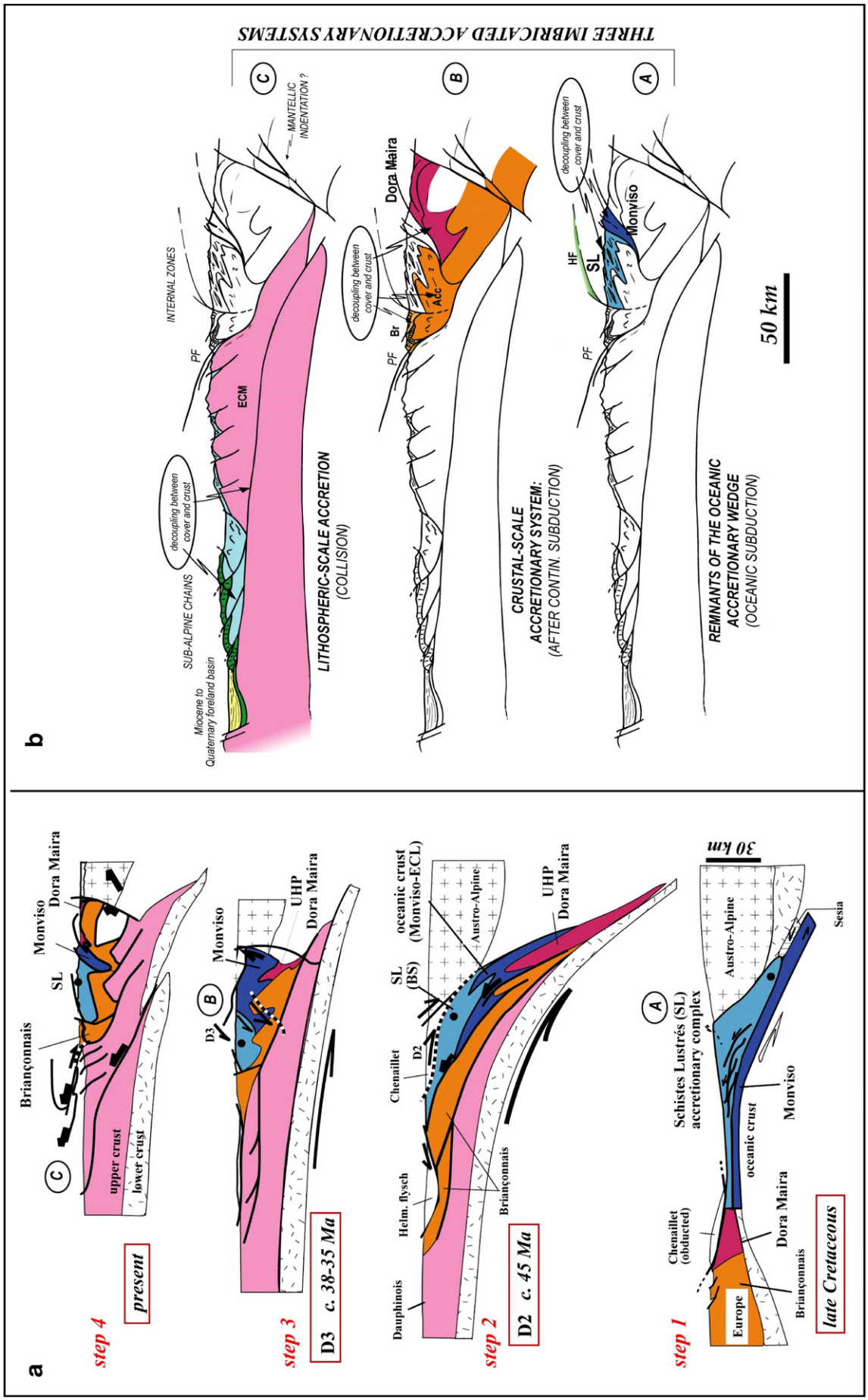

Fig. 6. (a) Geodynamic scenario for the evolution of the Western Alps (modified from Agard et al., 2002; BS: blueschist; ECL: eclogite; D2, D3: deformation stages). See text for details. (b) Lithospheric-scale cross-section (after Jolivet et al., 1996) showing the domains progressively incorporated in the Western Alpine orogen during oceanic subduction (1), continental subduction (2) and collision (3). The importance of sedimentary/crustal decoupling at each stage can also be noted. Abbreviations: Acc: Acceglio; Br: Briançonnais; HF: Helminthoid flysch; ECM: External Crystalline massifs; PF: Penninic front; SL: Schistes Lustrés complex.

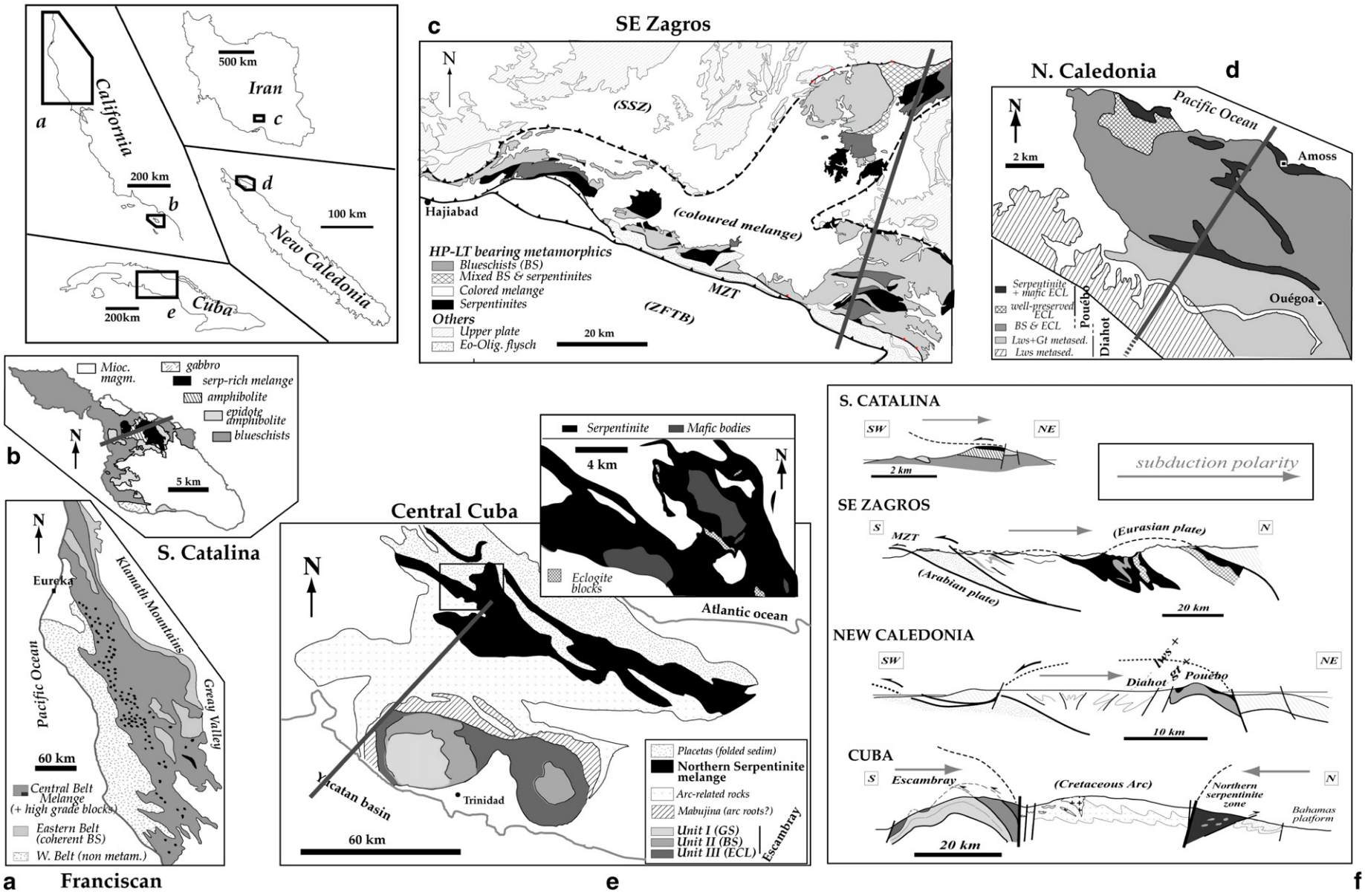

Fig. 7. Geological settings of some of the key areas considered in our study (Table 1). Profiles correspond to the cross-sections shown in panel f. (a) Main subdivisions of the Franciscan complex (after Cloos, 1985). (b) Geological map of Santa Catalina island (after Sorensen, 1988; Grove and Bebout, 1995). (c) Geological map of SE Zagros near Hajiabad (after Sabzehei et al., 1994; Agard et al., 2006). (d) Simplified geological map of NW New Caledonia (Pam Peninsula), showing the main unit subdivisions (adapted from Cluzel et al., 2001; Rawling and Lister, 2002; Fitzherbert et al., 2004, 2005). (e) Geological map of central Cuba simplified from Garcia-Casco et al. (2002) and Schneider et al. (2004). (f) Schematic cross-sections showing the position of the HP–LT rocks. Note the internal position of all mafic eclogitic units and serpentinites with respect to the subduction polarity, except for the Franciscan complex. The cross-section across NW New Caledonia was reinterpreted from available cross-sections (see above references).

2.6. Interpretation: structure and tectonic evolution of the W. Alps

This review of available *P–T–t* data therefore suggests a marked contrast between the Schistes Lustrés complex on the one hand, and the Monviso and Zermatt-Saas units on the other hand (the Voltri massif showing intermediate characteristics): the Monviso/Zermatt-Saas units show the greater *P–T* values, the greater exhumation velocities, the larger coherent tracts of mafic units, and were exhumed during the final stages of the subduction process (Fig. 5b). In addition, these two massifs crop out in the vicinity and wrap the continental units of the internal crystalline massifs (Fig. 3a). All this suggests that the exhumation of these deep-seated fragments of oceanic lithosphere is linked with continental subduction. This link is further strengthened by the exhumation rates for the UHP Dora Maira unit, which are often considered ≥1–5 cm/yr (for example, Duchêne et al., 1997b; Gebauer et al., 1997; Rubatto and Hermann, 2001).

Although a detailed discussion of the tectonic evolution of the Western Alps is beyond the scope of the present paper, a synthetic view on the geodynamic evolution from subduction to collision is shown in Fig. 6a (see Agard et al., 2002; Jolivet et al., 2003). This reconstruction places emphasis on the progressive shortening and accretion (e.g., Polino et al., 1990) which occurred during oceanic subduction (step 1, Fig. 6a), continental subduction (steps 2–3) and collision (step 4). The Alpine belt can thus be viewed as the imbrication of three successive accretionary wedges of different scale with time (from A to C: sedimentary, crustal, lithospheric; Fig. 6b). Within this frame, the Schistes Lustrés complex (and possibly the Voltri group) is exhumed during convergence in the oceanic accretionary wedge and/or in the subduction channel (step 1, Fig. 6a). The faster exhumation velocities, tighter *P–T* loops (Fig. 5a) and spatial association of the large oceanic crust bodies such as Monviso and Zermat-Saas with the HP–UHP continental units suggest a different exhumation mechanism. Their exhumation occurred later, during the locking of continental subduction and the exhumation of the crustal wedge associated with continental subduction (step 2, Fig. 6a). The final exhumation of these deep-seated oceanic units takes places through major extensional shear zones (step 3, Fig. 6a), such as those separating the blueschist from eclogitic Piemonte units (e.g., Kienast, 1973; Ballèvre et al., 1990; Ballèvre and Merle, 1993; Reddy et al., 1999), and may even involve some later, minor re-burial during the early collisional stages (Beltrando et al., 2007).

3. The exhumation of oceanic rocks worldwide

3.1. Data compilation

We present in Table 1 and in the Appendix a worldwide compilation of oceanic blueschists and eclogites from subduction zones formed mainly from the Cretaceous onwards (location on Fig. 2), whose geodynamic context and oceanic origin are reasonably well known. This compilation aims at identifying key parameters controlling the burial and exhumation of oceanic (sedimentary and crustal) rocks in subduction zones, at constraining exhumation processes and, to some extent, plate interactions at subduction zones.

This review lists the main sites where HP–LT rocks are exhumed worldwide, in various geodynamic contexts: those with high or low convergence velocities, followed or not by collision and/or obduction, with protracted or short-lived exhumation histories, etc. Major data, whenever available, are given in Table 1. Note that exhumation velocities herein are either taken from the literature or calculated from averaged

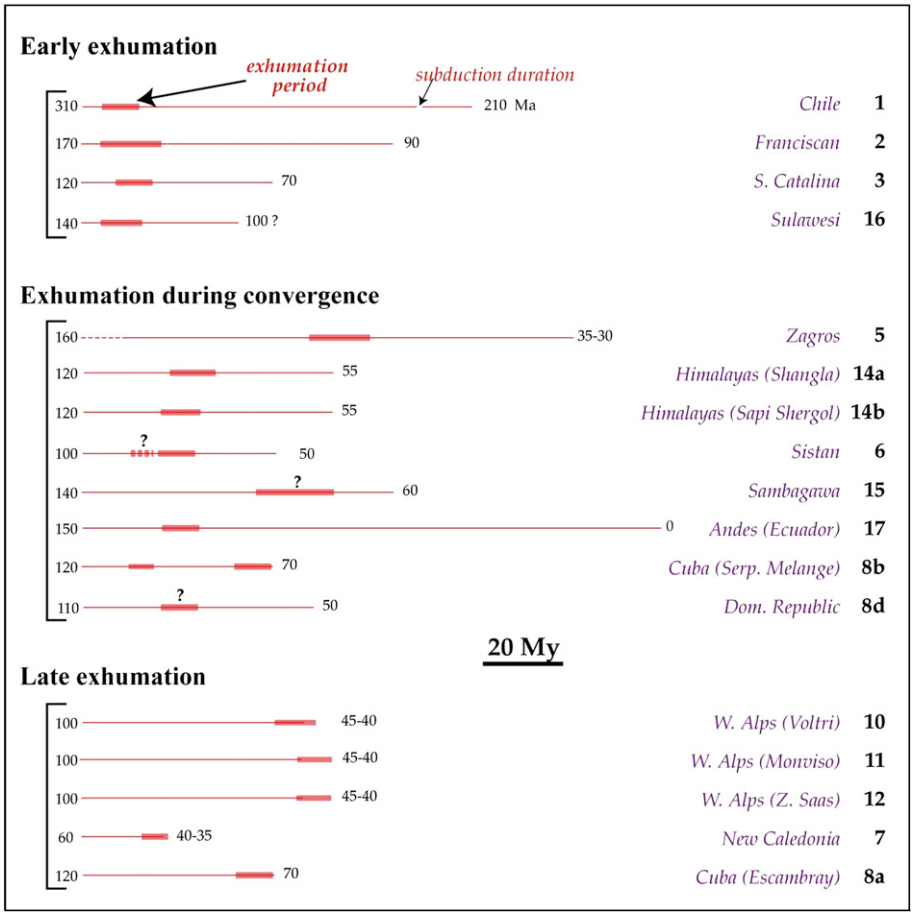

Fig. 8. Timing of oceanic crust exhumation (thick segments) with respect to the subduction history (whose duration is indicated by the thin line) in each of the investigated settings (numbers refer to ages in Ma). Numbers in the column to the right as for Table 1.

published radiometric ages pertaining to the various *P–T* equilibrium steps recognized on a given *P–T–t* path.

In order to both provide a brief description of the localities considered here and to ease reading, the overview of their geodynamic settings (size, nature of the material, main geological features) is placed in the Appendix. Several maps are given for the most representative localities (Fig. 7). For further details, the interested reader is referred to the selected bibliography in the Appendix and in Table 1.

3.2. Main conclusions from our survey

The following observations can be pointed out from the data of Table 1 (and Figs. 4–7):

(1) The timing of oceanic crust (+mantle) exhumation (thick lines in Fig. 8) with respect to the subduction duration is highly variable: it can either take place early (Chile, Franciscan, possibly Makran), in the midst of convergence (SE Zagros, Himalaya, Andes), or late (Western Alps, New Caledonia). Late exhumation of oceanic crust is observed in settings where continental subduction developed (New Caledonia; Zermatt-Saas and Monviso for the W. Alps), yet does not take place systematically (it is lacking in the Himalayas and SE Zagros, for example). Most importantly, Fig. 8 shows that the oceanic crust appears to be exhumed episodically, that is only during restricted, specific time windows.

(2) By contrast, sedimentary exhumation appears to be a long-lasting process: >50 My for Chile, ~50 My for the Franciscan complex, at least 25–30 My for the Alpine Schistes Lustrés (Table 1). The data also support the conclusion that exhumation returns larger volume proportions of subducted sediments (~80–90% and 30–50% for the Cascades and the W. Alps, respectively) than oceanic crust (+mantle). For example, <5% in the Western Alps, <<1% for the Himalayas, the Franciscan and SE Zagros.

(3) Oceanic crustal material is almost systematically associated with serpentinites, either as lenses wrapped in a serpentinite-rich (or exclusive) melange or as dispersed, isolated blocks. Serpentinites possibly originate from the hydrated mantle wedge (Guillot et al., 2001; Scambelluri et al., 2001; Fitzherbert et al., 2004; Guillot et al., 2004) or from the hydrothermalized slab mantle (as shown by the large oceanic pieces with gabbroic and basaltic successions of the W. Alps; Chalot-Prat et al., 2003; Li et al., 2004), or both (Hermann et

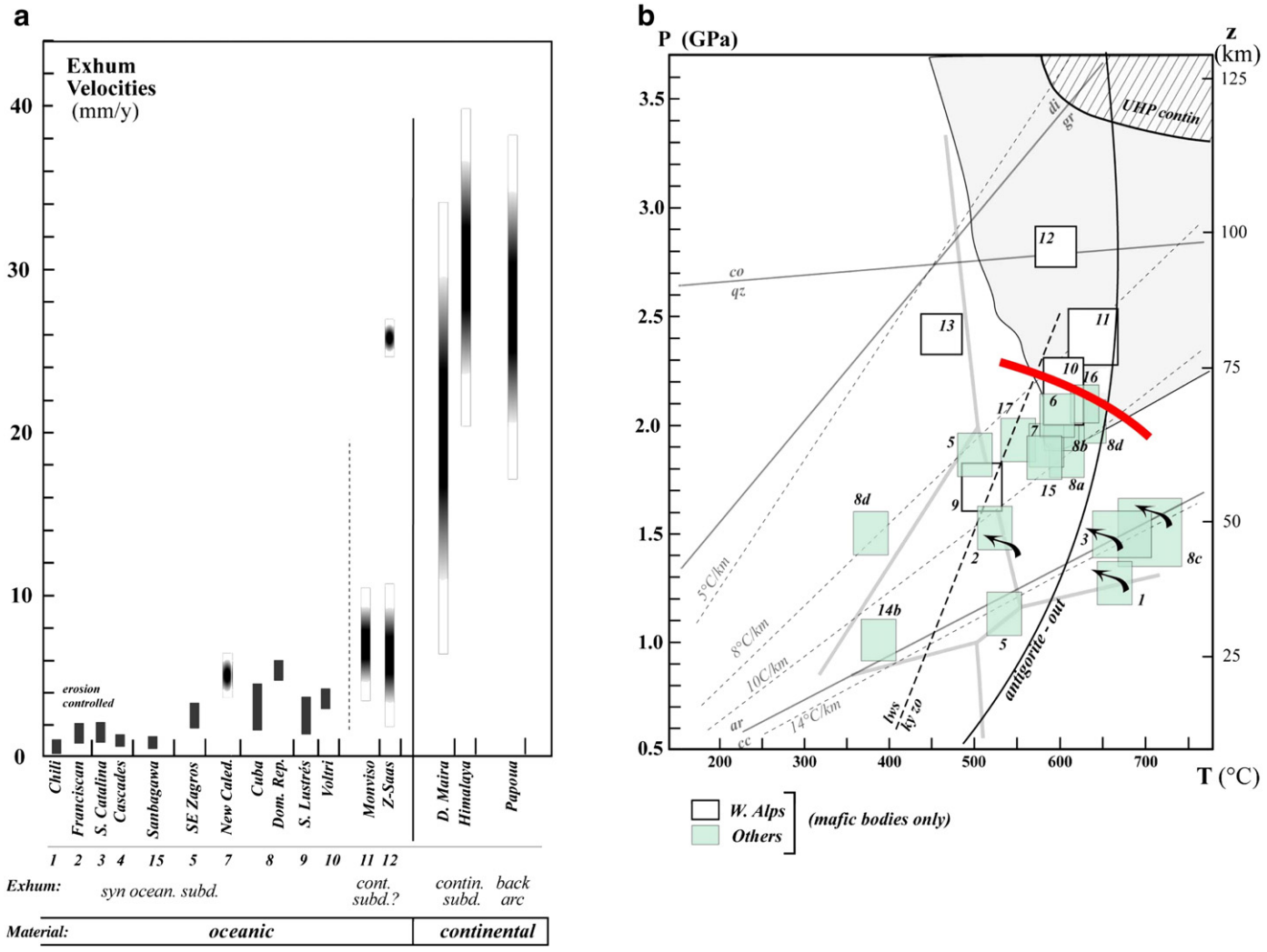

Fig. 9. (a) Plot of exhumation velocities listed in Table 1 (same numbers). Exhumation velocities herein are either taken from the literature or calculated from averaged published radiometric ages pertaining to the various *P–T* equilibrium steps recognized on a given *P–T–t* path. Note the sharp contrast between oceanic and continental rocks, and the highest rates for Monviso and Zermatt-Saas within the former category. (b) Plot of maximum *P–T* values reached by the oceanic crust in the various areas considered here (same numbers as for Table 1). Grey field: domain of negative buoyancy for the oceanic crust with respect to the adjacent mantle (see Fig. 13a and discussion). Hatched field: domain of ultra-high pressure conditions (UHP; for example D. Maira, W. Alps). Arrows: subduction settings providing evidence for cooling gradients following subduction initiation and/or for counter-clockwise *P–T–t* paths.

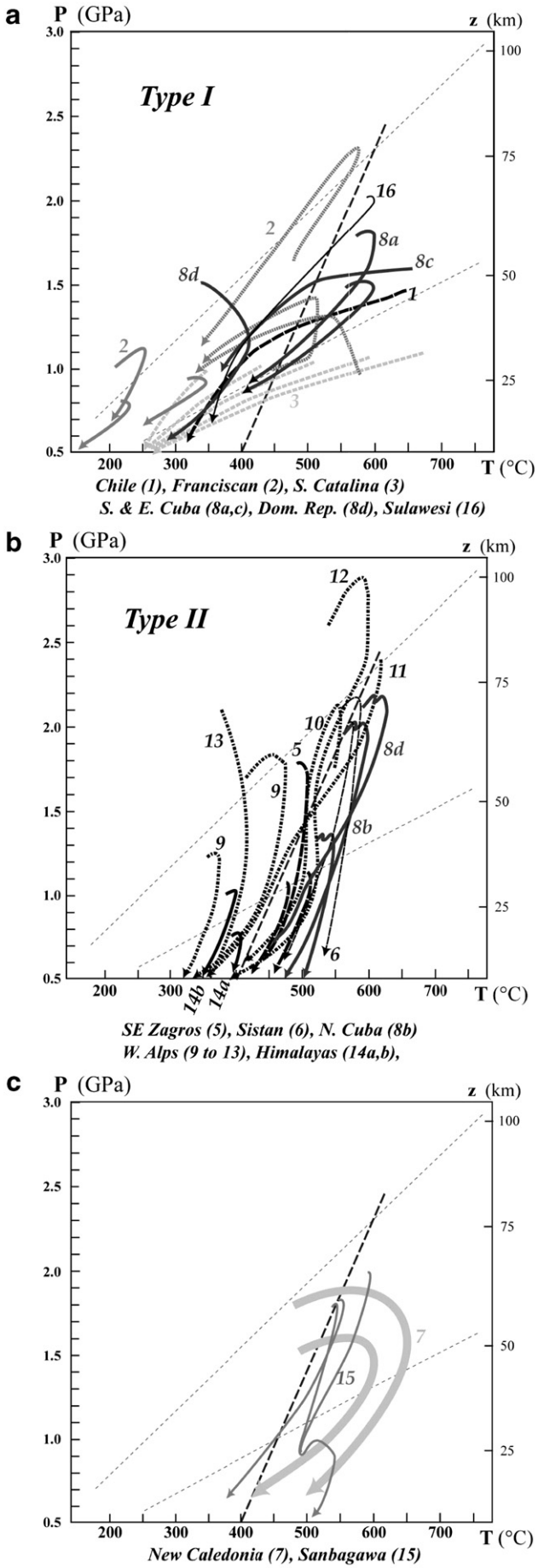

al., 2000). The data of Hattori and Guillot (2007) suggest that most Himalayan serpentinites originate from the mantle wedge, whereas Alpine serpentinites come from the slab mantle. Table 1 also shows that the exhumed oceanic crust generally occupies a structurally high, internal position, near the buttress (Fig. 7f). This is not the case, however, for the Franciscan complex, where coherent blueschist tracts are found at the rear of the wedge (Fig. 7a).

(4) Exhumation velocities range mainly between 1 and 5 mm/yr (Fig. 9a). Faster exhumation (>5–10 mm/yr) is only documented for Zermatt-Saas and Monviso in the Western Alps, and possibly for the Beigua unit in Voltri (see above). Exhumation velocities for New Caledonia, which lie in the upper bound too, further suggest that there is a link between faster exhumation rates and continental subduction. A word of caution is necessary, however, with respect to isolated blocks wrapped in serpentinites or in a weak matrix, for which exhumation velocities are not known with precision but were inferred to be low (Anczkiewicz et al., 2004; Glodny et al., 2005). Reappraisal of *P–T* conditions for the Franciscan blocks (Tsujimori et al., 2006) could lead to higher exhumation velocities than previously thought, since it is yet unclear at which *P–T* conditions the blocks were juxtaposed and later dispersed within the accreting metasediments.

(5) *P–T* gradients are in general ~8–10 °C/km, and in any case <15 °C/km (Fig. 9b). A number of settings provide evidence for cooling gradients following subduction initiation (Chile, Franciscan, Santa Catalina; arrows in Fig. 9b). *P–T* conditions are scattered but usually lower than 1.8–2.0 GPa for the metasediments and <2.0–2.3 GPa for the oceanic crust (Fig. 9b). A part of the Zermatt-Saas unit clearly went further down that this limit, and some of the Monviso and Voltri units (all of which belong to the W. Alps too) could have equilibrated 0.1–0.2 GPa higher. To date, the Zermatt-Saas occurrence is the deepest piece of subducted oceanic crust returned to the surface (Reinecke, 1991, 1998). Unlike continental rocks, however, no oceanic crustal rocks known to have returned from ultradeep conditions (that is 120–300 km, Fig. 1b; Green, 2005; Scambelluri et al., 2008 and references therein) have been found so far. Note that type B protoliths, as defined by Maruyama et al. (1996), experience pressure conditions largely >1.2 GPa (Table 1), contrary to the statement of these authors.

(6) *P–T* paths (shown in Fig. 10) essentially fall into two types, as noticed by Ernst (1988). Cooling *P–T* paths (Type I; Fig. 10a) characterize Chile, the Franciscan complex, Santa Catalina and most units in the Antilles, whereas isothermal (to slightly cooling) decompression paths characterize the W. Alps, Iran, the Himalayas and the Northern serpentinite melange from Cuba (Type II; Fig. 10b). All type I *P–T* paths (Fig. 10a), plus Corsica (Fig. 10b), stay on the low temperature side of the reaction identified by Zack et al. (2004; dotted line in Fig. 10) as the stability limit of lawsonite eclogite. Note that less typical paths are found for New Caledonia (Fig. 10c), and that the *P–T* paths for Sambagawa, despite the lack of subsequent collision, rather resemble those of Fig. 10b. Although these plots broadly

Fig. 10. *P–T* paths for the various HP–LT areas considered here (same numbers as for Table 1), grouped according to shape. Thin doted lines refer to the metamorphic gradients of 8 °C/km and 14 °C/km, respectively, as shown in Fig. 9. Thick dashed line: reaction lawsonite = kyanite + zoisite + SiO_2 + H_2O (after Schmidt and Poli, 1998). *P–T* conditions to the left of this curve favor the preservation of lawsonite eclogite according to Zack et al. (2004). (a) Type I: cooling paths. Several of them have allowed for the preservation of lawsonite eclogite (no. 2, 8d, 14). (b) Type II: isothermal to slightly cooling decompression paths (most of them lie to the right of the lawsonite eclogite preservation curve, apart from Corsica — no. 13). (c) Other paths contrasting with type I and type II (presented independently here for the sake of clarity): Sanbagawa (no. 18) and New Caledonia (no. 7).

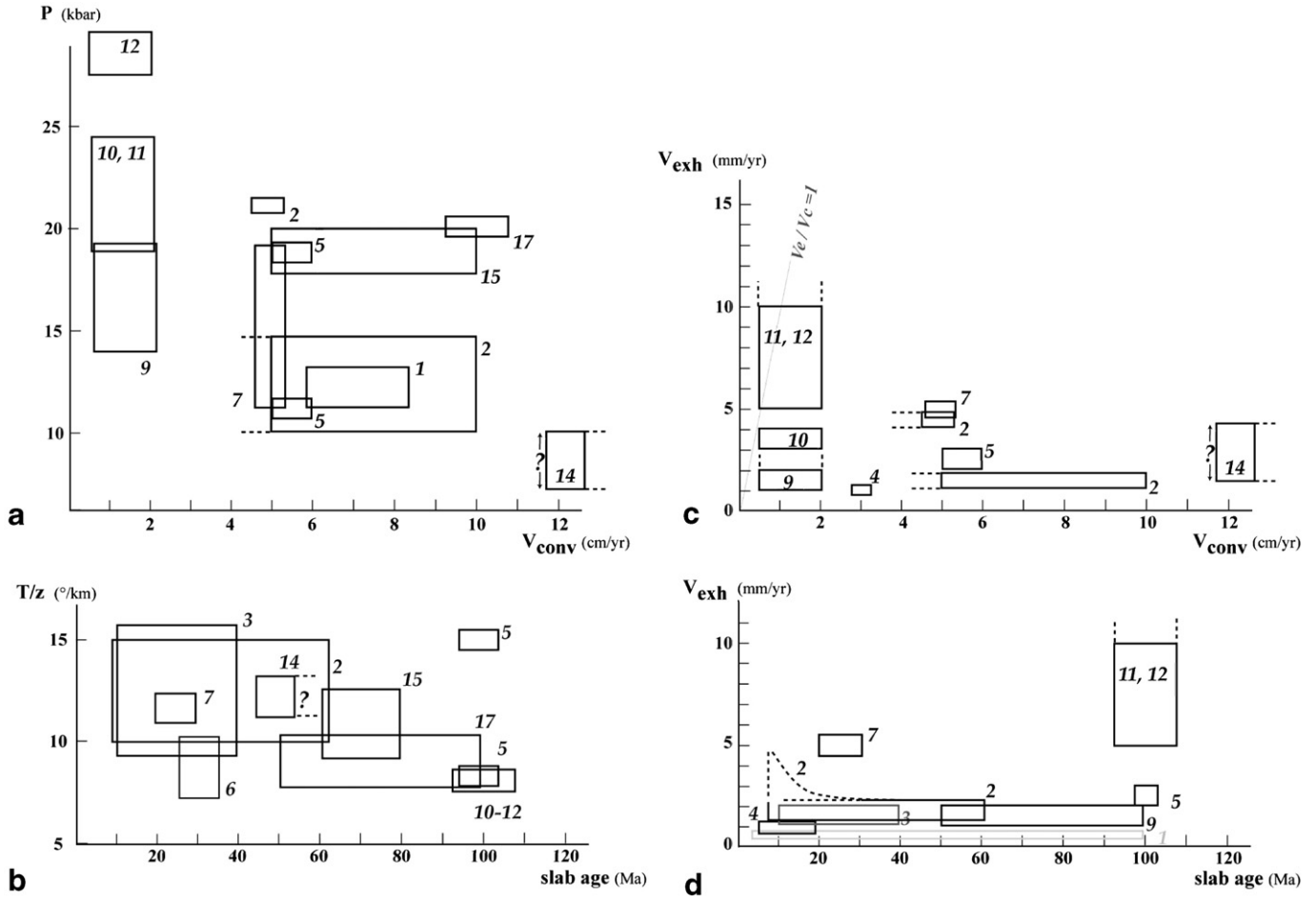

Fig. 11. Plots evidencing a weak correlation of convergence velocities or slab age on pressures and metamorphic gradients, respectively, and showing the lack of influence of these parameters on exhumation velocities (see also Table 1). (a) Plot of peak pressures versus convergence velocities. (b) Plot of metamorphic gradients versus slab age. (c) Plot of exhumation velocities versus convergence velocities. (d) Plot of exhumation velocities versus slab age.

confirm the conclusion that *P–T* paths fingerprint the tectonic history of subduction zones (Ernst, 1988), individual *P–T* paths should thus not be regarded as univocal (see also Matsumoto et al., 2003).

(7) Peak pressures seem to negatively correlate with convergence velocities (Fig. 11a), as broadly do metamorphic gradients with slab age (Fig. 11b). Yet data are very scattered and these two rather predictable correlations are not very robust at present. On the other hand, a number of parameters seem to have little or no influence on exhumation patterns and velocities (Table 1):

- Convergence velocities taken from the litterature do not affect exhumation rates (Fig. 11c). This observation points to the existence of strong decoupling between the upper, essentially sedimentary wedge and the subduction channel.
- No relationship is observed betwen subduction duration and exhumation velocities. This suggests that an exhumational steady state is reached at depth (as documented by Ring and Brandon, 1999 for the Franciscan complex).
- There is no correlation between the age of the subducting plate and exhumation velocities (Fig. 11d). The nature of the material, whether originating from a slow or fast spreading environment (with or without much ocean-floor serpentinites, respectively; Karson, 1998) could nevertheless be important (see below). On the other hand, young, warm plates (e.g. Franciscan complex, Santa Catalina; Table 1) obviously favor warm initial subduction gradients (15–16 °C/km).
- Assessing the role of slab dip is hampered by the lack of data.
- The presence (Franciscan, Himalayas; type B of Maruyama et al., 1996) or absence (W. Alps; type A) of arc-related magmatism in the upper plate does not seem to play a significant role.

4. Insights from subduction modelling

This section summarizes available data from experiments (mainly thermomechanical models) addressing the exhumation of HP–LT rocks in subduction zones during oceanic convergence, and emphasizes on the recent results obtained by our group (Yamato et al., 2007).

Analog modeling provides few insights on the exhumation of HP–LT rocks because it either focused on slab behavior during oceanic subduction (Faccenna et al., 2001; Regard et al., 2003; Funiciello et al., 2004) or dealt with continental subduction and the positive buoyancy of continental material (Chemenda et al., 1995, 2000, 2001; Boutelier et al., 2004). Similarly, most thermomechanical modelling studies dealt with the mechanisms of exhumation during continental subduction (Bousquet et al., 1997; Beaumont et al., 1999; Ellis et al., 1999; Pfiffner et al., 2000; Doin and Henry, 2001; Burov et al., 2001; Warren et al., 2008; Yamato et al., 2008; Burov and Yamato, 2008) rather than with oceanic subduction proper (Cloos, 1982; Gerya et al., 2002).

Reproducing the thermal regimes of blueschists and eclogites and their evolution through time was achieved in the early 1990s by Peacock (1987, 1990, 1996), based on the Franciscan and Santa Catalina examples, and refined until recently (for example, Peacock et al., 2005). Early thermomechanical models (Cloos, 1982, 1984; Allemand and Lardeaux, 1997; Schwartz et al., 2001) explored the circulation of particles in a deformable wedge (Dahlen, 1984). These models, however,

have a kinematically constrained geometry which strongly prescribes the geodynamic setting, and yield velocities too fast (1–4 cm/yr). Recent, essentially self-consistent numerical schemes (Burov et al., 2001; Gerya et al., 2002) allow to more realistically take into account the complex interplay of the different exhumation mechanisms (erosion, tectonic thinning, buoyancy, delamination, slab detachment: both superficial and lithospheric, as emphasized by Platt, 1993). These models also take into account the feedback between *P–T* dependent mineralogical phase changes and the mechanical response of the system (e.g., to density and rheological changes).

Burov et al. (2001) explored the behavior of the subduction channel during continental subduction and pointed out the existence of two distinct circulation levels at 0–30 km and 30–70 km, respectively, with slower exhumation rates for the upper level. Gerya et al. (2002) successfully modeled oceanic subduction and subduction channel processes with full phase and density changes and variable hydration of the mantle wedge. Their experiments were also applied to the Alpine case (Stöckhert and Gerya, 2005). Their models, however, predict too fast exhumation velocities for the metasediments and the oceanic crust (>1 cm/yr). Serpentinites are also randomly dispersed in the metasediments, contrary to the Western Alps and to most natural settings reported above (Figs. 4 and 7; Table 1).

Yamato et al. (2007) developed a model based on subduction experiments without pre-defined kinematic assumptions in the model (yet, with no hydration of the mantle wedge), and showed that:

- Exhumation velocities are ~1–2 mm/yr in the wedge (Fig. 12a). There is a turn-over circulation lasting ~15 My, which is consistent with constraints from the Schistes Lustrés and part of the Voltri units (W. Alps; Agard et al., 2002; Federico et al., 2005) but also with the Franciscan, Cascades and Chilean examples (Brandon et al., 1998, Ring and Brandon 1999; Batt et al., 2001; Glodny et al., 2005).
- The exhumation of oceanic crust is obtained only when serpentinites are present in the slab mantle, which is consistent with the Alpine case (Li et al., 2004; Hattori and Guillot, 2007), and exhumation velocities are 3–4 mm/yr (Fig. 12b).
- Oceanic crust is exhumed towards the rear of the subduction channel, in an internal position (Fig. 12b).
- No overpressures build up in the subduction channel.

5. Discussion: implication for subduction processes and exhumation concepts

5.1. Oceanic versus continental rocks: contrasting exhumation modes

From a number of recent studies in various settings worldwide, it is now apparent that the buoyant continental crust is exhumed during continental subduction, with velocities comparable to those of plate tectonics at mantle depths (1–5 cm/yr; Fig. 9a) and later decelerates (~mm/yr) in the upper crust (W. Alps: Duchêne et al., 1997a; Rubatto and Hermann, 2001; Papoua: Baldwin et al., 2004; Himalayas: De Sigoyer et al., 2000; O'Brien, 2006; Dabie Shan: Liu et al., 2006; Kokchetav: Hermann et al., 2001; Hacker et al., 2003a). As a first approximation, the buoyancy-driven exhumation of continental rocks takes place through extrusion (Chemenda et al., 1995), although in detail HP–UHP nappes are notably thinner (~100 m–1 km) than the thickness of a normal crust (~30–35 km; Jolivet et al., 2005). Note that slab breakoff could also provide an additional help for the buoyant rise of continental rocks (Von Blanckenburg and Huw Davies, 1995), although it is not required for exhumation (Warren et al., 2008; Yamato et al., 2008).

In contrast to the continental crust, our survey reveals that subducted ocean-floor sediments are exhumed at velocities ~mm/yr (Fig. 9a; Table 1). The sediments are efficiently decoupled from the oceanic crust and tend to accumulate in the accretionary wedge, as shown by the respective volumes for the W. Alps (Table 1; see also Fig. 6b). They circulate in the wedge under the combined effects of underthrusting (Gutscher et al., 1998; Glodny et al., 2005), erosion and tectonic thinning, whose respective contributions vary from one geodynamic setting to the other (highly erosive in the Franciscan complex; Platt, 1986, 1993; Ring and Brandon, 1999; highly tectonic in the W. Alps; Agard et al., 2002).

Most oceanic crust is to be irreversibly buried, yet it occasionnally returns to the surface at velocities ~mm/yr too, either wrapped in serpentinites or in a muddy/shaly, mechanically weak matrix melange. One finds m- (Franciscan) to hm- (Iran) or km-sized blocks (New Caledonia; W. Alps; Escambray, Cuba), which are either brought back early (Franciscan, Chili), during (SE Zagros, Himalayas) or late (W. Alps, New Caledonia; some parts of Cuba) in the subduction history (see next section). The dominantly internal position of oceanic crust (+mantle) with respect to sediments (Table 1), and frequently of eclogites on blueschists, either points to specific dynamics in the subduction channel and/or to the influence of the buttress and hydrated mantle wedge in channelling oceanic crust towards the surface (see also Fitzherbert et al., 2004). Mafic and ultramafic slices occupying such an internal position were also reported from Turkey (Okay et al., 1998).

Exhumation velocities for oceanic rocks are thus, contrary to continental ones, largely inferior to plate velocities. This is also the case when looking back at the few available Paleozoic examples: rates are <3 mm/yr for the ~470–460 Ma suture zones from Svalbard (Motalafjella; Agard et al., 2005a,b) and China (Qilian; Song et al., 2007-in review).

One exception is when the exhumation of oceanic crust (+mantle) directly results from the locking of subduction processes by continental subduction (W. Alps; Fig. 6a). Only in this case do we find large volumes preserved (Fig. 4), either as continuous slab pieces (Zermatt-Saas; Bucher et al., 2005) or as slices from contrasting depths (Monviso; Schwartz et al., 2000a,b). Similarly, in this case only are rocks brought back from UHP depths (Fig. 9b). We note that earlier, smaller subducted continental pieces (such as Sesia; Dal Piaz et al., 2001; Babist et al., 2006), some of which may represent extensional allochtons (Froitzheim and Manatschal, 1996; Manatschal, 2004), may have been too small to choke the subduction and provoke the exhumation of oceanic slices (see also Brun and Faccenna, 2008).

The scarcity of lawsonite eclogites worldwide (Fig. 2; Zack et al., 2004; Whitney and Davis, 2006; Tsujimori et al., in press), due to overprinting on exhumation, is consistent with the prevalence of rather low exhumation velocities (Fig. 9a). Fig. 10a,b, however, suggest that even at slow exhumation rates (Franciscan complex, Corsica), the preservation of lawsonite eclogite is possible if refrigerent conditions are maintained on exhumation.

This survey thus further strengthens the concept of subduction channel (Shreve and Cloos, 1986; Jolivet et al., 2003; Federico et al., 2007), by showing that a large amount of decoupling exists within the upper and lower parts of the channel. The detailed exhumation pathways of the slices of oceanic crust detaching from the sinking slab remain poorly constrained, however.

5.2. Continuous versus discontinuous oceanic crust exhumation?

A priori, two end-members situations can be expected for the exhumation of the oceanic crust:

- a continuous, steady state exhumation process. A good candidate would be a 'corner-flow' accretionary process (Cloos, 1982; Shreve and Cloos, 1986; Gerya et al., 2002; Gorczyk et al., 2007) with the incorporation of oceanic crust in the wedge, possibly enhanced by serpentinization (hydration of the slab mantle and/or serpentinite diapirs).
- a discontinuous, incidental exhumation process. In this case the oceanic crust would be exhumed only during specific time windows, for example in response to the entrance of buoyant

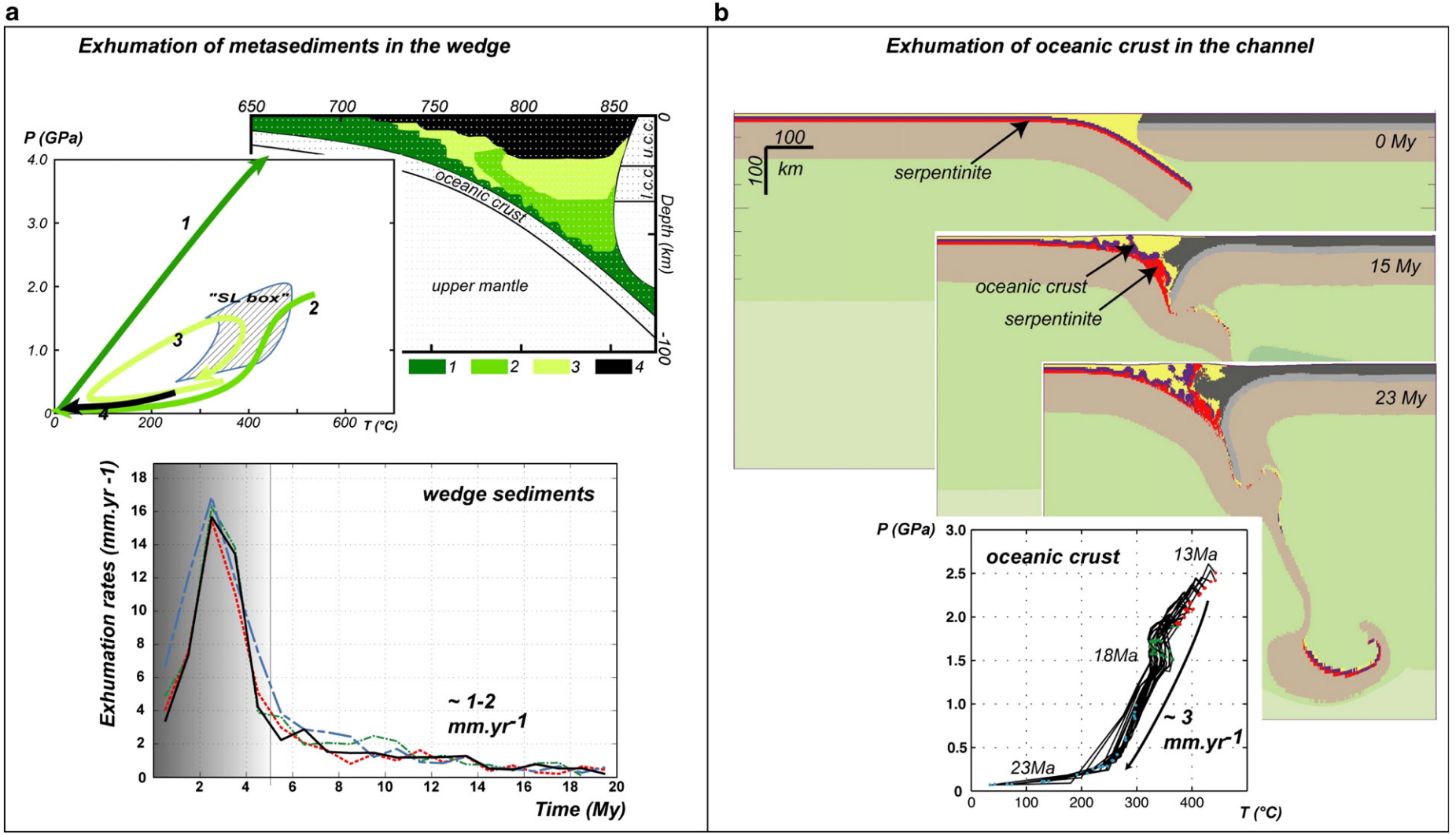

Fig. 12. Overview of the main results of the thermomechanical numerical study of Yamato et al. (2007) with application to the Western Alps. This large-strain model accounts for visco-elastic-plastic properties of the rocks, is thermally coupled, includes methamorphic phase changes and surface processes. Tracers are used to track particles and reproduce synthetic *P–T–t* paths that are compared with the observations (see text and Yamato et al., 2007 for details). (a) Schematic *P–T* paths followed by the sedimentary particles (grouped by colour) in the accretionary wedge and the subduction channel, showing that a number of them effectively enter the *P–T* field of the Schistes Lustrés (SL box). Exhumation velocities are a few mm/yr after a transient period. (b) Morphology obtained in the case of oceanic crust (blue) exhumation facilitated by the presence of an underlying serpentinized slab mantle (red). Note that the oceanic crust and serpentinites are exhumed at the rear of the wedge, at velocities ~3–4 mm/yr. (For interpretation of the references to colour in this figure legend, the reader is referred to the web version of this article.)

material in the subduction wedge (for example thinned continental margin, oceanic plateau, slab asperities; Ernst, 1988; Cloos, 1993; Arculus et al., 1999; Ernst, 2001), to the modification of the convergence setting (velocities, obliquity; Agard et al., 2006), or to the cessation of subduction (for example delamination of lower crust, slab-breakoff; Von Blanckenburg and Huw Davies, 1995).

Our worldwide survey of past subduction zones reveals the following contrasting behaviors (Fig. 8; Table 1):

(1) Short-lived early exhumation (Franciscan complex, Chile).In both cases, the geodynamic setting advocates for a warm, rapidly cooling subduction zone associated with the consumption of young oceanic lithosphere (Anczkiewicz et al., 2004; Glodny et al., 2005). The short-lived exhumation (lasting no longer than 10–15 My) suggests the existence of a transient state, both thermal and mechanical, following the initiation of subduction, as documented in our oceanic subduction models (Yamato et al., 2007). It could also be hypothetized that exhumation is no longer possible after a certain time period, once the mantle wedge has become too lubricated by water hydration (Iwamori, 1998; Arcay et al., 2005).

(2) Short-lived exhumation in the midst of convergence (SE Zagros, N. Cuba).In the case of SE Zagros, this short-lived exhumation (~15–20 My versus >120 My of subduction) coincided with a sharp rise of convergence velocities and with the onset of regional-scale obduction movements (Agard et al., 2006, 2007). The same ages are in fact obtained from Eastern Turkey (Sherlock et al., 1999) to Makran (Delaloye and Desmons, 1980) and the Himalayas (Anczkiewicz et al., 2000; Maluski and Matte, 1984), which indicates that this exhumation was contemporaneous and short-lived across thousands of km. This observation points to a major, regional-scale change in interplate mechanical coupling, which affected the whole Neotethyan subduction zone below Eurasia (Agard et al., 2006). In the case of Cuba, *P–T* fluctuations were deduced from oscillatory garnet zoning in eclogites taken hundreds of kilometers apart in the Northern Serpeninite melange zone (Garcia-Casco et al., 2002). These oscillations were interpreted to reflect slab rupture and episodic ascent of eclogitic slices incorporated into the mantle wedge serpentinites (Garcia-Casco et al., 2002).

(3) Exhumation towards the end of the oceanic subduction (W. Alps, New Caledonia).The role of continental subduction in triggering crustal exhumation has already been emphasized for the Western Alps (see above). The situation is probably similar for the rather short-lived New Caledonia subduction zone, except that collision did not fully develop. Some of the oceanic rocks were underplated below the mantle wedge (Fitzherbert et al., 2004), but were not significantly exhumed until the entrance of buoyant material in the subduction zone (Northfolk ridge; Cluzel et al., 2001; Spandler et al., 2005).

(4) Configurations in which the exhumation is (almost) impossible. This is obviously the case for the Andes and Java, and for the Himalayas and SE Zagros throughout most of their subduction history (Fig. 8). These settings correspond to gently-dipping, relatively fast subduction zones capped by well-developped calc-alkaline magmatic arcs. Where collision developed (Himalayas, SE Zagros), no oceanic rocks were brought back towards the end of subduction with UHP continental slices, unlike the W. Alps (and HP–UHP continental rocks are even lacking in SE Zagros). The reason is unclear, yet it can be noted that in such settings: 1) the extensive hydration of the mantle wedge, as indicated by the presence of the calc-alkaline arcs at the surface, may efficiently lubricate the subduction channel and prevent the detachment of oceanic slices from the slab, 2) in low-angle slabs, the positively buoyant continental material will less efficiently counterbalance the dense, rapidly subducting oceanic material during continental subduction.

A major conclusion is therefore that the exhumation of the oceanic crust metamorphosed under HP–LT conditions is highly discontinuous (or 'episodic'; Fig. 8). Further insights should perhaps be sought from adequate geodynamic settings such as the Antilles (particularly Cuba) and from geophysical data and modeling (section below).

5.3. Serpentinites: a great help down to limited depths?

Major unknowns in the deeper parts of the subduction channel are whether there are maximum depths for the exhumation of oceanic crust (+mantle), and whether oceanic crustal rocks are returned from specific depths (e.g., ~100 km, according to Bucher et al., 2005) or sampled at various depths along the subduction zone (Guillot et al., 2004; Fotoohi Rad et al., 2005). Evaluation is hampered by the difficulty of determining whether the inferred *P–T* conditions pertain to the entire series or to isolated blocks only (see the discussion by Wallis and Aoya, 2000; Fitzherbert et al., 2005; Stipska et al., 2006). In any case, the compilation from Fig. 9b clearly shows that exhumation is normally prohibited beyond 60–70 km (~2.0–2.3 GPa), except in the event of continental subduction (Zermatt-Saas, Monviso).

It was previously proposed that the exhumation of oceanic rocks was facilitated by their association with serpentinites, which would counterbalance their negative buoyancy and enhance mechanical decoupling (Hermann et al., 2000; Guillot et al., 2001; Schwartz et al., 2001; Pilchin, 2005). For example, Hermann et al. (2000) estimated that the density of the Beigua unit (Fig. 4d; Voltri, Western Alps), made of 90% of serpentinites and 10% of mafic eclogites, was lowered to 2.9 g/cm^3, and that of the Erro-Tobio unit, with variably serpentinized lherzolites and minor eclogites, to 3.1 g/cm^3 (Fig. 4d), hence lower than that of the mantle.

Our Fig. 9b, by showing that the exhumed oceanic crust from the various settings studied here lies within the mostly temperature-dependent antigorite stability field (<~650 °C; Hermann et al., 2000; Guillot et al., 2001; Hacker et al., 2003b), further supports the conclusions of these workers.

We also provide new insights by calculating, in the range 0–4 GPa and 0 to 1000 °C, the net buoyancy of the oceanic crust, which corresponds to the density difference between the oceanic crust and the surrounding mantle at a given *P–T* value (Fig. 13). This net buoyancy of the oceanic crust was computed using stables phases and equilibrium densities calculated by the Theriak thermodynamic code (De Capitani, 1994). Fig. 13a shows that all exhumed oceanic crust lies outside of the negative buoyancy domain, apart from the Alpine Zermatt-Saas and some of the Monviso and Voltri massifs, which nevertheless lie inside the antigorite stability field (Fig. 9b and 13b,c).

We therefore suggest that beyond maximum depths around 70 km there are in general either not enough serpentinites (because both the slab mantle and the mantle wedge are dehydrated) and/or they are not light enough to compensate the negative buoyancy of the crust. This depth range is consistent with the scarcity, in such settings, of garnet peridotites (typically equilibrated at depths >70–80 km) associated with oceanic crust (and, in those rare cases, the depths at which they were juxtaposed is unclear; e.g., Gorczyk et al., 2007). The existence of maximum depths explains the contrasting behavior of the oceanic crust from Zermatt-Saas (continuous slab with uniform *P–T* conditions) and Monviso (slices with contrasting *P–T* conditions) more satisfactorily than the concept of a specific return depth point (Bucher et al., 2005). We note that incidental exhumation from greater depths should nevertheless be occasionnally possible with the help of continental material (continental subduction demonstrably exhumed mantle rocks from depths >300 km!; Green, 2005 and references therein), whose buoyancy is much greater than that of serpentinite at *T*>600° and *P*>2.0–2.3 GPa (Fig. 13c; Hermann, 2002).

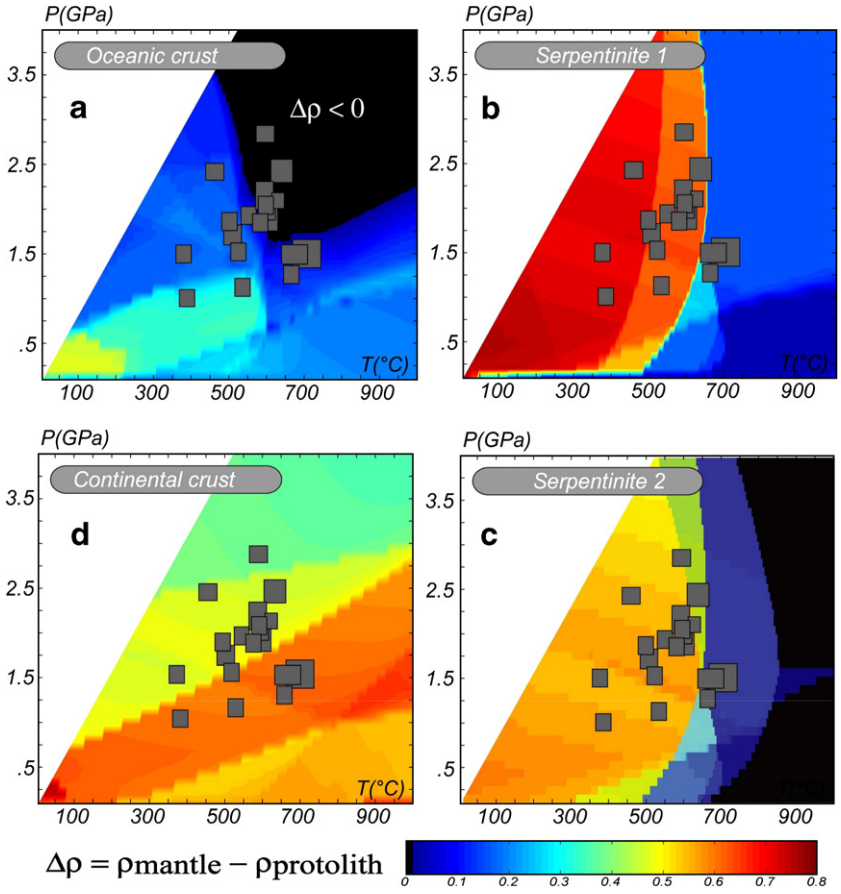

Fig. 13. Estimation of the net buoyancy of the oceanic crust (a), serpentinite (b, c) and continental crust (d), defined as the density difference between each of them, respectively, and the adjacent mantle. Serpentinite 1 corresponds to the pure Mg-rich end-member and average compositions for the oceanic and continental crust are taken from Yamato et al. (2007). Note that similar density contrasts are found for buoyancies calculated with other serpentinite compositions (Ulmer and Trommsdorff, 1995; Bromiley and Pawley, 2003). The most contrasting results are obtained for serpentinite 2 (plot c), which corresponds to the slightly Al-richer composition of Bromiley and Pawley (2003; their sample BM1913,87). Whatever the serpentinite composition, however, note that the sharp drop in buoyancy always occurs at the antigorite/forsterite reaction, whose position remains stable within 30 °C. Boxes as for Fig. 9b: maximum *P*–*T* values recorded by oceanic rocks in the subduction zones reviewed here. These diagrams, using stables phases and equilibrium densities calculated by the Theriak thermodynamic code (De Capitani, 1994), show that all exhumed oceanic crust lies outside of the negative buoyancy domain, apart from Monviso and Zermatt-Saas, which nevertheless lie inside the antigorite stability field.

5.4. Interplate mechanical coupling and exhumation processes at depth in the subduction channel

Although mantle wedge or slab mantle serpentinites obviously play a great role in the exhumation of oceanic crust, they alone do not explain how the crust (+mantle) detaches from the subducting slab. This problem of localization and detachment also exists for continental rocks (Jolivet et al., 2005). The great difference, however, is that continental rocks are intrinsically buoyant and effectively detach from the subducting plate (except perhaps in Zagros, where no HP–UHP continental rocks crop out), whereas oceanic lithosphere only rarely makes it to the surface (Fig. 8), despite the help from serpentinites.

Mechanisms based on mineral reactions triggering earthquakes were recently proposed for localization and detachment at depth in subduction zones. They include dehydration embrittlement (Kirby et al., 1996; Hacker et al., 2003b and references therein) and localized melting (Kanamori et al., 1994; pseudotachylites: Austrheim and Andersen, 2004; Andersen and Austrheim, 2006) followed by localization (Jolivet et al., 2005). Note that dehydration embrittlement will occur deeper in fast, cool subduction zones than in warm, moderately rapid ones (for example NE Japan v. SW Japan, respectively; Peacock and Wang, 1999). Once detached, the crust will encounter major decoupling interfaces such as the mantle wedge (Guillot et al., 2001; Gerya et al., 2002) and the 5–10 km thick hydrated crustal layer imaged by seismology in the upper part of the slab (Abers et al., 2006).

The fact that exhumation is discontinuous/episodic demonstrates that during most of the subduction process either the detachment from the slab and/or the later upward migration along the slab interface is inhibited. Examples of short-lived oceanic crust exhumation during convergence suggest that the interplate mechanical coupling conditions (Conrad et al., 2004) drastically changed, possibly in response to increased velocities (SE Zagros: Agard et al., 2006; Himalayas?), thermal instabilities (N. Cuba: Garcia-Casco et al., 2002) or slab rollback triggered by the entrance of continental blocks (Brun and Faccenna, 2008).

It is beyond the scope of the present paper to address in detail mechanical coupling and force balance at subduction zones (Scholz and Campos, 1995 and references therein). We point out, however, that the discontinuous exhumation of oceanic blueschists and eclogites, could be used as a proxy for interplate mechanical coupling and the mechanics of subduction zones.

From the preceeding examples, unfavorable interplate coupling conditions for exhumation seem to be that the oceanic crust is formed at fast spreading ridges (hence with a less hydrated slab mantle; for example Himalayas, Andes), with relatively low dip (too much friction and/or underplating below the upper plate at depth), at relatively fast rates (hence a cooler thermal regime: dehydration and detachment will take place deeper, where a counter-flow is no longer possible).

5.5. A general model for the exhumation of the oceanic crust

Although further carefully designed petrological and geophysical studies are needed, a provisional picture of processes operating at depth in subduction zones is shown in Fig. 14. It emphasizes that in general no steady state exhumation takes place, and that no exhumation is possible beyond a certain depth (Fig. 14a). Slab mantle and mantle wedge serpentinites play an important role on exhumation. By contrast, upper levels of the subduction channel are largely decoupled from the oceanic crust and circulate in the accretionary wedge (Fig. 14b; Yamato et al., 2007).

Early exhumation, in the first 5–15 My of oceanic subduction (Fig. 14c; Franciscan complex) occurs for relatively warm, rapidly cooling subduction zones (e.g. Anczkiewicz et al., 2004). Note that exhumation velocities associated with this process are still unclear. Given the characteristics of a young, warm subduction zone such as in SW Japan (Peacock and Wang, 1999), we propose that exhumation takes place through weakening resulting from the partial melting of the oceanic crust (as reported by Sorensen and Barton, 1987 for California), leading to boudinage and detachment of blocks in a weaker, sedimentary melange (Cloos, 1985; Anczkiewicz et al., 2004).

Once the subduction has cooled (particularly in subductions with velocities >~3 cm/y), dehydration reactions take place deeper down the subduction zone. In a relatively low-angle subduction channel, detachment will occur well below the upper plate and, given the pinch-out geometry, rocks can not be flushed back towards the surface along the slab interface (Fig. 14d). Mantle wedge hydration by continuous influx from the subducting slab, which results in increased interplate mechanical decoupling, further inhibites exhumation. Incidental exhumation, however, may happen in response to a major modification of boundary conditions (Himalayas, SE Zagros). Slab rollback developping in response to the subduction of large enough continental pieces can probably also significantly enhance the exhumation of oceanic material in some settings (Brun and Faccenna, 2008).

Finally, late exhumation associated with oceanic closure and continental subduction (and/or slab breakoff) will take place in relatively slow, steeply dipping subduction settings with a highly hydrated slab mantle (for example the W. Alps; Fig. 14e).

6. Conclusions

This study outlines the existence of three contrasting exhumation modes for sedimentary, oceanic crustal and continental rocks.

(1) Whereas the buoyancy-driven exhumation of continental rocks, possibly plucking ultradeep mantle rocks, proceeds at relatively fast rates at mantle depths (≥cm/yr; Duchêne et al., 1997a; Rubatto and Hermann, 2001; Ernst, 2001; Green, 2005), oceanic exhumation velocities for oceanic rocks, whether sedimentary or crustal, are usually on the order of the mm/yr.
(2) Underthrusting, detachment faulting and erosion, which are the driving exhumation mechanisms for the sediments, often preserve the continuity of the *P–T* conditions within the accreted sedimentary material (e.g. Agard et al., 2001a). In contrast, blueschist and eclogite mafic bodies are systematically associated with serpentinites and/or a mechanically weak matrix, and eclogites wrapped in serpentinites mostly crop out in an internal position in the orogen.
(3) Oceanic crust rarely records P conditions >2.0–2.3 GPa, which suggests maximum depths for the sampling of slab-derived oceanic crust. We propose that beyond such depths (~70 km), there are either not enough serpentinites (because both the slab mantle and the mantle wedge are dehydrated) and/or they are not light enough to compensate the negative buoyancy of the crust.
(4) Most importantly, this survey demonstrates that short-lived, discontinuous exhumation is the rule for the oceanic crust and associated mantle rocks: exhumation takes place either early (group 1: Franciscan, Chile), late (group 2: New Caledonia, W. Alps) or incidentally (group 3: SE Zagros, Himalayas, Andes, N. Cuba) during the subduction history. These conclusions are tentatively accounted by a comprehensive model in which exhumation is permitted by the specific thermal regime following the onset of a young, warm subduction (group 1), by continental subduction (group 2) or by a major, geodynamic modification of convergence across the subduction zone (group 3; change of kinematics, subduction of asperities, etc).

We finally stress the importance of understanding parameters controlling this short-lived exhumation and the detachment and migration of oceanic crustal slices along the subduction channel. In this respect, blueschists and eclogites are expected to shed light into the interplate mechanical coupling in subduction zones.

Acknowledgements

The authors apologize for the necessarily limited number of references cited here. J. Hermann and M. Scambelluri are greatly acknowledged for suggestions and improvement of the manuscript, as well as H. Engelen for the editorial handling of this article.

Appendix A

This section provides a brief geological description of the localities considered in our compilation of oceanic blueschists and eclogites from subduction zones across the world (location on Fig. 2; selected maps in Fig. 7; data in Table 1). For further details, the interested reader is referred to the selected bibliography (see also Table 1).

A.1. Chile

Within the metamorphic basement of the Coastal Cordillera of central Chile, the Western Series constitutes the HP–LT paleoaccretionary wedge of a fossil-paired metamorphic belt dominated by metagreywackes (Kato, 1985; Kato and Godoy, 1995). This subduction zone experienced a protracted accretion history (~50–100 My; Glodny et al., 2005) and moderate exhumation velocities (0.6 mm/yr; Glodny et al., 2005). In its eastern part, blocks derived from small lenses of garnet amphibolite with a blueschist facies overprint are locally intercalated and associated with serpentinite and garnet mica-schist (Willner et al., 2004). Those mafic blocks, dated at ~305 Ma, preserve a counter-clock-wise *P–T* path indicative of cooling early in the subduction history (Willner et al., 2004). Note that this is the only Paleozoic wedge considered here, because it escaped from later deformation (unlike Svalbard, for example; Ohta et al., 1986; Agard et al., 2005a).

A.2. California and Cascades

A.2.1. Franciscan complex

HP–LT rocks of the Franciscan Complex represent the prototypical, sediment-rich, fossil accretionary wedge. It was associated with the E-dipping subduction zone operating from c. 170 to 100 Ma (Cloos, 1985; Ring and Brandon, 1999; Anczkiewicz et al., 2004), which gave birth to the Sierra Nevada batholith (Ernst, 1970). A marked contrast exists between the essentially metasedimentary Eastern belt (Fig. 7a), composed of coherent tracts of blueschist facies metagraywackes (Cloos, 1982, 1985; Jayko et al., 1986; Ernst, 1993; Kimura et al., 1996), and the Central Belt, where meter-scale mafic high-grade blueschist and eclogite blocks (knockers) are found in a serpentinite- or shale-matrix melange (Oh and Liou, 1990; Wakabayashi, 1990; Krogh et al., 1994).

The Eastern belt blueschists reached *P–T* values <1.0–1.2 GPa and 400 °C, on average (Ernst, 1971; Jayko et al., 1986; Ernst, 1993), and were exhumed at velocities around 0.5–1 mm/yr (Ring and Brandon,

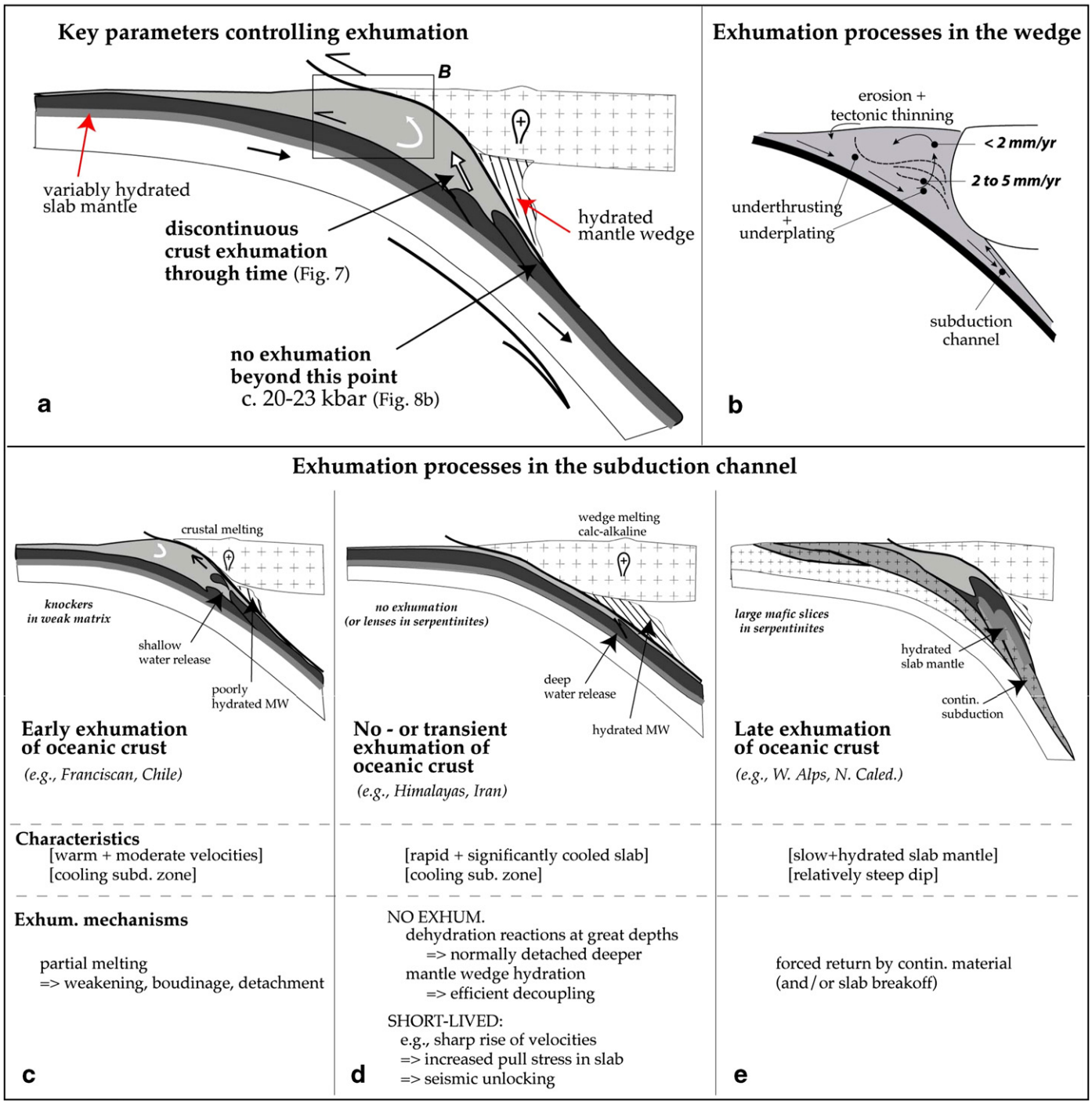

Fig. 14. Tentative model of processes controlling the exhumation of oceanic material in subduction zones. (a) In general no steady state exhumation of the oceanic crust takes place, and no exhumation is possible beyond a depth of ~70 km, corresponding to 2.0–2.3 GPa. Slab mantle and mantle wedge serpentinites play an important role on exhumation. (b) Sedimentary input is largely decoupled from the oceanic crust in the upper levels of the subduction channel and circulates in the accretionary wedge (dotted lines and dots: successive position of sedimentary interfaces). (c) Early exhumation, in the first 5–15 My of oceanic subduction may occur for relatively warm, rapidly cooling subduction zones. We propose that exhumation takes place through weakening resulting from the partial melting of the oceanic crust (Sorensen and Barton, 1987), leading to boudinage and detachement of high grade blocks in a weaker, sedimentary melange. (d) No steady-state exhumation of oceanic material takes place once the subduction has cooled (see text for details). Incidental exhumation, however, may happen in response to a major modification of boundary conditions (Himalayas, Zagros, Ecuador). (e) Late exhumation may be associated with continental subduction (and/or slab breakoff) in relatively slow, steeply dipping subduction settings with a highly hydrated slab mantle (such as the W. Alps).

1999). Mafic knockers were classically considered to have equilibrated at $P<1.2$–1.5 GPa, but recent findings point to pressures in excess of 20 kbars and exhumation velocities possibly as high as 5 mm/yr (Tsujimori et al., 2006). The Franciscan subduction zone is known to have cooled during a transient period which lasted ~10–15 My (Peacock, 1987; Anczkiewicz et al., 2004). Radiometric constraints for the high-grade blocks of oceanic crust suggest, as for Chile, that they were only exhumed during these early subduction stages (Cloos, 1985; Anczkiewicz et al., 2004).

A.2.2. Santa Catalina

This island corresponds to a small part of a later accretionary wedge formed after an outboard jump of the Franciscan subduction zone (Platt, 1986; Sorensen, 1988; Bebout, 1991; Grove and Bebout,

1995; Fig. 7b), and preserves evidence of transient, cooling metamorphic gradients associated with the onset of subduction (Peacock 1987). Age constraints suggest exhumation velocities from depths of 30–40 km at 1–2 mm/yr (Grove and Bebout, 1995).

A.2.3. Cascades

This Miocene accretionary wedge is only briefly alluded to here as a modern analogue of the Franciscan complex. Based on fission-track data, exhumation appears to be mostly erosion-driven (Brandon et al., 1998) and steady-state accretion and particle flow within the wedge, returning 80–90% of the sedimentary input, were deduced for the last 15 My (Batt et al., 2001). No deeply seated rocks have been exhumed so far.

A.3. Iran

A.3.1. Zagros

The Tertiary collisional Zagros orogen formed after a long-lived subduction of the Neotethys below Eurasia (~150–35 Ma; Agard et al., 2005b). HP–LT remnants are scarce, however, as for the Himalayas (see below). Blueschist facies rocks are only found in the southeasternmost corner of Zagros, near Makran (Fig. 7c; Sabzehei, 1974; Agard et al., 2006). They represent elongate hm- to km-sized mafic and volcanoclastic bodies, intimately associated with serpentinites, dispersed in a 'coloured' melange zone. Some serpentinite units contain lawsonite–omphacite–glaucophane-bearing blueschist knockers pointing to deeper *P–T* conditions (c. 1.8 GPa/500 °C). Age constraints point to a short-lived exhumation during the period 95–85 Ma, which coincided with regional-scale obduction movements (Coleman, 1971; Ricou, 1971) and followed a sharp rise of convergence velocities (Agard et al., 2006, 2007). This period also coincided with blueschist exhumation along adjacent segments of this subduction zone, in Turkey (Sherlock et al., 1999), Makran (Delaloye and Desmons, 1980) and Pakistan (Anczkiewicz et al., 2000).

A.3.2. Makran

Several blueschist facies outcrops of dominantly mafic material have been reported (McCall, 1997) at the rear of the Tertiary accretionary wedge (Platt et al., 1985). Radiometric dating pointed to ages of 87.9 ±5 Ma (Delaloye and Desmons, 1980) but *P–T* constraints are lacking.

A.3.3. Sistan (Eastern Iran)

Two serpentinite-rich accretionary complexes resulting from the closure of a small branch of the Neotethys (<600 km; Tirrul et al., 1983) are found in Eastern Iran. BS and eclogites, which form small lenses (metric to 200×100 m) exhibiting variable *P–T* conditions (Fotoohi Rad et al., 2005), were exhumed during convergence at least 20 My before collision (Tirrul et al., 1983). The lack of radiometric constraints unfortunately precludes the calculation of exhumation velocities for this geodynamic setting.

A.4. New Caledonia

Blueschist and eclogites found in New Caledonia represent one of the most extensive such outcrop in the world (Fig. 7d; Yokohama et al., 1986; Clarke et al., 1997). Its detailed structure and isograds, however, are still disputed (Rawling and Lister, 2002; Fitzherbert et al., 2005). Diahot blueschists and incipient eclogites correspond to clastic metasediments associated with an oceanic melange, whereas the eclogitic Pouébo terrane is dominated by mafic and volcanoclastic rocks intimately associated with serpentinites (Cluzel et al., 2001; Rawling and Lister, 2002; Fitzherbert et al., 2004, 2005). Mafic blocks in serpentinites preserve evidence for a 100–150 °C heating thought to result from the contact with the mantle wedge (Fitzherbert et al., 2004). This rather short-lived subduction zone (<15–25 My) is thought to have experienced the incorporation of several terranes (Diahot, Pouébo and Poya units) before choking when the continental Norfolk ridge attempted subduction (Cluzel et al., 2001; Fitzherbert et al., 2004; Spandler et al., 2005). This event resulted in the fore-arc obduction and exhumation of the HP–LT rocks (Cluzel et al., 2001), which later suffered contractional refolding (Rawling and Lister, 2002).

A.5. Antilles

The Antilles is a complex geodynamic setting with evidence of several subduction zones associated with the convergence between North and South America, whose timing and dip directions are still debated, either for Cuba (Iturralde-Vinent, 1994; Kerr et al., 1999; Schneider et al., 2004; Cobiella-Reguera, 2005; Garcia-Casco et al., 2006; Stanek et al., 2006) or for the Dominican Republic (Goncalves et al., 2000). These subductions have given rise to a variety of settings, from extensive, >500 km long serpentinite-rich zones with eclogite blocks (the so-called Northern serpentinite melange; Fig. 7e; Garcia-Casco et al., 2002), to highly deformed nappe stacks grading from blueschist to eclogite facies conditions, with clastics and mafic bodies wrapped in serpentinites (Escambray: Schneider et al., 2004; Stanek et al., 2006).

Contrasting *P–T* regimes are found, ranging from high temperature regimes associated with nascent subduction zones (for example Eastern Cuba; Garcia-Casco et al., 2006), to cold regimes associated with lawsonite–eclogite forming subduction zones (Dominican Republic; Zack et al., 2004; Krebs et al., 2008). One of the peculiar aspects of the subduction record is the evidence for transient thermal (and/or mechanical) instabilities in the subduction process, inferred from oscillatory zoning in garnets (Garcia-Casco et al., 2002, 2006).

A.6. The Himalayas

Sparsely distributed blueschists, mostly metavolcanics and volcanoclastics with minor serpentinites, crop out along the Indus–TsangPo suture zone, in the vicinity of the NW Himalayan syntaxis (Shangla: Anczkiewicz et al., 2000; Sapi-Shergol: Honegger et al., 1989). Age constraints point to exhumation periods similar to the one reported above for SE Zagros, at around 90–80 Ma (Maluski and Matte, 1984; Tonarini et al., 1993; Anczkiewicz et al., 2000). Compared to the vast amount of subducted oceanic lithosphere, the Himalayas have preserved only a very small percentage of HP–LT rocks. Besides, eclogites reported so far correspond exclusively to the metamorphosed continental Indian crust dragged below Asia and exhumed in the NW Himalayas (Pognante and Spencer, 1991; Guillot et al., 1997, 1999; De Sigoyer et al., 2000; O'Brien et al., 2001; Guillot et al., 2007), apart from one mafic eclogite from the Indus suture zone whose significance is still unclear (Le Fort et al., 1997).

A.7. Sambagawa

The Sanbagawa belt represents the fossil HP–LT part of one of Japan's paired metamorphic belts (Miyashiro, 1961; Banno, 1986; Takasu et al., 1994). It is mostly made of high grade blueschists and comprises rare eclogitic blocks encased in a mainly epidote–amphibolite weak pelitic matrix (Takasu et al., 1994; Enami, 1998), with only minor serpentinites. Recent petrological studies suggest, however, that eclogitic conditions may neither be as restricted as previously thought and may not be confined to isolated mafic blocks only (Wallis and Aoya, 2000; Ko et al., 2005). Whether this belt represents or not an accretionary melange is debated (Takasu et al., 1994; Wallis, 1998). *P–T* estimates yield 2.0–2.1 GPa and 600 °C in the Beshi area for isolated blocks and interleaved metapelites (Ko et al., 2005). Similar *P–T* values but contrasting exhumation paths were obtained in the Kotsu area (Matsumoto et al., 2003). Exhumation velocities are ≤1 mm/yr (Wallis et al., 2004), although few radiometric constraints are available, unfortunately, for the HP stages.

A.8. Others

A.8.1. Sulawesi

The Bantimala complex represents the exhumed wedge of a Cretaceous subduction and is mainly made of mafic bodies and volcanoclastics, with eclogite blocks embedded in serpentinites. Ultramafic units occupy an internal position. Miyazaki et al. (1996) inferred a cold *P–T* gradient of 8 °C/km and a cooling exhumation path.

A.8.2. Andes

The case of the Andes is considered here as an example where almost no exhumation of oceanic material takes place during convergence (Central Andes; Jaillard et al., 2002) despite active subduction along more than 4000 km from the Jurassic onwards. Accreted terranes testifying to restricted exhumation episodes are found, however, in the Northern Andes (Ecuador; Feininger, 1980; Kerr et al., 2002; Gabriele et al., 2003; Venezuela: Stöckhert et al., 1995; Maresch et al., 2000). The exhumation of the Raspas complex of Ecuador, in particular, is thought to result from the entrance of an oceanic plateau jamming the subuction zone during the lowermost Cretaceous (Arculus et al., 1999; Bosch et al., 2002).

References

Abers, G.A., van Keken, P.E., Kneller, E.A., Ferris, A., Stachnik, J.C., 2006. The thermal structure of subduction zones constrained by seismic imaging: implications for slab dehydration and wedge flow. Earth and Planet Science Letters 241, 387–397.

Agard, P., Lemoine, M., 2005. Faces of the Alps. Structure and Geodynamic Evolution. C.C.G.M. 48 pp.

Agard, P., Jolivet, L., Goffé, B., 2001a. Tectonometamorphic evolution of the Schistes Lustrés complex: implications for the exhumation of HP and UHP rocks in the Western Alps. Bull. Soc. Geol. Fr. 172 (5), 617–636.

Agard, P., Vidal, O., Goffé, B., 2001b. Interlayer and Si content of phengite in carpholite-bearing metapelites. Journal of Metamorphic Geology 19, 479–495.

Agard, P., Monié, P., Jolivet, L., Goffé, B., 2002. In situ laser probe $^{40}Ar/^{39}Ar$ dating of the Schistes Lustrés complex: implications for the exhumation of the Western Alps. Journal of Metamorphic Geology 20, 599–618.

Agard, P., Labrousse, L., Elvevold, S., Lepvrier, C., 2005a. Discovery of Palaeozoic Fe–Mg carpholite (Motalafjella, Svalbard Caledonides): a milestone for subduction zone gradients. Geology 33, 761–764.

Agard, P., Omrani, J., Jolivet, L., Mouthereau, F., 2005b. Convergence history across Zagros (Iran): constraints from collisional and earlier deformation. International Journal of Earth Sciences 94, 401–419.

Agard, P., et al., 2006. Transient, syn-obduction exhumation of Zagros blueschists inferred from P–T-deformation-time and kinematic constraints: implications for Neotethyan wedge dynamics. Journal of Geophysical Research 111, B11401. doi:10.1029/2005JB004103.

Agard, P., Jolivet, L., Vrielinck, B., Burov, E., Monié, P., 2007. Plate acceleration: the obduction trigger? Earth and Planetary Science Letters 258, 428–441.

Allemand, P., Lardeaux, J.-M., 1997. Strain partitioning and metamorphism in a deformable orogenic wedge: application to the Alpine belt. Tectonophysics 280, 157–169.

Amato, J.F., Johnson, C.M., Baumgartner, L.P., Beard, B.L., 1999. Rapid exhumation of the Zermatt-Saas ophiolite deduced from high-precision Sm–Nd and Rb–Sr geochronology. Earth and Planetary Science Letters 171, 425–438.

Anczkiewicz, R., Burg, J.P., Villa, I.M., Meier, M., 2000. Late Cretaceous blueschist metamorphism in the Indus Suture Zone, Shangla region, Pakistan Himalaya. Tectonophysics 324 (1–2), 111–134.

Anczkiewicz, R., Platt, J.P., Thirlwall, M.F., Wakabayashi, J., 2004. Franciscan subduction off to a slow start: evidence from high-precision Lu–Hf garnet ages on high grade-blocks. Earth and Planetary Science Letters 225, 147–161.

Andersen, T.B., Austrheim, H., 2006. Fossil earthquakes recorded by pseudotachylites in mantle peridotite from the Alpine subduction complex of Corsica. Earth and Planet Science Letters 242, 58–72.

Arcay, D., Tric, E., Doin, M.-P., 2005. Numerical simulations of subduction zones. Effect of slab dehydration on the mantle wedge dynamics. Physics of the Earth and Planetary Interiors 149, 133–153.

Arculus, R.J., Lapierre, H., Jaillard, E., 1999. Geochemical window into subduction and accretion processes: Raspas metamorphic complex, Ecuador. Geology 27, 547–550.

Austrheim, H., Andersen, T.B., 2004. Pseudotachylites from Corsica: fossil earthquakes from a subduction complex. Terra nova 16, 193–197.

Babist, J., Handy, M.R., Konrad-Schmolke, M., Hammerschmidt, K., 2006. Precollisional, multistage exhumation of subducted continental crust: the Sesia Zone, western Alps. Tectonics 25. doi:10.1029/2005TC001927.

Baldwin, S., 1996. Contrasting P–T–t histories for blueschists from the Western Baja Terrane and the Aegean: effects of synsubduction exhumation and backarc extension. In: Bebout, G.E., Scholl, D., Kirby, S., Platt, J.P. (Eds.), Subduction: Top to Bottom. Geophysical Monograph. AGU, pp. 135–141.

Baldwin, S., et al., 2004. Pliocene eclogite exhumation at plate tectonic rates in eastern Papua New Guinea. Nature 431, 263–267.

Ballèvre, M., Merle, O., 1993. The Combin fault: compressional reactivation of a late Cretaceous–early Tertiary detachment fault in the Western Alps. Schweizrische Mineralogische Petrografische Mitteilung 73, 205–227.

Ballèvre, M., Lagabrielle, Y., Merle, O., 1990. Tertiary ductile normal faulting as a consequence of lithospheric stacking in the western Alps. In: Roure, F., Heitzmann, P., Polino, R. (Eds.), Deep Structure of the Alps. Société Géologique de France, pp. 227–236.

Banno, S., 1986. The high-pressure metamorphic belts of Japan: a review, Blueschists and eclogites. Memoirs. Geological Society of America.

Barfety J., Lemoine M., de Graciansky P., Tricart P., 1995. Notice Explicative, Carte Geologique de la France (1: 50 000), Feuille Briancon (823), B.R.G.M.

Barnicoat, A.C., Fry, N., 1986. High-pressure metamorphism of the Zermatt-Saas ophiolite zone, Switzerland. Journal of the Geological Society of London 143, 607–618.

Barnicoat, A.C., Rex, D.C., Guise, G., Cliff, C.A., 1995. The timing of and nature of greenschist facies deformation and metamorphism in the upper Pennine Alps. Tectonics 14, 279–293.

Batt, G.E., Brandon, M.T., Farley, K.A., Roden-Tice, M., 2001. Tectonic synthesis of the Olympic mountains segment of the Cascadia wedge, using two-dimensiona thermal and kinematic modeling of thermochronological ages. Journal of Geophysical Research 106, 26731–26746.

Bearth, P., 1959. Uber Eklogite, Glaucophanschiefer, und metamorphe Pillowlaven. Schweizerische Mineralogische und Petrographische Mitteilungen 39, 267–286.

Beaumont, C., Ellis, S., Pfiffner, A., 1999. Dynamics of sediment subduction–accretion at convergent margins: short tem modes, long-term deformation, and tectonic implications. Journal of Geophysical Research 104, 17573–17601.

Bebout, G.E., 1991. Field-based evidence for devolatilization in subduction zones: implications for arc magmatism. Science 251, 413–416.

Bebout, G.E., 1996. Volatile transfer and recycling at convergent margins: mass-balance and insights from high-P/T metamorphic rocks. In: Bebout, G.E., Scholl, D., Kirby, S., Platt, J.P. (Eds.), Subduction: Top to Bottom. Geophysical monograph, pp. 179–193.

Bebout, G.E., 2007. Metamorphic chemical geodynamics of subduction zones. Earth and Planet Science Letters 260, 373–393.

Bebout, G.E., Barton, M.D., 2002. Tectonic and metasomatic mixing in a high-T, subduction zone mélange — insights into the geochemical evolution of the slab–mantle interface. Chemical Geology 187, 79–106.

Beltrando, M., Hermann, J., Lister, G.S., Compagnoni, R., 2007. On the evolution of orogens: pressure cycles and deformation mode switches. Earth and Planet Science Letters 256, 372–388.

Bonhomme, M.G., Saliot, P., Pinault, Y., 1980. Interpretation of potassium–argon isotopic data related to metamorphic events in south-western Alps. Schweizrische Mineralogische Petrografische Mitteilung 60, 81–98.

Bosch, D., Gabriele, P., Lapierre, H., Malfère, J.L., Jaillard, E., 2002. Geodynamic significance of the Raspas Metamorphic Complex (SW Ecuador): geochemical and isotopic constraints. Tectonophysics 345, 83–102.

Bousquet, R., Goffé, B., Henry, P., Le Pichon, X., Chopin, C., 1997. Kinematic, thermal and petrological model of the Central Alps; lepontine metamorphism in the upper crust and eclogitisation of the lower crust. Tectonophysics 273 (1–2), 105–127.

Bousquet, R., Goffé, B., Vidal, O., Patriat, M., Oberhänsli, R., 2002. The tectono-metamorphic history of the Valaisan domain from the Western to the Central Alps: new constraints for the evolution of the Alps. GSA Bulletin 114, 207–225.

Boutelier, D., Chemenda, A., Jorand, C., 2004. Continental subduction and exhumation of high-pressure rocks: insights from thermo-mechanical laboratory modelling. Earth and Planet Science Letters 222, 209–216.

Bowtell, S., Cliff, R.A., Barnicoat, A.C., 1994. Sm–Nd isotopic evidence of the age of eclogitization in the Zermatt-Saas ophiolite. Journal of Metamorphic Geology 12, 187–196.

Brandon, M.T., Roden-Tice, M.K., Garver, J.I., 1998. Late Cenozoic exhumation of the Cascadia accretionary wedge in the Olympic Mountains, NW Washington State. Geological Society of America Bulletin 110, 985–1009.

Bromiley, G.D., Pawley, A.R., 2003. The stability of antigorite in the systems $MgO–SiO_2–H_2O$ (MSH) and $MgO–Al_2O_3–SiO_2–H_2O$ (MASH): the effects of Al^{3+} substitution on high-pressure stability. American Mineralogist 88, 99–108.

Brun, J.P., Faccenna, C., 2008. Exhumation of high-pressure rocks driven by slab rollback. Earth and Planetary Science Letters 272, 1–7.

Brunet, C., Monié, P., Jolivet, L., Cadet, J.P., 2000. Migration of compression and extension in the Tyrrhenian Sea, insights from $^{40}Ar/^{39}Ar$ ages on micas along a transect from Corsica to Tuscany. Tectonophysics 321, 127–155.

Bucher, K., Fazis, Y., De Capitani, C., Grapes, R., 2005. Blueschists, eclogites, and decompression assemblages of the Zermatt-Saas ophiolite: high-pressure metamorphism of subducted Tethys lithosphere. American Mineralogist 90, 821–835.

Burov, E., Yamato, P., 2008. Continental plate collision, P-T-t-z conditions and unstable vs. stable plate dynamics: insights from thermo-mechanical modelling. Lithos 103, 178–204.

Burov, E.B., Jolivet, L., Le Pourhiet, L., Poliakov, A., 2001. A thermomechanical model of exhumation of HP and UHP methamorphic rocks in Alpine mountain belts. Tectonophysics 342, 113–136.

Caby, R., Bonhomme, G., 1982. Whole-rock and fine fraction K–Ar isotopic study of radiolarites affected by the alpine metamorphism. 5th International Conference on Geochemistry and Isotope Geology, p. 42.

Caron, J.M., Pequignot, G., 1986. The transition between blueschists and lawsonite-bearing eclogites based on observations from Corsica metabasalts. Lithos 19, 205–218.

Carson, C.J., Powell, R., Clarke, G.L., 1999. Calculated mineral equilibria for eclogites in $CaO–Na_2O–FeO–MgO–Al_2O_3–SiO_2–H_20$: application to the Pouébo Terrane, Pam Peninsula, New Caledonia. Journal of Metamorphic Geology 17, 9–24.

Cartwright, I., Barnicoat, A.C., 2002. Petrology, geochronology and tectonics of shear zones in the Zermatt-Saas and Combin zones of the Western Alps. Journal of Metamorphic Geology 20, 263–281.
Chalot-Prat, F., Ganne, J., Lombard, A., 2003. No significant element transfer from the oceanic plate to the mantle wedge during subduction and exhumation of the Tethys lithosphere (Western Alps). Lithos 69, 69–103.
Chemenda, A., Burg, J.P., Mattauer, M., 2000. Evolutionary model of the Himalaya–Tibet system: geopoem based on new modelling, geological and geophysical data. Earth and Planet Science Letters 174, 397–409.
Chemenda, A., Hurpin, D., Tang, J.C., Stephan, J.F., Buffet, G., 2001. Impact of arc-continent collision on the conditions of burial and exhumation of UHP/LT rocks: experimental and numerical modelling. Tectonophysics 342, 137–161.
Chemenda, A.I., Mattauer, M., Malavieille, J., Bokun, A.N., 1995. A mechanism for syn-collision rock exhumation and associated normal faulting: results from physical modelling. Earth and Planetary Science Letters 132, 225–232.
Chopin, C., 1984. Coesite and pure pyrope in high-grade blueschists of the western Alps: a first record and some consequences. Contributions to Mineralogy and Petrology 86, 107–118.
Chopin, C., 2003. Ultrahigh-pressure metamorphism: tracing continental crust into the mantle. Earth and Planet Science Letters 212, 1–14.
Chopin, C., Henry, C., Michard, A., 1991. Geology and petrology of the coesite-bearing terrain, Dora Maira massif, Western Alps. European Journal of Mineralogy 3, 263–291.
Clarke, G.L., Aitchison, J.C., Cluzel, D., 1997. Eclogites and blueschists of the Pam Peninsula, NE New Caledonia: a reappraisal. Journal of Petrology 38, 843–876.
Cliff, R.A., Barnicoat, A.C., Inger, S., 1998. Early Tertiary eclogite facies metamorphism in the Monviso ophiolite. Journal of Metamorphic Geology 16, 447–455.
Cloos, M., 1982. Flow melanges: numerical modelling and geologic constraints on their origin in the Franciscain subduction complex, California. Geological Society of America Bulletin 93, 330–345.
Cloos, M., 1984. Flow melanges and the structural evolution of accretionary wedges. In: Raymond, L.A. (Ed.), Melanges: Their Nature, Origin and Significance. Geological Society of America special paper. Geological Society of America, pp. 71–79.
Cloos, M., 1985. Thermal evolution of convergent plate margins: thermal modeling and re-evaluation of isotopic Ar-ages for blueschists in the Franciscan complex of California. Tectonics 4, 421–433.
Cloos, M., 1993. Lithospheric buoyancy and collisional orogenesis: subduction of oceanic plateaus, continental margins, island arcs, spreading ridges, and seamounts. Geological Society of America Bulletin 105, 715–737.
Cloos, M., Shreve, R.L., 1988. Subduction-channel model of prism accretion, melange formation, sediment subduction, and subduction erosion at convergent plate margins: 2. Implications and discussion. Pure and Applied Geophysics 128, 501–545.
Cluzel, D., Aitchison, J.C., Picard, C., 2001. Tectonic accretion nd underplating of mafic terranes in the Late Eocene intraoceanic fore-arc of New Caledonia (Southwest Pacific): geodynamic implications. Tectonophysics 340, 23–59.
Cobiella-Reguera, J.L., 2005. Emplacement of Cuban ophiolites. Geologica Acta 3, 273–294.
Coleman, R.G., 1971. Plate tectonic emplacement of upper mantle peridotites along continental edges. Journal of Geophysical Research 76, 1212–1222.
Conrad, C.P., Bilek, S., Lithgow-Bertelloni, C., 2004. Great earthquakes and slab-pull: interaction between seismic coupling and plate-slab coupling. Earth and Planet Science Letters 218, 109–122.
Coward, M. and Dietrich, D., 1989. Alpine tectonics — an overview. In: D.D. Coward M., Park R.G. (Editor), Alpine tectonics. Geological Society Special Publication, pp. 1–29.
Dahlen, F.A., 1984. Noncohesive critical coulomb wedges: an exact solution. Journal of Geophysical Research 89, 10125–10134.
Dal Piaz, G.V., 2001. History of tectonic interpretations of the Alps. Journal of Geodynamics 32, 99–114.
Dal Piaz, G.V., et al., 2001. Tertiary age and paleostructural inferences of the eclogitic imprint in the Austroalpine outliers and Zermatt-Saas ophiolite, western Alps. International Journal of Earth Sciences 90, 668–684.
Daniel, J.M., Jolivet, L., Goffé, B., Poinssot, C., 1996. Crustal-scale strain partitionning: footwall deformation below the Alpine Corsica Oligo-Miocene detachment. Journal of Structural Geology 18, 41–59.
De Capitani, C., 1994. Gleichgewichts-Phasendiagramme: Theorie und Software. Beihefte zum European Journal of Mineralogy-Jahrestagung der Deutschen Mineralogischen Gesellschaft, p. 48.
Delaloye, M., Desmons, J., 1976. K–Ar radiometric age determinations of white micas from the Piemonte zone, French–Italian Western Alps. Contributions to Mineralogy and Petrology 57, 297–303.
Delaloye, M., Desmons, J., 1980. Ophiolites and melange terranes in Iran: a geochronological study and its paleotectonic implications. Tectonophysics 68, 83–111.
Dercourt, J., et al., 2000. Atlas Peri-Tethys, Palaeogeographical Maps: 24 Maps and Explanatory Notes. CCGM/CGMW, Paris.
De Sigoyer, J., et al., 2000. Dating the Indian continental subduction and collisional thickening in the northwest Himalaya: multichronology of the Tso Morari eclogites. Geology 28, 487–490.
De Wever, P., Caby, R., 1981. Datation de la base des schistes lustrés postophiolitiques par des radiolaires (Oxfordien–Kimmeridgien moyen) dans les Alpes Cottiennes (Saint Véran, France). Comptes Rendus de l'Academie des Sciences 292, 467–472.
Dobrzhinetskaya, L.F., Green, H.W.I., Wang, S., 1996. Alpe Arami: a peridotite massif from depths of more than 300 kilometers. Science 271, 1841–1845.
Doin, M.-P., Henry, P., 2001. Subduction initiation and continental crust recycling: the roles of rheology and eclogitization. Tectonophysics 342, 163–191.
Duchêne, S., et al., 1997a. The Lu–Hf dating of Alpine Eclogites. Nature 387, 586–589.
Duchêne, S., Lardeaux, J.M., Albarède, F., 1997b. Exhumation of eclogites: insights from depth–time path analysis. Tectonophysics 280 (1–2), 125–140.
Ellis, S., Beaumont, C., Pfiffner, O.A., 1999. Geodynamic models of crustal-scale episodic tectonic accretion and underplating in subduction zones. Journal of Geophysical Research 104, 15169–15190.
Enami, M., 1998. Pressure–temperature path of Sanbagawa prograde metamorphism deduced from grossular zoning of garnet. Journal of Metamorphic Geology 16, 97–106.
Ernst, W.G., 1963. Petrogenesis of glaucophane schists. Journal of Petrology 4, 1–30.
Ernst, W.G., 1978. Petrochemical Study of Lherzolitic Rocks from the Western Alps. Journal of Petrology 19, 341–392.
Ernst, W.G., 1965. Mineral parageneses in Franciscan metamorphic rocks. Bulletin of the Geological Society of America 76, 879–914.
Ernst, W.G., 1970. Tectonic contact between the Franciscan melange and Great Valley sequence, crustal expression of a Late Mesozoic Benioff zone. Journal of Geophysical Research 75, 886–902.
Ernst, W.G., 1971. Petrologic reconnaissance of Franciscan Metagraywackes from the Diablo Range, Central California Coast Ranges. Journal of Petrology 12, 413–437.
Ernst, W.G., 1972. Occurrence and mineralogical evolution of blueschist belts with time. American Journal of Science 272, 657–668.
Ernst, W.G., 1988. Tectonic history of subduction zones inferred from retrograde blueschist P–T paths. Geology 16, 1081–1084.
Ernst, W.G., 1993. Metamorphism of Franciscan tectonostratigraphic assemblage, Pacheco Pass area, east-central Diablo Range, California Coast Ranges. Geological Society of America Bulletin 105, 618–636.
Ernst, W.G., 2001. Subduction, ultrahigh-pressure metamorphism, and regurgitation of buoyant crustal slices — implications for arcs and continental growth. Physics of the Earth and Planetary Interiors 127, 253–275.
Ernst, W.G., Dal Piaz, G.V., 1978. Mineral parageneses of eclogitic rocks and related mafic schists of the Piemonte ophiolite nappe, Breuil–St. Jacques area, Italian Western Alps. American Mineralogist 63, 621–640.
Ernst, W.G., Liou, J.G., 1995. Contrasting plate-tectonic styles of the Qinling–Dabie–Sulu and Franciscan metamorphic belts. Geology 23, 353–356.
Ernst, W.G., Maruyama, S., Wallis, S.R., 1997. Buoyancy-driven, rapid exhumation of ultrahigh-pressure metamorphosed continental crust. Proceedings of the National Academy of Sciences 94, 9532–9537.
Faccenna, C., Becker, T.W., Lucente, F.P., Jolivet, L., Rossetti, F., 2001. History of subduction and back-arc extension in the Central Mediterranean. Geophysical Journal International 145, 809–820.
Federico, L., Caponi, G., Crispini, L., Scambelluri, M., 2004. Exhumation of alpine high-pressure rocks: insights from petrology of eclogite clasts in the Tertiary Piemontese basin (Ligurian Alps, Italy). Lithos 74, 21–40.
Federico, L., Caponi, G., Crispini, L., Scambelluri, M., Villa, I.M., 2005. $^{39}Ar/^{40}Ar$ dating of high-pressure rocks from the Ligurian Alps: evidence for a continuous subduction–exhumation cycle. Earth and Planet Science Letters 240, 668–680.
Federico, L., Crispini, L., Scambelluri, M., Capponi, G., 2007. Ophiolite mélange zone records exhumation in a fossil subduction channel. Geology 35, 499–502.
Feehan, J.G., Brandon, M.T., 1999. Contribution of ductile flow to exhumation of low-temperature, high-pressure metamorphic rocks: San Juan-Cascade nappes, NW Washington state. Journal of Geophysical Research 104, 10883–10902.
Feininger, T., 1980. Eclogite and related high-pressure regional metamorphic rocks from the Andes of Ecuador. Journal of Petrology 21, 107–140.
Fitzherbert, J.A., Clarke, G.L., Marmo, B., Powell, R., 2003. Lawsonite–omphacite-bearing metabasites of the Pam Peninsula, NE New Caledonia: evidence for disrupted blueschist to eclogite facies conditions. Journal of Petrology 44, 1805–1831.
Fitzherbert, J.A., Clarke, G.L., Marmo, B., Powell, R., 2004. The origin and P–T evolution of peridotites and serpentinites of NE New Caledonia: prograde interaction between continental margin and the mantle wedge. Journal of Metamorphic Geology 22, 327–344.
Fitzherbert, J.A., Clarke, G.L., Powell, R., 2005. Preferential retrogression of high-P metasediments and the preservation of blueschist to eclogite facies metabasite during exhumation, Diahot terrane, NE New Caledonia. Lithos 83, 67–96.
Ford, M., Duchêne, S., Gasquet, D., Vanderhaeghe, O., 2006. Two-phase orogenic convergence in the external and internal SW Alps. Journal of the Geological Society — London 163, 815–826.
Fotoohi Rad, G.R., Droop, G.T.R., Amini, S., Moazzen, M., 2005. Eclogites and blueschists of the Sistan Suture Zone, eastern Iran: a comparison of P–T histories from a subduction melange. Lithos 84 (1–2), 1–24.
Fournier, M., Jolivet, L., Goffé, B., Dubois, R., 1991. The alpine Corsica metamorphic core complex. Tectonics 10, 1173–1186.
Froitzheim, N., Manatschal, G., 1996. Kinematics of Jurassic rifting, mantle exhumation, and passive-margin formation in the Austroalpine and Penninic nappes (eastern Switzerland). Geological Society of America Bulletin 108, 1120–1133.
Fryer, P., Wheat, C.G., Mottl, M.J., 1999. Mariana blueschist mud volcanism: implications for conditions within the subduction zone. Geology 27, 103–106.
Funiciello, F., Faccenna, C., Giardini, D., 2004. Role of lateral mantle flow in the evolution of subduction systems: insights from laboratory experiments. Geophysical Journal International 157, 1393–1406.
Gabriele, P., Ballèvre, M., Jaillard, E., Hernandez, J., 2003. Garnet–chloritoid–kyanite metapelites from the Raspas complex (SW Ecuador): a key eclogite-facies assemblage. European Journal of Mineralogy 15, 977–989.
Garcia-Casco, A., Torres-Roldan, R.L., Millan, G., Monié, P., Schneider, J., 2002. Oscillatory zoning in eclogitic garnet and amphibole, Northern Serpentinite Melange, Cuba: a

record of tectonic instability during subduction? Journal of Metamorphic Geology 20, 581–598.
Garcia-Casco, A., et al., 2006. High pressure metamorphism of ophiolites in Cuba. Geologica Acta 4, 63–88.
Gebauer, D., Schertl, H.P., Brix, M., Schreyer, W., 1997. 35 Ma old ultrahigh-pressure metamorphism and evidence for very rapid exhumation in the Dora Maira Massif, Western Alps. Lithos 41 (1–3), 5–24.
Gerya, T.V., Stöckhert, J.M., Perchuk, A.I., 2002. Exhumation of high-pressure metamorphic rocks in a subduction channel: a numerical simulation. Tectonics 21, 1–15.
Glodny, J., et al., 2005. Internal dynamics of a paleoaccretionary wedge: insights from combined isotope tectonochronology and sandbox modelling of the South-Central Chilean forearc. Earth and Planetary Science Letters 231 (1–2), 23–39.
Goffé, B., Velde, B., 1984. Contrasted metamorphic evolutions in thrusted cover units of the Briançonnais zone (French Alps): a model for the conservation of HP–LT metamorphic mineral assemblages. Earth and Planetary Science Letters 68, 351–360.
Goffé, B., Chopin, C., 1986. High-pressure metamorphism in the Western Alps: zoneography of metapelites, chronology and consequences. Schweizerische Mineralogische und Petrographische Mitteilungen 66, 41–52.
Goncalves, P., Guillot, S., Lardeaux, J.M., Nicollet, C., Mercier de Lepinay, B., 2000. Thrusting and sinistral wrenching in a pre-Eocene HP–LT Caribbean accretionary wedge (Samaná Peninsula, Dominican Republic). Geodinamica Acta 13, 119–132.
Gorczyk, W., Guillot, S., Gerya, T.V., Hattori, K., 2007. Asthenospheric upwelling, oceanic slab retreat, and exhumation of UHP mantle rocks: insights from the Greater Antilles. Geophysical Resarch Letters 34. doi:10.1029/2007GL031059.
Green, H.W.I., 2005. Psychology of a changing paradigm: 40+ years of high-pressure metamorphism. International Geology Review 47, 439–456.
Grove, M., Bebout, G.E., 1995. Cretaceous tectonic evolution of coastal southern California: insights from the Catalina Schist. Tectonics 14, 1290–1308.
Guillot, S., de Sigoyer, J., Lardeaux, J., Mascle, G., 1997. Eclogitic metasediments from the Tso Morari area (Ladakh, Himalaya): evidence for continental subduction during India–Asia convergence. Contributions to Mineralogy and Petrology 128, 197–212.
Guillot, S., Cosca, M., Allemand, P., Le Fort, P., 1999. Contrasting metamorphic and geochronologic evolution along the Himalayan belt. In: Macfarlane, A., Sorkhabi, R.B., Quade, J. (Eds.), Himalaya and Tibet: Mountain Roots to Mountain Tops. Geological Society of America, Boulder, Colorado. Special Paper.
Guillot, S., Hattori, K.H., de Sigoyer, J., Nägler, T., Auzende, A.-L., 2001. Evidence of hydration of the mantle wedge and its role in the exhumation of eclogites. Earth and Planetary Science Letters 193 (1–2), 115–127.
Guillot, S., Schwartz, S., Hattori, K., Auzende, A., Lardeaux, J., 2004. The Monviso ophiolitic Massif (Western Alps), a section through a serpentinite subduction channel. In: Beltrando, M., Lister, G., Ganne, J., Boullier, A. (Eds.), Evolution of the Western Alps: Insights from Metamorphism, Structural Geology, Tectonics and Geochronology. The Virtual Explorer. pp. Paper 3.
Guillot, S., Mahéo, G., de Sigoyer, J., Hattori, K. and Pêcher, A., 2007. Tethyan and indian subduction viewed from the Himalayan high- to ultra-high pressure metamorphic rocks, Out of Tethys: new geologic studies on the making of Asia, pp. in review.
Gutscher, M.-A., Kukowski, N., Malavieille, J., Lallemand, S., 1998. Material transfer in accretionary wedges from analysis of a systematic series of analog experiments. Journal of Structural Geology 20, 407–416.
Hacker, B.R., Calverta, A., Zhang, R.Y., Ernst, W.G., Liou, J.G., 2003a. Ultrarapid exhumation of ultrahigh-pressure diamond-bearing metasedimentary rocks of the Kokchetav Massif, Kazakhstan? Lithos 70, 61–75.
Hacker, B., Peacock, S., Abers, G.A., Holloway, S.D., 2003b. Subduction factory 2. Are intermediate-depth earthquakes in subducting slabs linked to metamorphic dehydration reactions? Journal of Geophysical Research 108. doi:10.1029/2001JB001129.
Hattori, K., Guillot, S., 2007. Geochemical character of serpentinites associated with high- to ultrahigh-pressure metamorphic rocks in the Alps, Cuba, and the Himalayas: recycling of elements in subduction zones. Geochemistry Geophysics Geosystems 8. doi:10.1029/2007GC001594.
Henry, C., Michard, A., Chopin, C., 1993. Geometry and structural evolution of ultra-high-pressure and high-pressure rocks from the Dora–Maira massif, western Alps, Italy. Journal of Structural Geology 15, 965–981.
Hermann, J., 2002. Experimental constraints on phase relations in subducted continental crust. Contributions to Mineralogy and Petrology 143, 219–235.
Hermann, J., Müntener, O., Scambelluri, M., 2000. The importance of serpentinite mylonites for subduction and exhumation of oceanic crust. Tectonophysics 327, 225–238.
Hermann, J., Rubatto, D., Korsakov, A., Shatsky, V.S., 2001. Multiple zircon growth during fast exhumation of diamondiferous, deeply subducted continental crust (Kokchetav Massif, Kazakhstan). Contributions to Mineralogy and Petrology 141, 66–82.
Heuret, A., Lallemand, S., 2005. Plate motions, slab dynamics and back-arc deformation. Physics of the Earth and Planetary Interiors 149, 31–51.
Honegger, K., Le Fort, P., Mascle, G., Zimmerman, J.L., 1989. The blueschists along the Indus Suture zone in Ladakh, NW Himalaya. Journal of Metamorphic Geology 7, 57–72.
Hoogerduijn Strating, E.H., Rampone, E., Piccardo, G.B., Drury, M.R., Vissers, R.L.M., 1993. Subsolidus emplacement of mantle peridotites during incipient oceanic rifting and opening of the Mesozoic Tethys (Voltri massif, NW Italy). Journal of Petrology 34, 901–927.
Hyndman, R.D., Yamano, M., Oleskevich, D.A., 1997. The seismogenic zone of subduction thrust faults. The Island Arc 6, 244–260.
Inui, M., Toriumi, M., 2002. Prograde pressure–temperature paths in the pelitic schists of the Sambagawa metamorphic belt, SW Japan. Journal of Metamorphic Geology 20, 563–580.
Iturralde-Vinent, M.A., 1994. Cuban geology: a new plate tectonic synthesis. Journal of Petroleum Geology 17, 39–70.
Iwamori, H., 1998. Trasnportation of H_2O and melting in subducting zones. Earth and Planet Science Letters 160, 65–80.
Jaillard, E., Hérail, G., Monfret, T., Wörner, G., 2002. Andean geodynamics: main issues and contributions from the 4th ISAG, Göttingen. Tectonophysics 345, 1–15.
Jayko, A.S., Blake, M.C., Brothers, R.N., 1986. Blueschist Metamorphism of the Eastern Franciscan Belt, Northern California, Blueschists and Eclogites. Geological Society of America, pp. 107–123.
Jolivet, L., Faccenna, C., 2000. Mediterranean extension and the Africa–Eurasia collision. Tectonics 16, 189–204.
Jolivet, L., et al., 1996. Miocene detachment in Crete and exhumation P–T–t paths of high pressure metamorphic rocks. Tectonics 15, 1129–1153.
Jolivet, L., Goffé, B., Bousquet, R., Oberhänsli, R., Michard, A., 1998a. Detachements in high-pressure mountain belts, Tethyan examples. Earth and Planetary Sciences Letters 160, 31–47.
Jolivet, L., et al., 1998b. Midcrustal shear zones in postorogenic extension: example from the northern Tyrrhenian Sea. Journal of Geophysical Research 103, 12123–12160.
Jolivet, L., Faccenna, C., Goffé, B., Burov, E., Agard, P., 2003. Subduction tectonics and exhumation of high-pressure metamorphic rocks in the Mediterranean orogens. American Journal of Science 303 (5), 353–409.
Jolivet, L., et al., 2005. Softening trigerred by eclogitization, the first step toward exhumation during continental subduction. Earth and Planetary Science Letters 237, 532–547.
Kanamori, H., Anderson, D.L., Heaton, T.H., 1994. Frictional melting during the rupture of the 1994 Bolivian earthquake. Science 279, 839–842.
Karson, J., 1998. Internal structure of oceanic lithosphere: a perspective from tectonic windows. In: Buck, W.R. (Ed.), Faulting and Magmatism at Mid-Ocean Ridges. Geophysical Monograph Series. AGU, Washington, D.C., pp. 177–217.
Kato, T.T., 1985. Pre-Andean orogenesis in the Coast ranges of Central Chile. Geological Society of America Bulletin 96, 918–924.
Kato, T.T., Godoy, E., 1995. Petroenesis and tectonic significance of Late Paleozoic coarse-crystalline blueschist and amphibolite boulders in the coastal range of Chile. International Geology Review 37, 992–1006.
Kerr, A.C., Iturralde-Vinent, M.A., Saunders, A.D., Babbs, A.D., Tarney, J., 1999. A new plate tectonic model of the Caribbean: implications from a geochemical reconnaissance of Cuban Mesozoic volcanic rocks. Geological Society of America Bulletin 111, 1581–1599.
Kerr, A.C., Aspden, J.A., Tarney, J., Pilatasig, L.F., 2002. The nature and provenance of accreted oceanic terrains in western Ecuador: geochemical and tectonic constraints. Journal of the Geological Society, London 159, 577–594.
Kienast, J.R., 1973. Sur l'existence de deux séries différentes au sein de l'ensemble des " Schistes Lustrés" à ophiolites du Val Tournanche. Comptes Rendus de l'Académie des Sciences 277, 1965–1968.
Kimura, G., Maruyama, S., Isozaki, Y., Terabayashi, M., 1996. Well-preserved underplating structure of the jadeitized Franciscan compex, Pacheco Pass, California. Geology 24 (1), 75–78.
Kirby, S., Engdahl, E.R., Denlinger, R., 1996. Intermediate-depth intraslab earthquakes and arc volcanism as physical expressions of crustal and uppermost mantle metamorphism in subducting slabs. In: Bebout, G.E., Scholl, D., Kirby, S., Platt, J.P. (Eds.), Subduction: Top to Bottom. Geophysical Monograph. AGU, pp. 195–214.
Ko, Z.W., Enami, M., Aoya, M., 2005. Chloritoid and barroisite-bearing pelitic schists from the eclogite unit iun the Beshi district, Sanbagawa metamorphic belt. Lithos 81, 79–100.
Krebs, M., et al., 2008. The dynamics of intra-oceanic subduction zones: a direct comparison between fossil petrological evidence (Rio San Juan Complex, Dominican Republic) and numerical simulation. Lithos 103, 106–137.
Krogh, E.J., Oh, C.W., Liou, J.G., 1994. Polyphase and anticlockwise P–T evolution for Franciscan eclogites and blueschists from Jenner, California, USA. Journal of Metamorphic Geology 12, 121–134.
Kurz, W., Froitzheim, N., 2002. The exhumation of eclogite-facies metamorphic rocks — a review of models confronted with examples from the Alps. International Geology Review 11, 702–743.
Lacombe, O., Jolivet, L., 2005. Structural and kinematic relationships between Corsica and the Pyrenees–Provence domain at the time of the Pyrenean orogeny. Tectonics 24. doi:10.1029/2004TC001673.
Lagabrielle, Y., Cannat, M., 1990. Alpine Jurassic ophiolites resemble the modern central Atlantic basement. Geology 18 (4), 319–322.
Lagabrielle, Y., Lemoine, M., 1997. Alpine, Corsican and Apennine ophiolites: the slow-spreading ridge model. Comptes Rendus de l'Academie des Sciences 325, 909–920.
Lahondère, D., Guerrot, C., 1997. Datation Sm–Nd du métamorphisme éclogitique en Corse Alpine: un argument pour l'existence au Crétacé Supérieur d'une zone de subduction active localisée sous le bloc Corso-Sarde. Géologie de la France 3, 3–11.
Lapen, T.J., et al., 2003. Burial rates during prograde metamorphism of an ultra-high-pressure terrane: an example from Lago di Cignana, western Alps, Italy. Earth and Planet Science Letters 215, 57–72.
Lardeaux, J.M., Spalla, M.I., 1991. From granulites to eclogites in the Sesia zone (Italian Western Alps): a record of the opening and closure of the Piedmont Ocean. Journal of Metamorphic Geology 9, 35–59.
Le Bayon, R., Pitra, P., Ballèvre, M., Bohn, M., 2006. Reconstructing P–T paths during continental collision using multi-stage garnet (Gran Paradiso nappe, Western Alps). Journal of Metamorphic Geology 24, 477–496.
Le Fort, P., Guillot, S., Pêcher, A., 1997. HP metamorphic belt along the Indus suture zone of NW Himalaya: new discoveries and significance. Comptes rendu de l'académie des Sciences de Paris 325, 773–778.
Lemoine, M., Tricart, P., 1986. Les Schistes Lustrés piémontais des Alpes Occidentales: approche stratigraphique, structurale et sédimentologique. Eclogae Geologicae Helvetiae 79, 271–294.
Lemoine, M., et al., 1984. Découverte de foraminifères planctoniques du Crétacé supérieur dans les schistes lustrés du Queyras (Alpes occidentales). Conséquences

paléogéographiques et tectoniques. Comptes Rendus de l'Academie des Sciences 229, 727–732.
Lemoine, M., et al., 1986. The continental margin of the Mesozoic Tethys in the Western Alps. Marine and Petroleum Geology 3, 179–199.
Lemoine, M., de Graciansky, P.C., Tricart, P., 2000. De l'océan à la chaîne de montagnes. Tectonique des plaques dans les Alpes. Gordon & Breach, Paris.
Le Pichon, X., Bergerat, F., Roulet, M.J., 1988. Plate kinematics and tectonics leading to the Alpine belt formation; a new analysis. Geological Society of America 11–131 (special issue 218).
Li, X.P., Rahn, M., Bücher, K., 2004. Serpentinites of the Zermatt-Saas ophiolite complex and their texture evolution. Journal of Metamorphic Geology 22, 159–177.
Liewig, N., Caron, J.M., Clauer, R., 1981. Geochemical and K–Ar isotopic behaviour of alpine sheet silicates during polyphased deformation. Tectonophysics 78, 273–290.
Liu, F.L., Gerdes, A., Liou, J.G., Xue, H.M., Liang, F.H., 2006. SHRIMP U–Pb zircon dating from Sulu–Dabie dolomitic marble, eastern China: constraints on prograde, ultrahigh-pressure and retrograde metamorphic ages. Journal of Metamorphic Geology 24, 569–589.
Lombardo, B., et al., 1978. Osservazioni preliminari sulle ofioliti metamorfiche del Monviso (Alpi Occidentali). Rendiconti della Societa Italiana di Mineralogia e Petrologia 34, 253–305.
Maekawa, H., Shozui, M., Ishii, T., Fryer, P., Pearce, J.A., 1993. Blueschist metamorphism in an active subduction zone. Nature 364, 520–523.
Mahéo, G., et al., 2006. Relicts of an intra-oceanic arc in the Sapi-Shergol mélange zone (Ladakh, NW Himalaya, India): implications for the closure of the Neo-Tethys Ocean. Journal of Asian Earth Sciences 26, 695–707.
Maluski, H., Matte, P., 1984. Ages of alpine tectonometamorphic events in the northwestern Himalaya (northern Pakistan) by $^{39}Ar/^{40}Ar$ method. Tectonics 3, 1–18.
Manatschal, G., 2004. New models for evolution of magma-poor rifted margins based on a review of data and concepts from West Iberia and the Alps. International Journal of Earth Sciences 93, 432–466.
Maresch, W.V., et al., 2000. Crustal history and plate tectonic development in the southern Caribbean. Sonderheft ZAG 1, 283–289.
Marmo, B.A., Clarke, G.L., Powell, R., 2002. Fractionation of bulk rock composition due to porphyroblast growth: effects on eclogitic facies mineral equilibria, Pam Peninsula, New Caledonia. Journal of Metamorphic Geology 20, 151–165.
Martin, S., Rebay, G., Kienast, J.R., Mevel, C., 2008. An eclogitized oceanic palaeo-hydrothermal field from the St Marcel valley (Italian Western Alps). Ofioliti 33, 49–63.
Maruyama, S., Liou, J.G., Terabayashi, M., 1996. Blueschist and eclogites of the world and their exhumation. International Geology Review 38, 485–594.
Matsumoto, K., et al., 2003. Petrological constraints on the formation conditions and retrograde P–T path of the Kotsu eclogite unit, Central Shikoku. Journal of Metamorphic Geology 21, 363–376.
McCall, G.J.H., 1997. The geotectonic history of the Makran and adjacent areas of southern Iran. Journal of Asian Earth Sciences 15 (6), 517–531.
Messiga, B., Scambelluri, M., 1991. Retrograde P-T-t path for the Voltri Massif eclogites (Ligurian Alps, Italy): some tectonic implications. Journal of Metamorphic Geology 9, 93–109.
Messiga, B., Scambelluri, M., Piccardo, G.B., 1995. Chloritoid-bearing assemblages in mafic systems and the eclogite-facies hydration of alpine Mg–Al metagabbros (Erro-Tobbio unit, Ligurian western Alps). European Journal of Mineralogy 7, 1149–1167.
Messiga, B., Kienast, J.R., Rebay, G., Riccardi, M.P., Tribuzio, R., 1999. Cr-rich magnesio-chloritoid eclogites from the Monviso ophiolites (Western Alps, Italy). Journal of Metamorphic Geology 17, 287–299.
Michard, A., Goffé, B., Chopin, C., Henry, C., 1996. Did the Western Alps develop through an Oman-type stage? The geotectonic setting of high pressure metamorphism in two contrasting Thethyan transects. Eclogae geol. Helv. 89 (1), 43–80.
Miyashiro, A., 1961. Evolution of metamorphic belts. Journal of Petrology 2, 277–311.
Miyazaki, K., Zulkarnain, I., Sopaheluwakan, J., Wakita, K., 1996. Pressure–temperature conditions and retrograde paths of eclogites, garnet–glaucophane rocks and schists from South Sulawesi, Indonesia. Journal of Metamorphic Geology 14, 549–563.
Molinaro, M., Leturmy, P., Guezou, J.C., Frizon de Lamotte, D., Eshraghi, S.A., 2005. The structure and kinematics of the southeastern Zagros fold-thrust belt, Iran: from thin-skinned to thick-skinned tectonics. Tectonics 24. doi:10.1029/2004TC001633.
Monié, P., Philippot, P., 1989. Mise en évidence de l'âge éocène moyen du métamorphisme de haute-pression dans la nappe eclogitique du Monviso (Alpes occidentales) par la methode $^{39}Ar–^{40}Ar$. Comptes Rendus de l'Academie des Sciences 309, 245–251.
Moore, D.E., Blake, M.C., 1989. New evidence for polyphase metamorphism of glaucophane schist and eclogite exotic blocks in the Franciscan complex, California and Oregon. Journal of Metamorphic Geology 7, 211–228.
O'Brien, P., 2006. Exhumation of UHP rocks: deciphering the petrologic and geochronologic evidence in Himalayan examples. EGU06, Vienna, pp. A–10573.
O'Brien, P.J., Zotov, N., Law, R., Khan, A.M., 2001. Coesite in Himalaya eclogite and implications for models of India–Asia collision. Geology 29, 435–438.
Oberhänsli, R., et al., 2004. Metamorphic Structure of the Alps. C.G.M.W., Paris.
Oh, C.W., Liou, J.G., 1990. Metamorphic evolution of two different eclogites in the Franciscan Complex, California, U.S.A. Lithos 25, 41–53.
Ohta, Y., Hirajima, T., Hiroi, Y., 1986. Caledonian High-Pressure Metamorphism in Central Western Spitsbergen, Blueschists and Eclogites. Geological Society of America, pp. 205–216.
Okay, A.I., 1989. Alpine–Himalayan blueschists. Annual Reviews of Earth and Planetary Sciences 17, 55–87.
Okay, A.I., Harris, N.B.W., Kelley, S.P., 1998. Exhumation of blueschists along a Tethyan suture in northwest Turkey. Tectonophysics 285, 275–299.
Orange, D.L., Geddes, D., Moore, J.C., Cox, R., Underwood, M., 1992. Constraining the temperature, pressure and fluid compositional evolution of an accretionary complex by an integrated study of cement stratigraphy and tectonics. In: Kharaka, D., Maest, J. (Eds.), Water–Rock Interaction. Balkema, Rotterdam.
Parkinson, C., 1998. Emplacement of the East Sulawesi Ophiolite: evidence from subophiolite metamorphic rocks. Journal of Asian Earth Sciences 16, 13–28.
Paul, A., Kaviani, A., Hatzfeld, D., Vergne, J., Mokhtari, M., 2006. Seismological evidence for crustal-scale thrusting in the Zagros mountain belt (Iran). Geophysical Journal International 166, 227–237.
Peacock, S., 1990. Numerical simulation of metamorphic pressure–temperature–time paths and fluid production in subduction slabs. Tectonics 9, 1197–1211.
Peacock, S., et al., 2005. Thermal structure of the Costa Rica–Nicaragua subduction zone. Physics of the Earth and Planetary Interiors 149, 187–200.
Peacock, S., Wang, K., 1999. Seismic consequences of warm versus cool subduction metamorphism: examples from southwest and northeast Japan. Science 286, 937–939.
Peacock, S.M., 1987. Creation and preservation of subduction-related metamorphic gradients. Journal of Geophysical Research 92 (12), 736–781.
Peacock, S.M., 1996. Thermal and Petrologic structure of subduction zones. In: Bebout, G.E., Scholl, D.W., Kirby, S.H., Platt, J.P. (Eds.), Subduction: Top to Bottom. Geophysical Monograph Ser. American Geophysical Union, Washington, D.C., pp. 119–133.
Pfiffner, O.A., Ellis, S., Beaumont, C., 2000. Collision tectonics in the Swiss Alps: insight from geodynamic modeling. Tectonics 19 (6), 1065–1094.
Philippot, P., 1990. Opposite vergence of nappes and crustal extension in the French–Italian Western Alps. Tectonics 9, 1143–1164.
Philippot, P., Blichert-Toft, J., Perchuk, A.L., Costa, S., Gerasimov, V.Y., 2001. Lu–Hf and Ar–Ar geochronology supports extreme rate of subduction zone metamorphism deduced from geospeedometry. Tectonophysics 342, 23–38.
Philippot, P., Kienast, J.-R., 1989. Chemical–microstructural changes in eclogite-facies shear zones (Monviso, Western Alps, north Italy) as indicators of strain history and the mechanism and scale of mass transfer. Lithos 23 (3), 179–200.
Pilchin, A., 2005. The role of serpentinization in exhumation of high- to ultra-high-pressure metamorphic rocks. Earth and Planet Science Letters 237, 815–828.
Platt, J.P., 1986. Dynamics of orogenic wedges and the uplift of high-pressure metamorphic rocks. Geological society of America Bulletin 97, 1037–1053.
Platt, J.P., 1993. Exhumation of high-pressure rocks: a review of concept and processes. Terra Nova 5, 119–133.
Platt, J.P., Leggett, J.K., Young, J., Raza, H., Alam, S., 1985. Large-scale sediment underplating in the Makran accretionary prism, southwest Pakistan. Geology 13, 507–511.
Pognante, U., 1991. Petrological constraints on the eclogite- and blueschist-facies metamorphism and P–T–t paths in the western Alps. Journal of Metamorphic Geology 9, 5–17.
Pognante, U., Spencer, D.A., 1991. First report of eclogites from the Himalayan belt, Kaghan valley (northern Pakistan). European Journal of Mineralogy 3, 613–618.
Polino, R., 1984. Les series oceaniques du Haut val de Suse (Alpes Cottiennes): analyse des couvertures sedimentaires. Ofioliti 9, 547–554.
Polino, R., Dal Piaz, G.V., Gosso, G., 1990. Tectonic erosion at the Adria margin and acretionary processes for the Cretaceous orogeny in the Alps. In: Roure, F., Heitzmann, P., Polino, R. (Eds.), Deep Structure of the Alps. Société Géologique de France, pp. 345–367.
Ravna, E.J., Krogh, E.J., Andersen, T.B., Jolivet, L., submitted for publication. New insights into the formation of lawsonite eclogites — constraints from prograde evolution of eclogitized pillow lava from Corsica. Lithos.
Rawling, T.J., Lister, G.S., 2002. Large-scale structure of the eclogite–blueschist belt of New Caledonia. Journal of Structural Geology 24, 1239–1258.
Reddy, S.M., Wheeler, J., Cliff, R.A., 1999. The geometry and timing of orogenic extension: an exemple from the Western Italian Alps. Journal of Metamorphic Geology 17, 573–589.
Reddy, S.M., et al., 2003. Kinematic reworking and exhumation within the convergent Alpine Orogen. Tectonophysics 365 (1–4), 77–102.
Regard, V., Faccenna, C., Martinod, J., Bellier, O., Thomas, J.-C., 2003. From subduction to collision: control of deep processes on the evolution of convergent plate boundary. Journal of Geophysical Research 108. doi:10.1029/2002JB001943.
Reinecke, T., 1991. Very high-pressure metamorphism and uplift of coesite-bearing metasediments from the Zermatt-Saas zone, Western Alps. European Journal of Mineralogy 3, 7–17.
Reinecke, T., 1998. Prograde high- to ultrahigh-pressure metamorphism and exhumation of oceanic sediments at Lago di Cignana, Zermatt-Saas Zone, western Alps. Lithos 42, 147–189.
Ricou, L.E., 1971. Le croissant ophiolitique péri-arabe, une ceinture de nappes mise en place au crétacé supérieur. Revue de géographie physique et de géologie dynamique 13, 327–350.
Ring, U. and Brandon, M.T., 1999. Ductile deformation and mass loss in the Franciscan subduction complex: implications for exhumation processes in accretionary wedges. In: B.M.T. Ring U., Willett S.D., Lister G.S. (Editor), Exhumation Processes: Normal Faulting, Ductile Flow and Erosion. Geological Society Special Publicatio, London, pp. 55–86.
Ring, U., Brandon, M.T., Willett, S.D. and Lister, G.S., 1999. Exhumation processes. In: B.M.T. Ring U., Willett S.D., Lister G.S. (Editor), Exhumation Processes: Normal Faulting, Ductile Flow and Erosion. Geological Society Special Publication, London, pp. 1–27.
Rosenbaum, G., Lister, G.S., 2005. The Western Alps from the Jurassic to Oligocene: spatio-temporal constraints and evolutionary reconstructions. Earth-Science Reviews 69, 281–306.
Roure, F., Polino, R., Nicolich, R., 1990. Early Neogene deformation beneath the Po plain: constraints of the post-collisional Alpine evolution. In: Roure, F., Heitzmann, P., Polino, R. (Eds.), Mémoires. Société Géologique de France, Paris, pp. 309–322.
Rubatto, D., Hermann, J., 2001. Exhumation as fast as subduction? Geology 29, 3–6.

Rubatto, D., Hermann, J., 2003. Zircon formation during fluid circulation in eclogites (Monviso, Western Alps): implications for Zr and Hf budget in subduction zones. Geochimica and Cosmochimica Acta 67, 2173–2187.
Rubatto, D., Scambelluri, M., 2003. U–Pb dating of magmatic zircon and metamorphic baddeleyite in the Ligurian eclogites (Voltri massif, Western Alps). Contributions to Mineralogy and Petrology 147, 341–355.
Rubatto, D., Gebauer, D., Fanning, M., 1998. Jurassic formation and Eocene subduction of the Zermatt-Saas-Fee ophiolites: implications for the geodynamic evolution of the Central and Western Alps. Contributions to Mineralogy and Petrology 132, 269–287.
Sabzehei, M., 1974. Les mélanges ophiolitiques de la région d'Esfandageh (Iran méridional). Etude pétrologique et structurale; interprétation dans le cadre Iranien. Ph-D Thesis, Univ. Grenoble, France, 306 pp.
Sabzehei, M., et al., 1994. Geological map of Hajiabad, 1/250.000 scale. Geological Survey of Iran.
Scambelluri, M., et al., 2001. Incompatible element-rich £uids released by antigorite breakdown in deeply subducted mantle. Earth and Planet Science Letters 192, 457–470.
Scambelluri, M., Pettke, T., van Roermund, H.L.M., 2008. Majoritic garnets monitor deep subduction fluid flow and mantle dynamics. Geology 36, 59–62.
Schellart, W.P., Lister, G.S., Toy, V.G., 2006. A Late Cretaceous and Cenozoic reconstruction of the Southwest Pacific region: tectonics controlled by subduction and slab rollback processes. Earth-Science Reviews 76, 191–233.
Schmid, S.M., Kissling, E., 2000. The arc of the Western Alps in the light of geophysical data on deep crustal structure. Tectonics 19, 62–85.
Schmidt, M.W., Poli, S., 1998. Experimentally-based water budgets for dehydrating slabs and consequences for arc magma generation. Earth and Planet Science Letters 163, 361–379.
Schneider, J., et al., 2004. Origin and evolution of the Escambray Massif (Central Cuba): an example of HP/LT rocks exhumed during intraoceanic subduction. Journal of Metamorphic Geology 22, 227–247.
Scholz, C.H., Campos, J., 1995. On the mechanism of seismic decoupling and back arc spreading at subduction zones. Journal of Geophysical Research 100, 22103–22115.
Schwartz, S., 2002. La zone Piémontaise des Alpes Occidentales: Un paléo-complexe de subduction. BRGM Thesis, Claude Bernard Lyon 1, Lyon, 313 pp.
Schwartz, S., Lardeaux, J.M., Guillot, S., Tricart, P., 2000a. Diversité du métamorphisme éclogitique dans le massif ophiolitique du Monviso (Alpes occidentales, Italie). Geodinamica Acta 13, 169–188.
Schwartz, S., Lardeaux, J.-M., Tricart, P., 2000b. La zone d'Acceglio (Alpes cottiennes): un nouvel exemple de croûte continentale éclogitisée dans les Alpes occidentales. Compte rendu de l'académie des Sciences de Paris 330, 859–866.
Schwartz, S., Allemand, P., Guillot, S., 2001. Numerical model of the effect of serpentinites on the exhumation of eclogitic rocks: insights from the Monviso ophiolitic massif (Western Alps). Tectonophysics 342, 193–206.
Searle, M., Corfield, R.I., Stephenson, B., McCarron, J., 1997. Structure of the North Indian continental margin in the Ladakh-Zanskar Himalayas: implications for the timing of obduction of the Spontang ophiolite, India–Asia collision and deformation events in the Himalaya. Geological Magazine 3, 297–316.
Sedlock, R.L., 1996. Syn-subduction forearc extension and blueschist exhumation in Baja California, Mexico. In: Bebout, G.E., Scholl, D., Kirby, S., Platt, J.P. (Eds.), Subduction: Top to Bottom. AGU, pp. 155–162.
Seno, S., Dallagiovanna, G., Vanossi, M., 2005. A kinematic evolutionary model for the Penninic sector of the central Ligurian Alps. International Journal of Earth Sciences 94, 114–129.
Sherlock, S.C., Kelley, S.P., Inger, S., Harris, N.B.W., Okay, A.I., 1999. $^{40}Ar/^{39}Ar$ and Rb–Sr geochronology of high-pressure metamorphism and exhumation history of teh Tavsanli zone, NW Turkey. Contributions to Mineralogy and Petrology 137, 46–58.
Shreve, R.L., Cloos, M., 1986. Dynamics of sediment subduction, melange formation, and prism accretion. Journal of Geophysical Research 91 (B10), 10229–10245.
Sinclair, H.D., Allen, P.A., 1992. Vertical versus horizontal motions in the Alpine orogenic wedge: stratigraphic response in the foreland basin. Basin Research 4, 215–232.
Smith, D.C., 1984. Coesite in clinopyroxene in the Caledonides and its implications for geodynamics. Nature 310 (641–644).
Sobolev, N.V., Shatsky, V.S., 1990. Diamond inclusions in garnets from metamorphic rocks: a new environment for diamond formation. Nature 343, 742–746.
Song, S.G., et al., 2007. Eclogite and carpholite-bearing meta-pelite in the North Qilian suture zone, NW China: implications for Early Paleozoic cold oceanic subduction. Journal of Metamorphic Geology: in review.
Sorensen, S.S., 1988. Petrology of amphibolite-facies mafic and ultramafid rocks from the Catalina Schist, southern California: metasomatism and migmatization in a subduction zone metamorphic setting. Journal of Metamorphic Geology 6, 405–435.
Sorensen, S.S., Barton, M.D., 1987. Metasomatism and partial melting in a subduction complex, Catalina schist, California. Geology 15, 115–118.
Spalla, M.I., Lardeaux, J.M., Dal Piaz, G.V., Gosso, G., Messiga, B., 1996. Tectonic significance of Alpine eclogites. Journal of Geodynamics 21 (3), 257–285.
Spandler, C., Rubatto, D., Hermann, J., 2005. Late Cretaceous–Tertiary tectonics of the southwest Pacific: insights from U–Pb sensitive, high-resolution ion microprobe (SHRIMP) dating of eclogite facies rocks from New Caledonia. Tectonics 24. doi:10.1029/2004TC001709.
Stampfli, G.M., et al., 1998. Subduction and obduction processes in the Swiss Alps. Tectonophysics 296, 159–204.
Stanek, K.P., Maresch, W.V., Grafe, F., Grevel, C., Baumann, A., 2006. Structure, tectonics and metamorphic development of the Sancti Spiritus Dome (eastern Escambray massif, Central Cuba). Geologica Acta 4, 151–170.
Stern, R.J., 2004. Subduction initiation: spontaneous and induced. Earth and Planetary Science Letters 226, 275–292.
Stipska, P., Pitra, P., Powell, R., 2006. Separate or shared metamorphic histories of eclogites and surrounding rocks? An example from the Bohemian Massif. Journal of Metamorphic Geology 24, 219–240.
Stöckhert, B., Gerya, T.V., 2005. Pre-collisional high pressure metamorphism and nappe tectonics at active continental margins: a numerical simulation. Terra Nova 17 (2), 102–110.
Stöckhert, B., et al., 1995. Tectonic history of Isla Margarita, Venezuela — a record of a piece of crust close to an active margin. Geology 23, 787–790.
Tagami, T., Dumitru, T.A., 1996. Provenance and thermal history of the Franciscan accretionary complex: constraints from zircon fision track thermochronology. Journal of Geophysical Research 101, 11353–11364.
Takasu, A., Wallis, S.R., Banno, S., Dallmeyer, R.D., 1994. Evolution of the Sambagawa metamorphic belt, Japan. Lithos 33, 119–133.
Takeshita, H., Shimoya, H., Itaya, T., 1994. White mica K–Ar ages of blueschist-facies rocks from the Piemonte 'calc-schists' of the Western Alps. The Island Arc 3, 151–162.
Takeshita, H., Ishii, K., Kanagawa, K., 2005. Flow kinematics in the deeper part of a subduction channel, as inferred from inclusion trails in plagioclase porphyroblasts from the Sambagawa metamorphic rocks, south-west Japan. Journal of Metamorphic Geology 23, 279–294.
Tirrul, R., Bell, I.R., Griffis, R.J., Camp, V.E., 1983. The Sistan Suture Zone of eastern Iran. Geological Society of America Bulletin 94, 134–150.
Todd, C.S., Engi, M., 1997. Metamorphic field gradients in the Central Alps. Journal of Metamorphic Geology 15, 513–530.
Tonarini, S., et al., 1993. Eocene age of eclogite metamorphism in Pakistan Himalaya: implications for India–Eurasia collision. Terra nova 5, 13–20.
Tsujimori, T., Matsumoto, K., Wakabayashi, J., Liou, J.G., 2006. Franciscan eclogite revisited: reeavaluation of the P–T evolution of tectonic blocks from Tiburon Peninsula, California, USA. Mineralogy and Petrology 88, 243–267.
Tsujimori, T., Sisson, V.B., Liou, J.G., Harlow, G.E. and Sorensen, S.S., Very-low-temperature record of the subduction process: a review of worldwide lawsonite eclogites. Lithos: in press.
Ulmer, P., Trommsdorff, V., 1995. Serpentine stability to mantle depths and subduction-related magmatism. Science 268, 858–861.
Van der Klauw, S.N.G.C., Reinecke, T., Stöckhert, B., 1997. Exhumation of ultrahigh-pressure metamorphic oceanic crust from Lago di Cignana, Piemontese zone, western Alps: the structural record in metabasites. Lithos 41, 79–102.
Van Roermund, HLM., Drury, M.R., 1998. Ultra-high pressure (P>6 GPa) garnet peridotites in Western Norway: exhumation of mantle rocks from >185 km depth, Terra Nova, 10, 295-301.
Vignaroli, G., et al., 2005. A counter-clockwise P–T path for the Voltri Massif eclogites (Ligurian Alps, Italy). Journal of Metamorphic Geology 23, 533–555.
Von Blanckenburg, F., Huw Davies, J., 1995. Slab breakoff: a model for syncollisional magmatism and tectonics in the Alps. Tectonics 14, 120–131.
Wain, A., 1997. New evidence for coesite in eclogite and gneisses: defining an ultra-high pressure province in the Western Gneiss region of Norway. Geology 25, 927–930.
Wakabayashi, J., 1990. Counterclockwise P–T–t paths from amphibolites, Franciscan complex, California: relics from the early stages of subduction zone metamorphism. Journal of Geology 98, 657–680.
Wallis, S.R., 1998. Exhuming the Sanbagawa metamorphic belt: the importance of tectonic discontinuities. Journal of Metamorphic Geology 16, 83–95.
Wallis, S.R., Aoya, M., 2000. A re-evaluation of eclogite facies metamorphism in SW Japan: proposal for an eclogite nappe. Journal of Metamorphic Geology 18, 653–664.
Wallis, S.R., Moriyama, Y., Tagami, T., 2004. Exhumation rates and age of metamorphism in the Sanbagawa belt: new constraints from zircon fission track analysis. Journal of Metamorphic Geology 22, 17–24.
Warren, C.J., Beaumont, C., Jamieson, R.A., 2008. Modelling tectonic styles and ultra-high pressure (UHP) rock exhumation during the transition from oceanic subduction to continental collision. Earth and Planet Science Letters 267, 129–145.
Whitney, D.L., Davis, P.B., 2006. Why is lawsonite eclogite so rare? Metamorphism and preservation of lawsonite eclogite, Sivrihisar, Turkey. Geology 34, 473–476.
Willner, A.P., Glodny, J., Gerya, T.V., Godoy, E., Massonne, H.-J., 2004. A counterclockwise PTt path of high-pressure/low-temperature rocks from the Coastal Cordillera accretionary complex of south-central Chile: constraints for the earliest stage of subduction mass flow. Lithos 75 (3–4), 283–310.
Yagi, K., Takeshita, H., 2002. Regional variation in exhumation and strain rate of the high-pressure Sambagawa metamorphic rocks in central Shikoku, south-west Japan. Journal of Metamorphic Geology 20, 633–647.
Yamato, P., Agard, P., Burov, E., Le Pourhiet, L., Jolivet, L., Tiberi, C., 2007. Burial and exhumation in a subduction wedge: mutual constraints from thermo-mechanical modeling and natural P-T-t data (Sch. Lustrés, W. Alps). Journal of Geophysical Research 112, B07410. doi:10.1029/2006JB004441.
Yamato, P., Burov, E., Agard, P., Le Pourhiet, L., Jolivet, L., 2008. HP–UHP exhumation during slow continental subduction: self-consistent thermodynamically and thermomechanically coupled model with application to the Western Alps. Earth and Planet Science Letters 271, 63–74.
Yokohama, K., Brothers, R.N. and Black, P.M., 1986. Regional eclogite facies in the high-pressure metamorphic belt of New Caledonia, blueschists and eclogites. Memoirs. Geological Society of America.
Zack, T., Rivers, T., Brumm, R., Kronz, A., 2004. Cold subduction of oceanic crust: Implications from a lawsonite eclogite from the Dominican Republic. European Journal of Mineralogy 16, 909–916.

GEOPHYSICAL RESEARCH LETTERS, VOL. 36, L07303, doi:10.1029/2008GL036942, 2009

Influence of surrounding plates on 3D subduction dynamics

P. Yamato,[1] L. Husson,[1] J. Braun,[1] C. Loiselet,[1] and C. Thieulot[2]

Received 9 December 2008; revised 4 March 2009; accepted 6 March 2009; published 3 April 2009.

[1] Our 3D modelling study shows that the presence of lithospheric plates around a subducting plate has a significant influence on subduction dynamics, in particular on trench retreat rate, slab dip, and lateral shortening of the subducting plate. Neighbouring plates prevent unrealistic plate behaviour with no need for complex rheologies. Because, at the Earth's surface, plates form a continuous shell, they should not be neglected. **Citation:** Yamato, P., L. Husson, J. Braun, C. Loiselet, and C. Thieulot (2009), Influence of surrounding plates on 3D subduction dynamics, *Geophys. Res. Lett.*, *36*, L07303, doi:10.1029/2008GL036942.

1. Introduction

[2] At the Earth's surface, tectonic plates form a complete shell and, therefore, no plate can be considered in isolation. A "complete" subduction system is thus made of four plates: the subducting, overriding and lateral plates.

[3] A variety of models have been proposed, using physical [e.g., *Bellahsen et al.*, 2005; *Funiciello et al.*, 2003a, 2006, 2008; *Schellart*, 2008], semi-analytical [*Royden and Husson*, 2006] and numerical methods [e.g., *Stegman et al.*, 2006; *Clark et al.*, 2008] to study the dynamics of subduction zones in 3D. However most studies, with the exception of a few [e.g., *Zhong and Gurnis*, 1995; *Royden and Husson*, 2006; *Espurt et al.*, 2008; *Regard et al.*, 2008; *Clark et al.*, 2008; *Bonnardot et al.*, 2008], considered the subducting plate in isolation, by focusing on its interactions with the surrounding mantle. In cases where the overriding plate is not included, one commonly assumes that it has no effect on mantle flow since it passively accompanies the retreating trench [*Bellahsen et al.*, 2005; *Funiciello et al.*, 2003b].

[4] However, because plates are stiffer and denser than the upper mantle, the presence or absence of lithospheric material in the upper mantle influences the velocity field in and around a subducting plate, and the dynamics of subduction will depart from the "intrinsic" dynamics of an isolated subduction system. Both the poloidal (downdip, in a vertical plane) and toroidal (at the slab edges, in a plane parallel to the surface) components of the return flow induced by the motion of the slab in the viscous upper mantle is not limited to the deepest parts of the subduction system but also reaches the surface; this flow may affect the motion of other plates and conversely, be influenced by them.

[5] In most models where the subducting plate is considered in isolation, the plate is not prevented from flowing laterally by the presence of neighbouring plates, as it is in natural systems. The deformation of the edges of the plate naturally occurs in purely viscous models, a phenomena that seems to be fortuitously limited in physical models by the possible action of surface tension or by the elastic properties of the material used [e.g., *Schellart*, 2008]. To prevent this artificial lateral flow, several *ad hoc* parameterizations have been used, including using a very high viscosity contrast between the plate and surrounding mantle, incorporating plasticity through a yield strength that is sufficiently high to prevent the horizontal deformation but small enough to permit slab bending [e.g., *Moresi and Solomatov*, 1998; *Stegman et al.*, 2006], imposing an arbitrary cut-off for stress transmission [*Husson*, 2006], or adding elasticity [e.g., *Bonnardot et al.*, 2008].

[6] Herein we quantify the impact of surrounding plates on subduction dynamics through a series of simple experiments carried out using a 3D numerical model of linear viscous fluid flow. It is not our purpose here to explore the many parameters of the system (e.g., geometry of the lithosphere, boundary conditions, viscosity, or density ratios): we choose a given setup in all our experiments and focus on the influence of surrounding plates.

2. Model Setup

[7] We have used the 3D code *DOUAR* described in details by *Braun et al.* [2008], originally designed for thermo-mechanical modelling. In this study, we are interested in understanding the basic interactions of a subducting plate with the surrounding mantle and adjacent plates; we have thus used a linear viscous rheology for all components of the system, neglecting non-linear effects arising from the thermal and stress-dependence of rheology.

[8] The initial model and the material parameters (effective viscosity and density) are presented in Figure 1a. Since the YZ plan at X = 0 in our model is a plane of symmetry, we only model one half of the slab along the left-hand side (X = 0) of the 3D box, leaving enough space to its right (i.e., between X = 0.5 and X = 1.0) to prevent most boundary effects. In all experiments, the initial geometry corresponds to an ongoing, though immature, subduction zone. The size of the square unit model box corresponds to 3000 km. The upper/lower mantle boundary is characterized by a viscosity jump at 660 km. The crust and mantle lithosphere are respectively 30 and 120 km thick. We chose thick lithosphere and crust in order to preserve a high resolution (additional tests are performed with thicknesses that are twice thinner). The resolution of the model is ~25 km between the top of the model and the upper-lower mantle boundary, where most of the deformation occurs, and 50 km elsewhere. The resolution is further improved by the *divFEM* algorithm used in *DOUAR* that can be tailored to represent density variations at an even smaller scale (~6 km)

[1] Geosciences Rennes, UMR6118, Université de Rennes 1, CNRS, Rennes, France.
[2] Department of Earth Sciences, Bergen University, Bergen, Norway.

0094-8276/09/2008GL036942$05.00

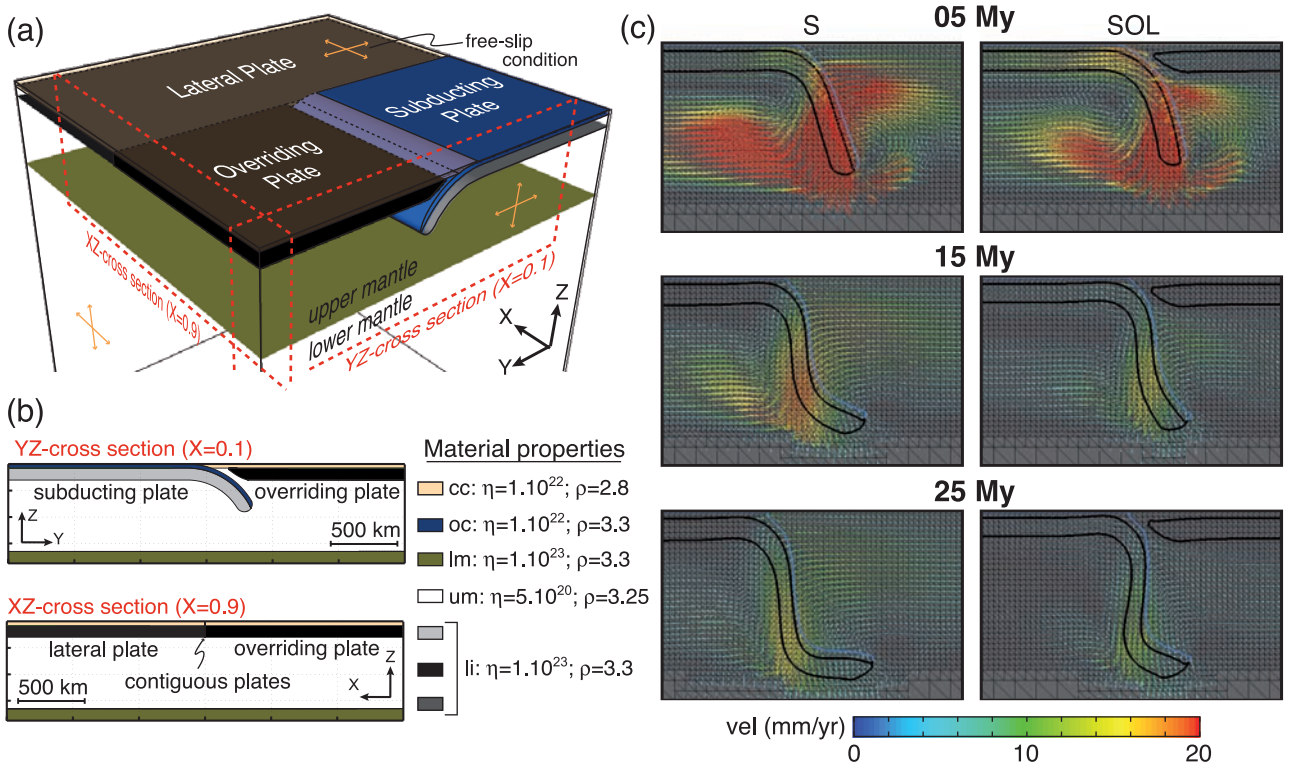

Figure 1. (a) 3D view of the model box at the beginning of the experiment. (b) Cross-sections showing plate stratification (crust and mantle) and material properties. *oc* and *cc*, oceanic and continental crust, *li*, *um* and *lm*: lithospheric, upper and lower mantle. Black, dark grey and light grey indicate overriding, lateral and subducting mantle lithosphere, respectively. (c) Subduction evolution during 25 My for the two models *S* and *SOL*. (YZ Cross-section taken at X = 0.1 corresponding to 300 km, see Figure 1a).

[*Braun et al.*, 2008]. Four configurations, that include respectively the Subducting plate only (S), the Subducting and Overriding plates only (SO), the Subducting and Lateral plates only (SL), and all plates together (SOL), were tested (Figure 1a). All models are nonetheless everywhere capped by a relatively buoyant, moderate viscosity crust, which in turns decreases the phenomena described below (e.g., trench retreat, lateral shortening and subduction).

[9] Material densities and viscosities are scaled to the upper mantle reference values (Figure 1b). In nature, the effective viscosity ratio between the subducting lithosphere and the upper mantle is thought to be in the range of 10 to 10^3 [e.g., *Hager*, 1984; *Davies and Richards*, 1992; *Mitrovica and Forte*, 2004]. We have thus used a viscosity ratio of 200, which also is a commonly used value that predicts realistic kinematics [e.g., *Funiciello et al.*, 2003a; *Schellart*, 2004, *Stegman et al.*, 2006, *Schellart*, 2008]. The lower mantle to lithosphere viscosity ratio is set to 1, high enough to limit slab penetration across the 660 km discontinuity. A crustal layer with a scaled viscosity of 20 caps the entire model; its scaled density is 1.015 over the subducting lithosphere and 0.8615 everywhere else (continental crust). All lithospheric mantle units are also contiguous, except for a rectangular gap between the subducting and the overriding lithosphere, where low viscosity material with upper mantle rheology facilitates the subduction process (Figure 1b). The crustal layer controls the kinematics [e.g., *Royden and Husson*, 2006] but the nature of this control is beyond our scope and we assign density and viscosity values that predict subduction velocities of a few mm.yr^{-1} (v-velocity component on Figure 2). Free-slip boundary conditions are imposed on all sides of the model and plate motion is resisted by the no-velocity conditions imposed at the plate boundaries (fixed plates, Figure 1a).

[10] This is an end-member situation in order to characterise the largest possible effect. Three-dimensional dynamic modelling of subduction zones is most relevant for small subduction zones. The behaviour of many small-sized subduction zones can thus be best approximated by the "fixed plate" setup we have used here, because their subduction rate is much faster than the plate convergence rate (e.g., Scotia, Hellenic, Tyrrhenian, Calabria...). We performed a few experiments with a free upper surface (no stress), but this required a much larger number of small time steps and did not lead to significantly different conclusions.

3. General Evolution of the Models

[11] In all experiments the subduction process evolves in three stages (Figure 1c) [see also *Bellahsen et al.*, 2005; *Stegman et al.*, 2006]: (1) the slab sinks in the upper mantle, (2) approaches the upper-lower mantle discontinuity and bends, (3) the slab tail (i.e., the bottom end of the slab) rests on the upper/lower mantle discontinuity and the system reaches a steady-state where further subduction is accompanied by trench retreat. The first sinking stage can be polluted by the initial geometry but can be assimilated to the transient stage existing between subduction initiation and

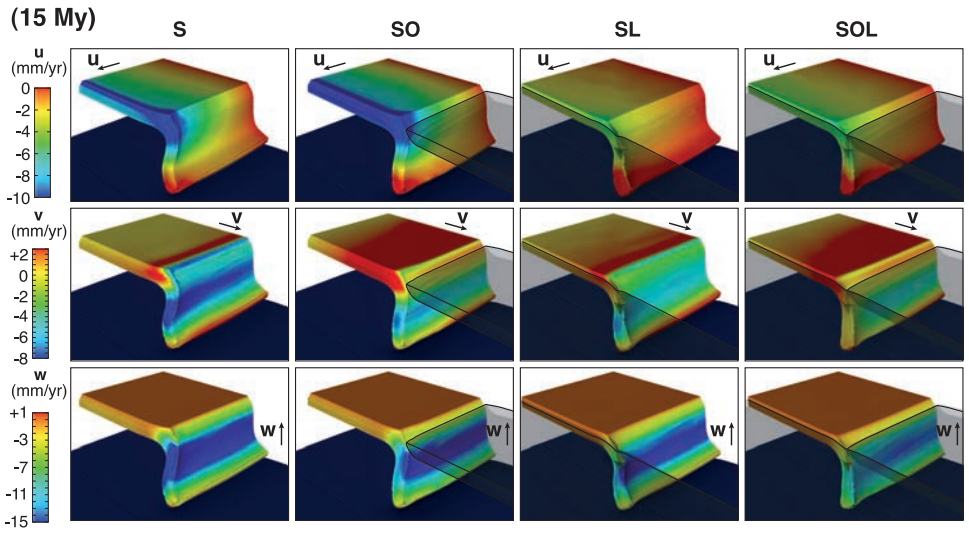

Figure 2. Velocity field components for the subducting plate for each experiment after 15 Myr. The shapes of the lateral and overriding lithospheres are presented as ghosts (the crust on the overriding and lateral plate is not shown).

'steady state' subduction. Trench retreat takes place when the slab approaches the 660 km discontinuity (stage 2), after an initial stage of advance (Figure 3a).

[12] In our models, the crust is advected in depth with the subducting lithosphere following the velocity field. The channel between the subducting and the overriding plates can thus evolve freely. The poloidal component of mantle flow is attenuated as the slab approaches the 660 km discontinuity (Figure 1c) because the upper mantle can no longer flow beneath the slab tail and the lower mantle.

[13] At intermediate depths (i.e., between 275 and 375 km), the slab dip is broadly similar in all experiments. During the first stage, slab dip increases from 60° to ~75–80°. In stage 2, it remains stable as the slab approaches the 660 km discontinuity, before increasing again during the bending of the slab tail along the 660 km discontinuity. In all experiments steady state is reached after ~20 Myr, with slab dips at intermediate depths ranging between 83° and 92°. The *SOL* and *SO* experiments display steeper slabs than in the *S* and *SL* experiments where slab dip is always lower than 90°.

4. Slab Rollback and Trench Retreat

[14] Subduction is accompanied by a faster rate of trench retreat in the experiments where the overriding plate is absent (y-component of the velocity field (*v*), mid. panel, Figure 2). This is illustrated in details in Figures 3a and 3b where the location (Figure 3a) and velocity (*v*-component, Figure 3b) of the trench are given as a function of time. Horizontal velocities, strain rates and deviatoric stresses along cross-sections from the models S and SOL are also given in the auxiliary material with description.[1]

[15] The poloidal flow induced by the sinking slab is made of two cylindrical cells, on either side of the slab. When the overriding plate is absent (Figure 1c), the cell in front of the slab extends from the slab tail to the surface. When the more viscous overriding plate is present, it does not extend to the surface but is limited to the base of the overriding plate. This difference influences subduction dynamics in two important ways. First, in the absence of overriding plate (*S* and *SL* experiments), the return flow amplifies trench retreat rates (Figure 2) by a factor of 2 to 5 (Figure 3b), as opposed to experiments with an overriding plate (*SO* and *SOL* experiments). Consequently, slab retreat rate will always be overestimated in experiments where the overriding plate is not accounted for. Secondly, the maximum velocity generated by the poloidal flow found at the top of the upper mantle, i.e. deeper with an overriding plate, explains the slightly higher slab dip values in *SO* and *SOL* than in *S* and *SL* (Figure 2).

5. Lateral Behaviour of the Subducting Plate

[16] Let's now consider the evolution of the slab in the third dimension (along the X axis, Figures 2, 3c, and S1). In both the *S* and *SO* experiments, the lateral edge of the subducting plate is not held by another plate alongside and is affected by trench parallel shortening (Figure 2, top). Significant shortening occurs for models with no lateral plate (Figure 3d) and is partly caused by subduction along the side of the subducting plate, driven by the negative buoyancy of the plate. The fact that the plate is fixed at the boundary induces additional extension on the plate, which stretches accordingly along the y-direction; this stretching has to be compensated by shortening along the x- and z-directions. Shortening is facilitated when the plate is not maintained laterally (*S* and *SO* experiments). After 20 Myr, total shortening values obtained are 3 times greater for the *S* and *SO* experiments (~15%) than for *SL* and *SOL* (~5%). As illustrated in Figure 3e where the maximum depth of the subducting plate measured along its edge is shown as a function of time for each of the four experiments, the presence of the neighbouring plate prevents shortening and thus the lateral subduction of the subducting plate.

[1] Auxiliary materials are available in the HTML. doi:10.1029/2008GL036942.

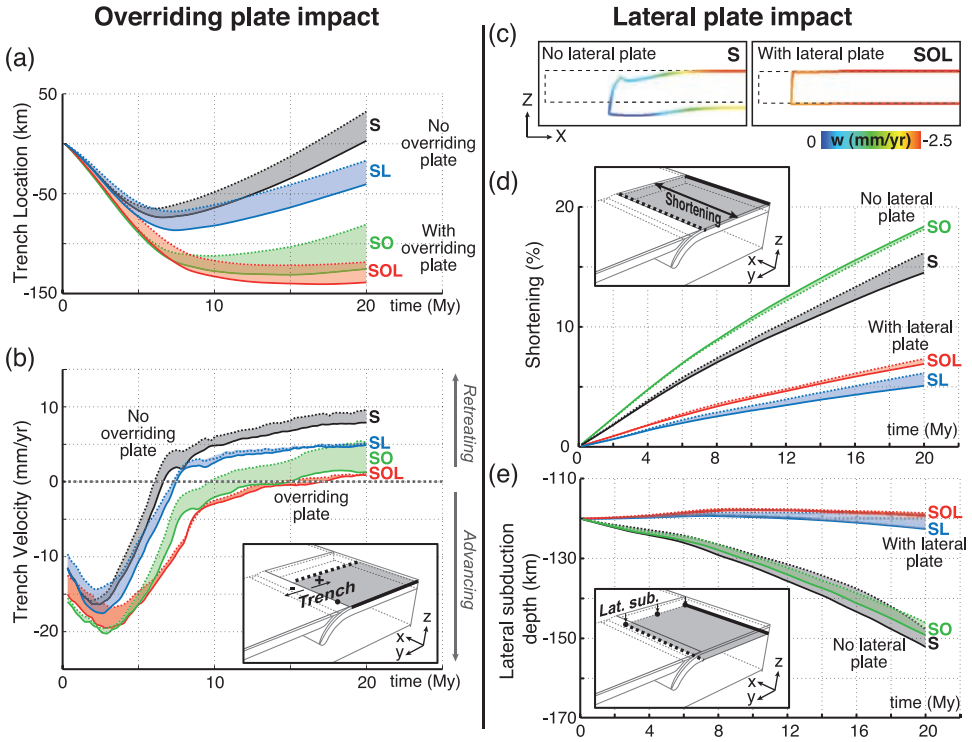

Figure 3. (a) Trench location and (b) velocity through time. Solid and dashed lines correspond to values calculated respectively at X = 0 and X = 0.35 (1050 km) from the right side of the model box (see inset). (c) Lateral behavior of the subducting lithosphere for the two models S and SOL after 20 Myr (XZ cross-section at Y = 0.1). Dashed and color lines correspond to the location of the subducting plate at t = 0 Myr and t = 20 Myr. (d) Lateral shortening of the subducting plate. (e) Maximum depth of lateral subduction (lat. sub.) reached by the lateral edge of the subducting plate. Solid and dashed lines correspond to the values at Y = 0 and Y = 0.4 (1200 km) from the backside of the model box (see inset).

Indeed, after 20 Myr, the plate edge has penetrated into the upper mantle to a depth of ~150 km for *S* and *SO* (Figure 3e), whereas it has remained at its initial depth when a lateral plate is included (*SL* and *SOL*, Figure 3c). Although the subducting lithosphere is equally gravitationally unstable in all four experiments and has thus the same tendency to subduct on all sides, the presence of a lateral plate reduces the negative buoyancy and thus prevents lateral subduction.

6. Conclusion and Discussion

[17] Surrounding plates in subduction systems affect the global dynamic of the subduction process in multiple ways. (1) The presence of an overriding plate modifies the poloidal flow generated by a subducting slab. Consequently, neglecting overriding plate leads to overestimating trench retreat velocities by a factor 2 to 5 and underestimating slab dips at depth. (2) The presence of a lateral plate prevents lateral shortening observed in many experiments where the subducting plate is considered in isolation; a phenomenon that leads to models including complex rheologies that prevent such undesirable effects [e.g., *Moresi and Solomatov*, 1998; *Stegman et al.*, 2006]. As previously shown [e.g., *King and Hager*, 1990; *Conrad and Hager*, 1999], 3D models composed of a single plate predict subduction velocities that have to be considered as upper bound values. However, in a purely viscous system, our experiments show that the absence of lateral plates leads to unrealistic lateral shortening and to the lateral subduction of the plate, which is not observed in natural subduction zones. Studies that do not account for the presence of surface plates may provide qualitative information that is only valid under the assumption that surrounding plates are weak (oceanic subduction in the presence of a well developed back-arc system, for instance). Our setup assumes that the plates are pinned to the sidewalls. When plates are "free", these effects are significantly reduced but still important. In real Earth, most small-scale subduction zones, for which our setup is relevant, are characterized by subduction rates that are much faster than the plate convergence rate (i.e., they are "fixed"). In addition, the large model crustal and mantle lithosphere thicknesses seemingly enhance our results. However, because the model is Newtonian, assigning thinner lithosphere and crust leads to comparable results for a given amount of subduction (not for a given time), as confirmed by additional tests.

[18] Our results suggest that all plates must be included in modelling-based studies, where the effects of many parameters characterizing a subduction system (e.g., lithosphere thickness, viscosity and density ratios, friction between plates, velocity/stresses boundary conditions...) are explored.

[19] **Acknowledgments.** This work was supported by the "Chair d'Excellence Senior de l'ANR" (J.B.). Constructive reviews by L. Fleitout, D. Stegman and an anonymous reviewer are gratefully acknowledged.

References

Bellahsen, N., C. Faccenna, and F. Funiciello (2005), Dynamics of subduction and plate motion in laboratory experiments: Insights into the "plate tectonics" behavior of the Earth, *J. Geophys. Res.*, *110*, B01401, doi:10.1029/2004JB002999.

Bonnardot, M. A., R. Hassani, E. Tric, E. Ruellan, and M. Régnier (2008), Effect of margin curvature on plate deformation in a 3-D numerical model of subduction zones, *Geophys. J. Int.*, *173*, 1084–1094, doi:10.1111/j.1365-246X. 2008.03752.x.

Braun, J., C. Thieulot, P. Fullsack, M. DeKool, C. Beaumont, and R. Huismans (2008), DOUAR: A new three-dimensional creeping flow numerical model for the solution of geological problems, *Phys. Earth Planet. Inter.*, *171*, 76–91, doi:10.1016/j.pepi.2008.05.003.

Clark, S. R., D. Stegman, and R. D. Müller (2008), Episodicity in back-arc tectonic regimes, *Phys. Earth Planet. Inter.*, *171*, 265–279, doi:10.1016/j.pepi.2008.04.012.

Conrad, C. P., and B. H. Hager (1999), Effects of plate bending and fault strength at subduction zones on plate dynamics, *J. Geophys. Res.*, *104*, 17,551–17,571.

Davies, G. F., and G. F. Richards (1992), Mantle convection, *J. Geol.*, *100*, 151–206.

Espurt, N., F. Funiciello, J. Martinod, B. Guillaume, V. Regard, C. Faccenna, and S. Brusset (2008), Flat subduction dynamics and deformation of the South American plate: Insights from analog modeling, *Tectonics*, *27*, TC3011, doi:10.1029/2007TC002175.

Funiciello, F., C. Faccenna, D. Giardini, and K. Regenauer-Lieb (2003a), Dynamics of retreating slabs: 2. Insights from three-dimensional laboratory experiments, *J. Geophys. Res.*, *108*(B4), 2207, doi:10.1029/2001JB000896.

Funiciello, F., G. Morra, K. Regenauer-Lieb, and D. Giardini (2003b), Dynamics of retreating slabs: 1. Insights from two-dimensional numerical experiments, *J. Geophys. Res.*, *108*(B4), 2206, doi:10.1029/2001JB000898.

Funiciello, F., M. Moroni, C. Piromallo, C. Faccenna, A. Cenedese, and H. A. Bui (2006), Mapping mantle flow during retreating subduction: Laboratory models analyzed by feature tracking, *J. Geophys. Res.*, *111*, B03402, doi:10.1029/2005JB003792.

Funiciello, F., C. Faccenna, A. Heuret, S. Lallemand, E. Di Giuseppe, and T. W. Becker (2008), Trench migration, net rotation and slab-mantle coupling, *Earth Planet. Sci. Lett.*, *271*, 233–240, doi:10.1016/j.epsl.2008.04.006.

Hager, B. H. (1984), Subducted slab and the geoid: Constraints on mantle rheology and flow, *J. Geophys. Res.*, *89*, 6003–6015.

Husson, L. (2006), Dynamic topography above retreating subduction zones, *Geology*, *34*, 741–744.

King, S. D., and B. H. Hager (1990), The relationship between plate velocity and trench viscosity in Newtonian and power-law subduction calculations, *Geophys. Res. Lett.*, *17*, 2409–2412.

Mitrovica, J. X., and A. M. Forte (2004), A new inference of mantle viscosity based upon joint inversion of convection and glacial isostatic adjustment data, *Earth Planet. Sci. Lett.*, *225*, 177–189, doi:10.1016/j.epsl.2004.06.005.

Moresi, L., and V. Solomatov (1998), Mantle convection with a brittle lithosphere: Thoughts on the global tectonic styles of Earth and Venus, *Geophys. J. Int.*, *133*, 669–682.

Regard, V., C. Faccenna, O. Bellier, and J. Martinod (2008), Laboratory experiments of slab break-off and slab dip reversal: Insight into the Alpine Oligocene reorganization, *Terra Nova*, *20*, 267–273.

Royden, L. H., and L. Husson (2006), Trench motion, slab geometry and viscous stresses in subduction systems, *Geophys. J. Int.*, *167*, 881–905.

Schellart, W. P. (2004), Quantifying the net slab pull force as a driving mechanism for plate tectonics, *Geophys. Res. Lett.*, *31*, L07611, doi:10.1029/2004GL019528.

Schellart, W. P. (2008), Kinematics and flow patterns in deep mantle and upper mantle subduction models: Influence of the mantle depth and slab to mantle viscosity ratio, *Geochem. Geophys. Geosyst.*, *9*, Q03014, doi:10.1029/2007GC001656.

Stegman, D. R., J. Freeman, W. P. Schellart, L. Moresi, and D. May (2006), Influence of trench width on subduction hinge retreat rates in 3-D models of slab rollback, *Geochem. Geophys. Geosyst.*, *7*, Q03012, doi:10.1029/2005GC001056.

Zhong, S., and M. Gurnis (1995), Mantle convection with plates and mobile, faulted plate margins, *Science*, *267*, 838–843.

J. Braun, L. Husson, C. Loiselet, and P. Yamato, Geosciences Rennes, UMR6118, Université de Rennes 1, CNRS, Bat. 15, F-35042 Rennes CEDEX, France. (philippe.yamato.rennes1@gmail.com)

C. Thieulot, Department of Earth Sciences, Bergen University, Allegaten 41, N-5007 Bergen, Norway.

Geophys. J. Int. (2009) **176,** 307–326 doi: 10.1111/j.1365-246X.2008.03977.x

Taiwan mountain building: insights from 2-D thermomechanical modelling of a rheologically stratified lithosphere

P. Yamato,[1] F. Mouthereau[2] and E. Burov[2]

[1] *Geosciences Rennes,* UMR 6118 CNRS*, Université de Rennes* 1*,* 35042 *Rennes Cedex, France*
[2] *Laboratoire de tectonique, Université Pierre et Marie Curie—Paris* 6*,* UMR 7072 CNRS, 4 *place Jussieu,* F-75005 *Paris, France.*
E-mail: frederic.mouthereau@lgs.jussieu.fr

Accepted 2008 September 12. Received 2008 September 11; in original form 2008 January 5

SUMMARY

The Taiwan orogen has long been regarded as a case example for studying mountain building in association with subduction processes. In this paper, we present a fully coupled thermomechanical modelling of the Taiwan collision based on a realistic viscous-elastic–plastic rheology. It satisfactorily reproduces available thermochronometric data, long-/short-term deformation patterns, heat flux and erosion/sedimentation distribution across the Taiwan orogeny. We found that a deep seated flux of Asian crustal material into the orogenic wedge should be invoked to counter-balance observed exhumation and erosion in the Central Range. However, in contrast with recent thermokinematic models of exhumation and deformation suggesting that underplating plays a significant role, we show that most constraints on exhumation and deformation can be more straightforwardly interpreted by the frontal accretion of the rheologically layered Asian crust. We finally infer that such a model is in better agreement with the basic expectation that the hot/young and buoyant Chinese continental margin should hardly be subducted beneath the cold/old and dense oceanic plate of the Philippines Sea.

Key words: Mechanics, theory, and modelling; Rheology: crust and lithosphere.

1 INTRODUCTION

Since the studies by Davis *et al.* (1983) and Dahlen *et al.* (1984) that popularized the critically tapered wedges approach of mountain building, Taiwan has become the key natural example of mountain belts for the development of critical wedge model. Assuming steady-state evolution, thermokinematic models presented in foremost papers by Barr & Dahlen (1989) and Dahlen & Barr (1989) have allowed for comparison between predicted particle paths entering orogenic wedges and observed *P–T* conditions, temperature distribution and heat flux with several applications to Taiwan. More recently, the increasing number of thermochronometric constraints has renewed our interest in investigating the mechanisms of exhumation in the Taiwan mountain belt (Willett & Brandon 2002; Willett *et al.* 2003; Fuller *et al.* 2006; Simoes & Avouac 2006; Simoes *et al.* 2007). One major conclusion brought by these recent models is that underplating can represent 50 to 100 per cent of the materials accreted to the Taiwan orogenic wedge, which is significantly larger than the initially proposed 10–25 per cent of underplating (Barr & Dahlen 1989).

Much of the models cited above are thermokinematic models in which the temperature is solved to allow for comparison with available thermochronometric or metamorphic data. They are not designed for the full description of mechanical processes during long-term orogenic processes. Actually, few models intended to produce a mechanically comprehensive representation of the Taiwan Mountain building so far. Chemenda *et al.* (2001) proposed an original analogue modelling approach in 2-D and 3-D in which oceanic and continental lithospheres have distinct plastic behaviour and overlie a low-viscosity asthenosphere. These models satisfactorily explain several particular tectonic features of Taiwan. First, they are successful in reproducing the so-called 'Taiwan paradox', that is, the apparent contradiction between the relative normal motion along the plate boundary fault and the observation that 30 per cent of the plate convergence is accommodated across this fault. Second, it also successfully reproduced the subduction reversal, its initiation being indirectly constrained by the age of the onset of a strong subsidence on the upper Philippine Sea Plate (PSP). Third, a major conclusion brought by the works of Chemenda *et al.* (2001) but less discussed by the authors is the limited subduction of the continental crust beneath the overriding plate. Indeed, as soon as the continental crust is subducted, collision processes initiate and the rapid exhumation or extrusion of the continental basement takes place. Thus, Chemenda's model disagrees with a long-standing continental subduction beneath Taiwan and rather predicts that Taiwan is the result of a transient collisional stage.

Unfortunately, this type of models was not designed to allow for comparison with the thermochronometric data such as the metamorphic grades observed throughout the belt or the fission-track age constraints. Furthermore, it is not accurate enough to provide quantitative interpretations of long-term deformation or short-term GPS-derived deformation patterns. Finally, because the lithosphere

rheology is limited to plasticity, exhumation processes assisted by viscous flow of rocks were not taken into account, which is, however, known to be a likely phenomenon in orogenies controlled by high erosion rates (Beaumont *et al.* 2001).

Fuller *et al.* (2006) presented a 2-D thermomechanical numerical modelling of the evolution of the Taiwan orogen constrained by thermochronometric data. The rheology of the crust is more realistic than numerical models already mentioned. A power-law viscosity is preferred at high temperature and a Coulomb criterion is used to simulate plastic failure in the crust. This model is also more sophisticated since it is able to provide thermal constraints and thus allows for comparison between predicted P–T paths and observations. However, owing to boundary conditions, there are some limitations for applying this category of models. Indeed, the plate boundary geometry between the subducting and the overriding plates, for example, the slab dip and the geometry of the backstop are fixed. Moreover, the deformation within the crustal wedge is quasi-static so large deformations are not permitted and changes in material fluxes are only permitted at the base of the growing orogenic wedge and at the surface where erosional processes are considered. More critical to our study is that underplating is simulated by adding numerically an upward velocity of particles (Fuller *et al.* 2006; Simoes *et al.* 2007). Thus, the flux of accretion by underplating and the width of the underplating window are imposed directly by initial boundary conditions rather than being outputs of the model.

Based on this brief review it appears that any further studies dealing with the modelling of the Taiwan mountain building require 2-D (ideally 3-D) fully-coupled thermomechanical modelling. Moreover, thermomechanical modelling of such subduction/collision processes becomes more and more common and sophisticated (e.g. Burov *et al.* 2001; Burg & Gerya 2005; Sobolev & Babeyko 2005; Currie *et al.* 2007; Faccenda *et al.* 2008; Gerya *et al*. 2008; Yamato *et al*. 2007, 2008; Warren *et al.* 2008). However, in relation to Taiwan, only a first attempt at using such kind of thermomechanical model with viscous-plastic and viscous-elastic–plastic rheology has been recently presented (Kaus *et al.* 2008).

In this paper, our objective is to provide a 2-D thermomechanical numerical model of Taiwan mountain building at the lithospheric-scale that accounts for a wide range of natural observations. All the dynamic parameters are fully coupled so that velocities, strength and the plate geometry change with model evolution. In this paper, we attempt to account for structural, metamorphic and thermochronometric data as well as fitting the short-/long-term shortening distribution, erosion–sedimentation distribution, heat flow data, which has never been attempted so far.

2 TECTONIC AND GEOLOGICAL SETTING

2.1 Overview

The Taiwan collision results from the convergence between the downgoing Chinese continental margin belonging to the Eurasian plate and the overriding oceanic PSP (Fig. 1). The collision likely started in the late Miocene–early Pliocene (Suppe 1981; Ho 1986; Lin *et al.* 2003; Tensi *et al.* 2006) about 20Myr after the initiation of the oceanic spreading in the South China Sea (Lee & Lawver 1995; Clift *et al.* 2002; Lin *et al.* 2003). The present-day convergence rate of the Luzon Arc relative to the Chinese continental margin is estimated to be 80 mmyr^{-1} in N58°W direction (e.g. Yu *et al.* 1997).

The Taiwan Island is classically divided into several tectonic units (Ho 1986). The Coastal Range (CoR) to the East, which represents a part of the northern Luzon Arc, accreted to the collided margin (Fig. 2). The CoR consists of a Miocene magmatic basement arc associated with intra-arc turbidites. This sequence is overlain by thick Plio-Pleistocene synorogenic deposits (3–4 km) that derived from the erosion of the Taiwan mountain belt (Huang *et al.* 1995). The Longitudinal Valley Fault (LVF) is the plate boundary fault between the CoR and the Central Range. The latter comprises the exhumed Palaeozoic–Mesozoic metamorphic basement (Tananao Schist, TS) that is overlain by the Palaeogene and Neogene slates of the Backbone Range (BR) and the Hsuehshan Range (HR). The western non-metamorphic fold–thrust belt, namely the Western Foothills (WF) is made of foreland and marginal deposits accreted to the growing orogenic wedge during the Pliocene. Further west, the Coastal Plain (CP) lies at the transition between the frontal thrust units and the western foredeep (Fig. 2). Much of the currently active faults or Quaternary faults are located between the CP and the WF (Bonilla 1977). The Chichi earthquake ($M_l = 7.6$) that occurred on 1999 September 21, related to the reactivation of a large reverse fault rupture, the Chelungpu–Sani Fault (CST in Fig. 2), constitutes a remarkable example for the seismic release of a significant part of the current plate convergence.

2.2 Metamorphic conditions and thermochronometric constraints

The TS contains black schists, marbles and gneiss bodies, which present the highest P–T metamorphic conditions recorded in Taiwan. After the Nanao orogeny in the Late Mesozoic, during which the TS recorded amphibolites metamorphism, the TS units were secondarily overprinted, during the Mio-Pliocene Penglai orogeny, by an upper to lower grade greenschist facies metamorphism (Fig. 2). The temperature–time history predicted for the Chipan gneiss in the north of the TS and P–T–t paths calculated by wedge modelling (Barr & Dahlen 1989; Simoes *et al.* 2007) show consistent peak metamorphism (up to $T = 500$°C and $P =$ 6–8 kb) and cooling history. Although these models suggest heating and burial prior to exhumation, only few Ar^{40}/Ar^{39} ages on biotite (Lo & Onstott 1995) allow the identification of a prograde path in the Chipan gneiss P–T history. Also, little evidence is found of high-pressure (HP) metamorphic facies. They are restricted to kilometric-scale exotic blocks of glaucophane schists (e.g. Juisui blueschist) in the Yuli Belt (Fig. 2). They are interpreted as oceanic rocks metamorphosed under HP–LT conditions ($T = 450$–500°C, $P > 8$ kb) possibly during the Late Miocene (Ernst 1981). In light of more recent thermodynamic databases, peak metamorphic conditions have been re-evaluated to $T = 550$°C and $P = 10$–12 kb (Beyssac *et al.* 2008). These authors further suggested that these HP rocks have been exhumed in two steps the final exhumation having occurred between 10 and 4.5 Ma.

Fig. 3 shows a synthesis of the thermochronometric constraints in Taiwan. Samples with ages lower than 5Myr are believed to be reset ages as they cooled through the closure isotherm of the studied thermochronometer. Predicted unreset ages are assumed to be close to depositional ages. We have arbitrarily fixed unreset ages to 30Myr, which is the averaged stratigraphic age for Palaeogene sediments where samples have been collected.

Cooling apatite fission track (AFT) ages in the TS are generally younger than 1Ma (Fig. 3a). Determination of zircon fission track (ZFT) ages also show reset zircons but with slightly older

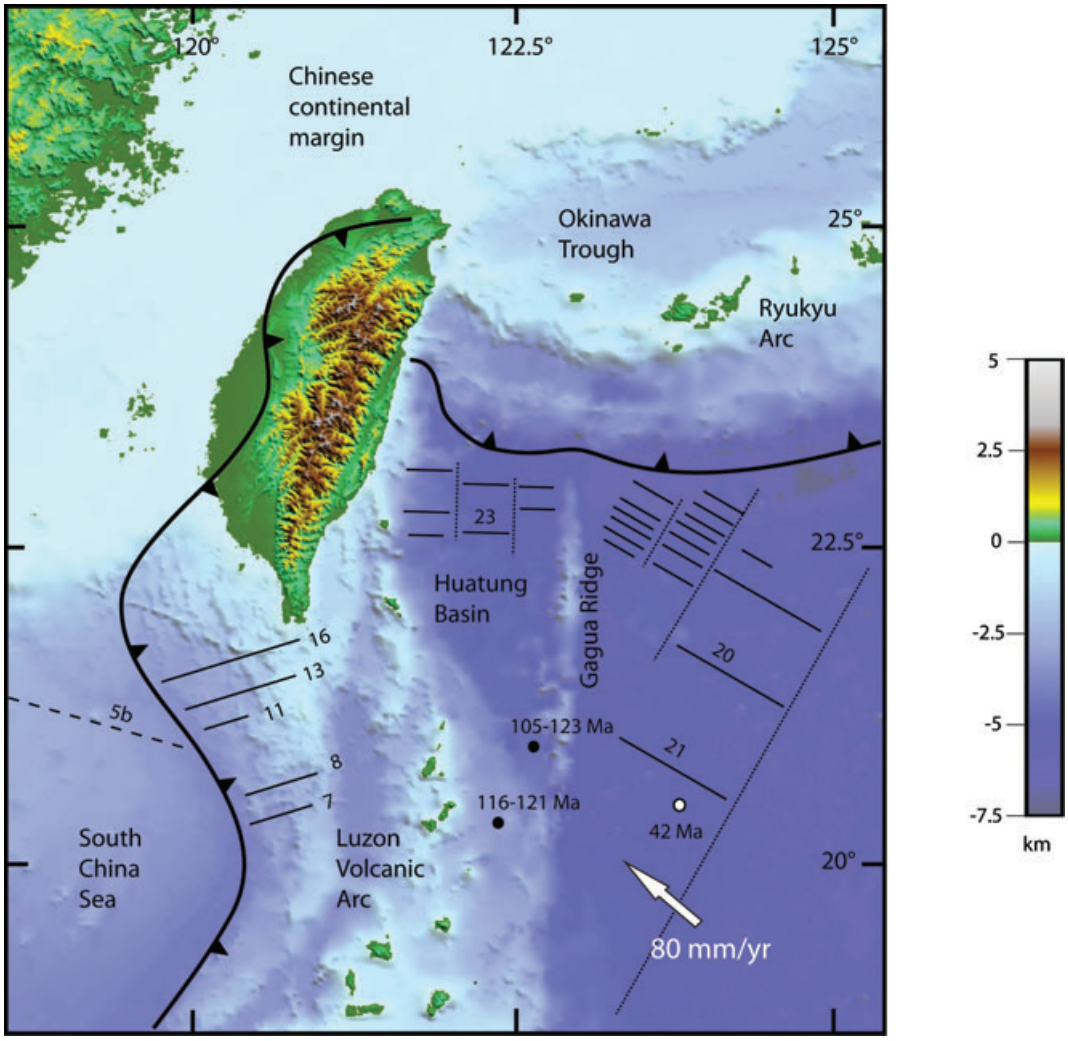

Figure 1. Geodynamic setting of the Taiwan arc–continent collision that developed in the context of two subduction zones with opposite vergence between the PSP and the Chinese continental margin. Magnetic anomalies suggest that spreading started at least 51 Ma (chron 23) in the West Philippine Basin (Huatung Basin). Dating in oceanic boreholes revealed older ages closer to 105–125 Ma (Deschamps *et al.* 2000). Eastward, the East PSP show younger ages ∼42 to 48 Ma (chron 21).

estimates between 3 and 0.9Ma (Fig. 3a). (U–Th)/He dating on zircons provides cooling ages younger than 1Ma close to AFT ages. Other constraints on peak temperatures revealed by Raman Spectroscopy of Carbonaceous Material (RSCM) techniques (Beyssac *et al.* 2008) indicate temperatures often higher than 450°C in the TS units.

The slates of the BR overlies the pre-Tertiary metamorphic basement. The BR is made of an assemblage of Eocene metasediments (Pilushan Formation), which are overlain unconformably by Miocene slates (Lushan Formation). These sediments have been metamorphosed during the ongoing collision under lower greenschist metamorphic conditions ($T = 300 \pm 50$ °C, $P = 4$ kb; Liou & Ernst 1984; Fig. 2). Reset AFT ages lower than 2 Myr, as well as reset ZFT ages younger than 3 Myr, are found in the Pilushan Formation. By contrast, the thermochronometric patterns in the Lushan Formation are more complex : partially reset or unreset AFT ages are in the range of 5.6 and 2 Myr (Fuller *et al.* 2006). Unreset samples with ZFT ages older than 30 Ma are reported together with ZFT ages younger than 3 Ma (Fig. 3a). Such FT ages have been alternatively interpreted as reset FT ages consistent with a two-stage collision (Lee *et al.* 2006). (U–Th)/He dating carried out on zircons also revealed partially reset and unreset zircons with ages ranging between 3.8 and 41 Ma (Fig. 3a). In the Pilushan slates all (U–Th)/He ages on zircons are reset with ages younger than 1 Ma. RSCM temperatures are usually lower than 350 °C.

The HR located to the west of the BR consists of Eocene–Oligocene slates metamorphosed at prehnyte–pumpellyite to lower greenschist facies ($T = 260 \pm 40$ °C, $P = 2$–3 kb; Liou & Ernst 1984). The HR is characterized by abnormally high peak RSCM temperatures locally larger than $T = 475$ °C similar to observations in the TS (Beyssac *et al.* 2007). This result is well correlated with reset AFT ages younger than 1 Ma, reset ZFT ages younger than 3 Ma and (U–Th)/He ages on zircons in the range of 1.5–2 Ma. All these data suggest a rapid exhumation of a minimum of 15 km (Beyssac *et al.* 2007). To explain such abnormal patterns, the HR can be viewed as a small-scale extensional basin originated in the rifted Chinese margin, which was subsequently inverted during the Penglai orogeny (Teng 1992; Clarck *et al.* 1993; Lee *et al.* 1997). In any case, the metamorphic data and model P–T paths for the BS and HR suggest a simple cooling and decompression from initial P–T conditions in the Chinese passive margin (Simoes *et al.* 2007).

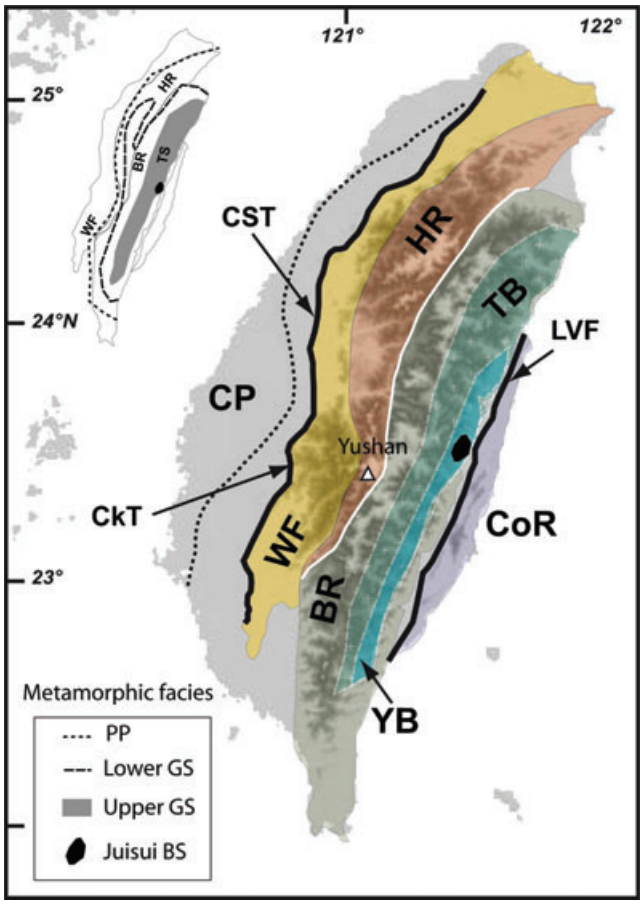

Figure 2. Simplified geological map of the Taiwan collision belt and metamorphic facies map (inset). Tectonic units are from East to West the Coastal Range (CoR), the Longitudinal Valley Fault (LVF), the Tailuko Belt (TB) and the Yuli Belt (YB) of the eastern Central Range, including the Juisui blueschist rocks, the Backbone Range (BR), the Hsuehshan Range (HR), the Western Foothills (WF) and the Coastal Plain (CP). The thick black lines depict the two main kinematic boundaries (reverse faults) accommodating the current plate convergence. They are the LVF to the East and the Chukou Thrust (CkT)-Chelungpu–Sani Thrust (CST) at the front. The white thin line corresponds to the Lishan Fault, a crustal scale backthrust that likely acted as a major faulted boundary accommodating the exhumation of the HR. Metamorphic facies map after Chen *et al.* (1983). GS, greenschist metamorphic facies; PP, prehnyte-pumpellyite metamorphic facies; BS, blueschist metamorphic facies.

Where thermochronometric constraints exist, the western foreland fold–thrust belt appears mostly characterized by unreset AFT, ZFT and ZHe ages. This is in agreement with the limited burial recorded by the outer frontal WF rocks. The highest metamorphic grades reported inner WF reveals prehnyte–pumpellyite conditions ($T = 150\ ^{\circ}$C, $P = 1$–2 kb; Liou & Ernst 1984).

2.3 Structural styles, finite strain and ductile fabrics

Crustal shortening across the whole Taiwan orogen has been first estimated to be 160–200 km (Suppe 1981). Based on modelling of foreland basin deposition patterns and age constraints on frontal thrusts, a shortening rate of 39–45 mm yr^{-1} over the past 2 Myr have been recently proposed (Simoes & Avouac 2006), consistently suggesting crustal shortening of 195–225 km over the past 5 Myr. Across the WF, finite shortening is greatly dependent on the importance assumed for basement-involved deformation with respect to thin-skinned style of deformation (Mouthereau & Lacombe 2006). Nevertheless, finite shortening in the WF should range between 15–20 km, increasing up to, for example, 42 km if thin-skinned deformation prevailed (Yue *et al.* 2005). Deformation in the HR is characterized by vertical folding in association with a pervasive steeply dipping pressure solution cleavage S1. By contrast, the BR is characterized by inclined folds in association with S1 dipping slightly to the SE. Studies on the finite ductile strain in the slate belt suggest that the HR was dominated by coaxial strain history and pure shear (Tillmann & Byrne 1995) with 130 to 450 per cent of vertical elongation (Fisher *et al.* 2002). By contrast, the BR shows top-to-the-west shear with an eastward-increasing magnitude of elongation from 40 to up to 460 per cent near the contact with the TS. The magnitude of ductile strain in the HR is low if compared with that predicted by thin-skinned critical wedge model (Clarck *et al.* 1993). This finding can be interpreted as the result of strain localization along out-of-sequence thrusts (Clark *et al.* 1993) or underplating (Simoes & Avouac 2007; Beyssac *et al.* 2007). The pre-Tertiary basement is also dominated by a single, penetrative fabric, S1, oriented NE and moderately dipping stretching lineation L1. In granitic gneiss (Chipan gneiss) L1 is defined by biotite, white mica and elongated quartz and by chlorite, actinolite, biotite and rarely white mica in metavolcanic phyllites. This penetrative fabric L1 is defined by greenschist minerals assemblage interpreted to be related to the Penglai orogeny (e.g. Lo & Onstott 1995). Taking into account the lack of evidence for prograde greenschist metamorphism, as mentioned in above section, we infer that the observed penetrative foliations that characterize the higher grade rocks in Taiwan are essentially post-peak metamorphism (i.e. retrograde). Kinematic analysis of the deformation associated with L1 is interpreted as related to lateral viscous extrusion of the TS between the slate belt and the CoR (Pulver *et al.* 2002).

2.4 Present-day kinematics

GPS velocity field derived from 1990–1995 geodetic surveys (Fig. 4) reveals that the current plate convergence is accommodated essentially across the LVF to the east and across the western frontal thrusts of the WF in agreement with the location of main active faults. In detail, shortening rates of 27–45 mm yr^{-1} are recorded across the LVF, over this period (Yu *et al.* 1997). Westward, the Central Range (BR and TS) shows a striking lack of shortening associated with a lack of seismicity (Fig. 4). The second kinematic boundary lies in the WF, where geodetic observations indicate interseismic shortening rates in the range of 4.6–27 mm yr^{-1}, across the frontal Chukou Fault (Fig. 4). On the other hand, northward, as a consequence of the Chichi earthquake, geodetic displacements in the hangingwall of the Chelungpu Thrust, still remain high with velocities of 30–45 mm yr^{-1} (Hu J.C. personal communication) but without significant modification of the first-order kinematic patterns.

2.5 Exhumation, erosion rates and heat flow

The number of available thermochronometric constraints yields quantitative estimates of the exhumation rates. For instance, on the basis of the locations of reset and unreset zones for apatite and zircon Willett *et al.* (2003) calculated erosion/exhumation rates in the range of 3–6 mm yr^{-1} in the eastern Central Range and 1.5–2.5 mm yr^{-1} in the western Central Range since ∼1 Myr. Based on assumptions for the geothermal gradient and comparison of AFT and ZFT ages, Lee *et al.* (2006) suggested a two-stage exhumation

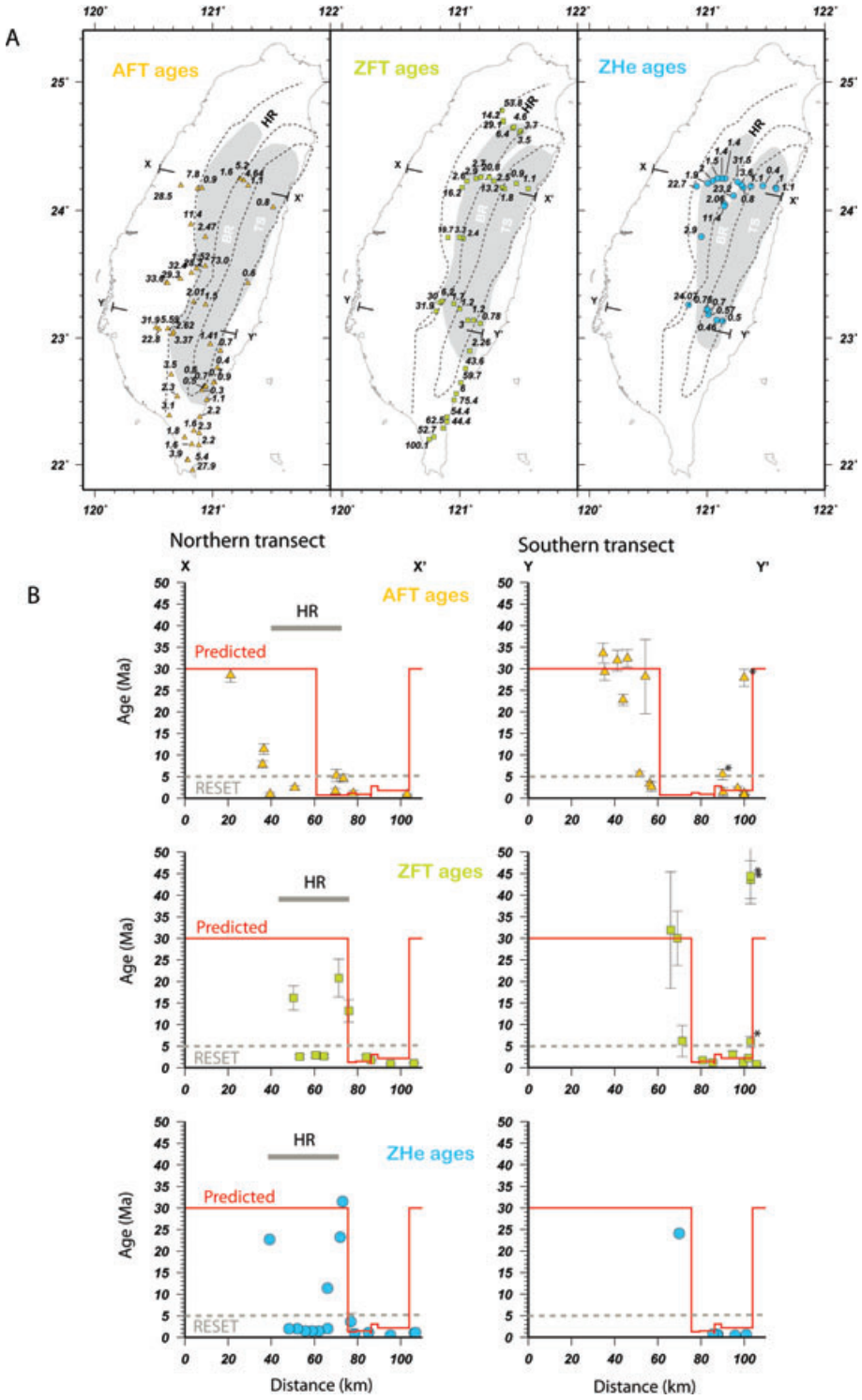

Figure 3. (a) Synthesis of thermochronometric constraints. FT ages are after compilation published in Fuller *et al.* (2006) and ZHe ages after Beyssac *et al.* (2007). Grey shading indicates inferred reset region for the studied low thermochronometer (same as Fuller *et al.* 2006 for AFT and ZFT ages). (b) Projection of observed AFT, ZFT and ZHe ages and model ages (red line) along northern and southern transects located in (a).

with low rates <1 mm yr^{-1} between 6–1 Ma followed by a rapid exhumation of 4–10 mm yr^{-1}.

Current erosion rates estimated using suspended sediments are about 3.9–5.2 mm yr^{-1} (Dadson *et al.* 2003) in agreement with former studies on stream load measurements (Li 1976), uplifted Holocene reefs and marine terraces (Peng *et al.* 1977). In addition to these constraints, fluxes of sediments supplied to the ocean have been estimated to be up to 500 Mt yr^{-1} (Dadson *et al.* 2003). They also showed that the mean annual suspended load of major rivers is strongly asymmetric across Taiwan as fluxes of erosion on the eastern slope of the orogen are 2 to 3.5 times higher than fluxes estimated from the western rivers.

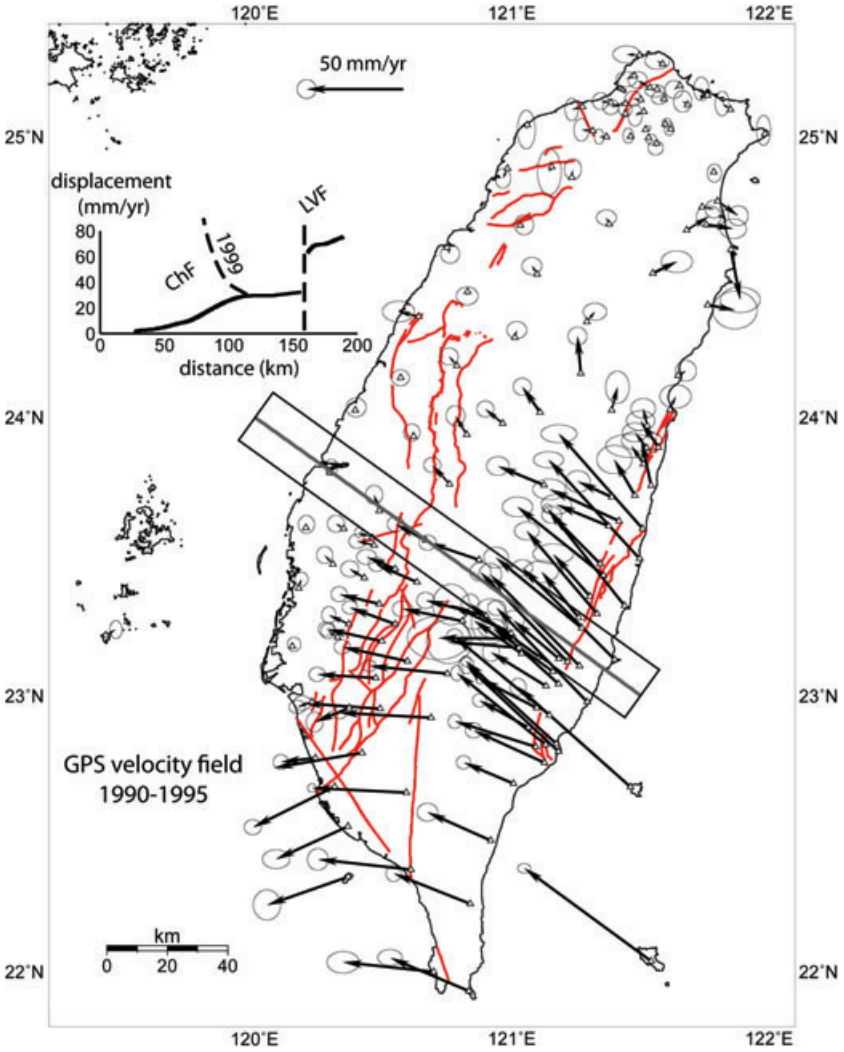

Figure 4. Present-day velocity field based on 1990–1995 geodetic surveys (after Yu *et al*. 1997). Red lines correspond to major known active faults. Horizontal geodetic velocities are plotted in cross-section (inset). The position of the main kinematic boundaries including the Longitudinal Valley Fault (LVF) and the Chelungpu–Sani Fault (ChF) are shown. Dashed lines show the departure from the 1990–1995 displacement field (solid line) that occurred in response to the activity of the ChF during the 1999 Chichi earthquake. Note that displacements are nearly constant through the Central Range, suggesting a lack of shortening in this region.

Heat flux values are characterized by maximum values of 150 mW m^{-2} in the Central Range, bounded by lower values of 50–70 mW m^{-2} in the western foreland and 70–100 mW m^{-2} to the east (Fig. 5). It is worth noting that the highest heat flux values mimic a dome-like feature centred in the Central Range. This suggests that rocks with high metamorphic grades are currently exhumed in the Central Range leading to upward deflection of the isotherms and hence local increase of heat flow.

3 A THERMODYNAMICALLY COUPLED THERMOMECHANICAL APPROACH

We have shown in the introduction that published numerical and analogue models of Taiwan had several limitations. Furthermore, the increasing number of geological and geophysical informations on the Taiwan orogen requires the use of more suitable lithospheric models that aim to account for the wide range of observations at a lithosphere scale. In this study we adopt the viscous-elastic–plastic thermomechanical numerical code PARA(O)VOZ (Poliakov *et al.* 1993) based on the FLAC (Fast Lagrangian Analysis of Continua) algorithm (Cundall 1989).

Compared to the previous versions, the code used for this study is thermodynamically coupled using THERIAK algorithm (De Capitani 1994) that evaluates equilibrium mineralogical phases and their densities as function of *P–T* conditions computed by the thermomechanical kernel of PARA(O)VOZ. The new densities and physical properties are dynamically re-integrated back to the thermomechanical kernel.

This thermomechanical kernel solves simultaneously the Newtonian equations of motion

$$\frac{\rho \partial v_i}{\partial t} - \frac{\partial \sigma_{ij}}{\partial x_j} - \rho g_i = 0, \tag{1}$$

$$\frac{D\sigma}{Dt} = F(\sigma, u, \nabla u, \ldots T \ldots), \tag{2}$$

and the heat transfer equation

$$k.\mathrm{div}(\nabla T) - \rho C_p \frac{\partial T}{\partial t} + H_r = \mathrm{v}\nabla \mathrm{T}, \tag{3}$$

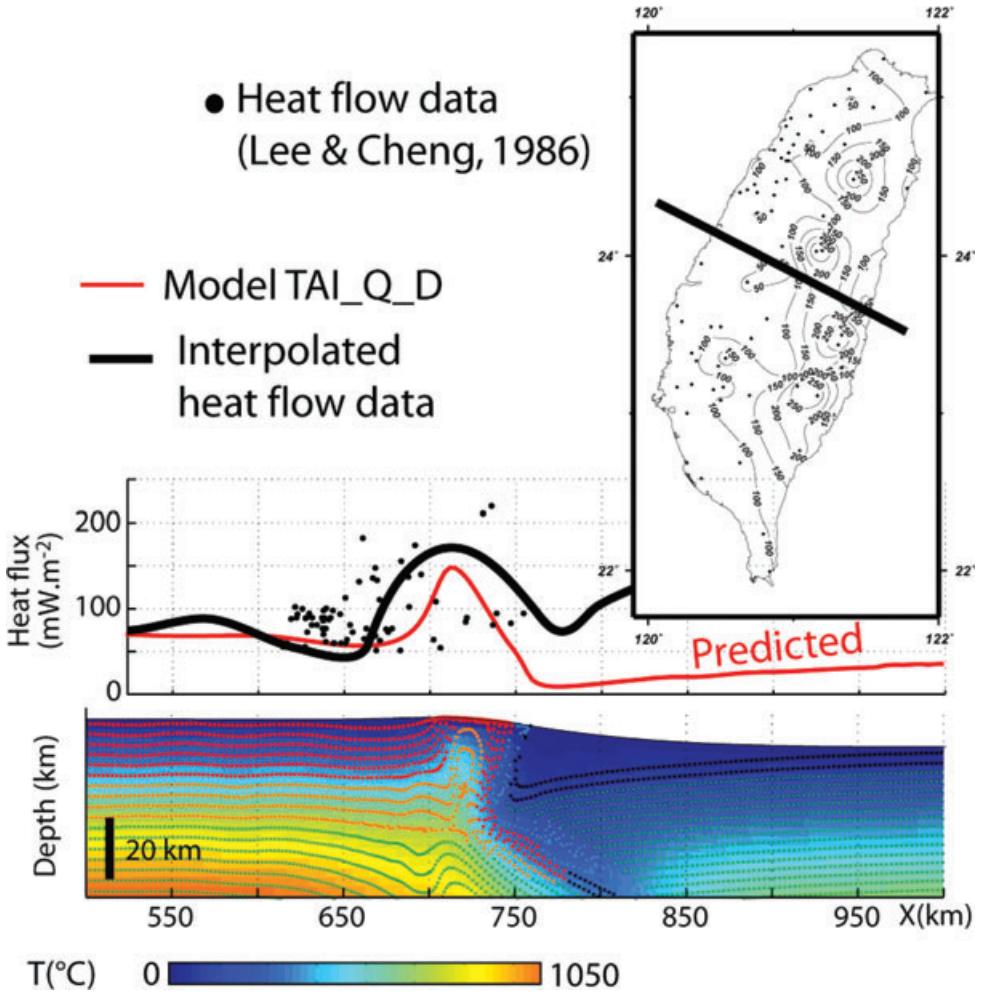

Figure 5. Comparison between observed (interpolated) heat flow data (Lee & Cheng 1986) and heat flow predicted in our preferred model Tai_Q_D (after 5 Myr of the numerical experiment). Spatial distribution of interpolated heat flow data (black thick solid line) is shown on map in the upper right inset. They are projected along NW–SE directed profile for comparison. Heat flow values larger than 300 mW m^{-2} and lower than 50 mW m^{-2} were excluded from this analysis because of the possible interference of geothermal circulation and groundwater movement (Lee & Cheng 1986).

in a large-strain Lagrangian formulation using Jauman's corrections for rotation of principal stress axis.

In eqs. 1–3 **u** is the displacement vector, **v** is velocity, ρ is density, t is time, g is the acceleration due to gravity, D is material objective derivative, σ is Lagrangian stress, T is temperature, C_p is the specific heat, k is the thermal conductivity and H_r is the internal heat production per unit volume. F denotes functional relationship for viscous-elastic–plastic constitutive law. We use Mohr–Coulomb criterion for plasticity and a non-linear power law for viscous flow.

The upper surface in all models is kept free and is additionally affected by erosion–sedimentation processes modelled with a diffusion law

$$\frac{\partial h}{\partial t} - \nabla(k_{\text{ero}} \nabla h) = 0, \tag{4}$$

where h, t and k_{ero} correspond to topography, time and coefficient of erosion, respectively.

The time-step for solving all these equations is of the order of 10 yr (Such a high resolution in time allows to handle all possible instabilities and non-linearities associated with complex rheologies and phase changes). Because it allows for large deformation it is particularly suitable for modelling long-term geological deformation at the lithospheric scale.

For our study, the thermomechanical code is thermodynamically coupled with the THERIAK algorithm (De Capitani 1994) back to the thermomechanical kernel to reproduce the changes in rocks density and thermal expansion/contraction, associated in particular with the eclogitization. THERIAK relies on the free energy minimization. To save computation time, the density field is pre-computed at the beginning of the computations for several typical bulk chemical compositions (see Yamato *et al.* 2007 for further details). Passive markers are incorporated within each grid cell of the model to track *P–T–z*-shortening histories of rocks and to improve the remeshing procedure (Yamato *et al.* 2007). Such markers enable us, for example, to track the thermal evolution of a given rock particle during deformation and hence allows for prediction of thermochronometric ages. In the same way, *P–T–t* paths can be computed. Owing to the particle-in-cell technique, local horizontal shortening rates and exhumation rates are traced during the computations. This allows us to study the long- and the short-term deformation distribution across the Taiwan orogen and to compare it with the geological data. The overall advantages of the numerical approach used is that it allows us to test a large number of parameters controlling the Taiwan orogen including erosion rates, crustal rheologies or convergence rates can be tested.

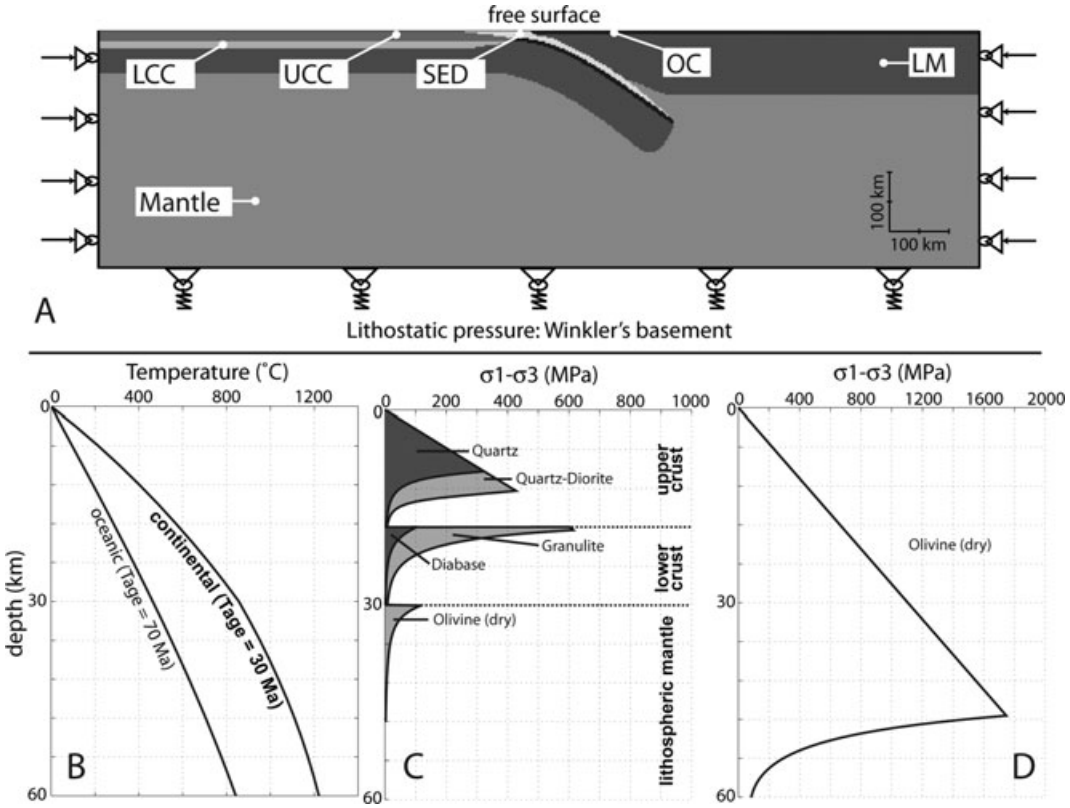

Figure 6. Model setup for all studied numerical experiments. (a) Initial plate geometry and boundary conditions applied on the model box. Abbreviations: LCC, lower continental crust; UCC, upper continental crust; SED, sediments; OC, oceanic crust; LM, lithospheric mantle. (b) Thermal profiles for the oceanic lithosphere of the PSP (thermal age is 70 Ma) and the continental lithosphere of the Chinese margin (thermal age is 30 Ma). (c) Yield strength envelopes computed for the thermal profiles in (b) for different composition of the continental crust used in the present study. (d) Yield strength envelope for the oceanic lithosphere.

Inside the model, all motions of material are free (i.e. there is no pre-imposed 'S' points or any internal forcing on solution). The free upper surface of the model is submitted to erosion/sedimentation tuned to the averaged values specific to the area. At the bottom of the model we apply Winkler's pliable basement condition, which corresponds to hydrostatic equilibrium with the underlying deep low-viscosity mantle assuming a small density contrast (10 kg m^{-3}).

We do not provide a more detailed description of PARA(O)VOZ algorithm because this is was already done in a number of recent publications (Burov *et al.* 2001; Le Pourhiet *et al.* 2004; Toussaint *et al.* 2004a,b; Yamato *et al.* 2007).

3.1 Boundary conditions

The boundary conditions refer to the common collision model setups used in previous studies (Burov *et al.* 2001; Toussaint *et al.* 2004a,b; Burov & Yamato 2007; Burov & Toussaint 2007; Yamato *et al.* 2007, 2008). The only boundary condition that is fixed in all numerical experiments is the plate velocity applied at both lateral sides of the model box. The velocities are dependent on the rate of convergence averaged since the beginning of the model, that is, since the beginning of the collision. In this respect, the convergence of the PSP relative to Eurasia is assumed to be 50 km Myr^{-1} to match the magnetic lineations in the Huatung Basin and below the Manila accretionary prism 15 Ma (chron 5b; Sibuet *et al.* 2002). The total convergence rate is divided into half velocities of 25 km Myr^{-1} applied on both sides of the model. The application of the total convergence rate on the left or the right border does not modify the model results.

3.2 Initial plate configuration

The initial plate configuration (Fig. 6a) refers to the time at which the Eurasian continental margin is supposed to initiate its subduction beneath the PSP in the Late Miocene. At this stage, the thinned continental lithosphere is attached to the oceanic lithosphere of the South China Sea and the initial dip angle of the oceanic slab is fixed at 30° in agreement with the average dips of current oceanic subduction slabs worldwide (see compilation by Cruciani *et al.* (2005)). It is worth noting that the continental margin has not yet been subducted and the continental slab is then assumed to be horizontal. This is a major difference with kinematic models in which an initial dip angle for the continental crust is fixed thus forcing the subduction of the continent.

Several lines of evidence, including the age of volcanism in the CoR and plate reconstruction, suggest that the E-directed subduction did not start before 15 Ma (Sibuet *et al.* 2002) of the collision considered to be between 9 and 6 Ma (Lin *et al.* 2003; Tensi *et al.* 2006). We thus infer that the oceanic subduction lasted 6 Ma before collision occurred (Sibuet & Hsu 2004). Given a fixed convergence rate of 50 km Myr^{-1} and uncertainties on the initiation of both the oceanic subduction and continental collision we have estimated the length of the oceanic slab to be 300 km.

In all numerical experiments presented in this study, the initial size of the 'model box' is 1482 km in length and 399 km in depth

with a spatial resolution (meshing) of 3 × 3 km. In each mesh of the model, 4 markers were added at the nodes of each element, 1 at the barycentre of the element and 4 at the barycentre of the four subtriangles constituting the element. The mineralogical compositions used for the calculation of the density of each material in the model correspond to commonly referred compositions, that is, composition of granite, MORB basalt, pelite and mantle for continental crust, oceanic crust, sediments and mantle, respectively (see Yamato *et al.* 2007 and references therein for further details).

The thickness of the continental crust is set to 30 km in agreement with geophysical data in the foreland (Rau & Wu 1995; Ma & Song 1997; Yen *et al.* 1998). The continental crust is believed to be rheologically layered; hence we have subdivided the crust into an upper (mainly brittle) continental crust and a lower (mainly viscous) crust (Fig. 6c) both *P*–*T*-dependent following the rheological parameters presented in Table 2. Based on the depth-distribution of seismicity and former rheological modelling of the Chinese margin (Mouthereau & Petit 2003) we set the thickness of the upper seismogenic crust having pressure-dependent rheology to 18 km. The remainder, that is, 12-km-thick layer corresponds to the viscous and nearly aseismic lower crust (Table 1). The thermomechanical characteristics of these two parts depend on the mineralogy considered for these two layers as detailed below and in Table 2.

3.3 Initial geotherm

The initial geotherm (Fig. 6b) is computed from plate-cooling models for oceanic (Parsons & Sclater 1977; Turcotte & Schubert 2002) and continental lithosphere (Burov & Diament 1995; Parsons & Sclater 1977) and consistent with the thermal (cooling) ages of both the oceanic and the continental lithospheres. The procedure used for computation of initial thermal structure is described in further details in Yamato *et al.* (2008). The thermal parameters are presented in Table 2. Thermal ages are defined by the last thermal event at which the plate cooling initiated. The thermal age of the PSP is constrained by geophysical studies and boreholes of the oceanic basement below the Huatung Basin (Deschamps *et al.* 2000). Magnetic anomalies suggest that spreading started at least ∼51 Ma (chron 23) in the northern Huatung Basin (Fig. 1). However, in the southern Huatung Basin dating of the oceanic floor using boreholes revealed older ages closer to 105–125 Ma (Fig. 2). Eastward, the East PSP show younger ages ∼42 to 48 Ma (chron 21). We hence adopt an average age of 70 Ma. For the continental part, the thermal structure (multilayer cooling half-space) is defined by setting its thermal age to 30 Ma (Fig. 6b) in agreement with the initiation of spreading in the South China Sea (Taylor & Hayes 1980; Lee & Lawver 1995). Figs 6(b)–(d) clearly show that the lithospheric mantle of the PSP is colder and stronger than the Eurasian margin. The first-order rheological contrast between both plates is a key parameter that constrains the development of the Taiwan mountain belt and the final geometry of the collision.

3.4 Rheological parameters

Viscous creep parameters of all model materials are presented in Table 2. PARA(O)VOZ code uses viscous-elastic–plastic rheologies, for description of each of which a total of seven material parameters are needed: three parameters for the viscous behaviour (n, A and E), two parameters for the elastic behaviour (the Lamé's coefficients λ and μ) and two parameters for the plastic law (cohesion Co and frictional angle ϕ). The values of elastic parameters (Table 1) were chosen assuming a lithosphere with a Poisson's ratio constant equal to 0.25 (which is equivalent to $\lambda = \mu$). For plastic behaviour, a frictional angle of 30° is considered for all crustal rocks according to Byerlee's law (Byerlee 1978). Cohesion values only differ for surface rocks. Although the elastic and plastic parameters of rocks are fairly well known, creep parameters used in the viscous law are less well constrained (e.g. Watts & Burov 2003). In our study, we have tested several material creep parameters in the crust that are presented in Table 2.

Table 1. Thermomechanical coefficients and boundary conditions used in our models.

Physical parameters	
All rocks	$\rho = f(P,T)$ calculated using Theriak (kg m^{-3})
	Friction angle = 30°
Upper continental crust (UCC)	Material: Quartz∗
	Thermal conductivity: 2.5 W m^{-1} °C^{-1}
	Thermal diffusivity: 8.3 × 10^{-7} m^2 s^{-1}
	Lamé constants: $\lambda = \mu = 3 \times 10^{10}$ Pa
	Cohesion: 20 x 10^6 Pa
Lower continental crust (LCC)	Material: Diabase∗
	Thermal conductivity: 2.5 W m^{-1} °C^{-1}
	Thermal diffusivity: 6.7 × 10^{-7} m^2 s^{-1}
	Lamé constants: $\lambda = \mu = 3 \times 10^{10}$ Pa
	Cohesion: 20 × 10^6 Pa
Sediments (SED)	Material: Quartz∗
	Thermal conductivity: 2 W m^{-1} °C^{-1}
	Thermal diffusivity: 8.3 × 10^{-7} m^2 s^{-1}
	Lamé constants: $\lambda = \mu = 1 \times 10^{10}$ Pa
	Cohesion: 1 × 10^6 Pa
Oceanic crust (OC)	Material: Olivine∗
	Thermal conductivity: 3.5 W m^{-1} °C^{-1}
	Thermal diffusivity: 8.75 × 10^{-7} m^2 s^{-1}
	Lamé constants: $\lambda = \mu = 3 \times 10^{10}$ Pa
	Cohesion: 20 × 10^6 Pa
Mantle	Material: Olivine∗
	Thermal conductivity: 3.5 W m^{-1} °C^{-1}
	Thermal diffusivity: 8.75 × 10^{-7} m^2 s^{-1}
	Lamé constants: $\lambda = \mu = 4 \times 10^{10}$ Pa
	Cohesion: 300 × 10^6 Pa
Thermal parameters	
*T*s; *T*hl	0 °C; 1330 °C
hl∗	120 km
Cont. *T*age∗	30 Ma
Oc. *T*age∗	70 Ma
hr, *H*c	10 km, 1.10^{-9} W kg^{-1}
Other parameters	
Huc	18 km
Hlc	12 km
keros∗	5000 m^2 yr^{-1}
Conv. rates∗	50 mm yr^{-1}

Note: Parameters presented with '∗' constitute those used in the reference numerical experiment (Tai_Q_D). They have been submitted to a parametric study presented in Table 3. For physical parameters section, abbreviations are similar to those presented in Fig. 3. *T*s and *T*hl correspond to the temperature at the surface and at the bottom of the continental lithosphere (hl), respectively. Thermal ages (*T*age) used to calculate the temperature profile for the continental lithosphere (Cont.) and the oceanic lithosphere (Oc.) are also reported. Concerning radiogenic heating, hr, corresponds to the decay depth where radiogenic heating is activated (only in the continental crust material) and *H*c is the value of the radiogenic production. *H*uc the thickness of the upper continental crust and *H*lc the thickness of the lower continental lithosphere are from (Mouthereau & Petit 2003); *k*eros is the coefficient of erosion; *Conv. rates*, Total convergence rate applied on our model.

Table 2. Creep parameters used in this study.

	n	A ($MPa^{-n}\ s^{-1}$)	E ($J\ mol^{-1}$)
Quartz∗	3	6.8×10^{-6}	1.56×10^5
Diabase∗	3.05	6.3×10^{-2}	2.76×10^5
Quartz-Diorite	2.4	3.01×10^{-2}	2.12×10^5
Mafic granulite	4.2	1.39×10^4	4.45×10^5
Olivine (dry) ∗	3	7×10^4	5.10×10^5

Note: Parameters presented with '∗' constitute those used in the reference numerical experiment (Tai_Q_D). Creep parameters data sources are from Ranalli & Murphy (1987) for quartz, Carter & Tsenn (1987) for diabase, Goetze (1978), Hansen & Carter (1982) and Wilks & Carter (1990) for quartz-diorite, mafic granulite and dry-olivine, respectively.

The Palaeogene sedimentary cover deposited onto the Chinese margin is included as part of the upper crust with the same rheological parameters. So the model inhibits the development of shallow low-dipping zone of weakness in the Chinese margin and thus decoupling in the shallow crust. This approach is validated *a posteriori* since deformation pattern are controlled, to first order, by the contrast of rheology between the upper and the lower crust.

4 MODEL RESULTS

From the examination of performed calculation runs we conclude that only the model Tai_Q_D is in good agreement with natural observations (Fig. 7). To demonstrate why this model is preferred we first present a full comparison between its predictions and natural observations. Then, the results of parameters variations are presented to identify the critical parameters of the reference model (see Table 3 and Section 6).

In this reference numerical experiment, quartz and diabase composition has been adopted for the upper and the lower crust, respectively. The average erosion coefficient, used in the diffusion equation (4) that simulates erosion, is 5000 $m^2\ yr^{-1}$. The age of the collision corresponding to the duration of the model is estimated to be 5 Myr, which is roughly in agreement with ages currently considered for Taiwan collision on the basis of stratigraphic studies and modelling of the basin subsidence in the western foreland basin (Teng 1990; Lin *et al.* 2003; Tensi *et al.* 2006).

4.1 Main tectonic features

4.1.1 Taiwan accretionary wedge

In this section, we summarize the main characteristic features of the collision model at the end of the numerical experiment. The contraction of the Chinese crust has led to the development of a typical collision wedge. The accretion of the Asian crust is accommodated by the decoupling in the lower crust and the westward nearly rigid displacement of the oceanic lithosphere. Strain rates clearly highlight the localization of the main decollements and other major shear zones within the collision belt (inset of Fig. 8a). The main PSP/EUR decoupling follows the moderately east-dipping subduction panel, then it flattens westward at the base of the orogenic wedge at a depth of ∼25 km and finally ramps up to the surface along a 40°-dipping frontal thrust. In the footwall of this frontal ramp, that is, below the western foreland, strain rates reveal that compressive deformation still remains significant especially in the lower crust and across rheological boundaries in the mid-crust and at the Moho.

Deformation within the orogenic wedge is remarkably dominated by the large-scale folding of the Asian crust controlled by the viscous thickening in the lower crust (Figs 7 and 8). This mechanism could be mistaken for underplating as proposed in recent models of Taiwan (Barr & Dahlen 1989; Simoes & Avouac 2006; Beyssac *et al.* 2007; Simoes *et al.* 2007). However, instead of being related to duplexing where the décollement is stepping down, the predicted upward advection of Asian material is rather the consequence of frontal accretion and viscous thickening of the incoming Asian lower crust. Such a frontal accretion of nearly the whole crust is well depicted by the model velocity field (Fig. 9). In addition, the exhumation at the rear of the wedge is permitted by the erosion and backthrusting. As a consequence, HT isotherms are deflected upward uplifting rocks that experienced greenschist and amphibole metamorphism.

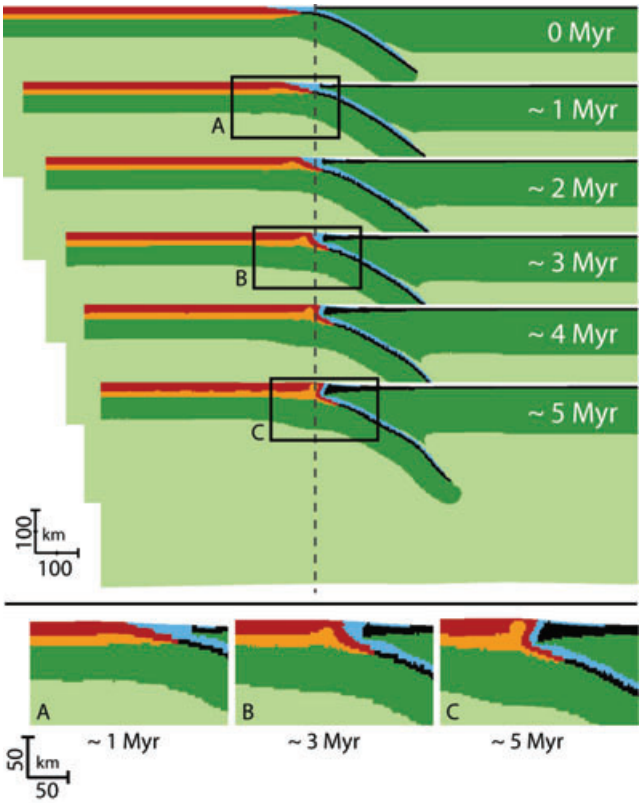

Figure 7. General evolution of the plate configuration during 5 Myr for the reference model (Tai_Q_D). The stage at 5 Myr (inset c) is believed to correspond to the present-day configuration. Note that as the Eurasian plate indents the PSP, the initial plate suture is moving toward the upper plate. Since no new passive markers are introduced, meshes of newly deposited sediments are stretched leading to increase artificially the thickness of the crust of the PSP. Black meshes should be viewed as a mix of sediments and oceanic crust rather than oceanic crust only.

4.1.2 The Philippines Sea Plate

The deflection of the PSP is clearly depicted on the eastern side of the model (Figs 7 and 8b). It is outlined by the development of a retro-foreland basin filled by synorogenic deposits eroded from the eastern side of the orogen. Such a deflection is likely caused by both the topographic loading arising from the mountain building and the intrinsic negative buoyancy of the PSP. The plate boundary, which is assumed to be represented by the Longitudinal Valley Fault, lies along the former Miocene oceanic accretionary wedge in a transitional area squeezed between the deformed PSP and the rapidly

Table 3. Parametric study.

Name of the numerical experiment	conv. rate (mm yr^{-1})	k_{eros} (m^2 yr^{-1})	Continental material Upper crust	Lower crust	Cooling/ exhumation.	PT	HF	Erosion/ Sediment.
Reference experiment								
Tai_Q_D (reference)	50	5000	Q	D	+	+	+	+
Influence of the erosion								
Tai_eros-	50	2500	Q	D	-	-	-	-
Influence of the convergence rate								
Tai_V+	100	5000	Q	D	-	-	-	-
Tai_V–	25	5000	Q	D				
Influence of the rheology								
Tai_QD_MG	50	5000	QD	MG	-	-	-	-
Tai_QD_D	50	5000	QD	D	-	-	-	-
Tai_Q_MG	50	5000	Q	MG	-	-	-	-

Numerical experiments for which the sensitivity to model parameters has been tested. Abbreviations: conv. rate, total convergence rate; k_{eros}, erosion coefficient used in the diffusion law; Q, quartz; D, diabase; QD, quartz-diorite; MG, mafic granulite. Modified parameters are shown with bold characters. ± signs refers to successful/unsuccessful reproduction of observations such as cooling/exhumation, *P–T* conditions (*PT*), Heat Flux (HF) and Erosion/sedimentation.

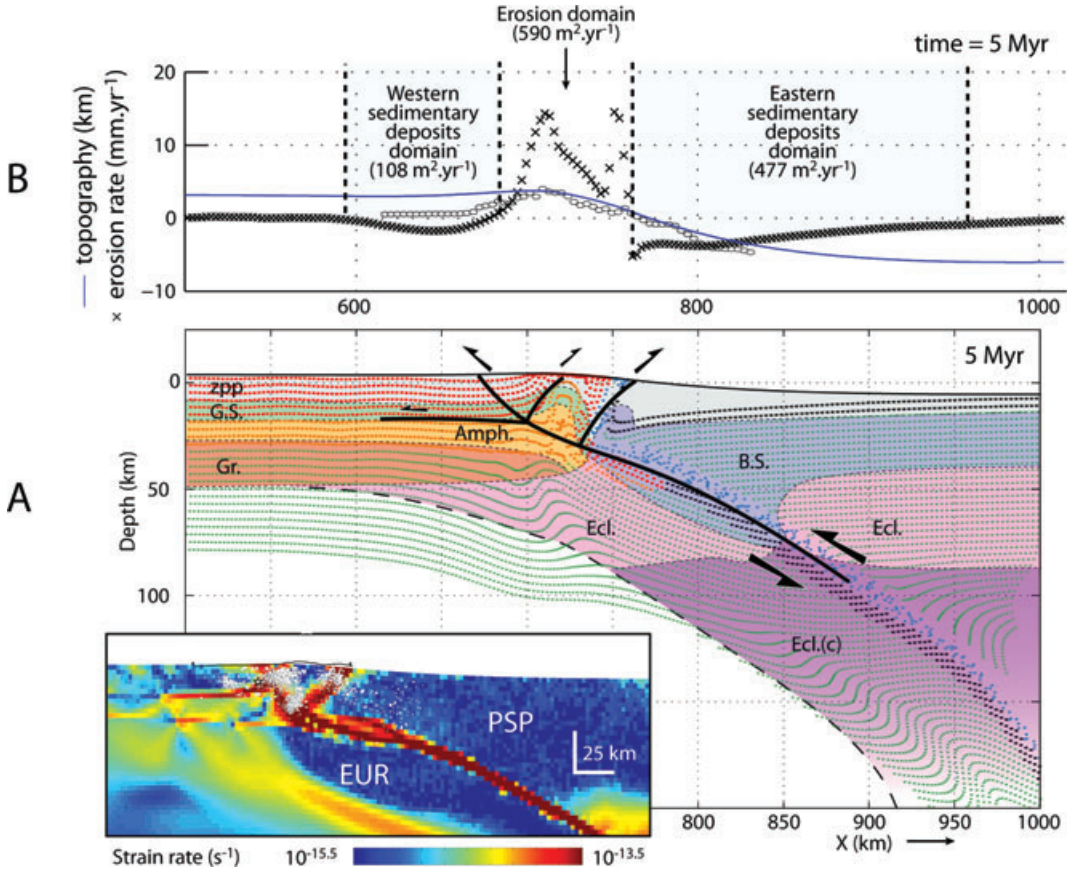

Figure 8. Detailed view of the reference model (Tai_Q_D) at the end of the model run, which corresponds to inset (c) of Fig. 7. Metamorphic facies zones presented in (a) are calculated from the *P–T* conditions at final stage at 5 Myr. For instance, no eclogitization is recorded in the lower crust of the Chinese margin beneath the Taiwan mountain belt. Location and motions along major fault zones are deduced from strain rates in the lower left-hand inset. Note that the strain rates distribution indicates that the lower crust can potentially release strain at fast rates and thus is able to produce earthquakes. Abbreviation: Amph., amphibolite facies; B.S., blueschist facies; Ecl., eclogite facies; Ecl.(c), eclogite with coesite; Gr., granulite facies; G.S., greenschist facies; zpp, zeolithe-prehnyte-pumpellyite facies. (b) Predicted (blue line) and observed topography (white dots). Erosion rates (and eroded/deposited areas) as well as erosion/sedimentation fluxes are calculated over the last computed increment of deformation and is equivalent to the current erosion rates.

uplifted collision wedge. At the end of the numerical experiment, this fault boundary, initially East-dipping, has rotated from its original position to become an east-vergent 80°-dipping reverse fault at the front of the indenting PSP.

4.2 Erosion–sedimentation distribution

Erosion rates (positive) and sedimentation rates (negative) calculated for the last increment of convergence show two adjacent

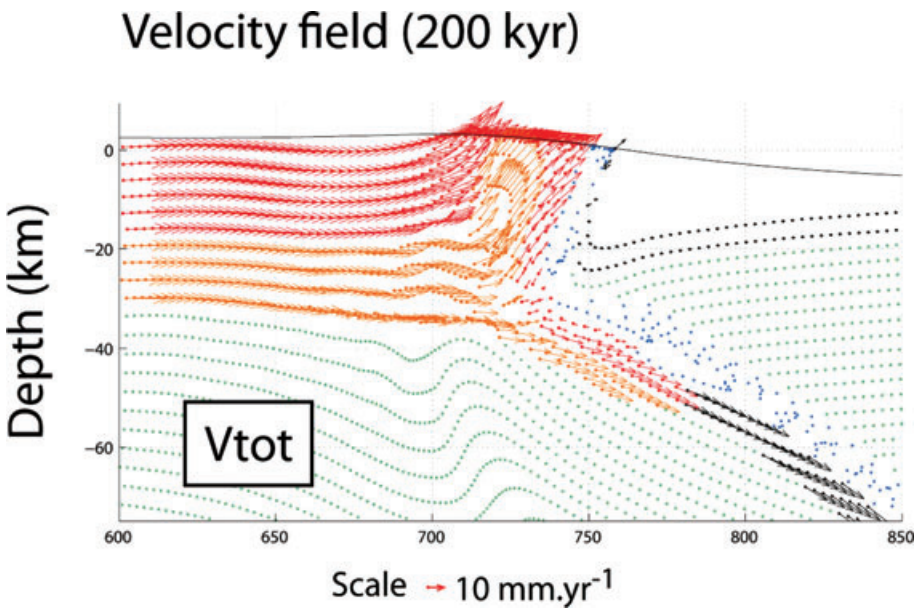

Figure 9. 2-D velocity field in the Chinese margin crust calculated over the past 200 kyr with respect to a fixed point in the PSP. Accretion of both the upper crust (red) and the lower crust (orange) is clearly depicted. Subduction of the Chinese margin can only be seen at depths deeper than 25 km beneath the suture zone (blue particles of the former accretionary prism), which is the depth of the basal shear zone observed in Fig. 5. Exhumation identified in the western frontal part of the belt results from the differential displacement between the upper and lower crustal rocks allowed by intracrustal decoupling. Exhumation at the rear results from the extrusion of the margin produced by the upward advection of lower crustal flow and shearing across the LVF.

flexural basins (Fig. 8b). Their widths are proportional to elastic thickness of plates on which they develop. Therefore the Western Foreland Basin is narrower ($\sim$ 100 km) with regard to the eastern (retro-)foreland basin ($\sim$ 180 km) since it developed on a weaker and younger plate. The sedimentation rates in the Western Foreland are about 2 mm yr^{-1} whereas in the eastern (retro-) foreland basin, sedimentation rates reach values of 3–4 mm yr^{-1} in accordance with maximum pleistocene depositional rates recorded in the West foreland basin (Lin *et al.* 2003; Tensi *et al*. 2006) and to some extent with the thick continent-derived flyschs observed in the CoR (Lundberg & Dorsey 1990; Huang *et al.* 1995). In details, except for local high values of 10 to 15 mm yr^{-1} in the vicinity of the highest mountain slopes, the erosion rates remain in the range of 3–10 mm yr^{-1}, which is in good agreement with the current erosion rates estimated based on sediment load or indirectly estimated using erosion law of FT data (Dadson *et al*. 2003, Willett *et al.* 2003). In our 2-D model, the total eroded material flux over the mountain range is estimated to be 590 m^2 yr^{-1}. 80 per cent are transported in the eastern retro-foreland basin (477 m^2 yr^{-1}) and the remainder is supplied to the Western foreland basin (108 m^2 yr^{-1}). These fluxes should be viewed as a first approximation as they do not take into consideration the 3-D plate configuration. Indeed, the development of longitudinal drainage, for example, in the western foredeep, likely removed sediments out of the plane of the section.

4.3 Heat flux

The distribution of the heat flux at the end of the modelling run is a very important constraint for evaluating our thermomechanical model in comparison to the documented thermal history and thermochronometers ages. We calculate heat flow q according to Fourier's law

$$q = -k.\frac{\mathrm{d}T}{\mathrm{d}z}, \tag{5}$$

using a thermal conductivity $k = 2.5$ W m^{-1} K^{-1} (Table 1) and determining the vertical temperature gradient dT/dz for the upper 6 km of the model.

Results are presented in Fig. 5. The spatial variations in the heat flux (Lee & Cheng 1986) are in good agreement (Fig. 5) regarding wavelengths and amplitudes. Heat flux values of 50 to 60 mW m^{-2} observed in the foreland are in good agreement with predicted heat flux of $\sim$62 mW m^{-2}. The decrease to the East of the heat flux due to the bending of the Chinese margin is also reproduced. This is followed by a sharp increase of heat flux in the central part of the orogen up to peak values of 150 mW m^{-2}, which are closer to the measurements in the eastern Central Range. One of the main characteristics of the observed heat flux is outlined by the decreasing heat flux toward the Longitudinal Valley. Our model consistently predicts lower values. However, although we predict values close to 20 mW m^{-2} on the floor of the cold PSP, observed heat fluxes are larger than 50 mW m^{-2} (Fig. 5). The apparent inconsistency between model heat flux and observation is related to the absence of the CoR in our models. Moreover, differences throughout the model may also arise from the fact that, in our models, frictional heat production was set to zero in contrast to previously presented models (e.g. Burg & Gerya 2005; Faccenda *et al.* 2008; Gerya *et al.* 2008).

5 COMPARISON OF PREDICTED AND OBSERVED DEFORMATION AND EXHUMATION PATTERNS

To better evaluate our model we have compared the long-term predicted thermochronometric ages and deformation distribution in our model with observations (see Introduction). To this aim, we have tracked eleven coloured markers having originally a regular spacing (Fig. 10). All these markers are initially located in the upper crust at the beginning of the numerical experiment. We chose

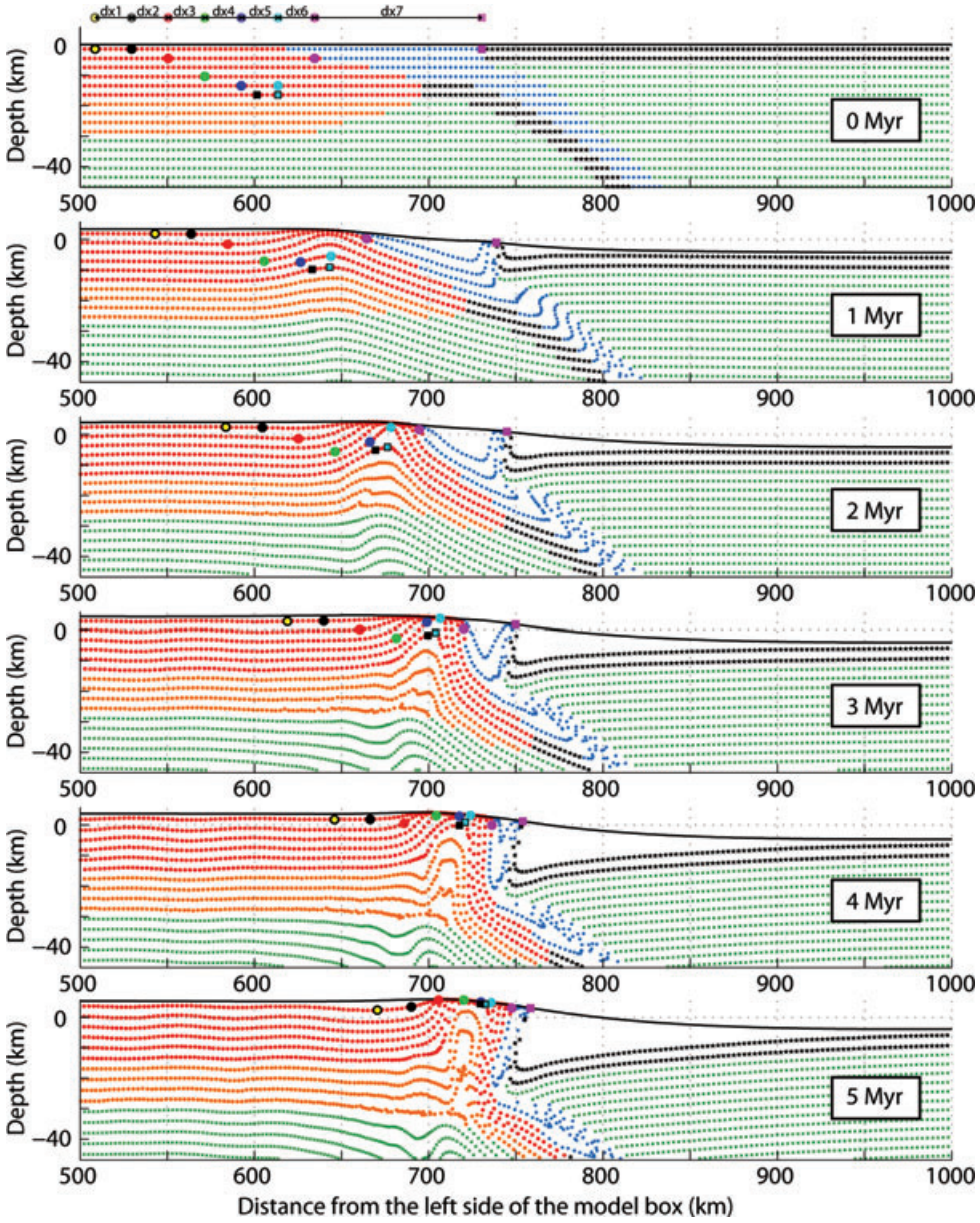

Figure 10. Close-up view of our preferred model (Tai_Q_D) in the collision area. The figure shows the evolution of the eleven markers shown as dots or squares with distinct colours. They are all located in the upper crust of the Eurasian margin and are thus consistent with a maximum exhumation of 16 km. At each time-step, we record the depth, the vertical and horizontal position, the pressure and the temperature for these markers during 5 Myr. In red, upper continental crust; orange, the lower continental crust is in orange; blue, sediments of the accretionary prism; black, oceanic crust and green, lithospheric mantle.

markers that are located close to the surface to facilitate the comparison with the present-day configuration in the Taiwan mountain belt.

5.1 Distribution of long-term and short-term shortening

We estimate that the total shortening associated with collision between Eurasia plate (yellow dot) and the PSP (magenta square) amounts to 133 km (Fig. 10). About 30 km of shortening must be added because of the deformation within the PSP (between magenta square and magenta dot). This shortening is taken up within the accretionary wedge and the weakest part of the PSP, for example, the Luzon Arc not modelled in our numerical experiment. Among these 133 km, less than half, that is, 48 km, are taken up within the Chinese continental margin. For instance, across the frontal thrusts (i.e. between yellow and red dots) our modelling predicts long-term shortening of ∼7 km amounting to 13 km if we consider deformation to the east (i.e. including the green particle). This represents 14.5 to 27 per cent of long-term deformation accommodated across the frontal part of the Taiwan mountain belt, which is fairly consistent with available constraints from cross-section balancing in the Western Foothills ranging between 10 and 30 per cent (Mouthereau *et al.* 2001; Mouthereau & Lacombe 2006). However, this result disagrees with thin-skinned interpretation of wedge deformation. We further estimate that 85 km of the total shortening, that is, 64 per cent were accommodated within the ancient oceanic wedge that currently forms the suture zone (LVF). Part of this ancient oceanic accretionary prism is now exposed in the Lichi mélange (southern CoR) and within the ophiolitic blocks exposed in the Yuli Belt including the HP-rocks exposed in the Juisui area.

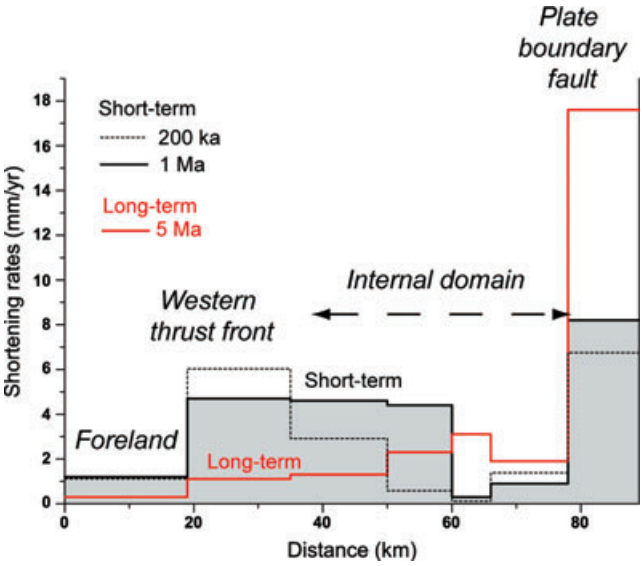

Figure 11. Long- (5 Myr) and short-term (1 Myr and 200 kyr) distribution of shortening in the reference model Tai_Q_D, calculated by considering the horizontal position of the studied particles (see Fig. 10). For instance, shortening in the foreland is assumed to represent the shortening calculated between yellow and black dots of Fig. 7. The accumulation of shortening currently recorded at the thrust front by active and seismogenic thrusting probably occurred in the past 1 Myr. This appears to be associated with a clear deficit of shortening in more internal domains. This trend seems to be more evident with the reduction of the time window considered. Note that the width W of the collision belt defined by the distance between the yellow dot and the magenta square is 89 km, which is equivalent to the present-day width of the Taiwan Island.

Fig. 11 reports both the long- and short-term shortening rates calculated in the model. The maximum long-term shortening rates of 17 km Myr^{-1} predicted by the model are located across the LVF, that is, across the suture zone. Westward, within the collision wedge, the cumulated long-term deformation reveals crustal shortening rates increasing from the front (∼1 km Myr^{-1}) to the rear of the Taiwan orogenic wedge (∼3–4 km Myr^{-1}, Fig. 11). Our model predicts a remarkable lack of shortening in a narrow domain of the most internal part of the collision belt. This narrow zone has also recorded little burial as seen in Fig. 10.

Although the rates of shortening across the wedge are of the order of rates estimated across the southern WF by cross-section balancing (Mouthereau *et al.* 2001) they appear significantly lower than the rates of shortening of 39–45 mm yr^{-1} calculated over the past 2 Myr (Simoes & Avouac 2006). We suggest that such a discrepancy might be caused by kinematic changes leading to the increase of shortening over the past 2 Myr. This possibility will be examined in the following section.

In an attempt to calibrate our preferred model with short-term geodetic deformation we have also calculated shortening rates over the last 1 Myr and 200 kyr (Fig. 11). Prior to comparison between predictions and observations it appears necessary to modify the short-term rates of deformation predicted by the modelling. Indeed, the geodesy (see Fig. 4) shows that the present-day plate convergence is 80 km Myr^{-1}, which is 1.6 times higher than the long-term convergence rate of 50 km Myr^{-1} used to reproduce most data. By assuming that increasing the rate of deformation by 1.6 over 1 Myr does not produce significant modifications of the bulk mechanics of the orogenic wedge, the incoming flux of material and the velocities in the wedge are likely to be increased by the same factor. Hence, we have multiplied the predicted shortening rates by a factor 1.6. The good agreement between results, presented in the following, and the observed rates validate this hypothesis.

For instance, prediction of shortening rates of 24 and 18 km Myr^{-1} over 1 Myr and 200 kyr across the whole orogen (i.e. between magenta square and yellow dot) give modified values of 38 and 30 km Myr^{-}1, respectively, for the periods considered. These values are comparable with the GPS-derived data indicating shortening rates between 27 and 45 mm yr^{-1} (Yu *et al.* 1997). Over the past 1 Myr, short-term distribution of shortening rates first highlights that deformation preferentially focuses on the most frontal thrusts at rates of 4–5 km Myr^{-1}. This trend is amplified over the past 200 kyr and the rate is 6 km Myr^{-1} (Fig. 11). This corresponds to rates of 6–10 km Myr^{-1} consistent with the lower bound of observed geodetic rates of 4.6 to 27 mm yr^{-1} across the frontal Chukou Fault or other estimates of 12 mm yr^{-1} across the HR (Yu *et al.* 1997) (Fig. 4). The abundant seismically released strain and the occurrence of the Chichi earthquake at the western front further supports this prediction. A consequence of increasing rates in the western front is the widening of the low deformation domain of the hinterland. The predicted rate of lower than 1 km Myr^{-1} is, however, in agreement with GPS studies (Fig. 4). As deformation increases to the West, shortening rates also diminish to 8.2 and even 6.7 km Myr^{-1} across the LVF in the same period. If we consider 4 km accommodated within the PSP, this gives 12.2 km Myr^{-1} in the past 1 Myr. Again by scaling this value with the current convergence rates the modified rates become 19.5 km Myr^{-1}. This value is close to the geodetic surveys for baseline between Lutao Island (Northern Luzon Arc) and the CoR (Fig. 4) as well as present-day estimates across the LVF (Yu *et al.* 1997). In summary, our model better fits the long-term and short-term deformation patterns only if we consider a recent increase of the plate convergence from 50 to 80 km Myr^{-1} in the past 1 Myr.

5.2 Long-term exhumation and metamorphic conditions

An age-distance plot of both predicted and observed AFT, ZFT and ZHe ages is shown in (Fig. 3b) to allow for comparison along the northern and southern transects. Predicted ages are generally in good agreement with observed thermochronometric constraints. Indeed, independent of the studied low thermochronometer the Western foreland is generally devoid of reset thermochronometers. And the eastern Central Range, where the highest metamorphic grades are exposed shows consistent reset ages compatible with the Penglai orogeny (Fig. 3b). A departure from this general decrease of ages toward the east is depicted, along the northern transect, where reset ages in the HR are not reproduced by our model. As a result, our model seems in better agreement with the exhumation pattern across the southern transect.

To allow for a more detailed comparison between predicted thermochronometer ages with thermochronometric constraints we plot the temperature against time recorded by each studied particle (Fig. 12a). The closure temperatures for ZFT, AFT and (U–Th)/He on zircons are assumed to be 220–235, 110 and 180 °C, respectively, in agreement with former studies (Liu *et al.* 2000; Beyssac *et al.* 2007). Fig. 12 shows that black and yellow particles, now exposed in the external part of the collision belt, were never buried below the closure temperature for fission-track annealing of apatite and zircon. As a result, the AFT and ZFT ages for these rocks are expected to be older or close to the depositional ages (unreset or detrital ages) in good consistency AFT and ZFT ages reported in

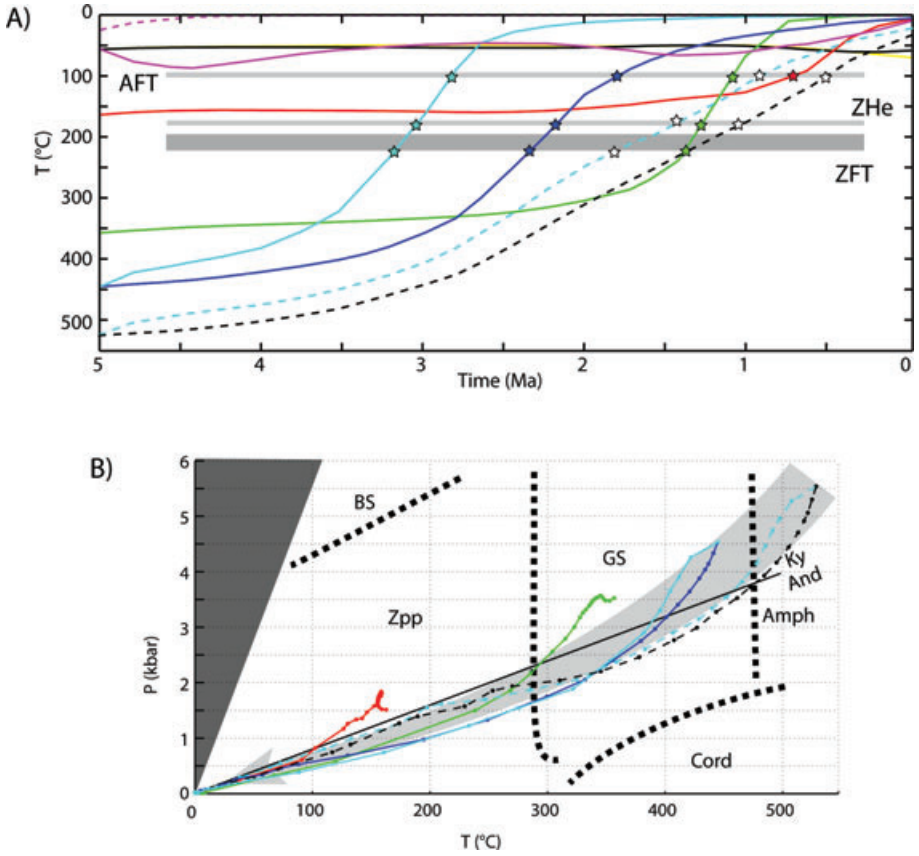

Figure 12. (a) Predicted *T*–*t* paths for particles shown in Fig. 10. Dashed lines correspond to light blue and black squares shown in Fig. 10. Stars show the expected cooling ages of particles with respect to a given thermochronometer. Particle position (not shown here) is recorded every 0.5 Myr. Abbreviations: AFT, closure temperature for Apatite fission tracks; ZFT, closure temperature for Zircon fission tracks; ZHe, closure temperature for (U–Th/He) ages on zircon. (b) *P*–*T* paths for particles studied in in (a). Colours as well as dashed or solid lines refer to captions in (a) (see text for explanation). Dots denote particles position recorded every 0.5 Myr. Such a retrograde evolution follows a classical barrovian HT–LP collisional gradient. Abbreviation: Amph, amphibolite facies; BS, blueschist facies; GS, green schist facies; Zpp, zeolithe-prehnyte-pumpellyite facies; Ky, Kyanite; And, Andalusite and Cord, Cordierite.

Western Taiwan (Fuller *et al.* 2006). The temperature–time trajectory of the red particle indicates unreset ZFT ages but a fully reset AFT age of ∼0.7 Ma. Eastward, the green particle denotes ZFT and AFT ages of 1.4 and 1.2 Ma, respectively consistent with zircon (U–Th/He) age of 1.3 Ma. Eastward, all AFT and ZFT ages appear younger than the Pliocene and thus agree with a cooling event coeval with the Penglai orogeny. Rocks exposed in this domain were all originated at depths greater than 13–14 km but their exhumation show different patterns. The youngest predicted AFT ages lower or close to 1 Ma and ZFT or ZHe ages of 1–2 Ma are associated with the exhumation of the light blue and black squares originated in the deep crust below 16 km. This domain fits well with the AFT ages in the TS that are generally younger than 1 Ma. Assuming a geothermal gradient dT/dz of 30–20 °C km^{-1}, these ages give exhumation rates of 3.6–5.5 mm yr^{-1} consistent with former studies (Willett *et al.* 2003; Lee *et al.* 2006). Eastward, ZFT and AFT ages for light blue and dark blue particles are older ∼3.2–2.4 and 1.8–2.85 Ma, respectively. This reveals that rocks originated at shallower crustal levels and to the west may have been exhumed earlier and thrusted onto rocks of higher metamorphic grades. These predicted ages seem to be in apparent contradiction with the general decrease of reset ages eastward (Fig. 3b). However, this prediction is in good agreement with FT ages of rocks currently exposed in the most immature portion of the southern Central Range (Willett *et al.* 2003; Lee *et al.* 2006). The absence of such rocks in the northern part of the Central Range is likely to be related to the subsequent stages of collision. Indeed, as plate convergence goes on particles with unreset FT ages are eroded and thus removed from the FT ages data set. We infer that rocks originally located east of the assumed TS domain will not record sufficient burial (or subduction) in the past 2 Ma. As a consequence, FT ages predicted in this particular domain are expected to be unreset or partially reset cooling ages in the continental margin. We cannot, however, rule out that some old FT ages may be consistent with an early cooling event during an initial stage of oceanic accretion (Lee *et al.* 2006) but no specific markers in the accretion wedge were studied in this study. We finally infer, based on predicted and observed particle paths, that exhumation of the Central Range agrees with the growth of a large-scale fold as outlined by reset ages along the fold axis and unreset ages on its flanks.

Throughout the modelling pressure–temperature conditions were also computed for all rocks studied in the above section (Fig. 12b). As collision began, the upper crustal rocks entering the orogenic wedge at depths deeper than 10 km, that is, in the greenschist facies or amphibolite facies, are exhumed in the stability field of upper and lower greenschist facies (Fig. 12b). This greenschist metamorphism is observed within the pre-Tertiary basement of the TS and the slates of the BR (Liou 1981). At the end of the modelling, the base of the undisturbed continental crust (lower crust) is in the amphibolite metamorphic facies even sometimes close to the granulite

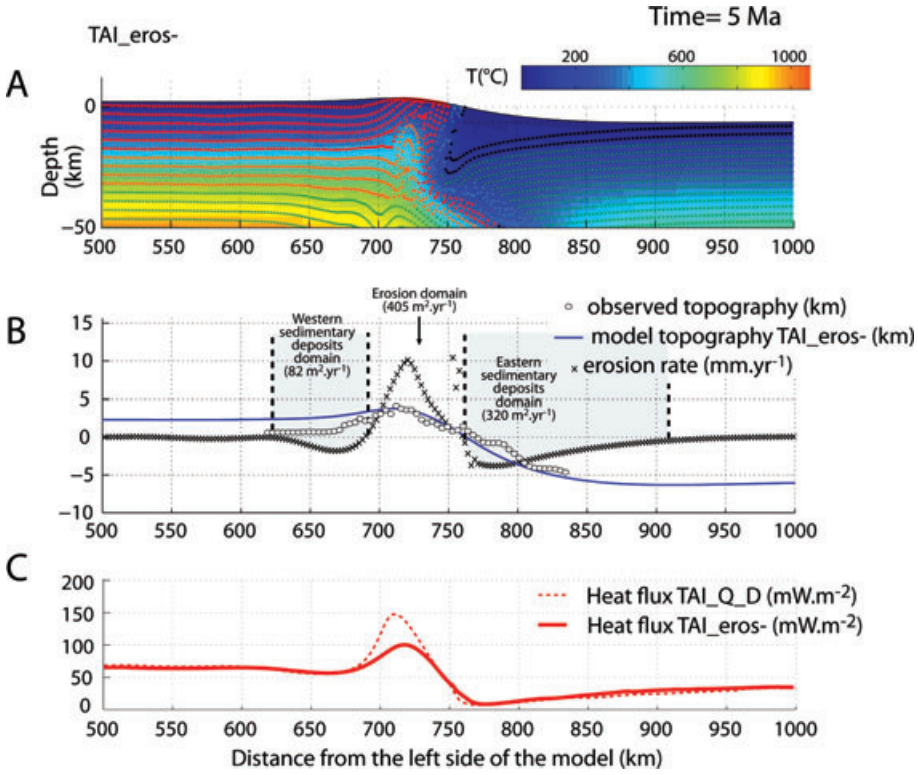

Figure 13. Model results obtained for an erosion coefficient of 2500 m^2 yr^{-1} instead of 5000 m^2 yr^{-1}. (a) Crustal and thermal structure as well as isotherms observed after ∼5 Myr of numerical experiment. (b) Topography and erosion rates associated. (c) Comparison with calculated heat flux of Fig. 5. Lower erosion rates clearly reduce the advection of hot lower crustal material.

metamorphic facies (Fig. 8). At shallower depths, the stable upper crust is under greenschist facies or in the upper grades of the greenschist facies. Peak temperatures recorded by the particles (Fig. 12b) are ranging between 350 (green particle) and 550 °C (dark blue and black particles).

6 SENSITIVITY TO MODEL PARAMETERS

6.1 Erosion rates

Erosion rates are well known to exert a strong control on the exhumation of rocks and hence on mountain building (e.g. Willett 1999). Fig. 13 shows the geotherm and erosion/sedimentation distribution for a model in which the coefficient of erosion is reduced to 2500 m^2 yr^{-1}. The total erosion rates are 402 m^2 yr^{-1} divided into a flux of detrital sediments in the western foreland basin of 82 and 320 m^2 yr^{-1} in the retro-foreland basin. As expected, the erosion rates (Fig. 13b) and consequently the outcoming flux of Eurasian material is lowered (Fig. 13a). The deep crustal isotherms are also less deflected hence reducing the total heat flux at the surface.

The reduction of erosion further leads to the decrease of the predicted cooling rates (Fig. 14a). Moreover only a fraction of the studied particles are exhumed at the end of the numerical experiment. The initiation of cooling is also delayed in time. For instance, the ZFT ages for the light blue and blue dots are estimated to be 2.5 and 0.7 Myr, that is, 1 to 2 Myr younger than observations. Also originally shallower particles (e.g. green and red) are still not exhumed after 5 Myr. Originally deeper particles such as blue squares are also not exhumed at the end of the modelling. This result can be explained by the fact that upward advection of viscous and hot material from the lower crust is inhibited by low erosion. We infer that a coefficient of erosion as high as 5000 m^2 yr^{-1} is required to maintain the long-term exhumation in Taiwan.

6.2 Plate convergence

Hereafter, we test the impact of modifying the plate convergence rates on the exhumation within the collision belt. We first examine the effect of reducing the plate convergence to 25 mm yr^{-1}. Fig. 14b shows that such a reduction obviously results in preventing the exhumation of the upper crust with respect to our preferred model. As a result none of the particles studied in the above sections are exhumed to the surface. For instance, blue particles, which are assumed to represent the most internal portions of the collision belt, are still not exhumed. Moreover, the width of the uplifted domain, which is defined by the intersection between the topographic surface and the crustal rocks, is larger than in our preferred model (Fig. 14b). Interestingly, these patterns of exhumation demonstrate that the reduction of the convergence rates by a factor of two is not equivalent to decrease the duration of the numerical experiment in our reference model. Indeed, a slower plate convergence prevents the decoupling between the upper and the lower crust and the overall strain localization in the model. As a consequence, more distributed shortening results in buckling of a larger portion of the Chinese margin. By contrast, a model for which the convergence rates are close to current geodetic values of 80 mm yr^{-1}, not shown here for the sake of clarity, promotes exhumation during the whole modelling. It finally results in the nearly complete removal of particles by erosion in the reference numerical experiment. We conclude that accelerating or lowering the plate convergence strongly affects the way and the rates to which crustal material are exhumed. This is because

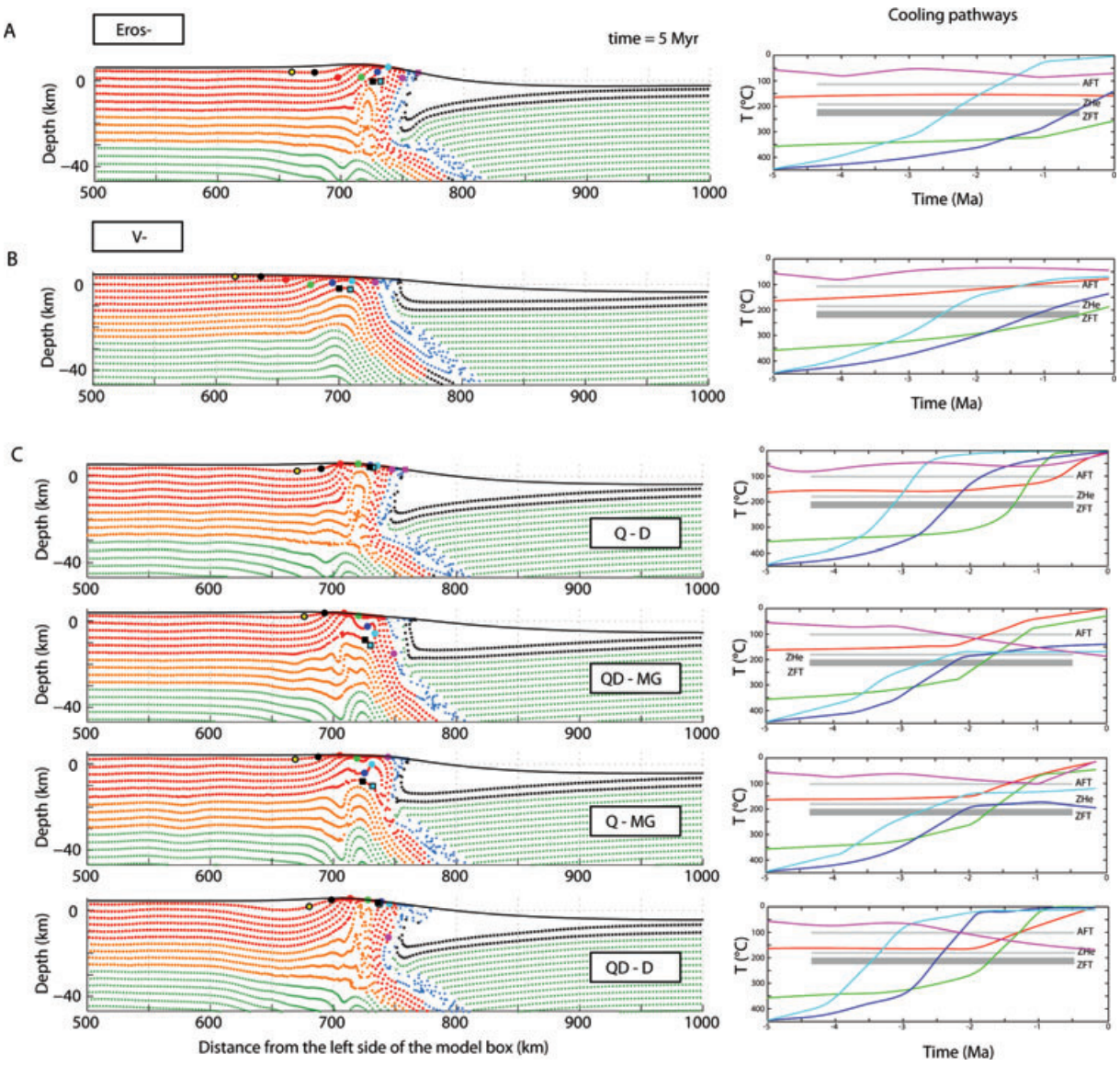

Figure 14. Crustal geometry and cooling history obtained for numerical experiments with reduced erosion, reduced plate convergence or for different combination of crustal composition. Abbreviations: Q, quartz; QD, quartz-diorite; D, diabase and G, mafic granulite. To first order, any modifications that consider (a) lower erosion rates, (b) lower plate convergence or (c) a stronger lower crust (mafic granulite) inhibit the exhumation of the Central Range. This suggests that a weak lower crust (Diabase), fast erosion (5000 m^2 yr^{-1}) and rapid plate convergence (at least 50 km Myr^{-1}) are more suitable for fitting the observed cooling rates.

the plate convergence controls the lithosphere rheology, leading to changes in localization/propagation during mountain building.

6.3 Initial rheology of the continental crust

In our reference numerical experiment, we have assumed a bi-layered continental crust, which was simulated by quartz and diabase rheologies. Alternatively, Mouthereau & Petit (2003) proposed a quartz-diorite and mafic granulite composition to model viscous properties for the upper and lower crust, respectively. Indeed, they showed that a quartz composition for the upper crust is unable to sustain enough stresses to explain the seismicity observed beneath the western foreland down to 12 km. Moreover, a mafic composition for the continental lower crust is acceptable regarding the petrology of the Chinese margin, which was affected by a period of Miocene post-rift magmatism.

Fig. 14c presents a set of models for different rheological profiles in the Eurasian crust together with the corresponding cooling history of particles. Basically, the addition of a stronger lower crust, like in models TAI_QD_MG or TAI_Q_MG (Fig. 14c), inhibits the exhumation process but, however, does not promote the subduction of the upper crust. To first order this seems to be independent of the choice of a relatively weaker (quartz) or stronger upper crust (quartz-diorite) as the exhumation history remains close to that observed in the reference model.

For numerical experiments TAI_ QD_MG and TAI_QD_D where the upper crust is stronger but keeping the lower crust weak we observe that subduction of the magenta dot beneath the PSP is promoted about 3 Ma, which is not observed in other models. In addition, the red particle is exhumed sooner in TAI_QD_D than in the reference experiment. We conclude that any models involving either a stronger upper crust or a stronger lower crust show important

deviation with regard to observations. To first order it is the rheology of the lower continental crust that is predominant in determining the timing of exhumation and hence the mechanism of mountain building. This result is consistent with more complete parametric studies recently conducted with application to Taiwan (Kaus *et al.* 2008).

7 ACCRETION/COLLISION VERSUS SUBDUCTION OF THE CHINESE CONTINENTAL CRUST

Exhumation and *P–T* conditions of rocks as well as the patterns of deformation predicted by our thermodynamic modelling show that crustal rocks of the Chinese margin do not experience significant burial and heating in the subduction zone prior to exhumation. As a result, subduction of the Chinese continental crust appears limited. Although this result may appear controversial it is supported by several evidences that are summarized in the following.

By means of thermochronometric constraints, partially reset or unreset FT data in the southern part of the Central Range, both in the West and in the East of the BS units suggest that part of the continental rocks currently exposed in the Central Range were not buried and reset during the Pliocene (Fig. 3). Moreover, too little evidence for prograde greenschist metamorphism is identified (e.g. in the Chipan gneiss) to definitely support continental subduction. The pervasive penetrative foliations that characterize the higher grade rocks appear consequently to be post-peak. Also, as inferred by previous models, the metamorphic data and model *P–T* paths in the BS suggest a simple cooling and decompression from initial *P–T* conditions in the Chinese passive margin (Simoes *et al.* 2007). In addition, HP-metamorphic rocks in the stable eastern Central Range are restricted to kilometric-scale blocks of metabasites in the Yuli Belt (Fig. 2) whose peak metamorphism is pre-collisional, that is, older than 5 Ma (Beyssac *et al.* 2008). As a consequence, there is currently no evidence for significant syn-subduction metamorphism of the Chinese margin crust.

On the other hand, evidence for fan-shaped slaty S1 cleavages within the TS (Crespi *et al.* 1996) as well as evidence that the marbles of the TS were folded rather than thrusted (Yui & Chu 2000) support the occurrence of a crust-scale fold that is explicitly reproduced in our model. Moreover, viscous deformation beneath the Central Range is currently supported by the low V_P/V_S ratio below 10 km and the relative lack of earthquakes in this area (Rau & Wu 1995; Wu *et al.* 1997; Wu *et al.* 2007). Together with geodetic deformation patterns indicating a lack of shortening beneath the Central Range, these kinematic constraints suggest the existence of an active viscous deformation in association with this large-scale folding. This observation is clearly reproduced in our model as it predicts that viscous thickening would prevail in the lower crust.

Though, some of these data can be accounted for by domains, along a steeply 17°-east-dipping detachment, where underplating vary in time and importance (Simoes *et al.* 2007), we suggest that much of the observations across Taiwan can be more straightforwardly interpreted by the present model. If correct, deformation and exhumation in Taiwan can be accounted for by nearly 100 per cent of frontal accretion of the Asian crust above a gently-dipping décollement located at a depth of ∼25 km.

8 CONCLUSIONS

In this study, we have presented a fully coupled thermomechanical numerical model that satisfactorily reproduces available thermochronometric data, long-/short-term deformation patterns as well as geological observations regarding the past 5 Myr evolution of the Taiwan mountain building. Our thermomechanical model supports earlier hypotheses, thick-skinned in type for which at least the upper 25 km of the Chinese margin crust are accreted in the collision process (Wu *et al.* 1997; Lin *et al.* 1998; Lin 2000). Also in agreement with the previous kinematic models (e.g. Simoes *et al.* 2007), we found that deep seated flux of material from the Chinese crust toward the orogenic wedge should be invoked to compensate for exhumation and erosion in the Central Range. However, instead of being related to underplating that focuses in domains that vary in time and length, it is the consequence of the frontal accretion of the whole bi-layered Asian continental crust. Modelling of *P–T* conditions illustrates that rocks of the Central Range mostly inherited their peak temperatures and pressures in the stable Chinese margin. This finding implies that the eastward increase of metamorphic grades observed across the orogen is likely to be related to the deeper initial position of rocks within the upper crust not to significant subduction prior to exhumation. In any case, the subduction of the Chinese continental crust appears limited. We finally infer that the model presented in this study is in good agreement with the basic expectation that the hot/young and buoyant Chinese continental margin should hardly be subducted beneath the cold/old and dense oceanic plate of the Philippines Sea.

ACKNOWLEDGMENTS

This work has been financially supported by the INSU/Relief program. The authors wish to thank Joerg Denner, T. Gerya and an anonymous reviewer for their insightful comments. Heat flow data were kindly provided by Prof. Kuo-Fong Ma. FM is particularly grateful to K.-F. Ma and A.T. Lin, from the Geophysics Department of NCU (Chungli, Taiwan). We also thank S. Castelltort and B. Kaus from ETH-Zurich for stimulating discussions.

REFERENCES

Barr, T.D. & Dahlen, F.A., 1989. Brittle frictional mountain builiding, 2: thermal structure and heat budget, *J. geophys. Res.,* **94**(B4), 3923–3947.

Beaumont, C., Jamieson, R.A., Nguyen, M.H. & Lee, B., 2001. Himalayan tectonics explained by extrusion of a low-viscosity crustal channel coupled to focused surface denudation, *Nature,* **414**(6865), 738–742.

Beyssac, O., Simoes, M., Avouac, J.P., Farley, K.A., Chen, Y.-G., Chan, Y.-C. & Goffé, B., 2007. Late Cenozoic metamorphic evolution and exhumation of Taiwan, *Tectonics,* **26**(TC6001), doi:10.1029/2006TC002064.

Beyssac, O., Negro, F., Simoes, M., Chan, Y.C. & Chen, Y.G., 2008. High-pressure metamorphism in Taiwan: from oceanic subduction to arc-continent collision? *Terra Nova,* **20,** 118–125.

Bonilla, M.G., 1977. Summary of quaternary faulting and elevation changes in Taiwan, *Geol. Soc. China Mem.,* **2,** 43–55.

Burg, J.-P. & Gerya, T.V., 2005. Viscous heating and thermal doming in orogenic metamorphism: numerical modeling and geological implications, *J. Metamorph. Geol.,* **23,** 75–95.

Burov, E.B. & Diament, M., 1995. Effective elastic thickness of the continental lithosphere—what does it really mean? *J. geophys. Res.,* **100,** 3905–3927.

Burov, E. & Toussaint, G., 2007. Surface processes and tectonics: forcing of continental subduction and deep processes, *Global Planet. Change (Topography of Europe)*, doi:10.1016/j.gloplacha.2007.02.009.

Burov, E. & Yamato, P., 2007. Continental plate collision, P-T-t-z conditions and unstable vs. stable plate dynamics: insights from thermo-mechanical modelling, *Lithos,* **103,** 178–204.

Burov, E., Jolivet, L., Le Pourhiet, L. & Poliakov, A., 2001. A thermomechanical model of exhumation of high pressure (HP) and ultra-high pressure

(UHP) metamorphic rocks in Alpine-type collision belts, *Tectonophysics,* **342**(1–2), 113–136.

Byerlee, J., 1978. Friction of rocks, *Pure appl. Geophys.,* **116,** 615–626.

Carter, N.L. & Tsenn, M.C., 1987. Flow properties of continental lithosphere, *Tectonophysics,* **136,** 27–63.

Chemenda, A.I., Yang, R.-K., Stephan, J.-F., Konstantinovskaya, E.A. & Ivanov, G.M., 2001. New results from physical modelling of arc-continent collision in Taiwan: evolutionary model, *Tectonophysics,* **333,** 159–178.

Chen, C.-H., Chu, H.-T., Liou, J.-G. & Ernst, W.-G., 1983. Explanatory notes for the metamorphic facies map of Taiwan, *Spec. Pub. Central Geol. Surv.,* **2,** 1–3.

Clarck, M.B., Fisher, D.M., Lu, C.-Y. & Chen, C.-H., 1993. Kinematic analyses of the Hsuehshan Range, Taiwan: a large-scale pop-up structure, *Tectonics,* **12,** 205–217.

Clift, P., Lin, J. & Barckhausen, U., 2002. Evidence of low flexural rigidity and low viscosity lower continental crust during continental break-up in the South China Sea, *Mar. Petrol. Geol.,* **19,** 951–970.

Crespi, J., Chan, Y.C. & Swaim, M.S., 1996. Synorogenic extension and exhumation of the Taiwan hinterland, *Geology,* **24**(3), 247–250.

Cruciani, C., Carminati, E. & Doglioni, C., 2005. Slab dip vs. lithosphere age: no direct function, *Earth planet. Sci. Lett.,* **238**(3–4), 298–310.

Cundall, P.A., 1989. Numerical experiments on localization in frictional materials, *Ing. Arch.,* **59,** 148–159.

Currie, C.A., Beaumont, C. & Huismans, R.S., 2007. The fate of subducted sediments: a case for backarc intrusion and underplating, *Geology,* **35,** 1111–1114.

Dadson, S.J. *et al*., 2003. Links between erosion, runoff variability and seismicity in the Taiwan orogen, *Nature,* **426,** 648–651.

Dahlen, F.A. & Barr, T.D., 1989. Brittle frictional mountain building, 1: deformation and mechanical energy budget, *J. geophys. Res.,* **94,** 3906–3922.

Dahlen, F.A., Suppe, J. & Davis, D., 1984. Mechanics of fold-and-thrust belts and accretionary wedges: cohesive coulomb theory, *J. geophys. Res.,* **89**(B12), 10 087–10 101.

Davis, D., Suppe, J. & Dahlen, F.A., 1983. Mechanics of fold-and-thrust belts and accretionary wedges, *J. geophys. Res.,* **88**(B2), 1153–1172.

De Capitani, C., 1994. Gleichgewichts-Phasendiagramme : Theorie und Software, Jahrestagung der Dtsch. Mineral. Ges., *Beihefte zum European J. Mineral,* **6,** 1–48.

Deschamps, A., Monie, P., Lallemand, S., Hsu, S.-K. & Yeh, K.Y., 2000. Evidence for Early Cretaceous oceanic crust trapped in the Philippine Sea Plate, *Earth planet. Sci. Lett.,* **179**(3–4), 503–516.

Ernst, W.G., 1981. Petrotectonic settings of glaucophane schist belts and some implications for Taiwan, *Geol. Soc. China Mem.,* **4,** 229–267.

Faccenda, M., Gerya, T.V. & Chakraborty, S., 2008. Styles of post-subduction collisional orogeny: influence of convergence velocity, crustal rheology and radiogenic heat production, *Lithos,* **103,** 257–287.

Fisher, D.M., Lu, C.-Y. & Chu, H.T., 2002. Taiwan Slate Belt: Insights into the ductile interior of an arc-continent collision, in *Geology and Geophysics of an Arc-Continent collision, Taiwan, Republic of China, Geological Society of America Special Paper,* Vol. 358, pp. 93–106, eds Byrne, T.B. & Liu, C.-S., GSA, Boulder, CO.

Fuller, C., Willett, S.D., Fischer, D. & Lu, C.-Y., 2006. A thermomechanical wedge model of Taiwan constrained by fission-track thermochronometry, *Tectonophysics,* **425,** 1–24.

Gerya, T.V., Perchuk, L.L. & Burg, J.-P., 2008. Transient hot channels: perpetrating and regurgitating ultrahigh-pressure, high temperature crust-mantle associations in collision belts, *Lithos,* **103,** 236–256.

Goetze, C., 1978. The mechanics of creep in Olivine, *Phil. Trans. R. Soc. Lond.,* **288,** 99–119.

Hansen, F.D. & Carter, N.L., 1982. Creep of selected crustal rocks at 1000 MPa, *EOS, Trans. Am. geophys Un.,* **63,** 437.

Ho, C.-S., 1986. A synthesis of the geologic evolution of Taiwan, *Tectonophysics,* **125,** 1–16.

Huang, C.-Y., Yuan, P.B., Song, S.-R., Lin, C.-W., Wang, C., Chen, M.-T., Shyu, C.-T. & Karp, B., 1995. Tectonics of short-lived intra-arc basins in the arc-continent collision terrane of the Coastal Range, eastern Taiwan, *Tectonics,* **14**(1), 19–38.

Kaus, B., Steeman, C. & Becker, T.W., 2008. From passive continental margin to mountain belt: insights from analytical and numerical models and application to Taiwan, *Phys. Earth planet. Int.,* doi:10.1016/j.pepl.2008.06.015.

Le Pourhiet, L., Burov, E. & Moretti, I., 2004. Rifting through a stack of inhomogeneous thrusts (the dipping pie concept), *Tectonics,* **23**(TC4005), doi:10.1029/2003TC001584.

Lee, C.-R. & Cheng, W.-T., 1986. Preliminary heat flow measurements in Taiwan, in *Proceedings of the Fourth Circum-Pacific Energy and Mineral Resources Conference,* 1986, Singapor.

Lee, T.-Y. & Lawver, L.A., 1995. Cenozoic plate reconstruction of Southeast Asia, *Tectonophysics,* **251,** 85–138.

Lee, J.-C., Angelier, J. & Chu, H.-T., 1997. Polyphase history and kinematics of a complex major fault zone in the northern Taiwan mountain belt : the Lishan fault, *Tectonophysics,* **274,** 97–115.

Lee, Y.-H., Chen, C.-C., Liu, T.-K., Ho, H.-C., Lu, H.-Y. & Lo, W, 2006. Mountain building mechanisms in the southern Central Range of the Taiwan orogenic belt from accretionary wedge deformation to arc-continent collision, *Earth planet. Sci. Lett.,* **252**, 413–422.

Li, Y.-H., 1976. Denudation of Taiwan Island since the Pliocene epoch, *Geology,* **4,** 105–107.

Lin, C.-H., 2000. Thermal modeling of continental subduction and exhumation constrained by heat flow and seismicity in Taiwan, *Tectonophysics,* **324,** 189–201.

Lin, C.-H., Yeh, Y.-H., Yen, H.-Y., Chen, K.-C., Huang, B.-S., Roecker, S.W. & Chiu, J.-M., 1998. Three-dimensional elastic wave velocity structure of the Hualien region of Taiwan: evidence of active crustal exhumation, *Tectonics,* **17**(1), 89–103.

Lin, A.T., Watts, A.B. & Hesselbo, S.P., 2003. Cenozoic stratigraphy and subsidence history of the South China Sea margin in the Taiwan region, *Basin Res.,* **15**(4), 453–478.

Liou, J.-G., 1981. Petrology of metamorphosed oceanic rocks in the Central Range of Taiwan, *Geol. Soc. China Mem.,* **4,** 291–341.

Liou, J.G. & Ernst, W.G., 1984. Summary of phanerozoic metamorphism in Taiwan, *Geol. Soc. China Mem.,* **6**(December 1984), 133–152.

Liu, T.-K., Chen, Y.-G., Chen, W.-P. & Jiang, S.-H., 2000. Rates of cooling and denudation of the early Penglai orogeny, Taiwan, as assessed by fission-track constraints, *Tectonophysics,* **320,** 69–82.

Lo, C.-H. & Onstott T.C., 1995. Rejuvenation of K-Ar systems for minerals in the Taiwan mountain belt, *Earth planet. Sci. Lett.,* **131,** 71–98.

Lundberg, N. & Dorsey, R.J., 1990. Rapid quaternary emergence, uplift, and denudation of the Coastal Range, eastern Taiwan, *Geology,* **18,** 638–641.

Ma, K.-F. & Song, D.-R., 1997. In velocity and Moho depth in Taiwan, *J. Geol. Soc. China,* **40,** 167–184.

Mouthereau, F. & Lacombe, O., 2006. Inversion of the Paleogene Chinese continental margin and thick-skinned deformation in the Western Foreland of Taiwan, *J. Struct. Geol.,* **28,** 1977–1993.

Mouthereau, F. & Petit, C., 2003. Rheology and strength of the Eurasian continental lithosphere in the foreland of the Taiwan collision belt : constraints from seismicity, flexure and structural styles, *J. geophys. Res.,* **108**(B11), 2512, doi:10.1029/2002JB002098.

Mouthereau, F., Lacombe, O., Deffontaines, B., Angelier, J. & Brusset, S., 2001. Deformation history of the southwestern Taiwan foreland thrust belt: insights from tectono-sedimentary analyses and balanced cross-sections, *Tectonophysics,* **333,** 293–322.

Parsons, B. & Sclater, J.G., 1977. An analysis of the variation of ocean floor bathymetry and heat flow with age, *J. geophys. Res.,* **82,** 803–827.

Peng, T.-H., Li, Y.H. & Wu, F.T., 1977. Tectonic uplift rates of the Taiwan island since the early Holocene, *Mem. Geol. Soc. China,* **2,** 57–69.

Poliakov, A., Podladchikov, Y. & Talbot, C.J., 1993. Initiation of salt diapirs with frictional overburden : numerical experiments, *Tectonophysics,* **228,** 199–210.

Pulver, M.H., Crespi, J.M. & Byrne, T.B., 2002. Lateral extrusion in a transpressional collision zone: an example from the pre-Tertiary metamorphic basement of Taiwan, in *Geology and Geophysics of an Arc-Continent collision, Taiwan, Republic of China, Geological Society of America Special Paper,* Vol. 358, pp. 107–120, eds Byrne, T.B. & Liu, C.-S. GSA, Boulder, CO.

Ranalli, G. & Murphy, D.C., 1987. Rheological stratification of the lithosphere, *Tectonophysics,* **132,** 281–295.

Rau, R.-J. & Wu, F.T., 1995. Tomographic imaging of lithospheric structures under Taiwan, *Earth planet. Sci. Lett.,* **133,** 517–532.

Sibuet, J.-C. & Hsu, S.-K., 2004. How was Taiwan created? *Tectonophysics,* **379,** 159–181.

Sibuet, J.-C., Hsu, S.-K., Le Pichon, X., Le Formal, J.P., Reed, D., Moore, G. & Liu, C.-S., 2002. East Asia tectonics since 15 Ma: constraints from the Taiwan region, *Tectonophysics,* **344,** 103–134.

Simoes, M. & Avouac, J.P., 2006. Investigating the kinematics of mountain building in Taiwan from the spatiotemporal evolution of the foreland basin and western foothills, *J. geophys. Res.,* **111**(B10401), doi:10.1029/2005JB004209.

Simoes, M., Avouac, J.-P., Beyssac, O., Goffe, B., Farley, K.A. & Chen, Y.-G., 2007. Mountain building in Taiwan: a thermokinematic model, *J. geophys. Res.,* **112**(B11405), doi:10.1029/2006JB004824.

Sobolev, S.V. & Babeyko, A.Y., 2005. What drives orogeny in the Andes? *Geology,* **33,** 617–620.

Suppe, J., 1981. Mechanics of mountain building and metamorphism in Taiwan, *Geol. Soc. China Mem.,* **4,** 67–89.

Taylor, B. & Hayes, D.E., 1980. The Tectonic Evolution of the South China Basin, in *The Tectonic and Geological Evolution of the Southeast Asian Seas and Islands, Geophysical Monograph Series,* Vol. 23, pp. 89–104, ed. Hayes, D.E., American Geophysical Union, Washington, D.C.

Teng, L.-S., 1990. Geotectonic evolution of late Cenozoic arc-continent in Taiwan, *Tectonophysics,* **183,** 67–76.

Teng, L.-S., 1992. Geotectonic evolution of Tertiary continental margin basins of Taiwan, *Petrol. Geol. Taiwan,* **27,** 1–19.

Tensi, J., Mouthereau, F. & Lacombe, O., 2006. Lithospheric bulge in the West Taiwan Basin, *Basin Res.,* **18**(3), 277–299.

Tillman, K.S. & Byrne, T.B., 1995. Kinematic analysis of the Taiwan slate belt, *Tectonics* **14**(7), 322–341.

Toussaint, G., Burov, E. & Jolivet, L., 2004a. Continental plate collision: unstable versus stable slab dynamics, *Geology,* **32**(1), 33–36.

Toussaint, G., Burov, E. & Avouac, J.-P., 2004b. Tectonic evolution of a continental collision zone: a thermo mechanical numerical model, *Tectonics,* **23,** TC6003, doi:10.1029/2003TC001604.

Turcotte, D.L. & Schubert, G., 2002. *Geodynamics: Applications of Continuum Mechanics to Geological Problems,* Cambridge University Press.

Watts, A.B. & Burov, E., 2003. Lithospheric strength and its relationship to the elastic and seismogenic layer thickness, *Earth planet. Sci. Lett.,* **213,** 113–131.

Warren, C.J., Beaumont, C. & Jamieson, R.A., 2008. Modelling tectonic styles and ultra-high pressure (UHP) rock exhumation during the transition from oceanic subduction to continental collision, *Earth. planet. Sci. Lett.,* **267,** 129–145.

Wilks, K.R. & Carter, N.L., 1990. Rheology of some continental lower crust, *Tectonophysics,* **182,** 57–77.

Willett, S.D., 1999. Orogeny and orography: the effects of erosion on the structure of mountain belts, *J. geophys. Res.,* **164**(B12), 28 957–28 981.

Willett, S.D. & Brandon, M.T., 2002. On steady states in mountain belts, *Geology,* **30,** 175–178.

Willett, S.D., Fischer, D., Fuller, C., Yeh, E.-C. & Lu, C.-Y., 2003. Erosion rates and orogenic-wedge kinematics in Taiwan inferred from fission-track thermochronometry, *Geology,* **31**(11), 945–948.

Wu, F.T., Rau, R.-J. & Salzberg, D., 1997. Taiwan orogeny: thin-skinned or lithospheric collision, *Tectonophysics,* **274,** 191–220.

Wu, Y.-M., Chang, C.-H., Zhao, L., Bruce, J., Shyu, H., Chen, Y.-G., Sieh, K. & Avouac, J.-P., 2007. Seismic tomography of Taiwan: improved constraints from a dense network of strong motion stations, *J. geophys. Res.,* **112**(B08312), doi:10.1029/2007JB004983.

Yamato, P., Agard, P., Burov, E., Le Pourhiet, L., Jolivet, L. & Tiberi, C., 2007. Burial and exhumation in a subduction wedge: Mutual constraints from thermomechanical modeling and natural P-T-t data (Schistes Lustrés, western Alps), *J. geophys. Res.,* **112**(B07410), doi:10.1029/2006JB004441.

Yamato, P., Burov, E., Agard, P., Le Pourhiet, L. & Jolivet, L., 2008. HP-UHP exhumation during slow continental subduction: Self-consistent thermodynamically and thermomechanically coupled model with application to the Western Alps, *Earth. planet. Sci. Lett.,* **271,** 63–74.

Yen, H.-Y., Yeh, Y.-H. & Wu, F.T., 1998. Two-dimensional crustal structures of Taiwan from gravity data, *Tectonics,* **17**(1), 104–111.

Yu, S.-B., Chen, H.-Y. & Kuo, L.-C., 1997. Velocity field of GPS stations in the Taiwan area, *Tectonophysics,* **274,** 41–59.

Yue, L.-F., Suppe, J. & Hung, J.-H., 2005. Structural geology of a classic thrust belt earthquake: the 1999 Chi-Chi earthquake Taiwan (Mw = 7.6), *J. Struct. Geol.,* **27,** 2058–2083.

Yui, T.-F. & Chu, H.-T., 2000. 'Overturned' marble layers: evidence for upward extrusion of the Backbone Range of Taiwan, *Earth planet. Sci. Lett.,* **179,** 351–361.

Geophysical Journal International

Geophys. J. Int. (2009) **179,** 1292–1300 doi: 10.1111/j.1365-246X.2009.04372.x

Episodic slab rollback fosters exhumation of HP–UHP rocks

Laurent Husson,[1] Jean-Pierre Brun,[1] Philippe Yamato[1,2] and Claudio Faccenna[3]

[1] *Géosciences Rennes, CNRS* UMR6118, *Université Rennes* 1, 35042 *Rennes, France. E-mail: laurent.husson@univ-rennes1.fr*
[2] *ETH-Zürich, NO-E31 Sonneggstrasse* 5, CH-8092 *Zürich, Switzerland*
[3] *Dip. Scienze Geologiche, Università degli Studi "Roma TRE", Largo S.Leonardo Murialdo* 1, 00146 *Roma, Italy*

Accepted 2009 August 26. Received 2009 June 16; in original form 2009 March 25

SUMMARY

The burial–exhumation cycle of crustal material in subduction zones can either be driven by the buoyancy of the material, by the surrounding flow, or by both. High pressure and ultrahigh pressure rocks are chiefly exhumed where subduction zones display transient behaviours, which lead to contrasted flow regimes in the subduction mantle wedge. Subduction zones with stationary trenches (mode I) favour the burial of rock units, whereas slab rollback (mode II) moderately induces an upward flow that contributes to the exhumation, a regime that is reinforced when slab dip decreases (mode III). Episodic regimes of subduction that involve different lithospheric units successively activate all three modes and thus greatly favour the exhumation of rock units from mantle depth to the surface without need for fast and sustained erosion.

Key words: Subduction zone processes; Continental margins: convergent; Dynamics of lithosphere and mantle; High strain deformation zones.

1 INTRODUCTION

The burial and exhumation cycle of rocks that underwent high pressure and low temperatures with respect to a mean crustal geotherm (HP metamorphism) is related to the subduction process. Metamorphosed stacks of blueschists or eclogites are widely found in mountain belts (e.g. Maruyama *et al.* 1996; Ring *et al.* 1999; Chopin 2003). But the fact that not all orogenic systems display high pressure (HP) or ultra high pressure (UHP) rocks at the surface is remarkable: blueschists and eclogites are essentially found in convergence zones in which the lower subducting plate was anything but a uniform oceanic lithosphere during the burial cycle: the Alps (e.g. Handy *et al.* 1999; Rosenbaum & Lister 2005), Zagros (e.g. Agard *et al.* 2006), and the Himalayas (e.g. Allègre *et al.* 1984), but also smaller systems of the Mediterranean domain (e.g. Stampfli 2000; Jolivet *et al.* 2008), like the Hellenides and Tyrrhenian systems (e.g. Brun & Faccenna 2008) encompass most of Cenozoic HP rocks occurrences, as opposed for instance to the Andes that barely show HP rocks at surface level.

Downgoing lithospheric plates convey stacks of crustal rocks at depth. These rocks are either the crustal cover of the downgoing plate or scrapped off the upper plate crust. Their downward journey into subduction zones straightforwardly follows that of the subducting slab. Conversely, the exhumation of HP rocks that follows the burial episode is less intuitive. A plethora of models, both analogue (e.g. Chemenda *et al.* 1995, 1996; Boutelier *et al.* 2004) and numerical (e.g. Pfiffner *et al.* 2000; Burov *et al.* 2001; Gerya *et al.* 2002; Gerya & Stöckhert 2002; Yamato *et al.* 2007, 2008; Warren *et al.* 2008) have been proposed to explain the second part of the cycle, in which the rock aggregate goes towards the surface, paradoxically seemingly against the overall downward flow. In all models, HP rocks are either driven upward by their own buoyancy or advected by the surrounding flow. The following severe conditions are to be met to validate the models: comprehensive analysis of HP rocks (e.g. Ring *et al.* 1999; Agard *et al.* 2009) show that HP rock slices were assembled at depth and exhumed together. The residence time at depth lasts for ∼5–10 Myr; exhumation occurs within ∼10 Myr or less, that is, at rates that are in the same range as rates of plate boundary displacement (e.g. Rubatto & Hermann 2001). Such rates (up to 40–50 mm/yr) are therefore significantly higher than the highest sustained erosion rates that could be expected on the long term (much less than 10 mm/yr). In fact, two-stage exhumation is often identified, with a fast exhumation at depth, up to 10 kbar (10^9 Pa), followed by a slower event that can be attributed to erosion (e.g. de Sigoyer *et al.* 2000; Ernst 2001; Rubatto & Herman 2001; Parra *et al.* 2002; Walsh & Hacker 2004; Yamato *et al.* 2008), up to surface level.

Most previous models arbitrarily consider a stationary trench location (e.g. Chemenda *et al.* 1995; Ernst *et al.* 1997; Beaumont *et al.* 1999; Pfiffner *et al.* 2000; Gerya *et al.* 2002); such choice is very unfortunate; first, because it prevents any substantial extension in the upper plate that could favour the exhumation of rocks and, second, because the associated downward flow in the wedge tends to counter an upward motion of rocks at depth. Because these models ignore the dynamics of the mantle wedge itself that may vary depending on the subduction regime, and the potential advection of the rock within the wedge, they most often invoke more complex mechanisms like for instance the so-called subduction channel (e.g. England & Holland 1979; Cloos 1982; Shreve & Cloos 1986). In fact, stationary trenches are seldom observed, regardless of the

reference frame (e.g. Lallemand *et al.* 2005), and slab rollback, that is, the motion of the entire subduction system (trench and subducting slabs) towards the foreland and relative to the lower mantle is the most natural behaviour of slabs (e.g. Funiciello *et al.* 2003). In addition, the subduction of a heterogeneous plate leads to transient subduction kinematics: subduction rate, trench migration rate and slab geometry very efficiently respond to heterogeneities in the plate rheology or buoyancy and are often unsteady (Martinod *et al.* 2005; Royden & Husson 2006). Thomson *et al.* (1998) or Brun & Faccenna (2008) noticed that such transient behaviour is observed in the Hellenides and in the Mediterranean domain in general (Royden 1993). Rollback-type settings favour the exhumation of HP rocks, chiefly because upper plate extension during rollback sets free space that can be filled up by rocks from underneath and therefore causes the exhumation of HP rocks (Gorczyk *et al.* 2007; Brun & Faccenna 2008; Faccenda *et al.* 2009).

The final exhumation of HP crustal slivers occurs inside the wedge. Field relationships and tectonic reconstructions show that their way back to the surface is often accompanied by 'syn-orogenic' extensional detachments positioned on the roof of the exhumed sliver (Platt 1986, 1993; Chemenda *et al.* 1995; Ring *et al.* 1999; Hacker *et al.* 2003; Jolivet *et al.* 2003, 2008). This deformation pattern suggests that during exhumation the overall backarc area was not under compression, although convergence and subduction were at work. This is typical of the Mediterranean realm, where exhumation was produced during the formation of the arc and often accompanied by backarc spreading (Jolivet *et al.* 2003; Brun & Faccenna 2008). In such tectonic context, most favourable to exhumation, the upper plate then plays a subordinate role, passively moving and deforming under the action of the return flow.

The aim of this work is to explore the advecting power of the sublithospheric wedge (simply referred to as 'wedge' in the following) and investigate how the poloidal flow in the wedge above the slab differently affects the upward journey of rock slices towards the surface. Our model can be pertinent to explore the movement of crustal buoyant sliver units detaching from the slab, penetrating into the mantle wedge and rising up at the boundary between the upper plate and subducting slab (i.e. the first stage of exhumation). With respect to previous work dealing with the interaction of a positively buoyant rock unit with the mantle flow excited by a purely downdip slab velocity (Hall & Kincaid 2001; Gerya & Yuen 2003; Manea *et al.* 2005; Castro & Gerya 2007), our study investigates the behaviour of units of variable buoyancies within a corner flow that is excited by different kinematical conditions, including slab rollback and oscillating slab dip.

In the following, because we consider the end-member situation where the upper plate has a negligible thickness, we do not consider the exhumation stage within the orogenic wedge but instead we explore the advecting power of the sublithospheric wedge (simply referred to as 'wedge' in the following) and investigate how the poloidal flow above the slab differently affects the upward journey of rock slices towards the surface. It is argued that slab rollback is more efficient than stationary trenches to exhume HP rocks, that slab shallowing does an even better job, and that the latter settings are commonly associated to HP rocks occurrences.

2 FORCES DRIVING EXHUMATION

In the wedge above the slab, a rock slice is primarily driven by two mechanisms: the buoyancy of the rock unit with respect to the surrounding material, and the flow of the material in the wedge that may advect it.

2.1 Intrinsic velocity of the HP rock units

Although there is no comprehensive description of HP rock units in terms of size and density, it seems that the vast majority is either neutrally or positively buoyant, that is, the mean density of the rock aggregate is equal or lower than that of the surrounding material and its natural velocity in a homogeneous viscous material is upward. A handful of units for which the density is higher than that of the surrounding material, like the Alpine eclogites (Zermatt–Saas, Monviso), is reported, but those units generally are embedded within serpentinite and/or continental crust rock units of lower density (e.g. Guillot *et al.* 2004; Agard *et al.* 2009) and it is unclear what the overall buoyancy is. Units of HP rocks are generally composed of stacks of rock slices that were assembled at depth. The observed characteristic size of the assemblage is tens to hundreds of kilometers. The vertical velocity of a unit scales with its size and, for a sphere in a viscous medium, its velocity v_0 is the Stokes velocity and increases like the squared radius of the sphere. It is therefore possible that HP rocks assemblages build up at depth until the intrinsic velocity of the assemblage is high enough to make it flow upwards. (Note, however, that the intrinsic velocity from the density of a rock stack in the wedge may depart from the Stokes velocity because the actual velocity of the particle also depends on many unknown parameters like the density contrast of course, but also the viscosity and the shape of the body of HP rocks itself).

This non-linear relationship in turn also implies that for a given density contrast between the rock stack at depth and surrounding material, there is a maximum size for the aggregate, after which rock units are removed faster than they are being aggregated: rocks stacks form at depth at a rate that is proportional to the subduction rate but the vertical velocity is not proportional to the volume of the body and therefore is not proportional to the rate at which rocks aggregate at depth. Removal of rock slices at depth is thus episodic and the period of removal is characterized by the balance between the 'productivity' of the subduction, that is, the rate at which rocks can be scrapped off the downgoing plate and accumulate at depth, and the rate at which the intrinsic velocity of the rock slice increases.

As emphasized in many studies (e.g. Chemenda *et al.* 1995; Ernst *et al.* 1997; Burov *et al.* 2001), the buoyancy of the aggregate is indeed a fundamental driving mechanism. But because the associated intrinsic velocity is generally too small (a few millimeters per year, Agard *et al.* 2009) and because the buoyancy of some units—eclogites for instance—is occasionally insufficient to achieve fast exhumation, other processes should be considered. Can the flow in which the aggregate moves be an additional contributor and efficiently advect it towards the surface?

2.2 Corner flow and subduction modes

Subduction zones have variable behaviours than can either be stationary, in which case the trench remains at the same location with respect to the lower mantle, or retreating (slab rollback) when the trench moves towards the foreland (and conversely, advancing). Because subducting lithospheres can be heterogeneous, subduction zones are often in transient regimes, and slab geometries varies accordingly (Garfunkel *et al.* 1986; Martinod *et al.* 2005; Royden & Husson 2006). For instance, the slab steepens when a

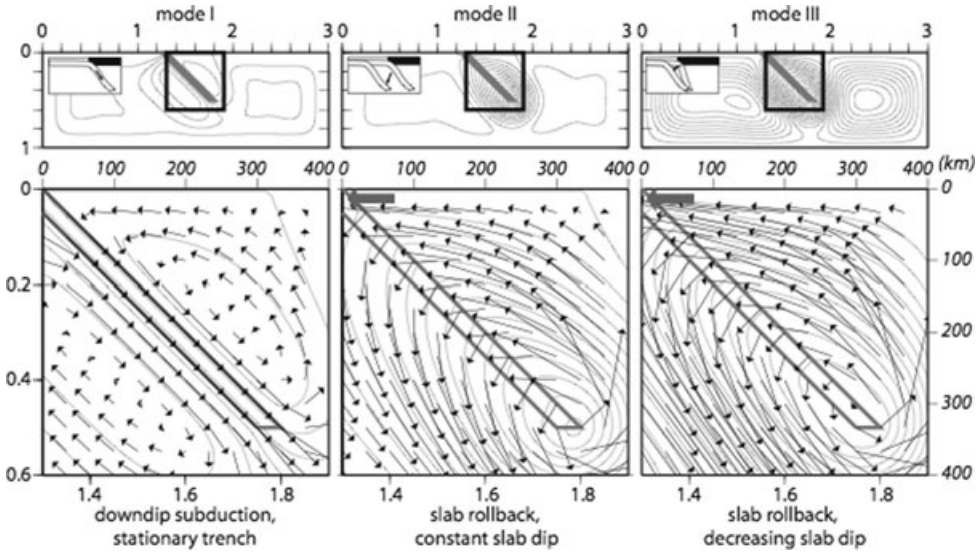

Figure 1. Flow field and streamlines in the mantle wedge for stationary trench (mode I); slab rollback (mode II); slab rollback accompanied by a decrease in slab dip (mode III). Top: cartoons and full models; bottom: zooms over the subduction wedges. Grey arrow denotes trench motion. Dimensionless and dimensional (italic) units.

unit of moderately negatively buoyant continent follows a highly negatively buoyant oceanic lithosphere. Examples can be found in the Banda and Tyrrhenian subduction zones (Royden & Husson 2009). Conversely, the subduction angle decreases when a negatively buoyant oceanic lithosphere follows the subduction of a less negatively buoyant unit like a continental island or an oceanic ridge embedded within a negatively buoyant lithosphere. The associated corner flow varies accordingly and can contribute to, or oppose, the exhumation of HP rocks. To compare the driving or resisting efficiency of the different subduction regimes, we solve for the poloidal flow of an isoviscous fluid within a two-dimensional domain (Fig. 1). It implies that return flow can always accommodate the displacement of the slab, although toroidal flow may also contribute and thus decreases the vigor of the poloidal flow (e.g. Piromallo *et al.* 2006; Stegman *et al.* 2006). The model can be naturally adimensionalized taking the subduction rate v_0, the upper mantle thickness H and the viscosity η_0 of the mantle (results are given in both dimensionless and dimensional values, computed for $v_0 = 40$ mm/yr, $H = 670$ km, and $\eta_0 = 10^{20}$ Pa s). The model represents a section of the upper mantle in which a subducting slab penetrates down to half the thickness of the upper mantle. The prescribed motion of a rigid panel that dips at 45° from the surface to a depth 0.5 (335 km) drives the flow. The fact that the slab only penetrates to half the upper mantle depth is designed to let the mantle flow freely in the poloidal field, because most small-scale slabs are dismantled at depth in the upper mantle, do not behave as consistent bodies all the way down to the top of the lower mantle, and therefore allow for poloidal flow originating at depth, around slab tails. This is opposed to many models of subduction zones (among many others, see Funiciello *et al.* 2003; Stegman *et al.* 2006; Royden & Husson 2006; Capitanio *et al.* 2007), but in fact more accurately reproduce the structure of the upper mantle as seen from geophysical observations (e.g. Faccenna *et al.* 2003 for the Mediterranean). We solve the stream function Ψ such that $\partial\Psi/\partial y = -u; \partial\Psi/\partial x = v$. For an incompressible fluid, Ψ verifies the biharmonic equation $\nabla^4\Psi = 0$. The stream function, and therefore the velocity, is prescribed at the boundaries and on the slab itself. The velocity at the boundaries is null and Ψ is defined on the slab such that the subduction rate v_0 is similar for all modes. The models are much simplified to allow for a comparison of the different subduction modes. To isolate the particular effect of variable corner flows, we assign the upper plate a null thickness, for it is supposed to play a passive role in the system. A thorough description of the flow in the wedge is beyond the scope of this work; we emphasize, however, that the comparison between simplified models is the most reliable way to quantify the relative contribution, in the exhumation process, of the corner flows within different modes of subduction.

The flow lines and velocity fields are shown on Fig. 1 for three different modes that highlight the contrasted, end-member flow patterns. For stationary trenches (mode I, Fig. 1a), where the slab does not change its dip or its location with respect to the mantle, slab motion is only downdip and two typical corner flow cells are well defined above and below the slab. The velocity field above the slab is downward and would not promote the exhumation of HP rocks. For purely retreating slabs (mode II, Fig. 1b), where the slab retreats with a velocity field that corresponds to a fixed foreland (the left hand side of the slab is fixed with respect to the bottom of the model), only one cell develops around the slab; above the slab the velocity field is essentially upward. The downdip velocity component along the slab is much smaller than the rollback component. Finally, for a decrease in slab dip (mode III, Fig. 1c), where the slab rotates around its tail that is anchored in the mantle, only one cell remains too, but the velocity field above the slab is strongly upward and higher than when the slab is only retreating without changing its dip. The downdip velocity component is neglected to more accurately represent the situation were only the shallowest part of the slab is dense enough to drive the subduction (see Section 4).

Amongst the three modes, two of them clearly show an upward velocity field above the slab: although a subduction zone with a stationary trench only drags the particles above the slab downward, a subduction zone with a retreating slab, and even more efficiently with a retreating slab whose dip decreases, induces an upward flow field that can only participates to the exhumation of high pressure rocks that are released from the slab at depth. Note that the velocities in the wedge are comparable in magnitude to that of the subducting slab. Other possible modes like slab steepening or trench advance are

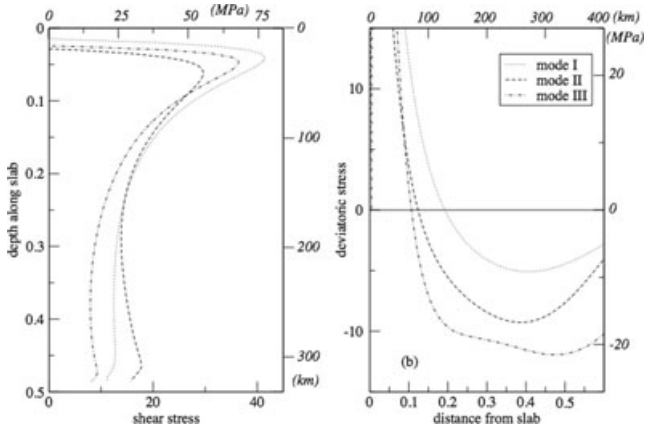

Figure 2. (a) Shear stresses along the surface of the slab and (b) deviatoric stresses at depth 0.1 (∼70 km) in front of the subducting slab. Dimensionless and dimensional (italic) units.

not considered here because they obviously oppose the exhumation of HP rocks.

In addition, the stress fields that are associated to the corner flows can also control the rate at which HP rocks make their way towards the surface. All three modes essentially display comparable positive shear stresses along the slab that favour the detachment of HP rock aggregates from the conveyor slab (Fig. 2a). Maximum shear stresses are found at depths lower than 0.1 (i.e. ∼70 km, typically the burial depth HP rocks reach before they are exhumed). Mode I, when the trench is stationary, favours the scrapping off rocks from the slab. Deviatoric stresses (measured in a horizontal plane) at a given depth (Fig. 2b, depth 0.1, ∼70 km) have comparable behaviours in all models, with localized strong compression (positive values) just above the slab and extension at larger distances. Horizontal extension is more than 2 times larger in mode III than in mode I, and ∼1.5 times larger than when in mode II. Extension favours the exhumation of HP aggregates throughout the wedge, rendering mode III more efficient than any other mode.

For all three modes, the very last episode of exhumation has to be driven either by extensional faulting or erosion, because the velocity field gradually becomes parallel to the surface, which of course reduces the advection capacity (Fig. 1).

3 KINEMATICS OF EXHUMATION

Once rocks are aggregated at depth and scrapped off the subducting slab, they may flow within the wedge and find their route to the surface. In the following, we test the relative influence of the buoyancy of a particle, which we characterize by its intrinsic velocity V_b, and of the wedge flow in the different modes.

3.1 Particle buoyancy and pathlines

The intrinsic velocity of the HP rock stack and the corner flow in which the aggregate is advected chiefly control the timing of exhumation. The corner flow can be driving (upward) or resisting (downward). We compare the kinematics of exhumation by tracking a particle released above the slab at a depth 0.15 (100 km) for the three modes. Unless otherwise specified, slab dip is 45° for modes I and II and the initial dip is 90° for mode III (slab dip varies in mode III and we start with the maximum dip to encompass the largest range of dip angles, from 90° to 0°).

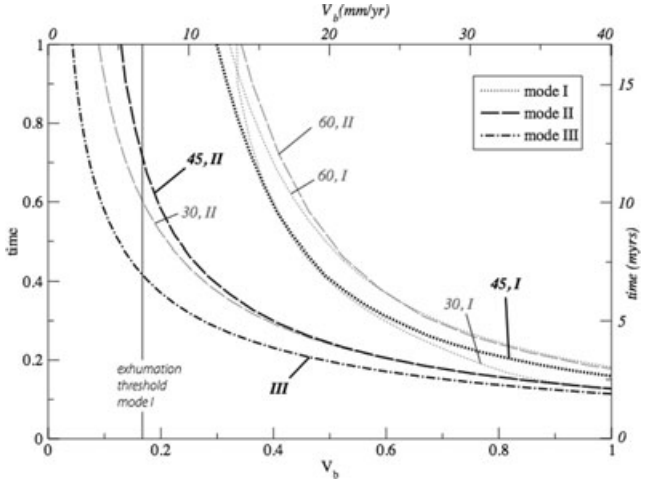

Figure 3. Delay for exhumation as a function of the intrinsic velocity of the rock unit V_b, subduction mode, and slab dip angle (labels give slab dip and mode). Vertical bar indicates the threshold under which exhumation is not achieved in mode I. Only one curve is displayed for mode III because its dip varies through time (initial dip is 90°). Dimensionless and dimensional (italic) units.

The total time necessary for the particle to reach the surface (Fig. 3) shows that mode III is much more efficient than mode I which on the contrary slows down the exhumation process. If the intrinsic particle velocity V_b is too small with respect to the corner flow velocities ($V_b < \sim 0.17 v_0$), mode I is unable to achieve the exhumation of the particle, as opposed to modes II and III that eventually drive the particle to the surface. In any mode, steep slabs are less prone to drive the particle upwards, but more drastically in mode II (Fig. 3). The differences in the timing of exhumation are related to the pathlines of the particles within the wedge velocity fields (Fig. 4). In mode I, the slab remains at its initial location.

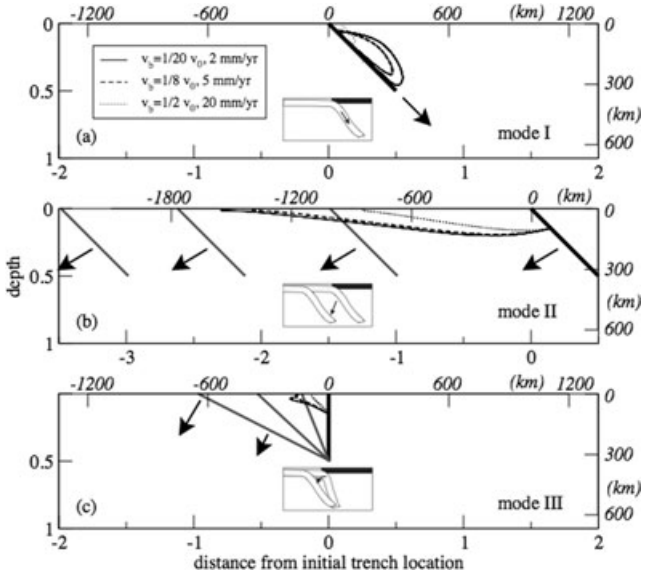

Figure 4. Flow lines for elementary rock units as a function of the ratio between intrinsic velocity of individual rock units V_b and subduction rate v_0 (1/20, solid curve; 1/8, dashed; 1/2, dotted. Dimensional values for $v_0 =$ 40 mm/yr). Arrows show slab motion. Bold black segment shows initial slab location, grey segments in modes II and III are the final locations. Overprinted path for $V_b = 1/20$ and $V_b = 1/8$ in mode I shows the multiple cycles. Dimensionless and dimensional (italic) units.

During subduction, the particles remain at a short distance from the slab until they reach the surface. But low buoyancy particles are in a first stage driven to large depths before they reach the surface. Because this result is inconsistent with the vast majority of observed maximum burial depths of presently outcropping rocks, it suggests that essentially very positively buoyant units can be exhumed in mode I. This nevertheless is in agreement with the fact that deeper exhumed rocks are rather of continental origin (e.g. Chopin 2003; Liou *et al.* 2004). Note that, as opposed to modes II and III for which brittle extension is expected at the surface, mode I can only fully achieve the burial–exhumation cycle if erosion is efficient enough.

Very low buoyancy (or neutrally buoyant) particles are not exhumed in mode I and remain in the mantle wedge cell (Fig. 1a). In modes II and III, the particles are gradually exhumed, and even low-buoyancy particles eventually reach the surface. Pathlines are shorter in mode III than in modes I and II (Fig. 4).

3.2 Delay of exhumation

Dimensional units make it easier to compare model results to natural examples, and we keep dimensional values in the following. The total delay of exhumation (Fig. 5) essentially depends on the buoyancy of the particle and the flow in the wedge. In an inactive subduction ($v_0 = 0$), the delay is simply D times V_b, where D is the initial depth of the particle. In the following, D is set to 100 km; because the velocity field tends to parallel the surface near surface level, we consider a depth of 6.5 km as the final depth (for otherwise total time tends to infinity if the particle has no intrinsic velocity); it also means that this final exhumation process needs to be attributed to another mechanism such as erosion or crustal extension (e.g. Yamato *et al.* 2008). Depending on the location of the particle in the wedge, the flow advects the particle with a variable vigour. It can either help or resist the ascension of the particle towards the surface. The combination often produces complex behaviours.

Mode I is almost systematically resisting: the faster the subduction, the longer the total time before exhumation (Fig. 5). If the intrinsic velocity of the particle cannot overcome the downward wedge flow, the particle permanently remains in the mantle wedge cell. In mode I, exhumation does not occur, even at low subduction rates, unless the particle has an intrinsic velocity V_b higher than ∼5 mm/yr (Fig. 6). Under some circumstances in mode I, the particle benefits from the upwelling mantle, or return flow (Fig. 1), that balances the downwelling effect. This is for instance outlined by the total time before exhumation of a particle that has an intrinsic velocity of 5 mm/yr in mode I (Fig. 5): for subduction rates that range from ∼22 mm/yr to ∼28 mm/yr the particle follows a peculiar pathline because it takes advantage of the return flow; as a consequence, the total delay of exhumation becomes shorter than for subduction rates lower than 22 mm/yr.

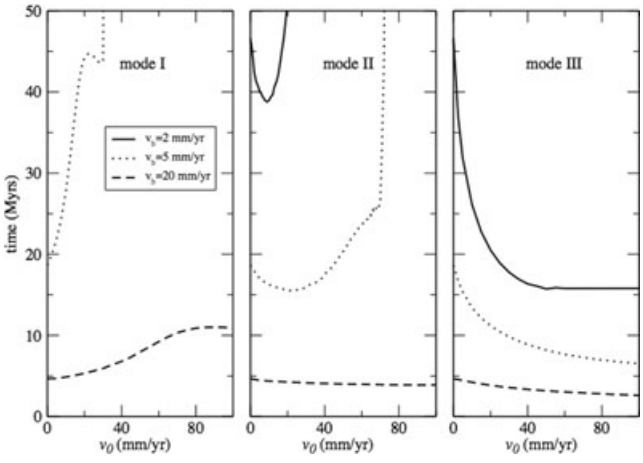

Figure 5. Total exhumation time for the three subduction modes, as a function of the intrinsic velocity of individual rock units V_b and subduction rate v_0. Dimensional units.

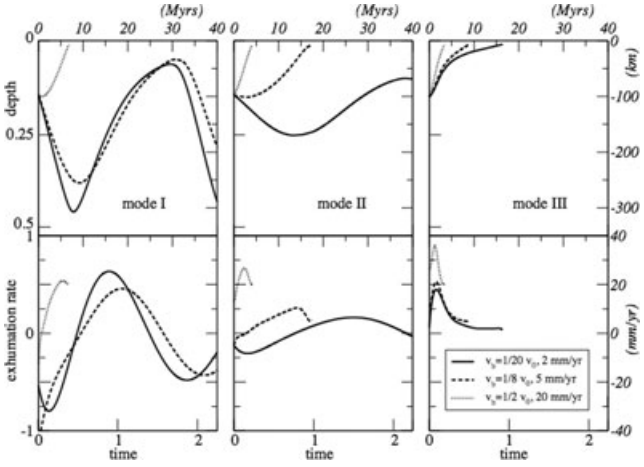

Figure 6. Burial depth (top) and exhumation rates (bot) of the rock units as a function of time and of the ratio between intrinsic velocity of individual rock units V_b and subduction rate v_0 (1/20, solid curve; 1/8, dashed; 1/2, dotted. Dimensional values for $v_0 = 40$ mm/yr). Dimensionless and dimensional (italic) units.

Mode II also shows a complex pattern (Fig. 5). Because at short distance from the slab the flow is downward, if subduction rates reach high values, the particle is dragged along with the slab and remains in the subduction cell. For instance, exhumation of a particle with an intrinsic velocity $V_b = 2$ mm/yr is fostered by subduction rates that are lower than ∼10 mm/yr, but higher rates increase the total exhumation delay. At rates higher than ∼28 mm/yr, the particle is never exhumed. Such scheme also holds for particles that have a higher intrinsic velocity: with $V_b = 5$ mm/yr, exhumation never occurs for subduction rates higher than ∼70 mm/yr.

Mode III is always helping exhumation. For a particle with $V_b =$ 2 mm/yr, the total delay of exhumation is divided by a factor 2 with a subduction rate of ∼10 mm/yr (from 50 to 25 m.yr between $v_0 =$ 0 mm/yr to $v_0 = 10$ mm/yr). A decrease in slab dip therefore very efficiently contributes to exhume HP rocks from depth.

3.3 Burial and exhumation

Because of these interactions between the vertical motion of a particle excited by its own intrinsic velocity and the wedge flow in which the particle is advected, the burial history is not monotonic (Figs 5 and 6). The most dramatic case is that of low buoyancy particles in mode I, that are stuck in the wedge cell. They are first driven to large depths before they are brought back to moderate depths and drown to large depths again, in a cyclic behaviour. The shape of the cell bounds the oscillation between depths of ∼300 and ∼50 km. The period of the cycle is controlled by the subduction rate v_0 (e.g. ∼30 m.yr for $v_0 = 40$ mm/yr). The vertical velocities are high (Fig. 6), comparable in magnitude to the tectonic velocities. In mode II, particles that have low intrinsic buoyancies are also caught in a comparable cyclic behaviour, although the vertical velocities are lower (<10 mm/yr) because the burial depths are

constrained within a thinner domain (between depths of ∼60 and ∼160 km). Such behaviour can be relevant to real Earth in the description of the wedge flow, but it would prevent the exhumation of HP rocks; of course, no observation can likely report such a pattern yet. Only if the positive buoyancy of the particle makes it overcome the advection in the wedge the particle reaches the surface. In that case, exhumation rates increase as the particles move away from the downwelling (see Fig. 1). The ascension eventually slows down as the particles approach the surface. Note that this is true in any mode because at surface level the velocity vectors tend to be parallel to the surface. In mode III, the vertical motion is always directed towards the surface, the larger the intrinsic velocity of the particle the faster it reaches the surface. With $v_0 = 40$ mm/yr, the fastest exhumation rates range between 20 and 40 mm/yr for particles with 2 mm/yr $< V_b <$ 20 mm/yr and gradually slow down to lower values as the particles approach the surface.

4 DISCUSSION

These models outline the first order behaviour of three subduction modes during the exhumation process of HP rocks. When the trench is stationary with respect to the lower mantle (mode I), the subduction zone is characterized by a powerful downwelling that drags to depth the HP rock aggregate released on the Benioff zone. It is therefore more efficient than any other mode to bury crustal material that may even be positively buoyant at large depths, but is rather inefficient to drive rocks to the surface except in cases implying high buoyancy material. Conversely, when the trench retreats during subduction (modes II and III), the wedge flow tends to advect the rock aggregate towards the surface. The vertical velocities can reach values that are comparable to tectonic velocities, that is, the velocity at which the plate subducts in the mantle. This result solves the apparent paradox based on observations that states that blueschists metamorphic rocks are often exhumed at a rate that is comparable to the rate at which the subduction panel enters the upper mantle (e.g. Thomson *et al.* 1998; Rubatto & Hermann 2001).

When trench retreat is associated to a decrease in slab dip (mode III, as opposed to mode II, where the slab uniformly retreats during subduction), the exhumation process is even more efficient. The timing of exhumation can typically be divided by a factor of two if the subduction rate increases from $v_0 = 0$ mm/yr to $v_0 =$ 40 mm/yr when mode III is excited. We conclude that slab rollback accompanied by a decrease in slab dip is the most efficient yet simple mechanism for HP rock exhumation, simply because it pumps material upwards. The closer to the surface, the more efficient this process is.

Because our simple models only address a single aspect of the exhumation process and neglect the rheological complexity of subduction zones, we emphasize that the qualitative results as well as the comparison of the models relative to each other hold, but the quantitative results should be considered with care, that is, as orders of magnitude. For instance, toroidal flow may decrease the vigour of the upward, poloidal flow, by a factor of 2 (Piromallo *et al.* 2006). Similarly, radial and lateral viscosity variations, or the presence of erosion, may distort our quantitative conclusions, but would not discard the return flow as a significant contributor for HP rocks exhumation. In our models the boundary conditions are that of a fixed upper plate, that is, backarc extension occurs when the trench retreats; changing the 'upper plate' boundary conditions to either free slip or fixed velocity (set to trench velocity) modifies the flow field (e.g. Yamato *et al.* 2009), but in a way that do not alter our conclusions because the upward flow near the surface is also close to the subducting slab. Our results indeed suggest that only slab rollback can provide enough power to drive the exhumation of rock aggregates that have low or neutral positive buoyancies at rates that are comparable to tectonic velocities, as inferred from P–T–t paths (e.g. Duchêne *et al.* 1997; Gebauer *et al.* 1997; Rubatto & Hermann 2001; Agard *et al.* 2009) and from the dynamics of real Earth systems (Brun & Faccenna 2008).

Our analysis compares models at a given subduction rate. However, because the buoyancy and viscosity structures of subducting plates are heterogeneous, subduction dynamics may vary significantly. Alternatively, the power—literally, the rate of energy spent to move the surrounding mantle around the slab—could have been used as a reference. Equal-power comparison would give slightly different results: mode II and mode III are the least and the most energy consuming regimes, respectively, possibly making mode II more efficient than mode III to advect HP rock aggregates towards the surface within a short delay. However, equal-power comparisons are not very satisfying either, because of the association of the modes to subduction velocities. For instance, mode III is likely associated to increasing subduction rates, for instance when a dense unit of oceanic lithosphere enters the subduction (e.g. Royden & Husson 2006). Likewise, mode I requires specific conditions that may slow down subduction.

The three modes are currently found on Earth, but mode I should be considered as an oddity, in which coincidentally the lower plate is pushed towards the upper plate at a rate that is equal to the subduction rate. A steady subduction is unlikely to prevail during the 20–40 Myr long burial–exhumation cycle. In many cases, in particular where subduction zones are narrow, the behaviour of the trenches and slabs are transient. Modes II and III would thus naturally occur more often than mode I. For instance, the termination of the subduction of the African plate beneath Eurasia is characterized by the many small-scale Mediterranean subduction zones in which the incoming lithosphere is heterogeneous, which leads to a chaotic behaviour of subduction zones, that may subsequently retreat, advance or remain stationary (e.g. Royden & Husson 2009). The Mediterranean subduction zones are remarkable in that sense. One can also establish similar observations for the SE Asian subduction zones assemblage. Complex settings like those, where subduction zones are believed to occur in a succession of different stages, generally yield HP rocks. Well-documented examples include the Tyrrhenian and Hellenic subduction zones (e.g. Jolivet *et al.* 2003), Oman (e.g. Breton *et al.* 2004) or Papua New Guinea (e.g. Baldwin *et al.* 2004). Conversely, modern blueschists and eclogites metamorphic rocks are seldom found in subduction zones that undergo a steadier regime, like the long-lived, massive circum Pacific subduction zones. Many of these examples where HP rocks outcrop—particularly the Mediterranean ones—also correspond to case studies for slab rollback (e.g. Malinverno & Ryan 1986; Royden 1993). This support the idea that slab rollback promotes exhumation for two reasons. The first reason is that the overriding plate is thinner: modes II and III that prevail during rollback drive the rock unit up to shallow depths before it hits the base of the upper plate. Only mild erosion and extension suffice for the final stage of exhumation. Our simplified model considers an upper plate of negligible thickness; this assumption holds for subduction zones where significant phase of trench retreat occurred prior to the release of the rock unit at depth. Nevertheless, the thickness of the overriding plate is thought to be thinner than 100 km, and generally about 60 km (Currie & Hyndman 2006) because of the effects of enhanced corner flow and slab dehydration (e.g. Arcay *et al.* 2006)

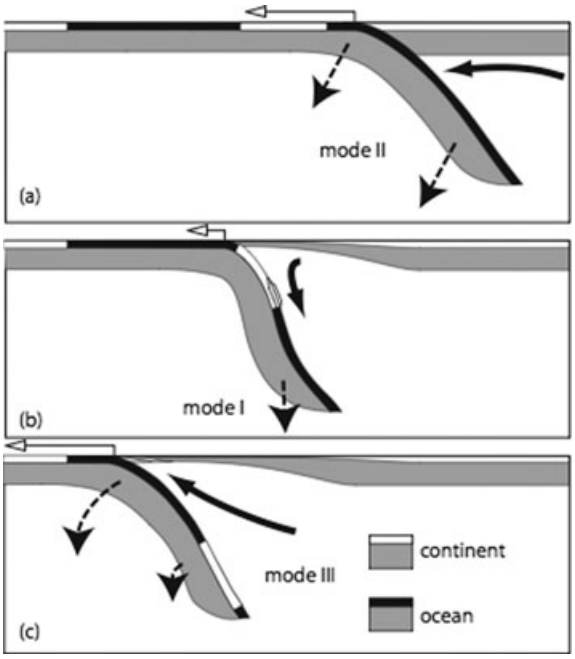

Figure 7. Sketch showing an episodic subduction triggering the burial–exhumation cycle of HP rocks. White arrow denotes trench migration rate, dashed arrows indicate slab motion and bold arrows show mantle flow.

and destabilization of the backarc lithosphere (Currie *et al.* 2008) and may tend to 0 km where backarc basins are active. Indeed, in the Mediterranean domain, overriding plates are thinned due to slab rollback (Royden 1993; Jolivet *et al.* 1994). Conversely there is, to our knowledge, no proven example where HP rocks are clearly associated with thick overriding lithospheres during the exhumation process: upper plates are thin in modern examples and older examples like the Alps or Himalayas are being debated. The second reason that we emphasize is that chaotic, or better-said episodic behaviour of subduction zones greatly promote the exhumation of HP rocks in a multi-stage story: following a subduction episode of dense oceanic lithosphere during which the trench retreats at a fast rate, in mode II (Fig. 7a); a fragment of less negatively buoyant continental lithosphere enters the subduction (Fig. 7b). The trench retreats slower and slab dip increases (although it seems counter intuitive, slab dip increases because negatively buoyant units at depth continue to sink, whereas the shallower, more buoyant units, resist subduction, Martinod *et al.* 2005; Royden & Husson 2006), entering mode I. The continental crust is buried and metamorphosed at high pressure and low temperatures. Because the wedge shears the Benioff zone and because the continental slices that are stacked in an aggregate of HP rocks have a constantly increasing upward force, the aggregate eventually detaches from the slab, at a depth at which shear stresses overcome the yield stress of the rock unit (e.g. Seno 2008). More negatively buoyant lithosphere enters the subduction and the slab rolls back again (Fig. 7c), and the dip of the slab decreases in mode III, inducing a wedge flow that triggers the exhumation of HP rocks from depth, with an upward velocity that is comparable to tectonic velocities and trench migration rate. The final exhumation stage is then promoted by the extensive strain in the upper plate. Throughout the entire cycle, the upper plate, therefore, never hampers the exhumation process. This cyclic episode can be followed by several other cycles that make it easy for HP rocks to be exhumed. More generally, any subduction zone that has a transient behaviour due to the presence of heterogeneities in the incoming lithosphere likely promotes the same mechanism.

ACKNOWLEDGMENTS

We are grateful to C. Beaumont and T. Gerya for their reviews, and G. Ernst for his comments on an earlier version of the manuscript. LH is funded by CNRS/INSU program SEDIT; PY thanks J. Braun for financial support from the ANR in Computational Geology.

REFERENCES

Agard, P. *et al*., 2006. Transient, synobduction exhumation of Zagros blueschists inferred from P-T, deformations, time, and kinematic constraints: implications for Neotethyan wedge dynamics, *J. geophys. Res.,* **111,** B11401, doi:10.1029/2005JB004103.

Agard, P., Yamato, P., Jolivet, L. & Burov, E., 2009. Exhumation of oceanic blueschists and eclogites in subduction zones: timing and mechanisms, *Earth Sci. Rev.,* doi:10.1016/j.earscirev.2008.11.002.

Allègre, C. *et al*., 1984. Structure and evolution of the Himalaya–Tibet orogenic belt, *Nature,* **307,** 17–22, doi:10.1038/307017a0.

Arcay, D., Doin, M.P., Tric, E., Bousquet, R. & de Capitani, C., 2006. Overriding plate thinning in subduction zones: localized convection induced by slab dehydration, *Geochem. Geophys. Geosyst.,* **7,** doi:10.1029/2005GC001061.

Baldwin, S., Monteleone, B.D., Webb, L.E., Fitzgerald, P.G., Grove, M. & Hill, E.J., 2004. Pliocene eclogite exhumation at plate tectonics rates in eastern Papua New Guinea, *Nature,* **431,** 263–267.

Beaumont, C., Ellis, S. & Pfiffner, A., 1999. Dynamics of sediment subduction-accretion at convergent margins: short-term modes, long term deformation, and tectonic implications, *J. geophys. Res.,* **104,** 17573–17601.

Boutelier, D., Chemenda, A. & Jorand, C., 2004. Continental subduction and exhumation of high-pressure rocks: insights from thermo-mechanical laboratory modelling, *Earth planet. Sci. Lett.,* **222,** 209–216.

Breton, J.-P., Béchennec, F., Le Métour, J., Moen-Maurel, L. & Razin, P., 2004. Eoalpine (Cretaceous) evolution of the Oman Tethyan continental margin: insights from a structural field study in Jabal Akhdar (Oman Mountains), *GeoArabia,* **9,** 1–18.

Brun, J.-P. & Faccenna, C., 2008. Exhumation of high-pressure rocks driven by slab rollback, *Earth planet. Sci. Lett.,* **272,** doi:10.1016/j.epsl.2008.02.038.

Burov, E., Jolivet, L., Le Pourhiet, L. & Poliakov, A., 2001. A thermomechanical model of exhumation of HP and UHP metamorphic rocks in Alpine mountain belts, *Tectonophysics,* **342,** 113–136.

Capitanio, F.A., Morra, G. & Goes, S., 2007. Dynamic models of downgoing plate-buoyancy driven subduction: subduction motions and energy dissipation, *Earth planet. Sci. Lett.,* **262,** 284–297.

Castro, A. & Gerya, T.V., 2007. Magmatic implications of mantle wedge plumes: experimental study, *Lithos,* **103,** 138–148.

Chemenda, A.I., Mattauer, M. & Bokun, A.N., 1996. Continental subduction and a mechanism for exhumation of high-pressure metamorphic rocks: new modeling and field data from Oman, *Earth planet. Sci. Lett.,* **143,** 173–182.

Chemenda, A.I., Mattauer, M., Malavieille, J. & Bokun, A.N., 1995. A mechanism for syn-collisional deep rock exhumation and associated normal faulting: results from physical modelling, *Earth planet. Sci. Lett.,* **132,** 225–232.

Chopin, C., 2003. Ultrahigh-pressure metamorphism: tracing continental crust into the mantle, *Earth planet. Sci. Lett.,* **212,** 1–14.

Cloos, M., 1982. Flow melanges: numerical modelling and geologic constraints on 299 their origin in the Franscican subduction complex, California, *Bull. Geol. Soc. Am.,* **93,** 330–345.

Currie, C.A. & Hyndman, R.D, 2006. The thermal structure of subduction zone backarcs, *J. geophys. Res.,* **111,** B08404, doi:10.1029/2005JB004024.

Currie, C.A., Huismans, R.S. & Beaumont, C., 2008. Thinning of continental backarc lithosphere by flow-induced gravitational instability, *Earth planet. Sci. Lett.,* **269,** 436–447.

De Sigoyer, J., Chavagnac, V., Blichert-Toft, J., Villa, I., Luais, B., Guillot, S., Cosca, M. & Mascle, G., 2000. Dating the Indian continental subduction and collisional thickening in the northwest Himalaya: multichronology of the Tso Morari eclogites, *Geology,* **28,** 487–490.

Duchêne, S., Lardeaux, J.M. & Albarède, F., 1997. Exhumation of eclogites: insights from depth-time path analysis, *Tectonophysics,* **280,** 125–140.

England, P.C. & Holland, T.J.B., 1979. Archimedes and the Tauern eclogites: the role of buoyancy in the preservation of exotic eclogite blocks, *Earth planet. Sci. Lett.,* **44,** 287–294.

Ernst, W.G., 2001. Subduction, ultrahigh-pressure metamorphism, and regurgitation of bouyant crustal slices — implications for arcs and continental growth, *Phys. Earth planet. Interiors,* **127,** 253–275.

Ernst, W.G., Maruyama, S. & Wallis, S., 1997. Buoyancy-driven, rapid exhumation of ultrahigh-pressure metamorphosed continental crust, *Proc. Natl. Acad. Sci.,* **94,** 9532–9537.

Faccenda, M., Minelli, G. & Gerya, T.V., 2009. Coupled and decoupled regimes of continental collision: numerical modeling, *Earth planet. Sci. Lett.,* **278,** 337–349.

Faccenna, C., Jolivet, L., Piromallo, C. & Morelli, A., 2003. Subduction and the depth of convection in the Mediterranean mantle, *J. geophys. Res.,* **108**(B2), 2099, doi:10.1029/2001JB001690.

Funiciello, F., Faccenna, C., Giardini, D. & Regenauer-Lieb, K., 2003. Dynamics of retreating slabs: 2. Insights from three-dimensional laboratory experiments, *J. geophys. Res.,* **108**(B4), 2207, doi:10.1029/2001JB000896.

Garfunkel, Z., Anderson, C.A. & Schubert, G., 1986. Mantle circulation and the lateral migration of subducted slabs, *J. geophys. Res.,* **91,** 7205–7223.

Gebauer, D., Schertl, H.P., Brix, M. & Schreyer, W., 1997. 35 Ma old ultrahigh-pressure metamorphism and evident for very rapid exhumation in the Dora Maira Massif, Western Alps, *Lithos,* **41,** 5–24.

Gerya, T.V., Stöckert, B. & Perchuk, A.L., 2002. Exhumation of high-pressure metamorphic rocks in a subduction channel: a numerical simulation, *Tectonics,* **21**(6), 1056, doi:10.1029/2002TC001406.

Gerya, T.V. & Stoeckhert, B., 2002. Exhumation rates of high pressure metamorphic rocks in subduction channels: the effect of rheology, *Geophys. Res. Lett.,* **29**(8), 1261, doi:10.1029/2001GL014307.

Gerya, T.V. & Yuen, D.A., 2003. RayleighTaylor instabilities from hydration and melting propel ''cold plumes'' at subduction zones, *Earth planet. Sci. Lett.,* **212,** 47–62.

Gorczyk, W., Guillot, S., Gerya, T.V. & Hattori, K., 2007. Asthenospheric upwelling, oceanic slab retreat and exhumation of UHP mantle rocks: insights from Greater Antilles, *Geophys. Res. Lett.,* **34,** L21309, doi:10.1029/2007GL031059.

Guillot, S., Schwartz, S., Hattori, K., Auzende, A. & Lardeaux, J., 2004. The Monviso ophiolitic Massif (Western Alps), a section through a serpentinite subduction channel, *J. Virtual Explorer,* **16,** paper 3.

Hacker, B.R., Andersen, T.B., Root, D.B., Mehl, L., Mattinson, J.M. & Wooden, J.L., 2003. Exhumation of high-pressure rocks beneath the Solund Basin, Western Gneiss Region of Norway, *J. Metamorph. Geol.,* **21,** 613–629.

Hall, P.S. & Kincaid, C., 2001. Diapiric flow at subduction zones: a recipe for rapid transport, *Science,* **292,** 2472–2475.

Handy, M.R., Franz, L., Heller, F., Janott, B. & Zurbriggen, R., 1999. Multistage accretion and exhumation of the continental crust (Ivrea crustal section, Italy and Switzerland), *Tectonics,* **18,** 1154–1177.

Jolivet, L., Daniel, J.M., Truffert, C. & Goffé, B., 1994. Exhumation of deep crustal metamorphic rocks and crustal extension in back-arc regions. *Lithos,* **33,** 3–30.

Jolivet, J., Faccenna, C., Goffé, B., Burov, E. & Agard, P., 2003. Subduction tectonics and exhumation of high-pressure metamorphic rocks in the Mediterranean orogens, *Am. J. Sci.,* **303,** 353–409.

Jolivet, L. *et al*., 2008. Subduction, convergence and the mode of backarc extension in the Mediterranean region. *Bull. Soc. Géol. France,* **179,** 525–550.

Lallemand, S., Heuret, A. & Boutelier, D., 2005. On the relationships between slab dip, back-arc stress, upper plate absolute motion, and crustal nature in subduction zones, *Geochem. Geophys. Geosyst.,* **6,** Q09006, doi:10.1029/2005GC000917.

Liou, J.G., Tsujimori, T., Zhang, R.Y., Katayama, I. & Maruyama, S., 2004. Global UHP metamorphism and continental subduction/collision: the Himalaya model. *Int. Geol. Rev.,* **46,** 1–27.

Malinverno, A. & Ryan, W.B.F., 1986. Extension of the Tyrrhenian Sea and shortening in the Apennines as result of a migration driven by sinking lithosphere, *Tectonics,* **5,** 227–245.

Manea, V.C., Manea, M., Kostoglodov, V. & Sewell, G., 2005. Thermomechanical model of the mantle wedge in Central Mexican subduction zone and a blob tracing approach for the magma transport, *Phys. Earth Planet. Inter.,* **149,** 165–186.

Martinod, J., Funiciello, F., Faccenna, C., Labanieh, S. & Regard, V., 2005. Dynamical effects of subducting ridges: insights from 3-D laboratory models, *Geophys. J. Int.,* **163,** 1137–1150, doi:10.1111/ j.1365-246X.2005.02797.x.

Maruyama, S., Liou, J.G. & Terabayashi, M., 1996. Blueschists and eclogites of the world, and their exhumation, *Int. Geol. Rev.,* **38,** 458–594.

Parra, T., Vidal, O. & Jolivet, L., 2002. Relation between the intensity of defor mation and retrogression in blueschist metapelites of Tinos Island (Greece) evidenced by chlorite–mica local equilibria, *Lithos,* **63,** 41–66.

Piromallo, C., Becker, T.W., Funiciello, F. & Faccenna, C., 2006. Three-dimensional instantaneous mantle flow induced by subduction, *Geophys. Res. Lett.,* **33,** L08304, doi:10.1029/2005GL025390.

Pfiffner, O.A., Ellis, S. & Beaumont, C., 2000. Collision tectonics in the Swiss Alps: insight from geodynamic modeling, *Tectonics,* **19,** 1065–1094.

Platt, J.P., 1986. Dynamics of orogenic wedges and the uplift of high-pressure metamorphic rocks, *Geol. Soc. Am. Bull.,* **97,** 1037–1053.

Platt, J.P., 1993. Exhumation of high-pressure rocks: a review of concept and processes, *Terra Nova,* **5,** 119–133.

Ring, U., Brandon, M.T., Willett, S. & Lister, G.S., 1999. Exhumation processes, in *Exhumation Processes: Normal faulting, ductile flow and erosion,* pp. 1–28, eds Ring, U., Brandon, M.T., Lister, G.S. & Willett, S., Special Publications Geological Soc., London.

Rosenbaum, G. & Lister, G.S., 2005. The Western Alps from the Jurassic to Oligocene: spatio-temporal constraints and evolutionary reconstructions, *Earth. Sci. Rev.,* **69,** 281–306.

Royden, L., 1993. Evolution of retreating subduction boundaries formed during continental collision, *Tectonics,* **12,** 629–638.

Royden, L. & Husson, L., 2006. Trench motion, slab geometry and viscous stresses in subduction systems, *Geophys. J. Int.,* **167,** 881–905, doi:10.1111/424 j.1365-246X.2006.03079.x.

Royden, L. & Husson, L. 2009. Subduction with variations in slab buoyancy: models and application to the Banda and Apennine systems, in *Subduction Zone Geodynamics, Frontiers in Earth Sciences,* Springer-Verlag, Berlin, doi:10.1007/978-3-540-87974-9.

Rubatto, D. & Hermann, J., 2001. Exhumation as fast as subduction? *Geology,* **29,** 3–6.

Seno, T., 2008. Conditions for a crustal block to be sheared off from the subducted continental lithosphere: what is an essential factor to cause features associated with collision?, *J. geophys. Res.,* **113,** B04414, doi:10.1029/2007JB005038.

Shreve, R.L. & Cloos, M., 1986. Dynamics of sediment subduction, melange formation, and prism accretion, *J. geophys. Res.,* **91,** 10229–10245.

Stampfli, G.M., 2000. Tethyan oceans, *Geol. Soc. London Spec. Publ.,* **173,** 1–23.

Stegman, D.R., Freeman, J., Schellart, W.P., Moresi, L. & May D., 2006. Influence of trench width on subduction hinge retreat rates in 3-D models of slab rollback, *Geochem. Geophys. Geosyst.,* **7,** Q03012, doi:10.1029/2005GC001056.

Thomson, S.N., Stockhert, B. & Brix, M.R., 1998. Thermochronology of the high-pressure metamorphic rocks of Crete, Greece: implications for the speed of tectonic processes, *Geology,* **26,** 259–262.

Warren, C., Beaumont, C. & Jamieson, R.A., 2008. Modelling tectonic styles and ultra-high pressure (UHP) rock exhumation during the transition

from oceanic to continental collision, *Earth planet. Sci. Lett.,* **267,** 129–145.

Yamato, P., Agard, P., Burov, E., Le Pourhiet, L., Jolivet, L. & Tiberi, C., 2007. Burial and exhumation in a subduction wedge: mutual constraints from thermomechanical modeling and natural P-T-t data (Sch. Lustrés, W. Alps), *J. geophys. Res.,* **112,** B07410, doi:10.1029/2006JB004441.

Yamato, P., Burov, E., Agard, P., Le Pourhiet, L. & Jolivet, L., 2008. HP-UHP exhumation during slow continental subduction: self-consistent thermodynamically and thermomechanically coupled model with application to the Western Alps, *Earth planet. Sci. Lett.,* **271,** 63–74, doi:10.1016/j.epsl.2008.03.049.

Yamato, P., Husson, L., Braun, J., Loiselet, C. & Thieulot, C., 2009. Influence of surrounding plates on 3D subduction dynamics, *Geophys. Res. Lett.,* **36,** L07303, doi:10.1029/2008GL036942.

Walsh, E.O. & Hacker, B.R., 2004. The fate of subducted continental margins: two-stage exhumation of the high-pressure to ultrahigh-pressure Western Gneiss Region, Norway, *J. Metamorphic Geol.,* **22,** 671–687.

Geochemistry Geophysics Geosystems G3

Article
Volume 11, Number 8
20 August 2010
Q08016, doi:10.1029/2010GC003172
ISSN: 1525-2027

Published by AGU and the Geochemical Society

Subducting slabs: Jellyfishes in the Earth's mantle

Christelle Loiselet
Géosciences Rennes, UMR 6118, Université de Rennes 1, CNRS, F-35042 Rennes, France

Now at Mineral Resources Division, BRGM, 3 avenue Claude Guillemin, BP 6009, F-45060 Orleans CEDEX 2, France (c.loiselet@brgm.fr)

Jean Braun
Géosciences Rennes, UMR 6118, Université de Rennes 1, CNRS, F-35042 Rennes, France

Now at Laboratoire de Géodynamique des Chaînes Alpines, Université Joseph Fourier de Grenoble, F-38041 Grenoble, France (jean.braun@bvra.ujf-grenoble.fr)

Laurent Husson
Géosciences Rennes, UMR 6118, Université de Rennes 1, CNRS, F-35042 Rennes, France

Also at Laboratoire de Planétologie et Géodynamique de Nantes, UMR 6112, CNRS, F-44322 Nantes, France (laurent.husson@univ-rennes1.fr)

Christian Le Carlier de Veslud
Géosciences Rennes, UMR 6118, Université de Rennes 1, CNRS, F-35042 Rennes, France (christian.le-carlier@univ-rennes1.fr)

Cedric Thieulot
Department of Earth Science, University of Bergen, N-5020 Bergen, Norway (cedric.thieulot@geo.uib.no)

Philippe Yamato
Géosciences Rennes, UMR 6118, Université de Rennes 1, CNRS, F-35042 Rennes, France (philippe.yamato@univ-rennes1.fr)

Djordje Grujic
Department of Earth Sciences, Dalhousie University, Halifax, Nova Scotia B3H 4J1, Canada (dgrujic@dal.ca)

[1] The constantly improving resolution of geophysical data, seismic tomography and seismicity in particular, shows that the lithosphere does not subduct as a slab of uniform thickness but is rather thinned in the upper mantle and thickened around the transition zone between the upper and lower mantle. This observation has traditionally been interpreted as evidence for the buckling and piling of slabs at the boundary between the upper and lower mantle, where a strong contrast in viscosity may exist and cause resistance to the penetration of slabs into the lower mantle. The distribution and character of seismicity reveal, however, that slabs undergo vertical extension in the upper mantle and compression near the transition zone. In this paper, we demonstrate that during the subduction process, the shape of low viscosity slabs (1 to 100 times more viscous than the surrounding mantle) evolves toward an inverted plume shape that we coin *jellyfish*. Results of a 3D numerical model show that the leading tip of slabs deform toward a rounded head skirted by lateral *tentacles* that emerge from the sides of the *jellyfish* head. The head is linked to the body of the subducting slab by a thin tail. A complete parametric study reveals that subducting slabs may achieve a variety of shapes, in good agreement

with the diversity of natural slab shapes evidenced by seismic tomography. Our work also suggests that the slab to mantle viscosity ratio in the Earth is most likely to be lower than 100. However, the sensitivity of slab shapes to upper and lower mantle viscosities and densities, which remain poorly constrained by independent evidence, precludes any systematic deciphering of the observations.

Components: 13,000 words, 11 figures, 2 tables.

Keywords: subduction; slab viscosity; mantle stratification; seismic tomography.

Index Terms: 8170 Tectonophysics: Subduction zone processes (1031, 3060, 3613, 8413); 8148 Tectonophysics: Planetary volcanism (5480, 8450); 0545 Computational Geophysics: Modeling (1952, 4255).

Received 13 April 2010; **Revised** 8 June 2010; **Accepted** 23 June 2010; **Published** 20 August 2010.

Loiselet, C., J. Braun, L. Husson, C. Le Carlier de Veslud, C. Thieulot, P. Yamato, and D. Grujic (2010), Subducting slabs: Jellyfishes in the Earth's mantle, *Geochem. Geophys. Geosyst.*, *11*, Q08016, doi:10.1029/2010GC003172.

1. Introduction

[2] The wide range of shapes observed among subducting oceanic lithospheres [*Isacks and Molnar*, 1971; *Kárason*, 2002; *Li et al.*, 2008] suggests a complex dynamical behavior for the penetration of slabs into the mantle. The lack of earthquake activity below 700 km depth and the compressive nature of the focal mechanisms of the deep earthquakes along the surface of the slabs have been interpreted as an effect of the resistance of slabs to penetration into the lower mantle [*Isacks and Molnar*, 1971]. Such observations are at least compatible with dynamic models of the long wavelength geoid anomalies associated with slabs requiring an increase in viscosity from the upper to the lower mantle by a factor 10–100 [*Hager and Richards*, 1989; *Lambeck and Johnston*, 1998; *Moresi and Gurnis*, 1996; *Peltier*, 1996; *Ricard et al.*, 1993] or more [*Kido and Cadek*, 1997]. But travel time tomography has also revealed that positive seismic anomalies attributed to slabs often extend into the lower mantle [*Creager and Jordan*, 1986; *Grand*, 1994; *Jordan*, 1977; *Jordan and Lynn*, 1974]. In the last decade, images from seismic tomography have improved in resolution and accuracy, and have revealed that slabs tend to thicken during penetration into the lower mantle, i.e., from the transition zone to mid-mantle depths [*Bijwaard et al.*, 1998; *Fukao et al.*, 2001; *Grand et al.*, 1997]. Examples thereof include the Central and South Americas [*Ren et al.*, 2007], southern Asia [*Kárason*, 2002; *Li et al.*, 2008] or the Hellenic slab [*Piromallo and Morelli*, 2003; *Wortel and Spakman*, 2000]. Slab thickening in the mid-lower mantle is often interpreted as evidence for periodic buckling of cold and stiff lithosphere as it penetrates into the mantle [*Gaherty and Hager*, 1994; *Guillou-Frottier et al.*, 1995; *Loubet et al.*, 2009; *Ribe et al.*, 2007]. However, the deformation of slabs going sinking through the mantle has also been interpreted as evidence that subducting plates could be very weak [*Bevis*, 1986; *Čížková et al.*, 2002; *Giardini and Woodhouse*, 1984; *Tao and O'Connell*, 1993]. Indeed, although they have not emphasized this aspect before, previous authors [e.g., *Christensen and Yuen*, 1984; *Zhong and Gurnis*, 1995; *Funiciello et al.*, 2003] do simulate (via numerical and analog modeling) comparable spherical shapes for weak descending plates. Only *Kárason* [2002] effectively associated the seismically observed morphology of slabs penetrating into the deep mantle to that of a thickened isoviscous slabs. He showed that the thickening of weak subducting slabs changes systematically with the viscosity contrast between the upper and lower mantles.

[3] Furthermore, the viscosity of the subducting plate strongly influences plate deformation and therefore its dynamics. In the literature, the range of assumed and predicted viscosity ratios between the slab and the surrounding mantle is large, comprised between 10^6 [*Kincaid and Griffiths*, 2003] and 1 [*Husson*, 2006; *Kárason*, 2002]. The values used in recent models are comprised between 10^2 and 10^3 [*Clark et al.*, 2008; *Faccenna et al.*, 2001; *Funiciello et al.*, 2003; *Schellart*, 2004; *Stegman et al.*, 2006; *Yamato et al.*, 2009]. Previous work from *Loiselet et al.* [2009] suggested that the viscosity ratio should be smaller than 10^2.

[4] In view of these most recent estimates of the viscosity ratio between the subducting plate and the surrounding mantle, we expanded on *Kárason*'s

[2002] work, exploring the possibility that a plate sinking into the mantle deforms and naturally thickens at mid-depths, without the need for a stiff lithosphere or a viscosity or density jump in the lower mantle. To demonstrate this point, we investigate here the role of the viscosity ratio between the plate and the surrounding fluid and, subsequently, the role of mantle stratification (corresponding to a viscosity or density jump) in forming a wide range of shapes, ranging from that of an undeformed slab to the characteristic shape of a downwelling plume that we refer to as a *jellyfish*. In the latter part of this paper, we further discuss our results in light of observed slab geometries, which we extract from seismic tomography images.

2. Methodology

[5] In order to explore the dynamic interactions between the subducting lithosphere and the surrounding viscous mantle, we evaluate the deformation pattern of a slab sinking into the mantle by means of a three-dimensional numerical model that is designed to track sharp, dynamically deforming interfaces. The 3D finite element code *DOUAR* [*Braun et al.*, 2008] solves for the conservation equations for mass, momentum and energy in the Boussinesq approximation, assuming that the mantle is an incompressible viscous medium. *DOUAR* is an ALE (Arbitrary Lagrangian Eulerian) Finite Element code based on an adaptive octree grid [*Thieulot et al.*, 2008] that is highly suited to solve geometry problems in three dimensions. An octree is the simplest hierarchical division of the unit cube into smaller cubes, obtained by dividing, where higher resolution is required, each cube into 8 smaller cubes, up to a given or desired resolution. The smallest or undivided cubes are called the "leaves" of the octree. In *DOUAR*, the computational domain is therefore a unit cube, the finite elements are the leaves of the octree and their density is adapted to represent the various material, density and viscosity interfaces with optimum accuracy. The flow is driven by the internal density difference $\Delta\rho$ between the subducting lithosphere and the surrounding mantle. We simplify our analysis by assuming an infinite Prandtl number in a fluid with very low Reynolds number (Re = 0) and a linear rheology for all components of the system. Under such conditions, the velocity field $\boldsymbol{u}$ and pressure p obey the following simplified form of Navier–Stokes equations, referred to as the Stokes equations:

$$\nabla.\mu\left(\nabla\mathbf{u}+\nabla\mathbf{u}^{\mathrm{T}}\right)-\nabla\mathrm{p}=\rho\mathbf{g} \tag{1}$$

and

$$\nabla.\mathbf{u}=0 \tag{2}$$

where ρ is the density, g the gravitational acceleration, p the pressure field, μ the dynamic viscosity and $\boldsymbol{u}$ the velocity.

[6] Interfaces (between the slab, upper mantle and lower mantle) are advected by using the computed velocity field and are tracked by a dual method combining Lagrangian particles for accuracy and level set functions for efficiency (see *Braun et al.* [2008] for further details on this method).

[7] The model setup is shown in Figure 1a and parameters are given in Table 1. The computational numerical domain is a unit cube (i.e., $1 \times 1 \times 1$ in x, y, z directions) representing a ~2750 km Cartesian box, corresponding to the Earth's mantle. The mantle is divided between an upper and lower mantle where a material discontinuity (i.e., that is advected with the flow) is imposed at $z_{660} = 0.24$ (~660 km). The grid counts $(64)^3$ (or level 6 octree) regularly spaced elements (or leaves) everywhere but in and around the slab where the resolution is increased to level 8, i.e., the element size is 1/256 of the size of the unit cube. Free slip is assumed on all boundaries. The experiment is initiated by placing a vertical (unless otherwise specified) plate of length, l = 0.066 (~182 km) and thickness h = 0.03 (~83 km) in the mantle between depths of 0.03 and 0.096 (~83 km to 264 km, Figure 1a).

[8] To ensure that the plate falling is controlled only by the buoyancy forces arising from the density contrast and by the viscosity ratio between the plate and the surrounding viscous fluid, the velocity at the top boundary of the plate is not fixed (i.e., not set to zero for the calculation of the velocity field). For the same raison, the top boundary of the slab is not attached to the top of the model box where the velocity component in the z-direction vanishes (free-slip conditions). However, since the slab is considered "infinite" in our simulation, slab material is constantly added from the top. To simulate that, we do not update the geometry of the upper boundary of the slab from the computed velocity field, such that it stays at the same level through time (i.e., at z = 0.03 from the top of the model box). Consequently, plate volume increases with time. In this way we discard any resistance to sinking that may arise in nature from the relative horizontal movement between the plate and the mantle. We assign a constant density contrast between the slab and the surrounding mantle. All viscosities are Newtonian and uniform within the slab and the

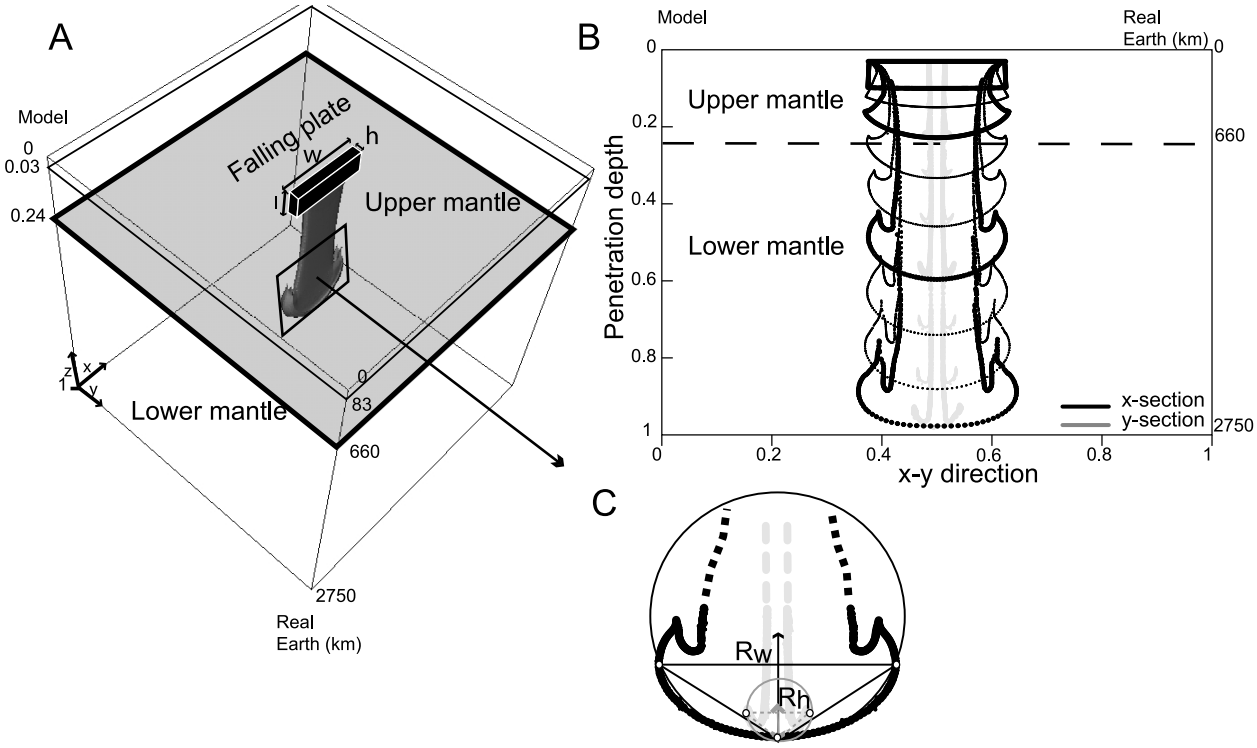

Figure 1. Reference model. (a) Model setup and variables: h is plate thickness, w is plate width, l is initial plate penetration. The black parallelepiped is the initial slab geometry and the gray body is a typical slab shape after subduction to mid-depth. (b) x- (black) and y- (gray) cross-section series of the plate at different stages (uniform time steps). Bold profiles denote notable stages (see text). (c) Vertical cross section along the x- (black) and y- (gray) sections of the leading edge of the subducting plate. R_w (black) (measured along the width w of the plate) and R_h (gray) (measured along its thickness h) give the radii of the circles that circumscribe the dotted triangles.

mantle; the upper mantle viscosity is taken as the reference viscosity (= 1). More complex rheologies may prevail in nature, especially rheologies that account for the influence of temperature on viscosity [e.g., *Billen and Gurnis*, 2005], but we chose to keep the model as simple as possible in order to quantify its behavior as a function of the effective slab to mantle viscosity ratio that we vary from $\mu_s = 0.01$ to

Table 1. Parameters Used in the Models

Description	Parameter	Model	Nature
		Slab	
Thickness	h	0.03	~83 km
Width	w	0.125/0.25[a]/0.5	344/688/1375 km
Dip angle	α	90[a]/70/45/30	90[a]/70/45/30
Density	ρ_s	0.1024	~3328 kg. m^{-3}
Viscosity ratio	μ_s	$10^{-2}/10^{0}/10^{1a}/10^{2}$	$10^{-2}/10^{0}/10^{1a}/10^{2}$
Uniform octree level	L_s	8 (0.0039)	~10.72 km
		Upper Mantle	
660 km boundary	z_{660}	0.24	660 km
Density	ρ_{um}	0.1	~3250 km.m^{-3}
Viscosity	μ_{um}	1	2.10^{-20}
Uniform octree level	L_{um}	6 (0.0156)	~43 km
		Lower Mantle	
Density	ρ_{lm}	0.1[a]/0.1012/0.1024/0.1032	~3250[a]/3289/3328/3434 kg.m^{-3}
Viscosity ratio	μ_l	$10^{0a}/10^{1}/10^{2}/10^{3}$	$10^{0a}/10^{1}/10^{2}/10^{3}$
Uniform octree level	L_l	6 (0.0156)	~43 km

[a]Reference value.

100. In our study, plate width, w, and initial slab dip, α, are also varied between 1/8, 1/4, and 1/2 of the box width and 90, 70, 60, 45 and 30° respectively.

3. Results

[9] We performed a series of 27 experiments to explore the dependence of the slab deformation on slab to lower mantle density contrast $\Delta\rho$, slab width w, slab dip α, slab to mantle viscosity ratio μ_s, and lower to upper mantle viscosity ratio μ_l. Some interesting features prevail regardless of the parameter values that we review below. To illustrate this point, we first show the results of a simple experiment (reference model) in which the plate viscosity is 10 times that of the upper mantle and where there is no viscosity or density contrast between the upper and lower mantle. The initial plate width is 0.25 (i.e., 1/4 of the box width) and the slab is vertical.

3.1. General Evolution of the Models

[10] During the sinking of the plate into the mantle, its shape evolves in a comparable way, to a large extent, to that of a reverse or descending plume (Figures 1a and 1b) [*Christensen and Yuen*, 1984; *Kárason*, 2002]. Note however that in most of our models the viscosity ratio is inverted in comparison to that of a typical rising mantle plume, which is characterized by a lower viscosity than the surrounding mantle. The shape of the slab is characterized by a rounded head at its leading tip, with two trailing "tentacles" along each narrow edge (Figure 1b), and connected to the surface by a long rectangular section tail. The initial rectangular shape probably promotes the development of the tentacles, but even when using plates with smooth edges, they still form. To a minor extent, the mantle also drags the longer edges and gently wraps them over the body of the slab (Figure 1b). In the following, we refer to the deformed shape of the slab as that of a *jellyfish*, for both our model slabs and real jellyfishes are characterized by comparable shapes that should minimize the viscous dissipation of energy while they move through the fluid. The jellyfish shape can be characterized by the longitudinal radius of curvature R_w and the lateral radius of curvature R_h (see Figure 1c). In practice, to calculate R_w and R_h, we compute the equation of the circle that circumscribes the triangle defined by the three vertices made by the leading tip (deepest point of the greatest z-value) and the two tips of the tentacles in the longitudinal direction (points of maximum and minimum x-value for R_w and y-value for R_h,). To further characterize the shape of the jellyfish and the flow it engenders in the mantle, we compute for each of the numerical experiments: (a) the velocity of the jellyfish head (measured on the slab at its maximum z-position) and its radius of curvature, (b) the maximum strain rate along the central vertical axis z, (c) the surface area of horizontal sections of the plate (distant by 0.03) as a function of depth and (d) the total viscous dissipation in the mantle.

[11] During the initial stages of subduction, the slab head becomes wider, thicker and curved (Figures 1b and 2a). The sinking velocity (measured at the jellyfish head) increases with plate deformation (Figure 2a). The radius of curvature R_w decreases rapidly (Figure 2b) as the slab tip evolves from a straight horizontal edge into a curved body. During this phase both the strain rate (Figure 3a) and the viscous dissipation in the mantle (Figure 3b) increase rapidly. When the slab tip reaches depths of 0.2 to 0.4, the head of the jellyfish is fully developed and an optimal curvature has been reached as indicated by the steady minimal value for R_w (Figure 2b).

[12] As the slab further penetrates into the mantle, the ratio between the lateral and longitudinal radii increases (Figure 2b), suggesting that the jellyfish head shape evolves toward a sphere (i.e., the radius of curvature is the same in all directions). During this stage, the sinking velocity continues to increase toward a maximum value (Figure 2a), yet the strain rate and mantle viscous dissipation remain steady (Figures 3a and 3b). In fact, once the jellyfish head is formed, only the "tentacles" continue to grow (Figure 1b). A neck forms above the jellyfish head, along the tail connecting the head to the surface (Figure 1b), its area remaining constant. At this stage, the jellyfish head area is respectively 1.5 and 2 times larger than the maximum (which is at the surface) and minimum (at the neck) surface areas of the tail (Figure 3d). According to the distribution of vertical strain (Figure 3c), the tail is lengthened near the surface while the head is shortened at depth (Figure 3c). Consequently, the head perimeter is as enlarged as the tail is thinned with respect to the original dimension of the slab before subduction. The final stage of evolution of the shape of the slab reflects the interaction of the jellyfish with the bottom of the box. The sinking velocity decreases to zero and the jellyfish head flattens.

[13] In the following paragraphs, we show how this general scheme is modulated by variable setup geometries and key parameters, in order to under-

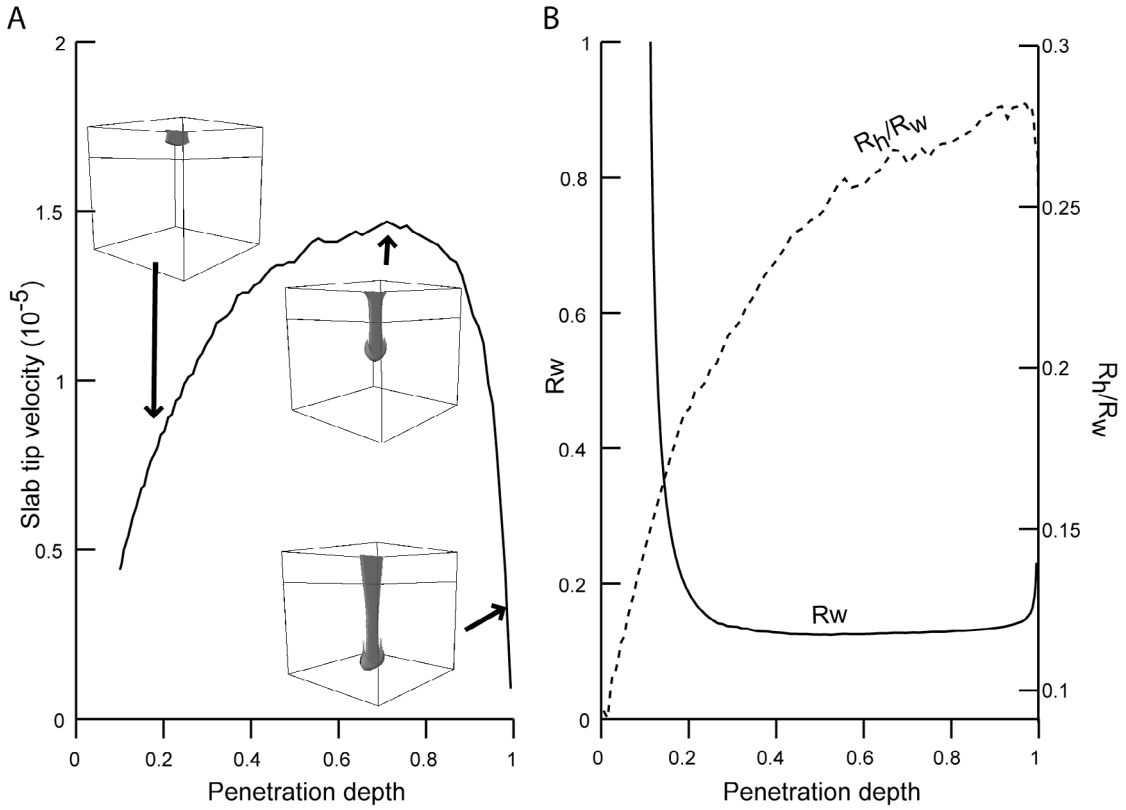

Figure 2. Reference model. (a) Velocity of the slab head as a function of penetration depth. (b) Radius of curvature R_w of the slab head across the x-profile (solid) and ratio between lateral (R_h) to longitudinal (R_w) radii of curvature of the jellyfish head (dashed).

stand the processes that control the behavior of the slab as it penetrates into the mantle.

3.2. Slab Width

[14] Plate width is known to influence the kinematics of subduction [*Di Giuseppe et al.*, 2008; *Loiselet et al.*, 2009; *Piromallo et al.*, 2006; *Schellart et al.*, 2007]. We evaluate its impact on the shape of the jellyfish by varying the plate width w between 0.125 and 0.5 (1/8 and 1/2 of the box width) while leaving the box size and plate thickness unchanged. Results show that, in all cases, the radius of curvature R_w of the jellyfish head decreases through time and tends toward a minimal value (Figure 4a). When normalized to slab width w and slab thickness h, R_w reaches a value comprised within a narrow range (~3/4) proportional to the sum of the width and thickness, i.e., the jellyfish head evolves toward a locally regular, spherical shape with a diameter proportional to 1.5 * (w+h). This is better illustrated by considering the R_h/R_w ratio (Figure 4b), which increases with slab penetration. Of course, the ratio between the initial slab width and thickness influences the curvature of the jellyfish head. If the plate has an initial square horizontal cross section, the slab diameter tends to 1 and R_w is always equal to R_h. Implicitly, the rate of formation of the jellyfish shape depends on the initial plate shape (i.e., w/h ratio): a narrow plate adopts the jellyfish shape faster than a wide plate.

3.3. Slab Dip

[15] In most natural cases, subduction does not initiate vertically: slabs tend to dip at a finite angle underneath the overriding plate. We explore the impact of slab dip on the jellyfish evolution by varying its value between 30 and 90°. Boundary conditions are the same as for the reference model. In Figure 5, we present results from two experiments, characterized by slab dips of 60 and 30°, respectively. The radius of the jellyfish head decreases and tends toward a minimal R_w value, regardless of the initially imposed slab dip. However, the morphology gets highly asymmetrical for shallow dipping slabs and the jellyfish shape transforms into a spoon shape (Figures 5a and 5b). Note that in our numerical

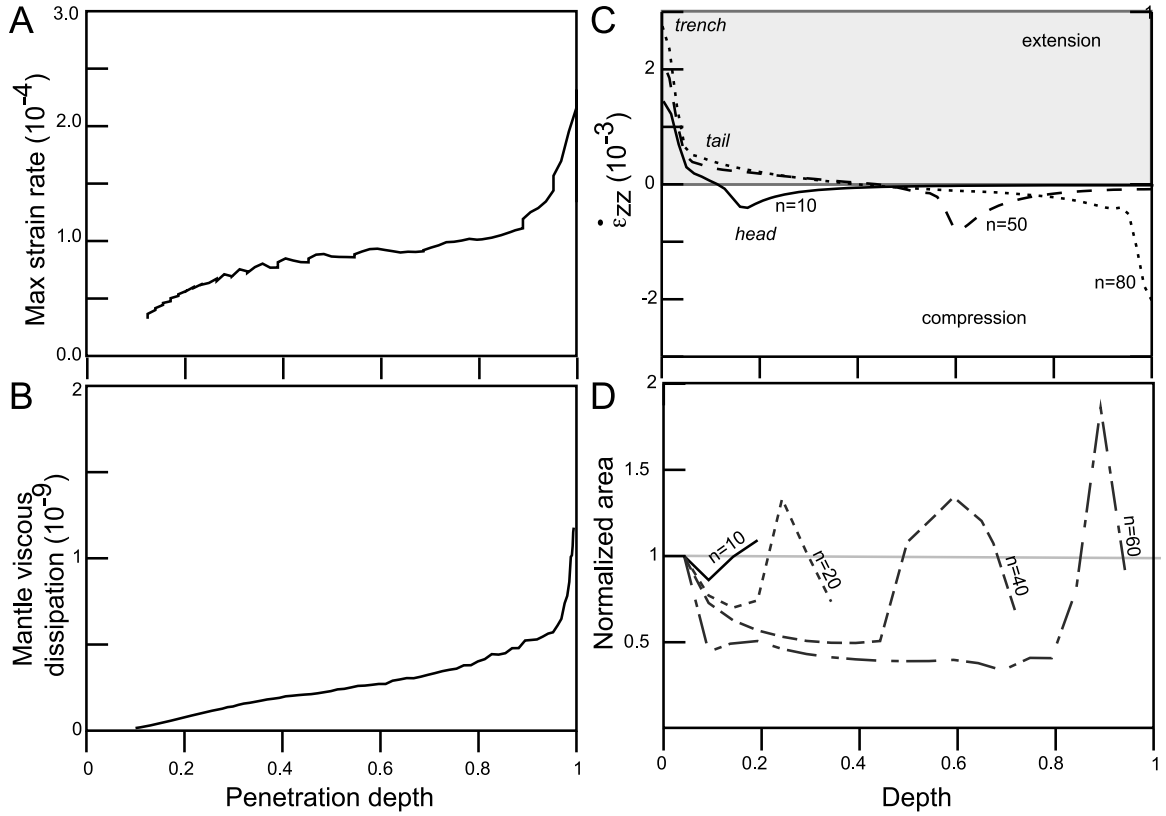

Figure 3. Reference model. (a) Maximum strain rate as a function of plate penetration depth. (b) Bulk viscous dissipation in the mantle as a function of plate penetration depth. (c) Vertical strain rate ($\dot{\varepsilon}_{zz}$) profile along the central axis of the plate (x = 0.5 and y = 0.5) at different time steps *n*. (d) Normalized areas of horizontal slab sections as a function of depth, at different time steps *n*.

setup, the location of the subduction zone at surface level remains fixed with respect to the underlying mantle while in nature, this may not be the case and slabs may gradually become vertical, thanks to the advance of the trench and/or retreat of the slab/head (Figures 5c and 5d). The dip does not seem to be a critical parameter in our parametric study and in the following numerical experiments we will only con-

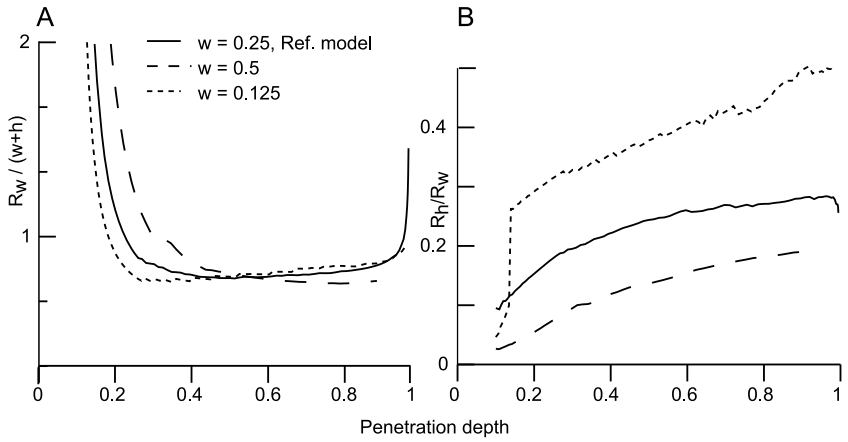

Figure 4. Reference model. (a) Radius of curvature R_w of the jellyfish head as function plate penetration depth, normalized to the sum of slab width *w* and slab thickness *h* for different slab width *w*, 0.25 (solid), 0.5 (dash) and 0.125 (dot). (b) Same as Figure 4a but for the ratio between lateral (R_h) and longitudinal (R_w) radii of curvature.

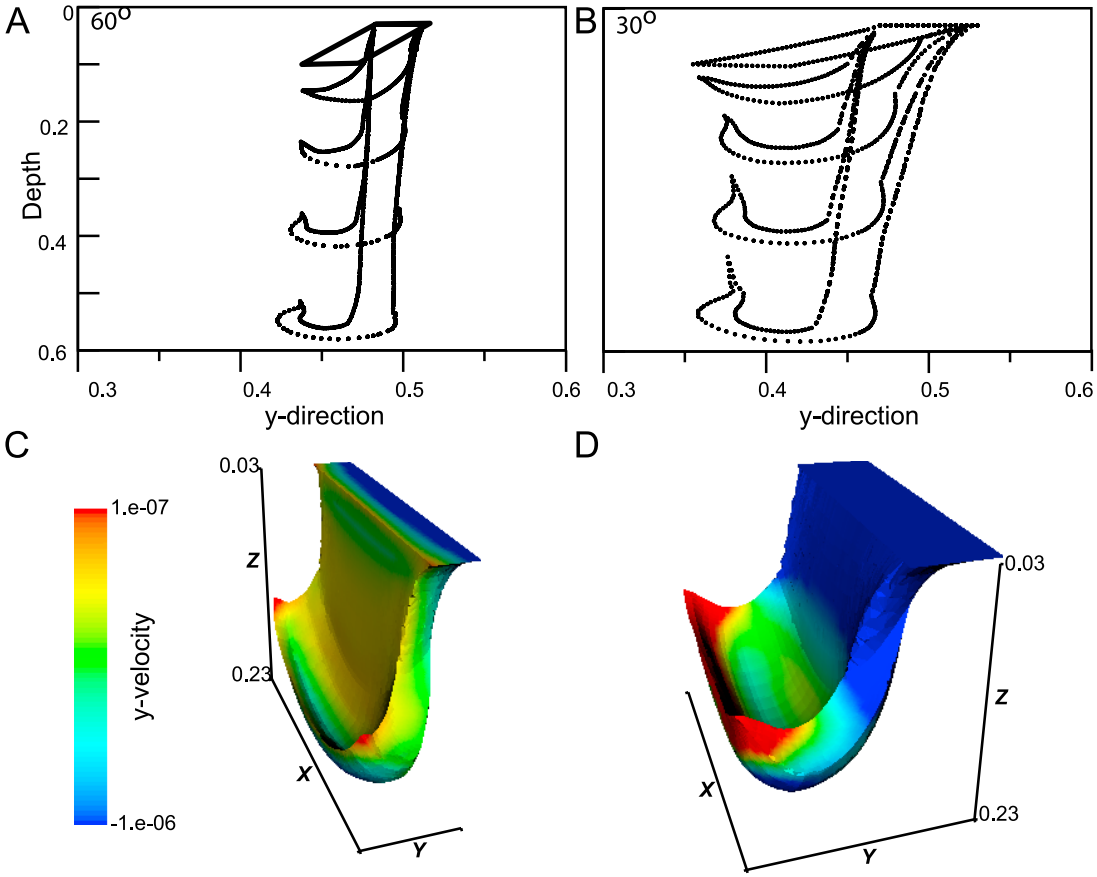

Figure 5. Geometry of the plate when subducted with an initial slab dip α: (a and c) $\alpha = 60°$ and (b and d) $\alpha = 30°$. Figures 5a and 5b show across-strike profiles, regularly sampled in time (n = 20), and Figures 5c and 5d give a 3D view of the plate geometry when it reaches ~660 km depth. The *y*-velocity on the surface of the plate is color-coded.

sider a 90° dip angle (or vertical slab), as set up in the reference model.

3.4. Slab to Mantle Viscosity Ratio

[16] We test different viscosity ratios (from 10^{-2} to 10^{2}) between the lithosphere slab and the surrounding mantle (Figure 6a). Note that in the absence of any viscosity difference between the slab and mantle, the flow is that of a *Stokes* sinker. Furthermore, because we neglect the potential and highly unknown dependence of mantle and lithospheric rock viscosity on pressure, temperature or stress, our viscosities must be considered as effective values. Expanding the work of *Olson and Singer* [1985] on creeping, rising plumes, we identify three classes of jellyfishes based on the development of the jellyfish head: (i) Cavity jellyfishes, for which the plate viscosity is lower than that of the mantle; they feature well rounded heads connected to tails upon which tentacles are retracted (Figure 6a, $\mu_s = 10^{-2}$). (ii) Diapiric jellyfishes develop when the system is isoviscous or close to it. They differ from cavity jellyfishes by their well-individualized tentacles and even better rounded head (Figure 6a, $\mu_s = 1$). (iii) Anvil jellyfishes develop when the viscosity ratio is much larger than 1. In this case, the slab grows into an inverted anvil-shaped cap (i.e., jellyfish head) along its leading edge (Figure 6a, $\mu_s = 10^{1}$–10^{2}). Because slab viscosity is higher than that of the surrounding mantle, anvil jellyfishes more likely apply to the Earth better than the other classes and in the following, we focus on this class. The deformation highly depends on the viscosity ratio, as illustrated by the strain rates along the vertical *z*-axis of the jellyfish (Figure 6b). The lower the viscosity ratio is, the higher the strain rates are, but they are always extensional in the tail and compressional in the head. Obviously, when $\mu_s \gg 100$, the slab does not deform and the head and tail do not develop.

[17] For high viscosity contrast, the radius of curvature R_w also decreases through time until it reaches a minimum value (Figure 6c). This indicates that, regardless of the viscosity ratio, the plate will tend toward an optimal shape (for an infinite domain

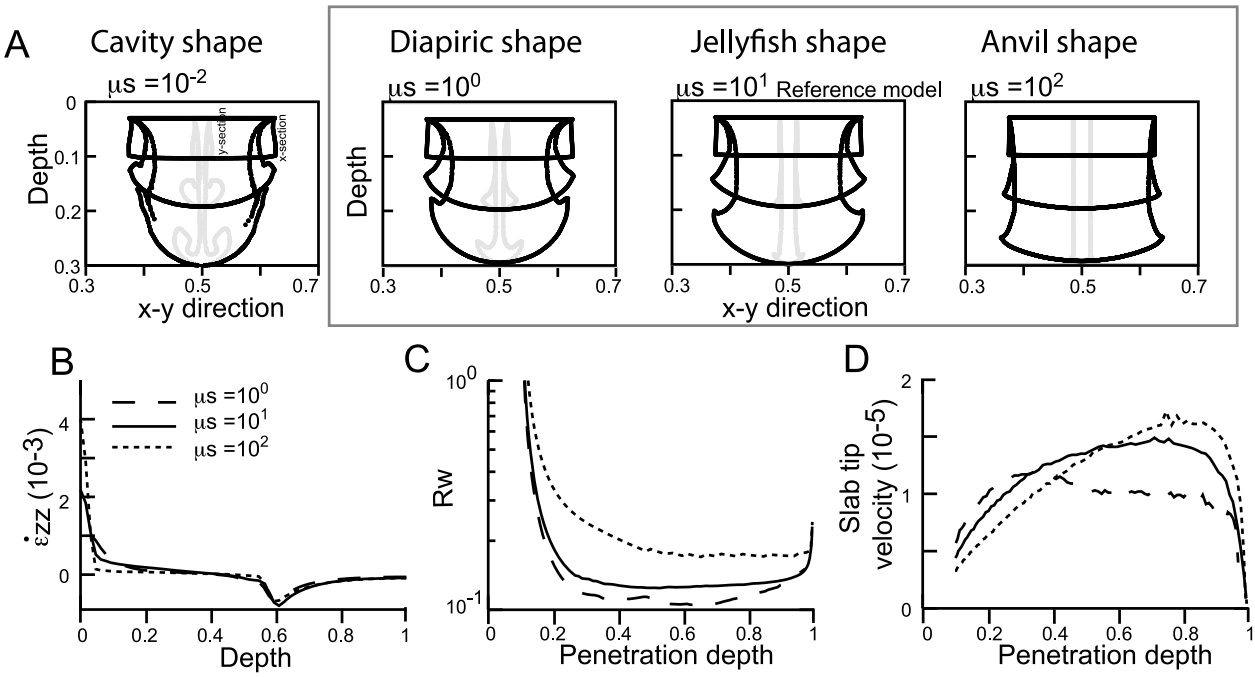

Figure 6. (a) Cross sections at selected depths along-strike (black) and across-strike (gray) and classification as function of the plate to upper mantle viscosity ratio μ_s (see Table 1). Framed profiles are a selection of geologically plausible scenarios. (b) Vertical strain rate $\dot{\varepsilon}_{zz}$ profile along the central axis of the plate (x = 0.5 and y = 0.5). (c) Radius of curvature of the jellyfish head R_w as a function of maximum penetration depth and μ_s. (d) Velocity of the plate head as a function of plate depth and μ_s.

in the vertical direction), although this might require a very long descent time for a very large viscosity ratio. In all cases, the velocity increases gradually during the early evolutionary stages of the jellyfish at shallow depths; it reaches a maximum value, and eventually decreases when plate penetration is hindered by the undeformable bottom of the model experiment (Figure 6d).

[18] Interestingly, the viscosity ratio affects the sinking velocity. The slab penetrates faster into the mantle when μ_s is high (μ_s = 100) and the velocity reaches its maximum value at greater depths than for less viscous slabs. When the viscosity ratio is low (μ_s = 1), the velocity starts to decrease at rather shallow depths (~0.35). These results can be explained by the joint effects of (i) the plate bulk mass (because the high viscous plate remained relatively undeformed, the boundary flux condition near the surface imposes a larger mass flux and thus larger negative buoyancy), (ii) plate stretching in the tail (which for low viscosity slabs, favors viscous dissipation in the surrounding mantle and prevents efficient stress transmission) and (iii) the passive resistance of the bottom of the mantle. Note that these results apparently differ from the solution obtained by *Hadamard* [1911] and *Rybczynski* [1911] which predicts that the sinking velocity should decrease as the viscosity contrast increases. This is actually not very surprising because the latter solution only applies to a constant volume, deforming spherical bubble characterized by a lower viscosity than the surrounding fluid.

[19] Both extensive and compressive strain rates are larger in the tails and in the heads of low viscosity jellyfishes than of the high viscosity ones, implying that the sinking velocity of low viscosity slabs tends more rapidly to the *Stokes* velocity of the jellyfish head; this velocity yet remains lower than the sinking velocity of highly viscous slabs that are more negatively buoyant simply because of the larger resulting plate volume.

3.5. Viscosity Stratification Between Upper Mantle and Lower Mantle

[20] Scaled analog experiments of the subduction process [*Funiciello et al.*, 2003; *Griffiths et al.*, 1995; *Guillou-Frottier et al.*, 1995; *Kincaid and Olson*, 1987; *Schellart*, 2004] and numerical studies of subduction systems [*Behounkova and Čížková*, 2008; *Christensen*, 1996; *Čížková et al.*, 2007; *Davies*, 1995; *Enns et al.*, 2005; *Gaherty*

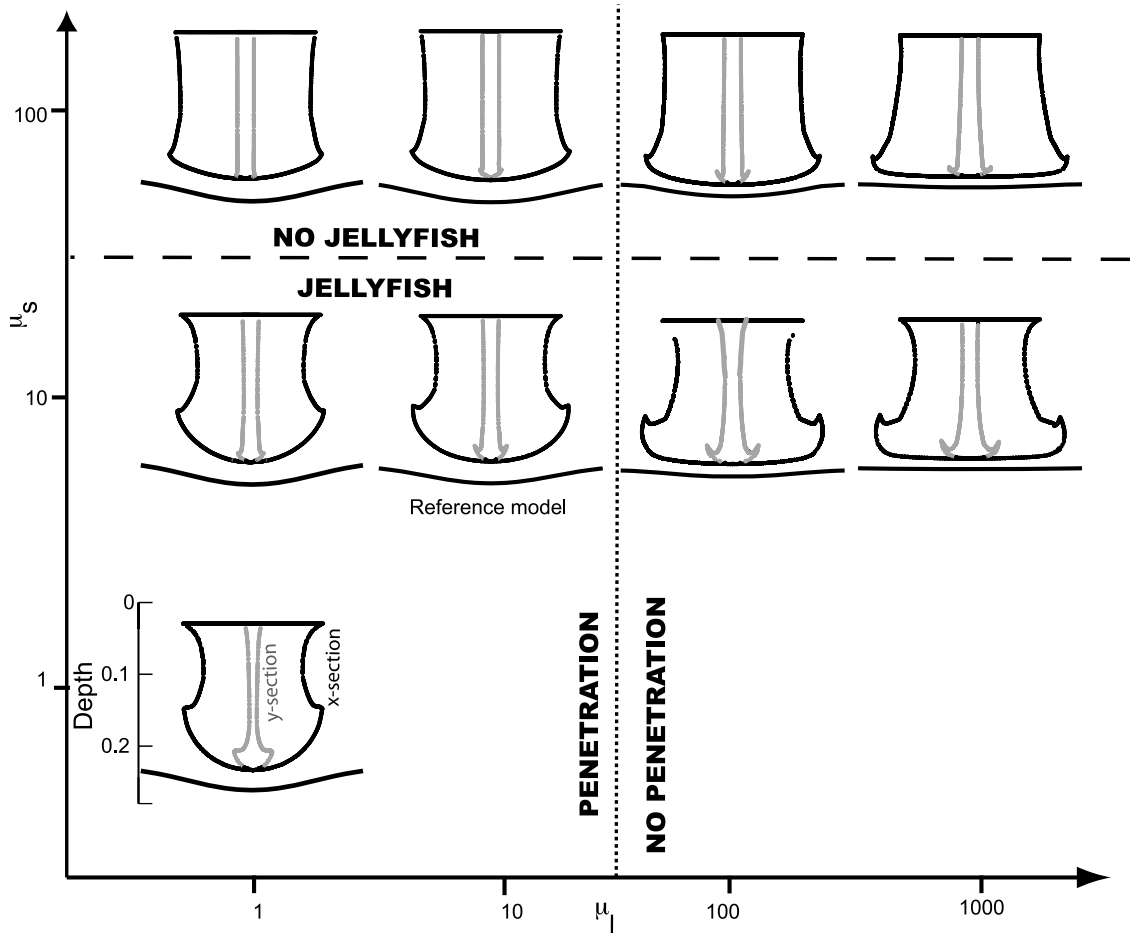

Figure 7. Different cases of slab geometry and slab penetration at the interface between the upper and lower mantle. Along-strike (black) and across-strike (gray) sections of the slab, as a function of the slab to upper mantle viscosity ratio μ_s and the lower mantle to upper mantle viscosity ratio μ_l. Solid black lines show the upper/lower mantle boundary.

and Hager, 1994; *Goes et al.*, 2008; *Houseman and Gubbins*, 1997; *Schellart et al.*, 2007; *Tackley*, 1993; *Tao and O'Connell*, 1993; *Yoshioka and Wortel*, 1995; *Zhong and Gurnis*, 1995] have already illustrated the modes of deformation of a stiff subducted slab reaching a fluid interface characterized by a viscosity and/or density increase. These studies have shown the importance of the density contrast [*Christensen and Yuen*, 1984] and viscosity ratio [*Kárason*, 2002; *Kincaid and Olson*, 1987] in governing whether the slab will lie along the interface, sink through it, or buckle and pile up at the interface [*Ribe*, 2003]. Here, we study the evolution of the jellyfish shape (i.e., low viscous slab) when the slab meets the 660 km boundary, which we either define as a viscosity or density contrast between the upper and lower mantle.

[21] Figure 7 summarizes the behavior of the plate as it forms a jellyfish shape and/or penetrates into the lower mantle as a function of μ_s, the viscosity ratio between the slab and the upper mantle, and μ_l, the viscosity ratio between the lower and upper mantle.

[22] We observe a range of subducting plate shapes, with or without stratification boundary penetration, an indication that several factors are involved in the style of slab deformation when a fluid interface is present. We can define four different cases:

[23] (a) Jellyfishing (i.e., formation of a jellyfish shape) and penetration ($\mu_s < 100$ and $\mu_l < 100$). The plate has a sufficiently low viscosity to transform into a jellyfish. The jellyfish head radius of curvature R_w is low (Figure 8a). The stratification is weak enough to permit the slab to sink into the lower mantle with minor deformation of the mantle stratification discontinuity. The plate continues to sink with a velocity decrease but without any interruption (Figure 8b). The interface deflects around the slab to form a blob and slowly collapses at the plate sinking velocity.

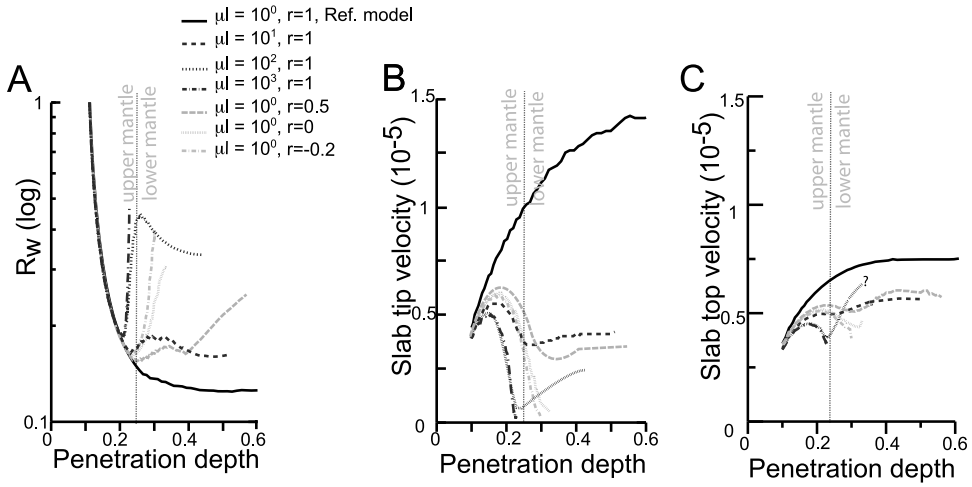

Figure 8. (a) Radius of curvature R_w, (b) velocity of slab tip, and (c) velocity of slab top measured as a function of the maximum plate penetration depth for different lower to upper mantle viscosity ratio μ_l (black), and density indices r (see text). The slab to upper mantle viscosity ratio μ_s is set to 10.

[24] (b) Jellyfishing and no penetration ($\mu_s < 100$ and $\mu_l > 100$). The plate transforms into jellyfish but does not penetrate the lower mantle. The plate stops close to the stratification boundary and the jellyfish head flattens. This case is also characterized by a rapid increase in R_w when the plate reaches the interface, followed by a phase of decreasing R_w (Figure 8a).

[25] (c) No jellyfishing and penetration ($\mu_s > 100$ and $\mu_l < 100$). The plate is too viscous and cannot evolve toward a jellyfish shape before it reaches the upper/lower mantle boundary but crosses it because the viscosity ratio μ_l is low enough. Consequently, the deflected interface collapses around the quasi-rigid slab. The viscosity ratio between the plate and the fluid decreases in the lower mantle allowing plate thickening in the lower fluid.

[26] (d) No jellyfishing and no penetration ($\mu_s > 100$ and $\mu_l > 100$). The plate does not cross the stratification boundary and keeps a slab shape because the viscosity ratio with the surrounding mantle is too high. Furthermore the strong viscosity contrast with lower mantle does not permit slab deformation and slab penetration. The interface stays straight.

[27] Our results therefore demonstrate that the penetration of the plate into the lower mantle mainly depends on mantle stratification while the widening of the slab tip and jellyfish formation mostly depends on the slab strength (i.e., viscosity ratio between the subducting plate and the surrounding mantle).

[28] Note that all slabs should ultimately penetrate if given sufficient time. Here, we define penetration mode when the characteristic slab sinking velocity is comparable to the characteristic penetration velocity, i.e., the slab does not pile up on the upper mantle/lower mantle interface.

3.6. Density Stratification Between Upper and Lower Mantle

[29] To investigate the influence of the various density contrasts between the sinking slab, upper mantle and lower mantle, we used the critical dimensionless parameter r defined by *Kincaid and Olson* [1987] (Figure 9) in which the slab/lower mantle density contrast is normalized by the slab/upper mantle density contrast: $r = (\rho_s - \rho_{lm})/(\rho_s - \rho_{um})$. $r = 1$ corresponds to a uniformly dense fluid (no density contrast between the upper and lower mantle), while negative values of r correspond to a denser lower mantle than the sinking slab. Results are given for $-0.2 < r < 1.0$ (Figures 8 and 9). We identify four cases in Figure 9:

[30] In Figure 9a, $r = -0.2$, which indicates strong stratification and no slab penetration. While the slab sinks through the upper mantle and reaches the discontinuity, its deformation is controlled by the viscosity ratio between the slab and the upper mantle. The leading edge thickens when it meets the undeformable interface. R_w increases and the sinking velocity decreases (Figures 8a and 8b).

[31] In Figure 9b, $r \sim 0$, which indicates partial slab penetration into the lower mantle. Sinking rates are lower than when $r = -0.2$. R_w increases (Figures 8a and 8b) when the slab reaches the mantle discontinuity. The leading edge of the slab reclines onto the

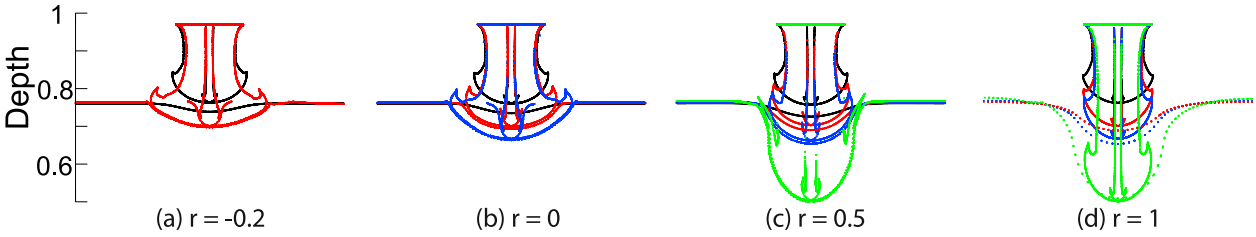

Figure 9. Across-strike and along-strike sections of the entire plate at four selected depths (0.24, black, 0.3 red, 0.34 blue and 0.5 green) for different values of the density parameter *r* (see text). The upper/lower mantle boundary is indicated by horizontal lines. Note some selected depths at r = −0.2 and r = 0 are missing when the plate does not cross the upper/lower mantle boundary.

interface. Buoyancy forces in the lower mantle are not strong enough to stall subduction until the slab has penetrated below the discontinuity (around 1/10 penetration in the lower mantle). Within this range of density contrasts the initial penetration is however always limited.

[32] In Figure 9c, r ~ 0.5, which indicates slab penetration. The slab sinks through the lower layer but only on a very long time scale because the sinking velocity decreases (Figure 8b). The deflected interface collapses around the slab into a blob. Both the slab and the deformed interface descend slowly.

[33] In Figure 9d, r > 0.5, which indicates weak stratification. The stratification is weak enough to permit the slab to sink into the lower mantle with only minor deformation of the interface. The slab acquires the jellyfish form as described in the above section. Both the viscosity and density stratification of the mantle intensify the decrease in slab sinking rates at its deep head, but also at the surface level (Figure 8c).

4. Comparison to the Real Earth

[34] Several types of seismically derived data address the problem of slab deformation within the mantle, as reviewed by *Lay* [1994]. The quasi-planar geometry of subducting slabs in the upper mantle was first defined from the distribution of large earthquakes along Wadati-Benioff zones [*Isacks and Barazangi*, 1977; *Jarrard*, 1986]. In addition, maps of earthquake focal positions [*Engdahl et al.*, 1998] provided high resolution three dimensional images of the seismogenic regions surrounding subduction zones that gave rise to general geometric and deformation models of mantle slabs, such as the *RUM* model [*Gudmundsson and Sambridge*, 1998]. Furthermore, global seismic tomography models [*Bijwaard et al.*, 1998; *Ding and Grand*, 1994; *Fukao*, 1992; *Grand*, 1994; *van der Hilst*, 1995; *van der Hilst and Widiyantoro*, 1997; *Wortel and Spakman*, 2000; *Becker and Boschi*, 2002] provide more insights into slab morphology, including those characterized by a relatively low seismicity [*Li et al.*, 2008], as well as the distribution of seismic velocity anomalies in the mantle surrounding the slabs. Most recently, seismic images have been interpreted in terms of the most probable density field yielding the observed seismic velocity anomalies, which in turn have been used to derive models of self-consistent mantle flow [e.g., *Becker*, 2006; *Conrad et al.*, 2007; *Conrad and Husson*, 2009; *Mitrovica and Forte*, 2004; *Moucha et al.*, 2007].

[35] All above mentioned methods are complementary and show that subducting slabs are significant structures in the upper mantle, that the majority of them penetrates into the lower mantle and that they are characterized by a rather complex three-dimensional deformation pattern (rather than being planar slabs) [*Yamaoka et al.*, 1986]. In many instances, which we will describe below, tomographic images suggest a characteristic shape for the slab, with a relatively narrow trace in the upper mantle and a wider anomaly in the mid-lower mantle [*Kárason and Van der Hilst*, 2001]. Clearly, subducted lithosphere is rarely imaged as a slab-shaped feature but rather as a spheroidal anomaly. As shown by *Kárason* [2002], using paleogeographic reconstitutions, geophysical observations are therefore consistent with our theoretical prediction that subducted slabs should deform as they penetrate into the mantle to take the shape of a jellyfish. The distribution of focal mechanisms shows that stresses within the subducted slab are characterized by downdip extension in its upper part (between 100 and 300 km depth), which is also associated with the narrow section of the slab, and by downdip compression in the deeper part of the slab, i.e., toward the 660 km boundary [*Apperson and Frohlich*, 1987; *Isacks and Molnar*, 1969; *Vassiliou et al.*, 1984], which is associated with the thickest section of the

Table 2. Geometrical Classification of Slabs and Subduction Parameters

Category	Name[a]	Vs[b] (mm/a)	Age[c] (My)	Φ[d] (km)
Type 1	N-Kuril	77.99	110	8591
	Central America	62.27	17.6	1089.26
	Alaska W	59.4	52	3091.92
	Alaska E	50.2	41.8	2128.45
	Peru	61.1	28.8	1756.51
	Java-Sumatra	47.39	69.93	3356.64
	Hellenic	42	100	5100
	North-central Chile	68.13	52.12	3542.07
Type 2	S-Kuril	75	120.4	9042.04
	Japan	89.75	129.5	11661.47
	Izu-Bonin	50	138.25	6943.23
	Tonga	157.25	107.25)	17754.16
Type 3	Mariana	40.11	151.61	6143.23
	Kermadec	55	99	5464.8
Type 4	Scotia	40	38.16	1525.63
	Aleutian	53.21	56.23	2945.32
	Caribbean	8	96.66	788.23
	North America	31	9.4	292.90
	South Chile	70	33.8	2376.47
	Ryuku	85.8	44.2	3777.33
	Calabria	50	80	4160

[a]Trench segmentation is based on *Gudmundsson and Sambridge* [1998].
[b]Vs = Vsub − Vt, where Vs is the average subduction velocity along the subduction zone segments, Vsub is the velocity of the subducting plate and Vt is the trench migration velocity (from the compilation of *Heuret and Lallemand* [2005]). The classification of slab deformation is based on the shape of the Wadati-Benioff zone inferred from deep seismicity [*Engdahl et al.*, 1998] and the results of the seismic tomography model of *Li et al.* [2008].
[c]Mean subduction age along the trench segments [from *Heuret and Lallemand*, 2005; after *Müller et al.*, 1997].
[d]Φ: Slab thermal parameter (age * Vs).

slab. Such a distribution of stress, and thus strain rate, along the subducting plate is identical to that predicted in our models of a slab transforming into a jellyfish (Figure 3c).

[36] By conducting a careful review of high resolution images of Wadati-Benioff zones derived from the accurate localization of seismicity [*Engdahl et al.*, 1998] and tomographic images obtained from P waves seismic travel time anomalies [*Li et al.*, 2008], we came to the conclusion that there are four main categories of slabs (defined in Table 2) in the Earth's mantle, varying in their shape (on whether subducted slabs thicken at depth or not) and interaction characteristics at/with the 660 km discontinuity (whether subducted slabs penetrate or not in the lower mantle). To illustrate these categories, we explored the structure of a variety of subduction systems and slab geometries in 2D and 3D views derived from a P wave seismic tomography model [*Li et al.*, 2008]. We selected well-defined examples that illustrate each category (Figure 10). These categories are:

[37] Type 1 is penetration and thickening (the Hellenic slab) (Figures 10a, 10e, 10i, and 10m). The subducted lithosphere crosses the 660 km boundary with a small perturbation in thickness, which increases in the mid-lower mantle. Below 660 km, a fast velocity anomaly appears in the subducting plate which widens to ~400 km in the mid-mantle (~1200 km depth). The penetration of the subducted slab through the 660 km discontinuity and slab thickening in the mid-mantle (~1200 km) are the two remarkable features that are observed in other tomographic studies of this region [*Piromallo and Morelli*, 2003; *Spakman et al.*, 1993]. Other subduction zones where comparable features are observed include Central America, N-Kuril [*Ding and Grand*, 1994], Java [*Fukao*, 1992; *Puspito et al.*, 1993; *Widiyantoro and van der Hilst*, 1996] and India-Tibet [*Bijwaard et al.*, 1998; *Grand et al.*, 1997].

[38] Type 2 is slab deflection with little or no penetration (the Izu-Bonin slab). In this category, slabs are significantly deflected above the 660 km discontinuity to form a sub-horizontal high seismic velocity zone. Vertical cross section in this area (Figures 10b, 10f, 10j, and 10n) clearly demonstrates that the slab has been strongly deflected at the 660 km discontinuity with only a slight hint that it may have penetrated in the lower mantle. The slabs in the Izu-Bonin [*Tajima and Grand*, 1998], in S-Kuril [*Tajima and Grand*, 1995] and Japan subduction systems are the best examples of this category.

[39] Type 3 is pure penetration (the Mariana slab). As shown in Figures 10c, 10g, 10k, and 10o and as seen in many tomographic studies [e.g., *Fukao*, 1992; *van der Hilst and Seno*, 1993; *Zhou*, 1988], the Mariana slab appears to penetrate the 660 km discontinuity to reach the mid-mantle without significant thickening. Another typical example is the Kermadec slab [*Zhao et al.*, 1997].

[40] Type 4 is no penetration and no thickening (the Scotia slab). This category includes the Calabria, Aleutian, Caribbean, Ryukyu and the Scotia slabs that do not penetrate into the lower mantle and do not seem to experience any thickening at their base (Figures 10d, 10h, 10l, and 10p). However, many slabs of this type may lay flat on the 660 km discontinuity because of slab rollback (e.g., Calabria or Scotia), which makes the comparison to our experiments more uncertain.

[41] In order to further characterize the shape of the subducting slabs, we mapped data from the tomographic model of *Li et al.* [2008] on a Cartesian grid using the *GMT* software [*Wessel and Smith*, 1991] to

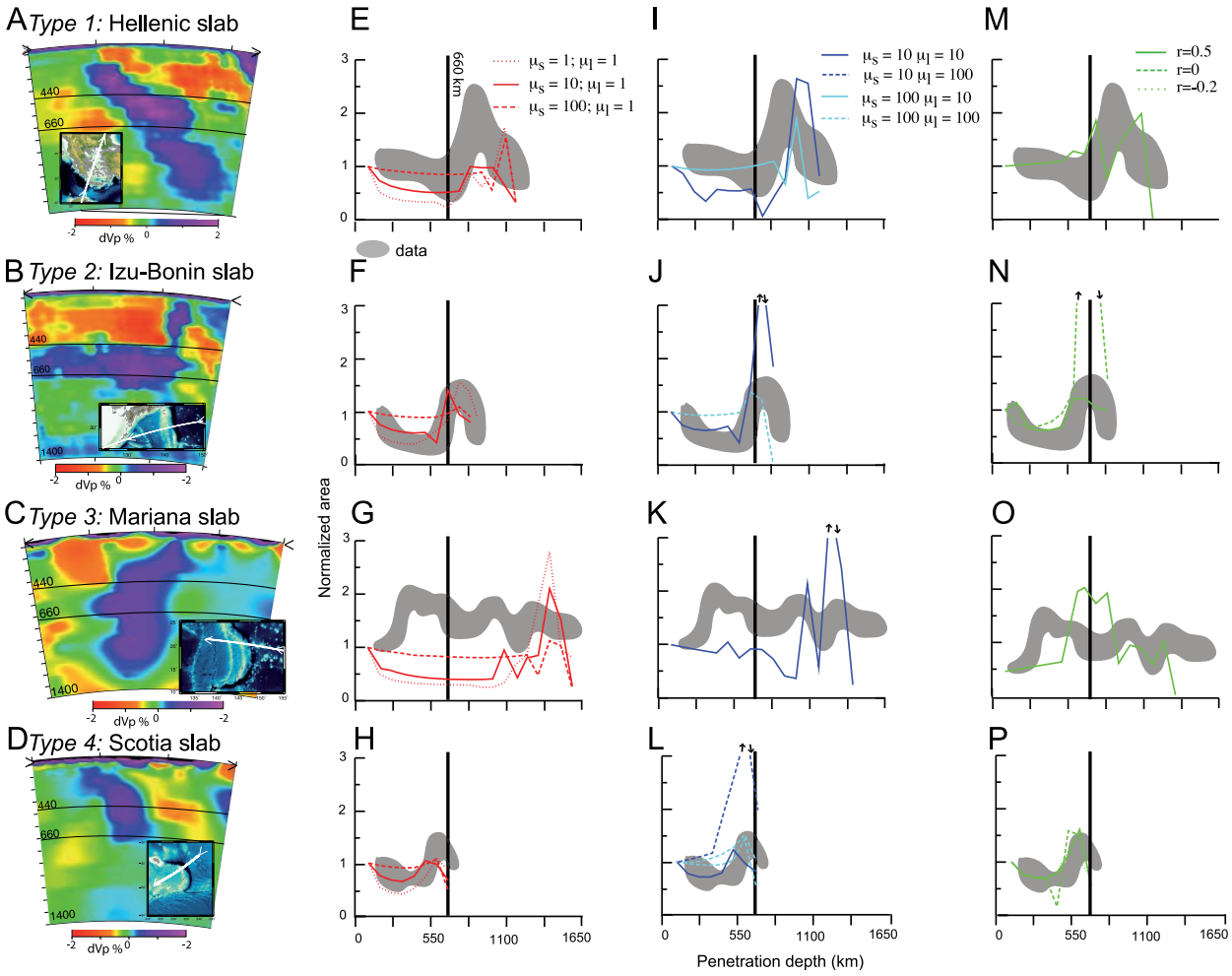

Figure 10. (a–d) Vertical profiles across seismic tomography model of *Li et al.* [2008] (global P wave model) and (e–p) slab thickening illustrated by the evolution of the predicted sectional area (by numerical models, color curves) and sectional area inferred from geophysical data (gray areas) as a function of maximum penetration depth. This is shown for ranges of slab to upper mantle viscosity ratio (red curves, Figures 10e–10h), lower to upper mantle viscosity ratio (blue curves, Figures 10i–10l), and density contrast between the slab and the lower mantle (green curves, Figures 10m–10p), for the Hellenic (Figures 10a, 10e, 10i, and 10m), Izu-Bonin (Figures 10b, 10f, 10j, and 10n), Mariana (Figures 10c, 10g, 10k, and 10o) and Scotia (Figures 10d, 10h, 10l, and 10p) subduction zones which are type 1, 2, 3 and 4 respectively. It is only for visualization/illustration purpose that the vertical sections of seismic tomography models are provided, and the comparison remains qualitative.

compute horizontal cross-sections at 100 km intervals of the seismic velocity anomalies from which we estimated the surface area of the slabs as they penetrate into the mantle, from 100 to 1400 km depths. In that way, we optimize the accuracy of estimates of the slab thinning/thickening with depth. In fact, at each depth, we considered three contours of the velocity anomaly contrast (minimum, mean and maximum relative velocities) to avoid artifacts arising from the inherent resolution of tomographic models. Note that no unique values for the seismic velocity contrasts can be selected for they vary with depth, in particular because of the thermal relaxation of the slabs during their downward route; contouring is therefore arbitrary and to some extent, subjective. We normalized the surface areas comprised inside each of the contours by the contour area at the surface to obtain dimensionless vertical profiles of the slab thickness (extracted from horizontal section). This procedure was also performed on some of our numerical model results (Figure 10).

[42] These values for slab thickness as they penetrate in the mantle are more relevant qualitatively than quantitatively. Although *Li et al.* [2008] suggest that the deep mantle parts of the slab structures are well resolved and are not affected by artifacts arising from the uneven distribution of seismic sources and

receivers, which suggest some robustness, we emphasize that the comparison of experiments to real Earth should be taken with care.

[43] For each of the four slab categories, we compared thickness profiles from the tomographic model to those obtained from numerical models in which we varied the viscosity ratio μ_s between 1 and 100, the viscosity ratio μ_l between 1 and 1000 and the density parameter r between −0.2 and 1 (Figure 10). To facilitate the comparison between data and models, we show model-predicted surface area profiles for model times that best correspond to subduction/penetration level suggested by each of the four tomographic images. The tentacles from the predicted model as described in results part are not considered (i.e., we include tentacles in surface area calculations) because the resolution of seismic tomography models is not sufficient to characterize their geometry.

[44] We first notice that, in both the numerical models, where the viscosity mantle stratification ($\mu_l > 1$) or the density mantle stratification ($r < 1$) impacts on plate penetration and on its deformation, and in some of the tomographic images, the formation of the jellyfish head and the corresponding thickening of the slab usually occurs deeper than the imposed viscosity/density jump at 660 km depth. This implies that, if in some cases the discontinuity impacts the thickening of the subducting slab, the formation of the jellyfish may take place at greater depths and is thus likely to result from an independent process, as advocated by our numerical model results.

[45] Then, in the first two categories, slab thickening occurs at (i.e., type 2, Izu Bonin slab, Figures 10b, 10f, 10j, and 10n) or below the 660 km discontinuity (i.e., type 1, Hellenic slab, Figures 10a, 10e, 10i, and 10m); comparing tomographic models and the results of the numerical models suggests that the formation of the jellyfish head is best explained either by a low increase in viscosity from upper to lower mantle ($\mu_l \sim 10$), consistent with previous studies based on the interpretation of the geoid [*Moresi and Gurnis*, 1996] or by a weak jump in density between the upper and lower mantle ($r \sim 0.5$), as suggested by other model results [*Christensen and Yuen*, 1984]. In nature, we found it impossible to discriminate the two causes; a combination of both is probably responsible for slab thickening. The observed surface area versus depth profiles are best explained with a relatively low slab viscosity (only ~10–100 times the mantle viscosity), which confirms the results of *Loiselet et al.* [2009].

[46] In the third category, the Mariana slab displays a rather different behavior that suggests that the slab may be stronger than slabs belonging to type 1, and does not evolve into a jellyfish shape as it descends through the upper mantle. The slight thickening that appears in the slab cross-sectional area observed at depths between 1100 and 1650 km may be due to the relatively poor resolution of the tomographic images at those depths or to a mild density or viscosity stratification as suggested by *Čížková et al.* [1996], *Hager and Richards* [1989], and *Lambeck and Johnston* [1998].

[47] In the fourth category, thickening of the Scotia slab as it approaches the 660 km discontinuity could be explained by the formation of a jellyfish head, which in turns requires a relatively low viscosity/strength subducting plate.

[48] In order to evaluate the relationship between the geometries derived from the analysis of a tomographic model, and the factors that might control it such as the density and/or viscosity of subducted slabs, we use the parameter Φ, introduced by *Wortel and Vlaar* [1988], defined as $\Phi = \text{age} * V_s$ (where *age* is the average age of lithosphere at the time of subduction and V_s is the average velocity of subduction along trench segments) (see Table 2). This parameter can be interpreted as a proxy for the thermal maturation of the slab, which affects both the viscosity and density of the slab. There is a clear distribution of slab categories (type 1, 2, 3 or 4) as a function of Φ (Figure 11): (i) slabs with small thermal parameters Φ (or hot slabs) more easily jellyfish (i.e., type 1) than those with larger values for Φ (i.e., type 3); and (ii) slabs with large values of Φ tend to subduct more easily for they are presumably stiffer and denser. For very small thermal parameters, thermal diffusion may have had enough time to heat up the slabs so that they do not show up in seismic tomography. Alternatively, heated slabs may have lost their initial negative buoyancy and are no longer able to continue to subduct to greater depths than the transition zone (type 4, Calabria, Scotia slabs). Last, slabs of type 2 seem to be at odds with our previous analysis, for they appear to pond on the 660 km discontinuity, whereas in our models stiff slabs are predicted to penetrate into the lower mantle and not to deform. The departure between our models and the predictions given by the thermal parameter Φ may however reflect the fact that this proxy does not apply for slabs of type 2 (Izu-Bonin, S-Kuril, Japan and Tonga slabs).

[49] In our numerical models, and thus in our interpretation of the various slab geometries suggested by

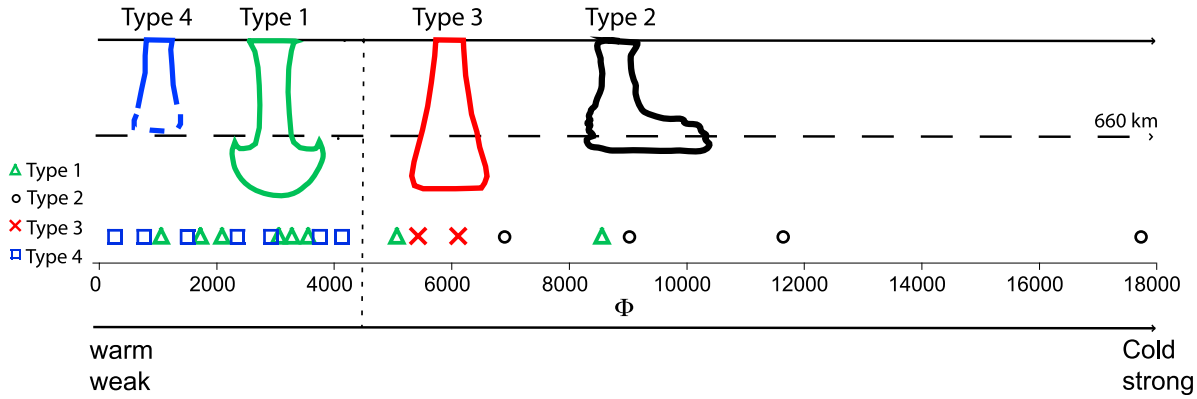

Figure 11. Geometrical classification of slabs (types 1 (green), 2 (black), 3 (red) and 4 (blue), see text) and correlation to the thermal parameter ϕ [*Wortel and Vlaar*, 1988]. Φ is the product of the average age of lithosphere and of the subduction rate (age * Vs) along the trench segment (defined from *Gudmundsson and Sambridge* [1998]).

tomographic models, we have assumed that slab motion is primarily driven by its buoyancy, i.e., the main force acting on the subducting oceanic lithosphere is the gravitational force arising from the high density of the plate with respect to the surrounding mantle. This has led us to interpret the observed thickening of weak slabs in the vicinity of the 660 km discontinuity as resulting from the formation of a jellyfish head in response to viscous drag between the slab and the mantle, potentially enhanced by the presence of a viscosity and/or density contrast between the upper and lower mantle. The former process (jellyfishing), in turn implies that the viscosity ratio between the slab and the mantle is relatively small (order 10), in other words that slabs are relatively weak. The latter process (interaction with the 660 km discontinuity) is supported by the compressive nature of the focal mechanisms of deep earthquakes [*Isacks and Molnar*, 1969], which clearly indicates the presence of resisting forces deeper than the transition zone, resulting from an increase in viscosity or a decrease in the density contrast between the slab and the surrounding mantle, and thus a decrease in the driving force.

[50] However, another explanation for the thickening of the slab along the 660 km discontinuity relies on the subduction (or penetration) velocity being imposed to the slab by other forces, either originating at the mid-ocean ridge (i.e., ridge push) or along other segments of the subducting lithosphere. If this is true and the trench migration velocity is significantly higher than the penetration velocity of the slab in the lower mantle (due to resistance force), slabs will have to deform on the 660 km discontinuity, to flatten and lie horizontally on it [*Christensen*, 1996; *Enns et al.*, 2005; *Griffiths et al.*, 1995; *Guillou-Frottier et al.*, 1995; *Olbertz et al.*, 1997; *Tagawa et al.*, 2007]. This scenario may explain why the Izu-Bonin slab flattens on the 660 km discontinuity [*van der Hilst and Seno*, 1993] whereas the Mariana slab penetrates it; similarly, the change in the style of subduction from the northern to southern Kuril [*Ding and Grand*, 1994; *Fukao*, 1992] is a potential illustration.

5. Discussion

[51] Seismic tomography images provide evidence for a strong deformation of some sections of the subducted lithosphere in the Earth's mantle. In the deep Earth's interior, some slabs may flatten and pond above or within the transition zone, such as beneath the Chilean Andes, the Aleutian, the S-Kuril, Japan, and Izu-Bonin. Other slabs tend to be deflected and lie sub-horizontally on the upper to lower mantle transition region before (at least for some of them) penetrating into the mid-lower mantle (such as in the N-Kuril, Hellenic, and the Philippines subduction systems), or well into the lower mantle (such as beneath the Peruvian Andes, Java, Mariana and Kermadec). In the latter case, slabs narrow in the upper mantle and anomalously thicken in the mid-lower mantle. Some authors explain this feature as resulting from a buckling instability [*Griffiths and Turner*, 1988; *Ribe et al.*, 2007]. Alternatively, *Christensen and Yuen* [1984] and *Kárason* [2002] showed that the large mid-mantle seismic anomaly could either be explained by geochemical and mineralogical changes in the slab as a function of depth or by the presence of a substantial viscosity jump at the 660 km discontinuity that modulates the penetration of an isoviscous plate.

[52] Here we propose, on the basis of the results of a large number of numerical experiments and their comparison to tomographic images, that the deformation of the subducting lithosphere mainly results from the interaction of a relatively weak slab with the surrounding viscous mantle, leading to the deformation of the planar lithosphere into a jellyfish.

[53] For each of the four subduction categories considered here, the comparison with model scenarios suggests that the viscosity ratios between the slab and the upper mantle ranges between 10 and 100. This is in accordance with *Husson* [2006] who found a good agreement between the topography observed above subduction zones and the dynamic topography computed assuming isoviscous flow in the mantle. *Čížková et al.* [2002] also found that slabs must be relatively weak in order to be deflected in the transition zone. Based on the results of analog experiments, [*Funiciello et al.*, 2008; *Schellart*, 2009] suggested that the observed trench and plate velocities and slab bending respectively are indicative of relatively weak slabs. More comprehensive reviews are given by *Billen* [2008] and *Becker and Faccenna* [2009].

[54] The low slab strength we predict here is at odds with the setup of many other analog and numerical models [*Capitanio et al.*, 2007; *Clark et al.*, 2008; *Conrad and Hager*, 1999; *Funiciello et al.*, 2003; *Morra et al.*, 2006; *Royden and Husson*, 2006; *Schellart*, 2004; *Stegman et al.*, 2006; *Zhong and Gurnis*, 1994] where the viscosity ratio between the subducted lithosphere and the surrounding mantle is set between 10^2 and 10^5. Although rock strength experiments also predict stiffer slabs than suggested here [see, e.g., *Kohlstedt et al.*, 1995], our predicted range of viscosity ratios is in accordance with global models [*Zhong and Davies*, 1999] that suggest that slabs should be 100 times more viscous than the upper mantle in order to fit geoid and dynamic topography data. *Loiselet et al.* [2009] independently suggest that the longitudinal curvature of slabs can only be achieved if the slab to mantle viscosity ratio is at most 10^2.

[55] In summary, any model that predicts a significant thickening of slabs descending in the upper mantle requires a weak subducted lithosphere, i.e., at most two orders of magnitude stiffer than the upper mantle. Higher than that, slabs are too strong to deform at the length-scale of the upper mantle. This result in turn indicates that slabs have limited time to acquire a characteristic jellyfish shape. Our interpretation of the seismically inferred thickening of slabs in the upper mantle applies well to young subduction zones, such as Scotia. In contrast, *Loubet et al.* [2009] have interpreted the apparent thickening of slabs in older, longer-lasting subduction zones as resulting from the periodic buckling of a relatively weak slab at the 660 km discontinuity by simple accumulation of subducting material.

[56] The comparison between our model predictions and seismic tomography data also suggests that the subducting plate should slow down and pond at the 660 km discontinuity if a viscosity or density contrast exists between upper and lower mantle, as already proposed by for example *Enns et al.* [2005]. The apparent slab widening at depth suggests that the slab is indeed stronger than the mantle but unfortunately an accurate estimate of the viscosity contrast cannot be obtained independently of any density variation that might exist across the 660 km discontinuity.

[57] Once the jellyfish penetrates into the lower mantle, the velocity of the subducting plate appears to remain constant, seemingly in contradiction with *Zhong and Gurnis* [1995] and *Christensen* [1996] who predicted an acceleration of the slab after penetrating the 660 km discontinuity. The difference in interpretation may occur because in their models there are (i) phase transitions with a negative Clapeyron slope along the 660-km discontinuity that foster subduction, or, (ii) alternatively, because the trench is actively retreating, while in our models, slabs subduct vertically.

6. Conclusions

[58] We have investigated the behavior of a slab subducting in the Earth's mantle driven by its negative buoyancy. We have showed that a relatively weak plate (at most two orders of magnitude times stiffer than the surrounding mantle) will form a characteristic jellyfish shape as it falls through the mantle. This is the optimal shape that a deformable object falling in a viscous fluid will acquire, regardless of its original shape, in order to probably minimize the viscous dissipation in the fluid. The jellyfish consists of a wide head experiencing vertical shortening and a long tail experiencing vertical lengthening. This pattern of deformation is consistent with the observed distribution of downdip extensional and compressional stresses along subducting slabs and with observed slab geometries at mid-mantle depths that are derived from tomographic images. This characteristic jellyfish shape

naturally evolves from that of a planar subducting plate, but the few other initial shapes that we tested numerically or in analog models also adopt similar behaviors and all tend to jellyfish shape. We have used a linear viscosity for both the slab and the mantle, which implies that strain rate and, subsequently, subduction velocity linearly scales with the imposed density contrast between the slab and the mantle. The value of the density contrast between the slab and the surrounding mantle thus does not influence the geometry of the subduction process nor the depth range over which the jellyfish head forms.

[59] The plate to mantle viscosity ratio is important to the deformation of the plate. Lithosphere strength is crucial physical parameter that controls the dynamics of subduction zone.

[60] By comparing model predictions with observations (inferred from seismic tomography and earthquake focal mechanism solutions) we therefore provide additional constrains on the viscosity contrast between subducting slabs and the surrounding mantle by suggesting that slabs are weak. The final jellyfish shape also depends on the initial slab width, or more precisely, its aspect ratio. Furthermore, in cases where the initial slab is not vertical, we have shown that the slab turns into an asymmetrical jellyfish. This "spoon" shape is consistent with many observed geometries (derived from seismic tomography and from the distribution of earthquakes in Wadati-Benioff zones); the Hellenic slab is one of the most striking examples of such spoon-shaped subducting slabs.

[61] Last, one way to reconcile the observation that some slabs are thickened around the 660 km discontinuity while others seem to thicken at mid- to lower mantle depths or deeper, is to consider (i) that the subducted plate is in general sufficiently weak to become a jellyfish during its fall in the upper mantle and (ii) that it meets at the 660 km depth a low viscosity and/or high density jump that lowers its sinking velocity.

Acknowledgments

[62] This work was supported by the College doctoral de Bretagne (Université Européenne de Bretagne) (C.L.) and by a "Chaire d'Excellence Senior de l'ANR" (J.B.). We thank P. Fullsack for stimulating discussions. Suggestions by anonymous reviewers and by Editor Thorsten Becker helped to greatly improve this paper.

References

Apperson, K. D., and C. Frohlich (1987), The relationship between Wadati-Benioff zone geometry and P, T and B axes of intermediate and deep focus earthquakes, *J. Geophys. Res.*, *92*, 13,821–13,831.

Becker, T. W. (2006), On the effect of temperature and strain-rate dependent viscosity on global mantle flow, net rotation, and plate-driving forces, *Geophys. J. Int.*, *167*, 943–957, doi:10.1111/j.1365-246X.2006.03172.x.

Becker, T. W., and L. Boschi (2002), A comparison of tomographic and geodynamic mantle models, *Geochem. Geophys. Geosyst.*, *3*(1), 1003, doi:10.1029/2001GC000168.

Becker, T. W., and C. Faccenna (2009), A review of the role of subduction dynamics for regional and global plate motions, in *Subduction Zone Geodynamics*, edited by S. Lallemand and F. Funiciello, pp. 3–34, doi:10.1007/978-3-540-87974-9_1, Springer, Berlin.

Behounkova, M., and H. Čížková (2008), Long-wavelength character of subducted slabs in the lower mantle, *Earth Planet. Sci. Lett.*, *275*, 43–53, doi:10.1016/j.epsl.2008.07.059.

Bevis, M. (1986), The curvature of Wadati-Benioff zones and the torsional rigidity of subducting plates, *Nature*, *323*, 52–53, doi:10.1038/323052a0.

Bijwaard, H., W. Spakman, and E. R. Engdahl (1998), Closing the gap between regional and global travel time tomography, *J. Geophys. Res.*, *103*(B12), 30,055–30,078.

Billen, M. I. (2008), Modeling the dynamics of subducting slabs, *Annu. Rev. Earth Planet. Sci.*, *36*(1), 325–356, doi:10.1146/annurev.earth.36.031207.124129.

Billen, M. I., and M. Gurnis (2005), Constraints on subducting plate strength within the Kermadec trench, *J. Geophys. Res.*, *110*, B05407, doi:10.1029/2004JB003308.

Braun, J., C. Thieulot, P. Fullsack, M. DeKool, C. Beaumont, and R. Huismans (2008), DOUAR: A new three-dimensional creeping flow numerical model for the solution of geological problems, *Phys. Earth Planet. Inter.*, *171*(1–4), 76–91, doi:10.1016/j.pepi.2008.05.003.

Capitanio, F. A., G. Morra, and S. Goes (2007), Dynamic models of downgoing plate-buoyancy driven subduction: Subduction motions and energy dissipation, *Earth Planet. Sci. Lett.*, *262*(1–2), 284–297, doi:10.1016/j.epsl.2007.07.039.

Christensen, U. R. (1996), The influence of trench migration on slab penetration into the lower mantle, *Earth Planet. Sci. Lett.*, *140*, 27–39, doi:10.1016/0012-821X(96)00023-4.

Christensen, U., and D. Yuen (1984), The interaction of a subducting lithosphere slab with a chemical or phase boundary, *J. Geophys. Res.*, *89*, 4389–4402, doi:10.1029/JB089iB06p04389.

Čížková, H., O. Čadek, D. A. Yuen, and H. Zhou (1996), Slope of the geoid spectrum and constraints on mantle viscosity stratification, *Geophys. Res. Lett.*, *23*(21), 3063–3066, doi:10.1029/96GL02257.

Čížková, H., J. van Hunen, A. P. van den Berg, and N. J. Vlaar (2002), The influence of rheological weakening and yield stress on the interaction of slabs with the 670 km discontinuity, *Earth Planet. Sci. Lett.*, *199*, 447–457, doi:10.1016/S0012-821X(02)00586-1.

Čížková, H., J. van Hunen, and A. van den Berg (2007), Stress distribution within subducting slabs and their deformation in the transition zone, *Phys. Earth Planet. Inter.*, *161*(3–4), 202–214, doi:10.1016/j.pepi.2007.02.002.

Clark, S. R., D. Stegman, and R. D. Muller (2008), Episodicity in back-arc tectonic regimes, *Phys. Earth Planet. Inter.*, *171*(1–4), 265–279, doi:10.1016/j.pepi.2008.04.012.

Conrad, C. P., and B. H. Hager (1999), Effect of plate bending and fault strength at subduction zones on plate dynamics, *J. Geophys. Res.*, *104*, 17,551–17,571, doi:10.1029/1999JB900149.

Conrad, C. P., and L. Husson (2009), Influence of dynamic topography on sea level and its rate of change, *Lithosphere*, *1*(2), 110–120, doi:10.1130/L32.1.

Conrad, C. P., M. D. Behn, and P. G. Silver (2007), Global mantle flow and the development of seismic anisotropy: Differences between the oceanic and continental upper mantle, *J. Geophys. Res.*, *112*, B07317, doi:10.1029/2006JB004608.

Creager, K. C., and T. H. Jordan (1986), Slab penetration into the lower mantle beneath the Mariana and other island arcs of the northwest Pacific, *J. Geophys. Res.*, *91*(B3), 3573–3589, doi:10.1029/JB091iB03p03573.

Davies, G. F. (1995), Penetration of plates and plumes through the mantle transition, *Earth Planet. Sci. Lett.*, *133*, 507–516, doi:10.1016/0012-821X(95)00039-F.

Di Giuseppe, E., J. van Hunen, F. Funiciello, C. Faccenna, and D. Giardini (2008), Slab stiffness control of trench motion: Insights from numerical models, *Geochem. Geophys. Geosyst.*, *9*, Q02014, doi:10.1029/2007GC001776.

Ding, X.-Y., and S. P. Grand (1994), Seismic structure of the deep Kurile subduction zone, *J. Geophys. Res.*, *99*(B12), 23,767–23,786, doi:10.1029/94JB02130.

Engdahl, E. R., R. van der Hilst, and R. Buland (1998), Global teleseismic earthquake relocation with improved travel times and procedures for depth determination, *Bull. Seismol. Soc. Am.*, *88*(3), 722–743.

Enns, A., T. W. Becker, and H. Schmeling (2005), The dynamics of subduction and trench migration for viscosity stratification, *Geophys. J. Int.*, *160*, 761–775, doi:10.1111/j.1365-246X.2005.02519.x.

Faccenna, C., F. Funiciello, D. Giardini, and P. Lucente (2001), Episodic back-arc extension during restricted mantle convection in central Mediterranean, *Earth Planet. Sci. Lett.*, *187*, 105–116, doi:10.1016/S0012-821X(01)00280-1.

Fukao, Y. (1992), Seismic tomogram of the Earth's mantle: Geodynamic implications, *Science*, *258*(5082), 625–630, doi:10.1126/science.258.5082.625.

Fukao, Y., S. Widiyantoro, and M. Obayashi (2001), Stagnant slabs in the upper and lower mantle transition region, *Rev. Geophys.*, *39*(3), 291–323, doi:10.1029/1999RG000068.

Funiciello, F., C. Faccenna, D. Giardini, and K. Regenauer-Lieb (2003), Dynamics of retreating slabs: 2. Insights from three-dimensional laboratory experiments, *J. Geophys. Res.*, *108*(B4), 2207, doi:10.1029/2001JB000896.

Funiciello, F., C. Faccenna, A. Heuret, S. Lallemand, E. Di Giuseppe, and T. W. Becker (2008), Trench migration, net rotation and slab-mantle coupling, *Earth Planet. Sci. Lett.*, *271*(1–4), 233–240, doi:10.1016/j.epsl.2008.04.006.

Gaherty, J. B., and B. H. Hager (1994), Compositional vs. thermal buoyancy and the evolution of subducted lithosphere, *Geophys. Res. Lett.*, *21*(2), 141–144, doi:10.1029/93GL03466.

Giardini, D., and J. H. Woodhouse (1984), Deep seismicity and modes of deformation in Tonga subduction zone, *Nature*, *307*, 505–509, doi:10.1038/307505a0.

Goes, S., F. Capitanio, and G. Morra (2008), Evidence of lower-mantle slab penetration phases in plate motions, *Nature*, *451*, 981–984.

Grand, S. P. (1994), Mantle shear structure beneath the Americas and surrounding oceans, *J. Geophys. Res.*, *99*(B6), 11,591–11,621, doi:10.1029/94JB00042.

Grand, S. P., R. D. Van der Hilst, and S. Widiyantoro (1997), Global seismic tomography: A snapshot of convection in the Earth, *GSA Today*, *7*, 1–7.

Griffiths, R. W., and S. Turner (1988), Folding of viscous plumes impinging on a density or viscosity interface, *Geophys. J.*, *95*(2), 397–419, doi:10.1111/j.1365-246X.1988.tb00477.x.

Griffiths, R. W., R. I. Hackney, and R. D. Van Der Hilst (1995), A laboratory investigation of effects of trench migration on the descent of subducted slabs, *Earth Planet. Sci. Lett.*, *133*, 1–17, doi:10.1016/0012-821X(95)00027-A.

Gudmundsson, Ó., and M. Sambridge (1998), A regionalized upper mantle (RUM) seismic model, *J. Geophys. Res.*, *103*(B4), 7121–7136, doi:10.1029/97JB02488.

Guillou-Frottier, L., J. Buttles, and P. Olson (1995), Laboratory experiments on the structure of subducted lithosphere, *Earth Planet. Sci. Lett.*, *133*, 19–34, doi:10.1016/0012-821X(95)00045-E.

Hadamard, J. S. (1911), Mouvement permanent lent d'une sphere liquide et visqueuse dans un fluide visqueux, *C. R. Acad. Sci.*, *152*, 1735.

Hager, B. H., and M. A. Richards (1989), Long wavelength variation in Earth's geoid: Physical models and dynamical implications, *Philos. Trans. R. Soc. London*, *328*, 309–327, doi:10.1098/rsta.1989.0038.

Heuret, A., and S. Lallemand (2005), Plate motions, slab dynamics and back arc deformation, *Phys. Earth Planet. Inter.*, *149*, 31–51, doi:10.1016/j.pepi.2004.08.022.

Houseman, G. A., and D. Gubbins (1997), Deformation of subducted oceanic lithosphere, *Geophys. J. Int.*, *131*(3), 535–551, doi:10.1111/j.1365-246X.1997.tb06598.x.

Husson, L. (2006), Dynamic topography above retreating subduction zones, *Geology*, *34*(9), 741–744, doi:10.1130/G22436.1.

Isacks, B., and M. Barazangi (1977), Geometry of Benioff zones: Lateral segmentation and downwards bending of the subducted lithosphere, in *Island Arcs, Deep Sea Trenches and Back-Arc Basins*, *Maurice Ewing Ser.*, vol. 1, edited by M. Talwani and W. C. Pitman III, pp. 99–144, AGU, Washington, D. C.

Isacks, B., and P. Molnar (1969), Mantle earthquake mechanisms and the sinking of the lithosphere, *Nature*, *223*, 1121–1124.

Isacks, B., and P. Molnar (1971), Distribution of stresses in the descending lithosphere from a global survey of focal mechanism solutions of mantle earthquakes, *Rev. Geophys.*, *9*, 103–174, doi:10.1029/RG009i001p00103.

Jarrard, R. D. (1986), Relations among subduction parameters, *Rev. Geophys.*, *24*, 217–284, doi:10.1029/RG024i002p00217.

Jordan, T. H. (1977), Lithospheric slab penetration into the lower mantle beneath the Sea of Okhots, *J. Geophys.*, *43*, 473–496.

Jordan, T. H., and W. S. Lynn (1974), A velocity anomaly in the lower mantle, *J. Geophys. Res.*, *79*, 2679–2685, doi:10.1029/JB079i017p02679.

Kárason, H. (2002), Constraints on mantle convection from seismic tomography and flow modeling, Ph.D. thesis, Mass. Inst. of Technol., Cambridge.

Kárason, H., and R. Van der Hilst (2001), Tomographic imaging of the lowermost mantle with differential times of refracted and diffracted core phases (PKP, Pai), *J. Geophys. Res.*, *106*, 6569–6587, doi:10.1029/2000JB900380.

Kido, M., and O. Cadek (1997), Inferences of viscosity from the oceanic geoid: Indication of a low viscosity zone below the 660-km discontinuity, *Earth Planet. Sci. Lett.*, *151*, 125–137, doi:10.1016/S0012-821X(97)81843-2.

Kincaid, C., and R. W. Griffiths (2003), Laboratory models of the thermal evolution of the mantle during rollback subduction, *Nature*, *425*(6953), 58–62, doi:10.1038/nature01923.

Kincaid, C., and P. Olson (1987), An experimental study of subduction and slab migration, *J. Geophys. Res.*, *92*, 13,832–13,840.

Kohlstedt, D. L., B. Evans, and S. J. Mackwell (1995), Strength of the lithosphere: Constraints imposed by laboratory experiments, *J. Geophys. Res.*, *100*(B9), 17,587–17,602, doi:10.1029/95JB01460.

Lambeck, K., and P. Johnston (1998), The viscosity of the mantle: Evidence from analysis of glacial-rebound phenomena, in *The Earth's Mantle: Composition, Structure, and Evolution*, edited by I. Jackson, pp. 461–502, Cambridge Univ. Press, Cambridge, U. K.

Lay, T. (1994), The fate of descending slabs, *Annu. Rev. Earth Planet. Sci.*, *22*, 33–61, doi:10.1146/annurev.ea.22.050194.000341.

Li, C., R. D. van der Hilst, E. R. Engdahl, and S. Burdick (2008), A new global model for *P* wave speed variations in Earth's mantle, *Geochem. Geophys. Geosyst.*, *9*, Q05018, doi:10.1029/2007GC001806.

Loiselet, C., L. Husson, and J. Braun (2009), From longitudinal slab curvature to slab rheology, *Geology*, *37*(8), 747–750, doi:10.1130/G30052A.1.

Loubet, N., N. M. Ribe, and Y. Gamblin (2009), Deformation modes of subducted lithosphere at the core-mantle boundary: An experimental investigation, *Geochem. Geophys. Geosyst.*, *10*, Q10004, doi:10.1029/2009GC002492.

Mitrovica, J. X., and A. M. Forte (2004), A new inference of mantle viscosity based upon joint inversion of convection and glacial isostatic adjustment data, *Earth Planet. Sci. Lett.*, *225*, 177–189, doi:10.1016/j.epsl.2004.06.005.

Moresi, L., and M. Gurnis (1996), Constraints on the lateral strength of slabs from three-dimentional dynamic flow models, *Earth Planet. Sci. Lett.*, *138*, 15–28, doi:10.1016/0012-821X(95)00221-W.

Morra, G., K. Regenauer-Lieb, and D. Giardini (2006), Curvature of oceanic arcs, *Geology*, *34*(10), 877–880, doi:10.1130/G22462.1.

Moucha, R., A. M. Forte, J. X. Mitrovica, and A. Daradich (2007), Lateral variations in mantle rheology: Implications for convection related surface observables and inferred viscosity models, *Geophys. J. Int.*, *169*(1), 113–135, doi:10.1111/j.1365-246X.2006.03225.x.

Müller, R., W. Roest, J. Y. Royer, L. Gahagan, and J. Sclater (1997), Digital isochrons of the world's ocean floor, *J. Geophys. Res.*, *102*, 3211–3214, doi:10.1029/96JB01781.

Olbertz, D., M. J. R. Wortel, and U. Hansen (1997), Trench migration and subduction zone geometry, *Geophys. Res. Lett.*, *24*, 221–224, doi:10.1029/96GL03971.

Olson, P., and H. Singer (1985), Creeping plumes, *J. Fluid Mech.*, *158*, 511–531.

Peltier, W. R. (1996), Mantle viscosity and ice-age ice sheet tomography, *Science*, *273*, 1359–1364, doi:10.1126/science.273.5280.1359.

Piromallo, C., and A. Morelli (2003), *P* wave tomography of the mantle under the Alpine-Mediterranean area, *J. Geophys. Res.*, *108*(B2), 2065, doi:10.1029/2002JB001757.

Piromallo, C., T. W. Becker, F. Funiciello, and C. Faccenna (2006), Three-dimensional instantaneous mantle flow induced by subduction, *Geophys. Res. Lett.*, *33*, L08304, doi:10.1029/2005GL025390.

Puspito, N. T., Y. Yamanaka, T. Miyatake, K. Shimazaki, and K. Hirahara (1993), Three-dimensional P wave velocity structure beneath the Indonesian region, *Tectonophysics*, *220*(1–4), 175–192, doi:10.1016/0040-1951(93)90230-H.

Ren, Y., E. Stutzmann, R. Van der Hilst, and J. Besse (2007), Understanding seismic heterogeneities in the lower mantle beneath the Americas from seismic tomography and plate tectonic history, *J. Geophys. Res.*, *112*, B01302, doi:10.1029/2005JB004154.

Ribe, N. M. (2003), Periodic folding of viscous sheets, *Phys. Rev. Lett.*, *E68*, 036305.

Ribe, N. M., E. Stutzmann, Y. Ren, and R. van der Hilst (2007), Buckling instabilities of subducted lithosphere beneath the transition zone, *Earth Planet. Sci. Lett.*, *254*(1–2), 173–179, doi:10.1016/j.epsl.2006.11.028.

Ricard, Y., M. A. Richards, C. Lithgow-Bertelloni, and Y. Le Stunff (1993), A geodynamic model of mantle density heterogeneity, *J. Geophys. Res.*, *98*, 21,895–21,909, doi:10.1029/93JB02216.

Royden, L. H., and L. Husson (2006), Trench motion, slab geometry and viscous stresses in subduction systems, *Geophys. J. Int.*, *167*, 881–905, doi:10.1111/j.1365-246X.2006.03079.x.

Rybczynski, W. (1911), Uber die fortschreitende Bewegung einer flussigen Kugel in einem zahen Medieum, *Bull. Acad. Sci. Cracovi, A*, *40*.

Schellart, W. P. (2004), Kinematics of subduction and subduction-induced flow in the upper mantle, *J. Geophys. Res.*, *109*, B07401, doi:10.1029/2004JB002970.

Schellart, W. P. (2009), Evolution of the slab bending radius and the bending dissipation in three-dimensional subduction models with a variable slab to upper mantle viscosity ratio, *Earth Planet. Sci. Lett.*, *288*, 309–319.

Schellart, W. P., J. Freeman, D. R. Stegman, L. Moresi, and D. May (2007), Evolution and diversity of subduction zones controlled by slab width, *Nature*, *446*(7133), 308–311, doi:10.1038/nature05615.

Spakman, W., S. van der Lee, and R. van der Hilst (1993), Travel-time tomography of the European-Mediterranean mantle down to 1400 km, *Phys. Earth Planet. Inter.*, *79*(1–2), 3–74, doi:10.1016/0031-9201(93)90142-V.

Stegman, D. R., J. Freeman, W. P. Schellart, L. Moresi, and D. May (2006), Influence of trench width on subduction hinge retreat rates in 3-D models of slab rollback, *Geochem. Geophys. Geosyst.*, *7*, Q03012, doi:10.1029/2005GC001056.

Tackley, P. J. (1993), Effects of strongly temperature-dependent viscosity on time-dependent, three-dimensional models of mantle convection, *Geophys. Res. Lett.*, *20*(20), 2187–2190, doi:10.1029/93GL02317.

Tagawa, M., T. Nakakuki, and F. Tajima (2007), Dynamical modeling of trench retreat driven by the slab interaction with the mantle transition zone, *Earth Planets Space*, *59*, 65–74.

Tajima, F., and S. P. Grand (1995), Evidence of high velocity anomalies in the transition zone associated with Southern Kurile Subduction Zone, *Geophys. Res. Lett.*, *22*(23), 3139–3142, doi:10.1029/95GL03314.

Tajima, F., and S. P. Grand (1998), Variation of transition zone high-velocity anomalies and depression of 660 km discontinuity associated with subduction zones from the southern Kuriles to Izu-Bonin and Ryukyu, *J. Geophys. Res.*, *103*(B7), 15,015–15,036.

Tao, W. C., and R. J. O'Connell (1993), Deformation of a weak subducted slab and variation of seismicity with depth, *Nature*, *361*(6413), 626–628, doi:10.1038/361626a0.

Thieulot, C., P. Fullsack, and J. Braun (2008), Adaptive octree-based finite element analysis of two- and three-dimensional indentation problems, *J. Geophys. Res.*, *113*, B12207, doi:10.1029/2008JB005591.

van der Hilst, R. (1995), Complex morphology of subducted lithosphere in the mantle beneath the Tonga trench, *Nature*, *374*(6518), 154–157, doi:10.1038/374154a0.

van der Hilst, R., and T. Seno (1993), Effects of relative plate motion on the deep structure and penetration depth of slabs below the Izu-Bonin and Mariana island arcs, *Earth Planet. Sci. Lett.*, *120*(3–4), 395–407, doi:10.1016/0012-821X(93)90253-6.

van der Hilst, R., and S. Widiyantoro (1997), Evidence for deep mantle circulation from global tomography, *Nature*, *386*, 578–584, doi:10.1038/386578a0.

Vassiliou, M. S., B. H. Hager, and A. Raefsky (1984), The distribution of earthquakes with depth and stress in subducting slabs, *J. Geodyn.*, *1*(1), 11–28, doi:10.1016/0264-3707(84)90004-8.

Wessel, P., and W. H. F. Smith (1991), Free software helps map and display data, *Eos Trans. AGU*, *72*, 441, doi:10.1029/90EO00319.

Widiyantoro, S., and R. van der Hilst (1996), Structure and evolution of lithospheric slab beneath the Sunda Arc, Indonesia, *Science*, *271*(5255), 1566–1570, doi:10.1126/science.271.5255.1566.

Wortel, M. J. R., and W. Spakman (2000), Subduction and slab detachment in the Mediterranean-Carpathian region, *Science*, *290*, 1910–1917, doi:10.1126/science.290.5498.1910.

Wortel, M. J. R., and N. J. Vlaar (1988), Subduction zone seismicity and the thermo-mechanical evolution of downgoing lithosphere, *Pure Appl. Geophys.*, *128*, 625–659, doi:10.1007/BF00874551.

Yamaoka, K. Y., Y. Fukao, and M. Kumazawa (1986), Spherical shell tectonics: Effects of sphericity and inextensibility on the geometry of the descending lithosphere, *Rev. Geophys.*, *24*, 27–53, doi:10.1029/RG024i001p00027.

Yamato, P., L. Husson, J. Braun, C. Loiselet, and C. Thieulot (2009), Influence of surrounding plates on 3D subduction dynamics, *Geophys. Res. Lett.*, *36*, L07303, doi:10.1029/2008GL036942.

Yoshioka, S., and M. J. R. Wortel (1995), Three-dimensional numerical modeling of detachment of subducted lithosphere, *J. Geophys. Res.*, *100*(B10), 20,223–20,244, doi:10.1029/94JB01258.

Zhao, D., Y. Xu, D. A. Wiens, L. M. Dorman, J. Hiderbrand, and S. C. Webb (1997), Depth extent of the Lau back-arc spreading center and its relation to subduction processes, *Science*, *278*, 254–257, doi:10.1126/science.278.5336.254.

Zhong, S., and G. F. Davies (1999), Effects of plate and slab viscosities on the geoid, *Earth Planet. Sci. Lett.*, *170*(4), 487–496, doi:10.1016/S0012-821X(99)00124-7.

Zhong, S., and M. Gurnis (1994), Controls on trench topography from dynamic models of subducted slabs, *J. Geophys. Res.*, *99*, 15,683–15,695, doi:10.1029/94JB00809.

Zhong, S., and M. Gurnis (1995), Mantle convection with plates and mobile, faulted plate margins, *Science*, *267*, 838–843, doi:10.1126/science.267.5199.838.

Zhou, H.-W. (1988), How well can we resolve the deep seismic slab with seismic tomography?, *Geophys. Res. Lett.*, *15*(12), 1425–1428, doi:10.1029/GL015i012p01425.

Geology, published online on 5 August 2011 as doi:10.1130/G32136.1

Dynamic constraints on the crustal-scale rheology of the Zagros fold belt, Iran

Philippe Yamato[1,2]*, Boris J.P. Kaus[2,3], Frédéric Mouthereau[4], and Sébastien Castelltort[2]
[1]Geosciences Rennes, UMR CNRS (Unité Mixte de Recherche, Centre National de la Recherche Scientifique) 6118, Université de Rennes 1, 35042 Rennes Cedex, France
[2]Department of Earth Sciences, E.T.H. Zürich, Sonnegstrasse 5, 8092 Zurich, Switzerland
[3]Department of Earth Sciences, University of Southern California–Los Angeles, Los Angeles, California 90089-0740, USA
[4]UPMC (Université Pierre et Marie Curie) Université Paris 06, UMR CNRS 7193, ISTeP (Institut des Sciences de la Terre de Paris), 75252 Paris Cedex 5, France

ABSTRACT

Thin-skinned fold-and-thrust belts are generally considered as the result of contractional deformation of a sedimentary succession over a weak décollement layer. The resulting surface expression frequently consists of anticlines and synclines spaced in a fairly regular manner. It is thus tempting to use this spacing along with other geological constraints to obtain insights into the dynamics and rheology of the crust on geological time scales. Here we use the Zagros Mountains of Iran as a case study, as it is one of the most spectacular, well-studied thin-skinned fold-and-thrust belts in the world. Both analytical and numerical models are employed to study what controls fold spacing and under what conditions folding dominates over thrusting. The models show that if only a single basal décollement layer is present underneath a brittle sedimentary cover, deformation is dominated by thrusting, which is inconsistent with the data of the Zagros fold belt. If we instead take into account additional décollement layers that have been documented in the field, a switch in deformation mode occurs and crustal-scale folding is obtained with the correct spacing and time scales. We show that fold spacing can be used to constrain the friction angle of the crust, which is ~5° in the Zagros fold belt. This implies that on geological time scales, the upper crust is significantly weaker than previously thought, possibly due to the effect of fluids.

INTRODUCTION

It is often assumed that fold belts can be explained by folding of a sedimentary layer above a basal detachment formed by a weak layer. As the spacing between folds in such belts is quite regular, we can consider them as a large-scale natural experiment of crustal deformation. Ideally, it should be possible to combine fold spacing with other geological data and theory to constrain parameters such as crustal rheology that are difficult or impossible to constrain from field observations alone.

The classical explanation of folds in fold belts is that they are due to a folding instability, which is well known for a homogeneous sedimentary sequence with either a power law viscous rheology or an elastic rheology (Schmalholz et al., 2002; Burg et al., 2004; Schmalholz, 2006). The dominant wavelength, λ_{dom}, for a viscous power law layer of viscosity η_{sed} and with exponent n overlying a linear viscous layer of viscosity η_{salt} is given by (Schmalholz et al., 2002):

$$\lambda_{dom} = 3.1\left(\frac{\eta_{sed}}{n\eta_{salt}}\right)^{\frac{1}{6}}\sqrt{\frac{H_{salt}}{H_{sed}}H_{sed}}, \qquad (1)$$

where H_{sed} and H_{salt} are the thicknesses of the sedimentary cover and of the salt, respectively. The growth rate (q_{dom}) of this instability non-dimensionalized over the background strain rate $\dot{\varepsilon}$ (Schmalholz et al., 2002) is given by:

$$\frac{q_{dom}}{\dot{\varepsilon}} = 2.5n\left(\frac{\eta}{n\eta_{salt}}\right)^{\frac{1}{3}}\frac{H_{salt}}{H_{sed}} = 2.5n\left(\frac{\lambda_{dom}}{3.1H_{sed}}\right)^{2}, \quad (2)$$

and a combination of numerical and analytical studies have shown that $q_{dom}/\dot{\varepsilon}$ should be >~20 for folding to form observable folds, rather than homogeneous thickening (e.g., Kaus et al., 2008).

The Zagros fold belt of Iran constitutes a classical example of such a folded belt that is geologically (e.g., Stocklin, 1968; Alavi, 2004; McQuarrie, 2004; Sherkati and Letouzey, 2004; Mouthereau et al., 2007) and geophysically (e.g., Jahani et al., 2009; Hatzfeld and Molnar, 2010; Nissen et al., 2010) well studied due to excellent exposure and extensive seismic and borehole data from exploration. The main tectonic and stratigraphic units are summarized in Figure 1 and show that a particular feature of the Zagros fold belt is a consistent spacing of folds with a wavelength (λ_{dom}) of 14 ± 3 km. These folds are generally explained as detachment folding of the post-Cambrian sedimentary sequence above a basal weak layer of the Hormuz salt.

The centroid depths of waveform-modeled earthquakes indicate that faulting is restricted to two structural levels located in the competent sediment cover units at 5–6 km depth and within the Precambrian basement at depths >11 km to 30 km (e.g., Talebian and Jackson, 2004; Nissen et al., 2010). Seismic reflection profiles (Jahani et al., 2009) and field observations in the Fars region (Mouthereau et al., 2007) show a lack of major thrust faults cutting the folded cover up to the surface. This confirms that detachment folding rather than thrusting is the dominant deformation mode in the Zagros fold belt. In this aspect, the Zagros Mountains differ from other fold-and-thrust belts such as the Jura Mountains, where large-offset faults are continuous across the stratigraphic sequence, well imaged through seismic studies (Simpson, 2009).

Detachment folding theory should thus be perfectly applicable to the Zagros fold belt. Equations 1 and 2 show that fold spacing depends strongly on the rheology of the overburden and on the thickness of the basal salt layer. In the Zagros, a linear viscous overburden (n = 1) and a viscosity contrast of 100 between salt and overburden requires a salt layer thickness of ~7.8 km to fit the observed spacing of folds (Equation 1). However, seismic data indicate that the thickness of the Hormuz salt is no more than 1 or 2 km (Mouthereau et al., 2006; Jahani et al., 2009). If the sedimentary cover has a power law rheology instead, its power law exponent should be n ~ 23 (Equation 2) to explain the data, considerably larger than estimates from rock creep experiments (Ranalli, 1995). Large power law exponents are often taken as evidence for a brittle rheology. Currently, however, there is no theory that can reliably predict the spacing of detachment folds in the case of a brittle overburden.

There is currently no satisfactory explanation for (1) why deformation in the Zagros fold belt is dominated by folding and not by thrusting, and (2) what controls the spacing of folds and how it is linked to crustal rheology. In order to address this, we performed thermomechanical numerical simulations to study the dynamics of detachment folding in the presence of a brittle sedimentary cover.

NUMERICAL MODEL

To study the effect of using visco-elasto-plastic rheologies on crustal dynamics, we have performed a series of numerical experiments using the finite element code MILAMIN_VEP (e.g., Kaus, 2010; see Item DR1 in the GSA Data Repository[1]). The viscosities of the weak layers are assumed to be linear and constant, a reasonable approximation for the rheology of salt. The brittle layers have a temperature-dependent

*E-mail: philippe.yamato@univ-rennes1.fr.

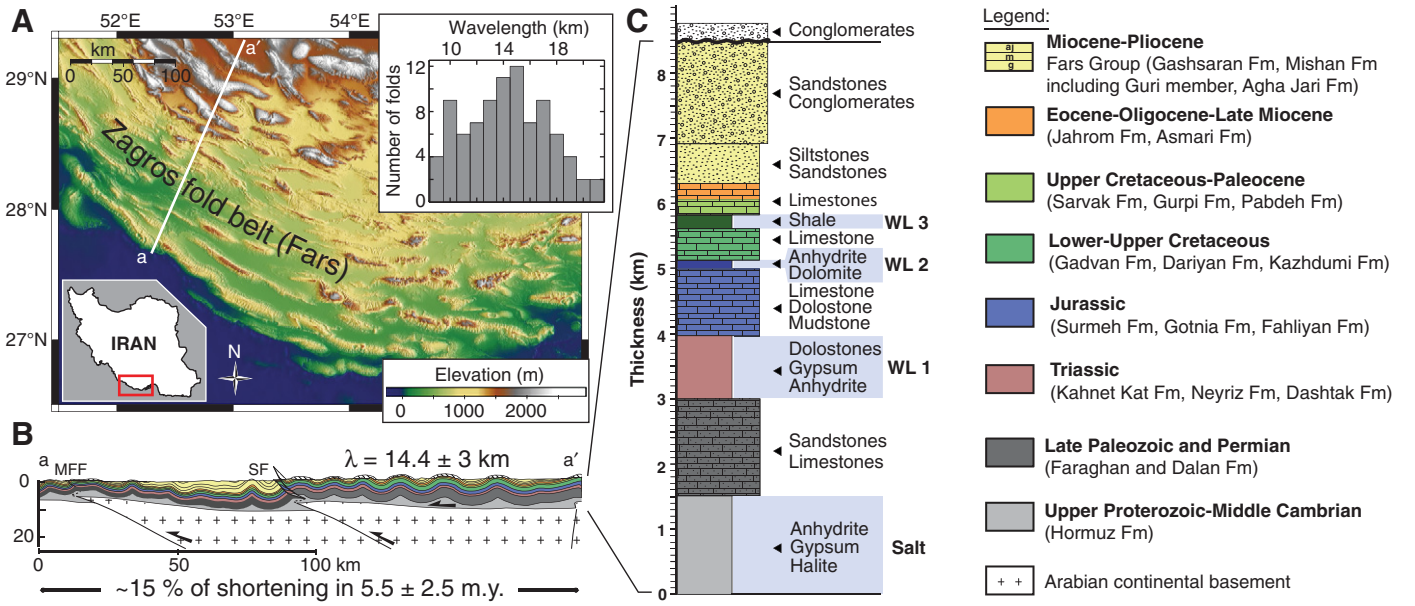

Figure 1. Field constraints for Zagros fold belt. A: Topography illustrates regular spacing of folds with amplitude ~500–1000 m over area of ~80,000 km². Fold crest lengths are ~50 km in average. Inset shows distribution of fold wavelengths measured for 88 anticlines from Zagros fold belt. B: Cross-section a-a′ across Zagros fold belt based on field measurement (Mouthereau et al., 2007). λ corresponds to average wavelength of folds. This value is slightly smaller than 15.8 ± 5.3 km from Mouthereau et al. (2007) that took into account folds from entire Fars area, including diapiric folds. MFF—Mountain Front fault; SF—Surmeh fault, associated with basement faulting. Vertical fold velocity is 0.3–0.6 mm yr^{-1}. C: Synthetic stratigraphic log where WL1, WL2, and WL3 correspond to weak layers in sedimentary sequence (Fm—Formation).

rheology of limestone (see Item DR1) that corresponds to the majority of rocks within the sedimentary cover (Fig. 1C; Mouthereau et al., 2007). A linear geotherm of 25 °C km^{-1} is initially applied (see Item DR1). For the low-temperature conditions of the Zagros fold belt, stresses are such that the rocks effectively deform in the brittle regime. Our model domain is initially 200 × 7.225 km (see Item DR1). The top boundary is a free surface with no erosion (see Item DR1), and a constant background strain rate of 10^{-15} s^{-1} is applied at the right of the model box, which results in 15% shortening after 5.5 m.y., consistent with geological constraints (see Item DR1). All other sides of the model have free slip conditions. Finally, to initiate the folding, the interface between the salt and the overburden rocks has random noise with maximum amplitude of 100 m. Model simulations were performed for 5.5 m.y., after which results were interpreted.

RESULTS FROM NUMERICAL SIMULATIONS

With a 1.5-km-thick single basal detachment layer underlying a homogeneous brittle sedimentary cover, the models develop faults rather than folds (Fig. 2B). Such faults develop at early stages with a spacing that is approximately twice the brittle layer thickness. Subsequent deformation is locked around these folds that have a box-fold geometry. Compared to the Zagros fold belt, we thus obtain a too large wavelength and an incorrect deformation style. Additional simulations where we varied the frictional parameters of the crust or the viscosity of the salt layer gave similar results (Fig. DR1 in the Data Repository). We thus infer that it is impossible to reproduce the observed finite wavelength of Zagros fold belt folds (Fig. 1) by considering only one weak basal décollement layer, unless this layer has an unrealistically large thickness.

A detailed look at the stratigraphic column, however, reveals that the sedimentary cover is not rheologically homogeneous. Instead there

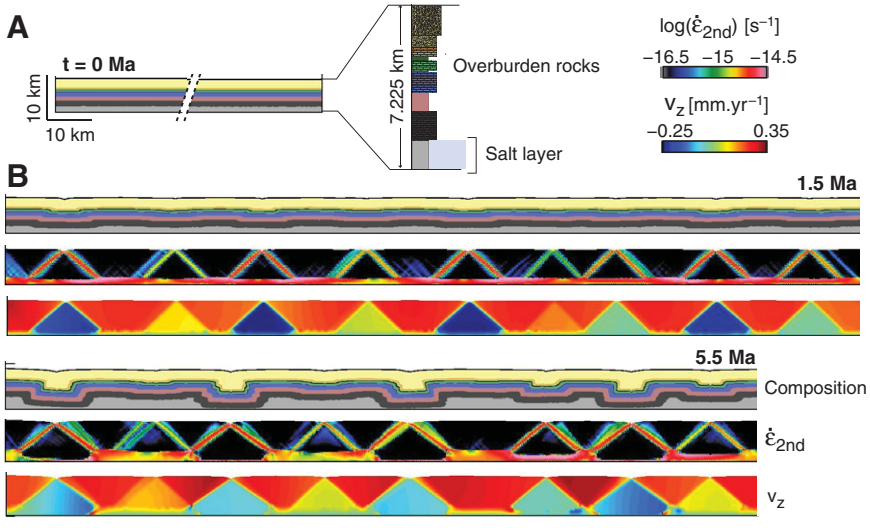

Figure 2. Simulation with basal décollement layer only. A: Initial setup with sedimentary thickness of 7.225 km. All rocks above basal salt layer are homogeneous and have friction angle of 5° and cohesion of 20 MPa. Background strain rate of 10^{-15} s^{-1} is imposed at right model boundary. t corresponds to time. B: Geometry, strain rate ($\dot{\varepsilon}$), and vertical velocities (V_z) after 1.5 Ma and 5.5 Ma, respectively. Deformation is localized along crustal-scale plastic shear zones and deformation structures are fault dominated.

[1]GSA Data Repository item 2011240, Item DR1 (description of the numerical code with more details on the setup, on the material properties and on the boundary conditions), Item DR2 (semianalytical method to predict fold spacing in the presence of a brittle overburden), and Figure DR1 (additional simulations with only a single basal décollement), is available online at www.geosociety.org/pubs/ft2011.htm, or on request from editing@geosociety.org or Documents Secretary, GSA, P.O. Box 9140, Boulder, CO 80301, USA.

are several layers that are composed of relatively weak rocks such as evaporites or shales (Figs. 1B and 1C; see detailed descriptions in McQuarrie, 2004; Sherkati et al., 2006; Mouthereau et al., 2007). A second set of simulations took this fine-scale rheological structure into account (Fig. 3). The results are remarkably different from the previous experiments: rather than being fault-dominated, deformation is now achieved by folding, with a final wavelength similar to the one observed in the Zagros fold belt (Fig. 3). An analysis of the simulation shows that the spacing of the folds is fixed at a very early stage, after which the individual structures grow without clear geometric pattern, in accordance with field constraints (Mouthereau et al., 2007). The initial fine-scale rheological stratification of the sediment cover of the Zagros fold belt thus has a first-order effect on the development of upper crustal–scale structures. These results are in full agreement with a recent study of active seismicity in the Zagros fold belt that showed that both the Hormuz salt layer and the intermediate layers are mechanically weak zones that form barriers to rupture for active faults (Nissen et al., 2010).

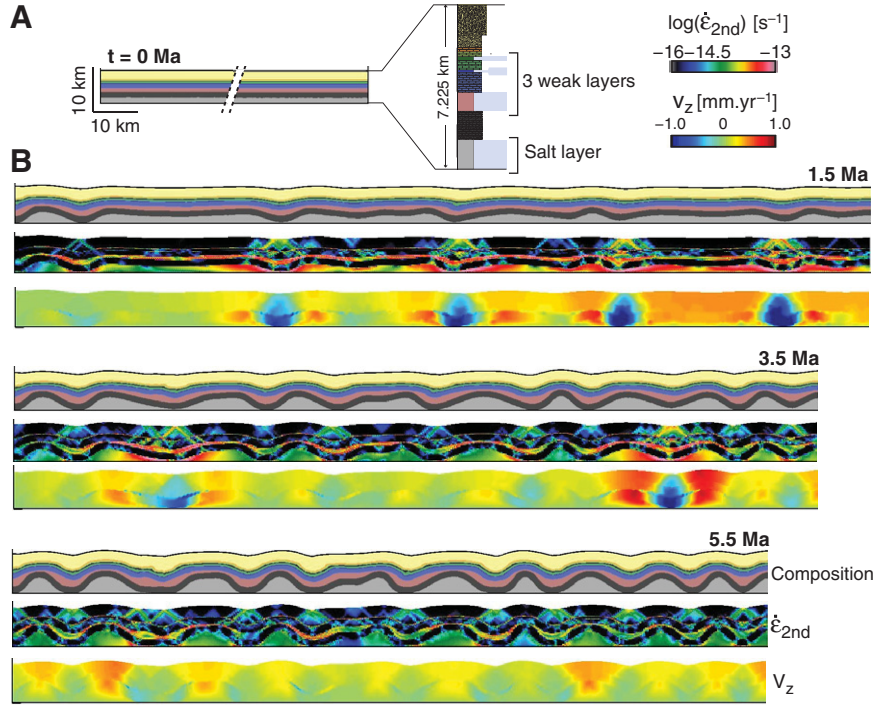

Figure 3. Simulation with intermediate crustal detachment layers. A: Initial setup as in Figure 2, but with three additional weak crustal detachment layers with 10^{18} Pa·s. B: Snapshots of geometry, strain rate ($\dot{\varepsilon}$), and vertical velocities (V_z) at different times (t), illustrating that crustal-scale folds rather than faults dominate deformation pattern. Note that folds do not grow continuously with time, but rather grow to a certain amplitude, after which activity switches to a different fold.

CONSTRAINTS ON CRUSTAL RHEOLOGY

The simulations presented in this study highlight the different modes of deformation that might occur in fold-and-thrust belts. However, they give limited insights into the underlying physics, as it remains unclear how sensitive the spacing of structures is to the rheology of the crust. For this reason, we developed a semi-analytical methodology, drastically reducing the computational requirements, that allows us to predict the outcome of numerical simulations in a large parameter space (see details in Item DR2). The resulting wavelength versus growth rate diagrams have a single maximum as a function of nondimensional wavelength (Fig. 4A). Rigorously, these semianalytical results are only valid for very small deformations. However, a comparison with numerical simulations reveals that they correctly predict the spacing of folds even after 5.5 m.y., which confirms that fold spacing is selected at a very early stage in the evolution of a fold-and-thrust belt (Fig. 4A).

Results for a homogeneous and brittle sedimentary cover reveal that the dominant growth rate is smaller than 20, which essentially means that folding will not be able to overcome background pure-shear thickening. Our numerical simulations indicate that this leads to fault-dominated deformation rather than folding (box folds, Fig. 2). If, however, weak layers are taken into account in the sedimentary sequence, the growth rate is significantly larger and the dominant wavelength is reduced (Fig. 4B). The addition of a single weak layer is sufficient to switch deformation styles from fault dominated to fold dominated, and elasticity has only a minor effect.

Using the same semianalytical methodology, we performed a large number of simulations and found that the two most important parameters are the viscosity of the salt (weak) layers and the friction angle of the crust, whereas rock density plays little to no role. Plots of dominant wavelength and growth rate versus those two parameters show an approximate equal dependence on the two parameters (Fig. 4). The results also show that weak layers in all cases yield growth rates that are sufficiently large for the folding instability to dominate faulting.

In the case of the Zagros fold belt, the effective viscosity of salt has been determined to be close to 10^{18} Pa·s, a value consistent with scaled laboratory derived values (Spiers et al., 1990) and other modeling studies (Van Keken et al., 1993; Mouthereau et al., 2006). If we combine this with our method, we estimate that the effective friction angle for the crust in the Zagros fold belt on geological time scales is ~5° ± 5° (Fig. 4B).

DISCUSSIONS AND CONCLUSIONS

Contrary to the common view of fold belts that often considers only a single major basal décollement, we demonstrate through the example of the Zagros Mountains that the entire stratigraphic sequence might influence the dynamics of the belt. Heterogeneities within the sedimentary cover, and weak layers in particular, control whether deformation is dominated by crustal-scale folds or by thrusts. The stratigraphy of a fold belt plays a much larger role than previously appreciated, and should thus be taken into account if one wishes to reconcile field observations with physically consistent models of geological processes.

Balancing geological cross sections in fold-thrust belts is a difficult exercise that aims at providing a consistent structural and kinematic interpretation of usually independent structural data. Our method paves the way for developing future generations of two- and three-dimensional dynamic reconstruction models for fold-and-thrust belts (e.g., Lechmann et al., 2010).

Moreover, we show that the regular spacing of folds puts constraints on the rheology of the crust on geological time scales. In the case of the Zagros fold belt, the value for the friction angle we obtained in this manner is small (<10°); this indicates that the crust was rather weak, potentially due to high fluid pressures (e.g., Huismans et al., 2005).

ACKNOWLEDGMENTS

This work benefited from fruitful discussions with L. Le Pourhiet, S. Schmalholz, and Y. Podladchikov. Constructive reviews from D. van Hinsbergen and two anonymous reviewers also contributed to improve the manuscript. B. Kaus was partly supported by European Research Council Starting Grant 258830.

REFERENCES CITED

Alavi, M., 2004, Regional stratigraphy of the Zagros fold-thrust belt of Iran and its proforeland evolution: American Journal of Science, v. 304, p. 1–20, doi:10.2475/ajs.304.1.1.

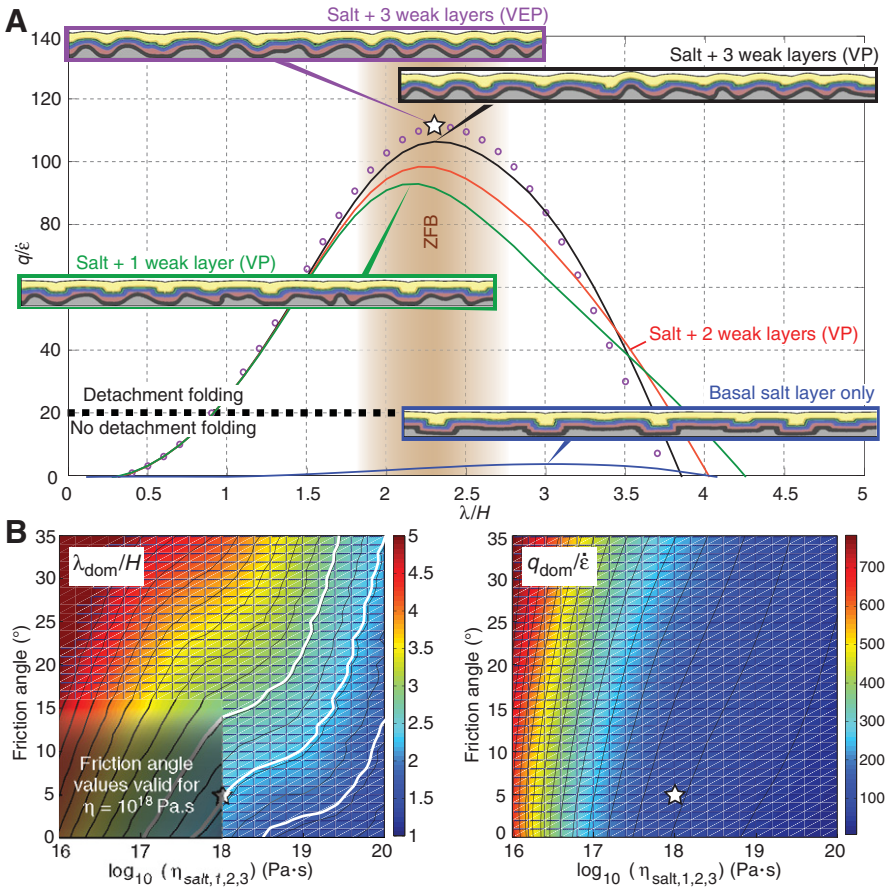

Figure 4. Influence of multiple weak layers and elasticity on folding. λ, *H*, *q*, and ė correspond to wavelength, total thickness, growth rate, and background strain rate, respectively. VP—viscoplastic simulation; VEP—viscoelastoplastic simulation. This diagram was produced using semianalytical approach described in Item DR2 (see footnote 1). A: Growth rate values obtained for given values of λ/*H* for 0, 1, 2, and 3 weak layers. For each case, characteristic wavelength value corresponds to highest value of growth rate (e.g., white star for case with three weak layers). Insets show results of numerical simulations after 5.5 m.y.; folds develop with spacing that is in excellent agreement with predicted characteristic wavelength. Single basalt décollement layer results in small folding growth rates and thrust-dominated deformation. Addition of one or more weak layers to brittle sedimentary cover results increases growth rate significantly and leads to folding-dominated deformation. ZFB area corresponds to λ/*H* ratio of Zagros fold belt. B: Diagrams of characteristic wavelength (left) and corresponding growth rate (right) versus viscosity of weak layers and friction angle of crust. Thick white lines show constraints for Zagros fold belt (average ±1 standard deviation). As in Zagros fold belt, salt viscosity is constrained independently; best-fit friction angle for crust is 5° ± 5°. White star corresponds to simulation of Figure 3.

Burg, J.-P., Kaus, B.J.P., and Podladchikov, Y.Y., 2004, Dome structures in collision orogens: Mechanical investigation of the gravity/compression interplay, *in* Whitney, D.L., et al., eds., Gneiss domes in orogeny: Geological Society of America Special Paper 380, p. 47–66, doi:10.1130/0-8137-2380-9.47.

Hatzfeld, D., and Molnar, P., 2010, Comparisons of the kinematics and deep structures of the Zagros and Himalaya and of the Iranian and Tibetan plateaus and geodynamic implications: Review of Geophysics, v. 48, RG2005, doi:10.1029/2009RG000304.

Huismans, R.S., Buiter, S.J.H., and Beaumont, C., 2005, Effect of plastic-viscous layering and strain softening on mode selection during lithospheric extension: Journal of Geophysical Research, v. 110, B02406, doi:10.1029/2004JB003114.

Jahani, S., Callot, J.P., Letouzey, J., and Frizon de Lamotte, D., 2009, The eastern termination of the Zagros Fold-and-Thrust Belt, Iran: Structures, evolution, and relationships between salt plugs, folding, and faulting: Tectonics, v. 28, TC6004, doi:10.1029/2008TC002418.

Kaus, B.J.P., 2010, Factors that control the angle of shear bands in geodynamic numerical models of brittle deformation: Tectonophysics, v. 484, p. 36–47, doi:10.1016/j.tecto.2009.08.042.

Kaus, B.J.P., Steedman, C., and Becker, T.W., 2008, From passive continental margin to mountain belt: Insights from analytical and numerical models and application to Taiwan: Physics of the Earth and Planetary Interiors, v. 171, p. 235–251, doi:10.1016/j.pepi.2008.06.015.

Lechmann, S.M., Schmalholz, S.M., Burg, J.-P., and Marques, F.O., 2010, Dynamic unfolding of multilayers: 2D numerical approach and application to turbidites in SW Portugal: Tectonophysics, v. 494, p. 64–74, doi:10.1016/j.tecto.2010.08.009.

McQuarrie, N., 2004, Crustal scale geometry of the Zagros fold-thrust belt, Iran: Journal of Structural Geology, v. 26, p. 519–535, doi:10.1016/j.jsg.2003.08.009.

Mouthereau, F., Lacombe, O., and Meyer, B., 2006, The Zagros folded belt (Fars, Iran): Constraints from topography and critical wedge modelling: Geophysical Journal International, v. 165, p. 336–356, doi:10.1111/j.1365-246X.2006.02855.x.

Mouthereau, F., Tensi, J., Bellahsen, N., Lacombe, O., De Boisgrollier, T., and Kargar, S., 2007, Tertiary sequence of deformation in a thin-skinned/thick skinned collision belt: The Zagros Folded Belt (Fars, Iran): Tectonics, v. 26, TC5006, doi:10.1029/2007TC002098.

Nissen, E., Yamini-Fard, F., Tatar, M., Gholamzadeh, A., Bergman, E., Elliott, J.R., Jackson, J.A., and Parsons, B., 2010, The vertical separation of mainshock rupture and microseismicity at Qeshm island in the Zagros fold-and-thrust belt, Iran: Earth and Planetary Science Letters, v. 296, p. 181–194, doi:10.1016/j.epsl.2010.04.049.

Ranalli, G., 1995, Rheology of the Earth (second edition): London, Chapman and Hall, 413 p.

Schmalholz, S.M., 2006, Scaled amplification equation: A key to the folding history of buckled viscous single-layers: Tectonophysics, v. 419, p. 41–53, doi:10.1016/j.tecto.2006.03.008.

Schmalholz, S.M., Podladchikov, Y., and Burg, J.-P., 2002, Control of folding by gravity and matrix thickness: Implications for large-scale folding: Journal of Geophysical Research, v. 107, 2005, doi:10.1029/2001JB000355.

Sherkati, S., and Letouzey, J., 2004, Variation of structural style and basin evolution in the central Zagros (Izeh zone and Dezful embayment): Iran: Marine and Petroleum Geology, v. 21, p. 535–554, doi:10.1016/j.marpetgeo.2004.01.007.

Sherkati, S., Letouzey, J., and Frizon de Lamotte, D., 2006, Central Zagros fold-thrust belt (Iran): New insights from seismic data, field observation, and sandbox modelling: Tectonics, v. 25, TC4007, doi:10.1029/2004TC001766.

Simpson, G.D.H., 2009, Mechanical modeling of folding versus faulting in brittle-ductile wedges: Journal of Structural Geology, v. 31, p. 369–381, doi:10.1016/j.jsg.2009.01.011.

Spiers, C.J., Schutjens, P.M.T.M., Brzesowsky, R.H., Peach, C.J., Liezenberg, J.L., and Zwart, H.J., 1990, Experimental determination of constitutive parameters governing creep of rocksalt by pressure solution, *in* Knipe, R.J., and Rutter, E.H., eds., Deformation mechanisms, rheology and tectonics: Geological Society of London Special Publication 54, p. 215–227, doi:10.1144/GSL.SP.1990.054.01.21.

Stocklin, J., 1968, Structural history and tectonics of Iran; a review: American Association of Petroleum Geologists Bulletin, v. 52, p. 1229–1258.

Talebian, M., and Jackson, J.A., 2004, Reappraisal of earthquake focal mechanisms and active shortening in the Zagros Mountains of Iran: Geophysical Journal International, v. 156, p. 506–526, doi:10.1111/j.1365-246X.2004.02092.x.

Van Keken, P.E., Spiers, C.J., Van den Berg, A.P., and Muyzert, E.J., 1993, The effective viscosity of rocksalt: Implementation of steady state creep laws in numerical models of salt diapirism: Tectonophysics, v. 225, p. 457–476, doi:10.1016/0040-1951(93)90310-G.

Manuscript received 2 February 2011
Revised manuscript received 14 March 2011
Manuscript accepted 1 April 2011

Printed in USA

Lithos 127 (2011) 222–238

Contents lists available at SciVerse ScienceDirect

Lithos

journal homepage: www.elsevier.com/locate/lithos

Subduction interface processes recorded by eclogite-facies shear zones (Monviso, W. Alps)

S. Angiboust [a,*], P. Agard [a], H. Raimbourg [b], P. Yamato [c], B. Huet [d]

[a] ISTEP, Université Paris 06-UPMC, UMR CNRS 7193, 75252 Cedex 05 PARIS, France
[b] ISTO, UMR CNRS 6113, Campus Géosciences, 1A rue de la Férolerie, 45071 ORLEANS cedex 2, France
[c] Geosciences Rennes, UMR CNRS 6118, Université de Rennes1 Campus Beaulieu CS 74205, F-35 042 Rennes Cedex France
[d] Department for Geodynamics and Sedimentology, University of Vienna, Althanstrasse 14, A-1090 Vienna, Austria

ARTICLE INFO

Article history:
Received 28 June 2011
Accepted 7 September 2011
Available online 16 September 2011

Keywords:
Subduction channel
Shear zone
Eclogite
Fluids
Monviso ophiolite

ABSTRACT

The Monviso ophiolite Lago Superiore Unit constitutes a well-preserved, almost continuous upper fragment of oceanic lithosphere subducted at c. 80 km depth, thereby providing a unique opportunity to study mechanical coupling processes and meter-scale fluid–rock interactions occurring at such depths in present-day subduction zones. It is made of (i) a variably thick (50–500 m) section of eclogitized basaltic crust (associated with minor calcschist lenses) overlying a 100–400 m thick metagabbroic body and of (ii) a c. 1 km thick serpentinite sole. We herein focus on the three major eclogite-facies shear zones found at the top of the unit, at the boundary between basalts and gabbros, and between gabbros and serpentinites, respectively. Strain localization occurred at lithological interfaces, irrespective of material strength. While ductile deformation dominates along the shear zones, local brittle behavior is demonstrated by the existence of numerous eclogite breccias of Fe–Ti metagabbros and widespread garnet fractures, possibly linked with intermediate-depth eclogite-facies (micro)seismicity. These m- to hm-sized fragments of Fe–Ti metagabbros were later sheared and disseminated within serpentinite schists along the gabbro–serpentinite boundary (Lower Shear zone; LSZ). Pervasive and focused fluid flow is attested in the LSZ by significant alteration of bulk rock compositions, weakening of the rocks and widespread crystallization of hydrous parageneses. By contrast, the Intermediate Shear zone (ISZ) shows evidence for more restricted, short-range fluid flow. The activity of both the ISZ and LSZ ceased during early lawsonite eclogite-facies exhumation, when deformation localized deeper within the serpentinite sole, allowing for the detachment (and preservation) of this large ophiolitic fragment.

1. Introduction

Characterisation of subduction interface dynamics is crucial to understand lithospheric-scale coupling between plates, vertical movements, material recycling and to better assess seismic hazard. The subduction interface is the target of numerous geophysical (e.g., Abers et al., 2006; Hilairet et al., 2007; Oncken and ANCORP working group, 2003; Raimbourg et al., 2007; Ranero et al., 2003; Zhao et al., 2002) and numerical modeling investigations (e.g., Gerya et al., 2002; Yamato et al., 2007). A wealth of field observations constrain mechanical processes occurring along the seismogenic zone at depth where megathrust earthquakes occur (15–35 km; Toyoshima, 1990; Ikesawa et al., 2003; Rowe et al., 2005; Bachmann et al., 2009; Meneghini et al., 2010; Fig. 1). In comparison, mechanical processes taking place deeper (>30–40 km) along the subduction interface, such as episodic tremor and slip events (Rogers and Dragert, 2003) or intermediate depth seismicity, are still poorly known due to the scarcity of well-preserved fault planes and shear zones within exhumed fragments detached beyond such depths (e.g. Austrheim and Andersen, 2004; John and Schenk, 2006; Healy et al., 2009; Fig. 1).

Large-scale, fossil shear zones from exhumed portions of subducted lithosphere may preserve the record of subduction interface processes (such as dynamic recrystallization, fluid flow and mass transfer) and shed light on interplate mechanical coupling and past seismic activity (e.g., Handy et al., 1999; John et al., 2009; Kirby, 1985; Montési and Hirth, 2003; Platt and Behr, 2011; White et al., 1980). However, contrary to eclogite facies shear zones from deeply subducted continental crust studied in the Norwegian Caledonides (e.g., Boundy et al., 1992; Fountain et al., 1994; Raimbourg et al., 2007; Terry and Heidelbach, 2006), few examples exist on large-scale, deeply subducted oceanic lithosphere remnants liable to give information on mechanisms acting during long-lived oceanic subduction (e.g., Hermann et al., 2000; Philippot and Van Roermund, 1992).

* Corresponding author at: ISTeP, Université Pierre et Marie Curie, Case 129, 46–00 3e, 4, place Jussieu, 75252 PARIS Cedex 05, France. Tel.: +33 1 44274904; fax: +33 1 44275085.
E-mail address: samuel.angiboust@upmc.fr (S. Angiboust).

0024-4937/$ – see front matter © 2011 Elsevier B.V. All rights reserved.
doi:10.1016/j.lithos.2011.09.004

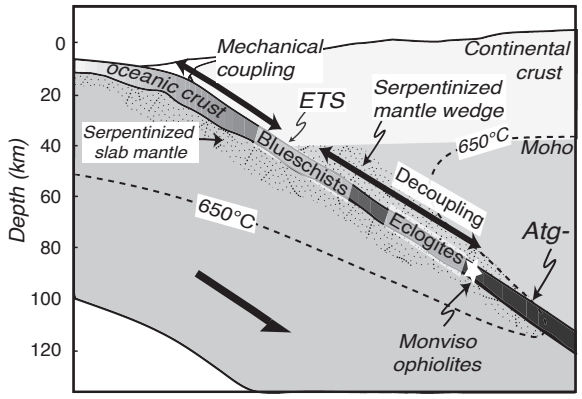

Fig. 1. Sketch showing a typical subduction zone and some of the key processes occurring along the plate interface. Mechanical coupling is maximum along the seismogenic zone (between 10 and 35 km) where the plate boundary is possibly sealed (Audet et al., 2009). Episodic tremor and slip events (ETS) generally occur at the base of the seismogenic zone. Decoupling is believed to occur below due to fluid transfer across the plate interface and serpentinization of the overlying mantle wedge. Note that the oceanic mantle is also believed to be partially serpentinized before entering the trench.

This paper aims at filling this gap and focuses on eclogite-facies shear zones formed at c. 80 km depth during oceanic subduction, which are found in the Monviso ophiolite, a well-preserved fragment of Tethyan oceanic lithosphere (W. Alps, Italy; Lombardo et al., 1978; Lagabrielle and Lemoine, 1997; Groppo and Castelli, 2010; Spandler et al., 2011; Angiboust et al., in press).

We herein present detailed petrological and deformation data, from the kilometer scale to the mineral scale, on the three largest shear zones found in the Monviso ophiolite, as identified from previous mapping and recently published P–T determinations (Angiboust et al., in press). The field relationships and petrography, mineralogy and chemistry of the three major shear zones are successively presented and a detailed petro-tectonic evolution is then proposed. We then discuss implications for fluid-flow, strain partitioning and subduction dynamics, and for the detachment and migration of km-scale fragments along the subduction interface.

2. Geological setting and structure of the Lago Superiore Unit

The Western Alps result from successive subduction, accretion and collision between the European and Apulian/African plates from the Cretaceous to the Oligocene (Agard et al., 2002; Coward and Dietrich, 1989; Polino et al., 1990; Rosenbaum and Lister, 2005). The internal Western Alps represent the W-verging stack of continental and oceanic nappes formed during subduction and (partial) exhumation of the Jurassic Tethyan seafloor and associated European thinned margin below the Apulian plate (e.g., Agard et al., 2002; Angiboust et al., 2009; Bearth, 1967; Beltrando et al., 2010; Dal Piaz et al., 1972; Oberhänsli and Goffé, 2004; Rubatto and Hermann, 2003). Remnants of this slow-spreading ocean form the Liguro-Piemontese domain, now sandwiched between the Penninic front and eclogitized portions of the European continental margin (e.g., Dora Maira, Gran Paradiso; Fig. 2, inset). Eclogitized portions of the Liguro-Piemontese oceanic lithosphere are found 200 km along-strike, from the Zermatt-Saas area (in the north) to the Monviso area (in the south), and constitute some of the largest and deepest ophiolitic slices detached from a subduction zone (Angiboust et al., 2009; Bucher et al., 2005; Reinecke, 1998).

The southern extent of the Liguro-Piemontese domain can be divided in two main tectono-metamorphic domains. To the west (Queyras area), the external Liguro-Piemontese zone corresponds to a fossil accretionary wedge, the Schistes Lustrés domain *s.s.*, where m- to hm-sized blocks and lenses of mafics and ultramafics are embedded in blueschist-facies, late Mesozoic metasedimentary rocks (e.g., Agard et al., 2001, 2002; Deville et al., 1992; Lagabrielle and Cotten, 1984; Schwartz et al., 2000; Tricart et al., 2004; Fig. 2, inset). To the East, the Monviso ophiolite forms the structural base of the Liguro-Piemontese domain and is separated from the adjacent Schistes Lustrés *s.s.* domain by an extensional shear zone (Ballèvre et al., 1990). The Monviso ophiolite is in turn separated from the underlying continental Dora Maira massif (Sampeyre and Dronero units) by another extensional shear zone (Blake and Jayko, 1990; Fig. 2a,b). These deep tectonic contacts, originally thrust planes, were thus reactivated as detachment zones during the Monviso exhumation history (e.g. Philippot and Van Roermund, 1992).

Based on tectono-stratigraphy, the Monviso ophiolitic massif was earlier divided into six units separated by W-dipping ductile tectonic contacts (Lombardo et al., 1978; Schwartz et al., 2001). All the rocks of the massif show evidence for recrystallization under eclogite-facies conditions followed by retrogression under epidote-blueschist facies and greenschist facies (Blake et al., 1995; Lombardo et al., 1978). Ages for eclogitization of the ophiolite range between 50 and 40 Ma (Cliff et al., 1998; Duchene et al., 1997; Monié and Philippot, 1989; Rubatto and Hermann, 2003). Several studies suggested variable maximum P–T conditions for the Monviso ophiolite (from *c.* 450 °C/12 kbar to 620 °C/24 kbar; Blake et al., 1995; Messiga et al., 1999; Schwartz et al., 2001) and argued for the presence of a deep subduction mélange where tectonic slices detached from different depths accumulated in a weak serpentinized subduction channel (e.g., Guillot et al., 2004). However, Angiboust et al. (in press) recently demonstrated that the Monviso ophiolite can be divided in two main coherent tectono-metamorphic units (Fig. 2b): (i) the Monviso Unit to the W, which reached *c.* 480 °C/22 kbar and (ii) the Lago Superiore Unit to the E, which recrystallized within lawsonite eclogite facies close to the coesite stability field (*c.* 550 °C/26 kbar; similar estimates were obtained on a lawsonite-eclogite assemblage by Groppo and Castelli, 2010). These two units are separated by a ductile shear zone named "Upper Shear Zone" (USZ) in this study (Fig. 2).

The Lago Superiore Unit is a well-preserved, relatively undisturbed section of oceanic lithosphere, cut across by two major shear zones (referred to as the "Intermediate" and "Lower Shear Zones": ISZ and LSZ; Fig. 2b; Angiboust et al., in press; Philippot and Kienast, 1989). The upper portion of the section is composed of a variably thick and heterogeneous, dominantly mafic sequence containing (i) metabasalts and associated interpillow material (60–80%), (ii) metadiabases and Fe–Ti metagabbro layers (10–20%) and (iii) calcschists (5–10%; Fig. 2b). The middle part of the section is composed of a 200–300 m thick Mg–Al metagabbro capped by a discontinuous (generally 5–20 m thick) layer of Fe–Ti metagabbros. The bottom of the sequence is mainly composed of serpentinites derived from hydrothermally altered abyssal peridotites (Hattori and Guillot, 2007; Monviso, 1980; Figs. 2b, 3a).

3. Field observations in the three major shear zones

The three main shear zones, which cut across the Monviso ophiolite, are either localized at the boundary between units with different P–T histories (USZ) or along major lithological boundaries (ISZ, LSZ; Figs. 2b, 3). By contrast, m-sized shear zones found in the field show limited spatial continuity and lack well-developed mylonites or blocks embedded in serpentinite. For the sake of clarity, field observations for each of the shear zones are summarized in Table 1 and detailed geological maps of the shear zones are given as Supplementary material 1.

3.1. The Upper Shear Zone (USZ)

The USZ can be followed over 15 km from Colle Armoine in the north to south of Passo Gallarino in the south (Fig. 2a). This USZ is

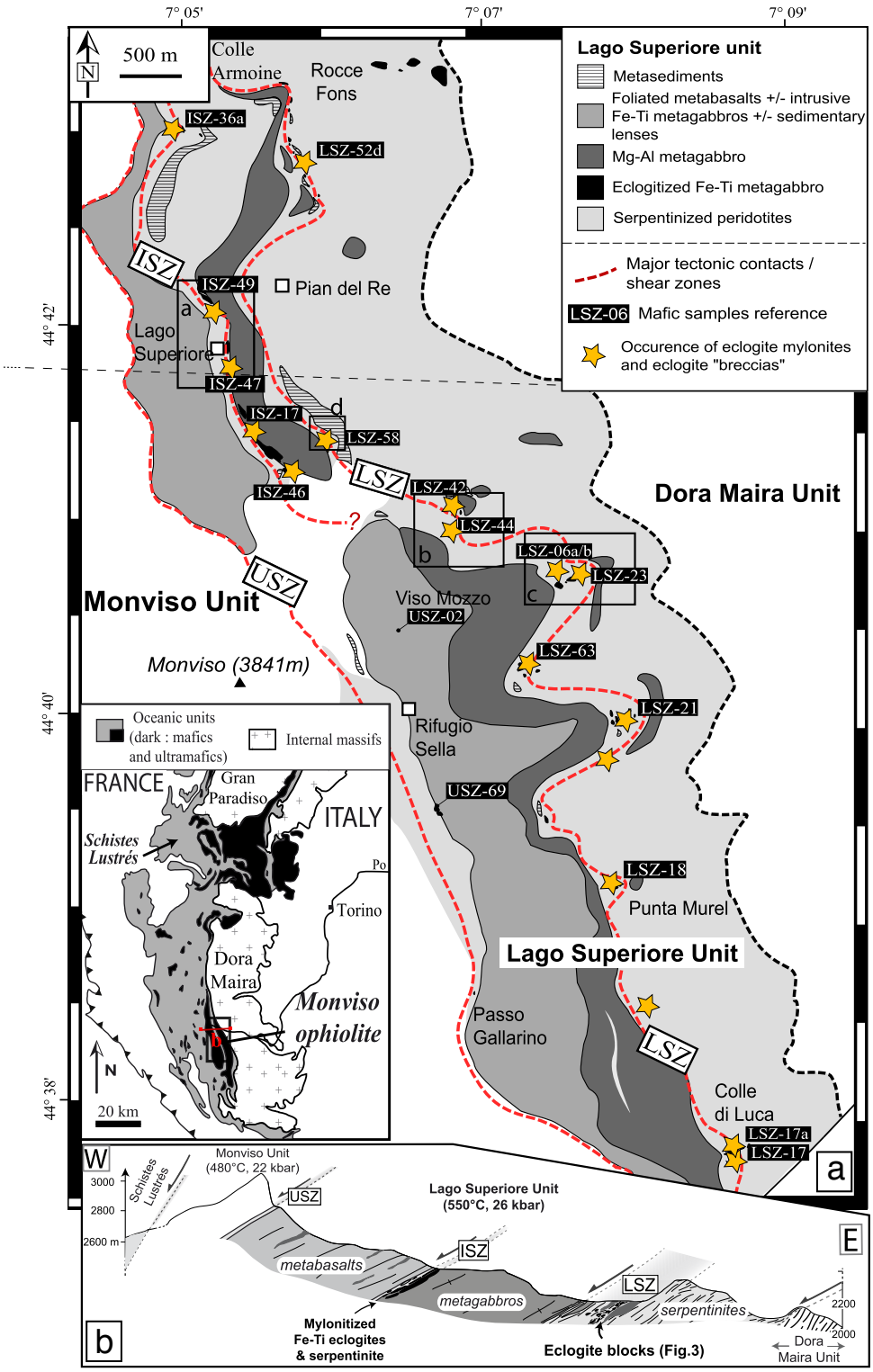

Fig. 2. a. Geological map of the working area showing the location of the main shear zones, the position of the units and the location of samples mentioned in text (modified after Lombardo et al., 1978 and Angiboust et al., in press). The inset localizes the Monviso ophiolite within the Western Alps. b. Section across the Monviso ophiolite showing the disposition of the main tectonic units and tectonic relationships between them (dotted transect on Fig. 2a).

lined up by a variably thick (between 1 and 30 m) serpentinite sliver, in which m-sized flattened lenses of Fe–Ti metagabbros are randomly dispersed, together with rare Mg–Al gabbro lenses and metasediments (dominantly calcschists). Metabasaltic rocks forming the lower margin of the USZ are commonly dragged and sliced along the shear zone. Meter-sized mylonite serpentinite slivers are also interleaved with strongly retrogressed metabasalts in the vicinity of the USZ. Importantly, eclogitic lenses found along the USZ do not record evidence for strong and pervasive eclogite-facies mylonitization as for other shear zones deeper in the ophiolite pile (see below). The USZ was intensively reactivated as an extensional detachment zone during later exhumation stages, as testified by the formation of

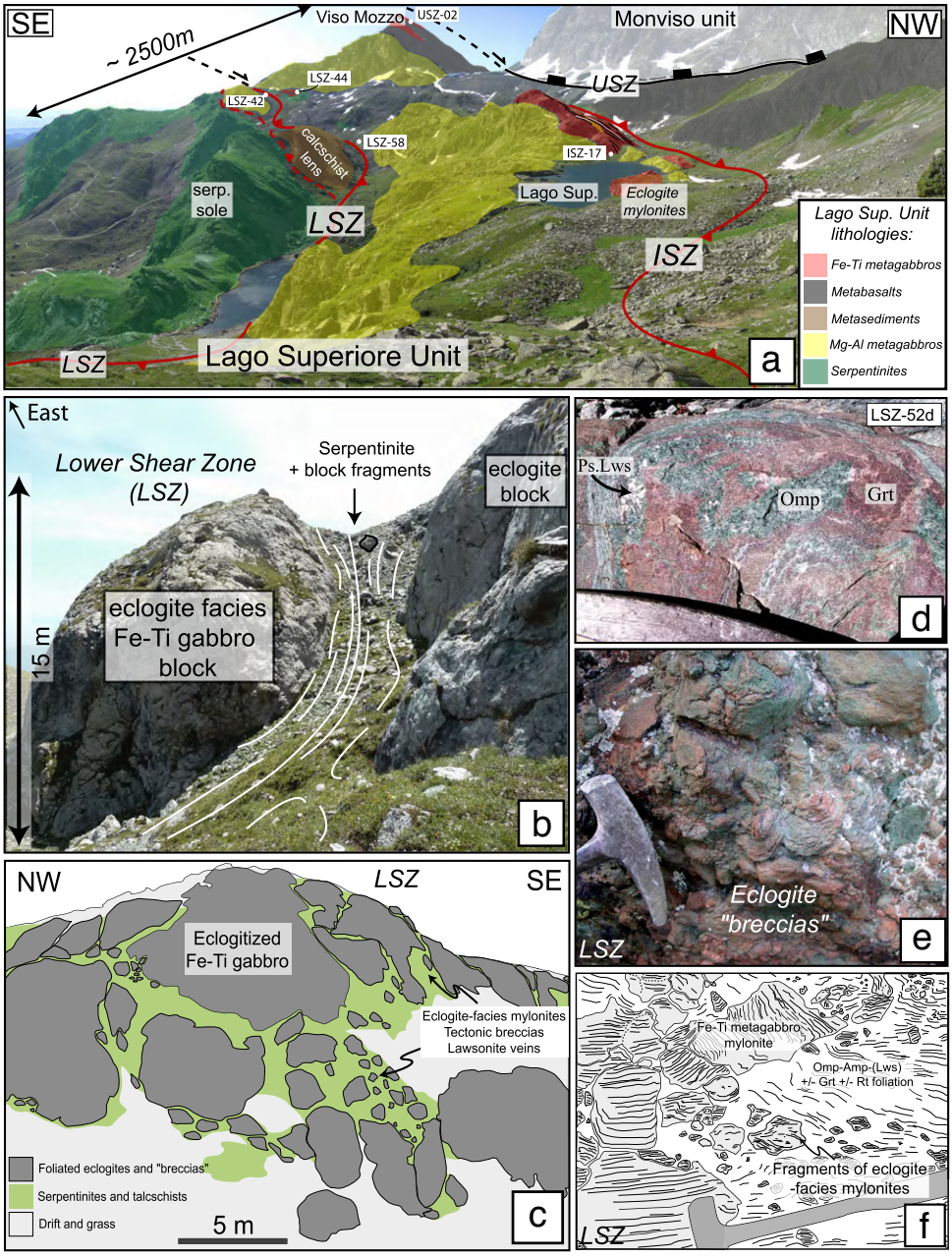

Fig. 3. a. Field view of the Lago Superiore Unit showing the various lithologies and the location of the three main shear zones (USZ, ISZ, LSZ: upper, intermediate and lower shear zones, respectively) together with samples mentioned in the text. Deep shear zones (in red) are marked as thrusts on the picture. The USZ, reactivated as a major detachment zone during late exhumation processes, is lined by dark black rectangles. b. Field view of a rounded block of Fe–Ti metagabbro embedded within LSZ serpentinites (Punta Forcione: N 44° 40′ 38.1″; E 07° 07′ 39.8″). c. Drawing illustrating a disaggregated block and associated disseminated fragments within a serpentinite/talcschist matrix (Punta Murel: N 44° 39′ 00.5″; E 07° 07′ 55.4″). d. A strongly foliated mylonite where omphacite (Omp) and garnet (Grt) have been clearly segregated in two distinct domains (hammer for scale). Note that whitish pseudomorphs after lawsonite (Ps. Lws) are concentrated in omphacite domains. e. Picture of typical eclogite breccias found at the surface of blocks embedded within the Lower Shear Zone (LSZ), showing variably sized and oriented fragments of eclogite facies mylonites cemented by omphacite. f. Drawing of the foliation trend within an eclogite-facies breccia from Colle di Luca (Fig. 2a) emphasizing the rotation of the fragments at the block surface. (For interpretation of the references to color in this figure legend, the reader is referred to the web version of this article.)

ubiquitous W-dipping shear bands and L-tectonites at the transition between epidote blueschist facies and greenschist facies conditions (9 kbar, 420 °C; Schwartz et al., 2000).

3.2. The Intermediate Shear Zone (ISZ)

The ISZ, which is more limited spatially than the other two, is well expressed in the Lago Superiore area and pinches out southwards in the Viso Mozzo area and northwards (Figs. 2a, 3a). In the Lago Superiore area (Supplementary material 1a), Mg–Al metagabbros, which constitute the bulk of the sequence, are capped by a 2–50-meter-thick discontinuous sequence of dark Fe–Ti metagabbros (ISZ-17; Fig. 3a) exhibiting a mylonitic foliation sub-parallel to the ISZ. The absence of large porphyroblasts in the mylonitic foliation, however, prevents identification of the dominant sense of shear.

These eclogites are heterogeneously deformed, showing an alternation of highly and intermediately strained samples at the outcrop scale (Philippot and Kienast, 1989). Intermediate to highly strained mylonites represent over 90% of the volume outcrop in the Lago Superiore area. High strain, non-coaxial deformation and folding

Table 1
Summary of field, structural and petrological observations with emphasis on the lenses and/or blocks dispersed within the three main shear zones. Thermobarometric results are from Angiboust et al. (in press).

	Upper Shear Zone (USZ)	Intermediate Shear Zone (ISZ)	Lower Shear Zone (LSZ)
Serpentinite thickness	3–20 m	2–10 m	>50 m
Serpentinite rel. amount	Highly variable along-strike (decreasing northwards)	Between 20 and 80%	Over 90%
Penetrativity of SZ eclogite facies deformation	Hanging wall (Monviso Unit): ? footwall (Lago Superiore Unit): low	Hanging wall: ? footwall: very strong (20–25 m)	Hanging wall: strong (20–30 m) footwall: strong (50–100 m)
Relative abundance/typical thickness of:			
Fe–Ti gabbro	+/2–5 m	+++/5–8 m	+++/0.1–15 m
Mg–Al gabbro	0	+/5–8 m	+/5–10 m
Sediment	−/2–5 m	+/3–7 m	+/1–35 m
Basalt	++/2–5 m	++/3–7 m	0
Eclogite-facies mylonites	Not observed	Frequent, mainly "dry"	Frequent, mainly "hydrated"
Peak paragenesis of Fe–Ti gabbros	Grt-Omp-Gln-Rt+/−Ph+/−Zo	Grt-Omp-Rt-Ap+/−Lws	Grt-Omp-Rt-Ap-Lws+/−Chl+/−Tlc+/−Ph
Veins	Not observed	Fairly rare (between 1 and 5 vol.%, mainly Omp)	Frequent (between 5 and 15 vol.%, mainly omp and lws)
Mylonite "breccias"	Not observed	Rare	Frequent
Garnet structure	Well-preserved zoning pattern, rarely fractured and any healed fractures	Strongly fractured, cemented by a Mg-rich composition	Strongly fractured, cemented by a Mg-rich composition. Possibly multiple episodes of fracturation
Ps. Lws abundance	Rare (<2 vol.%)	0–10 vol.%	0–20 vol.% in mylonites 0–80 vol.% in veins
Peak P–T conditions	480–500 °C/23 kbar (Monviso Unit) 515–540 °C/26–27 kbar (Lago Sup. Unit)	530–550 °C/26–27 kbar	530–570 °C/26–27 kbar
Grade and intensity of retrogression	Epidote blueschist—high, greenschist—very high and pervasive	Epidote blueschist—moderate, greenschist—relatively low and localized	Epidote blueschist—low and well localized, greenschist—low and localized

interferences led to the formation of N–S trending cigar-shaped boudins (10 m × 1 m) in the Lago Superiore area (Philippot, 1987). Tensile fractures with fibrous omphacite perpendicular to the vein walls (and with the mylonitic foliation only occasionally deflected around these veins) represent a few percents of the rock volume (Philippot and Kienast, 1989). The different generations of omphacite epitaxial fillings along these veins were interpreted as marking successive incremental crack-seal processes associated with mylonitization and cm-scale, fluid-assisted mass transfer (Nadeau et al., 1993).

Several metabasaltic lenses, and to a minor extent metasediments, are found along the ISZ within serpentinite mylonites, lying subparallel to the main gently dipping foliation (~N005 15–30° W). P–T estimates show that these rocks underwent a metamorphic history similar to that of the walls of the shear zone (Angiboust et al., in press). The apparent meter-scale structural complexity therefore results from a tectonic juxtaposition of rocks constituting the walls of the ISZ together with variably thick serpentinite slivers (0–10 m; Table 1). The presence of an allochtonous serpentinite sliver between gabbros and basalts (Fig. 2a, Lago Superiore Area) indicates that the ophiolitic sequence was disrupted along the ISZ. Retrogression under epidote blueschist-facies is attested by the formation of glaucophane, chlorite, epidote and albite instead of garnet and omphacite). It dominantly affects the metabasalts from the hanging wall, whereas mylonitized Fe–Ti metagabbros are remarkably well-preserved.

3.3. The Lower Shear Zone (LSZ)

The LSZ runs at the base of the main Mg–Al gabbro body, at the boundary with the underlying serpentinite sole, and can be traced over 15 km in the studied area from Rocce Fons in the north to Colle di Luca in the south (Fig. 2a). The LSZ ranges in thickness from 40 to 150 m (Supplementary material 1b, c, d). The upper boundary of the LSZ is well defined by the Mg–Al gabbro interface but its lower margin, towards the serpentinite sole, is much more diffuse.

Finite deformation linked to the activity of the LSZ is characterized by (i) a W-dipping foliation (generally 20–30°) and the flattening of the Mg–Al gabbros of the hanging wall and (ii) an extremely pervasive schistosity in serpentinites. This serpentinized tectonic contact is lined by many irregularly dispersed lenses and aggregates of metagabbroic and metasedimentary rocks (Fig. 2b; Table 1). Rare lenses of metasediments (mainly calcschists, carbonates and garnet–chloritoid quartzites) are intercalated within serpentinites and metagabbro aggregates in the LSZ. Most of these flattened lenses are generally meter-sized except a large lens located at the southeast of the Lago Superiore reaching several hundred meters in length and ca. 50 m in thickness (Supplementary Material 1d, Figs. 2a; 3a) showing slightly higher maximum temperatures than adjacent rocks (Tmax = 550–570 °C vs. 530–550 °C, respectively; see Angiboust et al., in press). Rare meter-sized blocks of jadeitite (Compagnoni et al., 2007) after plagiogranite and rodingite veins (Castelli et al., 2002; Lombardo et al., 1978) are found in blocks and veins in the LSZ and within the underlying serpentinite sole, respectively. Metabasalts were neither observed within the LSZ nor within the serpentinite sole.

Fe–Ti metagabbros generally constitute large (10–20 m-sized) rounded aggregates, internally made of several independent, rounded blocks (Fig. 3b–d), wrapped by a mixture of antigorite schists, tremolite schists and talcschists. The abundance of these small rounded fragments (0.1–0.5 m sized), dispersed within the serpentinite in the vicinity of the major aggregates decrease away from the aggregate core. Importantly, small (<20 cm) angular mylonite fragments are dispersed upon the rough block surface (Fig. 3b) and cemented by an omphacite-rich matrix.

Some of the meter-scale blocks are made of eclogitic breccias (Fig. 3e,f), where internal rotation is attested by the strong variability in strike and dip of the main mylonitic foliation planes (Fig. 3f) and omphacite cementation is also conspicuous.

Fe–Ti eclogitic blocks expose remarkably well-preserved peak mylonitic assemblages and underwent only minor and very localized retrogression under epidote blueschist-facies and greenschist facies (Table 1). These rocks are characterized by the ubiquitous presence of whitish layers or patchy aggregates (up to 1 cm in length) of pseudomorphs after lawsonite, which is now dominantly replaced by epidote and paragonite (e.g. Lombardo et al., 1978; Fig. 4). They occur either along the mylonitic foliation (Fig. 4a,d) but also as porphyroblasts associated with omphacite or as vein-filling material (Fig. 4a, b,c; Table 1). In locality LSZ-21 (Fig. 2a), a block exhibiting a mylonitic fabric is wrapped by a banded eclogite mainly composed of strongly folded, milky (0.5 to 2 cm-thick) layers of pseudomorphed lawsonite

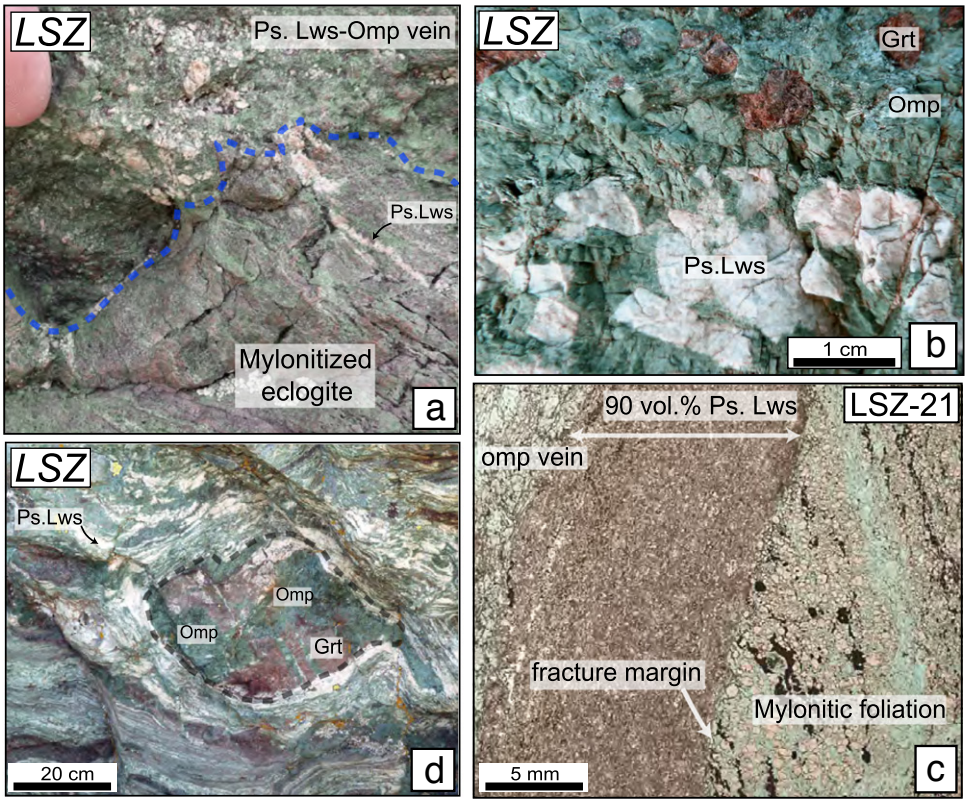

Fig. 4. a. Contact between a mylonitized eclogite fragment and a vein filled by omphacite and pseudomorphs after lawsonite at the surface of a brecciated eclogitic block from the LSZ (N 44° 39′ 52.8″; E 07° 07′ 50.3″). b. Lawsonite eclogite sample occurring in a low-strained domain at the block surface showing remarkably large lawsonite pseudomorphs (up to 1 cm in length) in a weakly deformed matrix (Punta Murel; Fig. 2a). c. A mylonitic foliation consisting of garnet, omphacite and rutile (right) crosscut by a vein (left) filled by lawsonite and omphacite (lawsonite is now pseudomorphed by epidote and paragonite). d. Boudinaged mylonitic fragment wrapped within a later foliation consisting of omphacite, garnet and lawsonite (LSZ). Mineral abbreviations as in Fig. 3.

and foliated fined-grained omphacite (Fig. 4d). Primary crack-seal omphacite-bearing fractures similar to those from the ISZ near Lago Superiore, are locally preserved and commonly associated with pseudomorphed lawsonite veins (Fig. 4a,c). Textural relationships with the mylonitic fabric are often erased by later ductile deformation.

4. Mineralogy of shear zones eclogites

Eighteen samples from the three main shear zones (Fig. 2a) were selected from a set of 75 samples collected across the study area. We focus below on the eclogitic Fe–Ti gabbro with well-preserved peak assemblages and the extent to which they record the activity of these shear zones beyond 50 km depth. The detailed peak rock paragenesis are presented in Table 2. Analytical methods used to track mineralogical and compositional changes are described in Appendix A.

4.1. Upper Shear Zone eclogites (USZ)

Rare lenses of eclogitized Fe–Ti gabbros, locally retrogressed under blueschist-facies conditions, are dispersed throughout the USZ serpentinites. One characteristic sample was collected at the south of rifugio Sella (USZ-69; Figs. 2a, 5a). The texture of these low strain Fe–Ti metagabbros consists of former corona features with garnet growing at the boundary of pseudomorphed magmatic crystals (see also Lombardo et al., 1978; Pognante and Kienast, 1987; Philippot and van Roermund, 1992). Clinopyroxene porphyroblasts in sample USZ-69 have been rotated, fractured and disseminated along the foliation plane. Plastic deformation is suggested by the elongated shape of recrystallized omphacite crystals. Garnet porphyroblasts are only rarely fractured (but not healed) and always show a typical “alpine” zoning pattern (i.e. Mn–Ca rich cores and Fe–Mg enriched rims; Fig. 5b; Supplementary material 2). Phengite is randomly dispersed in the clinopyroxene matrix and dismembered rutile ribbons after magmatic ilmenite define a crude foliation together with clinopyroxene. Brecciated garnet and eclogite-facies mylonites such as those described hereafter for the other shear zones have not been observed along the USZ.

4.2. Intermediate Shear Zone eclogites (ISZ)

These eclogites are characterized by a marked grain size reduction of omphacite down to 5–10 μm and a relatively strong crystal preferred orientation within the foliation plane, interpreted as the result of plastic dynamic recrystallization by dislocation creep (Lardeaux et al., 1986; Philippot and Kienast, 1989; Philippot and Van Roermund, 1992). Brittle deformation is attested by the presence of fractured, 10 to 300 μm large garnet porphyroblasts (Fig. 5d–f; initially part of coronitic structures: Pognante and Kienast, 1987). Omphacite-cored atoll garnet commonly occurs along the mylonitic foliation (Fig. 5c) but is systematically absent from low-strained Fe–Ti metagabbros. Phengite and glaucophane are rare (<0.5 vol.%) and generally aligned between omphacite crystals along the foliation. Pseudomorphs after lawsonite (much smaller than those from LSZ eclogites) generally occur as millimeter-sized ribbons or aggregates dispersed along the mylonitic foliation (sample ISZ-17, Fig. 5c).

Zoning patterns in garnet from ISZ mylonitic eclogites show embayments and healed fractures, suggesting a combination of dissolution and cementation (Fig. 5d). In the least fractured garnets, the original pattern with Ca/Mn-rich cores and Fe/Mg enriched rims is preserved. In addition, a sharp depletion in grossular content commonly occurs towards garnet rims, associated with a marked increase in pyrope content (Fig. 5e,f). The outermost parts of garnet rims are

Table 2
Synthesis of peak paragenesis and relative phase abundances in the selected set of samples from the three shear zones described in the text.

	Sample ref.	Veins	Grt	Omp	Ph	Tlc	Lws ps.	Chl	Gln	Ep	Aln	Qz	Rt
USZ	*USZ-02*		+	+++					+	+		-	+
	USZ-69		+	+++	+				−	−		−	+
ISZ	*ISZ-17*		++	++	−		+		−			−	+
	ISZ-36a		++	++								−	
	ISZ-49	*Omp*	++	++	−								+
LSZ	*LSZ-05*		++	++	−			−				−	+
	LSZ-06		+	+++			+						+
	LSZ-06b		+	++		+							+
	LSZ-17b	*Omp, Lws*	++	++			+						+
	LSZ-18	*Omp, Chl*		+++		+	−	+				−	−
	LSZ-18b		−	++			++	+			−		−
	LSZ-21	*Lws, Omp*	+	+++	−		+					−	+
	LSZ-23		++	+	+	+							
	LSZ-42		+	++	+		+		−			−	+
	LSZ-44	*Lws*	++	++	−		+				−	+	+
	LSZ-52 d	*Lws*	++	++			+					−	−
	LSZ-58		++	++	−			+			−		+

Key: +++ over 70 vol.%; ++ 25 to 70 vol.%; + 1 to 25 vol.%; − less than 1 vol.%.

slightly enriched in Mn compared to garnet mantles (see Angiboust et al., in press, for further chemical data on these garnets). Garnet filling the fractures, which are generally 5–10 μm wide, is marked by a sharp enrichment in pyrope content too (from 8 mol% to 16 mol%; Supplementary material 3) and a slight depletion in grossularite and almandine contents. Some samples (ISZ-36a, ISZ-49) exhibit very small truncated garnet fragments with limited evidence of post-fracturing healing.

4.3. Lower Shear Zone eclogites (LSZ)

The LSZ contains numerous blocks of Fe–Ti metagabbros, some almost identical to those found in the ISZ. It nevertheless displays a much wider diversity of rock types than along the ISZ, suggesting a somewhat different post-mylonitic metamorphic history. A common feature to those diverse rock types only encountered in the LSZ is the presence of large and widespread hydrated mineral phases (Fig. 4b). By contrast, eclogites similar to those found in the ISZ will be referred here to as "dry" eclogites.

Within dry eclogites showing textural affinities with the highly strained ISZ eclogites (i.e., brecciation, cementation and grain-size reduction), some display a marked banding exemplified by almost monomineralic layers of garnet and omphacite (e.g., samples LSZ 52d and LSZ-21; Figs. 3d, 4d). Garnet-rich layers consist of over 75 vol.% of coalesced (50–100 μm-sized) garnet crystals with intergranular spaces filled by very fine grained omphacite (c. 10–30 μm). Omphacite-rich layers contains less than 5 vol.% garnet and preferentially host millimeter-sized aggregates of pseudomorphs after lawsonite (Fig. 3d).

Hydrated eclogites, which are found only in the LSZ (Fig. 3b–f), can be grouped in two main categories:

- *lawsonite-bearing eclogites (LSZ-17, 18, 21, 42 and 44)*
  Lawsonite-bearing eclogites occur on the rims of the blocks of Fe–Ti metagabbros, with centimetric (Fig. 4b,d) or millimetric lawsonite fringes along the mylonitic foliation (Fig. 4a). The rims of the smaller block fragments typically comprise garnet and omphacite-bearing layers with variable amounts (0–30 vol.%) of variably-sized euhedral lawsonite pseudomorphs (from 10 μm to up to 1 cm in length; Fig. 4b). Fragments scattered at the block surface are cemented by an omphacite–lawsonite+/−garnet assemblage that ranges from weakly (Fig. 4a,b) to highly strained (Fig. 4c). Garnet diameter ranges from 20 μm up to 1 cm (Fig. 4b). A complex fracture network is generally preserved within garnet, as in ISZ eclogites. These garnet crystals exhibit 10 to 20 μm-wide chemical oscillations associated with dissolution-precipitation processes (showing striking similarities to "cloudy" garnets described in Martin et al., 2011). One sample (LSZ-42; Fig. 5h) shows large phengite laths (0.5–4 mm in length; Si^{4+} = [3.6–3.7 p.f.u]) in apparent textural equilibrium with subidioblastic garnet and fine grained omphacite aligned along the mylonitic foliation. Phengite has not been observed included within garnet cores. Small lawsonite pseudomorphs (c. 100 μm long) are preferentially scattered in the phengite-rich layers (Fig. 5h).
- *chlorite and talc-bearing eclogites (LSZ-06, LSZ-23 and LSZ-58)*
  Talc- (LSZ-06) and chlorite-bearing (LSZ-23; LSZ-58) eclogites randomly occur on the rims of Fe-Ti metagabbro blocks. They exhibit garnet crystals with two distinct generations intensively fractured and healed by a pyrope-rich garnet. Talc or chlorite (up to 10 vol.%) occur as elongated laths along the foliation between omphacite and garnet but have not been observed as inclusion within garnet cores. Talc-bearing domains are often associated with glaucophane shear bands and chlorite aggregates cutting across and postdating the mylonitic foliation.

Complex fracture patterns are found in the garnets. As an example, five successive tectono-metamorphic events were recorded by a single garnet grain from a chlorite–eclogite (sample LSZ-23; Fig. 6a,b). The boundary between garnet I and garnet II is lined by an embayment rich in Mn and Ca (respectively up to 10 mol% and 25 mol%). Pyrope content increases rimwards within garnet II, from c. 15 mol% to 25 mol%. Several "fossilized" fracture networks lined by a slightly Mg-enriched composition can also be identified (Fig. 6a,b).

5. Chemical variations in shear zones eclogites

Shear zones have been long recognized as a preferred locus for fluid-assisted mass transfer leading to bulk rock chemical alteration, as well as isotopic mixing (Austrheim, 1987; Dipple and Ferry, 1992; Keller et al., 2004; White and Knipe, 1978). In order to evaluate the degree of fluid circulation, the major element compositions of all rock-types encountered in the ISZ and LSZ were compared. The procedure used to obtain reliable compositions is given in Appendix B and detailed compositions are available in Supplementary material 4.

Fig. 7a shows that low-strained and dry mylonitized Fe–Ti eclogites compositions (whether from the ISZ or the LSZ) plot in the middle of the ACF diagram. "Dry" mylonitized Fe–Ti metagabbros generally have a bulk composition which lies very close to the Lago Superiore area eclogites studied by Schwartz et al. (2000). By contrast, lawsonite-rich hydrated eclogites (dominantly cropping out in the LSZ) exhibit a

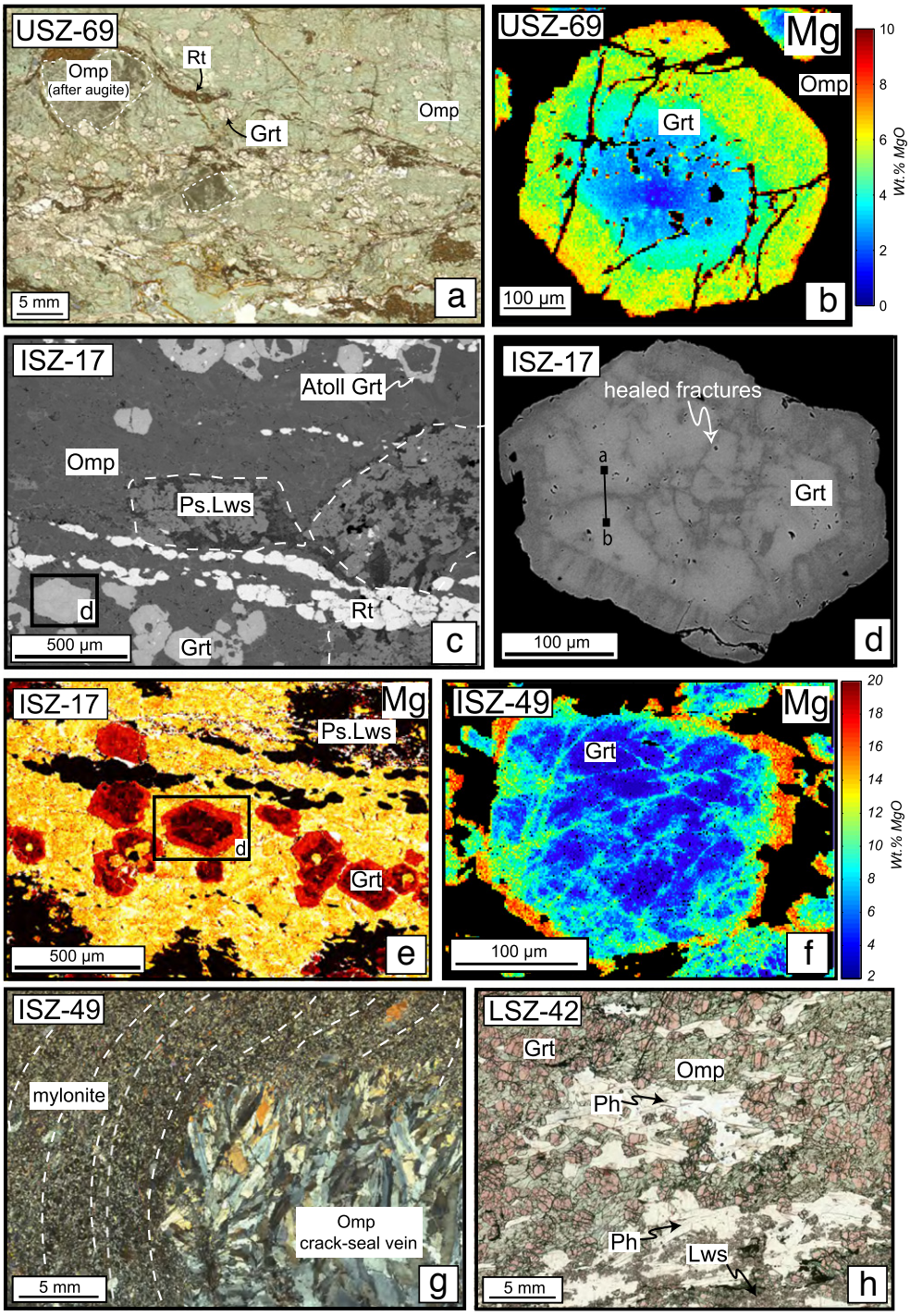

Fig. 5. a. Scanned thin section of a moderately strained eclogite from a block embedded within serpentinite from USZ (Fig. 2a), showing relatively well preserved relicts of omphacite porphyroclasts (after augite) embedded within an omphacite-rich foliated domain. b. Quantified chemical map of a garnet crystal magnesium content (wt.%) of sample USZ-69, showing a typical zoning pattern (enrichment in Mg towards the rims) and the absence of healed fractures. c. Back-scattered Electron (BSE) view of an Fe–Ti metagabbro mylonite from Lago Superiore Area showing pseudomorphs after lawsonite growing along the omphacitic foliation. Dismembered rutile ribbons underline the foliation. d. BSE picture of a garnet showing two distinct garnet generations with a clear Ca-rich core and a dark Mg-rich rim. A dark complex network of healed Mg-rich fractures connected on the garnet rim crosscuts the garnet core. Garnet chemical composition across the fracture (transect a–b) is given in Supplementary material 3. e. Chemical map of Mg content (counts) of the mylonitic matrix from sample ISZ-17. f. Chemical map of Mg content (wt.%) of a garnet from sample ISZ-49 exhibiting a very complex pattern of Mg-enriched healed fractures. g. Scanned thin section of a mylonitic sample showing the mylonitic foliation deflected around an omphacite-filled crack-seal vein. h. Scanned thin section of sample LSZ-42 (courtesy of D. Waters) showing numerous phengite and pseudomorphed lawsonite crystals along the eclogitic foliation. Abbreviations after Whitney and Evans (2010).

striking depletion in FeO (−8 wt.%; Fig. 7a). This feature is also observed for lawsonite and omphacite-bearing veins sampled between brecciated fragments, whose composition largely differs from that of the undeformed Fe–Ti metagabbro (Fig. 7a).

Mg-chlorite and talc-bearing mylonites, where pseudomorphed lawsonite has not been observed, are significantly enriched in MgO: talc-bearing mylonites range from 9 to 16 wt.% MgO (Fig. 7a; low strained Fe–Ti metagabbros typically contain 6 wt.% MgO). Similar

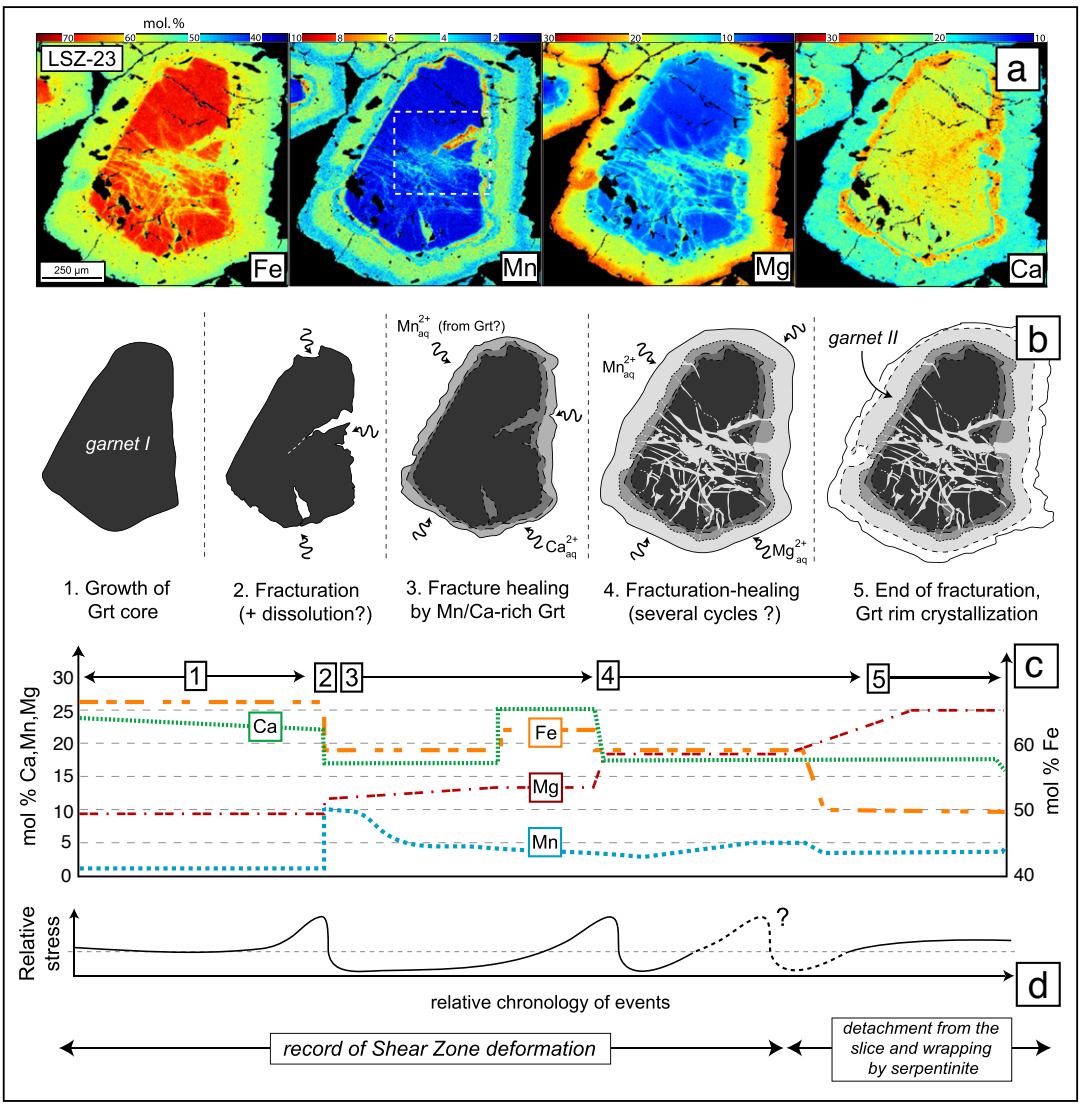

Fig. 6. a. Chemical maps of a garnet from a chlorite–eclogite sample from the LSZ (LSZ-23). b. Sketches depicting the successive steps of garnet growth. A first garnet (Garnet I) generation is fractured and healed by a Mn–Ca rich garnet composition (white dotted line square). A second fracturing episode is attested by the presence of a very complex fracture pattern cemented by a Mg-rich composition (Garnet II). c. Core to rim zoning profiles of the garnet composition. d. These successive events can be interpreted in terms of cyclic variation of relative shear stress associated with movement along the shear zone. See discussion for details.

bulk rock estimates for the phengite-bearing Fe–Ti metagabbro (LSZ-42) show that the K_2O bulk rock content of this sample is close to 1.5 wt.%, i.e. more than 5 times higher than the average K_2O content of Monviso Fe–Ti metagabbros (see Lombardo et al., 1978 and Schwartz et al., 2000).

A striking depletion in FeO is also recorded by garnet rims from LSZ eclogites (Fig. 7b), which are systematically depleted in almandine content, and corresponds to the transition between GrtI and GrtII (Fig. 6a). Garnet rim values for all samples are surprisingly similar (Fig. 7b) and generally trend towards 55% of almandine content. Such a trend is absent from the ISZ (and USZ) samples (Fig. 7b).

6. Discussion

6.1. Petrological evolution during shear zone activity at 80 km depth

Our data (field relationships and petrography, mineralogy, chemical trends) suggest that eclogite-facies deformation of Fe–Ti metagabbros and fluid infiltration led to the formation of various mylonite types. Their relative timing of formation is presented in Fig. 8a and set back against P–T conditions (taken from Angiboust et al., in press). We stress that the four steps described in Fig. 8a successively took place between 70 and 80 km depth under lawsonite eclogite facies conditions, as testified by the presence of lawsonite pseudomorphs all along the textural evolution (as porphyroblasts and/or in veins). Steps 2 to 4 occurred in a relatively narrow P–T range as demonstrated by similar thermobarometric estimates obtained on these texturally different assemblages (detailed calculations given in Angiboust et al., in press).

"Dry" mylonites (Fig. 8a-step2) are common along the ISZ and also occur in the LSZ. By contrast, the presence in the LSZ of strongly hydrated parageneses and extensive bulk rock alteration demonstrates that the blocks of Fe–Ti metagabbros dispersed along this shear zone recrystallized in a much more fluid-rich environment. Chemical data (Fig. 7a,b) indicate contrasting degrees of bulk rock alteration, ranging from slightly (in the ISZ) to strongly altered (in the LSZ). Similarities in terms of rock types, P–T conditions and textures (garnet zoning and brecciation; lawsonite pseudomorphs) between the ISZ and LSZ suggest that the LSZ recorded a broadly coeval (i.e., at the same

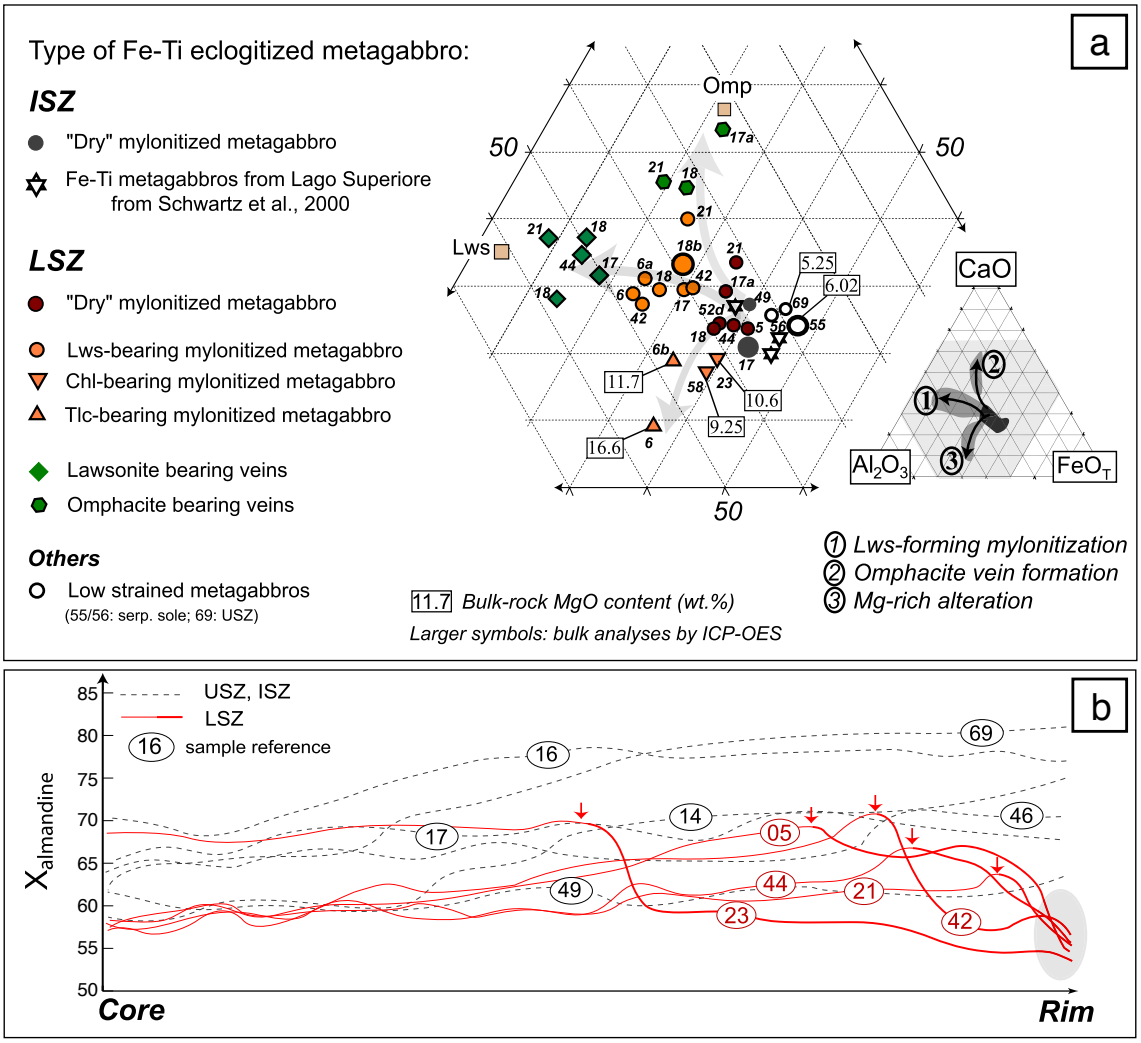

Fig. 7. a. Plot of the bulk rock composition in the ACF triangle (with F = FeO) for the mylonites sampled in the Intermediate (ISZ) and Lower (LSZ) Shear Zones distinguishing the different types of mylonites identified on petrographic observation and the trend in FeO depletion associated with water-saturated mylonitization (growth of lawsonite). b. Smoothed, normalized garnet core-rim transects for eleven samples from the three different shear zones. Iron depletion is systematically observed at the rim of garnet from LSZ while it is absent within garnet from unaltered or ISZ samples. The red arrow localizes the relative position of incipient depletion.

depths) yet slightly longer tectonic history than the ISZ, with marked fluid and mass transfer. This is consistent with the much more intense fragmentation of eclogite blocks and the larger spatial extension of the LSZ in the field (Figs. 2a, 3b,c). These additional stages of deformation and fluid influx, mostly recorded in the LSZ, are shown in Fig. 8a, as steps 3 (compare with Fig. 3e–f) and 4 (compare with Fig. 4d).

We finally point out that the presence of eclogitic breccias (Fig. 3e), garnet fractures (Fig. 6a) and block boudinage (Fig. 4d) attests to switches between brittle and ductile deformation, as shown in steps 2 through 4 (Fig. 8a). In the following sections, we use this petro-tectonic evolution to provide critical information on deformation patterns, fluid–rock interactions and rheological processes occurring within the eclogitized oceanic lithosphere, down dip in the subduction zone.

6.2. Contrasting ranges of fluid flow

The above data suggest a contrasting amount of fluid flow for the ISZ and the LSZ (Fig. 8b), whose spatial extent is further discussed here.

The detailed analysis of ISZ garnets shows a complex zoning pattern (overgrowths, oscillations; Fig. 5f, supplementary material 2; see also Spandler et al., 2011), suggesting chemical system opening and deformation-assisted fluid circulation. Manganese, which is strongly partitioned within garnet cores, may have been dissolved during fracturing of garnet cores and subsequently precipitated after advective transport (for examples of garnet embayment within an ISZ eclogite, see Angiboust et al., in press; their Fig. 3g). However, undeformed Fe–Ti metagabbros and "dry" ISZ mylonite samples are chemically indistinguishable (Fig. 7a). Moreover, garnet rim almandine content from ISZ Fe–Ti eclogites is similar to that of undeformed, unaltered samples (Fig. 7b). Even if a very local infiltration of external fluid is possible (Spandler et al., 2011), our results support the predominance of relatively short range (i.e. meter-scale) fluid flow along the ISZ, as first inferred for Lago Superiore area eclogite mylonites from the presence of omphacitic crack-seal veins (e.g., Philippot and Selverstone, 1991; Nadeau et al., 1993; Table 1; Fig. 7a). Sharp interfaces between (omphacite filled) tensile cracks and mylonitized wall rock also suggest short-lived, incremental fluid–rock interaction and short vein lifetime (Philippot and Van Roermund, 1992).

In the LSZ, by contrast, our data point to larger-scale fluid flow and substantial metasomatism (Fig. 7a; with noticeable chemical

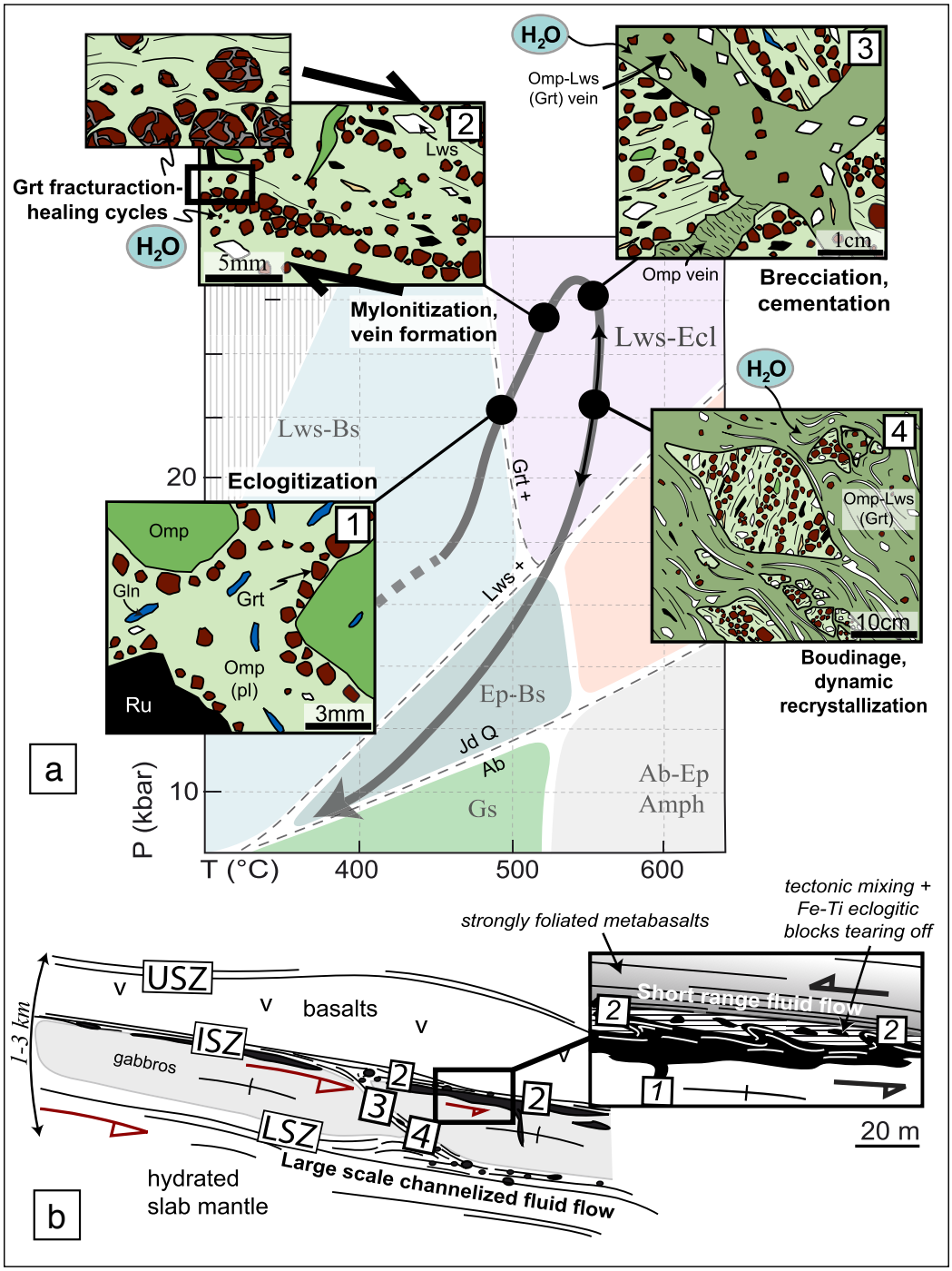

Fig. 8. a. Relative chronology of events (and associated P–T position) observed on eclogite Fe–Ti metagabbro mylonites boudins along the ISZ and LSZ. Igneous texture (step 1) is progressively blurred by mylonitization processes (step 2) leading to grain size reduction, garnet fracturing and phase segregation. Variable amounts of hydrous phases crystallized depending on the amount of water available during mylonitization. Eclogite facies breccias (step 3), commonly found along the LSZ are generally cemented by omphacite +/− lawsonite +/− garnet. These brecciated fragments (Fig. 3f) may be embedded as boudins in a later lawsonite eclogite-facies foliation (step 4). The P–T diagram at the background shows the P-T path for the LSU ophiolite, the location of the main metamorphic facies and the relative position of the four steps identified. Note that the presence of lawsonite (now pseudomorphed by epidote), omphacite and garnet in all textural positions constrains these events to the lawsonite-eclogite facies. b. Schematic drawing at the scale of the Lago Superiore unit, showing the location of the different shear zones and the location of the four steps mentioned above. Our results indicate that substantial fluid flow occurred along the LSZ, whereas only short range localized fluid flow within the ISZ.

potential gradients in H_2O, SiO_2 and FeO; e.g., Ferry, 1979) between the serpentinite matrix and the blocks of Fe–Ti metagabbros (see Fig. 8a, steps 3–4). Dissolution figures and associated overgrowths (Fig. 6a,c) show that the garnet surface was successively enriched in Mn–Ca then in Mg. This sharp boundary between Grt I and Grt II in LSZ eclogites (Figs. 6a,c; 7b) requires the advection of elements (and chemical system opening) close to peak conditions. The decrease of garnet almandine content within core–rim profiles for all LSZ samples towards a similar value (Fig. 7b) strongly suggests a buffering and input of Mg by the adjacent thick serpentinite sole (Figs. 2b,3b).

Eclogite porosity is generally limited to microfractures, isolated pores, cleavage planes and mineral boundaries (e.g. Mibe et al., 2003), connectivity is presumably very limited (Davies, 1999; Watson

and Brenan, 1987) and eclogite permeability is estimated at six orders of magnitude lower than for serpentinite mylonites (10^{-18} m^2; Morrow et al., 1984). We thus suggest that serpentinite-bearing shear zones, particularly the LSZ, acted as true conduits for fluid flow, despite the fact that the relatively low permeability of the blocks possibly deflected most of the flow through the matrix and limited deep infiltration into the blocks (Ague, 2007).

Whether fluids channelized within the LSZ originate from antigorite breakdown (which occurs close, yet slightly deeper than estimated peak conditions: ~650 °C, 25–30 kbar; Scambelluri et al., 1995; Ulmer and Trommsdorff, 1995) or derive from dehydration of the adjacent Mg–Al gabbro body during prograde reactions remains uncertain (see also the discussion on ISZ veins by Spandler et al., 2011). Chemical exchange and the formation of metasomatic rinds in any case facilitated the transposition of fabrics and enhanced fragment disaggregation, as observed on the block rims along the LSZ (Fig. 3c; for similar blackwall examples: Bebout and Barton, 2002; Catlos and Sorensen, 2003; Breeding et al., 2004).

6.3. Rheology of the subducting lithosphere and strain localization at depth

The Lago Superiore Unit provides a unique opportunity to document deep deformation processes occurring in subducted oceanic lithosphere, from the kilometer scale to the mineral scale, and to compare it with theoretical rheological parameters derived from rock flow laws based on experimental data (e.g., Kirby, 1983).

6.3.1. Rheological behavior at the kilometer scale

Bulk cumulative strain inferred from field observations is shown in Fig. 9b (and set back against the cross-section of Fig. 9c). This profile shows that the main shear zones are preferentially located along the major lithological contrasts, i.e. at the boundary between materials with significantly different strengths and viscosities. In agreement with theoretical studies of multilayered media (e.g., Strömgård, 1973; Treagus, 1981), this confirms that interfaces between rocks with different competencies are the loci of maximized shear strain.

For the sake of comparison, we tentatively evaluated the strength of each layer of the column using available dislocation creep flow laws for similar materials (Fig. 9a). This profile has been calculated using a constant strain rate of 10^{-14} s^{-1}. Other details of the calculation method are given in Appendix C. Our field observations (Fig. 9b) qualitatively strengthen the rheological envelope inferred from laboratory experiments (Fig. 9a) in showing that gabbros are indeed stronger than the overlying metabasaltic sequence under peak conditions (in agreement with preliminary observations; Burg and Philippot, 1991). However, the geometry of the whole system (stack of layers) implies that the different shear zones were active for the same range of shear

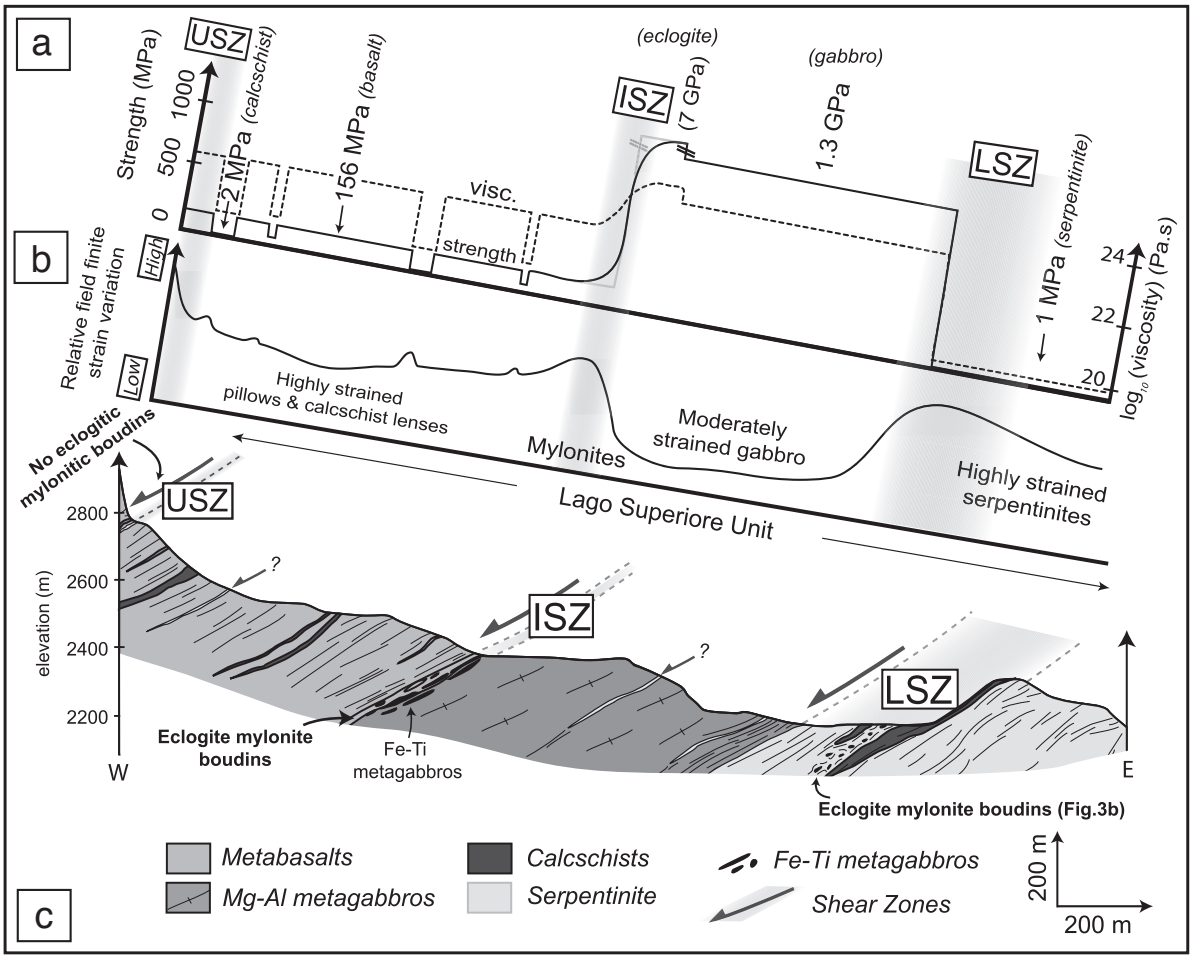

Fig. 9. a. Plot of differential strength (thick line) and viscosities (dotted line) against the same cross-section using the following flow laws: calcschists (micaschist: Shea and Kronenberg, 1992), basalts (omphacitite: Zhang et al., 2006), gabbros Fe–Ti (eclogite: Jin et al., 2001), gabbros Mg–Al (diabase: Mackwell et al., 1995), serpentinite (serpentinite: Hilairet et al., 2007) at 550 °C and with a strain rate of 10^{-14}. More details on the construction of the profile are given in Appendix C. b. Finite strain envelope across the described section, inferred from field observations and strain markers, showing that strain is strongly localized along the shear zones. c. Section across the Lago Superiore Unit showing the lithologies and the location of the three main shear zones. Arrows along the shear zones represent normal movement during late exhumation processes (Philippot and Van Roermund, 1992).

stresses, a statement at variance with the very large strength contrasts derived from dislocation creep flow laws (Fig. 9a). In particular, in spite of the presence of a thick serpentine sole supposedly so weak as to accommodate all the deformation, not only the shear zones (where serpentinite slivers are commonly found) but also the bulk of the metabasalt unit was pervasively deformed. This relative weakness of eclogites, not well reflected in experimental flow laws (Fig. 9a), could be related to their high water content, as rock strength is known to be significantly reduced by the presence of dissolved water ("hydrolytic weakening"; Griggs, 1967; Rybacki and Dresen, 2000; Zhang and Green, 2007), particularly within omphacite (whose H_2O content commonly reaches 1000 ppm in natural eclogites; e.g. Katayama et al., 2006).

Although ductile deformation dominates the deep evolution of this ophiolite, brittle deformation is apparent in veins (Fig. 5g) and in the breccia structures on the rims of the blocks of the LSZ (Fig. 3c–e; 4c). These observations are consistent with the experimental results describing a "semi-brittle" mode of deformation, in particular for clinopyroxene (Kirby and Kronenberg, 1984; Philippot and Van Roermund, 1992; Rutter, 1986). It should be noted that the "clasts" of these breccia are mylonite fragments, and that the whole breccia is generally reworked by ductile deformation, i.e., brecciation is bracketed by two phases of mylonitization (Fig. 8a, step4). Pseudotachylytes marking brittle rupture (Andersen and Austrheim, 2006; Austrheim and Boundy, 1994) have not been observed within the Lago Superiore Unit, despite extensive investigations. This could be due to the fact that pseudotachylites preferentially develop in extremely water-poor protoliths (John et al., 2009), whereas the Lago Superiore Unit shear zones show ample evidence for abundant fluid circulation.

6.3.2. At the cm-scale: phase segregation and garnet fracturing

Phase segregation between omphacite and garnet (Figs. 3d, 4d, 8a—step 2) was described in shear zones from the Tauern, Dabie Sulu, Caledonides (Holland, 1979; Ji et al., 2003; Terry and Heidelbach, 2006) and in experimentally deformed eclogites under high shear strain (Zhang and Green, 2007), but at temperatures much higher than those reported for Lago Superiore eclogites. Mechanisms invoked for phase segregation include mineral reactions, deformation-related processes such as dynamic recrystallization associated with grain size reduction (Mauler et al., 2000; Philippot and Van Roermund, 1992; Terry and Heidelbach, 2006) and/or the presence of a free fluid phase (e.g., Essene and Fyfe, 1967; Holland, 1979; Schliestedt, 1990; Selverstone et al., 1992).

We suggest that the segregation of garnet (otherwise behaving as rotating rigid spheres in a matrix of weaker omphacite) into lenses or layers may well explain their fracturing (Fig. 8b) as a result of indentation at garnet-to-garnet contacts. This does not preclude the contribution of other processes, such as hydraulic fracturing (Spandler et al., 2011), but does not require the presence of a very high pore fluid pressure. In principle, with increasing strain such angular fragments can be disseminated along the foliation by cataclastic flow (e.g., Tullis and Yund, 1987). This is locally observed in some very dry eclogite mylonites along the ISZ (ISZ-49; Fig. 2a), but most garnet fractures, within both ISZ and LSZ samples, are healed without evidence of relative displacement (Figs. 5d, 6a). Fast healing of garnet requires efficient element mobility, which is fostered by a free fluid phase (Erambert and Austrheim, 1993) and by grain size reduction (Rutter and Brodie, 1995). The preservation of an almost undisturbed garnet I shape at the core of garnet II also suggests the existence of a stress drop after fracturing (Fig. 6d), since garnet fragments would otherwise have been disseminated by ongoing strain. This result is consistent with the very large minimum stress drops associated with very small earthquakes, inferred from pseudotachylytes of Corsica (Andersen et al., 2008). These observed deformation and growth patterns thus potentially relate to co-seismic deformation and intermediate-depth coupling processes (see also Erambert and Austrheim, 1993). On the other hand, phase segregation and healed fractures also point to a key contribution to small-scale deformation processes from dissolution-precipitation, in addition to creep. Dissolution-precipitation may indeed be an important deformation mechanism within omphacite-rich domains, which are particularly subject to channelized fluid circulation (Piepenbreier and Stöckhert, 2001), or within garnets (as shown by the propagation of crack-tips; Prior, 1993).

6.4. Implications for km-scale, geodynamic processes at the subduction interface

Our results demonstrate that the Lago Superiore ophiolite was affected by intense shearing dominantly accommodated along three major shear zones defined by eclogite-facies mylonites and/or serpentinite slivers (Fig. 8b). Lenses and blocks dispersed along these shear zones, as well as the whole of the Lago Superiore, display similar P–T conditions (Angiboust et al., in press), suggesting spatially limited tectonic mixing. The error bar associated with the thermobarometric methods used here (i.e. ± 20 °C and ± 1.5 kbar) implies that less than c. 12 km of cumulative displacement occurred along these shear zones (considering a dip of 45° for the plate interface). The slightly hotter temperatures reported in a calcschist lens embedded within the LSZ (Fig. 3a; 560–570 °C; Angiboust et al., in press) may reflect the fact that the lower portion of the ophiolite reached slightly greater depths ($\leq$3 km deeper) than the overlying portions of the Lago Superiore ophiolite (Fig. 10a). These shear zones, particularly the LSZ, represent an example of network widening (in the sense of Schrank et al., 2008, for example) and not a subduction mélange formed by extensive mixing along the subduction interface (Blake et al., 1995; Guillot et al., 2004). The above description of deformation patterns within the Lago Superiore ophiolite thus suggests that caution is needed before interpreting former eclogite-facies shear zones as serpentinite mélanges, particularly in areas with limited surface exposures (e.g., Voltri; Brouwer et al., 2002; Federico et al., 2007).

We emphasize that mylonitized Fe–Ti metagabbros blocks found dispersed within serpentinite in the LSZ originate from the ISZ for two reasons: (i) the main source of Fe–Ti gabbros is structurally located at the top of the Mg–Al gabbroic body (Figs. 3a, 8b) (ii) mylonitization of such eclogites cannot happen once the blocks are embedded within the rheologically much weaker serpentinite. Such Fe–Ti metagabbros thus constitute markers of the relative displacement along the shear zones. The blocks from the LSZ successively underwent mylonitization along the ISZ (Fig. 10a), shearing and detachment from the ISZ by a ball-bearing mechanism before being embedded in the serpentinites schists of the LSZ (Fig. 10b). Note that displacement of eclogitic blocks from ISZ to LSZ through the gabbroic body could have been facilitated by the presence of an inherited structural weakness (such as bending-related faults; e.g. Ranero et al., 2003), tectonically reactivated as a thrust during deep shearing.

The final detachment of the Lago Superiore ophiolitic slice as a whole implies that deformation migrated towards the base of the serpentinite sole (Fig. 10c). Strain localization within the ultramafic section of the lithosphere probably occurs at the transition between highly and midly serpentinized peridotite (i.e., at depths of a few hundred meters to a few km below the oceanic Moho; Minshull et al., 1998; Iyer et al., 2010). It is likely that from this stage onwards (Fig. 10c) both the ISZ and LSZ were less active, and consequently preserved from extensive overprinting.

The behavior of the Lago Superiore ophiolite after detachment remains somewhat speculative but is closely linked (as discussed by Agard et al., 2009) with the upward, buoyancy-driven exhumation of light continental material ($\rho \sim 2700$ kg.m^{-3}) dragging these dense ($\rho = 3300$–3400 kg.m^{-3}; e.g. Stern, 2004; Lapen et al., 2007; Angiboust

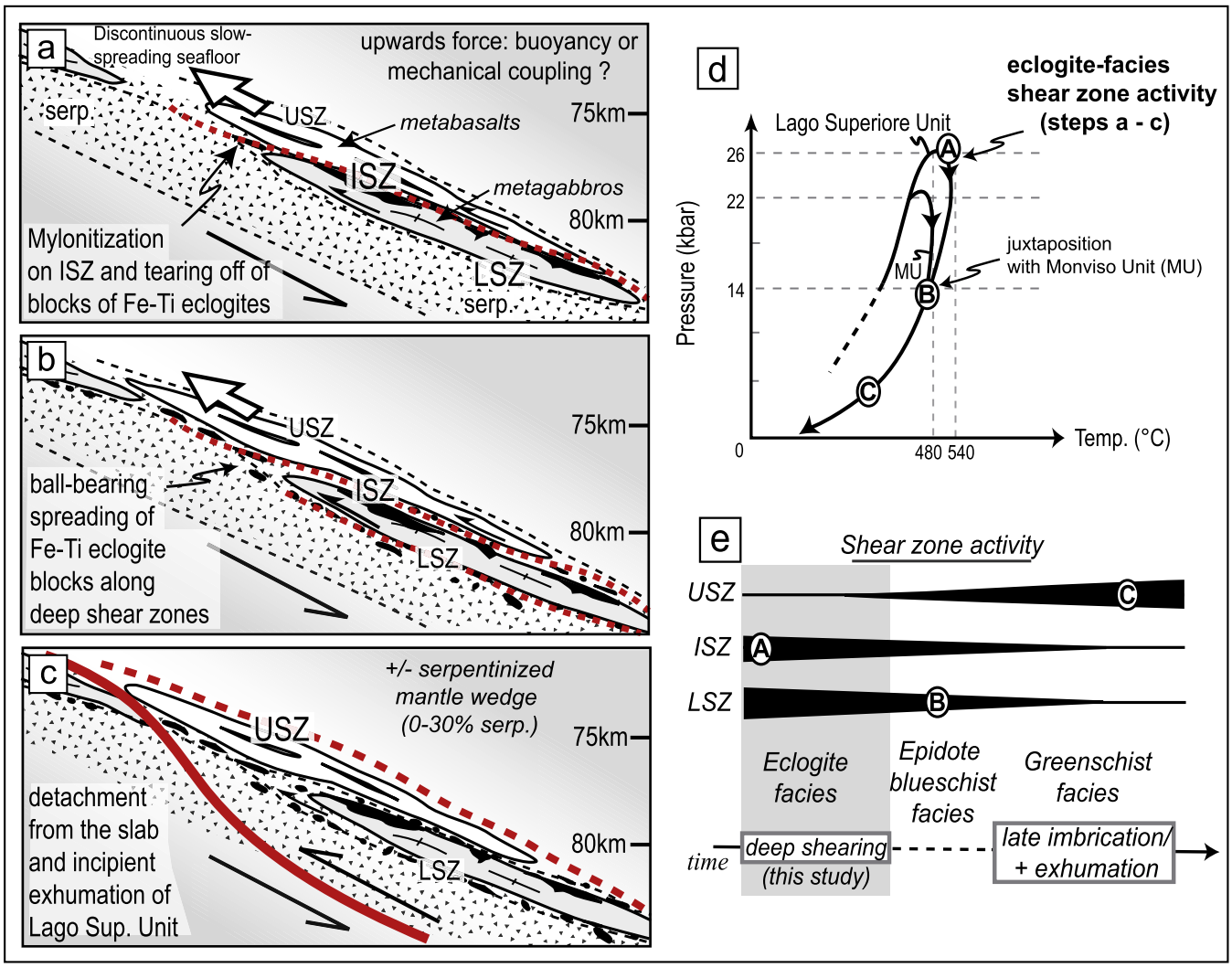

Fig. 10. a. Sketch representing the Lago Superiore ophiolite slice at the onset of mylonitization. Deformation is first localized on the ISZ, at the boundary between basalts and gabbros (red dotted line). b. Ongoing shearing along the plate interface is responsible for dismembering and fragmentation of eclogite blocks detached from the ISZ. c. The whole Lago Superiore unit finally detaches from the downgoing slab and the bulk of the deformation is now localized at the base of the serpentinite sole. Monviso unit, which detaches from the slab at c. 65–70 km is not represented here. d. P–T paths from Angiboust et al. (in press) for both Monviso and Lago Superiore Units. e. Eclogite facies shear zone activity is restricted to the vicinity of peak conditions (i.e. 550 °C, 26 kbar). Juxtaposition with the adjacent Monviso Unit occurs in the epidote blueschist facies during exhumation in the subduction channel (Schwartz et al., 2000). The relative timing of shear zone activity is based on the intensity of metamorphism recorded by the rocks from the different shear zones. (For interpretation of the references to color in this figure legend, the reader is referred to the web version of this article.)

and Agard, 2010) portions of eclogitized oceanic lithosphere along the subduction interface. Accordingly, younger peak ages recorded in the adjacent, continental Dora Maira internal crystalline massif (c. 35–40 Ma v. 40–45 Ma for Monviso; Tilton et al., 1991; Duchene et al., 1997; Rubatto and Hermann, 2001) would imply that the ophiolite remained at depth for ~5 My before being dragged upwards by the Dora Maira unit. In the meantime, the Lago Superiore slice may have remained buoyant enough thanks to the buoyant serpentinite sole at the base of the section (300–500 m; $\rho = 2900$ kg m^{-3}; Schwartz et al., 2001; Guillot et al., 2004) and/or to the overall fluid content in the mafic section (Angiboust and Agard, 2010). Further geochronological data are now required to better constrain the relative timing of deformation and deep thrusting processes responsible for detachment and exhumation of the Monviso ophiolite and its relationships with the underlying Dora Maira unit.

7. Conclusions

The Lago Superiore Unit, which exposes a very well-preserved lithospheric-scale tectonic ophiolitic slice returned from c. 80 km depth in the Alpine subduction zone, is crosscut by a network of three km-scale shear zones. It therefore provides a unique opportunity to study strain localization and rheological weakening in the subducting lithosphere. Our results show that:

(i) Strain was strongly localized within eclogite-facies shear zones at the interface between layers presenting rheological contrasts (i.e. between basalts, gabbros and serpentinites).
(ii) Dominantly short-range fluid flow occurred at the basalt–gabbro boundary (ISZ) through repeated fracturing processes associated with mylonitization of the shear zone. By contrast, we identified a longer-lived, pervasive deformation-enhanced fluid pathway at the gabbro–serpentinite interface (LSZ) leading to strong metasomatism, mechanical weakening and dismembering of the block fragments within serpentinite schists.
(iii) The presence of eclogite "breccias", preserving numerous healed fractured garnet crystals, suggest a local brittle behavior of the oceanic crust, possibly associated with co-seismic deformation.

(iv) The activity of both the ISZ and LSZ stopped during early lawsonite eclogite-facies exhumation when deformation localized deeper within the serpentinite sole, allowing for the detachment (and preservation) of this large ophiolitic fragment.

Supplementary materials related to this article can be found online at doi:10.1016/j.lithos.2011.09.004.

Acknowledgements

We acknowledge Loïc Labrousse, Dave Waters, Anne Verlaguet, Laetitia Le Pourhiet and Alexandre Schubnel for insightful remarks and discussions. Ryan Langdon, Christian Chopin and Alexandre Dimanov are thanked for technical assistance. This paper benefited from thoughtful reviews from Jane Selverstone and Torgeir Andersen. Marco Scambelluri is acknowledged for careful reading and editorial handling. This work has been funded with an INSU grant to P.A.

Appendix A. Analytical methods

Mineral abbreviations used in this work are after Whitney and Evans (2010).

The mineral analyses were performed using a Cameca SX100 electron microprobe (Camparis, Univ. Paris 6; a Cameca SX50 was also used for additional conventional analyses). Classical analytical conditions were adopted for spot analyses [15 kV, 10 nA, wavelength-dispersive spectroscopy (WDS) mode], using Fe_2O_3 (Fe), $MnTiO_3$ (Mn, Ti), diopside (Mg, Si), CaF_2 (F), orthoclase (Al, K), anorthite (Ca) and albite (Na) as standards. Chemical maps of garnet were obtained at the SX100 electron microprobe using 15 kV, 20 nA and a counting time of 100 ms. Quantifications were derived from the automated Cameca ZAF quantification procedure.

Chemical composition of microdomains (~3 mm × 1.5 mm) studied for bulk rock composition analysis were obtained at the Geology Laboratory of the Ecole Normale Supérieure (Paris) using a Zeiss Sigma field-emission-gun SEM with an X-max Oxford detector (50 mm^2), an acceleration voltage of 20 kV and a counting time of 1 min per domain.

Three additional whole-rock chemical analyses were undertaken at the SARM (CRPG Nancy) from c. 5 cm^3 of each representative rock sample (ISZ-17, sole-55 and LSZ-18-2). The major elements were analysed by inductively coupled plasma-optical emission (ICP-OES) spectroscopy after fusion with $LiBO_3$ and dissolution in HNO_3. More details on the method are given in Carignan et al. (2001). H_2O content was determined by loss on ignition.

Appendix B. Bulk rock composition analysis

Chemical composition of fifteen thin sections from USZ, ISZ and LSZ were calculated either by averaging of several surface compositions scans using a FEG-SEM (average between 2 and 5 surface analyses) or by a combination of visual percentage estimated modes (Terry and Chilinger, 1955) and averaged EMP chemical analyses. Detailed chemical compositions, average values and sampling GPS coordinates are given in Supplementary material 4.

Appendix C. Construction of the rheological profile

In order to compare rheological properties of the materials, fixed value of $10^{-14}\ s^{-1}$ has been chosen for the calculation. Note that integrated strain rates for subduction zones, generally between 10^{-13} and $10^{-14}\ s^{-1}$ may be substantially higher along shear zones (between 10^{-9} and $10^{-12}\ s^{-1}$; Sibson, 1986; Stöckhert, 2002; Burg and Gerya, 2005), leading to significant increase of rock strength and a marked decrease of rock viscosity

For the basaltic upper section (Fig. 9a), we use an omphacite power law creep rheology (Zhang et al., 2006) to describe its behavior because omphacite appears to be the dominant (c. 75%) mineral under eclogite-facies conditions. This assumption is justified by the fact that garnet (less than 15 vol.% in the eclogitized basaltic crust) does not exhibit a strong fabric and generally behaves as a rotating rigid body during plastic deformation of eclogite (e.g. Mainprice et al., 2004). For Fe–Ti metagabbros, where the relative amount of garnet locally reaches 40 vol.%, an eclogite flow law is considered to be more appropriate (Jin et al., 2001). We also consider that Mg–Al gabbro is rheologically similar to diabase, whose mineralogy is also composed of a Ca-rich plagioclase and clinopyroxene (Mackwell et al., 1995). As Fe–Ti metagabbros are included in the uppermost portion of the Mg–Al metagabbro, the whole gabbroic unit is believed to behave as a coherent body (Fig. 9). Serpentinite exhibits a viscosity which is over 4 orders of magnitude lower than metagabbros (following the flow law for antigorite from Hilairet et al., 2007).

Experimental parameters for the eclogite flow law (calculated for 50% garnet, 40% omphacite, and 10% quartz; Jin et al., 2001) yield an unrealistic rock strength of 7 GPa for Fe–Ti metagabbros under these relatively cold conditions (T = 550 °C; Fig. 9a). This value will likely be lowered in our samples since garnet, considered as responsible for strengthening of the eclogites in the dislocation creep regime (Jin et al., 2001) represents only 25–30 vol.%. Pervasive ductile deformation of metagabbros contrasts with the presence of omphacite-bearing crack-seal veins (earlier reported in eclogite-facies mylonites from the Lago Superiore Area; Philippot, 1987), which constitute one of the rare examples attesting to local brittle behavior of oceanic crust under HP-LT conditions.

References

Abers, G.A., van Keken, P.E., Kneller, E.A., Ferris, A., Stachnik, J.C., 2006. The thermal structure of subduction zones constrained by seismic imaging: implications for slab dehydration and wedge flow. Earth and Planetary Science Letters 241 (3–4), 387–397.

Agard, P., Jolivet, L., Goffé, B., 2001. Tectonometamorphic evolution of the Schistes Lustre's complex: implications for the exhumation of HP and UHP rocks in the western Alps. Bulletin De La Societe Geologique De France 172 (5), 617–636.

Agard, P., Monie, P., Jolivet, L., Goffé, B., 2002. Exhumation of the Schistes Lustres complex: in situ laser probe Ar-40/Ar-39 constraints and implications for the Western Alps. Journal of Metamorphic Geology 20 (6), 599–618.

Agard, P., Yamato, P., Jolivet, L., Burov, E., 2009. Exhumation of oceanic blueschists and eclogites in subduction zones: timing and mechanisms. Earth-Science Reviews 92 (1–2), 53–79.

Ague, J.J., 2007. Models of permeability contrasts in subduction zone mélange: implications for gradients in fluid fluxes, Syros and Tinos Islands, Greece. Chemical Geology 239 (3–4), 217–227.

Andersen, T.B., Austrheim, H., 2006. Fossil earthquakes recorded by pseudotachylytes in mantle peridotite from the Alpine subduction complex of Corsica. Earth and Planetary Science Letters 242 (1–2), 58–72.

Andersen, T.B., Mair, K., Austrheim, H., Podladchikov, Y., Vrijmoed, J.C., 2008. Stress release in exhumed intermediate and deep earthquakes determined from ultramafic pseudotachylyte. Geology 36 (12), 995–998.

Angiboust, S., Agard, P., 2010. Initial water budget: the key to detaching large volumes of eclogitized oceanic crust along the subduction channel? Lithos 120, 453–474.

Angiboust, S., Agard, P., Jolivet, L., Beyssac, O., 2009. The Zermatt-Saas ophiolite: the largest (60-km wide) and deepest (c. 70–80km) continuous slice of oceanic lithosphere detached from a subduction zone? Terra Nova 21, 171–180.

Angiboust, S., Langdon, R., Agard, P., Waters, D., Chopin, C., in press. Eclogitization of the Monviso ophiolite and implications on subduction dynamics. Journal of Metamorphic Geology. doi:10.1111/j.1525-1314.2011.00951.x.

Audet, P., Bostock, M.G., Christensen, N.I., Peacock, S.M., 2009. Seismic evidence for overpressured subducted oceanic crust and megathrust fault sealing. Nature 457 (7225), 76–78.

Austrheim, H., 1987. Eclogitization of lower crustal granulites by fluid migration through shear zones. Earth and Planetary Science Letters 81 (2–3), 221–232.

Austrheim, H., Andersen, T.B., 2004. Pseudotachylytes from Corsica: fossil earthquakes from a subduction complex. Terra Nova 16 (4), 193–197.

Austrheim, H., Boundy, T.M., 1994. Pseudotachylytes generated during seismic faulting and eclogitization of the deep crust. Science 265 (5168), 82–83.

Bachmann, R., Glodny, J., Oncken, O., Seifert, W., 2009. Abandonment of the South Penninic-Austroalpine palaeosubduction zone, Central Alps, and shift from subduction erosion to accretion: constraints from Rb/Sr geochronology. Journal of the Geological Society 166 (2), 217–231.

Ballèvre, M., Lagabrielle, Y., Merle, O., 1990. Tertiary ductile normal faulting as a consequence of lithospheric stacking in the western Alps. Deep structure of the Alps. Societe Geologique de France 156, 227–236.
Bearth, P., 1967. Die Ophiolite der zone von Zermatt-Saas Fee. Materiaux pour la Carte Geologique de la Suisse. Neue Folge 132, 1–130.
Bebout, G.E., Barton, M.D., 2002. Tectonic and metasomatic mixing in a high-T, subduction-zone mélange—insights into the geochemical evolution of the slab-mantle interface. Chemical Geology 187 (1–2), 79–106.
Beltrando, M., Rubatto, D., Manatschal, G., 2010. From passive margins to orogens: the link between ocean-continent transition zones and (ultra)high-pressure metamorphism. Geology 38 (6), 559–562.
Blake Jr., M.C., Moore, D.E., Jayko, A.S., 1995. The role of serpentinite melanges in the unroofing of ultrahigh-pressure metamorphic rocks: an example from the Western Alps. Ultrahigh pressure metamorphism. Cambridge University Press. 182–205 pp.
Blake, M.C., Jayko, A.S., 1990. Uplift of very high pressure rocks in the western Alps: evidence for structural attenuation along low-angle faults. Mémoire de la Société Géologique de France 156, 237–246.
Boundy, T.M., Fountain, D.M., Austrheim, H., 1992. Structural development and petrofabrics of eclogite facies shear zones, Bergen Arcs, western Norway: implications for deep crustal deformational processes. Journal of Metamorphic Geology 10 (2), 127–146.
Breeding, C.M., Ague, J.J., Bröcker, M., 2004. Fluid-metasedimentary rock interactions in subduction-zone mélange: implications for the chemical composition of arc magmas. Geology 32 (12), 1041–1044.
Bucher, K., Fazis, Y., De Capitani, C., Grapes, R., 2005. Blueschists, eclogites, and decompression assemblages of the Zermatt-Saas ophiolite: high-pressure metamorphism of subducted Tethys lithosphere. American Mineralogist 90 (5–6), 821–835.
Brouwer, F.M., Vissers, R.L.M., Lamb, W.M., 2002. Metamorphic history of eclogitic metagabbro blocks from a tectonic mélange in the Voltri massif, Ligurian Alps, Italy. Ofioliti 27 (1), 1–16.
Burg, J.P., Gerya, T.V., 2005. The role of viscous heating in Barrovian metamorphism of collisional orogens: thermomechanical models and application to the Lepontine Dome in the Central Alps. Journal of Metamorphic Geology 23 (2), 75–95.
Burg, J.-P., Philippot, P., 1991. Asymmetric compositional layering of syntectonic metamorphic veins as way-up criterion. Geology 19 (11), 1112–1115.
Carignan, J., Hild, P., Mevelle, G., Morel, J., Yeghicheyan, D., 2001. Routine analyses of trace elements in geological samples using flow injection and low pressure on-line liquid chromatography coupled to ICP-MS: a study of geochemical reference materials BR, DR-N, UB-N, AN-G and GH. Geostandards Newsletter 25 (2–3), 187–198.
Castelli, D., Rostagno, C., Lombardo, B., 2002. Jd-Qtz-bearing metaplagiogranite from the Monviso meta-ophiolite (Western Alps). Ofioliti 27, 81–90.
Catlos, E.J., Sorensen, S.S., 2003. Phengite-based chronology of K- and Ba-Rich fluid flow in two paleosubduction zones. Science 299 (5603), 92–95.
Cliff, R.A., Barnicoat, A.C., Inger, S., 1998. Early Tertiary eclogite facies metamorphism in the Monviso Ophiolite. Journal of Metamorphic Geology 16 (3), 447–455.
Compagnoni, R., Rolfo, F., Manavella, F., Salusso, F., 2007. Jadeitite in the Monviso meta-ophiolite, Piemonte Zone, Italian western Alps. Periodico di Mineralogia 76 (2), 79–89.
Coward, M., Dietrich, D., 1989. Alpine tectonics — an overview. Geological Society, London, Special Publications 45 (1), 1–29.
Dal Piaz, G.V., Hunziker, J.C., Martinotti, G., 1972. La Zona Sesia-Lanzo e l'evoluzione tettonino-metamorphica delle Alpi nordoccidentali interne. Mem. Societa, 11. Geologica Italiana, Roma, pp. 433–472.
Davies, J.H., 1999. The role of hydraulic fractures and intermediate-depth earthquakes in generating subduction-zone magmatism. Nature 398 (6723), 142–145.
Deville, E., Fudral, S., Lagabrielle, Y., Marthaler, M., Sartori, M., 1992. From oceanic closure to continental collision: a synthesis of the “Schistes lustrés” metamorphic complex of the Western Alps. Geological Society of America Bulletin 104 (2), 127–139.
Dipple, G.M., Ferry, J.M., 1992. Metasomatism and fluid flow in ductile fault zones. Contributions to Mineralogy and Petrology 112 (2), 149–164.
Duchene, S., Lardeaux, J.M., Albarede, F., 1997. Exhumation of eclogites: insights from depth–time path analysis. Tectonophysics 280 (1–2), 125–140.
Erambert, M., Austrheim, H., 1993. The effect of fluid and deformation on zoning and inclusion patterns in poly-metamorphic garnets. Contributions to Mineralogy and Petrology 115 (2), 204–214.
Essene, E.J., Fyfe, W.S., 1967. Omphacite in Californian metamorphic rocks. Contributions to Mineralogy and Petrology 15 (1), 1–23.
Federico, L., Crispini, L., Scambelluri, M., Capponi, G., 2007. Ophiolite melange zone records exhumation in a fossil subduction channel. Geology 35 (6), 499–502.
Ferry, J.M., 1979. A map of chemical potential differences within an outcrop. American mineralogist 64 (9–10), 966–985.
Fountain, D.M., Boundy, T.M., Austrheim, H., Rey, P., 1994. Eclogite-facies shear zones—deep crustal reflectors? Tectonophysics 232 (1–4), 411–424.
Gerya, T.V., Stockhert, B., Perchuk, A.L., 2002. Exhumation of high-pressure metamorphic rocks in a subduction channel: a numerical simulation. Tectonics 21 (6), 1–19.
Griggs, D., 1967. Hydrolytic Weakening of Quartz and Other Silicates*. Geophysical Journal of the Royal Astronomical Society 14 (1–4), 19–31.
Groppo, C., Castelli, D., 2010. Prograde P–T evolution of a lawsonite eclogite from the Monviso metaophiolite (Western Alps): dehydration and redox reactions during subduction of oceanic FeTI-oxide gabbro. Journal of Petrology 51 (12), 2489–2514.
Guillot, S., Schwartz, S., Hattori, K., Auzende, A., Lardeaux, J., 2004. The Monviso ophiolitic Massif (Western Alps), a section through a serpentinite subduction channel. Evolution of the western Alps: insights from metamorphism, structural geology, tectonics and geochronology, The Virtual Explorer. pp. Paper 3.
Handy, M.R., Wissing, S.B., Streit, L.E., 1999. Frictional-viscous flow in mylonite with varied bimineralic composition and its effect on lithospheric strength. Tectonophysics 303 (1–4), 175–191.
Hattori, K.H., Guillot, S., 2007. Geochemical character of serpentinites associated with high- to ultrahigh-pressure metamorphic rocks in the Alps, Cuba, and the Himalayas: recycling of elements in subduction zones. Geochemistry Geophysics Geosystems 8 (9), Q09010.
Healy, D., Reddy, S.M., Timms, N.E., Gray, E.M., Brovarone, A.V., 2009. Trench-parallel fast axes of seismic anisotropy due to fluid-filled cracks in subducting slabs. Earth and Planetary Science Letters 283 (1–4), 75–86.
Hermann, J., Müntener, O., Scambelluri, M., 2000. The importance of serpentinite mylonites for subduction and exhumation of oceanic crust. Tectonophysics 327 (3–4), 225–238.
Hilairet, N., et al., 2007. High-pressure creep of serpentine, interseismic deformation, and initiation of subduction. Science 318, 1910.
Holland, T., 1979. High water activity in the generation of high-pressure kyanite eclogite of the Tauern window, Austria. Journal of Geology 87, 1–27.
Ikesawa, E., Sakaguchi, A., Kimura, G., 2003. Pseudotachylyte from an ancient accretionary complex: evidence for melt generation during seismic slip along a master decollement? Geology 31 (7), 637–640.
Iyer, K., Rüpke, L.H., Morgan, J.P., 2010. Feedbacks between mantle hydration and hydrothermal convection at ocean spreading centers. Earth and Planetary Science Letters 296 (1–2), 34–44.
Ji, S., et al., 2003. Microstructures, petrofabrics and seismic properties of ultra high-pressure eclogites from Sulu region, China: implications for rheology of subducted continental crust and origin of mantle reflections. Tectonophysics 370 (1–4), 49–76.
Jin, Z.M., Zhang, J., Green, H.W., Jin, S., 2001. Eclogite rheology: implications for subducted lithosphere. Geology 29 (8), 667–670.
John, T., et al., 2009. Generation of intermediate-depth earthquakes by self-localizing thermal runaway. Nature Geosciences 2 (2), 137–140.
John, T., Schenk, V., 2006. Interrelations between intermediate-depth earthquakes and fluid flow within subducting oceanic plates: constraints from eclogite facies pseudotachylytes. Geology 34 (7), 557–560.
Katayama, I., Nakashima, S., Yurimoto, H., 2006. Water content in natural eclogite and implication for water transport into the deep upper mantle. Lithos 86 (3–4), 245–259.
Keller, L.M., Abart, R., Stünitz, H., De Capitani, C., 2004. Deformation, mass transfer and mineral reactions in an eclogite facies shear zone in a polymetamorphic metapelite (Monte Rosa nappe, western Alps). Journal of Metamorphic Geology 22 (2), 97–118.
Kirby, S.H., 1983. Rheology of the lithosphere. Reviews of Geophysics 21 (6), 1458–1487.
Kirby, S.H., 1985. Rock mechanics observations pertinent to the rheology of the continental lithosphere and the localization of strain along shear zones. Tectonophysics 119 (1–4), 1–27.
Kirby, S.H., Kronenberg, A.K., 1984. Deformation of clinopyroxenite: evidence for a transition in flow mechanisms and semibrittle behavior. Journal of Geophysical Research 89 (B5), 3177–3192.
Lagabrielle, Y., Cotten, J., 1984. Le matériel détritique ophiolitique des séries océaniques liguro-piémontaises. L'exemple du Haut Queyras. Contribution à l'étude des prasinites. Ofioliti 9, 43–66.
Lagabrielle, Y., Lemoine, M., 1997. Alpine, Corsican and Apennine ophiolites: the slow-spreading ridge model. Comptes Rendus de l'Académie des Sciences - Series IIA - Earth and Planetary Science 325 (12), 909–920.
Lapen, T., et al., 2007. Coupling of oceanic and continental crust during Eocene eclogite-facies metamorphism: evidence from the Monte Rosa nappe, western Alps. Contributions to Mineralogy and Petrology 153, 139–157.
Lardeaux, J.-M., Caron, J.-M., Nisio, P., Péquignot, G., Boudeulle, M., 1986. Microstructural criteria for reliable thermometry in low-temperature eclogites. Lithos 19 (3–4), 187–203.
Lombardo, B., et al., 1978. Osservazioni preliminari sulle ofioliti metamorfiche del Monviso (Alpi occidentali). Rendiconti Societa Italiana Mineralogia Petrologia 34, 253–305.
Mackwell, S., Zimmermann, M., Kohlestdt, D., Scherber, D., 1995. Experimental deformation of dry Columbia diabase: implications for tectonics of Venus. In: Daemen, J., Schultz, R. (Eds.), Rock mechanics: proceedings of the 35th U.S. Symposium, University of Nevada. Reno/5–7 June 1995.
Mainprice, D., Bascou, J., Cordier, P., Tommasi, A., 2004. Crystal preferred orientations of garnet: comparison between numerical simulations and electron back-scattered diffraction (EBSD) measurements in naturally deformed eclogites. Journal of Structural Geology 26 (11), 2089–2102.
Martin, L.A.J., Ballèvre, M., Boulvais, P., Halfpenny, A., Vanderhaeghe, O., Duchêne, S., Deloule, E., 2011. Garnet re-equilibration by coupled dissolution–reprecipitation: evidence from textural, major element and oxygen isotope zoning of ‘cloudy’ garnet. Journal of Metamorphic Geology 29 (2), 213–231.
Mauler, A., Burlini, L., Kunze, K., Philippot, P., Burg, J.P., 2000. P-wave anisotropy in eclogites and relationship to the omphacite crystallographic fabric. Physics and Chemistry of the Earth, Part A: Solid Earth and Geodesy 25 (2), 119–126.
Meneghini, F., Di Toro, G., Rowe, C.D., Moore, J.C., Tsutsumi, A., Yamagushi, A., 2010. Record of mega-earthquakes in subduction thrusts: the black fault rocks of Pasagshak Point (Kodiak Island, Alaska). Geological Society of America Bulletin 122 (7–8), 1280–1297.
Messiga, B., Kienast, J.R., Rebay, G., Riccardi, M.P., Tribuzio, R., 1999. Cr-rich magnesiochloritoid eclogites from the Monviso ophiolites (Western Alps, Italy). Journal of Metamorphic Geology 17 (3), 287–299.
Mibe, K., Yoshino, T., Ono, S., Yasuda, A., Fujii, T., 2003. Connectivity of aqueous fluid in eclogite and its implications for fluid migration in the Earth's interior. Journal of Geophysical Research 108 (B6), 2295.

Minshull, T.A., Muller, M.R., Robinson, C.J., White, R.S., Bickle, M.J., 1998. Is the oceanic Moho a serpentinization front? Geological Society of London. Special Publications 148 (1), 71–80.
Monié, P., Philippot, P., 1989. Mise en évidence de l'âge éocène moyen du métamorphisme de haute pression dans la nappe ophiolitique du Monviso (Alpes Occidentales) par la méthode 39 Ar–40 Ar. Comptes Rendus de l'Academie des Sciences 309, 245–251.
Montési, L.G.J., Hirth, G., 2003. Grain size evolution and the rheology of ductile shear zones: from laboratory experiments to postseismic creep. Earth and Planetary Science Letters 211 (1–2), 97–110.
Monviso, 1980. The Monviso ophiolite complex. Extract from "Ophiolites: Proceedings International Ophiolite Symposium", Cyprus 1979, pp. 332–340.
Morrow, C.A., Shi, L.Q., Byerlee, J.D., 1984. Permeability of fault gouge under confining pressure and shear stress. Journal of Geophysical Research 89 (B5), 3193–3200.
Nadeau, S., Philippot, P., Pineau, F., 1993. Fluid inclusion and mineral isotopic compositions (HCO) in eclogitic rocks as tracers of local fluid migration during high-pressure metamorphism. Earth and Planetary Science Letters 114 (4), 431–448.
Oberhänsli, R., Goffé, B., 2004. Metamorphic Structure of the Alps. C.C.G.M, Paris.
Oncken, O., ANCORP working group, 2003. Seismic imaging of a convergent continental margin and plateau in the central Andes (Andean Continental Research Project 1996 (ANCORP'96)). Journal of Geophysical Research 108 (B7), 2328.
Philippot, P., 1987. Crack-seal vein geometry in eclogitic rocks. Geodinamica acta 3, 171–181.
Philippot, P., Kienast, J.-R., 1989. Chemical-microstructural changes in eclogite-facies shear zones (Monviso, Western Alps, north Italy) as indicators of strain history and the mechanism and scale of mass transfer. Lithos 23 (3), 179–200.
Philippot, P., Selverstone, J., 1991. Trace-element-rich brines in eclogitic veins: implications for fluid composition and transport during subduction. Contributions to Mineralogy and Petrology 106 (4), 417–430.
Philippot, P., van Roermund, H.L.M., 1992. Deformation processes in eclogitic rocks: evidence for the rheological delamination of the oceanic crust in deeper levels of subduction zones. Journal of Structural Geology 14 (8–9), 1059–1077.
Piepenbreier, D., Stöckhert, B., 2001. Plastic flow of omphacite in eclogites at temperatures below 500°C - implications for interplate coupling in subduction zones. International Journal of Earth Sciences 90 (1), 197–210.
Platt, J.P., Behr, W.M., 2011. Lithospheric shear zones as constant stress experiments. Geology 39 (2), 127–130.
Pognante, U., Kienast, J.-R., 1987. Blueschist and eclogite transformations in Fe–Ti gabbros: a case from the Western Alps ophiolites. Journal of Petrology 28 (2), 271–292.
Polino, R., Dal Piaz, G.V., Guido, G., 1990. Tectonic erosion at the Adria margin and accretionnary processes for the Cretaceous orogeny of the Alps. Mémoire de la Société Géologique de France 156, 345–367.
Prior, D.J., 1993. Sub-critical fracture and associated retrogression of garnet during mylonitic deformation. Contributions to Mineralogy and Petrology 113 (4), 545–556.
Raimbourg, H., Jolivet, L., Leroy, Y., 2007. Consequences of progressive eclogitization on crustal exhumation, a mechanical study. Geophysical Journal International 168 (1), 379–401.
Ranero, C.R., Phipps Morgan, J., McIntosh, K., Reichert, C., 2003. Bending-related faulting and mantle serpentinization at the Middle America trench. Nature 425 (6956), 367–373.
Reinecke, T., 1998. Prograde high- to ultrahigh-pressure metamorphism and exhumation of oceanic sediments at Lago di Cignana, Zermatt-Saas Zone, western Alps. Lithos 42 (3–4), 147–189.
Rogers, G., Dragert, H., 2003. Episodic tremor and slip on the Cascadia subduction zone: the chatter of silent slip. Science 300 (5627), 1942–1943.
Rosenbaum, G., Lister, G.S., 2005. The Western Alps from the Jurassic to Oligocene: spatio-temporal constraints and evolutionary reconstructions. Earth-Science Reviews 69 (3–4), 281–306.
Rowe, C.D., Moore, J.C., Meneghini, F., McKeirnan, A.W., 2005. Large-scale pseudotachylytes and fluidized cataclasites from an ancient subduction thrust fault. Geology 33 (12), 937–940.
Rubatto, D., Hermann, J., 2001. Exhumation as fast as subduction? Geology 29 (1), 3–6.
Rubatto, D., Hermann, J., 2003. Zircon formation during fluid circulation in eclogites (Monviso, Western Alps): implications for Zr and Hf budget in subduction zones. Geochimica et Cosmochimica Acta 67 (12), 2173–2187.
Rutter, E.H., 1986. On the nomenclature of mode of failure transitions in rocks. Tectonophysics 122 (3–4), 381–387.
Rutter, E.H., Brodie, K.H., 1995. Mechanistic interactions between deformation and metamorphism. Geological Journal 30 (3–4), 227–240.
Rybacki, E., Dresen, G., 2000. Dislocation and diffusion creep of synthetic anorthite aggregates. Journal of Geophysical Research 105 (B11), 26017–26036.
Scambelluri, M., Muntener, O., Hermann, J., Piccardo, G.B., Trommsdorff, V., 1995. Subduction of water into the mantle: history of an Alpine peridotite. Geology 23 (5), 459–462.
Schliestedt, M., 1990. Occurrences and stability conditions of low-temperature eclogites. Eclogite Facies Rocks, 1990. Blackie.
Schrank, C.E., Handy, M.R., Fusseis, F., 2008. Multiscaling of shear zones and the evolution of the brittle-to-viscous transition in continental crust. Journal of Geophysical Research 113 (B01407).
Schwartz, S., Allemand, P., Guillot, S., 2001. Numerical model of the effect of serpentinites on the exhumation of eclogitic rocks: insights from the Monviso ophiolitic massif (Western Alps). Tectonophysics 342 (1–2), 193–206.
Schwartz, S., Lardeaux, J.M., Guillot, S., Tricart, P., 2000. The diversity of eclogitic metamorphism in the Monviso ophiolitic complex, western Alps, Italy. Geodinamica Acta 13 (2–3), 169–188.
Selverstone, J., Franz, G., Thomas, S., Getty, S., 1992. Fluid variability in 2 GPa eclogites as an indicator of fluid behavior during subduction. Contributions to Mineralogy and Petrology 112 (2), 341–357.
Shea, W.T., Kronenberg, A.K., 1992. Rheology and deformation mechanisms of an isotropic mica schist. Journal of Geophysical Research 97 (B11), 15201–15237.
Sibson, R.H., 1986. Earthquakes and rock deformation in crustal fault zones. Annual Review of Earth and Planetary Sciences 14 (1), 149–175.
Spandler, C., Pettke, T., Rubatto, D., 2011. Internal and external fluid sources for eclogite-facies veins in the Monviso meta-ophiolite, Western Alps: implications for fluid flow in subduction zones. Journal of Petrology 52 (6), 1207–1236.
Stern, R.J., 2004. Subduction initiation: spontaneous and induced. Earth and Planetary Science Letters 226 (3–4), 275–292.
Stöckhert, B., 2002. Stress and deformation in subduction zones: insight from the record of exhumed metamorphic rocks. Geological Society, London, Special Publications 200 (1), 255–274.
Strömgård, K.-E., 1973. Stress distribution during formation of boudinage and pressure shadows. Tectonophysics 16 (3–4), 215–248.
Terry, M.P., Heidelbach, F., 2006. Deformation-enhanced metamorphic reactions and the rheology of high-pressure shear zones, Western Gneiss Region, Norway. Journal of Metamorphic Geology 24 (1), 3–18.
Terry, R.D., Chilinger, G.V., 1955. Comparison charts for visual estimation of percentage composition. Journal of Sediment Petrology 25, 229–234.
Tilton, G.R., Schreyer, W., Schertl, H.P., 1991. Pb–Sr–Nd isotopic behavior of deeply subducted crustal rocks from the Dora Maira Massif, Western Alps, Italy—II: What is the age of the ultrahigh-pressure metamorphism? Contributions to Mineralogy and Petrology 108 (1), 22–33.
Toyoshima, T., 1990. Pseudotachylite from the Main Zone of the Hidaka metamorphic belt, Hokkaido, northern Japan. Journal of Metamorphic Geology 8 (5), 507–523.
Treagus, S.H., 1981. A theory of stress and strain variations in viscous layers, and its geological implications. Tectonophysics 72 (1–2), 75–103.
Tricart, P., Schwartz, S., Sue, C., Lardeaux, J.-M., 2004. Evidence of synextension tilting and doming during final exhumation from analysis of multistage faults (Queyras Schistes lustrés, Western Alps). Journal of Structural Geology 26 (9), 1633–1645.
Tullis, J., Yund, R.A., 1987. Transition from cataclastic flow to dislocation creep of feldspar: mechanisms and microstructures. Geology 15 (7), 606–609.
Ulmer, P., Trommsdorff, V., 1995. Serpentine stability to mantle depths and subduction-related magmatism. Science 268 (5212), 858–861.
Watson, B., Brenan, J., 1987. Fluids in the lithosphere, 1. Experimentally-determined wetting characteristics of CO2H2O fluids and their implications for fluid transport, host-rock physical properties, and fluid inclusion formation. Earth and Planetary Science Letters 85 (4), 497–515.
White, S.H., Burrows, S.E., Carreras, J., Shaw, N.D., Humphreys, F.J., 1980. On mylonites in ductile shear zones. Journal of Structural Geology 2 (1–2), 175–187.
White, S.H., Knipe, R.J., 1978. Transformation- and reaction-enhanced ductility in rocks. Journal of the Geological Society 135 (5), 513–516.
Whitney, D.L., Evans, B.W., 2010. Abbreviations for names of rock-forming minerals. American Mineralogist 95 (1), 185–187.
Yamato, P., Agard, P., Burov, E., Le Pourhiet, L., Jolivet, L., Tiberi, C., 2007. Burial and exhumation in a subduction wedge: mutual constraints from thermomechanical modeling and natural P-T-t data (Schistes Lustres, western Alps). Journal of Geophysical Research-Solid Earth 112 (B7).
Zhang, J., Green, H.W., 2007. Experimental investigation of eclogite rheology and its fabrics at high temperature and pressure. Journal of Metamorphic Geology 25 (2), 97–115.
Zhang, J., Green, H.W., Bozhilov, K.N., 2006. Rheology of omphacite at high temperature and pressure and significance of its lattice preferred orientations. Earth and Planetary Science Letters 246 (3–4), 432–443.
Zhao, D., Mishra, O.P., Sanda, R., 2002. Influence of fluids and magma on earthquakes: seismological evidence. Physics of The Earth and Planetary Interiors 132 (4), 249–267.

Tectonophysics 526–529 (2012) 97–109

Contents lists available at ScienceDirect

Tectonophysics

journal homepage: www.elsevier.com/locate/tecto

Numerical modelling of magma transport in dykes

P. Yamato [a,b,*], R. Tartèse [a], T. Duretz [b], D.A. May [b]

[a] Géosciences Rennes, CNRS UMR 6118, Université de Rennes 1, 35042 Rennes Cedex, France
[b] Institute of Geophysics, Department of Earth Science, ETH-Zurich, Sonneggstrasse 5, CH-8092 Zurich, Switzerland

ARTICLE INFO

Article history:
Received 30 December 2010
Received in revised form 16 May 2011
Accepted 18 May 2011
Available online 15 June 2011

Keywords:
Dyke
Magma ascent
Numerical modelling
Crystal rotation
Magmatic differentiation

ABSTRACT

The rheology and dynamics of an ascending pure melt in a dyke have been extensively studied in the past. From field observations, it is apparent that most dykes actually contain a crystalline load. The presence of a crystalline load modifies the effective rheology of such a system and thus the flow behaviour. Indeed, the higher density and viscosity of each crystal, compared to the melt, cause a decrease of the ascent velocity and modify the shape of the velocity profile, from a typical Poiseuille flow, to a Bingham-type flow. A common feature observed in the field is the arrangement of crystals parallel or at a very low angle to the edge of the dyke. Such a structural arrangement is often interpreted as the result of magma flow, which caused the crystals to rotate and align within the flow direction, but this process remains unclear. Another issue related to the introduction of a crystalline load concerns the possibility for crystals to be segregated from a viscous granitic melt phase during magma ascent. The implications of such a process on magmatic differentiation have not previously been considered, nor has such a process been previously investigated via numerical models. In this study, we examine the flow dynamics of a crystal bearing granitic melt ascending in a dyke via numerical models. In our models, both the crystal and melt phases are represented as highly viscous fluids in a Stokes regime. Our results reveal that the presence of crystals in the melt modifies the magma velocity profile across the dyke. Furthermore, we observe that whilst crystals continually rotate in the shear flow, over one period of revolution, their major axis has a high probability to be aligned parallel to the flow direction. Moreover, some experiments showed that the melt phase can effectively be squeezed out from a crystal-rich magma when subjected to a given pressure gradient range. This demonstrates that crystal-melt segregation in dykes during granitic magma ascent constitutes a viable mechanism for magmatic differentiation.

1. Introduction

The processes related to magma ascent from source zones towards emplacement sites of magmatic intrusions in the upper crust constitute a major subject of interest in Earth sciences, especially in terms of understanding intra-crustal differentiation. In particular, the mechanism leading to granitic melt migration towards the upper continental crust (represented by the "diapirism" and "dyking" end-members) has been controversially discussed throughout the 20th century (see reviews by Clemens, 1998; Petford, 2003). Nevertheless, since the study of Clemens and Mawer (1992), it is now largely agreed that the most viable mechanism for the migration of magma, from the deep partial melting zone where they form, to the upper crust where they emplace, is dyking (e.g., Clemens, 1998, 2003; Clemens and Petford, 1999; Petford et al., 1994; Scaillet et al., 1998).

The rheology and the behaviour of a multiphase magma (i.e., composed of suspended crystals carried by a viscous medium) subject to a given pressure gradient are governed by the amount of crystals and their geometry (e.g., Bagdassarov and Dorfman, 1998). Here we do not consider the effect of gas bubbles because the processes that we study occur at a depth where volatiles are dissolved in the melt phase. When the amount of crystals is small, silicate melts are considered as Newtonian fluids and their behaviour follows the Einstein–Roscoe relations (Einstein, 1906; Roscoe, 1953). Above a critical solid fraction of suspended crystals, depending on their size, shape and distribution in the magma, the suspension can form a rigid skeleton (Philpotts et al., 1998), which introduces a yield stress in the magmatic suspension and thus results in an effective non-Newtonian rheology (e.g. Kerr and Lister, 1991). The volume of crystals at which the transition from a Newtonian to a non-Newtonian rheology occurs has been estimated somewhere between 15 and 50 vol.% (Champallier et al., 2008; Hallot et al., 1996; Kerr and Lister, 1991; Petford, 2003; Petford and Koenders, 1998; Walsh and Saar, 2008). When the magma contains ca. 55% of solid particles, only residual liquids can escape the rigid skeleton formed by crystals, an effect known as the "rigid percolation threshold" (Vigneresse et al.,

* Corresponding author at: Géosciences Rennes, CNRS UMR 6118, Université de Rennes 1, 35042 Rennes Cedex, France. Tel.: +33 2 23 23 60 95.
E-mail address: philippe.yamato@univ-rennes1.fr (P. Yamato).

0040-1951/$ – see front matter © 2011 Elsevier B.V. All rights reserved.
doi:10.1016/j.tecto.2011.05.015

1996). According to these authors, when ca. 75% of crystallisation occurs, the entire system becomes totally locked, preventing further mechanical melt percolation from occurring.

Field observations of crystal arrangement in frozen dykes reveal that both their repartitions and their orientations are not random (e.g., Chistyakova and Latypov, 2010; Paterson, 2009; Smith, 2002). In many instances, the crystals are found to be orientated with their major axis parallel, or at a low angle, to the edges of the dyke following the magma flow direction. However, the processes of crystal re-orientation and of their spatial organisation acting during magma transport cannot be directly observed and thus have to be modelled. The rotation of solids immersed in a deforming viscous medium has been addressed in numerous analogue experiments (e.g., Arbaret et al., 1996, 2001; Marques and Burlini, 2008; Marques and Coelho, 2001, 2003; Van den Driessche and Brun, 1987; Willis, 1977) and numerical studies (Bons et al., 1996; Mandal et al., 2001; Marques et al., 2005a, 2005b; Samanta et al., 2002; Schmid, 2005). Also, observations of the crystal size distribution within dykes often show that the crystals are sorted by their size, increasing from the edges of the dyke to the centre (e.g., Nkono et al., 2006 and references therein). This can be attributed to their mechanical segregation during the magmatic transport, a phenomenon known as the "Bagnold effect" (e.g., Bagnold, 1954; Barrière, 1976; Bhattacharji, 1967; Komar, 1972a, 1972b). Besides the fact that these two phenomena should occur coevally during crystal-bearing magma transport in dykes, this complex mechanism remains poorly constrained. Numerous experimental (e.g., Bagdassarov and Dorfman, 1998) and numerical (e.g., Deubelbeiss et al., 2010) studies have been undertaken on magmatic suspension containing particles. However, they mainly addressed the issue of quantifying the effective viscosity of the crystal-melt system and the related rheological consequences, with an emphasis on volcanism (Caricchi et al., 2007; Costa et al., 2007; Dingwell, 1996; Melnik and Sparks, 1999; Papale, 1999; Taisne and Jaupart, 2011).

Finally, another fundamental aspect of magma dynamics is the capacity of crystal-melt segregation to occur during magma ascent in dykes, which has important consequences for magmatic differentiation processes. Crystal-melt fractionation is controlled by factors such as the density difference between the solid and liquid phases, the viscosity of the melt phase, the crystal size and the dynamics of the system. In granitic rocks, such a process is considered to be difficult to initiate, because of (i) the common belief that granitic melts are highly viscous and (ii) the lack of a sufficiently high density difference between the minerals and the residual liquid. Granitic melt viscosities are in the range 10^4–10^6 Pa.s (e.g., Clemens, 1998; Scaillet et al., 1998), and the density difference between the melt and common crystals is typically in the range of 200–400 kg.m^{-3}.

To our knowledge, numerical modelling has not been used to study crystal-melt segregation processes that might take place in dykes at depth. In order to address this issue, we propose to use a fluid dynamic description of creeping flow (Stokes) to represent both the crystal and melt phases in one coupled system. We first verify that the numerical method developed can reproduce the known behaviour of highly viscous, or rigid, inclusion subject to both simple and pure shear boundary conditions. In these tests, we quantitatively compared our numerical results to analytical solutions. Then, we describe a model setup that can be used to understand field observations such as crystal orientation in dykes. Finally, we show that crystal-melt segregation is actually a viable mechanism during granitic magma ascent. In this paper, we present examples where all of the crystals introduced possess identical material properties and geometry.

2. Numerical model

In order to study the dynamics of a crystal suspension in an ascending magmatic flow, we define the system to be composed of highly viscous fluids. The equations governing creeping flow in two-dimensions are given by the Stokes equations (Eqs. (1)–(2)) subject to the incompressibility constraint (Eq. (3)):

$$-\frac{\partial P}{\partial x}+\frac{\partial \tau_{xx}}{\partial x}+\frac{\partial \tau_{xz}}{\partial z}=0, \tag{1}$$

$$-\frac{\partial P}{\partial z}+\frac{\partial \tau_{zz}}{\partial z}+\frac{\partial \tau_{zx}}{\partial x}=\rho g, \tag{2}$$

$$\frac{\partial Vx}{\partial x}+\frac{\partial Vz}{\partial z}=0, \tag{3}$$

where P, τ_{ij}, ρ and g correspond to the pressure, the deviatoric stress tensor, the density, and the gravitational acceleration, respectively. Vx and Vz are the two components of the velocity vector in 2D (x,z) Cartesian coordinate system.

We consider both the crystals and the melt as a linear viscous material. Their constitutive relationship is expressed as follows:

$$\tau_{ij}=2\eta\dot{\varepsilon}_{ij}, \tag{4}$$

where η is the shear viscosity and $\dot{\varepsilon}_{ij}$ is the strain rate tensor defined as:

$$\dot{\varepsilon}_{ij}=\frac{1}{2}\left(\frac{\partial V_i}{\partial x_j}+\frac{\partial V_j}{\partial x_i}\right), \tag{5}$$

We approximate the crystals as an infinitely rigid material by prescribing a viscosity which is large compared to the viscosity of the surrounding fluid. This ensures that the strain rate inside the crystal is approximately zero. Thus, the crystal "rigidity" is defined by the viscosity ratio between the crystal and melt.

The use of Stokes flow to describe the evolution of the crystal-melt system is only valid if the flow in the dyke is laminar (i.e. Reynolds number lower than 1). The Reynolds number is given by:

$$Re=\frac{\rho_{melt}\cdot V\cdot W}{\eta_{melt}}, \tag{6}$$

where ρ_{melt}, η_{melt}, V and W are respectively the density of the melt, the viscosity of the melt, the flow velocity and the width of the channel. As the presence of crystals leads to a significant decrease of the velocity in the dyke, the highest value of the Reynolds number Re is obtained for a dyke comprised only of melt (i.e., without crystals). For a melt density of 2400 kg.m^{-3} and a large range of acceptable velocities (lower than 0.1 m.s^{-1}) and viscosities (higher than 10^4 Pa.s), the value of Re does not exceed ~0.0125 for a 0.5 m wide dyke. Consequently, viscous forces dominate the inertial forces, thereby justifying the use of Stokes equations to model crystal-melt dynamics in dykes.

We solve the Eqs. (1)–(3) numerically using a code which employs an Eulerian staggered grid finite difference, particle-in-cell method (Gerya and Yuen, 2003; 2007). The material properties, viscosity and density are defined on a set of Lagrangian particles that move through the model domain. To evaluate the finite difference stencil for the discrete stress tensor and the force term on the right hand side of Eqs. (1)–(2), we interpolate the particle viscosity and density onto the finite difference grid. The interpolation used between the particles and the grid is described in Section 3.1. Following the solution of Eqs. (1)–(3) the particles are advected using a fourth-order accurate in space, first-order accurate in time, Runge–Kutta scheme. At each stage of the Runge–Kutta scheme, we define the velocity field at each marker position by interpolating the velocity field from the staggered grid using a bilinear function.

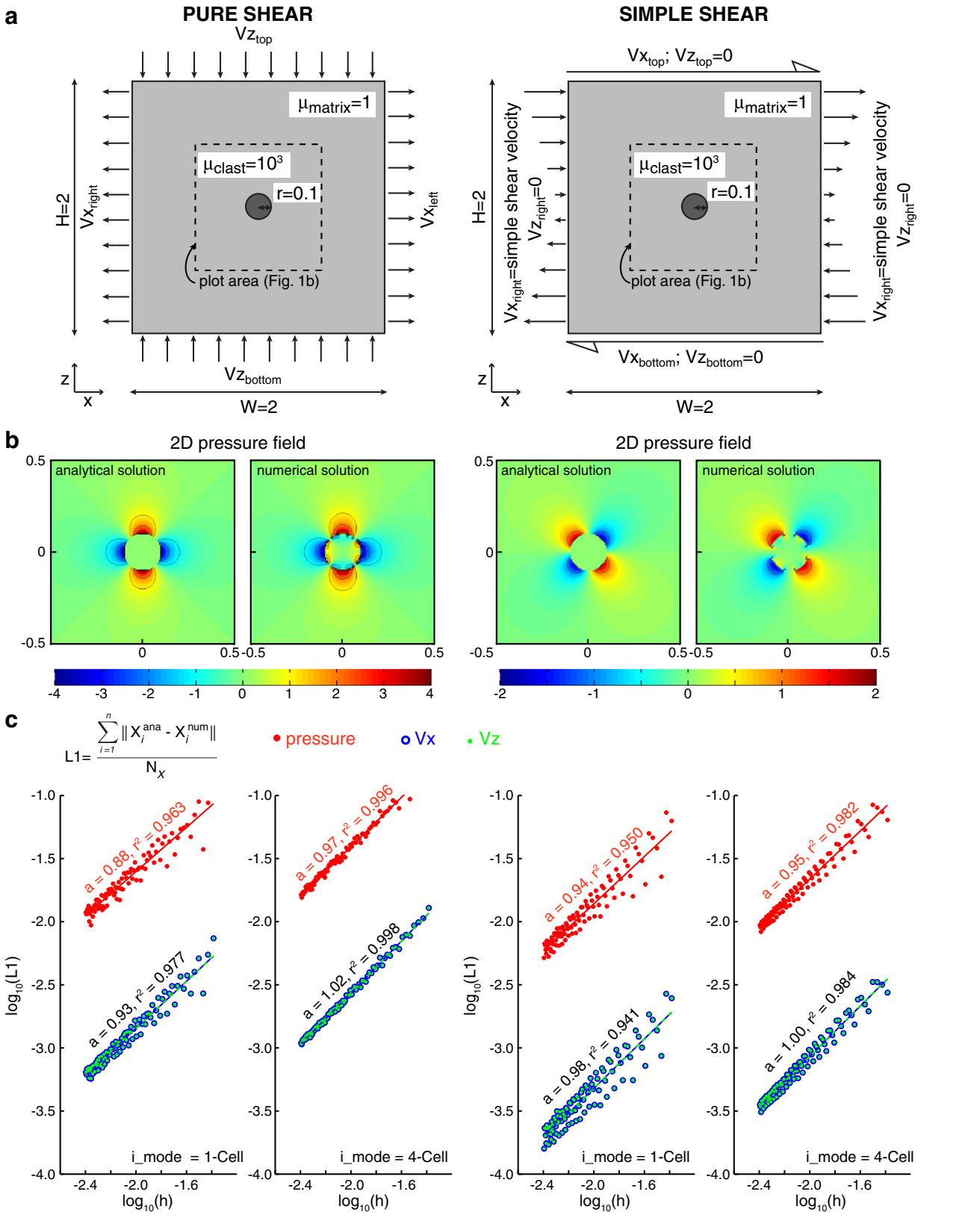

Fig. 1. Comparison of numerical results with analytical solutions for a rigid circular inclusion in a pure shear (left) and simple shear (right) regimes. a) Model setup (see text for details). b) Comparison of the computed 2D pressure field with the analytical solution. In this example, the resolution of the model is 280×280 grid points with 9 particles per cell c) Error between our results and the analytical solution ($L1$) vs. the cell size (h) for two different interpolation modes (see text for details). The $L1$ value corresponds to the sum of the difference between the numerical and the analytical value for the field X at each point i divided by the number of points considered (Nx). X can thus be the pressure (P), the x-component of the velocity vector (Vx), or the z-component of the velocity vector (Vz). Using a staggered grid, in a model with nx nodes in the x direction and ny nodes in the z direction, the value of Nx is $(nx-1)\times(nz-1)$, $nx\times(nz-1)$ and $(nx-1)\times nz$ for P, Vx and Vz respectively.

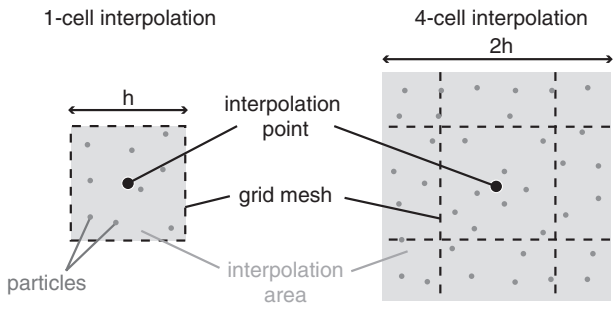

Fig. 2. Interpolation mode definitions. The different modes of interpolations are based on the size of the interpolation area. Here, we illustrate an example of interpolation from the particles, to the centre of the cell, for a case with 9 particles per cell. On the left, 1-cell interpolation mode: the weighted interpolation is performed using all the particles included in a 1-cell area around the interpolation point. The length of the square edge including the particles used is thus *h*, which corresponds to the size of the cell. On the right, 4-cell interpolation mode: the weighted interpolation is performed using all the particles included in a 4-cell area around the interpolation point.

3. Verification of the numerical scheme

Before using our code to study flows with randomly distributed crystals, we performed several experiments involving a viscous inclusion for which we had an analytic solution for the velocity and pressure field. These tests were conducted in order to understand the discretisation errors associated with the method, and to verify that these discretisation errors decreased at the appropriate rate as the numerical resolution in the model was increased. In the crystal-free case, the flow induced by a pressure gradient is characterised by a Poiseuille-type flow. It was already shown that the shear component, particularly close to the edges of the dyke, causes pre-existing crystals to orient their major axis parallel to the flow direction (e.g., Petford and Koenders, 1998). Before examining the case of magmatic suspensions, it is important to verify that our numerical model is capable of correctly simulating both pure and simple shear regimes, and a Poiseuille flow.

3.1. High viscosity inclusion in pure and simple shear regimes

The first test verifies the accuracy of the velocity and the pressure fields for a model defining a circular inclusion of high viscosity, subject to a pure shear boundary condition (Schmid and Podladchikov, 2003). The viscosity ratio between the inclusion and the matrix has been set to 1000 (Fig. 1a) to allow direct comparison of the results with previous studies (e.g. Deubelbeiss and Kaus, 2008; Schmid and Podladchikov, 2003). Zero density difference is prescribed between the inclusion and

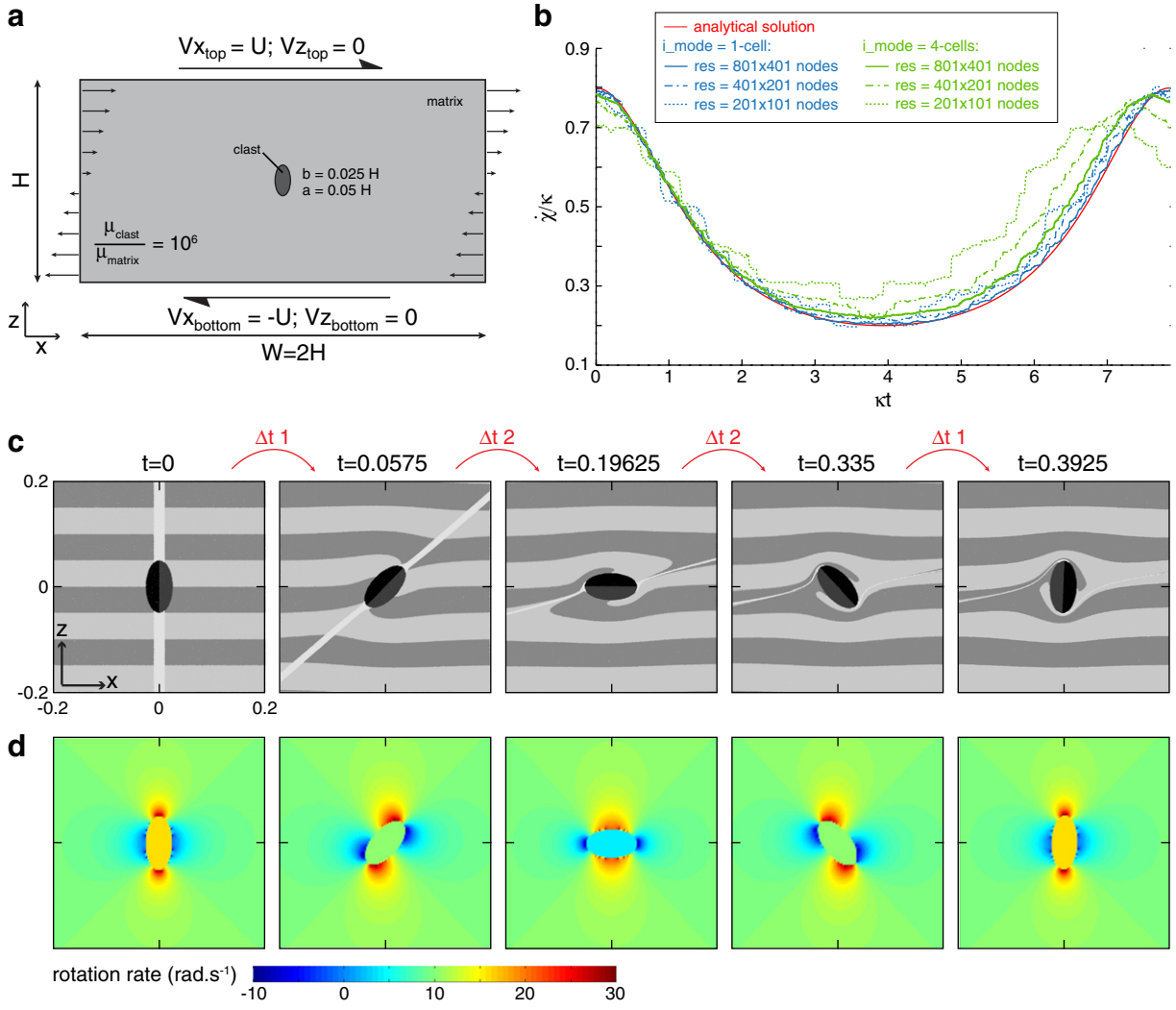

Fig. 3. Comparison of the numerical results with the analytical solution for a rigid elliptical body in a simple shear flow. a) Model setup, identical to the one of Feng and Joseph (1995). Here, $U = 10$ m.s^{-1} and $H = 1$ m. *a* and *b* correspond to the major and minor semi-axes of the elliptical inclusion, respectively. b) Variation of the angular velocity χ vs. time obtained for different grid resolutions and interpolation modes (see text for details). c) Evolution of the ellipse through time. The two horizontal light grey layers in the matrix and the two dark grey regions in the ellipse have been added for visualisation only. d) Evolution of the rotation rate of the ellipse through time.

the matrix. In order to impose the strain rate boundary conditions similar to those used in Schmid and Podladchikov (2003), we evaluated the analytic velocity field at the boundary of the model domain, and used these values as Dirichlet boundary conditions. The initial setup and the results obtained for different numerical resolutions are shown on Fig. 1 (left panels). These results (Fig. 1b, left), which can also be compared with those of Deubelbeiss and Kaus (2008), show that our numerical model provides a very close approximation of the analytical solution of Schmid and Podladchikov (2003).

We also considered an additional simple shear experiment (Fig. 1, right panels). As in the pure shear tests, we used a viscosity ratio of 10^3 and constant density. The results from our model for the simple shear experiment (Fig. 1b, right) are again in good visual agreement with the analytic solution of Schmid and Podladchikov (2003). In both the pure and simple shear cases, we computed the difference between the numerical and analytical solutions using an *L1* norm, where *L1* corresponds to a measure of the discretisation error (see Fig. 1c). The *L1* error for velocity and pressure is observed to decrease, with decreasing grid spacing h (Fig. 1c). In these models, each cell is a square (same resolution in x and z directions). Fig. 1c displays a slope of ~1 in the $\log_{10}(L1)$ vs. $\log_{10}(h)$ plot which means that the discretisation error decreases by a factor 2 when the grid spacing is divided by 2.

In addition, we also performed several tests designed to evaluate two different interpolation schemes (i_mode, Fig. 1c), which are used to map the material properties (viscosity and density) from the markers to the grid. The interpolation mode corresponds to how the viscosity and the density values are interpolated from the particles to the cell vertices, and the cell centres (Fig. 2). The values of viscosity and density are required at these locations to define the finite difference stencil. An interpolation mode over 1 cell (denoted via i_mode = 1-cell in Fig. 1c) corresponds to a distance weighted interpolation using all the particles included in a one cell area around the interpolation point, whereas a 4-cell interpolation (i_mode = 4-cell in Fig. 1c) uses all particles contained in four cell areas for this operation (Fig. 2). The interpolation calculation is performed using the same method as described in Gerya and Yuen (2003). The only difference concerns the area of interpolation and thus, the number of particles taken into account. The main advantage of the 4-cell interpolation is that, for a given number of markers per cell, more markers are used for the interpolation calculation. However, the increase in the interpolation area can increase the error of the interpolated field (see discussion in Section 3.2 and Fig. 3b). Concerning our test of a highly viscous inclusion in pure and simple shear regimes, the convergence rates obtained using 1-cell or 4-cell averaging are very similar, however the pressure field obtained using the 4-cell average is less noisy (Fig. 1c).

3.2. Rigid ellipse in a simple shear regime

The first series of tests verified that the finite difference, particle-in-cell method produces convergent velocity and pressure fields for systems containing a stationary, circular viscous inclusion. In nature, crystals are non-circular and would rotate in a simple shear flow. Here, we consider several tests designed to verify that our code correctly models systems with these characteristics. Jeffery (1922) developed analytical solutions predicting the 3D trajectory and the angular velocity of a rigid ellipsoidal particle, as a function of its aspect ratio and the applied background shear strain. However, no analytical solution exists for the motion of a 2D rectangular body in a simple shear regime. In order to verify our numerical code, we decided to use the solution derived from the study by Jeffery (1922) and already used several times (e.g., Feng and Joseph, 1995; Ghosh and Ramberg, 1976). We regard this solution appropriate for the purpose of code verification, as the geometry of the inclusion is an approximation of the rectangular crystal geometry we wish to model. This second test allowed us to check if the rotation rates computed numerically are correct and to choose a viscosity ratio between the crystal and melt which ensures that the crystal behaves as a rigid body. The rotation rate for the elliptical inclusion is given by:

$$\dot{\chi} = \frac{\kappa}{a^2 + b^2}\left(a^2 \cos^2\chi + b^2 \sin^2\chi\right) \tag{7}$$

with,

$$\tan\chi = \frac{a}{b}\tan\frac{ab\kappa t}{a^2 + b^2}, \tag{8}$$

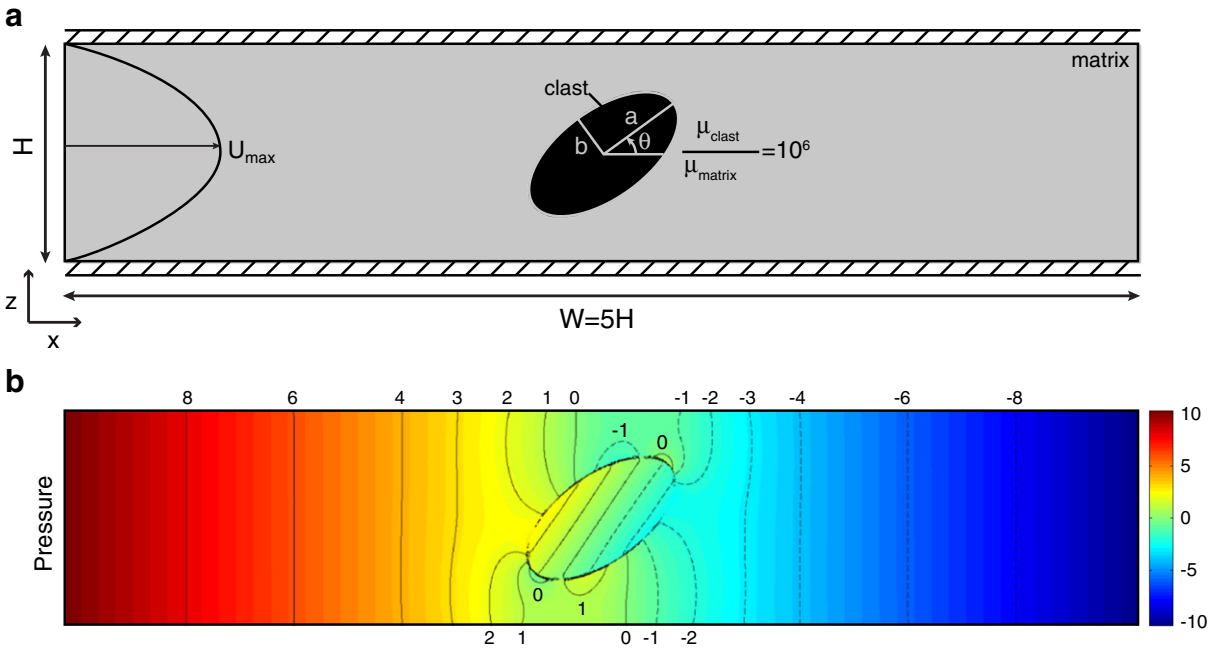

Fig. 4. Rigid ellipse in a Poiseuille flow. a) Model setup, similar to the one of Sugihara-Seki (1993); $H = 1$, $a = 0.4$, $b = 0.2$ and $\theta = 0.2\,\pi$, the viscosity of the matrix μ_{matrix} is 1 and U_{max} is set to 10 (non-dimensional values) as in his experiment. b) Pressure field computed. As in Sugihara-Seki (1993), the colour scale denotes $(p - p_m)d/\mu U_{max}$ where p_m represents the average of the upstream ($x = 0$) and downstream ($x = W$) pressures.

where $\dot{\chi}$, a, b, κ and t are the rotation rate, the half-length of the major axis, the half-length of the minor axis, the shear rate and the time, respectively. The same model setup as in Feng and Joseph (1995) is used and presented in Fig. 3a. The viscosity ratio between the clast (considered as a rigid ellipse) and the matrix is set to 10^6 to mimic a rigid body.

The two interpolation modes were also tested here (Fig. 3b). In comparison with the analytic solution (solid red line), 4-cell interpolation is observed to be less accurate than the 1-cell interpolation. We observe that the interpolation over 4 cells leads to an overestimated rotation rate. This can be explained by the fact that a larger interpolation area decreases the accuracy of the interpolation. The high viscosity at the edge of the ellipse is then computed with an effective viscosity ratio lower than the imposed one. As a consequence, in the following models of asymmetric rigid bodies, we have thus preferred an interpolation mode over 1 cell. Given that the numerical solution is in close agreement with the analytic solution, we can also conclude that our choice of viscosity ratio of 10^6 between the crystal and melt is sufficient to approximate rigid bodies.

According to Jeffery's theory (1922), the rotation rate is higher when the ellipse is perpendicular to the shear direction and slower when the major axis of the ellipse is parallel to the shear (Fig. 3c and d). The fact that the rotation rate is much lower when the ellipse is parallel to the shear flow, compared to when it is perpendicular, leads on average over one period of revolution, to a preferential orientation of the major axis of the ellipse along the shear flow direction.

3.3. Rigid ellipse in a Poiseuille flow

Direct comparison of our numerical results with the analytical solution given by Feng and Joseph (1995) for a Poiseuille flow configuration is not possible because these authors included the inertia of both the ellipse and the fluid in their formulation. Since we are interested in studying low Reynolds numbers flows, we compared our results with those of Sugihara-Seki (1993) who performed similar experiments to Feng and Joseph (1995) but without inertia, using a 2D finite element code (Fig. 4). The results we obtained for the longitudinal velocity of a neutrally buoyant elliptical cylinder (measured at the centreline) in a Poiseuille flow are in good visual agreement with the results of Sugihara-Seki (1993; refer to Table 1). The differences in non-dimensional velocities computed with the Sugihara-Seki (1993) solutions are always lower than 10^{-3} for resolutions higher than 201×41 nodes. This Poiseuille flow setup constitutes a supplementary test for the pressure computation in our code. Visually we obtain a similar pressure field to that of Sugihara-Seki, thus providing further confirmation of the accuracy of our pressure solution (Fig. 4b).

All these tests indicate that our code gives a good approximation of solutions for problems of rigid bodies in pure shear, simple shear and in Poiseuille flow conditions. It can now be used in more complex cases such as the simulation of magma transport in dykes involving "rigid" crystals suspended in a Newtonian melt. Following these results, for the remainder of this paper, a viscosity ratio of 10^6 and the 1-cell averaging scheme are used for all calculations.

4. Application to magma transport in dykes

4.1. Model setup

Our model setup is constructed in a manner to produce an effective pressure gradient between the base and the top of a channel (simulating the dyke), by using a rigid piston pushed in a fluid perforated by a hole (Fig. 5). The fluid corresponds to the melt phase of the magmatic material that can be filled with crystals. The term magmatic, as in a mineralogical point of view, means a mixture composed of both melt and crystals (as in Fig. 5). The two main advantages of such a model are

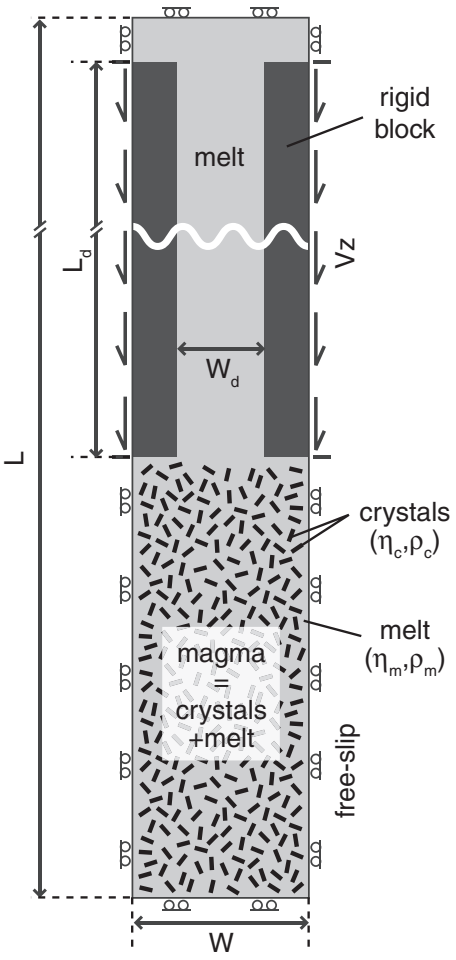

Fig. 5. Rigid piston setup (not shown to scale). The lengths L, L_d, W and W_d correspond to the length of the model, the length of the dyke, the width of the model and the width of the dyke, respectively. In our models $L >> W$, thus for clarity only a portion of the model domain is shown (the wavy white line denotes the cut). The model is thus composed of two parts: a reservoir, filled with magma (80% of melt + 20% of crystals) at the bottom, and the dyke located above. η_c, ρ_c, η_m and ρ_m correspond to the viscosity and the density of the crystals and of the melt, respectively.

(1) that a large volume of crystal mush can easily be used to supply the dyke since the reservoir is included in the model domain and (2) that the mass balance is respected and that the effective background fluid pressure gradient (P_{driv}) over the depth of the channel can be controlled by the velocity imposed at the edges of the two rigid blocks. In this way, no internal kinematic constraints are required within the model in order to drive the magmatic fluid.

In all the simulations we present here, we used a regular grid containing 401×1551 nodes, the interpolation between particles and nodes was carried out over 1 cell area (i_mode = 1-cell). Length units are fixed at 1 m, 0.5 m, 7.75 m and 5 m for W, W_d, L and L_d, respectively (Fig. 5). In such a configuration, the resolution (i.e. the grid spacing) is thus 2.5 mm and 5 mm in the x and z directions, respectively. The size of each crystal is chosen to be 2.5×7.5 cm in order to always ensure that each crystal is sufficient well resolved throughout the simulation. Such crystal sizes are quite large but not uncommon in granitic magma (Vernon and Paterson, 2008a, 2008b). However, since our flow is in a Stokes regime and we use a linear rheology, the principle of dynamic similarity can be applied. This implies that the dynamics is independent of the scale. For example, dividing all length scales in the model by a factor of two will lead to identical flow patterns, but the velocity field will be two times larger. Moreover, since this study is not focused on the influence of the crystal size, but rather on the influence of their presence in the melt,

we consider this size suitable. The amount of crystals in the reservoir is set to 20% (Fig. 5). We first performed several resolution tests to confirm that the grid size used is appropriate to resolve the features of the crystalline flow (Fig. 6). Whilst the location and orientation of a particular crystal may slightly differ between the four panels in Fig. 6, the global evolution of the crystals remains consistent with one another and shows excellent visual agreement. We chose a relatively high grid resolution in order to avoid any artificial crystal clustering, which can occur if a too low numerical resolution is used. However, this resolution test shows that, in the future, simulations with a smaller crystal size could be run using the same grid resolution.

The viscosities of the melt and the crystals are chosen to be 10^4 Pa.s and 10^{10} Pa.s, corresponding to a viscosity ratio of 10^6. This ratio is used to simulate crystals as rigid bodies. The densities used in the models are 2400 kg.m^{-3} and 2700 kg.m^{-3} for the melt and the crystals, respectively. For the rigid blocks, a viscosity of 10^{11} Pa.s was chosen, and in order to avoid any influence between the block and the imposed velocity, the density of the block was chosen to be equal to that of the melt. Hence, no negative or positive buoyancy forces due to a density difference can perturb the vertical velocity we want to impose via these rigid blocks which act as pistons. Four cases are presented here, in which we tested the driving pressure gradient parameter (P_{driv}) imposed through the dyke. This driving pressure gradient controls the magma ascent, and depends on the velocity of the lateral falling blocks (Fig. 5). In a pure melt dyke, the driving pressure gradient is such as:

$$P_{driv} = -\frac{24 \cdot \eta_m \cdot Vz_{block}}{W_d^2}, \quad (9)$$

where η_m, Vz_{block} and W_d correspond to the viscosity of the magma, the velocity of the lateral falling blocks and the dyke width, respectively (see Appendix A). Indeed, imposing the sinking velocity of the rigid blocks corresponds to a pressure gradient. When the applied velocity is zero (experiment $Vz=0$), the only force acting on the magma is its buoyancy. As a result, when considering pure melt and $Vz=0$, the pressure gradient is equal to 24,000 Pa.m^{-1} ($\rho_{melt}.g = 2400 \times 10 = 24{,}000$). This value corresponds to the force needed to compensate the weight of the melt column, ensured by the free-slip boundary condition at the bottom, which prevents the material from leaving the model domain. In order to move the magma upward, the applied pressure gradient must be higher than this buoyancy value, i.e. the system below the piston needs to be over-pressured. In the three cases presented below, this pressure gradient is ensured by using imposed velocities at the edges of the blocks of 5.10^{-2} m.s^{-1} (experiment *High Vz*), 1.10^{-4} m.s^{-1} (experiment *Intermediate Vz*) and 5.10^{-5} m.s^{-1} (experiment *Low Vz*). Using the equation (Eq. (9)) and assuming a 50 cm width dyke, we thus obtain realistic absolute driving pressure gradient values for P_{driv} of 48,000, 96 and 48 Pa.m^{-1}, respectively (e.g., Wilson and Head, 1988).

4.2. Effect of crystalline load on the dyke's flow profile

The presence of crystals in an ascending magma alters the vertical velocity profile across the width of the dyke. In the crystal-free simulations, the fit between the computed vertical velocity and the analytical solution is very good (Fig. 7a). This velocity profile is typical of that expected in a Poiseuille flow. The Fig. 7b shows that the presence of crystals radically alters the parabolic shape of the vertical velocity profile. Low vertical velocities characterise regions where crystals are concentrated. On the other hand, crystal-free areas are preferential corridors in which the melt quickly ascends. This is illustrated in Fig. 7c where several vertical velocity profiles from different heights in the dyke are shown. Vertical velocity profiles computed at $Z=-5$ m and $Z=-5.5$ m are similar, displaying both

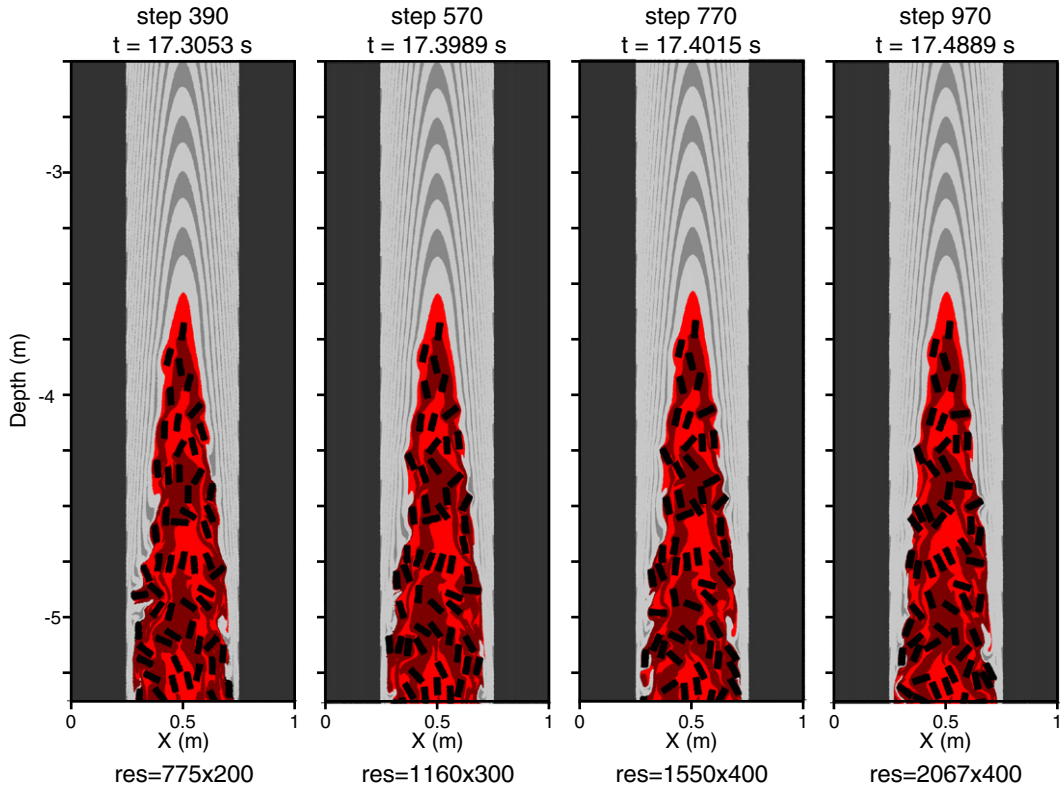

Fig. 6. Resolution tests performed for the *High Vz* experiment (see text for details of the setup). "*res*" corresponds to the grid resolution (number of nodes in the *x* direction multiplied by the number of nodes in the *z* direction). Both the light grey layering and red layering constitute the same material property (melt). They are added here to facilitate visualisation of the deformation field. Red melt corresponds to the melt originally located in the reservoir, which contains crystals. Grey melt denotes the melt already in the channel when the experiment starts. Crystals are plotted in black and the dark grey corresponds to the dyke walls (i.e., the rigid blocks). Results show a good visual agreement, even when using the lowest grid resolution.

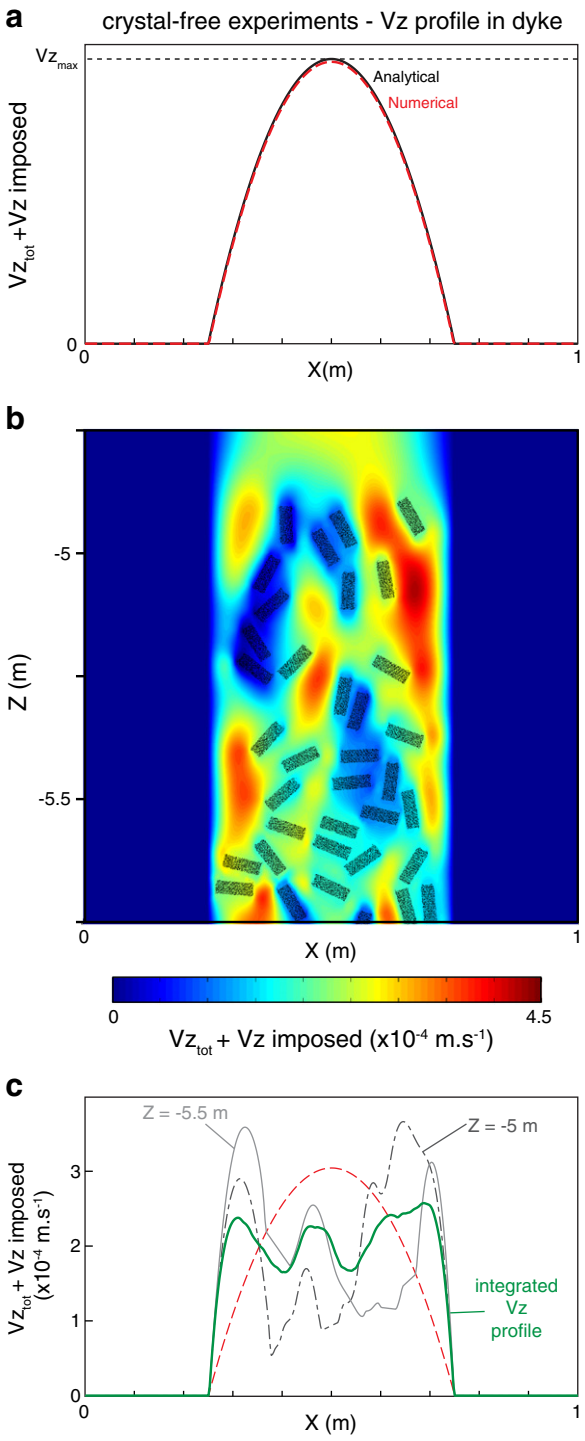

Fig. 7. Real vertical velocity component within the dyke ($Vz_{tot} + Vz_{imposed}$). Indeed, in order to obtain a vertical velocity equal to zero at the dyke walls (i.e. fix walls), the velocities presented here correspond to the vertical velocity component computed (called Vz_{tot}) added to the vertical velocity imposed at the edges of the rigid block (called $Vz_{imposed}$). a) Velocity profile computed in the middle of the dyke for all experiments without any crystal load. Vz_{max} values are then 0.15 m.s^{-1}, 3.10^{-4} m.s^{-1} and 1.5.10^{-4} m.s^{-1} for *High Vz*, *Intermediate Vz* and *Low Vz* experiments, respectively. b) *Vz* plot in the dyke at $t \sim 6000$ s for the *Intermediate Vz* experiment. Crystals are shown as black ghosts. c) In red, vertical velocity profile obtained in the crystal-free model under the same conditions as the *Intermediate Vz* experiment. The grey profiles correspond to 2 individual transects at $Z = -5$ m (plain) and $Z = -5.5$ m (dots). The green profile corresponds to an average of all the velocity profiles integrated between $Z = -5.75$ m and $Z = -4.75$ m.

high and low velocity zones. An interesting feature is that vertical velocities are the highest along the dyke margins, and this value can be larger than the maximum theoretical velocity calculated in the crystal-free case. This illustrates the mechanism of lubrication along the conduit margins already highlighted by Nkono et al. (2006). The integrated velocity profiles over 2 m (green curve in Fig. 7c) shows a roughly defined flat plateau. The irregular shape of this plateau is attributed to the large size of the crystals. Decreasing the size of the crystals (and thus increasing the number of crystals required to maintain the same percentage by volume) would necessarily smooth this plateau. This plateau shape is typical of a Bingham flow, which is representative of crystal-bearing magmatic flows (e.g. Walsh and Saar, 2008).

4.3. Crystal displacement toward the centre of the dyke

Analogue experiments conducted by Bhattacharji (1967) have shown that magma flow provokes an accumulation of the pre-existing solid particles toward the centre of the dyke, due to the Bagnold effect (Bagnold, 1954), even at relatively low crystal content of ca. 15 vol.%. Analytical calculations have confirmed this phenomenon, showing that a hydrodynamic grain dispersive pressure regroups phenocrysts in the centre of the dyke, provided that their volume concentration reaches ca. 8% (Komar, 1972a, 1972b). The size of the phenocrysts is an important parameter in this process; the larger their size, the more efficient the sorting is (Barrière, 1976; Komar, 1972a, 1972b). In our numerical experiments, we do not observe this phenomenon. This could be due to the fact that all the crystals in the numerical experiments have the same size and shape. Indeed, as mentioned above, crystal size is a major parameter controlling this process. Additional experiments utilising various crystal sizes, shapes and distributions of crystal sizes are needed to understand the absence of the Bagnold effect in our numerical models.

4.4. Crystal rotation during magma flow

We demonstrated above that the numerical code we have developed is capable of modelling the rotation rates of a rigid inclusion immersed in a viscous liquid undergoing simple shear. In a Poiseuille flow, the velocity field is parabolic and represents a simple shear component that increases linearly from the centre to the edge. Suspended crystals carried by the melt phase continually rotate during magma ascent. Crystals located in the left part of the dyke rotate counter-clockwise whilst, in contrast, crystals located in the right part of the dyke rotate clockwise. As mentioned in Section 3.2 and according to Jeffery's theory (1922), advected crystals are continuously rotating. Therefore, no specific crystal orientations should be stable. However, for the crystal aspect ratio employed, the rotation rate is about 3 times larger when the major axis is perpendicular to the flow (i.e. the *z*-axis or the wall plane) and slower when the major axis of the ellipse is parallel to the flow. For each crystal, this variation of rotation rate that occurs over one period of revolution explains why crystals are more often found orientated parallel or at a very low angle to the flow direction rather than perpendicular to it. This is illustrated in Fig. 8. Histograms of the crystal orientation in the dyke show that the more the magma ascends, the more the statistical orientation of the crystals tends to be parallel to the flow direction. This may explain why field observations of dyke textures usually show aligned crystals in the flow direction (e.g. Paterson, 2009; Smith, 2002). The observed statistical orientation of the crystals is also in good agreement with the anisotropy of magnetic susceptibility (AMS) studies that show that the statistical alignment of the major axes of phenocrysts (magnetic lineation K1) is parallel or at low angle to the flow direction (e.g., Arbaret et al., 1996; Geoffroy et al., 2002; Ildefonse et al., 1992). In addition, the fact that crystals located to the right of the dyke centre rotate clockwise and those located to the left of the dyke centre rotate counter clockwise

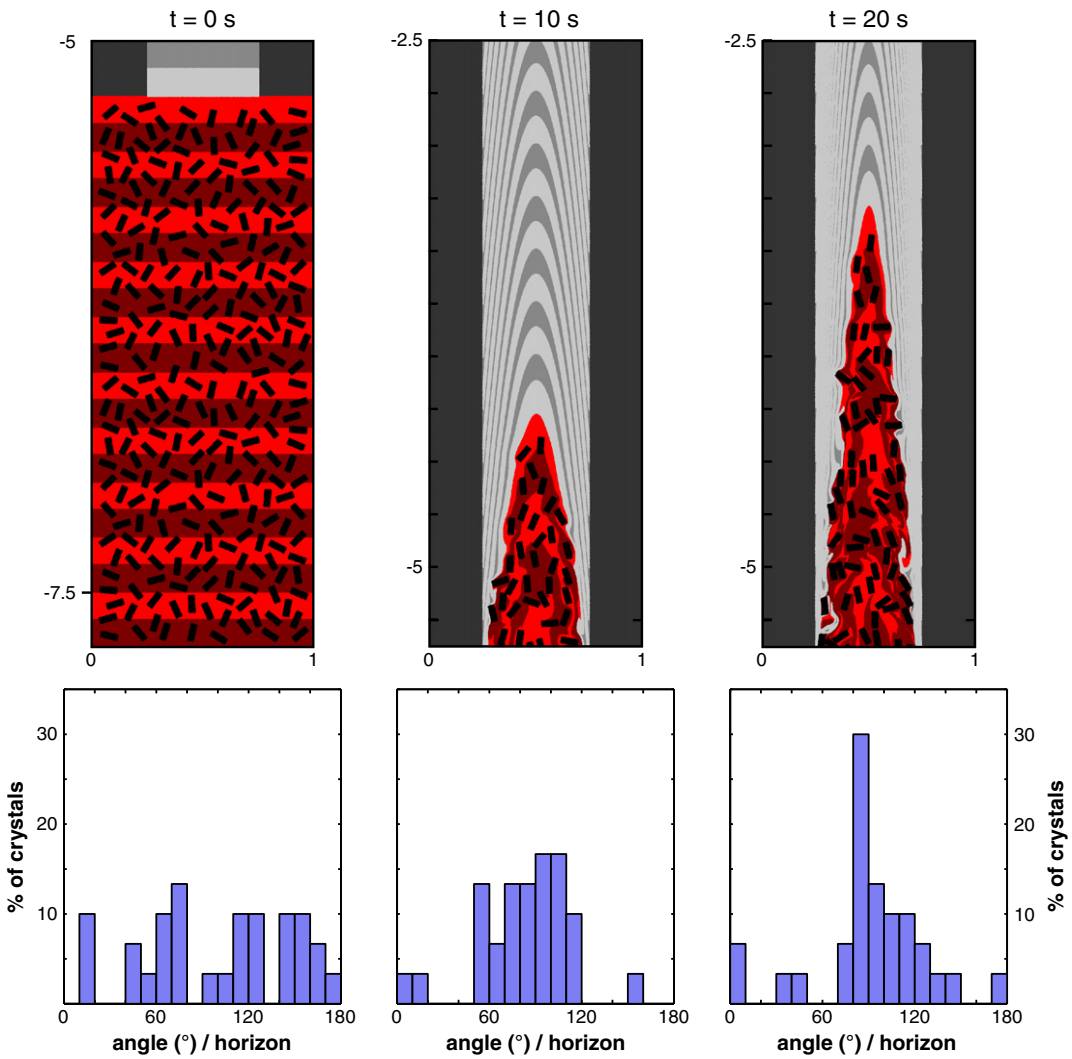

Fig. 8. Crystal rotation during magma flow. Snapshots have been taken at 0, 10 and 20 s in the *High Vz* experiment (upper part). The statistical orientation of the first 30 crystals entered in the dyke has been computed and is displayed as frequency histograms (lower part). The colours represent the same quantities defined in Fig. 6.

leads to the tilling of the crystals (see Fig. 8 at t = 20 s, or Fig. 9, *High Vz* experiment) with a superposition angle in agreement with the sense of the magma flow as determined from AMS studies (e.g., Geoffroy et al., 2002; Knight and Walker, 1988; Varga et al., 1998).

4.5. Crystal-melt segregation and magmatic differentiation

Based on petrographical observations and geochemical data, Tartèse and Boulvais (2010) proposed a mechanism of magmatic differentiation "en route" to the surface. With this mechanism, suspended crystals are segregated from the carrying melt phase at depth during magma ascent in dykes. As a result of this process, the larger the vertical distance the ascending magma has travelled, the more differentiated the resulting magma becomes. The main controls on this process of crystal-melt fractionation are physical factors like melt viscosity, crystal size or the density difference between the melt and the crystals. If crystal fractionation from the melt in mafic magmas is well accepted as a mechanism of differentiation (e.g., Philpotts et al., 1998), such a process is usually considered as unlikely in granitic magmas because of the belief that they are too viscous, and that the density difference between the melt and the crystals is not sufficient.

In the simulations presented in Fig. 9, the melt phase can effectively be squeezed out from the crystalline network. The primary control on this mechanism is the pressure gradient applied on the magma. On one hand, if the pressure gradient is low, the magma cannot rise into the dyke and the crystals fall to the base of the tank (*Vz = 0* experiment in Fig. 9, bottom). Conversely, when the applied pressure gradient is large, the magma rises very quickly, preventing any crystal-melt segregation to occur (*High Vz* experiment in Fig. 9). In the simulations presented Fig. 9, the melt phase is segregated from the crystal-rich mush in the *Low Vz* and *Intermediate Vz* experiments, which corresponds to a driving pressure gradient of 48 and 96 $Pa.m^{-1}$, respectively.

5. Conclusion and perspectives

In this study we have presented a numerical technique to model magmatic flows within a dyke. The main results can be summarised as follow:

(1) Our code has been verified against several analytical solutions that possess characteristics similar to those found in crystal-melt systems. These tests indicate that the marker to node interpolation using 1-cell area is more accurate for problems that include rotating, non-circular rigid-bodies.
(2) The simulations presented here clearly illustrate that crystals rotate continually in an ascending magma, and why field

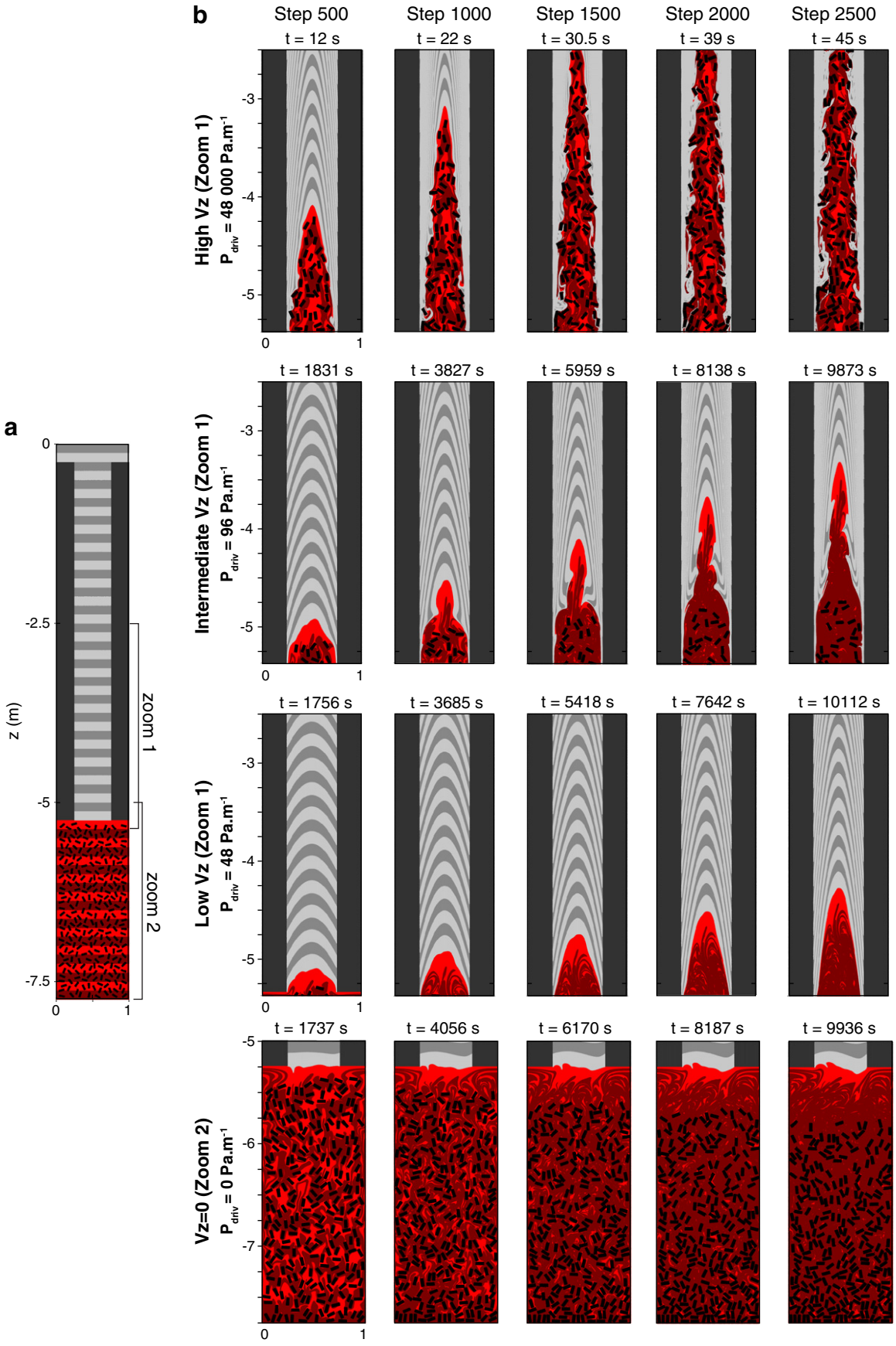

Fig. 9. Results of the experiments as a function of the applied driving pressure gradient (P_{driv}). The colours represent the same quantities defined in Figs. 6 and 8. a) Initial configuration showing the location of the zoom regions presented in b. b) Evolution of the models through time (see text for detailed description).

observations of frozen dykes typically display crystals with their major axis usually orientated parallel to the flow direction.

(3) The presence of crystals modifies the velocity profile from a typical parabolic shape (Poiseuille flow) to a Bingham-type shape. Thus, despite the usage of a linear rheology, the presence of rigid crystals introduces an effective bulk non-Newtonian behaviour.

(4) The segregation of granitic melt from an ascending crystal-rich magma is physically possible for the classical values of viscosity (10^4 Pa.s) and density of granitic material (2400 and 2700 kg.m^{-3} for the melt and the crystals, respectively).

The numerical modelling technique developed here can be readily applied to many different types of crystal-melt studies. In particular, it would be straightforward to apply this type of model to evaluate the effective viscosity of magmas with different types of crystalline loads (various crystal sizes and shapes), and to examine the influence of dyke morphology in conjunction with various crystal sizes.

Acknowledgments

We first thank F.O. Marques and the GeoMod2010 team for the workshop organisation where multiple discussions and debates have initiated this work. Discussions with B. Kaus and M. Dabrowski were greatly appreciated. A special "спасибо" is addressed to T. Gerya for his constant support and enthusiasm during coding using the M-I-C method. Multiple stimulating discussions with E. Hallot, K. Gallagher, P. Boulvais, M. Poujol, W. Husson and B. Cordonnier were also appreciated. Finally, we also thank D. Schmid and an anonymous reviewer for their constructive reviews that have substantially improved the manuscript. Author DAM was financially supported by the ETH Zurich Postdoctoral Fellowship Program. High-resolution simulations were performed on the ETH brutus cluster. Author TD was supported by the SNF-EU research grant 20TO21-120535 (TOPO-4D).

Appendix A. Maximum velocity in dyke and driving pressure gradient calculation

The advantage of our setup is that it provides a way to control the effective pressure gradient (and thus, the maximum vertical velocity) in the dyke via the imposed velocity of the lateral blocks (see Fig. 5). In the case of a pure melt dyke (see Fig. A1), we can derive an expression which relates the applied velocity of the rigid blocks Vz_{block}, to the driving pressure gradient P_{driv}:

Over one time step (dt), the area of the block buried in the fluid (A_{block}) is:

$$A_{block} = W_b \cdot Vz_{block} \cdot dt, \tag{A.1}$$

where W_b and Vz_{block} correspond, respectively, to the width of the rigid block and to the imposed velocity (Fig. A1). In the same time, melt is expulsed in the dyke following a quadratic Poiseuille flow. In 2D, the amount of melt expulsed corresponds to the area located below the parabola describing this flow (A_{parab}, see Fig. A1). The area under the parabola (A_{parab}) is given by

$$A_{parab} = \frac{2}{3} \cdot W_d \cdot Vz_{max} \cdot dt, \tag{A.2}$$

where W_d and Vz_{max} are, respectively, the width of the dyke and the maximum vertical velocity of the Poiseuille flow (Fig. A1). Since the fluid we consider is incompressible, mass flow across horizontal interfaces defining the bottom of the blocks must be conserved. That is, we require that

$$2A_{block} = A_{parab}, \tag{A.3}$$

noting that the factor two comes from the fact that we have a block on each side of the dyke. In this study, the rigid block width (W_b) is always two times thinner than the dyke width (W_d), i.e. $W_d = 2\,W_b$. Equating Eqs. (A.1) and (A.2) and using the mass conservation condition in Eq. (A.3), we obtain the following expression for the maximum vertical velocity of the flow (Vz_{max}) as a function of the velocity imposed to each rigid block (Vz_{block}):

$$Vz_{max} = 3 \cdot Vz_{block}, \tag{A.4}$$

The vertical velocity profile equation in a Poiseuille flow is given by:

$$Vz(x) = -\frac{1}{2\eta_m}\left(\rho_m g + \frac{dP}{dz}\right)\left(xW_d - x^2\right), \tag{A.5}$$

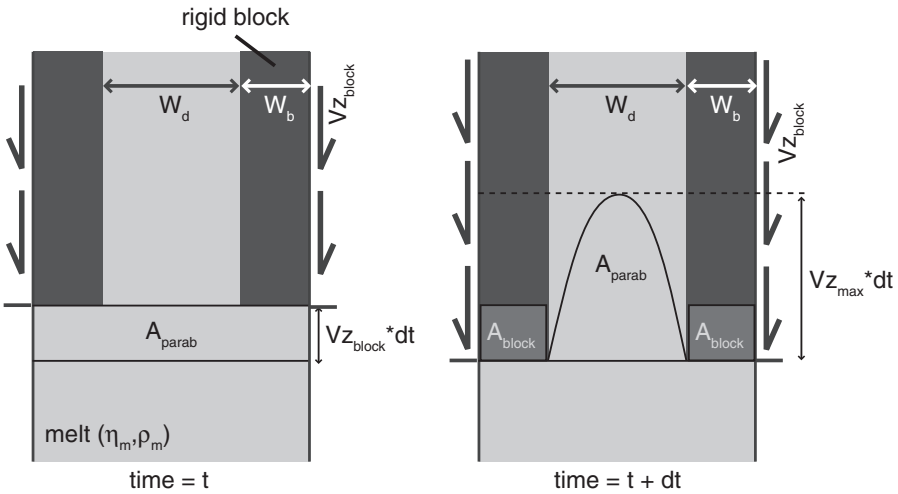

Fig. A1. Schematic evolution of a model constituted by pure melt with a viscosity η_m and a density ρ_m between the time t (left) and the time $t+dt$ (right). The imposed velocity (Vz_{block}) is applied at the edges of the rigid blocks as described in our model setup. Since the volumes are conserved and considering a dyke width (W_d) two times larger than a rigid body width (W_b), the amount of melt entering in the dyke (A_{parab}) corresponds to four times the amount of rigid block buried in depth (A_{block}).

where η_m, ρ_m, g and $\frac{dP}{dz}$ are the viscosity of the melt, the density of the melt, the gravitational acceleration and the total pressure gradient through the dyke.

Using Eq. (A.5), in the middle of the dyke (i.e., at $x = 0.5\ W_d$), where the vertical velocity is maximum (Vz_{max}), we can write:

$$Vz_{max} = -\frac{1}{8\eta_m} \cdot P_{driv} \cdot W_d^2, \tag{A.6}$$

where P_{driv} corresponds to the driving pressure gradient resulting from both the melt weight and the pressure gradient induced by the rigid lateral blocks such as:

$$P_{driv} = \rho_m g + \frac{dP}{dz}, \tag{A.7}$$

The driving pressure gradient can thus be expressed in function of the imposed velocity on the rigid block combining the Eqs. (A.4) and (A.6):

$$P_{driv} = -\frac{24 \cdot \eta_m \cdot Vz_{block}}{W_d^2}, \tag{A.8}$$

In addition, these values of Vz_{max} and P_{driv} have also been calculated numerically in our simulations and give the same results.

References

Arbaret, L., Diot, H., Bouchez, J.L., 1996. Shape fabrics of particles in low concentration suspensions: 2D analogue experiments and application to tiling in magma. J. Struct. Geol. 18, 941–950.

Arbaret, L., Mancktelow, N.S., Burg, J.P., 2001. Effect of shape and orientation on rigid particle rotation and matrix deformation in simple shear flow. J. Struct. Geol. 23, 113–125.

Bagdassarov, N., Dorfman, A., 1998. Granite rheology: magma flow and melt migration. J. Geol. Soc. 155, 863–872.

Bagnold, R.A., 1954. Experiments on a gravity-free dispersion of large solid spheres in a Newtonian fluid under shear. R. Soc. Lond. Proc. 225, 49–63.

Barrière, M., 1976. Flowage differentiation: limitation of the "Bagnold effect" to the narrow intrusions. Contrib. Mineral. Petrol. 55, 139–145.

Bhattacharji, S., 1967. Mechanics of flow differentiation in ultramafic and mafic sills. J. Geol. 75, 101–111.

Bons, P.D., Barr, T.D., ten Brink, C.E., 1996. The development of δ-clasts in non-linear viscous materials: a numerical approach. Tectonophysics 270, 29–41.

Caricchi, L., Burlini, L., Ulmer, P., Gerya, T., Vassalli, M., Papale, P., 2007. Non-Newtonian rheology of crystal-bearing magmas and implications for magma ascent dynamics. Earth Planet. Sci. Lett. 264, 402–419.

Champallier, R., Bystricky, M., Arbaret, L., 2008. Experimental investigation of magma rheology at 300 MPa: from pure hydrous melt to 76 vol.% of crystals. Earth Planet. Sci. Lett. 267, 571–583.

Chistyakova, S., Latypov, R., 2010. On the development of internal chemical zonations in small mafic dykes. Geol. Mag. 147, 1–12.

Clemens, J.D., 1998. Observations on the origins and ascent mechanisms of granitic magmas. J. Geol. Soc. 155, 843–851.

Clemens, J.D., 2003. S-type granitic magmas-petrogenetic issues, models and evidence. Earth Sci. Rev. 61, 1–18.

Clemens, J.D., Mawer, C.K., 1992. Granitic magma transport by fracture propagation. Tectonophysics 204, 339–360.

Clemens, J.D., Petford, N., 1999. Granitic melt viscosity and silicic magma dynamics in contrasting tectonic settings. J. Geol. Soc. 156, 1057–1060.

Costa, A., Melnik, O., Sparks, R.S.J., Voight, B., 2007. Control of magma flow in dykes on cyclic lava dome extrusion. Geophys. Res. Lett. 34, L02303.

Deubelbeiss, Y., Kaus, B.J.P., 2008. Comparison of Eulerian and Lagrangian numerical techniques for the Stokes equations in the presence of strongly varying viscosity. Phys. Earth Planet. Inter. 171, 92–111.

Deubelbeiss, Y., Kaus, B.J.P., Connolly, J.A.D., 2010. Direct numerical simulation of two-phase flow: effective rheology and flow patterns of particle suspensions. Earth Planet. Sci. Lett. 290, 1–12.

Dingwell, D.B., 1996. Volcanic dilemma: flow or blow? Science 273, 1054–1055.

Einstein, A., 1906. Eine neue Bestimmung der Moleküldimensionen. Ann. Phys. 19, 289–306.

Feng, J., Joseph, D.D., 1995. The unsteady motion of solid bodies in creeping flows. J. Fluid Mech. 303, 83–102.

Geoffroy, L., Callot, J.P., Aubourg, C., Moreira, M., 2002. Magnetic and plagioclase linear fabric discrepancy in dykes: a new way to define the flow vector using magnetic foliation. Terra Nova 14, 183–190.

Gerya, T.V., Yuen, D., 2003. Characteristics-based marker-in-cell method with conservative finite-differences schemes for modeling geological flows with strongly variable transport properties. Phys. Earth Planet. Inter. 140, 293–318.

Gerya, T.V., Yuen, D., 2007. Robust characteristics method for modelling multiphase visco-elasto-plastic thermo-mechanical problems. Phys. Earth Planet. Inter. 163, 83–105.

Ghosh, S.K., Ramberg, H., 1976. Reorientation of inclusions by combination of pure shear and simple shear. Tectonophysics 34, 1–70.

Hallot, E., Davy, P., de Bremond d'Ars, J., Auvray, B., Martin, H., Van Damme, H., 1996. Non-Newtonian effects during injection in partially crystallised magmas. J. Volcanol. Geotherm. Res. 71, 31–44.

Ildefonse, B., Launeau, P., Bouchez, J.L., Fernandez, A., 1992. Effect of mechanical interactions on the development of shape preferred orientation: a two-dimensional experimental approach. J. Struct. Geol. 14, 73–83.

Jeffery, G., 1922. The motion of ellipsoidal particles immersed in a viscous fluid. Proc. R. Soc. Lond. A102, 201–211.

Kerr, R.C., Lister, J.R., 1991. The effects of shape on crystal settling and on the rheology of magmas. J. Geol. 99, 457–467.

Knight, M.D., Walker, G.P.L., 1988. Magma flow direction in dykes of the Koolau complex, Oahu, determined from magnetic fabric studies. J. Geophys. Res. 93, 4301–4319.

Komar, P.D., 1972a. Mechanical interactions of phenocrysts and flow differentiation of igneous dykes and sills. Geol. Soc. Am. Bull. 83, 973–988.

Komar, P.D., 1972b. Flow differentiation in igneous dikes and sills: profiles of velocity and phenocryst concentration. Geol. Soc. Am. Bull. 83, 3443–3448.

Mandal, N., Samanta, S.K., Chakraborty, C., 2001. Numerical modeling of heterogeneous flow fields around rigid objects with special reference to particle paths, strain shadows and foliation drag. Tectonophysics 330, 177–194.

Marques, F.O., Burlini, L., 2008. Rigid inclusions rotate in geologic materials as shown by torsion experiments. J. Struct. Geol. 30, 1368–1371.

Marques, F.O., Coelho, S., 2001. Rotation of rigid elliptical cylinders in viscous simple shear flow: analogue experiments. J. Struct. Geol. 23, 609–617.

Marques, F.O., Coelho, S., 2003. 2-D shape preferred orientations of rigid particles in transtensional viscous flow. J. Struct. Geol. 25, 841–854.

Marques, F.O., Taborda, R., Antunes, J., 2005a. Influence of a low-viscosity layer between rigid inclusion and viscous matrix on inclusion rotation and matrix flow: a numerical study. Tectonophysics 407, 101–115.

Marques, F.O., Taborda, R.M., Antunes, J.V., 2005b. 2D rotation of rigid inclusions in confined bulk simple shear flow: a numerical study. J. Struct. Geol. 27, 2171–2180.

Melnik, O., Sparks, R.S.J., 1999. Nonlinear dynamics of lava dome extrusion. Nature 402, 37–41.

Nkono, C., Féménias, O., Diot, H., Berza, T., Demaiffe, D., 2006. Flowage differentiation in an andesitic dyke of the Motru Dyke Swarm (Southern Carpathians, Romania) inferred from AMS, CSD and geochemistry. J. Volcanol. Geoth. Res. 154, 201–221.

Papale, P., 1999. Strain-induced magma fragmentation in explosive eruptions. Nature 397, 425–428.

Paterson, S.R., 2009. Magmatic tubes, pipes, troughs, diapirs, and plumes: late-stage convective instabilities resulting in compositional diversity and permeable networks in crystal-rich magmas of the Tuolumne batholith, Sierra Nevada, California. Geosphere 5, 496–527.

Petford, N., 2003. Rheology of granitic magma during ascent and emplacement. Annu. Rev. Earth Planet. Sci. 31, 399–427.

Petford, N., Koenders, M.A., 1998. Granular flow and viscous fluctuations in low Bagnold number granitic magmas. J. Geol. Soc. 155, 873–881.

Petford, N., Lister, J.R., Kerr, R.C., 1994. The ascent of felsic magmas in dykes. Lithos 32, 161–168.

Philpotts, A.R., Shi, J., Brustman, C., 1998. Role of plagioclase crystal chains in the differentiation of partly crystallized basaltic magma. Nature 395, 343–346.

Roscoe, R., 1953. Suspensions. In: Hermans, J.J. (Ed.), Flow Properties of Disperse Systems. North Holland, Amsterdam, pp. 1–38.

Samanta, S.K., Mandal, N., Chakraborty, C., 2002. Development of structures under the influence of heterogeneous flow field around rigid inclusions; insights from theoretical and numerical models. Earth Sci. Rev. 58, 85–119.

Scaillet, B., Holtz, F., Pichavant, M., 1998. Phase equilibrium constraints on the viscosity of silicic magmas. 1. Volcanic–plutonic comparison. J. Geophys. Res. 103, 27257–27266.

Schmid, D.W., 2005. Rigid polygons in shear. In: Bruhn, D., Burlini, L. (Eds.), High strain zones: structure and physical properties: Geol. Soc. London Spec. Pub., 245, pp. 421–431.

Schmid, D.W., Podladchikov, Y.Y., 2003. Analytical solutions for deformable elliptical inclusions in general shear. Geophys. J. Int. 155, 269–288.

Smith, J.V., 2002. Structural analysis of f low-related textures in lavas. Earth Sci. Rev. 57, 279–297.

Sugihara-Seki, M., 1993. The motion of an elliptical cylinder in channel flow at low Reynolds numbers. J. Fluid Mech. 257, 575–596.

Taisne, B., Jaupart, C., 2011. Magma expansion and fragmentation in a propagating dyke. Earth Planet. Sci. Lett. 301, 146–152.

Tartèse, R., Boulvais, P., 2010. Differentiation of peraluminous granites "en route" to the surface. Lithos 114, 353–358.

Van den Driessche, J., Brun, J.P., 1987. Rolling structures at large shear strain. J. Struct. Geol. 9, 691–704.

Varga, R.J., Gee, J.S., Staudigel, H., Tauxe, L., 1998. Dykes surface lineation as magma flow indicators within the sheeted dyke complex of the Troodos ophiolite, Cyprus. J. Geophys. Res. 103, 5241–5256.

Vernon, R.H., Paterson, S.R., 2008a. How late are K-feldspar megacrysts in granites? Lithos 104, 327–336.
Vernon, R.H., Paterson, S.R., 2008b. How extensive are subsolidus grain-shape changes in cooling granites? Lithos 105, 85–97.
Vigneresse, J.L., Barbey, P., Cuney, M., 1996. Rheological transitions during partial melting and crystallisation with application to felsic magma segregation and transfer. J. Petrol. 37, 1579–1600.
Walsh, S.D.C., Saar, M.O., 2008. Numerical models of stiffness and yield stress growth in crystal-melt suspensions. Earth Planet. Sci. Lett. 267, 32–44.
Willis, D.G., 1977. A kinematic model of preferred orientation. Geol. Soc. Am. Bull. 88, 883–894.
Wilson, L., Head, J.W., 1988. Nature of magma storage zones and geometry of conduit systems below basaltic eruption sites: Pu'u 'O'o, Kilauea East Rift, Hawaii example. J. Geophys. Res. 93 (B12), 14785–14792.

Tectonophysics 611 (2014) 204

Contents lists available at ScienceDirect

Tectonophysics

journal homepage: www.elsevier.com/locate/tecto

Corrigendum

Corrigendum to "Numerical modelling of magma transport in dykes" [Tectonophysics 526–529 (2012) 97–109]

P. Yamato [a,b,*], R. Tartèse [a], T. Duretz [b], D.A. May [b]

[a] Géosciences Rennes, CNRS UMR 6118, Université de Rennes 1, 35042 Rennes Cedex, France
[b] Institute of Geophysics, Department of Earth Science, ETH-Zurich, Sonneggstrasse 5, CH-8092 Zurich, Switzerland

The results presented in Figure 9 were obtained using an imposed block velocity (Vz_{block}) and the corresponding pressure gradients (P_{driv}) assuming an incorrect dyke thickness (W_d) of 1 m, instead of the correct value of $W_d = 0.5$ m. According to Equation 9, for a given Vz_{block}, the value of P_{driv} should be 4 times lower in a 1 m dyke than in a 0.5 m dyke. Hence, in order to correctly scale the results (i.e., to obtain the same behaviour in 0.5 m dyke than in a 1 m dyke), the time scales shown in Figure 9 need to be increased by a factor 4 and values of P_{driv} reported need to be decreased by a factor 4.

As an example, the corrected Figure 9 for *Intermediate Vz* experiment thus becomes:

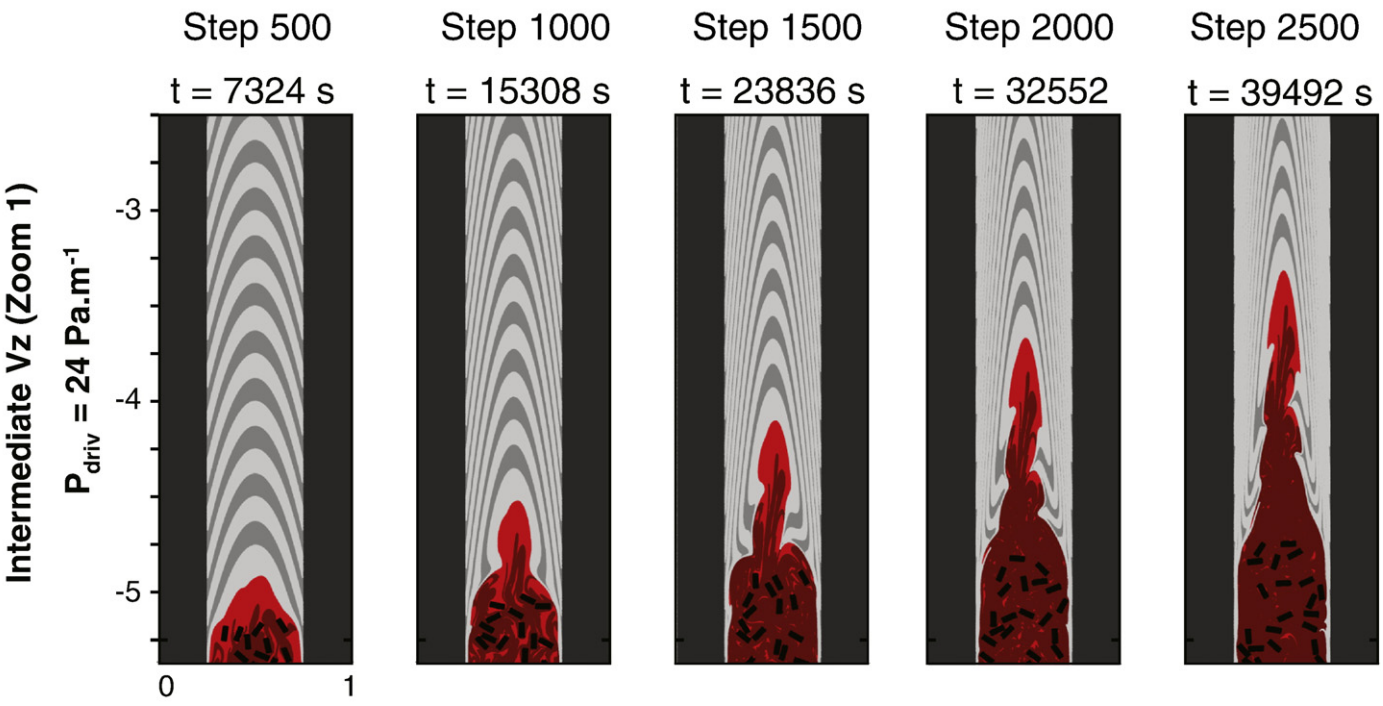

The authors apologise for this mistake, which nevertheless, do not affect the general conclusions of this paper.

DOI of original article: http://dx.doi.org/10.1016/j.tecto.2011.05.015.
* Corresponding author: Géosciences Rennes, CNRS UMR 6118, Université de Rennes 1, 35042 Rennes Cedex, France. Tel.: +33 2 23 23 60 95.
E-mail address: philippe.yamato@univ-rennes1.fr (P. Yamato).

http://dx.doi.org/10.1016/j.tecto.2013.11.031

Eclogite breccias in a subducted ophiolite: A record of intermediate-depth earthquakes?

S. Angiboust[1]*, P. Agard[1], P. Yamato[2], and H. Raimbourg[3]
[1]ISTEP, UMR CNRS 7193, UPMC Sorbonne Universités, F-75005 Paris, France
[2]Geosciences Rennes, Université Rennes1, F-35 042 Rennes, France
[3]ISTO, Université d'Orléans, F-45071 Orléans, France

ABSTRACT

Understanding processes acting along the subduction interface is crucial to assess lithospheric-scale coupling between tectonic plates and mechanisms causing intermediate-depth seismicity. Despite a wealth of geophysical studies aimed at better characterizing the subduction interface, we still lack critical data constraining processes responsible for seismicity within oceanic subduction zones. We herein report the finding of eclogite breccias, formed at ~80 km depth during subduction, in an almost intact 10-km-scale fragment of exhumed oceanic lithosphere (Monviso ophiolite, Western Alps). These eclogite breccias correspond to meter-sized blocks made of 1–10 cm fragments of eclogite mylonite cemented by interclast omphacite, lawsonite, and garnet, and were later embedded in serpentinite in a 30–150-m-wide eclogite facies shear zone. At the mineral scale, omphacite crack-seal veins and garnet zoning patterns also show evidence for polyphased fracturing-healing events. Our observations suggest that a possible seismic brecciation occurred in the middle part of the oceanic crust, accompanied by the input of externally derived fluids. We also conclude that these eclogite breccias likely mark the locus of an ancient fault zone associated with intraslab, intermediate-depth earthquakes at ~80 km depth.

INTRODUCTION

Most intermediate-depth (70–300 km) earthquakes worldwide concentrate in subduction zones along 2 or 3 distinct seismic layers separated vertically by a 10–40-km-thick weakly seismic core (Yamasaki and Seno, 2003; Fig. 1A). Accurate relative relocations (Rietbrock and Waldhauser, 2004) suggest that the upper seismic layer may correlate with the top, crustal part of the slab, where massive dehydration of minerals formed by seawater alteration takes place through metamorphic reactions (Green and Houston, 1995; Hacker et al., 2003), whereas the lower layer may correspond to the top, most hydrated part of the slab mantle (Yamasaki and Seno, 2003). Eclogitization of the basaltic crust (i.e., crystallization of garnet and omphacite) is known to dramatically affect the structure, density, mineralogy, fluid content, and stress state of the downgoing slab sinking into the Earth mantle (e.g., Rondenay et al., 2008).

The exact location (absolute depths are known within 3–5 km only; Rietbrock and Waldhauser, 2004) and mechanical process at the origin of this seismicity (e.g., hydraulic fracturing or dehydration embrittlement; Davies, 1999; Hacker et al., 2003) are still debated (Kuge et al., 2010). In addition, few studies have documented the brittle behavior of eclogitized oceanic crust in exhumed ophiolitic belts (e.g., Philippot and van Roermund, 1992; John and Schenk, 2006; Healy et al., 2009). We herein present a fossil example of oceanic crust brecciation under eclogite facies conditions from the Lago Superiore Unit of the Monviso ophiolite (Western Alps; Fig. 1B; Agard et al., 2009), that attests to brittle behavior of oceanic crust at intermediate depths.

GEOLOGICAL SETTING

This several-kilometer-long, almost intact section (Fig. 1C) of the Tethyan ocean reached lawsonite-eclogite facies conditions at ~80 km depth between 50 and 40 Ma (Angiboust et al., 2012). The Lago Superiore Unit is crosscut by two major (kilometer scale) eclogite facies shear zones, located at the boundaries between basalts and gabbros and between gabbros and serpentinites (intermediate and lower shear zones; ISZ

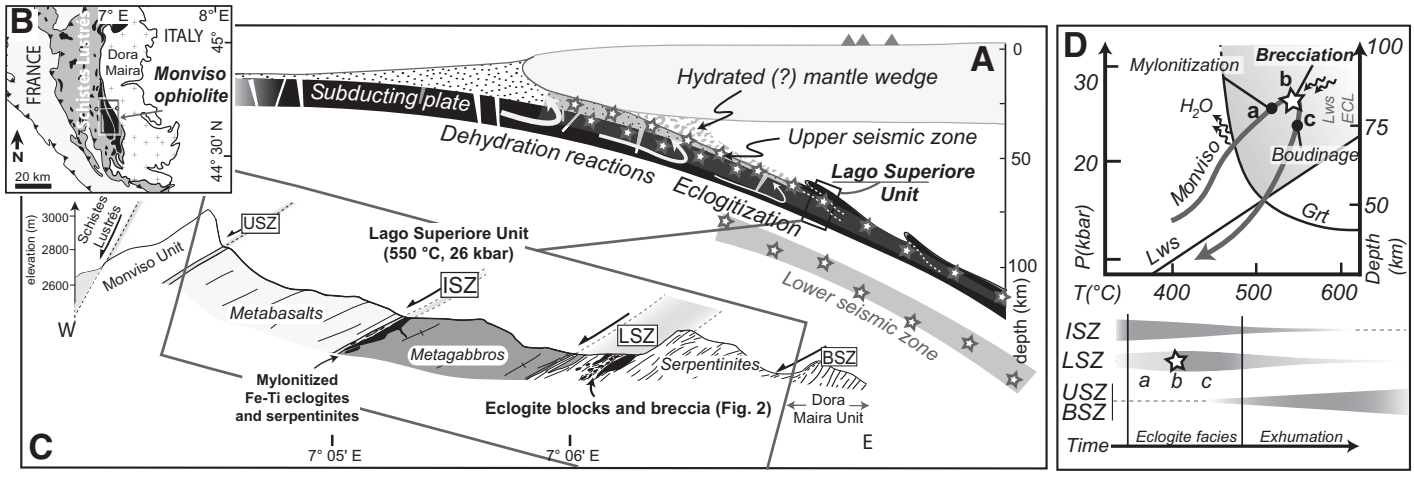

Figure 1. A: Schematic view of subduction zone featuring double seismic zone (after Hacker et al., 2003) and showing slicing of Lago Superiore Unit at ~80 km depth. B: Location of Monviso ophiolite within western Alpine belt. C: Section across LSU showing four main shear zones: upper (USZ), intermediate (ISZ), lower (LSZ), and basal (BSZ). D: Pressure-temperature (*P-T*) path of LSU and relative timing of shear zone activity (mapping and thermobarometric data from Angiboust et al., 2011, 2012, respectively). Lws—lawsonite; Grt—garnet; Lws-ECL—lawsonite-eclogite facies.

*E-mail: samuel.angiboust@upmc.fr.

and LSZ in Fig. 1C; Angiboust et al., 2011). Mylonitic eclogite facies Fe-Ti metagabbros, which cap the top of the thick Mg-Al metagabbroic body along the ISZ (Fig. 1C), host omphacite-filled crack-seal veins previously interpreted as dehydration reaction products of the downgoing crust (Philippot and van Roermund, 1992). Similar eclogitized Fe-Ti metagabbros are found in the LSZ (Fig. 1C); they were torn off the ISZ by intense subduction-parallel shearing, and later embedded within serpentinite in the LSZ. Fe-Ti metagabbros from both the ISZ and LSZ fossilize deformation events that took place near peak burial of the Lago Superiore Unit, in a narrow pressure-temperature (*P-T*) range within the lawsonite-eclogite facies (i.e., 500–550 °C and 22–26 kbar; Fig. 1D). Over this range of *P-T* conditions, estimated internal fluid release amounts to ~1 wt% in the upper mafic crust (with glaucophane-lawsonite-chlorite proportions shifting from 9, 11, and 5 wt% to 3, 8, and 0 wt%, respectively; Angiboust et al., 2012).

ECLOGITIC BRECCIAS AND OTHER EVIDENCE OF BRITTLE FAILURE

A specificity of the LSZ is the existence of eclogite blocks (cropping out >10 km along strike) consisting of rounded meter- to decameter-sized pods of highly strained Fe-Ti metagabbros embedded within a strongly foliated serpentinite and talc schist matrix. Blocks are for the most part spectacularly fresh eclogitic breccias (Figs. 2A and 2B) made of coalesced fragments of mylonitic eclogite with discordant foliation and sharp edges, showing variable disruption (further mesoscopic and microscopic breccia images are shown in Fig. DR1 in the GSA Data Repository[1]). To our knowledge, this is the first report of such eclogitic breccias. Most fragments within the eclogite breccia are between 1 and 10 cm in length (see clast size distribution in Fig. DR2) and exhibit a marked mylonitic foliation identical to the fabric reported along the ISZ (Lago Superiore area; Philippot and van Roermund, 1992). In the rare outcrops where post-breccia deformation was limited, the breccia clasts are chaotically oriented (Woodcock and Mort, 2008) and the corresponding texture is among the "wear abrasion" and/or "fluid-assisted brecciation" types defined by Jébrak (1997, p. 115; see the Data Repository for further discussion). Note that many of these clasts were disseminated in the block vicinity within the weak serpentinite-rich matrix.

The matrix cementing the mylonitic clasts is composed of as much as 30 vol% lawsonite (now pseudomorphed by epidote), omphacite, and garnet (100–1000 µm diameter; Fig. DR1F). Garnet from the interclast matrix is generally weakly zoned, in contrast to garnet derived from the mylonitic clasts, which preserves prograde zoning, and systematically exhibits a marked increase in Mg content rimward (Fig. DR3).

Most blocks also exhibit fractures dominantly filled by omphacite and lawsonite pseudomorphs (Fig. DR1C). These water-rich recrystallized domains (>2–3 wt% H_2O, as opposed to Fe-Ti metagabbro mylonites containing <1 wt% H_2O after eclogitization; Spandler et al., 2011) point to a significant fluid input during brecciation. No such eclogitic breccias were found in the ISZ. On the contrary, omphacite-filled crack-seal veins reported in the ISZ (Philippot and van Roermund, 1992) are also found in the LSZ as folded veins intermingled with eclogite mylonite clasts on the block surface (Fig. DR1C).

Fracturing processes are also observable at the mineral scale, where several brittle events are fossilized in an interclast eclogite sample (Figs. 2C and 2D) exhibiting a first garnet generation (garnet I, Fig. 2E) fractured and healed by a Mn-enriched garnet overgrowth. A second fracturing episode is attested to by the presence of a complex fracture pattern cemented by Mg-enriched composition (garnet II, Fig. 2E). The final, outer garnet rim is devoid of fractures and fossilizes these two successive fracturing events (Fig. 2E). These fractures healed rapidly before the next deformation increment (as indicated by the preservation of the pre-fracturing garnet geometry), suggesting a post-fracturing stress drop, as for seismic cycle patterns (Sibson,

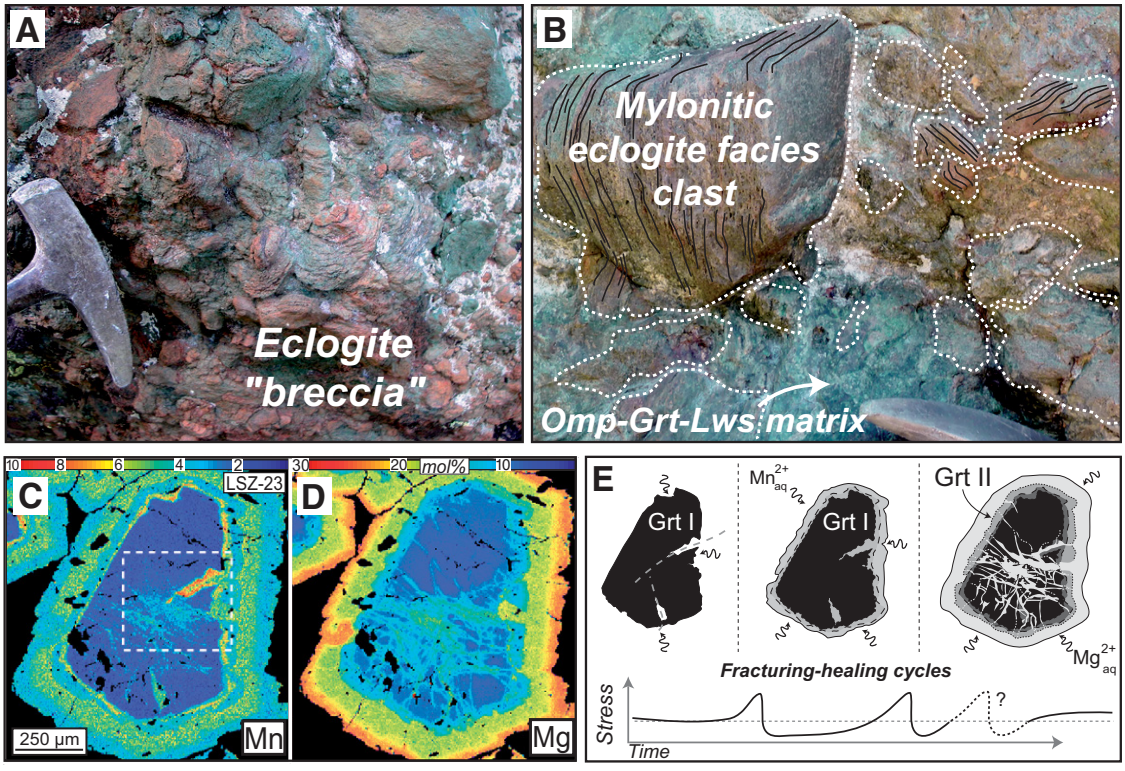

Figure 2. Multiscale fracturing recorded by eclogite breccias. A: Eclogite breccia from lower shear zone (LSZ). Hammer head is 18 cm. B: Centimeter-sized mylonitic clasts cemented by lawsonite (Lws) eclogite facies paragenesis. Omp—omphacite; Grt—garnet. C, D: Mn and Mg content (mol%) X-ray chemical maps of garnet from LSZ eclogite showing several healed fossilized fracture networks. E: Interpretative sketch of same garnet showing presence of two main garnet generations: first one exhibits Mn-rich oscillatory patterns, and second is characterized by Mg-rich overgrowth sealing fractures. Successive fracturing events are tentatively related to seismic cycle (see text for details).

[1]GSA Data Repository item 2012197, Figure DR1 (additional eclogite breccia pictures), Figure DR2 (clast size distribution histogram), and Figure DR3 (additional petrological and *P-T* constrains on eclogite breccia formation), is available online at www.geosociety.org/pubs/ft2012.htm, or on request from editing@geosociety.org or Documents Secretary, GSA, P.O. Box 9140, Boulder, CO 80301, USA.

1986). The latest garnet overgrowth (in the outermost rim; Figs. 2D and 2E), which shows the same Mg-buffered composition in all LSZ Fe-Ti metagabbros, points to element transfer from externally (serpentinite) derived fluids (Angiboust et al., 2011).

INTERPRETATION

Structural, chemical (such as chemically buffered interclast garnet composition; Fig. DR3), and thermobarometric results strongly suggest that the three successive deformation increments observed occurred in a narrow *P-T* range, between 70 and 80 km depth (Figs. 1D and 3; Angiboust et al., 2012; see the Data Repository).

Crack-seal vein formation accompanying mylonitization first occurred along the ISZ (Fig. 3A; Philippot and van Roermund, 1992). A later, larger-scale fracturing episode (Fig. 3B) led to the formation of eclogite breccias in the LSZ and to the rotation of the 1–10 cm mylonite clasts (Figs. 2A, 2B, and 3B) in the presence of externally derived fluids. This brecciation may have reactivated the rheologically weaker tensile omphacite-bearing veins (Fig. 3A, inset; Zhang and Green, 2007). After brecciation, ongoing deformation within the eclogite breccia was only limited, as evidenced by the sharp edges of mylonite fragments (Fig. 3B; Fig. DR1) and by the absence of mylonitization of the interclast material. By contrast, eclogite facies ductile deformation continued around the eclogite breccia (Fig. 3C), suggesting that brittle deformation was short lived and rapidly sealed (i.e., frozen in and taken over) by ductile deformation around the blocks. Subsequent shearing and migration along the LSZ led to significant block rotation and minor disaggregation within serpentinite by a ball bearing mechanism, and to an overall rheological weakening of the LSZ. Embedding within serpentinite also prevented the eclogite breccias from pervasive retrogression and allowed for their preservation.

These observations lead us to infer important consequences.

1. This short-lived mesoscopic eclogite facies brecciation, as well as microscopic fracturing, was likely seismic and could correspond to a relict damage zone (as shown by fragmented and rotated clasts preserving an inherited structural fabric, and by pulverization as seen from relict garnet cores; see McGrath and Davison, 1995; Doan and Gary, 2009). These breccias probably formed within a few meters of the fault core, at the most, as indicated by the linear density of macrofractures (~100/m, as inferred from averaged field estimates; Mitchell and Faulkner, 2009). The fault core has not been observed in the field (or pseudotachylites, which preferentially form in water-poor protoliths; Andersen and Austrheim, 2006), but it could have recrystallized under eclogite facies conditions or been overprinted by later ductile deformation.

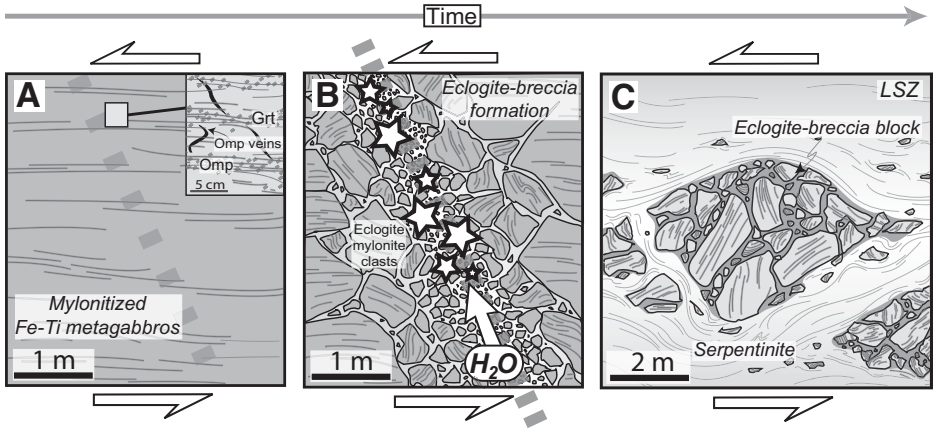

Figure 3. Eclogite breccia-forming evolution. A: Top of gabbroic layer (Fig. 1C), lined up with Fe-Ti metagabbros, underwent pervasive eclogite facies mylonitization leading to marked grain size reduction and segregation of garnet (Grt) and omphacite (Omp) beds. Note omphacite veins cutting across mylonitic fabric (inset). Gray dotted line represents inferred inherited structural weakness. B: Intermediate-depth intraslab earthquake (star) produces faulting of Fe-Ti metagabbro mylonites, rotation of mylonitic fabrics, and infiltration of external H_2O-rich fluids (white arrow). C: Present-day occurrence of preserved lower shear zone (LSZ) eclogite breccia showing serpentinite foliation deflected around block.

2. Fluids played a key role, as shown by the abundance of lawsonite, chemical trends in garnet, and the fact that fractures must have been rapidly healed by efficient, fluid-mediated element transfer. This is further supported by the lack of any such brecciation in the ISZ, where fluid ingression was much more limited (Angiboust et al., 2011; Spandler et al., 2011).

3. Brittle deformation leading to eclogite brecciation is found only in the LSZ and in resistant lithologies (Fe-Ti metagabbros) formerly located within the oceanic crustal section along the ISZ. Brecciation thus necessarily took place at the junction of the LSZ and ISZ (Fig. 4A), which we infer to be the locus of the relict damage zone. We propose that an intermediate-depth earthquake fractured a large part of the crust, cutting through the Mg-Al gabbros and the ISZ Fe-Ti gabbros (Fig. 4A); further fluid ingression and subsequent rheological weakening localized deformation along this fault plane, which became the LSZ (and along which eclogite breccias were dispersed by later deformation; Figs. 3C and 4B).

IMPLICATIONS

Our data provide a refined view, at the meter to kilometer scale, of possibly earthquake-related deformation processes in a subducting slab and the coexistence of viscous and frictional mechanisms at these depths (see also Handy et al., 2007). These processes can be set back precisely

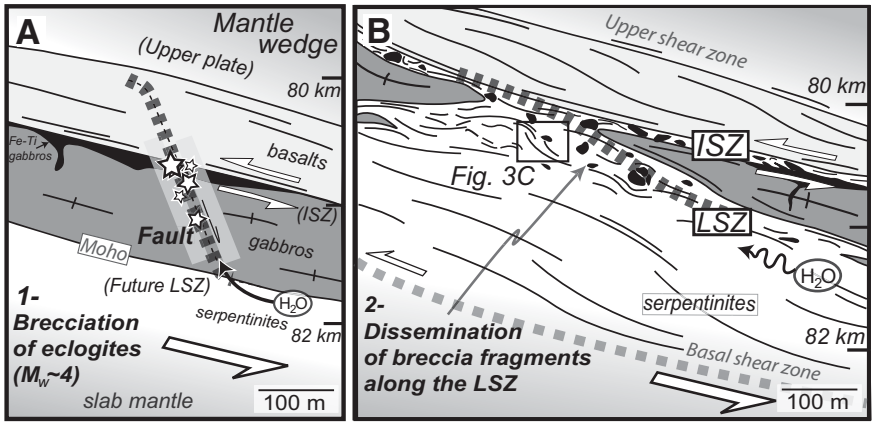

Figure 4. Tectonic scenario for formation and dissemination of eclogite breccias along lower shear zone (LSZ). A: Faulting (possibly reactivating inherited fault) allowed formation of eclogite facies breccias, infiltration of external fluids, and connection of intermediate shear zone (ISZ) and LSZ. Stars represent intermediate-depth intraslab seismicity, causing seismic events to M_w = 4. B: Ongoing shearing along eclogite facies shear zones and injection of serpentinite along fault breccia account for dissemination of breccia fragments along LSZ. Jump of deformation along basal shear zone permitted preservation of complete upper lithospheric section.

within the oceanic crust of the slab (Fig. 4A) and correspond to: (1) short-lived, most likely seismic, mesoscopic brecciation of eclogites along the LSZ accompanied by significant fluid input from the hydrated slab mantle beneath (i.e., from antigorite breakdown at ~90–100 km; van Keken et al., 2011), and (2) deformation through shearing in the ISZ before (and possibly after) brecciation with evidence of brittle failure at the mineral scale (garnet fractures and crack-seal veins), but only limited fluid input.

The former type can be related to the largest magnitude intermediate-depth earthquakes observed in active subduction zones (i.e., relatively few earthquakes with steep fault plane solutions and Mw ~ 3–4.5; e.g., Cassidy and Waldhauser, 2003), which were interpreted as fault planes cutting across the entire crust. Magnitudes recorded for these largest intermediate-depth earthquakes match displacements required to produce the eclogitic breccia (Mw ~ 3.5–4.5, considering several centimeter-scale displacements along a kilometer-scale fault zone). Although this shear zone has an overall reverse offset at present, we cannot determine whether initial faulting was normal or reverse (Rietbrock and Waldhauser, 2004; Igarashi et al., 2001, respectively), or whether faulting may have reworked inherited structures (Ranero et al., 2003). By contrast, the second type of process (shearing and microcracks along the ISZ, probably too small to be detected seismically) could correspond to minor deformation accompanying the somewhat smaller, yet more frequent, dominantly along-plane microseismicity reported for the upper seismic layer (i.e., Mw < 2.5; Rietbrock and Waldhauser, 2004).

We herein document the complex interplay between ductile shearing, brittle failure, and fluid ingression accompanying intermediate-depth intraslab seismicity (Figs. 3 and 4). Most authors envision brittle failure at depth as triggered by in situ fluid release and dehydration embrittlement (Hacker et al., 2003) or by hydrofracturing (Davies, 1999). In principle, crustal dehydration embrittlement could explain the crack-seal veins of the ISZ. It cannot account for eclogitic brecciation, however, as shown by (1) the very low H_2O content of the Fe-Ti metagabbros at such depths (<0.5 wt%), which precludes a massive release of in situ fluids, and (2) the clear evidence for externally derived fluids (Spandler et al., 2011). From field evidence, we thus conclude that crustal dehydration embrittlement is insufficient to break the entire crust and suggest, instead, that a large faulting event (and possibly coeval hydrofracturing by fluids released by antigorite breakdown occurring ~10 km deeper) is a more likely mechanism.

ACKNOWLEDGMENTS

We thank S. Guillot, L. Labrousse, and A. Schubnel for insightful discussions, assistance, and/or comments on the ideas. We benefited from the thoughtful comments from J.G. Barreiro, C. Balica, and an anonymous reviewer.

REFERENCES CITED

Agard, P., Yamato, P., Jolivet, L., and Burov, E., 2009, Exhumation of oceanic blueschists and eclogites in subduction zones: Timing and mechanisms: Earth-Science Reviews, v. 92, p. 53–79, doi:10.1016/j.earscirev.2008.11.002.

Andersen, T.B., and Austrheim, H., 2006, Fossil earthquakes recorded by pseudotachylytes in mantle peridotite from the Alpine subduction complex of Corsica: Earth and Planetary Science Letters, v. 242, p. 58–72, doi:10.1016/j.epsl.2005.11.058.

Angiboust, S., Agard, P., Raimbourg, H., and Yamato, P., 2011, Subduction interface processes recorded by eclogite facies shear zones: Lithos, v. 127, p. 222–238, doi:10.1016/j.lithos.2011.09.004.

Angiboust, S., Langdon, R., Agard, P., Waters, D., and Chopin, C., 2012, Eclogitization of the Monviso ophiolite and implications on subduction dynamics: Journal of Metamorphic Geology, v. 30, p. 37–61, doi:10.1111/j.1525-1314.2011.00951.x.

Cassidy, J.F., and Waldhauser, F., 2003, Evidence for both crustal and mantle earthquakes in the subducting Juan de Fuca plate: Geophysical Research Letters, v. 30, 1095, doi:10.1029/2002GL015511.

Davies, J.H., 1999, The role of hydraulic fractures and intermediate-depth earthquakes in generating subduction-zone magmatism: Nature, v. 398, p. 142–145, doi:10.1038/18202.

Doan, M.-L., and Gary, G., 2009, Rock pulverization at high strain rate near the San Andreas fault: Nature Geoscience, v. 2, p. 709–712, doi:10.1038/ngeo640.

Green, H.W.I., and Houston, H., 1995, The mechanics of deep earthquakes: Annual Review of Earth and Planetary Sciences, v. 23, p. 169–213, doi:10.1146/annurev.ea.23.050195.001125.

Hacker, B.R., Peacock, S.M., Abers, G.A., and Holloway, S.D., 2003, Subduction factory 2. Are intermediate-depth earthquakes in subducting slabs linked to metamorphic dehydration reactions?: Journal of Geophysical Research, v. 108, 2030, doi:10.1029/2001JB001129.

Handy, M.R., Hirth, G., and Bürgmann, R., 2007, Fault structure and rheology from the frictional-viscous transition downward, *in* Handy, M.R., et al., eds., Tectonic faults—Agents of change on a dynamic Earth: Dahlem Workshop Report 95: Cambridge, Massachusetts, MIT Press, p. 139–181.

Healy, D., Reddy, S.M., Timms, N.E., Gray, E.M., and Brovarone, A.V., 2009, Trench-parallel fast axes of seismic anisotropy due to fluid-filled cracks in subducting slabs: Earth and Planetary Science Letters, v. 283, p. 75–86, doi:10.1016/j.epsl.2009.03.037.

Igarashi, T., Matsuzawa, T., Umino, N., and Hasegawa, A., 2001, Spatial distribution of focal mechanisms for interplate and intraplate earthquakes associated with the subducting Pacific plate beneath the northeastern Japan arc: A triple-planed deep seismic zone: Journal of Geophysical Research, v. 106, p. 2177–2191, doi:10.1029/2000JB900386.

Jébrak, M., 1997, Hydrothermal breccias in vein-type ore deposits: A review of mechanisms, morphology and size distribution: Ore Geology Reviews, v. 12, p. 111–134, doi:10.1016/S0169-1368(97)00009-7.

John, T., and Schenk, V., 2006, Interrelations between intermediate-depth earthquakes and fluid flow within subducting oceanic plates: Constraints from eclogite facies pseudotachylytes: Geology, v. 34, p. 557–560, doi:10.1130/G22411.1.

Kuge, K., Kase, Y., Urata, Y., Campos, J., and Perez, A., 2010, Rupture characteristics of the 2005 Tarapaca, northern Chile, intermediate-depth earthquake: Evidence for heterogeneous fluid distribution across the subducting oceanic plate?: Journal of Geophysical Research, v. 115, B09305, doi:10.1029/2009JB007106.

McGrath, A.G., and Davison, I., 1995, Damage zone geometry around fault tips: Journal of Structural Geology, v. 17, p. 1011–1024, doi:10.1016/0191-8141(94)00116-H.

Mitchell, T.M., and Faulkner, D.R., 2009, The nature and origin of off-fault damage surrounding strike-slip fault zones with a wide range of displacements: A field study from the Atacama fault system, northern Chile: Journal of Structural Geology, v. 31, p. 802–816, doi:10.1016/j.jsg.2009.05.002.

Philippot, P., and van Roermund, H.L.M., 1992, Deformation processes in eclogitic rocks: Evidence for the rheological delamination of the oceanic crust in deeper levels of subduction zones: Journal of Structural Geology, v. 14, p. 1059–1077, doi:10.1016/0191-8141(92)90036-V.

Ranero, C.R., Phipps Morgan, J., McIntosh, K., and Reichert, C., 2003, Bending-related faulting and mantle serpentinization at the Middle America trench: Nature, v. 425, p. 367–373, doi:10.1038/nature01961.

Rietbrock, A., and Waldhauser, F., 2004, A narrowly spaced double-seismic zone in the subducting Nazca plate: Geophysical Research Letters, v. 31, L10608, doi:10.1029/2004GL019610.

Rondenay, S., Abers, G.A., and van Keken, P.E., 2008, Seismic imaging of subduction zone metamorphism: Geology, v. 36, p. 275–278, doi:10.1130/G24112A.1.

Sibson, R.H., 1986, Earthquakes and rock deformation in crustal fault zones: Annual Review of Earth and Planetary Sciences, v. 14, p. 149–175, doi:10.1146/annurev.ea.14.050186.001053.

Spandler, C., Pettke, T., and Rubatto, D., 2011, Internal and external fluid sources for eclogite-facies veins in the Monviso meta-ophiolite, Western Alps: Implications for fluid flow in subduction zones: Journal of Petrology, v. 52, p. 1207–1236, doi:10.1093/petrology/egr025.

van Keken, P.E., Hacker, B.R., Syracuse, E.M., and Abers, G.A., 2011, Subduction factory: 4. Depth-dependent flux of H_2O from subducting slabs worldwide: Journal of Geophysical Research, v. 116, B01401, doi:10.1029/2010JB007922.

Woodcock, N.H., and Mort, K., 2008, Classification of fault breccias and related fault rocks: Geological Magazine, v. 175, p. 435–440, doi:10.1017/S0016756808004883.

Yamasaki, T., and Seno, T., 2003, Double seismic zone and dehydration embrittlement of the subducting slab: Journal of Geophysical Research, v. 108, 2212, doi:10.1029/2002JB001918.

Zhang, J., and Green, H.W., 2007, Experimental investigation of eclogite rheology and its fabrics at high temperature and pressure: Journal of Metamorphic Geology, v. 25, p. 97–115, doi:10.1111/j.1525-1314.2006.00684.x.

Manuscript received 17 October 2011
Revised manuscript received 17 February 2012
Manuscript accepted 26 February 2012

Printed in USA

Earth and Planetary Science Letters 357-358 (2012) 238–248

Contents lists available at SciVerse ScienceDirect

Earth and Planetary Science Letters

journal homepage: www.elsevier.com/locate/epsl

Effect of fluid circulation on subduction interface tectonic processes: Insights from thermo-mechanical numerical modelling

S. Angiboust [a,c,*], S. Wolf [a], E. Burov [a], P. Agard [a], P. Yamato [b]

[a] ISTEP 46-00, 3e case 129, UMR CNRS 7193, UPMC Sorbonne Universités, F-75252 Cedex 05, Paris, France
[b] Geosciences Rennes, UMR CNRS 6118, Université de Rennes1 Campus Beaulieu CS 74205, F-35 042 Rennes Cedex, France
[c] Helmholtz-Zentrum – Deutsches GeoForschungsZentrum, Telegrafenberg, D-14473 Potsdam, Germany

ARTICLE INFO

Article history:
Received 25 April 2012
Received in revised form
7 September 2012
Accepted 12 September 2012
Editor: T. Spohn
Available online 23 October 2012

Keywords:
numerical modelling
fluids
subduction
exhumation

ABSTRACT

Both geophysical and petrological data suggest that large amounts of water are released in subduction zones during the burial of oceanic lithosphere through metamorphic dehydration reactions. These fluids are generally considered to be responsible for mantle wedge hydration, mechanical weakening of the plate interface and to affect slab-interface seismicity. In order to bridge the gap between subduction dynamics and the wealth of field, petrological and experimental data documenting small-scale fluid circulation at mantle depths, we designed a bi-phase model, in which fluid migration is driven by rock fluid concentrations, non-lithostatic pressure gradients and deformation. Oceanic subduction is modelled using a forward visco-elasto-plastic thermo-mechanically and thermodynamically coupled code (FLAMAR) following the previous work by Yamato et al. (2007). After 16.5 Myr of convergence, deformation is accommodated along the subduction interface by a low-strength shear zone characterised by a weak (10–25% of serpentinite) and relatively narrow (5–10 km) serpentinized front in the reference experiment. Dehydration associated with eclogitization of the oceanic crust (60–75 km depth) and serpentinite breakdown (110–130 km depth) significantly decreases the mechanical strength of the mantle at these depths, thereby favouring the detachment of large slices of oceanic crust along the plate interface. The geometries obtained are in good agreement with reconstructions derived from field evidence from the Alpine eclogite-facies ophiolitic belt (i.e., coherent fragments of oceanic crust detached at ca.80 km depth in the Alpine subduction zone and exhumed along the subduction interface). Through a parametric study, we further investigate the role of various parameters, such as fluid circulation, oceanic crustal structure and rheology, on the formation of such large tectonic slices. We conclude that the detachment of oceanic crust slices is largely promoted by fluid circulation along the subduction interface and by the subduction of a strong and originally discontinuous mafic crust.

1. Introduction and geological constraints

An increasing number of geophysical (Hebert et al., 2009; Kuge et al., 2010; Gerya and Meilick, 2011; van Keken et al., 2011), petrological (Bachmann et al., 2009; Padron-Navarta et al., 2010) and experimental studies (Hilairet and Reynard, 2009; Kawano et al., 2011) confirmed the fundamental role of fluids on intermediate depths interplate rheological and mechanical subduction processes.

Prior to subduction, huge amounts of water are also added to the oceanic lithosphere by hydrothermal alteration and/or downward percolation of seawater through fractures in the bending lithosphere entering trenches (Watts et al., 1980; McAdoo and Martin, 1984; Burov and Diament, 1995; Rüpke et al., 2004). During subduction, dehydration reactions accompanying prograde metamorphism transfer part of these fluids to the Earth mantle: (1) to the upper plate mantle wedge, ultimately causing arc magmatism and affecting subduction zone rheology and mechanical coupling along the plates interface (Iwamori, 1998; Oncken et al., 1999; Peacock and Hyndman, 1999; van Keken, 2003; Arcay et al., 2005; Wada et al., 2008; Bachmann et al., 2009), (2) to the upper part of the lower plate oceanic mantle (Schmidt and Poli, 1998; Ranero et al., 2003; Zhang et al., 2004; Faccenda et al., 2009; Contreras-Reyes, Carrizo, 2011; Fig. 1), and beyond (Green et al., 2010).

Such dehydration reactions are considered to be partly responsible for the observed intermediate-depth seismicity in the Wadati–Benioff zone (e.g. Green and Houston, 1995; Peacock, 2001; Hacker et al., 2003), together with hydraulic fracturing and reactivation of inherited faults (Davies, 1999; Rietbrock and

* Corresponding author. Now at GFZ Potsdam, Germany.
Tel.: +49 331 288 1363; fax: +49 331 288 1370.
E-mail address: samuel.angiboust@gmail.com (S. Angiboust).

0012-821X/$ - see front matter © 2012 Elsevier B.V. All rights reserved.
http://dx.doi.org/10.1016/j.epsl.2012.09.012

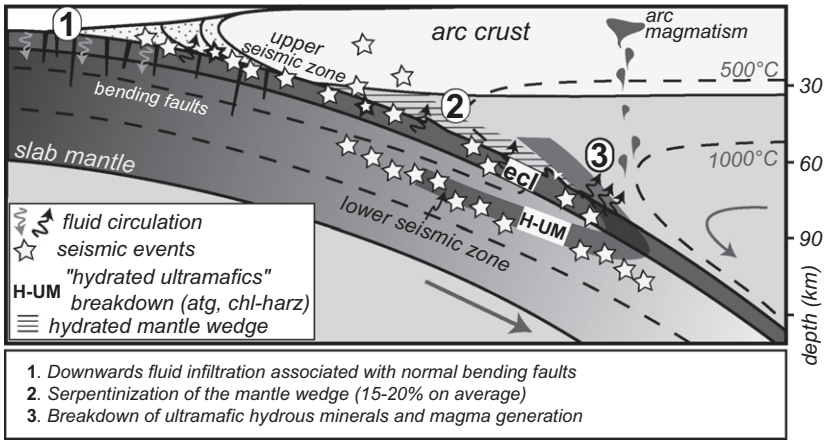

Fig. 1. Schematic view of a typical subduction zone showing the main fluid transfer processes and the location of the recorded seismic events.

Waldhauser, 2004; Angiboust et al., 2012a). The coupling between these prograde dehydration and hydration reactions (such as mantle serpentinization) could also be responsible for the detachment of tens of kilometres long coherent fragments of the downgoing slab, such as those found in the exhumed ophiolitic terranes in the Western Alps (where they detached along crustal-scale shear zones channelising fluids: Angiboust et al., 2009, 2011) or as those imaged by geophysical data on active subduction zones (Singh et al., 2008; Toda et al., 2008).

Geophysical observations notably through low S-velocity zones, seismic anisotropies and high Poisson ratios suggest the existence of a hydrous layer on the top of the subduction interface, between the slab and the mantle wedge (e.g. Kodaira et al., 2004; Abers, 2005; Audet et al., 2009; Jung, 2011; Fig. 1). This layer is however not robustly detectable since its thickness (generally ranging from 2 to 10 km) appears to be at the limits of resolution of seismic studies (Abers, 2005; Hilairet and Reynard, 2009). This hydrous layer is thought to be dominantly composed of serpentinite and, to a lesser extent, of talc and/or brucite (e.g. Peacock and Hyndman, 1999). Heat flux measurements also indicate that, except for some relatively "warm" subduction zones (such as the Cascades or Nankai; van Keken et al., 2011), serpentinization of the mantle wedge should be dominantly restricted to the vicinity of the plate interface (Wada et al., 2008 and references therein) and rarely exceed 20–30% (see Hyndman and Peacock, 2003). The mechanical weakening associated with serpentinization is in particular thought to account for the observed lack of seismicity within the mantle wedge.

Despite this recent wealth of data, constraints on the mechanisms allowing fluid extraction and circulation across and/or along the subduction interface and on their mechanical effect on interplate coupling are still critically lacking (e.g. Miller et al., 2003; Hacker et al., 2003; Wada et al., 2008). We herein attempt to bring additional constraints through thermomechanically and thermodynamically coupled numerical modelling. While Arcay et al. (2005) assumed that fluids released by metamorphic dehydration reactions only migrate upwards, recent works proposed that local gradients in tectonic pressure may strongly control fluid flow at depth in subduction zone environments (Faccenda and Mancktelow, 2010; Faccenda et al., 2012; see also Connolly and Podladchikov, 2004). Based on water contents derived from phase diagrams and tectonic pressure gradients, we herein implement fluid migration in an Alpine-type ocean–continent subduction setting (Yamato et al., 2007). In particular, we propose a methodology that enables reproducing the complex interplay between the rock fluid content and the physical and mechanical rock properties at mantle depths in a subduction environment. This kilometre-scale fluid circulation algorithm permits assessing the spatial extent of fluid migration and evaluating the effect of fluids on interplate mechanical coupling. The associated parametric study enables a better understanding of the key parameters controlling the formation of these large mafic slices along the plate interface in "cold" subduction zone settings. Comparison of numerical modelling results with natural data from exhumed ophiolitic belts provides an opportunity to validate the numerical approach herein followed.

2. Numerical modelling method and model setup

2.1. Thermo-mechanical model description

The numerical code FLAMAR v12 (derived from Paravoz; Poliakov et al., 1993, and based on the FLAC algorithm, Cundall, 1989) has been used in this study to assess the impact of fluid transfer processes on interplate subduction dynamics (more details on the numerical method are available in Burov et al., 2001, Yamato et al., 2007 and in Appendix A in supplementary material). The algorithm accounts for (1) large strains, (2) visco-elasto-plastic rheologies including Mohr–Coulomb failure (faulting) and pressure (P) – temperature (T) strain-rate dependent ductile creep, (3) density and rheology changes due to metamorphic reactions, (4) internal heat sources, and (5) free surface boundary conditions combined with erosion/sedimentation processes. The model setup is similar to the one used in the previous work by Yamato et al. (2007), but with a narrower accretionary wedge and a discontinuous oceanic crust, in order to match the seafloor structure of a slow-spreading ocean, such as for the Tethyan seafloor (Fig. 2a; Western Alps; Lagabrielle and Cannat, 1990; see also Gorczyk et al., 2007 for a close initial seafloor structure). The oceanic crust is composed of flat-lying mafic bodies separated by serpentinized mantle (such as inferred for Western Alps ophiolitic domains; Lagabrielle and Lemoine, 1997, or after geophysical observation; Cannat et al., 1997). We imposed the presence of a 6 km-thick partly serpentinized layer below the oceanic mafic crust in order to match recent numerical models demonstrating the existence of a downgoing serpentinization front in slow-spreading contexts (Iyer et al., 2010 and references therein). Thermal structure, boundary conditions and other fixed parameters are identical to those described by Yamato et al. (2007). Input lithologies, chemical compositions and flow laws for the different materials used in the model are given in Table 1. Density and maximum water contents are updated dynamically as function of pressure–temperature (P–T)

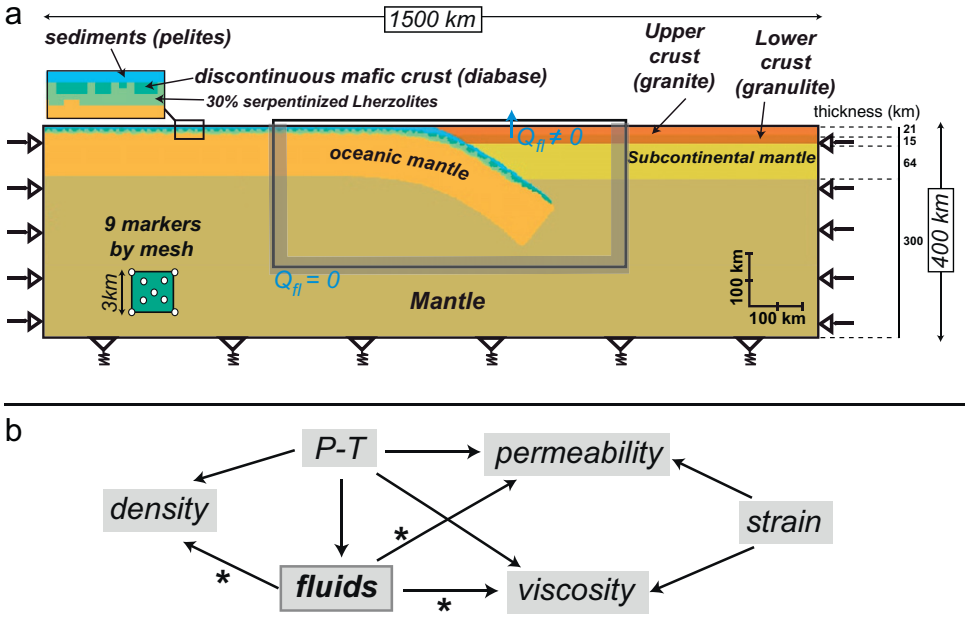

Fig. 2. (a) Initial setup for our oceanic subduction models with a close-up showing the detailed structure of the oceanic lithosphere (see Yamato et al., 2007 for further information on the setup). The fluid flow is computed only in the rectangle surrounding the subduction zone (see Appendix B in supplementary material for details). The amount of fluid is set to zero on the boundary of this box ($Q_{fl}=0$) except at the surface where the total fluid flux outwards the mesh elements is cancelled ($Q_{fl} \neq 0$) (that is, the quadrangles at the top of the mesh are not allowed to retain any fluid). (b) Sketch showing the complex interplays between all the variables considered in this study. *, relationship considered only for ultramafic material (serpentinites and peridotites).

conditions using thermodynamic free-energy minimisation (Connolly, 2005; Yamato et al., 2007).

2.2. Fluid circulation model

Given that metamorphic rocks porosity is extremely low, we considered as a first approximation that the instantaneous total water content equals the mineral-bounded water content. As an example, an element of the model made of serpentinite is considered to carry 12 wt.% H_2O. In our model, the instantaneous fluid content (which for instance may vary with prograde metamorphic dehydration reactions) is automatically derived from P–T-[H_2O] grids calculated with PerpleX (Connolly, 2005; Fig. 2b).

Although previous numerical models considered that fluids released by metamorphic reactions dominantly migrate upwards by porous flow along the vertical pressure gradient (e.g. Iwamori, 1998; Arcay et al., 2005), an increasing number of recent studies evoke the possibility that fluids do not necessarily migrate purely upwards but could also flow downwards or trenchwards (Hacker et al., 2003; Faccenda et al., 2009; Faccenda and Mancktelow, 2010; Kawano et al., 2011; van Keken et al., 2011). In order to better reproduce the complex coupling between deformation and fluid flow at depth in subduction zones, we formulated an alternative algorithm enabling released free fluids to migrate along the non-lithostatic pressure gradients, i.e., without any prescribed condition on the flow direction (e.g. Connolly and Podladchikov, 2004; Faccenda and Mancktelow, 2010). Fluid pressure in each element of the model is therefore proportional to non-lithostatic pressure (Appendix B in supplementary material) and the expelled fluid is forced to migrate from higher to lower non-lithostatic pressure domains (i.e., where deformation generally concentrates). The idea that these tectonic pressure gradients play a more important role than the vertical pressure gradient is supported by the fact that (i) pore connectivity is extremely low in metamorphic rocks (free fluids pressure therefore approaches lithostatic values; Etheridge et al., 1983; Connolly, 1997) and (ii) fractures, faults and shear zones constitute higher-permeability drains for fluids in natural systems (e.g. Cox, 2001; Ague, 2003; Miller et al., 2003; Angiboust et al., 2011).

In our model, fluid circulation also depends on the relative water saturation of the material (that is, in domains where non-lithostatic pressure is roughly constant, water flows from hydrated to anhydrous material; Appendix B in supplementary material). We also defined a “dynamic permeability” parameter, which itself depends on the strain rate (that is, fluid flow will be channelised within domains undergoing active deformation) and on P–T conditions (following the permeability-depth relationship of Ingebritsen and Manning, 1999). Introduction of a deformation-dependant permeability term enables considering the strong effect of an anisotropic fabric (that develop within rocks undergoing deformation) on fluid channelization (e.g. Kawano et al., 2011). This new algorithm was designed (i) to reproduce large-scale fluid circulation processes in order to take into account serpentinization processes (e.g. as in Gerya et al., 2002; Arcay et al., 2005; Iyer et al., 2010), (ii) to allow for a feedback between fluid content and mantle viscosities, densities and permeabilities (Fig. 2b). Detailed equations, constitutive relations and references are presented in Appendix B in supplementary material.

The fluid circulation starts after 2.5 Myr of convergence in order to first achieve a thermally and mechanically stable subduction environment (Yamato et al., 2007). While sediments are initially water-saturated, the oceanic mantle and the oceanic crust are considered to be initially moderately hydrated (~30% serpentinization; Ranero et al., 2003, and 2 wt.% H_2O, respectively; Carlson, 2003; Table 1). Note that the use of P–T-[H_2O] grids derived from pseudosection modelling implies that we assume that thermodynamic equilibrium is reached for each element of the model. Since our numerical experiments primarily aim at understanding the main parameters controlling the formation of large mafic slices in a serpentinized environment along the plate interface in relatively

Table 1
Chemical and rheological parameters used in the experiments.

Phase	Chemical composition (ox. wt.%)	Material	Reference	Initial water amount (wt.%)	Flow law reference	Experimental material	Viscosity parameters $\log_{10}(A)$ ($MPa^{-n} s^{-1}$)	n	Q (kJ mol^{-1})
Sediments	Si(50)Al(11.2)Fe(9.5)Mg(4.9)K(4)	Fe–Mg rich pelite	Yamato et al. (2007)	Saturated	Shea and Kronenberg (1992)	Micaschist	−67	31	98
					Ranalli and Murphy (1987)	Wet quartzite	−5.16	3	156
Serpentinite	Si(42.5)Al(1)Fe(6)Mg(42) Ca(1.5)	Serpentinized lherzolite	Li et al. (2004)[a]	4%	Hilairet et al. (2007)	Serpentinite	−12.6	5.8	18
Oceanic mafic crust	Si(49.8)Al(16.3)Fe(10.6)Mg(6.7)Ca(10.9)Na(3.1)	Basalt	Carmichael (1989)	2%	Caristan (1980)	Maryland diabase	−1.2	3.1	276
Upper continental crust	Si(70.2)Al(14.1)Fe(3.6)Mg(0.2)Ca(1.7)Na(3)K(6)	Granite	Carmichael (1989)	1%	Hansen and Carter (1983)	Wet westerly granite	−3.7	1.9	141
Lower continental crust	Si(50.1)Al(18.4)Fe(8.1)Mg(7.2)Ca(9.9)Na(3.4)	Mafic granulite	Forster et al. (2010)[a]	1%	Caristan (1980)	Maryland diabase	−1.2	3.1	276
Oceanic lithospheric mantle	Si(44.7)Al(3.9)Fe(8.2)Mg(36.7)Ca(3.2)	Abyssal peridotite	Workman and Hart (1995)	0%	Goetze and Evans (1979)	Dry olivine	3.84	3	510
Subcontinental mantle	Si(44)Al(2.3)Fe(8.4)Mg(41.4)Ca(2.15)	Spinel peridotite	McDonough (1990)	0%	Karato and Jung (2003)	Wet olivine	2.9	3	470
Mantle	Si(45)Al(4.5)Fe(8.1)Mg(37.8) Ca(3.6)	Primitive mantle	McDonough and Sun (1995)	0%	Goetze and Evans (1979)	Dry olivine	3.84	3	510

[a] Averaged chemical composition; Elastic parameters, cohesion, friction angle, thermal conductivity and diffusivity are identical to Yamato et al. (2007).

"cold" subduction zone settings, partial melting processes were ignored. In addition, phase relationships, melt formation and extraction processes are still debated (e.g. Poli and Schmidt, 2002) and have so far yielded contrasting numerical models (Hebert et al., 2009; Gerya and Meilick, 2011 and references therein).

3. Experiments and results

The following parameters were systematically varied in a series of experiments (summarised in Table 2): (i) the presence of fluid circulation, (ii) the structure of oceanic crust, (iii) the rheology of both the oceanic crust and sediments and (iv) the convergence rate. The best match with the behaviour inferred from field observations in the Western Alps was achieved in experiment Sub45, hereafter referred to as the reference experiment.

3.1. Reference experiment (sub45)

The results of this numerical experiment after 16.5 Myr of convergence are presented in the compositional map of Fig. 3a and in Table 2 (see Appendix C in supplementary material for the associated thermal structure, density, and strain rate maps). The oceanic lithosphere is buried along a rather cold gradient (~7°/km) in agreement with the prograde *P–T* path reported for the *W.* Alps ophiolitic domains (Agard et al., 2001; Angiboust et al., 2012b; Fig. 3b). We observe large pluri-kilometric fragments of oceanic crust, decoupled from the downgoing slab and accreted along the plate interface (Fig. 3a). Discontinuities within the oceanic crust (initially separated by serpentinized mantle directly overlain by sediments; Fig. 2a) are activated as thrusts during the detachment of these slices. Note that this slicing systematically occurs along pre-existing weakness zones, preserving a relatively undisturbed lateral continuity within individualised tectonic bodies. Importantly, these slices undergo very limited upwards motion but rather remain stacked along the plate interface, decoupled from the downgoing plate.

These fragments are underlain by a relatively thick (10–20 km) and buoyant, partly serpentinized sole (20–25% serpentinization; Fig. 4c). Sediments, which are the dominant material at shallow depths (0–40 km) along the subduction interface, are restricted to a narrow strip at mantle depths. The overlying mantle wedge appears stagnant under the continental Moho but is dragged beyond depths of 150 km together with the downgoing plate (Fig. 3a). After 16.5 Myr of convergence, most of the sedimentary material is scraped off and accreted within the accretionary wedge by underplating (as in Yamato et al., 2007; Plunder et al., 2012). At this stage, our model shows that the subduction channel is composed of 15% sediments, 31% mafics and 54% serpentinite between 60 and 100 km depth (i.e., typical depths exposed in the Western Alps internal high-pressure domain; Guillot et al., 2004; Angiboust and Agard, 2010; Table 2).

The dynamic permeability map (Fig. 3b; Appendix B in supplementary material) suggests the existence of 10–100 times higher permeability zones located below and at the top of the oceanic crust. Fluids produced by dehydration metamorphic reactions will therefore be drained along these "channels" where deformation is localised. The highest water contents (up to 6 wt.%) are reached in the accretionary wedge (Fig. 4a), where sedimentary material is close to saturation (Fig. 4b). The water content, originally comprised between 2 and 6 wt.% within the subducting lithosphere, decreases at the tip of the wedge to reach 2–3% on average (Fig. 4a). Note that even if the rocks are located at *P–T* conditions where major water release occurs (40–70 km depth), they remain undersaturated (Fig. 4b; i.e., water content is 2–3 times lower than theoretical maximum water contents,

Table 2
Summary of the numerical experiments, compared with the reference model (Sub45). Parameters changed with respect to Sub45 are highlighted by gray boxes. Sign "+" means presence.

Parametric study	**Parameter tested**				**Results**				
					Oceanic crust rheology				
	Plate velocity (cm yr^{-1})	**Fluid circulation**	**Serp. sole**	**Oceanic crust structure**	**Mafic crust**	**Sediments**	**Stability of subduction**	**Detachment of crustal fragments at 60–100 km depth and timing**	**Prop. of subd. channel crustal material at 60–100 km depth at 16 Ma**
Sub45 (ref. experiment)	2	+	+	Disc.	Maryland diabase	Micaschist	Stable	Large mafic fragments at ~10 Ma	$Sed_{15}Mafic_{31}Serp_{54}$
Sub45nofl	2			Disc.	Maryland diabase	Micaschist	Stable	No detachment	$Sed_{40}Mafic_{26}Serp_{34}$
Sub46	2	+		Disc.	Maryland diabase	Micaschist	Stable	No detachment	$Sed_{25}Mafic_{75}$
Sub46nofl	2			Disc.	Maryland diabase	Micaschist	Stable	No detachment	$Sed_{63}Mafic_{37}$
Sub48	2	+	+	Cont.	Maryland diabase	Micaschist	Stable	No detachment	$Sed_{24}Mafic_{45}Serp_{31}$
Sub43	2	+	+	Disc.	Maryland diabase	Wet quartzite	Slab breakdown at 13 Ma	Sedimentary "plume" in the mantle wedge at ~9.5 Ma	$Sed_{22}Mafic_{33}Serp_{45}$
Sub43nofl	2		+	Disc.	Maryland diabase	Wet quartzite	Stable	Accretion of sediments along the plate interface	$Sed_{65}Mafic_{22}Serp_{13}$
Sub43bis	2	+	+	Disc.	Wet quartzite	Wet quartzite	Slab breakdown at 10 Ma	Medium-sized fragments in a mélange at 6.6 Ma	No crust
Sub49	1	+	+	Disc.	Maryland diabase	Micaschist	Stable	Medium-sized slices at ~13 Ma	$Sed_{34}Mafic_{30}Serp_{36}$
Sub50	4	+	+	Disc.	Maryland diabase	Micaschist	Slab breakdown at 12 Ma	Medium-sized slices at ~10 Ma	$Sed_{25}Mafic_{45}Serp_{30}$
								Western Alps HP ophiolites proportions:	$Sed_{8}Mafic_{44}Serp_{48}$

assuming thermodynamic equilibrium). At greater depths (>100 km), water contents become very low (<1 wt.%), but the three orders of magnitude lower dynamic permeabilities prevent fluid draining, which explains the presence of oversaturated domains along and below the subduction interface down to ca. 300 km (Fig. 4b).

In order to better understand the extent of fluid infiltration within the mantle surrounding the subducted crust, we calculated the degree of serpentinization (i.e., the instantaneous water content divided by 12%, which is the amount of water within fully serpentinized peridotite; Fig. 4c). Maximum water contents calculated in the reference model suggest that a serpentinite-rich, fully hydrated mantle can theoretically be preserved down to ~90 km depth within the subducting slab (Fig. 3c). They also indicate that the upper mantle wedge, immediately below the continental Moho (40–50 km), may be fully hydrated (with 12 wt.% H_2O) for such a thermal regime of the subduction zone (Fig. 3c). A narrower (10–15 km thick) front located at the top of the subduction interface also develops down to 150 km depth (where Mg-chlorite breaks down at ca. 800 °C; Fig. 3b) and exhibits slightly lower serpentinization degree, on the order of 5–15% (Fig. 4c). The extent of initial serpentinization of the oceanic mantle (around 35% prior to subduction) progressively decreases to reach ~15–20% at 100 km depth (Fig. 4c). As expected, slab bending produces intensive normal faulting in the hinge area (Ranero et al., 2003; Faccenda et al., 2012), thereby increasing mantle permeability and permitting fluid infiltration down to ca. 30 km depth within the mantle (Figs. 3 and 4; Appendix C in supplementary material).

3.2. Parametric study

In order to first evaluate the mechanical impact of fluids on subduction interface dynamics, the fluid circulation algorithm was turned off in experiment sub45nofl, keeping all other parameters as in the reference model. Results (Table 2) show that in absence of fluid circulation, no fragments of oceanic crust are ever detached from the downgoing slab during the experiment (20 Myr). A larger sedimentary component is also observed along the plate interface (40% sediments instead of 15% in the reference model).

In order to evaluate the influence of an initial serpentinite sole (as expected from seafloor serpentinization of the oceanic mantle; e.g. Iyer et al., 2010), another experiment was performed in which the discontinuous oceanic crust directly lies on the dry oceanic mantle (sub46). This configuration yields results similar to the previous experiment and does not lead to the detachment of oceanic crust fragments, whether or not activating the fluid circulation algorithm (sub46nofl; Fig. 5a). Note that the subduction of an initially continuous oceanic crust (sub48) also prevents the slice detachment observed in the reference experiment (cf. Table 2).

The use of different rheological flow laws is known to be a major source of discrepancies between numerical models (e.g. Kaus et al., 2009). Evaluating the effect of sediment rheology is therefore of critical importance for the modelling of subduction processes because their properties partly control the mechanical strength of the plate interface. While a micaschist flow law was used for the reference experiment (Shea and Kronenberg, 1992), an alternative wet quartzite flow law, substantially weaker (viscosity is 1.3 order of magnitude lower at 500 °C) and commonly used in geodynamic numerical modelling (e.g. Currie et al., 2007; Yamato et al., 2007; Warren et al., 2008; Gerya and Meilick, 2011), was used in exp. Sub43 (Table 2; Fig. 5b). We observe the formation of a buoyant sedimentary "plume" (similar to those first described by Gerya and Yuen, 2003) after 4 Myr of

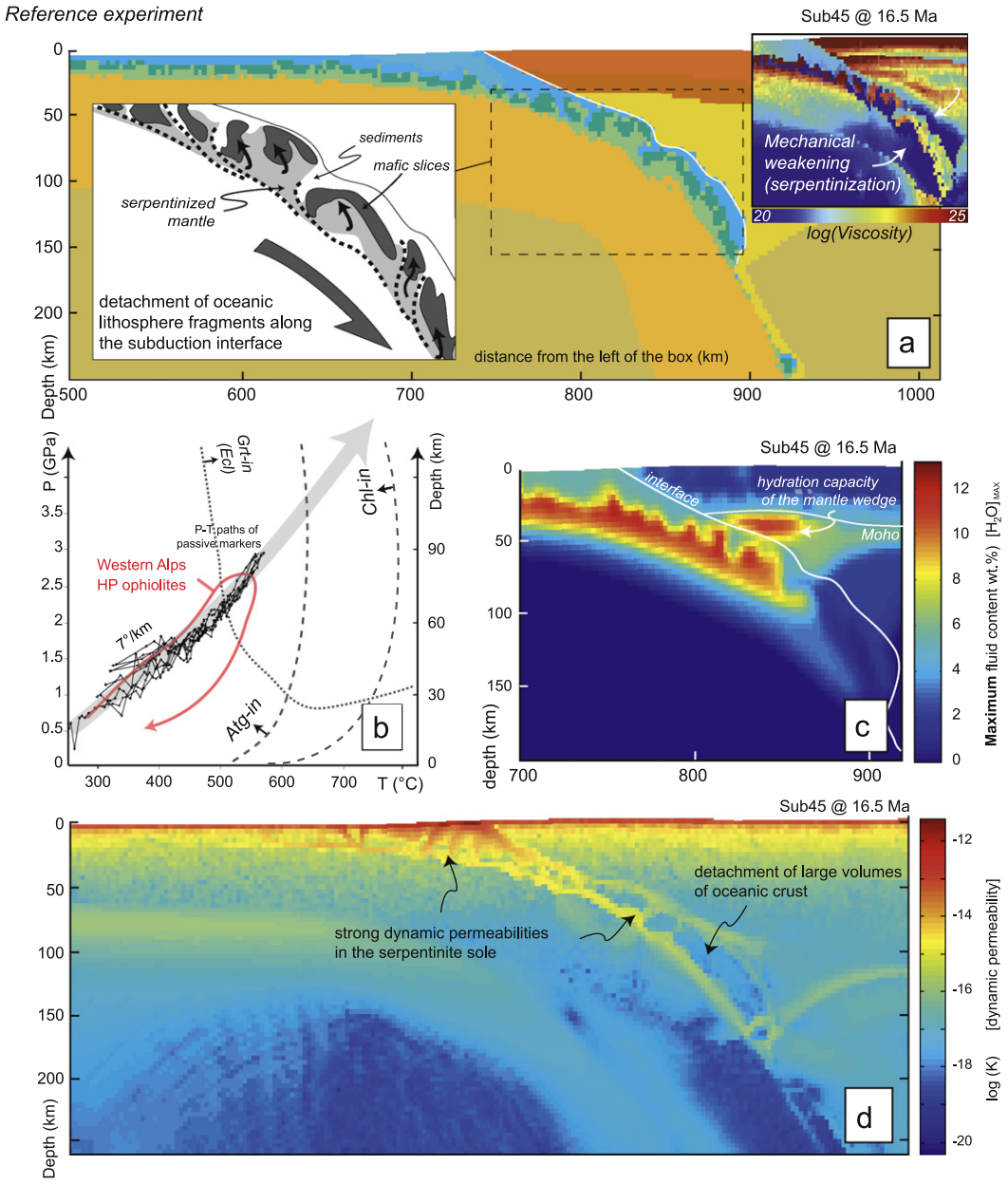

Fig. 3. (a) Morphology of our reference experiment (Sub45) after 16.5 Myr of convergence (i.e., the time step at which tectonic slices were the most obvious during model evolution). The inset shows the distribution of effective viscosity within the subduction zone for the same time-step. (b) Burial *P–T* paths obtained for downgoing oceanic lithosphere showing excellent agreement with prograde *P–T* paths from the literature for eclogite-facies Alpine ophiolitic units (see references in the text). Also shown three major water-producing phase transitions associated with eclogitization of the oceanic crust and the breakdown of antigorite and chlorite within ultramafics. (c) Close-up view showing the maximum fluid content (in wt.% H_2O) theoretically permitted, computed for each element of the mesh (based on thermodynamic data using the program PerpleX). (d) "Dynamic permeability" structure of the reference experiment after 16.5 Myr of convergence showing the presence of higher-permeability channels forming in deforming areas (with higher strain rates; Appendix C in supplementary material), surrounding lower-permeability domains (decoupled oceanic crust).

convergence. This low-viscosity, buoyant instability develops within the hydrated mantle wedge (Hebert et al., 2009) and progressively reaches the continental Moho. In this case a break-off of the downgoing slab takes place at ca. 13 Myr. Note that the same experiment run without fluid circulation (sub43-nofl) produces a very thick accretionary wedge along the subduction interface down to ca.90 km depth, probably in response to changes in interplate mechanical coupling.

We also tested the effect of the presence of a very weak mafic oceanic crust by using a wet quartzite flow law instead of the diabase rheology (Gerya and Meilick, 2011; sub43bis; Table 2; Fig. 5c). An accretionary complex (similar to the one formed in experiment sub43nofl) formed after 6 Myr of convergence, showing a very complex tectonic mixing between the oceanic lithosphere fragments and the mantle wedge. Weakening of the oceanic crust thus does not promote the detachment of large tectonic slices along the subduction interface between 60 and 100 km depth but apparently rather favours the formation of various types of sediment-rich accretionary complexes and/or plume-like sedimentary instabilities.

Finally, only minor changes with respect to the reference experiment are observed when dividing the convergence rate by two (Sub49): these are (i) a higher sediment fraction along the subduction interface and (ii) the detachment of slightly smaller tectonic slices (Table 2). On the contrary, doubling the convergence rate (up to 4 cm yr^{-1}; Sub50) causes a break-off of the oceanic lithosphere at 12 Myr, following the detachment of similar medium-sized tectonic slices along the plate interface.

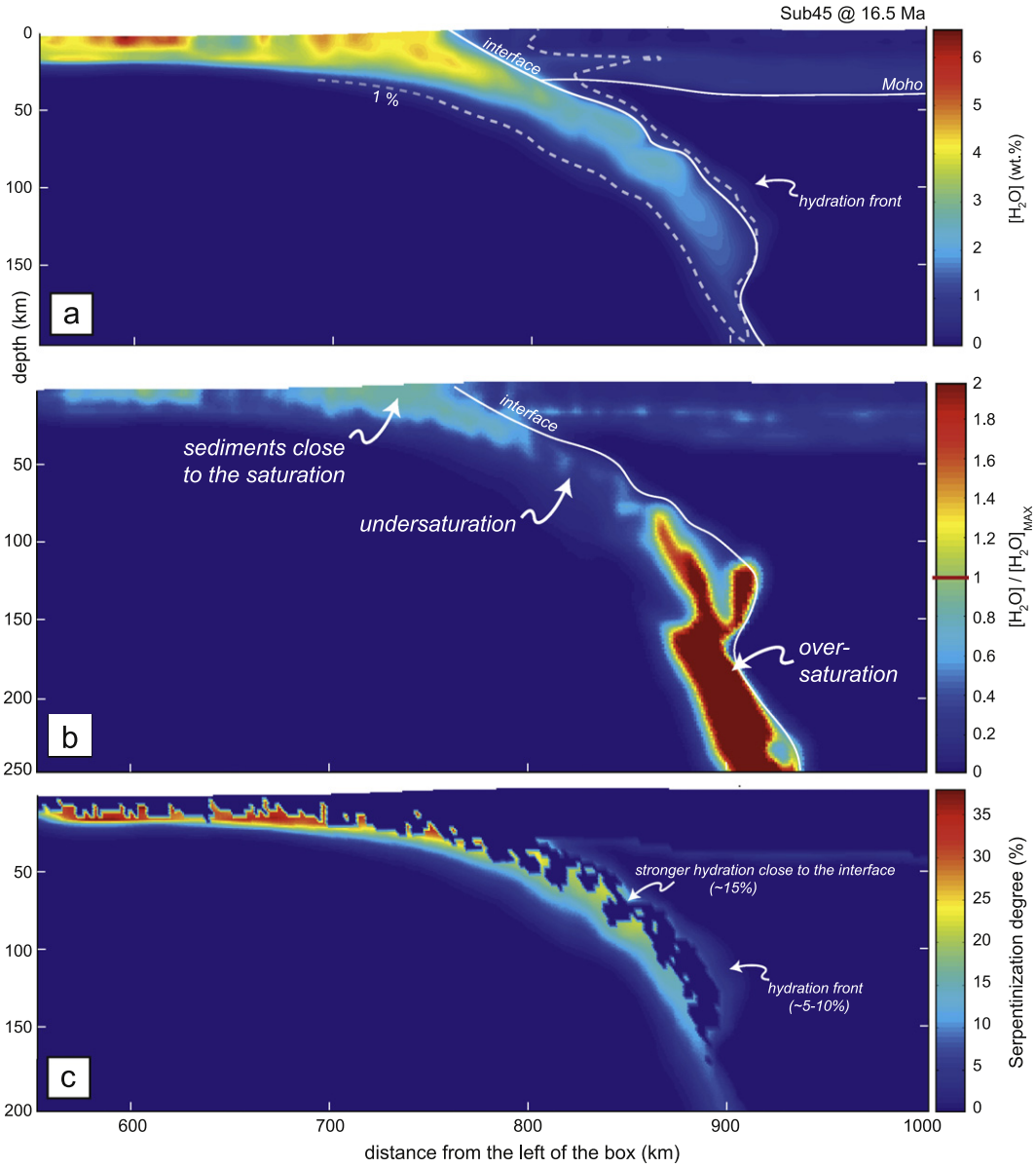

Fig. 4. (a) Water content of the reference experiment after 16.5 Myr of convergence showing a water-enriched accretionary wedge and decreasing water content with increasing depth. (b) Saturation ratio (obtained by normalising instantaneous water content by the maximum water content thermodynamically permitted for each material) for the reference experiment showing strong along-strike variations. Note that "over-saturated" domains exist at depth (100–250 km) below the subduction interface, where permeability is too low for fluid expulsion. (c) Serpentinization degree (calculated by dividing the instantaneous amount of fluid by 12 wt.%, i.e., the maximum weight amount of water within serpentinite) for the reference experiment at 16.5 Myr illustrating (i) the decrease of the serpentinization degree of oceanic peridotites with burial and (ii) the formation of a weak, diffuse hydration front close to the subduction interface at mantle depths.

4. Implications for subduction interface processes

These results throw light on the nature of the subduction interface and potentially help interpreting geophysical observations on active subduction zones. Comparing these results with field evidence from exhumed ophiolitic terrains also provides new insights on interplate petrological and tectonic processes acting in the mantle depth interval between 50 and 150 km.

4.1. Fluids: a key parameter controlling the formation of large oceanic lithosphere slices

Our experiments show that large pluri-kilometric volumes of oceanic lithosphere can be accreted between 50 and 110 km along the subduction interface. Although buoyancy is commonly regarded as a critical parameter permitting the exhumation and preservation of HP ophiolitic domains (Hermann et al., 2000; Schwartz et al., 2001; Yamato et al., 2007), our results suggest that this condition alone is not sufficient to enable slicing of the oceanic crust in the subduction channel (in line with Angiboust and Agard, 2010). The detachment of the sliced fragments is herein controlled by the interplay between buoyancy forces and the significant mechanical weakening resulting from the serpentinization of the subduction interface (mantle viscosity decreases by one to two orders of magnitude, in agreement with Billen and Gurnis, 2001; Hilairet et al., 2007; Appendix C in supplementary material; Table 2). These experiments also indicate that the existence of an initially discontinuous mafic crust facilitates the "basal decoupling" responsible for the detachment of these slices. We consequently hypothesise that slow-spreading oceans may be more subject to slice individualisation and detachment than those with a thick, continuous oceanic crust.

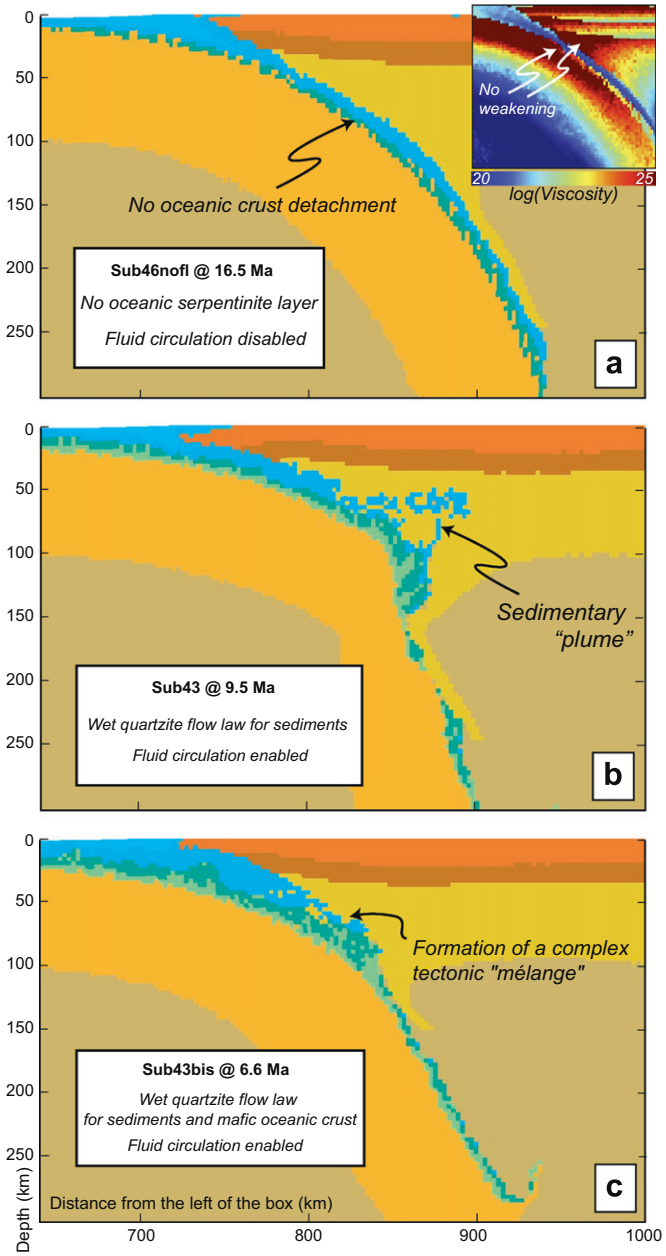

Fig. 5. (a) Morphology of the experiment Sub46nofl after 16.5 Myr of convergence showing the absence of detachment of large oceanic crust fragments. The inset shows the effective viscosity distribution for the same time-step in the absence of fluids. (b) Morphology of the experiment Sub43 after 9.5 Myr of convergence showing the formation of a "sedimentary plume" in the mantle wedge. (c) Morphology of the experiment Sub43bis after 6.6 Myr of convergence showing the formation of a complex tectonic mélange along the subduction interface where mantle wedge peridotites, oceanic crust and oceanic serpentinites are chaotically gathered.

Internal high-pressure ophiolitic massifs from the W. Alps or Alpine Corsica, exhumed from ca. 80 km depth (Angiboust et al., 2009; Vitale-Brovarone et al., 2011), indeed generally exhibit a striking primary first-order structural coherency, characterised by the presence of a relatively thick (~1 km) serpentinized oceanic mantle sole at the bottom of the ophiolitic pile (Angiboust and Agard, 2010). This suggests that a basal decoupling, taking place below the oceanic Moho, possibly at the transition between highly and weakly serpentinized peridotites, controlled the detachment of these slices. Note that the existence of reversed polarity km-sized ophiolitic tectonic slices in the Alpine orogen (e.g. Monviso Unit, Lombardo et al., 1978; Angiboust et al., 2012b) supports the possibility that kilometre-scale dragging folds formed during the detachment of the slice or on exhumation (Fig. 6).

The presence of such large slices in active subduction settings has been recently demonstrated by seismic data in the depth interval from 40 to 80 km beneath Tokyo (Toda et al., 2008). Our results suggest that such slab fragments may detach in subduction zones in response to a strong hydration of the oceanic lithosphere and/or in association with the scrapping off of downgoing asperities (such as seamounts; Ranero and Von Huene, 2000; Wang and Bilek, 2011) and/or mega-earthquakes (Singh et al., 2011). Although the subduction interface in the depth range 50–110 km is the source area of these tectonic slices in our models, we stress that (i) these slices underwent very limited upwards motion (few kilometres at the most) and that (ii) none of these slices escaped the subduction channel to reach the tip of the accretionary wedge (i.e., above ca. 35 km). Despite the fact that such a slicing of the oceanic lithosphere may be a long-lived process in active subduction zones, we indeed recall that the exhumation of HP rocks is only a transient process likely taking place during geodynamic perturbations of the subduction regime (Agard et al., 2007, 2009; Brun and Faccenna, 2008; Guillot et al., 2009). In the Western Alps, the exhumation and preservation of large volumes of eclogitized oceanic lithosphere were probably enabled by the entrance and rapid exhumation of buoyant continental material (i.e., internal crystalline massifs such as Dora Maira, Monte Rosa) plucking back the ophiolitic nappe-stack out of the subduction channel (e.g. Angiboust and Agard, 2010).

4.2. Constraints on subduction channel rheology

Fluids generated by prograde metamorphic dehydration reactions are channelised in our models in weaker materials (i.e., sediments and serpentinites), where deformation concentrates, and deflected around fragments of stronger, less permeable oceanic crust (Fig. 6). Subduction-parallel upwards fluid flux apparently dominates over subduction-perpendicular fluid infiltration, in close agreement with recent experimental studies on serpentinite permeability anisotropy (Kawano et al., 2011).

Our results suggest that the overlying mantle wedge only undergoes a slight serpentinization (10–15%) restricted to the vicinity of the plate interface (generally ~10 km-thick). These values, predicted for an Alpine-type subduction setting, are in agreement with geophysical studies suggesting the existence of a narrow, heterogeneous, slightly serpentinized mantle wedge in relatively "cold" subduction settings (~20%; Hyndman and Peacock, 2003; Chou et al., 2009). Note that in the reference experiment, material from the overlying mantle wedge is not dragged within the subduction channel, in line with geochemical data suggesting that serpentinized peridotites from the Western Alps effectively belong to the exhumed oceanic mantle (e.g. Hattori and Guillot, 2007). Interestingly, our models showed that dragging of mantle wedge material within the subduction channel occurs dominantly when the downgoing oceanic crust is modelled using weaker lithologies (Fig. 5c) and when the overriding mantle wedge is partly serpentinized.

The oceanic mantle also undergoes a slightly stronger downward serpentinization (10–20%) down to 20–30 km, in agreement with recent models suggesting that plate bending favours downward fluid flow inside the slab (Faccenda and Mancktelow, 2010). This deeper infiltration may potentially trigger seismic activity due to elevated pore fluid pressures (Fig. 4c), which in turn may explain the lower seismic plane frequently observed within active subduction zones (e.g. Hacker et al., 2003; Faccenda et al., 2012; Figs. 1 and 6). Our models do not permit to discriminate

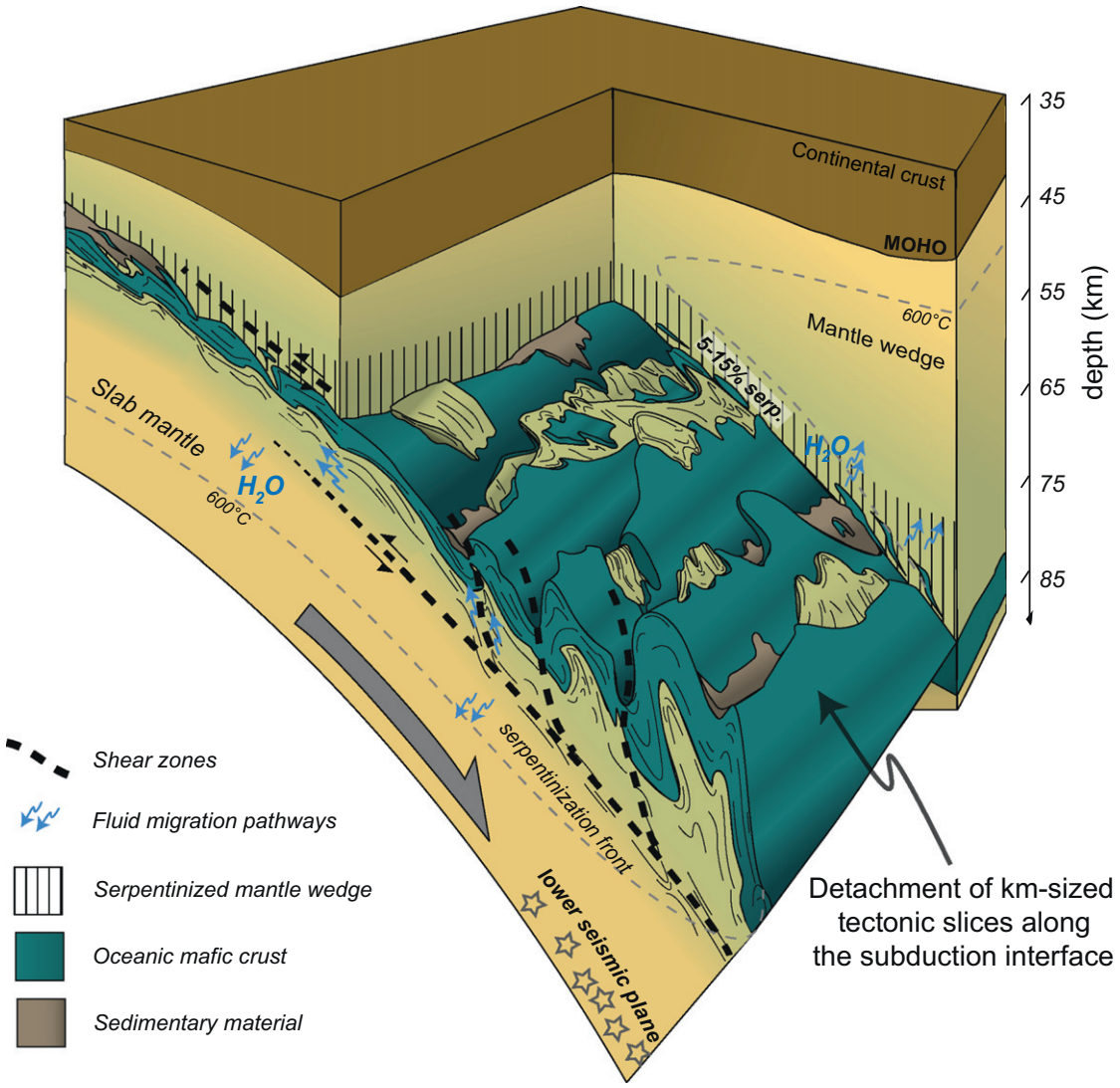

Fig. 6. Schematic view of a subduction zone between 35 and 85 km depth based on our numerical model results (and to a lesser extent on exhumed ophiolitic terrains) showing inferred morphologies and the detachment of large folded slices of oceanic lithosphere, accreted along the plate interface. This figure also illustrates the main deformation-enhanced fluid pathways (associated with deep serpentinite producing/consuming reactions), dominantly at the boundary between material with marked rheological contrasts.

accurately the origin of the upper plane seismicity (hydraulic fracturing and/or dehydration embrittlement; Davies, 1999; Hacker et al., 2003). The formation of a slightly serpentinized layer on the top of the subduction interface is generally believed to inhibit the formation of subduction thrust earthquakes (e.g. Hirauchi et al., 2010) because shear stress would be preferentially accommodated by plastic flow. Our results nevertheless show that pre-subduction segmentation of the oceanic lithosphere controls the formation of tectonic slices by reactivating inherited structural features (see also Butler, 1989). The latter could potentially cause intra-slab seismic events, as recorded within fossil and active subduction zones (Oncken et al., 1999; Rietbrock and Waldhauser, 2004; Marot et al., 2012; Angiboust et al., 2012a).

We finally stress that natural data (structure and lithological composition) from the W. Alps ophiolitic belt was better reproduced using relatively stronger rheologies for the oceanic crust (see Table 2). The choice of weaker rheologies for the sediments and mafic crust not only increases the thickness of the channel (and the relative fraction of sediments), but also influences the deformation style by promoting the formation of an accretionary complex (Fig. 5c) in which chaotic mixing and plume-like instabilities may develop (i.e., one of the characteristic features reported for several ophiolitic suture zones such as in Cuba or in the Franciscan complex; Cloos, 1982; Blanco-Quintero et al., 2011; Gerya and Meilick, 2011).

5. Conclusions

Thermo-mechanically and thermodynamically coupled numerical experiments accounting for fluid circulation enable a new understanding of the complex interplay between fluid and deformation at mantle depths within subduction zones. These experiments notably provide constraints on interplate mechanical coupling and on processes responsible for the detachment of oceanic lithosphere fragments.

Our results provide constraints on the rheology of the subduction interface between 50 and 150 km depth and suggest that the exhumation style within subduction zones (i.e., large tectonics slices versus complex mélanges) is partly controlled by the strength of subducted crustal material. In particular, we showed that a weak downgoing oceanic crust apparently promotes the formation of large mélange-like accretionary complexes while

large tectonic slices rather require a stronger, discontinuous oceanic crust overlying a serpentinized mantle.

These results (i) corroborate field evidence from large eclogitized tectonic slices of ophiolitic material showing homogeneous *P–T* conditions (i.e., tens of kilometres along-strike, as in the Western Alps) and (ii) are strongly supported by recent geophysical studies imaging the presence of decoupled oceanic material fragments in active subduction zones. We thus hypothesise that the detachment of such slices from the subducting plate represents a fraction of the intermediate-depth seismicity presently recorded within active subduction zones.

Acknowledgements

We thank Laetitia Le Pourhiet, Peter Van Keken, Benjamin Huet and Thomas François for insightful discussions and technical assistance. This paper benefited from thoughtful and careful reviews from Taras Gerya and Clare Warren.

Appendix A. Supporting information

Supplementary data associated with this article can be found in the online version at http://dx.doi.org/10.1016/j.epsl.2012.09.012.

References

Abers, G.A., 2005. Seismic low-velocity layer at the top of subducting slabs: observations, predictions, and systematics. Phys. Earth Planet. Inter. 149, 7–29.
Agard, P., Jolivet, L., Goffé, B., 2001. The Schistes lustrés complex: a key for understanding the exhumation of HP and UHP rocks in the Western Alps? Bull. Soc. Geol. Fr. 172, 617–636.
Agard, P., Jolivet, L., Vrielynck, B., Burov, E., Monié, P., 2007. Plate acceleration: the obduction trigger? Earth Planet. Sci. Lett. 258, 428–441.
Agard, P., Yamato, P., Jolivet, L., Burov, E., 2009. Exhumation of oceanic blueschists and eclogites in subduction zones: timing and mechanisms. Earth Sci. Rev. 92, 53–79.
Ague, 2003. Fluid flow in the deep crust. In: Rudnick, R.L. (Ed.), Treatise in Geochemistry. Elsevier.
Angiboust, S., Agard, P., Yamato, P., Raimbourg, H., 2012a. Eclogite breccias in a subducted ophiolite: a record of intermediate-depth earthquakes? Geology 40, 707–710.
Angiboust, S., Langdon, R., Agard, P., Waters, D., Chopin, C., 2012b. Eclogitization of the Monviso ophiolite and implications on subduction dynamics. J. Metamorph. Geol. 30, 37–61.
Angiboust, S., Agard, P., Raimbourg, H., Yamato, P., Huet, B., 2011. Subduction interface processes recorded by eclogite-facies shear zones. Lithos 127, 222–238.
Angiboust, S., Agard, P., 2010. Initial water budget: the key to detaching large volumes of eclogitized oceanic crust along the subduction channel? Lithos 120, 453–474.
Angiboust, S., Agard, P., Jolivet, L., Beyssac, O., 2009. The Zermatt-Saas ophiolite: the largest (60-km wide) and deepest (c. 70–80 km) continuous slice of oceanic lithosphere detached from a subduction zone? Terra Nova 21, 171–180.
Arcay, D., Tric, E., Doin, M.P., 2005. Numerical simulations of subduction zones: effect of slab dehydration on the mantle wedge dynamics. Phys. Earth Planet. Inter. 149, 133–153.
Audet, P., Bostock, M.G., Christensen, N.I., Peacock, S.M., 2009. Seismic evidence for overpressured subducted oceanic crust and megathrust fault sealing. Nature 457, 76–78.
Bachmann, R., Oncken, O., Glodny, J., Seifert, W., Georgieva, V., Sudo, M., 2009. Exposed plate interface in the European Alps reveals fabric styles and gradients related to an ancient seismogenic coupling zone. J. Geophys. Res. 114, B05402.
Billen, M.I., Gurnis, M., 2001. A low viscosity wedge in subduction zones. Earth Planet. Sci. Lett. 193, 227–236.
Blanco-Quintero, I.F., Garcia-Casco, A., Gerya, T.V., 2011. Tectonic blocks in serpentinite melange (eastern Cuba) reveal large-scale convective flow of the subduction channel. Geology 39, 79–82.
Brun, J.P., Faccenna, C., 2008. Exhumation of high-pressure rocks driven by slab rollback. Earth Planet. Sci. Lett. 272, 1–7.
Burov, E., Jolivet, L., Le Pourhiet, L., Poliakov, A., 2001. A thermomechanical model of exhumation of high pressure (HP) and ultra-high pressure (UHP) metamorphic rocks in Alpine-type collision belts. Tectonophysics 342, 113–136.
Burov, E.B., Diament, M., 1995. The effective elastic thickness (Te) of continental lithosphere: what does it really mean? J. Geophys. Res. 100 (B3), 3905–3927.
Butler, R.W.H., 1989. The Influence of Pre-existing Basin Structure on Thrust System Evolution in the Western Alps, 44. Geological Society, London (Special Publication), pp. 105–122.
Cannat, M., Lagabrielle, Y., Bougault, H., Casey, J., De Coutures, N., Dmitriev, L., Ultramafic and gabbroic exposures at the Mid-Atlantic ridge: geological mapping in the 15°N region. Tectonophysics 279, 197–213.
Caristan, Y., 1980. High Temperature Mechanical Behavior of Maryland Diabase. Ph.D. thesis, MIT, Cambridge, MA.
Carlson, R.L., 2003. Bound water content of the lower oceanic crust estimated from modal analyses and seismic velocities of oceanic diabase and gabbro. Geophys. Res. Lett. 30 (22), 2142.
Carmichael, R., 1989. Practical Handbook of Physical Properties of Rocks and Minerals. CRC Press, Boca Raton, FL 741 pp.
Chou, H.C., Kuo, B.Y., Chiao, L.Y., Zhao, D., Hung, S.H., 2009. Tomography of the westernmost Ryukyu subduction zone and the serpentinization of the fore-arc mantle. J. Geophys. Res. 114, B12301.
Cloos, M., 1982. Flow Melanges -– numerical modeling and geologic constraints on their origin in the franciscan subduction complex, California. Geol. Soc. Am. Bull. 93, 330–345.
Connolly, J.A.D., 2005. Computation of phase equilibria by linear programming: a tool for geodynamic modeling and its application to subduction zone decarbonation. Earth Planet. Sci. Lett. 236, 524–541.
Connolly, J.A.D., Podladchikov, Y.Y., 2004. Fluid flow in compressive tectonic settings: implications for midcrustal seismic reflectors and downward fluid migration. J. Geophys. Res. 109, B04201.
Connolly, J.A.D., 1997. Deformation-generated fluid pressure and deformation-propagated fluid flow during regional metamorphism. J. Geophys. Res. 102, 18149–18173.
Contreras-Reyes, E., Carrizo, D., 2011. Control of high oceanic features and subduction channel on earthquake ruptures along the Chile–Peru subduction zone. Phys. Earth Planet. Inter. 186, 49–58.
Cox, S.F., 2001. Fluid flow in mid- to deep crustal shear systems: experimental constraints, observation on exhumed high fluid flux shear systems, and implications on seismogenic processes. Earth Planets Space 54, 1121–1125.
Cundall, P.A., 1989. Numerical experiments on localization in frictional materials. Arch. App. Mech. 59, 148–159.
Currie, C.A., Beaumont, C., Huismans, R.S., 2007. The fate of subducted sediments: a case for backarc intrusion and underplating. Geology 35, 1111–1114.
Davies, J.H., 1999. The role of hydraulic fractures and intermediate-depth earthquakes in generating subduction-zone magmatism. Nature 398, 142–145.
Etheridge, M.A., Wall, V.J., Cox, S.F., 1983. High fluid pressures during regional metamorphism and deformation: implications for mass transport and deformation mechanism. J. Geophys. Res. 86, 4344–4358.
Faccenda, M., Gerya, T.V., Burlini, L., 2009. Deep slab hydration induced by bending-related variations in tectonic pressure. Nat. Geosci. 2, 790–793.
Faccenda, M., Gerya, T.V., Mancktelow, N.S., Moresi, L., 2012. Fluid flow during slab unbending and dehydration: implications for intermediate-depth seismicity, slab weakening and deep water recycling. Geochem. Geophys. Geosyst. 13, Q01010.
Faccenda, M., Mancktelow, N.S., 2010. Fluid flow during unbending: implications for slab hydration, intermediate-depth earthquakes and deep fluid subduction. Tectonophysics 494, 149–154.
Forster, H.J., Forster, A., Oberhansli, R., Stromeyer, D., 2010. Lithospheric composition and thermal structure of the Arabian Shield in Jordan. Tectonophysics 481, 29–37.
Gerya, T.V., Meilick, F.I., 2011. Geodynamic regimes of subduction under an active margin: effects of rheological weakening by fluids and melts. J. Metamorph. Geol. 29, 7–31.
Gerya, T.V., Stockhert, B., Perchuk, A.L., 2002. Exhumation of high-pressure metamorphic rocks in a subduction channel: a numerical simulation. Tectonics, 21.
Gerya, T.V., Yuen, D.A., 2003. Rayleigh-Taylor instabilities from hydration and melting properties of cold plumes at subduction zones. Earth Planet. Sci. Lett. 212, 47–62.
Goetze, C., Evans, B., 1979. Stress and temperature in the bending lithosphere as constrained by experimental rock mechanics. Geophys. J. R. Astron. Soc. 59, 463–478.
Gorczyk, W., Guillot, S., Gerya, T.V., Hattori, K., 2007. Asthenospheric upwelling, oceanic slab retreat, and exhumation of UHP mantle rocks: insights from Greater Antilles. Geophys. Res. Lett., 34.
Green, H.W., Houston, H., 1995. The mechanics of deep earthquakes. Ann. Rev. Earth Planet. Sci. 23, 169–213.
Green, H.W., Chen, W.P., Brudzinski, M.R., 2010. Seismic evidence of negligible water carried below 400-km depth in subducting lithosphere. Nature 467, 828–831.
Guillot, S., Schwartz, S., Hattori, K., Auzende, A., Lardeaux, J., 2004. The Monviso Ophiolitic Massif (Western Alps), A Section Through a Serpentinite Subduction Channel. Evolution of the Western Alps: Insights from Metamorphism, Structural Geology, Tectonics and Geochronology, The Virtual Explorer, Paper 3.
Guillot, S., Hattori, K., Agard, P., Schwartz, S., Vidal, O., 2009. Exhumation Processes in Oceanic and Continental Subduction Contexts: A Review, Subduction Zone Geodynamics. Frontiers in Earth Sciences. Springer Berlin Heidelberg, pp. 175–205.

Hacker, B.R., Peacock, S.M., Abers, G.A., Holloway, S.D., 2003. Subduction factory – 2. Are intermediate-depth earthquakes in subducting slabs linked to metamorphic dehydration reactions? J. Geophys. Res.-Solid Earth 108 (B1).
Hansen, F.D., Carter, N.L., 1983. Semibrittle Creep Of Dry And Wet Westerly Granite At 1000 MPa. Conference paper: The 24th U.S. Symposium on Rock Mechanics (USRMS), June 20–23, 1983. College Station, TX.
Hattori, K.H., Guillot, S., 2007. Geochemical character of serpentinites associated with high- to ultrahigh-pressure metamorphic rocks in the Alps, Cuba, and the Himalayas: recycling of elements in subduction zones. Geochem. Geophys. Geosyst. 8, Q09010.
Hebert, L.B., Antoshechkina, P., Asimow, P., Gurnis, M., 2009. Emergence of a low-viscosity channel in subduction zones through the coupling of mantle flow and thermodynamics. Earth Planet. Sci. Lett. 278, 243–256.
Hermann, J., Müntener, O., Scambelluri, M., 2000. The importance of serpentinite mylonites for subduction and exhumation of oceanic crust. Tectonophysics 327, 225–238.
Hilairet, N., et al., 2007. High-pressure creep of serpentine, interseismic deformation, and initiation of subduction. Science 318, 1910–1913.
Hilairet, N., Reynard, B., 2009. Stability and dynamics of serpentinite layer in subduction zone. Tectonophysics 465, 24–29.
Hirauchi, K.-i., Katayama, I., Uehara, S., Miyahara, M., Takai, Y., 2010. Inhibition of subduction thrust earthquakes by low-temperature plastic flow in serpentine. Earth Planet. Sci. Lett. 295, 349–357.
Hyndman, R.D., Peacock, S.M., 2003. Serpentinization of the forearc mantle. Earth Planet. Sci. Lett. 212, 417–432.
Ingebritsen, S.E., Manning, C.E., 1999. Geological implications of a permeability-depth curve for the 178 continental crust. Geology 27, 1107–1110.
Iwamori, H., 1998. Transportation of H_2O and melting in subduction zones. Earth Planet. Sci. Lett. 160, 65–80.
Iyer, K., Rüpke, L.H., Morgan, J.P., 2010. Feedbacks between mantle hydration and hydrothermal convection at ocean spreading centers. Earth Planet. Sci. Lett. 296, 34–44.
Jung, H., 2011, Seismic anisotropy produced by serpentine in mantle wedge. Earth Planet. Sci. Lett. 307, 535–543.
Karato, S.-i., Jung, H., 2003. Effects of pressure on high-temperature dislocation creep in olivine. Philos. Mag., 83.
Kaus, B.J.P., Liu, Y., Becker, T.W., Yuen, D.A., Shi, Y., 2009. Lithospheric stress-states predicted from long-term tectonic models: influence of rheology and possible application to Taiwan. J. Asian Earth Sci. 36, 119–134.
Kawano, S., Katayama, I., Okazaki, K., 2011. Permeability anisotropy of serpentinite and fluid pathways in a subduction zone. Geology 39, 939–942.
Kodaira, S., et al., 2004. High pore fluid pressure may cause silent slip in the Nankai Trough. Science 304, 1295–1298.
Kuge, K., Kase, Y., Urata, Y., Campos, J., Perez, A., 2010. Rupture characteristics of the 2005 Tarapaca, northern Chile, intermediate-depth earthquake: evidence for heterogeneous fluid distribution across the subducting oceanic plate? J. Geophys. Res. 115 (B9), B09305.
Lagabrielle, Y., Lemoine, M., 1997. Alpine, Corsican and Apennine ophiolites: the slow-spreading ridge model. C. R. Acad. Sci.–Ser. IIA – Earth Planet. Sci. 325, 909–920.
Lagabrielle, Y., Cannat, M., 1990. Alpine Jurassic ophiolites resemble the modern central Atlantic basement. Geology 18, 319–322.
Li, X.P., Rahn, M., Bucher, K., 2004. Serpentinites of the Zermatt-Saas ophiolite complex and their texture evolution. J. Metamorph. Geol. 22, 159–177.
Lombardo, B., Nervo, R., Compagnoni, R., Messiga, B., Kienast, J.R., Mevel, C., Fiora, L., Piccardo, G., Lanza, R., 1978. Osservazioni preliminari sulle ofioliti metamorfiche del Monviso (Alpi occidentali). Rend. Soc. Ital. Mineral. Petrol. 34, 253–305.
Marot, M., Monfret, T., Pardo, M., Ranalli, G., Nolet, G., 2012. An intermediate-depth tensional earthquake (MW 5.7) and its aftershocks within the Nazca slab, central Chile: a reactivated outer rise fault? Earth Planet. Sci. Lett. 327–328, 9–16.
McAdoo, D.C., Martin, C.F., 1984. Seasat observations of lithospheric flexure seaward of trenches. J. Geophys. Res. 89 (B5), 3201–3210.
McDonough, W.F., 1990. Constraints on the composition of the continental lithospheric mantle. Earth Planet. Sci. Lett. 101, 1–18.
McDonough, W.F., Sun, S.S., 1995. The composition of the Earth. Chem. Geol. 120, 223–253.
Miller, S.A., van der Zee, W., Olgaard, D.L., Connolly, J.A.D., 2003. A fluid-pressure feedback model of dehydration reactions: experiments, modelling, and application to subduction zones. Tectonophysics 370, 241–251.
Oncken, O., the ANCORP working group, 1999. Seismic reflexion image revealing offset of Andean subduction zone earthquakes into oceanic mantle. Nature 397, 341–344.
Padron-Navarta, J.A., Tommasi, A., Garrido, C.J., Sánchez-Vizcaíno, V.L., Gómez-Pugnaire, M.T., Jabaloy, A., Vauchez, A., 2010. Fluid transfer into the wedge controlled by high-pressure hydrofracturing in the cold top-slab mantle. Earth Planet. Sci. Lett. 297, 271–286.
Peacock, S.M., 2001. Are the lower planes of double seismic zones caused by serpentine dehydration in subducting oceanic mantle? Geology 29, 299–302.
Peacock, S.M., Hyndman, R.D., 1999. Hydrous minerals in the mantle wedge and the maximum depth of subduction thrust earthquakes. Geophys. Res. Lett. 26 (16), 2517–2520.
Plunder A., Agard P., Dubacq B., Chopin C., Bellanger M., 2012. How continuous and precise is the record of *P–T* paths? Insights from combined thermobarometry and thermodynamic modelling into subduction dynamics (Schistes Lustrés, W. Alps). J. Metamorph. Geol., 30, 223–246.
Poli, S., Schmidt, M.W., 2002. Petrology of subducted slabs. Ann. Rev. Earth Planet. Sci. 30, 207–235.
Poliakov, A.N.B., Podladchikov, Y., Talbot, C., 1993. Initiation of salt diapirs with frictional overburdens – numerical experiments. Tectonophysics 228, 199–210.
Ranalli, G., Murphy, D.C., 1987. Rheological stratification of the lithosphere. Tectonophysics 132, 281–295.
Ranero, C.R., Phipps Morgan, J., McIntosh, K., Reichert, C., 2003. Bending-related faulting and mantle serpentinization at the Middle America trench. Nature 425, 367–373.
Ranero, C.R., Von Huene, R., 2000. Subduction erosion along the Middle America convergent margin. Nature 404, 748–752.
Rietbrock, A., Waldhauser, F., 2004. A narrowly spaced double-seismic zone in the subducting Nazca plate. Geophys. Res. Lett. 31 (10), L10608.
Rüpke, L.H., Morgan, J.P., Hort, M., Connolly, J.A.D., 2004. Serpentine and the subduction zone water cycle. Earth Planet. Sci. Lett. 223, 17–34.
Schmidt, M.W., Poli, S., 1998. Experimentally based water budgets for dehydrating slabs and consequences for arc magma generation. Earth Planet. Sci. Lett. 163, 361–379.
Schwartz, S., Allemand, P., Guillot, S., 2001. Numerical model of the effect of serpentinites on the exhumation of eclogitic rocks: insights from the Monviso ophiolitic massif (Western Alps). Tectonophysics 342, 193–206.
Shea, W.T., Kronenberg, A.K., 1992. Rheology and deformation mechanisms of an isotropic mica schist. J. Geophys. Res. 97 (B11), 15201–15237.
Singh, S.C., Carton, H., Tapponnier, P., Hananto, N.D., Chauhan, A.P.S., Hartoyo, D., Bayly, M., Moeljopranoto, S., Bunting, T., Christie, P., Lubis, H., Martin, J., 2008. Seismic evidence for broken oceanic crust in the 2004 Sumatra earthquake epicentral region. Nat. Geosci. 1, 777–781.
Singh, S.C., Hananto, N., Mukti, M., Robinson, D.P., Das, S., Chauhan, A., Carton, H., Gratacos, B., Midnet, S., Djajadihardja, Y., Harjono, H., 2011. Aseismic zone and earthquake segmentation associated with a deep subducted seamount in Sumatra. Nat. Geosci. 4, 308–311.
Toda, S., Stein, R.S., Kirby, S.H., Bozkurt, S.B., 2008. A slab fragment wedged under Tokyo and its tectonic and seismic implications. Nat. Geosci. 1, 771–776.
van Keken, P.E., 2003. The structure and dynamics of the mantle wedge. Earth Planet. Sci. Lett. 215, 323–338.
van Keken, P.E., Hacker, B.R., Syracuse, E.M., Abers, G.A., 2011. Subduction factory: 4. Depth-dependent flux of H_2O from subducting slabs worldwide. J. Geophys. Res. 116 (B1), B01401.
Vitale-Brovarone, A., Beltrando, M., Malavieille, J., Giuntoli, F., Tondella, E., Groppo, C., Beyssac, O., Compagnoni, R., 2011. Inherited ocean–continent Transition zones in deeply subducted terranes: insights from Alpine Corsica. Lithos 124, 273–290.
Wada, I., Wang, K., He, J., Hyndman, R.D., 2008. Weakening of the subduction interface and its effects on surface heat flow, slab dehydration, and mantle wedge serpentinization. J. Geophys. Res. 113 (B4), B04402.
Wang, K., Bilek, S., 2011. Do subducting seamounts generate or stop large earthquakes? Geology 39, 819–822.
Warren, C.J., Beaumont, C., Jamieson, R.A., 2008. Modelling tectonic styles and ultra-high pressure (UHP) rock exhumation during the transition from oceanic subduction to continental collision. Earth Planet. Sci. Lett. 267, 129–145.
Watts, A.B., Bodine, J.H., Steckler, M.S., 1980. Observations of flexure and the state of stress in the oceanic lithosphere. J. Geophys. Res. 85 (B11), 6369–6376.
Workman, R.K., Hart, S.R., 1995. Major and trace element composition of the depleted MORB mantle (DMM). Earth Planet. Sci. Lett. 231, 53–72.
Yamato, P., Agard, P., Burov, E., Le Pourhiet, L., Jolivet, L., Tiberi, C., 2007. Burial and exhumation in a subduction wedge: mutual constraints from thermomechanical modeling and natural P–T–t data (Schistes Lustres, western Alps). J. Geophys. Res. Solid Earth 112 (B7).
Zhang, J., Green, H.W., Bozhilov, K., Jin, Z., 2004. Faulting induced by precipitation of water at grain boundaries in hot subducting oceanic crust. Nature 428, 633–636.

Tectonophysics 608 (2013) 812–831

Contents lists available at ScienceDirect

Tectonophysics

journal homepage: www.elsevier.com/locate/tecto

Major role of shear heating in intracontinental inverted metamorphism: Inference from a thermo-kinematic parametric study

S. Duprat-Oualid [a,*], P. Yamato [a,b], P. Pitra [a]

[a] Géosciences Rennes, UMR6118, Université de Rennes 1 & CNRS, 35042 Rennes, France
[b] ETH-Zurich, Sonneggstrasse 5, CH-8092 Zurich, Switzerland

ARTICLE INFO

Article history:
Received 3 May 2013
Received in revised form 16 July 2013
Accepted 30 July 2013
Available online 13 August 2013

Keywords:
Inverted metamorphism
Shear heating
Numerical modelling
Thermal properties of the lithosphere

ABSTRACT

Inverted metamorphism corresponds to the stacking of high-temperature metamorphic units structurally on top of lower-temperature units and is commonly observed along main thrusts in major orogens. Yet, in spite of many existing models, the origin and preservation of the metamorphic inversion in intracontinental collision belts are still debated. In this study, we use a crustal-scale 2D thermo-kinematic model in order to investigate the key parameters controlling the inversion of the geothermal gradient at crustal scale. Our results confirm that the kinematic framework strongly impacts the thermal evolution around the thrust. Erosion velocity and thermal conductivity of rocks are two parameters that control the spatial location of the thermal perturbation and the intensity of inversion, respectively. However, even in extreme kinematic configurations, i.e., convergence velocities >3 cm·yr^{-1} and relatively high thrust dip angles ~30°, the thermal inversion is fleeting and thrust temperatures cannot reach the high temperature peak values characteristic of natural occurrences (>600 °C) if shear heating is not taken into account. Conversion of mechanical energy into heat represents a main contribution to the thermal budget along main crustal shear zones. It leads to high temperature conditions in the thrust zone and our results attest that it is the only process that allows the preservation through time of an intense thermal inversion. Our quantification shows that shear heating is much more efficient than other processes such as accretion and surface denudation and is compatible with the observations of inverted metamorphism in the Himalayan or Variscan belts, for example. This comparison with natural occurrences suggests that the formation and preservation of intracontinental inverted metamorphism require shear zone viscosity values of the order of 10^{20}–10^{21} Pa·s for convergence velocities between 1 and 3 cm·yr^{-1}.

1. Introduction and state of the art

An inverted metamorphic sequence is characterised by an upward intensification of metamorphism, typically an increase of the metamorphic peak temperature. Inverted metamorphism is mostly related to major thrusts, where convergence velocities are high. The major occurrences can be ascribed to one of three distinct geological contexts: (i) metamorphic soles beneath ophiolites (e.g., Abd El-Naby et al., 2000; Hacker, 1991; Jamieson, 1986; Williams and Smyth, 1973); (ii) oceanic subduction zones (e.g., Platt, 1975; Toksöz et al., 1971); and (iii) major thrusts in continental collision (e.g., Kohn, 2008; LeFort, 1975).

The present study is focused on the third geological setting. The best documented example is the inverted metamorphic sequence associated with the Main Central Thrust (MCT) zone in the southern Himalayas (e.g., Arita, 1983; Caddick et al., 2007; Frank et al., 1973; Harrison et al., 1997, 1998, 1999; Henry et al., 1997; Hubbard, 1989; Jain and Manickavasagam, 1993; Kohn, 2008; LeFort, 1975; Sinha-Roy, 1982), but other examples were described in the Variscan belt (Arenas et al., 1995; Ballèvre et al., 2009; Burg et al., 1984; Pitra et al., 2010; Štípská and Schulmann, 1995), in the Caledonian belt (Andreasson and Lagerblad, 1980; Johnson and Strachan, 2006; Mason, 1984; Watkins, 1985) or in the Appalachian belt (Camiré, 1995). The pressure and temperature conditions within such thrust zones attest to a medium pressure, medium-high temperature metamorphism. As an example, inverted metamorphic sequences in both the Himalayas and the Variscan belt have recorded peak temperatures between 500 and 700 °C and peak pressures between 8 and 11 kbar (e.g., Burg et al., 1984; Corrie and Kohn, 2011; Guillot, 1999; Kohn, 2008; Macfarlane, 1995; Pitra et al., 2010). Natural intracontinental metamorphic inversions are thus characterised by inverted thermal gradients between 10 and 50 °C·km^{-1} (e.g., Kohn, 2008; Pitra et al., 2010). Such intense thermal perturbations over a thickness of several kilometres necessarily imply geodynamic processes at crustal or even lithospheric scale. Several numerical models have been developed, most of them constrained by or aiming to fit data from the Himalayan belt (e.g., Bollinger et al., 2006; Henry et al., 1997; Jamieson et al., 1996, 2004; Kohn, 2008). They suggest two alternative hypotheses to explain the metamorphic inversion.

* Corresponding author. Tel.: +33 223236783.
E-mail address: sylvia.duprat-oualid@univ-rennes1.fr (S. Duprat-Oualid).

0040-1951/$ – see front matter © 2013 Elsevier B.V. All rights reserved.
http://dx.doi.org/10.1016/j.tecto.2013.07.037

On the one hand, the inverted zonation is the result of a post-metamorphic deformation of a preexisting "normal" metamorphic sequence. This may result from late thrusts cutting through the initial metamorphic sequence (e.g., Brunel and Kienast, 1986), passive deformation of metamorphic isograds within a ductile shear zone (e.g., Gibson et al., 1999; Grujic et al., 1996; Jain and Manickavasagam, 1993) or crustal-scale folding (e.g., Searle and Rex, 1989; Stephenson et al., 2000).

On the other hand, the inverted zonation may result from a temporary spatial perturbation of crustal isotherms (Burg and Schmalholz, 2008; Jamieson et al., 1996, 2004; LeFort, 1975; Peacock, 1987a). In this hypothesis, metamorphism is synchronous with the deformation event. Some authors propose that inverted metamorphism occurs due to a diffusive heat transfer across the major thrust from the hotter upper unit to the colder subjacent unit (e.g., England and Molnar, 1993; LeFort, 1975; Shi and Wang, 1987). Particularly, the thermal inversion may be due to a "channel flow", i.e., the extrusion of deep hot crustal rocks above a colder plate (e.g., Grujic et al., 1996; Jamieson et al., 1996, 2004). This model presents the advantage of reproducing the ranges of metamorphic pressures and temperatures characterising the outcroping sections of the MCT (Beaumont et al., 2001). However, it requires strong erosion localised on the thrust front and specific internal physical properties in terms of viscosity and angle of friction. Furthermore, it fails to reproduce some important metamorphic and geochronological records on both sides of the MCT (Kohn, 2008).

Beyond the first-order role of the kinematic framework and thermal diffusion, several studies have specifically focused on the contribution of radiogenic heat, including the accretion of radioactive material across the active thrust, and on the role of erosion (Bollinger et al., 2006; Huerta et al., 1996, 1998, 1999; Royden, 1993; Ruppel and Hodges, 1994). Accretion models allowing the accumulation of highly radioactive material over a duration longer than 30 Myr can lead to a significant increase of temperature within the hanging wall (e.g., Huerta et al., 1996, 1998). However, such studies involve disputable initial assumptions. As an example, the orogenic accretionary wedges of these models (e.g., Huerta et al., 1998) are deeply rooted at 30 to 60 km depths. Reasonable accretion velocities associated with lower, realistic erosion velocities lead to wedges several hundreds of kilometres wide at the surface. Outcrouping rocks across such wide zones should consequently be characterised by a continuous intense deformation and none of the known frontal thrusts displays such a configuration. Moreover, in most cases, strong accretion alone cannot reproduce the high temperatures observed in natural inverted metamorphic sequences. On the contrary, accretion leads to progressive cooling of the active thrust plane to steady temperatures lower than 400 °C at 30 km depth with no significant thermal inversion (Royden, 1993). Concomitant surface denudation characterised by an erosion velocity greater than the accretion velocity is necessary to raise the temperatures in the thrust zones (e.g., Bollinger et al., 2006; Royden, 1993).

In the absence of accretion processes, moderate erosion velocities can lead to thrust temperatures of the order of 600 °C and to the development of inverted isotherms comparable to those observed in natural inverted metamorphic sequences (Royden, 1993). However, these conclusions require a thrust activity lasting for more than 70 Myr and exhumation of ultra-high pressure metamorphic rocks from more than 100 km depth (Royden, 1993). Such implications are not compatible with natural cases where rocks recorded metamorphic peak pressures of 8 to 11 kbar. From a mechanical approach, erosion catalyses the development of main orogenic structures (e.g., Burg and Schmalholz, 2008), and some models highlight the important influence of both the erosion and the exhumation on the thermal perturbation (e.g., Beaumont et al., 2004; Bollinger et al., 2006; Jamieson et al., 1996; Kohn, 2008).

The role of heat production by conversion of mechanical energy into thermal energy in a major shear zone (shear heating) was also considered to complete the thermal budget and the possible development of thermal inversion around a thrust (Burg and Gerya, 2005; Burg and Schmalholz, 2008; England and Molnar, 1993; England and Thompson, 1984; Graham and England, 1976; LeFort, 1975; Minear and Toksöz, 1970; Molnar and England, 1990; Pavlis, 1986; Scholz, 1980; Toksöz et al., 1971), but without real quantification. Kidder et al. (2013) specifically refute the importance of shear heating under high convergence velocity (~10 cm·yr^{-1}) and attribute the thermal inversion to accretion process.

The demonstration provided by Kidder et al. (2013) that shear heating is not a cause of inverted metamorphism in accretion domains is based on an oceanic subduction beneath an active arc (Kidder and Ducea, 2006). The very high convergence velocity (~10 cm·yr^{-1}) and the high initial geothermal gradients characterising the overriding forearc (Kidder and Ducea, 2006) and the subducting oceanic plate easily and rapidly lead to intense thermal inversion. With low shear heating (~10^{-5} W·m^{-3} implying very low viscosities of about 10^{17} Pa·s), heat advection and conduction dominate the thermal budget: both the overriding plate and the slab are rapidly cooled and the subducting material is progressively and slowly heated. Consequently, the rocks accumulated in the accretion zone are representative of the thermal state of the thrust plane. Understandingly, the thermal peaks are thus colder from the top to the base of the accretion area and such thermal inversion is compatible with the thermochronologic data from the Pelona Schist of southern California (Kidder et al., 2013). Considering a stronger shear heating along the active thrust, which is superposed on the overall cooling pattern, decreases the thermal inversion intensity recorded in the accreted sediments. Nevertheless, such shear heating assumptions are not generally applicable because very low shear stress and viscosities are involved to balance the high strain rate (10^{-12} to 10^{-11} s^{-1}).

Previous studies of syn-deformational intracontinental inverted metamorphism used various models with very different degrees of complexity (e.g., England and Molnar, 1993; Jamieson et al., 2004; Shi and Wang, 1987). However, none of the proposed models is commonly accepted to give a general explanation to the development of syn-deformation inverted metamorphism. Whereas analytical studies provide good mathematical solutions for understanding the respective influence of kinematics and heat diffusion on the thermal evolution, the other factors involved (e.g., erosion, various heat sources, variable kinematic configuration, thermo-dependence laws) are difficult to address analytically but can be solved and quantified numerically.

In the present paper, our goal is not to fit a particular natural case (e.g., the Himalayas). Rather, using a systematic approach, we aim to explore and provide a detailed synthesis of the different conditions required for the formation and preservation of crustal-scale inverted metamorphism along one intracontinental thrust. We define and compare the relative importance of each of the parameters and processes involved: kinematic setting, thrust geometry, erosion velocity, rock properties (in particular the thermal diffusivity), accretion velocity, radiogenic heat production and shear heating. The goal is to infer (i) the conditions required to locally invert the thermal field; (ii) the exact impact of each one of these parameters on the intensity, the location and the duration of the inversion and (iii) the conditions required to preserve the thermal inversion through time. Finally, we discuss how and why shear heating is crucial for the formation and preservation of inverted thermal gradients under realistic kinematic settings.

2. Numerical model

2.1. Initial setup

In order to test independently the influence of the various parameters and processes on the thermal evolution of a crustal thrust, a simple numerical model is defined in which each component can be controlled. The 2D-model setup (Fig. 1a) is focused on the first 80 km of a continental lithosphere, which includes a 30 km thick crust. In order to study the thermal evolution of a major continental thrust zone, a thrust cutting through the whole continental crust with a dip angle θ is simulated by

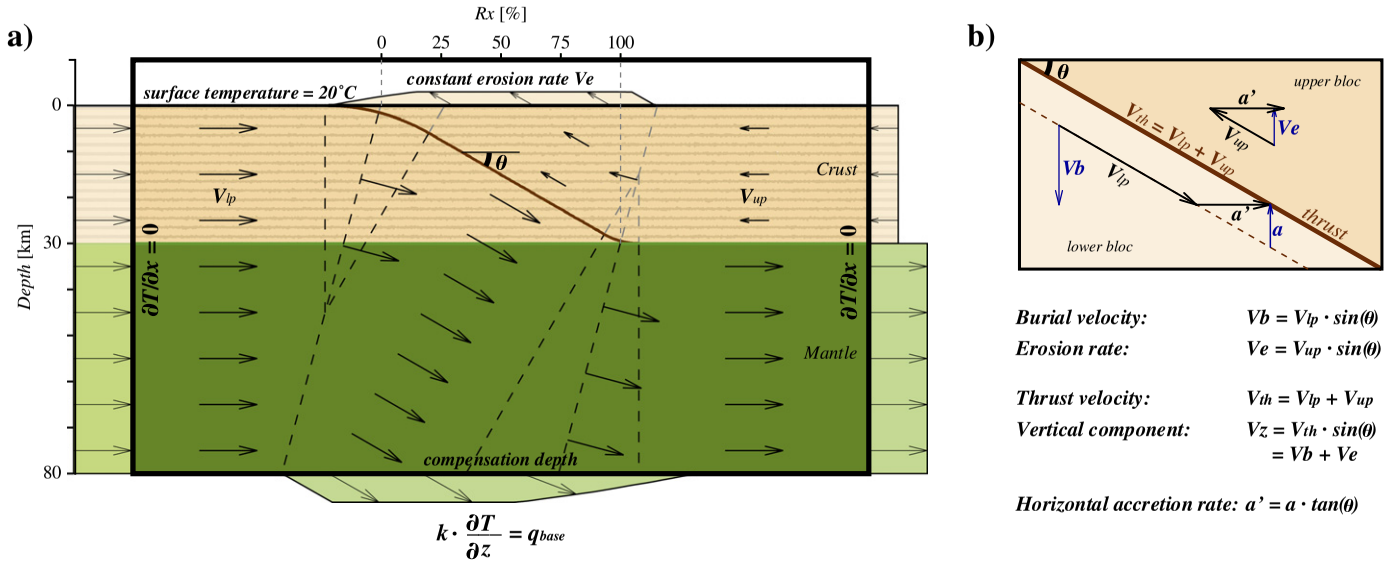

Fig. 1. a) Model setup showing the initial morphology, the imposed velocity field and the thermal boundary conditions. Lower and upper continental blocks are converging at fixed velocities of V_{lp} and V_{up} respectively. θ is the maximum thrust dip angle. The compensation depth for isostatic balancing corresponds to the base of the model. Both surface temperature and mantle heat flux q_{base} are constant. k corresponds to the thermal conductivity. Lateral heat flux is considered to be nil. Rx represents the ratio between the distance to the thrust front and the width of the area concerned by the slanted part of the thrust. b) Terminology of the velocity fields used in this study. V_{th}, Vb, Ve and Vz correspond to the convergence velocity, the burial velocity of the lower plate, the erosion velocity and the vertical component of the thrust velocity, respectively. Accretion is defined by the vertical accretion velocity a. In order to keep the thrust zone fixed with respect to the reference frame, accretion is simulated by imposing a horizontal accretion velocity a' to the entire model. The dashed line represents the theoretical active thrust shifting due to accretion.

imposing a velocity contrast between the downgoing plate and the upper plate, moving with a velocity V_{lp} and V_{up}, respectively (Fig. 1). The convergence velocity V_{th} is consequently given by $V_{th} = V_{lp} + V_{up}$. The thrust is mainly represented by a straight segment, the dip angle of which, however, progressively decreases towards both the base of the crust and the surface in order to avoid any advection errors due to local strong velocity direction contrasts. Since the present study focuses on the slanted part of the thrust and because the temperature evolution around the thrust and in the deepest levels of the fault is not noticeably affected by the configuration of the lower block velocity field beneath the first 30 km (see Appendix A, Fig. A.1), the downgoing plate intentionally lies flat under the upper crust to simplify the boundary conditions and the isostasy computation.

The initial geotherm is defined in the whole model according to the following equation:

$$T(x,z,t_0) = T_{surface} + z \cdot \frac{q_{base}}{k} + T_{source}(x,z) \quad (1)$$

where $T_{surface}$, q_{base}, k and T_{source} are the surface temperature, the mantle heat flux, the thermal conductivity and the possible local heat sources, respectively. Initially, the only implemented heat source is the radiogenic heat production. It is considered as a permanent property of the material and is defined according to the following decreasing exponential law from Turcotte and Schubert (2002):

$$Q(z,t_0) = Q_0 \cdot \exp\left(\frac{-z}{z_r}\right) \quad (2)$$

where Q_0 is the surface radiogenic heat production, and z_r corresponds to the length scale for the decrease in Q with depth (Turcotte and Schubert, 2002) controlling the curvature of the vertical profile of Q. Eq. (2) allows to easily test a wide range of possible distributions of radiogenic production and both parameters Q_0 and z_r, were independently tested. In the presence of radiogenic heat sources, Eq. (1) is then only z-dependent and becomes:

$$T(z,t_0) = T_{surface} + z \cdot \frac{q_{base}}{k} + \frac{Q_0 \cdot {z_r}^2}{k} \cdot \left(1 - \exp\left(\frac{-z}{z_r}\right)\right). \quad (3)$$

2.2. Computation methods

Both kinematic and thermal computations are based on a regular Eulerian grid with a space resolution of 1 km. During the thrust activity, at each time step, advection and thermal diffusion are realised separately in order to minimise the numerical diffusion of temperature inside a non-static environment by using the marker-in-cell method (Gerya, 2010). The advection of rock properties and temperature is ensured by a field of initially randomly distributed particles (see Appendix A for more details). Three kinematic parameters can be distinguished here (Fig. 1b). The first one is the burial velocity Vb of the downgoing plate corresponding to the vertical component of the velocity field V_{lp} and defined by:

$$Vb = V_{lp} \cdot \sin(\theta). \quad (4)$$

The second parameter defines the vertical accretion velocity a. As in previous studies (e.g., Huerta et al., 1996, 1998, 1999; Royden, 1993), accretion is realised at each time step by adding a horizontal velocity component a' (Fig. 1b) in the whole model so that both the active thrust position and the convergence velocity remain fixed. Both parameters are related according to:

$$a' = a \cdot \tan(\theta). \quad (5)$$

The third kinematic parameter corresponds to the maximum erosion velocity Ve linked to the upper plate velocity V_{up} by the following equation:

$$Ve = V_{up} \cdot \sin(\theta). \quad (6)$$

The erosion velocity Ve controls the upper plate velocity V_{up} in the models (Fig. 1b, see Appendix A for more details).

Compared to the tectonic advection times, the isostatic balance is reached instantaneously (Crough, 1977). Thus, at each time step, the isostatic response is calculated in the entire model thereby producing a realistic topography associated with the thrust.

Then, for the thermal part, the following heat equation is solved by using the implicit finite difference method on the Eulerian grid. In order to limit numerical diffusion, the Eulerian computation is coupled with intermediate thermal interpolations with the Lagrangian particles (see Appendix A for more details):

$$\rho \cdot Cp \cdot \frac{\partial T}{\partial t} - \frac{\partial}{\partial x}\left(k\frac{\partial T}{\partial x}\right) - \frac{\partial}{\partial z}\left(k\frac{\partial T}{\partial z}\right) = Q + Hs. \quad (7)$$

The heat equation (Eq. (7)) is composed of a heat diffusion part where ρ, Cp and k are respectively the density, the heat capacity and the thermal conductivity (left side of Eq. (7)) and of a heat production part (right side of Eq. (7)) where Q and Hs represent the radiogenic heat production and the shear heating, respectively.

The parameters ρ, Cp, and k define the capacity of the material to diffuse heat. This property can be reduced to one parameter, the thermal diffusivity κ, defined as $\kappa = k/(\rho \cdot Cp)$. Each one of these three parameters depends on the lithology, but also on the physical environment of the rock (e.g., pressure, temperature). Various empirical laws describe the temperature and pressure dependence of these parameters in rocks (e.g., Abdulagatov et al., 2006; Hofmeister, 2007; Seipold, 1995, 1998; Whittington et al., 2009; Zoth and Hänel, 1988). In the present study, we tested independently the influence of a range of realistic values for each parameter on the thermal evolution around the thrust (see Table 1). First, these values were considered constant in the crust and in the mantle. In a second time, their temperature and pressure dependences are considered and their influence on the thermal field investigated. These results are discussed in Section 3.3.2.

Table 1
Parameters tested in the model.

Symbol	Parameter	Range of tested values	Unit
Kinematic parameters:			
θ	Thrust dip angle	10–35	°
V_{th}	Thrust velocity (convergence rate)	0.5–5	$cm \cdot yr^{-1}$
Vz	Vertical component of V_{th}	$V_{th} \cdot \sin(\theta)$	$cm \cdot yr^{-1}$
V_{lp}	Lower plate velocity	0.5–5	$cm \cdot yr^{-1}$
Vb	Burial velocity	$V_{lp} \cdot \sin(\theta)$	$cm \cdot yr^{-1}$
V_{up}	Upper plate velocity	$V_{th} - V_{lp}$	$cm \cdot yr^{-1}$
Ve	Erosion rate	$V_{up} \cdot \sin(\theta)$	$cm \cdot yr^{-1}$
a	Vertical accretion rate	0–0.2	$cm \cdot yr^{-1}$
a'	Horizontal accretion rate	$a' \cdot \tan(\theta)$	$cm \cdot yr^{-1}$
Rock thermal properties:			
ρc	Crust density	2800	$kg \cdot m^{-3}$
ρm	Mantle density	3300	$kg \cdot m^{-3}$
Cp	Heat capacity	800–1200	$J \cdot kg^{-1} \cdot K^{-1}$
k	Thermal conductivity	2–4	$W \cdot m^{-1} \cdot K^{-1}$
κ	Thermal diffusivity in the crust	$k/(\rho c \cdot Cp)$	$m^2 \cdot s^{-1}$
Heat sources:			
q_{base}	Mantle heat flux	20–40	$mW \cdot m^{-2}$
Q	Radiogenic heat production		$\mu W \cdot m^{-3}$
Q_0	Surface radiogenic heat production	0–4	$\mu W \cdot m^{-3}$
z_r	Specific depth where $Q = Q_0 \cdot e^{-1}$	5–20	km
Hs	Shear heating		$\mu W \cdot m^{-3}$
η	Thrust effective viscosity	10^{19}–10^{21}	Pa·s

Shear heating *Hs* results from the transformation of mechanical energy into heat during deformation and is recognised as a major component of the total energy budget (e.g., Brun and Cobbold, 1980; Chester et al., 2005; Lachenbruch and Sass, 1980). Shear heating is a function of the strain rate and stress tensors ($\dot{\varepsilon}_{ij}$ and σ_{ij} respectively) and is computed according to the following equation:

$$Hs = \sigma_{xx} \cdot \dot{\varepsilon}_{xx} + \sigma_{zz} \cdot \dot{\varepsilon}_{zz} + 2\sigma_{xz} \cdot \dot{\varepsilon}_{xz}. \quad (8)$$

The strain rate tensor is defined as $\dot{\varepsilon}_{ij} = 0.5\left[(\partial V_i/\partial j) + (\partial V_j/\partial i)\right]$ where $\partial V_i/\partial j$ corresponds to the variation of the velocity of the component i in the direction j and the same convention applies for $\partial V_j/\partial i$. Because shear zones related to inverted metamorphism can be several kilometres thick (e.g., Grujic et al., 1996), ductile rheology is generally attributed to the whole thrust (e.g., Jamieson et al., 1996; Kidder and Ducea, 2006; Searle and Rex, 1989). In the present study, the shear zone thickness is space resolution dependent and is thus approximately 1 km. Shear heating is computed in a ductile manner, where stress and strain rate are linked by the effective viscosity η of the material constituting the thrust:

$$\sigma_{ij} = 2 \cdot \eta \cdot \dot{\varepsilon}_{ij}. \quad (9)$$

Viscosity depends on temperature, strain rate and creep parameters (e.g., Carter and Tsenn, 1987; Goetze and Evans, 1979; Ranalli and Murphy, 1987). It tends to decrease with increasing strain rate and temperature (Meissner and Mooney, 1998). Inversely, both the rock deformation and the associated shear heating depend on the viscosity (e.g., Burg and Schmalholz, 2008; Hartz and Podladchikov, 2008). However, in order to better define the first order role of viscosity, we simplified the problem by using a constant viscosity η all within the thrust (see discussion in Section 3.4).

3. Model results

3.1. Burial velocity effects

In order to test the validity of our numerical model, we first realised a comparative study with analytical solutions from England and Molnar (1993). The results are described in Appendix B.

In extreme kinematic configurations (e.g., $V_{th} = 5$ cm·yr^{-1}, $\theta = 30°$), which favour the development of thermal inversion, the thermal evolution around the thrust and in the whole model can be best characterised. In this case, because the initial geotherm is linear, the thermal inversion starts on a large part of the thrust with a relatively homogeneous intensity. Then, the affected area progressively deepens and widens and the maximum intensity is localised towards the deepest levels of the thrust. On each point of the thrust, the vertical temperature gradient $\partial T/\partial z$ first decreases, reaches a minimum value (negative when thermal inversion occurs) and then increases again until a steady state when the temperature advection and the heat diffusion are completely balanced. Nevertheless, even under such extreme kinematic settings, none of the (V_{th}, θ) combinations allows the preservation of the thermal inversion in time beyond the first 6 Myr (see Appendix B, Fig. B.2).

3.2. Erosion effects

In our model, erosion can be activated and is only controlled by the erosion velocity *Ve* (Eq. (6), Fig. 1 and Table 1). In this case, contrary to the previous analysis (Section 3.1, Appendix B), the thrust velocity V_{th} is given by a combination of the lower and the upper plates velocities (V_{lp} and V_{up}, see Fig. 1b). Consequently, in order to test the influence of the erosion velocity independently of the kinematic setting, either the downgoing plate velocity V_{lp} or the thrust velocity V_{th} has to be fixed. Here, we chose to keep constant the thrust velocity V_{th} for two reasons. (i) Kinematic simulations having the same vertical component *Vz* of the thrust velocity (Fig. 1b) are characterised by very similar thermal evolutions (see Appendix B). Each given *Vz* value corresponds to a group of (V_{th}, θ) combinations. This allows us to easily make connections and distinctions between the thermal evolution around the thrust and, on the one hand, the erosion velocity, and on the other hand, the convergence velocity and the thrust dip angle. In comparison with the MCT in the Himalayas which is characterised by a high downgoing velocity of the Indian plate of ~2 cm·yr^{-1} for the last 10 to 20 Myr (e.g., Bilham et al., 1997; Lavé and Avouac, 2000) and a dip angle of ~15 (e.g., Kaneko et al., 2003), *Vz* values of the order of 0.5 cm·yr^{-1} are realistic and greater values are excessive. (ii) A further parametric analysis concerning the shear heating (Section 3.4) takes into account the velocity contrast on the thrust as a major parameter. Controlling the thrust velocity instead of the downgoing plate velocity is thus more practical to compare the combined effects of the kinematic setting, the erosion velocity and the shear heating. The distribution of the velocity field on both sides of the thrust can be described as the ratio between the erosion velocity *Ve* and the vertical component *Vz* of the thrust velocity (see Fig. 1).

Erosion and motion of the upper plate, for a constant V_{th}, do not lead to significant variations of the reached intensity (Fig. 2a) and of the thickness of the affected area (Fig. 2b) of the thermal inversion during the thrust activity. However, it strongly influences its space and time locations. Increasing erosion and hence displacement of the upper plate tends to localise the thermal inversion at shallower depths along the thrust (Fig. 2). Taking out crustal material by erosion leads to progressive cooling of the remaining shallowest material controlled by surface thermal conditions. The maximum thermal inversion intensity is not restricted to the base of the slanted part of the thrust but moves to the surface with increasing erosion velocities. However, because erosion velocities are not sufficiently high to efficiently balance the thermal diffusion, even for extreme cases, thermal inversion cannot occur at very superficial levels along the thrust.

The time of maximum inversion is not significantly changed, even if a slight delay can be noticed. The duration of the thermal inversion is widely extended with erosion. However, if for extreme kinematic and erosion values thermal inversion can be preserved until the steady state, the most realistic kinematic setting tested (corresponding to $Vz = 0.5$ cm·yr^{-1}) never leads to a thermal inversion, whatever the applied erosion velocity (Fig. 2).

Hence, when the displacement along the thrust is entirely ensured by the downgoing plate ($Ve = 0$), temperature on each point along the thrust is continually decreasing until the steady state. When the upper plate velocity V_{up} approximates the lower plate velocity V_{lp}, (i.e., $Ve \approx 0.5Vz$), the thermal evolution along the thrust tends to be reversed. Thus, for $Ve > 0.5Vz$, temperature at a given point of the thrust starts to increase in the beginning of the thrust activity (Fig. 2a, case $Ve = 2Vz/3$) due to the fast exhumation of the deep hot portions of the upper plate. This trend increases with the vertical component *Vz* of the thrust velocity. After reaching a local temperature peak, maximum thermal inversion is quickly reached and the temperature along the whole thrust decreases until the steady state. Actually, the thrust profile flattening in depth limits the temperature increase because the deepest rocks involved in the thrust come from the base of the upper continental block and cannot thus be hotter than the initial Moho temperature.

To summarise, erosion tends to localise the thermal inversion towards shallower depths of the thrust and significantly increases the thermal inversion duration. Nevertheless, it does not affect the intensity and the thickness of the thermal inversion. Furthermore, even in extreme cases, the initial temperature increase on the thrust is limited (maximum 25 °C) and is far from sufficient to account for the high temperatures known in major thrust zones associated with inverted metamorphism.

3.3. Rock properties effects

In the lithosphere, conduction is generally the predominant heat transport mechanism ahead of convection and radiation (Abdulagatov

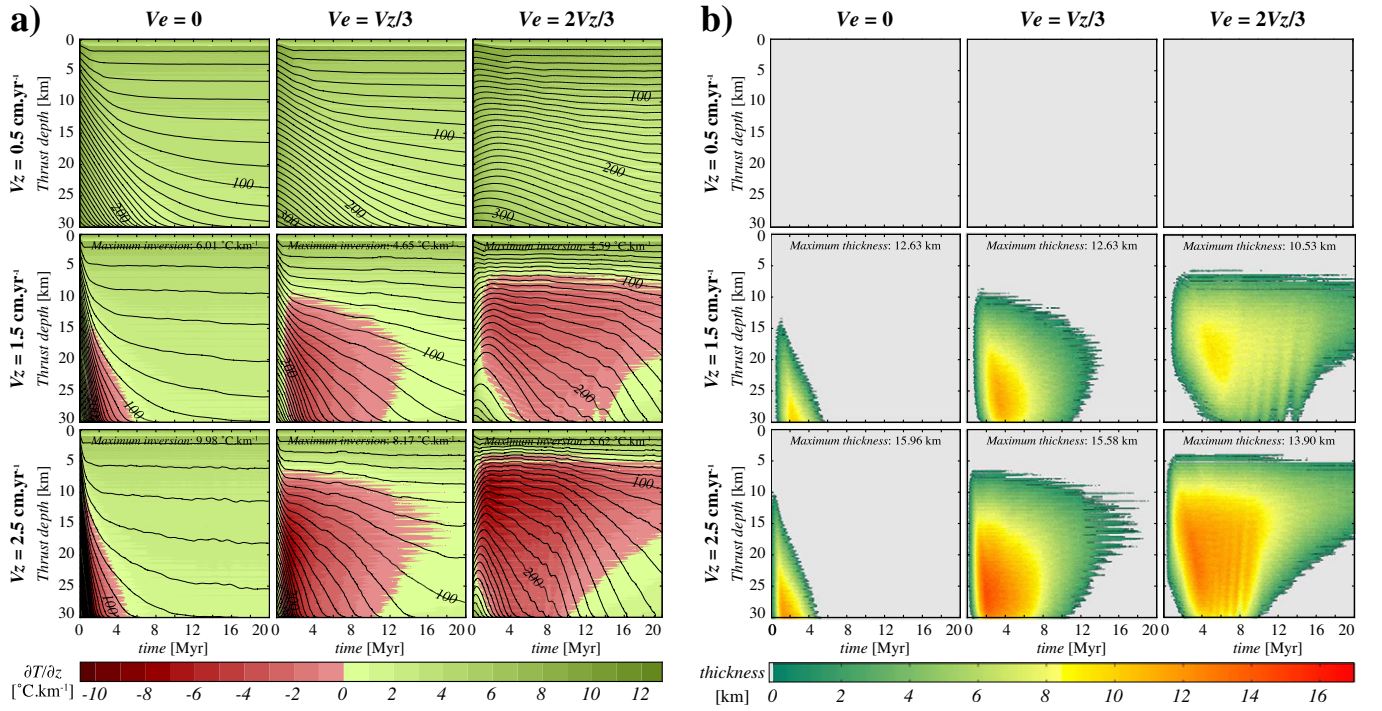

Fig. 2. Thermal evolution along the thrust as a function of the vertical component *Vz* of the thrust velocity and the relative erosion velocity *Ve*. a) Vertical thermal gradient and isotherms along the thrust. b) Vertical thickness of the area affected by the thermal inversion at each point of the thrust.

et al., 2006; Lachenbruch and Sass, 1980). As shown previously in Section 2.2, ρ, *Cp* and *k* constitute the three rock properties involved in the heat diffusion equation. Moreover, as defined by Eq. (3), the initial geotherm in the lithosphere is controlled not only by *k* and the radiogenic heat sources, but also by the basal mantle heat flux q_{base}. These thermal parameters are here considered independently and the impact of the radioactive character of the crust on the thermal evolution around the thrust is also discussed.

3.3.1. Heat diffusion properties and the mantle heat flux

The ranges of realistic values (Table 1) for each thermal parameter depend strongly on the lithology. On the one hand, the *k* values are generally comprised between 2 $W \cdot m^{-1} \cdot K^{-1}$ and 4 $W \cdot m^{-1} \cdot K^{-1}$ (Clauser and Huenges, 1995; Turcotte and Schubert, 2002). This high degree of variability of more than 100% proportionally controls the thermal diffusivity κ with the same order of magnitude. On the other hand, the heat capacity *Cp* varies up to ~50%, from 800 to 1200 $J \cdot kg^{-1} \cdot K^{-1}$ (Waples and Waples, 2004), involving maximum differences for κ of ~30%. Depending on the lithology, the crustal rock density ρ varies from ~2400 $kg \cdot m^{-3}$ for sedimentary rocks to ~3300 $kg \cdot m^{-3}$ for basic eclogites as an extreme case, but is generally comprised between 2500 and 3000 $kg \cdot m^{-3}$ with an associated variability of ~20%. Heat diffusion is therefore mainly controlled by the variation of thermal conductivity, and the influence of the variations of density and heat capacity is less significant (see Appendix C, Fig. C.1). This has two reasons:

First, the hotter is the geotherm (obtained for a low thermal conductivity in the crust or a high mantle heat flux), the higher is the thermal inversion (Fig. 3a, c). The basal heat flux, q_{base}, only involved in the initial and boundary conditions, influences the intensity of the thermal inversion proportionally to the magnitude of its variability. For example, between $q_{base} = 20$ $mW \cdot m^{-2}$ and $q_{base} = 40$ $mW \cdot m^{-2}$, the initial thermal gradient is two times higher and the thermal inversion intensity reached on each point of the thrust is doubled (Fig. 3c). Proportionally to a q_{base} increase, the intensification of the inversion with decreasing *k* is more significant. From $k = 3$ to 2 $W \cdot m^{-1} \cdot K^{-1}$, the thermal inversion is approximately two times higher (Fig. 3a). Thus, the initial thermal structure of the lithosphere, defined by the distribution of both q_{base} and *k*, constitutes a key parameter controlling the intensity reached by the thermal inversion. Nevertheless, the location of the inversion, both in space and time, is mostly insensitive to either q_{base} or *k* (Fig. 3).

Second, the strong correlation between κ and *k* leads the latter to strongly influence the heat diffusion through the thrust. A low thermal conductivity decreases the heat diffusion and thus favours thermal inversion during thrusting. For this reason, the influence of both *k* and q_{base} on the thermal evolution around the thrust is different (Fig. 3). A decrease of *k* induces a more significant intensification of the inversion than an increase of q_{base} (Fig. 3a, c). Furthermore, contrary to the intensification of the basal heat flux, a decrease of *k* induces a widening of the thrust part affected by the inversion, a thickening of the area where the thermal inversion occurs (Fig. 3b, d) and a continuation in time of the thermal inversion (Fig. 3).

3.3.2. Temperature and pressure dependences

Thermal properties also vary as a function of temperature and pressure. Various experiments have been realised and some empirical laws have been proposed in order to define the thermal dependence of the thermal conductivity *k* (Abdulagatov et al., 2006; Clauser and Huenges, 1995; Horai and Susaki, 1989; Seipold, 1998; Voosten and Schellschmidt, 2003; Whittington et al., 2009; Zoth and Hänel, 1988) and heat capacity *Cp* (Waples and Waples, 2004; Whittington et al., 2009). Generally, with increasing temperature, *k* decreases, whereas *Cp* increases. Conversely, thermal conductivity tends to increase with increasing pressure (Abdulagatov et al., 2006; Hofmeister, 2007; Horai and Susaki, 1989; Kukkonen et al., 1999; Osako et al., 2004; Seipold, 1992). However, the pressure effect is limited compared to the influence of temperature (Abdulagatov et al., 2006).

The reported variation of each thermal property as a function of temperature and pressure lies within the range of constant values tested in our numerical simulations (Table 1). Only the variability of *k* has a significant impact on the thermal evolution around the thrust. However,

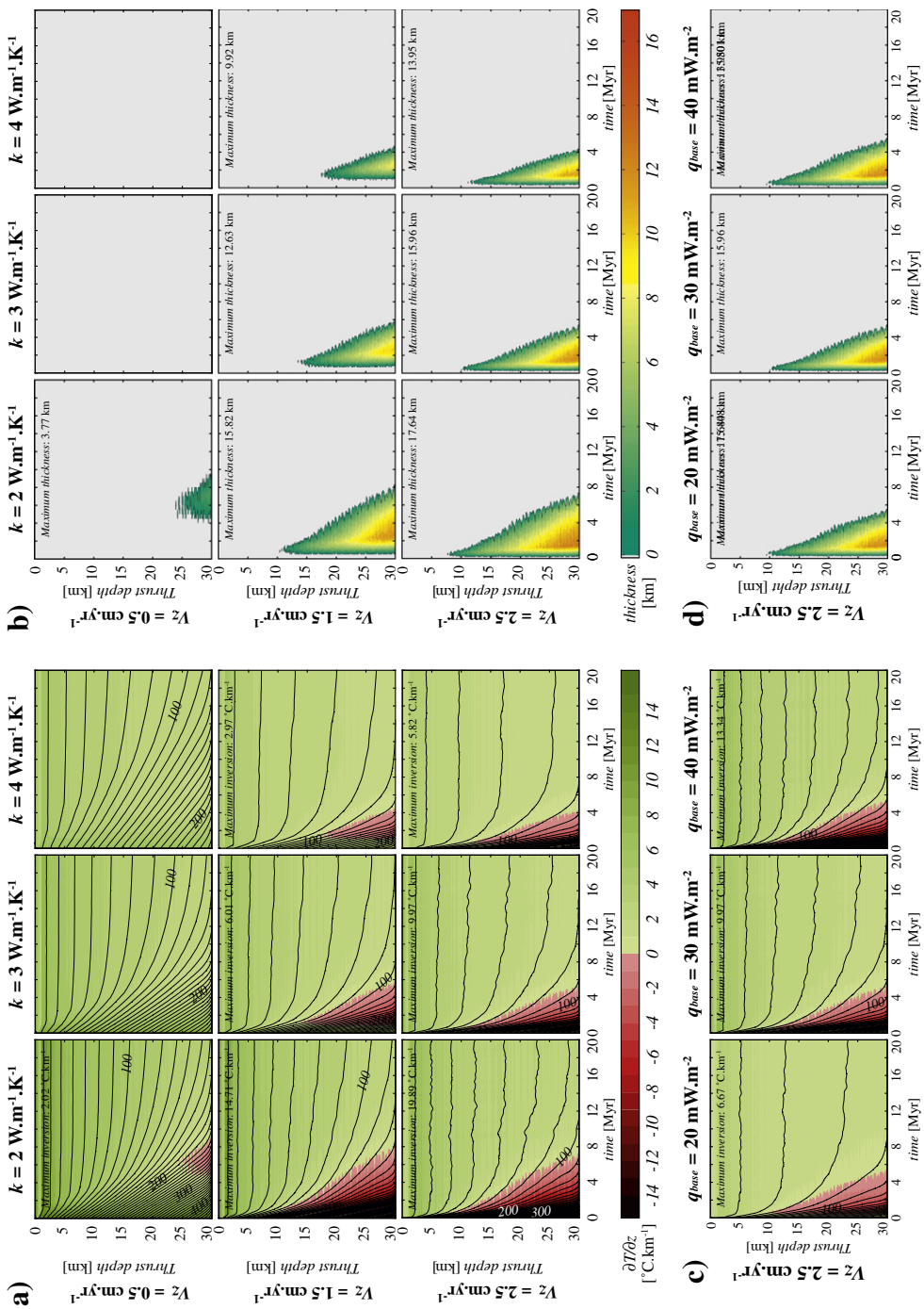

Fig. 3. Thermal evolution along the thrust as a function of the vertical component *Vz* of the thrust velocity and the thermal conductivity *k* (a and b) and the mantle heat flux q_{base} (c and d). Erosion is switched off and no internal heat sources are taken into account. a) and c) Vertical thermal gradient and isotherms along the thrust. b) and d) Vertical thickness of the area affected by the thermal inversion at each point of the thrust.

k depends on both the lithology and the physical environment, and this impact is difficult to quantify. Indeed, in spite of the numerous laboratory experiments (e.g., Abdulagatov et al., 2006; Čermák and Rybach, 1982; Osako et al., 2004), none of the proposed empiric laws (Abdulagatov et al., 2006; Clauser and Huenges, 1995; Seipold, 1998; Voosten and Schellschmidt, 2003; Whittington et al., 2009; Zoth and Hänel, 1988) appears to be undisputable (Fig. 4). Diverse equations relative to the same lithology appear inconsistent with one another (Fig. 4c, d). Furthermore, they are associated with large uncertainties (e.g., Seipold, 1998, Fig. 4a) and rarely integrate both temperature and pressure dependences in the same time (Abdulagatov et al., 2006; Kukkonen et al., 1999).

Regarding only the vertical distribution of the theoretical lithologies (after Turcotte and Schubert, 2002), the thermal conductivity increases from the superficial levels (sediments) to the mantle rocks. On the other hand, within each lithology, k decreases significantly with temperature (and hence depth; Fig. 4). This progressive drop may reach 30–50% from 0 to 600 °C. Concerning the pressure influence, k increases with depth in the shallowest crustal levels due to the reduction of the pore volume (Abdulagatov et al., 2006). Beyond ~100 MPa, k tends to reach a linear behaviour (Abdulagatov et al., 2006; Clauser and Huenges, 1995; Horai and Susaki, 1989), and is supposed to evolve following the thermo-dependence law appropriate for the considered lithology.

To sum up, within the range of realistic values, both Cp and ρ have negligible effects on the thermal evolution of the lithosphere, and the diffusive transport of heat is controlled by the variability of k. The temperature and pressure dependences do not change the order of variability, but they can lead to different thermal behaviours inside the lithosphere (Maierová et al., 2012). In particular, the dependence of the k value on temperature for a given lithology and pressures >100 MPa favours the thermal inversion in depths. These physical and lithologic dependences are generally not taken into account in the numerical models although the values allocated to the thermal conductivity have to be considered with caution (Nabelek et al., 2010).

3.3.3. Radiogenic heat production

As for the heat diffusion properties (Section 3.3.1, Appendix C), numerical simulations were realised in an extreme kinematic context ($V_{th} = V_{lb} = 5$ cm·yr^{-1} and $\theta = 30°$) in order to quantify the effect of the radiogenic heat production. They show that although the radiogenic heat production contributes to the initial geothermal profile, it does not influence the thermal inversion around the thrust in terms of intensity and localisation (Appendix C, Fig. C.2).

The previous analysis revealed that the burial velocity, the erosion velocity and the thermal conductivity of rocks are the main parameters controlling the thermal evolution around a crustal scale thrust. Nevertheless, considering realistic kinematic settings ($V_{th} < 3$ cm·yr^{-1}), none of these parameters allows the preservation of an established thermal inversion in time.

3.4. Shear heating effects

Shear heating constitutes a part of the conservation of energy and a study of the thermal evolution around a thrust during its activity requires taking into account the relative displacement between the two crustal blocks as a source of heat (Brun and Cobbold, 1980; Pavlis, 1986; Toksöz et al., 1971). By considering shear heating in the viscous way, two parameters have to be examined: the strain rate $\dot{\varepsilon}$ and the effective viscosity η within the thrust (Section 2.2, Eqs. (8) and (9)). Since the velocity field is not mechanically computed in our numerical models but imposed, both $\dot{\varepsilon}$ and η can be considered independently. The initial kinematic conditions used here are based on realistic cases for continental collision: the maximum dip angle θ of the thrust set to 15° and the velocity thrust values between 1 and 3 cm·yr^{-1}, implying strain rates from $3 \cdot 10^{-13}$ to 10^{-12} s^{-1}.

In rocks, viscosity is temperature- and strain rate-dependent. Considering an undeformed crust, the viscosity field is characterised by a decrease from ~10^{25} Pa·s in the cold upper crust to ~10^{21} Pa·s in the hot lower crust (e.g., Burg and Gerya, 2005). The interdependence of strain rate and viscosity tends to a steady state and, as an example, with a convergence velocity of 2 cm·yr^{-1}, the viscosity drops to values of 10^{19} to 10^{21} Pa·s within major shear zones (Burg and Gerya, 2005). Consequently, we chose to apply this range of viscosity values, constant in time and space along the thrust. In our kinematic models, the strain field is only localised along the thrust (Fig. 1) thus limiting the frictional heat production to the shear zone. In order to highlight the effects of shear heating, no additional heat source is taken into account, and the erosion is not considered so that the downgoing plate only ensures the displacement along the thrust.

The theoretical amount of heat produced (Eq. (8)) along the thrust is very sensitive to even small variations of viscosity (Fig. 5c). Considering the lowest viscosity ($\eta = 10^{19}$ Pa·s) and strain rate ($\dot{\varepsilon} = 3.17 \cdot 10^{-13}$s^{-1}), the resulting frictional heat produced ($Hs \approx 4$ μW·m^{-3}) is of the same order of magnitude as the maximum realistic radiogenic heat production (Table 1). A viscosity increase induces a proportional increase of shear heating along the thrust. For example, an increase of $10^{0.25}$ Pa·s will typically result in an elevation of ~$10^{0.25} = 178\%$ of the produced heat (Fig. 5c). This way, (i) shear heating can efficiently balance the diffusive cooling of the overriding plate. For high viscosity values, the thermal gradient above the thrust

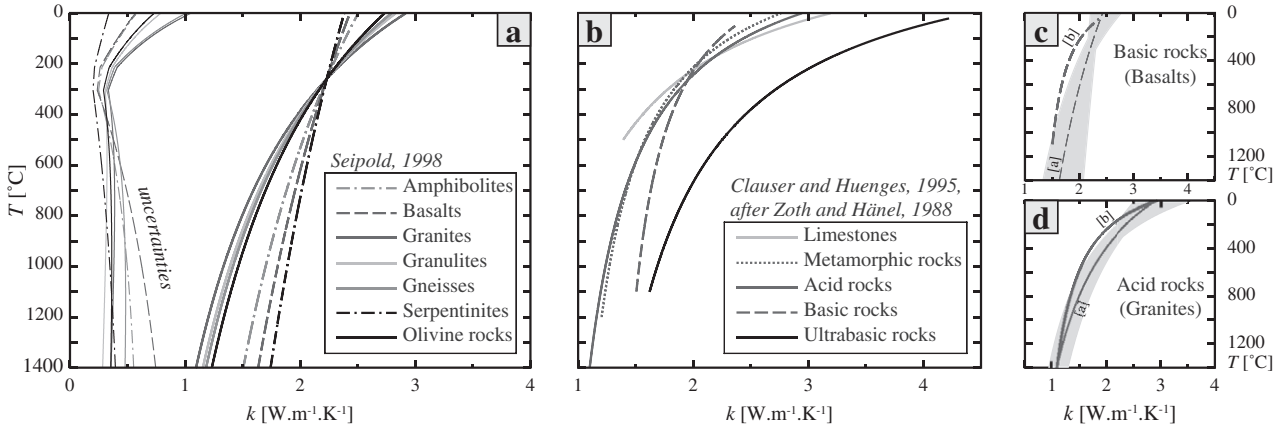

Fig. 4. Empirical thermo-dependence laws for k for various lithologies. a) Seipold (1998). Fine lines show the variations of the uncertainty for each rock type as a function of temperature. b) Clauser and Huenges (1995), after the relation proposed by Zoth and Hänel (1988). Uncertainties are unknown. c) and d) Comparison of thermo-dependence laws illustrated in (a) and (b) for two rock types: basic (c) and acid (d). Grey band is the uncertainty from (a).

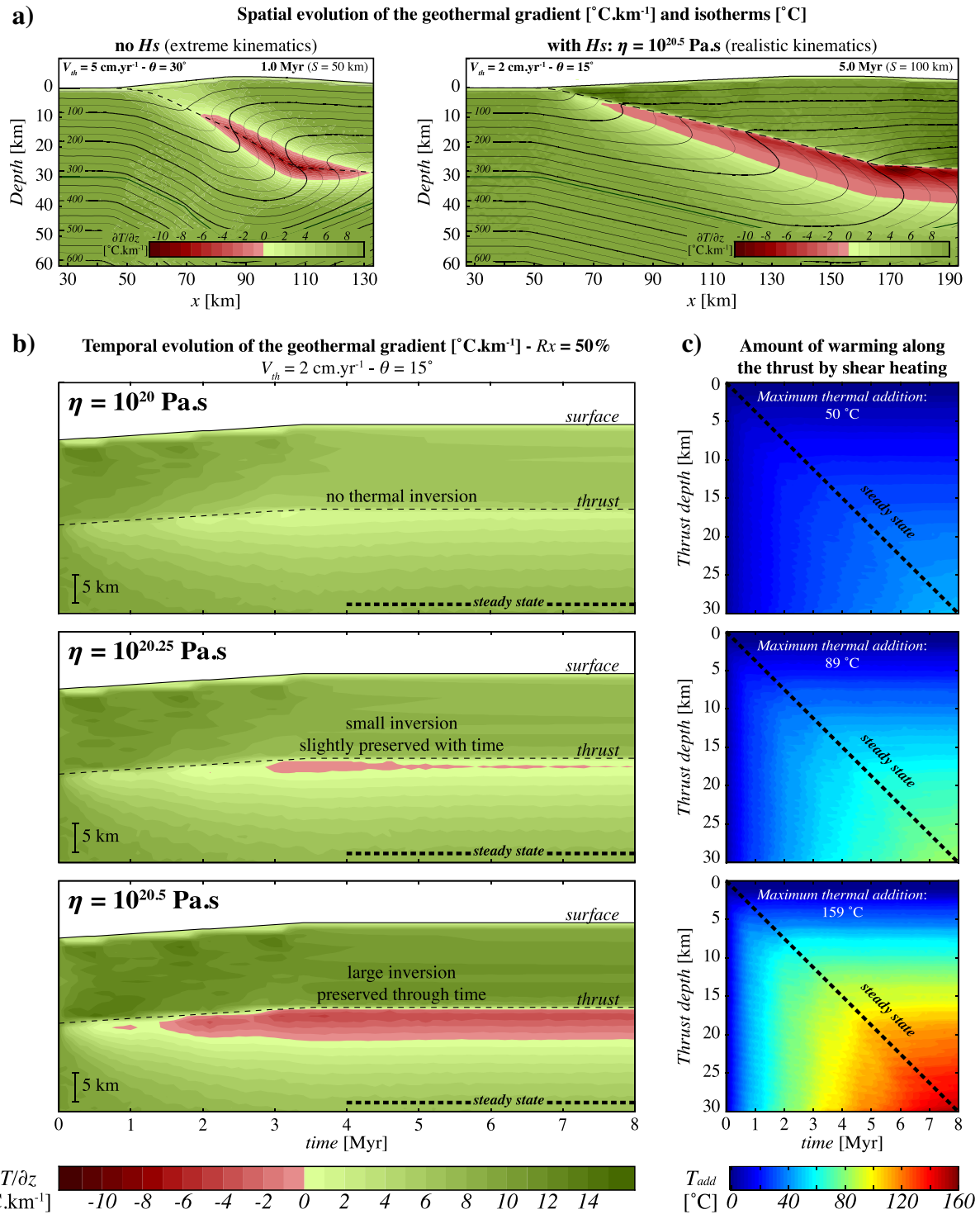

Fig. 5. a) Influence of the shear heating *Hs* on the spatial evolution of the geothermal gradient and isotherms, and on the location of thermal inversion. [Left] Without shear heating and under extreme kinematic conditions ($\theta = 30°$ and $V_{th} = 5$ cm·yr^{-1}). Thermal evolution 1 Myr after the thrust activity starting, i.e., at the maximum thermal inversion. [Right] Thermal evolution with shear heating at viscosity $\eta = 10^{20.5}$ Pa·s after 5 Myr, when the thermal steady state has been reached (kinematic conditions are: $\theta = 15°$ and $V_{th} = 2$ cm·yr^{-1}, i.e., $\dot{\varepsilon} = 6.34 \cdot 10^{-13}$ s^{-1}). *S* is the cumulative shortening. b) Temporal evolution of the geothermal gradient along a vertical profile located in the centre of the model (*Rx* = 50%, Fig. 1) according to three different constant viscosities: $\eta = 10^{20}$ Pa·s, $\eta = 10^{20.25}$ Pa·s and $\eta = 10^{20.5}$ Pa·s. c) Corresponding thermal increment by shear heating along the thrust during its activity.

can be elevated beyond the initial crustal geotherm. Consequently, if the heating produced by shearing becomes higher than the cooling driven by the underthrusting of cold material, the surface heat flow at the top of the upper block increases during thrusting (Hartz and Podladchikov, 2008). (ii) The thermal budget at the top of the downgoing crust has two sources: the transfer by diffusion of the heat inherited in the upper block and the shear heating along the thrust. Consequently, in the presence of shear heating, the maximum thermal perturbation appears and develops under the thrust, whereas it straddles the thrust when shear heating is not considered (Fig. 5a, b).

As shown in Fig. 6, the amount of heat produced by shearing leads to an intense thermal inversion characterised by a significant thickening of

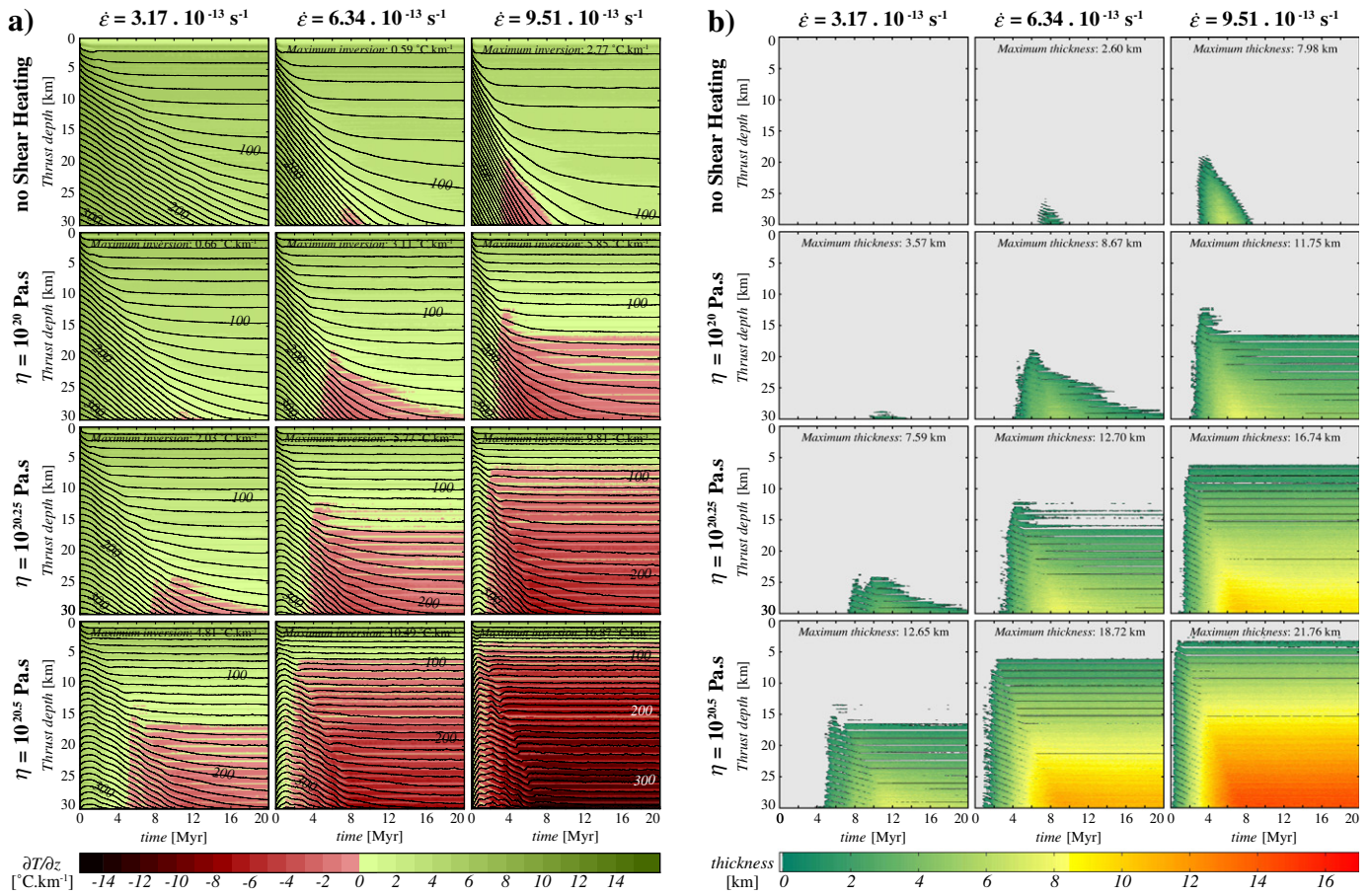

Fig. 6. Impact of shear heating on the thermal evolution along the thrust during the convergence as a function of strain rate $\dot{\varepsilon}$ and viscosity η. a) Vertical thermal gradient (colour scale) and isotherms (black lines) at 1 km under the thrust, i.e., close to the maximum thermal inversion for each vertical profile across the crust. b) Vertical thickness of the area affected by the thermal inversion on each point of the thrust.

the area affected and to a long duration. Unlike the other situations considered, shear heating allows the preservation of the thermal inversion in time until the steady state under realistic kinematic settings (V_{th} = 1–3 cm·yr^{-1}; Figs. 5b and 6).

Thermal inversion intensities, even at shallow depths, can exceed 100 °C·km^{-1} and temperatures extend up to more than 1000 °C (Fig. 7). Both ranges of temperatures between 500 and 700 °C and of thermal inversion intensities from 10 to 50 °C·km^{-1} are reached between 20 and 30 km depths for different combinations of viscosity and convergence velocity (Fig. 8). Consequently, shear heating alone can reproduce and preserve in time thermal features comparable to natural occurrences of inverted metamorphic sequences. Furthermore, our model suggests that, in these cases, viscosity values within the thrust zone have to range between 10^{20} and 10^{21} Pa·s (Fig. 8).

In short, for small variations of viscosity or strain rate across a thrust (constant width of the sheared area), the thermal inversion is strongly influenced by shear heating in terms of intensity, space and time location. Although shear heating does not necessary imply an inversion, it plays a major role in the preservation of the perturbation in time.

3.5. Shear heating, accretion and radiogenic heat production competition

Accretion processes were implemented while keeping shear heating in action along the active thrust. As previously, the thrust dip angle θ was set to 15°. The convergence velocity V_{th} was fixed at 2 cm·yr^{-1} and no erosion process was considered. The vertical accretion velocities a tested were 1 and 2 mm·yr^{-1} and are comparable to the values used in previous works (Bollinger et al., 2006; Huerta et al., 1996, 1998, 1999; Kidder et al., 2013; Royden, 1993). In order to evaluate the thermal influence of accumulation of radioactive material in the accretion prism, an elevated accretion velocity (a = 2 mm·yr^{-1}) was considered and two radiogenic profiles (Eqs. (2) and (3)) characterised by a common surface radiogenic heat production Q_0 = 2 μW·m^{-3} but differing in the specific depth z_r were tested: (i) a realistic configuration with z_r = 15 km and (ii) an extreme case with z_r = 30 km such that the whole continental crust is highly enriched in radioactive elements. Mantle flux was adapted to each thermal configuration in order to ensure a realistic initial temperature at the base of the crust between 420 and 500 °C.

Results are synthesised in Fig. 9 in terms of maximum thermal inversion intensity and maximum temperatures reached in the thrust zone after the thermal steady state is attained. Whether we take into account accretion and radiogenic heat production or not, no significant thermal inversion occurs if the viscosity η is lower than $10^{20.25}$ Pa·s. Low viscosity implying low amounts of shear heating (Eqs. (8) and (9)), it follows that, in the framework of realisitc kinematic and thermal settings, it is impossible to reproduce metamorphic inversions comparable to natural observations by considering accretion processes only. Conversely, if η exceeds 10^{21} Pa·s, temperatures and geothermal gradients within the thrust zone are excessively elevated whatever the depth considered. Thus, under a given kinematic context, the range of viscosities leading to realistic thermal inversions is relatively narrow, of the order of 10^{20} to 10^{21} Pa·s (Figs. 8 and 9).

The concomitance of accretion and shear heating implies that material previously deformed and warmed within the thrust zone is accumulated in the hanging wall while subjacent volumes are in turn sheared and heated. For low amounts of shear heating, upward heat transfer by

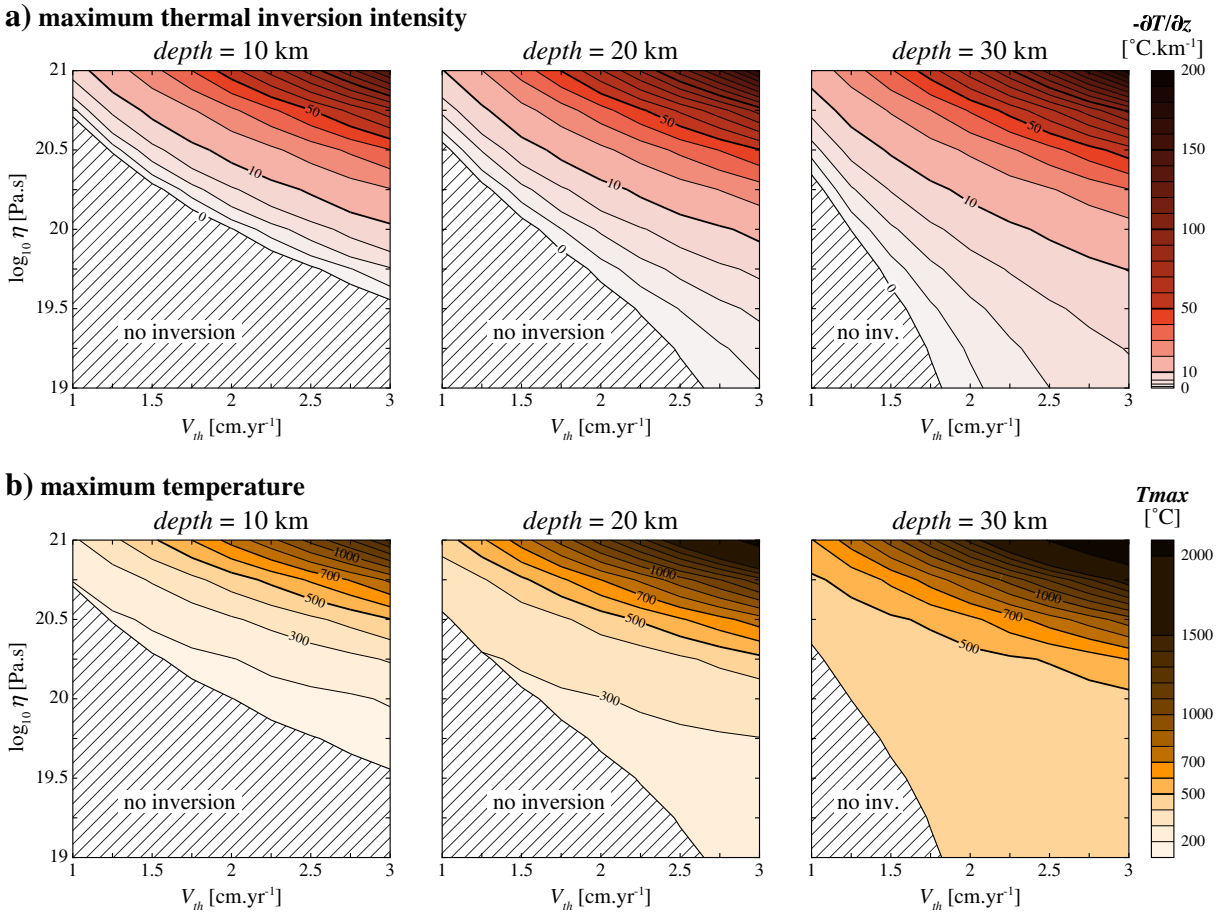

Fig. 7. a) Maximum thermal inversion intensity reached beneath the thrust zone in the presence of shear heating and after the thermal steady state has been reached (10 Myr). Mantle heat flux is set to 40 $mW \cdot m^{-2}$ and no radiogenic heating is considered such as the initial Moho temperature is 420 °C. The thrust dip angle is defined to 15°. Results are given as a function of convergence velocity V_{th}, viscosity η and depths (10, 20 and 30 km). b) Maximum temperature. Hatched areas indicate the combinations (V_{th}, η) for which no thermal inversion occurs.

accretion leads to a smaller perturbation on the geothermal gradient around the active thrust (Fig. 9a) and no change in the maximum temperatures (Fig. 9b). Conversely, when shear heating is significant, accretion of hot material efficiently reduces the heat diffusion from the thrust zone to the overriding plate. Thermal inversion in the active thrust zone is consequently more intense and this trend is more pronounced in depth. However, because the material heated in the shear zone is continuously moved upwards out of the active shear zone, the maximum temperatures are significantly lower (e.g., about 50 °C lower with a 2 $mm \cdot yr^{-1}$ accretion velocity and $\eta = 10^{20.5}$ Pa·s. and almost 100 °C lower with a 1 $mm \cdot yr^{-1}$ accretion velocity and $\eta = 10^{20.75}$ Pa·s.) (Fig. 9b).

Accretion of radioactive material associated with shear heating has no significant effect on the maximum intensity of thermal inversion, even if extremely radioactive crustal material is considered (Fig. 9a).

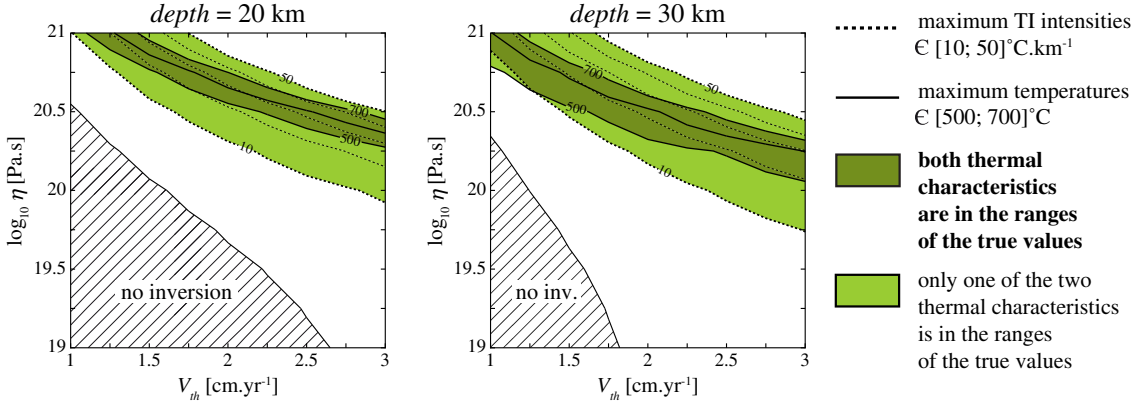

Fig. 8. Combination of maximum thermal inversion intensity and maximum temperature from results presented in Fig. 7 at 20 and 30 km depth. Ranges of values are selected with respect to the reported thermal characteristics of intracontinental inverted metamorphic sequences. Maximum temperatures are drawn for values of 500, 600 and 700 °C (continuous lines). Maximum inverted geothermal gradients are represented from 10 to 50 $°C \cdot km^{-1}$ (dashed lines). Dark green areas represent the combinations (V_{th}, η) for which both thermal characteristics are in the range of values considered as "realistic". Hatched areas indicate the combinations (V_{th}, η) for which no thermal inversion occurs.

Because the top of the downgoing plate is highly radioactive, the maximum temperatures reached along the thrust are obviously hotter than without radiogenic heating.

In short, whatever the accretion velocity or the radiogenic heat production, even in extreme cases, none of these processes can lead to thermal inversion without shear heating in the framework of realistic kinematic and thermal settings. Furthermore, maximum thermal features in the thrust zone are more influenced by small viscosity variations than by high changes of the accretion velocity and of the amount of radiogenic heating.

3.6. Shear heating and erosion

On the one hand, surface denudation enhances the localisation of the thermal inversion at shallower depths and can lead to increased temperatures along the thrust (see Section 3.2). On the other hand, shear heating strongly influences the crustal thermal budget and highly intensifies the thermal inversion (see Sections 3.4 and 3.5). Consequently, numerical simulations taking into account both processes are necessary to complete our parametric study (Fig. 9). Here again, tests were performed with a thrust dipping 15° and a convergence velocity V_{th} of 2 cm·yr^{-1}. Accretion and radiogenic heat production were switched off. Viscosities ranged between 10^{19} and 10^{21} Pa·s and erosion velocity was set to $Ve = 2$ mm·yr^{-1}. This results in 38% of the thrust velocity V_{th} being ensured by the upper plate velocity V_{up}.

When the hanging wall velocity partially ensures the convergence (i.e., erosion is taken into account), maximum temperatures attained in and along the thrust zone are significantly rised (Fig. 9b). As an example, at 20 km depth, a 2 mm·yr^{-1} erosion velocity induces an increase of the maximum temperature of 80° for $\eta = 10^{20.25}$ Pa·s, of 110° for $\eta = 10^{20.5}$ Pa·s and of 140° for $\eta = 10^{20.75}$ Pa·s. This thermal jump increases with the viscosity. More generally, the maximum temperatures recorded along the thrust for a such erosion velocity ($Ve = 2$ mm·yr^{-1}) show an increase of 10 to 18% at 30 km depth, of 20 to 25% at 20 km depth and 19 to 32% at 10 km depth. Thermal influence of erosion is thus significantly intensified when shear heating is important, whereas it is almost negligible at low frictional heat production. However, if exhumation of the overthrusting rocks favours the thermal raise, its influence is inconsiderable with regard to the thermal perturbation intensity (Fig. 9a). Erosion velocities greater than 2 mm·yr^{-1} yield similar results and follow the same trend.

To sum up, concomitance of erosion processes with shear heating along a major thrust in realistic configurations (i.e., $Ve < Vb$) does not lead to significant variations in the maximum thermal inversion intensity. But the maximum temperatures reached along the thrust are highly increased by several tens of degrees.

4. Discussion and conclusions

Through the present parametric study, we tested and compared the relative influences of the different processes and parameters involved in

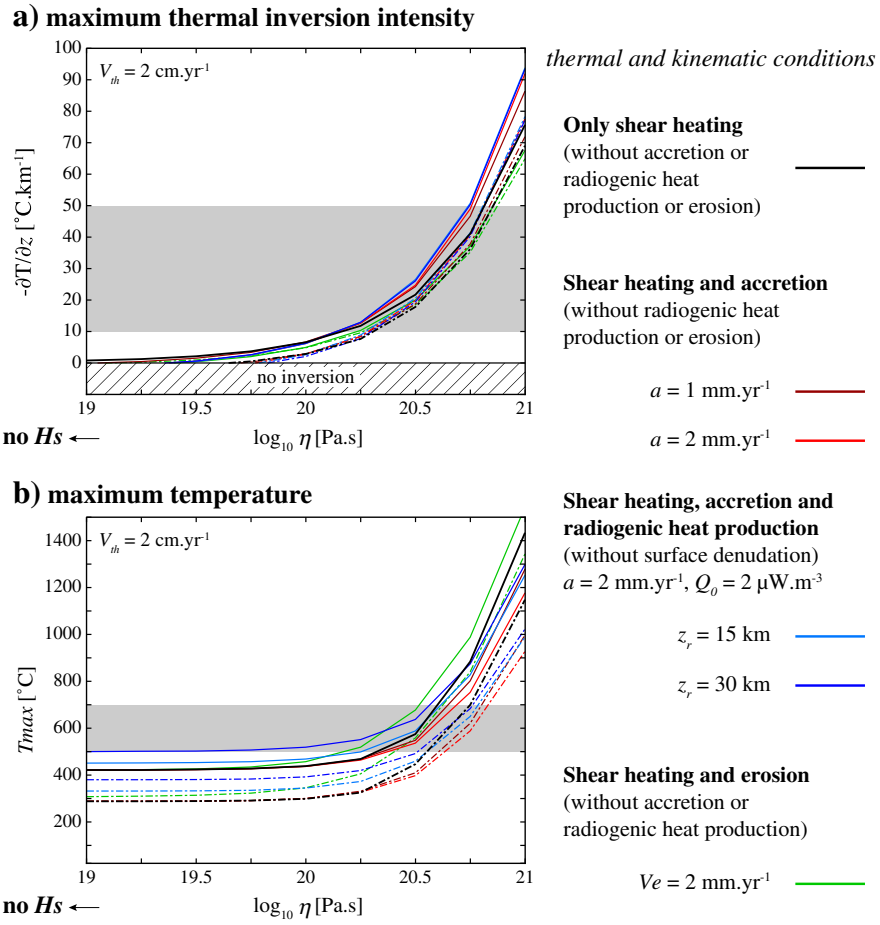

Fig. 9. a) Maximum thermal inversion intensity and b) maximum temperature from the thrust zone in the presence of shear heating, accretion processes and/or radiogenic heat production or surface denudation after 10 Myr (thermal steady state is reached). Results are given as a function of the viscosity η and are plotted for 20 km (dashed lines) and 30 km depth (continuous lines). The numerical simulations were realised at a convergence velocity V_{th} set to 2 cm·yr^{-1}, with a thrust dip angle $\theta = 15°$ and a mantle heat flux $q_{base} = 40$ mW·m^{-3}. The grey areas correspond to the ranges of inverted thermal gradients and metamorphic peak temperatures characterising natural intracontinental inverted metamorphic sequences (see Sections 3.5 and 3.6 for details about the radiogenic, accretion and erosion conditions). Hatched area in (a) delimits the range of geothermal gradients not inverted.

the thermal evolution in space and time of the continental crust around a major thrust zone:

(i) the kinematic configuration of the thrust, i.e., the thrust dip angle, the convergence velocity, and the distribution of the thrust velocity on both sides of the shear zone (expressed here as the erosion velocity);
(ii) the thermal rock properties controlling the heat diffusion across the rocks, i.e., the thermal conductivity, the heat capacity and the density;
(iii) the heat sources, i.e., the basal mantle flux, the internal radiogenic heat production, including the accretion of radioactive material, and the mechanical energy converted into heat along the thrust during its activity (shear heating).

The initial kinematic configuration plays a major role. Whereas the thermal perturbation around the thrust increases in depth with increasing burial velocity of the downgoing plate, erosion localises the perturbation towards shallower depths of the crust and significantly increases its duration. However, for identical convergence velocities, any changes in the erosion velocity do not impact the intensity and the thickness of the thermal inversion contrary to the thermal conductivity. Nevertheless, whereas a limited and transient thermal inversion can be achieved in extreme kinematic configurations, inversion is never observed in the range of reasonable (reported from nature) values of these parameters. Among all the processes and parameters tested, only shear heating allows the preservation of an intense thermal inversion through time under realistic kinematic schemes.

4.1. The thermal conductivity problem

The thermal conductivity, in the range of realistic values (i.e., between 2 and 4 $W \cdot m^{-1} \cdot K^{-1}$), has a major influence on the heat transfer by diffusion and on the initial geothermal gradient. Consequently, it strongly influences the local thermal gradient during the thrust activity, and when thermal inversion occurs, the intensity of this perturbation (Appendix C). As a rule, the initial thermal structure of the lithosphere is an important parameter to take into account in the models. However, tests comparing the thermal evolution of crusts with an identical initial temperature field but different thermal conductivities (the slope of the initial geotherm is thus balanced by the amount of mantle heat flux) attest to the significant effect of k on the intensity and duration of the thermal inversion (Appendix C).

Whereas the thermal conductivity (or thermal diffusivity) is generally considered to be constant in numerical models, it strongly depends on both the lithology and the physical environment, more particularly the temperature. The choice of the k values (Maierová et al., 2012; Nabelek et al., 2010) and corresponding empirical laws chosen in the numerical thermal models are capital and can lead to significant differences of the thermal behaviour of the lithosphere. For pressures higher than 100 MPa, the pressure effect is negligible and the thermal influence dominates with a strong decrease of k of ~1 $W \cdot m^{-1} \cdot K^{-1}$ for temperatures ranging from the surface to the base of the crust. Empirical thermo-dependence laws for various rock types were developed for atmospheric pressures. Empirical laws describing the evolution of k as a function of temperature under pressures higher than 100 MPa should give a better estimation of the thermal conductivity field in the crust for a given lithology. Furthermore, metamorphic reactions occurring along and across the thrust, the varying amount of fluids in the rocks and the possible associated chemical changes linked to their circulation and/or chemical diffusion have also an impact on the evolution of the thermal conductivity of a given rock. These parameters are difficult to integrate in the models at present, but may have significant effects.

4.2. Shear heating, the key parameter

Shear heating, as defined in this paper and in the majority of other numerical models, considers that the whole energy required to overcome the fault friction is converted into thermal energy. However, this is a simplification and other energy transfers should be taken into account and their influence on the formation and preservation of the inverted thermal gradient tested. (i) The energy dissipated during a continuous deformation is not entirely converted into heat but can also be used to change the physical properties of the rock inside the sheared area (e.g., the rock microstructure; Brun and Cobbold, 1980). (ii) Metamorphic reactions occurring within and astride the shear zone can significantly consume or release heat (Anderson et al., 1978; DeVore, 1983; Oxburgh and Turcotte, 1976; Peacock, 1987a, 1987b, 1990). (iii) Potential strain and gravitational energy (Kanamori and Rivera, 2006) can be transformed into pressurisation heat without displacement along the fault. Although these aspects should be taken into account in order to refine the general picture, they are not expected to modify the first-order message delivered by the modelling presented here.

Indeed, our results show that without shear heating, the occurrence of thermal inversion requires extreme kinematic configurations (e.g., Kidder et al., 2013) and is systematically transient (a few million years), and the inversion paroxysm is reached astride the thrust. In such a case, in order to preserve the trace of the thermal inversion in metamorphic parageneses (i.e., to avoid that any other metamorphic event significantly overprints the inverted record), exhumation of the whole sequence needs to be initiated during the short period of time concerned by the inversion (some Myr) and to be extremely fast with a very high associated erosion velocity. On the other hand, under realistic kinematic configurations for intracontinental thrusts (up to 3 $cm \cdot yr^{-1}$), shear heating is the only parameter which allows the preservation of the thermal inversion in time until the thermal steady state. It also significantly influences the spatial location and extent of the thermal inversion: (i) frictional heating along the thrust causes the localisation of the inversion area under rather than astride the thrust, within the uppermost levels of the lower plate, and (ii) the more frictional heat is produced, the thicker is the area affected by the thermal inversion leading to inversion zones up to tens of kilometres thick. The amount of heat produced depends on the local strain rate and the shear zone viscosity (Eq. (8)). The values of both parameters, and particularly the effective viscosity, strongly influence the crustal scale thermal perturbation, especially in terms of thermal inversion intensity.

The present study attests that shear heating is the key-parameter and allows to reproduce thermal features coming from natural inverted metamorphic sequences (Fig. 8). Both the high metamorphic peak temperatures (500–700 °C at 8–11 kbar; e.g., Corrie and Kohn, 2011; Guillot, 1999; Pitra et al., 2010) and the thermal inversion intensities (generally comprised between 10 and 50 $°C \cdot km^{-1}$; e.g., Kohn, 2008; Pitra et al., 2010) can be reproduced. In parallel, our results suggest that the development and preservation of such inverted metamorphic zoning in realistic kinematic and thermal setting require that the viscosity of the material involved has to be between 10^{20} and 10^{21} Pa·s.

4.3. Applicability to the Himalayan inverted metamorphism

The MCT in the Himalayas is characterised by a dip angle of 15° (e.g., Kaneko et al., 2003) and a downgoing velocity of the Indian plate of 2 $cm \cdot yr^{-1}$. (e.g., Bilham et al., 1997; Lavé and Avouac, 2000). High metamorphic temperature peaks within the MCT reach 600 to 650 °C and pressure peaks are of 8 to 11 kbar (e.g., Corrie and Kohn, 2011; Guillot, 1999; Macfarlane, 1995), corresponding to depths of about 30–40 km (assuming that these pressures correspond to lithostatic pressures). In agreement with the kinematical constraints, Fig. 8 shows that shear zone viscosity of $10^{20.5}$ to $10^{20.6}$ Pa·s is required to reproduce such maximum temperatures. The corresponding steady state

thermal inversion intensity is 20 to 30 °C·km^{-1}, hence matching the estimates extracted from Kohn (2008).

By taking into account erosion and accretion of radioactive rocks, as proposed by previous studies (e.g., Bollinger et al., 2006; Huerta et al., 1998) the range of consistent viscosities is slightly extended to $10^{20.35}$ to $10^{20.65}$ Pa·s and the corresponding maximum thermal inversion intensity spreads between 20 and 40 °C·km^{-1} (Fig. 9). Whether or not accretion and surface denudation are considered, the thermal features of the inverted metamorphic zoning across the MCT can simply be reproduced by using shear heating and involving viscosities in the shear zone close to those commonly expected (e.g., Burg and Gerya, 2005).

Hence, our model, without pretending to explain the inverted metamorphism related to the MCT, shows that the downgoing of the Indian plate under the Himalayan belt with kinematical constraints from previous works associated with shear heating can reconcile: (i) the simultaneous increase of pressure and temperature conditions within the lower unit; (ii) the metamorphic temperature peaks recorded within the thrust zone as maximum temperatures reached and representative of the thermal steady state; (iii) the order of thermal inversion intensity and (iv) the location of such a thermal inversion mainly below and across the thrust zone. Furthermore it does not contradict the possible concomitance of accretion processes and surface denudation that, in a very lesser extent compared to shear heating, modify the characteristics of the thermal inversion.

Acknowledgements

We thank L. Le Pourhiet, T. Duretz and D. May for fruitful discussions and their numerical advices. Stimulating discussions with M. Ballèvre and P. Gautier at the onset of this work were greatly appreciated. We also thank P. Tackley and D. May for the material support (ETH Brutus cluster). This paper benefited from thoughtful and careful revisions from S. Guillot, S. Schmalholz and an anonymous reviewer.

Appendix A. Computation method complements

A.1. Continental collision vs. continental subduction

The velocity field configuration of the downgoing plate beneath the first 30 km has a negligible influence on the thermal evolution around the thrust (Fig. A.1).

A.2. Interpolation computations between nodes and particles

They are realised by using a weight interpolation scheme (Gerya, 2010) between the Lagrangian particles and the Eulerian nodes. The interpolation from particles to nodes is realised on 1 cell by using at least 25 particles per cell. This constitutes a good compromise between the time needed for interpolation calculations and the generated numerical error (Yamato et al., 2012).

A.3. Advection computations

At each time step, the velocity field corresponding to the tectonic advection (both V_{lp} and V_{up}) is computed on each particle. The velocity direction of each particle is defined as parallel to the nearest segment of the thrust. In order to avoid a sharp variation of the velocity field on particles, the thrust profile was intentionally smoothed at the border of its slanted part (Fig. 1). The magnitude and the sign of each particle velocity are defined by its location relative to the thrust. Particles are then advected by using the Runge–Kutta method. A Courant criterion maximising the advection to a half-cell by time step associated with the second-order Runge–Kutta method leads to an accurate advection

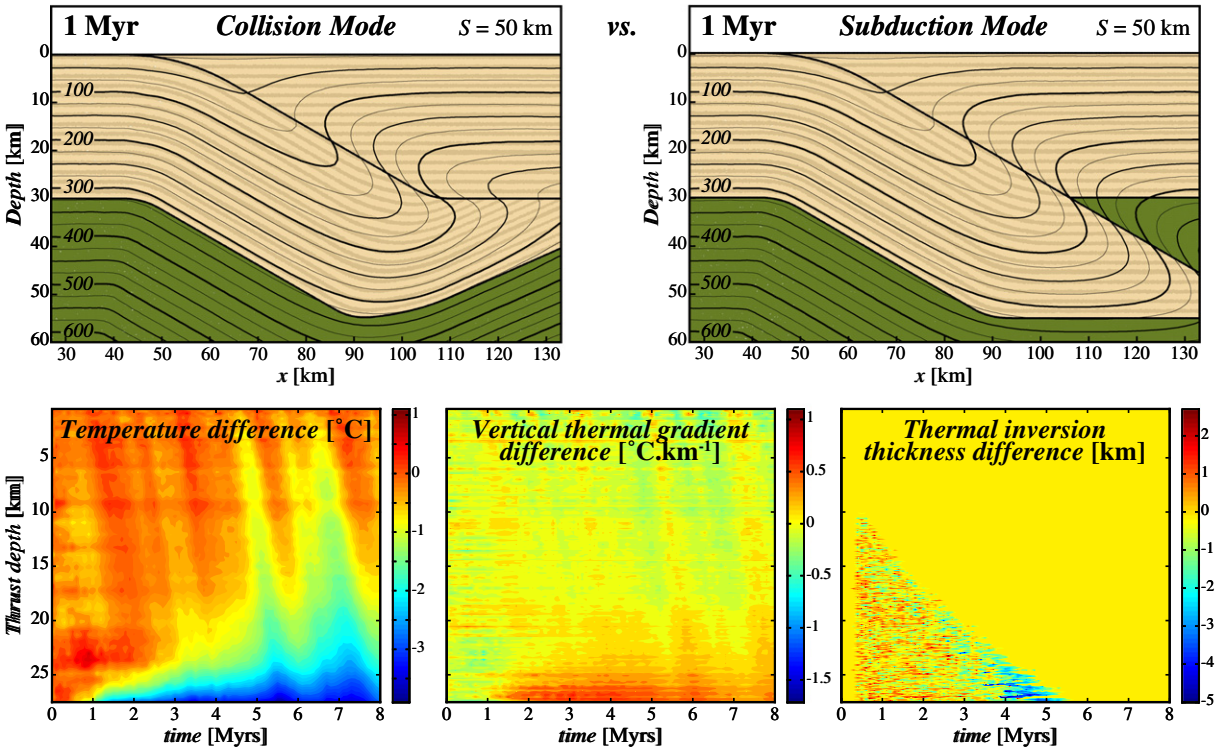

Fig. A.1. Comparison between two velocity field configurations: "Collision mode", in which the downgoing plate lies flat under the crustal part of the upper plate, and "Subduction mode", in which it subducts into the mantle without change of direction. Isostatic balance is switched off. In order to highlight the thermal characteristics differences between both models, computations were realised under extreme kinematic conditions: $V_{th} = 5$ cm·yr^{-1} and $\theta = 30°$. [top] Snapshots and corresponding isotherms (in °C) of both models after a 1 Myr convergence (amount of shortening $S = 50$ km), i.e., when the thermal inversion reached its paroxysm. [bottom] Differences of characteristic values of the thermal evolution along the thrust between the "Collision mode" and the "Subduction mode": temperature, vertical thermal gradient and thickness of the thermal inversion, respectively from left to right. For each characteristic value, the difference between both models is minor compared to the absolute values.

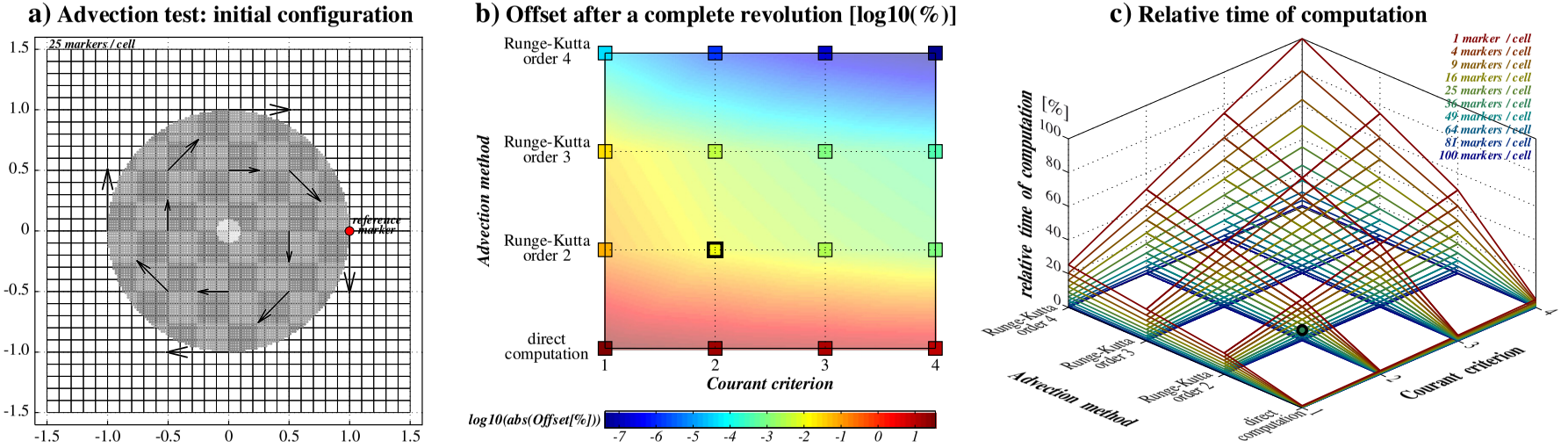

Fig. A.2. Influence of the computation mode of the velocity field on particles mode and of the Courant criterion on total advection. a) Initial test setup and corresponding velocity field. The dimensionless 2D-model represents a disc composed by regularly emplaced particles. The imposed velocity field is circular in order to make the disc rotate around its centre. Time step is defined according to the Courant criterion applied on the maximum local velocity, i.e., on the disc border. For example, a Courant criterion of 3 thus maximises the advection to a third-cell by time step. A reference marker is localised on this border. Velocity field on particles was computed according to four different modes: on the one hand, direct computation is only characterised by linearly interpolating the velocity field from the nodes to the particles, while on the other hand, advection is realised according to the Runge–Kutta approximations of order 2, 3 or 4. Tests were also realised for a range of particles amount, from 1 to 100 per cell. Number of particles does not impact on the effective advection. b) Offset after a complete revolution. Every test leads to a certain numerical error, i.e., the reference marker does not keep constant its distance to the disc centre. While direct computation is characterised by a terminal offset of about 10 to 40%, the Runge–Kutta methods allow a significant improvement of the particles advection leading to total offset of about 10^{-2} to 10^{-3}% for the orders 2 and 3, and for less than 10^{-4}% for the order 4. In the present test, the offset is positive for the direct computation and the 2nd order of Runge–Kutta methods, i.e., the disc tends to dilate, whereas it is negative for the other two Runge–Kutta orders. This explains why the 2nd and 3rd orders are very similar in absolute. The Courant criterion also plays a main role in numerical advection. In the present test, increasing it with a factor 2 assures the reduction of the space error (offset) of a factor 2 for the simple computation, of a factor 8 for the Runge–Kutta methods of order 2 and 3, and of a factor 32 for the 4th order. c) Relative time of computations normalised to the maximum time (i.e., for the 4th order of the Runge–Kutta approximation, with a Courant criterion of 4 and 100 particles/cell). Results are given in percents. Time of computation linearly increases with the Courant criterion, with the amount of particles and also with the order of the used Runge–Kutta method. Even if there is an important gap between the calculation times of the direct computation and the 2nd order of the Runge–Kutta approximation, the benefit of space advection precision significantly prevails. The present test reveals an advection error (offset) of only 0.0098% and an associated computation time more than 2 times lower than for the 3rd order and approximately 4 times better than for the 4th order. Consequently, these observations lead us to use a Courant criterion of 2 associated with the 2nd order of the Runge–Kutta method for a good compromise between the advection approximation and the computation time.

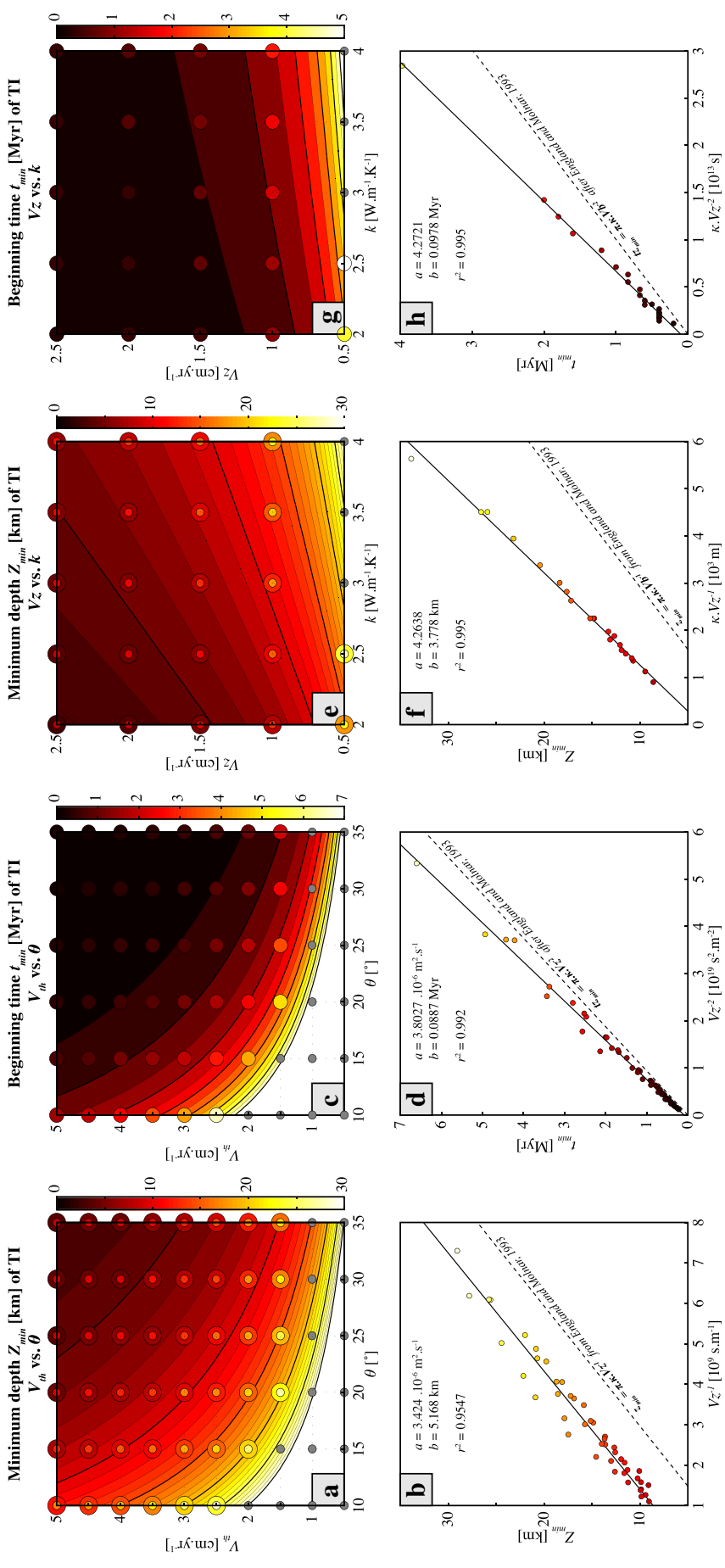

Fig. B.1. Role of the kinematic conditions (V_{th} and θ) and the thermal conductivity k: validation of the numerical model with respect to analytical developments. Erosion and accretion are switched off. Rock thermal properties are set to the reference values (Table 1). a) Minimum depth Z_{min} of thermal inversion reached during the thrust activity as a function of V_{th} and θ. Comparison between our numerical results (coloured circles) and the analytical solution from England and Molnar (1993) (Eq. (B.2)) (background). Small circles: real computed depth. Grey points correspond to the cases where no thermal inversion occurs. Large circles: real computed depth minored by 5.168 km (see text for details). b) Numerical Z_{min} as a function of Vz^{-1} (coloured circles). The linear regression is represented by the continuous line. The straight dashed line corresponds to the analytical linear law from England and Molnar (1993). c) Time t_{min} of the thermal inversion start as a function of V_{th} and θ. Comparison between our numerical results (coloured circles) and the analytical solution for tz_{min} developed after England and Molnar (1993) (Eq. (B.3)) (background). d) Numerical t_{min} as a function of Vz^{-2} (coloured circles). The linear regression is represented by the continuous line. The dashed straight line corresponds to the analytical linear law after England and Molnar (1993). e) Minimum depth Z_{min} in function of Vz and k. Comparison between our numerical results (coloured circles) and the analytical solution from England and Molnar (1993) (Eq. (B.2)) (background). Small circles: real computed depth. Grey points correspond to the cases where no thermal inversion occurs. Large circles: real computed depth minored by 5.168 km (see b). f) Numerical Z_{min} as a function of $\kappa.Vz^{-1}$ (coloured circles). The linear regression is represented by the continuous line. The dashed straight line corresponds to the analytical linear law from England and Molnar (1993).g) Time t_{min} of the thermal inversion start in function of Vz and k. Comparison between our numerical results (coloured circles) and the analytical solution for tz_{min} developed after England and Molnar (1993) (Eq. (B.3)) (background). h) Numerical t_{min} as a function of $\kappa.Vz^{-2}$ (coloured circles). The linear regression is represented by the continuous line. The dashed straight line corresponds to the analytical linear law after England and Molnar (1993).

while limiting the computation time (Fig. A.2). The differences between the fourth, third and second orders of the Runge–Kutta method are negligible.

A.4. Erosion computation

To simulate erosion, each particle advected above the topography is then numerically considered as part of the atmospheric domain by changing each one of the properties it carries. This way, erosion does not perturb the topography and consequently the crustal thickness that controls the vertical displacements linked to the isostatic balancing. The mass balance is assured by adding the corresponding amount of material laterally to the upper plate.

A.5. Thermal computations

Heat diffusion Eq. (7) is solved by using the implicit finite difference method on the Eulerian grid. Then, the computed temperature difference

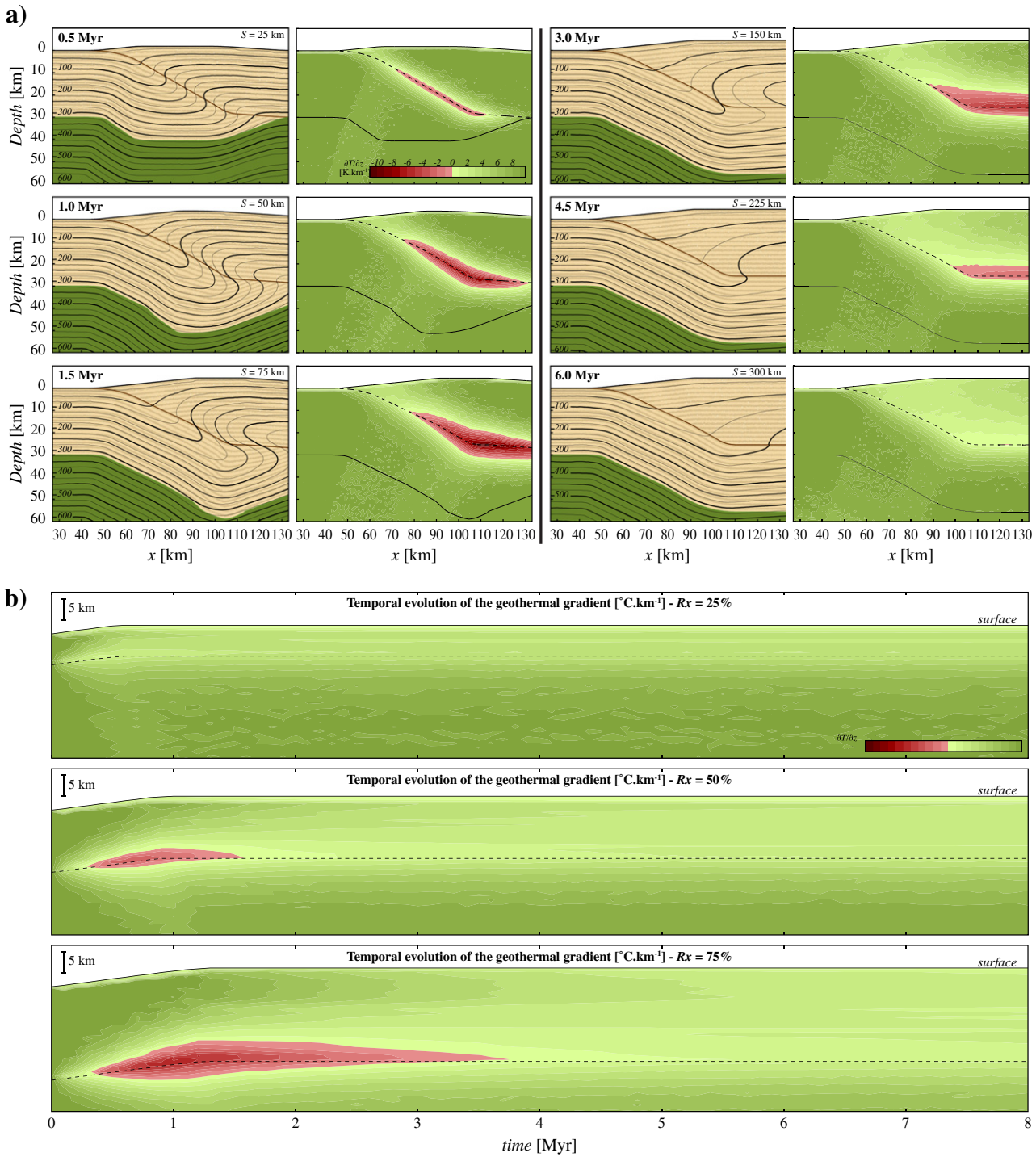

Fig. B.2. Thermal evolution for an extreme kinematic setting: $V_{th} = 5$ cm·yr^{-1}, $\theta = 30°$. a) Evolution during the thrust activity: geometry of the lithosphere and isotherms (left) and vertical thermal gradient (right). S is the amount of shortening. b) Temporal evolution of the geothermal gradient along 3 profiles corresponding to Rx = 25%, 50% and 75% (Fig. 1). Steady state is more rapidly reached in the shallowest part of the thrust, and thermal inversion duration in depths does not exceed 6 Myr.

on nodes ΔT between the current and the previous time step is interpolated from the grid to the particles. Finally, the new temperature is computed by adding the interpolated ΔT to the previous particle temperature. By ensuring the advection by particles, this method has the advantage of defining precisely the new temperature field directly on the particles.

Appendix B. Numerical model validation

England and Molnar (1993) and Molnar and England (1990), by using a series of simplifications, proposed mathematical derivations of the fundamental equations controlling the heat transfer in the lithosphere. This way, without additional heat sources, they defined the tectonic conditions for the occurrence of a thermal inversion on each point of the thrust such as:

$$\frac{Z_f \cdot V_{th} \cdot \sin(\theta)}{\pi \cdot \kappa} \geq 1 \tag{B.1}$$

where Z_f is the depth of the considered point on the fault. This can be used to provide the minimum depth $Z_{\min}$ where thermal inversion appears:

$$Z_{\min} = \frac{\pi \cdot \kappa}{V_{th} \cdot \sin(\theta)} = \frac{\pi \cdot \kappa}{Vz}. \tag{B.2}$$

Considering a point in the downgoing plate located at the thrust front, it will reach the depth $Z_{\min}$ after a time $tz_{\min}$:

$$tz_{\min} = \frac{Z_{\min}}{Vz} = \frac{\pi \cdot \kappa}{Vz^2}. \tag{B.3}$$

Whereas England and Molnar considered θ constant along the entire slanted part of the fault, θ represents here the maximum dip angle of the thrust and an exact fit with the analytical solutions (B.2) and (B.3) cannot be expected and the thermal inversion is slightly underestimated.

The numerical minimum depth $Z_{\min}$ and start time $t_{\min}$ of the thermal inversion as a function of V_{th} and θ show a good agreement with the general trend of the analytical values given by or deduced from England and Molnar (1993) (Fig. B.1a, c). This consistency is confirmed by the linear regressions (Fig. B.1b, d) resulting from the set of numerical values. In spite of an overestimation of the minimum depth $Z_{\min}$ of about 5 km, the slope of the linear regression law between $Z_{\min}$ and Vz^{-1} is very close to the coefficient $\pi \cdot \kappa$ from Eq. (B.2) (Fig. B.1b). In the same way, the numerical times $t_{\min}$ show also a good agreement with the trend defined by the analytical solutions for $tz_{\min}$ (Eq. (B.3) and Fig. B.1c, d). Shifts between the analytical laws and linear regressions are essentially due to the smoothed thrust profile we used (Fig. 1).

Advection effects on the thermal evolution within a thrust zone can be thus described as a function of the vertical component of the thrust velocity Vz (Fig. 1). In Fig. B.1e, g, the results for a range of numerical simulations with different (Vz, k) combinations are treated in the same way as previously. Even if the slopes a relative to the linear regression laws corresponding to the minimum depth $Z_{\min}$ and time $t_{\min}$ (Fig. B.1f, h) of the beginning of the thermal inversion are rather far from the coefficient π predicted by England and Molnar (1993) (Eqs. (B.2) and (B.3)), both the high similarity between our two regression slopes a and the very good correlation coefficients r confirm the tendencies of the analytical equations.

Appendix C. Rock thermal properties, mantle heat flux and radiogenic heat production effects

Heat capacity Cp crustal scale thermo-dependence law, from Whittington et al. (2009) (T in K):

$$\begin{cases} Cp_{crust}(T<846K) = 899.54 + 0.3864 \cdot T - 2.25 \cdot 10^{-5} \cdot T^{-2} \\ Cp_{crust}(T>846K) = 1034.0 + 0.1456 \cdot T - 21.59 \cdot 10^{-5} \cdot T^{-2}. \end{cases} \tag{C.1}$$

Thermal conductivity k thermo-dependence laws as a function of the lithology, from Clauser and Huenges (1995) and Zoth and Hänel (1988) (T in °C):

$$\begin{cases} k_{crust}(T) = k_{metamorphic}(T) = 705/(T+350) + 0.75 \\ k_{mantle}(T) = k_{ultra-basic}(T) = 1293/T + 350 + 0.73 \end{cases} \tag{C.2}$$

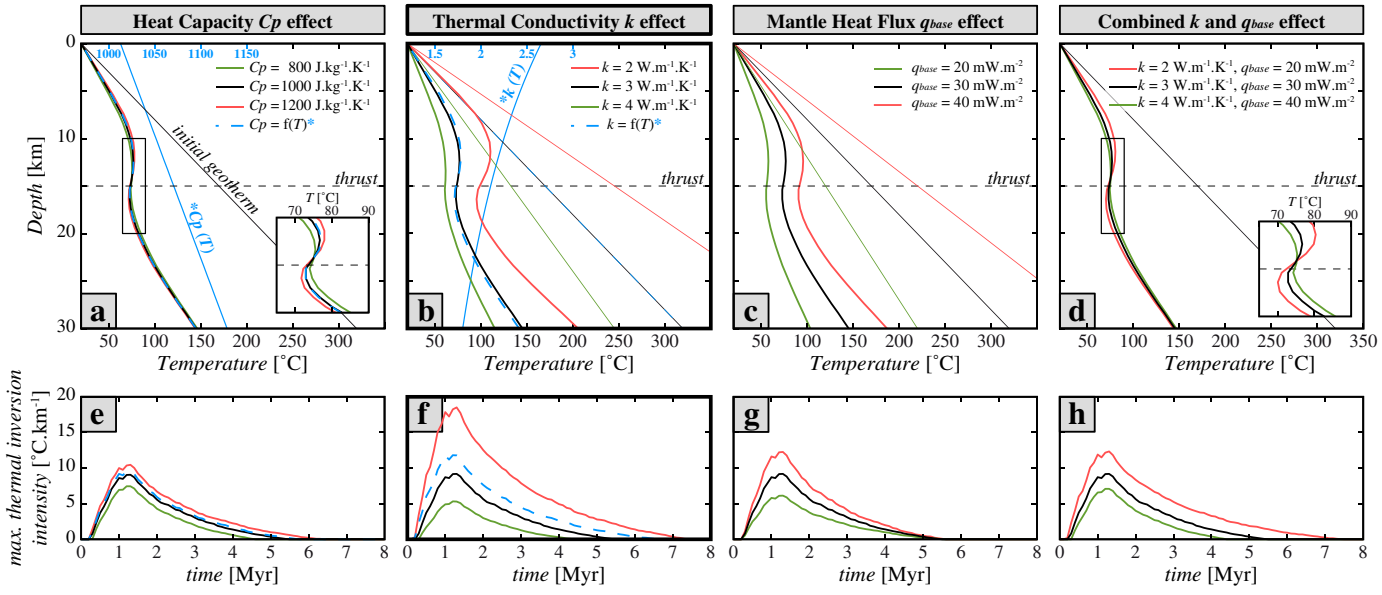

Fig. C.1. Rock thermal properties and mantle heat flux effects on the thermal inversion under extreme kinematic conditions (V_{th} = 5 cm·yr^{-1}, θ = 30°). a) and e) Heat capacity Cp effects. b) and f) Thermal conductivity effects. c) and g) Mantle heat flux q_{base} effects. d) and h) Combined k and q_{base} effects, considering identical initial geotherms. [Top] Thick lines are geotherms after a 1 Myr convergence (amount of shortening S = 50 km) along the central crustal profile, i.e., Rx = 50% (Fig. 1). Fine lines represent the corresponding initial geotherms. [Bottom] Evolution of the maximal intensity of the thermal inversion reached along the thrust. Solid blue lines (and numbers) show the variation of Cp and k with depth (and hence with temperature) for the initial geotherm. Dashed blue lines are the results of the corresponding simulations.

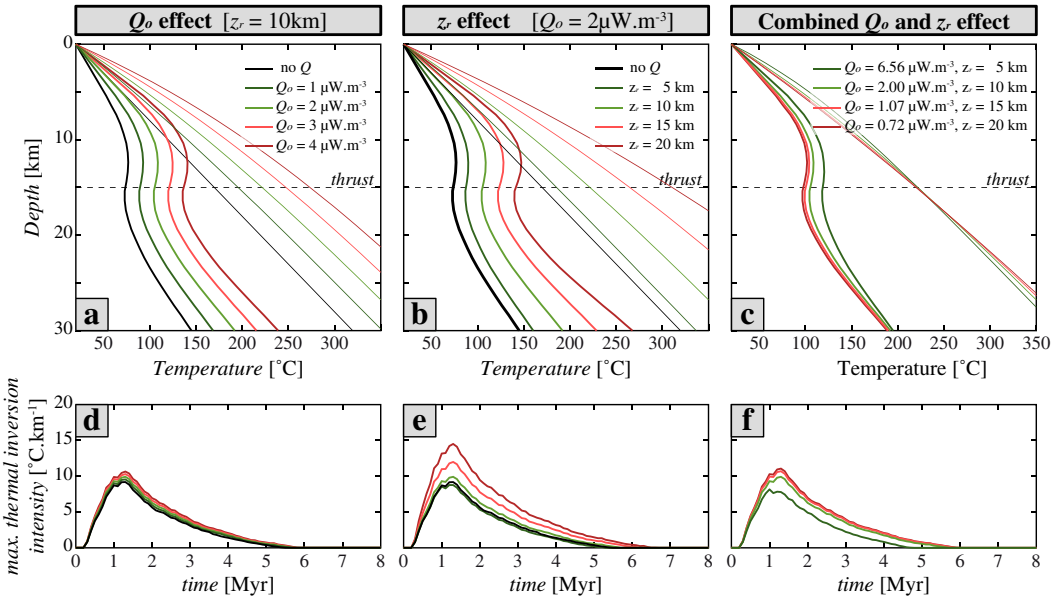

Fig. C.2. Radiogenic heat production effects on the thermal inversion under extreme kinematic conditions: $V_{th} = 5$ cm·yr^{-1} and $\theta = 30°$. a) and d) Surface radiogenic heat production Q_0 effects. b) and e) Specific depth z_r effects. c) and f) Combined Q_0 and z_r effects such as the initial mean crustal radiogenic heat productions are the same. [Top] Thick lines are geotherms after a 1 Myr convergence (amount of shortening $S = 50$ km) along the central crustal profile, i.e., $Rx = 50\%$ (Fig. 1). Fine lines represent the corresponding initial geotherms. [Bottom] Evolution of the maximal intensity of the thermal inversion reached along the thrust.

References

Abd El-Naby, H., Frisch, W., Hegner, E., 2000. Evolution of the Pan-African Wadi Haimur metamorphic sole, Eastern Desert, Egypt. J. Metamorph. Geol. 18 (6), 639–651.

Abdulagatov, I.M., Emirov, S.N., Abdulagatoca, Z.Z., Askerov, S.Y., 2006. Effect of pressure and temperature on the thermal conductivity of rocks. J. Chem. Eng. Data 51 (1), 22–33.

Anderson, R.N., DeLong, S.E., Schwarz, W.M., 1978. Thermal model of subduction with dehydration in the downgoing slab. J. Geol. 86, 731–739.

Andreasson, P.G., Lagerblad, B., 1980. Occurrence and significance of inverted metamorphic gradients in the western Scandinavian Caledonides. J. Geol. Soc. 137 (3), 219–230.

Arenas, R., Rubio Pascual, F.J., Diaz Garcia, F., Martinez Catalan, J.R., 1995. High-pressure micro-inclusions and development of an inverted metamorphic gradient in the Santiago Schists (Ordenes Complex, NW Iberian Massif, Spain): evidence of subduction and syncollisional decompression. J. Metamorph. Geol. 13 (2), 141–164.

Arita, K., 1983. Origin of the inverted metamorphism of the lower Himalayas, Central Nepal. Tectonophysics 95 (1–2), 43–60.

Ballèvre, M., Bosse, V., Ducassou, C., Pitra, P., 2009. Palaeozoic history of the Armorican Massif: models for the tectonic evolution of the suture zones. C. R. Geosci. 341, 174–201.

Beaumont, C., Jamieson, R.A., Nguyen, M.H., Lee, B., 2001. Himalayan tectonics explained by extrusion of a low-viscosity crustal channel coupled to focused surface denudation. Nature 414 (6865), 738–742.

Beaumont, C., Jamieson, R.A., Nguyen, M.H., Medvedev, S., 2004. Crustal channel flows: 1. Numerical models with applications to the tectonics of the Himalayan–Tibetan orogen. J. Geophys. Res. 109, B06406.

Bilham, R., Larson, K., Freymueller, J., 1997. GPS measurements of present-day convergence across the Nepal Himalaya. Nature 386 (6620), 61–64.

Bollinger, L., Henry, P., Avouac, J.P., 2006. Mountain building in the Nepal Himalaya: thermal and kinematic model. Earth Planet. Sci. Lett. 244, 58–71.

Brun, J.P., Cobbold, P.R., 1980. Strain heating and thermal softening in continental shear zones: a review. J. Struct. Geol. 2 (1/2), 149–158.

Brunel, M., Kienast, J.R., 1986. Etude pétro-structurale des chevauchements ductiles himalayens sur la transversale de l'Everest-Makalu (Népal oriental). Can. J. Earth Sci. 23, 1117–1137.

Burg, J.P., Gerya, T.V., 2005. The role of viscous heating in Barrovian metamorphism of collisional orogens: thermomechanical models and application to the Lepontine Dome in the Central Alps. J. Metamorph. Geol. 23, 75–95.

Burg, J.P., Schmalholz, S.M., 2008. Viscous heating allows thrusting to overcome crustal-scale buckling: numerical investigation with application to the Himalayan syntaxes. Earth Planet. Sci. Lett. 274, 189–203.

Burg, J.P., Leyreloup, A., Marchand, J., Matte, P., 1984. Inverted metamorphic zonation and large-scale thrusting in the Variscan Belt: an example in the French Massif Central. Geol. Soc. Lond. Spec. Publ. 14 (1), 47–61.

Caddick, M.J., Bickle, M.J., Harris, N.B.W., Holland, T.J.B., Horstwood, M.S.A., Parrish, R.R., Ahmad, T., 2007. Burial and exhumation history of a Lesser Himalayan schist: Recording the formation of an inverted metamorphic sequence in NW India. Earth Planet. Sci. Lett. 264, 375–390.

Camiré, G., 1995. Development of inverted metamorphic gradient in the internal domain of the Taconian belt, Gaspé Peninsula. Can. J. Earth Sci. 32, 37–51.

Carter, N.L., Tsenn, M.C., 1987. Flow properties of continental lithosphere. Tectonophysics 136 (1–2), 27–63.

Čermák, V., Rybach, L., 1982. Thermal conductivity and specific heat of minerals and rocks. In: Angenheister, G. (Ed.), Landolt-Börnstein: Numerical Data and Functional Relationships in Science and Technology, New Series, Group V (Geophysics and Space Research), Volume Ia, (Physical Properties of Rocks). Springer, Berlin-Heidelberg, pp. 305–343.

Chester, J.S., Chester, F.M., Kronenberg, A.K., 2005. Fracture surface energy of the Punchbowl fault, San Andreas system. Nature 437 (7055), 133–136.

Clauser, C., Huenges, E., 1995. Thermal conductivity of rocks and minerals. AGU Reference Shelf 3 Rock Physics and Phase Relations. A Handbook of Physical Constants, pp. 105–125.

Corrie, S.L., Kohn, M.J., 2011. Metamorphic history of the central Himalaya, Annapurna region, Nepal, and implications for tectonic models. Geol. Soc. Am. Bull. 123 (9–10), 1863–1879.

Crough, S.T., 1977. Isostatic rebound and power-law flow in the asthenosphere. Geophys. J. Roy. Astron. Soc. 50 (3), 723–738.

DeVore, G.W., 1983. Relations between subduction, slab heating, slab dehydration and continental growth. Lithos 16 (4), 255–263.

England, P., Molnar, P., 1993. The interpretation of inverted metamorphic isograds using simple physical calculations. Tectonics 12 (1), 145–157.

England, P.C., Thompson, A.B., 1984. Pressure–temperature–time paths of regional metamorphism. I. Heat transfer during the evolution of regions of thickened continental crust. J. Petrol. 25 (4), 894–928.

Frank, W., Hoinkes, G., Miller, C., Purtscheller, F., Richter, W., Thöni, M., 1973. Relations between metamorphism and orogeny in a typical section of the Indian Himalayas. Tschermaks Mineral. Petrogr. Mitt. 20 (4), 303–332.

Gerya, T.V., 2010. Introduction to Numerical Geodynamic Modelling. Cambridge University Press, New York.

Gibson, H.D., Brown, R.L., Parrish, R.R., 1999. Deformation-induced inverted metamorphic field gradients: an example from the southeastern Canadian Cordillera. J. Struct. Geol. 21, 751–767.

Goetze, C., Evans, B., 1979. Stress and temperature in the bending lithosphere as constrained by experimental rock mechanics. Geophys. J. Roy. Astron. Soc. 59 (3), 463–478.

Graham, C.M., England, P.C., 1976. Thermal regimes and regional metamorphism in the vicinity of overthrust faults: an example of shear heating and inverted metamorphic zonation from southern California. Earth Planet. Sci. Lett. 31, 142–152.

Grujic, D., Casey, M., Davidson, C., Hollister, L.S., Kündig, R., Pavlis, T.L., Schmid, S.M., 1996. Ductile extrusion of the Higher Himalayan Crystalline in Bhutan: evidence from quartz microfabrics. Tectonophysics 260, 21–43.

Guillot, S., 1999. An overview of the metamorphic evolution of central Nepal. In: Upreti, B.N., Le Fort, P. (Eds.), Geology of Nepal. Journal of Asian Earth Sciences, 17, pp. 713–725.

Hacker, B.R., 1991. The role of deformation in the formation of metamorphic gradients: ridge subduction beneath the Oman Ophiolite. Tectonics 10 (2), 455–473.

Harrison, T.M., Ryerson, F.J., Le Fort, P., Yin, A., Lovera, O.M., Catlos, E.J., 1997. A late Miocene–Pliocene origin for the central Himalayan inverted metamorphism. Earth Planet. Sci. Lett. 146, E1–E7.

Harrison, T.M., Grove, M., Lovera, O.M., Catlos, E.J., 1998. A model for the origin of Himalayan anatexis and inverted metamorphism. J. Geophys. Res. 103 (B11), 27017–27032.

Harrison, T.M., Grove, M., Lovera, O.M., Catlos, E.J., d'Andrea, J., 1999. The origin of Himalayan anatexis and inverted metamorphism: models and constraints. J. Asian Earth Sci. 17, 755–772.
Hartz, E.H., Podladchikov, Y.Y., 2008. Toasting the jelly sandwich: the effects of shear heating on lithospheric geotherms and strength. Geology 36, 331–334.
Henry, P., Le Pichon, X., Goffé, B., 1997. Kinematic, thermal and petrological model of the Himalayas: constraints related to metamorphism within the underthrust Indian crust and topographic elevation. Tectonophysics 273 (1–2), 31–56.
Hofmeister, A.M., 2007. High–pressure geoscience special feature: pressure dependence of thermal transport properties. Proc. Natl. Acad. Sci. 104 (22), 9192–9197.
Horai, K., Susaki, J., 1989. The effect of pressure on the thermal conductivity of silicate rocks up to 12 kbar. Phys. Earth Planet. Inter. 55 (3–4), 292–305.
Hubbard, M.S., 1989. Thermobarometric constraints on the thermal history of the Main Central Thrust Zone and Tibetan Slab, eastern Nepal Himalaya. J. Metamorph. Geol. 7 (1), 19–30.
Huerta, A.D., Royden, L.H., Hodges, K.V., 1996. The interdependence of deformational and thermal processes in mountain belts. Science 273, 637–639.
Huerta, A.D., Royden, L.H., Hodges, K.V., 1998. The thermal structure of collisional orogens as a response to accretion, erosion, and radiogenic heating. J. Geophys. Res. Solid Earth 103, 15287–15302.
Huerta, A.D., Royden, L.H., Hodges, K.V., 1999. The effects of accretion, erosion and radiogenic heat on the metamorphic evolution of collisional orogens. J. Metamorph. Geol. 17, 349–366.
Jain, A.K., Manickavasagam, R.M., 1993. Inverted metamorphism in the intracontinental ductile shear zone during Himalayan collision tectonics. Geology 21 (5), 407.
Jamieson, R.A., 1986. P–T paths from high temperature shear zones beneath ophiolites. J. Metamorph. Geol. 4 (1), 3–22.
Jamieson, R.A., Beaumont, C., Hamilton, J., Fullsack, P., 1996. Tectonic assembly of inverted metamorphic sequences. Geology 24 (9), 839–842.
Jamieson, R.A., Beaumont, C., Medvedev, S., Nguyen, M.H., 2004. Crustal channel flows: 2. Numerical models with implications for metamorphism in the Himalayan–Tibetan orogen. J. Geophys. Res. 109, B06407.
Johnson, M.R.W., Strachan, R.A., 2006. A discussion of possible heat sources during nappe stacking: the origin of Barrovian metamorphism within the Caledonian thrust sheets of NW Scotland. J. Geol. Soc. 163 (4), 579–582.
Kanamori, H., Rivera, L., 2006. Energy partitioning during an earthquake. Geophysical Monograph, Series 170, Earthquakes: Radiated Energy and the Physics of Faulting 3–13.
Kaneko, Y., Katayama, I., Yamamoto, H., Misawa, K., Ishikawa, M., Rehman, H.U., Kausar, A.B., Shiraishi, K., 2003. Timing of Himalayan ultrahigh-pressure metamorphism: sinking rate and subduction angle of the Indian continental crust beneath Asia. J. Metamorph. Geol. 21 (6), 589–599.
Kidder, S., Ducea, M.N., 2006. High temperatures and inverted metamorphism in the schist of Sierra de Salinas, California. Earth Planet. Sci. Lett. 241, 422–437.
Kidder, S.B., Herman, F., Saleeby, J., Avouac, J.P., Ducea, M.N., Chapman, A., 2013. Shear heating not a cause of inverted metamorphism. Geology. http://dx.doi.org/10.1130/G34289.1.
Kohn, M.J., 2008. P–T–t data from central Nepal support critical taper and repudiate large-scale channel flow of the Greater Himalayan sequence. Geol. Soc. Am. Bull. 120 (3/4), 259–273.
Kukkonen, I.T., Jokinen, J., Seipold, U., 1999. Temperature and pressure dependencies of thermal transport properties of rocks: implications for uncertainties in thermal lithosphere models and new laboratory measurements of high-grade rocks in the central Fennoscandian shield. Surv. Geophys. 20, 33–59.
Lachenbruch, A.H., Sass, J.H., 1980. Heat flow and energetics of the San Andreas fault zone. J. Geophys. Res. 85 (B11), 6185–6222.
Lavé, J., Avouac, J.P., 2000. Active folding of fluvial terraces across the Siwaliks Hills, Himalayas of central Nepal. J. Geophys. Res. 105 (B3), 5735–5770.
LeFort, P., 1975. Himalayas: the collided range — present knowledge of the continental arc. Am. J. Sci. 275 (A), 1–44.
Macfarlane, A.M., 1995. An evaluation of the inverted metamorphic gradient at Langtang National Park, Central Nepal Himalaya. J. Metamorph. Geol. 13 (5), 595–612.
Maierová, P., Chust, T., Steinle-Neumann, G., Čadek, O., Čížková, H., 2012. The effect of variable thermal diffusivity on kinematic models of subduction. J. Geophys. Res. 117 (B7).
Mason, R., 1984. Inverted isograds at Sulitjelma, Norway: the result of shear-zone deformation. J. Metamorph. Geol. 2, 77–82.
Meissner, R., Mooney, W., 1998. Weakness of the lower continental crust: a condition for delamination, uplift, and escape. Tectonophysics 296 (1–2), 47–60.
Minear, J.W., Toksöz, M.N., 1970. Thermal regime of a downgoing slab. Tectonophysics 10 (1–3), 367–390.
Molnar, P., England, P., 1990. Temperatures, heat flux, and frictional stress near major thrust faults. J. Geophys. Res. 95 (B4), 4833–4856.
Nabelek, P.I., Whittington, A.G., Hofmeister, A.M., 2010. Strain heating as a mechanism for partial melting and ultrahigh temperature metamorphism in convergent orogens: implications of temperature-dependent thermal diffusivity and rheology. J. Geophys. Res. 115 (B12) B12417.
Osako, M., Ito, E., Yoneda, A., 2004. Simultaneous measurements of thermal conductivity and thermal diffusivity for garnet and olivine under high pressure. Phys. Earth Planet. Inter. 143–144, 311–320.
Oxburgh, E., Turcotte, D., 1976. The physico-chemical behaviour of the descending lithosphere. Tectonophysics 32 (1–2), 107–128.
Pavlis, T.L., 1986. The role of strain heating in the evolution of megathrusts. J. Geophys. Res. 91 (B12), 12407–12422.
Peacock, S.M., 1987a. Creation and preservation of subduction-related inverted metamorphic gradients. J. Geophys. Res. 92 (B12), 12763–12781.
Peacock, S.M., 1987b. Thermal effects of metamorphic fluids in subduction zones. Geology 15 (11), 1057.
Peacock, S.M., 1990. Numerical simulation of metamorphic pressure–temperature–time paths and fluid production in subducting slabs. Tectonics 9 (5), 1197.
Pitra, P., Ballèvre, M., Ruffet, G., 2010. Inverted metamorphic field gradient towards a Variscan suture zone (Champtoceaux Complex, Armorican Massif, France). J. Metamorph. Geol. 28, 183–208.
Platt, J.P., 1975. Metamorphic and deformational processes in the Franciscan Complex, California: some insights from the Catalina Schist terrane. Geol. Soc. Am. Bull. 86 (10), 1337–1347.
Ranalli, G., Murphy, D.C., 1987. Rheological stratification of the lithosphere. Tectonophysics 132 (4), 281–295.
Royden, H.L., 1993. The steady state thermal structure of eroding orogenic belts and accretionary prisms. J. Geophys. Res. 98, 4487–4507.
Ruppel, C., Hodges, K.V., 1994. Pressure–temperature–time paths from two-dimensional thermal models: prograde, retrograde, and inverted metamorphism. Tectonics 13, 17–44.
Scholz, C.H., 1980. Shear heating and the state of stress on faults. J. Geophys. Res. 85, 6174–6184.
Searle, M.P., Rex, A.J., 1989. Thermal model for the Zankstar Himalaya. J. Metamorph. Geol. 7, 127–134.
Seipold, U., 1992. Depth dependance of thermal transport properties for typical crustal rocks. Phys. Earth Planet. Inter. 69, 299–303.
Seipold, U., 1995. The variation of thermal transport properties in the Earth's crust. J. Geodyn. 20 (2), 145–154.
Seipold, U., 1998. Temperature dependance of thermal transport properties of crystalline rocks — a general law. Tectonophysics 291 (1–4), 161–171.
Shi, Y., Wang, C.Y., 1987. Two-dimensional modeling of the P–T–t paths of regional metamorphism in simple overthrust terranes. Geology 15, 1048–1051.
Sinha-Roy, S., 1982. Himalayan main central thrust and its implications for Himalayan inverted metamorphism. Tectonophysics 84 (2–4), 197–224.
Stephenson, B.J., Waters, D.J., Searle, M.P., 2000. Inverted metamorphism and the Main Central Thrust: field relations and thermobarometric constraints from the Kishtwar Window, NW Indian Himalaya. J. Metamorph. Geol. 18, 571–590.
Štípská, P., Schulmann, K., 1995. Inverted metamorphic zonation in a basement-derived nappe sequence; eastern margin of the Bohemian Massif. Geol. J. 30, 385–413.
Toksöz, M.N., Minear, J.W., Julian, B.R., 1971. Temperature field and geophysical effects of a downgoing slab. J. Geophys. Res. 76 (5), 1113–1138.
Turcotte, D.L., Schubert, G., 2002. Geodynamics, 2nd edition. Cambridge University Press.
Voosten, H.D., Schellschmidt, R., 2003. Influence of temperature on thermal conductivity, thermal capacity and thermal diffusivity for different types of rock. Phys. Chem. Earth. 28, 499–509.
Waples, D., Waples, J., 2004. A review and evaluation of specific heat capacities of rocks, minerals, and subsurface fluids. Part 1: minerals and nonporous rocks. Nat. Resour. Res. 13 (2), 97–122.
Watkins, K.P., 1985. Geothermometry and geobarometry of inverted metamorphic zones in the W central Scottish Dalradian. J. Geol. Soc. 142 (1), 157–165.
Whittington, A.G., Hofmeister, A.M., Nabelek, P.I., 2009. Temperature-dependent thermal diffusivity of the Earth's crust and implications for magmatism. Nature 458, 319–321.
Williams, H., Smyth, W.R., 1973. Metamorphic aureoles beneath ophiolite suites and alpine peridotites; tectonic implications with west Newfoundland examples. Am. J. Sci. 273 (7), 594–621.
Yamato, P., Tartèse, R., Duretz, T., May, D.A., 2012. Numerical modelling of magma transport in dykes. Tectonophysics 526–529, 97–109.
Zoth, G., Hänel, R., 1988. Thermal conductivity. In: Hänel, R., Rybach, L., Stegena, L.K. (Eds.), Handbook of Terrestrial Heat Flows Density Determination. Dordrecht, pp. 449–468.

TECTONICS, VOL. 32, 1559–1570, doi:10.1002/2013TC003375, 2013

Passive margins getting squeezed in the mantle convection vice

Philippe Yamato,[1] Laurent Husson,[1,2] Thorsten W. Becker,[3] and Kevin Pedoja[4]

Received 21 May 2013; revised 10 September 2013; accepted 16 October 2013; published 19 December 2013.

[1] Passive margins often exhibit uplift, exhumation, and tectonic inversion. We speculate that the compression in the lithosphere gradually increased during the Cenozoic, as seen in the number of mountain belts found at active margins during that period. Less clear is how that compression increase affects passive margins. In order to address this issue, we design a 2-D viscous numerical model wherein a lithospheric plate rests above a weaker mantle. It is driven by a *mantle conveyor belt*, alternatively excited by a lateral downwelling on one side, an upwelling on the other side, or both simultaneously. The lateral edges of the plate are either free or fixed, representing the cases of free convergence, and collision (or slab anchoring), respectively. This distinction changes the upper mechanical boundary condition for mantle circulation and thus, the stress field. Between these two regimes, the flow pattern transiently evolves from a free-slip convection mode toward a no-slip boundary condition above the upper mantle. In the second case, the lithosphere is highly stressed horizontally and deforms. For a constant total driving force, compression increases drastically at passive margins if upwellings are active. Conversely, if downwellings alone are activated, compression occurs at short distances from the trench and extension prevails elsewhere. These results are supported by Earth-like models that reveal the same pattern, where active upwellings are required to excite passive margins compression. Our results substantiate the idea that compression at passive margins is in response to the underlying mantle flow that is increasingly resisted by the Cenozoic collisions.

Citation: Yamato, P., L. Husson, T. W. Becker, and K. Pedoja (2013), Passive margins getting squeezed in the mantle convection vice, *Tectonics*, *32*, 1559–1570, doi:10.1002/2013TC003375.

1. Introduction

[2] Paleogeographic reconstructions [e.g., *Blakey*, 2008] suggest that the Earth had much less topographic relief during the time of maximum continental dispersion, during the Late Cretaceous. Since then, continents continuously contract, and the many Cenozoic mountain belts at active margins best record this worldwide change. However, not only the active margins are exposed to deformation, and mounting evidence suggests that passive margins also undergo contraction—yet more subtle—and they are now often colloquially referred to as *not-so-passive margins*.

[3] A range of arguments is indicative of gentle shortening at passive margins. First, elevation is often anomalously high with respect to the surrounding continent (>2000 m at short distances from the coastline) [e.g., *Japsen et al*., 2012a and Figure 1]. Second, passive margins are also rapidly uplifting, as indicated by abundant, widespread, Upper Cenozoic sequences of paleocoasts (e.g., marine terrace, beach-ridges, and coral terraces) developed on the coasts located in such settings [*Pedoja et al*., 2011 and Figure 1]) and post-rift marine sediments (for instance, in NE Brazil [*Morais Neto et al*., 2006; *Martill*, 2007] and West Greenland [*Piasecki et al*., 1992; *Japsen et al*., 2006]). Third, ubiquitous exhumation at passive margins occurs during the Cenozoic (Figure 1). A variety of examples are found, among others, in India [*Gunnell and Fleitout*, 1998]; in the South Atlantic in general [*Gallagher and Brown*, 1999], Western Africa [*Lavier et al*., 2001], Morocco [*Ghorbal et al*., 2008], Southern Africa [*Partridge and Maud*, 1987; *Brown et al*., 2002; *Roberts and White*, 2010] and Brazil [*Cobbold et al*., 2001; *Cogné et al*., 2011, 2012; *Japsen et al*., 2012b], in particular; in the North Atlantic in general [*Japsen and Chalmers*, 2000; *Cloetingh and Van Wees*, 2005; *Cloetingh et al*., 2008], Greenland [e.g., *Japsen et al*., 2006; *Thomson et al*., 1999; *Japsen et al*., 2012a], Barents Sea and the Alaskan north slope [*Green and Duddy*, 2010], Norway [*Lundin and Doré*, 2002; *Ritchie et al*., 2008], the British Isles [*Hillis et al*., 2008a; *Holford et al*., 2008, 2009; *Smallwood*, 2008], and North Sea basin [*Japsen*, 1998], in particular. As pointed out by *Japsen et al*. [2012a], exhumation generally follows a period of subsidence and only occurs long after breakup, and might even be episodic. Lastly, tectonic inversion affects many margins (Figure 1). Again, examples are found in Brazil [*Gomes Sant'Anna et al*., 1997; *Riccomini*

[1]Geosciences Rennes, UMR 6118 CNRS, Université de Rennes 1, Rennes, France.
[2]LPGN, UMR 6112 CNRSS, Université de Nantes, Nantes, France.
[3]Department of Earth Sciences, University of Southern California, Los Angeles, California, USA.
[4]M2C, UMR 6143 CNRS, Université de Caen, Caen, France.

Corresponding author: P. Yamato, Geosciences Rennes, UMR 6118 CNRS, Université de Rennes 1, Rennes, France. (philippe.yamato@univ-rennes1.fr)

0278-7407/13/10.1002/2013TC003375

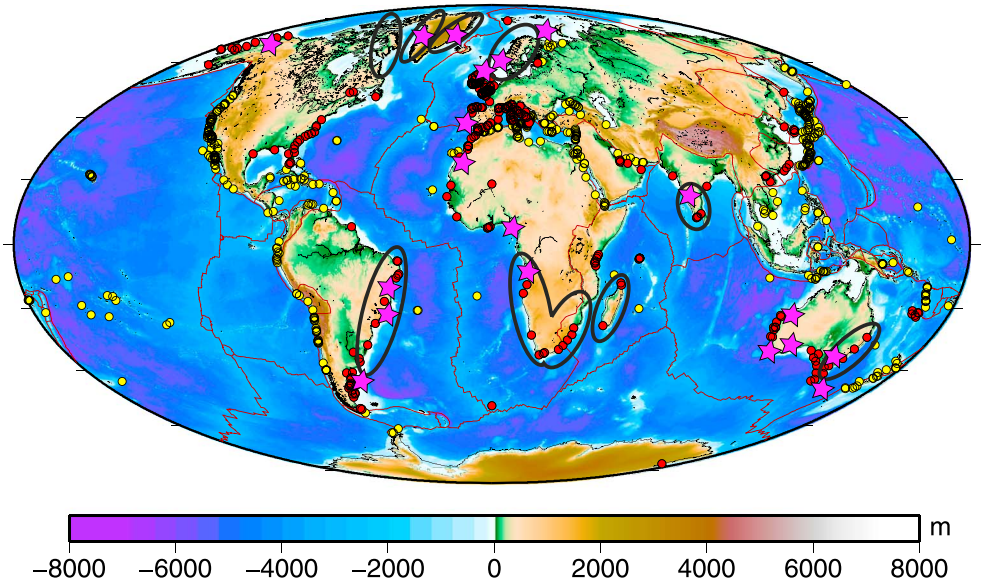

Figure 1. Synthetic map showing the following: (i) anomalously elevated passive margins (topography and black ellipses, after *Japsen et al*., 2012a), (ii) coastal sequence including the last interglacial maximum benchmark (125 ka) (dots, after *Pedoja et al*. [2011]; passive margins are plotted in red, others in yellow), and, (iii), exhumed and tectonically inverted passive margins during the Cenozoic (magenta stars, see text for details and references).

and Assumpcao, 1999; *Cobbold et al*., 2007; *Cogné et al*., 2011, 2012] and Patagonia [*Rodriguez and Littke*, 2001], in the British Isles [*Andersen and Boldreel*, 1995; *Lundin and Doré*, 2002; *Smallwood*, 2008] and in the North Atlantic [*Doré et al*., 1997], Norway [*Brekke*, 2000], West Africa [*Hudec and Jackson*, 2002; *Jackson et al*., 2005; *Briggs et al*., 2009], Moroccan Meseta [*Ghorbal et al*., 2008], India [*Gunnell and Fleitout*, 1998], Iberia [*Masson et al*., 1994; *Peron-Pinvidic et al*., 2008], and Australia [*Hillis et al*., 2008b; *Bishop and Goldrick*, 2000]. Here we refer to tectonic inversion when former normal faults are tectonically inverted and unambiguously reveal compression. Exhumation itself may not be as symptomatic and may be caused by mantle rather than lithospheric activity.

[4] Several mechanisms, for instance, dynamic support from the underlying mantle flow in West Africa [e.g., *Lithgow-Bertelloni and Silver*, 1998], flexure due to sedimentary loading [e.g., *Gunnell and Fleitout*, 1998], and enhanced erosion due to climate change [*Clift*, 2010] partially explain these observations on regional scales. In fact, such mechanisms satisfactorily explain uplift and exhumation but fail to explain tectonic inversions. Only subduction initiation at passive margins may trigger modest compression, uplift, and exhumation [e.g., *Nikolaeva et al*., 2010]. Moreover, because most margins appear affected in a similar fashion, these observations suggest a general process that applies at least at the scale of the Atlantic, where most passive margins are found at present, but likely also on global scales.

[5] Exhumation and tectonic inversion in many instances occur at conjugate margins (e.g., Brazil and Western Africa, [*Japsen et al*., 2012b] and the margins of the North Atlantic [*Japsen et al*., 2012a]). Even more intriguing is the fact that phases of tectonic inversion at passive margins appear to be coeval to periods of tectonic activity at their active counterparts. This is observed in South America [*Cobbold et al*., 2007] where the Peruvian, Incaic, Quechua phases of Andean deformation match the deformation at the Brazilian margin [*Cogné et al*., 2012], or Iberia where tectonic inversion is synchronous to the Alpine deformation [*Peron-Pinvidic et al*., 2008]. This observation suggests that a general process leads to compression at both margins. Plate tectonics and continental deformation are, of course, ultimately linked to mantle convection. Sublithospheric mantle tractions are thought to be relevant for relative plate motions, trench motions, and lithospheric deformation [e.g., *Steinberger et al*., 2001; *Becker and O'Connell*, 2001; *Conrad and Lithgow-Bertelloni*, 2002; *Lithgow-Bertelloni and Guynn*, 2004; *Husson*, 2012]. In the Indian Ocean [*Becker and Faccenna*, 2011], the South Atlantic [*Husson et al*., 2012], or along the entire global plate circuit [*Faccenna et al*., 2013], approximately cylindrical, whole mantle convection cells underneath the drifting plates successfully explain the time evolution of active orogens at convergent boundaries. These previous studies explored how mantle "conveyor belts" need to be simultaneously excited by active upwellings and downwellings, as opposed to large-scale return flow, in order to match the observed kinematics. Downwellings associated with subduction pull the plates trenchward and are therefore essentially a source of extension in the lithosphere. Conversely, if upwellings are located close to spreading centers ("ridges"), they can serve to push plates from ridges to trenches and are a source of compression. Of course, because of conservation of mass, an upwelling is necessarily associated to, at least, one downwelling (and vice versa) but the importance of their contributions is a matter of (i) focusing (slab-like, focused downwellings can be counterbalanced by upwellings that are either diffuse or localized, underneath oceanic ridges in particular); and (ii) their respective buoyancies that render them either active or passive. In the present-day plate configuration, upwellings, chiefly fuelled by the African superswell, appear

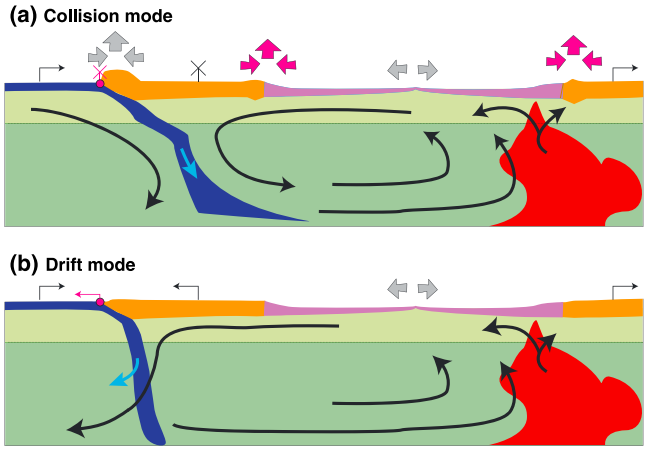

Figure 2. Sketch of the mantle convective cell flow in (a) collision mode and (b) drift mode. In the collision mode, the anchored slab does not retreat and prevents the trench-ward motion of the upper plate and is thus blocked. In drift mode, the subducting slab is retreating and accommodates the oceanic lithosphere convergence that can freely move. Thick black and blue arrows show mantle flow and slab motion, respectively. Thin black and magenta arrows correspond to the lithosphere and trench displacements, respectively. These thin arrows are replaced by crosses when the motion is zero with respect to the upwelling. Large grey and magenta arrows correspond to compressional and extensional areas at active and passive plate margins, respectively.

to significantly contribute to the force balance, and in particular compress the upper plates. The prominent consequence is the formation of compressive belts at active plate boundaries. Because upwellings and downwellings on each side of the convection cell combine together, it is the entire plate that rides the convection cell that likely undergoes compression (Figure 2a) and collateral damage may occur anywhere in the plate, including at passive margins. The relative contributions of the upwelling and downwelling force appear critical to the wholesale compression of the plate.

[6] Slab anchoring in the lower mantle modifies the flow pattern underneath the lithosphere. If rollback freely occurs, or if it occurs faster than the oceanward motion of the upper plate, mantle flow does not dramatically interfere with the slab. Conversely, if the mantle flows faster than rollback, the convection cell gets circumscribed by the downgoing slab, on the one hand, and by the upwelling, on the other hand (Figure 2b). This modifies the state of stress in the lithosphere, and the latter will promote compression in the upper plate, at least at its active margin [*Jolivet and Faccenna*, 2000]. However, we speculate that the same regime applies to the passive counterpart. We thereafter refer to these two end members as drift mode and collision mode, respectively.

[7] Post-rift tectonic inversion at passive margins has been addressed kinematically [e.g., *Leroy et al.*, 2004], where deformation reacts to an imposed convergence rate. Here we emphasize the role of basal drag excited by mantle flow, alternatively driven by upwellings and downwellings. We therefore set out to test how upwelling and downwelling forces act on the lithosphere depending on the configuration of the lithospheric plates and to explore the required conditions that promote contraction at passive margins, when the system switches from drift to collision mode.

[8] We only consider large-scale active upwellings and downwellings. Ridge-push, and its temporal variations, are assumed to be insufficient to trigger phases of compression. We thus only test the hypothesis that compression is triggered by large-scale mantle flow and ignore lithosphere-scale processes. This study possibly best applies to the South Atlantic system, an idealized version of which we used to design the experimental setup. However, the obtained results are also applicable to other cases (e.g., Australia and Africa, see Figure 1) where the main lines of dynamics appear to be akin to that of the South Atlantic in many aspects.

2. Numerical Model

2.1. Equations Solved

[9] In our numerical code (see full description in *Yamato et al.* [2012]), we solve the Stokes equations in 2-D (equations (1) and (2)) subject to the incompressibility constraint (equation (3))

$$-\frac{\partial P}{\partial x}+\frac{\partial \tau_{xx}}{\partial x}+\frac{\partial \tau_{xz}}{\partial z}=0, \tag{1}$$

$$-\frac{\partial P}{\partial z}+\frac{\partial \tau_{zz}}{\partial z}+\frac{\partial \tau_{zx}}{\partial x}=\rho g, \tag{2}$$

$$\frac{\partial Vx}{\partial x}+\frac{\partial Vz}{\partial z}=0, \tag{3}$$

where P, τ_{ij}, ρ, and g correspond to the pressure, deviatoric stress tensor, density, and gravitational acceleration, respectively. V_x and V_z are the two components of the velocity vector in a 2-D (x, z) Cartesian coordinate system. These equations are solved numerically on a Eulerian-staggered grid by a finite difference method [*Gerya and Yuen*, 2003, 2007]. Field properties such as viscosities and densities are originally set on Lagrangian particles that can be advected following a Runge-Kutta scheme within the model domain. The numerical scheme was already intensively tested [*Yamato et al.*, 2012] and is well suited for problems involving linear viscous materials as will be used here throughout. Since we are interested in the first-order dynamics of passive margin deformation, we do not invoke more complex rheologies or

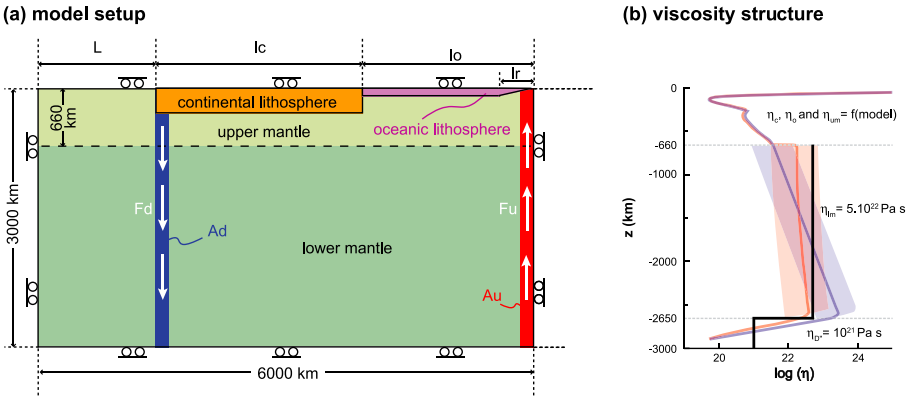

Figure 3. Initial configuration of the model. (a) Model setup. L: length of mantle space between the left-hand side of the box and the continental lithosphere; l_c: length of continental lithosphere; l_o: length of oceanic lithosphere; l_r: length corresponding to the thinning of the lithosphere due to the ridge; F_d: downwelling force; F_u: upwelling force. These buoyancy forces are implemented by setting variable densities in the red and blue columns. The area of the columns is A_d and A_u for the downwelling and the upwelling force, respectively. See also text for details. (b) Viscosity structure. η_c, η_o, and η_{um} correspond to the viscosity of the continental lithosphere, oceanic lithosphere, and upper mantle, respectively. The viscosity of the lower mantle corresponds to a simplified profile (black line). The viscosity models from *Cizkova et al.* [2012] are also provided (Family-A model in red and Family-B model in blue) as references.

geometries which introduce necessarily new parameters (e.g., temperature and stress dependent rheologies, subduction angle, passive margin morphology, oceanic lithosphere age, etc.) that would likely only blur our analysis. This also ensures the reproducibility of our results that can be easily tested by any code-solving Stokes equations with free-slip boundary conditions.

2.2. Model Setup

[10] Our model approximates a part of the Earth's mantle located between the core-mantle boundary and the surface. Our model geometry is purposely kept as simple as possible (Figure 3a). The Cartesian box is 6000 km wide and 3000 km deep. The grid resolution used is of 601 × 301 nodes which corresponds to a spatial resolution of 10 km. We consider this resolution sufficient because (i) the wavelength of the expected perturbations are typically one order of magnitude higher and (ii) we performed resolution tests; by increasing the resolution by factors of 2 and 4 that lead to very similar velocity fields. All the mechanical boundary conditions are free slip and all the viscosities in our model are linear viscous.

[11] A continental lithosphere adjacent to an oceanic lithosphere at its right-hand side is located on the top of the model (Figure 3a). The left-hand side of the continental lithosphere rests above a body of negative buoyancy that models a downwelling zone (slab in subduction zone). It integrates to a downward force F_d. Tuning the density contrast between the whole mantle and this prescribed domain (in blue in Figure 3a) sets the value of F_d. At the opposite, the right side of the oceanic lithosphere rests above a domain of positive buoyancy, which integrates to an upward force F_u and that similarly models an upwelling zone (in red in Figure 3a). In this last case, the density difference between the upwelling material and the mantle is then negative. These two forces (F_d and F_u) are the only driving forces in our model, and they are balanced by viscous dissipation in the mantle. We do not consider other effects, whose contributions (e.g., details of slab bending, interplate friction as resisting forces, and gravitational sliding of the cooling oceanic lithosphere ("ridge push") as driving forces) may explain local departures from the general behavior that we test here because our model is more conceptual than applied to a given setting.

[12] The net values of these internal forces are, however, not well known. For the South Atlantic, the sum of F_d and F_u is supposed to be on the order of $\sim 10^{13}\,\mathrm{N\,m^{-1}}$ [*Husson et al.*, 2012], for example. To facilitate comparison between all of our models, we decided to keep the net force ($F_u + F_d$) that excites the mantle convection cell constant. In that way, this total force can be easily distributed between the upwelling and/or downwellings (see section 3.2). This total force is somewhat arbitrarily set to $2 \cdot 10^{13}\,\mathrm{N\,m^{-1}}$ in all our models, corresponding to typical plate tectonic value (slab pull, [see e.g., *Turcotte and Schubert*, 1982]). This choice does not restrict generality: since everything is linear in our experiments, should this force be modified by a given factor, our quantitative results would scale accordingly, but our conclusions would not be altered. In addition, the same results can be obtained for other values by adjusting the viscosities by an appropriate factor. In that sense, we could have opted for a dimensionless analysis, but for an easiest comparison with natural data, we decided to keep dimensional values.

[13] In our models, continental and oceanic lithospheres are modeled by rectangular bodies. The "ridge side" of the oceanic lithosphere ends as a triangle over 500 km (i.e., l_r = 500 km, Figure 3a). The oceanic lithosphere is not attached to the right-hand side of the box, for one upper mantle cell separates it from the model box edge. This ensures that the lithosphere is free to move laterally and is not affected by the free-slip boundary condition imposed at the right side, which would impose $V_x = 0$ at the lithosphere edge. Setting different values for l_r only modifies the results by no more than $1\,\mathrm{mm\,yr^{-1}}$ and yields overall very similar kinematics. For this reason, we thus chose to stick to a value of l_r set to 500 km in all our computations.

[14] The influence of the thickness of both the oceanic and continental lithospheres is not presented here either for two reasons. First, by testing different values for the thickness of the oceanic lithosphere and considering that the continental lithosphere thickness is larger than the oceanic one, the results are identical. Second, since these parameters can be inferred from geophysical data, they do not constitute a real unknown parameter. We thus fixed typical thicknesses to 200 km and 100 km [e.g., *Conrad and Lithgow-Bertelloni*, 2006] for the continental and the oceanic lithosphere, respectively. The width of the continental lithosphere is similarly set in all our models to 2000 km.

[15] In our model, the density is generally uniform and set to $\rho_{\mathrm{ref}} = 3250\ \mathrm{kg\,m^{-3}}$ everywhere in the model box. Density differences are only assigned to the upwelling and the downwelling zones that drive, by buoyancy, the convection cell (Figure 3a). The density value in the upwelling (ρ_u) and in the downwelling (ρ_d) areas depends on the buoyancy force applied and are expressed as follows:

$$\rho_u = \rho_{\mathrm{ref}} - \frac{F_u}{\rho_{\mathrm{ref}} \cdot g \cdot A_u} \tag{4}$$

$$\rho_d = \rho_{\mathrm{ref}} + \frac{F_d}{\rho_{\mathrm{ref}} \cdot g \cdot A_d} \tag{5}$$

where F_u and F_d correspond to the absolute values of the upwelling and downwelling forces, respectively, and g is the gravitational acceleration (set to $9.81\ \mathrm{m\,s^{-2}}$). These upwelling and downwelling forces are thus evenly distributed over the surfaces A_u and A_d, respectively (see Figure 3a). Here we focus on the tractions caused by convective flow in the mantle. However, we are aware that the complete lithospheric stress field will also have contributions due to lateral variations in the gravitational potential energy due to differences in the vertical density structure above the compensation depth. In particular, the mean continental plate stress state is strongly affected by the density of the lithospheric mantle and crustal thickness [*Fleitout and Froidevaux*, 1983]. Any such effects will be superimposed on the patterns we discuss here.

[16] The viscosity profile used in our models is presented in Figure 3b. The viscosity in the lower mantle corresponds to a very simplified profile: From 660 km to 2650 km depth, the viscosity is set to $\eta_{\mathrm{um}} = 5 \cdot 10^{22}$ Pa s. Below, the viscosity is set to 10^{21} Pa s (D″ layer). Experiments have also been done by using a B-family profile (see details in *Cizkova et al*. [2012]). However, since the results yield identical conclusions, we thus choose to use the simplest 1-D viscosity profile for this study. Above the lower mantle, the viscosities are not well resolved and therefore need to be tested (section 3.1). To simplify, we considered the viscosity of the continental lithosphere, of the oceanic lithosphere, and of the upper mantle as linear and constant. Implementing nonlinear rheologies would at the largest scales mainly affect rates but not patterns of mantle flow, and likely by an amount that is not critical to our aims of conceptual exploration [see e.g., *Becker*, 2006]. Our simplified rheology also implicitly discards the effect of slab stiffness that will modulate the surrounding mantle flow [e.g., *Conrad and Lithgow-Bertelloni*, 2002; *Loiselet et al*., 2010]. In fact, because there is no proper slab-like structure—besides the density of the negatively buoyant unit—the models where the downwelling zone is remote from the box edge correspond to a subduction zone that offers no resistance to the upper plate, i.e., a subduction zone where the rate of rollback adjusts to the rate at which the upper plate migrates toward the subduction zone. Conversely, models where the downwelling zone is at the box edge corresponds to a situation where the slab offers an absolute resistance to upper plate drift. These situations shall thus be considered as the two end members Earth-like regimes of subduction.

[17] The aim of our study is (i) to quantify the influence of the force balance between downwelling and upwelling on the deformation of the lithosphere, and (ii) to highlight the consequences of the current continental aggregation that, to some extent, corresponds to the transition from a continent that is free to ride over the mantle (drift mode) to a continent that is blocked by the adjacent subducting or colliding plates (collision mode). However, since it is impossible to address this problem without some knowledge of the viscosities of the lithospheres and upper mantle, they thus need to be constrained first. We thus proceed to test the influence of the upper mantle and of the continental/oceanic lithosphere viscosities.

3. Results

[18] As the natural observation described in section 1 corresponds to the actual state of the lithosphere, we first focused our study on the collision mode ($L = 0$, see Figure 3a). This configuration corresponds to the actual state of the South American plate blocked at its eastern margin by the subduction of the Nazca plate, anchored underneath the Andes [*Husson et al*., 2012]. This reference model will be used later for a study through time (in drift mode) by using different values for L (see Figure 3a). This allows us to constrain (i) the suitable radial viscosity structure and (ii) the force balance needed to match the model results (velocity and strain rate) with observations. These parameters will form the basis upon which we further elaborate our analysis of the time evolution of this system.

3.1. Setting Up the Radial Viscosity Structure

[19] In the collision mode, $L = 0$ and the lithosphere cannot move freely above the convection cell (see Figure 1a). As noted in section 1, the net driving force involved in this example amounts to $2 \cdot 10^{13}\ \mathrm{N\,m^{-1}}$. This total force is evenly distributed ($F_u = F_d = 10^{13}\ \mathrm{N\,m^{-1}}$). The influence of this partitioning of the total force is discussed later in section 3.2. Figure 4 shows the results obtained with an identical viscosity for both oceanic and continental lithospheres and a range of viscosities for the upper mantle.

[20] In such configurations, for an acceptable range of values of the upper mantle viscosity η_{um} (from 10^{19} to 10^{21} Pa s), the viscosity of the continental lithosphere η_{c} should be close to 10^{22} Pa s in order to get strain rates in the lithosphere that compare to the observations, for the Andes in particular. Indeed, in these models (i) the strain rate reaches its maximal value close to the collision area (corresponding to the Andes) and (ii) the second invariant strain rate profile is between 10^{-15} and $10^{-16}\ \mathrm{s^{-1}}$ over ~500 km width decreasing from the west to the east, which is comparable to the value inferred from the World Strain Rate Map (WSRM) of *Kreemer et al*. [2003]. For higher viscosities ($\eta_{\mathrm{c}} = \eta_{\mathrm{o}} = 10^{23}$ Pa s), deformation in the collision area becomes

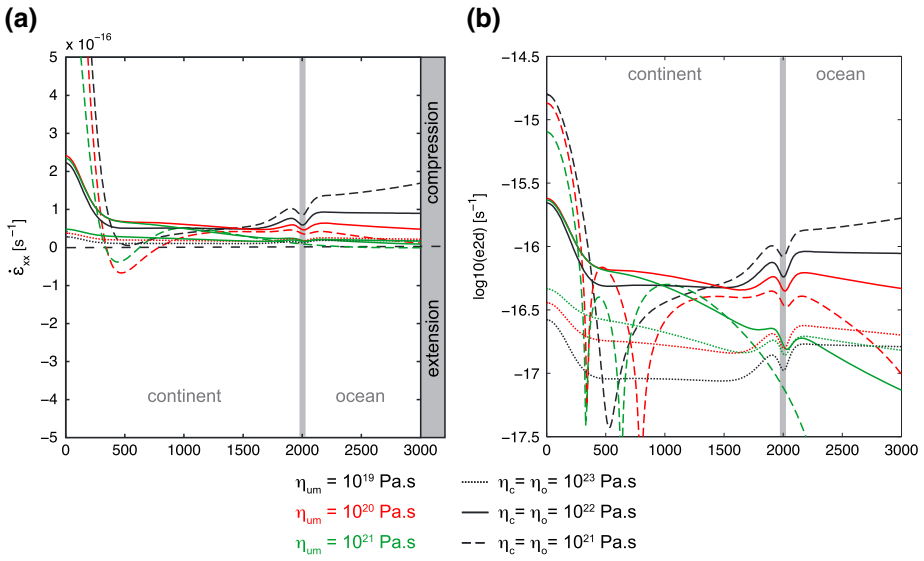

Figure 4. (a) Shortening rate $\dot{\varepsilon}_{xx}$ (horizontal component of the strain rate tensor) at the surface across the 3000 km long continental and oceanic lithospheres ($L = 0$ km, $l_c = 2000$ km, $F_d = F_u = 10^{13}$ N m^{-1}, see Figure 3a). Positive values of $\dot{\varepsilon}_{xx}$ correspond to compression. (b) Logarithm of the second invariant of the strain rate (e2d) along the same profile.

too small ($< 10^{-16}$ s^{-1}, Figure 4a) and the corresponding second invariant of the strain rate (Figure 4b, dotted lines) is low ($< 10^{-16}$ s^{-1}). Moreover, this leads to deformation at the passive margin with the same order of magnitude as that at the active margin, which is obviously not the case in reality. The second invariant of the strain rate at passive margins is close to zero in the WSRM because strain rates are much lower than that at the active margins. However, the World Strain Rate Map should, of course, be taken with caution because its usefulness is inherently limited to regions where there is sufficient (geodetic) data coverage, and this is generally not the case for passive margins.

[21] For lower continental lithosphere viscosities, deformation in the collisional area (Andes) is also high and extends over ~500 km width; however, these models yield unrealistic extension at the back (Figure 4a, dashed lines), which is also incompatible with the case of the South American plate in particular. This acceptable value of 10^{22} Pa s is in good agreement with values found for the effective viscosity of the deforming Andean lithosphere [e.g., *Husson and Ricard*, 2004]. As to the viscosity ratio between the lithosphere and upper mantle, our models show that it should be ~100 to produce both realistic strain rates of passive margins and a limited deformation of the oceanic lithosphere. For a higher viscosity ratio, no deformation of the passive margin occurs (Figure 4a, green lines). If, conversely, this viscosity ratio is too low, deformation of the oceanic lithosphere becomes higher than that at the passive margin, in disagreement with observations [e.g., *Kreemer et al.*, 2003]. Within the framework of our model simplifications, the average viscosity of the lithosphere is hence quite well constrained: the viscosity of the continental lithosphere has to be ~10^{22} Pa s and ~100 times that of the upper mantle. These values are in good agreement with those obtained from postglacial rebound and convection studies (see e.g., *Mitrovica and Forte*, 2004; and discussion in *Cizkova et al.* [2012]), even if lateral viscosity variations can trade-off with such average layer estimates [e.g., *Yoshida and Nakakuki*, 2009; *Ghosh et al.*, 2010].

[22] However, constant viscosity for both continental and oceanic lithosphere is problematic because in such a configuration, the strain rate in the oceanic lithosphere is higher than that at the passive margin (Figure 4a). Increasing the viscosity ratio between the oceanic and continental lithospheres yields more acceptable predictions. Results are

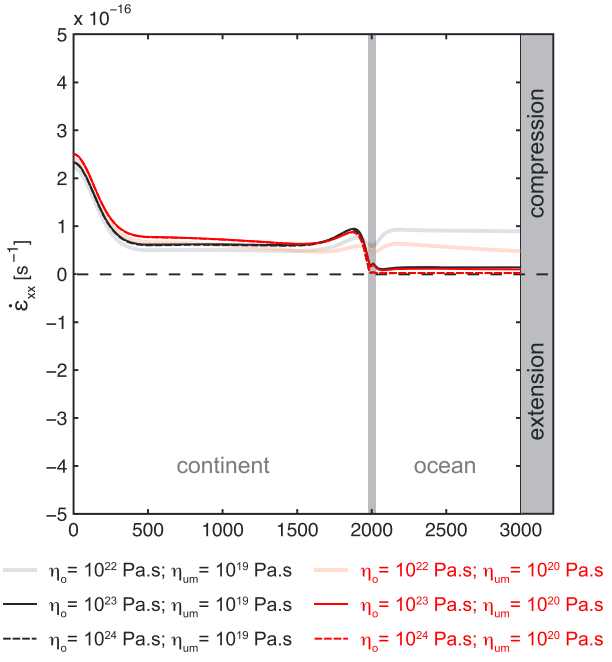

Figure 5. Horizontal component of the strain rate ($\dot{\varepsilon}_{xx}$) across the 3000 km long continental and oceanic lithospheres ($L = 0$ km and $l_c = 2000$ km, see Figure 3a), for a variety of oceanic η_o and upper mantle η_{um} viscosities. The viscosity of the continental lithosphere η_c is set to 10^{22} Pa s.

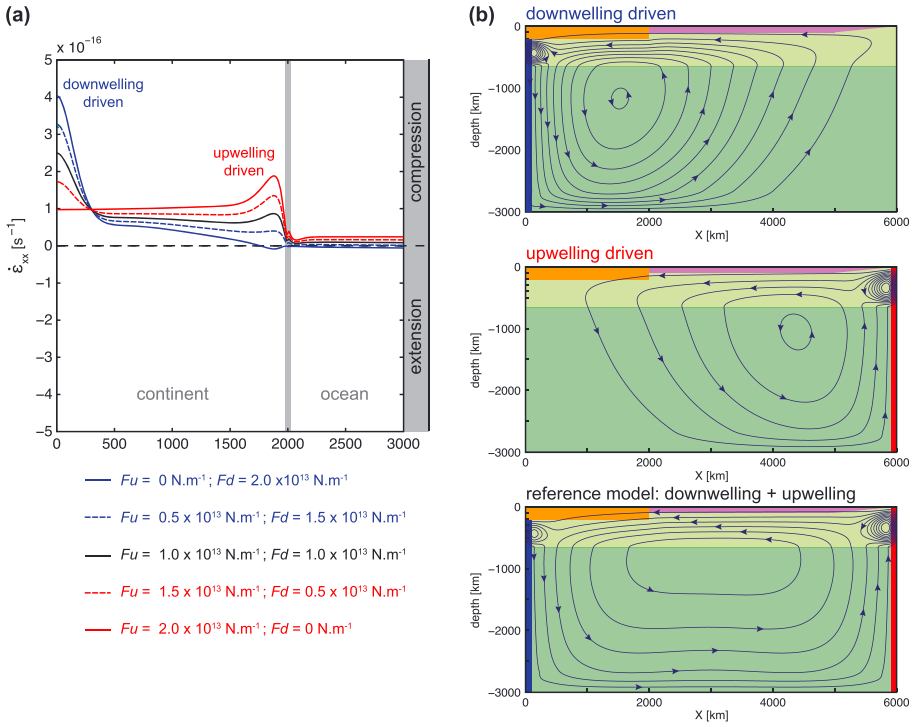

Figure 6. (a) Strain rate at the surface across the 3000 km long continental and oceanic lithospheres ($L = 0$ km and $l_c = 2000$ km, see Figure 3a). (b) Streamlines obtained for the downwelling driven model ($F_u = 0\ \mathrm{N\,m^{-1}}$, $F_d = 2 \cdot 10^{13}\ \mathrm{N\,m^{-1}}$), the upwelling driven model ($F_u = 2 \cdot 10^{13}\ \mathrm{N\,m^{-1}}$, $F_d = 0\ \mathrm{N\,m^{-1}}$), and the reference model ($F_u = 10^{13}\ \mathrm{N\,m^{-1}}$, $F_d = 10^{13}\ \mathrm{N\,m^{-1}}$).

shown in Figure 5 for different viscosity values for the oceanic lithosphere (from 10^{22} to 10^{24} Pa s) and upper mantle (10^{19} and 10^{20} Pa s).

[23] These results show that regardless of the absolute viscosity of the oceanic lithosphere, similar results are obtained provided that the oceanic lithosphere is more viscous than the continental counterpart. This choice is plausible given the globally uneven distribution of intraplate seismicity [e.g., *Gordon*, 2000] and the rheological inference that the strength of the oceanic lithosphere at a passive margin should be higher than the continental one for ages older than ~100 Myr [e.g., *Kohlstedt et al.*, 1995]. Indeed, similar viscosities have been used by *Leroy et al.* [2004] to explore the deformation at passive margins.

[24] In summary, these results show that—at least in a collisional mode—the best parameters that yield results that are in agreement with the observations are: (i) a viscosity for the continental lithosphere (η_c) of about 10^{22} Pa s, (ii) a stiffer oceanic than continental lithosphere ($\eta_o > \eta_c$), and (iii) an upper mantle viscosity (η_{um}) in the range from 10^{19} to 10^{20} Pa s. We accordingly use $\eta_c = 10^{22}$ Pa s; $\eta_o = 10^{23}$ Pa s and $\eta_{um} = 10^{20}$ Pa s for our reference model.

3.2. Influence of the Force Balance: Upwellings Versus Downwellings

[25] We build upon our reference experiment to explore the respective influence of the downwelling and upwelling forces. In a collisional mode, our reference model is driven by a mantle convection cell excited by both the lateral downwelling and the upwelling ($F_u = F_d = 10^{13}\ \mathrm{N\,m^{-1}}$). To test the respective effect of the downwelling and the upwelling forces on the strain rate profile in the lithosphere, we modified their respective contribution but kept the net sum of these forces unchanged throughout all models.

[26] The strain rate profiles in the lithosphere are presented in Figure 6a and the streamlines of global mantle flow in Figure 6b. Increasing the downwelling force relative to the upwelling force leads to an increase of the compressive deformation on the active margin side and to a decrease of the compressive deformation on the passive margin side. More interestingly, if the upwelling force is completely switched off, the passive margin undergoes extension. Conversely, increasing the upwelling force compared to the downwelling force fosters compression at the passive margin. Strain rates are equal at both passive and active margins when the upwelling force amounts to ~1/3 of the downwelling force.

[27] From these results, we suggest that upwellings play a major role on the stress regime of the lithosphere located above the convection cell. In the absence of upwellings at the ridge end of the cell, passive margins are in extension because upwellings push plates and thus only add compression. Downwellings conversely pull the plates toward the subduction zones. In principle, by doing so, they add extension. But these observations only hold at large distances from the trench; in the mantle wedge next to the trench, corner flow (Figure 6b) causes sublithospheric horizontal shear stress to increase away from the trench, up to a certain distance that scales with the thickness of the upper mantle. This flow compresses the lithosphere next to the trench; a mechanism that has been previously envisioned as a driver for the Andean orogeny [e.g., *Wdowinski and O'Connell*, 1991]. Moreover, the ratio between upwelling and downwelling

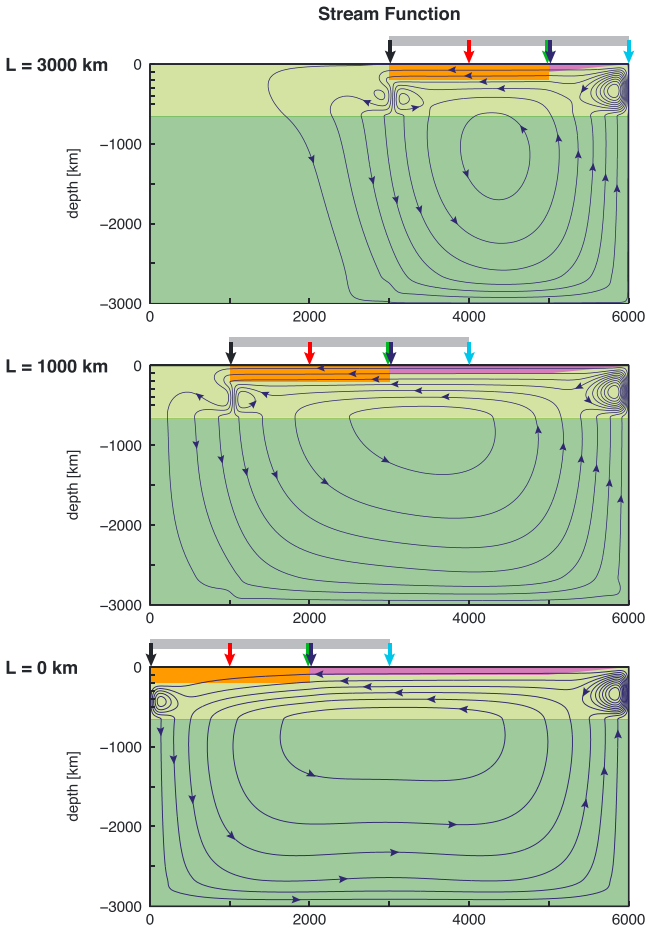

Figure 7. Streamlines (in blue) for three models where the only difference is the distance (L) from the left-hand side of the box to the continental lithosphere. Arrows with different colors correspond to the locations of the different vertical profiles shown in Figure 8. The gray segment shows the location of the strain profiles of Figure 9.

forces should be close to 1 and larger than ~1/3 to produce both high strain rates in the collision zone (typically the Andes) and smaller rates at passive margins, in agreement with general observations, and with the South American plate in particular.

[28] To fit with observations of the strain rate occurring both at the active and at the passive margin, the preferred setting in the collision mode seems to be the one where upwellings and downwellings act in comparable fractions of the net driving force. In order to test the evolution of the strain regime through time between the drift mode and the collision mode, we thus choose to use equal upwelling and downwelling forces (i.e., $F_u = F_d = 10^{13}\,\mathrm{N\,m^{-1}}$).

3.3. Drift Versus Collision Mode

[29] At the opposite of the collision mode, where the continental lithosphere is blocked by an anchored subducting plate (or similarly, by a collision), the drift mode corresponds to a case of free motion of the lithosphere located over the convection cell (see Figure 2). To address the consequences of the transition from drift to collision mode, we performed experiments by placing the continental lithosphere and the downwelling at different distances (L) from the left-hand side of our model box (see Figure 3a). These instantaneous experiments mimic the time evolution of the dynamics of the system during this transition.

[30] Figure 7 shows the streamlines obtained for $L = 3000$ km, $L = 1000$ km (i.e., in drift mode), and $L = 0$ km (i.e., in collision mode). Viscosity parameters are the same as for the reference model ($\eta_{um} = 10^{20}$ Pa s, $\eta_c = 10^{22}$ Pa s, and $\eta_o = 10^{23}$ Pa s) and the force balance is set as follows: $F_u = 10^{13}\,\mathrm{N\,m^{-1}}$ and $F_d = 10^{13}\,\mathrm{N\,m^{-1}}$. The size of the convection cell increases with time when L is decreasing. Consequently, since the total force in the system is kept constant ($F_u + F_d = 2 \cdot 10^{13}\,\mathrm{N\,m^{-1}}$), the volume of mantle that enters in motion increases with the dimension of the cell, and the velocity in the horizontal direction of the lithosphere located over the mantle is then decreasing. This can be observed on Figure 8 where vertical profiles of the horizontal velocity are provided for the three different cases, at different locations in the model (see arrows on Figure 7). Indeed, at the surface, the velocity (V_x) decreases from $L = 3000$ km to $L = 1000$ km (difference between dashed and dotted lines on Figure 8).

[31] Figures 7 and 8 show that the flow below the lithosphere is dramatically different between these two modes. In drift mode (dashed and dotted lines, Figure 8), mantle circulation resembles a Poiseuille flow with a free surface. As the lithosphere approaches the end wall and therefore is no longer free to move laterally, the upper mantle circulation gradually converts into a Poiseuille flow in the strict sense,

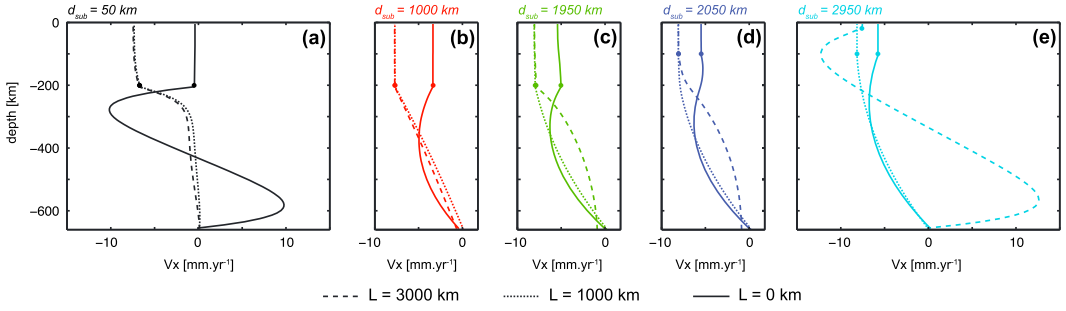

Figure 8. Vertical profiles through the model box showing the evolution of the horizontal velocity with time when the distance L is decreasing. These profiles are computed at different distances (d_{sub}) from the left edge of the continental lithosphere (subduction zone). Colors correspond to these locations represented by color arrows in Figure 7. (a), (b), and (c) Profiles that pass across the continental lithosphere and (d) and (e) profiles that pass across the oceanic lithosphere. The dots correspond to the lithosphere-upper mantle transition.

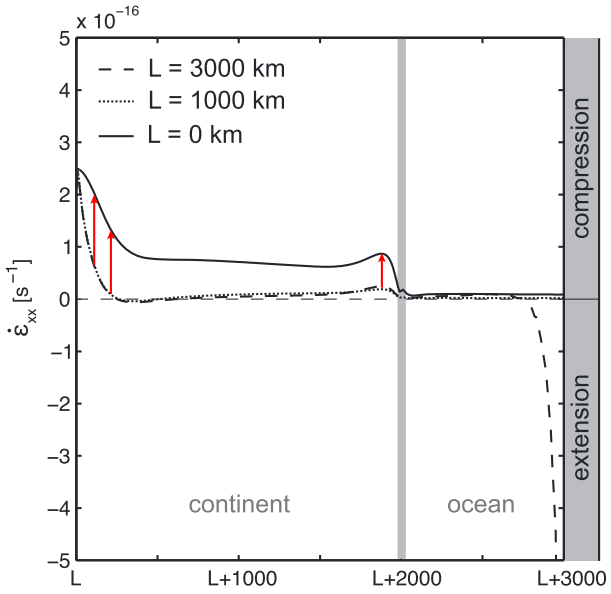

Figure 9. Horizontal component of the strain rate ($\dot{\varepsilon}_{xx}$) at the surface across the 3000 km long continental and oceanic lithospheres. Red arrows show the jump that occurs at the transition from drift mode to collision mode.

between two units that deform at much slower rates, namely the lithosphere and the lower mantle. This behavior is akin to the transition from a mobile lid to a sluggish lid regime of mantle convection. The horizontal velocities at the surface are also different along the lithosphere, indicating that large deformation occurs. The mantle flow just below the lithosphere switches from a convex shape oriented toward the upwelling (convex-right in Figure 8, dashed and dotted lines) to a convex shape oriented toward the downwelling (convex-left in Figure 8, solid line) when the system switches from drift to collision mode.

[32] Since it reflects the variation of the horizontal velocity field in the lithosphere, the same conclusions are achieved when plotting the resulting horizontal strain rate profile in the lithosphere (Figure 9). This graph clearly shows that strain rates are boosted at the transition between the drift mode and the collision mode (red arrows). In drift mode, large deformation occurs at the active margin, but this compression is restricted to the first ~250 km from the trench. Strain rates do not vary in drift mode at the active margin, which is unaffected by the distance to the upwelling. The continental lithosphere is not deformed at all excepted at the passive margin where we clearly see the influence of the upwelling. When the upwelling is closer to the passive margin ($L = 3000$ km, dashed line), the force acting on the lithosphere is bigger because the convection cell is smaller and less viscous dissipation occurs in the mantle. The deformation then decreases during ocean spreading (e.g., $L = 1000$ km, dotted line) until the system enters the collision mode. Then, strain rates dramatically increase at the active margin, further in the continent, and at the passive margin. The joint effects of upwellings and downwellings are thus essential in collision mode but not in drift mode.

4. Discussion

[33] To first order, the compression at passive margins can be reproduced under certain conditions: (i) the motion of the lithosphere above the convection cell has to be prevented or impeded by slab anchoring, continental collision, or any mechanism suited to restrain plate motion, (ii) upwellings have to be active, as the downwellings alone do not trigger compression at passive margins, (iii) the oceanic lithosphere has to be stronger than the continental lithosphere, and (iv) the viscosity ratio between the lithosphere and the upper mantle has to be ~100.

[34] Under these conditions, even our simple models yield results that agree with observations. The magnitude of compression at passive margins is likely sufficient to trigger viscous compression but also tectonic inversion, uplift and exhumation of passive margins. These models present, however, certain crude assumptions, in particular because they rely on linear viscous rheology which only varies with depth. However, the aim of this study is not to perfectly fit the data but to test the plausibility of a mechanism, i.e., to explore how upwelling and downwelling forces in the mantle stress the lithosphere, and may or may not supply the necessary conditions for passive margin inversion when the system switches from drift to collision mode.

[35] Perfectly fitting the data is outside the scope of this study, as too many unknowns such as the precise value of the total driving force, its partitioning between upwellings and downwellings, the departure from an idealized convection cell, and more accurate rheological parameters should be accounted for. In particular, the viscosity structure could be tuned because continental margins (both active and passive) are probably weaker than the continental lithosphere itself, because of the stress and temperature dependence of the rheology. By tuning such parameters, it may be possible to obtain a closer resemblance to nature, but the global dynamics will likely be the same as in our abstract models. Passive margin compression could not be achieved without a convection regime that approaches that of a sluggish lid, and without the active support from an upwelling force at the ridge side of the convection cell, in addition to the ridge-push, whose magnitude and above all, the magnitude of its temporal changes, are smaller and would not significantly alter the force balance.

[36] The simplified model setup that we designed here is mostly conceptual and does not allow for a close examination of the location of expected locations of compression. We therefore also conducted tests using more "realistic," 3-D spherical models (Figure 10), using the global mantle flow modeling setup as discussed by *Becker and Faccenna* [2011]. We explore models where mantle flow is alternatively driven by density anomalies inferred from seismic tomography—and therefore includes both downwellings at subduction zones and upwellings above the superswells—and density anomalies that correspond to subducting slabs only. While the second scenario (Figure 10a) mostly compresses the active margins of upper plates and leaves other areas at rest, the first scenario (Figure 10b) efficiently compresses passive margins where the geological record reveals their uplift, exhumation, and tectonic inversion. This confirms the conclusions from the simplified 2-D models.

[37] Such effects are particularly clear for the South American plate, where only the active margin is under compression if flow is driven by the descending Nazca slab alone, and both active and passive margins are compressed when mantle upwellings drive the system. This finding also

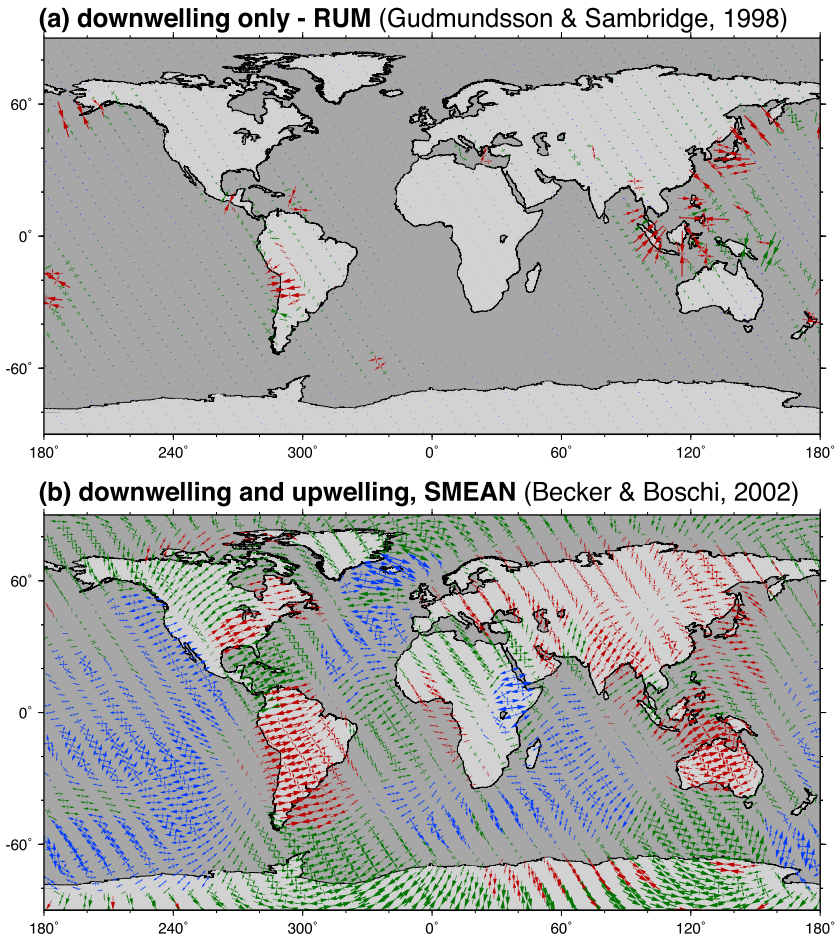

Figure 10. Global, 3-D spherical circulation models. Red, green, and blue arrows correspond to compressive, transform, and extensive areas, respectively. Arrow sizes relate to the magnitude. Results are obtained using density anomalies corresponding to (a) subducting slabs only (RUM: Regionalized upper mantle model [*Gudmundsson and Sambridge*, 1998]) and (b) results obtained when the flow include both downwellings at subduction zones and upwellings above the superswells (SMEAN: Composite *S* wave model by *Becker and Boschi* [2002]). See *Becker and Faccenna* [2011] for details.

holds along passive margins from western Africa, Eastern North America, Scandinavia and the British Isles, and in Australia, providing a good match with the examples of Figure 1. Unlike these more Earth-like global circulation models, the simplified model setup that we designed here is mostly conceptual and does not allow for a close examination of the location of expected locations of compression. The advanced regional specificity of the global models also helps to explain for instance that observed tectonic inversion and exhumation sometimes occur remotely from the strict ocean-continent boundary (Figure 1).

[38] The large-scale, deep mantle flow mechanisms that we discuss here may well interact with local, self-destabilization and subduction initiation effects at passive margins, in particular along the Atlantic [*Nikolaeva et al*., 2010, 2011]. Gravitational instabilities arise due to the effectively positively buoyant continental lithosphere, and may lead to underthrusting of the oceanic lithosphere beneath the continental lithosphere, if this latest is sufficiently weak to flow. *Nikolaeva et al*. [2010] show that such instabilities may occasionally trigger modest compression and uplift. The far-field forces due to the underlying mantle convection, that act as a vice, would facilitate this destabilization, foster underthrusting, uplift, and exhumation of the passive margin.

[39] Also, some regional settings deserve particular attention. For instance, Greenland does not clearly fit in our simplified model setup because it is surrounded by passive margins. Yet this situation is even more prone to compression (modeling shows that sea floor spreading compresses plates, subduction extends them). However, our global circulation models do not reveal compression but strike slip in the region. This result may be due to the fact that the model lacks definition for shorter wavelength patterns of mantle flow because the resolution of the input tomographic model compares to that of Greenland itself.

5. Conclusions

[40] In summary, both our simplified theoretical models and more Earth-like global circulation models reveal that the combined buoyancy forces from upwellings and downwellings play a prominent role in the tectonic reactivation of passive margins, their uplift, and exhumation. Plate convergence is assisted by pulsating deep mantle upwellings which transiently

actively stimulate plate motion at the other end, on the ridge-side. The Cenozoic is the time during which many mountain belts grew worldwide. It is also the time during which the free drift of continents above the mantle became gradually hampered by multiple collisions, like Africa-Eurasia, Arabia-Eurasia, India-Eurasia, Australia-Eurasia, and slab anchoring underneath South America [*Husson et al*., 2012]. These events are contemporaneous with the disappearance of many subduction zones (most of the Tethys and Farallon), while total ridge length remained steady. All of these events contribute to an increase of the compression in the lithosphere. Most emblematic is the development of the American cordilleras and Alpine chains. However, the same mechanism may also have led to compression at passive margins, as shown by the simultaneous morphotectonic events at passive margins (as discussed for South America by *Cogné et al*. [2012], for example). Such compressive events, both at active and passive margins, were likely boosted by active mantle upwellings. The activity of those upwellings may be somewhat irregular, leading us to suggest that morphotectonic activity at both passive and active margins is strongly affected by the transient bursts that may occur on the ridge side of tectonic plates, e.g., due to pulsating thermochemical, deep mantle plumes. Indeed, other upwelling pulses may have occurred at other times, as highlighted for instance by post-rift vertical movements and horizontal deformation observed in the eastern margin of the Central Atlantic before the Cenozoic [*Bertotti and Gouiza*, 2012]. In principle, this mechanism could thus have prevailed during other compressive phases (Hercynian, for instance), and this would be an indirect proxy to evaluate the respective roles of upwellings and downwellings in the past, as well as their geometrical distribution. Unfortunately, deformation at passive margins is most certainly too subtle to be preserved earlier than the current collision phase. For the more recent times, however, the not-so-passive margins may hold useful, and as of yet no fully exploited clues, for unraveling the dynamics of plate tectonics.

[41] **Acknowledgments.** We thank Gael Choblet for the fruitful discussions at the beginning this work. P.Y. thanks Thibault Duretz and Dave May for the help during the code development. We also highly appreciated the constructive comments of the Associate Editor, Giovanni Bertotti, an anonymous reviewer, and Peter Japsen.

References

Andersen, M. S., and L. O. Boldreel (1995), Tertiary compression structures in the Faeroe-Rockall area, *Geol. Soc. London Spec. Publ.*, *90*, 215–216.

Becker, T. W. (2006), On the effect of temperature and strain-rate dependent viscosity on global mantle flow, net rotation, and driving forces, *Geophys. J. Int.*, *167*, 943–957.

Becker, T. W., and L. Boschi (2002), A comparison of tomographic and geodynamic mantle models, *Geochem. Geophys. Geosyst.*, *3*(1), 1003, doi:10.1029/2001GC000168.

Becker, T. W., and C. Faccenna (2011), Mantle conveyor beneath the Tethyan collisional belt, *Earth Planet. Sci. Lett.*, *310*, 453–461.

Becker, T. W., and R. J. O'Connell (2001), Predicting plate velocities with mantle circulation models, *Geochem. Geophys. Geosyst.*, *2*, doi:10.1029/2001GC000171.

Bertotti, G., and M. Gouiza (2012), Post-rift vertical movements and horizontal deformations in the eastern margin of the Central Atlantic: Middle Jurassic to Early Cretaceous evolution of Morocco, *Int. J. Earth Sci.*, *101*, 2151–2165.

Bishop, P., and G. Goldrick (2000), Geomorphological evolution of the East Australian continental margin, in *Geomorphology and Global Tectonics*, edited by M. A. Summerfield, pp. 227–255, Wiley, Chichester, U. K.

Blakey, R. C. (2008), Gondwana paleogeography from assembly to breakup —A 500 m.y. odyssey, *Geol. Soc. Am. Spec. Pap.*, *441*, 1–28.

Brekke, H. (2000), The tectonic evolution of the Norwegian Sea Continental Margin with emphasis on the Vøring and Møre Basins, *Geol. Soc. London Spec. Publ.*, *167*, 327–378.

Briggs, S. E., R. J. Davies, J. Cartwright, and R. Morgan (2009), Thrusting in oceanic crust during continental drift offshore Niger Delta, equatorial Africa, *Tectonics*, *28*, TC1004, doi:10.1029/2008TC002266.

Brown, R. W., M. A. Summerfield, and A. J. W. Gleadow (2002), Denudational history along a transect across the Drakensberg Escarpment of southern Africa derived from apatite fission track thermochronology, *J. Geophys. Res.*, *107*(B12), 2350, doi:10.1029/2001JB000745.

Cizkova, H., A. P. van den Berg, W. Spakman, and C. Matyska (2012), The viscosity of Earth's lower mantle inferred from sinking speed of subducted lithosphere, *Phys. Earth Planet. Inter.*, *200–201*, 56–62.

Clift, P. D. (2010), Enhanced global continental erosion and exhumation driven by Oligo-Miocene climate change, *Geophys. Res. Lett.*, *37*, L09402, doi:10.1029/2010GL043067.

Cloetingh, S., and J. D. Van Wees (2005), Strength reversal in Europe's intraplate lithosphere: Transition from basin inversion to lithospheric folding, *Geology*, *33*, 285–288.

Cloetingh, S., F. Beekman, P. A. Ziegler, J. D. Van Wees, and D. Sokoutis (2008), Post-rift compressional reactivation potential of passive margins and extensional basins, *Geol. Soc. Spec. Publ.*, *306*, 27–70.

Cobbold, P. R., K. Meisling, and V. S. Mount (2001), Reactivation of an obliquely rifted margin, Campos and Santos basins, southeastern Brazil, *Am. Assoc. Pet. Geol. Bull.*, *85*, 1925–1944.

Cobbold, P. R., E. A. Rossello, P. Roperch, C. Arriagada, L. A. Gomez, and C. Lima (2007), Distribution, timing, and causes of Andean deformation across South America, *Geol. Soc. London Spec. Publ.*, *272*, 321–343.

Cogné, N., K. Gallagher, and P. R. Cobbold (2011), Post-rift reactivation of the onshore margin of southeast Brazil: Evidence from apatite (U-Th)/He and fission-track data, *Earth Planet. Sci. Lett.*, *309*, 118–130.

Cogné, N., K. Gallagher, P. R. Cobbold, C. Riccomini, and C. Gautheron (2012), Post-breakup tectonics in southeast Brazil from thermochronological data and combined inverse-forward thermal history modeling, *J. Geophys. Res.*, *117*, B11413, doi:10.1029/2012JB009340.

Conrad, C. P., and C. Lithgow-Bertelloni (2002), How mantle slabs drive plate tectonics, *Science*, *298*, 207–209.

Conrad, C. P., and C. Lithgow-Bertelloni (2006), Influence of continental roots and asthenosphere on plate-mantle coupling, *Geophys. Res. Lett.*, *33*, L05312, doi:10.1029/2005GL025621.

Doré, A. G., E. R. Lundin, C. Fichler, and O. Olesen (1997), Patterns of basement structure and reactivation along the NE Atlantic margin, *J. Geol. Soc.*, *154*, 85–92.

Faccenna, C., T. W. Becker, C. P. Conrad, and L. Husson (2013), Mountain building and mantle dynamics, *Tectonics*, *32*, 80–93, doi:10.1029/2012TC003176.

Fleitout, L., and C. Froidevaux (1983), Tectonic stresses in the lithosphere, *Tectonics*, *2*, 315–324.

Gallagher, K., and R. Brown (1999), The Mesozoic denudation history of the Atlantic margins of southern Africa and southeast Brazil and the relationship to offshore sedimentation, in *The Oil and Gas Habitats of the South Atlantic*, Geol. Soc. Spec. Publ., vol. 153, edited by N. R. Cameron, R. H. Bate, and V. S. Clure, pp. 41–53.

Gerya, T. V., and D. Yuen (2003), Characteristics-based marker-in-cell method with conservative finite-differences schemes for modeling geological flows with strongly variable transport properties, *Phys. Earth Planet. Inter.*, *140*, 293–318.

Gerya, T. V., and D. Yuen (2007), Robust characteristics method for modelling multiphase visco-elasto-plastic thermo-mechanical problems, *Phys. Earth Planet. Inter.*, *163*, 83–105.

Ghorbal, B., G. Bertotti, J. Foeken, and P. Andriessen (2008), Unexpected Jurassic to Neogene vertical movements in 'stable' parts of NW Africa revealed by low temperature geochronology, *Terra Nova*, *20*, 355–363.

Ghosh, A., T. W. Becker, and S. J. Zhong (2010), Effects of lateral viscosity variations on the geoid, *Geophys. Res. Lett.*, *37*, L01301, doi:10.1029/2009GL040426.

Gomes Sant'Anna, L., H. D. Schorscher, and C. Riccomini (1997), Cenozoic tectonics of the Fonseca Basin Region, eastern Quadrilátero Ferrífero, MG, Brazil, *J. South Am. Earth Sci.*, *10*, 275–284.

Gordon, R. G. (2000), Diffuse oceanic plate boundaries: Strain rates, vertically averaged rheology, and comparisons with narrow plate boundaries and stable plate interiors, in *History and Dynamics of Global Plate Motions*, Geophysical Monograph, vol. 121, edited by M. A. Richards, R. G. Gordon, and R. D. Van der Hilst, pp. 143–159, AGU, Washington, D. C.

Green, P. F., and I. R. Duddy (2010), Synchronous exhumation events around the Arctic including examples from Barents Sea and Alaska North Slope, in *Petroleum Geology: From Mature Basins to New Frontiers—Proceedings of the 7th Petroleum Geology Conference*, edited by B. A. Vining and S. C. Pickering, pp. 633–644, Geological Society, London.

Gudmundsson, O., and M. Sambridge (1998), A regionalized upper mantle (RUM) seismic model, *J. Geophys. Res.*, *103*, 7121–7136.

Gunnell, Y., and L. Fleitout (1998), Shoulder uplift of the Western Ghats passive margin, India: A denudational model, *Earth Surf. Processes Landforms*, *23*, 391–404.

Hillis, R. R., S. P. Holford, P. F. Green, A. G. Doré, R. W. Gatliff, M. S. Stoker, K. Thomson, J. P. Turner, J. R. Underhill, and G. A. Williams (2008a), Cenozoic exhumation of the southern British Isles, *Geology*, *36*, 371–374.

Hillis, R. R., M. Sandiford, S. D. Reynolds, and M. C. Quigley (2008b), Present-day stresses, seismicity and Neogene-to-Recent tectonics of Australia's 'passive' margins: intraplate deformation controlled by plate boundary forces, *Geol. Soc. Spec. Publ.*, *306*, 71–90.

Holford, S. P., P. F. Green, J. P. Turner, G. A. Williams, R. R. Hillis, D. R. Tappin, and I. R. Duddy (2008), Evidence for kilometric-scale Neogene exhumation driven by compressional deformation in the Irish Sea basin system, *Geol. Soc. Spec. Publ.*, *306*, 91–119.

Holford, S. P., J. P. Turner, P. F. Green, and R. R. Hillis (2009), Signature of cryptic sedimentary basin inversion revealed by shale compaction data in the Irish Sea, western British Isles, *Tectonics*, *28*, TC4011, doi:10.1029/2008TC002359.

Hudec, M. R., and M. P. A. Jackson (2002), Structural segmentation, inversion, and salt tectonics on a passive margin: Evolution of the Inner Kwanza Basin, Angola, *Geol. Soc. Am. Bull.*, *114*, 1222–1244.

Husson, L. (2012), Trench migration and upper plate strain over a convecting mantle, *Phys. Earth Planet. Inter.*, *212–213*, 32–43.

Husson, L., and Y. Ricard (2004), Stress balance above subduction: Application to the Andes, *Earth Planet. Sci. Lett.*, *222*, 1037–1050.

Husson, L., C. P. Conrad, and C. Faccenna (2012), Plate motions, Andean orogeny, and volcanism above the South Atlantic convection cell, *Earth Planet. Sci. Lett.*, *317–318*, 126–135.

Jackson, M. P. A., M. R. Hudec, and K. A. Hegarty (2005), The great West African Tertiary coastal uplift: Fact or fiction? A perspective from the Angolan divergent margin, *Tectonics*, *24*, TC6014, doi:10.1029/2005TC001836.

Japsen, P. (1998), Regional velocity-depth anomalies, North Sea Chalk: A record of overpressure and Neogene uplift and erosion, *AAPG Bull.*, *82*, 2031–2074.

Japsen, P., and J. A. Chalmers (2000), Neogene uplift and tectonics around the North Atlantic: Overview, *Global Planet. Change*, *24*, 165–173.

Japsen, P., J. M. Bonow, P. F. Green, J. A. Chalmers, and K. Lidmar-Bergström (2006), Elevated, passive continental margins: Long-term highs or Neogene uplifts? New evidence from West Greenland, *Earth Planet. Sci. Lett.*, *248*, 330–339.

Japsen, P., J. A. Chalmers, P. F. Green, and J. M. Bonow (2012a), Elevated, passive continental margins: Not rift shoulders, but expressions of episodic, post-rift burial and exhumation, *Global Planet. Change*, *90–91*, 73–86.

Japsen, P., J. M. Bonow, P. F. Green, P. R. Cobbold, D. Chiossi, R. Lilletveit, L. P. Magnavita, and A. J. Pedreira (2012b), Episodic burial and exhumation history of NE Brazil after opening of the South Atlantic, *GSA Bull.*, *124*, 800–816.

Jolivet, L., and C. Faccenna (2000), Mediterranean extension and the Africa-Eurasia collision, *Tectonics*, *19*, 1095–1106.

Kohlstedt, D. L., B. Evans, and S. J. Mackwell (1995), Strength of the lithosphere: Constraints imposed by laboratory experiments, *J. Geophys. Res.*, *100*, 17,587–17,602.

Kreemer, C., W. E. Holt, and A. J. Haines (2003), An integrated global model of present-day plate motions and plate boundary deformation, *Geophys. J. Int.*, *154*, 8–34.

Lavier, L. L., M. S. Steckler, and F. Brigaud (2001), Climatic and tectonic control on the Cenozoic evolution of the West African margin, *Mar. Geol.*, *178*, 63–80.

Leroy, M., O. Dauteuil, and P. R. Cobbold (2004), Incipient shortening of a passive margin: The mechanical roles of continental and oceanic lithospheres, *Geophys. J. Int.*, *159*, 400–411.

Lithgow-Bertelloni, C., and J. H. Guynn (2004), Origin of the lithospheric stress field, *J. Geophys. Res.*, *109*, B01408, doi:10.1029/2003JB002467.

Lithgow-Bertelloni, C., and P. G. Silver (1998), Dynamic topography, plate driving forces and the African superswell, *Nature*, *395*, 269–272.

Loiselet, C., J. Braun, L. Husson, C. Le Carlier de Veslud, C. Thieulot, P. Yamato, and D. Grujic (2010), Subducting slabs: Jellyfishes in the Earth's mantle, *Geochem. Geophys. Geosyst.*, *11*, Q08016, doi:10.1029/2010GC003172.

Lundin, E., and A. G. Doré (2002), Mid-Cenozoic post-breakup deformation in the 'passive' margins bordering the Norwegian-Greenland Sea, *Mar. Pet. Geol.*, *19*, 79–93.

Martill, D. M. (2007), The age of the Cretaceous Santana Formation fossil Konservat Lagerstätte of north-east Brazil: A historical review and an appraisal of the biochronostratigraphic utility of its palaeobiota, *Cretaceous Res.*, *28*, 895–920.

Masson, D. G., J. A. Cartwright, L. M. Pinheiro, R. B. Whitmarsh, M.-O. Beslier, and H. Roeser (1994), Compressional deformation at the ocean-continent transition in the NE Atlantic, *J. Geol. Soc.*, *151*, 607–613.

Mitrovica, J. X., and A. M. Forte (2004), A new inference of mantle viscosity based upon a joint inversion of convection and glacial isostatic adjustment data, *Earth Planet. Sci. Lett.*, *225*, 177–189.

Morais Neto, J. M., K. A. Hegarty, and G. D. Karner (2006), Preliminary constraints on paleotemperature and landscape evolution in and around Araripe Basin, northeastern Brazil, using apatite fission track analysis, *Bol. Geoc. Petrobras*, *14*, 113–119.

Nikolaeva, K., T. V. Gerya, and F. O. Marques (2010), Subduction initiation at passive margins: Numerical modeling, *J. Geophys. Res.*, *115*, B03406, doi:10.1029/2009JB006549.

Nikolaeva, K., T. V. Gerya, and F. O. Marques (2011), Numerical analysis of subduction initiation risk along the Atlantic American passive margins, *Geology*, *39*, 463–466.

Partridge, T. C., and R. R. Maud (1987), Geomorphic evolution of southern Africa since the Mesozoic, *S. Afr. J. Geol.*, *90*, 179–208.

Pedoja, K., et al. (2011), Relative sea-level fall since the last interglacial stage: Are coasts uplifting worldwide?, *Earth Sci. Rev.*, *108*, 1–15.

Peron-Pinvidic, G., G. Manatschal, S. M. Dean, and T. A. Minshull (2008), Compressional structures on the West Iberia rifted margin: Controls on their distribution, *Geol. Soc. Spec. Publ.*, *306*, 169–183.

Piasecki, S., L. M. Larsen, A. K. Pedersen, and G. K. Pedersen (1992), Palynostratigraphy of the Lower Tertiary volcanics and marine clastic sediments in the southern part of the West Greenland Basin: Implications for the timing and duration of the volcanism, *Grønlands Geol. Und. Rapp.*, *154*, 13–31.

Riccomini, C., and M. Assumpcao (1999), Quaternary tectonics in Brazil, *Episodes*, *22*, 221–225.

Ritchie, J. R., H. Johnson, M. F. Quinn, and R. W. Gatliff (2008), The effect of Cenozoic compression within the Faroe-Shetland Basin and adjacent area, *Geol. Soc. Spec. Publ.*, *306*, 121–136.

Roberts, G. G., and N. White (2010), Estimating uplift rate histories from river profiles using African examples, *J. Geophys. Res.*, *115*, B02406, doi:10.1029/2009JB006692.

Rodriguez, J. F. R., and R. Littke (2001), Petroleum generation and accumulation in the Golfo San Jorge Basin, Argentina: A basin modeling study, *Mar. Pet. Geol.*, *18*, 995–1028.

Smallwood, J. R. (2008), Uplift, compression and the Cenozoic Faroe-Shetland sediment budget, *Geol. Soc. Spec. Publ.*, *306*, 137–152.

Steinberger, B., H. Schmeling, and G. Marquart (2001), Large-scale lithospheric stress field and topography induced by global mantle circulation, *Earth Planet. Sci. Lett.*, *186*, 75–91.

Thomson, K., P. F. Green, A. G. Whitham, S. P. Price, and J. R. Underhill (1999), New constraints on the thermal history of North-East Greenland from apatite fission-track analysis, *GSA Bull.*, *111*, 1054–1068.

Turcotte, D. L., and G. Schubert (1982), *Geodynamics: Applications of Continuum Physics to Geological Problems*, 450 pp., J. Wiley, New York.

Wdowinski, S., and R. J. O'Connell (1991), Deformation of the Central Andes (15°−27°S) derived from a flow model of subduction zones, *J. Geophys. Res.*, *96*, 12,245–12,255.

Yamato, P., R. Tartèse, T. Duretz, and D. A. May (2012), Numerical modelling of magma transport in dykes, *Tectonophysics*, *526–529*, 97–109.

Yoshida, M., and T. Nakakuki (2009), Effects on the long-wavelength geoid anomaly of lateral viscosity variations caused by stiff subducting slabs, weak plate margins and lower mantle rheology, *Phys. Earth Planet. Inter.*, *172*, 278–288.

Gondwana Research 25 (2014) 464–493

Contents lists available at ScienceDirect

Gondwana Research

journal homepage: www.elsevier.com/locate/gr

Mechanisms of continental subduction and exhumation of HP and UHP rocks

Evgene Burov [a,b,*], Thomas Francois [a,b], Philippe Yamato [c], Sylvie Wolf [a,b]

[a] UPMC SORBONNE UNIVERSITES, ISTEP UMR 7193, Université Pierre et Marie Curie, F-75005, Paris, France
[b] CNRS, ISTEP, UMR 7193, F-75005, Paris, France
[c] Géosciences Rennes, CNRS UMR 6118, Université de Rennes 1, 35042 Rennes Cedex, France

ARTICLE INFO

Article history:
Received 9 May 2012
Received in revised form 5 September 2012
Accepted 20 September 2012
Available online 6 November 2012

Keywords:
Continental collision
Subduction
Orogeny
Metamorphism
HP/UHP exhumation
Eclogites
Modeling
Rheology

ABSTRACT

We discuss possible scenarios of continental collision, and their relation to mechanisms of exhumation of HP and UHP rocks, inferred from thermo-mechanical numerical models accounting for thermo-rheological complexity of the continental lithosphere. Due to this complexity, mechanisms of continental convergence are versatile and different, in many aspects from those that control oceanic subduction. Elucidating these mechanisms from conventional observations is difficult, and requires additional constraints such as those derived from petrological data. Indeed, exhumation of HP/UHP rocks is an integral part of convergent processes, and burial/exhumation dynamics inferred from metamorphic *P–T–t* paths provides strong constraints on the collision scenarios. Metamorphic rocks also play an active role due to their contrasting physical properties (rheology, density, fluid transport capacity). Numerical thermo-mechanical experiments suggest that HP/UHP exhumation can only be produced in subduction contexts, as well as that long-lasting (>10 Myr) continental subduction can only occur in case of cold strong lithospheres (T_{Moho}<550 °C, the equivalent elastic thickness T_e>50 km) and of relatively high convergence rates (>3–5 cm yr^{-1}). In this case, high density UHP material in the crustal part of subduction interface provides additional pull on the slab and is not always exhumed to the surface. In case of slower convergence and/or weaker lithosphere (T_e<40 km), continental subduction is a transient process that takes a limited time span in the evolution of collision zone. Under these conditions, hot mechanically weak UHP rocks enhance decoupling between the upper and lower plate while their exhumation may be rapid (faster than convergence rate) and abundant. Therefore, the UHP exhumation paths can be regarded as sensitive indicators of subduction. Rheological changes and fluid exchanges associated with low-to-middle pressure phase transitions along the subduction interface, such as serpentinization during the oceanic phase and schisting, play a major role producing necessarily mechanical softening of the subduction interface and of the hydrated mantle wedge. The oceanic UHP rocks are exhumed thanks to mixing with low-density continental crustal units during transition from oceanic to continental subduction. At the continental phase, the UHP exhumation occurs as a result of a multi-stage process: at the deep stage (<40 km depth) the exhumation is rapid and is driven by buoyancy of partly metamorphosed (or partly molten) UHP material often mixed with non-metamorphosed crustal volumes. At final stages, exhumation takes common slow path through the accretion prism mechanism and the erosional denudation. The experiments suggest that formation of UHP rocks requires that continental subduction starts at higher oceanic subduction rate. It then may progressively slow down until the lockup of the subduction interface and/or slab-break-off. A rate of ~1–2 cm yr^{-1} is generally sufficient to drive continental subduction during the first several Myr of convergence, but pertinent subduction requires faster convergence rates (>3–5 cm yr^{-1}). We suggest that most continental orogenic belts could have started their formation from continental subduction but this process has been generally limited in time.

1. Introduction

In continents, subduction is only one of the four possible mechanisms of accommodation of tectonic shortening (Fig. 1): pure-shear thickening; simple shear subduction or underplating; folding (Cloetingh et al., 1999; Burg and Podladchikov, 2000), and gravitational (Raleigh–Taylor (RT)) instabilities in thickened, negatively buoyant lithosphere (e.g., Houseman and Molnar, 1997) dubbed here "unstable subduction." All these scenarios can be superimposed in nature. For instance, "megabuckles" created by lithospheric folding (Burg and Podladchikov, 2000) can localize and evolve into subduction-like thrust zones or result in the development of Rayleigh–Taylor instabilities. On the other hand, RT and boudinage instabilities leading to slab-break-off may occur in subducting lithosphere when it loses its mechanical strength due to conductive heating from the surrounding mantle (Pysklywec et al., 2000).

General physical conditions for subduction include (1) presence of sufficient slab-pull/push forces, (2) strong mechanical decoupling between the upper and lower plate (i.e., weak subduction interface)

* Corresponding author.
E-mail address: evgenii.burov@upmc.fr (E. Burov).

1342-937X/$ – see front matter
http://dx.doi.org/10.1016/j.gr.2012.09.010

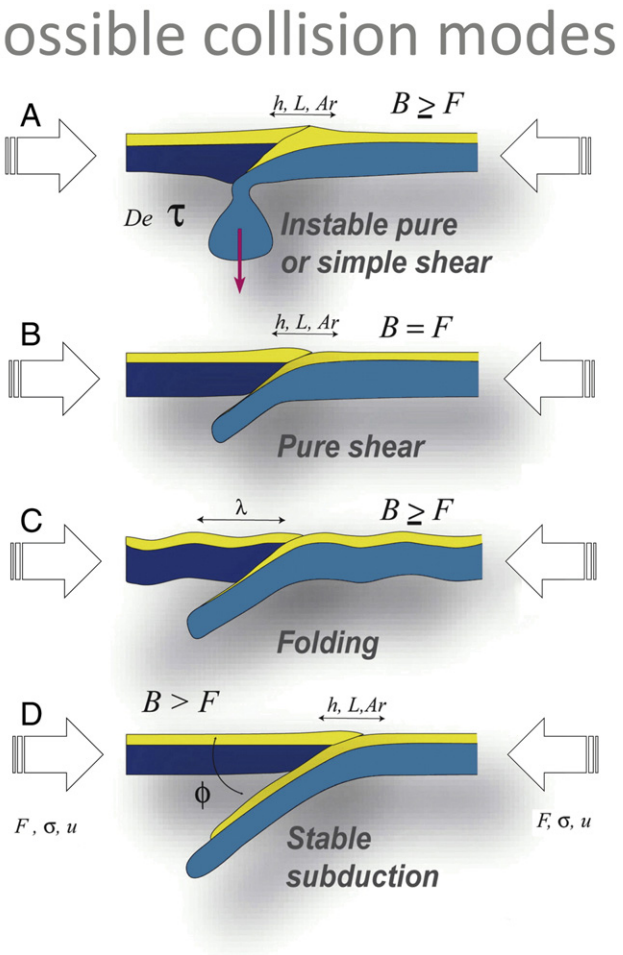

Fig. 1. Possible collision scenarios: (A) unstable (Rayleigh–Taylor) pure or simple shear instability; (B) pure shear in stable mode and (C) unstable mode (folding); (D) simple shear in stable mode (subduction). Related large-scale parameters characterising collision style, lithospheric strength and rheology: T_e, F, σ, u, De, τ_m, h, L, λ, ϕ. T_e is equivalent elastic thickness. F, σ , u are respectively the horizontal force, stress and convergence/extension velocity, that are linked to the lithospheric strength and possible deformation styles. *De* and τ_m are respectively Deborah number and relaxation time related to viscosity contrasts in the lithosphere. λ is the characteristic wavelength of unstable deformation related to the thickness of the competent layers in the lithosphere. h, L are respectively the vertical and horizontal scale for process-induced topography supported by lithospheric strength, Argand number $Ar = \rho g h L/F$. φ is subduction or major thrust fault angle that is indicative of the brittle properties and of the overall plate strength.

and (3) sufficient mechanical strength of the lower plate assuring preservation of its geometric and mechanical integrity during subduction. Additional mechanisms are also needed for subduction initialization and for downward bending of strong lithosphere when it slides below the upper plate (Cloetingh et al., 1982). In oceans, lithospheric buoyancy and flexural strength (measured in terms of the equivalent elastic thickness, T_e) are functions of plate age and thus of the distance from the ridge (Watts, 2001). Hence, when the lithosphere attains negative buoyancy needed for subduction, it also reaches maximal flexural strength that prevents slab from downward bending (Cloetingh et al., 1982). This controversy has been resolved by showing that pre-subduction bending of the oceanic lithosphere is possible due to localized inelastic flexural weakening, that is, ductile yielding and "plastic hinging" produced by high flexural stresses near the peripheral bulge (Burov and Diament, 1995a, 1995b, 1992; Burov, 2011). Flexural weakening is then enhanced by rheological softening due to metamorphic reactions produced by fluids penetrating in small normal faults created by tensional flexural strains in the upper parts of the peripheral bulge (Faccenda et al., 2009a, 2009b). In continental settings subduction initialization is "natural" since the continental lithosphere follows the path open by the preceding oceanic subduction.

Since the slab pull/push forces can be roughly estimated from gravitational force balance, the most uncertain conditions refer to the mechanisms of weakening of the subduction interface and to the preservation of slab strength during subduction. The former seem to be ultimately related to the metamorphic processes. In oceans, it is already generally agreed that the subduction interface is lubricated due to the presence of serpentinize mantle layer below the oceanic crust and the reactions with free and hydrous fluids released or absorbed during metamorphic reactions (e.g., Guillot et al., 2000, 2001, 2009). In continents, the governing weakening mechanisms are not clear but the presence of thick, relatively weak and rheologically stratified crust as well as strength drops and density changes due to metamorphic transformations also appear to be of primary importance (e.g., Burov et al., 2001a, 2001b; Yamato et al., 2008). Preservation of slab integrity is a major problem for continental subduction, since continental convergence occurs at much slower rates than in oceans. In case of oceanic subduction (at rates of 5–15 cm yr^{-1}), slab has no time to heat up due to the thermal diffusion from the surrounding asthenosphere. As a consequence, it loses its strength only by the moment when it is already sunk to a great depth. In continents, convergence rates are much slower, sometimes not exceeding several mm yr^{-1}. Under these conditions, the lithosphere may heat up, thermally weaken and break-off before it reaches the HP depth.

Despite all complications, continental subduction appears to be a pervasive process, as indicated by geological and geophysical observations (e.g., Ford et al., 2006; Zhang et al., 2009; Handy et al., 2010; Tetsuzo and Rehman, 2011). However, in difference from oceans, here we do not dispose such clear evidences for subduction as Benioff zones, tomographic images of subducting slabs or straight kinematic inferences from paleomagnetic data. In continents, all data are highly "blurred", so that probably the most straightforward evidence for continental subduction refers to the presence of HP and UHP metamorphic material in convergence zones (e.g., Guillot et al., 2000, 2001, 2009; Li et al., 2009; Ernst, 2010; Maruyama et al., 2010; Shigenori et al., 2010; Lanari et al., 2012). The high- to ultrahigh-pressure (HP/UHP) metamorphic belts are believed to be witnessing subduction processes as the exhumed continental blocks appear to bear a strong overprint of the subduction record as they return to surface (e.g. Ring et al., 2007; Zhang et al., 2009; Hacker et al., 2010; Diez Fernández et al., 2012). This evidence is generally preserved in small and disconnected lenses (Teyssier et al., 2010), as mineral relicts within a dominant low- to medium-pressure metamorphic matrix, and more rarely as relatively large HP/UHP units (e.g., Yamato et al., 2008). If one assumes *P–T* conditions inferred for subduction zones, then UHP material should have been buried to depths of 100–150 km and brought back to the surface. Consequently, if the UHP depth estimates are correct (e.g., Spear, 1993), the HP/UHP rocks can be regarded as direct markers of continental subduction and their *P–T–t* paths can be used for reconstruction of subduction dynamics and of the conditions at the subduction interface. Under these assumptions, detailed studies of HP/UHP rocks provide direct constraints on thermo-mechanical processes in subduction zones (Coleman, 1971; Ernst, 1973, 2010). These data would provide insights on mechanisms of exhumation as well, since different processes and contexts would potentially result in different styles of deformation and hence exhumation *P–T–t* paths. In particular, based on the analysis of metamorphic data (Ernst, 2010) it has been suggested that two main types of continental convergence can be distinguished: fast "Pacific underflow" , where continental subduction is preceded by that of thousands of km of oceanic lithosphere, and slow "Alpine closure" of an intervening oceanic basin leading to short-lived continental subduction soon followed by pure shear collision. It has been also pointed out that the exhumed HP–UHP complexes display low-aggregate bulk densities (e.g., Ernst, 2010), while the exhumation rates in some cases largely exceed the convergence rates (e.g., Yamato et al., 2008), jointly suggesting a buoyancy-driven ascent mechanism.

Large-scale nappes folding and other complex deformation processes occurring at subduction interface largely distort kinematic imprint of subduction (e.g. Diez Fernández et al., 2012; Tirel et al., submitted for publication), hence justifying a numerical modeling approach for decrypting and matching structural and metamorphic observations. For this reason, in most recent approaches, the data from HP and UHP rocks are treated in conjunction with synthetic *P–T–t* paths predicted from thermo-mechanical numerical models of convergent processes. This provides key validation of the inferred concepts of convergent dynamics and thermo-mechanical properties of oceanic and continental subduction zones (e.g., Yamato et al., 2007, 2008; Li and Gerya, 2009). However, both, the mechanisms of continental convergence and of exhumation of HP/UHP material are still very much in debate, and the ideas on the interpretation of metamorphic data and mechanisms of convergence require further investigation. In particular, for each given context it should be demonstrated, in independent way, that: (1) continental subduction is a viable mechanism of accommodation of tectonic shortening; (2) it is possible to propose a particular mechanism of HP/UHP exhumation compatible both with the *P–T–t* data and with the proposed subduction dynamics.

It is noteworthy that alternative mechanisms have been also proposed both to explain the mechanics of continental convergence, as well as the formation and exhumation of HP/UHP material. Some of the suggested mechanisms of convergence are more or less directly associated with the mechanisms of exhumation, some not. For example, Petrini and Podladchikov (2000) suggest tectonic overpressure as the mechanism of formation of UHP rocks that, in this case, have no deep origins and their *P–T–t* paths do not contain interpretable information on the mechanism of collision. Other workers (e.g., Raimbourg et al., 2007) choose another extremity by ultimately linking UHP exhumation to geometric "subduction channel" concept. However, recently developed numerical thermo-mechanical models of collision and exhumation coupled with thermodynamic processes suggest that buoyancy/pressure driven channel flow concepts are not really applicable for explanation of UHP exhumation mechanisms (Burov et al., 2001a, 2001b; Pysklywec, 2006; Yamato et al., 2008), even in the oceanic contexts (Angiboust et al., 2012). According to observations (e.g., Ernst, 2010; Diez Fernández et al., 2012) and recent modeling results (e.g., Burov and Yamato, 2008; Yamato et al., 2008; Li and Gerya, 2009), exhumation and collision mechanisms are versatile, in particular, poly-phase. It also comes out from the numerical experiments that continental subduction provides a physically most consistent explanation to formation and exhumation of the HP/UHP material. At same time, the numerical models show that exhumation of the UHP material goes by context-dependent multi-stage mechanisms (Burov et al., 2001a, 2001b; Yamato et al., 2008).

By now, a large number of modeling studies have investigated various factors influencing subduction processes (e.g., Chemenda et al., 1995; Pysklywec et al., 2000; Doin and Henry, 2001; Gerya et al., 2002a, 2002b; Sobouti and Arkani-Hamed, 2002; Pysklywec, 2006; Yamato et al., 2007,2008; Warren et al., 2008a, 2008b; Gray and Pysklywec, 2010, 2012; Sizova et al., 2010). However, not all of the existing models match the task. The analogue models are largely inadequate because of impossibility to incorporate phase changes, rheological simplifications, absent or poorly controlled thermal coupling. The numerical models are often limited by simplified visco-plastic rheologies or by the rigid top/"sticky air" upper-boundary condition, which is widely used instead of the paramount free-surface boundary condition. The use of rigid-top upper-boundary condition forces stable subduction (Doin and Henry, 2001; Sobouti and Arkani-Hamed, 2002), attenuates pure shear, cancels folding and does not allow for consistent prediction of topography evolution. Many models also do not incorporate surface processes which are key forcing factors of continental collision (e.g., Avouac and Burov, 1996) and an integral part of the final stages of exhumation. Some studies also force a specific convergence mode, in particular, subduction, via prescription of favoring boundary conditions, for example, by putting an additional boundary condition (e.g., "S-point") inside the model (e.g., Beaumont et al., 1996; Beaumont et al., 2000). Some other models favor pure shear collision by including a weak zone in the plate shortened in the direction opposite to the pre-imposed mantle flow (Pysklywec et al., 2002). Models operating in deviatoric stress formulation (e.g., Navier Stokes approximation) may also have specific problems with evaluation of total pressure needed for tracing of *P–T–t* conditions and correct account for brittle deformation. Even though some earlier modeling studies (Burov et al., 2001a, 2001b; Gerya et al., 2002a, 2002b; Toussaint et al., 2004a,b; Burg and Gerya, 2005) have considered phase changes, fully coupled models with progressive phase changes directly derived from thermodynamic relations have emerged only few years ago (Stöckhert and Gerya, 2005; Yamato et al., 2007; Li and Gerya, 2009; Li et al., 2011).

Summarizing the requirements to the numerical models of collision and exhumation, we can note that they should: (1) allow for all modes of deformation, (2) account for viscous-elastic-plastic rheology and thermal evolution, (3) thermodynamically coupled, i.e. account for phase changes (and at best for fluid circulation), (4) account for surface processes and free-surface boundary condition (or at least incorporate "sticky air" approximation of the free surface), (5) provide an accurate solution for total pressure.

It is hence evident that a joint approach considering collision processes in direct relation to exhumation and formation of HP/UHP material is the most promising one for understanding both the mechanisms of continental convergence and of exhumation. The goal of this paper is therefore two-fold: we first discuss physical and rheological conditions allowing for subduction in continental settings, with a specific focus on the conditions allowing for preservation of slab integrity. We next revise the conditions for HP/UHP exhumation. We finally link all processes together attempting to obtain better insights on the mechanisms of continental convergence, and, by proxy, of formation and exhumation of the HP/UHP material.

2. Physical conditions for preservation of slab integrity

Subduction implies preservation of slab integrity, hence small bulk deformation of the lower plate during convergence: a subducting plate only bends without significantly changing its length and thickness. The slab should also to provide an efficient stress guide for driving push/pull forces. To meet the above conditions, it is clear that the lithosphere has to preserve sufficient mechanical strength as it sinks into the asthenosphere. Otherwise it will stretch or thicken, break-off, stagnate or drip-off under the action of the external shear, push–pull forces and viscous gravitational (Raleigh–Taylor) instabilities. Preservation of slab integrity (= small internal strain rate) is also equivalent to nearly invariable plate-parallel component of plate velocity. Since slab push–pull, shear and body forces acting on the opposite ends of the plate are largely different, this condition can be also satisfied only if the slab stays strong even at great depth.

Olivine-rich rocks flow at temperatures above 500–600 °C in oceans ($P>0.4$ GPa) and at 700–800 °C ($P>1.2$ GPa) in continents (e.g., Goetze and Evans, 1979). Hence, to preserve its strength, slab should remain cold, i.e. rapidly descent in the asthenosphere and have no time to heat up - hence weaken - due to heat diffusion from hot environment (>1330 °C). Therefore, one can characterize minimal thermo-rheological condition for stable subduction by "subduction Péclet number" Pe_s:

$$Pe_s = u^2 t_s/\kappa \quad (1)$$

where t_s is a characteristic time scale, u is plate-parallel (horizontal at surface) plate velocity and κ is thermal diffusivity ($\approx$ on the order of 10^{-6} m^2 s^{-1}). The corresponding thermal diffusion length is $l_d = (t_s\,\kappa)^{1/2}$. The characteristic time scale t_s hence corresponds to the average life span of stable subduction, i.e. to the time interval between the onset of subduction and the moment when simple shear is

no more dominant deformation mode, being progressively suppressed by other mechanisms such as pure shear shortening, RT instabilities, or folding (Fig. 1). After that, heat advection mechanism is no more directly dependent on convergence rate, and the Eq. (1) does not hold anymore.

For preservation of considerable slab strength by time t_s, l_d should be significantly less than h_k, where h_k is the apparent thickness of strong , nearly elastic mechanical core of the lithosphere when it arrives at the subduction zone. Strong core is a condition for transmission of intra-plate stresses with minimal internal shortening of the lithosphere. This condition is equivalent to assumption that heat advection is primarily dependent on the convergence rate u, as expressed by the Eq. (1). Let us assume $l_d \leq 0.25\ h_k$, that is, a maximum factor of 2 reduction of the thermo-mechanical thickness of the slab by time t_s (slab heats up both from its upper and lower interface $(0.25\times 2)^{-1}=(0.5)^{-1}$). Hence, the characteristic time scale of subduction is:

$$t_s \approx {l_d}^2/\kappa \approx 0.0625 h_k^2/\kappa, \tag{2}$$

and the minimal condition for stable subduction is:

$$Pe_s >> Pe_k = u h_k/\kappa \tag{3}$$

If Pe_s is smaller than Pe_k, thermal weakening of the slab, caused by heat diffusion, prohibits stable subduction process (Toussaint et al., 2004a). As also follows from Eq. (2), if Eq. (3) is satisfied, then characteristic subduction length d_s (the length of "subductable" lithosphere) , can be roughly estimated as:

$$d_s \approx u t_s \approx 0.0625 u h_k^2/\kappa, \tag{4}$$

which means that maximal stable subduction depth for lower crustal units (initial crustal thickness h_c plus d_s multiplied by tangent of the dip angle) is (1) linearly proportional to subduction rate and (2) quadratically proportional to the mechanical thickness of the lithosphere at surface. Hence, convergence rate is a secondary factor compared to the initial mechanical strength of the lithosphere, which is thus of major importance for subduction. The above estimations are very approximate. One can complement them by evaluating also a hard limit on the duration of the subduction, that is, the maximal time t_{bmax} of slab break-off, which will happen no later when the mechanical core of the lithosphere vanishes, i.e. when $(t\kappa)^{½} \sim 0.5 h_k$.

$$t_{bmax} < 0.25 h_k^2/\kappa, \tag{5a}$$

with maximal slab-brak-off depth, d_{sbmax},

$$d_{sbmax} < u t_{bmax}. \tag{5b}$$

This yields t_{bmax} of 7–10 Myr for lithosphere with initial $T_e = 20$–30 km (e.g., Western Alps), 20 Myr for lithosphere with initial $T_e =$ 50 km (e.g., Zagros), and up to 65 Myr for lithosphere with $T_e = 70$–90 km (India–Himalaya collision). Surprisingly, these simple estimates match the inferences from observations and thermo-mechanical models for the respective regions (e.g., Toussaint et al., 2004b; Yamato et al., 2008; Francois et al., 2012, in press; Angiboust et al., 2012). Nevertheless, the Eqs. (5a), (5b) may not hold well for slow convergence settings (e.g. $u<2$ cm yr^{-1}) because of strong influence of thermo-mechanical instabilities that may develop at similar time scale.

The thickness of the mechanical core of the lithosphere h_k can be constrained from observations of plate flexure that reveal significant plate strength in zones of oceanic subduction and in many zones of continental collision (Watts, 2001). The observed equivalent elastic thickness of the lithosphere, $T_e \sim h_k$, is a direct proxy for the long-term integrated strength, B, of the lithosphere (see Watts, 2001). For example, for a single-layer plate of mechanical thickness h_m with $T_e = T_{e\_ocean}$:

$$B = \int_0^\infty \sigma^f(x,z,t,\dot{\varepsilon})\mathrm{d}z \text{ while } T_{e\_ocean} = \left(12\left(\frac{\partial \sigma^f_{xx}}{\partial z}\right)^{-1} \overbrace{\int_0^{h_m} \sigma^f_{xx}(z-Z_n)\mathrm{d}z}^{M_x(x)} \right)^{\frac{1}{3}};\ T_{e\_ocean} < h_m, \tag{6}$$

where x, z, t, $\dot{\varepsilon}$ are horizontal and vertical (with respect to local plate coordinates) coordinate, time and strain rate, respectively, Z_n is the position of the neutral fiber within the plate, σ^f_{xx} is bending stress and M_x is bending moment (Burov and Diament, 1995a, 1995b). For inelastic rheology and rheologically stratified lithosphere, T_e, is smaller than h_m. In this case T_e has no geometrical interpretation, and can be identified with our definition for h_k (apparent mechanical thickness of the lithosphere). T_e varies spatially due to its dependence on local bending stress that leads to localized plate weakening (called plastic or ductile hinging) in the areas of utmost flexure, e.g. near subduction zones (at the peripheral bulge) or below mountains and islands. As discussed in previous sections, ductile-plastic hinging is important property allowing for subduction.

Typical values of T_e of the oceanic lithosphere correlate with the depth of 500–600 °C geotherm and are roughly equal to 30–50 km near subduction zones (e.g., Burov and Diament, 1995a, 1995b; Watts, 2001). By analogy with the oceanic plates, which, as we know, do subduct, we can assume same minimal T_e value for subduction of continental lithosphere. Continental plates are characterized by T_e values varying between 15 to 90 km (e.g., Burov and Diament, 1995a, 1995b; Cloetingh and Burov, 1996; Pérez-Gussinyé and Watts, 2005). Hence, only some of them are strong enough to develop oceanic-type subduction provided that other conditions (e.g., buoyancy versus shear force balance) are also favorable. For example, consider a convergence rate u of 1 cm yr^{-1}. Assuming a value for h_k of 50 km we obtain $Pe_k = 15$. Then, from $l_d \leq 0.25\ h_k$, one obtains $t_s \leq 5$ Myr. For t_s greater than 5 Myr, Pe_s is smaller than Pe_k , suggesting that sustainable long-lasting subduction is improbable (characteristic stable subduction length $\sim u t_s = 50$ km; maximal slab-break-off depth $ut_{bmax} < 200$ km) at such a slow convergence rate. However, for $u = 5$ cm yr^{-1}, $Pe_k = 75$ and $Pe_s = 400$ suggesting that stable subduction (characteristic subduction length $ut_s = 250$ km) is possible even for time spans greater than 5 Myr. As extreme example, we can consider India-Asia collision ($h_k \approx 80$–90 km (Watts, 2001), $t_s \sim 12$–15 Myr, $u = 5$ cm yr^{-1}). For these conditions we obtain minimal $Pe_s > 953$ and minimal $Pe_k = 127$, which implies that subduction is dominating mode and that at least 600–750 km ($= ut_s$) of the Himalayan convergence could have been accommodated in subduction regime. The maximal amount of subduction could be even much more important ($ut_{bmax} > 2500$ km), meaning that slab-break off would never happen if the Indian slab was sinking at a steep angle into the upper mantle (the reality is more complex since Indian plate appears to underplate the Tibetan plateau). These rough estimates are comparable with interpretations (500–1000 km of subduction, up to 1500 km of total convergence) of geological and paleomagnetic data (Patriat and Achache, 1984 ; Chen et al., 1993; Patzelt et al., 1996; Avouac, 2003).

The first-order estimations reasonably comply with the results of recent geodynamic thermo-mechanical models. In particular, Yamato et al. (2008) have shown that slow (<1 cm yr^{-1}) Alpine subduction could have lasted no more than 5–10 Myr (between 30 Ma and 35 Ma) and that soon after the lithosphere had to enter into unstable mode or pure shear collision mode. In this case, slab was not simply descending at convergence rate but also stretching, and an early slab break-off at about 200–250 km depth resulted in cessation of continental subduction. Slab stretching has actually allowed to bring rocks to 120 km depth. On the contrary, for the fast (5 cm yr^{-1}) convergence

such as the India-Asia collision (Toussaint et al., 2004a, 2004b; Burov and Yamato, 2008) or past collision between North China and Yangtze craton (Li and Gerya, 2009; Li et al., 2011), it has been shown that sustainable subduction could continue for a very long period of time absorbing considerable amounts of tectonic shortening (e.g., at least 700–800 km for Indian collision). In such settings, slab break-off either does not occur or has a little effect on the collision mode. In particular, slab-break-off depth increases with the increasing subduction rate and strength of the lithosphere, so in cases of fast subduction, slab-break off, if happens, takes place far deep from the surface (at distance l, $ut_s<l<ut_{bmax}$) and thus has a limited impact on surface evolution (Eqs. (5a), (5b)).

One can suggest on the base of this discussion that maximal subduction rate is linked to the initial strength of mantle lithosphere. Fast (>2–3 cm yr^{-1}) continental subduction appears to be only possible in case of strong mantle lithosphere.

Numerical models have also shown that the rheological properties of the continental subduction interface and, therefore, of metamorphic reactions transforming host rocks into weaker and denser phases, are of primary importance for the evolution of continental convergence (Burov and Yamato, 2008; Warren et al., 2008a, 2008b). It has been demonstrated that subduction takes place only when the interface between the colliding plates has low mechanical strength allowing for sliding of the lower plate below the upper plate. Early studies (Hassani et al., 1997) have found that the effective friction angle of the subduction interface has to be as low as 5° for sustainable subduction. Since real rocks have practically invariable internal friction angle (~30°), it is evident that lubrication of the subduction interface is produced by non-brittle mechanisms such as ductile flow in weak metamorphosed layers, assisted by shear heating and fluids. In case of the oceanic lithosphere, the lubrication of subduction interface is provided by very weak serpentine layer that forms at the crust–mantle interface due to infiltration of fluids through flexurally induced normal faults and fractures (Jolivet et al., 1994, 2005; Yamato et al., 2007; Faccenda et al., 2009a, 2009b; Angiboust et al., 2012). Hydrated serpentinite layer transports fluids to great depths along the subduction interface; these fluids are then released due to dehydration of serpentinite at high pressure/temperature conditions. Fluid release produces further weakening of the subduction interface. It also results in partial melting that leads to weakening of the subduction wedge and the back-arc zone (Gerya et al.,

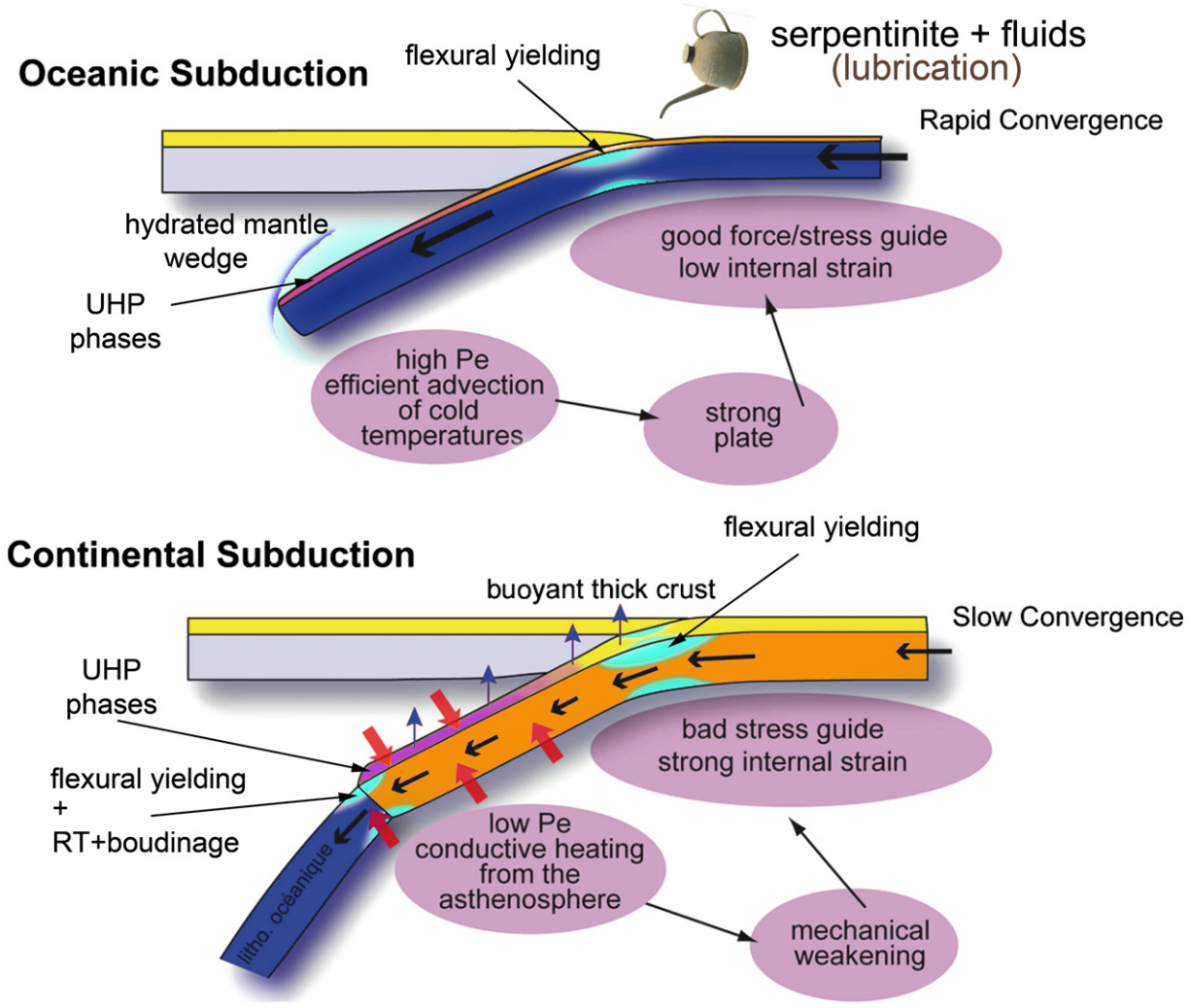

Fig. 2. Oceanic subduction versus continental subduction. Oceanic subduction is favoured by several factors such as fast convergence rate, negative buoyancy, high bulk plate strength, flexural plastic hinging (yielding) , serpentinization of the crust–mantle interface, hydration of the mantle wedge and shear heating. Many of these factors are absent in case of continental subduction which is disfavored by overall positive buoyancy of the lithosphere, slow convergence (leading to additional thermal buoyancy, mechanical weakening and rapid slab break-off) and the lack of lubrication of the subduction interface. One of the frequently evoked (possibly important) factors favouring continental subduction refers to metamorphic (LP/MP/HP) reactions leading to weakening of the subduction interface and the UHP eclogitisation of the crust (leading to negative buoyancy) and low ductile strength of the intermediate and lower crust.

2008). In case of continental subduction, the lithosphere has a lower, than oceanic lithosphere, ability to transfer fluids to depth, and metamorphic phases, presented by shists and higher grade facies, in particular, eclogites, are mechanically stronger than serpentine. Hence, for given subduction rate, the resistance of the continental subduction interface may be higher than in case of the oceanic subduction. In addition, thick continental crust has positive buoyancy that creates body forces opposing slab pull/push forces (Fig. 2). Therefore, in most cases the duration of continental subduction should be limited; at the beginning it is facilitated by the pull of the oceanic slab, which decreases with time, and by initially higher convergence velocity. The latter hypothesis is confirmed for collision zones where paleomagnetic and geological records allow for reconstruction of convergence rates (Patriat and Achache, 1984). Apart of lubrication of the subduction interface and plastic hinging of the plate at the peripheral bulge, several other conditions should be satisfied to allow for development of continental subduction (e.g., Afonso and Zlotnik, 2011). In particular, growth rates of the competing modes of deformation (RT instability, folding, pure shear) should be small, and the upward drag (eduction force) due to the buoyant crust and viscous shear must be smaller than tectonic and slab pull forces. The combined effect of these multiple factors can be only assessed through numerical modeling (e.g., Toussaint et al., 2004a, 2004b; Burov and Watts, 2006; Faccenda et al., 2008, 2009a, 2009b; Sizova et al., 2010; Duretz et al., 2011). These parametric studies have shown that continental subduction can occur and remain sustained over tens of million years only if the lithosphere is initially cold, and remains cold during subduction, which, in case of continental lithosphere (e.g., Toussaint et al., 2004a, 2004b) implies initial Moho temperatures of less than 550 °C, and convergence rates higher than 2–3 cm yr^{-1}. It is therefore reasonable to assume that after the onset of collision between, for example, India and Eurasia, when the convergence rate was about 10 cm yr^{-1} (Patriat and Achache, 1984), the oceanic subduction turned into subduction of the Indian continental lithosphere (Avouac, 2003; Toussaint et al., 2004b).

Despite these complexities, geologic and geophysical observations suggest that continental subduction took place even in very disfavoring (slow, weak lithosphere) settings such as Alpine collision (e.g., Chopin,

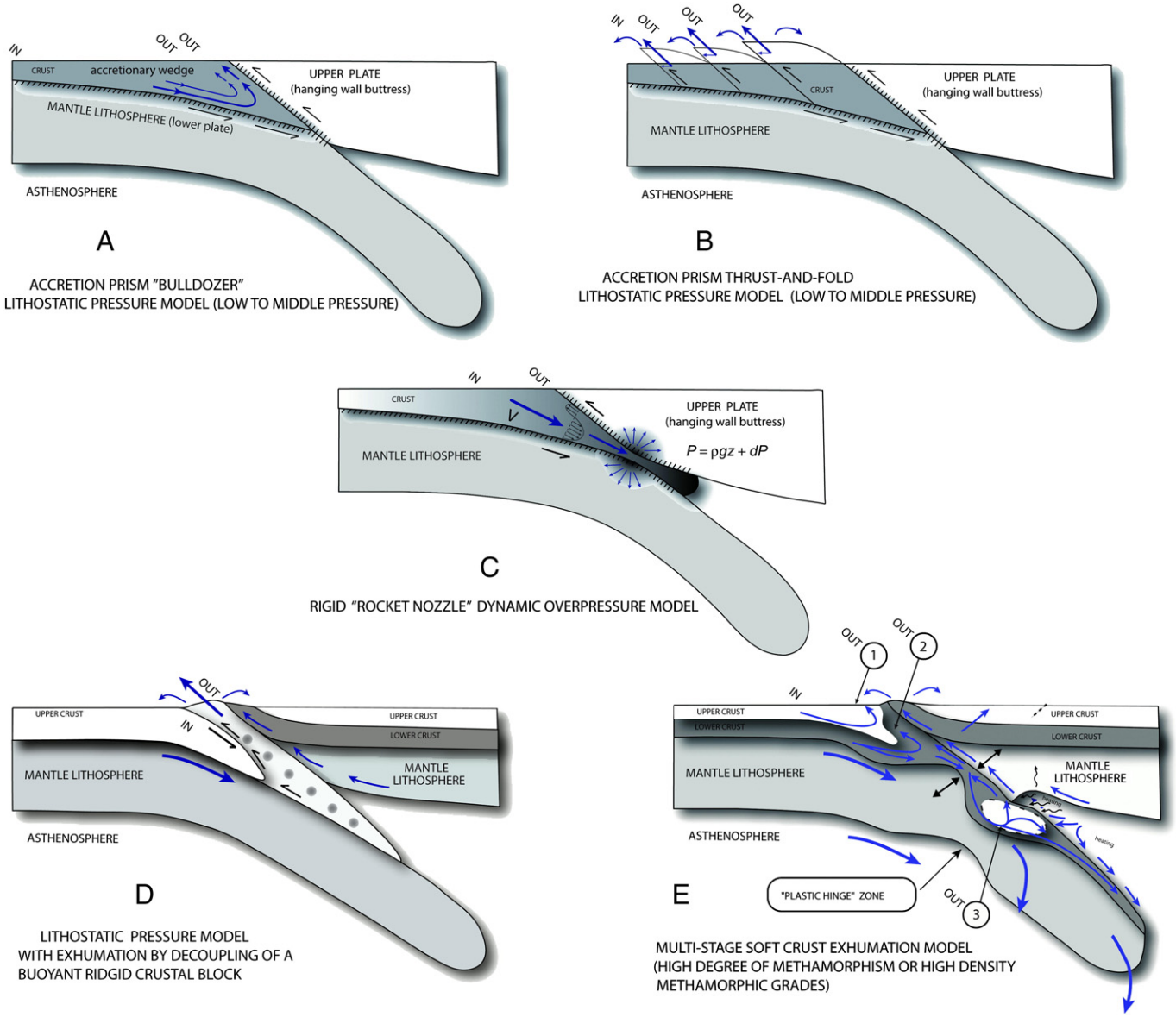

Fig. 3. Various exhumation/collision concepts linked to different ideas on collision mechanics: (A) classical accretion prism mechanisms for LP-LT to MP-MT conditions (Davis et al., 1983; Dahlen and Suppe, 1988; Dahlen, 1990); (B) Thrusting model, superimposed here onto accretion prism mechanism (LP-LT to MP-MT conditions, e.g., Jolivet et al., 1994); (C) Mancktelow's (1995) "rocket nozzle" dynamic overpressure model (LP to UHP conditions, Mancktelow, 1995); (D) rigid block UHP exhumation model (Chemenda et al., 1995); (E) multi-stage soft crust exhumation model (LP to UHP conditions, high or low degree of metamorphism, or high or low density of the metamorphic grades, Burov et al., 2001a, 2001b) that may be combined with the hot channel mechanism suggested by Gerya et al. (2008).

1984). The key observation here is the presence of UHP metamorphic rocks (eclogite facies) of continental origin regurgitated to the surface from the depths exceeding 120 km.

Hence, understanding the mechanisms of continental subduction requires additional considerations. First of all, the negative effect of the positive buoyancy of the lithosphere can be neutralized if a part of low-density crust early separates from the mantle (Cloos, 1993) or if it soon undergoes metamorphic changes and becomes dense and strong (Austrheim, 1991; Le Pichon et al., 1992; Burov et al., 2001a, 2001b). The second factor allowing for continental subduction should refer to the initially higher convergence rates that should favor continental subduction before it is replaced by pure shear, folding or RT instabilities as the convergence rate slows down. In most cases, one can expect that change in the force balance after the first slab break-off might slow down or cancel continental subduction phase.

3. Compatibility of the proposed mechanisms of HP-UHP exhumation with the mechanisms of continental convergence

3.1. Conceptual models and general considerations

Apart of the role of metamorphic rocks as of markers of subduction processes, it is also expected that metamorphic changes , specifically those leading to formation of weak and/or denser facies such as schists and eclogites, provide important controls on subduction interface dynamics, largely due to their weakening and lubricating effect, and also, in case of large quantities, due to their high density. The UHP rocks are considerably denser than the surrounding matrix and hence would not flow up on their own. Consequently, understanding the mechanisms controlling their journey to the depth and their return back to the surface is largely equivalent to elucidation of the convergence mechanisms in general.

Indeed, exhumation of these high density rocks (e.g. eclogite density may exceed by 400–800 kg/m^3 that of the normal crust and by 100 kg/m^3 that of the mantle) is particularly difficult to explain within the conventional exhumation models developed for LP and MP rocks (e.g., Platt, 1986). Existing subduction/exhumation models can be roughly sub-divided onto (1) shallow kinematically driven exhumation models (Fig. 3, see Platt, 1993 for review) such as the accretion prism model, which is limited to exhumation from depths above the 40 km limit, (2) shallow overpressure models that can only work either if the "subduction channel" walls are undeformable (Mancktelow, 1995, Fig. 3) or in the absence of dominant simple shear deformation (Petrini and Podladchikov, 2000), and (3) deep basically hydrodynamically and buoyancy driven HP-UHP exhumation models (Fig. 3, Chemenda et al, 1995; Burov et al., 2001a, 2001b; Yamato et al., 2008).

Subduction and exhumation of deep crustal material is generally considered as resulting from competition between the buoyancy of partially metamorphosed crust and the downward viscous drag exerted on the subduction interface (Couette flow). If one oversimplifies the problem, the viscous buoyancy forces returning the crustal material to the surface can be treated in the framework of the Poiseuille flow (e.g., Platt, 1993), so that the return flow of the exhumed material to the surface results from competition between the downward Couette and upward Poiseuille flow (Raimbourg et al., 2007). Yet this mechanism cannot work on practice since it implies a largely undeformable subduction channel while most recent studies show a much more complicated picture of the subduction interface (e.g., Yamato et al., 2008). The assumption of Poiseuille flow can be only satisfied if the strong parts of both the subducting

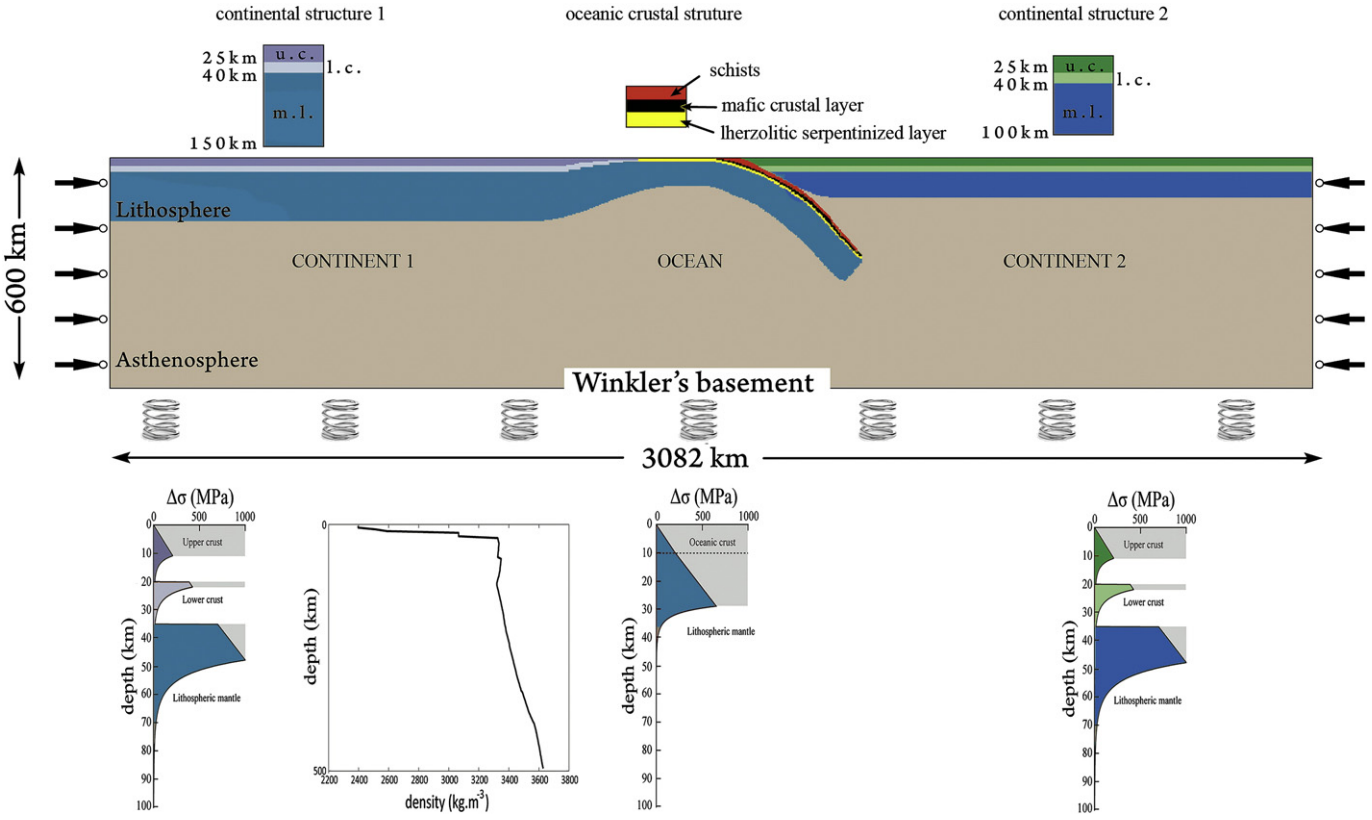

Fig. 4. Representative model setup. The experiment starts from the oceanic subduction that transforms into continental collision / subduction. The upper boundary condition is a free surface combined with surface erosion and sedimentation in case of continental lithosphere. The bottom boundary condition is pliable Winkler basement. The lateral boundary conditions are velocities. The brittle–elastic–ductile rheology is different for the upper crust, lower crust, mantle lithosphere, slab, sediments, asthenosphere and deep mantle (Tables 1, 2, Fig. 5). The model eclogites have the same (weak) rheology as the upper crust, but higher density (up to 3400 kg/m^3).

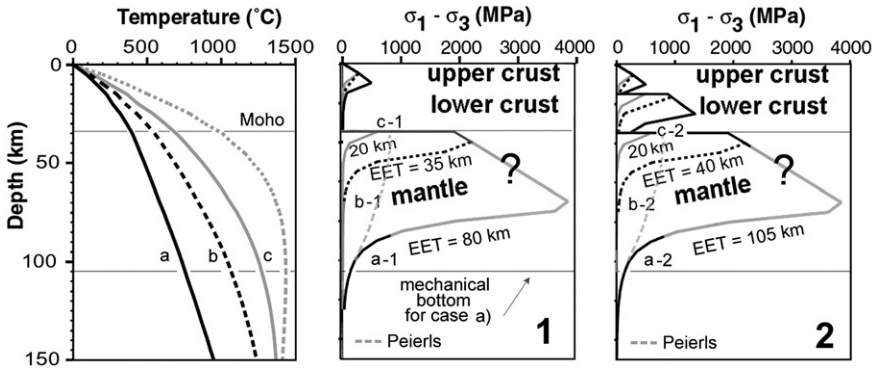

Fig. 5. Representative thermal and rheology profiles for continental lithosphere as function of thermo-tectonic age. EET = T_e is Equivalent Elastic Thickness, directly measurable proxy (from isostatic observations) to the integrated strength of the lithosphere. Initial geotherms (left) and associated rheological strength profiles (middle and right) are computed for lithosphere with a 40-km-thick crust, deforming at a strain rate of 10^{-15} s^{-1}. Middle (1): Weak lower crust. Right (2): Strong lower crust. Black line: cold lithosphere (thermotectonic age = 450 m yr, T_{Moho} = 400–450 °C); black dashed lines: intermediate lithosphere (150 m yr, 550 °C); gray line: hot lithosphere (75 m yr, 650–700 °C); gray dashed line: very hot lithosphere (25 m yr, 1000 °C). Note also that the maximal strength of the mantle lithosphere is limited by Peierls flow law when the predicted dislocation or brittle strength is higher than Peierls strength.

plate and the overriding plate are rigid thus allowing for deviations from lithostatic pressure. Or, it has been shown that "subduction channel" walls are deformable so it cannot support any significant over- or under-pressure (Burov et al., 2001a, 2001b). Therefore it is more appropriate to consider Stokes problem for the return flow in the subduction zone.

If one accepts lithostatic pressure conditions (see discussion in Burov and Yamato, 2008) for the subduction interface settings, then the exhumation depth of HP and UHP rocks must exceed 80–120 km. It was demonstrated (e.g., Platt, 1993) that commonly evoked exhumation mechanisms, that is, kinematically driven circulation in the critical wedge of an accretion prism (Fig. 3, Davis et al., 1983; Dahlen and Suppe, 1988; Dahlen, 1990), cannot bring metamorphic material to the surface from depths exceeding 40 km. This hard limit is related to the fact that the accretion prism mechanism requires, at one side, a relatively high viscosity, needed to drag host rocks to depth and bring their metamorphic facies back to the surface, but on the other side, the viscosity cannot be higher than 10^{19} Pa s to permit circulation of material and to maintain a realistic geometry of the sedimentary prism (Emerman and Turcotte, 1983). At temperatures corresponding to the 40 km depth, most metamorphic rocks have low viscosity, specifically in case of partial melting, and it becomes impossible to build a sufficiently high viscous force to drag up such a weak material. As a result, large part of the material will remain at the bottom of the accretion prism and/or carried down with the subducting mantle.

Another classical kinematic exhumation model evokes foreland fold-and-thrust mechanisms allowing thrusting (nappe stacking) one rock unit on top of another (Jolivet et al., 1994, Fig. 3). The kinematic thrust-and-fold and nappes stacking models exploit the possibility of detachment at the base of the accretion prism. In this case the lower accreted units may be folded and thrusted on top of the upper units. This stacking modesl appear to be consistent with field observations for LP and MP conditions. This mechanism, ultimately linked to simple shear deformation and hence subduction, probably can also work at final stages of HP/UHP exhumation when small volumes of UHP/HP material are included in partly metamorphosed LP/MP matrix.

Finally, one should mention a number of concepts of continental collision that consider mechanical alternatives to subduction and propose specific mechanisms of formation of HP/UHP rocks and their exhumation. For example, Thompsons' "tooth paste" model (e.g., Thompson et al., 1997) suggests that rocks may be squeezed up to the surface, for example as a result of closure of the accretion prism. The model of Thompson et al. (1997) can be discarded since it requires quite specific rheological properties for the colliding blocks and does not imply realistic structural features. Burg and Podladchikov (2000) have suggested a specific collision model that implies tectonic overpressure (as in Petrini and Podladchikov, 2000) and megabuckling of mechanically coupled strong colliding plates. In this model, there is no upper and lower plate but the crustal rocks are brought down within a gigantic syncline formed as a result of a compressional instability. Due to tectonic overpressure, these rocks are formed at twice smaller depth (than usually inferred for HP/UHP material) and then exhumed to the surface by denudation processes and possibly by squeezing like in Thompson's model. The possibility of megabuckling or, more general, of "symmetric" collision, has been also discussed in a number of studies (e.g., Burov et al., 1990; Cloetingh et al., 1999). However, this kind of scenario might be limited to some very specific places in the world such as Himalayan syntaxes or Tien-Shan.

3.2. "Working" mechanisms of UHP exhumation

Chemenda et al. (1995) have suggested a highly elaborated and elegant analogue model of continental subduction scenario with a lithostatic UHP mechanism, in which the rigid cold crust is first brought down with the subducting mantle because its initial viscosity is high allowing for adherence to the mantle lithosphere. Partly metamorphosed, therefore still buoyant and sufficiently rigid, large crustal blocks return to the surface when they delaminate from the mantle. The delamination is caused by reduction of the ductile strength of

Table 1
Summary of thermal and mechanical parameters used in model calculations (Turcotte and Schubert, 2002; Burov, 2010a, 2010b).

Type	Definition	Units
Thermal	Surface temperature (0 km depth)	0 °C
	Temperature at the base of thermal lithosphere	1330 °C
	Temperature at the base of upper mantle (650 km)	1700° ±100 °C
	Thermal conductivity of crust	2.5 Wm^{-1} $°C^{-1}$
	Thermal conductivity of mantle	3.5 Wm^{-1} $°C^{-1}$
	Thermal diffusivity of mantle	10^{-6} m^2 s^{-1}
	Radiogenic heat production at surface	9.5×10^{-10} W kg^{-1}
	Radiogenic heat production decay length	10 km
	Thermo-tectonic age of the lithosphere	50 to 600 Myr
Mechanical	Density of the upper crust[a]	2700 kg m^{-3}
	Density of lower crust[a]	2900 kg m^{-3}
	Density of oceanic crust[a]	2900 kg m^{-3}
	Density of sediment[a]	2600 kg m^{-3}
	Density of undepleted mantle[a]	3330 kg m^{-3}
	Density of asthenosphere[a]	3310 kg m^{-3}
	Lamé elastic constants λ , G (Here, λ = G)	30 GPa
	Byerlee's law — Friction angle	30°
	Byerlee's law — Cohesion	20 MPa

[a] We here provide average densities, in thermo-dynamically coupled models densities are derived directly from the assumed mineralogical composition as function of pressure and temperature conditions.

Table 2
Example of ductile flow parameters assumed in model calculations. Compilation of Mackwell et al. (1998), who used data from Gleason and Tullis (1995), Wilks and Carter(1990), Kirby et al. (1991), Ranalli (1995), Hirth and Kohlstedt (1996), Chopra and Paterson (1981). More recent data (see compilation in Bürgmann and Dresen, 2008) predict slightly different values for ductile flow parameters. However, on practice these differences are negated by adjusting geotherms or thicknesses of the rheological layers in way that the integral strength of the lithosphere matches the observed T_e values.

Layer	Composition	Pre-exponential stress constant A MPa^{-n} s^{-1}	Power law exponent n	Activation energy, Q kJ mol^{-1}
Upper Crust	Wet Quartzite	1.1×10^{-4}	4	223
Lower Crust	Dry Maryland Diabase	8 ± 4	4.7 ± 0.6	485 ± 30
	Undried Pikwitonei granulite	1.4×10^{4}	4.2	445
Mantle or	Dry Olivine	4.85×10^{4}	3.5	535
Oceanic lithosphere	Wet Olivine	417	4.48	498
	Diffusion creep	1.92×10^{-4}	1	3.0×10^{5}
	Peierls law	$10^{7.8}\times10^{-12}$	Peierls stress = 5 GPa	5.35×10^{5}

the crust as its temperature increases with depth. The heavy UHP units are brought to the surface in solid state with the buoyant low density matrix. Once at the surface, the matrix is eroded exposing less erodible UHP material. As can be seen, the key point of this model relates to the net floatability of the exhumed crustal blocks that are supposed to be only partly converted into metamorphic material. Another condition is that this model requires high erosion rates at final stages of the exhumation processes. The model of Chemenda et al., 1995 has been successfully tested mechanically, but it still requires validation in terms of the *P–T* conditions because, because, as most analogue models, it is not thermally coupled and the predicted *P–T* conditions are out of control. In particular, one needs to demonstrate that the crustal blocks can remain sufficiently rigid at the moment of their decoupling from the mantle. It should be also kept in mind that phase transitions result in reduction of the ductile strength and depend on the presence of fluids, which remain to be a poorly constrained factor of the subduction process. With these reservations, one can suggest that the "rigid block model" may work in particular settings characterized by exhumation of relatively small volumes of non-deformed UHP rock. Recent thermally coupled numerical models (Sizova et al., 2010) have demonstrated that Chemenda' model of exhumation is indeed physically viable. Yet, it is still to be validated on a real-life case such as Himalaya collision, for which it was originally designed for.

In difference from the Chemenda model, in some collision settings such as the Western Alps (e.g., Agard et al., 2001,2009; Burov et al., 2001a, 2001b; Yamato et al., 2007, 2008), the amounts of exhumed UHP material are important (large HP volumes up to 50 km wide with up to 200 m thick UHP units). To exhume this material, one needs to create sufficient space (e.g. via slab roll-back or by applying strong surface erosion, yet the latter scenario is not applicable to the Alps). This material is also strongly deformed by ductile deformation. These observations reduce the possibility that the metamorphic terrains were exhumed as small inclusions within a rigid matrix. For this reason, Burov et al. (2001a, 2001b) have suggested an alternative model, in which the subduction interface zone breaks into a shallow (1) and mid-depth (2) accretion prism and (3) a deep zone of accumulated crustal material formed near the base of the upper plate (this zone is dubbed "crustal pocket"). For each of these three levels there is a specific mechanism of exhumation. The two accretion prism zones exhume LP and MP pressure rocks and also HP and UHP rocks that penetrate in the prism with return flow in the subduction interface zone. This return flow is driven both by up-thrusting of the upper plate and small-scale convective movements and gravitational instabilities in the more or less metamorphosed and partially molten subducted crust and in the "crustal pocket" that sometimes may underplate the overriding plate at the 50–120 km depth. At this depth, the weakened subduction interface zone breaks down onto two parts, the upper and the lower one (i.e., "crustal pocket" with potentially partially molten rock), separated from each other by a more or less narrow "neck". Starting from this depth, a large part of the upper and adjacent lower crustal material does not subduct anymore, this material is accumulated below the upper plate and heats up due to direct contact with hot ($T=1330°$) asthenosphere. Thermal expansion due to heating initiates small-scale convection and RT instabilities in the "crustal pocket". These processes drive the metamorphic material (possibly partially molten and mixed up with non-metamorphosed low density crustal units) back to the intermediate crustal depths (40–50 km). From these depths, the UHP material is exhumed to the surface in the "normal way", by the accretion prism mechanism. Each stage of this poly-phase exhumation has its characteristic exhumation rate. The exhumation rate characterizing the convection stage may be much more rapid (10–15 cm yr^{-1}) than the tectonic convergence and uplift rates because the ascent Stokes velocity, V_s , is conditioned by the density contrast and the non-Newtonian viscosity μ_{eff} of the rocks (Weinberg and Podladchikov, 1994; Burov et al., 2001a, 2001b):

$$V_s \approx \Delta\rho g r^2/3\mu_{eff} = 3^{-(n-1)}\cdot r^{n+1}\cdot A\cdot((\alpha\rho_0\Delta T+\Delta\rho_c)g)^n/\left(3\cdot6^{n-1}\cdot\exp(Q/RT)\right) \quad (7)$$

where r is the approximate half-size of the ascending crustal body, $\Delta\rho_c$ is compositional density contrast , n, A, Q, T are the power law exponent (typically 2–3), material constant, activation enthalpy and temperature of the embeddings, respectively, R is the gas constant (8.314 $Jmol^{-1}$ $°C^{-1}$), g is the acceleration due to gravity (9.8 $m\cdot s^{-2}$), ρ_0 is reference mean density (at 0 °C), α is thermal expansion coefficient (typically $3\cdot10^{-5}$ $°C^{-1}$). Let us consider following typical conditions: background temperatures of about 600 °C, $\Delta\rho$ ranging from 20 to 200 kg m^{-3} and temperature contrasts between the ascending material and embeddings ranging from 100 °C to 300 °C. Whatever the embedding is, quartz-rich crust ($n=3$, $H=190$ k $Jmol^{-1}$, $A=5\cdot10^{-12}$ Pa^{-n} s^{-1}, $\rho_0=2600$–2900 kg m^3) or mantle olivine ($n=3$, $H=520$ k $Jmol^{-1}$, $A=7\cdot10^{-14}$ Pa^{-n} s^{-1}, $\rho=3300$ kg m^{-3}) (Burov et al., 1999, 2001a, 2001b), one can find that these conditions would be largely sufficient to drive up a 10–20 km-thick body at 10–20 cm yr^{-1} rate. For larger temperature or density contrasts the estimated values of v_y become very high suggesting the possibility of very fast material ascent from great depths, slowing down near the surface due to the decreasing

Fig. 6. Example of implementation of the collision model that starts from the oceanic subduction phase with progressive transition to continental subduction (Zagros collision settings) after slab-break off (Francois et al., 2012). Shown are the logarithm of the effective viscosity (ratio of shear stress to strain rate) and surface topography. The star symbol corresponds to the slab break-off zone, and the number near the star — to the number of break-off event (there are three consecutive slab break-offs in this experiment).

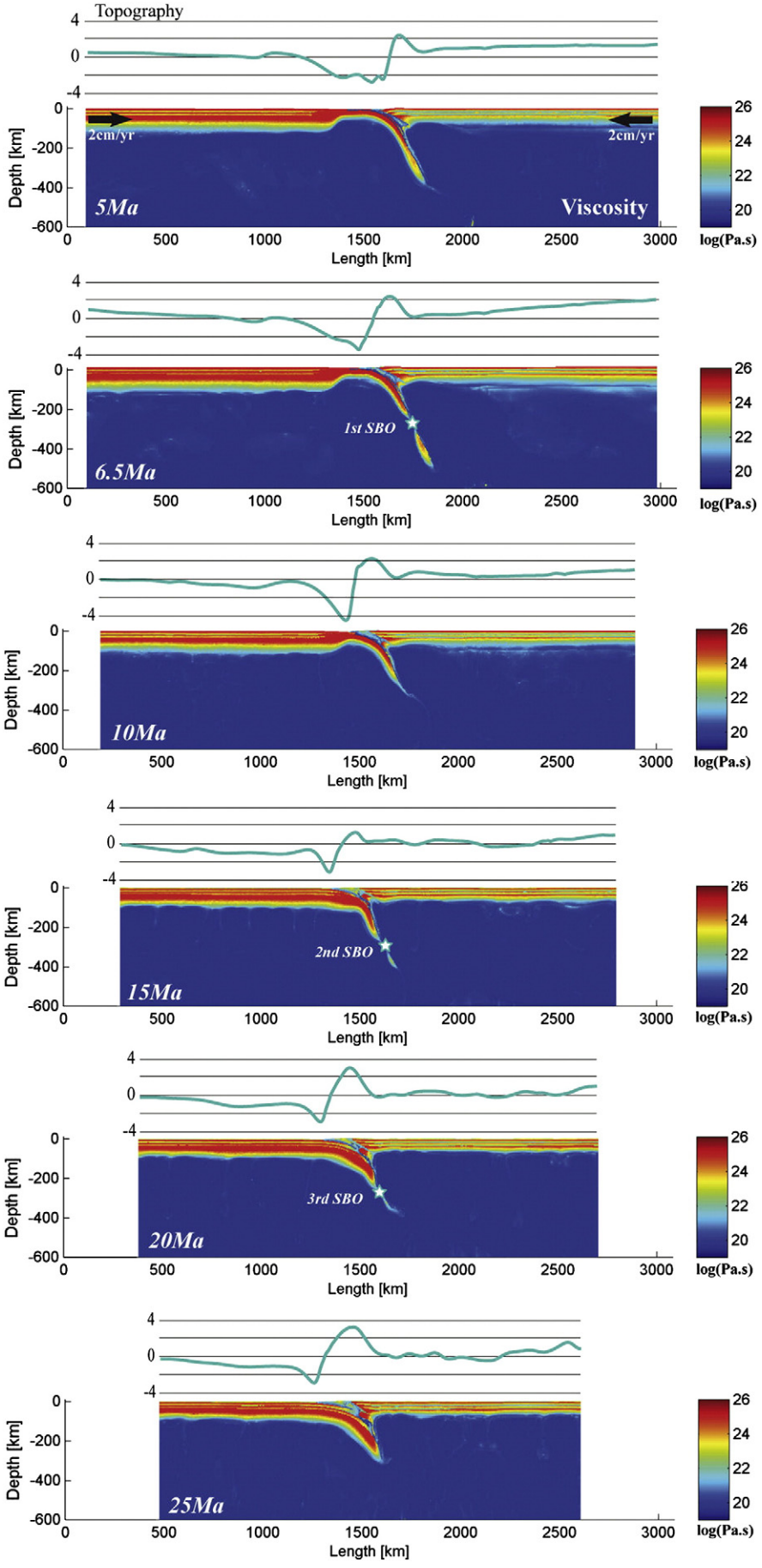
Topography
2cm/yr
2cm/yr
5Ma
Viscosity
1st SBO
6.5Ma
10Ma
2nd SBO
15Ma
3rd SBO
20Ma
25Ma
Depth [km]
Length [km]
log(Pa.s)

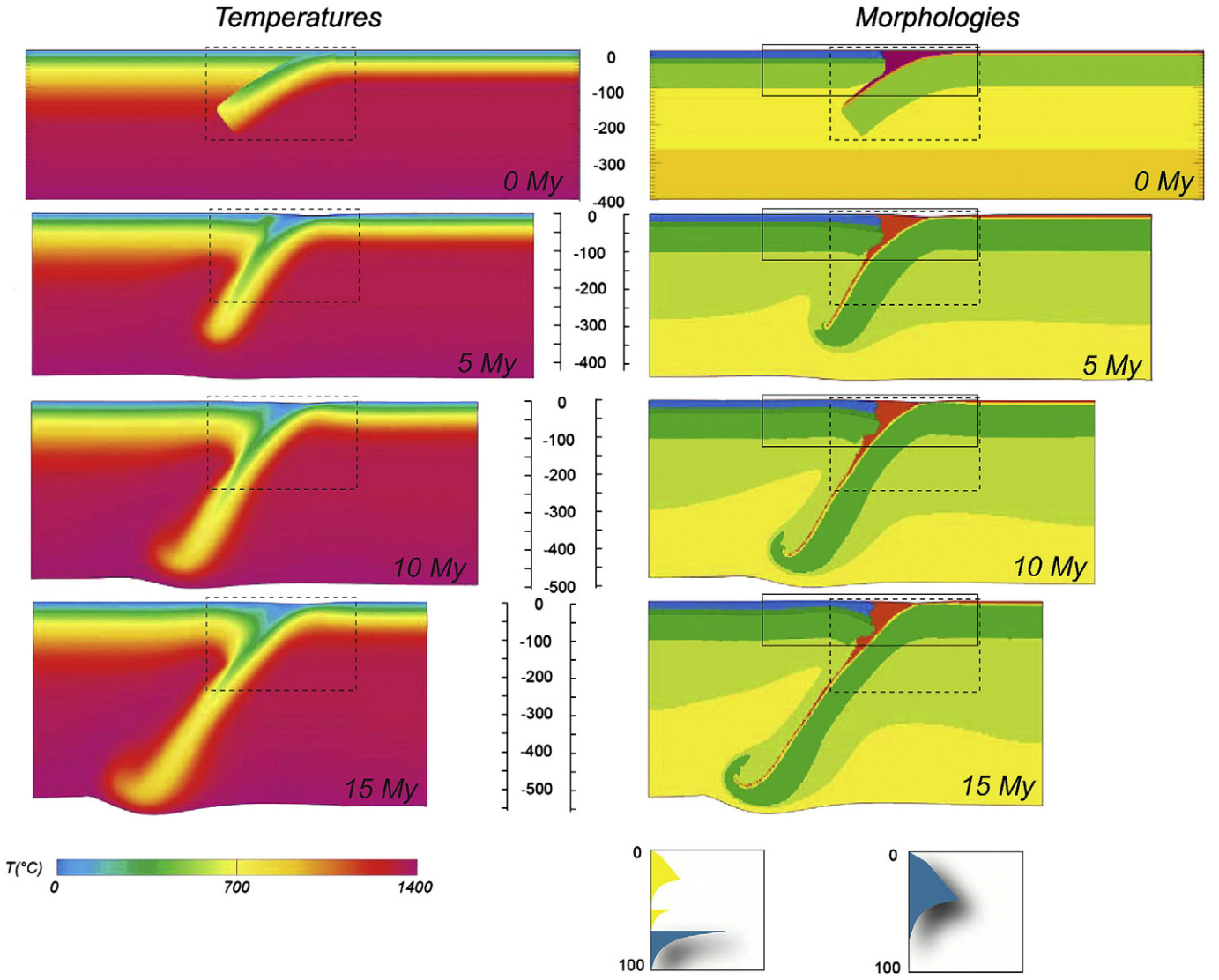

Fig. 7. Example of self-consistent oceanic subduction experiments (Yamato et al., 2007), for the case of an oceanic plate subducting below a 160 Myr old continental lithosphere. This experiment referred below as "*Std*" implements thermo-dynamically consistent phase changes. Densities for all material phases are computed using the algorithm THERIAK (1987, De Capitani, 1994; Tables 1, 2, Appendix A). Squared zones show the position of zoom area shown in Fig. 8. Shown at the bottom are the assumed rheological profiles, for the continental (left) and oceanic plate (right). The profiles were derived for the mentioned thermotectonic age under assumption of quartz-rich upper continental crust, diabase lower crust, and olivine mantle (Tables 1, 2). Olivine is used for the entire oceanic lithosphere.

temperature. These estimates are highly sensitive to the material parameters, for example in case of a crustal quartzite-rich body ascending through olivine background ($\Delta\rho = 430$ kg m^{-3}), the ascent rate may vary from 1^{-4} m yr^{-1} for embedding temperature of 600 °C to 1 m yr^{-1} for the embedding temperature of 900–1000 °C. In case of much more temperature sensitive quartzite embeddings (hot crust material ascends through cold crustal embeddings), the scatter in possible vertical velocities becomes important, including a possibility of turbulent flow inside and outside the crustal body (Burov et al., 2001a, 2001b).

The velocity contrast between the exhuming material, mantle and crustal material of the upper plate induces formation of a large-scale shear zone, which works as a normal fault with a relative upward motion of the footwall. This is quite similar at a first glance to what Chemenda et al. (1995,1996,1997) have predicted from analogue laboratory experiments. There are, however, some principal differences between the two models. In the Chemenda's model, continental crust is exhumed as a large rigid block, which detaches from the mantle and glides up between the downgoing slab and the upper plate. This ascent is driven by density contrast between the crust and mantle. In the Burov et al., 2001a, 2001b model, the exhumed body presents a deformed crustal volume included between a thrust zone forming along the Moho boundary of the lower plate and a normal fault zone forming between the lower and upper plate. In this model the exhumed material is not rigid, but ductile due to high temperature. Contrary to that, Chemenda's model is incompatible with long exposure of the subducted crust to high temperatures. The second important difference relates to the geometry of the downgoing slab. In the Burov et al., 2001a, 2001b model high buoyancy experiment, the downgoing slab has a tendency to rotate upward below the upper plate, due to a positive flexural moment created by cumulative effect of remaining low density crustal layer and of asthenopsheric upflow below the overriding plate. The third principal difference is that in this model there is no important accumulation of crustal material below the upper plate as would be observed in the Chemenda's model in case of weak crustal rheology or hot surroundings. The fourth, less important difference is related to the presence of active extension within the upper plate provoked by the upwelling asthenosphere.

The equation for Stokes velocity of exhumation of buoyant crust does not directly consider its capacity to drag heavier metamorphic

facies that under some condition can still sink in opposite direction. This additional condition can be roughly defined by "internal" Stokes velocity V_i if these metamorphosed facies within the exhumed crustal body:

$$V_i \approx \Delta\rho' g l^2 / 3\mu_{eff\_c} \quad (8)$$

where $\Delta\rho'$ is the density contrast between the metamorphosed part of the exhuming crustal volume and the crust, l is the characteristic size of the metamorphic inclusions and μ_{eff_c} is the effective viscosity of the crust. Logically, exhumation of metamorphic inclusions within lighter crustal units is possible under condition that

$$|V_s| - |V_i| > 0 \quad (9)$$

As long as l is sufficiently small (l<0.25 r–0.5r) the above ratio is positive meaning that large crustal volumes can effectively drag upward smaller metamorphic inclusions. These analytical considerations are largely oversimplified neglecting, for example, the non-linear downward drag due to subduction, which justifies a fully numerical approach.

Burov et al. (2001a, 2001b) suggest that their mechanism can work for a limited amount of time during the initial stages of continental subduction, but do not preclude the possibility of delayed exhumation of the eventually partially molten UHP material from the "crustal pocket" that underlies the overriding plate in their model. This model has received further development in the models Yamato et al. (2007, 2008) and Li and Gerya (2009), which account for thermo-dynamically consistent metamorphic phase changes, and allow for tracing metamorphic P–T–t paths used for validation of the model-predicted collision dynamics. These models, discussed in full detail in the next sections, belong to the latest generation of thermo-dynamically coupled collision/subduction models (see also Sizova et al., 2010) where material properties are dynamically adjusted in full consistency with thermodynamic conditions.

Recent numerically inspired oceanic and continental UHP exhumation concepts by Gerya and Stoeckhert (2005), Stöckhert and Gerya (2005), Beaumont et al. (2009), Li and Gerya (2009), Duretz et al., (2011) and Sizova et al. (2010) added new elements to our understanding of exhumation mechanisms, reinforcing, for example, the role of Rayleigh–Taylor instabilities both in the subduction interface zone and the hydrated mantle wedge. Rayleigh–Taylor instabilities may develop in the subduction interface zone due to partial hydration and melting and even propel low density "cold plumes" ascending towards the surface (Gerya and Yuen, 2003); back-arc or back-stop exhumation may be partly explained by the formation of rotating rigid "wheels" trapped into the weakened material in the subduction channel (Gorczyk et al., 2006), or by partial melting in the above discussed deep crustal pockets forming as a result of partial underplating (Burov et al., 2001a, 2001b; Li and Gerya, 2009).

The "hot channel" model (Gerya et al., 2008) of continental collision complements the poly-phase model of Burov et al. (2001a, 2001b) by emphasizing the role of the heating-weakening mechanism, in which the subducting crustal material may be over-heated by viscous shear heating and radiogenic elements. In this model, heating is also associated with flow of aqueous fluids relieved by rapid dehydration (deserpentinization) of the overriding mantle lithosphere that has been hydrated during previous subduction stages. The channel can penetrate along the plate interface down to the bottom of the lithosphere of the overriding plate (150–200 km) and is characterized by temperatures reaching 700 to 900 °C. The low effective viscosity of rocks caused by increased temperature, partial melting and fluid infiltration permits profound mixing of hydrated mantle and crustal rocks. The hot channel exists during the early stage of collision only, but rapidly produces large amounts of ultrahigh-pressure, high temperature rocks. Further collision closes the channel through squeezing rheologically weak, partially molten, buoyant rocks between the strong lithospheric mantles of the two colliding plates.

The role of tectonic heritage has been studied by Tirel et al. (submitted for publication) , who have suggested, in application to Aegean subduction, that deep stacking of continental terrains inherited from the previous tectonic history can explain deep burial and exhumation in appropriate contexts. In the intensively studied Aegean back-arc domain, HP belts represent small continental blocks buried and exhumed back during subduction and slab roll-back of the African lithospheric plate. Numerical models integrating multi-disciplinary observations show that slab buoyancy variations resulting from successive subduction of continental blocks can be responsible for episodic rollback-exhumation cycles. The model of Tirel et al. (submitted for publication) succeeds in reproducing major structural patterns and pressure-temperature-time (P–T–t) paths of the HP rocks in the Eastern Mediterranean and as such exemplifies a new concept for exhumation of deeply buried continental crust.

The specific features of the Burov et al. (2001a, 2001b) and (Burg and Gerya, 2005; Gerya et al., 2008; Yamato et al., 2008; Li and Gerya, 2009) models refer to the presence of several stages or levels of exhumation, with different exhumation rates (and mechanisms) at each stage/level. These models predict high exhumation rates at depth that may be several times higher than the horizontal convergence rates or denudation rates at surface. The predicted rates reach, for example, 10–15 cm yr^{-1} in the Alpine context, where the convergence rates, currently almost negligible, were in average less than 1 cm yr^{-1}, with initial values not higher than 3–5 cm yr^{-1} (Burov et al., 2001a, 2001b; Yamato et al., 2008).

4. Numerical experiments on continental subduction and HP/UHP exhumation

We next discuss the lower and upper bounds on the parameters controlling continental subduction and thus UHP-HP exhumation. We asses various factors controlling continental collision/subduction by using state-of-the art numerical thermo-mechanical models coupled with thermodynamic processes. In these models, density and other physical properties of the material are computed by minimization of free Gibbs energy as function of P–T conditions (e.g., Connolly, 2005) and re-iterated back to the thermo-mechanical part of the model (see Appendix A).

4.1. General method used

We use as representative examples the recent models based on the FLAMAR code (Appendix A). This code, originating from Parovoz-FLAC algorithm (Fast Langrangian Analysis of Continua, Cundall, 1989; Poliakov et al., 1993; Appendix A), has all major features that are necessary for consistent modeling of continental collision. It implements explicit time-marching, large-strain Lagrangian algorithm to locally solve Newtonian equations of motion in continuum mechanics approximation. This viscous-elastic-plastic code is written in full stress formulation, which allows for accurate computation of total pressure, P, as a trace of the full stress tensor. Solution of motion equations is coupled with constitutive equations, heat-transfer, fluid circulation, surface transport and thermodynamic equations. The algorithm also handles explicit free-surface boundary condition. The metamorphic phase changes are treated using free energy minimization algorithms (De Capitani, 1994; Connolly, 2005). The surface processes (erosion and sedimentation) are incorporated using linear and non-linear diffusion formulation (Avouac and Burov, 1996). Fluid transport algorithm is based on enhanced variant of Darcy's flow approximation with strain-rate dependent permeability (Angiboust et al., 2012). The Lagrangian grid is supplemented by a denser particle-in-cell sub-grid (9 to 30 particles, or passive markers, per grid element), which allows for diffusion-free interpolation of grid quantities between remeshings, as well as for tracing

trajectories of selected particles, allowing, for example, for construction of synthetic *P–T–t* paths.

4.2. Numerical setup

4.2.1. Initial configuration

To achieve continental subduction phase in "natural" way, without prescribing it in the beforehand, most recent models of continental collision start from the oceanic phase of subduction (Yamato et al., 2008). Oceanic subduction "prepares" conditions for the continental phase by creating weak subduction interface and providing initial slab pull on the continental lithosphere. Oceanic accretion prism also provides weak material for start-up lubrication of the continental subduction interface (Figs. 4, 5). Further lubrication of the subduction interface is provided by weak rheology of metamorphic and crustal rocks including constant supply of sedimentary material produced by erosion of the uplifting topography.

4.2.2. Mechanical and thermal boundary and initial conditions

The upper boundary condition is free surface. The lateral boundary conditions are kinematic (horizontal velocities). The Winkler's hydrostatic pliable bottom is used as the bottom boundary condition. This semi-free condition allows for reduction of the vertical size of the model by up to 25% compared to the fixed-bottom configuration, allowing the slab to deflect the lower boundary of the model when it approaches the bottom. In subduction zones, the downward translation of a cold slab material produces complex thermal structures (Royden, 1993; Davies, 1999). To account for this complexity, the initial thermal structure (see Appendix A) relies on the oceanic plate cooling model for the oceanic part of the model, while the continental part is based on the continental plate cooling model (Parsons and Sclater, 1977; Appendix A) with a thermo-tectonic age of 160 Ma. The corresponding thermal boundary conditions include zero flux in lateral direction, and fixed temperatures at the upper surface and the bottom of the model. For the entire model, the initial thermal distribution is computed from combination of the plate cooling models (oceanic or continental) for the upper lithospheric part with the adiabatic thermal gradient for the underlying mantle. One first solves the plate cooling problem assuming $T = 0$ °C at the surface and $T = 1330$ °C at the bottom of the lithosphere (Appendix A). Then the initial adiabatic temperature gradient in the underlying mantle is computed by equalizing the temperature at its top with the temperature at the bottom of the lithosphere (1330 °C) and by adjustment the mantle heat flux in a way that the temperature at the bottom of the upper mantle (650 km depth) fits 1700 ± 100 °C (e.g., Turcotte and Schubert, 2002). We re-adjust the initial thermal thickness and, if necessary, the thermotectonic age of the plate to equalize heat fluxes at the mantle-lithosphere boundary. We control both the values of the surface and mantle heat flux to ensure that they fall in the expected range (30–80 mW m^{-2} at the surface and 10–30 mW m^{-2} in the mantle depending on plate age and thickness). The initial bottom and surface temperatures and zero lateral heat flow are kept fixed during further computations. There is a particular difficulty of thermal computations in the accretion prism that refers to the fact that thermal conductivity of sedimentary materials varies from 1 to 5 W m^{-1} K^{-1}, with low values for shales and sandstones (~1,2–4,2 W m^{-1} K^{-1}) and higher values for limestones and dolomites (2–5 W m^{-1} K^{-1}) (Turcotte and Schubert, 2002). The value used in reference simulation is 2 W m^{-1} K^{-1}, but a twice higher thermal conductivity was also tested.

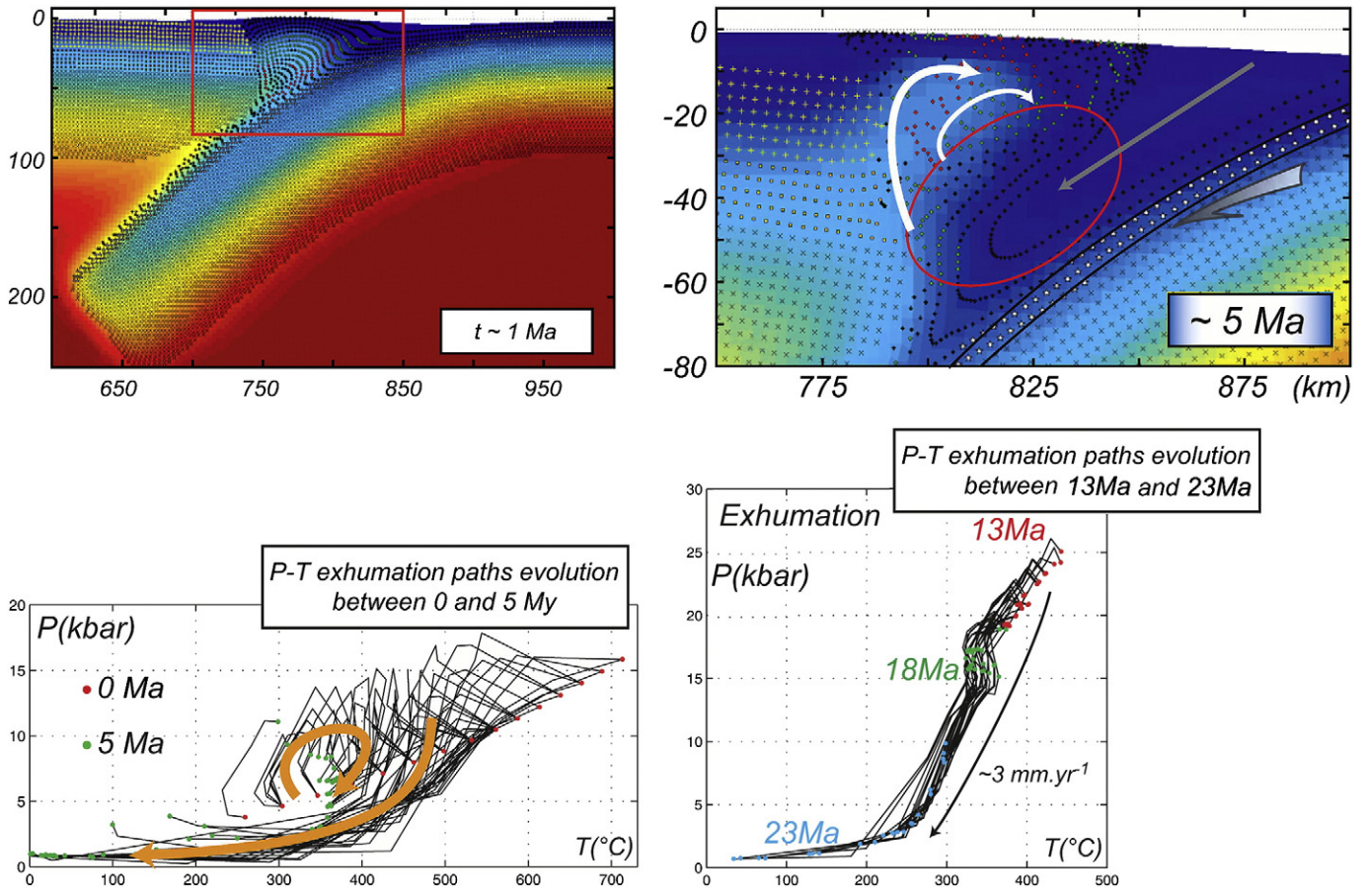

Fig. 8. Zoom to the oceanic subduction interface, for the experiments shown in Fig. 7. Marker field at 5 Myr traces the movements of the particles, which allows us to trace *P–T–t* paths at each moment of time (bottom). In this model, exhumation of HP rocks was achieved at 10–13 Myr under assumption of low viscosity of the serpentinite layer. All markers used for the construction of the *P–T–t* paths were initially located in the normal (un-subducted) oceanic sediments (the uppermost 2 km layer of the crust).

4.2.3. Intermediate conditions for continental subduction

In the models, continental subduction, or, eventually other collision mode, follows the oceanic subduction. For this reason, the initial continental convergence rate equals the rate of the oceanic subduction (for example, two-sided initial closing rate of 2×1.5–3 cm yr^{-1} during the first 5–10 My). The values tested in this study do not exceed the present-day continental collision rates, which are at maximum 3–6 cm yr^{-1}. These rates are on the order of smallest present-day

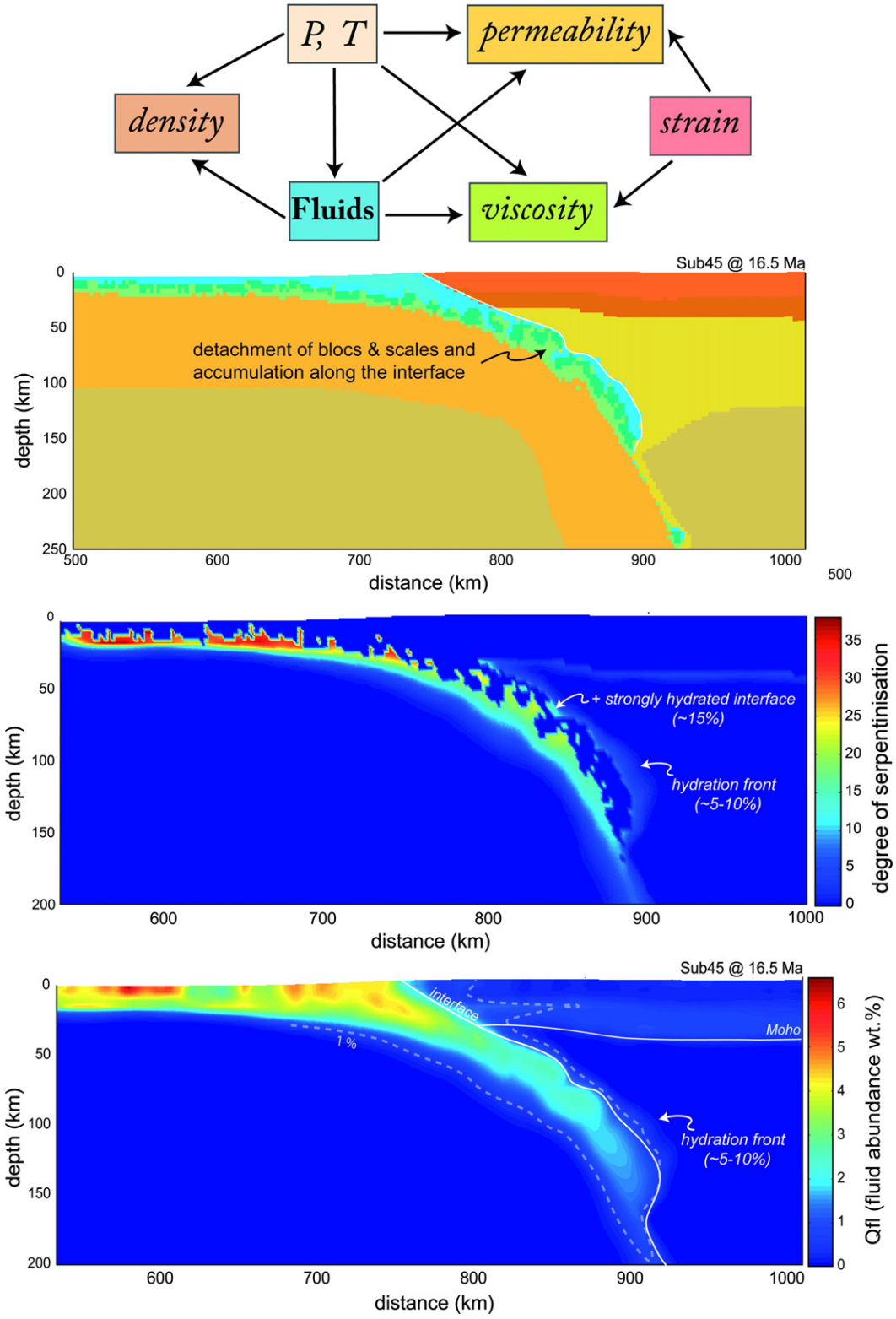

Fig. 9. Example of two-phase flow version of the experiments of Figs. 7, 8 (Angiboust et al., 2012) in which thermo-mechanical and themodynamic model is coupled with porous flow model (top). As can be seen, hydration/dehydration reactions result in strong changes of fluid content in the oceanic subduction interface zone. A 1–2% fluid content variation is sufficient to drop viscous strength by a factor of 10. As result, the interface zone and the mantle wedge are essentially weakened allowing for stable subduction. This weak interface zone is re-used by the arriving continental lithosphere at the initial stages of the continental subduction.

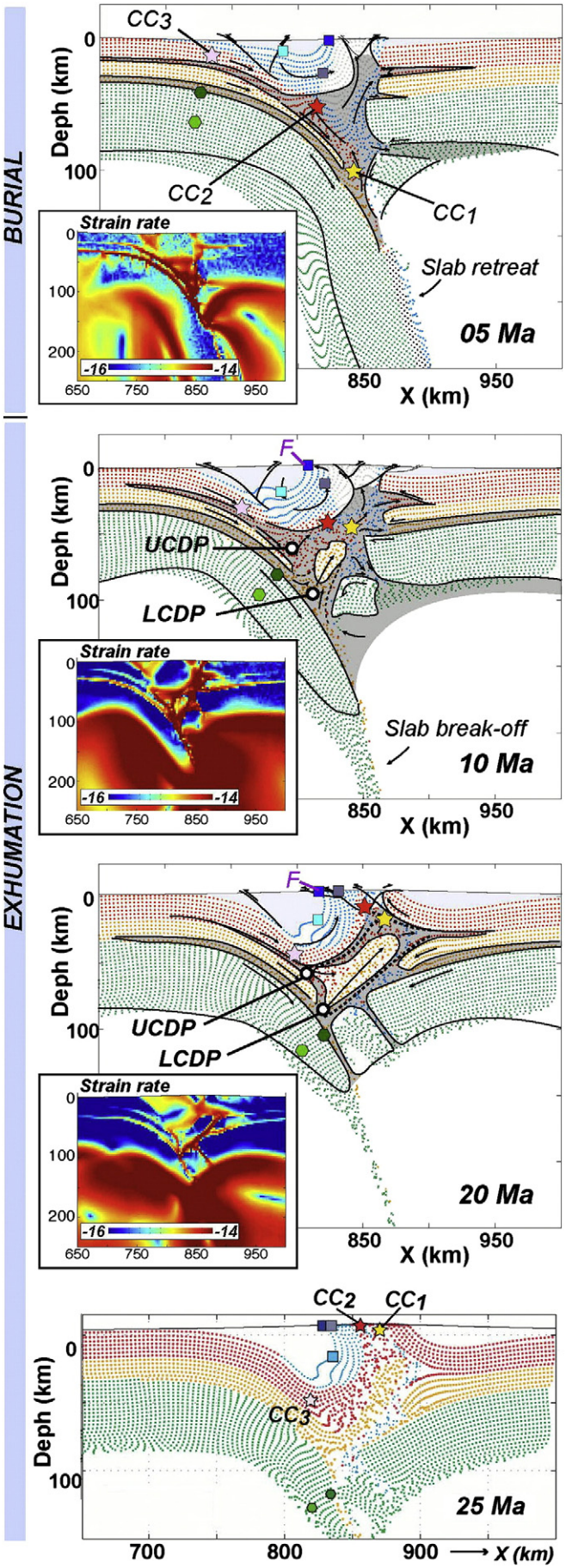

oceanic subduction rates, and are also smaller than the past continental convergence rates for some particularly active continental collisions such as the India-Asia collision (2×4 to 2×5 cm yr^{-1}) during the first 10 m yr. (Patriat and Achache, 1984).

4.2.4. Rheological structure

For continental and oceanic collision models, we assume commonly inferred crustal structure and rheology parameters derived from rock mechanics (Tables 1, 2). As in nature, the topography growth is strongly affected by surface erosion, which is modeled using diffusion erosion with diffusion coefficient varied from 50 m^2 yr^{-1} to 11000 m^2 yr^{-1} (the practical range is 100 m^2 yr^{-1} to 3000 m^2 yr^{-1} , Avouac and Burov, 1996; Burov et al., 2001a, 2001b). For continental collision, as for the case of the upper plate in the experiments on oceanic subduction, the initial geotherm is derived from the half-space cooling model modified to take into account internal heat production and structure of the continental lithosphere (e.g., Parsons and Sclater, 1977; Burov and Diament, 1995a, 1995b; Yamato et al., 2008; Appendix A).

4.2.5. Variable model parameters

One of the universal controlling variable parameters of all experiments is the initial geotherm, which is defined by the thermotectonic age (Burov and Diament, 1995a, 1995b; Toussaint et al., 2004a, 2004b) and is largely characterized by Moho temperature T_m (Fig. 6). The geotherm controls major mechanical properties of the system through its strong impact on the rheological strength profile. By varying the geotherm, one can account for the whole possible range of lithospheres, from very old, cold, and strong plates to very young, hot, and weak ones. The second variable parameter for continental models is the composition of the lower crust, which, together with the geotherm, controls the degree of crust–mantle coupling. We generally considered both weak (quartz dominated) and strong (diabase) lower-crustal rheology and also strong and weak (dry versus wet olivine) mantle rheology (Tables 1, 2). In high resolution experiments, intermediate crust has been also included in the models (Yamato et al., 2008).

As discussed in the previous sections, for given thermo-rheological strength profile, the convergence rate is the main factor defining the mode of continental collision via its impact on the critical Peclet number of the system. In nature, there is obviously a correlation between the convergence rate, the mechanical strength and thermal state of the subducting lithosphere (Mouthereau et al., 2012) so that all major controlling parameters are inter-dependent. We here consider 3 representative cases: (1) very slow collision of weak lithosphere (Alps), (2) intermediate-rate collision (Zagros) of middle-strong lithosphere and (3) fast subduction of very strong Indian lithosphere (Himalaya). The tested convergence velocities vary from $2\times$ 3 mm yr^{-1} to 2×3 cm

Fig. 10. Thermo-dynamically coupled high-resolution model of Alpine collision (Yamato et al., 2008) revealing fine details of subduction and exhumation mechanics in slow convergent context. Marker regions of blue and grey colour correspond to initial sediments (grey markers are those totally eroded after the 20 Myr of experiment). Red and orange markers correspond, respectively, to the upper crust and the lower crust. Green markers represent lithospheric mantle and black ones the oceanic crust. Abbreviations: CC, continental crust; SL, accretionary wedge sediments of the "Schistes Lustrés". The position of the "F point" in the sedimentary accretionary wedge is virtually stable as well as that of two other characteristic points (UCDP and LCDP, Upper and Lower Crustal Decoupling Points, respectively). Note that within the pre-existing subjacent sedimentary accretionary wedge, sediments form a "rigid block", which stays non-deformed and moves, by rotation, around the stable point F. This mechanism can explain why "Schistes Lustrés" found at this place in the Western Alps are dated from the oceanic subduction. The markers shown with stars (CC1,CC2,CC3) correspond, respectively, to the units of Dora Maira, Gran Paradiso, and to formerly surface unit currently buried at great depth. CC1 and CC2 are exhumed at surface at the end of the experiment (25 Ma) after traveling to a more than a 100 km depth (CC1).

yr^{-1}. We then test the influence of most important metamorphic changes such as serpentization, schisting and eclogitization (at $P>1.5$ GPa and $T>550$ °C, see Tables 1, 2).

4.3. Results and discussion

Fig. 6 provides a representative example of continental collision experiments (Francois et al., 2012) in Zagros collision context that occurs at intermediate convergence rates. The experiments start from the oceanic subduction phase (Figs. 4, 5) and, after several slab break-off episodes arrive at the stage of continental subduction that occurs progressively, as a result of subduction of the continental margin pulled by the oceanic plate. The repetitive character of slab-break off process in case of intermediate convergence rates (2 cm yr^{-1}) is an important feature potentially explaining the possibility of repetitive changes in deformation styles, topography evolution and exhumation events observed at the surface. We will later discuss the results of these experiments in full detail, but at this stage Zagros collision experiments were used just as a representative example demonstrating the importance of oceanic subduction phase in continental collision models.

4.3.1. Stage I: pre-continental (oceanic) subduction phase (slow convergence)

As mentioned, oceanic subduction phase plays an important role in the development of continental collision, specifically in case of slow convergence rates. We hence start a detailed discussion of collision/exhumation models from description of the oceanic phase for particularly slow Alpine convergence settings. Figs. 7–9 show experiments on the oceanic phase of Alpine convergence implemented by Yamato et al., 2007 as initial phase of their continental collision model (Yamato et al., 2008, Fig. 7). In this model the oceanic plate subducts at a rate of 6 cm yr^{-1} below the overriding continental plate. These experiments target the Alpine collision and are aimed, in particular, to test the idea of the possibility of continental subduction as follow-up of the oceanic subduction in slow convergence settings. In these experiments, the thermo-mechanical model was coupled with a thermo-dynamic model using the thermodynamic algorithm THERIAK (De Capitani, 1994, see Appendix A) that predicts mineralogical phases and their density by minimizing free Gibbs energy for P–T conditions computed within the thermo-mechanical part of the model. The experiment successfully reproduces the burial and exhumation in a subduction wedge (Fig. 8), in terms of correspondence between the predicted synthetic and observed P–T–t trajectories and the structural and exhumation patterns. The model is tested and parameterized on the well constrained Schistes Lustrés complex (SL; Western Alps), which is thought to represent the fossil accretionary wedge of the Liguro-Piemontese ocean. For convergence rates comparable to the oceanic phase of the Alpine subduction (~3 cm yr^{-1}), the best fitting results are obtained for high viscosity, low density wedge sediments and/or a strong lower continental crust. After a short transition period of 3–5 My, the modeled accretionary wedges reach a steady state which lasts over 20 My. Over this time span, a significant part (~35%) of sediments entering the wedge undergoes P–T conditions typical of the SL complex (~15–20 kbar; 350–450 °C) with similar P–T loops. Computed exhumation rates (<6 mm yr^{-1}) are in the agreement with observations (1–5 mm yr^{-1}) hence validating the choices of thermo-rheological parameters and conforming the viability of accretion prism concept of LP/MP exhumation. The model confirms the crucial importance of the mechanical weakening due to metamorphic reactions in the subduction interface zone by showing that in presence of a serpentinite layer below the oceanic crust, exhumation of oceanic material takes place at realistic rates approaching 3 mm yr^{-1}. The importance of metamorphic reactions was well demonstrated in later follow-up of this study by Angiboust et al. (2012) who have developed a two-phase flow model in the oceanic subduction context by coupling the Alpine subduction model with porous-matrix fluid transport equations (Fig. 9). In this model, dehydration of serpentinite layer provokes fluid release forming a hydration front in the mantle around the subduction interface. As the result, the mantle wedge is strongly weakened (e.g., Guillot et al., 2000; 2001) allowing for more efficient uncoupling between the lower and overriding plate. Fluid migration algorithm is coupled with thermo-mechanical counterpart so that the fluids are free to migrate through a permeable matrix, driven by rock fluid concentrations, non-lithostatic pressure gradients and deformation. These experiments show that deformation is accommodated along the subduction interface by a low-strength shear zone parallel to the wall of the subduction thrust interface, and characterized by a weak (10–25% of serpentinite) and relatively narrow (5–10 km) serpentinized front. Dehydration associated with eclogitization of the oceanic crust (60–75 km depth) and serpentinite breakdown (110–130 km depth) significantly decreases the mechanical strength of the mantle at these depths, thereby favoring the detachment of large slices of oceanic crust along the plate interface. In these experiments, the resulting morphologies are in good agreement with reconstructions derived from structural field observations from the Alpine eclogite-facies ophiolitic belt (corresponding to, i.e., coherent fragments of oceanic crust detached at ~80 km depth in the Alpine subduction zone and exhumed along the

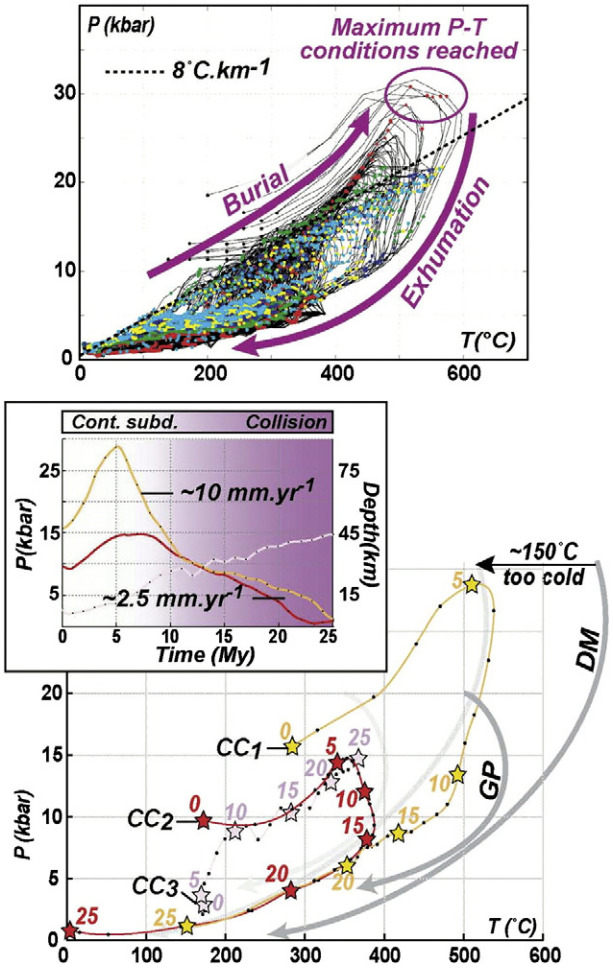

Fig. 11. P–T–t paths of particles (passive markers) coming from the upper continental crust and comparison with the observed P–T paths of the Western Alps (experiment of Fig. 10). Color and symbols as for GP: Gran Paradiso; DM: Dora Maira. See caption to Fig. 10 for other notations. The experiments predict P–T trends that are very similar to nature, assuring that the models realistically reproduce subduction/collision dynamics. Temperature shift of 100–150 °C can be explained by underestimated contribution of shear heating.

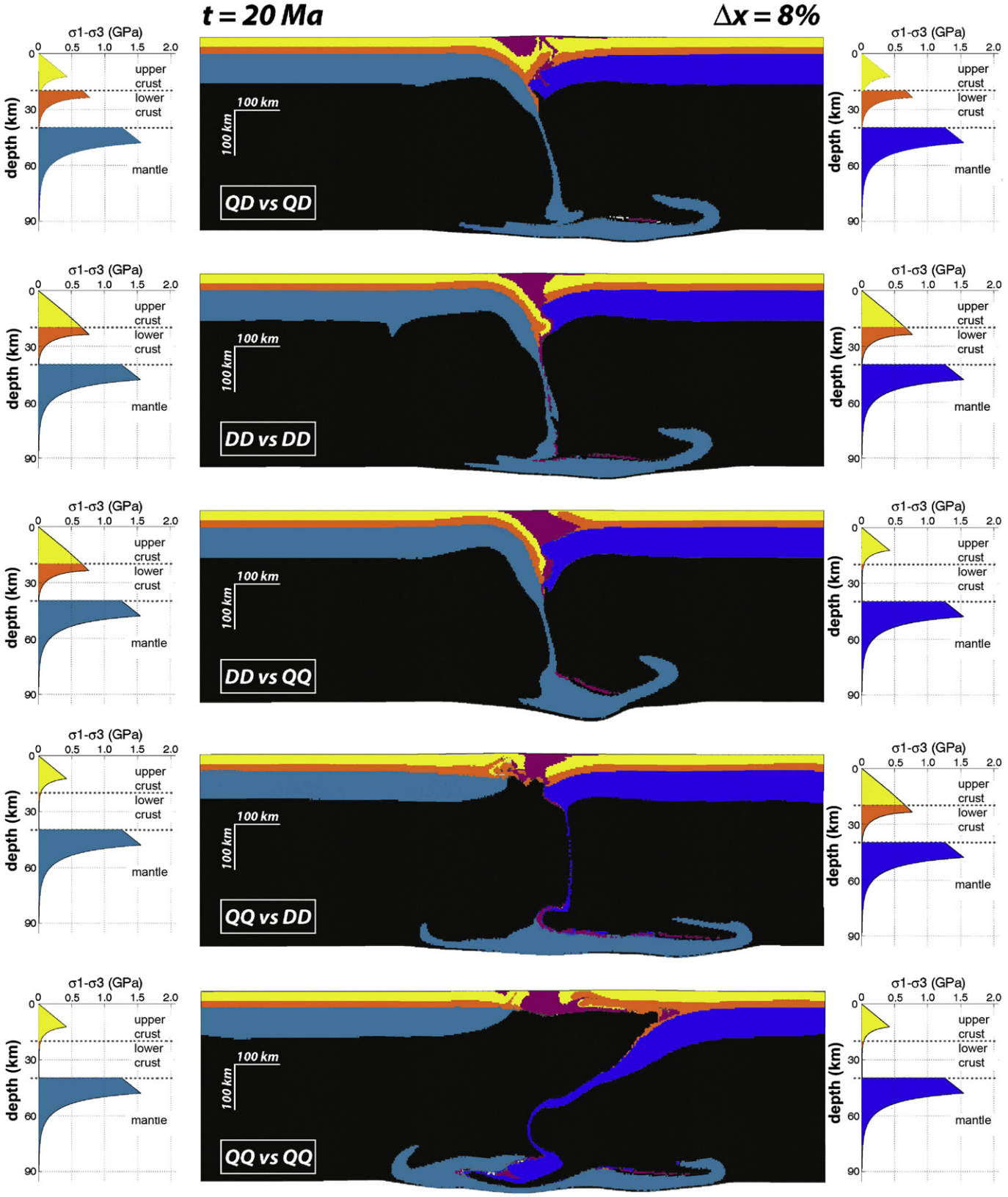

Fig. 12. Influence of crustal rheology on the collision style in case of slow (6 mm yr^{-1}) Alpine-type collision (weak lithosphere). The general setup of experiments corresponds to that of Fig. 10. Shown are morphologies for the models at 20 Myr for different crustal strength profiles. QD: quartz–diabase double-layer crustal structure (upper and lower crust, respectively). QQ: quartz–quartz double-layer crustal structure; DD: strong single-layer structure simulated by diabase. Color code: blue — mantle, orange — lower crust, yellow — upper crust, dark — asthenosphere and sub-lithosphere mantle.

subduction interface). It can be suggested that overall weakening of the plate contact-zone during oceanic subduction creates necessary conditions for the continental subduction at later stages.

4.3.2. Stage II: subduction of a weak lithosphere (T_e<30 km) at slow convergence rate (<1.5 cm yr^{-1}) showing strong dependence on crustal and lithosphere mantle rheology

The second phase of Alpine convergence corresponds to continental subduction occurring at slow convergence rate and hence at near critical Peclet numbers. Slow convergence settings present a particularly important framework for studying continental convergence due to the extreme dependence, in this case, of the collision mode on thermo-rheological assumptions (Yamato et al., 2008). The well-studied Alps are an excellent example being characterized by both very small convergence rates and by weak lithosphere, as attested by T_e data (Watts, 2001). In the study by Yamato et al. (2008), various crustal compositions have been tested, starting from "all-granite" (very weak) crust and ending by "all-diabase" (very strong) crust (Tables 1, 2). It is difficult to constrain the range of the convergence rates in the Alpine orogeny at the eve of the collision stage, that is, back to 30 myr. The present day convergence rates are at the limit of accuracy of geodetic measurements (<0.5 mm yr^{-1}); while the average amount of shortening estimated from structural paleoreconstructions, divided by the duration of the convergence, also yields very small values on the order of 0.8 mm yr^{-1}. Exhumation of UHP rocks of continental origin within the first 5 Myr of collision from depths in excess of 100–120 km, suggests, however, that at this stage the convergence rate had to be much faster, on the order of 2×(0.75–1) cm yr^{-1}. The UHP exhumation data hence is

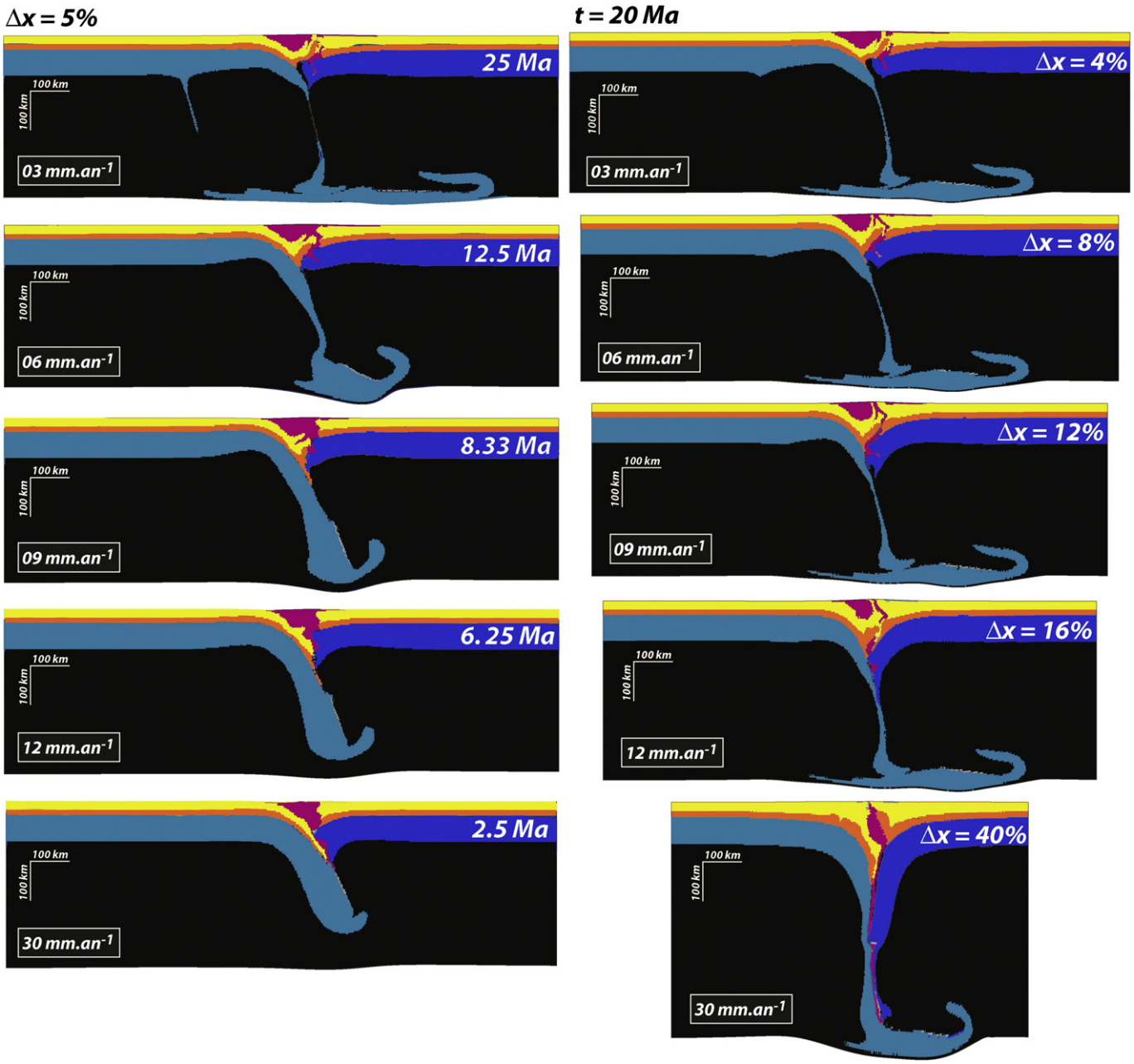

Fig. 13. Morphologies of the Alpine (weak lithosphere with T_e~30 km) collision models for different convergence rates. The general setup of the experiments corresponds to that of Fig. 10 (shortening with a constant rate at both sides, the rheology profile corresponds to the top experiment "QD"–"QD" of Fig. 12); colors correspond to definitions of Fig. 12. Left: configuration after 5% of shortening (compared to the initial width of the box). Right: configuration at 20 Ma since onset of convergence. As can be seen, high convergence rate promotes sustainable subduction while at slow rate slab break-off and RT instabilities shorten the duration of the subduction stage. Color code: see caption to Fig. 12.

practically the only observation allowing us to constrain the dynamics of the collision zone during the first 5–15 Myr. The most reasonable idea is hence to suggest that during the initial several Myr the continental subduction continued at rates that were comparable to those of the preceding oceanic subduction. This reinforces the idea that the oceanic slab pull is an important component of the initial force balance at the onset of the continental collision phase. It can be also argued that the initial subduction rates were even higher than the estimates obtained from dating exhumed rocks versus the exhumation depth. In particular, some part of UHP rock could be buried deeper without being exhumed (which is probably the case of fast collision zones such as Himalaya). At the agnostic side, we cannot also exclude that the exhumed rocks are not representative of the bulk circulation of the metamorphic material in the subduction wedge.

The experiments shown in Supplementary Fig. 1 illustrate historically first numerical model of Alpine collision that has been successful in reproducing continental subduction and UHP exhumation in the Alpine context (Burov et al., 2001a, 2001b). This model has been enhanced by (Yamato et al., 2008) who have coupled it with thermodynamic processes while significantly increasing the numerical resolution (Figs. 10, 11). This model, accounting for multilayered rheological structure of the continental crust, shows that UHP exhumation may occur due to mechanical decoupling of the subducted lower or middle crustal layer from both mantle lithosphere and the upper crustal layer. A large part of the layer tip tears off and flows up at the rear of the accretion wedge, between the subducting and overriding plates, in agreement with the field observations for the Western Alps. The predicted bi-phase exhumation rate and *P–T* trends match well the observational data thus justifying the model (Fig. 11). This high resolution model was first used to parameterize the rheological choices by exploring the impact of the convergence rate and rheology in case of the relatively weak Alpine lithosphere (Fig. 12). These experiments demonstrate extremely high sensitivity of the models to the rheological parameters thus allowing for robust elimination of those thermo-rheological profiles that are mechanically incompatible with the considered convergence scenario. Surprisingly, the models have demonstrated that some rather "classical" rheological choices such as that of all-quartz-rich crust are entirely incompatible with the dynamics of the Alpine collision (Fig. 12) , hence opening a new way of linking the laboratory derived rheology laws to geological scales. Figs. 13, 14 also show the impact of convergence velocity for the case of best fitting rheological structure derived for the Alps on the base of the experiments shown in Fig. 12. It can be seen that very slow rates (<3 mm yr^{-1}) result in Rayleigh–Taylor instabilities and slab-breakoff, while very high velocities, in case of weak lithosphere, (2×3 cm yr^{-1}) lead to development of unusual double-sided symmetric subduction. Also, the predicted exhumation rates are directly comparable with the observations thus allowing for elimination of incompatibly high convergence rates. The other remarkable results refer to the prediction that higher convergence rates result in slower UHP exhumation just until its complete disappearance at rates exceeding 30 mm yr^{-1}. This result provides some elements for explanation why UHP rocks of continental origin are rare or absent in faster convergence settings such as Zagros or Himalaya. It can be thus once again concluded that the convergence rates and the integrated strength of the lithosphere are interlinked, probably because that higher convergence rate requires higher slab pull/push forces while such forces can be only exerted on the lithosphere if the latter is strong enough to sustain them.

4.3.3. Intermediate (1.5–3 cm/myr) to fast convergence rates (>3 cm/myr), intermediately strong (T_e~50 km) to strong (T_e>70 km) lithosphere. Impact of convergence rate partitioning

We here discuss the results of experiments (Supplementary Fig. 2) studying the amount of continental subduction as function of convergence rate assuming strong cold lithosphere with T_e values on the order of 70 km (e.g., Indian craton, Watts, 2001). Even for such a strong lithosphere, the experiments show significant dependence of the amount of subduction on the convergence rate, for equivalent amounts of tectonic shortening. In the experiments, the amount of subduction is characterized by "subduction number" S which is the ratio of the subduction length to the total amount of shortening. As demonstrated by these experiments, S number approaches 1 (100% subduction) only for convergence rates>3 cm yr^{-1} (subduction Peclet number>10). At smaller rates, an essential amount of shortening is accommodated by pure shear thickening and partly by folding.

Francois et al. (2012) have also studied the conditions of the intermediate rate Zagros collision (Figs. 4–6, 15, 16), which some workers regard as a "mini-Himalayan collision" (Hatzfeld and Molnar, 2010) due to the fact that in both cases an old strong cratonic plate slides below a younger weaker overriding plate resulting in rise of an elevated plateau. However, the similarities between these two collision zones probably do not go much further. In particular, the Iranian plateau is much shorter and lower than the Tibetan plateau and has a pronounced elevation trend; Zagros mountain belt is also much lower than Himalaya, and it has been also suggested that relatively early slab break-off could have affected Zagros collision whereas in the Himalayan case slab break-off event did not probably take place. The respective integrated strength of the Arabean plate (T_e~50 km) is also much smaller than that of the Indian plate (T_e~70–90 km), but both plates are much stronger than the Alpine lithosphere. Last but not least, the convergence rate in Zagros is about 2 times smaller than in Himalaya.

Fig. 15 shows zooms to the subduction interface zone for the major stages of the evolution of the "Zagros collision" experiments

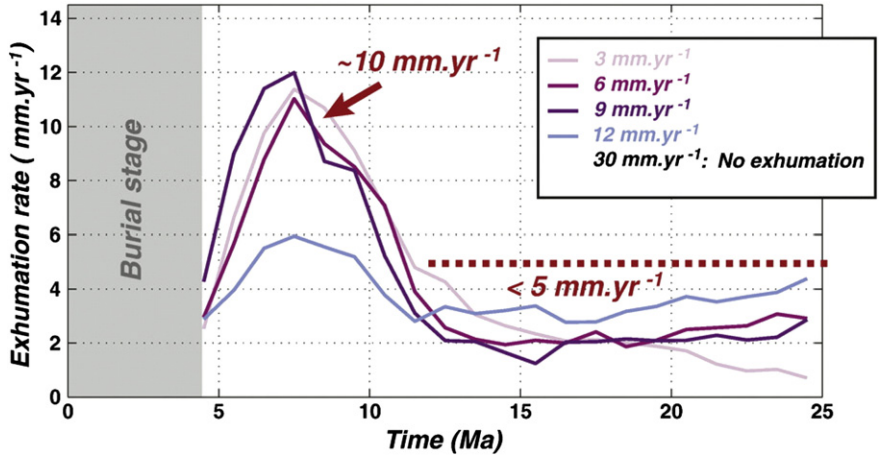

Fig. 14. UHP exhumation rates for the experiments shown in Fig. 13. Note that high convergence rates reduce exhumation rates until fully negating them.

from Fig. 5. As can be seen, quite contrary to common expectations, several consequent slab-break-offs may occur before the exhumation of HP/UHP continental crust without producing major topographic response at the surface. It is also remarkable that oceanic HP/UHP material is exhumed only at the onset of the continental collision, when it is pushed/dragged up by low buoyancy continental crustal rocks. Similarly, exhumation of small amount of HP/UHP material occurs during the initial stages of collision (at 25 Myr of model time). It is also insightful in these settings most exhuming HP/UHP rocks get stacked a few km below the surface. This explains the practical absence of UHP material in Zagros. It can be also concluded that even if the presence of UHP material at surface can serve as indicator of subduction processes, its absence, on the contrary, does not prove the absence of such. Furthermore, it follows from these and previously shown experiments that only limited part of possible *P–T* paths gets to the surface such, appealing for a thorough study of their representativity for the bulk exhumation and collision mechanisms.

Francois et al. (2012) have found that for intermediate and high convergence rates, collision style is highly dependent not only on the total value of the convergence rate but also on the partitioning of the convergence rates between the overriding and subducting plate. The explicit presence of absolute advection velocity terms (Eq. (1); Appendix A) in the heat transfer equation results in sensibility of the behavior of the thermo-mechanical system to the partitioning of the convergence rates between the two sides of the model. For example, applying total velocity at the border of the subducting plate enhances the amount of subduction and increases plate dip, while doing so at the opposite side of the model has an opposite effect. In these particular experiments, the difference between dip angles reached almost 40° at 20 Myr (37%), from nearly 80° in case of convergence from the side of the subducting plate to about 45° in case of convergence from the opposite side, with an intermediate value for double-sided convergence. This effect is contra-intuitive, since simple mechanical non-inertial inertial system should be indifferent to distribution of absolute velocities at the borders (as in case of analog models). Yet, thermo-mechanical coupling changes this rule, since absolute velocities imposed at the borders define horizontal and vertical thermal advection rates, which, in their turn, affect the mechanical properties, thermal buoyancy and phase changes. As a result, absolute velocity distribution matters, specifically because in nature many collision zones are converging only from one side, e.g. the Himalayas. In some cases the absolute velocities are not as certain and hence evaluation of absolute tectonic movements represents a great challenge for the future.

4.3.4. Strong lithosphere, various convergence rates

Studies of fast continental collision (>3 cm yr^{-1}; Toussaint et al., 2004a, 2004b) of strong lithosphere have shown that at rapid convergence rates and strong lower plate, continental subduction, once initialized, may continue for a very long period of time, i.e., practically for the entire life span of convergence. However, in this case the impact of convergence rate cannot be treated separately from that of the surface denudation/erosion/sedimentation processes. In fast collision zones, there should be a strong feedback between the surface processes and tectonic forcing. For pure-shear collision settings this has been demonstrated by Avouac and Burov (1996) who have shown that stable growth of orogenic topography requires a strong feedback between the erosion rate and the tectonic convergence rate. In opposite case, the orogenic topography tends to collapse. Even stronger impact of surface processes is expected for continental subduction (Lavier and Steckler, 1997; Toussaint et al., 2004a, 2004b; Burov and Toussaint, 2007, Fig. 17, Supplementary Figs. 3 and 4), since sedimentary loading and erosional unloading have primary effect on the force balance and integrated strength of the lithosphere (flexural yielding/unyielding, thermal blanketing etc.) in the collision zone. In particular, excessive topography , if not timely removed, exerts closing pressure on the subduction interface, increasing plate coupling and hence preventing subduction (e.g., case S = 0.8 and S = 1.0, Fig. 17). More surprisingly, very fast erosion (e.g., cases S = 0.1, 0.21, 0.33,0.42, 0.5, Fig. 17) also reduces the amount of subduction by producing dynamic unloading and hence elastic unbending of the subducting plate causing lock-up of the subduction interface. The experiments show that pure shear thickening or folding occur instead of simple shear subduction when erosion is either too strong (e.g., $k>3000$ m^2 yr^{-1} for convergence rates $<2\times2$ cm yr^{-1}), in that case any topographic irregularity is "too" rapidly erased by surface processes (Fig. 17), or when erosion is too weak ($k<50$ m^2 yr^{-1}). In case of slow erosion, surface elevations are unrealistically high (Fig. 17, Supplementary Fig. 4) which leads to vertical over-loading causing flexural yielding of the lithosphere and growth of the frictional force along the major thrust fault. As consequence, the major thrust fault is locked leading to coupling between the upper and lower plate; this results in overall buckling or folding of the region whereas the crustal root below the range starts to spread out laterally with formation of a high flat "pancake-shaped" topographies. On the contrary, in case of a dynamic balance between surface and subsurface processes (e.g., k = 2000×3000 m^2 yr^{-1}, for convergence rates $>2\times2$ cm yr^{-1} or k = 500–1000 m^2 yr^{-1} for convergence rates <3 cm yr^{-1}) erosion/sedimentation results in long-term localization of the major thrust fault that keeps working during 10 My. It is noteworthy that in the experiments with k = 500–1000 m^2 yr^{-1} (moderate feedback between surface and subsurface processes), the major thrust fault and topography were almost stationary (Supplementary Fig. 4). In case of a stronger feedback (k = 2000–5000 m^2 yr^{-1}) the mountain range and the thrust fault migrated horizontally in the direction of the subducting plate ("India"). This generally happened when both the mountain range and the foreland basin reached some critical size. In this case, the "initial" mountain range and major thrust fault were abandoned after about 500 km of subduction, and a new thrust fault, foreland basin and range were formed "to the south" (i.e. towards the subducting plate) of the initial location. The numerical experiments confirm the previous ideas that intercontinental orogenies could arise from coupling between surface/climatic and tectonic processes, without involvement of special mechanisms of strain localization (Avouac and Burov, 1996). Last but not least, the experiments from Fig. 18 also test the influence of eclogite UHP facies and the possibility of their exhumation as function of the erosion and convergence rate (assuming 100% transformation of crustal material to eclogites at corresponding *P–T* conditions). The experiments suggest that this transformations occurs at much deeper depths in case of fast convergence settings so that subducting crust remains too cold (for UHP phase transition) even at important depth, thus leaving less chance for backward exhumation of the UHP rocks. Yet, exhumation does take place in cases when the subduction interface zone thickens and becomes large allowing for great volumes of light crustal material to delaminate from the mantle and flow back to the surface dragging up UHP material (e.g., case S = 1.1., Fig. 17). It has to be also stated that eclogitization has little effect on the development of subduction.

4.4. Fast convergence, influence of the thermo-rheological structure

We here summarize the results of numerous experiments that tested the influence of rheological structure on the amount of subduction and collision style in most favoring fast convergence settings (2×1.5 cm yr^{-1}). These experiments reveal several types of collision scenarios as function of the thermotectonic age (geotherm, also characterized by temperature at Moho depth, T_m) and rheology profile:

4.4.1. Cold geotherm ($T_m<450$ °C, "jelly sandwich" rheology)

An initially cold geotherm allows the collision to evolve into stable, oceanic-type subduction (Fig. 18, thermo-rheological profile

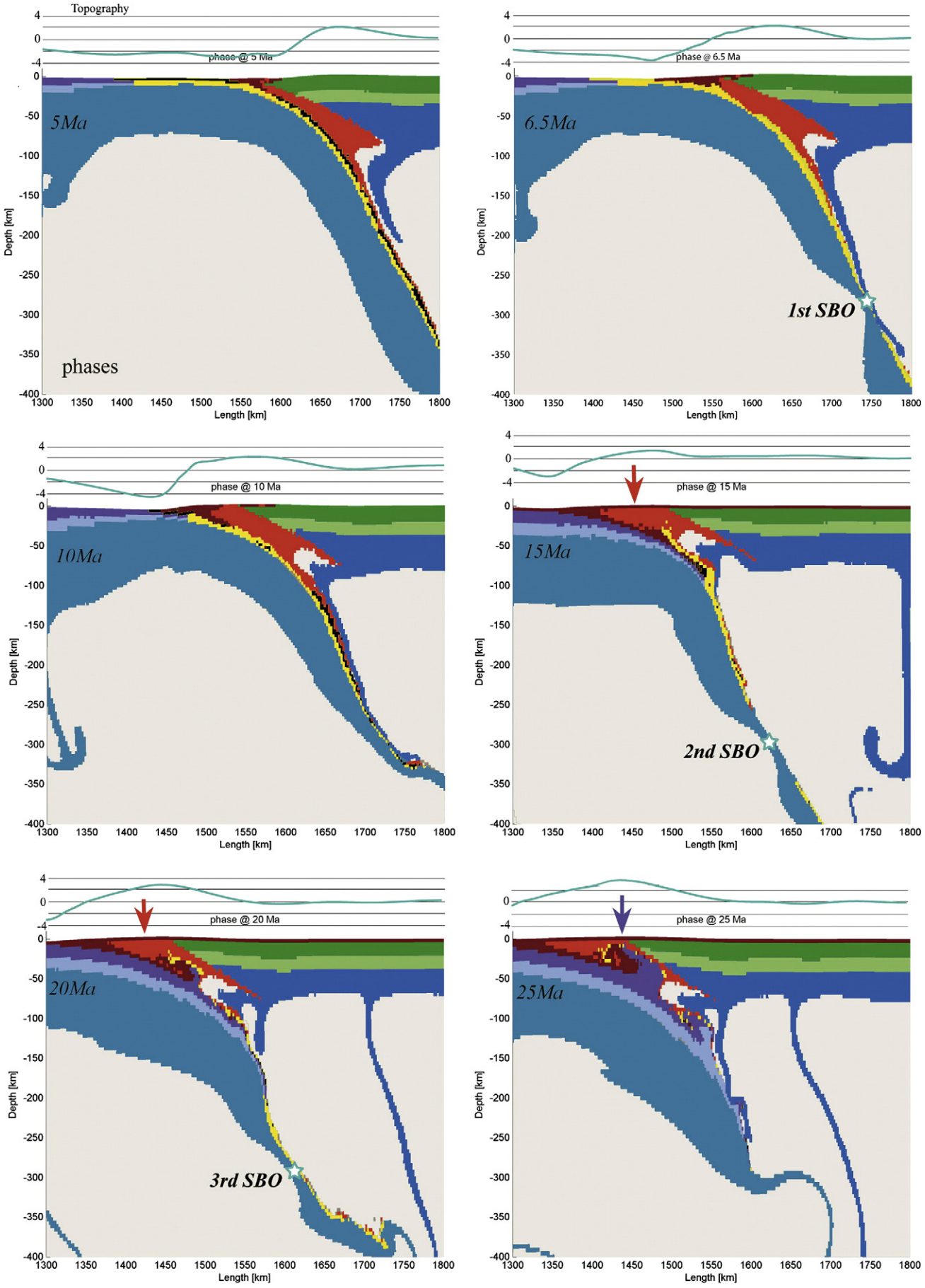
Topography
phase @ 5 Ma
5Ma
phases
phase @ 6.5 Ma
6.5Ma
1st SBO
phase @ 10 Ma
10Ma
phase @ 15 Ma
15Ma
2nd SBO
phase @ 20 Ma
20Ma
3rd SBO
phase @ 25 Ma
25Ma
Depth [km]
Length [km]

"C_1", Fig. 17 case S = 1.1, Supplementary Fig. 3). Almost all shortening is accommodated by subduction both of the continental lower crust and mantle. Because of low Moho temperature, the lower crust is highly resistant to decoupling and remains "welded" to the lithospheric mantle. It can be dragged to as deep as 250 km depth in spite of its positive buoyancy. However, the mechanical resistance of the major part of the upper crust remains lower than the buoyancy-induced stresses. It early separates from the lower crust and remains at surface or mid crustal depth, only small amounts of the upper crust are dragged to the depth. In these experiments, crustal material is brought down to important depths (>>120–150 km) allowing for UHP and HP metamorphism. These experiments closely resemble those from (Toussaint et al., 2004b) that modeled India-Asia collision. Supplementary Fig. 3 shows formation of large-scale thrust-and-fold structures that are conditioned by the crust–mantle decoupling and resemble those typically observed in the field. This process explains the eventual complexity of the *P–T–t* paths, with a limited amount of UHP material exhumed at the beginning of subduction.

4.4.2. Intermediate geotherm (T_m = 450–600 °C, "jelly sandwich" rheology)

Stable subduction of the lithospheric mantle leads the lower crust to decouple from the mantle (Fig. 18, thermo-rheological profile "C"). For intermediate geotherms, shortening is still largely accommodated by subduction, but positively buoyant lower crust separates from negatively buoyant lithospheric mantle and stagnates at some intermediate level (between 100 and 200 km depth), sometimes forming a double crustal zone (possible analogy is Northern Apennines, Ponziani et al., 1995). The crustal part of the subduction interface is divided onto the accretion prism and a lower crustal "pocket". The geometry of the downgoing lithospheric mantle is affected by the ascent of the buoyant lower crust: the slab adopts a very low angle of subduction. As a consequence, the oceanic slab early detaches and sinks into the deep mantle. Small-amplitude (1000 m) long-wavelength (350–400 km) lithospheric folding also accommodates some part of the shortening, specifically in the upper plate. The crustal material is brought down to 100–120 km depth allowing for UHP and HP metamorphism.

4.4.3. Hot geotherm (T_m = 600–700 °C, "jelly sandwich" rheology)

Subduction and pure-shear thickening (Fig. 18, thermo-rheological profile "C_{-1}") are the results of collision under the conditions of a hot geotherm. At a Moho temperature of 650 °C, pure-shear thickening and moderate-amplitude (1500 m) lithospheric folding (wavelength 200–250 km) accommodate a significant part of shortening. This behavior is a result of thermal weakening of the lithosphere, which makes volumetric thickening mechanically easy. The base of the overriding lithospheric plate is also weakened and can be dragged downward with the sinking lower plate. The crustal material basically does not arrive to depths larger than 60–80 km, except for very early stage of subduction (first 5 Myr). Hence, formation and exhumation of HP/UHP is possible only at very beginning of subduction.

4.4.4. Very hot geotherm ("jelly sandwich" rheology) or weak mantle ("crème brulée" rheology, T_m > 750 °C for weak lower crust and dry olivine mantle, or T_m > 600 °C for wet or dry diabase lower crust and wet olivine mantle)

Pure-shear thickening and RT instabilities (Fig. 18), thermo-rheological profiles "D" and "B" dubbed "crème brulée" (Burov and Watts, 2006) result from very hot geotherms. For such a hot, weak lithosphere, stable subduction (hence HP/UHP exhumation) and lithospheric folding are impossible: convergence at the borders is entirely accommodated by pure-shear thickening and RT instabilities. Because of high temperatures, the effective viscosity at the base of the lithosphere is reduced, whereas its density is still higher than that of the asthenosphere; these two factors promote rapid (in < 1 m yr) development of RT instabilities. The slab thins in a "chewing gum" fashion, and a "cold spot" forms (possible natural examples: Vrancia body in the Romanian Carpathians, e.g., Wenzel, 2002; Cloetingh et al., 2004). The rate of "subduction" in this case is not controlled by the convergence rate but by the internal growth rate of the RT instability. We dubb this style of deformation "unstable subduction." In the conditions of these experiments, the crust is not brought down to depth below 40 km . Hence, HP/UHP metamorphism is impossible in this case.

4.5. Case of strong lower crustal rheology

The experiments of the previous section (shown in Fig. 18) were repeated assuming strong dry diabase rheology (Table 2) for the lower crust. The resulting end-member scenarios (stable subduction vs. unstable subduction) are roughly the same as in the previous experiments. Yet, there are some noticeable differences in the intermediate cases.

4.5.1. Cold lithosphere

For experiments with very cold lithospheres (T_m < 450 °C), the convergence produces stable subduction. However, the results of these experiments differ in many ways from homologue experiments with "weak" (undried granulite) lower crust. In particular, subduction involves the entire continental crust, including the upper crust and its sedimentary rocks. The lithosphere also has a much higher tendency for folding while the predicted topography is 20–30% higher than in the experiments with weak lower crust.

4.5.2. Intermediate-temperature lithospheres

For higher Moho temperatures (T_m = 450–750 °C), stable subduction is progressively replaced by pure-shear thickening and by large-scale lithospheric folding. Folding is favored by stronger rheology of the lower crust, which ensures its mechanical coupling with the lithospheric mantle. Note that for the same temperature range, but for a weak lower crust, subduction was a dominant mechanism of deformation.

4.5.3. Very hot lithosphere

The results of very "warm" experiments (T_m > 750 °C, case D, Fig. 18) are similar to the corresponding experiments with weak lower crust (case B, Fig. 18) from the previous section (no subduction), despite the fact that the integrated strength of the lithosphere in this case is the same in case C_{-1} from Fig. 18. Therefore, it can be concluded that strong mantle lithosphere is a paramount condition for continental subduction and, consequently, for formation and exhumation of HP/UHP rocks. These results showing that strong crust cannot "replace" strong mantle in subduction mechanics can be easily interpreted: in difference from mantle lithosphere, the lower crust is highly buoyant. It cannot subduct by its own, without being dragged by a negatively buoyant strong mantle. If such strong mantle layer is absent, the crust will stay at surface.

Fig. 15. Experiments testing the impact of intermediate convergence rate of 2 cm yr^{-1} (Zagros collision model, Francois et al., 2012). Shown are zooms to the subduction interface zone for the major stages of the evolution of the experiments from Fig. 5. Color code: same is in Fig. 4. See also (Figs. 4–6). SBO means "Slab break-off". (There consequent slab-break-offs occur before the first exhumation of HP/UHP continental crust). Red arrows show the area of initial exhumation of metamorphosed HP/UHP oceanic material. Purple (violet) arrow shows the area of the first exhumation of HP/UHP continental crustal material. Note that oceanic HP/UHP materials exhumes at the onset of the continental collision, when it is pushed/dragged up by low buoyancy continental crustal rocks. It is noteworthy that most exhuming HP/UHP rocks get blocked just few km below the surface.

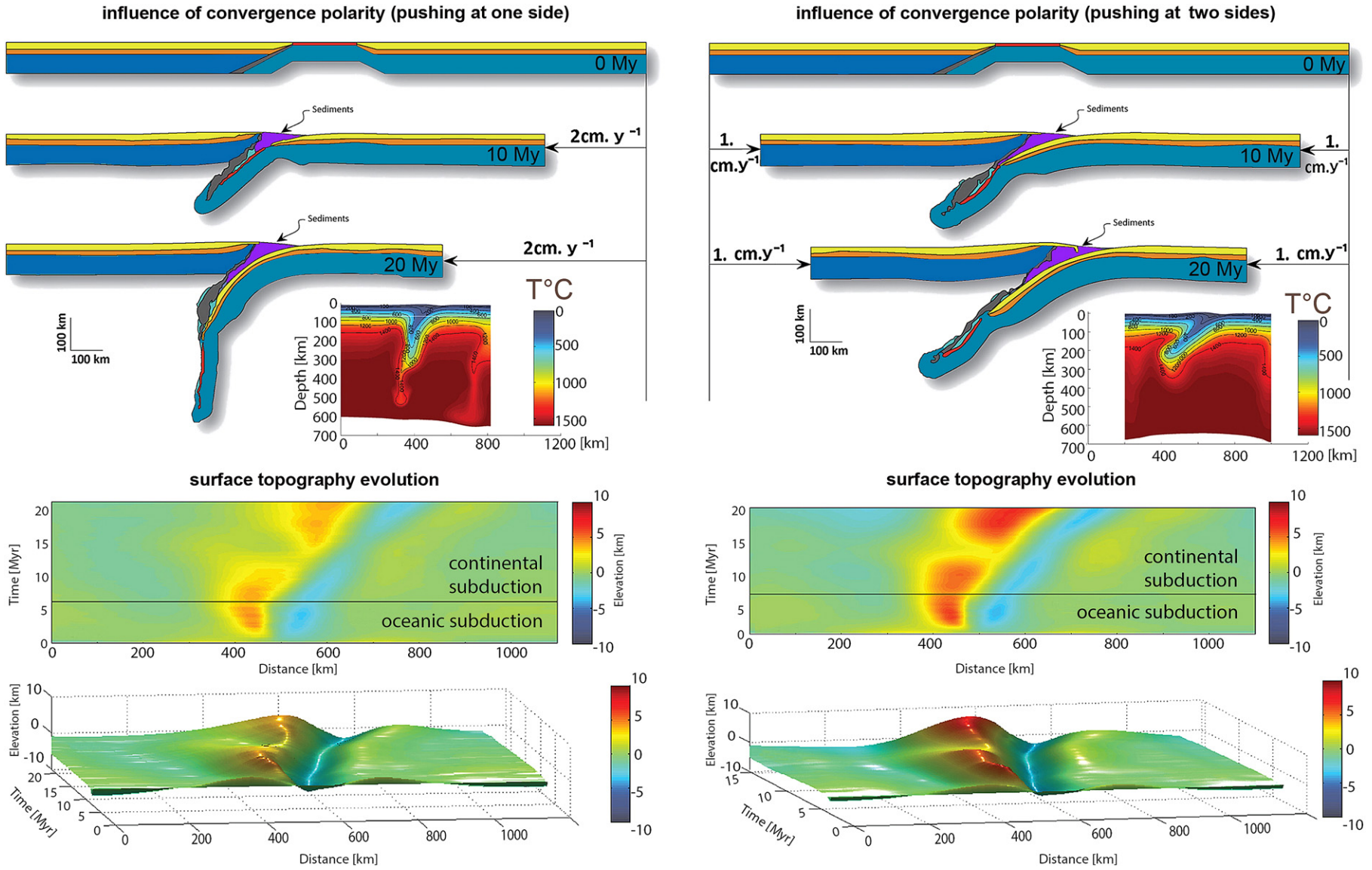

Fig. 16. Importance of the boundary velocity partitioning (Zagros collision model, Francois et al., 2012). The models inspired by Zagros collision settings (Figs. 4–6, 15) test the model sensitivity to the choice of partitioning of convergence velocities between the borders of the model. It is commonly assumed that distribution of velocities between the borders is of no importance in case of non-inertial systems. However, thermal coupling results in appearance of explicit advective terms in the equations describing the thermo-mechanical problem (Appendix A). Hence, the way how the velocities are distributed between the opposite borders of the model becomes highly important, specifically because the ductile properties are exponential function of temperature. As can be seen, applying shortening velocity at one side of the model or at both sides changes the final amount of subduction and slab dip (hence also affecting the amount of slab roll-back and back-arc extension and the timing of slab-break off). These experiments illustrate the importance of exact knowledge of the absolute plate tectonic velocities in nature (absolute plate tectonics versus relative plate tectonics). Color code: blue — mantle, orange — lower crust, yellow — upper crust, red — oceanic crust, grey — initial material of oceanic subduction interface, purple — sediments.

4.6. Summary of the results concerning the role of LP/MP/HP metamorphic phase changes and fluids in subduction processes

Low, middle and high pressure metamorphic facies potentially produce a major impact on the subduction evolution due to their weak rheology that reduces mechanical coupling between the subducting and the overriding plate (Gerya et al., 2008; Angiboust et al., 2012). The role of low or medium grade metamorphism is essential for weakening of the subduction interface by creating or propagating weak shear zones at lithospheric scale. The low-grade facies have very low rheological strength, which allows for lubrication of the subduction interface controlled by the formation of shear zones localizing the deformation. In oceans, serpentinite layer forming at crust–mantle interface and fluid release due to its dehydration at depth play a major role in weakening of the subduction channel allowing for stable subduction (Faccenda et al., 2009a, 2009b).

The major effect of UHP metamorphic changes (eclogitisation) appears to resume in better decoupling between the subducting and the overriding plate and a steeper subduction angle of the continental slab. The experiments suggest that eclogite phase changes do not significantly improve chances for "normal" subduction: when the Moho temperature exceeds 550–600 °C (temperature of onset of UHP metamorphism), subduction is not a dominant mechanism, whatever the degree of eclogite metamorphism is. This statement is valid for common assumption of weak eclogite rheology (about the same as quartz rheology) adopted in most experiments. Any assumptions on the badly constrained eclogite rheology may be questioned while the degree of eclogitization may also vary in a wide range. Additional experiments hint that the assumption of strong eclogite rheology (such as that of dry granulites) would be equivalent, in terms of the mechanical behavior, to additional slab pull, improving the chances for continental subduction (effect equivalent to the assumption of a colder denser plate with Moho temperature of about 150–200 °C lower than in the reference case).

5. Conclusions

The experiments show strong association between the continental subduction and the HP/UHP exhumation processes, so that the presence of HP/UHP material can be regarded as evidence for subduction and may be quantitatively explored for reconstruction of subduction/collision dynamics.

Tectonic collision styles and, in particular, the possibility and duration of subduction, are primary conditioned by convergence rate and thermo-

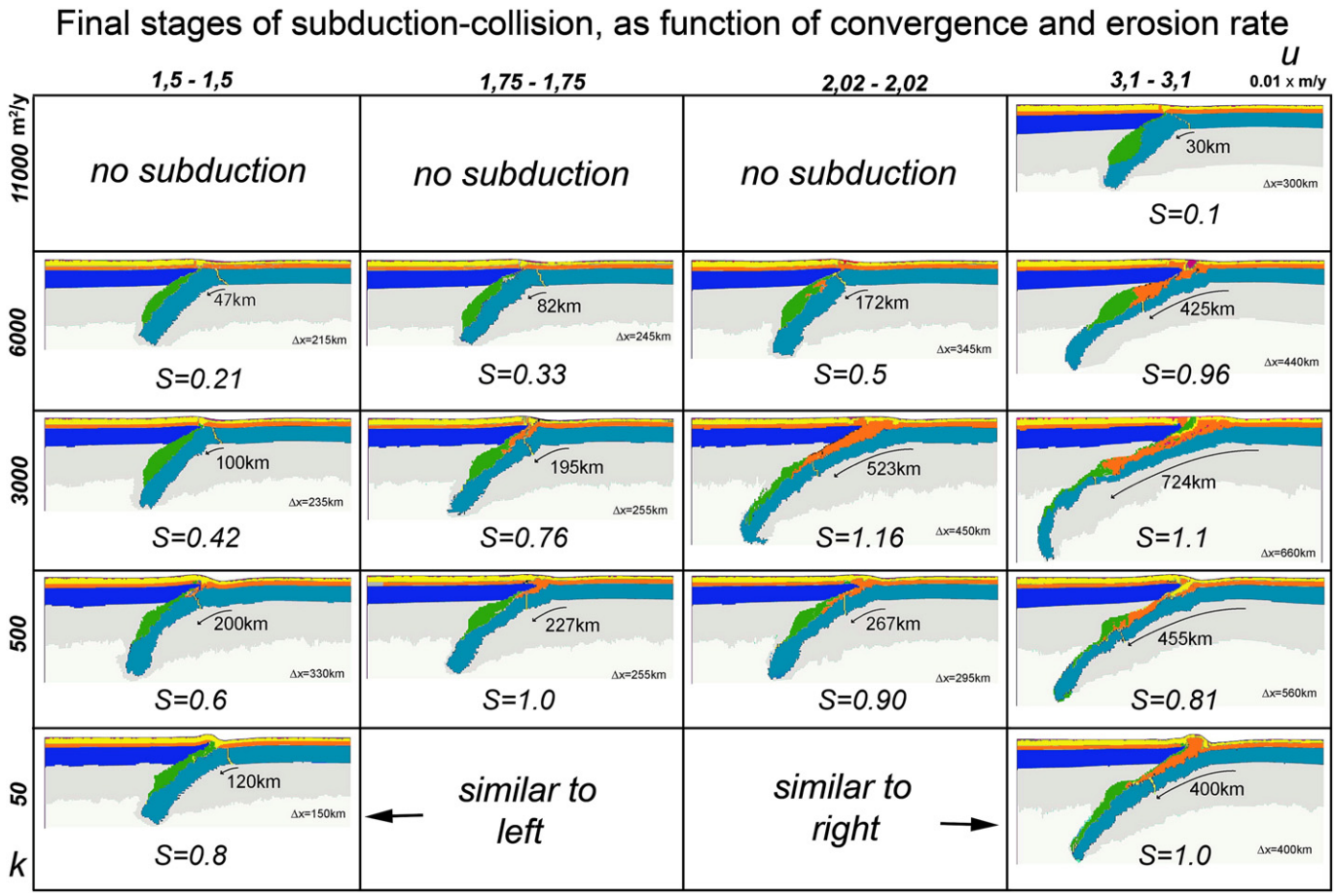

Fig. 17. Interaction between surface erosion rate and tectonic convergence rate in fast collision settings (Burov and Toussaint, 2007), strong lithosphere ("Indian craton" type, the initial rheology profile is equivalent to that used for the experiments of Supplementary Fig. 2). Green color indicates the eclogitized crust produced at the beginning of the experiment but later metamorphic changes are not shown with specific colors. Other colors are explained in caption to Fig. 12. Surface erosion/depositon rate has a major impact on the collision style and amount of subduction, specifically for high convergence rates u (up to 100% variation of the total amount of subduction). Summary of the results of the numerical experiments show the dependence of the "subduction number" S (S = amount of subduction to the total amount of shortening) on the erosion coefficient, k, for different values of the convergence rate (values are given for each side of the model, $k = 50, 100, 500, 1000, 3000, 6000$ and $11000\ m^2\ yr^{-1}$). Note local maximum on the S–k–u for $u > 1.75\ cm\ yr^{-1}$ and $k > 1000\ m^2\ yr^{-1}$. Numbers below the subducting plate correspond to the maximal number of subduction achieved in the corresponding experiment. As can be seen, the amount of subduction strongly depends on the degree of feedback between the tectonic forcing and surface processes, with more than factor of 2 difference between the cases of strong balance between the tectonic input and surface reaction and those characterized by strong misbalance. It can be seen that exhumation of initially buried UHP material is quite rare, as well as the later buried material also returns to the surface only in a few cases.

rheological state of the lithosphere. The experiments (summarized in Figs. 18,19) suggest a wide variety of scenarios for development of collision zones. Sustainable continental subduction and HP-UHP exhumation is possible only in case of relatively strong mantle lithosphere characterized by Moho temperatures below T_m<550–600 °C and relatively fast initial convergence rates (>3 cm yr^{-1}<10 cm yr^{-1}). In this context, only a little portion of UHP material exhumes to the surface, but large UHP volumes can be formed at depth and provide additional pull on the subducting lithosphere. For hotter or slower settings, continental subduction is only a transient process that basically ends soon after the slab break-off. Since the critical values of convergence rates are close to normal oceanic subduction rates, it is reasonable to assume that most continental collision zones might have gone through a continental subduction phase at the initial stages (5–20 Myr) of their evolution. In the case of weak mantle lithospheres (or slower convergence), alternative deformation mechanisms may prevail: (2) lithospheric folding (500 °C<T_m<650 °C); (3) pure-shear thickening (550 °C<T_m<650 °C), and (4) RT instabilities (T_m>650 °C). In some cases, folding may also develop in case of overall strong rheology and fast convergence rate. Both folding and pure shear are unlikely to be associated with HP/UHP exhumation.

It can be overall concluded that the convergence rates and the integrated strength of the lithosphere are interlinked, probably because higher convergence rates require higher slab pull/push forces while such forces can be only exerted on the lithosphere if the latter is strong enough to sustain them. Fig. 19 illustrates this idea by summarizing the results for representative thermo-rheological profiles treated in this study ("Alps", "Zagros", "Indian craton").

The next counter-intuitive finding refers to the demonstrated dependence of the convergence style (slab dip, time of slab break-off, eventually amount of subduction) on the partitioning of the absolute convergence velocities at the borders of the convergent zone. For example, applying total convergence rate at the side of the subducting plate may increase the slab dip by 40° compared to the case where

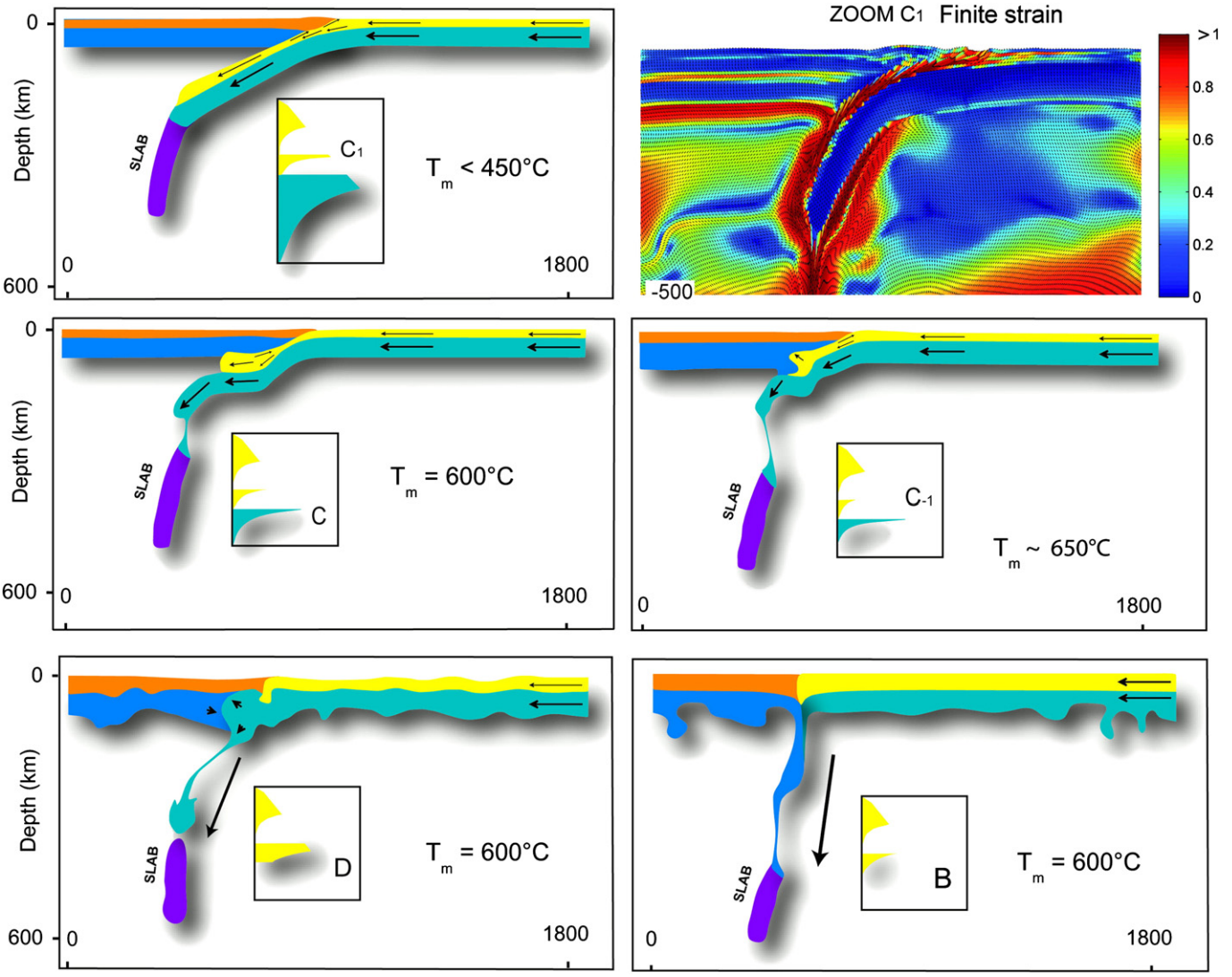

Fig. 18. Summary of continental collision/subduction styles predicted by numerical experiments, as function of rheology profile (Toussaint et al., 2004a, 2004b; Burov and Yamato, 2008). The tested rheology profiles incorporate either weak lower crust (experiments "C"), or strong lower crust ("D" and "B"). Snapshots at 5.5 My, convergence rate 2×3 cm yr^{-1}. Moho temperatures are, respectively, 450 °C, 600 °C, 650 °C (profiles C_1, C, C_{-1}), and 600 °C (profiles D and B). Profiles C correspond to dry olivine mantle, wet quartz-rich upper crust and wet diabase lower crust. Profile D corresponds to the thermo-rheological hypothesis of Mackwell et al. (1998) that combines common wet quartz rheology for the upper crust with strong dry diabase rheology for the lower crust and a weak wet olivine rheology for the mantle. The profile C_1 was used in Toussaint et al. (2004b) to model the initial stages of India-Asia collision (see also Fig. 17). The length of arrows is proportional to material velocity. The insert shows the effective strain distribution for the central part of the "Indian" experiment C_1 superimposed with a 'marker grid' — a grid connecting markers initially placed at the nodes of the starting regular Lagrangian grid. Distortion of the "marker grid" illustrates relative displacement of different units and deformation in the subduction channel.

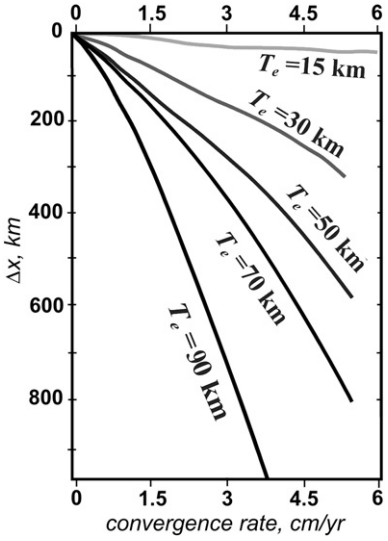

Fig. 19. Graph showing dependence of the amount of subduction (before the slab break-off) on the convergence rate and the integrated strength (T_e) of the lithosphere (according to the results of the experiments shown in Figs. 13–18, and those from Burov and Yamato, 2008; Yamato et al., 2008; Yamato et al., 2009; Sizova et al., 2010).

the convergence rate is imposed on the other side (Fig. 16), with obvious consequences for evolution of the collision and exhumation of deep material. These results emphasize the importance of elucidation of absolute plate tectonic movements.

The role of UHP rocks in collision mechanisms is multifold: their relatively weak rheology (including dehydration melting) enhances lubrication of the subduction interface; their high density also creates an additional pull on the subducting slab. The UHP metamorphism influences deep slab geometry, but does not necessarily promote stable subduction, at least in case of weak eclogite rheologies (It probably does so in case of strong eclogite rheologies). However, by now it is very difficult to quantify the degree of metamorphic changes at depth and hence evaluate their contribution to the force balance at the subduction interface.

The exhumation of HP/UHP material occurs at initial stages of subduction and is favoured in slow convergence settings (<2 cm yr^{-1}). Hence, there is a trade-off between the range of convergence rates favoring subduction, and the range of convergence rates favoring maximal amount of exhumation.

The exhumation of UHP rocks is a poly-phase process driven by different physical mechanisms occurring in the subduction interface zone: (1) the LP and MP rocks are exhumed by the classical accretion prism mechanism and erosion; the final stages (above 40 km depth) of HP/UHP exhumation also take the same path; (2) within the HP/UHP depth interval, the HP and UHP rocks are largely exhumed by buoyancy, within relatively small partly metamorphosed low-density crustal units, slices or malanges, as a result of RT instabilities and small-scale convection and viscous drag in the deep crustal pockets created by separation of the subducting crust from the mantle below 80–120 km depth. The buoyancy is enhanced by heating, and possibly by partial melting.

Deep exhumation is therefore mainly conditioned by viscosity drop and floatability rise due to (1) heat transfer from the asthenosphere below the upper plate; (2) shear heating; (3) viscosity drop due to metamorphic reactions; (4) additional heating due to radioactive heat sources carried down with the sediments and the upper crustal material, (5) dehydration and some case-specific mechanisms (Gerya et al., 2008). The efficiency of the proposed mechanisms depends on the degree of metamorphism, i.e. on the mean density and viscosity of the metamorphic rocks and of their non-metamorphosed environment. Consequently, it largely depends on the presence of fluids that activate metamorphic reactions and weaken both, metamorphic and host rocks. Like for the oceanic lithosphere (e.g. Faccenda et al., 2008; Angiboust et al., 2012), further in-depth developments should thoroughly study fluid exchanges in continental settings. These processes are yet to be understood and quantified.

As suggested by Stöckhert and Gerya (2005), it is also not excluded that mechanisms of deep exhumation can be complemented by diapiric RT instabilities that can bring a part of the material vertically, avoiding the subduction interface zone, resulting in exhumation in the backstop area (for low–middle pressure facies back-stop exhumation can be purely kinematic).

Rheological stratification, i.e. crust–mantle decoupling and upper crust/intermediate crust decoupling (Yamato et al., 2008) allowing for detachment of crustal units are important rheological factors of HP/UHP exhumation.

In specific cases (small volumes of undeformed UHP rock), the rigid crustal block exhumation model (Chemenda et al., 1995) may be also applicable (Sizova et al., 2010) . Even though this model still needs validation on local case study, one can imagine that at least smaller scale nappes-stacking may contribute to UHP exhumation.

In addition, it can be proposed that exhumation of the oceanic UHP rocks occurs during the transition from the oceanic to continental subduction phase, when these dense rocks can be dragged to the surface by positively buoyant delaminated continental crustal units.

Finally, we note that the subduction interface is devoid of significant deviations from lithostatic pressure gradient (Burov et al., 2001a, 2001b; Burov and Yamato, 2008; Li et al., 2010). Small under-pressures may be produced at depths below 40–50 km. The surrounding lithosphere may be both under- and overpressured with pressures reaching up 1.6–2 times lithostatic, but these zones of anomalous pressure do not participate in the exhumation turn-over (Burov and Yamato, 2008). In the particular, Li et al. (2010) show that the main overpressure region that may influence the *P–T* paths of HP-UHP rocks is located in the bottom corner of the wedge-like confined channel with the characteristic magnitude of pressure deviation on the order of<=0.3 GPa and 10–20% from the lithostatic values. Consequently, in most cases, UHP *P–T–t* data can be decoded in terms of exhumation depth using lithostatic pressure assumptions.

The considered models do not account for tectonic heritage. Account for pre-existing structures such as ridges or embedded terrains might be of great importance but would require thorough case-by-case regional studies (Tirel et al., submitted for publication).

Supplementary data to this article can be found online at http://dx.doi.org/10.1016/j.gr.2012.09.010.

Acknowledgements

We thank two anonymous reviewers and the Guest Editor T. Gerya for providing insightful comments on the manuscript. Different parts of the MS have also benefited from discussions with *L.* Le Pourhiet, Ph. Agard and B. Huet. This publication was partly supported by INSU SEDIT program.

Appendix A. Numerical algorithm

A1. Thermo-mechanical module

The mixed finite-element volume/finite difference code FLAMAR (outgrowth of Paravoz by Poliakov et al., 1993) is based on the FLAC algorithm (Cundall, 1989). It solves simultaneously Newtonian dynamic equations of motion (A1), in a Lagrangian formulation, coupled with visco-elasto-plastic constitutive Eq. (A2), heat transport Eq. (A3) and state Eq. (A4) (see Appendix A, (Burov et al., 2001a, 2001b; Le Pourhiet et al., 2004) for details concerning numerical implementation).

$$\rho\frac{Du_i}{Dt}-\frac{\partial\sigma_{ij}}{\partial x_j}=\rho g_i \tag{A1}$$

$$\frac{D\sigma}{Dt} = F(\sigma, \mathbf{u}, \mathbf{v}, \nabla\mathbf{v}, \ldots T \ldots) \quad (A2)$$

$$\rho C_p(\partial T/\partial t + u\nabla T) - \nabla(k\nabla T) - H_r - \text{frac} \times \sigma_{II}\partial\varepsilon_{II}/\partial t = 0 \quad (A3)$$

$$\rho = f(P, T) \quad (A4)$$

Here u, σ, *g*, *k* are the respective terms for velocity, stress, acceleration due to body forces and thermal conductivity. The terms *t*, ρ, C_p, *T*, H_r, α, frac× $\sigma_{II}\partial\varepsilon_{II}/\partial t$ designate respectively time, density, specific heat, temperature, internal heat production, thermal expansion coefficient and shear heating term moderated by experimentally defined *frac* multiplier (*frac* is set to 0.1 in most experiments). The terms $\partial/\partial t$, $D\sigma/Dt$, *F* are a time derivative, an objective (Jaumann) stress time derivative and a functional, respectively. In the Lagrangian framework, the incremental displacements are added to the grid coordinates allowing the mesh to move and deform with the material. This enables solution of large-strain problems locally using small-strain formulation: on each time step the solution is obtained in local coordinates, which are then updated in the large strain mode. Volume / density changes due to phase transitions are accounted via application of equivalent stresses to affected material elements.

Solution of (A1) provides velocities at mesh points used for computation of element strains and of heat advection $\mathbf{u}\nabla T$. These strains are used in (A2) to calculate element stresses, and the equivalent forces are used to compute velocities for the next time step.

All rheological terms are implemented explicitly. The rheology model is serial viscous-elastic-plastic (Tables 1, 2). The plastic term is given by explicit Mohr-Coulomb plasticity (non-associative with zero dilatency) assuming linear Navier-Coulomb criterion. We imply internal friction angle ϕ of 30° and maximal cohesion *S* of 20 Mpa, which fit best the experimental Byerlee's law of rock failure (Byerlee, 1978):

$$\tau = S + \sigma_n \text{tg}\phi \quad (A5)$$

where τ is the shear stress and σ_n is the normal stress. Linear cohesion softening is used for better localization of plastic deformation ε_p ($S(\varepsilon_p) = S_0$ min (0, $1 - \varepsilon_p/\varepsilon_{p0}$) where ε_{p0} is 0.01). Specific properties are applied to soft serpentinised rock (Hassani et al., 1997).

The ductile-viscous term is represented by non-linear power law with three sets of material parameters (Tables 1, 2) that correspond to the properties of four lithological layers: upper crust (quartz), middle-lower crust (quartz-diorite), mantle and asthenosphere (olivine):

$$\eta_{\text{eff}} = \left(\frac{\partial\varepsilon}{\partial t}\right)_{II}^{d(1-n)/n} (A^*)^{-1/n} \exp(H/nRT) \quad (A6)$$

where $\left(\frac{\partial\varepsilon}{\partial t}\right)_{II}^{d} = \left(Inv_{II}\left(\left(\frac{\partial\varepsilon}{\partial t}\right)_{II}^{d}\right)\right)^{1/2}$ is the effective strain rate and $A^* = \frac{1}{2}A \cdot 3^{(n+1)/2}$ is the material constant, *H* is the activation enthalpy, $H = Q + PV$ where *Q* is activation energy and *V* is molar volume, *R* is the gas constant, *n* is the power law exponent (Table 2). The elastic parameters (Tables 1, 2) correspond to commonly inferred values from Turcotte and Schubert (2002).

The surface processes are taken into account by diffusing (A7) the topographic elevation *h* of the free surface along *x* using conventional Culling erosion model (Culling, 1960) with a diffusion coefficient k_{ero}.

$$\frac{\partial^2 h}{\partial t^2} = k_{ero}\frac{\partial^2 h}{\partial x^2} \quad (A7)$$

This simple model is well suited to simulate fan deltas, which can be taken as a reasonably good analogue of typical foreland basin deposits. This model is not well adapted to model slope dependent long-range sedimentation, yet, it accounts for some most important properties of surface processes such as dependency of the erosion/sedimentation rate on the roughness of the relief (surface curvature).

The fluid transport algorithm is based on an enhanced variant of Darcy's flow approximation with strain-rate dependent permeability (Angiboust et al., 2012). In this algorithm it is assumed that the fluid flux q_f is driven by fluid pressure gradient through a medium with dynamic permeability *K*, as follows:

$$q_f = -K\nabla P_{fl}^* \quad (A8)$$

where fluid pressure P^*_{fl} is related to the non-lithostatic pressure δ*P* through a fluid "saturation factor" $[H_2O]/[H_2O]_{sat}$ as follows:

$$P_{fl}^* = \delta P \frac{[H_2O]}{[H_2O]_{sat}}, \quad (A9)$$

where $[H_2O]$ is the current water content (in wt.%) in the material for each element of the numerical grid and $[H_2O]_{sat}$ is the maximum water content thermodynamically calculated for the same material as a function of *P*–*T* conditions. The dynamic permeability *K* is defined as a function of the intrinsic permeability, strain rate and inversed viscosity of the fluid (Angiboust et al., 2012).

FLAMAR allows for large displacements and strains in particular owing to an automatic remeshing procedure, which is implemented each time the mesh becomes too destorted to produce accurate results. The remeshing criterion is imposed by a critical angle of grid elements. This angle is set to 10° to reduce frequency of remeshing and thus limit the associated numerical diffusion. The numerical diffusion was effectively constrained by implementation of the passive marker algorithm. This algorithm traces passively moving particles that are evenly distributed in the initial grid. This allows for accurate recovering of stress, phase and other parameter fields after each remeshing. FLAMAR has been already tested on a number of geodynamical problems for subduction/collision context (Burov et al., 2001a, 2001b; Toussaint et al., 2004a, 2004b).

A.2. Thermodynamic coupling

Buoyancy (and, eventually, rheology changes) is an important component of the force balance at subduction zone (Bousquet et al., 1997; Burov et al., 2001a, 2001b; Doin and Henry, 2001). For this reason, the thermodynamic THERIAK (de Capitani, 1994) and PERPLE_X (Connolly, 2005) algorithms have been incorporated to introduce progressive density changes during evolution. Both algorithms (THERIAK is used for sedimentary rocks, PERPLE_X - for the rest) minimize free Gibbs energy for a given chemical composition to calculate an equilibrium mineralogical assemblage for given *P*–*T* conditions (de Capitani and Brown, 1987).

$$G = \sum_{i=1}^{n} \mu_i N_i \quad (A8)$$

where μ_i is the chemical potential and N_i the moles number for each component *i* constitutive of the assemblage. Given the mineralogical composition, the computation of the density is then straightforward.

Mineralogical composition and hence density, is re-evaluated every 10^4 time steps (~200 kyr) according to the current *P*–*T* conditions. Equivalent stresses are applied to the elements to account for volume-density changes associated with the metamorphic transitions.

Unfortunately, changes in rheological properties of the metamorphic facies cannot be implemented in the same way as the density changes, due to the lack of the appropriate experimental data. We took into account rheology changes only for key facies such as serpentinite and eclogite.

A.3. Initial thermal structure

To compute the initial continental geotherm T_{cont}, one can use the Eq. (A9) taking into account, in T_{std}, the stationary part of the

geotherm and contribution due to the radiogenic heat production H_s in the crust, and correction $T(age)$ due to transient cooling of the lithpshere that depends on its age.

$$T_{cont}(z, age, H_s) = T_{std}(z, H_s) + T(age) \quad \text{(A9)}$$

Radiogenic contribution T_r in the crust depends of the thickness of the crust h_c, density ρ_c, radiogenic production H_s, radiogenic production decay depth h_r, and thermal conductivity coefficient k_c (A10):

$$T_r = \frac{\rho_c \cdot H_s \cdot h_r^2}{k_c} \cdot \left(1 - \exp^{-\frac{h_c}{h_r}}\right) \quad \text{(A10)}$$

Temperature T_m at Moho depth, h_c , is used for the calculation of the temperature for depths below the Moho and is given by :

$$T_m = T_0 + \frac{q_m}{k_c} \cdot h_c + T_r \quad \text{(A11)}$$

where T_0 and q_m correspond, respectively, to the temperature at the surface and the heat flux calculated at the Moho. This heat flux is given by:

$$q_m = \frac{T_{hl} - T_0 - T_r}{\frac{h_c}{k_c} + \frac{h_l - h_c}{k_m}} \quad \text{(A12)}$$

where T_{hl} is temperature at the thermal base of lithosphere (of a thickness h_l) and k_m is coefficient of thermal conductivity for the mantle.

Temperature at a depth z can thus be calculated as:

$$-If\ z \le h_c: \qquad T_{std}(z) = T_0 + \frac{q_m}{k_c} \cdot z + T_r \quad \text{(A13)}$$

$$-If\ z > h_c: \qquad T_{std}(z) = T_m + q_m \cdot \frac{(z - h_c)}{k_m} \quad \text{(A14)}$$

This obtained temperature is then corrected fot transient cooling that depends on thermotectonic age (age) of the lithosphere using formulation from Parsons and Sclater (1977) adapted for the continental lithosphere.

$$T(\text{age}) = \frac{2}{\pi} \cdot \left(T_{h_l} - T_0\right) \cdot TT(\text{age}) \quad \text{(A15)}$$

where

$$TT(\text{age}) = \sum_{n=1}^{\infty} \frac{(-1)^{n+1}}{n} \cdot \exp\left(\frac{-k_m \cdot \pi^2 \cdot \text{age} \cdot n^2}{\rho_m \cdot C_m \cdot h_l^2}\right) \cdot \sin\left(\frac{n \cdot \pi \cdot z}{h_l}\right) \quad \text{(A16)}$$

with C_m and ρ_m are respectively the specific heat capacity and the density for the mantle. Values for the parameters used for the initial geotherm are given in Tables 1, 2.

References

Afonso, J.C., Zlotnik, S., 2011. The subductability of continental lithosphere: the before and after story, arc-continent collision. Frontiers in Earth Sciences 53–86 http://dx.doi.org/10.1007/978-3-540-88558-0_3 (Part 1).

Agard, P., Jolivet, L., Goffé, B., 2001. Tectonometamorphic evolution of the Schistes Lustrés complex: implications for the exhumation of HP and UHP rocks in the Western Alps. Bulletin de la Societe Geologique de France 172 (5), 617–636.

Agard, P., Yamato, P., Jolivet, L., Burov, E., 2009. Exhumation of oceanic blueschists and eclogites in subduction zones: timing and mechanisms. Earth Sciences Reviews 92, 53–79.

Angiboust, S., Wolf, S., Burov, E., Agard, P., Yamato, P., 2012. Fluid circulation at the subduction interface: insights from thermo-mechanical numerical modelling. Earth and Planetary Science Letters 358, 238–248.

Austrheim, H., 1991. Eclogite formation and the dynamics of crustal roots under continental collision zones. Terra Nova 3, 492–499.

Avouac, J.P., 2003. Mountain building, erosion and the seismic cycle in the Nepal Himalaya. Advances in Geophysics 46, 1–80.

Avouac, J.P., Burov, E.B., 1996. Erosion as a driving mechanism of intracontinental mountain growth. Journal of Geophysical Research-Solid Earth 101 (B8), 17747–17769.

Beaumont, C., Kamp, P.J.J., Hamilton, J., Fullsack, P., 1996. The continental collision zone, South Island, New Zealand: comparison of geodynamical models and observations. Journal of Geophysical Research 101, 3333–3359.

Beaumont, C., Muñoz, J.A., Hamilton, J., Fullsack, P., 2000. Factors controlling the Alpine evolution of the central Pyrenees inferred from a comparison of observations and geodynamical models. Journal of Geophysical Research 105 (B4), 8121–8146.

Beaumont, C., Jamieson, R.A., Butler, J.P., Warren, C.J., 2009. Crustal structure: a key constraint on the mechanisms of ultra-high-pressure rock exhumation. Earth and Planetary Science Letters 287, 116–129.

Bousquet, R., Goffe, B., Henry, P., Le Pichon, X., Chopin, C., 1997. Kinematic, thermal and petrological model of the central Alps: lepontine metamorphism in the upper crust and eclogitisation of the lower crust. Tectonophysics 273, 105–127.

Burg, J.-P., Gerya, T.V., 2005. Viscous heating and thermal doming in orogenic metamorphism: numerical modeling and geological implications. Journal of Metamorphic Geology 23, 75–95.

Burg, J.-P., Podladchikov, Y., 2000. From buckling to asymmetric folding of the continental lithosphere: numerical modelling and application to the Himalayan syntaxes. In: Khan, M.A., et al. (Ed.), Tectonics of the Nanga Parbat syntaxis and the western Himalaya: Geological Society of London Special Publication, 170, pp. 219–236.

Bürgmann, R., Dresen, G., 2008. Rheology of the lower crust and upper mantle: evidence from rock mechanics, geodesy, and field observations. Annual Review of Earth and Planetary Sciences 36, 531–567 http://dx.doi.org/10.1146/annurev.earth.36.031207.124326.

Burov, E., 2010a. The equivalent elastic thickness (Te), seismicity and the long-term rheology of continental lithosphere: time to burn-out "crème brûlée"?: Insights from large-scale geodynamic modeling. Tectonophysics http://dx.doi.org/10.1016/j.tecto.2009.06.013.

Burov, E., 2010b. Thermo-Mechanical Models for Coupled Lithosphere-Surface Processes: Applications to Continental Convergence and Mountain Building Processes. In: Cloetingh, S., Negendank, J. (Eds.), New Frontiers in Integrated Solid Earth Sciences, International Year of Planet Earth. Springer Science + Business Media, pp. 103–143 http://dx.doi.org/10.1007/978-90-481-2737-5_4.

Burov, E., 2011. Rheology and strength of the lithosphere. Marine and Petroleum Geology 28–8, 1402–1443 http://dx.doi.org/10.1016/j.marpetgeo.2011.05.008.

Burov, E.B., Diament, M., 1992. Flexure of the continental lithosphere with multilayered rheology. Geophysical Journal International 109, 449–468.

Burov, E.B., Diament, M., 1995a. Effective elastic thickness of the continental lithosphere — what does it really mean? Journal of Geophysical Research 100, 3905–3927.

Burov, E.B., Diament, M., 1995b. The effective elastic thickness (Te) of continental lithosphere: what does it really mean? Journal of Geophysical Research 100, 3895–3904.

Burov, E., Toussaint, G., 2007. Surface processes and tectonics: forcing of continental subduction and deep processes. Global and Planetary Change, Special volume on Topography of Europe 58, 141–164.

Burov, E., Watts, A.B., 2006. The long-term strength of continental lithosphere: "jelly-sandwich" or "crème-brûlé"? GSA Today 16, 4–10.

Burov, E., Yamato, Ph, 2008. Continental plate collision, P–T–t–z conditions and unstable vs. stable plate dynamics: insights from thermo-mechanical modelling. Lithos 103, 178–204.

Burov, E.B., Kogan, M.G., Lyon-Caen, H., Molnar, P., 1990. Gravity anomalies, the deep structure, and dynamic processes beneath the Tien Shan. Earth and Planetary Science Letters 96, 367–383.

Burov, E.B., Podladchikov, Y., Grandjean, G., Burg, J.-P., 1999. Validation of multidisciplinary data using thermo-mechanical modelling: application to the Western and Nothern Alps. Terra Nova 11, 124–131.

Burov, E.B., Jolivet, L., Le Pourhiet, L., Poliakov, A., 2001a. A thermemechanical model of exhumation of HP and UHP methamorphic rocks in Alpine mountain belts. Tectonophysics 342, 113–136.

Burov, E., Jolivet, L., Le Pourhiet, L., Poliakov, A., 2001b. A thermomechanical model of exhumation of high pressure (HP) and ultrahigh pressure (UHP) metamorphic rocks in Alpine-type collision belts. Tectonophysics 342, 113–136.

Byerlee, J.D., 1978. Friction of rocks. Pure and Applied Geophysics 116, 615–629.

Chemenda, A.L., Mattauer, M., Malavieille, J., Bokun, A.N., 1995. A mechanism for syn-collisional deep rock exhumation and associated normal faulting: results from physical modelling. Earth and Planetary Science Letters 132, 225–232.

Chen, Y., Cogne, J.-P., Courtillot, V., Tapponnier, P., Zhou, X.Y., 1993. Cretaceous paleomagnetic results from western Tibet and tectonic implications. Journal of Geophysical Research 98, 17981–18000.

Chopin, C., 1984. Coesite and pure pyrope in high-grade blueschists of the western Alps: a first record and some consequences. Contributions to Mineralogy and Petrology 96, 253–274.

Chopra, P.N., Paterson, M.S., 1981. The experimental deformation of dunite. Tectonophysics 78, 453–473.

Cloetingh, S., Burov, E., 1996. Thermomechanical structure of European continental lithosphere: constraints from rheological profiles and EET estimates. Geophysical Journal International 124, 695–723.

Cloetingh, S.A.P.L., Wortel, M.J.R., Vlaar, N.J., 1982. Evolution of passive continental margins and initiation of subduction zones. Nature 297, 139–142.

Cloetingh, S., Burov, E., Poliakov, A., 1999. Lithosphere folding: primary response to compression? (from central Asia to Paris Basin). Tectonics 18, 1064–1083.

Cloetingh, S.A.P.L., Burov, E., Matenco, L., Toussaint, G., Bertotti, G., Andriessen, P.A.M., Wortel, W.J.R., Spakman, W., 2004. Thermomechanical controls on the model of continental collision in the SE Carpathians (Romania). Earth and Planetary Sciences Letters 218, 57–76.

Cloos, M., 1993. Lithospheric buoyancy and collisional orogenesis: subduction of oceanic plateaus, continental margins, island arcs, spreading ridges and seamounts. Geological Society of America Bulletin 105, 715–737.
Coleman, R.G., 1971. Plate tectonic emplacement of upper mantle peridotites along continental edges. Journal of Geophysical Research 76, 1212–1222.
Connolly, J.A.D., 2005. Computation of phase equilibria by linear programming: a tool for geodynamic modeling and its application to subduction zone decarbonation. Earth and Planetary Sciences Letters 236, 524–541.
Culling, W.E.H., 1960. Analytical theory of erosion. Journal of Geology 68, 333–336.
Cundall, P.A., 1989. Numerical experiments on localization in frictional material. Ingenieur-Archiv 59, 148–159.
Dahlen, F.A., 1990. Critical taper model of fold-and-thrust belts and accretionary wedges. Annual Review of Earth and Planetary Science 18, 55–99.
Dahlen, F.A., Suppe, J., 1988. Mechanics, growth and erosion of mountain belts. Geological Society of America, Special Paper 218, 161–178.
Davies, J.H., 1999. Simple analytic model for subduction zone thermal structure. Geophysical Journal International 139, 823–828.
Davis, D.M., Suppe, J., Dahlen, F.A., 1983. Mechanics of fold-and-thrust belts and accretionary wedges. Journal of Geophysical Research 88 (B2), 1153–1172.
De Capitani, C., 1994. Gleichgewichts-Phasendiagramme: Theorie und Software. Beihefte zum European Journal of Mineralogy-Jahrestagung der Deutschen Mineralogischen Gesellschaft 48.
de Capitani, C., Brown, T.H., 1987. The computation of chemical equilibrium in complex systems containing non-ideal solutions. Geochimica et Cosmochimica Acta 51, 2639–2652.
Diez Fernández, R., Martínez Catalán, J.R., Arenas, R., Abati, J., 2012. The onset of the assembly of Pangaea in NW Iberia: constraints on the kinematics of continental subduction. Gondwana Research 22, 20–25.
Doin, M.-P., Henry, P., 2001. Subduction initiation and continental crust recycling: the roles of rheology and eclogitization. Tectonophysics 342, 163–191.
Duretz, T., Gerya, T.V., May, D.A., 2011. Numerical modelling of spontaneous slab breakoff and subsequent topographic response. Tectonophysics 502, 244–256.
Emerman, S.H., Turcotte, D.L., 1983. A fluid model for the shape of accretionary wedges. Earth and Planetary Science Letters 63, 379–384.
Ernst, W.G., 1973. Blueschist metamorphism and P–T regimes in active subduction zones. Tectonophysics 17, 255–272.
Ernst, W.G., 2010. Subduction-zone metamorphism, calc-alkaline magmatism, convergent-margin crustal evolution. Gondwana Research 18, 8–16.
Faccenda, M., Gerya, T.V., Chakraborty, S., 2008. Styles of post-subduction collisional orogeny: influence of convergence velocity, crustal rheology and radiogenic heat production. Lithos 103, 257–287.
Faccenda, M., Gerya, T.V., Burlini, L., 2009a. Deep slab hydration induced by bending related variations in tectonic pressure. Nature Geoscience 2, 790–793.
Faccenda, M., Minelli, G., Gerya, T.V., 2009b. Coupled and decoupled regimes of continental collision: numerical modeling. Earth and Planetary Science Letters 278, 337–349.
Ford, M., Duchêne, S., Gasquet, D., Vanderhaeghe, O., 2006. Two-phase orogenic convergence in the external and internal SW Alps. Journal of the Geological Society of London 163, 1–12.
Francois, T., Burov, E., Agard, P., Meyer, B., 2012. Evaluating the effect of rheology on the evolution of continental collision: application to the Zagros orogen. Geophysical Research Abstracts 14 (EGU2012-10283, 2012, EGU General Assembly).
Francois, T., Burov, E., Meyer, B., Agard, P., in press. Surface topography as key constraint on thermo-rheological structure of stable cratons. Tectonophysics, http://dx.doi.org/10.1016/j.tecto.2012.10.009.
Gerya, T.V., Stoeckhert, B., 2005. 2-D numerical modeling of tectonic and metamorphic histories at active continental margins. International Journal of Earth Sciences http://dx.doi.org/10.1007/s00531-005-0035-9.
Gerya, T.V., Yuen, D.A., 2003. Rayleigh–Taylor instabilities from hydration and melting propel "cold plumes" at subduction zones. Earth and Planet Sciences Letters 212, 47–62.
Gerya, T.V., Stöckhert, B., Perchuk, A.L., 2002a. Exhumation of high-pressure metamorphic rocks in a subduction channel: a numerical simulation. Tectonics 26 (6), 1–15.
Gerya, T.V., Stöckert, B., Perchuck, A.L., 2002b. Exhumation of high pressure metamorphic minerals in subduction channels: a numerical simulations. Tectonics 21, 1056 http://dx.doi.org/10.1029/2002TC001406.
Gerya, T.V., Perchuk, L.L., Burg, J.-P., 2008. Transient hot channels: perpetrating and regurgitating ultrahigh-pressure, high temperature crust–mantle associations in collision belts. Lithos 103, 236–256.
Gleason, G.C., Tullis, J., 1995. A flow law for dislocation creep of quartz aggregates determined with the molten salt cell. Tectonophysics 247, 1–23.
Goetze, C., Evans, B., 1979. Stress and temperature in the bending lithosphere as constrained by experimental rock mechanics. Geophysical Journal of Royal Astronomy Society 59, 463–478.
Gorczyk, W., Gerya, T.V., Connolly, J.A.D., Yuen, D.A., Rudolph, M., 2006. Large-scale rigid-body rotation in the mantle wedge and its implications for seismic tomography. Geochemistry, Geophysics, Geosystems 7 http://dx.doi.org/10.1029/2005GC001075.
Gray, R., Pysklywec, R.N., 2010. Geodynamic models of Archean continental collision and the formation of mantle lithosphere keels. Geophysical Research Letters 37, L19301 http://dx.doi.org/10.1029/2010GL043965.
Gray, R., Pysklywec, R.N., 2012. Geodynamic models of mature continental collision: evolution of an orogen from lithospheric subduction to continental retreat/delamination. Journal of Geophysical Research http://dx.doi.org/10.1029/2011JB008692.
Guillot, S., Hattori, K., de Sigoyer, J., 2000. Mantle wedge serpentinization and exhumation of eclogites: insights from eastern Ladakh, northwest Himalaya. Geology 28, 199–202.
Guillot, S., Hattori, K., Sigoyer de, J., Nägler, T., Auzende, A.L., 2001. Evidence of hydration of the mantle wedge and its role in the exhumation of eclogites. Earth Planetary Sciences Letters 193, 115–127.
Guillot, S., Hattori, K., Agard, P., Schwartz, S., Vidal, O., 2009. Exhumation processes in oceanic and continental subduction contexts: a review. In: Lallemand, S., Funiciello, F. (Eds.), Subduction Zone Dynamics. Springer-Verlag Berlin Heidelberg, pp. 175–204 http://dx.doi.org/10.1007/978-3-540-87974-9.
Hacker, B.R., Andersen, T.B., Johnston, S., Kylander-Clark, A.R.C., Peterman, E.M., Walsh, E.O., Young, D., 2010. High-temperature deformation during continental-margin subduction & exhumation: the ultrahigh-pressure Western Gneiss Region of Norway. Tectonophysics 480 (1–4), 149–171.
Handy, M.R., Schmid, S.M., Bousquet, R., Kissling, E., Bernoulli, D., 2010. Reconciling plate-tectonic reconstructions of Alpine Tethys with the geological–geophysical record of spreading and subduction in the Alps. Earth-Science Reviews 102, 121–158.
Hassani, R., Jongmans, D., Chery, J., 1997. Study of plate deformation and stress in subduction processes using two-dimensional numerical models. Journal of Geophysical Research 102 (B8), 17951–17965.
Hatzfeld, D., Molnar, P., 2010. Comparisons of the kinematics and deep structures of the Zagros and Himalaya and of the Iranian and Tibetan plateaus and geodynamic implications. Reviews of Geophysics 48, RG2005 http://dx.doi.org/10.1029/2009RG000304 (48 pp.).
Hirth, G., Kohlstedt, D.L., 1996. Water in the oceanic upper mantle: implications for rheology, melt extraction and the evolution of the lithosphere. Earth and Planetary Sciences Letters 144, 93–108.
Houseman, C.A., Molnar, P., 1997. Gravitational (Rayleigh–Taylor) instability of a layer with nonlinear viscosity and convergence thinning of continental lithosphere. Geophysical Journal International 128, 125–150.
Jolivet, L., Daniel, J.M., Truffert, C., Goffé, B., 1994. Exhumation of deep crustal metamorphic rocks and crustal extension in back-arc regions. Lithos 33, 3–30.
Jolivet, L., Raimbourg, H., Labrousse, L., Avigad, D., Leroy, Y., Austrheim, H., Andersen, T.B., 2005. Softening trigerred by eclogitization, the first step toward exhumation during continental subduction. Earth Planetary Sciences Letters 237, 532–547.
Kirby, S.H., Durham, W., Stern, L., 1991. Mantle phase changes and deep-earthquake faulting in subducting lithosphere. Science 252, 216–225.
Lanari, P., Guillot, S., Schwartz, S., Vidal, O., Tricart, P., Riel, N., Beyssac, O., 2012. Diachronous evolution of the alpine continental subduction wedge: evidence from P–T estimates in the Briançonnais Zone houillère (France–Western Alps). Journal of Geodymics http://dx.doi.org/10.1016/j.jog.2011.09.006.
Lavier, L., Steckler, M., 1997. The effect of sedimentary cover on the flexural strength of continental lithosphere. Nature 389, 476–479.
Le Pichon, X., Fournier, M., Jolivet, L., 1992. Kinematics, topography, shortening and extrusion in the India–Eurasia collision. Tectonics 11, 1085–1098.
Le Pourhiet, L., Burov, E., Moretti, I., 2004. Rifting through a stack of inhomogeneous thrusts (the dipping pie concept). Tectonics 23 (4), TC4005 http://dx.doi.org/10.1029/2003TC001584.
Li, Z., Gerya, T.V., 2009. Polyphase formation and exhumation of HP-UHP rocks in continental subduction zone: numerical modeling and application to the Sulu UHP terrane in eastern China. Journal of Geophysical Research 114, B09406 (Article Number).
Li, Sanzhong, Kusk Timothy, M., Xiaochun, Liu, et al., 2009. Two-stage collision-related extrusion of the western Dabie HP-UHP metamorphic terranes, central China: evidence from quartz c-axis fabrics and structures. Gondwana Research 16, 294–309.
Li, Z.H., Gerya, T.V., Burg, J.-P., 2010. Influence of tectonic overpressure on P–T paths of HP–UHP rocks in continental collision zones: thermomechanical modeling. Journal of Metamorphic Geology 28 (3), 227–247.
Li, Z.H., Xu, Z.Q., Gerya, T.V., 2011. Flat versus steep subduction: contrasting modes for the formation and exhumation of high- to ultrahigh-pressure rocks in continental collision zones. Earth and Planetary Science Letters 301, 65–77.
Mackwell, S.J., Zimmerman, M.E., Kohlstedt, D.L., 1998. High-temperature deformation of dry diabase with applications to tectonics on Venus. Journal of Geophysical Research 103, 975–984.
Mouthereau, F., Watts, A.B., Burov, E., 2012. Linkage between crustal shortening in collisional orogens and the long-term strength of the continental lithosphere. Geophysical Research Abstracts 14, 11832 (EGU General Assembly 2012).
Mancktelow, N., 1995. Nonlithostatic pressure during sediment subduction and the development and exhumation of high pressure metamorphic rocks. Journal of Geophysical Research 100, 571–583.
Maruyama, S., Masago, H., Katayama, I., Iwase, Y., Toriumi, M., Omori, S., et al., 2010. A new perspective on metamorphism and metamorphic belts. Gondwana Research 18, 106–137.
Parsons, B.E., Sclater, J.G., 1977. An analysis of the variation of ocean floor bathymetry and heat flow with age. Journal of Geophysical Research 82, 803–827.
Patriat, P., Achache, J., 1984. India–Eurasia collision chronology has implications for crustal shortening and driving mechanism of plates. Nature 311, 615–621.
Patzelt, A., Li, H., Wang, J., Appel, E., 1996. Palaeomagnetism of Cretaceous to Tertiary sediments from southern Tibet: evidence for the extent of the northern margin of India prior to the collision with Eurasia. Tectonophysics 259, 259–284.
Pérez-Gussinyé, M., Watts, A.B., 2005. The long-term strength of Europe and its implications for plate-forming processes. Nature 436 http://dx.doi.org/10.1038/nature03854.
Petrini, K., Podladchikov, Yu., 2000. Lithospheric pressure–depth relationship in compressive regions of thickened crust. Journal of Metamorphic Geology 18, 67–78.
Platt, J.P., 1986. Dynamics of orogenic wedges and the uplift of high-pressure metamorphic rocks. Geological Society of America Bulletin 97, 1037–1053.
Platt, J.P., 1993. Exhumation of high-pressure rocks: a review of concept and processes. Terra Nova 5, 119–133.

Poliakov, A.N.B., Podladchikov, Yu., Talbot, C., 1993. Initiation of salt diapirs with frictional overburden: numerical experiments. Tectonophysics 228, 199–210.
Ponziani, F., De Franco, R., Minelli, G., Biella, G., Federico, C., Pialli, G., 1995. Crustal shortening and duplication of the Moho in the Northern Apennines: a view from seismic refraction data. Tectonophysics 252, 391–418.
Pysklywec, R.N., 2006. Surface erosion control on the evolution of the deep lithosphere. Geology 269 (34(4)), 225–228.
Pysklywec, R., Beaumont, C., Fullsack, P., 2000. Modeling the behavior of the continental mantle lithosphere during plate convergence. Geology 28, 655–658.
Pysklywec, R.N., Beaumont, C., Fullsack, P., 2002. Lithospheric deformation during the early stages of continental collision: numerical experiments and comparison with South Island, New Zealand. Journal of Geophysical Research 107 (B7) http://dx.doi.org/10.1029/2001JB000252.
Raimbourg, H., Jolivet, L., Leroy, Y., 2007. Consequences of progressive eclogitization on crustal exhumation, a mechanical study. Geophysical Journal International 168, 379–401.
Ranalli, G., 1995. Rheology of the Earth, 2nd ed. Chapman and Hall, London . (413 pp.).
Ring, U., Will, T., Glodny, J., Kumerics, C., Gessner, K., Thomson, S., Gungor, T., Monie, P., Okrusch, M., Druppel, K., 2007. Early exhumation of high-pressure rocks in extrusion wedges: cycladic blueschist unit in the eastern Aegean, Greece, and Turkey. Tectonics 26 (2), TC2001 http://dx.doi.org/10.1029/2005tc001872.
Royden, L.H., 1993. The steady state thermal structure of eroding orogenic belts and accretionary prisms. Journal of Geophysical Research 98 (B3), 4487–4507.
Shigenori, Maruyama, Masago, H., Katayama, I., et al., 2010. A new perspective on metamorphism and metamorphic belts. Gondwana Research 18, 106–137.
Sizova, E., Gerya, T., Brown, M., Perchuk, L.L., 2010. Subduction styles in the precambrian: insight from numerical experiments. Lithos 116, 209–229.
Sobouti, F., Arkani-Hamed, J., 2002. Thermo-mechanical modeling of subduction of continental lithosphere. Physics of the Earth and Planetary Interiors 131, 185–203.
Spear, F.S., 1993. Metamorphic phase equilibria and pressure–temperature–time paths. Mineralogical Society of America (800 pp.).
Stöckhert, B., Gerya, T.V., 2005. Pre-collisional high pressure metamorphism and nappe tectonics at active continental margins: a numerical simulation. Terra Nova 17 (2), 102–110.
Tetsuzo, S., Rehman, H.U., 2011. When and why the continental crust is subducted: examples of Hindu Kush and Burma. Gondwana Research 19, 327–333.
Teyssier, C., Whitney, D.L., Toraman, E., Seaton, N.C.A., 2010. Lawsonite vorticity and subduction kinematics. Geology 38 (12), 1123–1126.
Thompson, A.B., Jezek, J., Schulmann, K., 1997. Extrusion tectonics and rapid elevation of lower crustal metamorphic rocks in convergent orogens. Geology 25, 491–494.
Tirel, C., Brun, J.-P., Burov, E., Wortel, M.J.R., Lebedev, S., submitted for publication. A plate tectonics oddity: caterpillar-walk exhumation of subducted continental crust. Geology.
Toussaint, G., Burov, E., Jolivet, L., 2004a. Continental plate collision: unstable versus stable slab dynamics. Geology 32 (1), 33–36.
Toussaint, G., Burov, E., Avouac, J.-P., 2004b. Tectonic evolution of a continental collision zone: a thermo mechanical numerical model. Tectonics 23.
Turcotte, D.L., Schubert, G., 2002. Geodynamics, Second edition. Cambridge University Press, Cambridge . (456 pp.).
Warren, C.J., Beaumont, C., Jamieson, R.A., 2008a. Modelling tectonic styles and ultra-high pressure (UHP) rock exhumation during the transition from oceanic subduction to continental collision. Earth and Planetary Science Letters 267 (1–2), 129–145.
Warren, C.J., Beaumont, C., Jamieson, R.A., 2008b. Formation and exhumation of ultra-high-pressure rocks during continental collision: role of detachment in the subduction channel. Geochemistry, Geophysics, Geosystems 9 (4) http://dx.doi.org/10.1029/2007GC001839.
Watts, A.B., 2001. Isostasy and Flexure of the Lithosphere. Cambridge University Press . (458 pp.).
Weinberg, R.F., Podladchikov, Y., 1994. Diapiric ascent of magmas through power law crust and mantle. Journal of Geophysical Research 99, 9543–9559.
Wenzel, F., 2002. Seismic experiments target earthquake-prone region in Romania. Eos Transactions, American Geophysical Union 83, 462–463.
Wilks, K.R., Carter, N.L., 1990. Rheology of some continental lower crustal rocks. Tectonophysics 182, 57–77.
Yamato, P., Agard, P., Burov, E., Le Pourhiet, L., Jolivet, L., Tiberi, C., 2007. Burial and exhumation in a subduction wedge: mutual constraints from thermo-mechanical modelling and natural p–t–t data (sch. Lustres, w. Alps). Journal of Geophysical Research 112, B07410 http://dx.doi.org/10.1029/2006JB004441.
Yamato, P., Burov, E., Agard, P., Le Pourhiet, L., Jolivet, L., 2008. HP-UHP exhumation processes during continental subduction (W. Alps): when thermomechanical models reproduce P–T–t data. Earth and Planetary Sciences Letters 271, 63–75.
Yamato, P., Mouthereau, F., Burov, E., 2009. Taiwan mountain building: insights from 2D thermo-mechanical modelling of a rheologically-stratified lithosphere. Geophysical Journal International 176, 307–326 http://dx.doi.org/10.1111/j.1365-246X.2008.03977.x.
Zhang, R.Y., Liou, J.G., Ernst, W.G., 2009. The Dabie-Sulu continental collision zone: A comprehensive review. Gondwana Research 16, 1–26.

AGU PUBLICATIONS

JGR

Journal of Geophysical Research: Solid Earth

RESEARCH ARTICLE

10.1002/2013JB010453

Key Points:
- The MPG model predicts the viscosity of polyphase rocks having power law phases
- The MPG model provides a better fit with experimental data than existing models
- The MPG model offers good potential in structural geology and numerical modeling

Supporting Information:
- Readme
- Text S1

Correspondence to:
B. Huet,
benjamin.huet@univie.ac.at

Citation:
Huet, B., P. Yamato, and B. Grasemann (2014), The Minimized Power Geometric model: An analytical mixing model for calculating polyphase rock viscosities consistent with experimental data, *J. Geophys. Res. Solid Earth*, *119*, doi:10.1002/2013JB010453.

Received 21 JUN 2013
Accepted 4 APR 2014
Accepted article online 9 APR 2014

The Minimized Power Geometric model: An analytical mixing model for calculating polyphase rock viscosities consistent with experimental data

B. Huet[1], P. Yamato[2,3], and B. Grasemann[1]

[1]Department of Geodynamics and Sedimentology, University of Vienna, Vienna, Austria, [2]Géosciences Rennes, Université de Rennes 1 - UMR 6118, Rennes, France, [3]Géosciences Rennes, CNRS - UMR 6118, Rennes, France

Abstract Here we introduce the Minimized Power Geometric (MPG) model which predicts the viscosity of any polyphase rocks deformed during ductile flow. The volumetric fractions and power law parameters of the constituting phases are the only model inputs required. The model is based on a minimization of the mechanical power dissipated in the rock during deformation. In contrast to existing mixing models based on minimization, we use the Lagrange multipliers method and constraints of strain rate and stress geometric averaging. This allows us to determine analytical expressions for the polyphase rock viscosity, its power law parameters, and the partitioning of strain rate and stress between the phases. The power law bulk behavior is a consequence of our model and not an assumption. Comparison of model results with 15 published experimental data sets on two-phase aggregates shows that the MPG model reproduces accurately both experimental viscosities and creep parameters, even where large viscosity contrasts are present. In detail, the ratio between experimental and MPG-predicted viscosities averages 1.6. Deviations from the experimental values are likely to be due to microstructural processes (strain localization and coeval other deformation mechanisms) that are neglected by the model. Existing models that are not based on geometric averaging show a poorer fit with the experimental data. As long as the limitations of the mixing models are kept in mind, the MPG model offers great potential for applications in structural geology and numerical modeling.

1. Introduction

Lower crustal and upper mantle rocks are typically polyphase materials that deform in creep regimes. Their effective viscosities depend on temperature, strain rate, and anisotropy, as well as on composition (rheology and amounts of the constituting minerals). The mechanical control of the later factor is strong [*Kirby*, 1985]. The best natural examples of this interrelation are the ductile shear zones that show strain localization due to weakening by metamorphic reactions [*Pennacchioni*, 1996; *Furusho and Kanagawa*, 1999; *Handy and Stünitz*, 2002; *Gueydan et al.*, 2003; *Jolivet et al.*, 2005; *Terry and Heidelbach*, 2006; *Hobbs et al.*, 2010; *Oliot et al.*, 2010; *Angiboust et al.*, 2011; *Grasemann and Tschegg*, 2012]. Quantifying the viscosity of polyphase rocks and its changes with metamorphic reactions is therefore of crucial importance for understanding the strength of the lower crust and upper mantle. It is, though, still an open issue [*Bürgmann and Dresen*, 2008].

Several laboratory [*Jordan*, 1987; *Tullis et al.*, 1991; *Bloomfield and Covey-Crump*, 1993; *Bons and Urai*, 1994; *Tullis and Wenk*, 1994; *Dresen et al.*, 1998; *Bruhn et al.*, 1999; *Ji et al.*, 2001; *Jin et al.*, 2001; *Xiao et al.*, 2002; *Rybacki et al.*, 2003; *Barnhoorn et al.*, 2005; *Dimanov and Dresen*, 2005] and numerical [*Tullis et al.*, 1991; *Treagus and Lan*, 2000; *Madi et al.*, 2005; *Takeda and Griera*, 2006; *Groome et al.*, 2006; *Jessell et al.*, 2009; *Dabrowski et al.*, 2012] experiments on two-phase aggregates have already addressed this issue. They characterized the way the bulk viscosity of a few aggregates changes with their composition. These studies also improved our understanding of the processes occurring in polyphase rocks during deformation. However, unlike the diversity of natural rocks, the number of experiments is limited. An accurate experimental description of all the polyphase rocks is, therefore, not available.

Theoretically, mixing models can be used to estimate the viscosity of any polyphase rock if the amounts and the mechanical behaviors of its constituting minerals are known. Such models can be classified into three families: (1) phenomenological models [*Voigt*, 1928; *Reuss*, 1929; *Tullis et al.*, 1991; *Ji and Zhao*, 1993; *Handy*, 1994a, 1994b; *Ji et al.*, 2003; *Ji*, 2004], (2) models based on minimization of the mechanical power

[*Hutchinson*, 1976; *Zhou*, 1995; *Jiang et al.*, 2005], and (3) models derived with the self-consistent approach [*Budiansky*, 1965; *Hill*, 1965; *Duva*, 1984; *Yoon and Chen*, 1990; *Treagus*, 2002; *Jiang*, 2013].

Applying these models to lower crustal and mantle rocks is, however, not straightforward. They are indeed either designed only for two-phase materials [*Budiansky*, 1965; *Hill*, 1965; *Duva*, 1984; *Yoon and Chen*, 1990; *Tullis et al.*, 1991; *Handy*, 1994a, 1994b; *Treagus*, 2002], depend on approximately constrained empirical parameters [*Ji and Zhao*, 1993; *Ji et al.*, 2003; *Ji*, 2004], provide viscosity bounds [*Voigt*, 1928; *Reuss*, 1929; *Hutchinson*, 1976; *Zhou*, 1995; *Jiang et al.*, 2005], or require an iteration process [*Ji and Zhao*, 1993; *Zhou*, 1995; *Ji et al.*, 2003; *Jiang et al.*, 2005].

In this paper, we present a new mixing model based on constrained minimization of the mechanical power: the Minimized Power Geometric model (MPG model). This minimization is, for the first time, carried out analytically with the Lagrange multipliers method. We thus provide a fast and precise way to estimate the bulk viscosity of any polyphase rock, as well as its bulk creep parameters and the strain rate and stress in its constituting phases.

The method and the derivation of the MPG model are presented first. The results are then analyzed, and the estimates of the MPG model are compared with existing laboratory and numerical experiments. Our model is also compared with existing mixing models in order to assess the ability of all these models to reproduce the experimental data sets. The limitations and the advantages of our model are finally discussed.

2. Theory and Method of Calculation

This section, which presents the theory and the method used to develop the new mixing model, formalizes and extends a method introduced in geology by *Handy* [1990]. Materials considered here are assumed to have isotropic properties and incompressible behaviors that do not depend on pressure. The derivations are carried out with the second invariants of the deviatoric strain rate and stress tensors, e and s, which are hereafter simply called strain rate and stress. The notations used in the paper are presented in the Notation.

2.1. Mechanical Power Dissipated in a Power Law Material

In a viscous material, the viscosity η relates strain rate e to stress s:

$$s = 2\eta e. \tag{1}$$

Laboratory experiments suggest that the steady state behavior of creeping minerals and rocks can be described by a power law equation:

$$e = As^n \exp\left(\frac{-Q}{RT}\right), \tag{2}$$

where n, Q, A, R, and T stand respectively for the stress exponent, activation energy, preexponential factor, gas constant, and absolute temperature [*Kohlstedt et al.*, 1995]. The creep parameters n, Q, and A are material factors, and A can include the effect of average grain size as well as the water and oxygen fugacities. To simplify the following derivations, a condensed form of the power law equation is adopted:

$$e = Bs^n, \tag{3}$$

where

$$B = A \exp\left(\frac{-Q}{RT}\right). \tag{4}$$

Combining equations (1) and (3), the behavior of a homogeneous power law material can thus be described by an effective viscosity that depends on either strain rate or stress:

$$\eta = \frac{e^{(1-n)/n}}{2B^{1/n}} = \frac{s^{1-n}}{2B}. \tag{5}$$

Viscous creep is accompanied by dissipation of mechanical power [*Ranalli*, 1995]:

$$P = 2\eta e^2 = \frac{s^2}{2\eta}, \tag{6}$$

The mechanical power dissipated in a homogeneous power law material is then given by substituting equation (5) into equation (6):

$$P = \frac{e^{(n+1)/n}}{B^{1/n}} = Bs^{n+1}. \tag{7}$$

2.2. Mechanical Power Dissipated in a Polyphase Rock

A polyphase rock is an aggregate of N different phases i with volumetric fractions ϕ_i (the fractions sum up to 1). Each phase corresponds to all grains of a mineral. For example, the phases constituting granite are quartz, mica, plagioclase, and alkaline feldspar. In that particular case, $N = 4$.

In the following, we make three assumptions:

1. The distribution of the different phases constituting the aggregate is homogeneous and isotropic, and these phases do not present any shape- or crystallographic-preferred orientation. This allows us to consider constant ϕ_i sets and to avoid theoretical problems related to anisotropic viscosity.
2. The only deformation mechanism is incompressible viscous creep of each phase i, described by a power law with known parameters n_i, A_i and Q_i. Even if elastic deformation must be present, the contribution of elastic strain rate close to steady state is considered to be negligible.
3. All the grains from the same phase i have the same strain rate e_i and stress s_i.

These assumptions have been used more or less implicitly for developing previous mixing models [*Handy*, 1990; *Tullis et al.*, 1991; *Handy*, 1994a, 1994b; *Ji*, 2004; *Ji and Zhao*, 1993; *Ji et al.*, 2003; *Jiang et al.*, 2005; *Zhou*, 1995]. They are also crucial for the development of our model. It must, however, be noted that the third assumption is very strong because it leads locally to a contradiction with the equations of stress and strain rate continuity. While ensuring continuity between the grains belonging to the same phase, it does not respect this principle at the boundary between grains belonging to different phases. The validity and consequences of these conditions are extensively discussed in section 7.

The bulk viscosity of a polyphase rock $\bar{\eta}$ can be calculated in the same way as for homogeneous material, as the ratio of the bulk stress $\bar{s}$ over the bulk strain rate $\bar{e}$:

$$\bar{\eta} = \frac{\bar{s}}{2\bar{e}}. \tag{8}$$

On the one hand, the bulk mechanical power can be expressed with this bulk viscosity according to equation (6):

$$\bar{P} = 2\bar{\eta}\bar{e}^2 = \frac{\bar{s}^2}{2\bar{\eta}}. \tag{9}$$

On the other hand, assumption 2 allows us to calculate the mechanical power dissipated in a polyphase rock by summing the mechanical power dissipated in each phase P_i weighted by the phase fraction ϕ_i [*Handy*, 1990] such that

$$\bar{P} = \sum_i \phi_i P_i. \tag{10}$$

Throughout the paper, sums and products are calculated over the N phases when no lower and upper bounds are specified. Using assumptions 2 and 3, equations (7) and (10) can be combined to express $\bar{P}$ as a function of phase strain rates or stresses:

$$\bar{P} = \sum_i \phi_i B_i^{-1/n_i} e_i^{(n_i+1)/n_i} = \sum_i \phi_i B_i s_i^{n_i+1}. \tag{11}$$

In equation (11), the sets of e_i and s_i are unknown. Here we calculate the e_i and s_i that minimize the mechanical power dissipated in the polyphase rock. Minimizing the power dissipated in a polyphase aggregate for calculating a bulk viscosity has been proposed for the first time by *Handy* [1994a, 1994b] and applied in the studies of *Zhou* [1995] and *Jiang et al.* [2005]. This amounts to using the principle of least action that is commonly used in elastic polycrystals studies (see the review by *Markov* [1999]). It must be emphasized that the principle of least action has been developed for transition between equilibrium states with conservation of energy and that its application to nonequilibrium process leads to steady state if the relationship between the driving force (the stress) and the flux (the strain rate) is linear [*de Groot and Mazur*, 1984].

It is then possible to estimate the bulk viscosity $\bar{\eta}$ as follows: once the set of e_i (resp. s_i) that minimizes $\bar{P}$ is determined for a given bulk strain rate $\bar{e}$ (resp. stress $\bar{s}$), the mechanical power is calculated with equation (11) and the effective viscosity of the aggregate is calculated with equation (9).

2.3. Which Constraint for the Minimization?

The absolute minimum of the mechanical power is zero. This value implies that the phases of a deformed polyphase rock do not deform. As this is in contradiction to assumption 2, an additional relation between the phase and bulk strain rates (resp. stresses) is therefore required. Such a relation has to describe the strain rate (or stress) partitioning between the phases for a given bulk strain rate (resp. stress). This will be used as a constraint for the minimization. Different types of constraints can be considered.

2.3.1. Homogeneity Constraints

Homogeneous strain rate ($e_i = \bar{e}$, $1 \leq i \leq N$) and homogeneous stress ($s_i = \bar{s}$, $1 \leq i \leq N$) only apply to layered media loaded along specific directions [*Markov*, 1999], which correspond to a limited number of cases. In these cases, the mechanical power cannot be minimized because the e_i or the s_i are fixed. The homogeneity constraints are therefore not consistent with minimization of the power. They are also unrealistic for most rocks [*Tullis et al.*, 1991].

2.3.2. Arithmetic Mean Constraints

A simple equation describes the strain rate partitioning in a layered material loaded perpendicular to its layering. The bulk strain rate is the arithmetic mean of the phase strain rates:

$$\sum_i \phi_i e_i - \bar{e} = 0. \tag{12}$$

Similarly, loading of a layered material parallel to its layering leads to a simple expression for the stress partitioning. The bulk stress is the arithmetic mean of the phase stresses:

$$\sum_i \phi_i s_i - \bar{s} = 0. \tag{13}$$

These two types of partitioning, which are in theory only valid for layered materials, have been used as constraints for minimizing the dissipated power in isotropic materials [*Zhou*, 1995].

A constraint derived from equation (12) has subsequently been proposed for taking into account strain distribution at grain size scale [*Jiang et al.*, 2005]. Since the deformation of minor weak phases is controlled by the stronger phase skeleton, they cannot experience an excessively large strain rate and their strain rates can be approximated by the bulk strain rate. This amounts to setting e_i to $\bar{e}$ for the minor weak phases in equation (12), and the corresponding derivation can therefore be adapted from the one using equation (12).

2.3.3. Geometric Mean Constraints

Following the use of the arithmetic mean of the phase strain rate or stress by *Zhou* [1995], we here use geometric mean constraints. These are derived from the previous constraints by simply replacing the arithmetic mean with the geometric mean. The geometric mean of strain rate is expressed by

$$\prod_i e_i^{\phi_i} - \bar{e} = 0 \tag{14}$$

and the geometric mean of stress is expressed by

$$\prod_i s_i^{\phi_i} - \bar{s} = 0. \tag{15}$$

There are two reasons to consider geometric averaging as a constraint. The first one is based on a theoretical argument [*Aleksandrov and Aizenberg*, 1966; *Matthies and Humbert*, 1993] that states that a function f which allows to average a physical property x

$$\bar{x} = f^{-1}\left(\sum_i \phi_i f(x_i)\right), \tag{16}$$

and its inverse property $y = x^{-1}$

$$\bar{y} = f^{-1}\left(\sum_i \phi_i f(y_i)\right), \tag{17}$$

so that

$$\bar{x} = \overline{x^{-1}}^{-1}, \tag{18}$$

provides an improvement in comparison to the arithmetic and harmonic means. The geometric mean fulfills this condition. The second reason is empirical and comes from the fact that mixing models based on the geometric mean provide a good fit with experimental data (see section 6 below).

The constraints (14) and (15) are used below to develop the MPG model. The arithmetic mean constraints having already been considered together with a numerical approach [*Zhou*, 1995], they are used here to develop an analytical version of the mixing models of *Zhou* [1995], to which the MPG model will be later compared (see sections 4 and 6.2).

2.4. The Lagrange Multipliers Approach

Previous studies used numerical iterations for minimizing the dissipated mechanical power [*Zhou*, 1995; *Jiang et al.*, 2005]. Here we use the Lagrange multipliers method [e.g., *Stewart*, 2002] outlined here. A supplementary function L is defined by the mechanical power and the constraint C:

$$L = \bar{P} - \lambda C, \tag{19}$$

where $\bar{P}$ is given by equation (11), λ is the Lagrange multiplier, and C is the chosen constraint given by equations (12), (13), (14), or (15). The constrained minimum of the mechanical power is found by setting simultaneously the $N + 1$ partial derivatives of L (N phase strain rates or stresses and one Lagrange multiplier) to zero. Since the stress exponent in power laws is larger or equal to 1, $\bar{P}$ is convex up. The value found with the Lagrange multiplier method is therefore a unique minimum.

3. Theoretical Determination of the Mixing Models

For each of the four constraints described in sections 2.3.2 and 2.3.3, one mixing model can be determined. These four models are referred to as Minimized Power Geometric/Arithmetic strain rate/stress models (MPG*e*, MPG*s*, MPA*e*, and MPA*s* models). Geometric or Arithmetic describes the type of mean used in the constraint, and strain rate or stress describes the quantity used in the constraint. In this section, we detail the determination of the MPG*e* model. The determination of the three other models follows the same steps and is presented in the supporting information. As section 3 mainly contains the derivations, the reader who is not interested can turn directly to section 4 where the results of theses calculations are provided.

The supplementary function is built by inserting equation (11) and constraint (14) into equation (19):

$$L\left(\ldots, e_i, \ldots, \lambda\right) = \sum_i \phi_i B_i^{-1/n_i} e_i^{(n_i+1)/n_i} - \lambda\left(\prod_i e_i^{\phi_i} - \bar{e}\right). \tag{20}$$

Setting all the partial derivatives of L to zero leads to a system of N equations:

$$\phi_i B_i^{-1/n_i} \frac{n_i + 1}{n_i} e_i^{1/n_i} = \phi_i \lambda e_i^{\phi_i - 1} \prod_{j \neq i} e_j^{\phi_j}, 1 \leq i \leq N, \tag{21}$$

together with

$$\prod_i e_i^{\phi_i} = \bar{e}. \tag{22}$$

3.1. Determination of the Strain Rate Partitioning

One phase i is considered ($1 \leq i \leq N$). Equation (21) is first simplified by isolating e_i^{1/n_i} in the left-hand side:

$$e_i^{1/n_i} = B_i^{1/n_i} \frac{n_i}{n_i + 1} \lambda e_i^{\phi_i - 1} \prod_{j \neq i} e_j^{\phi_j}. \tag{23}$$

Equation (23) is then multiplied by e_i:

$$\begin{aligned} e_i^{(n_i+1)/n_i} &= B_i^{1/n_i} \frac{n_i}{n_i + 1} \lambda e_i^{\phi_i} \prod_{j \neq i} e_j^{\phi_j}, \\ &= B_i^{1/n_i} \frac{n_i}{n_i + 1} \lambda \prod_i e_i^{\phi_i}. \end{aligned} \tag{24}$$

and simplified with equation (22):

$$e_i^{(n_i+1)/n_i} = B_i^{1/n_i} \frac{n_i}{n_i + 1} \lambda \bar{e}. \tag{25}$$

We then introduce the N effective viscosities of the phases calculated for homogeneous strain rate, as in equation (5):

$$\eta_i = \frac{\bar{e}^{(1-n_i)/n_i}}{2B_i^{1/n_i}}, \tag{26}$$

which gives an expression for the B_i:

$$B_i = \left[\frac{\bar{e}^{(1-n_i)/n_i}}{2\eta_i}\right]^{n_i}. \tag{27}$$

The introduction of this notation does not imply that homogeneous strain rate is assumed.

Equation (27) is inserted into equation (25):

$$\begin{aligned} e_i^{(n_i+1)/n_i} &= \frac{n_i}{2(n_i+1)}\frac{\lambda}{\eta_i}\bar{e}\bar{e}^{(1-n_i)/n_i}, \\ &= \frac{n_i}{2(n_i+1)}\frac{\lambda}{\eta_i\bar{e}}\bar{e}^{(n_i+1)/n_i}. \end{aligned} \tag{28}$$

We also introduce a scaled Lagrange multiplier ξ:

$$\xi = \frac{\lambda}{\bar{e}}. \tag{29}$$

A relation between the N phase strain rates and the bulk strain rate is then found by setting equation (28) to the power $n_i/(n_i+1)$ and using the definition of the scaled Lagrange multiplier:

$$e_i = \bar{e}\left(\frac{n_i}{2(n_i+1)}\frac{\xi}{\eta_i}\right)^{n_i/(n_i+1)}. \tag{30}$$

Hence, these N equations give the value of the strain rate in each phase of the aggregate.

3.2. Determination of the Scaled Lagrange Multiplier ξ

The e_i are eliminated from equation (22) by introducing the N equations (30):

$$\begin{aligned} \bar{e} &= \prod_i \bar{e}^{\phi_i}\left(\frac{n_i}{2(n_i+1)}\frac{\xi}{\eta_i}\right)^{\phi_i n_i/(n_i+1)}, \\ &= \bar{e}\left(\frac{\xi}{2}\right)^{\sum_i \phi_i n_i/(n_i+1)}\prod_i\left(\frac{n_i}{\eta_i(n_i+1)}\right)^{\phi_i n_i/(n_i+1)}. \end{aligned} \tag{31}$$

A new set of parameters is introduced:

$$a_i = \prod_{j\neq i}(n_j+1). \tag{32}$$

The powers in equation (31) are then simplified with

$$\frac{\phi_i n_i}{n_i+1} = \frac{\phi_i a_i n_i}{\prod_j(n_j+1)} \tag{33}$$

and

$$\sum_i \frac{\phi_i n_i}{n_i+1} = \frac{\sum_i \phi_i a_i n_i}{\prod_i(n_i+1)}. \tag{34}$$

Equation (31) then becomes

$$\bar{e} = \bar{e}\left(\frac{\xi}{2}\right)^{\sum_i \phi_i a_i n_i/\prod_i(n_i+1)}\prod_i\left(\frac{n_i}{\eta_i(n_i+1)}\right)^{\phi_i a_i n_i/\prod_j(n_j+1)} \tag{35}$$

and the value of the scaled Lagrange multiplier is

$$\xi = 2\prod_i\left(\eta_i\frac{n_i+1}{n_i}\right)^{\phi_i a_i n_i/\sum_j \phi_j a_j n_j}. \tag{36}$$

3.3. Determination of the Bulk Viscosity

The minimum value of the mechanical power is calculated by inserting successively equations (30), (27), and (36) into equation (11):

$$\begin{aligned}\bar{P} &= \sum_i \phi_i B_i^{-1/n_i} \dot{e}_i^{(n_i+1)/n_i},\\ &= \sum_i \phi_i 2\eta_i \bar{\dot{e}}^{(n_i-1)/n_i} \frac{n_i}{2(n_i+1)} \frac{\xi}{\eta_i} \bar{\dot{e}}^{(n_i+1)/n_i},\\ &= 2\bar{\dot{e}}^2 \prod_i \left(\eta_i \frac{n_i+1}{n_i}\right)^{\phi_i a_i n_i / \sum_i \phi_j a_j n_j} \sum_i \frac{\phi_i n_i}{n_i+1}.\end{aligned} \tag{37}$$

Combining equations (9) and (37) gives the value of the bulk viscosity for the MPG*e* model:

$$\bar{\eta} = \sum_i \frac{\phi_i n_i}{n_i+1} \prod_i \left(\eta_i \frac{n_i+1}{n_i}\right)^{\phi_i a_i n_i / \sum_i \phi_j a_j n_j}. \tag{38}$$

3.4. Determination of the Bulk Creep Parameters

The strain rate and temperature dependency of the bulk viscosity are explicitly stated by introducing equations (4) and (26) in equation (38):

$$\bar{\eta} = \sum_i \frac{\phi_i n_i}{n_i+1} \times \prod_i \left(\frac{\bar{\dot{e}}^{(1-n_i)/n_i}}{2A_i^{1/n_i}} \exp\left(\frac{Q_i}{n_i RT}\right) \frac{n_i+1}{n_i}\right)^{\phi_i a_i n_i / \sum_i \phi_j a_j n_j}. \tag{39}$$

This equation can be simplified into a product of three terms:

$$\bar{\eta} = \left[\bar{\dot{e}}^{\sum_i \phi_i a_i (1-n_i)/\sum_i \phi_i a_i n_i}\right] \times \left[\exp\left(\frac{1}{RT} \frac{\sum_i \phi_i a_i Q_i}{\sum_i \phi_i a_i n_i}\right)\right] \times \left[\sum_i \frac{\phi_i n_i}{n_i+1} \prod_i \left(\frac{n_i+1}{2A_i^{1/n_i} n_i}\right)^{\phi_i a_i n_i / \sum_i \phi_j a_j n_j}\right]. \tag{40}$$

If the bulk behavior obeyed a power law, the bulk effective viscosity could be calculated with equation (5):

$$\bar{\eta} = \left[\bar{\dot{e}}^{(1-\bar{n})/\bar{n}}\right] \left[\exp\left(\frac{\bar{Q}}{\bar{n}RT}\right)\right] \left[\frac{1}{2\bar{A}^{1/\bar{n}}}\right], \tag{41}$$

where $\bar{n}$, $\bar{Q}$, and $\bar{A}$ would be the bulk creep parameters.

In equations (40) and (41), the bulk viscosity is split into three factors: a factor with a power of the bulk strain rate, an Arrhenius-type factor depending on temperature, and a factor containing only material parameters. The power of the bulk strain rate that appears in the first factor of equation (40) is treated first:

$$\frac{\sum_i \phi_i a_i (1-n_i)}{\sum_i \phi_i a_i n_i} = \frac{1 - \frac{\sum_i \phi_i a_i n_i}{\sum_i \phi_i a_i}}{\frac{\sum_i \phi_i a_i n_i}{\sum_i \phi_i a_i}}. \tag{42}$$

The first factors of equations (40) and (41) match exactly for

$$\bar{n} = \frac{\sum_i \phi_i a_i n_i}{\sum_i \phi_i a_i}. \tag{43}$$

Using the definition of the bulk stress exponent that has just been determined, the second factors match for

$$\bar{Q} = \frac{\sum_i \phi_i a_i Q_i}{\sum_i \phi_i a_i}. \tag{44}$$

The bulk preexponential factor is calculated by identifying the third factors of equations (40) and (41):

$$\frac{1}{2\bar{A}^{1/\bar{n}}} = \sum_i \frac{\phi_i n_i}{n_i+1} \prod_i \left(\frac{n_i+1}{2A_i^{1/n_i} n_i}\right)^{\phi_i a_i n_i / \sum_i \phi_j a_j n_j}. \tag{45}$$

Introducing the value of the bulk stress exponent, given by equation (43), into equation (45) leads to

$$\bar{A} = \left(\frac{1}{2\sum_i \frac{\phi_i n_i}{n_i+1}}\right)^{\bar{n}} \prod_i \left(\frac{2A_i^{1/n_i} n_i}{n_i+1}\right)^{\bar{n}\phi_i a_i n_i / \sum_i \phi_j a_j n_j}. \tag{46}$$

Table 1. Bulk Viscosity, Phase Strain Rates or Phase Stresses, and Scaled Lagrange Multiplier for the Four Mixing Models

Mixing Model	Bulk Viscosity $\bar{\eta}$ [a]	Phase Strain Rates e_i or Phase Stresses s_i	Scaled Lagrange Multiplier ξ [b]
MPG*e*	$\sum_i \frac{\phi_i n_i}{n_i+1} \prod_i \left(\eta_i \frac{n_i+1}{n_i}\right)^{\frac{\phi_i a_i n_i}{\sum_i \phi_j a_j n_j}}$	$\bar{e}\left(\frac{n_i}{2(n_i+1)} \frac{\xi}{\eta_i}\right)^{\frac{n_i}{n_i+1}}$	$2\prod_i \left(\eta_i \frac{n_i+1}{n_i}\right)^{\frac{\phi_i a_i n_i}{\sum_i \phi_j a_j n_j}}$
MPG*s*	$\frac{1}{\sum_i \frac{\phi_i}{n_i+1}} \prod_i \left(\eta_i \frac{1}{n_i+1}\right)^{\frac{\phi_i a_i}{\sum_i \phi_j a_j}}$	$\bar{s}\left(\frac{2}{n_i+1} \frac{\eta_i}{\xi}\right)^{\frac{1}{n_i+1}}$	$2\prod_i \left(\eta_i \frac{1}{n_i+1}\right)^{\frac{\phi_i a_i}{\sum_i \phi_j a_j}}$
MPA*e*	$\sum_i \phi_i \eta_i \left(\frac{n_i}{2(n_i+1)} \frac{\xi}{\eta_i}\right)^{n_i+1}$	$\bar{e}\left(\frac{n_i}{2(n_i+1)} \frac{\xi}{\eta_i}\right)^{n_i}$	$\sum_i \phi_i \left(\frac{n_i}{2(n_i+1)} \frac{\xi}{\eta_i}\right)^{n_i} = 1$
MPA*s*	$\left(\sum_i \frac{\phi_i}{\eta_i} \left(\frac{2}{n_i+1} \frac{\eta_i}{\xi}\right)^{\frac{n_i+1}{n_i}}\right)^{-1}$	$\bar{s}\left(\frac{2}{n_i+1} \frac{\eta_i}{\xi}\right)^{\frac{1}{n_i}}$	$\sum_i \phi_i \left(\frac{2}{n_i+1} \frac{\eta_i}{\xi}\right)^{\frac{1}{n_i}} = 1$

[a] For the MPG*e* and MPA*e* models, $\eta_i = \bar{e}^{(1-n_i)/n_i} / 2B_i^{1/n_i}$. For the MPG*s* and MPA*s* models, $\eta_i = \bar{s}^{1-n_i} / 2B_i$; $a_i = \prod_{j \neq i}(n_j + 1)$.

[b] The scaled Lagrange multiplier is the solution of a nonlinear equation for the two MPA models.

Further simplification give the value of the bulk preexponential factor:

$$\bar{A} = \left(\sum_i \frac{\phi_i n_i}{n_i + 1}\right)^{-\bar{n}} \prod_i \left(\frac{n_i}{n_i + 1}\right)^{\phi_i a_i n_i / \sum_i \phi_j a_j} \prod_i A_i^{\phi_i a_i / \sum_i \phi_j a_j}. \tag{47}$$

Bulk creep parameters that correspond to a power law and that do not depend on temperature and on bulk strain rate can be determined for the MPG*e* model. Thus, if the phases follow a power law behavior, the bulk behavior defined by the MPG*e* model is also a power law behavior.

4. Analysis of the Mixing Models

The four mixing models determined in both section 3 (for the MPG*e* model) and supporting information (for the MPG*s*, MPA*e*, and MPA*s* models) are analyzed here. This section demonstrates the predictions of the four models for an anorthite-diopside aggregate in the wet dislocation creep regime. This example has been chosen because of the large difference in creep parameters and viscosity between anorthite (the weak phase) and diopside (the strong phase).

4.1. The Equations Defining the Mixing Models

The equations defining the four mixing models are summarized in Table 1. The two MPG models are fully analytical while the two MPA models are semianalytical. Their scaled Lagrange multipliers are calculated numerically by solving a nonlinear equation. The solution of this equation is then used for calculating the bulk viscosity and the strain rate or the stress in the phases.

For the four models, the bulk viscosity appears as a weighted mean of the phase viscosities calculated for homogeneous strain rate or stress. The type of mean in these equations depends on the constraint: geometric mean for the MPG models, arithmetic mean for the MPA*e* model, and harmonic mean for the MPA*s* model. The weights are combinations of volumetric fractions, stress exponents, viscosities, and scaled Lagrange multiplier. Similar combinations appear in the expressions of the phase strain rates and stresses.

The equations in Table 1 are intricate because the stress exponents of the phases are different. They simplify for a homogeneous stress exponent. This simple case corresponds to a rock in which all the phases deform by diffusion creep ($n = 1$). It is also an approximation for a rock in which the phases deform by dislocation creep with stress exponents close to 3. In such cases, both MPG models predict the same bulk viscosity:

$$\bar{\eta} = \prod_i \eta_i^{\phi_i}, \tag{48}$$

which is exactly the geometric mean of the viscosities of the phases calculated for a homogeneous strain rate or a homogeneous stress. The scaled Lagrange multiplier of the MPA models can be calculated analytically for homogeneous stress exponents. The bulk viscosity defined by the MPA*e* model is given by the

generalized mean of the phase viscosities calculated for homogeneous strain rate, with an exponent equal to $-n$:

$$\bar{\eta} = \left(\sum \phi_i \eta_i^{-n} \right)^{-1/n}. \quad (49)$$

For the MPA*s* model, the bulk viscosity is given by the generalized mean of the phase viscosities calculated for homogeneous stress, with an exponent equal to $1/n$:

$$\bar{\eta} = \left(\sum \phi_i \eta_i^{1/n} \right)^{n}. \quad (50)$$

Equations (49) and (50) simplify to a harmonic and arithmetic mean, respectively, for a polyphase rock containing phases deforming by diffusion creep.

4.2. The Bulk Viscosity

Figure 1a presents the bulk viscosity of an anorthite-diopside aggregate as a function of its diopside fraction. The predictions of the four mixing models are plotted together. The mixing models show three similar characteristics. The viscosity calculated for the two end-member compositions is similar to the end-member viscosity. The viscosity increases while the fraction of diopside increases. The models constrained by stress partitioning predict larger bulk viscosities than those constrained by strain rate partitioning. The first two characteristics are expected for any mixing model.

There are, however, major differences between the MPG models and the MPA models. The viscosity curves calculated with the MPG models have a smooth slope and are almost undistinguishable. The two MPG models therefore predict bulk viscosities which are very similar. The trend of the curves on Figure 1a is close to linear. Since the *y* axis uses a logarithmic scale, this means that the bulk viscosity is close to the one calculated with a simple geometric mean. The viscosity curves calculated with the MPA models are in contrast significantly different from each other (by several orders of magnitude), and the estimates of the MPA models bound those of the MPG models. The MPA*e* model leads to the lowest calculated viscosities with a convex down curve. The predicted bulk viscosity is close to the viscosity of anorthite when the aggregate contains less than 80% of diopside. It steepens up dramatically for larger diopside fractions. The evolution of the viscosity curve predicted by the MPA*s* model shows an opposite behavior.

4.3. The Partitioning of Strain Rate and Stress

The strain rate and stress in anorthite and diopside are presented as functions of the diopside fraction (Figures 1b and 1c). These curves characterize the partitioning of strain rate and stress predicted by the four mixing models. Both strain rates and stresses are normalized on the bulk values.

The evolutions of the curves predicted by the four mixing models are similar. For a given aggregate composition, the strain rate in anorthite is larger than the bulk strain rate, and the stress is lower than the bulk stress. Further, the normalized strain rate increases, and the normalized stress decreases while the fraction of anorthite decreases. For anorthite fractions tending to zero, the limit value of its strain rate and stress is finite. The evolution of strain rate and stress in diopside is similar. The strain rate curves are translated at values lower than the bulk one, and the stress curves are translated at values larger than the bulk ones. This evolution implies that both the weak and the strong phases deform at higher strain rates while the aggregate gets richer in the strong phase and hence stronger.

However, the way that partitioning is quantified is model dependent. The evolution predicted by the two MPG models is characterized by a fairly constant slope, and both models predict almost identical partitioning. In contrast, the MPA*e* model predicts a dramatic increase of the phase strain rates (5 orders of magnitude for anorthite and 12 orders of magnitude for diopside) and an almost homogeneous stress close to the bulk value. In contrast, the MPA*s* model predicts a dramatic increase of the phase stresses and an almost homogeneous strain rate close to the bulk value. The MPA models therefore behave almost like models based on homogeneous strain rate or stress, such behaviors being generally unrealistic [*Tullis et al.*, 1991].

4.4. The Bulk Creep Parameters

The bulk creep parameters of the MPG models determined in section 3 and supporting information are presented in Table 2. They only depend on the phase creep parameters and fractions and do not vary with temperature, strain rate, or stress. Thus, an aggregate of power law phases defined by the MPG models also

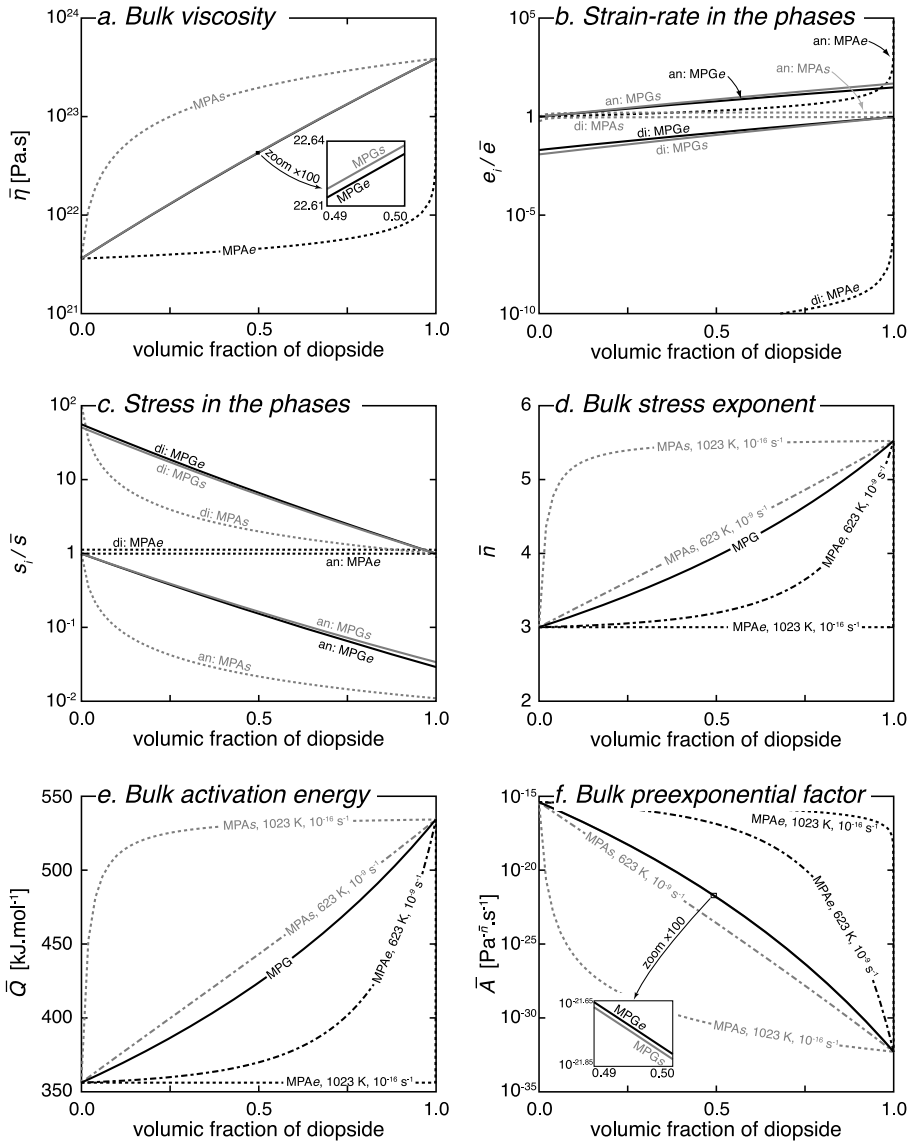

Figure 1. Mechanical behavior of anorthite-diopside aggregates as a function of the diopside fraction predicted by the MPG*e* (black solid curves), the MPG*s* (grey solid curves), the MPA*e* (black dotted curves), and the MPA*s* (grey dotted curves) models. (a) Bulk viscosity. (b) Normalized strain rate in the phases (an: anorthite, weak phase, di: diopside, strong phase). (c) Normalized stress in the phases. (d) Bulk stress exponent. (e) Bulk activation energy. (f) Bulk preexponential factor. The phase strain rates and the stresses are normalized on the bulk values. Predictions are calculated for temperature of 1023 K and strain rate of 10^{-16} s^{-1}. The bulk creep parameters are also calculated at other conditions in order to show that the bulk creep parameters predicted by the MPA models depend on temperature and strain rate. The creep parameters of anorthite and diopside correspond to the dislocation creep regime in wet conditions [*Dimanov and Dresen*, 2005].

follows a power law. The transmission of this behavior from the phases to the aggregate is not an assumption of the MPG models. Such a transmission has also been recognized in phenomenological mixing models based on geometric averaging [*Tullis et al.*, 1991; *Ji and Zhao*, 1993; *Ji et al.*, 2003] and is consequence of the geometric mean used in the constraints. Essentially speaking, multiplying strain rates, stress, or viscosities together allows the powers in the phases power laws to be regrouped together, leading to a bulk power law.

The two MPG models give the same bulk stress exponent $\bar{n}$ and the same bulk activation energy $\bar{Q}$ (Table 2). These bulk parameters are calculated as the arithmetic mean of the phase parameters weighted by $\phi_i a_i$. For homogeneous phase stress exponents, the bulk stress exponent simplifies to the phase stress exponents, and the bulk activation energy simplifies to the arithmetic mean of the values of the separate phases

Table 2. Bulk Creep Parameters Calculated for the Minimized Power Geometric Models

Mixing Model	Bulk Stress Exponent $\bar{n}$ [a]	Bulk Activation Energy $\bar{Q}$ [a]	Bulk Preexponential Factor $\bar{A}$ [a]
MPG*e*	$\sum_i \phi_i a_i n_i \,/\, \sum_i \phi_i a_i$	$\sum_i \phi_i a_i Q_i \,/\, \sum_i \phi_i a_i$	$\prod_i A_i^{\phi_i a_i / \sum_i \phi_j a_j} \times \left(\sum_i \frac{\phi_i n_i}{n_i+1}\right)^{-\bar{n}} \prod_i \left(\frac{n_i}{n_i+1}\right)^{\phi_i a_i n_i / \sum_i \phi_j a_j}$
MPG*s*	$\sum_i \phi_i a_i n_i \,/\, \sum_i \phi_i a_i$	$\sum_i \phi_i a_i Q_i \,/\, \sum_i \phi_i a_i$	$\prod_i A_i^{\phi_i a_i / \sum_i \phi_j a_j} \times \sum_i \frac{\phi_i}{n_i+1} \prod_i (n_i+1)^{\phi_i a_i / \sum_i \phi_j a_j}$
Homogeneous n_i [b]	n_i	$\sum_i \phi_i Q_i$	$\prod_i A_i^{\phi_i}$

[a] $a_i = \prod_{j \neq i}(n_j + 1)$.
[b] For homogeneous stress exponent, both MPG*e* and MPG*s* models provide the same bulk creep parameters.

(Table 2). As expected from their expressions, the evolution of $\bar{n}$ and $\bar{Q}$ with increasing diopside fraction shows a regular and close to linear increase from the anorthite value to the diopside value (Figures 1d and 1e).

The bulk preexponential factor $\bar{A}$ of the MPG*e* and MPG*s* models are different (Table 2). The ratio between these expressions lies between 0.25 and 1 (see Appendix A). This implies that the value of $\bar{A}$ corresponding to the MPG*e* model is larger than the one corresponding to the MPG*s* model (Figure 1f). This also implies that the bulk viscosity predicted by the MPG*e* model is always lower than the bulk viscosity predicted by the MPG*s* model, as observed on Figure 1a. However, the bulk viscosity predicted by the two MPG models falls within the same order of magnitude. For homogeneous stress exponents, both MPG models predict the same bulk preexponential factor: the geometric mean of the phase preexponential factors (Table 2). In spite of the complexity of the expression which define it, the predicted bulk preexponential factor of anorthite-diopside aggregates decreases regularly when the diopside fraction increases (Figure 1f).

In contrast, the bulk creep parameters that correspond to the MPA models cannot be calculated analytically (see supporting information). Figures 1d–1f show the evolution of these parameters, calculated numerically for anorthite-diopside aggregates at different conditions of temperature and strain rate. The values of $\bar{n}$, $\bar{Q}$, and $\bar{A}$ predicted by the MPA models depend on temperature and on strain rate. Thus, even if the phases have a power law behavior, this characteristic is not transmitted to the bulk behavior described by the MPA models.

5. Comparison With Experiments

The MPG*e* and MPG*s* models predict values of the bulk preexponential factor that are almost similar. This is the only difference between these two models, and it is the reason they predict similar bulk viscosities and partitioning. Below, these two models are thus referred to as a single MPG model, and only the predictions of the MPG*e* model are shown.

In this section, the predictions of the MPG model are compared with the published results of 15 experimental data sets on two-phase materials. The predictions of the MPG model are calculated with the experimental end-member viscosities and stress exponents using equation (38). When bulk creep parameters have been determined experimentally for the aggregates of intermediate compositions, bulk creep parameters are also calculated using equations (43), (44), and (47). Experiments which have been shown by *Ji* [2004] not to fall within the theoretical bounds are not considered here. In the following figures, the experimental data together with their errors (when reported) are represented by open symbols, and the predictions are represented by solid curves.

5.1. Enstatite-Forsterite Aggregates

In the experiments carried out by *Ji et al.* [2001], forsterite is stronger than enstatite, with a viscosity contrast lower than 1 order of magnitude (Figure 2a). The same deformation mechanisms were observed in the phases deformed alone and in the two-phase aggregates. Since the deformation mechanisms do not change, it is legitimate to calculate the bulk viscosity of the aggregates using the end-member values. The evolution of the viscosity with increasing forsterite fraction shows a trend close to logarithmic (Figure 2a). This evolution is complicated by an S-shape trend which has been interpreted as the effect of microstruc-

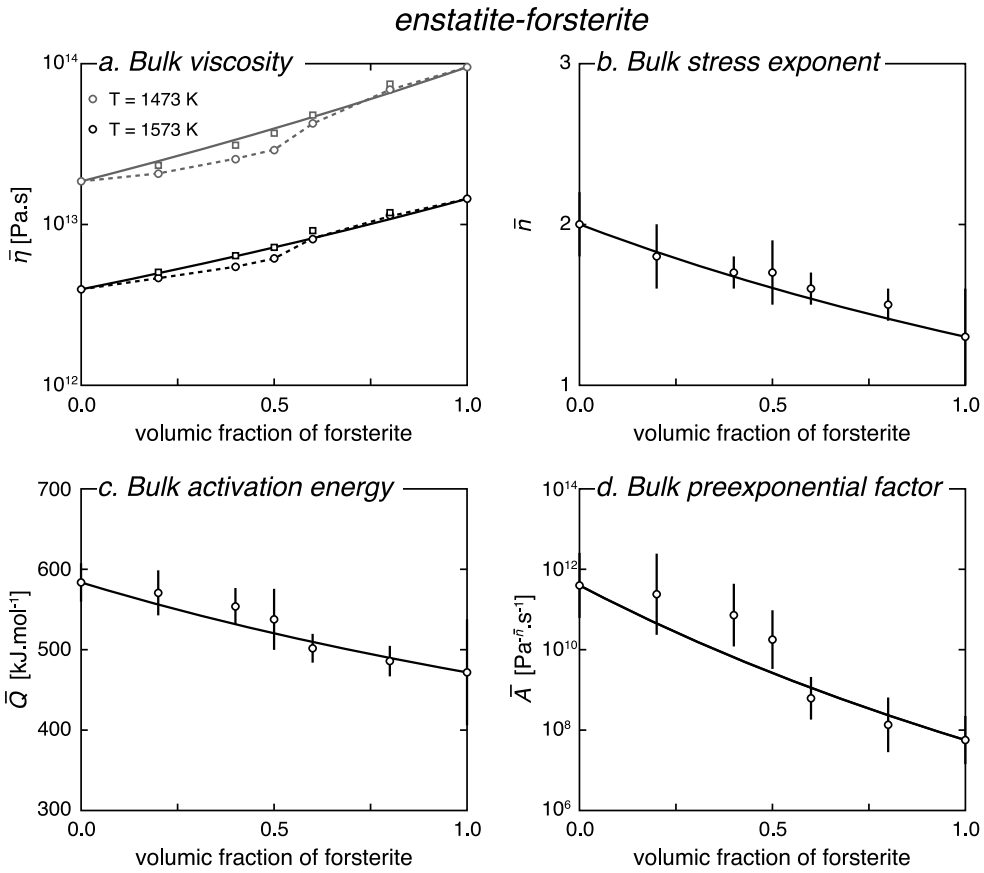

Figure 2. (a–d) Bulk viscosity and bulk creep parameters of enstatite-forsterite aggregates as a function of the forsterite fraction: comparison between the experimental data set of *Ji et al.* [2001] (open circles) and the MPG model (solid curves). The experimental S-shape trend is highlighted with a dotted line. Viscosity values corrected for the porosity [*Ji*, 2004] are also shown (open squares). The vertical bars correspond to the fitting errors calculated during the regression of the creep parameters. Bulk strain rate: 10^{-6} s^{-1}, temperature: 1473–1573 K, confining pressure: 0.1 MPa.

tural changes [*Ji et al.*, 2001]. For low forsterite fractions (lower than 0.4), the structure is weak-phase supported, whereas for large forsterite fractions (larger than 0.6), it is strong-phase supported. For intermediate forsterite contents (0.4–0.6), deformation is controlled by a transitional regime. Even if the MPG model fits the general trend very well (Figure 2a), it fails to reproduce the S-shape trend. If the experimental viscosity is corrected for the aggregate porosity [*Ji*, 2004], the S-shape trend is smoothed, which improves the agreement between the data and the model.

Comparison of both the bulk stress exponent and the bulk activation energy with their predicted counterparts shows that the predicted values fall within the experimental errors of the experimental data (Figures 2b and 2c). The quality of fit is poorer for the bulk preexponential factor even if the difference between the experimental and predicted values is lower than 1 order of magnitude (Figure 2d). Note that the error on the preexponential factor usually does not take into account the regression errors of the stress exponent and activation energy, on which it also relies. A larger experimental error would then lead to a better agreement.

5.2. Omphacite-Garnet Aggregates

In the experiments of *Jin et al.* [2001], omphacite and garnet were deformed by dislocation creep, with a viscosity difference of 1 order of magnitude (Figure 3a). Since no experiment was conducted for pure garnet aggregates, the viscosity value for pure garnet was deduced by *Jin et al.* [2001] using a mixing model [*Tullis et al.*, 1991]. The experimental data set has a logarithmic trend, even without the data for pure garnet (Figure 3a). Stress exponents from the literature (omphacite: $n = 3.5$ [*Zhang et al.*, 2006], garnet: $n = 2.7$ [*Karato*, 1995]) were used to predict the aggregate bulk viscosity. The predictions of the geometric

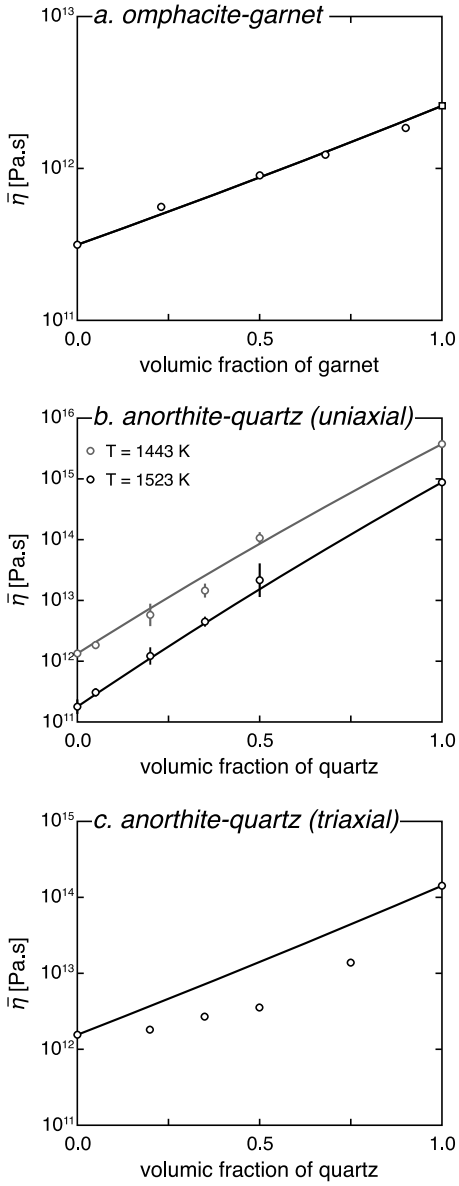

Figure 3. (a) Bulk viscosity of omphacite-garnet aggregates as a function of the fraction of garnet: comparison between the experimental data set of *Jin et al.* [2001] (open circles) and the predictions of the MPG model (solid curve). The viscosity of pure garnet (open square) is not experimental but has been calculated with the help of a mixing model [*Jin et al.*, 2001]. Bulk strain rate: 4.6 10^{-4} s^{-1}, temperature: 1500 K, confining pressure: 3 GPa. (b and c) Viscosity of anorthite-quartz aggregates as a function of the fraction of quartz under uniaxial conditions in Figure 3b and triaxial conditions in Figure 3c: comparison between the experimental data set of *Xiao et al.* [2002] (open circles) and the predictions of the MPG model (solid curves). The vertical bars indicate the experimental dispersion of the viscosity. Uniaxial experiments: normalized for bulk stress: 10 MPa, temperature: 1443 and 1523 K, confining pressure: 0.1 MPa. Triaxial experiments: normalized for bulk stress: 10 MPa, temperature: 1393 K, confining pressure: 300 MPa.

mixing model are in very good agreement with the experimental data for the whole range of aggregate compositions.

5.3. Anorthite-Quartz Aggregates

In the experiments of *Xiao et al.* [2002], anorthite deformed by grain boundary diffusion creep and showed similar deformation mechanisms when pure and when mixed with quartz. Quartz behaved almost like rigid grains and recorded intense deformation at its rim with an increase in dislocation densities (uniaxial experiments) or showed partly dislocation free grains (triaxial experiments). The viscosity of quartz was, in the experimental conditions, 2 to 3 orders of magnitude larger than that of anorthite (Figures 3b and 3c).

Under uniaxial conditions, the viscosity of the anorthite-quartz aggregates shows a logarithmic increase with increasing quartz content (Figure 3b). Both the trend and the values are well reproduced by the MPG model. Under triaxial conditions, the MPG model overestimates systematically the experimental values by up to half an order of magnitude at maximum (Figure 3c). The difference of behavior between the two sets of experiments was interpreted by a reduced load transfer to the quartz grains through the weak anorthite matrix at high confining pressure [*Xiao et al.*, 2002]. However, since no experiment was carried out on pure quartz under triaxial conditions, the creep parameters from another experimental study [*Brodie and Rutter*, 2000] are used to calculate the bulk viscosity with the MPG model. If the viscosity of pure quartz was approximately 1 order of magnitude lower than the one calculated with the *Brodie and Rutter* [2000] parameters, the match between the experimental data and the MPG model would be much better. Such a difference can be expected if the sample preparation or the experimental setup are different.

5.4. Anorthite-Diopside Aggregates

Dimanov and Dresen [2005] carried out experiments on anorthite-diopside aggregates in the diffusion and dislocation creep regimes in dry and wet conditions. The mechanical data and the microstructures suggest that anorthite, diopside, and their aggregates deformed by linear viscous grain boundary diffusion creep at low stress and by power law dislocation creep at higher stress. At intermediate stress, a mixed diffusion-dislocation creep regime was observed. Under the experimental conditions, the viscosity of diopside was 2 to 3 orders of magnitude greater than the viscosity of anorthite (Figure 4). For the two deformation regimes and in both dry and wet conditions, the experimental viscosity increases along an S-shape trend with increasing diopside fraction. The

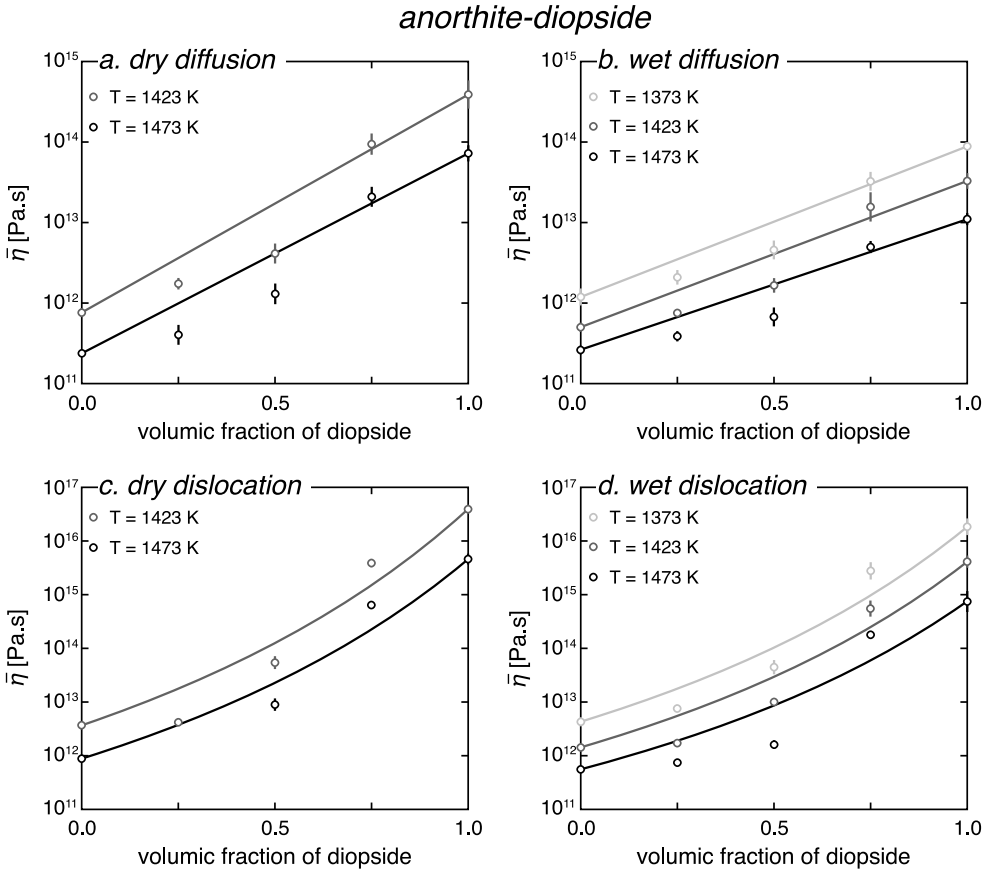

Figure 4. Viscosity of anorthite-diopside aggregates as a function of the fraction of diopside: comparison between the experimental data set of *Dimanov and Dresen* [2005] (open circles) and the predictions of the MPG model (solid curves). (a) Diffusion experiments in dry conditions. (b) Diffusion experiments in wet conditions. (c) Dislocation experiments in dry conditions. (d) Dislocation experiments in wet conditions. The vertical bars indicate the experimental dispersion of the viscosity. Recalculated for bulk stress of 10 MPa (diffusion experiments) and 100 MPa (dislocation experiments), temperature: 1373, 1423, and 1473 K, confining pressure: 300 MPa.

inflection point lies at diopside fractions in the range 0.5–0.75. This evolution suggests a weak-phase supported microstructure at diopside fractions lower than 0.5 and a strong-phase supported microstructures at diopside fraction larger than 0.75. This might be due to the contrasting grain size between anorthite and diopside in the experiments, which could promote the formation of weak- and strong-phase supported structures.

Bulk viscosities have been calculated with stress exponents of 1 for both anorthite and diopside in the diffusion creep regime and higher values in the dislocation creep regime (anorthite: $n = 3$, diopside: $n = 5.5$ [*Dimanov and Dresen*, 2005]). The predicted evolution is logarithmic for the diffusion experiments (Figures 4a and 4b) and is convex up for the dislocation experiments (Figures 4c and 4d). Thus, even if the difference between the predicted and the experimental viscosity is generally less than half an order of magnitude, the MPG model fails to reproduce the experimental S-shape trend. More precisely, it overestimates the viscosity for the diopside fractions of 0.25 and 0.5 and underestimates it for the diopside fraction of 0.75.

The experimental data in the diffusion creep regime are consistent with bulk stress exponents of 1 for anorthite, diopside, and aggregates of intermediate composition. This is predicted by the MPG model (see Table 2). In the dislocation creep regime, the experimental and predicted bulk stress exponents are in good agreement even if the model does not reproduce the smooth S-shape experimental trend (Figure 5a). The experimental values of the bulk activation energy are well reproduced by the predicted one for the diffusion creep regime and the dry dislocation creep regime (Figure 5b). The agreement is, however, not as good for the wet dislocation creep regime. For the bulk preexponential factor (Figure 5c), the agreement between experimental and predicted values varies from very good (wet diffusion creep) to very poor (dislocation

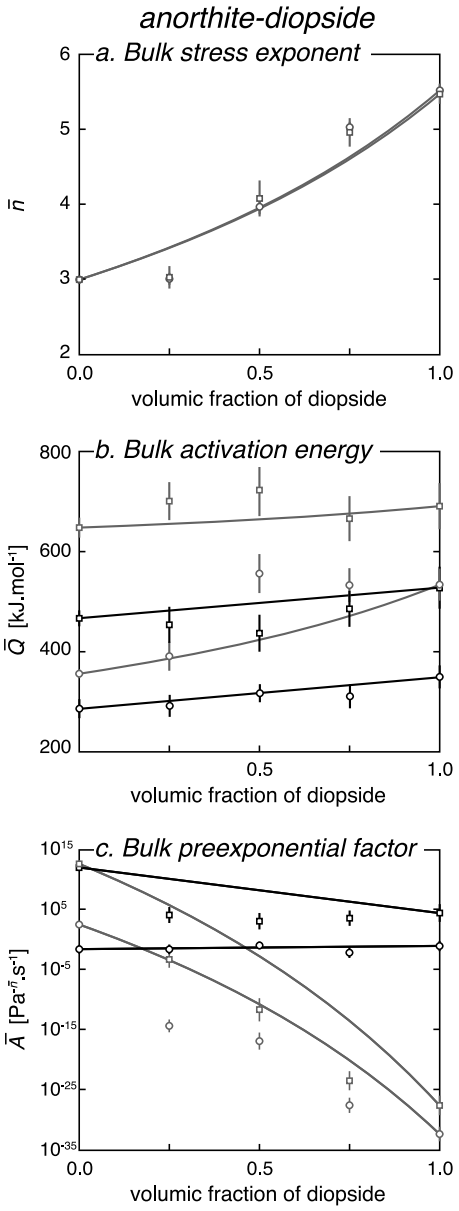

Figure 5. (a–c) Bulk creep parameters of anorthite-diopside aggregates as a function of the fraction of diopside: comparison between the experimental data set of *Dimanov and Dresen* [2005] (open symbols) and the predictions of the MPG model (solid curves). The black (resp. grey) color corresponds to diffusion (resp. dislocation) creep experiments. Open circles (resp. squares) correspond to wet (resp. dry) conditions. The vertical bars correspond to the fitting errors calculated during the regression of the creep parameters.

creep). Since the stress exponent is regressed first and the preexponential factor is regressed third, the decrease in the agreement between experiments and predictions, from stress exponent to preexponential factor, might be an artifact of the regression process of the creep parameters. Small errors in the determination of the bulk stress exponent and activation energy might lead to large errors in the determination of the bulk preexponential factor.

5.5. Halite-Calcite Aggregates

In the experiments of *Jordan* [1987] and [*Bloomfield and Covey-Crump* 1993], calcite is 1 order of magnitude stronger than halite (Figure 6a). Calcite deformed partly by intracrystalline plasticity with twinning and partly by cataclasis, whereas halite deformed by dislocation glide. The experimental viscosities show a logarithmic increase with increasing calcite fraction. The predictions of the MPG model have been calculated with stress exponents determined in other experimental studies (halite: $n = 5.3$ [*Carter et al.*, 1993], calcite: $n = 7.8$ [*Schmid et al.*, 1980]). For both experimental data sets, the values calculated with the MPG model reproduce the experimental values very well, even if cataclastic flow of calcite which is not strictly modeled by a power law was active in the experiments.

5.6. Calcite-Anhydrite Aggregates

In the experiments of *Barnhoorn et al.* [2005], calcite and anhydrite have viscosities of the same order of magnitude (Figure 6b). They deformed (separately and together) in the dislocation creep regime with exception of one experiment (70% of anhydrite) where anhydrite deformation was controlled by diffusion creep or grain boundary sliding. The viscosity measured in a torsion apparatus (used for these experiments) depends on the stress exponent of the material. *Barnhoorn et al.* [2005] suggest that 5 is the most likely value for the stress exponent of most of the aggregates. In the aggregates having a calcite-anhydrite ratio of 1:1, their preferred value is 3. The dispersion due to variations of stress exponent between 1 and 5 is shown, in addition to the experimental viscosity values (Figure 6b). The viscosity of the aggregate containing 70% of anhydrite is lower than the viscosity of the two end-members, which is due to a change in the deformation mechanism of anhydrite. This data point is therefore not considered here. The predictions of the MPG model have been calculated with a stress exponent of 5 for both calcite and anhydrite. Variation of the end-member stress exponent induces a minor dispersion of the predicted viscosity (grey background on Figure 6b). If the outlier value is not considered, the predicted values are very similar to the experimental data.

5.7. Octachloropropane-Camphor Aggregates

Octachloropropane (OCP) and camphor are crystalline organic materials that creep at room temperature and low stress. In the three constant load experiments of *Bons and Urai* [1994], the viscosity shows the

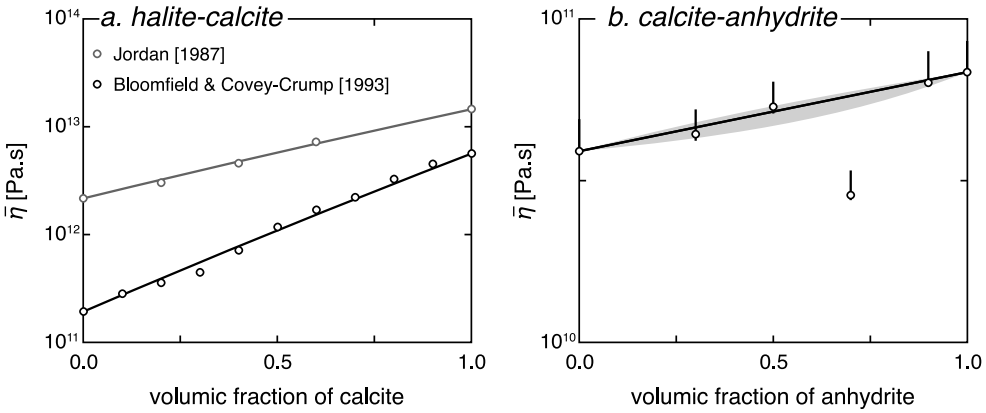

Figure 6. (a) Viscosity of halite-calcite aggregates as a function of the fraction of calcite: comparison between the experimental data sets of *Jordan* [1987] (grey open circles) and *Bloomfield and Covey-Crump* [1993] (black open circles), on the one hand, and the predictions of the MPG model (solid curves), on the other hand. The viscosity corresponds to 10% strain for *Jordan* [1987] experiments and 20% strain for *Bloomfield and Covey-Crump* [1993] experiments. Bulk strain rate: 10^{-5} s^{-1}, temperature: 473 K, confining pressure: 200 MPa. (b) Viscosity of calcite-anhydrite aggregates as a function of the fraction of anhydrite: comparison between the experimental data set of *Barnhoorn et al.* [2005] (open circles) and the predictions of the MPG model (solid curves). The vertical bars indicate the range in viscosity due to variations of the end-member stress exponents between 1 and 5. The grey background indicates the range in predicted viscosity due to the variations of the end-member stress exponent. The viscosity corresponds to the peak stress (shear strain of approximately 0.5). Bulk strain rate: 10^{-3} s^{-1}, temperature: 1873 K, confining pressure: 300 MPa.

same parallel evolution. It increases regularly over 3 orders of magnitude with increasing camphor fraction (Figure 7a). Predictions with the MPG model have been calculated with the stress exponents derived from the stepping load experiments (OCP: $n = 4.5$, camphor: $n = 3.3$). The three predicted viscosity curves are also parallel and follow the experimental trend. However, the predictions slightly overestimate the experimental values with a maximum difference of approximately half an order of magnitude.

The bulk stress exponent and bulk constant factor of OCP-camphor aggregates have been determined with stepping load experiments at constant temperature [*Bons and Urai*, 1994]. The stress exponent values of the aggregates of intermediate composition are close to the one of OCP (Figure 7b). Furthermore, the bulk stress exponent shows a bell-shape evolution with increasing camphor fraction. This increased nonlinearity might be the effect of grain-scale mechanical interactions between OCP and camphor grains. This is probably why the predictions of the MPG model fail to reproduce both the experimental values and trend. The experimental bulk constant factor (which includes the preexponential factor and the thermal part of the power law) decreases regularly with the increasing camphor fraction (Figure 7c). The predicted evolution of the bulk constant factor reproduces the experimental trend. However, the predictions slightly underestimate the experimental values, which is consistent with the overestimation of the viscosity (Figure 7a). Because of the surprising evolution of the bulk stress exponent, the very weak OCP has been suggested to control the deformation of the aggregate, even at large camphor contents [*Bons and Urai*, 1994]. This mechanical control is not in line with the regular experimental evolution of the bulk viscosity (Figure 7a) and bulk constant factor (Figure 7c) reproduced by the MPG model.

5.8. Ammonia Dihydrate-Water Ice Aggregates

In the experiments of *Durham et al.* [1993], both ammonia dihydrate ($NH_3 \cdot 2H_2O$) and water ice deformed by dislocation creep. Water ice was 1 order of magnitude stronger than ammonia dihydrate (Figure 8a). The viscosity value for pure ammonia dihydrate (open square on Figure 8a) was deduced by *Durham et al.* [1993] from the experimental data set with the mixing model of *Tullis et al.* [1991]. Even without this model-dependent point, the evolution of bulk viscosity with increasing water ice content is close to logarithmic. The viscosity predicted by the MPG model are calculated with the stress exponents determined by *Durham et al.* [1993]. The predictions of the MPG model slightly overestimate the experimental data. Another value for the poorly constrained viscosity of pure ammonia dihydrate (which could not be synthesized) could lead to an even better agreement.

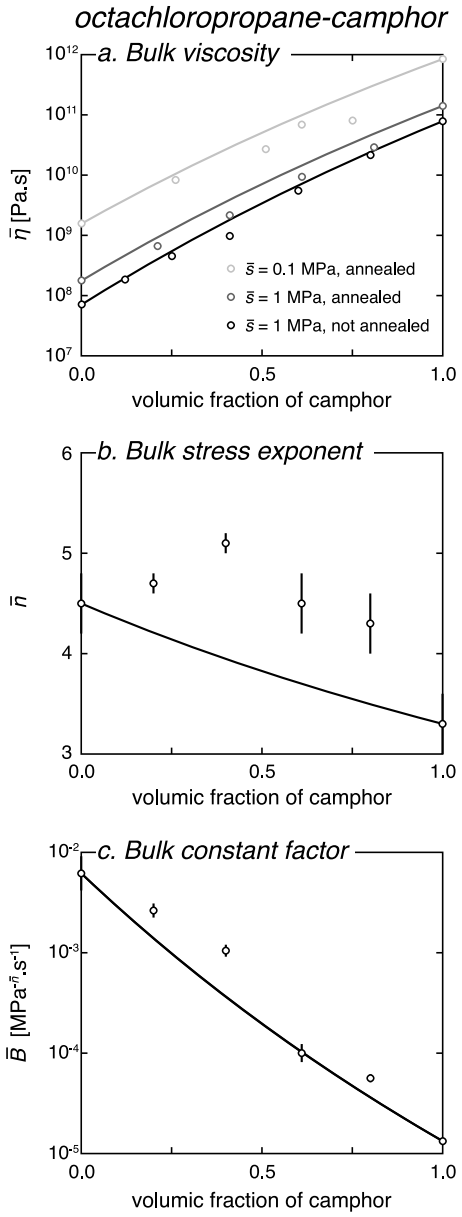

Figure 7. (a–c) Viscosity and bulk creep parameters of octachloropropane (OCP)-camphor aggregates as a function of the fraction of camphor: comparison between the experimental data set of *Bons and Urai* [1994] and the predictions of the MPG model (solid curves). The vertical bars correspond to the fitting errors calculated during the regression of the creep parameters. Temperature: 301 K, confining pressure: 0.6 MPa.

5.9. Water Ice-Sodium Sulfate Hydrate Salt Aggregates

In the experiments of *Durham et al.* [2005], both water ice and sodium sulfate hydrate salt ($Na_2SO_4.10H_2O$, NS10) deformed in the dislocation creep regime. NS10 had a viscosity 1 order of magnitude larger than water ice calculated using the parameters for pure ice I [*Durham and Stern*, 2001] (Figure 8b). The predictions of the MPG model, which are calculated with the end-member viscosities and the stress exponent of water ice ($n = 4$ [*Durham and Stern*, 2001]) and NS10 ($n = 5.4$ [*Durham et al.*, 2005]), systematically overestimate the viscosity of the aggregates by half an order of magnitude (Figure 8b). Further, the experimental values have a convex-up trend, whereas the predicted curve is convex down. Note, however, that the values for pure ice come from another experimental data set [*Durham and Stern*, 2001].

5.10. Matrix-Porphyroblast Numerical Aggregates

Several numerical studies have been published on the topics of two-phase aggregates. Here we only consider the study of *Groome et al.* [2006], since the other studies either have too little experimental data [*Tullis et al.*, 1991; *Madi et al.*, 2005], or consider very simplified geometries [*Treagus and Lan*, 2000; *Takeda and Griera*, 2006], or deal with anisotropic viscosities that cannot be treated with our approach [*Treagus*, 2003; *Dabrowski et al.*, 2012].

Groome et al. [2006] studied the mechanical effect of strong porphyroblasts (dimensionless linear viscosity of 100) growing in a weak matrix (dimensionless linear viscosity of 1). The numerical experiments were performed under simple shear boundary conditions. The bulk viscosity of the numerical aggregates shows a close to logarithmic increase with increasing porphyroblast fraction (Figure 8c). The evolution predicted by the MPG model is perfectly logarithmic, since linear viscous materials are considered (see equation (48)). The agreement between the numerical experiment and the predictions is excellent.

6. Comparison With Other Mixing Models

The MPG model makes good predictions of the bulk viscosity and the bulk creep parameters for the most of the two-phase experiments. Here a qualitative and quantitative comparison is made between the MPG model and nine representative mixing models from the literature.

6.1. Qualitative Comparison

Three classes of models are distinguished.

6.1.1. The Bounding Models

The first class of models provides bounds for the viscosity of a polyphase aggregate. The Reuss lower and Voigt upper bounds are respectively calculated as the weighted harmonic and arithmetic means of the

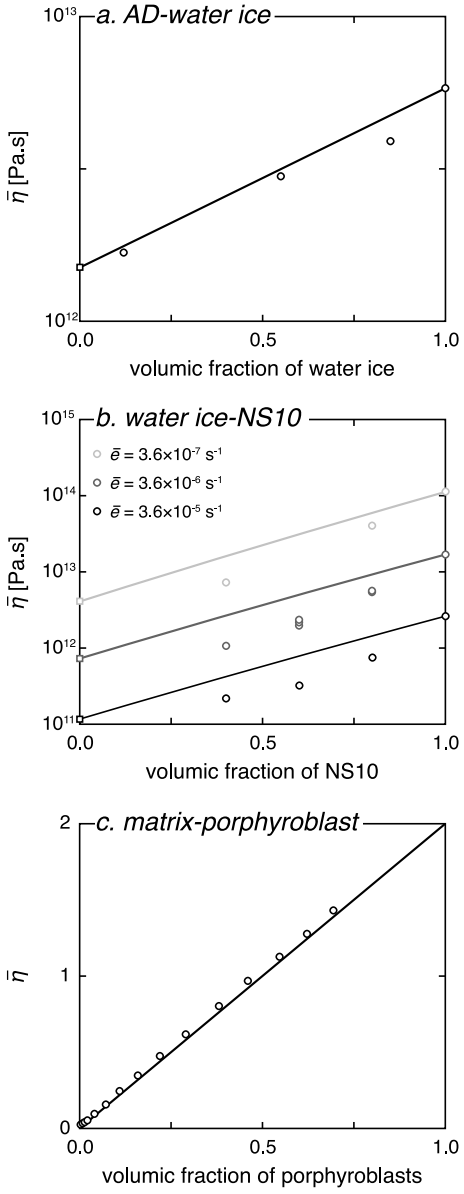

Figure 8. (a) Viscosity of ammonia dihydrate (AD)-water ice aggregates as a function of the fraction of water ice: comparison between the experimental data sets of *Durham et al.* [1993] (open circles) and the predictions of the MPG model (solid curves). Bulk strain rate: 3.5 10^{-6} s^{-1}, temperature: 167 K, confining pressure: 50 MPa. (b) Viscosity of water ice-sodium sulfate hydrate salt (NS10) aggregates as a function of the fraction of NS10: comparison between the experimental data sets of *Durham and Stern* [2001] (open circles) and the predictions of the geometric mixing models (solid curves). Bulk strain rate of 3.5 10^{-5}, 3.5 10^{-6}, and 3.5 10^{-7} s^{-1}, temperature: 233 K, confining pressure: 50 MPa. (c) Adimensioned viscosity of numerical aggregates of strong porphyroblasts embedded in a weak matrix as a function of the fraction of porphyroblasts: comparison between the numerical experiments of *Groome et al.* [2006] (open circles) and the predictions of the MPG model (solid curve).

phase viscosities [*Voigt*, 1928; *Reuss*, 1929]. Both are valid for layered aggregates of linear viscous material deformed with special boundary conditions. The mixing models for "interconnected weak layer" and "load-bearing framework" microstructures [*Handy*, 1994a, 1994b] lead to values which are close to these bounds. Theoretically, the bulk viscosity of any aggregate must lie between the Reuss and Voigt bounds [*Markov*, 1999]. Violations of the Reuss lower bound have, however, been reported [*Tullis and Wenk*, 1994; *Bruhn et al.*, 1999]. They are interpreted to be the result of anisotropies, grain growth inhibition, or enhanced diffusion along the grain boundaries.

Refined bounds have been proposed for power law materials [*Zhou*, 1995]. They are calculated by minimizing the power under constraints of arithmetic strain rate or stress partitioning. These bounds which were originally calculated numerically have been revised in this paper and correspond to the semianalytical MPA models (Zhou lower bound: MPA*e* model, Zhou upper bound: MPA*s* model). The analysis of these models (see section 4.3) reveals that the MPA*e* (resp. MPA*s*) model leads to an almost homogeneous stress (resp. strain rate) in the aggregate. This suggests that the Zhou bounds must generally lie close to the Reuss and Voigt bounds.

The bounding models predict evolutions which are either convex up or convex down (Figure 9a). A sharp increase of the viscosity with increasing fraction of the strong phase is also predicted at approximately 0.2 fraction of the strong phase for the upper bounds and at approximately 0.8 fraction of the strong phase for the lower bound. Such predictions are not consistent with either the almost logarithmic evolution of the viscosity or the S-shape trend which have been identified in most experimental data sets (see section 5). However, the lower bounds might produce good approximations when the microstructures are weak-phase supported until large fractions of the strong phase are present.

6.1.2. The Geometric Models

The second class of models is based on a geometric averaging procedure. The geometric mean (GM on Figure 9b) is one particular case of the generalized mean model [*Ji*, 2004]. The use of such a mean has no physical basis. It can, however, be considered as a good approximation for two-phase aggregates [*Ji*, 2004]. It also provides good results for averaging the elastic properties of aggregates [*Matthies and Humbert*, 1993; *Mainprice and Humbert*, 1994].

Tullis et al. [1991] proposed an empirical mixing model for aggregates of two power law materials. This assumes that the bulk behavior also follows a power law with a bulk stress exponent calculated as

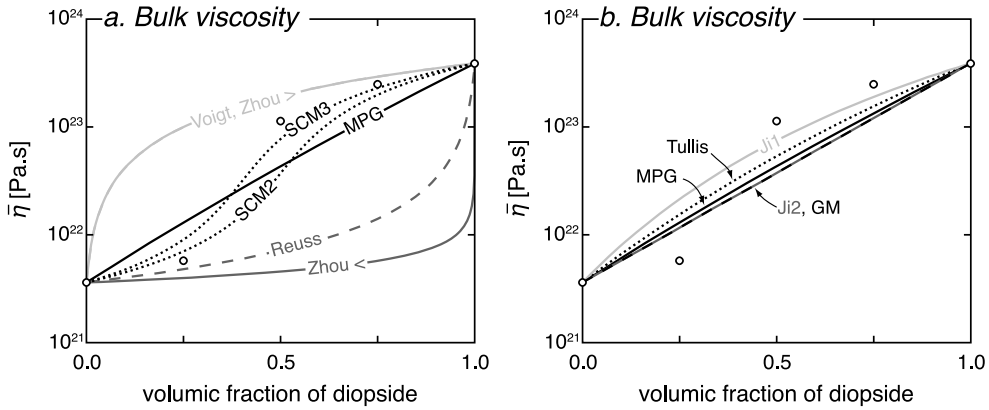

Figure 9. (a) Bulk viscosity of anorthite-diopside aggregates as a function of the diopside fraction predicted by the MPG model, the Voigt and Reuss bounds, the Zhou lower and upper bounds, and the self-consistent model for 2-D geometry (SCM2) [*Treagus*, 2002, equation (9)] and for 3-D geometry (SCM3) [*Treagus*, 2002, equation (22)]. (b) Bulk viscosity of anorthite-diopside aggregates as a function of the diopside fraction predicted by the Minimized Power Geometric (MPG) model, the geometric mean (GM), and the first and second Ji models. Predictions are calculated for temperature of 1023 K and strain rate of 10^{-16} s^{-1}. The creep parameters of anorthite and diopside correspond to the dislocation creep regime in wet conditions [*Dimanov and Dresen*, 2005]. Also shown is the viscosity calculated with the creep parameters determined for aggregates of intermediate composition (open circles). The good fit between the experimental data and the SCM model is here exceptional (see section 6.2).

the weighted geometric mean of the end-member stress exponents. This model also assumes that the bulk viscosity at a given temperature is equal to the isoviscous point of the two end-members.

Other power law models based on geometric averaging have also been proposed by *Ji and Zhao* [1993] and *Ji et al.* [2003]. The first Ji model (Ji1 on Figure 9b) assumes a homogeneous stress in the aggregate and geometric strain rate partitioning, while the second Ji model (Ji2 on Figure 9b) assumes homogeneous strain rate and geometric stress partitioning. Since neither a homogeneous strain rate nor a homogeneous stress are generally realistic [*Tullis et al.*, 1991], iterations can be used to find a more accurate model [*Ji and Zhao*, 1993; *Ji et al.*, 2003]. Results of this iterative procedure are almost identical to those of the *Tullis et al.* [1991] model [*Ji and Zhao*, 1993; *Ji et al.*, 2003].

All the geometric models predict the same close to logarithmic evolution with very similar viscosities (Figure 9b). The MPG model belongs to this group.

6.1.3. The Self-Consistent Model

The self-consistent model (SCM) approximates an aggregate of two linear elastic phases as a homogeneous aggregate made of an ellipsoidal inclusion embedded in a matrix [*Budiansky*, 1965; *Hill*, 1965; *Jiang*, 2013]. This model can also be applied to linear viscous materials [*Treagus*, 2002]. Amongst all the mixing models considered here, the SCM is the only one which is based on Newton's equation of motion. It predicts an S-shape curve with an inflection point at 0.4 strong phase fraction for 3-D geometry and 0.5 strong phase fraction for 2-D geometry (Figure 9a). Even if the SCM is not based on a transition between weak- and strong-phase supported microstructures, it could be a good approximation for such a transition.

Models for nonlinear viscous materials have also been developed using a self-consistent approach [*Duva*, 1984; *Yoon and Chen*, 1990]. They are not considered here because they assume that the strong phase of the aggregate is rigid. This results in unrealistic viscosities for aggregate compositions close to the strong end-member.

6.2. Quantitative Comparison

The ability of all the 10 models to reproduce the 15 experimental data sets presented in section 5 is assessed in a quantitative way. For each set of experimental data set and mixing model, two misfits are calculated (see Appendix B for their definitions). The mean standard deviation misfit, $\Delta\bar{\eta}$, estimates the order of magnitude of the absolute misfit between experimental and predicted bulk viscosities. The mean misfit, $\delta\bar{\eta}$, estimates the order of magnitude of the relative misfit between experimental and predicted bulk viscosities. The smaller the absolute value of the misfits are, the better the fit is. Absolute values of $\Delta\bar{\eta}$ and $\delta\bar{\eta}$ of 0.2, 0.4, and 1 indicate that the ratio between the experimental viscosities and the predicted ones is on average

Table 3. Misfits Between the Experimental and Predicted Viscosity

Experimental Data Set	Misfit	MPG	Reuss	Voigt	Zhou<	Zhou>	GM	Tullis	Ji1	Ji2	SCM[l]
en-fo[a]	$\Delta\bar{\eta}$	0.07	0.06	0.18	0.14	0.18	0.09	0.06	0.05	0.09	0.10
$N = 10$	$\delta\bar{\eta}$	+0.05	−0.02	+0.16	−0.11	+0.17	+0.07	+0.04	+0.01	+0.07	+0.09
omph-grt[b]	$\Delta\bar{\eta}$	0.04	0.17	0.17	0.40	0.17	0.04	0.04	0.05	0.04	0.07
$N = 4$	$\delta\bar{\eta}$	+0.00	−0.16	+0.17	−0.38	+0.17	+0.01	−0.01	−0.03	+0.01	+0.05
an-qtz (uni.)[c]	$\Delta\bar{\eta}$	0.11	1.04	1.88	1.04	1.88	0.13	0.11	0.13	0.11	0.50
$N = 8$	$\delta\bar{\eta}$	+0.01	−0.88	+1.85	−0.88	+1.85	−0.05	+0.01	−0.05	+0.06	−0.02
an-qtz (tri.)[c]	$\Delta\bar{\eta}$	0.50	0.17	1.21	0.17	1.14	0.52	0.50	0.52	0.48	0.68
$N = 4$	$\delta\bar{\eta}$	+0.49	−0.08	+1.20	−0.08	+1.13	+0.51	+0.49	+0.51	+0.47	+0.62
an-di (dry diff.)[d]	$\Delta\bar{\eta}$	0.39	0.86	1.36	0.86	1.36	0.39	0.39	0.39	0.39	0.68
$N = 6$	$\delta\bar{\eta}$	+0.28	−0.67	+1.24	−0.67	+1.24	+0.28	+0.28	+0.28	+0.28	+0.53
an-di (wet diff.)[d]	$\Delta\bar{\eta}$	0.27	0.49	0.82	0.49	0.82	0.27	0.27	0.27	0.27	0.38
$N = 9$	$\delta\bar{\eta}$	+0.18	−0.37	+0.74	−0.37	+0.74	+0.18	+0.18	+0.18	+0.18	+0.31
an-di (dry disl.)[d]	$\Delta\bar{\eta}$	0.46	1.58	2.14	1.58	1.03	0.67	0.50	0.67	0.46	1.37
$N = 5$	$\delta\bar{\eta}$	+0.09	−1.28	+1.92	−1.28	+0.90	+0.49	+0.24	+0.49	−0.01	+1.18
an-di (wet disl.)[d]	$\Delta\bar{\eta}$	0.47	1.21	2.08	1.21	0.91	0.68	0.52	0.68	0.45	1.13
$N = 9$	$\delta\bar{\eta}$	+0.17	−0.84	+1.88	−0.84	+0.78	+0.52	+0.30	+0.52	+0.09	+0.89
ha-cc[e]	$\Delta\bar{\eta}$	0.02	0.15	0.17	0.32	0.17	0.02	0.04	0.07	0.02	0.03
$N = 3$	$\delta\bar{\eta}$	+0.01	−0.14	+0.16	−0.29	+0.17	−0.00	+0.03	+0.07	−0.00	+0.02
ha-cc[f]	$\Delta\bar{\eta}$	0.05	0.43	0.41	0.77	0.41	0.05	0.06	0.11	0.05	0.09
$N = 9$	$\delta\bar{\eta}$	−0.00	−0.40	+0.36	−0.68	+0.36	−0.02	+0.04	+0.09	−0.02	+0.06
cc-anh[g]	$\Delta\bar{\eta}$	0.02	0.02	0.02	0.06	0.02	0.02	0.02	0.02	0.02	0.02
$N = 3$	$\delta\bar{\eta}$	+0.01	−0.01	+0.02	−0.05	+0.02	+0.01	+0.01	+0.01	+0.01	+0.01
OCP-camphor[h]	$\Delta\bar{\eta}$	0.21	1.09	1.23	1.09	0.70	0.12	0.17	0.12	0.24	0.54
$N = 13$	$\delta\bar{\eta}$	+0.18	−1.02	+1.17	−1.02	+0.68	+0.06	+0.14	+0.06	+0.22	+0.34
AD-water ice[i]	$\Delta\bar{\eta}$	0.05	0.04	0.11	0.21	0.11	0.05	0.05	0.05	0.05	0.07
$N = 3$	$\delta\bar{\eta}$	+0.04	−0.02	+0.10	−0.18	+0.10	+0.04	+0.04	+0.04	+0.04	+0.06
water ice-NS10[j]	$\Delta\bar{\eta}$	0.31	0.17	0.64	0.50	0.64	0.30	0.34	0.38	0.30	0.40
$N = 8$	$\delta\bar{\eta}$	+0.30	−0.13	+0.61	−0.43	+0.61	+0.29	+0.33	+0.37	+0.29	+0.39
matrix-porph.[k]	$\Delta\bar{\eta}$	0.03	0.49	0.64	0.49	0.64	0.03	0.03	0.03	0.03	0.15
$N = 15$	$\delta\bar{\eta}$	−0.03	−0.37	+0.59	−0.37	+0.59	−0.03	−0.03	−0.03	−0.03	−0.07
average	$\Delta\bar{\eta}$	0.20	0.53	0.87	0.62	0.68	0.22	0.21	0.23	0.20	0.41
	$\delta\bar{\eta}$	+0.12	−0.43	+0.81	−0.51	+0.63	+0.16	+0.14	+0.17	+0.11	+0.30

[a]Enstatite-forsterite (en-fo) aggregates [*Ji et al.*, 2001].
[b]Omphacite-garnet (omph-grt) aggregates [*Jin et al.*, 2001].
[c]Anorthite-quartz (an-qtz) aggregates under uniaxial (uni.) and triaxial conditions (tri.) [*Xiao et al.*, 2002].
[d]Anorthite-diopside (an-di) aggregates in dry and wet, diffusion (diff.), and dislocation (disl.) creep regimes [*Dimanov and Dresen*, 2005].
[e]Halite-calcite (ha-cc) aggregates [*Jordan*, 1987].
[f]Halite-calcite (ha-cc) aggregates [*Bloomfield and Covey-Crump*, 1993].
[g]Calcite-anhydrite (cc-anh) aggregates [*Barnhoorn et al.*, 2005].
[h]OCP-camphor aggregates [*Bons and Urai*, 1994].
[i]AD-water ice aggregates (AD: ammonium dihydrate) [*Durham and Stern*, 2001].
[j]Water ice-NS10 aggregates (NS10: sodium sulfate hydrate salt) [*Durham et al.*, 2005].
[k]Matrix-porphyroblast aggregate [*Groome et al.*, 2006].
[l]The SCM for 3-D geometry is used for all laboratory experiments, and the SCM for 2-D geometry is used for the matrix-porphyroblast experiment of *Groome et al.* [2006].

$10^{0.2} \approx 1.6$, $10^{0.4} \approx 2.5$, and $10^{1} = 10$, respectively. Positive (resp. negative) values of $\delta\bar{\eta}$ indicate that the considered mixing model overestimates (resp. underestimates) the experimental viscosity. The values of the misfits for the 15 experimental data sets and the 10 mixing models are presented in Table 3. Values of the misfits averaged over the 15 experimental data sets are also given. The separation in three classes of models is also highlighted by the misfits values.

The bounding models (Reuss, Voigt, Zhou<, and Zhou> models in Table 3) have the largest $\Delta\bar{\eta}$ values. Their misfits are larger than 0.4 for more than half of the experimental data sets. Further, values larger than 1 also occur. This means that the bounding models can fail at reproducing the experimental viscosity within 1 order of magnitude. As expected, the lower bounds underestimate the experimental viscosity (average $\delta\bar{\eta}$ misfit lower than −0.4). Conversely, the upper bounds overestimate the experimental viscosity (average $\delta\bar{\eta}$ misfit larger than +0.6). The experimental data sets on anorthite-quartz aggregates under triaxial conditions [*Xiao et al.*, 2002] and NS10-water ice aggregates [*Durham and Stern*, 2001] are, in that respect,

exceptional. The Reuss bound has the lowest $\Delta\bar{\eta}$ misfit for them. Such an agreement is due to the convex-up trend of the experimental viscosity (see Figures 3c and 8b), similar to the trend of the Reuss bound. It must be emphasized that the viscosity of one end-member of these three data sets does not come from the same experiments as the other viscosities. Therefore, we conclude that the bounding models do not provide a good fit to the experiments on two-phase aggregates, with a few dubious exceptions.

The geometric models (MPG, GM, Tullis, Ji1, and Ji2 models in Table 3) generally have the lowest $\Delta\bar{\eta}$ values. Their misfits are larger than 0.4 for only two experimental data sets and lower than 0.1 for seven experimental data sets. The $\delta\bar{\eta}$ is almost always positive which means that this class of models tends to overestimate the experimental bulk viscosity. For aggregates of linear viscous materials, all the geometric models predict the same viscosities as indicated by the identical misfit values. All the geometric models have an average $\Delta\bar{\eta}$ misfit which is close to 0.2. This means that they reproduce the experimental viscosities very well. The best fit is achieved for the MPG and the second Ji (Ji2) models.

The SCM has variable $\Delta\bar{\eta}$ misfits which can be larger than 1. It also overestimates almost systematically the bulk viscosity. The largest $\Delta\bar{\eta}$ misfits are calculated for the experiments on anorthite-diopside aggregates in dislocation creep regime [*Dimanov and Dresen*, 2005]. Interestingly, these data sets show an S-shape trend which could be similar to the one predicted by the SCM. In these cases, the large values of both misfits indicate that the predicted S-shape curve has its inflection point at smaller fractions of the strong phase than the experimental trend. Despite the interesting trend of the bulk viscosity predicted by the SCM model, this model fails to accurately fit with the experiments on two-phase aggregates.

Finally, note that some experimental data sets are easier to fit than others. The experiments on end-members having close viscosities are fitted very well by all the models, like, for example, the calcite-anhydrite experiments [*Barnhoorn et al.*, 2005]. Similarly, there are experiments which are relatively poorly fitted by all the models, like, for example, anorthite-diopside experiments in dislocation creep regime [*Dimanov and Dresen*, 2005]. These experiments have been carried out with end-members having very different viscosities and also show microstructural complexities. This does not mean, however, that experiments with end-members having very different viscosities are not fitted by the models of the geometric group and, especially, by the MPG model.

7. Discussion and Conclusions

Since assumptions were necessary to develop the MPG model (see section 2.2), we propose to discuss their geological validity here in more details. Indeed, if the MPG model appears to be one of the best models for reproducing accurately experimental data, it comprises some limitations that have to be kept in mind.

7.1. Isotropy and Homogeneity of the Aggregate

The first assumption requires that there exists a scale at which the considered polyphase rock can be considered as homogeneous. Thus, the scale at which the MPG model is used has therefore to be considered with caution. It has to be much larger than the grain scale and much smaller than the characteristic length scale of chemical, mineralogical, and lithological variations.

Isotropy has also been assumed even if most rocks deformed in the ductile field are initially anisotropic or become anistropic after a minor amount of strain due to the development of a grain shape [*Lister and Snoke*, 1984; *Schmid et al.*, 1987; *Shelley*, 1989; *Herwegh and Handy*, 1998] or lattice [*Wilson*, 1975; *Etchecopar*, 1977; *Lister and Price*, 1978; *Jessell*, 1987] preferred orientations. This limitation can be overcome if the scale of the anisotropy is much larger than the grain scale. Otherwise, since the MPG model lies between the theoretical Reuss and Voigt bounds, the error is expected to be reasonable.

7.2. Unicity of the Deformation Mechanism

Viscous creep with known creep parameters has been considered as the only deformation mechanism. First, this assumption simplifies considerably the grain-scale processes that accommodate deformation. Indeed, the MPG model does not consider any interaction between the phases. Enhanced diffusion along the grain boundaries [*Bruhn et al.*, 1999], secondary mineral phases [*Herwegh et al.*, 2003], and chemical reactions between the phases [*Sundberg and Cooper*, 2008] tend to reduce the bulk viscosity with respect to the end-member viscosities. The generally good agreement between the predictions of the MPG model and the experiments indicates that these processes have a reduced impact, at least in the laboratory experiments considered here. Second, the pressure-dependent deformation mechanisms are neglected by the

MPG model. This simplification can, however, be tested by comparing the stress which is necessary for brittle failure and cataclasis with the stress predicted by the MPG model (in both polyphase rock and phases). Third, dynamic processes like grain-size reduction and metamorphic reaction are not included. They can, however, be implemented in a time- or a strain-dependent scheme together with the MPG model. This is then used to calculate the stress in the grains, and piezometers are used to calculate a consistent grain size.

The creep parameters of the phases which are used as inputs of the MPG model are also a limitation. Detailed experiments have not been carried out on all the major rock-forming minerals. Even though the rheological behaviors of quartz, feldspar, pyroxene, olivine, garnet, and calcite are fairly well understood [*Herwegh et al.*, 2005; *Bürgmann and Dresen*, 2008; *Karato*, 2008], other important minerals (phyllosilicates, amphiboles, and calcsilicates) are poorly constrained. Further, the temperature, strain rate, and stress conditions that are relevant for geological problems require extrapolations of the creep parameters far out of the range of experimental conditions. Such extrapolations have, however, been suggested to be valid as long as the deformation mechanisms are similar [*Dimanov and Dresen*, 2005].

7.3. Physical Formulation of the Model

The third assumption of the MPG models states that all the grains from phase *i* have the same strain rate e_i and stress s_i. While ensuring stress and strain rate continuity between the grains belonging to the same phase, this assumption does not respect the continuity equations at the boundary between grains belonging to different phases. If this is valid for a single ellipsoidal inclusion embedded in an infinite matrix with a coupled interface [*Eshelby*, 1957], this is not valid anymore in other cases (e.g., decoupling between the phases or power law materials). Numerical experiments show that the strain rate and stress fields within the same phase are heterogeneous, even for very simple geometries [*Schmid*, 2005; *Dabrowski et al.*, 2012; *Le Pourhiet et al.*, 2013; *Mancktelow*, 2013]. In natural rocks, heterogeneous stress fields in porphyroclasts are highlighted, for example, by core-and-mantle structures [*White*, 1976], mechanical twinning of leftover grains [*Burkhard*, 1993], or myrmekite growth in the compressional quadrants of K feldspar [*Simpson and Wintsch*, 1989].

However, it has to be noted that this third assumption has been made, most often implicitly, in previous papers developing mixing models [*Handy*, 1990; *Tullis et al.*, 1991; *Handy*, 1994a, 1994b; *Ji*, 2004; *Ji and Zhao*, 1993; *Ji et al.*, 2003; *Jiang et al.*, 2005; *Zhou*, 1995]. It has always been considered as a reasonable simplification up to now. It is clear that the consistency with the continuity equations should be the prerequisite of any exact mixing model. Such a model is, however, impossible to develop since it would require a perfect statistical knowledge of the aggregate geometry, which is, unfortunately, impossible in practice [*Markov*, 1999]. Two types of simplifications have therefore been considered so far.

1. On the one hand, one can assume a simple geometry for which the strain rate and stress fields can be calculated. This is the approach of the *Reuss* [1929] and *Voigt* [1928] models in which the different phases are linked in series and in parallel, respectively. This is also the approach of the self-consistent model [*Budiansky*, 1965; *Hill*, 1965; *Jiang*, 2013] that assumes that the stress and strain rate distribution corresponds to the one of an elliptical inclusion welded to its matrix. Each of these mixing models is exact only for a simple given geometry. It constitutes thus an approximation for all other more complex geometries.
2. On the other hand, one can assume simplified strain rate and stress fields that are not necessarily consistent with the continuity of strain rate and stress at grain scale. This means that the local mechanical constraints are relaxed in such a mixing model. This is the choice we made here in our study, as in several other previous studies [*Handy*, 1990; *Tullis et al.*, 1991; *Handy*, 1994a, 1994b; *Ji*, 2004; *Ji and Zhao*, 1993; *Ji et al.*, 2003; *Jiang et al.*, 2005; *Zhou*, 1995].

Mixing models are, therefore, approximations. Thus, assessing a mixing model has to be done through a comparison of its predictions with laboratory and numerical experiments. If the model is able to predict a reliable bulk strain rate (or stress) for a given experimental bulk stress (or strain rate), it can be used to describe accurately the bulk behavior of the aggregate, even though it does not describe exactly its local internal behavior (by assuming a specific geometry or a simplified stress and strain rate field). The comparison with experiments carried out in the present study (see sections 5 and 6) shows that our model provides one of the best fits. Especially, in spite of the local contradiction with the continuity principle, the predictions of the MPG model are in very good agreement with the matrix-porphyroblast numerical experiments [*Groome et al.*, 2006] that are precisely relying in this principle.

The reason the MPG model is able to reproduce accurately the experiment data sets while contradicting at local scale the continuity equation remains unclear. One explanation could be that the constant phase strain rates and stresses can be viewed as mean values. The geometric partitioning (used in the constrained minimization) would then allow a relatively good description of the partitioning once the strain rate and stress is averaged phase by phase. This explanation can be tested by numerical modeling which is able to track precisely the strain rate and stress fields.

Moreover, we used the principle of least action out of its application range in the case of nonequilibrium thermodynamics (see section 2.2). This implies that the viscosity calculated with the MPG model does not necessarily correspond to steady state. Here again, in spite of this assumption, comparison between the predictions of the MPG model and experimental data shows good agreement. This might indicate that an aggregate described with the MPG model is close enough to equilibrium (so that nonequilibrium thermodynamics is not needed) and that our use of the principle of least action is partly valid.

7.4. Advantages of the MPG Model

The MPG model is thus affected by several limitations, and hence, its predictions have to be tested by natural data. However, these limitations are inherent to all the mixing models. To that extent, the MPG model is as good as the existing models. However, compared to them, it also has important advantages.

1. The MPG model provides a good fit with the experimental data, even for large viscosity contrasts, as shown by the ratio of experimental and predicted viscosities (1.6 on average, see section 6.2 and Table 3). Such a good fit does not occur with the existing models, except for those based on geometric averaging [*Tullis et al.*, 1991; *Ji and Zhao*, 1993; *Ji et al.*, 2003; *Ji*, 2004].
2. Experimental work has shown that creep of most single-mineral aggregates can be described by a power law. It has also shown that the rocks made with these minerals also follow a power law. The processes responsible for this transmission are very complex and are not explicitly taken into account in our model. Instead, the geometric mean constraints are responsible for it. We suggest, therefore, that these constraints can be considered as a way to approximate complex microstructural processes occurring in a polyphase rock in one simple equation. Thus, the bulk power law behavior does not have to be assumed a priori by the MPG model.
3. The MPG model predicts the partitioning of strain rate and stress in the phases. This has interesting implications for upscaling the stress estimated by paleopiezometry. For example, stress values deduced from quartz present together with stronger minerals will underestimate the bulk stress.
4. The MPG model is analytical, which means that computations are straightforward and do not need any iteration process. It is also possible to apply it to polyphase rocks containing any number of phases with a power law behavior. Its implementation into numerical models accounting for metamorphic reactions is therefore easy. Since some metamorphic reactions lead to important viscosity changes, such an implementation would have important consequences on the mechanical behavior of the modeled rocks.

Appendix A: Ratio of the Preexponential Factors of the MPG Models

The ratio of the bulk viscosities predicted by the two MPG models depends mainly on the ratio of the bulk preexponential factors. In this appendix, we bound this ratio. The ratio between the two bulk preexponential factors is equal to

$$R = \frac{\bar{A}_s}{\bar{A}_e} = \frac{\sum_i \frac{\phi_i}{n_i+1} \prod_i (n_i+1)^{\phi_i a_i / \sum_j \phi_j a_j}}{\left(\sum_i \frac{\phi_i n_i}{n_i+1}\right)^{-\bar{n}} \prod_i \left(\frac{n_i}{n_i+1}\right)^{\phi_i a_i n_i / \sum_j \phi_j a_j}}. \tag{A1}$$

In order to simplify this ratio, we introduce the notation

$$X = \sum_i \frac{\phi_i}{n_i+1} \tag{A2}$$

and use the following properties:

$$X = \frac{\sum_i \phi_i a_i}{\prod_i (n_i+1)}, \tag{A3}$$

$$1 - X = \sum_i \frac{\phi_i n_i}{n_i + 1} = \frac{\sum_i \phi_i a_i n_i}{\prod_i (n_i + 1)}, \tag{A4}$$

and

$$\bar{n} = \frac{\sum_i \phi_i a_i n_i}{\sum_i \phi_i a_i} = \frac{1 - X}{X}. \tag{A5}$$

The ratio between the bulk preexponential factors can then be simplified:

$$\begin{aligned} R &= \frac{X \prod_i (n_i + 1)^{\phi_i a_i / \sum_i \phi_j a_j}}{(1 - X)^{(X-1)/X} \prod_i \left(\frac{n_i}{n_i+1}\right)^{\phi_i a_i n_i / \sum_i \phi_j a_j}}, \\ &= X(1 - X)^{(1-X)/X} \prod_i \left(\frac{n_i + 1}{n_i^{n_i/(n_i+1)}}\right)^{\phi_i a_i (n_i+1) / \sum_i \phi_j a_j}, \\ &= \left(X^X (1 - X)^{(1-X)}\right)^{1/X} \prod_i \left(\frac{n_i + 1}{n_i^{n_i/(n_i+1)}}\right)^{1/X}, \\ &= \left(X^X (1 - X)^{(1-X)} \prod_i \left(\frac{n_i + 1}{n_i^{n_i/(n_i+1)}}\right)^{\phi_i}\right)^{1/X} \end{aligned} \tag{A6}$$

In order to remove the powers in equation (A6), we now consider $r = \ln R^X$:

$$r = X \ln(X) + (1 - X) \ln(1 - X) + \sum_i \phi_i \ln\left(\frac{n_i + 1}{n_i^{n_i/(n_i+1)}}\right). \tag{A7}$$

The function $\mathrm{H}(x) = x \ln(x) + (1 - x) \ln(1 - x)$ is introduced. Thus,

$$r = \mathrm{H}(X) + \sum_i \phi_i \ln\left(\frac{n_i + 1}{n_i^{n_i/(n_i+1)}}\right). \tag{A8}$$

The indexed variable of the summation in equation (A7) is expended as follows:

$$\begin{aligned} \ln\left(\frac{n_i + 1}{n_i^{n_i/(n_i+1)}}\right) &= \ln(n_i + 1) - \frac{n_i}{n_i + 1} \ln n_i, \\ &= -\ln\left(\frac{1}{n_i + 1}\right) - \frac{n_i}{n_i + 1} \ln n_i, \\ &= -\frac{n_i + 1}{n_i + 1} \ln\left(\frac{1}{n_i + 1}\right) - \frac{n_i}{n_i + 1} \ln n_i, \\ &= -\frac{1}{n_i + 1} \ln\left(\frac{1}{n_i + 1}\right) - \frac{n_i}{n_i + 1} \ln\left(\frac{n_i}{n_i + 1}\right), \\ &= -\frac{1}{n_i + 1} \ln\left(\frac{1}{n_i + 1}\right) - \left(1 - \frac{1}{n_i + 1}\right) \ln\left(1 - \frac{1}{n_i + 1}\right), \\ &= -\mathrm{H}\left(\frac{1}{n_i + 1}\right). \end{aligned} \tag{A9}$$

Equations (A2), (A8), and (A9) lead to a simple expression of r:

$$r = \mathrm{H}\left(\sum_i \phi_i \frac{1}{n_i + 1}\right) - \sum_i \phi_i \mathrm{H}\left(\frac{1}{n_i + 1}\right). \tag{A10}$$

Since H is a convex-up function,

$$\mathrm{H}\left(\sum_i \phi_i \frac{1}{n_i + 1}\right) \leq \sum_i \phi_i \mathrm{H}\left(\frac{1}{n_i + 1}\right). \tag{A11}$$

Therefore, $r \leq 0$ and R is lower than 1. In equation (A10), the values at which H is evaluated lie between 0 and 1. In this range, H is bounded by $-\ln(2)$ and 0. This property provides a lower bound for r:

$$r \geq -\ln(2). \tag{A12}$$

A lower bound for R is thus $1/2^{1/X}$. Since the minimum stress exponent in rocks is 1, X is lower than $1/2$, and $1/X$ is larger than 2. Finally, R is larger than 1/4. The ratio of the bulk preexponential factors corresponding to the two MPG models lies between 0.25 and 1.

Appendix B: The Misfit Parameters

One experimental data set is characterized by M subsets of experiments conducted under the same temperature and stress/strain rate conditions. In each subset j, there are N_j experiments on aggregates of different intermediate compositions. The end-member viscosities being always fitted by the models, they are not taken into account in the calculation of the misfits. The mean standard deviation misfit estimates the order of magnitude of the absolute misfit between the experimental values $\bar{\eta}^e$ and the values predicted by the mixing models $\bar{\eta}^m$:

$$\Delta\bar{\eta} = \frac{1}{M}\sum_{j=1}^{M}\sqrt{\frac{1}{N_j}\sum_{i=1}^{N_j}(\log\bar{\eta}_i^m - \log\bar{\eta}_i^e)^2}. \tag{B1}$$

This misfit, without the logarithmic scaling, has been used to assess the quality of brittle failure criterion [*Colmeranes and Zoback*, 2002; *Benz and Schwab*, 2008]. The logarithmic scaling is used to put all the misfits at the same order of magnitude (between 0 and 3). $\Delta\bar{\eta}$ values of 1 and 2 indicate an absolute difference of 1 and 2 orders of magnitude between the experimental viscosities and the predicted ones. $\Delta\bar{\eta}$ values of 0.2, 0.4, 0.6, and 0.8 indicate on average a ratio of $10^{0.2} \approx 1.6$, $10^{0.4} \approx 2.5$, $10^{0.6} \approx 4.0$, and $10^{0.8} \approx 6.3$ between the experimental and predicted viscosity. The mean misfit estimates the order of magnitude of the relative misfit between the experimental and the predicted values:

$$\delta\bar{\eta} = \frac{1}{M}\sum_{j=1}^{M}\frac{1}{N_j}\sum_{i=1}^{N_j}\left(\log\bar{\eta}_i^m - \log\bar{\eta}_i^e\right). \tag{B2}$$

Positive (resp. negative) values of $\delta\bar{\eta}$ indicate that the considered mixing model tends to overestimate (resp. underestimate) the experimental viscosity.

Notation

Term definition and unit.

- a_i a function of the phase stress exponents.
- A preexponential factor, $Pa^{-n}\ s^{-1}$.
- B product of the preexponential factor and the Arrhenius term in a power law, $Pa^{-n}\ s^{-1}$.
- C constraint for the minimization, s^{-1} or Pa.
- e second invariant of the deviatoric strain rate tensor, s^{-1}.
- i index of the current phase.
- L auxiliary function introduced for the Lagrange multiplier method, $W\ m^{-3}$.
- M number of experiments in the same conditions.
- n stress exponent.
- N number of phases in the polyphase rock.
- P dissipated mechanical power, $W\ m^{-3}$.
- Q activation energy, $J\ mol^{-1}$.
- R universal gas constant, $J\ mol^{-1}\ K^{-1}$.
- s second invariant of the deviatoric stress tensor, Pa.
- T absolute temperature, K.
- $\delta\bar{\eta}$ mean misfit.
- $\Delta\bar{\eta}$ standard deviation misfit.

η effective viscosity, Pa s.
λ Lagrange multiplier, Pa or s^{-1}.
ξ scaled Lagrange multiplier, Pa s.
ϕ_i volumetric fraction of phase *i*.

Acknowledgments
B.H. would like to thank Laetitia Le Pourhiet (for mentioning the mechanical applications of the geometric mean), Étienne Ghys (for showing the very nice convexity trick in the bounding of the preexponential factors ratio), Neil Mancktelow, Giorgio Pennacchioni, Florian Lehner, Martin Schöpfer, and Marta Adamuszek (for fruitful discussions even though they might disagree with the content of the paper), and Marvin Pentz Gaye (for his inspiring initials). P.Y. and B.H. thank the INSU Syster program that funded partially this work. Hugh Rice is thanked for editing very carefully the English. We are also grateful to Tom Parsons for editorial handling, Reid Cooper, an anonymous Associate Editor, Brian Evans, and an anonymous reviewer for their thoughtful remarks which highly improved the quality of the manuscript.

References

Aleksandrov, K. S., and L. A. Aizenberg (1966), Method of calculating physical constants of polycrystalline materials, *Dokl. Akad. Nauk SSSR*, *167*, 1028–1031.
Angiboust, S., P. Agard, H. Raimbourg, P. Yamato, and B. Huet (2011), Subduction interface processes recorded by eclogite-facies shear zones (Monviso, W. Alps), *Lithos*, *127*, 222–238.
Barnhoorn, A., M. Bystricky, K. Kunze, L. Burlini, and J.-P. Burg (2005), Strain localisation in bimineralic rocks: Experimental deformation of synthetic calcite–anhydrite aggregates, *Earth Planet. Sci. Lett.*, *240*, 748–763.
Benz, T., and R. Schwab (2008), A quantitative comparison of six rock failure criteria, *Int. J. Rock Mech. Min. Sci.*, *45*, 1176–1186.
Bloomfield, J. P., and S. J. Covey-Crump (1993), Correlating mechanical data with microstructural observations in deformation experiments on synthetic two-phase aggregates, *J. Struct. Geol.*, *15*, 1007–1019.
Bons, P. D., and J. L. Urai (1994), Experimental deformation of two-phase rock analogues, *Mater. Sci. Eng.*, *A175*, 221–229.
Budiansky, B. (1965), On the elastic moduli of some heterogeneous materials, *J. Mech. Phys. Solids*, *13*, 223–227.
Burkhard, M. (1993), Calcite-twins, their geometry, appearance and significance as stress-strain markers and indicators of tectonic regime: A review, *J. Struct. Geol.*, *15*, 351–368.
Brodie, K., and E. Rutter (2000), Deformation mechanisms and rheology: Why marble is weaker than quartzite, *J. Geol. Soc.*, *157*, 1093–1096.
Bruhn, D. F., D. L. Olgaard, and L. N. Dell'Angelo (1999), Evidence for enhanced deformation in two-phase rocks: Experiments on the rheology of calcite-anhydrite aggregates, *J. Geophys. Res.*, *104*, 707–724.
Bürgmann, R., and G. Dresen (2008), Rheology of the lower crust and upper mantle: Evidence from rock mechanics, geodesy, and field observations, *Ann. Rev. Earth Planet. Sci.*, *36*, 531–567.
Carter, N. L., S. T. Horseman, J. E. Russell, and J. Handin (1993), Rheology of rocksalt, *J. Struct. Geol.*, *15*, 1257–1271.
Colmeranes, L. M., and M. D. Zoback (2002), A statistical evaluation of intact rock failure criteria constrained by polyaxial test data for five different rocks, *Int. J. Rock Mech. Min. Sci.*, *39*, 695–729.
Dabrowski, M., D. W. Schmid, and Y. Y. Podladchikov (2012), A two-phase composite in simple shear: Effective mechanical anisotropy development and localization potential, *J. Geophys. Res.*, *117*, B08406, doi:10.1029/2012JB009183.
de Groot, S. R., and P. Mazur (1984), *Non-Equilibrium Thermodynamics,* Dover, New York.
Dimanov, A., and G. Dresen (2005), Rheology of synthetic anorthite-diopside aggregates: Implications for ductile shear zones, *J. Geophys. Res.*, *110*, B07203, doi:10.1029/2004JB003431.
Dresen, G., B. Evans, and D. L. Olgaard (1998), Effect of quartz inclusions on plastic flow in marble, *J. Geophys. Res.*, *8*, 1245–1248.
Durham, W. B., and L. A. Stern (2001), Rheological properties of water ice—Applications to satellites of the outer planets, *Ann. Rev. Earth Planet. Sci.*, *29*, 295–330.
Durham, W. B., S. H. Kirby, and L. A. Stern (1993), Flow of ices in the ammonia-water system, *J. Geophys. Res.*, *98*, 17,667–17,682.
Durham, W. B., L. A. Stern, T. Kubo, and S. H. Kirby (2005), Flow strength of highly hydrated Mg- and Na-sulfate hydrate salts, pure and in mixtures with water ice, with application to Europa, *J. Geophys. Res.*, *110*, E12010, doi:10.1029/2005JE002475.
Duva, J. M. (1984), A self-consistent analysis of the stiffening effect of rigid inclusions on a power-law material, *J. Eng. Mater. Tech.*, *106*, 317–321.
Eshelby, J. D. (1957), The determination of the elastic field of an ellipsoidal inclusion, and related problems, *Proc. R. Soc. London*, *241*, 376–396.
Etchecopar, A. (1977), A plane kinematic model of progressive deformation in a polycrystalline aggregate, *Tectonophysics*, *50*, 481–505.
Furusho, M., and K. Kanagawa (1999), Transformation-induced strain localization in a lherzolite mylonite from the Hidaka metamorphic belt of central Hokkaido, Japan, *Tectonophysics*, *313*, 411–432.
Grasemann, B., and C. Tschegg (2012), Localization of deformation triggered by chemo-mechanical feedback processes, *Geol. Soc. Am. Bull.*, *124*, 737–745, doi:10.1130/B30504.1.
Groome, W. G., S. E. Johnson, and P. Koons (2006), The effects of porphyroblast growth on the effective viscosity of metapelitic rocks: Implications for the strength of the middle crust, *J. Metamorph. Geol.*, *24*, 389–407.
Gueydan, F., Y. Leroy, L. Jolivet, and P. Agard (2003), Analysis of continental midcrustal strain localization induced by microfracturing and reaction-softening, *J. Geophys. Res.*, *108*, 2064, doi:10.1029/2001JB000611.
Handy, M. R. (1990), The solid-state flow of polymineralic rocks, *J. Geophys. Res.*, *95*, 8647–8661.
Handy, M. R. (1994a), Flow laws for rocks containing two non-linear viscous phases: A phenomenological approach, *J. Struct. Geol.*, *16*, 287–301.
Handy, M. R. (1994b), The energetics of steady state heterogeneous shear in mylonitic rock, *Mater. Sci. Eng.*, *A175*, 261–272.
Handy, M. R., and H. Stünitz (2002), Strain localisation by fracturing and reaction weakening—A mechanism for initiating exhumation of subcontinental mantle beneath rifted margins, in *Deformation Mechanisms, Rheology and Tectonics: Current Status and Future Perspectives*, vol. 200, edited by S. De Meer et al., pp. 387–407, Geol. Soc. Spec. Publ., London, U. K.
Herwegh, M., X. Xiao, and B. Evans (2003), The effect of dissolved magnesium on diffusion creep in calcite, *Earth Planet. Sci. Lett.*, *212*, 457–470.
Herwegh, M., J. De Bresser, and J. Ter Heege (2005), Combining natural microstructures with composite flow laws: An improved approach for the extrapolation of lab data to nature, *J. Struct. Geol.*, *27*, 503–521.
Herwegh, M., and M. R. Handy (1998), The origin of shape preferred orientations in mylonite: Inferences from in-situ experiments on polycrystalline norcamphor, *J. Struct. Geol.*, *20*, 681–694.
Hill, R. (1965), A self-consistent mechanics of composite materials, *J. Mech. Phys. Solids*, *13*, 213–222.
Hobbs, B., A. Ord, M. I. Spalla, G. Gosso, and M. Zucali (2010), The interaction of deformation and metamorphic reactions, in *Advances in Interpretation of Geological Processes: Refinement of Multi-Scale Data and Integration in Numerical Modelling*, vol. 332, edited by M. I. Spalla, A. M. Marotta, and G. Gosso, pp. 189–223, Geol. Soc. Spec. Publ., London, U. K.
Hutchinson, J. W. (1976), Bounds and self-consistent estimates for creep of polycrystalline materials, *Proc. R. Soc. London*, *348*, 101–127.
Jessell, M. A. (1987), Grain-boundary migration microstructures in a naturally deformed quartzite, *J. Struct. Geol.*, *9*, 1007–1014.

Jessell, M. A., P. D. Bons, A. Griera, L. A. Evans, and C. J. L. Wilson (2009), A tale of two viscosities, *J. Struct. Geol.*, *31*, 719–736.
Ji, S. (2004), A generalized mixture rule for estimating the viscosity of solid-liquid supensions and mechanical properties of polyphase rocks and composite materials, *J. Geophys. Res.*, *109*, B10207, doi:10.1029/2004JB003124.
Ji, S., and P. Zhao (1993), Rheology of multiphase rocks in terms of the volume fractions and flow laws of the constituent phases, *Earth Planet. Sci. Lett.*, *117*, 181–187.
Ji, S., Z. Wang, and R. Wirth (2001), Bulk flow strength of forsterite–enstatite composites as a function of forsterite content, *Tectonophysics*, *341*, 69–93.
Ji, S., P. Zhao, and B. Xia (2003), Flow laws of multiphase materials and rocks from end-member flow laws, *Tectonophysics*, *370*, 129–145.
Jiang, D. (2013), The motion of deformable ellipsoids in power-law viscous materials: Formulation and numerical implementation of a micromechanical approach applicable to flow partitioning and heterogeneous deformation in Earth's lithosphere, *J. Struct. Geol.*, *50*, 22–34.
Jiang, Y., S. Zang, and R. Wei (2005), Decibel error test and flow law of multiphase rocks based on energy dissipation theory, *Earth Planet. Sci. Lett.*, *235*, 200–210.
Jin, Z. M., J. Zhang, and H. W. Green II (2001), Eclogite rheology: Implications for subducted lithosphere, *Geology*, *29*(8), 667–670.
Jolivet, L., H. Raimbourg, L. Labrousse, D. Avigad, Y. Leroy, H. Austrheim, and T. B. Andersen (2005), Softening trigerred by eclogitization, the first step toward exhumation during continental subduction, *Earth Planet. Sci. Lett.*, *237*, 532–547.
Jordan, P. G. (1987), The deformational behaviour of bimineralic limestone-halite aggregates, *Tectonophysics*, *135*, 185–197.
Karato, S. I. (1995), Plastic deformation of garnets: Systematics and implications for the rheology of the mantle transition zone, *Earth Planet. Sci. Lett.*, *130*, 13–30.
Karato, S. I. (2008), *Deformation of Earth Materials: An Introduction to the Rheology of Solid Earth,* Cambridge Univ. Press, Cambridge.
Kirby, S. H. (1985), Rock mechanics observations pertinent to the rheology of the continental lithosphere and the localization of strain along shear zones, *Tectonophysics*, *119*, 1–27.
Kohlstedt, D., B. Evans, and S. J. Mackwell (1995), Strength of the lithosphere: Constraints imposed by laboratory experiments, *J. Geophys. Res.*, *100*, 17,587–17,602.
Le Pourhiet, L., B. Huet, P. Agard, L. Labrousse, L. Jolivet, and K. Yao (2013), Strain localisation in mechanically layered rocks, insights from numerical modelling, *Solid Earth*, *4*, 1165–1204, doi:10.5194/sed-4-1165-2012.
Lister, G., and G. P. Price (1978), Fabric development in a quartz-feldspar mylonite, *Tectonophysics*, *49*, 37–78.
Lister, G., and A. W. Snoke (1984), S-C mylonites, *J. Struct. Geol.*, *6*, 617–638.
Madi, K., S. Forest, P. Cordier, and M. Boussuge (2005), Numerical study of creep in two-phase aggregates with a large rheology contrast: Implications for the lower mantle, *Earth Planet. Sci. Lett.*, *237*, 223–238.
Mainprice, D., and M. Humbert (1994), Methods of calculation petrophysical properties from lattice preferred orientation data, *Surv. Geophys.*, *15*, 575–592.
Mancktelow, N. S. (2013), Behaviour of an isolated rimmed elliptical inclusion in 2D slow incompressible viscous flow, *J. Struct. Geol.*, *46*, 235–254.
Markov, K. Z. (1999), Elementary micromechanics of heterogeneous media, in *Heterogeneous Media: Modelling and Simulation*, vol. 1, edited by K. Z. Markov and L. Preziosi, pp. 1–162, Birkhäuser, Boston, Mass.
Matthies, S., and M. Humbert (1993), The realization of the concept of a geometric mean for calculating physical constants of polycrystalline materials, *Phys. Stat. Sol. (b)*, *177*, 47–50.
Oliot, E., P. Goncalvez, and D. Marquer (2010), Role of plagioclase and reaction softening in a metagranite shear zone at mid-crustal conditions (Gotthard massif, Swiss Central Alps), *J. Metamorph. Geol.*, *28*, 849–871.
Pennacchioni, G. (1996), Progressive eclogitization under fluid-present conditions of pre-Alpine mafic granulites in the Austroalpine Mt Emilius Klippe (Italian Western Alps), *J. Struct. Geol.*, *18*, 549–561.
Ranalli, G. (1995), *Rheology of the Earth,* 2nd ed., Chapman and Hall, London, U. K.
Reuss, A. (1929), Berechnung der Fliessgrenze von Mischkristallen auf Grund der Plastizitätsbedingung für Einkristalle, *Zeitschrift für Angewandte Mathematik und Mechanik*, *9*, 49–58.
Rybacki, E., M. Paterson, R. Wirth, and G. Dresen (2003), Rheology of calcite-quartz aggregates deformed to large strain in torsion, *J. Geophys. Res.*, *108*, 2089, doi:10.1029/2002JB001833.
Schmid, D. W. (2005), Rigid polygons in shear, in *High-Strain Zones: Structure and Physical Properties*, vol. 254, edited by D. Bruhn and L. Burlini, pp. 421–431, Geol. Soc. Spec. Publ., London.
Schmid, S. M., M. S. Paterson, and J. N. Boland (1980), High temperature flow and dynamic recrystallization in Carrara marble, *Tectonophysics*, *65*, 245–280.
Schmid, S. M., R. Panozzo, and S. Bauer (1987), Simple shear experiments on calcite rocks: Rheology and microfabric, *J. Struct. Geol.*, *9*, 747–778.
Shelley, D. (1989), Plagioclase and quartz preferred orientations in a low-grade schist: The roles of primary growth and plastic deformation, *J. Struct. Geol.*, *11*, 1029–1037.
Simpson, C., and R. P. Wintsch (1989), Evidence for deformation-induced K-feldspar replacement by myrmekite, *J. Metamorph. Geol.*, *7*, 261–275.
Stewart, J. (2002), *Calculus,* 5th ed., Brooks Cole, Pacific Grove, Calif.
Sundberg, M., and R. F. Cooper (2008), Crystallographic preferred orientation produced by diffusional creep of harzburgite: Effects of chemical interactions among phases during plastic flow, *J. Geophys. Res.*, *113*, B12208, doi:10.1029/2008JB005618.
Takeda, Y.-T., and A. Griera (2006), Rheological and kinematical responses to flow of two-phase rocks, *Tectonophysics*, *427*, 95–114.
Terry, M. P., and F. Heidelbach (2006), Deformation-enhanced metamorphic reactions and the rheology of high-pressure shear zones, Western Gneiss Region, Norway, *J. Metamorph. Geol.*, *24*, 3–20.
Treagus, S. H. (2002), Modelling the bulk viscosity of two-phase mixtures in terms of clast shape, *J. Struct. Geol.*, *24*, 57–76.
Treagus, S. H. (2003), Viscous anisotropy of two-phase composites, and applications to rocks and structures, *Tectonophysics*, *372*, 121–133.
Treagus, S. H., and L. Lan (2000), Pure shear deformation of square objects, and applications to geological strain analysis, *J. Struct. Geol.*, *22*, 105–122.
Tullis, J., and H. R. Wenk (1994), Effect of muscovite on the strength and lattice preferred orientations of experimentally deformed quartz aggregates, *Mater. Sci. Eng.*, *175*, 209–220.
Tullis, T. E., F. G. Horowitz, and J. Tullis (1991), Flow laws of polyphase aggregates from end-member flow laws, *J. Geophys. Res.*, *96*, 8081–8096.
Voigt, W. (1928), *Lehrbuch der Kristallphysik,* Teubner, Leipzig.
Wilson, C. J. L. (1975), Preferred orientation in quartz ribbon mylonites, *Bull. Geol. Soc. Am.*, *86*, 968–974.

White, S. H. (1976), The role of dislocation processes during tectonic deformation with special reference to quartz, in *The Physics and Chemistry of Minerals and Rocks*, edited by R. J. Strens, pp. 75–91, Wiley, London.

Xiao, W., R. Wirth, and G. Dresen (2002), Diffusion creep of anorthite-quartz aggregates, *J. Geophys. Res.*, *107*, 2279, doi:10.1029/2001JB000789.

Yoon, C. K., and I. W. Chen (1990), Superplastic flow of two-phase ceramics containing rigid inclusions—Zirconia/mullite composites, *J. Am. Ceram. Soc.*, *73*, 1555–1565.

Zhang, J., H. W. Green II, and K. N. Bozhilov (2006), Rheology of omphacite at high temperature and pressure and significance of its lattice preferred orientations, *Earth Planet. Sci. Lett.*, *24*, 432–443.

Zhou, S. (1995), Bounds on steady state flow strengths of multiphase rocks: Theory and test with experimental data, *J. Geodyn.*, *20*, 199–217.

Tectonophysics xxx (2014) xxx–xxx

Contents lists available at ScienceDirect

Tectonophysics

journal homepage: www.elsevier.com/locate/tecto

Invited Review

Rheological and geodynamic controls on the mechanisms of subduction and HP/UHP exhumation of crustal rocks during continental collision: Insights from numerical models

Evgene Burov [a,b], Thomas Francois [a,b], Philippe Agard [a,b], Laetitia Le Pourhiet [a,b], Bertrand Meyer [a,b], Celine Tirel [c], Sergei Lebedev [c], Philippe Yamato [d], Jean-Pierre Brun [d]

[a] Sorbonne Universités, UPMC Univ Paris 06, UMR 7193, Institut des Sciences de la Terre Paris (iSTeP), F-75005 Paris, France
[b] CNRS, UMR 7193, Institut des Sciences de la Terre Paris (iSTeP), F-75005 Paris, France
[c] Dublin Institute for Advanced Studies, Geophysics Section, 5 Merrion Square, Dublin 2, Ireland
[d] Géosciences Rennes, CNRS UMR 6118, Université de Rennes 1, F-35042 Rennes, France

ARTICLE INFO

Article history:
Received 30 November 2013
Received in revised form 9 April 2014
Accepted 21 April 2014
Available online xxxx

Keywords:
Continental collision
Subduction
Rheology
Numerical modeling
Metamorphism
HP/UHP exhumation

ABSTRACT

While subduction of crustal rocks is increasingly accepted as a common scenario inherent to convergent processes involving continental plates and micro-continents, its occurrence in each particular context, as well as its specific mechanisms and conditions is still debated. The presence of ultra-high pressure(UHP) terranes is often interpreted as a strong evidence for continental subduction (subduction of continental crust) since the latter is seen as the most viable mechanism of their burial to UHP depths, yet if one admits nearly lithostatic pressure conditions in the subduction interface (or "channel"). The presumed links of continental subduction to exhumation of high- and ultra-high-pressure (HP/UHP) units also remain a subject of controversy despite the fact that recent physically consistent thermo-mechanical numerical models of convergent processes suggest that subduction can create specific mechanisms for UHP exhumation. We hence review and explore possible scenarios of subduction of continental crust, and their relation to exhumation of HP and UHP rocks as inferred from last generation of thermo-mechanical numerical models accounting for thermo-rheological complexity and structural diversity of the continental lithosphere. The inferences from these models are matched with the petrology data, in particular, with P–T–t paths, allowing for better understanding of subtleties of both subduction and burial/exhumation mechanisms. Numerical models suggest that exhumation and continental subduction are widespread but usually transient processes that last for less than 5–10 Myr, while long-lasting (>10–15 Myr) subduction can take place only in rare cases of fast convergence of cold strong lithospheres (e.g. India). The models also show that tectonic heritage can play a special role in subduction/exhumation processes. In particular, when thicker continental terrains are embedded in subducting oceanic plate, exhumation of UHP terranes results in the formation of versatile metamorphic belts and domes and in series of slab roll-back and exhumation events with remarkably different P–T–t records.

Contents

http://dx.doi.org/10.1016/j.tecto.2014.04.033
0040-1951/

1. Introduction

Continental subduction and the mechanisms of formation and exhumation of UHP rocks are two enigmatic processes that are closely linked together (e.g., Ernst, 2001). From geodynamic point of view, the occurrence of HP–UHP rocks raises two types of questions related to the mechanisms of their burial, and to those of their return to the surface. So far the occurrence of HP–UHP rocks in zones of continental convergence is most often interpreted as evidence for subduction (e.g., Hacker and Gerya, 2013; Kylander-Clark et al., 2011; Smith, 1984). In most cases it is supposedly linked to subduction of passive margins and early stages of intercontinental collision associated with subduction of continental lithosphere (Burov et al., 2001; Burtman and Molnar, 1993; Yamato et al., 2007). In other cases UHP exhumation is produced during late stages of oceanic subduction, during the transition from oceanic subduction to continental collision (Hacker and Gerya, 2013; Angiboust et al., 2009) or when small thick continental terrains (i.e., buoyant microcontinents) embedded in "normal" lithosphere are forced down together with the subducting plate and exhumed as a consequence of slab roll-back (Ernst, 2001; Brun and Faccenna, 2008; Husson et al., 2009; Tirel et al., 2013). More specific mechanisms linked to subduction have also been inferred, yet, for the moment, without quantitative match with in-situ P–T-paths. These include slab "eduction" (Andersen and Austrheim, 2008; Duretz et al., 2012), "subduction erosion" leading to diapiric rise of UHP terranes (Gerya and Stöckhert, 2006; von Huene et al., 2004), and foundering of orogenic roots (Hacker and Gerya, 2013).

It is worth mentioning that alternative "non-lithostatic" interpretations for the occurrence of UHP terranes exist (e.g., Mancktelow, 1995, 2008; Petrini and Podladchikov, 2000; Schmalholz and Podladchikov, 2013; Schmalholz et al., this volume), suggesting that non-lithostatic overpressure of different nature may alter pressure levels recorded by the UHP material by up to a factor of 2, so that the UHP rocks may be formed at about 50 km depth and hence do not need to be transported to such great "subduction" depths (>100–200 km) inferred from the lithostatic hypothesis. It is hence argued that the occurrence of UHP material does not present evidence for continental subduction and, by extrapolation, that the latter might not exist, or at least is not needed for explanation of the occurrence of the UHP terranes. The overpressure models inherently imply that P–T–t data are of limited use as markers of dynamic processes. Indeed, if subduction does not take place, then overpressure can be build up in the compressed media at levels determined exclusively by the local yield strength and loading conditions, which depend on many uncertain factors such as rheological properties, fluid content, porous pressure, etc., resulting in almost +100% error on depth estimations. Alternatively, full-scale subduction models (e.g., Li et al., 2010; Toussaint et al., 2004a) predict no significant non-lithostatic pressures in non-locked subduction channel (<20% below 50 km depth) allowing for reliable interpretation of P–T/P–T–t data. It should also be emphasized, that the "non-lithostatic" models do not explain why the same P/T gradients are found for both oceanic and continental HP/UHP rocks in a given setting (~8-10°C/km; e.g., Agard et al., 2001) and amongst the various continental subduction regimes (Agard and Vitale-Brovarone, 2013), nor why continental HP/UHP material was only found in places where subducted, dense (oceanic) slab material is imaged by tomography at depths.

At the outcome, elucidation of the mechanisms of formation and exhumation of the UHP rocks is of utmost importance both for understanding the mechanisms of continental convergence (e.g. subduction versus pure shear or folding) and for evaluation of the degree of utility of the petrology data for constraining geodynamic processes.

Indeed, "anti-subduction" models of UHP rock formation (e.g., Petrini and Podladchikov, 2000; Schmalholz et al., this volume) arise from reasonable doubts in physical plausibility of crustal subduction in continental settings where slow convergence rates and high buoyancy of continental crust are largely unfavorable to subduction processes. Subduction is only one of the four possible mechanisms of accommodation of tectonic shortening (Fig. 1): pure-shear thickening; simple shear subduction or underplating; folding (Burg and Podladchikov, 2000; Cloetingh et al., 1999), and gravitational (Raleigh–Taylor (RT)) instabilities in thickened, negatively buoyant lithosphere (e.g., Houseman and Molnar, 1997) dubbed here "unstable subduction." Whereas in oceans subduction is a dominating mode of accommodation of tectonic compression, in continents all of the above scenarios can be superimposed to some degree. For instance, "megabuckles" created by lithospheric folding (Burg and Podladchikov, 2000) can in theory localize and evolve into mega-thrust zones or result in the development of Rayleigh–Taylor (RT)

Please cite this article as: Burov, E., et al., Rheological and geodynamic controls on the mechanisms of subduction and HP/UHP exhumation of crustal rocks during continental coll..., Tectonophysics (2014), http://dx.doi.org/10.1016/j.tecto.2014.04.033

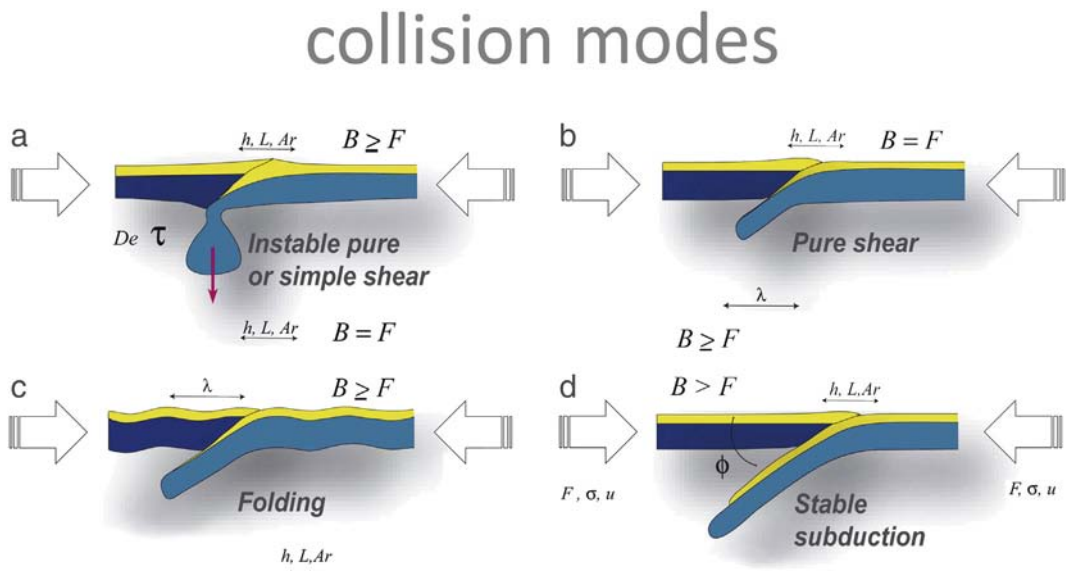

Fig. 1. Possible collision scenarios: (a) unstable (Rayleigh–Taylor) pure or simple shear instability; (b) pure shear in stable mode and (c) unstable mode (folding); (d) simple shear in stable mode (subduction). Related large-scale parameters characterizing collision style, lithospheric strength and rheology: T_e, F, σ, u, De, τ_m, h, L, λ, ϕ. T_e is equivalent elastic thickness. F, σ, u are respectively the horizontal force, stress and convergence/extension velocity, that are linked to the lithospheric strength and possible deformation styles. De and τ_m are respectively Deborah number and relaxation time related to viscosity contrasts in the lithosphere. λ is the characteristic wavelength of unstable deformation related to the thickness of the competent layers in the lithosphere. h, L are respectively the vertical and horizontal scale for process-induced topography supported by lithospheric strength, Argand number $Ar = \rho ghL / F$. φ is subduction or major thrust fault angle that is indicative of the brittle properties and of the overall plate strength.

instabilities. On the other hand, RT and boudinage instabilities leading to slab-break-off may also occur in subducting lithosphere leading to interruption of the subduction process (Pysklywec et al., 2000).

However, it is not only the presence of UHP material but also a host of structural (e.g., Hacker et al., 2006) and geophysical data (e.g., Ford et al., 2006; Handy et al., 2010; Tetsuzo and Rehman, 2011; Zhang et al., 2009) that provide a support for the idea that continental subduction takes place at some stages of continental convergence (e.g., Toussaint et al., 2004a,b). For example, at least 700 km of Indian continental crust are "missing" from surface since India–Asia collision (e.g., DeCelles et al., 2002), and hence had to be buried in some way at depth. Physical conditions for subduction include (1) presence of sufficient far-field slab-pull/push forces, (2) weak mechanical coupling between the upper and lower plates (i.e., weak subduction interface) and (3) sufficient mechanical strength of the lower plate assuring preservation of its geometric and mechanical integrity during subduction. In oceans, additional strain localization and plate weakening mechanisms are needed for subduction initialization and for downward bending of strong lithosphere when it slides below the upper plate (Cloetingh et al., 1982; McAdoo et al., 1985; Watts, 2001). Enhanced pre-subduction bending of the lithosphere is possible due to inelastic flexural weakening, that is, ductile yielding and "plastic hinging" produced by high flexural stresses near the peripheral bulge (Burov, 2010a, 2011; Burov and Diament, 1995; McAdoo et al., 1985). Flexural weakening of oceanic lithosphere is amplified by pressure reduction due to pore fluids and rheological softening due to metamorphic reactions, e.g., serpentinization, produced by fluids penetrating in normal faults created by tensional flexural strains in the uppermost parts of the peripheral bulge (e.g., Angiboust et al., 2012; Faccenda et al., 2009a; Hacker et al., 2010; Kylander-Clark et al., 2011; Ranero et al., 2003). In continental settings, subduction initialization is actually less problematic since the continental lithosphere follows the path opened by the preceding oceanic subduction.

Since the slab pull/push forces can be directly estimated from gravitational force balance (e.g., Bott, 1993), the most uncertain conditions here refer to the mechanisms of weakening of the subduction interface and to the preservation of slab strength (and integrity) during subduction. The former seem to be influenced by metamorphic processes, at least in two aspects: one concerning the role of the metamorphic materials in enabling subduction processes, and the other concerning the capacity of the lithosphere to transport crustal rocks — future high-pressure metamorphic materials — to a great depth. As mentioned above, it is generally agreed, based both on models and observations, that oceanic subduction is possible due to lubrication of the subduction interface by serpentinized mantle layer formed along crust–mantle interface, and due to mechanical weakening resulting from reactions with free and hydrous fluids released or absorbed during metamorphic phase changes (e.g., Angiboust et al., 2012; Faccenda et al., 2009a; Hacker et al., 2010; Kylander-Clark et al., 2011; Ranero et al., 2003). In continents, the governing weakening mechanisms are not well established but the presence of thick, relatively weak and rheologically stratified crust appear to be of primary importance (e.g., Burov et al., 2001; Yamato et al., 2008). Strength reduction and density changes due to metamorphic transforms in LP–HP range and the associated partial melting should also play a certain role (Yamato et al., 2008), but the impact of UHP transforms on subduction may be of minor importance (Toussaint et al., 2004a), specifically because some UHP transforms occur during the exhumation stage only and therefore cannot influence slab behavior at most crucial initial subduction stage (Peterman et al., 2009). Preservation of slab integrity is a major problem for continental subduction, since continental convergence occurs at much slower rates than in oceans. In the case of oceanic subduction (at rates of 5–15 $cm \cdot yr^{-1}$), the slab has no time to heat up due to the thermal diffusion from the surrounding asthenosphere. As a consequence, it loses its strength only at a great depth. In continents, convergence rates are much slower, sometimes not exceeding a few $mm \cdot yr^{-1}$. Under these conditions, the lithosphere may heat up, thermally weaken and drip-off before it reaches the UHP depth (e.g., Yamato et al., 2008).

Oceanic subduction has numerous lines of direct evidence such as Benioff zones, straight kinematic inferences from paleomagnetic data, relatively "sharp" tomographic images and gravity anomalies. For continental subduction, on the other hand, the corresponding observational data is much more "blurred", such that probably one of the most straightforward evidences for continental subduction refers to the presence of HP and UHP continental material in convergence zones (e.g., Ernst, 2010; Guillot et al., 2000, 2001, 2009; Hacker et al., 2006; Lanari et al., 2012; Maruyama et al., 2010; Sanzhong et al., 2009). The high- to ultrahigh-pressure (HP/UHP) metamorphic belts are believed to be witnessing subduction processes as the exhumed continental blocks appear to bear an overprint of the subduction record as they

Please cite this article as: Burov, E., et al., Rheological and geodynamic controls on the mechanisms of subduction and HP/UHP exhumation of crustal rocks during continental coll..., Tectonophysics (2014), http://dx.doi.org/10.1016/j.tecto.2014.04.033

return to surface (e.g. Diez Fernández et al., 2012; Hacker et al., 2010; Ring et al., 2007; Zhang et al., 2009). This evidence can be preserved in small and disconnected lenses (eclogite blocks in blocks in a quartzofeldspathic matrix, see Hacker et al., 2006 for review), as mineral relicts within a dominant low- to medium-pressure metamorphic matrix (e.g., Guillot et al., 2009), or as relatively large HP/UHP units (e.g., Yamato et al., 2008). If one assumes lithostatic P–T conditions commonly inferred for subduction zones, then UHP material should have been buried to depths of 100–170 km and brought back to the surface. Consequently, if the UHP depth estimates are valid (e.g., Spear, 1993), the HP/UHP rocks can be regarded as passive markers of continental subduction and their P–T–t paths can be used for reconstruction of subduction dynamics and of the conditions at the subduction interface. Under these assumptions, detailed studies of HP/UHP rocks can provide constraints on thermo-mechanical processes in subduction zones (Coleman, 1971; Ernst, 1973, 2010). These data provide insights on exhumation mechanisms as well, since different processes and contexts potentially result in different styles of deformation and, hence, in different exhumation P–T–t paths. In particular, based on the analysis of metamorphic data (e.g., Ernst, 2010) it has been suggested that two main types of continental convergence can be distinguished: fast "Pacific underflow", where continental subduction is preceded by that of thousands of km of oceanic lithosphere, and slow "Alpine closure" of an intervening oceanic basin leading to short-lived continental subduction soon followed by pure shear collision. It is indeed possible to make a disctinction (Agard and Vitale-Brovarone, 2013) between 1) long-lived subduction (~20-40 Myr) of large-scale continental fragments, containing both lower and upper crustal material, exhumed from UHP (and HP) depths (Hacker et al., 2006) and 2) limited volumes of essentially upper crustal material exhumed over shorter time-scales (5-10 Myr), either from HP/UHP depths (Alps, Himalaya; Guillot et al., 2009) or only HP depths (continental subduction beneath obducted ophiolites: Oman, New Caledonia; Agard et al., 2010; aborted collision: Corsica; punctuated exhumation of microcontinents: Aegean, Turkey; Brun and Faccenna, 2008). It has also been pointed out that the exhumed HP–UHP complexes display low-aggregate bulk densities (e.g., Ernst, 2010), while the exhumation rates in some cases largely exceed the convergence rates (e.g., Yamato et al., 2008), jointly suggesting a buoyancy-driven ascent mechanism.

Large-scale nappe stacking and folding, and other complex deformation processes occurring at the subduction interface largely distort kinematic imprint of subduction (e.g. Diez Fernández et al., 2012; Tirel et al., 2013), hence justifying a numerical modeling approach for decrypting and matching structural and metamorphic observations. For this reason, in recent approaches, the data from HP and UHP rocks are treated in conjunction with synthetic P–T–t paths predicted from thermo-mechanical numerical models of convergent processes. This provides validation of the inferred concepts of convergent dynamics and thermo-mechanical properties of oceanic and continental subduction zones (e.g., Li and Gerya, 2009; Yamato et al., 2007, 2008). Since the mechanisms of continental convergence and exhumation of HP/UHP material are still very much in debate, and the ideas on the interpretation of metamorphic data and on the mechanisms of convergence require further investigation. In particular, for each given context it should be demonstrated, in an independent way, that: (1) continental subduction is a viable mechanism of accommodation of tectonic shortening; and (2) it is possible to propose a particular mechanism of HP/UHP exhumation compatible both with the P–T–t data and with the proposed subduction dynamics.

According to observations (e.g., Diez Fernández et al., 2012; Ernst, 2010) and recent modeling results (e.g., Burov and Yamato, 2008; Li and Gerya, 2009; Yamato et al., 2008), the mechanisms of exhumation of deeply buried, HP-LT continental units and collision are versatile and in general poly-phase. However, it comes out from regional-scale numerical experiments that continental subduction provides a physically most consistent background for formation and exhumation of the HP/UHP material. The numerical models also reproduce the observations suggesting that exhumation of the UHP material goes by context-dependent multi-stage mechanisms. In particular, exhumation of the UHP material from depths in excess of typical crustal depths (40–50 km) may occur by Stokes flow mechanism at a high rate controlled by buoyancy and viscosity of the matrix, while, when the UHP material reaches 40–50 km depth it is more slowly dragged to the surface within the accretionary prism, or by simple shear upward sliding of semi-brittle crustal slices and large multi-kilometer scale segments (Burov et al., 2001; Yamato et al., 2008; Angiboust et al., 2009).

Whatever is the mechanism of UHP exhumation, one can conclude that in case of stable subduction, the subduction interface should be devoid of significant deviations from lithostatic pressure conditions (Burov et al., 2001; Burov and Yamato, 2008; Li et al., 2010). In case of stable subduction, only small under-pressures and overpressures (20%, or <0.3 GPa) may be produced in the subduction interface at depths below 40–50 km (Burov and Yamato, 2008; Li et al., 2010; Toussaint et al., 2004a,b), even though the surrounding lithosphere constituting the upper and lower wall of the interface may experience pressure deviations of up to 50% of lithostatic level (e.g., Li et al., 2010; Toussaint et al., 2004a). The in-wall over- and under pressures are basically caused by bending stress concentrations, yet, these zones do not belong to the subduction interface walls and do not participate in the exhumation turn-over (Burov and Yamato, 2008). Consequently, all studies converge to the point that if subduction takes place, the UHP P–T–t data can be decoded in terms of exhumation depth within 10–20% accuracy using lithostatic pressure gradients.

By now, a large number of modeling studies have investigated various factors influencing subduction processes (e.g., Chemenda et al., 1995, 1996; Doin and Henry, 2001; Gerya et al., 2002; Arcay et al., 2005; Pysklywec, 2006; Gray and Pysklywec, 2010, 2012; Li and Gerya, 2009; Li et al., 2010; Pysklywec et al., 2000; Sizova et al., 2012; Sobouti and Arkani-Hamed, 2002; Warren et al., 2008a,b; Yamato et al., 2007, 2008). However, not all of the existing models are sufficiently consistent. The analog models are largely inadequate because of impossibility to incorporate phase changes, rheological simplifications, absent or poorly controlled thermal coupling (not mentioning that it is practically impossible to extract PT paths from these models). The numerical models are often limited by simplified visco-plastic rheologies or by the rigid top/"sticky air" upper-boundary condition, which is widely used instead of the paramount free-surface boundary condition. The use of rigid-top upper-boundary condition forces stable subduction (Doin and Henry, 2001; Sobouti and Arkani-Hamed, 2002), attenuates pure shear, cancels folding and does not allow for consistent prediction of topography evolution. Many models also do not incorporate surface processes which are key forcing factors of continental collision (e.g., Avouac, 2003; Avouac and Burov, 1996; Burov, 2010b; Burov and Toussaint, 2007; Toussaint et al., 2004b) and an integral part of the final stages of exhumation. Some studies also force a specific convergence mode, in particular, subduction, via prescription of favoring boundary conditions, for example, by putting an additional boundary condition (e.g., "S-point") inside the model (e.g., Beaumont et al., 1996, 2000). Some other models favor pure shear collision by including a weak zone in the plate shortened in the direction opposite to the pre-imposed mantle flow (Pysklywec et al., 2002). Some older codes operating in deviatoric stress formulation (e.g., Navier–Stokes approximation) had specific problems with accurate evaluation of total pressure needed for tracing of P–T–t conditions and correct account for brittle deformation (this problem was fixed in most of the recent codes). Even though some earlier modeling studies (Burg and Gerya, 2005; Burov et al., 2001; Gerya et al., 2002; Toussaint et al., 2004a,b) have considered phase changes, fully coupled models with progressive phase changes directly derived from thermodynamic relations have emerged only few years ago (Francois et al., submitted for publication; Li and Gerya, 2009; Li et al., 2010, 2011; Stöckhert and Gerya, 2005; Yamato et al., 2007, 2008).

Summarizing the requirements to the new generation of numerical models of collision and exhumation, we therefore can note that they

should: (1) consider the entire regional context, i.e. encompass lateral spatial scales from 1500 km and vertical scales from 400 km; (2) allow for all modes of deformation, (3) account for viscous-elastic–plastic rheology and thermal evolution, (4) be thermodynamically coupled, i.e. account for phase changes (and ideally also for fluid circulation), (5) account for surface processes and free-surface boundary condition (or at least incorporate "sticky air" approximation of the free surface), and (6) provide an accurate solution for total pressure and report P–T paths based on the dynamic total pressure, rather than based on depth.

It is hence evident that a joint approach considering subduction processes in direct relation to exhumation and formation of HP/UHP material is the most promising one for understanding both the mechanisms of continental convergence and of exhumation.

The goal of this paper is therefore multi-fold: we start from discussing different concepts linking continental convergence with formation and exhumation of UHP terranes. We then discuss physical and rheological conditions allowing for subduction in continental settings, with a specific focus on the conditions allowing for preservation of slab integrity. We next revise the conditions for HP/UHP exhumation. We finally link all processes together attempting to obtain better insights on the mechanisms of continental convergence, and, by proxy, of formation and exhumation of the HP/UHP material.

2. Non-lithostatic models of formation and exhumation of UHP rocks during continental collision

As mentioned, several alternative mechanisms have been proposed both to explain the mechanics of continental convergence, and formation and exhumation of HP/UHP material. Their common feature refers to the idea that the UHP material comes from shallower depths than is commonly inferred from the assumption of the lithostatic pressure gradient. This implies a presence of static or dynamic overpressure during UHP rock formation which can be created by different mechanisms most of which are incompatible with continental subduction. The major thrust of these models is therefore that (1) continental subduction does not exist or is incapable to bring crust to important depth and (2) that P–T/P–T–t data cannot be directly interpreted in terms of depth at trajectories of the exhumed units.

Some of the suggested mechanisms of convergence are more or less directly associated with the mechanisms of exhumation, some not. For example, in the second case, Petrini and Podladchikov (2000) suggested tectonic overpressure as the mechanism of formation of UHP rocks that, according to the concept, originate from potentially twice smaller depths (50–75 km) than the usually inferred lithostatic depths of 100–170 km. These authors infer, consequently, that continental subduction does not take place or at least is not the most probable mechanism for UHP rock formation. This conceptually straightforward and formally mechanically consistent conceptual model has, however, a number of narrow places. In particular, it requires that the entire lithosphere reaches the yield state, which needs tectonic forces one or two orders of magnitude higher than estimated slab push/pull forces (~10^{12} N per unit length, Turcotte and Schubert, 2002). Even though the latter limitation may be bypassed by assuming only localized stress concentrations in 50–80 km depth interval, the maximal over-pressure values may be still limited in nature due to the fact that Byerlee's law is relayed by "weaker" Peierl's or GBS creep at mantle lithosphere depths (e.g. Burov, 2011). Another drawback of this concept refers to the fact that it does not provide a particular mechanism for burial and exhumation to-and-from the 50–80 km depths while the "common" accretionary prism mechanism is limited to 40 km depth (Platt, 1993) due to the exponential drop of the viscosity of prism material with depth/temperature. Furthermore, it does not explain why the same P/T gradient is found for HP/UHP oceanic (subducted without doubt) and continental material, nor why HP/UHP material is generally spatially associated with (and partly responsible for the exhumation of) oceanic eclogites (Angiboust et al., 2009).

Other workers (e.g., Raimbourg et al., 2007) have chosen another extremity by ultimately linking UHP exhumation to the conventional "subduction channel" concept, in which rocks are dragged down with plate interface by Couette flow, and returned back by Poiseuille flow associated with positive buoyancy of crustal material (Mancktelow, 1995). As mentioned, the "Couette" component of this mechanism cannot work at depths in extent of 40–50 km due to the exponentially rapid drop of channel viscosity with depth. Therefore it has been suggested (Mancktelow, 1995) that dynamic overpressure builds inside the channel due to a hypothesized decrease of channel width with depth. This is supposed to produce dynamic overpressure by "rocket nozzle" effect (Bernulli's effect) and reduce the depth of the UHP rock formation to 40–50 km. However, Bernulli's effect can be persistent only if channel walls are rigid and remain unmovable, while it is widely observed that the lithosphere and hence the subduction channel bends under flexural loads and tectonic forces of less than 10^{12} N per unit length as well as it locally widens when, for example, a seamount subducts at trench axis (Watts, 2001). Indeed, an overpressure of ~2 GPa (needed to divide the UHP depth by a factor of 2) in a 50 km long channel would yield an expansion force on the order of 10^{14} N per unit length acting on channel walls. Such force is sufficient not only to widen the channel but simply to break apart the entire lithosphere. Even if one considers a much smaller effective channel length of 1 km (assuming small-scale localized overpressure anomalies), the repulsive force (10^{12} N per unit length) will be high enough to push the colliding plates apart, hence widening the channel and automatically canceling the overpressure. In this relation it is noteworthy that metamorphic terranes often exhibit multi-kilometer scales (Hacker et al., 2006), which means that UHP conditions should be created at multi-kilometer scales as well. Further numerical thermo-mechanical models of subduction have confirmed these arguments by showing that pressure-driven channel overpressure concepts cannot explain UHP burial/exhumation (Burov et al., 2001; Li et al., 2010; Toussaint et al., 2004a; Yamato et al., 2008), even in the oceanic contexts (Angiboust et al., 2012; Yamato et al., 2007). According to these models, underpressure or overspressure in the subduction channel produces its "ballooning", "deflating" or out-of plane flow leading to automatic re-establishment of pressure balance with the environment. As result, pressure deviations from lithostatic conditions do not exceed 20% at depths in excess of 50 km (e.g., Li et al., 2010; Toussaint et al., 2004a) while significant overpressures (yet, according to the experiments, not exceeding 50% of lithostatic pressure) can be indeed created by flexural stresses and fiber forces within the channel walls.

As a matter of fact, most overpressure models remain at conceptual stage and are not really testable against observations. The only exception refers to the work by Schmalholz and Podladchikov (2013) and Schmalholz et al. (this volume), who have presented a thermo-mechanical overpressure numerical model in tectonic-scale shear bands that technically has got all necessary features allowing for prediction of testable PT paths, surface and structural evolution. Yet, this numerically state-of-the-art model is still far from being convincing: it is based on local-scale setup and therefore is not tested in regional tectonic context; the model-predicted PT paths are different from those typically observed; the predicted surface uplift rates (hence, probably intraplate forces) are far too high, with 5 km of surface uplift in about 2 Myr (Schmalholz et al., this volume). This model has potential for further development and future will show if it can be finally applied within regional context and match the observations at same extent as the recent subduction models.

Despite the shortcomings of the existing overpressure models, one must agree that strong overpressures are possible in some contexts. For example, volumetric expansion of mineral inclusions in locally stiff rock matrix can result in important overpressures inside the mineral seeds protected by the matrix (even in the UHP context, as in Norway, e.g. Kylander-Clark et al., 2011). Consequently, small and sparse UHP inclusions cannot be considered as evidence for continental subduction.

Please cite this article as: Burov, E., et al., Rheological and geodynamic controls on the mechanisms of subduction and HP/UHP exhumation of crustal rocks during continental coll..., Tectonophysics (2014), http://dx.doi.org/10.1016/j.tecto.2014.04.033

3. Preservation of slab integrity as paramount condition of subduction

Subduction implies preservation of slab integrity, hence small bulk deformation of the lower plate during convergence: a subducting plate bends without significantly changing its length and thickness. The slab should also provide an efficient stress guide for push/pull forces that drive subduction. To meet the above conditions, the lithosphere has to preserve sufficient mechanical strength as it sinks into the asthenosphere. Otherwise it would stretch or thicken, break-off, stagnate or drip-off under the action of the external shear, push–pull forces and viscous gravitational Raleigh–Taylor instabilities. Preservation of slab integrity (= small internal strain rate) is also equivalent to nearly invariable plate-parallel component of plate velocity. Since slab push–pull, shear and body forces acting on the opposite ends of the plate are largely different, this condition can be satisfied only if the slab stays strong even at great depth.

Olivine-rich rocks of lithosphere mantle exhibit important ductile deformation at temperatures above 500–600 °C in oceans (P > 0.4 GPa) and at 700–800 °C (P > 1.2 GPa) in continents (e.g., Goetze and Evans, 1979). The higher yield-strength temperature in continents is related to higher pressure (depth) at equivalent temperature. Hence, to preserve its strength, slab should remain cold, i.e. rapidly descend in the asthenosphere and have no time to heat up — hence weaken — due to heat diffusion from hot environment (>1330 °C). Therefore, one can characterize the minimal thermo-rheological condition for stable subduction by "subduction Péclet number" Pe_s:

$$Pe_s = u^2 t_s/\kappa \tag{1}$$

where t_s is a characteristic time scale, u is plate-parallel (horizontal at surface) plate velocity and κ is thermal diffusivity ($\approx$on the order of 10^{-6} m^2 s^{-1}). The corresponding thermal diffusion length is $l_d = (t_s\kappa)^{½}$. The characteristic time scale t_s hence corresponds to the average life span of stable subduction, i.e. to the time interval between the onset of subduction and the moment when simple shear is no more dominant deformation mode, being progressively suppressed by other modes such as pure shear shortening, RT instabilities, or folding (Fig. 1). After that, heat advection mechanism is no more directly dependent on the convergence rate, and Eq. (1) does not hold anymore. This condition can be also used to characterize the prograde parts of the metamorphic P–T–t paths.

For preservation of considerable slab strength for a time t_s, l_d should be significantly less than h_k, where h_k is the apparent thickness of strong, nearly elastic mechanical core of the lithosphere when it arrives at the subduction zone. Having a strong core is a condition for transmission of intra-plate stresses with minimal internal shortening of the lithosphere, which is equivalent to assuming that heat advection is primarily dependent on the convergence rate u, as expressed by Eq. (1). Let us assume $l_d \le 0.25h_k$, that is, a maximum factor of 2 reduction of the thermo-mechanical thickness of the slab by time t_s (slab heats up both from its upper and lower interface, $(0.25 \times 2)^{-1} = (0.5)^{-1}$). Hence, the characteristic time scale of subduction is:

$$t_s \approx {l_d}^2/\kappa \approx 0.0625{h_k}^2/\kappa, \tag{2}$$

and the minimal condition for stable subduction is:

$$Pe_s \gg Pe_k = uh_k/\kappa. \tag{3}$$

If Pe_s is smaller than Pe_k, thermal weakening of the slab, caused by heat diffusion, prohibits stable subduction (Toussaint et al., 2004a). As also follows from Eq. (2), if Eq. (3) is satisfied, then the characteristic subduction length d_s (the length of "subductable" lithosphere), can be roughly estimated as:

$$d_s \approx ut_s \approx 0.0625u{h_k}^2/\kappa, \tag{4}$$

which means that maximal stable subduction depth for lower crustal units (initial crustal thickness h_c plus d_s multiplied by tangent of the dip angle) is (1) linearly proportional to subduction rate and (2) quadratically proportional to the mechanical thickness of the lithosphere at the surface. Hence, convergence rate is a secondary factor compared to the initial mechanical strength of the lithosphere, which is thus of major importance for subduction. The above estimations are only crude approximations. One can complement them by evaluating an additional strong limit on the duration of the subduction, that is, the maximal time t_{bmax} of slab break-off, which will happen no later than when the mechanical core of the lithosphere vanishes, i.e. when $(t\kappa)^{½} \sim 0.5h_k$.

$$t_{bmax} < 0.25{h_k}^2/\kappa, \tag{5a}$$

with maximal slab-break-off depth, d_{sbmax},

$$d_{\mathrm{sbmax}} < ut_{bmax}. \tag{5b}$$

This yields t_{bmax} of 3–7 Myr for lithosphere with initial T_e = 20–30 km (e.g., Western Alps), 20 Myr for lithosphere with initial T_e = 50 km (e.g., Zagros), and up to 39–64 Myr for lithosphere with T_e = 70–90 km (India–Himalaya collision). Surprisingly, these simple estimates match the inferences from observations and thermo-mechanical models for the respective regions (e.g., Angiboust et al., 2012; Francois et al., 2012; Francois et al., submitted for publication; Toussaint et al., 2004b; Yamato et al., 2008). Nevertheless, the Eqs. (5a) and (5b) may not hold well for slow convergence settings (e.g. $u < 2$ cm·yr^{-1}) because of strong influence of thermo-mechanical instabilities that may develop at similar time scale.

The thickness of the mechanical core of the lithosphere h_k can be constrained from observations of plate flexure that reveal significant plate strength in zones of oceanic subduction and in many zones of continental collision (Watts, 2001). The observed equivalent elastic thickness of the lithosphere, $T_e \sim h_k$, is a direct proxy for the long-term integrated strength, B, of the lithosphere (see Watts, 2001). For example, for a single-layer plate of mechanical thickness h_m with $T_e = T_{e\_ocean}$:

$$B = \int_0^{\infty} \sigma^f(x,z,t,\dot{\varepsilon})dz \quad \text{while} \quad T_{e\_ocean} = \left(12\left(\frac{\partial \sigma^f_{xx}}{\partial z}\right)^{-1}\int_0^{h_m}\sigma^f_{xx}(z-Z_n)dz\right)^{\frac{1}{3}}_{M_x(x)}; \quad T_{e\_ocean} < h_m, \tag{6}$$

where x, z, t and $\dot{\varepsilon}$ are horizontal and vertical (with respect to local plate coordinates) coordinates, time and strain rate, respectively, Z_n is the position of the neutral fiber within the plate, σ^f_{xx} is bending stress and M_x is bending moment (Burov and Diament, 1995). For inelastic rheology and rheologically stratified lithosphere, T_e, is smaller than h_m. In this case T_e has no geometrical interpretation, and can be identified with our definition for h_k (apparent mechanical thickness of the lithosphere). T_e varies spatially due to its dependence on local bending stress that leads to localized plate weakening (called plastic or ductile hinging) in the areas of utmost flexure, e.g. near subduction zones (at the peripheral bulge) or below mountains and islands. As discussed in previous sections, ductile-plastic hinging is an important property allowing for subduction.

Typical values of T_e of the oceanic lithosphere correlate with the depth of 500°–600 °C geotherm and are roughly equal to 30–50 km near subduction zones (e.g., Burov and Diament, 1995; Watts, 2001). By analogy with oceanic plates, we can assume the same minimal T_e value for subduction of continental lithosphere. Continental plates are characterized by T_e values varying between 15 and 90 km (e.g., Burov and Diament, 1995; Cloetingh and Burov, 1996; Pérez-Gussinyé and Watts, 2005). Hence, only some of them are strong enough to develop oceanic-type subduction provided that other conditions (e.g., buoyancy

Please cite this article as: Burov, E., et al., Rheological and geodynamic controls on the mechanisms of subduction and HP/UHP exhumation of crustal rocks during continental coll..., Tectonophysics (2014), http://dx.doi.org/10.1016/j.tecto.2014.04.033

versus shear force balance) are also favorable. For example, consider a convergence rate u of 1 cm·yr^{-1}. Assuming a value for h_k of 50 km we obtain $Pe_k \sim 16$. Then, from $l_d \leq 0.25h_k$, one obtains $t_s \leq 5$ Myr. For t_s greater than 5 Myr, Pe_s is smaller than Pe_k, suggesting that sustainable long-lasting subduction is improbable (characteristic stable subduction length ~ $ut_s = 50$ km; maximal slab-break-off depth $ut_{bmax} < 200$ km) at such a slow convergence rate. However, for $u = 5$ cm·yr^{-1}, $Pe_k \sim 80$ and $Pe_s \sim 400$ suggesting that stable subduction (characteristic subduction length $ut_s = 250$ km) is possible even for time spans greater than 5 Myr. As extreme example, we can consider India–Asia collision ($h_k \approx$ 80–90 km (Watts, 2001), $t_s \sim$ 12–15 Myr, $u = 5$ cm·yr^{-1}). For these conditions we obtain minimal $Pe_s > 953$ and minimal $Pe_k = 127$, which implies that subduction is dominating mode and that at least 600–750 km ($= ut_s$) of the Himalayan convergence could have been accommodated in subduction regime. The maximal amount of subduction could be even much more important ($ut_{bmax} > 2500$ km), meaning that slab-break off would never happen if the Indian slab was sinking at a steep angle into the upper mantle (the reality is more complex since the Indian plate appears to underplate the Tibetan plateau). These very rough estimates are, however, comparable with interpretations (500–1000 km of subduction, up to 1500 km of total convergence) of geological and paleomagnetic data (Avouac, 2003; Chen et al., 1993; Patriat and Achache, 1984; Patzelt et al., 1996).

The first-order estimations reasonably comply with the results of recent geodynamic thermo-mechanical models. In particular, Yamato et al. (2008) have shown that slow (<1 cm·yr^{-1}) Alpine subduction could have lasted no more than 5–10 Myr (between 30 Ma and 35 Ma) and that soon after that the lithosphere had to enter into unstable mode or pure shear collision mode. In this case, the slab was no longer simply descending at the convergence rate but also stretching, and an early slab break-off at about 200–250 km depth resulted in cessation of continental subduction. Slab stretching has actually allowed the bringing of rocks to 120 km depth. On the contrary, for the fast (5 cm·yr^{-1}) convergence such as the India–Asia collision (Burov and Yamato, 2008; Toussaint et al., 2004a,b) or past collision between North China and Yangtze craton (Li and Gerya, 2009; Li et al., 2011), it has been shown that sustainable subduction could continue for a very long period of time absorbing considerable amounts of tectonic shortening (e.g., at least 700–800 km for Indian collision). In such settings, slab break-off either does not occur or has little effect on the collision mode. In particular, slab-break-off depth increases with increasing subduction rate and strength of the lithosphere, so in cases of fast subduction, slab-break off, if it happens, takes place far deep from the surface (at distance l, $ut_s < l < ut_{bmax}$) and thus has a limited impact on surface evolution (Eqs. (5a) and (5b)).

One can suggest on the base of this discussion that subduction rates are closely tied to the initial strength of the mantle lithosphere. Fast (>2–3 cm·yr^{-1}) continental subduction appears to be only possible in the presence of a strong mantle lithosphere.

Numerical models have also shown that the rheological properties of the continental subduction interface and, therefore, of metamorphic reactions transforming host rocks into weaker phases, are of potentially primary importance for the evolution of continental convergence (Burov and Yamato, 2008; Warren et al., 2008a,b), even though the role of the UHP material in this process may be of no importance in some cases (e.g., Western Gneiss Region in Norway, Peterman et al., 2009). It has been demonstrated that subduction takes place only when the interface between the colliding plates has a low mechanical strength allowing for sliding of the lower plate below the upper plate. Early studies (Hassani et al., 1997) found that the effective friction angle of the subduction interface has to be as low as 5° for sustainable subduction to occur. Since real rocks have practically invariable internal friction angle (~30°), it is evident that lubrication of the subduction interface is produced by non-brittle mechanisms such as ductile flow in weak metamorphosed layers, assisted by shear heating and fluids. In the case of oceanic lithosphere, the lubrication of the subduction interface is provided by very weak serpentine layers that form at the crust–mantle interface due to infiltration of fluids through flexurally induced normal faults and fractures (Angiboust et al., 2012; Faccenda et al., 2009a; Jolivet et al., 2005; Yamato et al., 2007). Hydrated serpentinite layers transport fluids to great depths along the subduction interface; these fluids are then released due to dehydration of serpentinite at high pressure/temperature conditions, further weakening the subduction interface (Hermann et al., 2000; Guillot et al., 2001) and causing partial melting that leads to weakening of the subduction wedge and the back-arc zone (Gerya et al., 2008). In the case of continental subduction, the lithosphere has less ability to transfer fluids to depth, and metamorphic phases, present in HP pelitic schists and higher grade UHP facies like eclogites are mechanically stronger than serpentine. Hence, for a given subduction rate, the resistance of the continental subduction interface may be higher than in the case of oceanic subduction. In addition, thick continental crust has a positive buoyancy that creates body forces opposing slab pull/push forces (Fig. 2). Therefore, in most cases the duration of continental subduction should be limited; at the beginning it is facilitated by the pull of the oceanic slab, which decreases with time, and by initially higher convergence velocity. The latter hypothesis is confirmed for collision zones where paleomagnetic and geological records allow for reconstruction of convergence rates (Patriat and Achache, 1984). Apart of lubrication of the subduction interface and plastic hinging of the plate at the peripheral bulge, several other conditions should be satisfied to allow for the development of continental subduction (e.g., Afonso and Zlotnik, 2011). In particular, growth rates of the competing modes of deformation (RT instability, folding, pure shear) should be small, and the upward drag (eduction force) due to the buoyant crust and viscous shear must be smaller than tectonic and slab pull forces. The combined effect of these multiple factors can be only assessed through numerical modeling (e.g., Burov and Watts, 2006; Duretz et al., 2011; Faccenda et al., 2008, 2009a,b; Sizova et al., 2012; Toussaint et al., 2004a,b). These parametric studies have shown that continental subduction can occur and remain sustained over tens of million years only if the lithosphere is initially cold, and remains cold during subduction, which, in the case of continental lithosphere (e.g., Toussaint et al., 2004a,b) implies initial Moho temperatures of less than 550 °C, and convergence rates higher than 2–3 cm·yr^{-1}. It is therefore reasonable to assume that after the onset of collision between, for example, India and Eurasia, when the convergence rate was about 10 cm·yr^{-1} (Patriat and Achache, 1984), the oceanic subduction turned into subduction of the Indian continental lithosphere (Avouac, 2003; Toussaint et al., 2004b). The critical values of Moho temperature (550 °C) corresponds to the reference rheology profile (e.g. Toussaint et al., 2004b). Drier and more basic crustal compositions will result in stronger crust and hence critical "subduction" temperature may be higher in this case (600°–650 °C) also provided that the lithosphere mantle is controlled by strong dry olivine-dominated rheology. Inversely, wet crustal and mantle rheologies may prohibit crustal subduction even for lower Moho temperatures.

Despite these complexities, geologic and geophysical observations suggest that continental subduction took place even under very disfavoring (slow, weak lithosphere) settings such as the Alpine collision (e.g., Chopin, 1984), Western Norway orogen (e.g., Kylander-Clark et al., 2009; Labrousse et al., 2002) or Qinling–Dabie orogen (Central Asia, e.g., Hacker et al., 2004). The key observation here, as well as in many other convergent zones, is the presence of UHP metamorphic rocks (eclogite facies, Fig. 3a, b) of continental origin regurgitated to the surface from the depths of 120–180 km (assuming lithostatic pressure gradient). In particular, Western Norway (Kylander-Clark et al., 2009) and Dabie (Central Asia, e.g., Hacker et al., 2004; Li and Gerya, 2009) present a prominent example of fast UHP exhumation in case of hot lithosphere and slow subduction (Kylander-Clark et al., 2009). Some of these orogens (Alps, Yamato et al., 2008) have been successfully modeled using self-consistent thermo-mechanical thermo-dynamically coupled models showing that slow continental subduction of hot lithosphere is actually possible for limited intervals of time and for specific crustal rheological structures. Finally, in some contexts deep exhumation has

Please cite this article as: Burov, E., et al., Rheological and geodynamic controls on the mechanisms of subduction and HP/UHP exhumation of crustal rocks during continental coll..., Tectonophysics (2014), http://dx.doi.org/10.1016/j.tecto.2014.04.033

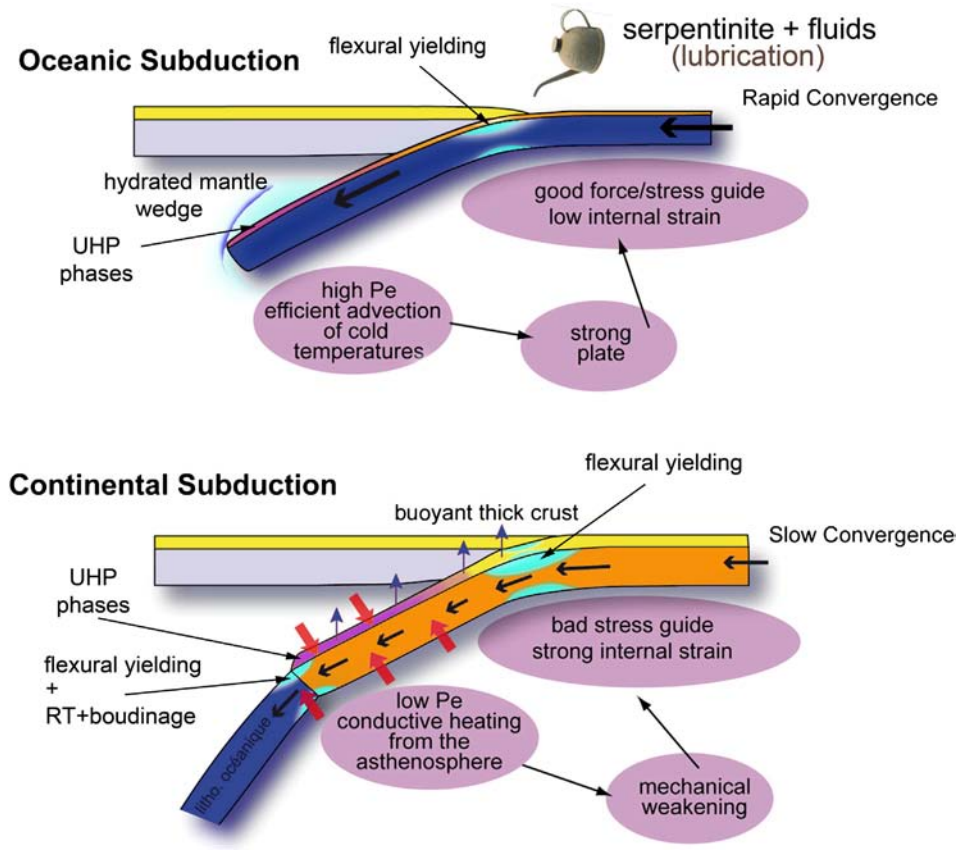

Fig. 2. Oceanic subduction versus continental subduction. Oceanic subduction is favored by several factors such as fast convergence rate, negative buoyancy, high bulk plate strength, flexural plastic hinging (yielding), serpentinization of the crust–mantle interface, hydration of the mantle wedge and shear heating. Many of these factors are absent in case of continental subduction which is disfavoured by overall positive buoyancy of the lithosphere, slow convergence (leading to additional thermal buoyancy, mechanical weakening and rapid slab break-off) and the lack of lubrication of the subduction interface. One of the frequently evoked (possibly important) factors favoring continental subduction refers to metamorphic (LP/MP/HP) reactions leading to weakening of the subduction interface and the UHP eclogitization of the crust (leading to negative buoyancy) and low ductile strength of the intermediate and lower crust.

been tentatively explained by diapiric RT instabilities bringing a part of the material vertically in the backstop area (Gerya and Stöckhert, 2006).

Hence, understanding the mechanisms of continental subduction requires a number of additional considerations. First of all, the counteracting effect of the positive buoyancy of the lithosphere can be neutralized if a part of low-density crust early separates from the mantle (Cloos, 1993) or if it soon undergoes metamorphic changes and becomes dense and strong (Austrheim, 1991; Burov et al., 2001; Le Pichon et al., 1992). The second factor allowing for continental subduction should refer to the initially higher convergence rates that should favor continental subduction before it is replaced by pure shear, folding or RT instabilities as the convergence rate slows down. Such initially higher continental subduction rates could be a natural consequence of transition from faster oceanic subduction to slower continental collision, which must be a progressive process (e.g., in the above mentioned case of India–Asia collision), the initial oceanic convergence rates of up to 15 $cm \cdot yr^{-1}$ have been progressively reduced to 10 $cm \cdot yr^{-1}$ at the onset of the continental collision stage to the present 4–5 $cm \cdot yr^{-1}$ within many tens of Myr (Patriat and Achache, 1984; Hatzfeld and Molnar, 2010). Later stages, one can expect that changing the force balance after the first slab break-off might slow down or cancel continental subduction phase.

4. Mechanisms of HP–UHP exhumation and their relation to the mechanisms of continental subduction

4.1. General concepts

Apart of the role of metamorphic rocks as of markers of subduction processes, it is also expected that metamorphic changes, specifically those leading to the formation of weak and/or denser rocks such as schists and eclogites, provide important controls on subduction interface dynamics, largely due to their weakening and lubricating effect, and also, in case of large quantities, due to their high density. The UHP rocks are considerably denser than the surrounding matrix and hence would not flow up on their own. Yet, nearly all UHP terranes are dominated by quartzofeldspathic rock that is buoyant under UHP conditions (e.g., Kylander-Clark et al., 2011); the density of eclogite, as long as it is included in a quartzofeldspathic matrix, is unimportant in terms of the average density of the exhumed bodies. Thus, the positive net buoyancy of the UHP assemblages is generally regarded as major factor of exhumation in the HP–UHP depth interval (e.g., Burov et al., 2001). Yet, to make buoyancy-driven exhumation possible, the matrix viscosity should (1) remain sufficiently high to allow for passive drag of the UHP inclusions back to the surface, and (2) sufficiently low to permit detachment of the exhumed bodies from the subducting lithosphere. (3) In addition, the viscosity of the intra-channel embeddings surrounding the ascending bodies should be sufficiently low (while the width of the channel should be sufficiently large) to permit their ascent through the channel. Consequently, understanding the mechanisms allowing for the journey of the crustal rocks to the UHP depths and back to the surface is largely equivalent to elucidation of the convergence mechanisms in general.

Without assuming such mechanisms it would be difficult to explain the exhumation of dense UHP rocks (e.g. eclogite density may exceed by 400–800 kg/m^3 the density of the normal crust and by 100 kg/m^3 that of the mantle) within the exhumation models developed for LP and MP rocks, which can be roughly sub-divided onto: (1) shallow, kinematically driven exhumation models (Fig. 3c, see also Platt, 1986, 1993; Hacker and Gerya, 2013 for review) such as the accretion prism model limited to exhumation from depths above the 40 km limit (e.g., Platt, 1993), (2) shallow overpressure models that can only work if the "subduction

Please cite this article as: Burov, E., et al., Rheological and geodynamic controls on the mechanisms of subduction and HP/UHP exhumation of crustal rocks during continental coll..., Tectonophysics (2014), http://dx.doi.org/10.1016/j.tecto.2014.04.033

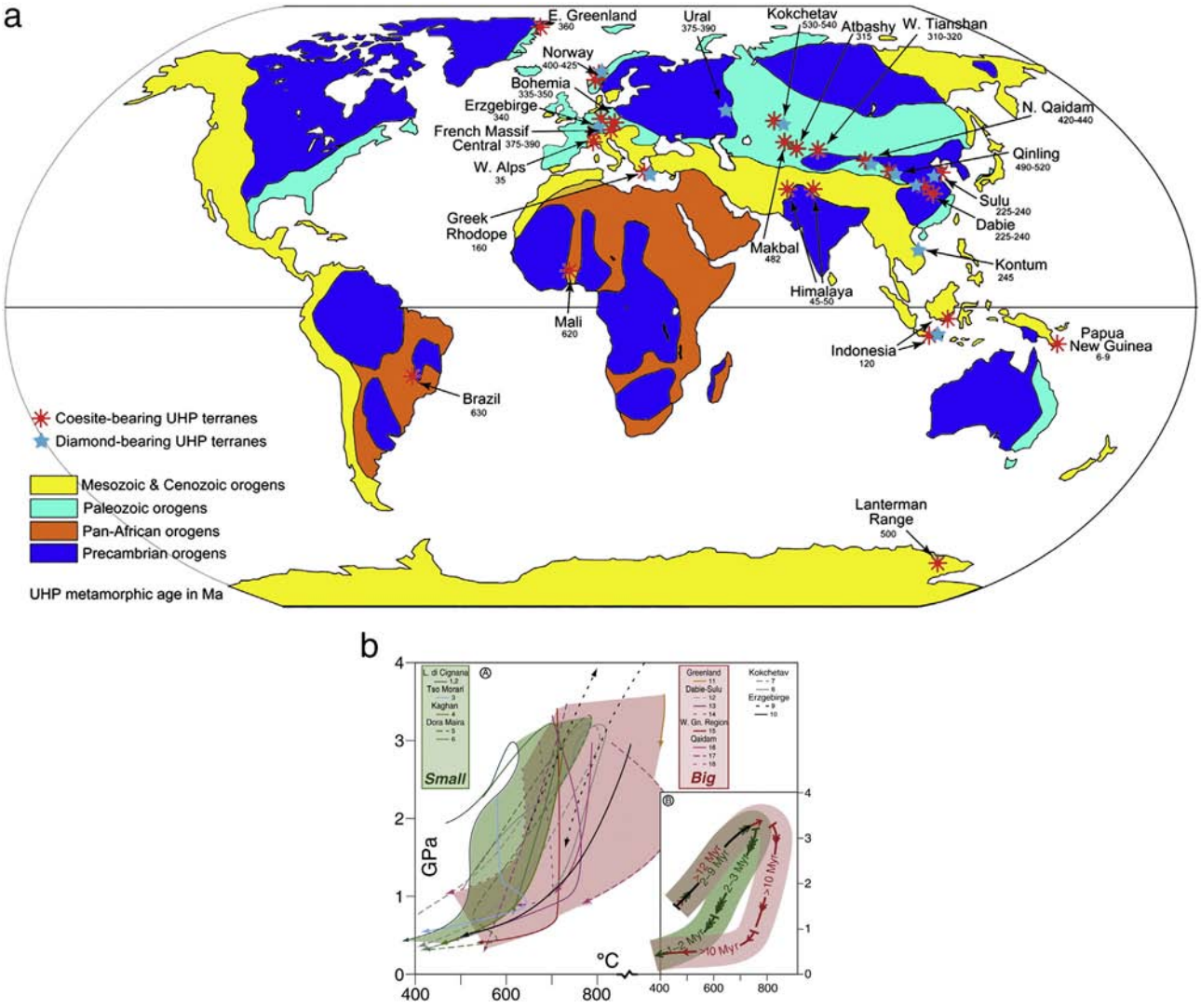

Fig. 3. a. Global distribution of UHP terranes recognized in continental subduction zones (coesite or diamond bearing). b. Pressure–temperature paths of UHP terranes (after Kylander-Clark et al., 2011). Large (Big), slowly formed terranes in red/orange define a region (pink) with higher overall temperatures than the small (Small), slowly formed terranes (blue and green). The Kokchetav terranes is not associated with a group and shown in gray. c. Various exhumation/collision concepts linked to different ideas on collision mechanics: (A) classical accretion prism mechanisms for LP–LT to MP–MT conditions (Dahlen, 1990; Dahlen and Suppe, 1988; Davis et al., 1983); (B) Thrusting model, superimposed here onto accretion prism mechanism (LP–LT to MP–MT conditions, e.g., Jolivet et al., 1994); (C) Mancktelow's (1995) "rocket nozzle" dynamic overpressure model (LP to UHP conditions, Mancktelow, 1995); (D) rigid block UHP exhumation model (Chemenda et al., 1995); (E) multi-stage soft crust exhumation model (LP to UHP conditions, high or low degree of metamorphism, or high or low density of the metamorphic grades, Burov et al., 2001) that is also compatible with the hot channel mechanism, "sub-lithosphere plume" and diapiric hot magma uprise mechanism developed in detail by Gerya et al. (2008) and Li and Gerya (2009); (G) "eduction" model, in which the subductiong plate rebounds after slab break-off bringing crustal volumes back to the surface (Duretz et al., 2012).
Panel a is modified from Zheng (2012) and Liou et al. (2009). The numbers in the legend of panel b correspond to the references in Kylander-Clark et al. (2011).

channel" walls are undeformable (Mancktelow, 1995, 2008, Fig. 3c) or in the absence of a dominant simple shear deformation (Petrini and Podladchikov, 2000), and (3) deep basically hydrodynamically and buoyancy driven HP–UHP exhumation models (Fig. 3c, Burov et al., 2001; Chemenda et al., 1995; Duretz et al., 2012; Li et al., 2010; Yamato et al., 2008).

Subduction and exhumation of deep crustal material is more and more considered as result of the competition between the buoyancy of partially metamorphosed crust and downward viscous drag exerted on the subduction interface (Couette flow). A simplistic view of this problem is that the buoyancy forces and the related inverse pressure gradients return the crustal material to the surface within the Poiseuille flow (Fig. 3c(C), Platt, 1993), so that the return flow of the exhumed material to the surface results from a trade-off between the downward Couette and upward Poiseuille flow (Beaumont et al., 2009; Raimbourg et al., 2007). Yet, as discussed in Section 2, this mechanism should not work in practice since it required undeformable subduction channel with rigid walls while physical consideration and recent studies show that "subduction channel" walls are deformable so that the channel would rather inflate instead of maintaining any significant over- or under-pressure (Burov and Yamato, 2008; Burov et al., 2001). Therefore, in case of simple shear subduction, is more appropriate to consider near-normal pressure conditions and an exhumation mechanism related to Stokes return flow.

If one follows the results of full-scale geodynamic models (Burov and Yamato, 2008; Li et al., 2010; Toussaint et al., 2004a) that have confirmed nearly lithostatic pressure conditions inside the subduction channel, then the exhumation depth of HP and UHP rocks must exceed 80–120 km. It was demonstrated (e.g., Platt, 1993) that kinematically driven circulation in the critical wedge of an accretion prism (Fig. 3c(A), Dahlen, 1990; Dahlen and Suppe, 1988; Davis et al., 1983) cannot bring metamorphic material to the surface from depths exceeding 40 km. This hard limit is established from the fact that the accretion prism mechanism requires, at one side, a relatively high viscosity, needed to drag host rocks to depth and bring their metamorphic facies back to the surface, but on the other side, the viscosity cannot be higher than 10^{19} Pa s to permit

Please cite this article as: Burov, E., et al., Rheological and geodynamic controls on the mechanisms of subduction and HP/UHP exhumation of crustal rocks during continental coll..., Tectonophysics (2014), http://dx.doi.org/10.1016/j.tecto.2014.04.033

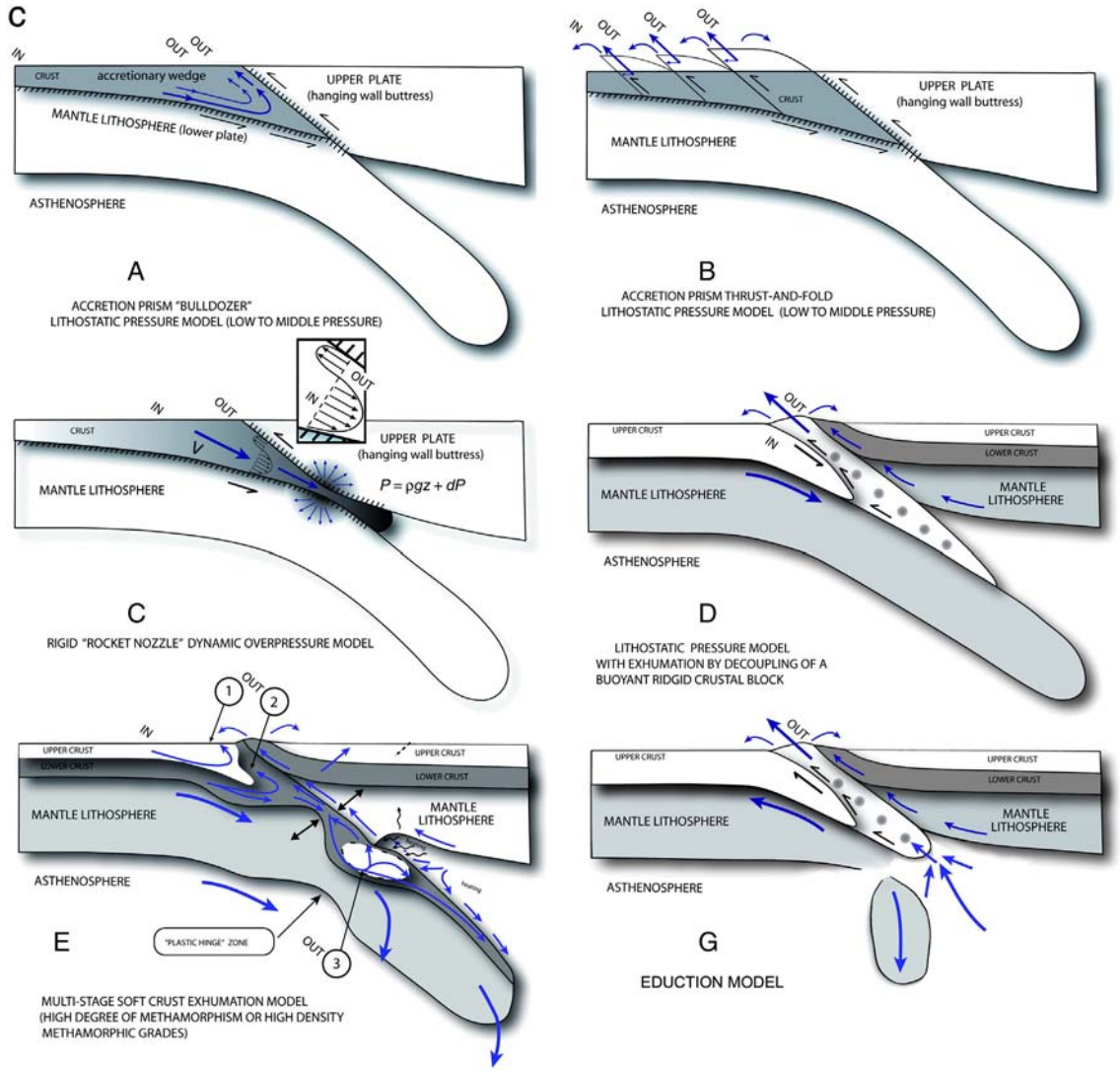

Fig. 3 (*continued*).

circulation of material and to maintain realistic geometry of the sedimentary prism (Emerman and Turcotte, 1983). At temperatures corresponding to the 40 km depth, most metamorphic bodies have low viscosity and it becomes impossible to build a sufficiently high viscous force to drag such a weak material up. As a result, large part of the material will remain at the bottom of the accretion prism and/or carried down with the subducting mantle. However, despite their presumably low viscosity, a part of exhumed rocks (Norway, Dabie, e.g. Kylander-Clark et al., 2011; Turkey: Okay et al., 1988, Plunder et al., 2013) show little deformation, which poses additional questions concerning the mechanisms of their exhumation.

Another classical kinematic exhumation model evokes foreland fold-and-thrust mechanisms allowing thrusting (nappe stacking) of one rock unit on top of another (Jolivet et al., 1994, Fig. 3c(B)). The kinematic thrust-and-fold and nappes stacking models exploit the possibility of detachment at the base of the accretion prism. In this case the lower accreted units may be folded and thrusted on top of the upper units. These stacking models appear to be consistent with field observations for LP and MP conditions. This mechanism, ultimately linked to simple shear deformation and hence subduction, probably can also work at final stages of HP/UHP exhumation when small volumes of UHP/HP material are included in partly metamorphosed LP/MP matrix. At larger scale, a similar mechanism may work in case of subduction of terrains embedded in the "normal" lithosphere (Tirel et al., 2013).

Finally, a number of concepts of continental collision consider mechanical alternatives to subduction and propose customized mechanisms for HP/UHP rocks formation and exhumation. For example, Thompsons' "tooth paste" model (e.g., Thompson et al., 1997) suggests that rocks may be squeezed up to the surface, for example as a result of closure of the accretion prism. The model of Thompson et al. (1997) can be discarded since it requires quite uncommon rheological properties for the colliding blocks and does not imply realistic structural features. Burg and Podladchikov (2000) have suggested a specific collision model that implies tectonic overpressure (as in Petrini and Podladchikov, 2000) and megabuckling of mechanically coupled strong colliding plates. In this model, there is no upper and lower plates. Instead, crustal rocks are brought down within a gigantic syncline formed as a result of a compressional instability. Due to tectonic overpressure, these rocks are formed at twice smaller depth (than usually inferred for HP/UHP material) and then exhumed to the surface by denudation processes and possibly by squeezing a bit like in Thompson's model. The possibility of megabuckling or, more general, of "symmetric" collision, has been also discussed in a number of studies (e.g., Burov et al., 1990; Cloetingh et al., 1999). However, this kind of scenario might be limited to some very specific places in the world such as Himalayan syntaxes or Tien-Shan.

Please cite this article as: Burov, E., et al., Rheological and geodynamic controls on the mechanisms of subduction and HP/UHP exhumation of crustal rocks during continental coll..., Tectonophysics (2014), http://dx.doi.org/10.1016/j.tecto.2014.04.033

4.2. Most generally considered mechanisms of UHP exhumation

Chemenda et al. (1995) have suggested a highly elaborated and elegant analog model of continental subduction scenario with a lithostatic UHP mechanism, in which the rigid cold crust is brought down with the subducting mantle because its initial viscosity is high allowing for adherence to the mantle lithosphere. Partly metamorphosed, therefore still buoyant and sufficiently rigid, large crustal blocks return to the surface when they delaminate from the mantle. The delamination is caused by reduction of the ductile strength of the crust as its temperature increases with depth. The UHP units are brought to the surface in solid state with the buoyant low density matrix. Once at the surface, the matrix is eroded exposing less erodible UHP material. As can be seen, the key point of this model relates to the net floatability of the exhumed crustal blocks that are supposed to be only partly converted into metamorphic material. Another condition is that this model requires high erosion rates at final stages of the exhumation processes. The model of Chemenda et al. (1995) has been successfully tested mechanically, but by the time it has been published it still required validation in terms of the P–T conditions because, as most analog models, it is not thermally coupled and the predicted P–T conditions are out of control. In particular, it was important to demonstrate that the crustal blocks can remain sufficiently rigid at the moment of their decoupling from the mantle. It should also be kept in mind that phase transitions result in reduction of the ductile strength and depend on the presence of fluids, which remain to be a poorly constrained factor of the subduction process. With these reservations, one can suggest that the "rigid block model" may work in particular settings characterized by exhumation of relatively small volumes of non-deformed UHP rock. Recent thermally coupled numerical models (Sizova et al., 2012) have demonstrated that Chemenda's model of exhumation is physically viable. Yet, the model is still to be validated with a thermo-mechanical model on a real-life case such as Himalaya collision (in particular, Dabieshan, Hacker et al., 2000), for which it was originally designed for. In particular, it is noteworthy that nappe stacking still occurs under particular conditions in the model by Sizova et al. (2012), i.e. in the presence of a rather strong lower crust. So far the only existing thermo-mechanical model that reproduced UHP exhumation for Dabieshan–Sulu (Li and Gerya, 2009) infers a mechanism that is more close to the multi-phase exhumation mechanism suggested by Burov et al. (2001, Fig. 3c(E), see below) than the rigid-block exhumation mechanism of Chemenda et al. (1995).

In difference from the geological contexts considered in the Chemenda' model, there is number of well-studied collision settings such as the Western Alps (Fig. 3c(E); Agard et al., 2001, 2009; Burov et al., 2001; Yamato et al., 2007, 2008) where the fraction of the exhumed UHP material is relatively important, even though HP volumes of 50 km wide with 200 m thick UHP units observed in this area are not exceptionally large (Kylander-Clark et al., 2009). To exhume this material, one needs to create sufficient space (e.g. via slab roll-back or by applying strong surface erosion, yet the latter scenario is not applicable to the Alps). This material is also strongly deformed by ductile deformation. These observations reduce the possibility that the metamorphic terranes were exhumed as small inclusions within a rigid matrix. For this reason, Burov et al. (2001) have suggested an alternative model, in which the subduction interface zone breaks into a shallow (1) and mid-depth (2) accretion prism and (3) a deep zone of accumulated crustal material formed near the base of the upper plate (this zone is dubbed "crustal pocket"). For each of these three levels there is a specific mechanism of exhumation. The two accretionary prism zones exhume LP and MP pressure rocks and also HP and UHP rocks that penetrate in the prism with return flow in the subduction interface zone. This return flow is driven both by up-thrusting of the upper plate and small-scale convective movements and gravitational instabilities in the more or less metamorphosed and partially molten subducted crust and in the "crustal pocket" that sometimes may underplate the overriding plate at the 50–120 km depth. At this depth, the weakened subduction interface zone breaks down onto two parts, the upper and the lower ones (i.e., "crustal pocket" with potentially partially molten rock), separated from each other by a more or less narrow "neck". Starting from this depth, a large part of the upper and adjacent lower crustal material does not subduct anymore, this material is accumulated below the upper plate and heats up due to direct contact with hot (T = 1330°) asthenosphere. Thermal expansion due to heating initiates small-scale convection and RT instabilities in the "crustal pocket". These processes drive the metamorphic material, possibly partially molten (in extreme, but not yet observed cases, Little et al., 2011) and mixed up with non-metamorphosed low density crustal units back to crustal depths of 40–50 km. From these depths, the UHP material is exhumed to the surface in the "normal way", through the accretionary prism mechanism. Each stage of this poly-phase exhumation process has its characteristic exhumation rate. The exhumation rate characterizing the convection stage may be much more rapid (10–15 $cm \cdot yr^{-1}$) than the tectonic convergence and uplift rates because the ascent Stokes velocity, V_s, is conditioned by the density contrast and the non-Newtonian viscosity μ_{eff} of the rocks (Burov et al., 2001; Weinberg and Podladchikov, 1994):

$$V_s \approx 2^{1-n} 3^{1-2n} r^{n+1} A (\alpha \Delta T \rho_0 g + \Delta \rho_c g)^n e^{-Q/RT} \quad (7)$$

where r is the approximate half-size of the ascending crustal body, $\Delta\rho_c$ is compositional density contrast, n, A, Q, and T are the power law exponent (typically 2–3), material constant, activation enthalpy and temperature of the embeddings, respectively, R is the gas constant (8.314 J mol^{-1} K^{-1}), g is the acceleration due to gravity (9.8 $m \cdot s^{-2}$), ρ_0 is reference mean density (at 0 °C), α is thermal expansion coefficient (typically $3 \cdot 10^{-5}$ $°C^{-1}$). It is noteworthy that the Eq. (7) holds for a spherical blob in an infinite matrix, and hence provides a maximal estimate for the ascent velocity, because in nature the ascent velocity is progressively reduced as the exhumed body approaches the surface, or, more exactly, the depth of brittle–ductile transition (e.g., Burov et al., 2003). However, since brittle–ductile transition depth in the subduction channel/interface and normal crust is likely to be above 20–30 km (Yamato et al., 2008), a large part of UHP exhumation may still occur at velocities described by Eq. (7).

Let us consider following typical conditions: background temperatures of about 600 °C, $\Delta\rho$ ranging from 20 to 200 kg m^{-3} and temperature contrasts between the ascending material and embeddings ranging from 100 °C to 300 °C. Whatever the embedding lithologies, quartz-rich crust ($n = 3$, $H = 190$ kJ mol^{-1}, $A = 5 \cdot 10^{-12}$ Pa^{-n} s^{-1}, $\rho_0 =$ 2600–2900 kg m^{-3}) or mantle olivine ($n = 3$, $H = 520$ kJ mol^{-1}, $A = 7 \cdot 10^{-14}$ Pa^{-n} s^{-1}, $\rho = 3300$ kg m^{-3}) (Burov et al., 1999, 2001), one can find that these conditions would be largely sufficient to drive up a 10–20 km-thick body at 10–20 $cm \cdot yr^{-1}$ rate. For larger temperature or density contrasts the estimated values of v_y become very high suggesting the possibility of very fast material ascent from great depths, slowing down near the surface due to the decreasing temperature. These estimates are highly sensitive to the material parameters, for example in case of a crustal quartzite-rich body ascending through olivine background ($\Delta\rho = 430$ kg m^{-3}), the ascent rate may vary from 1^{-4} $m \cdot yr^{-1}$ for embedding temperature of 600 °C to 1 $m \cdot yr^{-1}$ for the embedding temperature of 900–1000 °C. In case of much more temperature sensitive quartzite embeddings (hot crust material ascends through cold crustal embeddings), the scatter in possible vertical velocities becomes important, including a possibility of turbulent flow inside and outside the crustal body (Burov et al., 2001).

The velocity contrast between the exhuming material, mantle and crustal material of the upper plate induces formation of a large-scale shear zone, which works as a normal fault with a relative upward motion of the footwall. This is quite similar at a first glance to what Chemenda et al. (1995, 1996) have predicted from analog laboratory experiments. There are, however, some principal differences between the two models. In the Chemenda's model, continental crust is exhumed as a large rigid block, which detaches from the mantle and glides up

Please cite this article as: Burov, E., et al., Rheological and geodynamic controls on the mechanisms of subduction and HP/UHP exhumation of crustal rocks during continental coll..., Tectonophysics (2014), http://dx.doi.org/10.1016/j.tecto.2014.04.033

between the downgoing slab and the upper plate. This ascent is driven by density contrast between the crust and mantle. In the Burov et al. (2001) model, the exhumed body presents a deformed crustal volume included between a thrust zone forming along the Moho boundary of the lower plate and a normal fault zone forming between the lower and upper plates. In this model the exhumed material is not rigid, but ductile due to high temperature. Contrary to that, Chemenda's model is incompatible with long exposure of the subducted crust to high temperatures. The second important difference relates to the geometry of the downgoing slab. In the Burov et al. (2001) model high buoyancy experiment, the downgoing slab has a tendency to rotate upward below the upper plate, due to a positive flexural moment created by cumulative effect of remaining low density crustal layer and of asthenopsheric upflow below the overriding plate. The third principal difference is that in this model there is no important accumulation of crustal material below the upper plate as would be observed in the Chemenda's model in case of weak crustal rheology or hot surroundings. The fourth, less important difference is related to the presence of active extension within the upper plate provoked by the upwelling asthenosphere.

The equation for Stokes velocity of exhumation of buoyant crust does not directly consider its capacity to drag heavier metamorphic facies that under some condition can still sink in opposite direction. This additional condition can be roughly defined by "internal" Stokes velocity V_i of these metamorphosed facies within the exhumed crustal body:

$$V_i \approx \Delta\rho' g l^2 / 3\mu_{eff\_c} \quad (8)$$

where $\Delta\rho'$ is the density contrast between the metamorphosed part of the exhuming crustal volume and the crust, l is the characteristic size of the metamorphic inclusions and μ_{eff_c} is the effective viscosity of the crust. Logically, exhumation of metamorphic inclusions within lighter crustal units is possible under condition that

$$|V_s|-a|-V_i|-|V_{suv}|>0 \quad (9)$$

where $a \approx z_e/s_b$ is the ratio of the exhumation depth z_e to the characteristic vertical dimension of the body, s_b, and V_{suv} is the vertical component of the subduction rate. As long as l is sufficiently small ($l < 0.25r$–$0.5r$) the above ratio is positive meaning that large crustal volumes can effectively drag upward smaller metamorphic inclusions. These analytical considerations are largely oversimplified neglecting, for example, the non-linear downward drag due to subduction, which justifies a fully numerical approach. Burov et al. (2001) suggest that their mechanism can work for a limited amount of time during the initial stages of continental subduction, but do not preclude the possibility of delayed exhumation of the eventually partially molten UHP material from the "crustal pocket" that underlies the overriding plate in their model. This model has received further development in the models developed by Yamato et al. (2007, 2008) and Li and Gerya (2009), which account for thermodynamically consistent metamorphic phase changes, and allow for tracing metamorphic P–T–t paths used for validation of the model-predicted collision dynamics. These models, discussed in full detail in the next sections, belong to the latest generation of thermodynamically coupled collision/subduction models (see also Sizova et al., 2012) where material properties are dynamically adjusted in full consistency with thermodynamic conditions.

Recent numerically inspired oceanic and continental UHP exhumation concepts (e.g., Beaumont et al., 2009; Duretz et al., 2011; Gerya and Stöckhert, 2006; Li and Gerya, 2009; Li et al., 2013; Sizova et al., 2012; Stöckhert and Gerya, 2005) added new elements to our understanding of exhumation mechanisms, reinforcing, for example, the role of Rayleigh–Taylor instabilities both in the subduction interface zone and the hydrated mantle wedge. Rayleigh–Taylor instabilities may develop in the subduction interface zone due to partial hydration and melting and even propel low density "cold plumes" ascending toward the surface (Gerya and Yuen, 2003; Marschall and Schumacher, 2012); back-arc or back-stop exhumation may be partly explained by the formation of rotating rigid "wheels" trapped into the weakened material in the subduction channel (Gorczyk et al., 2006), or by partial melting in the above discussed deep crustal pockets forming as a result of partial underplating (Burov et al., 2001; Li and Gerya, 2009).

The "hot channel" model of continental collision (Gerya et al., 2008) complements the poly-phase model of Burov et al. (2001) by emphasizing the role of the internal heating–weakening mechanism, in which the subducting crustal material may be over-heated by viscous shear heating and radiogenic elements. In this model, heating is also associated with flow of aqueous fluids relieved by rapid dehydration (deserpentinization) of the overriding mantle lithosphere that has been hydrated during previous subduction stages. The channel can penetrate along the plate interface down to the bottom of the lithosphere of the overriding plate (150–200 km) and is characterized by temperatures reaching 700 to 900 °C. The low effective viscosity of rocks caused by increased temperature, partial melting and fluid infiltration permits profound mixing of hydrated mantle and crustal rocks. The hot channel exists during the early stage of collision only, but rapidly produces large amounts of ultrahigh-pressure, high temperature rocks. Further collision closes the channel through squeezing rheologically weak, partially molten, buoyant rocks between the strong lithospheric mantles of the two colliding plates.

Finally, the role of tectonic heritage has been studied by Tirel et al. (2013), who have suggested, in application to Aegean subduction, that deep stacking of continental terrains inherited from the previous tectonic history can explain deep burial and exhumation in appropriate contexts. In the intensively studied Aegean back-arc domain, HP belts represent small continental blocks buried and exhumed back during subduction and slab roll-back of the African lithospheric plate (Brun and Faccenna, 2008). Numerical models integrating multi-disciplinary observations show that slab buoyancy variations resulting from successive subduction of continental blocks can be responsible for episodic rollback–exhumation cycles. The model of Tirel et al. (2013) succeeds in reproducing major structural patterns and pressure–temperature–time (P–T–t) paths of the HP rocks in the Eastern Mediterranean and as such exemplifies a new concept for exhumation of deeply buried continental crust.

The specific features of Burov et al. (2001), Burg and Gerya (2005), Gerya et al. (2008), Li and Gerya (2009) and Yamato et al. (2008) models refer to the presence of several stages or levels of exhumation, with different exhumation rates (and mechanisms) at each stage/level. These models predict high exhumation rates at depth that may be several times higher than the horizontal convergence rates or denudation rates at surface. The predicted rates reach, for example, 10–15 $cm \cdot yr^{-1}$ in the Alpine context, where the convergence rates (currently almost negligible) were in average less than 1 $cm \cdot yr^{-1}$, with initial values not higher than 3–5 $cm \cdot yr^{-1}$ (Burov et al., 2001; Yamato et al., 2008).

5. Successful numerical models of continental subduction and HP/UHP exhumation

We next discuss the lower and upper bounds on the parameters controlling continental subduction and thus HP-UHP rocks exhumation. We assess various factors controlling continental collision/subduction by using state-of-the art numerical thermo-mechanical models coupled with thermodynamic processes. In these models, density and other physical properties of the material are computed by minimization of free Gibbs energy as function of P–T conditions (e.g., Connolly, 2005) and re-iterated back to the thermo-mechanical part of the model (see Appendix A).

5.1. Common modeling approach

We here discuss the general methodology of subduction/collision models using as representative examples recent modeling studies based on the FLAMAR code (Appendix A). This code, originating from

Please cite this article as: Burov, E., et al., Rheological and geodynamic controls on the mechanisms of subduction and HP/UHP exhumation of crustal rocks during continental coll..., Tectonophysics (2014), http://dx.doi.org/10.1016/j.tecto.2014.04.033

Parovoz-FLAC algorithm (Fast Langrangian Analysis of Continua, Cundall, 1989; Poliakov et al., 1993; Appendix A), has all major features that are present in consistent models of continental collision. It implements explicit time-marching, large-strain Lagrangian algorithm to locally solve Newtonian equations of motion in continuum mechanics approximation. This code is viscous–elastic–plastic and written in full stress formulation, which allows for accurate computation of total pressure, P, as a trace of the full stress tensor. Solution of motion equations is coupled with constitutive equations, heat-transfer, fluid circulation, surface transport and thermodynamic equations. The algorithm also handles explicit free-surface boundary condition. The metamorphic phase changes are treated using free energy minimization algorithms (Connolly, 2005; De Capitani, 1994). The surface processes (erosion and sedimentation) are incorporated using linear and non-linear diffusion formulation (Avouac and Burov, 1996). The fluid transport algorithm is based on an enhanced variant of Darcy's flow with strain-rate dependent permeability (Angiboust et al., 2012). The Lagrangian grid is supplemented by a denser particle-in-cell sub-grid (9 to 30 particles, or passive markers, per grid element), which allows for diffusion-free interpolation of grid quantities between remeshings, as well as for tracing trajectories of selected particles, allowing, for example, for construction of synthetic P–T–t paths.

5.2. Numerical setup

5.2.1. Initial configuration

To achieve continental subduction phase in "natural" way, without prescribing it from the beginning, recent models of continental collision start from the oceanic phase of subduction (Fig. 4; Yamato et al., 2008). Oceanic subduction "prepares" conditions for the continental phase by creating a weak subduction interface and providing initial slab pull on the continental lithosphere. The oceanic accretion prism also provides weak material to start-up lubrication of the continental subduction interface (Figs. 4, 5). Further lubrication of the subduction interface is provided by the weak rheology of metamorphic and crustal rocks including the supply of sedimentary material produced by erosion of the uplifting topography.

5.2.2. Mechanical and thermal boundary and initial conditions

The most appropriate upper boundary condition for geotectonic modeling is a free surface. This condition is explicitly implemented in Flamar, which uses Lagrangian framework. It is noteworthy that many Eulerian codes based on Stokes flow formulation use surrogate "sticky air" approximation of the free surface (Sizova et al., 2012). If the required topography precision is not high, the "sticky air" approximation is quite acceptable provided the viscosity of the "air" is sufficiently low and the thickness of the "air" layer is sufficiently large. However, the absolute precision of nodal vertical and horizontal displacements in implicit Eulerian Stokes flow codes is typically on the order of half element size (e.g. 0.5 km for 1×1 km element size) because they are obtained indirectly, from interpolation of positions of passive markers. In the Lagrangian codes like Flamar, the practical accuracy of nodal positions is about two orders of magnitude better (e.g. 0.01 km for 1×1 km element size), because the nodes move with the velocity field (e.g., Francois et al., submitted for publication) and their coordinates are updated directly without interpolation.

In all existing models the lateral boundary conditions are kinematic (horizontal velocities). The Winkler's hydrostatic pliable bottom is often used as the bottom boundary condition. This semi-free condition allows for reduction of the vertical size of the model by up to 25% compared to the fixed-bottom configuration, allowing the slab to deflect the lower boundary of the model when it approaches the bottom. In subduction zones, the downward translation of a cold slab material produces complex thermal structures (Davies, 1999; Royden, 1993). To account for this complexity, the initial thermal structure (see Appendix A) relies on the oceanic plate cooling model for the oceanic part of the model, while the continental part is based on the continental plate cooling model (Parsons and Sclater, 1977; Appendix A) with a thermo-tectonic age of 160 Ma. The corresponding thermal boundary conditions include zero flux in lateral direction, and fixed temperatures at the upper surface

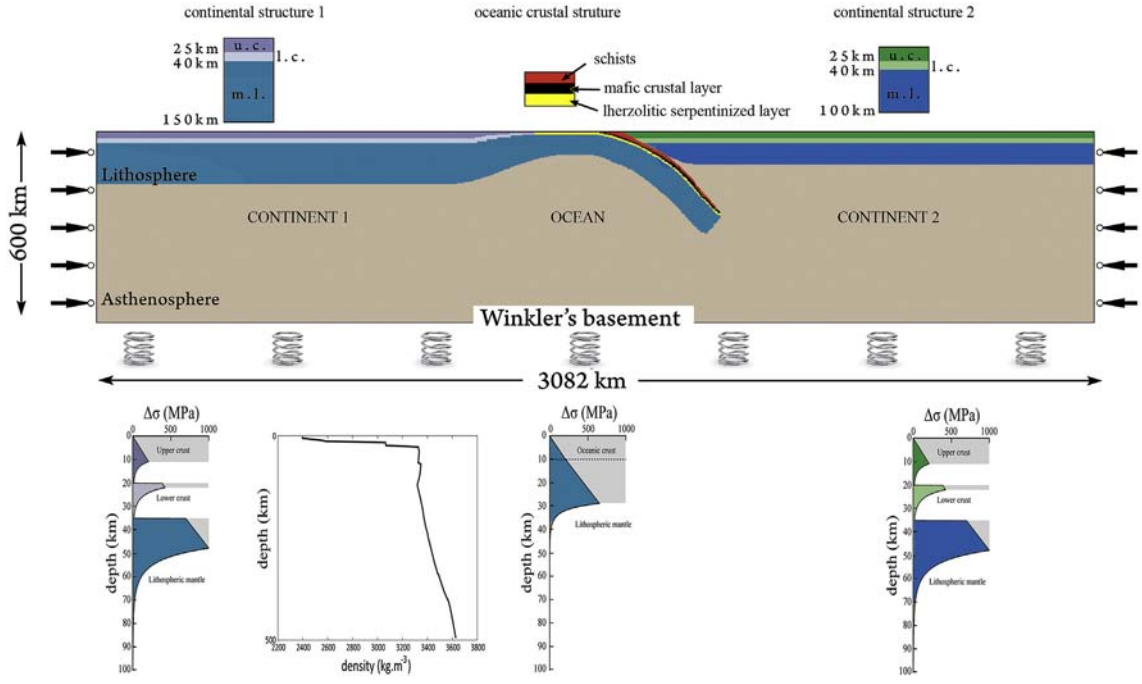

Fig. 4. Representative model setup (e.g., Francois et al., submitted for publication). The experiment starts from the oceanic subduction that transforms into continental collision/subduction. The upper boundary condition is a free surface combined with surface erosion and sedimentation in case of continental lithosphere. The bottom boundary condition is pliable Winkler basement. The lateral boundary conditions are velocities. The brittle–elastic–ductile rheology is different for the upper crust, lower crust, mantle lithosphere, slab, sediments, asthenosphere and deep mantle (Tables 1a and 1b, Fig. 5). The model eclogites have the same (weak) rheology as the upper crust, but higher density (up to 3400 kg/m^3). The crustal lithological and rheology profile that assumes mafic lower crust is consistent with seismic and gravity data. This assumption may not be generally valid, however (Hacker et al., 2011).

Please cite this article as: Burov, E., et al., Rheological and geodynamic controls on the mechanisms of subduction and HP/UHP exhumation of crustal rocks during continental coll..., Tectonophysics (2014), http://dx.doi.org/10.1016/j.tecto.2014.04.033

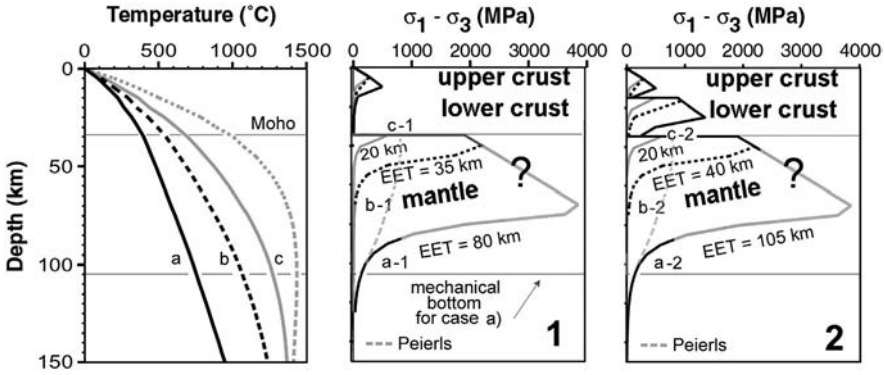

Fig. 5. Representative thermal and rheology profiles for continental lithosphere as function of thermo-tectonic age. EET = T_e is equivalent elastic thickness, directly measurable proxy (from isostatic observations) to the integrated strength of the lithosphere. Initial geotherms (left) and associated rheological strength profiles (middle and right) are computed for lithosphere with a 40-km-thick crust, deforming at a strain rate of 10^{-15} s^{-1}. Middle (1): Weak lower crust. Right (2): Strong lower crust. Black line: cold lithosphere (thermotectonic age = 450 m.y., T_{Moho} = 400–450 °C); black dashed lines: intermediate lithosphere (150 m.y., 550 °C); gray line: hot lithosphere (75 m.y., 650–700 °C); gray dashed line: very hot lithosphere (25 m.y., 1000 °C). Note also that the maximal strength of the mantle lithosphere is limited by Peierls flow law when the predicted dislocation or brittle strength is higher than Peierls strength.

and the bottom of the model. For the entire computational domain, the initial thermal distribution is computed through a combination of plate cooling models (oceanic or continental) for the upper lithospheric part with the adiabatic thermal gradient for the underlying mantle. One first solves the plate cooling problem assuming T = 0 °C at the surface and T = 1330 °C at the bottom of the lithosphere (Appendix A). Then the initial adiabatic temperature gradient in the underlying mantle is computed by equalizing the temperature at its top with the temperature at the bottom of the lithosphere (1330 °C) and by adjusting the mantle heat flux in a way that the temperature at the bottom of the upper mantle (650 km depth) fits 1700 ± 100 °C (e.g., Turcotte and Schubert, 2002). We re-adjust the initial thermal thickness and, if necessary, the thermotectonic age of the plate to satisfy heat fluxes at the mantle–lithosphere boundary. We control both the values of the surface and mantle heat flux to ensure that they fall in the expected range (30–80 mW m^{-2} at the surface and 10–30 mW m^{-2} in the mantle depending on plate age and thickness). The bottom and surface temperatures and zero lateral heat flow are fixed during all computations. There is a particular difficulty of thermal computations in the accretion prism that refers to the fact that thermal conductivity of sedimentary materials varies from 1 to 5 $W \cdot m^{-1} \cdot K^{-1}$, with low values for shales and sandstones (~1.2–4.2 $W \cdot m^{-1} \cdot K^{-1}$) and higher values for limestones and dolomites (2–5 $W \cdot m^{-1} \cdot K^{-1}$) (Turcotte and Schubert, 2002). The value used in reference simulation is 2 $W \cdot m^{-1} \cdot K^{-1}$, but a twice higher thermal conductivity was also tested.

5.2.3. Intermediate conditions for continental subduction

In the models, continental subduction, or, eventually other collision modes, follows the oceanic subduction. For this reason, the initial continental convergence rate equals the rate of the oceanic subduction (for example, two-sided initial closing rate of 2 × 1.5–3 $cm \cdot yr^{-1}$ during the first 5–10 My). The values tested in this study do not exceed the present-day continental collision rates, which are at maximum 3–6 $cm \cdot yr^{-1}$. These rates are on the order of smallest present-day oceanic subduction rates, and are also smaller than the past continental convergence rates for some particularly active continental collisions such as the India–Asia collision (2 × 4 to 2 × 5 $cm \cdot yr^{-1}$ during the first 10 $m \cdot yr^{-1}$) (Patriat and Achache, 1984).

5.2.4. Rheological structure

For continental and oceanic subduction/collision models, we assume that commonly inferred crustal structure and rheology parameters derived from rock mechanics (Tables 1a and 1b). As in nature, topography growth is strongly affected by surface erosion, which is modeled using diffusion erosion with a diffusion coefficient varied from 50 m^2 yr^{-1} to 11,000 m^2 yr^{-1} (the practical range is 100 m^2 yr^{-1} to 3000 m^2 yr^{-1}, Avouac and Burov, 1996; Burov et al., 2001). For continental collision, as for the case of the upper plate in the experiments on oceanic subduction, the initial geotherm is derived from the half-space cooling model modified to take into account internal heat production and structure of the continental lithosphere (e.g., Burov and Diament, 1995; Parsons and Sclater, 1977; Yamato et al., 2008; Appendix A).

5.2.5. Variable model parameters

One of the universal controlling variable parameters of all experiments is the initial geotherm, which is defined by the thermotectonic age (Burov and Diament, 1995; Toussaint et al., 2004a,b) and is largely characterized by the Moho temperature T_m (Fig. 5). The geotherm controls the major mechanical properties of the system through its strong impact on the rheological strength profile. By varying the geotherm, one can account for the whole possible range of lithospheres, from very old, cold, and strong plates to very young, hot, and weak ones. The second variable parameter for continental models is the composition of the lower crust, which, together with the geotherm, controls the degree of crust–mantle coupling. We generally considered both weak (quartz dominated) and strong (diabase) lower-crustal rheology and also strong and weak (dry versus wet olivine) mantle rheologies

Table 1a
Summary of thermal and mechanical parameters used in model calculations (Burov, 2010a, b, 2011; Ranalli, 1995; Turcotte and Schubert, 2002).

Type	Definition	Units
Thermal	Surface temperature (0 km depth)	0 °C
	Temperature at the base of thermal lithosphere	1330 °C
	Temperature at the base of upper mantle (650 km)	1700° ± 100 °C
	Thermal conductivity of crust	2.5 W m^{-1} $°C^{-1}$
	Thermal conductivity of mantle	3.5 Wm^{-1} $°C^{-1}$
	Thermal diffusivity of mantle	10^{-6} $m^2 \cdot s^{-1}$
	Radiogenic heat production at surface	9.5 ×10^{-10} W kg^{-1}
	Radiogenic heat production decay length	10 km
	Thermo-tectonic age of the lithosphere	50 to 600 Myr
Mechanical	Density of the upper crust[a]	2700 kg m^{-3}
	Density of lower crust[a]	2900 kg m^{-3}
	Density of oceanic crust[a]	2900 kg m^{-3}
	Density of sediment[a]	2600 kg m^{-3}
	Density of undepleted mantle[a]	3330 kg m^{-3}
	Density of asthenosphere[a]	3310 kg m^{-3}
	Lamé elastic constants λ, G (Here, λ = G)	30 GPa
	Byerlee's law — friction angle	30°
	Byerlee's law — cohesion	20 MPa

[a] We here provide average densities, in thermo-dynamically coupled models densities are derived directly from the assumed mineralogical composition as function of pressure and temperature conditions.

Please cite this article as: Burov, E., et al., Rheological and geodynamic controls on the mechanisms of subduction and HP/UHP exhumation of crustal rocks during continental coll..., Tectonophysics (2014), http://dx.doi.org/10.1016/j.tecto.2014.04.033

Table 1b
Example of ductile flow parameters assumed in model calculations. Compilation of Mackwell et al. (1998), who used data from Gleason and Tullis (1995), Wilks and Carter (1990), Hirth and Kohlstedt (1996) and Chopra and Paterson (1981). More recent data (see compilation in Bürgmann and Dresen, 2008) predict slightly different values for ductile flow parameters. However, in practice these differences are negated by adjusting geotherms or thicknesses of the rheological layers in way that the integral strength of the lithosphere matches the observed T_e values.

Layer	Composition	Pre-exponential stress constant A MPa^{-n} s^{-1}	Power law exponent n	Activation energy, Q KJ mol^{-1}
Upper crust	Wet quartzite	1.1×10^{-4}	4	223
Lower crust	Dry Maryland diabase	8 ± 4	4.7 ± 0.6	485 ± 30
	Undried Pikwitonei granulite	1.4×10^{4}	4.2	445
Mantle or oceanic lithosphere	Dry olivine	4.85×10^{4}	3.5	535
	Wet olivine	417	4.48	498
	Diffusion creep	1.92×10^{-4}	1	3.0×10^{5}
	Peierls law	$10^{7.8} \times 10^{-12}$	Peierls stress = 5 GPa	5.35×10^{5}

(Tables 1a and 1b). In high resolution experiments, intermediate crust has been also included in the models (Yamato et al., 2008).

As discussed in the previous sections, for a given thermo-rheological strength profile, the convergence rate is the main factor defining the mode of continental collision via its impact on the critical Peclet number of the system. In nature, there is a correlation between the convergence rate, the mechanical strength and thermal state of the subducting lithosphere (Mouthereau et al., 2013) such that all major controlling parameters are inter-dependent. We here consider 3 representative cases: (1) very slow collision of weak lithosphere (Alps), (2) intermediate-rate collision (Zagros) of middle-strong lithosphere and (3) fast subduction of very strong Indian lithosphere (Himalaya). The tested convergence velocities vary from 2×3 mm·yr^{-1} to 2×3 cm·yr^{-1}. We then test the influence of most important metamorphic changes such as, for instance, serpentinization, schisting and eclogitization (at P > 1.5 GPa and T > 550 °C, see Tables 1a and 1b).

5.3. Comparison of end-member cases of continental subduction

Fig. 6 provides a representative example of continental collision experiments (Francois et al., submitted for publication) in a Zagros collision context that occurs at intermediate convergence rates. The experiments start from an oceanic subduction phase (Figs. 4, 5) and, after several slab break-off episodes arrive at the stage of continental subduction that occurs progressively, as a result of subduction of the continental margin pulled by the oceanic plate. The repetitive character of slab-break off process in case of intermediate convergence rates (2 cm·yr^{-1} on both sides) is an important feature potentially explaining the possibility of repetitive changes in deformation styles, topography evolution and exhumation events observed at the surface. We will later discuss the results of these experiments in full detail, but at this stage Zagros collision experiments were used as a representative example demonstrating the importance of the oceanic subduction phase in continental collision models.

5.3.1. Stage I: Pre-continental (oceanic) subduction phase (slow convergence)

As mentioned, the oceanic subduction phase plays an important role in the development of continental collision, specifically in case of slow convergence rates. We hence start detailed discussion of collision/exhumation models from description of the oceanic phase for particularly slow Alpine convergence settings. Figs. 7–9 show experiments on the oceanic phase of Alpine convergence implemented by Yamato et al., 2007 as initial phase of their continental collision model (Yamato et al., 2008, Fig. 7). In this model the oceanic plate subducts at a rate of 6 cm·yr^{-1} below the overriding continental plate. These experiments target the Alpine collision and are aimed, in particular, to test the idea of the possibility of continental subduction as follow-up of the oceanic subduction in slow convergence settings. In these experiments, the thermo-mechanical model was coupled with a thermo-dynamic model using the thermodynamic algorithm THERIAK (De Capitani, 1994, see Appendix A) that predicts mineralogical phases and their density by minimizing free Gibbs energy for P–T conditions computed within the thermo-mechanical part of the model. The experiment successfully reproduces the burial and exhumation in a subduction wedge (Fig. 8), in terms of correspondence between the predicted synthetic and observed P–T–t trajectories and the structural and exhumation patterns. The model is tested and parameterized on the well constrained Schistes Lustrés complex (SL; Western Alps), which is thought to represent

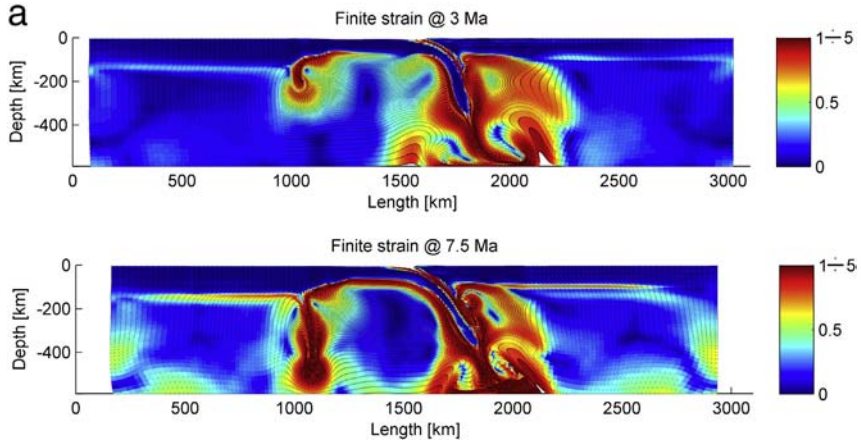

Fig. 6. a. Example of implementation of a numerical collision model (see Fig. 4) that starts from the oceanic subduction phase with progressive transition to continental subduction (Zagros collision settings) after slab-break off (Francois et al., 2012). The figure shows finite strain distributions during the oceanic subduction phase demonstrating extreme strain localization around the slab and at the LAB. The model lithosphere is shortening with a rate of 4 cm·yr^{-1} on both sides. b. Progressive transition from oceanic to continental subduction in the experiment similar to the one shown in Fig. 6a, with same total convergence rate of 4 cm·yr^{-1}. Note earlier slab break-off at 6.5 Myr. Shown are the logarithm of the effective viscosity (ratio of shear stress to strain rate) and surface topography. The star symbol corresponds to the slab break-off zone, and the number near the star — to the number of break-off event (there are three consecutive slab break-offs in this experiment).

Please cite this article as: Burov, E., et al., Rheological and geodynamic controls on the mechanisms of subduction and HP/UHP exhumation of crustal rocks during continental coll..., Tectonophysics (2014), http://dx.doi.org/10.1016/j.tecto.2014.04.033

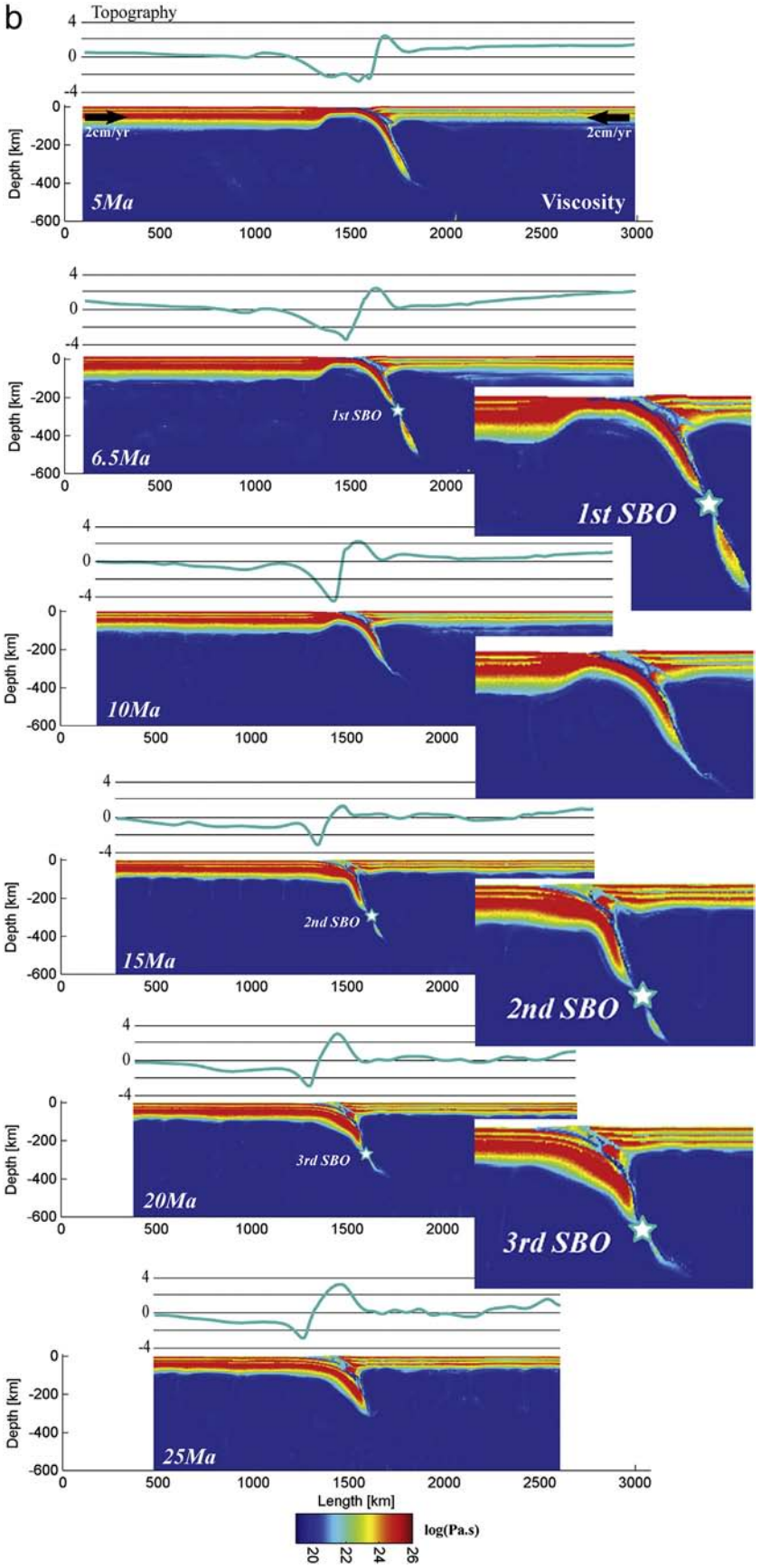

Fig. 6 (*continued*).

Please cite this article as: Burov, E., et al., Rheological and geodynamic controls on the mechanisms of subduction and HP/UHP exhumation of crustal rocks during continental coll..., Tectonophysics (2014), http://dx.doi.org/10.1016/j.tecto.2014.04.033

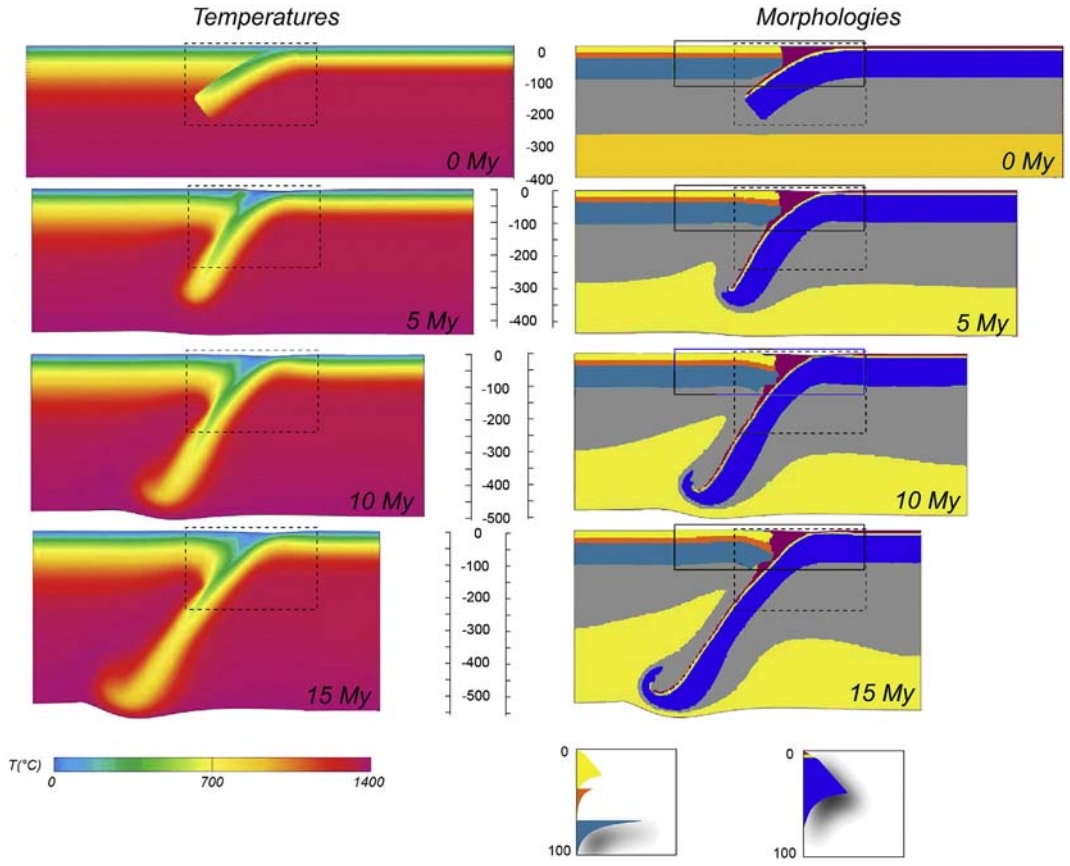

Fig. 7. Oceanic phase of Alpine convergence: example of self-consistent subduction experiments (Yamato et al., 2006), for the case of an oceanic plate subducting below a 160 Myr old continental lithosphere. This experiment implements thermo-dynamically consistent phase changes. Densities for all material phases are computed using the algorithm THERIAK (De Capitani, 1994; Tables 1a and 1b, Appendix A). Squared zones show the position of zoom area shown in Fig. 8. Shown at the bottom are the assumed rheological profiles, for the continental (left) and oceanic plate (right). The profiles were derived for the mentioned thermotectonic age under assumption of quartz-rich upper continental crust, diabase lower crust, and olivine mantle (Tables 1a and 1b). Olivine is used for the entire oceanic lithosphere.

the fossil accretionary wedge of the Liguro-Piemontese ocean. For convergence rates comparable to the oceanic phase of the Alpine subduction (~3 cm·yr^{-1}), the best fitting results are obtained for high viscosity, low density wedge sediments and/or a strong lower continental crust. After a short transition period of 3–5 My, the modeled accretionary wedges reach a steady state which lasts over 20 My. Over this time span, a significant part (~35%) of sediments entering the wedge undergoes P–T conditions typical of the SL complex (~15–20 kbar; 350–450 °C) with similar P–T loops. Computed exhumation rates (<6 mm·yr^{-1}) are in the agreement with observations (1–5 mm·yr^{-1}) hence validating the choices of thermo-rheological parameters and conforming the viability of accretion prism concept of LP/MP exhumation. The model confirms the crucial importance of the mechanical weakening due to metamorphic reactions in the subduction interface zone by showing that in presence of a serpentinite layer below the oceanic crust, exhumation of oceanic material takes place at realistic rates approaching 3 mm·yr^{-1}. The importance of metamorphic reactions was well demonstrated in later follow-up of this study by Angiboust et al. (2012) who have developed a two-phase flow model in the oceanic subduction context by coupling the Alpine subduction model with porous-matrix fluid transport equations (Fig. 9). In this model, dehydration of serpentinite layers provokes fluid release forming a hydration front in the mantle around the subduction interface. As a result, the mantle wedge is strongly weakened (e.g., Guillot et al., 2000, 2001) allowing for more efficient uncoupling between the lower (subducting) and overriding plate. A fluid migration algorithm is coupled with thermo-mechanical counterpart so that the fluids are free to migrate through a permeable matrix, driven by rock fluid concentrations, non-lithostatic pressure gradients and deformation. These experiments show that deformation is accommodated along the subduction interface by a low-strength shear zone parallel to the wall of the subduction thrust interface, and characterized by a weak (10–25% of serpentinite) and relatively narrow (5–10 km) serpentinized front. Dehydration associated with eclogitization of the oceanic crust (60–75 km depth) and serpentinite breakdown (110–130 km depth) significantly decreases the mechanical strength of the mantle at these depths, thereby favoring the detachment of large slices of oceanic crust along the plate interface. In these experiments, the resulting morphologies are in good agreement with reconstructions derived from structural field observations from the Alpine eclogite-facies ophiolitic belt (i.e., corresponding to coherent fragments of oceanic crust detached at ~80 km depth in the Alpine subduction zone and exhumed along the subduction interface; Angiboust et al., 2009; Angiboust and Agard, 2010). It can be suggested that overall weakening of the plate contact-zone during oceanic subduction creates necessary conditions for the continental subduction at later stages.

5.3.2. Stage II: Subduction of a weak lithosphere (T_e < 30 km) at slow convergence rate (<1.5 cm·yr^{-1}) showing strong dependence on crustal and lithosphere mantle rheology

The second phase of Alpine convergence corresponds to continental subduction occurring at slow convergence rate and hence at near critical Peclet numbers. Slow convergence settings present a particularly important framework for studying continental convergence due to the extreme dependence, in this case, of the collision mode on thermo-rheological assumptions (Yamato et al., 2008). The well-studied Alps are an excellent example for this that is characterized by both very small convergence rates and by a weak lithosphere, as attested by T_e data (Watts, 2001). In the study by Yamato et al. (2008), various crustal

Please cite this article as: Burov, E., et al., Rheological and geodynamic controls on the mechanisms of subduction and HP/UHP exhumation of crustal rocks during continental coll..., Tectonophysics (2014), http://dx.doi.org/10.1016/j.tecto.2014.04.033

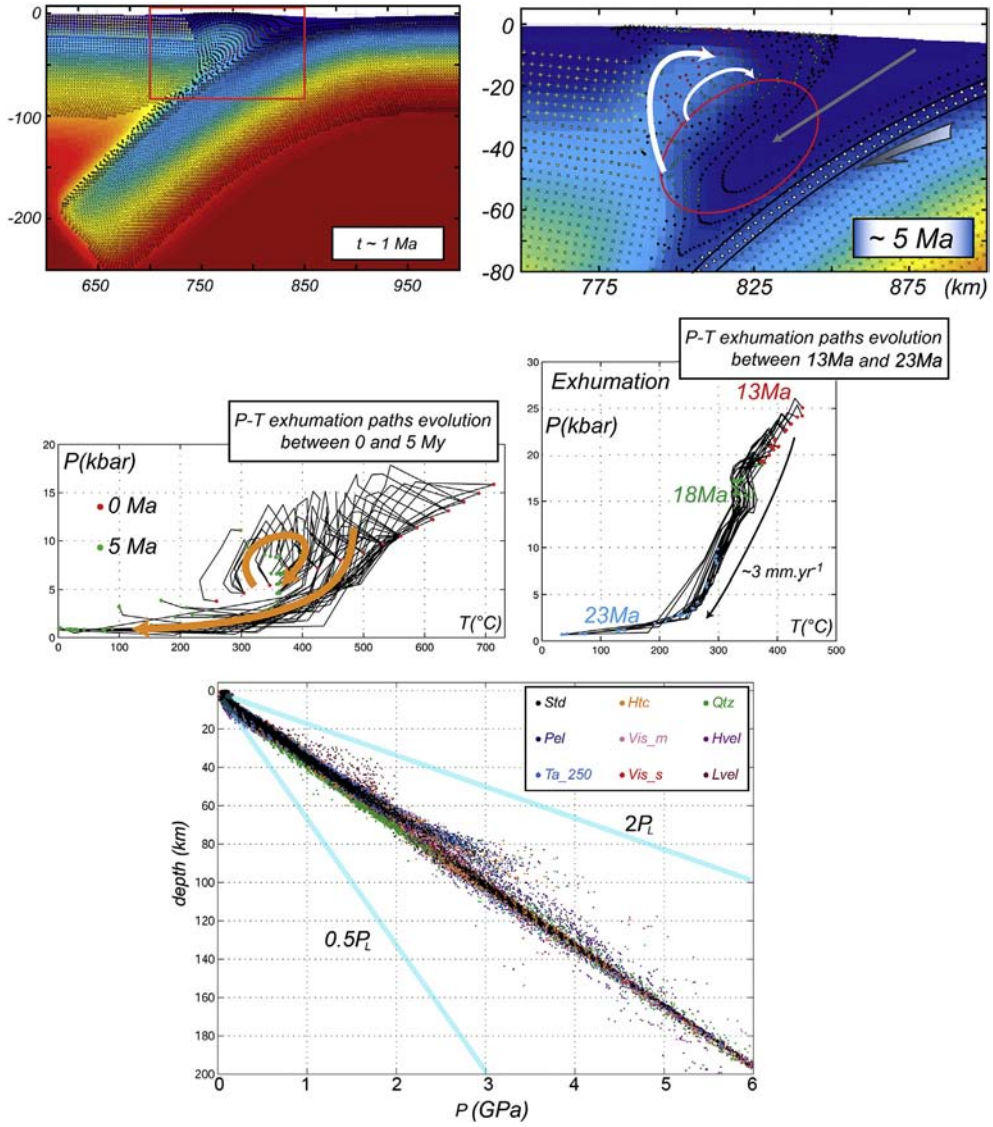

Fig. 8. Zoom to the oceanic subduction interface, for the experiments shown in Fig. 7. Marker field at 5 Myr traces the movements of the particles, which allows us to trace P–T–t paths at each moment of time (bottom). In this model, exhumation of HP rocks was achieved at 10–13 Myr under assumption of low viscosity of the serpentinite layer. All markers used for the construction of the P–T–t paths were initially located in the normal (un-subducted) oceanic sediments (the uppermost 2 km layer of the crust). The lower panel shows pressure distribution in the subduction channel/interface compared to theoretically admissible upper and lower bounds (double lithostatic and half-lithostatic). Note less than 20% deviations from the lithostatic gradient.

compositions have been tested, starting from an "all-granite" (very weak) crust and ending by "all-diabase" (very strong) crust (Tables 1a and 1b). It is difficult to constrain the range of the convergence rates in the Alpine orogeny at the eve of the collision stage, that is, back to 30 $m \cdot yr^{-1}$. The present day convergence rates are at the limit of accuracy of geodetic measurements (<0.5 $mm \cdot yr^{-1}$); while the average amount of shortening estimated from structural paleoreconstructions, divided by the duration of the convergence, also yields very small values on the order of 0.8 $mm \cdot yr^{-1}$ (Ford et al., 2006). Exhumation of UHP rocks of continental origin within the first 5 Myr of collision from depths in excess of 100–120 km, suggests, however, that at this stage the convergence rate had to be much faster, on the order of 2× (0.75–1) $cm \cdot yr^{-1}$. The UHP exhumation data hence is practically the only observation allowing us to constrain the dynamics of the collision zone during the first 5–15 Myr. The most reasonable idea is hence to suggest that during the initial several Myr the continental subduction continued at rates that were comparable to those of the preceding oceanic subduction. This reinforces the idea that the oceanic slab pull is an important component of the initial force balance at the onset of the continental collision phase. It can be also argued that the initial subduction rates were even higher than the estimates obtained from dating exhumed rocks versus the exhumation depth. In particular, some part of UHP rock could be buried deeper without being exhumed (which is probably the case of fast collision zones such as Himalaya, and certainly the case for the Zagros; Agard et al., 2011). At the agnostic side, we cannot also exclude that the exhumed rocks are not representative of the bulk circulation of the metamorphic material in the subduction wedge. It is however unlikely that the exhumed UHP material is formed as a result of local stress concentrations and/or overpressure since the UHP facies are present at a large scale, in vast continuous volumes (Yamato et al., 2008) and in systematic spatial association with oceanic HP/UHP units (Agard et al., 2009).

The experiments shown in Supplementary Fig. 1 illustrate the historically first numerical model of Alpine collision that has been successful in reproducing continental subduction and UHP exhumation in the Alpine context (Burov et al., 2001). This model has been enhanced by Yamato et al. (2008) who have coupled it with thermodynamic processes while significantly increasing the numerical resolution (Figs. 10, 11). This model, accounting for multilayered rheological structure of the continental crust, shows that UHP exhumation may occur due to mechanical decoupling of the subducted lower or middle crustal layer from both mantle lithosphere and the upper crustal layer. A large part of the layer tip tears off and flows up at the rear of the accretion wedge,

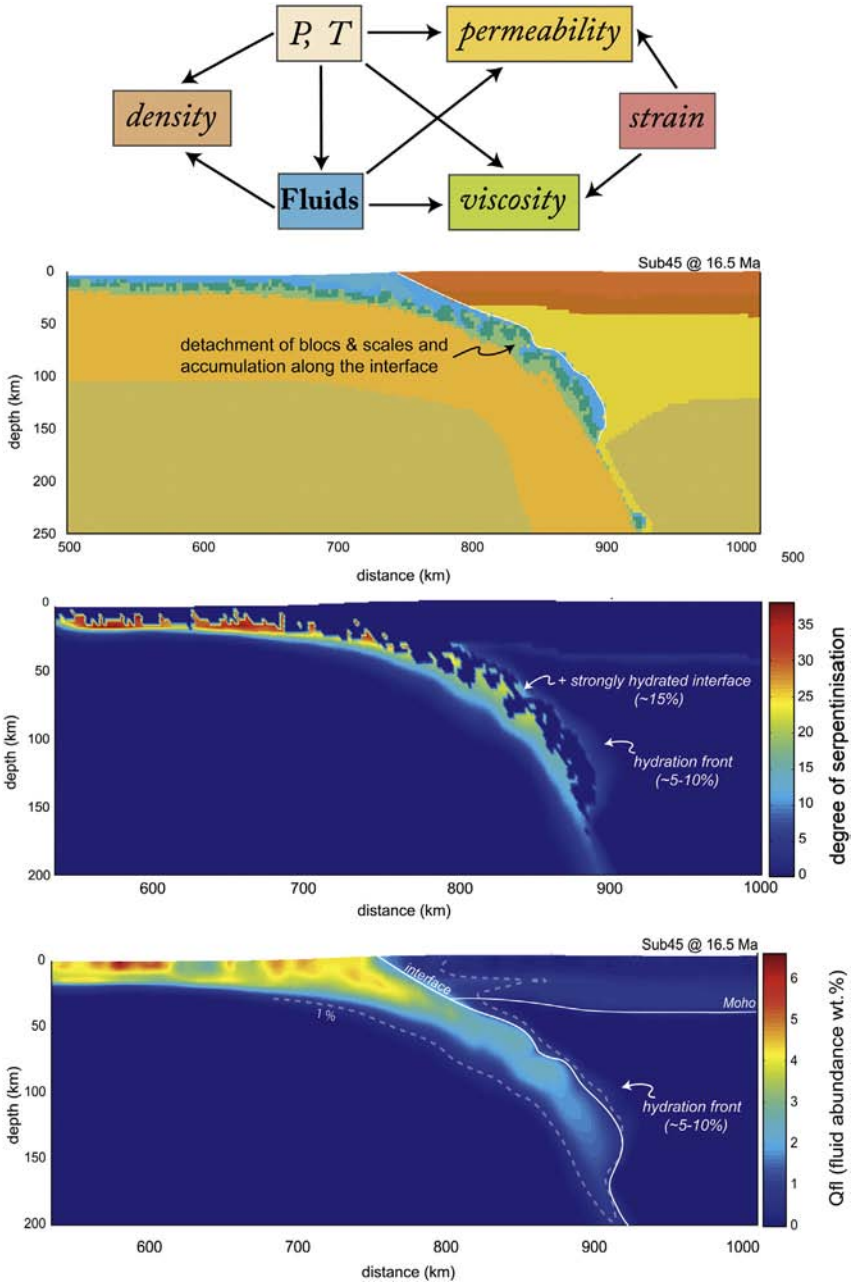

Fig. 9. Example of two-phase flow version of the Alpine subduction (oceanic phase) experiments shown in Figs. 7–8 (Angiboust et al., 2012), in which thermo-mechanical and thermo-dynamic model is coupled with porous flow model (top) where permeability and viscosity are functions of strain rate, pressure and temperature. As can be seen, hydration/dehydration reactions result in strong changes of fluid content in the oceanic subduction interface zone. A 1–2% fluid content variation is sufficient to drop viscous strength by a factor of 10. As result, the interface zone and the mantle wedge are essentially weakened allowing for stable subduction. This weak interface zone is re-used by the arriving continental lithosphere at the initial stages of the continental subduction.

between the subducting and overriding plates, in agreement with the field observations for the Western Alps. The predicted bi-phase exhumation rate and P–T trends match well the observational data thus justifying the model (Fig. 11). This high resolution model was first used to parameterize the rheological choices by exploring the impact of the convergence rate and rheology in case of the relatively weak Alpine lithosphere (Fig. 12). These experiments demonstrate extremely high sensitivity of the models to the rheological parameters thus allowing for robust elimination of those thermo-rheological profiles that are mechanically incompatible with the considered convergence scenario. Surprisingly, the models have demonstrated that some rather "classical" rheological choices such as that of all-quartz-rich crust are entirely incompatible with the dynamics of the Alpine collision (Fig. 12), hence opening a new way of linking the laboratory derived rheology laws to geological scales. Figs. 13, 14 also show the impact of convergence velocity for the case of best fitting rheological structure derived for the Alps on the base of the experiments shown in Fig. 12. It can be seen that very slow rates (<3 mm·yr^{-1}) result in Rayleigh–Taylor instabilities and slab-breakoff, while very high velocities, in case of weak lithosphere (2×3 cm·yr^{-1}), lead to development of unusual double-sided symmetric subduction. Also, the predicted exhumation rates are directly comparable with the observations thus allowing for elimination of incompatibly high convergence rates. The other remarkable results refer to the prediction that higher convergence rates result in slower UHP exhumation just until its complete disappearance at rates exceeding 30 mm·yr^{-1}. This result rovides some elements for explanation why UHP rocks of continental origin are rare or absent in faster convergence settings such as Zagros or Himalaya. It can be thus once again concluded that the convergence

Please cite this article as: Burov, E., et al., Rheological and geodynamic controls on the mechanisms of subduction and HP/UHP exhumation of crustal rocks during continental coll..., Tectonophysics (2014), http://dx.doi.org/10.1016/j.tecto.2014.04.033

rates and the integrated strength of the lithosphere are interlinked, probably because that higher convergence rate requires higher slab pull/push forces while such forces can be only exerted on the lithosphere if the latter is strong enough to sustain them.

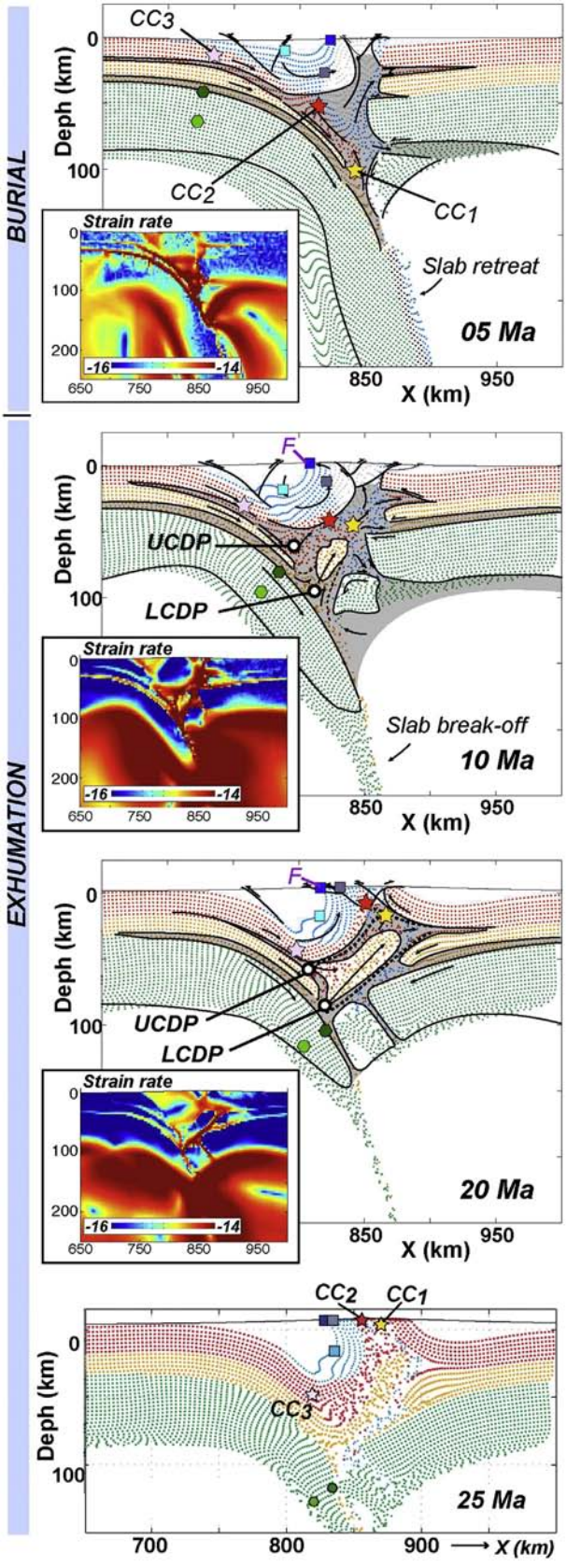

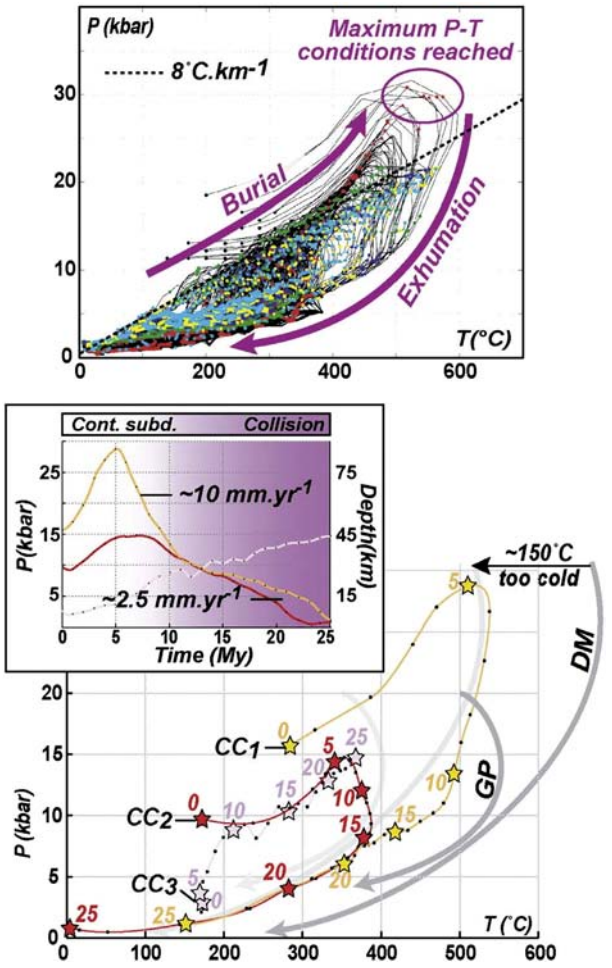

Fig. 11. P–T–t paths of particles (passive markers) coming from the upper continental crust and comparison with the observed P–T paths of the Western Alps (experiment of Fig. 10). Color and symbols as for GP: Gran Paradiso; DM: Dora Maira. See caption to Fig. 10 for other notations. The experiments predict P–T trends that are very similar to nature, assuring that the models realistically reproduce subduction/collision dynamics. Temperature shift of 100–150 °C can be explained by underestimated contribution of shear heating.

5.3.3. Intermediate (1.5–3 cm/myr) to fast convergence rates (>3 cm/myr), intermediately strong (T_e ~ 50 km) to strong (T_e > 70 km) lithosphere. Impact of convergence rate partitioning

We here discuss the inferences from the experiments (Supplementary Fig. 2) studying the amount of continental subduction as function of convergence rate assuming strong cold lithosphere with T_e values on the order of 70 km (e.g., Indian craton, Watts, 2001). Even for such a strong lithosphere, the experiments show significant dependence of the

Fig. 10. Thermo-dynamically coupled high-resolution model of continental phase of Alpine collision (Yamato et al., 2008) revealing fine details of subduction and exhumation mechanics in slow convergent context. Marker regions of blue and gray color correspond to initial sediments (gray markers are those totally eroded after the 20 Myr of experiment). Red and orange markers correspond, respectively, to the upper crust and the lower crust. Green markers represent lithospheric mantle and black ones the oceanic crust. Abbreviations: CC, continental crust; SL, accretionary wedge sediments of the "Schistes Lustrés". The position of the "F point" in the sedimentary accretionary wedge is virtually stable as well as that of two other characteristic points (UCDP and LCDP, Upper and Lower Crustal Decoupling Points, respectively). Note that within the pre-existing subjacent sedimentary accretionary wedge, sediments form a "rigid block", which stays non-deformed and moves, by rotation, around the stable point F. This mechanism can explain why "Schistes Lustrés" found at this place in the Western Alps are dated from the oceanic subduction. The markers shown with stars (CC1, CC2, CC3) correspond, respectively, to the units of Dora Maira, Gran Paradiso, and to formerly surface unit currently buried at great depth. CC1 and CC2 are exhumed at surface at the end of the experiment (25 Ma) after traveling to a more than a 100 km depth (CC1).

Please cite this article as: Burov, E., et al., Rheological and geodynamic controls on the mechanisms of subduction and HP/UHP exhumation of crustal rocks during continental coll..., Tectonophysics (2014), http://dx.doi.org/10.1016/j.tecto.2014.04.033

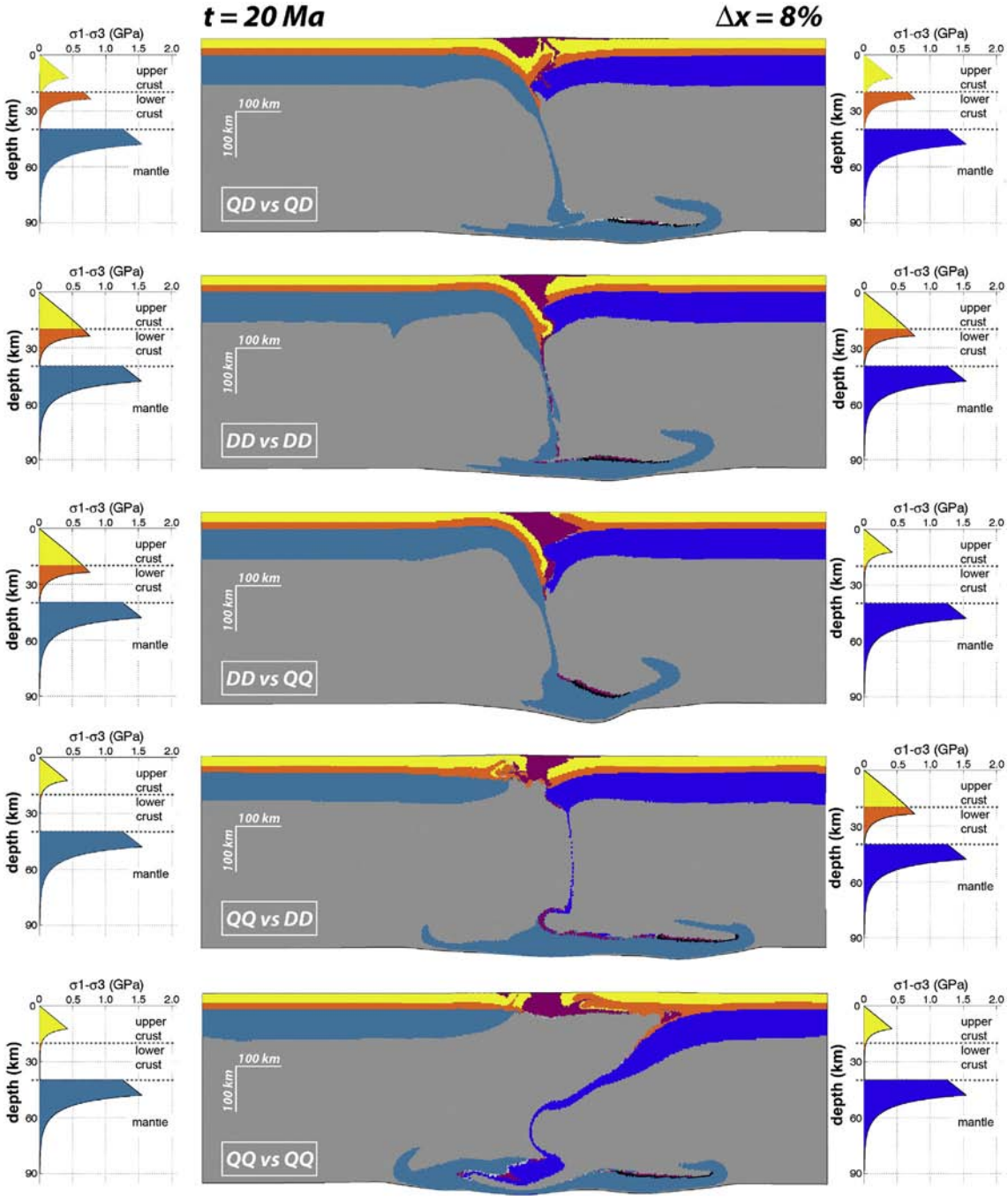

Fig. 12. Influence of crustal rheology on the collision style in case of slow (6 mm·yr^{-1}) Alpine-type collision (weak lithosphere). The general setup of experiments corresponds to that of Fig. 10. Shown are morphologies for the models at 20 Myr for different crustal strength profiles. QD: quartz–diabase double-layer crustal structure (upper and lower crust, respectively). QQ: quartz–quartz double-layer crustal structure; DD: strong single-layer structure simulated by diabase. Color code: blue — mantle, orange — lower crust, yellow — upper crust, gray — asthenosphere and sub-lithosphere mantle.

amount of subduction on the convergence rate, for equivalent amounts of tectonic shortening. In the experiments, the amount of subduction is characterized by "subduction number" S which is the ratio of the subduction length l to the total amount of shortening Δx ($S = l/\Delta x$). l is measured as a plate-parallel displacement of a virtual vertical passive marker line (Supplementary Fig. 2), initially placed in the lower plate at some distance from the major thrust. That is, when $S = 1$, all of the tectonic shortening is accommodated by subduction (in some cases $S > 1$ due to the additional stretching of the slab). If $S < 1$, then some part of shortening is accommodated in pure shear or by folding of the lower plate. As demonstrated by these experiments, S number approaches 1 (100% subduction) only for convergence rates >3 cm·yr^{-1} (subduction Peclet number > 10). At smaller rates, an essential amount of shortening is accommodated by pure shear thickening and partly by folding. The physical reason for that is that at higher convergence rates, heat diffusion cannot affect plate viscosity (and hence plate strength and buoyancy) before the plate reaches an important depth. At smaller rates heat diffusion results in plate weakening and buoyancy rise, which hampers the possibility of subduction.

Francois et al. (submitted for publication) have also studied the conditions of the intermediate rate Zagros collision (Figs. 4–6, 15, 16), which some workers regard as a "mini-Himalayan collision" (Hatzfeld and Molnar, 2010) due to the fact that in both cases an old strong cratonic plate slides below a younger weaker overriding plate resulting

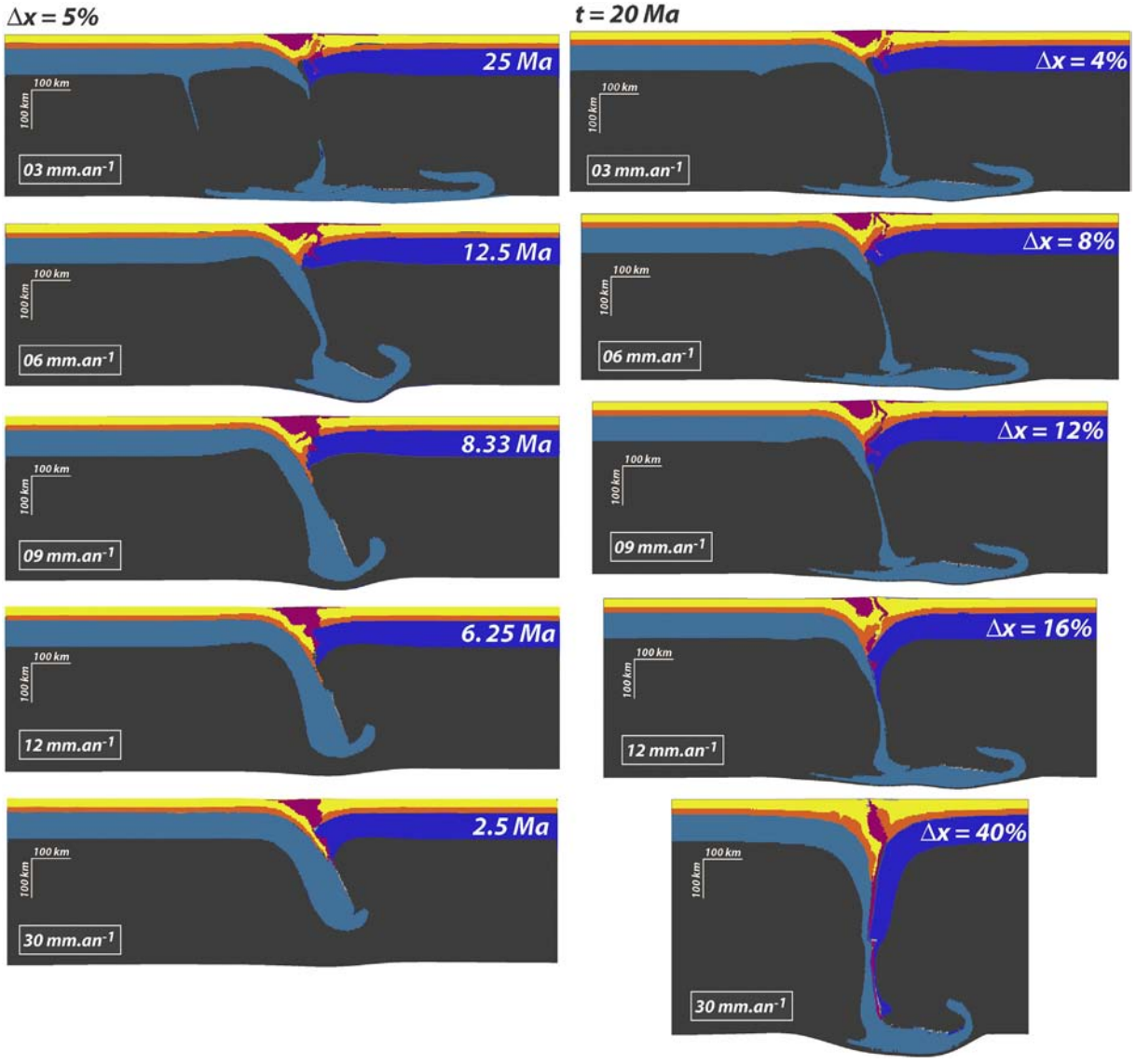

Fig. 13. Morphologies of the Alpine (weak lithosphere with $T_e \sim 30$ km) collision models for different convergence rates. The general setup of the experiments corresponds to that of Fig. 10 (shortening with a constant rate at both sides, the rheology profile corresponds to the top experiment "QD"–"QD" of Fig. 12); colors correspond to definitions of Fig. 12. Left: configuration after 5% of shortening (compared to the initial width of the box). Right: configuration at 20 Ma since onset of convergence. As can be seen, high convergence rate promotes sustainable subduction while at slow rate slab break-off and RT instabilities shorten the duration of the subduction stage. Color code: see caption to Fig. 12.

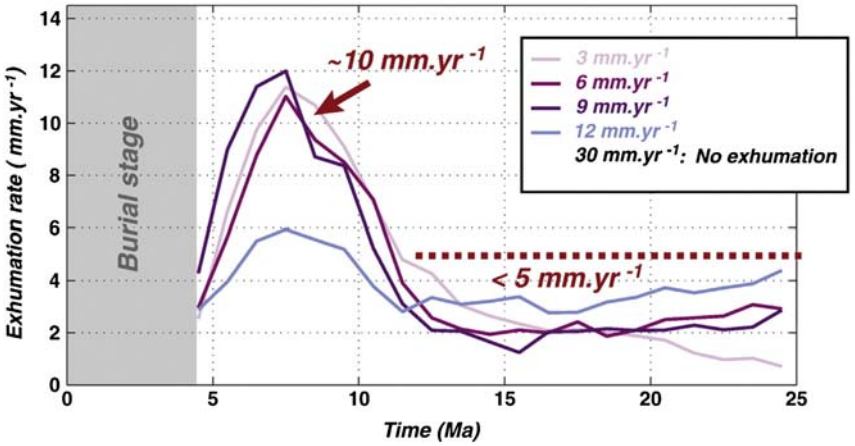

Fig. 14. UHP exhumation rates for the experiments shown in Fig. 13. Note that high convergence rates reduce exhumation rates until fully prohibiting UHP exhumation.

Please cite this article as: Burov, E., et al., Rheological and geodynamic controls on the mechanisms of subduction and HP/UHP exhumation of crustal rocks during continental coll..., Tectonophysics (2014), http://dx.doi.org/10.1016/j.tecto.2014.04.033

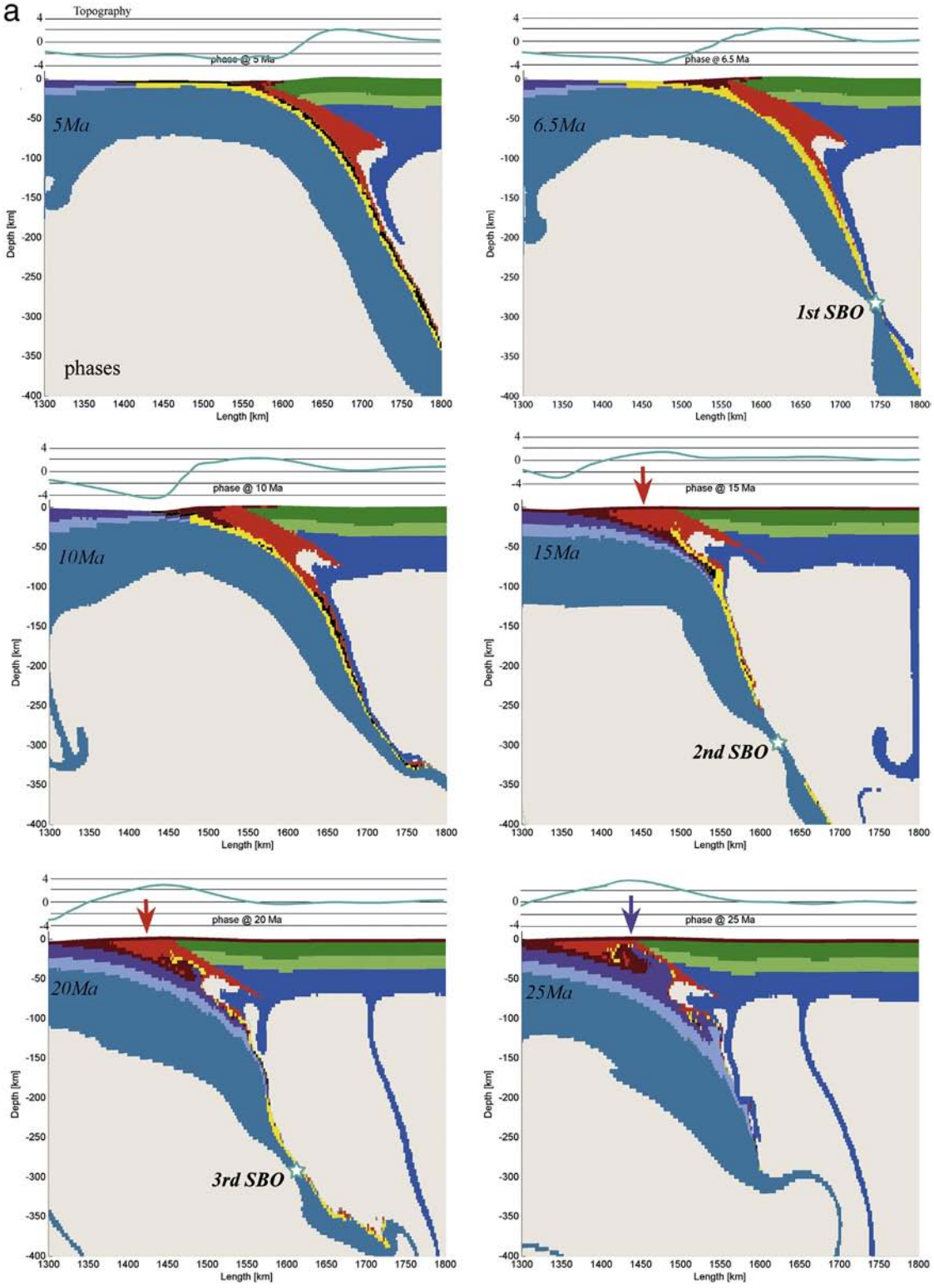

Fig. 15. a. Continental subduction experiments testing the case of intermediate convergence rate of 2 cm·yr^{-1} (Zagros collision model, Francois et al., 2012). Shown are zooms to the subduction interface zone for the major stages of the evolution of the experiments from Figs. 4–6. Note formation of a "crustal pocket" at depth of 100–150 that may eventually serve as a source for HP or UHP exhumation. Color code: same is in Fig. 4. See also (Figs. 4–6). SBO means "Slab break-off". (There consequent slab-break-offs occur before the first exhumation of HP/UHP continental crust). Red arrows show the area of initial exhumation of metamorphosed HP/UHP oceanic material. Purple (violet) arrow shows the area of the first exhumation of HP/UHP continental crustal material. Note that oceanic HP/UHP materials exhumes at the onset of the continental collision, when it is pushed/dragged up by low buoyancy continental crustal rocks. It is noteworthy that most exhuming HP/UHP rocks get blocked just few km below the surface. Shown is material field (1 pixel — one grid element). b. Exhumation of the oceanic crust as a result of the onset of continental subduction (top panels). The bottom panel shows corresponding P–T-paths (blue curves correspond to P-T paths in the exhumed continental crust, brown curve corresponds to P-T path in the oceanic crust. Stars show timing of pressure picks. 24 Ma corresponds to the time of simultaneous pressure maximum in the exhumed oceanic and continental crustal units. Note that HP oceanic units are exhumed at the continental subduction stage). See caption to Fig. 15a for further details. c. Similar exhumation mechanism reproduced in the study by Li and Gerya (2009) applied to Sulu terranes in eastern China. These authors used the term "sub-lithosphere plume" for what Burov et al. (2001) have called "crustal pocket" — a deep area of crustal underplating that serves as a source for eventually fast periodic HP/UHP exhumation (see also Fig. 3c(E)). Bottom panel — predicted PT paths. Shown is passive marker field (1 pixel — 1 marker, there are tens of markers per grid element. The real grid resolution is coarser). Color squares in the bottom panel correspond to the representative marker domains shown by the same symbols in the upper and middle panel.

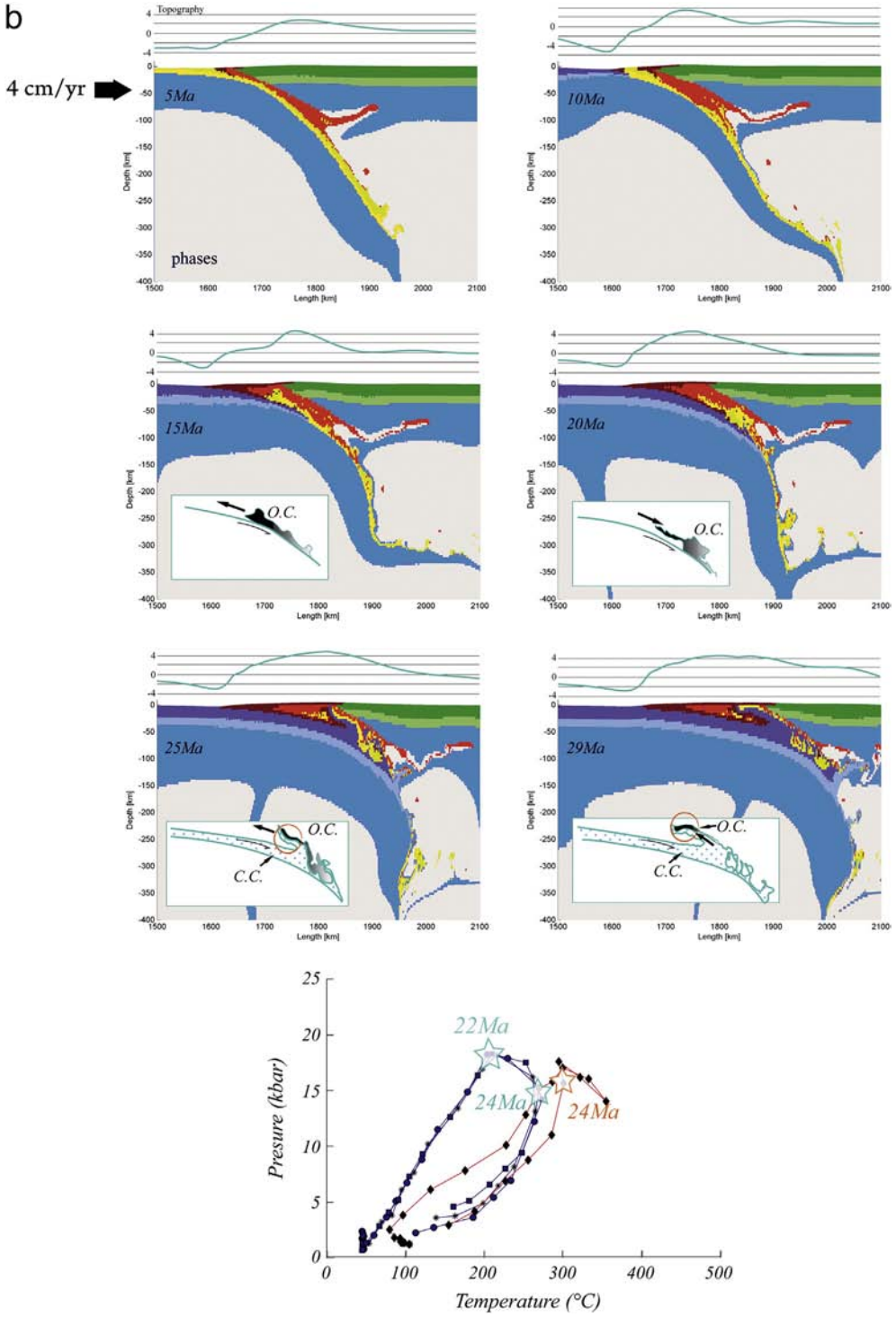

Fig. 15 (*continued*).

in rise of an elevated plateau. However, the similarities between these two collision zones probably do not go much further. In particular, the Iranian plateau is much shorter and lower than the Tibetan plateau, has a pronounced elevation trend, even though it is subject, as Tibetan plateau, to significant extension in the direction normal to convergence (England and Houseman, 1989); the Zagros mountain belt is also much lower than Himalaya, and it has been also suggested that relatively early slab break-off could have affected Zagros collision whereas in the Himalayan case slab break-off event did not probably take place (Toussaint et al., 2004a,b). The respective integrated strength of the Arabian plate (T_e ~ 50 km) is also much smaller than that of the Indian plate (T_e ~ 70–90 km), but both plates are much stronger than the Alpine lithosphere. Last but not least, the convergence rate in Zagros is about 2 times smaller than in Himalaya.

Fig. 15a–b shows zooms to the subduction interface zone for the major stages of the evolution of the "Zagros collision" experiments from Fig. 4. As in Burov et al. (2001) this model shows formation of a crustal UHP "pocket" or , "sub-lithosphere plume" (Fig. 3c(E)) at 100–150 km depth from which the rock can be eventually exhumed to the surface at rates largely controlled by local viscosity and density contrast (Eq. (7)). Crustal "pocket exhumation mechanism" has been reproduced in a number of recent studies, for example by Li and

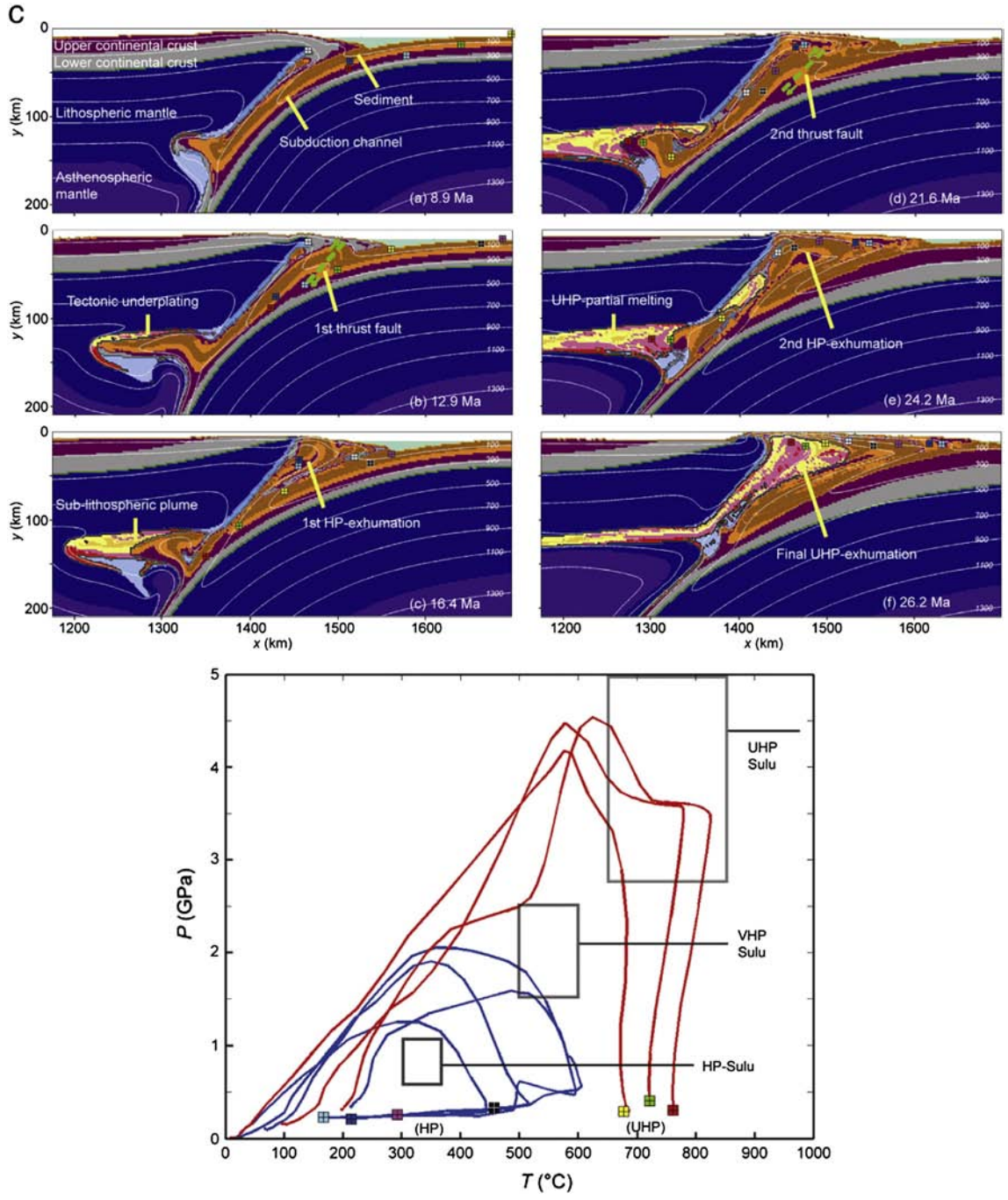

Fig. 15 *(continued).*

Gerya (2009, Fig. 15c) for HP–UHP Sulu terrain in eastern China. As can be seen from Fig. 15a, quite contrary to common expectations, several consequent slab-break-offs may occur before the exhumation of HP/UHP continental crust without producing major topographic response at the surface. It is also remarkable that oceanic HP/UHP material is exhumed only at the onset of the continental collision, when it is pushed/dragged up by low buoyancy continental crustal rocks. Similarly, exhumation of small amounts of HP/UHP material occurs during the initial stages of collision (at 25 Myr of model time). Interestingly, the majority of exhuming HP/UHP rocks get stacked a few km below the surface. This explains the practical absence of UHP material in Zagros. It can be also concluded that even if the presence of UHP material at surface can serve as indicator of subduction processes, its absence, on the contrary, does not prove the absence of such. Furthermore, it follows from these and previously shown experiments that only limited parts of possible P–T paths arrive at the surface, appealing for a thorough study of their representativity for the bulk exhumation and collision mechanisms.

Francois et al. (submitted for publication) have found that for intermediate and high convergence rates, collision style is highly dependent not only on the total value of the convergence rate but also on the partitioning of the convergence rates between the overriding and subducting plate. The explicit presence of absolute advection velocity terms (Eq. (1); Appendix A) in the heat transfer equation explains the sensitivity of the behavior of the thermo-mechanical system to the partitioning of the convergence rates between the two sides of the model. For example, applying total velocity at the border of the subducting plate enhances the amount of subduction and increases plate dip, while doing so at the opposite side of the model has an

Please cite this article as: Burov, E., et al., Rheological and geodynamic controls on the mechanisms of subduction and HP/UHP exhumation of crustal rocks during continental coll..., Tectonophysics (2014), http://dx.doi.org/10.1016/j.tecto.2014.04.033

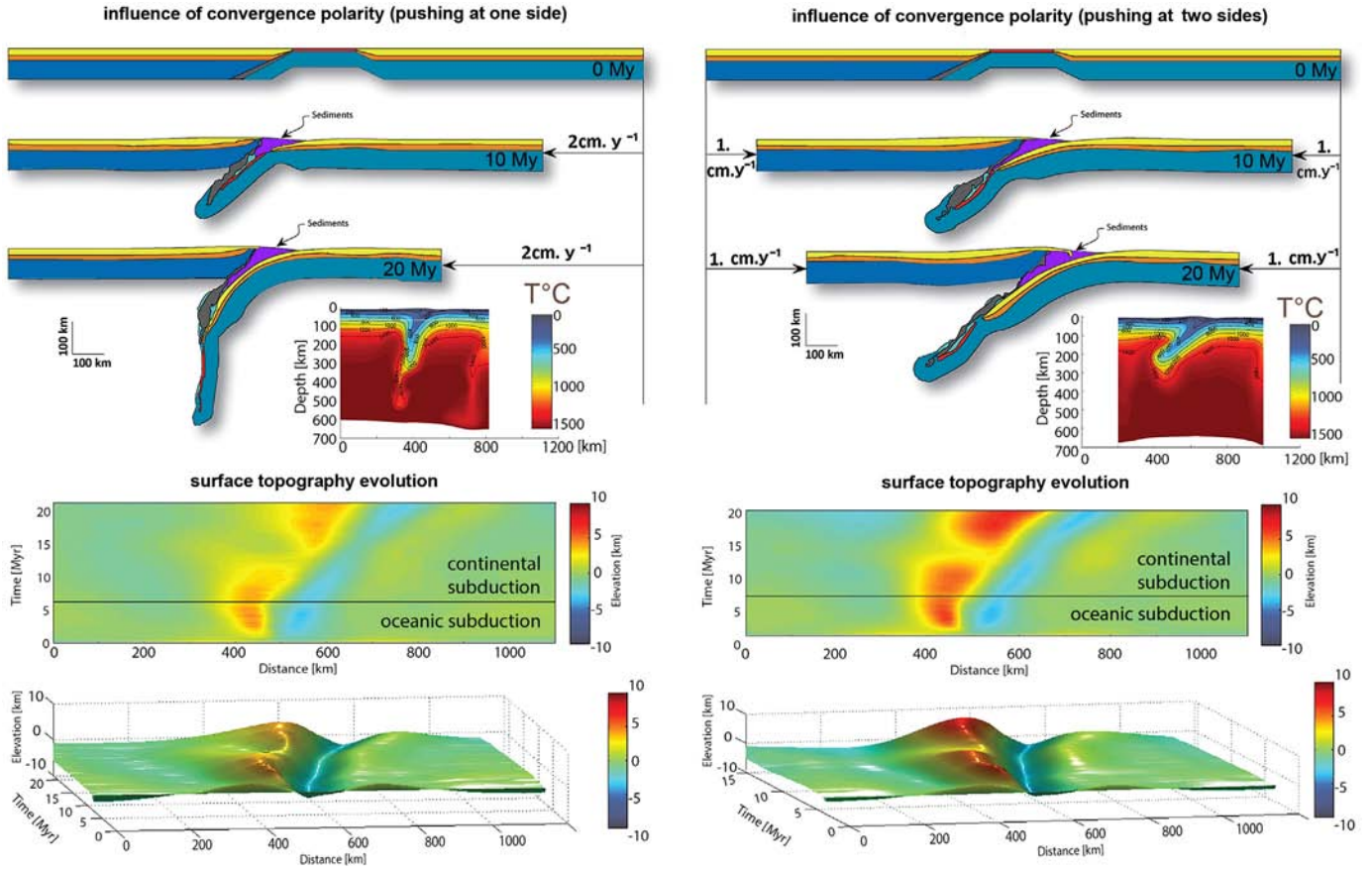

Fig. 16. Importance of the boundary velocity partitioning (Zagros collision model, Francois et al., 2012). The models inspired by Zagros collision settings (Figs. 4–6, 15) test the model sensitivity to the choice of partitioning of convergence velocities between the borders of the model. It is commonly assumed that distribution of velocities between the borders is of no importance in case of non-inertial systems. However, thermal coupling results in appearance of explicit advective terms in the energy equations describing the thermo-mechanical problem (Appendix A). In additions, slab interaction with mantle wind may be also dependent on absolute slab velocity. Hence, the way how the velocities are distributed between the opposite borders of the model becomes highly important, specifically because the ductile properties are exponential function of temperature. As can be seen, applying shortening velocity at one side of the model or at both sides changes the final amount of subduction and slab dip (hence also affecting the amount of slab roll-back and back-arc extension and the timing of slab-break off). These experiments illustrate the importance of exact knowledge of the absolute plate tectonic velocities in nature (absolute plate tectonics versus relative plate tectonics). Color code: blue — mantle, orange — lower crust, yellow — upper crust, red — oceanic crust, gray — initial material of oceanic subduction interface, purple — sediments.

opposite effect. In these particular experiments, the difference between dip angles reached almost 40° at 20 Myr (37%), from nearly 80° in case of convergence from the side of the subducting plate to about 45° in case of convergence from the opposite side, with an intermediate value for double-sided convergence. This effect is contra-intuitive, since simple mechanical non-inertial inertial system should be indifferent to distribution of absolute velocities at the borders (as in case of analog models). Yet, thermo-mechanical coupling changes this rule, since absolute velocities imposed at the borders define horizontal and vertical thermal advection rates, which, in their turn, affect the mechanical properties, thermal buoyancy and phase changes. As a result, absolute velocity distribution matters, specifically because in nature many collision zones are converging only from one side, e.g. the Himalayas. In some cases the absolute velocities are not as certain and hence evaluation of absolute tectonic movements represents a great challenge for the future.

5.3.4. Strong lithosphere, various convergence rates

Studies of fast continental collision (>3 cm·yr^{-1}; Toussaint et al., 2004a,b) of strong lithosphere have shown that for rapid convergence rates and strong lower plates, continental subduction, once initialized, may continue for a very long period of time, i.e., practically for the entire life span of convergence. However, in this case the impact of convergence rate cannot be treated separately from that of surface denudation/erosion/sedimentation processes. In fast collision zones, there should be a strong feedback between surface processes and tectonic forcing. For pure-shear collision settings this has been demonstrated by Avouac and Burov (1996) who have shown that stable growth of orogenic topography requires a strong feedback between the erosion rate and the tectonic convergence rate. If that feedback is not present, the orogenic topography tends to collapse. An even stronger impact of surface processes is expected for continental subduction (Burov and Toussaint, 2007; Lavier and Steckler, 1997; Toussaint et al., 2004a,b, Fig. 17, Supplementary Figs. 3 and 4), since sedimentary loading and erosional unloading have a primary effect on the force balance and integrated strength of the lithosphere (flexural yielding/unyielding, thermal blanketing etc.) in the collision zone. In particular, excessive topography, if not timely removed, exerts closing pressure on the subduction interface, increasing plate coupling and hence preventing subduction (e.g., case S = 0.8 and S = 1.0, Fig. 17). More surprisingly, very fast erosion (e.g., cases S = 0.1, 0.21, 0.33, 0.42, 0.5, Fig. 17) also reduce the amount of subduction by producing dynamic unloading and hence elastic unbending of the subducting plate causing lock-up of the subduction interface). The experiments show that pure shear thickening or folding occur instead of simple shear subduction when erosion is either too strong (e.g., k > 3000 m^2·yr^{-1} for convergence rates <2 × 2 cm·yr^{-1}), in that case any topographic irregularity is "too" rapidly erased by surface processes (Fig. 17), or when erosion is too weak (k < 50 m^2·yr^{-1}). In case of slow erosion, surface elevations are unrealistically high (Fig. 17, Supplementary Fig. 4) which leads to vertical over-loading causing flexural yielding of the lithosphere and growth of the frictional force along the major thrust fault. As a consequence, the major thrust fault is locked leading to coupling between the upper and lower plates; this results

Please cite this article as: Burov, E., et al., Rheological and geodynamic controls on the mechanisms of subduction and HP/UHP exhumation of crustal rocks during continental coll..., Tectonophysics (2014), http://dx.doi.org/10.1016/j.tecto.2014.04.033

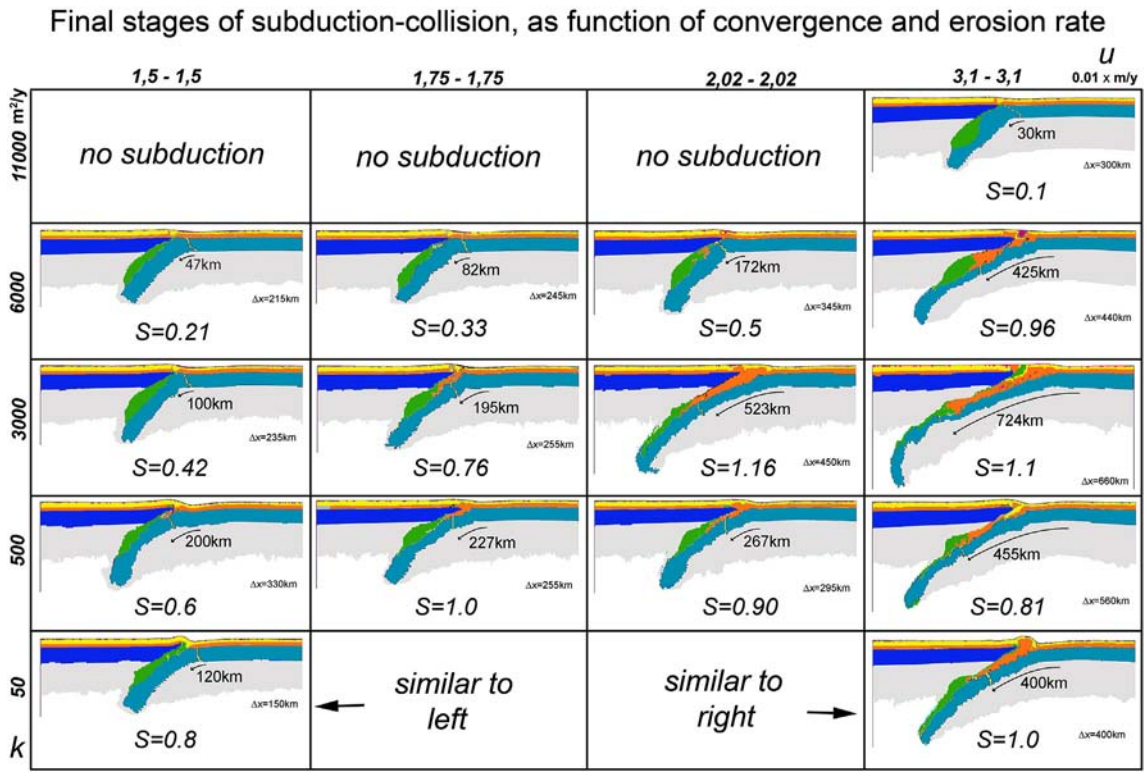

Fig. 17. Interaction between surface erosion rate and tectonic convergence rate in fast collision settings (Burov and Yamato, 2008), strong lithosphere ("Indian craton" type, the initial rheology profile is equivalent to that used for the experiments of Supplementary Fig. 2). Green color indicates the eclogitized crust produced at the beginning of the experiment but later metamorphic changes are not shown with specific colors. Other colors are explained in caption to Fig. 12. Surface erosion/deposition rate has a major impact on the collision style and amount of subduction, specifically for high convergence rates u (up to 100% variation of the total amount of subduction). Summary of the results of the numerical experiments show the dependence of the "subduction number" S (S = amount of subduction to the total amount of shortening) on the erosion coefficient, k, for different values of the convergence rate (values are given for each side of the model, k = 50, 100, 500, 1000, 3000, 6000 and 11,000 $m^2 \cdot yr^{-1}$). Note local maximum on the S − k − u for $u > 1.75$ $cm \cdot yr^{-1}$ and $k > 1000$ $m^2 \cdot yr^{-1}$. Numbers below the subducting plate correspond to the maximal number of subduction achieved in the corresponding experiment. As can be seen, the amount of subduction strongly depends on the degree of feedback between the tectonic forcing and surface processes, with more than a factor of 2 difference between the cases of strong balance between the tectonic input and surface reaction and those characterized by strong misbalance. It can be seen that exhumation of initially buried UHP material is quite rare, as well as the later buried material also returns to the surface only in a few cases.

in overall buckling or folding of the region whereas the crustal root below the range starts to spread out laterally with formation of a high flat "pancake-shaped" topographies. On the contrary, in the case of a dynamic balance between surface and subsurface processes (e.g., k = 2000–3000 $m^2 \cdot yr^{-1}$, for convergence rates $>2 \times 2$ $cm \cdot yr^{-1}$ or k = 500–1000 $m^2 \cdot yr^{-1}$ for convergence rates <3 $cm \cdot yr^{-1}$) erosion/sedimentation results in long-term localization of the major thrust fault that keeps working during 10 My. It is noteworthy that in the experiments with k = 500–1000 $m^2 \cdot yr^{-1}$ (moderate feedback between surface and subsurface processes), the major thrust fault and topography were almost stationary (Supplementary Fig. 4). In case of a stronger feedback (k = 2000–5000 $m^2 \cdot yr^{-1}$) the mountain range and the thrust fault migrated horizontally in the direction of the subducting plate ("India"). This generally happened when both the mountain range and the foreland basin reached some critical size. In this case, the "initial" mountain range and major thrust fault were abandoned after about 500 km of subduction, and a new thrust fault, foreland basin and range were formed "to the south" (i.e. toward the subducting plate) of the initial location. The numerical experiments confirm the previous ideas that intercontinental orogenies could arise from coupling between surface/climatic and tectonic processes, without involvement of special mechanisms of strain localization (Avouac and Burov, 1996). Last but not least, the experiments shown in Figs. 17–18 also test the influence of UHP metamorphism and the possibility of exhumation of eclogite rocks as a function of erosion and convergence rate (assuming 100% transformation of crustal material to eclogites at corresponding P–T conditions). The experiments suggest that prograde metamorphism transformations occur at much deeper depths in case of fast convergence settings so that subducting crust remains too cold (even at important depth), thus leaving less chance for exhumation of the UHP rocks. Yet, exhumation does take place in cases when the subduction interface zone thickens and becomes large allowing for great volumes of light crustal material to delaminate from the mantle and flow back to the surface dragging up UHP material (e.g., case S = 1.1, Fig. 17). It has to be also stated that, in this case, eclogitization has little effect on the development of subduction.

5.4. Fast convergence, influence of the thermo-rheological structure

We here summarize the results of numerous experiments (Figs. 18–19) that tested the influence of rheological structure on the amount of subduction and collision style in most favoring fast convergence settings (2×1.5 $cm \cdot yr^{-1}$). These experiments reveal several types of collision scenarios as a function of the thermotectonic age (geotherm, also characterized by temperature at Moho depth, T_m) and rheology profile.

5.4.1. Cold geotherm ($T_m < 450$ °C, "jelly sandwich" rheology)

An initially cold geotherm allows the collision to evolve into stable, oceanic-type subduction (Fig. 18a, thermo-rheological profile "C_1", Fig. 17 case S = 1.1, Supplementary Fig. 3). Almost all shortening is accommodated by subduction both of the continental lower crust and mantle. Because of low Moho temperatures, the lower crust is highly resistant to decoupling and remains "welded" to the lithospheric mantle. It can be dragged to as deep as 250 km depth in spite of its positive buoyancy. However, the mechanical resistance of the major part of the

Please cite this article as: Burov, E., et al., Rheological and geodynamic controls on the mechanisms of subduction and HP/UHP exhumation of crustal rocks during continental coll..., Tectonophysics (2014), http://dx.doi.org/10.1016/j.tecto.2014.04.033

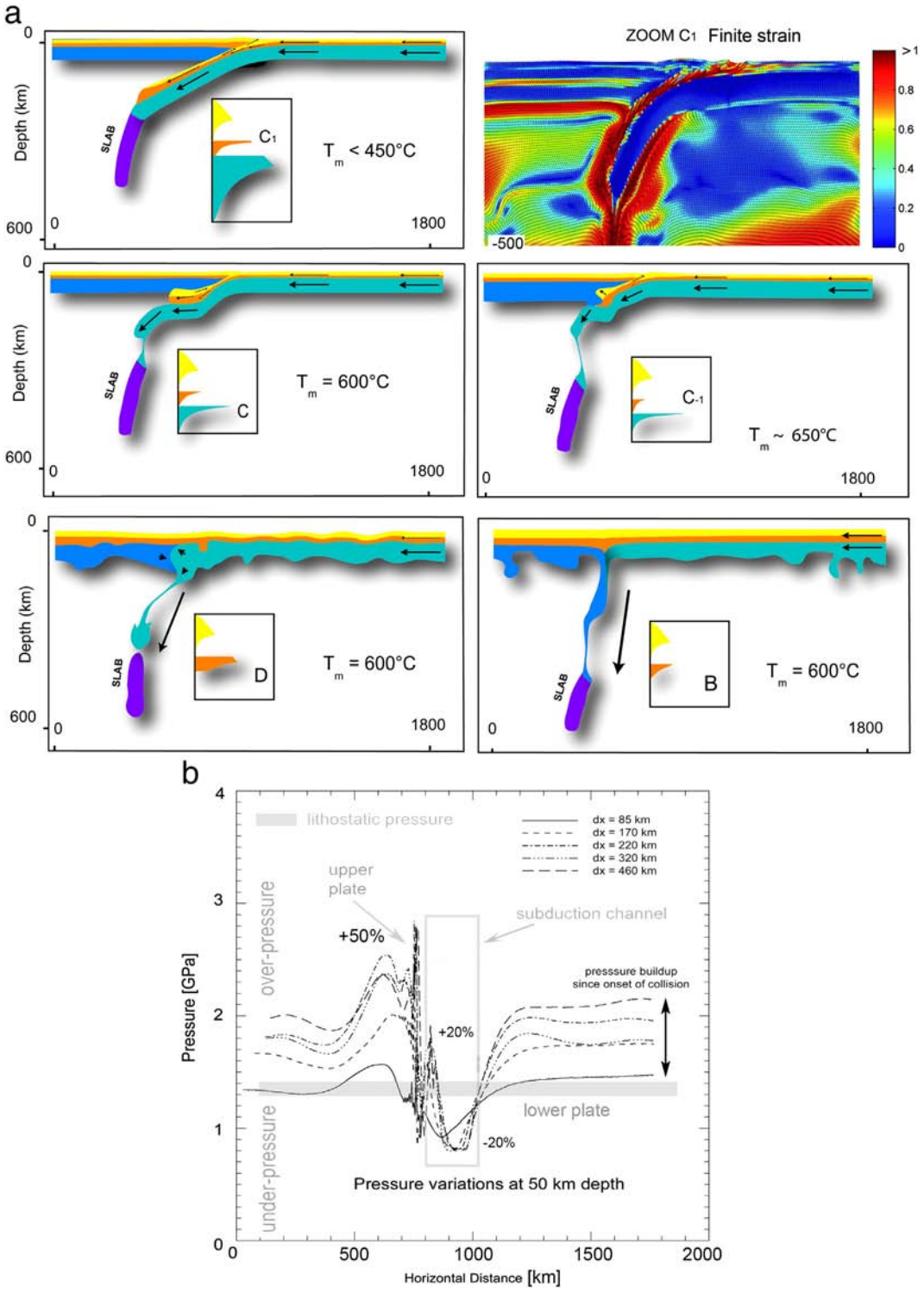

Fig. 18. a. Summary of continental collision/subduction styles predicted by numerical experiments, as function of rheology profile (Burov and Yamato, 2008; Toussaint et al., 2004a,b). The tested rheology profiles incorporate either weak lower crust (experiments "C"), or strong lower crust ("D" and "B"). Snapshots at 5.5 My, convergence rate 2×3 cm·yr^{-1}. Moho temperatures are, respectively, 450 °C, 600 °C, 650 °C (profiles C_1, C, C_{-1}), and 600 °C (profiles D and B). Profiles C correspond to dry olivine mantle, wet quartz-rich upper crust and wet diabase lower crust. Profile D corresponds to the thermo-rheological hypothesis of Mackwell et al. (1998) that combines common wet quartz rheology for the upper crust with strong dry diabase rheology for the lower crust and a weak wet olivine rheology for the mantle. The profile C_1 was used in Toussaint et al. (2004b) to model the initial stages of India–Asia collision (see also Fig. 17). The length of arrows is proportional to material velocity. The insert shows the effective strain distribution for the central part of the "Indian" experiment C_1 superimposed with a 'marker grid' — a grid connecting markers initially placed at the nodes of the starting regular Lagrangian grid. Distortion of the "marker grid" illustrates relative displacement of different units and deformation in the subduction channel. b. Non-lithostatic pressure distributions for experiment C_1 of Toussaint et al. (2004a) shown in Fig. 18a (left upper panel) at various amounts of subduction, dx (from 85 km to 460 km). Shown are horizontal total pressure profiles at depth of 50 km, which corresponds to the strong core of the lithosphere mantle everywhere outside the subduction channel. This depth is chosen as it represents targeted depth of overpressure models for UHP rocks (e.g., Petrini and Podladchikov, 2000). Overpressure (up to +50%) occurs in the upper crustal and mantle layer outside the subduction channel, which undergoes only small underpressures and overpressures at 50 km depth (<20% or 0.3 GPa). It is noteworthy that this experiment presents an extreme case (very fast convergence), so the predicted deviations from the lithostatic pressure correspond to upper-bound values. The values of overpressure may be overestimated because of the use of the Byerlee's law and kinematic boundary conditions and due to the neglect by shear heating (in these experiments). The subduction channel remains ±20% lithostatic during almost 500 km of subduction, while its walls are exposed to moderate overpressures and under-pressures produced by flexural stresses in the upper and lower plates.

upper crust remains lower than the buoyancy-induced stresses. It separates from the lower crust and remains at surface or mid crustal depth at an early stage, only small amounts of the upper crust are dragged to larger depth. In these experiments, crustal material is brought down to significant depths (≫120–150 km), allowing UHP and HP metamorphism to develop in the conditions devoid of significant over-pressure (Fig. 18b). These experiments closely resemble those from (Toussaint et al., 2004b) that modeled India–Asia collision. Supplementary Fig. 3 shows the formation of large-scale thrust-and-fold structures that result from crust–mantle decoupling and resemble those typically observed in the field. This process explains the eventual complexity of the P–T–t paths, with a limited amount of UHP material exhumed at the beginning of subduction.

5.4.2. Intermediate geotherm (T_m = 450–600 °C, "jelly sandwich" rheology)

Stable subduction of the lithospheric mantle results in decoupling of the lower crust from the mantle (Fig. 18a, thermo-rheological profile "C"). For intermediate geotherms, shortening is still largely accommodated by subduction, but positively buoyant lower crust separates from negatively buoyant lithospheric mantle and stagnates at some intermediate level (between 100 and 200 km depth), sometimes forming a double crustal zone (a possible analogy are the Northern Apennines, Ponziani et al., 1995). The crustal part of the subduction interface is divided into an accretion prism and a lower crustal "pocket" (Burov et al., 2001). The geometry of the downgoing lithospheric mantle is affected by the ascent of the buoyant lower crust: the slab adopts a very low angle of subduction. As a consequence, the oceanic slab detaches early and sinks into the mantle. Small-amplitude (1000 m) long-wavelength (350–400 km) lithospheric folding also accommodates some part of the shortening, specifically in the upper plate. The crustal material is brought down to 100–120 km depth allowing for UHP and HP metamorphism.

5.4.3. Hot geotherm (T_m = 600–700 °C, "jelly sandwich" rheology)

Subduction and pure-shear thickening (Fig. 18a, thermo-rheological profile "C_{-1}") are the results of collision under the conditions of a hot geotherm. At a Moho temperature of 650 °C, pure-shear thickening and moderate-amplitude (1500 m) lithospheric folding (wavelength 200–250 km) accommodate a significant part of shortening. This behavior is a result of thermal weakening of the lithosphere, which makes volumetric thickening mechanically easy. The base of the overriding lithospheric plate is also weakened and can be dragged downward with the sinking lower plate. The crustal material basically does not arrive to depths larger than 60–80 km, except for very early stage of subduction (first 5 Myr). Hence, formation and exhumation of HP/UHP is possible only at the very beginning of subduction.

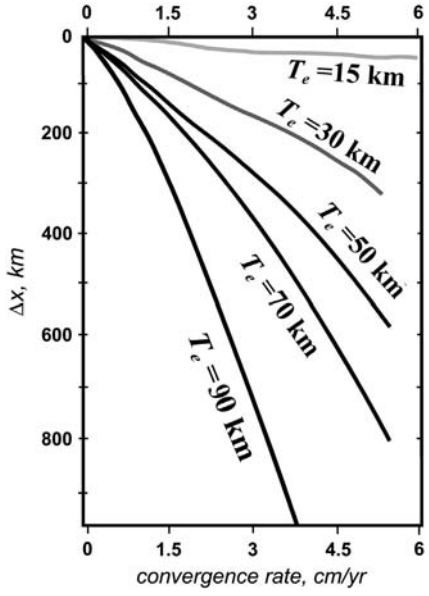

Fig. 19. Graph showing dependence of the amount of subduction (before the slab break-off) on the convergence rate and the integrated strength (T_e) of the lithosphere according to the results of the experiments shown in Figs. 13–18, and those from Burov and Yamato (2008), Sizova et al. (2012) and Yamato et al. (2008, 2009).

5.4.4. Very hot geotherm ("jelly sandwich" rheology) or weak mantle ("crème brulée" rheology, T_m > 750 °C for weak lower crust and dry olivine mantle, or T_m > 600 °C for wet or dry diabase lower crust and wet olivine mantle)

Pure-shear thickening and RT instabilities (Fig. 18a), thermo-rheological profiles "D" and "B" dubbed "crème brulée" (Burov and Watts, 2006) result from very hot geotherms. For such a hot, weak lithosphere, stable subduction (hence HP/UHP exhumation) and lithospheric folding are impossible: convergence at the borders is entirely accommodated by pure-shear thickening and RT instabilities. Because of high temperatures, the effective viscosity at the base of the lithosphere is reduced compared to older models, whereas its density is still higher than that of the asthenosphere; these two factors promote rapid (in <1 m.y.) development of RT instabilities. The slab thins in a "chewing gum" fashion, and a "cold spot" forms (possible natural examples: Vrancia body in the Romanian Carpathians, e.g., Wenzel, 2002; Cloetingh et al., 2004). The rate of "subduction" in this case is not controlled by the convergence rate but by the internal growth rate of the RT instability. We dub this style of deformation "unstable subduction." In the conditions of these experiments, the crust is not brought down to depths below 40 km. Hence, HP/UHP metamorphism is impossible in this case.

5.5. Case of strong lower crustal rheology

The experiments of the previous section (shown in Fig. 18a) were repeated assuming strong dry diabase rheology (Table 1b) for the lower crust. The resulting end-member scenarios (stable subduction vs. unstable subduction) are roughly the same as in the previous experiments. Yet, there are some noticeable differences in the intermediate cases.

5.5.1. Cold lithosphere

For experiments with very cold lithospheres (T_m < 450 °C), the convergence produces stable subduction. However, the results of these experiments differ in many ways from homologue experiments with "weak" (undried granulite) lower crust. In particular, subduction involves the entire continental crust, including the upper crust and its sedimentary rocks. The lithosphere also has a much higher tendency for folding while the predicted topography is 20–30% higher than in the experiments with weak lower crust.

5.5.2. Intermediate thermal gradients in the lithosphere

For higher Moho temperatures (T_m = 450–750 °C), stable subduction is progressively replaced by pure-shear thickening and by large-scale lithospheric folding. Folding is favored by a stronger rheology of the lower crust, which ensures its mechanical coupling with the lithospheric mantle and has a positive effect on the growth rate of folding instability. Note that for the same temperature range, but for a weak lower crust, subduction was a dominant mechanism of deformation.

5.5.3. Very hot lithosphere

The results of very "warm" experiments (T_m > 750 °C, case D, Fig. 18a) are similar to the corresponding experiments with weak lower crust (case B, Fig. 18a) from the previous section (no subduction), despite the fact that the integrated strength of the lithosphere in this case is the same in case C_{-1} from Fig. 18a. Therefore, it can be concluded that strong mantle lithosphere is a paramount condition for continental subduction and, consequently, for formation and exhumation of HP/UHP rocks. These results

showing that strong crust cannot "replace" strong mantle in subduction mechanics can be easily interpreted: different than the mantle lithosphere, the lower crust is positively buoyant. It cannot subduct by its own, without being dragged by a negatively buoyant strong mantle. If such strong mantle layer is absent, the crust will not subduct.

5.6. Summary of the results concerning the role of LP/MP/HP metamorphic phase changes and fluids in subduction processes

Metamorphic phase transformation have potentially weakening impact on crustal rheology (e.g., Wassmann and Stockhert, 2013) and, hence, on subduction evolution reducing mechanical coupling between the subducting and the overriding plate (Angiboust et al., 2012; Gerya et al., 2008). The role of low or medium grade metamorphism is essential for weakening of the subduction interface by creating or propagating weak shear zones at lithospheric scale. The low-grade facies have very low rheological strength, which lubricates the subduction interface controlled by the formation of the localized shear zones. In oceans, serpentinite layers forming at crust–mantle interface and fluid release due to its dehydration at depth play a major role in weakening of the subduction channel allowing for stable subduction (Faccenda et al., 2009a).

The major effect of UHP metamorphic changes (eclogitization) is that it better decouples the subducting and the overriding plate and results in a steeper subduction angle of the continental slab. The experiments suggest that eclogite phase changes do not significantly improve the chances for "normal" subduction: when the Moho temperature exceeds 550–600 °C (temperature of onset of UHP metamorphism), subduction is not a dominant mechanism, whatever the degree of eclogite metamorphism is. This statement is valid for the commonly used assumption that eclogite has a weak rheology (about the same as quartz rheology), which was used in most experiments. Any assumptions on the badly constrained eclogite rheology may be questioned while the degree of eclogitization may also vary in a wide range. Additional experiments hint that the assumption of strong eclogite rheology (such as that of dry granulites) would be equivalent, in terms of the mechanical behavior, to additional slab pull, improving the chances for continental subduction with an effect that is equivalent to the assumption of a colder denser plate with Moho temperature of about 150–200 °C lower than in the reference case.

5.7. Burial/exhumation of small continental terranes and their impact on the subduction cycle

In the previous sections, we have considered a general scenario in which continental crust subducts as a part of large-scale plate convergence process that starts from oceanic subduction and evolves into continental collision (e.g., Alps, Himalaya). However, a number of situations exist in which continental crust can be buried with the oceanic lithosphere. This refers to subduction of relatively small continental terrains embedded within oceanic plate, which further exhumation gives birth to formation of the impressive high-pressure (HP) metamorphic belts that comprise rocks regurgitated to the Earth's surface from depths of up to 150 km (Tirel et al., 2013 and references therein). In the intensively studied Aegean back-arc domain in the Mediterranean (Fig. 20) , P-wave anomalies and the origin of the diverse HP belts appear to be related to the continuous subduction of the same African lithospheric plate, which indicates that their exhumation is a transient and recurrent process (Jolivet et al., 2012; Tirel et al., 2013 and references therein). Here we discuss thermo-mechanical numerical experiments that test this idea and show that successive subduction of multiple continental blocks — and the associated variations in slab buoyancy and subsequent rollback rate may be responsible for the episodic rollback–exhumation cycles (Brun and Faccenna, 2008). In these experiments, a single self-consistent model reproduces the major structural patterns and pressure–temperature–time (P–T–t) paths of the HP rocks in different parts of the Aegean and elucidates a new fundamental mechanism of HP exhumation.

Structural complexity of subducting oceanic plates, in particular the presence of small continental blocks within them, influenced the Tertiary evolution and rate of retreat of the subduction zones in the Mediterranean; it must also have had an effect on the HP rock burial and exhumation cycles (Fig. 20a,b).

The eclogites and blueschists in the northernmost Cyclades Islands derived from Pindus oceanic material were exhumed in two stages, first from the mantle to lower crustal depths (at 45–37 Ma) and then up to the upper crustal depths (30–14 Ma) (Fig. 20c). The blueschists atop Adria's granitic basement were subducted below Pelagonia up to the middle Eocene in the Cyclades and up to the Oligocene in Peloponnese and Crete, where they recorded pressures of up to 17 kbar around 26 Ma and reached upper crustal depths around 12–10 Ma (Fig. 20d).

We thus assume an initial geometry with an already initiated oceanic subduction and with two blocks of continental crust (Pelagonia and Adria) located on the subducting plate, each destined to be accreted (at ~55 and ~30 Ma, respectively) to the overriding plate in the course of the experiment (Fig. 21). In this model, subduction is unforced, i.e. driven by the slab pull force while the opposite sides of the plates are attached to the model walls. This assumption is realistic because both European and African lithosphere represent very large continental blocks, which far field dynamics would not be affected by a small subduction zone.

Fig. 22a shows the step-by-step evolution of the model at the upper-mantle scale. Two continental blocks are subducted and then exhumed one after the other during the continuous retreat of the subduction zone. It is noteworthy that the subduction of a continental block induces an increase in the slab dip angle and a decrease in the subduction velocity, due to the change in slab buoyancy. The slab, heated by the hotter ambient mantle, breaks at its weakest points, the former location of the continental blocks (such slab break-off is not seen in the tomography at this location 3, but it has little effect on HP exhumation).

Structural development associated with the two subduction–exhumation cycles is summarized in the key snapshots in Fig. 22b. Pressure–temperature (PT) paths through time (t) of material points within the block 2 are illustrated using colored markers (Fig. 22b, c). At the onset (6.1 Ma), the subducting slab drags down the tip of the overriding plate, inducing asthenospheric ascent below the extending overriding continental lithosphere. Extension is driven by slab rollback, caused by the negative buoyancy of the slab. The subducting continental block reaches HP–UHP metamorphic conditions and is progressively delaminated from the mantle lithosphere, as it is thrust beneath the accretionary wedge. Despite the deep burial, continental-crust rocks remain cold, partially insulated from the warm asthenosphere by the lithospheric-mantle material of the upper plate that is being dragged down. The delaminated rear part of the subducting block then moves back to the surface along an extensional detachment that reactivates the suture zone, while the front part continues to move downward (12.3 Myr), to be exhumed later. When back to the surface, the crustal block is delaminated completely from the underlying lithospheric mantle, and the asthenosphere flows into the wedge that opens (36.6 Myr). During the exhumation process (6.1–36.6 Myr), the block-scale deformation mimics one step of a caterpillar walk, with the block's tail slipping along a basal décollement, approaching the head and making a large buckle, which then unrolls as soon as the entire block is delaminated. This caterpillar walk process is accommodated structurally, first, by stacking of thrust slices at the rear of the block and, then, by extensional detachment at the rear when the thrusting reaches the front of the block. When exhumed completely, the block undergoes extension almost along its entire length. It is noteworthy that small slices of oceanic lithosphere that are thrust on top of the continental-block rear are then exhumed together with the continental block. These oceanic slices correspond to ophiolites that undergo HP–UHP metamorphism prior to their thrust emplacement atop continental crust at the surface.

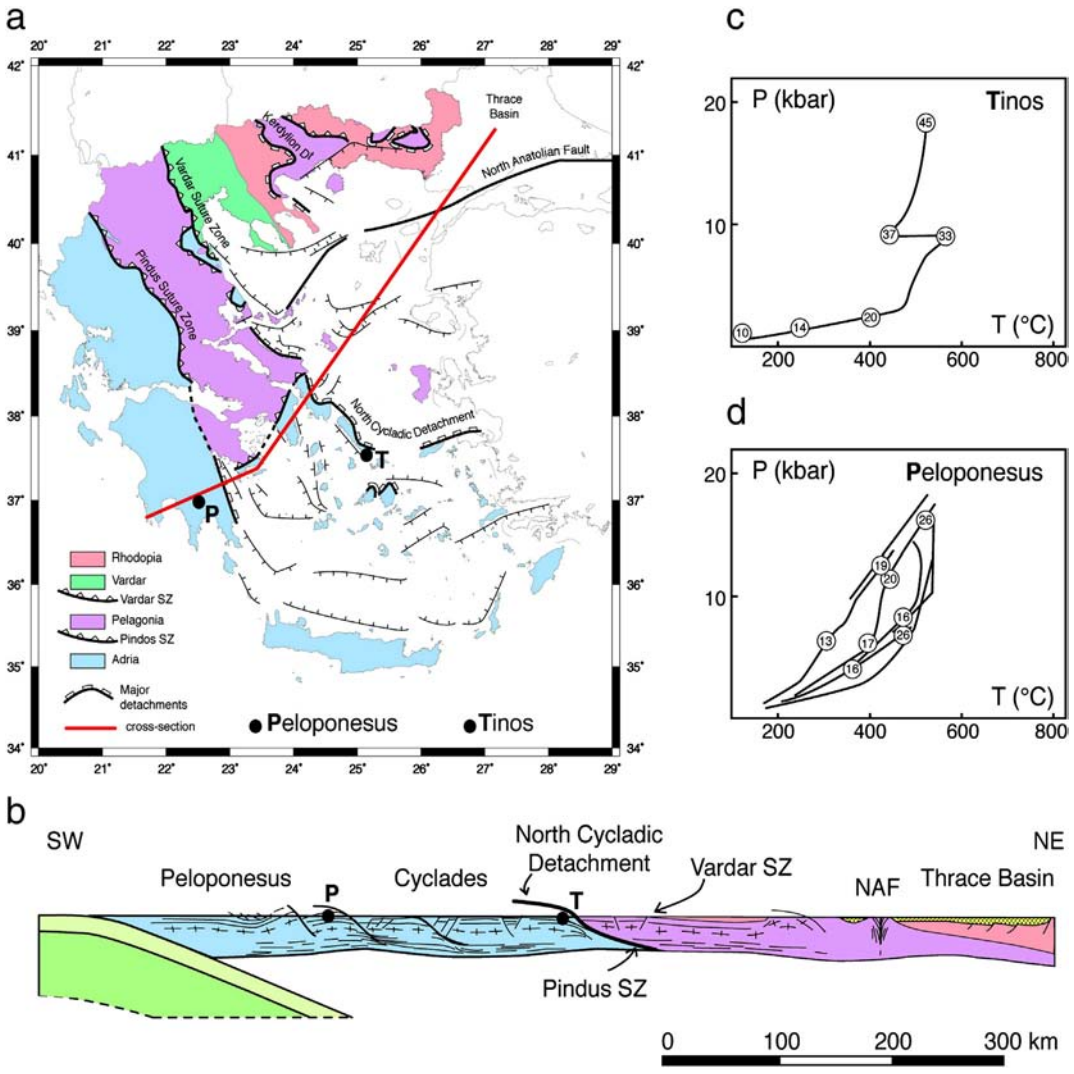

Fig. 20. Tectonic set-up of the Aegean and P–T–t paths of HP rocks. The three main continental blocks and other major features of the Aegean are shown in map view (a) and in cross-section (b), KD, VSZ, PSZ, NCD, NAF and TB are Kerdylion Detachment, Vardar Suture Zone, Pindos Suture Zone, North Cycladic Detachment, North Anatolian Fault and Thrace Basin, respectively. P–T–t paths are from northwest Cyclades, Tinos (point T) (c) and from Peloponnese (point P) (d).
After Tirel et al. (2013).

When block 2 enters the subduction zone, it undergoes subduction and exhumation as block 1 before it (36.6–70.4 Myr). The ascent of the asthenosphere due to the slab-dip increase causes strong heating and thermal weakening of the first, exhumed continental block. Consequently, the exhumed block 1 undergoes extension during the exhumation of block 2, with extensional reactivation of thrust faults and development of high-temperature (HT) metamorphic core complexes (MCC). The yellow marker (Fig. 22) shows that this isobaric heating can reach 700 °C beginning at about 10 kbar. Pervasive flow in the middle and lower crust accommodates considerable stretching, with the Moho remaining flat.

The modeled deformation sequence during the subduction–exhumation cycle of a continental block (Figs. 22 and 23) shows remarkable similarity to the evolution of the blueschists and eclogites of the Adria block (Fig. 20): i) thrust emplacement of HP ophiolites on top of continental crust at the block rear is observed in the northwest Cyclades; ii) the stacking of thrust slices starting at the block rear and propagating frontward directly corresponds to the thrusting in the middle Eocene in the Cyclades, ending in the Oligocene in the external Hellenides; iii) block exhumation accommodated by the extensional reactivation of the suture zone — coeval with the last stages of the thrusting at the block front 4 — is illustrated by the reactivation of the Vardar suture zone at the front (relative to its entrance in subduction) of the Adria block (Fig. 20); iv) partial melting and HT core-complex development in the exhumed block is observed, for example, in Naxos, central Cyclades, pervasive flow in the lower crust associated with the MCC development in the Cyclades is evidenced by seismic anisotropy; v) distributed extension of the exhumed block is seen in the widespread development of sedimentary basins across the Aegean since the late Miocene; and vi) the modeled P–T–t paths closely match those observed in the northern Cyclades (including the isobaric increase of temperature at the Adria block front; Fig. 20c) and in Peloponnese (Adria block rear; Fig. 20d).

These numerical experiments show that the subduction of small continental blocks, as documented in the Mediterranean, is followed by rapid exhumation of HP metamorphic belts, driven, fundamentally, by slab rollback. Because it is the space created by the trench retreat that allows the block to reach the surface, the rate of the exhumation of the block depends on the velocity of the trench retreat. During the entire process, the block delamination (by thrusting) and exhumation are driven by the buoyancy of the crust. Tectonically, exhumation promoted by slab rollback invokes extensional reactivation of a suture zone and accounts for the emplacement at the surface of HP rock units with a horizontal envelope at regional scale that keep their

Please cite this article as: Burov, E., et al., Rheological and geodynamic controls on the mechanisms of subduction and HP/UHP exhumation of crustal rocks during continental coll..., Tectonophysics (2014), http://dx.doi.org/10.1016/j.tecto.2014.04.033

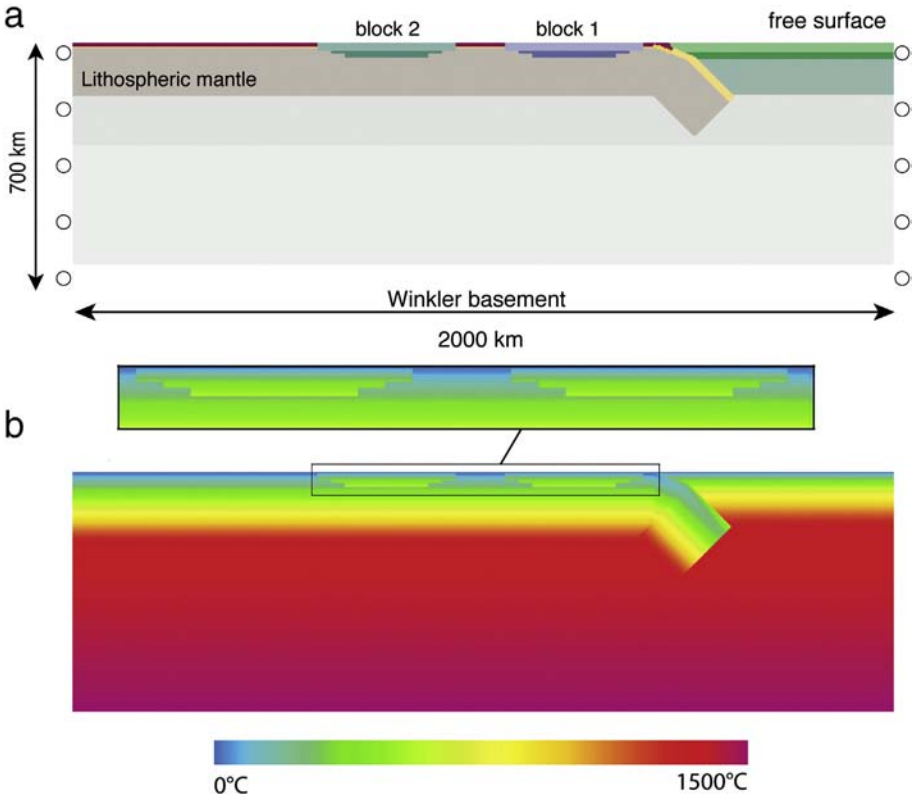

Fig. 21. Setup for the model studying the impact of subduction of continental terrains embedded in the oceanic lithosphere. In this experiment, two continental terrains are considered (Tirel et al., 2013). Pliable Winkler hydrostatic basement allows the accommodation of vertical flow associated with subduction.

lithological–stratigraphical continuity over long distances (several hundred kilometers) along the direction of trench retreat. These results also show that subduction and fast return of a small continental block does not indicate, strictly speaking, a collisional setting. Subduction of a small continental block that rapidly returns to the surface as subduction continues does not indicate, strictly speaking, a collisional setting. This may have been difficult to establish, until now, due to the fact that HP units exhumed in this way are often squeezed, subsequently, in a continental collision zone.

5.8. 3D configuration of plate boundaries and UHP exhumation

Deviations from 2D cylindrical geometry may result in sometimes strong spatial variations of the subduction and UHP exhumation conditions. One of the evident examples refers to the Himalayan syntaxes (Chemenda et al., 1995) where deep structures and geodynamic conditions are very different from those in the Central Himalayas. Few models have investigated so far the effect of 3D geometry on continental subduction (e.g., Li et al., 2013, Fig. 24) to show, in particular, the possibility of lateral propagation of the tearing of the slab leading to spatially progressive along-strike exhumation of the subducted continental crust. The 3D effects can also include along-strike corrugations of the subduction interface and hence to spatially periodic or punctual UHP exhumation.

6. Discussion and conclusions

(1) The numerical experiments discussed here show that subduction processes can result in the formation and exhumation of HP/UHP terranes for physically reasonable parameter ranges. When subduction takes place, the UHP P–T–t data can be decoded in terms of the exhumation depths within 10–20% accuracy from lithostatic pressure gradients. Yet, the presence of UHP rocks can be regarded as solid evidence for subduction only in association with subduction-compatible P–T/P–T–t data and structural evolution, and under condition that the UHP assemblages are statistically representative for the targeted area. In this study we have discussed application of subduction models to the Alps, Zagros and Himalaya. A lot of observational work on the UHP rocks has been done in a number of other orogens such as in Dabie (e.g., Hacker et al., 2004), Norway (e.g., Kylander-Clark et al., 2009), and Kokchetav (Hacker et al., 2003), where the presence of UHP terranes and mechanisms of their exhumation may eventually receive a different interpretation, even though, at a first glance, all these areas can be treated in the framework of the subduction hypothesis. It cannot be excluded that at some stages of collision evolution, various (tectonic or local) overpressure mechanisms can affect formation of the UHP rocks. However, the all overpressure hypotheses need to be tested through complete regional modeling approach, so that the adequate models should reproduce all stages of burial and exhumation of the UHP material while generating realistic P–T/P–T–t paths, surface and geotectonic evolution.

(2) The possibility and duration of the subduction phase is mainly conditioned by the convergence rate and thermo-rheological structure of the crust and lithosphere (e.g., Figs. 12–13 and 18–19) that have major control both on the possibility of subduction and exhumation. The experiments suggest a wide variety of continental subduction scenarios. Sustainable continental subduction and HP–UHP exhumation is possible only in the case of a relatively strong mantle lithosphere (Moho temperatures below $T_m < 550$–600 °C) and relatively fast initial convergence rates (>1–3 cm·yr^{-1} < 10 cm·yr^{-1}). Yet, only a small portion of UHP material probably is probably exhumed to the surface, compared to the large UHP volumes that can be formed at depth. For hot ($T_m > 650$ °C) or slow convergence settings (<1 cm·yr^{-1}) continental subduction is possible as follow-up of the oceanic subduction stage and represents a

Please cite this article as: Burov, E., et al., Rheological and geodynamic controls on the mechanisms of subduction and HP/UHP exhumation of crustal rocks during continental coll..., Tectonophysics (2014), http://dx.doi.org/10.1016/j.tecto.2014.04.033

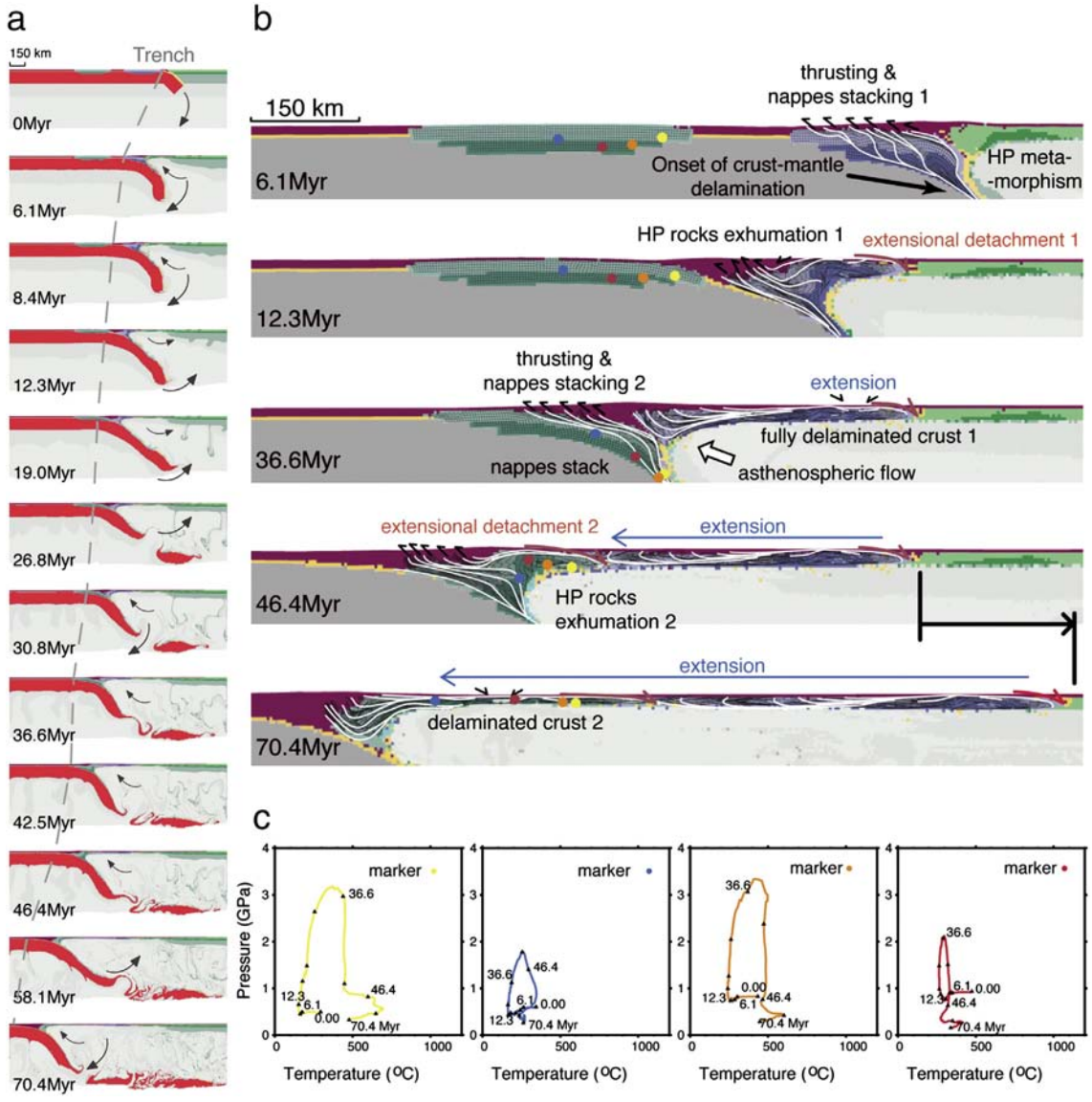

Fig. 22. Step-by-step development of the subduction–exhumation cycles. (a) The evolution at the lithosphere–upper mantle scale (gray color: subducting lithosphere mantle). Dashed line shows the retreat of the trench. (b) Zooms to block deformation during the subduction–exhumation cycle (here lithosphere mantle is marked with gray color). Interpreted shear zones are plotted with white lines. (c) P–T–t paths of the color-coded markers shown in (b).
After Tirel et al. (2013).

transient process that lasts less than 5–10 Myr. It probably ends after the slab break-off (Yamato et al., 2008).

(3) It can be overall concluded that the convergence rates and the integrated strength of the lithosphere are interlinked (Fig. 19), since higher convergence rates require higher slab pull/push forces while such forces can only be exerted if the lithosphere is sufficiently strong to sustain them.

(4) A rather counter-intuitive finding refers to the dependence of the convergence style (slab dip, time of slab break-off, eventually amount of subduction) on the partitioning of the absolute convergence velocities at the borders of the convergent zone (Fig. 16). These results emphasize the importance of elucidation of absolute plate tectonic movements and sub-lithospheric mantle flow directions.

(5) The exhumation of HP/UHP material might be most favored during the initial stages of continental subduction and is promoted by slow convergence settings (<2 cm·yr^{-1}), which is rather in the lower limit of the convergence rate range favoring subduction. There is, hence, a trade-off between the range of convergence rates favoring subduction and the range of the convergence rates favoring maximal amounts of exhumation. It can be thus also proposed that exhumation of the oceanic UHP rocks occurs during the transition from the oceanic to continental subduction phase, when the subduction slows down (Eq. (9)) and the UHP rocks can be effectively dragged to the surface by positively buoyant delaminated continental crustal units (Agard et al., 2009; Angiboust et al., 2009).

(6) The exhumation of UHP units is a poly-phase process driven by different physical mechanisms occurring at the subduction interface zone: (1) the LP and MP rocks are exhumed by a classical accretion prism mechanism and erosion; the final stages (above 40 km depth) of HP/UHP exhumation also take the same path; and (2) within the HP/UHP domain, small-to-middle sized HP and UHP terranes can be largely exhumed by buoyancy, within partly metamorphosed low-density crustal units, slices or melanges, as a result of RT instabilities and small-scale convection and viscous drag in

Please cite this article as: Burov, E., et al., Rheological and geodynamic controls on the mechanisms of subduction and HP/UHP exhumation of crustal rocks during continental coll..., Tectonophysics (2014), http://dx.doi.org/10.1016/j.tecto.2014.04.033

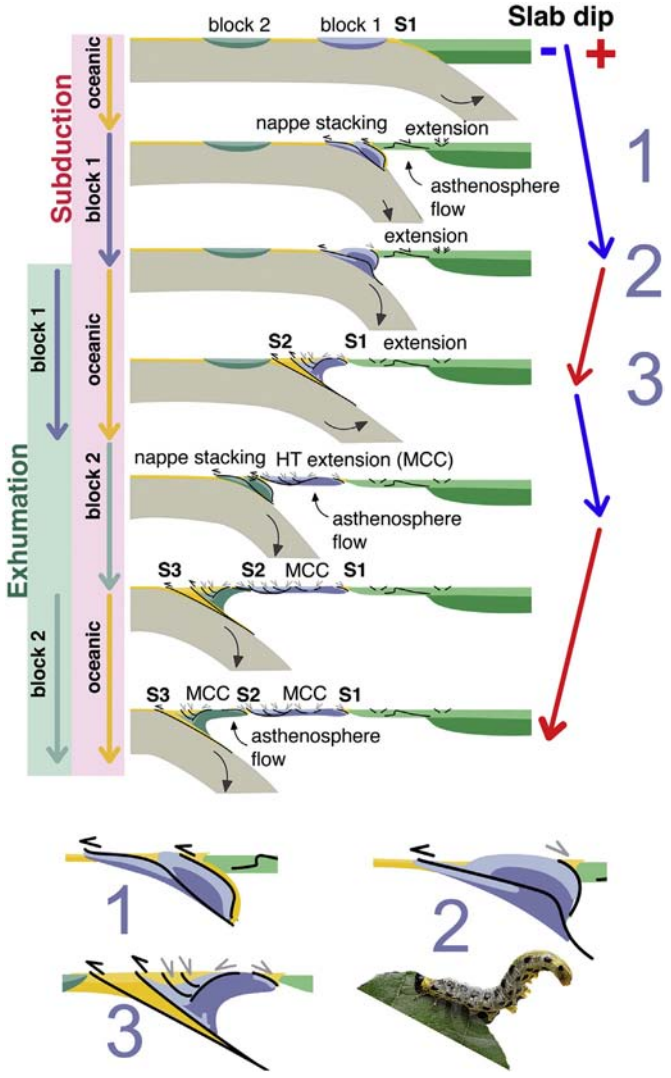

Fig. 23. Summary of the revealed relationship between the continental-block subduction and *caterpillar walk* exhumation, slab dip changes and crustal deformation. Numbers "1, 2, 3" indicate turning buckles in the *caterpillar walk* of the exhuming crustal blocks. After Tirel et al. (2013).

the deep "crustal pockets" created due to separation of the subducting crust from the mantle below 80–120 km depth. Large UHP terranes can be exhumed by buoyancy, within large multi-decakilometer blocks of intermediate or lower crust that delaminate from the mantle lithosphere and are additionally pushed to the surface by tectonic forces (e.g., Fig. 10, Yamato et al., 2008). One can suggest that deep exhumation is mainly conditioned by viscosity and buoyancy within and around the metamorphic bodies. Since metamorphic reactions are activated by fluids, which presence is not always granted during the burial path, some UHP material may form only during exhumation.

(7) UHP exhumation may occur in slab-roll back context when oceanic lithosphere embeds one or more continental terrains (Tirel et al., 2013). Successive subduction of continental terrains results in pulsating regime, with periodical roll-backs and episodes of exhumation. Sliding of the blocks one below the other may results in versatile metamorphic evolution with, for example, simultaneous exhumation of cold and hot rocks.

(8) 3D geometries of plate boundaries may have strong impact on timing and localization of exhumation of UHP terranes.

Supplementary data to this article can be found online at http://dx.doi.org/10.1016/j.tecto.2014.04.033.

Acknowledgments

We are very much thankful to the both reviewers, Boris Kaus and Brad Hacker for their very helpful comments and suggestions. Boris Kaus is also thanked for many useful corrections concerning manuscript wording and style. Different parts of the MS have benefited from discussions with T. Gerya, S. Wolf and B. Huet. This publication was supported by the Advanced ERC Grant Rheolith.

Appendix A. Numerical algorithm

A.1. Thermo-mechanical module

The mixed finite-element volume/finite difference code FLAMAR (outgrowth of Paravoz by Poliakov et al., 1993) is based on the FLAC algorithm (Cundall, 1989). It solves simultaneously Newtonian dynamic equations of motion (Eq. (A1)), in a Lagrangian formulation, coupled with visco-elasto-plastic constitutive equation (Eq. (A2)), heat transport equations (Eq. (A3)) and state equation (Eq. (A4)) (see Appendix A, (Burov and Yamato, 2008; Burov et al., 2001, 2003; Le Pourhiet et al., 2004; Burov and Cloetingh, 2009) for details concerning numerical implementation).

$$\rho\frac{Du_i}{Dt}-\frac{\partial\sigma_{ij}}{\partial x_j}=\rho g_i \tag{A1}$$

$$\frac{D\sigma}{Dt}=F(\sigma,\mathbf{u},\mathbf{v},\nabla\mathbf{v},\ldots,T,\ldots) \tag{A2}$$

$$\rho C_p(\partial T/\partial t+\mathbf{u}\nabla T)-\nabla(k\nabla T)-H_r-H_a-frac\times\sigma_{II}\partial\varepsilon_{II}/\partial t=0 \tag{A3}$$

$$\rho=f(P,T) \tag{A4}$$

Here $\mathbf{u}$, σ, g, k are the respective terms for velocity, stress, acceleration due to body forces and thermal conductivity. The terms t, ρ, C_p, T, H_r, H_a, α, $frac\times\sigma_{II}\partial\varepsilon_{II}/\partial t$ designate respectively time, density, specific heat, temperature, internal heat production, adiabatic heating/cooling term, thermal expansion coefficient and shear heating term moderated by experimentally defined *frac* multiplier (*frac* is set to conservative value of 0.1 in most experiments. It is noteworthy that some studies advocate for stronger efficiency of shear heating, advancing *frac* values on the order of 0.9 (Thielmann and Kaus, 2012). However, in the absence of direct observational data we decided to keep *frac* at relatively low level). The terms $\partial/\partial t$, $D\sigma/Dt$, F are a time derivative, an objective (Jaumann) stress time derivative and a functional, respectively. In the Lagrangian framework, the incremental displacements are added to the grid coordinates allowing the mesh to move and deform with the material. This enables solution of large-strain problems locally using small-strain formulation: on each time step the solution is obtained in local coordinates, which are then updated in the large strain mode. Volume/density changes due to phase transitions are accounted via application of equivalent stresses to affected material elements. It is noteworthy that the inertial term (first parameter in Eq. (A1)) is negligible for geodynamic applications. It is retained here because the FLAC method is written in fully dynamic formulation. While modeling geodynamic processes this term is still present, yet for numerical reasons since FLAC then employs an artificial inertial dampening

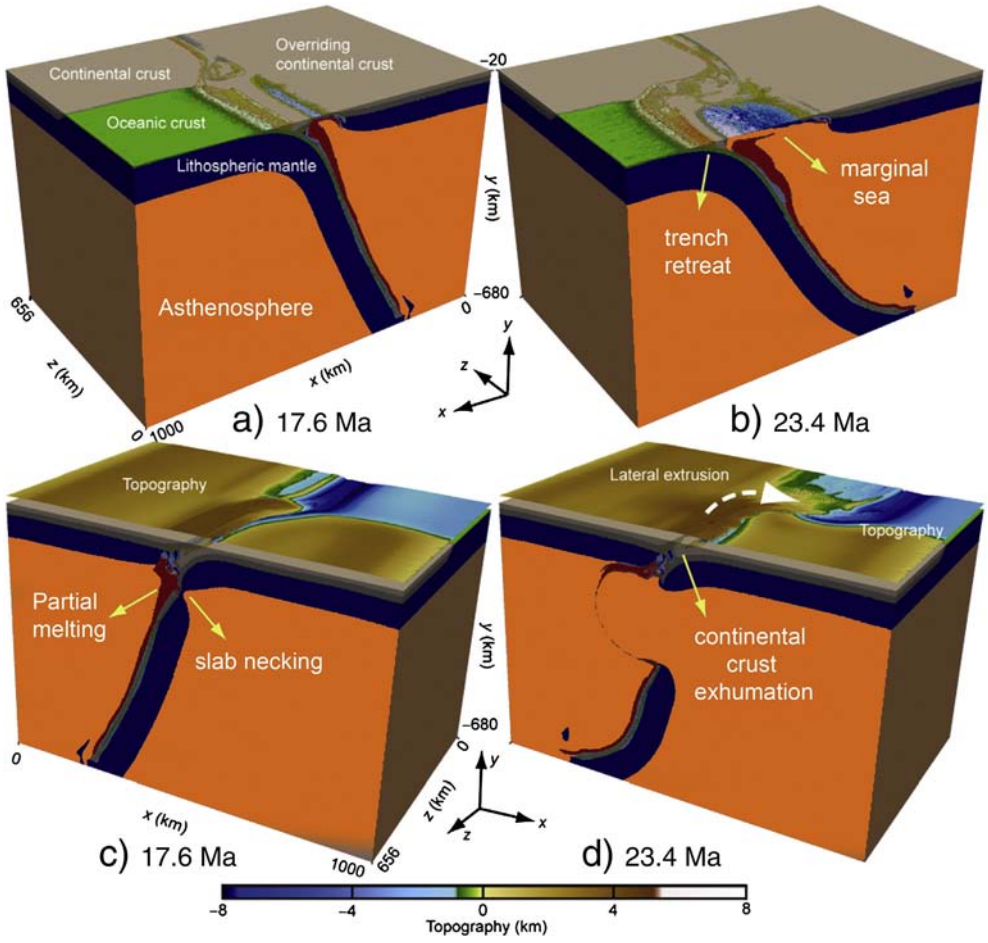

Fig. 24. 3-D numerical model for the collision of continental corner with progressively decreasing convergence velocity. The slow-down of the convergence results in slab-retreat followed by slab break-off and exhumation of continental crustal material. (a, b) View from the oceanic subduction side. (c,d) View from the continental collision side.
Modified from Li et al. (2013).

density allowing to slow-down the elastic waves and hence advance with much larger time steps (Cundall, 1989) than would be required in a fully inertial mode.

Solution of Eq. (A1) provides velocities at mesh points used for computation of element strains and of heat advection $\mathbf{u}\nabla T$. These strains are used in Eq. (A2) to calculate element stresses, and the equivalent forces are used to compute velocities for the next time step.

All rheological terms are implemented explicitly. The rheology model is serial viscous-elastic–plastic (Tables 1a and 1b). The plastic term is given by explicit Mohr–Coulomb plasticity (non-associative with zero dilatancy) assuming linear Navier–Coulomb criterion. We imply internal friction angle ϕ of 30°, maximal cohesion S of 20 MPa, and dilatation angle φ of 0°, which fit best the experimental Byerlee's law of rock failure (Byerlee, 1978):

$$\tau = S + \sigma_n tg\phi \tag{A5}$$

where τ is the shear stress and σ_n is the normal stress that accounts both for rock and fluid pressure. Linear cohesion softening is used for better localization of plastic deformation ε_p ($S(\varepsilon_p) = S_0 \min(0, 1 - \varepsilon_p / \varepsilon_{p0})$ where ε_{p0} is 0.01). Specific properties are applied to soft serpentinized rock (Hassani et al., 1997).

The ductile–viscous term is represented by non-linear power law with three sets of material parameters (Tables 1a and 1b) that correspond to the properties of four lithological layers: upper crust (quartz), middle-lower crust (quartz–diorite), mantle and asthenosphere (olivine):

$$\eta_{eff} = \left(\frac{\partial \varepsilon}{\partial t}\right)_{II}^{d(1-n)/n} (A^*)^{-1/n} \exp(H/nRT) \tag{A6}$$

where $\left(\frac{\partial \varepsilon}{\partial t}\right)_{II}^{d} = \left(Inv_{II}\left(\left(\frac{\partial \varepsilon}{\partial t}\right)_{II}^{d}\right)\right)^{1/2}$ is the effective strain rate and $A^* = \frac{1}{2}A \cdot 3^{(n+1)/2}$ is the material constant, H is the activation enthalpy, $H = Q + PV$ where Q is activation energy and V is molar volume, R is the gas constant, n is the power law exponent (Table 1b). The elastic parameters (Tables 1a and 1b) correspond to commonly inferred values from Turcotte and Schubert (2002).

The surface processes are taken into account by diffusing (Eq. (A7)) the topographic elevation h of the free surface along x using conventional Culling erosion model (Culling, 1960) with a diffusion coefficient k_{ero}.

$$\frac{\partial^2 h}{\partial t^2} = k_{ero} \frac{\partial^2 h}{\partial x^2} \tag{A7}$$

This simple model is well suited to simulate fan deltas, which can be taken as a reasonably good analog of typical foreland basin deposits. This model is not well adapted to model slope dependent long-range sedimentation, yet, it accounts for some most important properties of

Please cite this article as: Burov, E., et al., Rheological and geodynamic controls on the mechanisms of subduction and HP/UHP exhumation of crustal rocks during continental coll..., Tectonophysics (2014), http://dx.doi.org/10.1016/j.tecto.2014.04.033

surface processes such as dependency of the erosion/sedimentation rate on the roughness of the relief (surface curvature).

The fluid transport algorithm is based on an enhanced variant of Darcy's flow approximation with strain-rate dependent permeability (Angiboust et al., 2012). In this algorithm it is assumed that the fluid flux q_f is driven by fluid pressure gradient through a medium with dynamic permeability K, as follows:

$$q_f = -K\nabla P^*_{fl}, \tag{A8}$$

where fluid pressure P^*_{fl} is related to the non-lithostatic pressure δP through a fluid "saturation factor" $[H_2O]/[H_2O]_{sat}$ as follows:

$$P^*_{fl} = \delta P \frac{[H_2O]}{[H_2O]_{sat}}, \tag{A9}$$

where $[H_2O]$ is the current water content (in wt.%) in the material for each element of the numerical grid and $[H_2O]_{sat}$ is the maximum water content thermodynamically calculated for the same material as a function of P–T conditions. The dynamic permeability K is defined as a function of the intrinsic permeability k, normalized strain rate and inversed viscosity of the fluid (Angiboust et al., 2012):

$$K = \frac{k}{\mu_f} \times \frac{\dot{\varepsilon}}{\varepsilon_0} \tag{A10}$$

where $\mu_f = 2.414 \times 10^{-5} \times 10^{\frac{247.8}{T-140}}$ and $\varepsilon_0 = 10^{-14}\,s^{-1}$ are respectively temperature dependent experimentally defined fluid viscosity and reference strain rate.

FLAMAR allows for large displacements and strains in particular owing to an automatic remeshing procedure, which is implemented each time the mesh becomes too destorted to produce accurate results. The remeshing criterion is imposed by a critical angle of grid elements. This angle is set to 10° to reduce frequency of remeshing and thus limit the associated numerical diffusion. The numerical diffusion was effectively constrained by implementation of the passive marker algorithm. This algorithm traces passively moving particles that are evenly distributed in the initial grid. This allows for accurate recovering of stress, phase and other parameter fields after each remeshing. FLAMAR has been already tested on a number of geodynamical problems for subduction/collision context (Burov et al., 2001; Toussaint et al., 2004a,b).

A.2. Thermodynamic coupling

Buoyancy (and, eventually, rheology changes) is an important component of the force balance at subduction zone (Bousquet et al., 1997; Burov et al., 2001; Doin and Henry, 2001). For this reason, the thermodynamic THERIAK (De Capitani, 1994) and PERPLE_X (Connolly, 2005) algorithms have been incorporated to introduce progressive density changes during evolution. Both algorithms (THERIAK is used for sedimentary rocks, PERPLE_X — for the rest) minimize free Gibbs energy for a given chemical composition to calculate an equilibrium mineralogical assemblage for given P–T conditions (De Capitani, 1994).

$$G = \sum_{i=1}^{n} \mu_i N_i \tag{A11}$$

where μ_i is the chemical potential and N_i the moles number for each component i constitutive of the assemblage. Given the mineralogical composition, the computation of the density is then straightforward.

Mineralogical composition and hence density, is re-evaluated every 10^4 time steps (~200 kyr) according to the current P–T conditions. Equivalent stresses are applied to the elements to account for volume–density changes associated with the metamorphic transitions. Unfortunately, changes in rheological properties of the metamorphic facies cannot be implemented in the same way as the density changes, due to the lack of the appropriate experimental data. We took into account rheology changes only for key facies such as serpentinite and eclogite.

A.3. Initial thermal structure

To compute the initial continental geotherm T_{cont}, one can use the Eq. (A12) taking into account, in T_{std}, the stationary part of the geotherm and contribution due to the radiogenic heat production H_s in the crust, and correction $T(age)$ due to transient cooling of the lithosphere that depends on its age.

$$T_{cont}(z, age, H_s) = T_{std}(z, H_s) + T(age) \tag{A12}$$

Radiogenic contribution T_r in the crust depends of the thickness of the crust h_c, density ρ_c, radiogenic production H_s, radiogenic production decay depth h_r, and thermal conductivity coefficient k_c (Eq. (A10)):

$$T_r = \frac{\rho_c \cdot H_s \cdot h_r^2}{k_c} \cdot \left(1 - e^{-\frac{h_c}{h_r}}\right). \tag{A13}$$

Temperature T_m at Moho depth, h_c, is used for the calculation of the temperature for depths below the Moho and is given by:

$$T_m = T_0 + \frac{q_m}{k_c} \cdot h_c + T_r \tag{A14}$$

where T_0 and q_m correspond, respectively, to the temperature at the surface and the heat flux calculated at the Moho. This heat flux is given by:

$$q_m = \frac{T_{hl} - T_0 - T_r}{\frac{h_c}{k_c} + \frac{h_l - h_c}{k_m}} \tag{A15}$$

where T_{hl} is temperature at the thermal base of lithosphere (of a thickness h_l) and k_m is coefficient of thermal conductivity for the mantle.

Temperature at a depth z can thus be calculated as:

$$-\text{If } z \le h_c: \quad T_{std}(z) = T_0 + \frac{q_m}{k_c} \cdot z + T_r \tag{A16}$$

$$-\text{If } z > h_c: \quad T_{std}(z) = T_m + q_m \cdot \frac{(z - h_c)}{k_m} \tag{A17}$$

This obtained temperature is then corrected for transient cooling that depends on thermotectonic age (age) of the lithosphere using formulation from Parsons and Sclater (1977) adapted for the continental lithosphere.

$$T(age) = \frac{2}{\pi} \cdot \left(T_{h_l} - T_0\right) \cdot TT(age) \tag{A18}$$

where

$$TT(age) = \sum_{n=1}^{\infty} \frac{(-1)^{n+1}}{n} \cdot \exp\left(\frac{-k_m \cdot \pi^2 \cdot age \cdot n^2}{\rho_m \cdot C_m \cdot h_l^2}\right) \cdot \sin\left(\frac{n \cdot \pi \cdot z}{h_l}\right) \tag{A19}$$

with C_m and ρ_m are respectively the specific heat capacity and the density for the mantle. Values for the parameters used for the initial geotherm are given in Tables 1a and 1b.

References

Afonso, J.C., Zlotnik, S., 2011. The subductability of continental lithosphere: the before and after story, arc–continent collision. Front. Earth Sci. Part 1, 53–86. http://dx.doi.org/10.1007/978-3-540-88558-0_3.

Please cite this article as: Burov, E., et al., Rheological and geodynamic controls on the mechanisms of subduction and HP/UHP exhumation of crustal rocks during continental coll..., Tectonophysics (2014), http://dx.doi.org/10.1016/j.tecto.2014.04.033

Agard, P., Jolivet, L., Goffé, B., 2001. Tectonometamorphic evolution of the Schistes Lustrés complex: implications for the exhumation of HP and UHP rocks in the Western Alps. Bull. Soc. Geol. Fr. 172 (5), 617–636.

Agard, P., Searle, M.P., Alsop, G.I., Dubacq, B., 2010. Crustal stacking and expulsion tectonics during continental subduction: P-T deformation constraints from Oman. Tectonics 29. http://dx.doi.org/10.1029/2010TC002669.

Agard, P., Omrani, J., Jolivet, L., Whitechurch, H., Vrielynck, B., Spakman, W., Monié, P., Meyer, B., Wortel, R., 2011. Zagros orogeny: a subduction-dominated process. Geological Magazine. http://dx.doi.org/10.1017/S001675681100046X.

Agard, P., Vitale-Brovarone, P., 2013. Thermal regime of continental subduction: the record from exhumed HP-LT terranes (New Caledonia, Oman, Corsica). Tectonophysics 601, 206–215.

Agard, P., Yamato, P., Jolivet, L., Burov, E., 2009. Exhumation of oceanic blueschists and eclogites in subduction zones: timing and mechanisms. Earth Sci. Rev. 92, 53–79.

Andersen, T.B., Austrheim, H., 2008. The Caledonian infrastructure in the Fjord-region of Western Norway; with special emphasis on formation and exhumation of high- and ultrahigh-pressure rocks, late- to post-orogenic tectonic processes and basin formation. Field Trip Guidebook 33 IGC excursion No 29 p. 88 (August 15–22nd).

Angiboust, S., Agard, P., Jolivet, L., Beyssac, O., 2009. The Zermatt-Saas ophiolite : the largest (60 km-wide) and deepest (c. 70–80 km) continuous slice of oceanic lithosphere detached from a subduction zone? Terra Nova 21, 171–180. http://dx.doi.org/10.1111/j.1365-3121.2009.00870.x.

Angiboust, S., Agard, P., 2010. Initial water budget: the key to detaching large volumes of eclogitized oceanic crust along the subduction channel? Lithos. http://dx.doi.org/10.1016/j.lithos.2010.09.007.

Angiboust, S., Wolf, S., Burov, E., Agard, Ph., Yamato, P., 2012. Effect of fluid circulation on subduction interface tectonic processes: insights from thermo-mechanical numerical modelling. Earth Planet. Sci. Lett. 357–358, 238–248.

Arcay, D., Tric, E., Doin, M.-P., 2005. Numerical simulations of subduction zones. Effect of slab dehydration on the mantle wedge dynamics. Physics of the Earth and Planetary Interiors 149, 133–153.

Austrheim, H., 1991. Eclogite formation and the dynamics of crustal roots under continental collision zones. Terra Nova 3, 492–499.

Avouac, J.P., 2003. Mountain building, erosion and the seismic cycle in the Nepal Himalaya. Adv. Geophys. 46, 1–80.

Avouac, J.P., Burov, E.B., 1996. Erosion as a driving mechanism of intracontinental mountain growth. J. Geophys. Res. Solid Earth 101 (B8), 17747–17769.

Beaumont, C., Kamp, P.J.J., Hamilton, J., Fullsack, P., 1996. The continental collision zone, South Island, New Zealand: comparison of geodynamical models and observations. J. Geophys. Res. 101, 3333–3359.

Beaumont, C., Muñoz, J.A., Hamilton, J., Fullsack, P., 2000. Factors controlling the Alpine evolution of the central Pyrenees inferred from a comparison of observations and geodynamical models. J. Geophys. Res. 105 (B4), 8121–8146.

Beaumont, C., Jamieson, R.A., Butler, J.P., Warren, C.J., 2009. Crustal structure: a key constraint on the mechanisms of ultra-high-pressure rock exhumation. Earth Planet. Sci. Lett. 287, 116–129.

Bott, M.H.P., 1993. Modelling the plate-driving mechanism. Journal of the Geological Society of London 150, 941–951.

Bousquet, R., Goffé, B., Henry, P., Le Pichon, X., Chopin, C., 1997. Kinematic thermal and petrological model of the Central Alps: Lepontine metamorphism in the upper crust and eclogitisation of the lower crust. In: Touret, J.R.L., Austrheim, H., et al. (Eds.), Collision Orogens: Zones of Active Transfers between Crust and Mantle. Tectonophysics, 273, n°1-2, pp. 105–127.

Brun, J.-P., Faccenna, C., 2008. Exhumation of high-pressure rocks driven by slab rollback. Earth Planet. Sci. Lett. 272, 1–7.

Burg, J.-P., Gerya, T.V., 2005. Viscous heating and thermal doming in orogenic metamorphism: numerical modeling and geological implications. J. Metamorph. Geol. 23, 75–95.

Burg, J.-P., Podladchikov, Y., 2000. From buckling to asymmetric folding of the continental lithosphere: numerical modelling and application to the Himalayan syntaxes. In: Khan, M.A., et al. (Eds.), Tectonics of the Nanga Parbat Syntaxis and the Western Himalaya. Geological Society of London Special Publication, 170, pp. 219–236.

Bürgmann, R., Dresen, G., 2008. Rheology of the lower crust and upper mantle: evidence from rock mechanics, geodesy, and field observations. Annu. Rev. Earth Planet. Sci. 36, 531–567. http://dx.doi.org/10.1146/annurev.earth.36.031207.124326.

Burov, E., 2010a. The equivalent elastic thickness (Te), seismicity and the long-term rheology of continental lithosphere: time to burn-out "crème brûlée"? Insights from large-scale geodynamic modeling. Tectonophysics 484, 4–26. http://dx.doi.org/10.1016/j.tecto.2009.06.013.

Burov, E., 2010b. Thermo-mechanical models for coupled lithosphere-surface processes: applications to continental convergence and mountain building processes. In: Cloetingh, S., Negendank, J. (Eds.), New Frontiers in Integrated Solid Earth Sciences. International Year of Planet Earth. Springer Science + Business Media, pp. 103–143. http://dx.doi.org/10.1007/978-90-481-2737-5_4.

Burov, E., 2011. Rheology and strength of the lithosphere. Mar. Pet. Geol. 28, 8,1402–8,1443. http://dx.doi.org/10.1016/j.marpetgeo.2011.05.008.

Burov, E., Cloetingh, S., 2009. Controls of mantle plumes and lithospheric folding on modes of intra-plate continental tectonics: differences and similarities. Geophys. J. Int. 178 (3), 1691–1722.

Burov, E.B., Diament, M., 1995. Effective elastic thickness of the continental lithosphere — what does it really mean? J. Geophys. Res. 100, 3905–3927.

Burov, E., Toussaint, G., 2007. Surface processes and tectonics: forcing of continental subduction and deep processes. Glob. Planet. Chang. 58, 141–164 (Special volume on Topography of Europe).

Burov, E., Watts, A.B, 2006. The long-term strength of continental lithosphere: "jelly-sandwich" or "crème-brûlé"? GSA Today 16, 4–10.

Burov, E., Yamato, Ph., 2008. Continental plate collision, P–T–t–z conditions and unstable vs. stable plate dynamics: insights from thermo-mechanical modelling. Lithos 103, 178–204.

Burov, E.B., Kogan, M.G., Lyon-Caen, H., Molnar, P., 1990. Gravity anomalies, the deep structure, and dynamic processes beneath the Tien Shan. Earth Planet. Sci. Lett. 96, 367–383.

Burov, E.B., Podladchikov, Y., Grandjean, G., Burg, J.-P., 1999. Validation of multidisciplinary data using thermo-mechanical modelling: application to the Western and Nothern Alps. Terra Nova 11, 124–131.

Burov, E.B., Jolivet, L., Le Pourhiet, L., Poliakov, A., 2001. A thermomechanical model of exhumation of HP and UHP methamorphic rocks in Alpine mountain belts. Tectonophysics 342, 113–136.

Burov, E., Jaupart, C., Guillou-Frottier, L., 2003. Emplacement of magma reservoirs in the upper crust. J. Geophys. Res. 108 (B4), 2177–2189.

Burtman, V.S., Molnar, P., 1993. Geological and geophysical evidence for deep subduction of continental crust beneath the Pamir. Geol. Soc. Am. Spec. Pap. 281, 1–76.

Byerlee, J.D., 1978. Friction of rocks. Pure Appl. Geophys. 116, 615–629.

Chemenda, A.I., Mattauer, M., Malavieille, J., Bokun, A.N., 1995. A mechanism for syncollisional rock exhumation and associated normal faulting: results from physical modelling. Earth Planet. Sci. Lett. 132, 225–232.

Chemenda, A.I., Mattauer, M., Bokun, A.N., 1996. Continental subduction and a mechanism for exhumation of high-pressure metamorphic rocks: new modeling and field data from Oman. Earth Planet. Sci. Lett. 143, 173–182.

Chen, Y., Cogne, J.-P., Courtillot, V., Tapponnier, P., Zhou, X.Y., 1993. Cretaceous paleomagnetic results from western Tibet and tectonic implications. J. Geophys. Res. 98, 17981–18000.

Chopin, C., 1984. Coesite and pure pyrope in high-grade blueschists of the western Alps: a first record and some consequences. Contrib. Mineral. Petrol. 96, 253–274.

Chopra, P.N., Paterson, M.S., 1981. The experimental deformation of dunite. Tectonophysics 78, 453–473.

Cloetingh, S., Burov, E., 1996. Thermomechanical structure of European continental lithosphere: constraints from rheological profiles and EET estimates. Geophys. J. Int. 124, 695–723.

Cloetingh, S.A.P.L., Wortel, M.J.R., Vlaar, N.J., 1982. Evolution of passive continental margins and initiation of subduction zones. Nature 297, 139–142.

Cloetingh, S., Burov, E., Poliakov, A., 1999. Lithosphere folding: primary response to compression? (from central Asia to Paris Basin). Tectonics 18, 1064–1083.

Cloetingh, S.A.P.L., Burov, E., Matenco, L., Toussaint, G., Bertotti, G., Andriessen, P. A.M., Wortel, W.J.R., Spakman, W., 2004. Thermomechanical controls on the model of continental collision in the SE Carpathians (Romania). Earth Planet. Sci. Lett. 218, 57–76.

Cloos, M., 1993. Lithospheric buoyancy and collisional orogenesis: subduction of oceanic plateaus, continental margins, island arcs, spreading ridges and seamounts. Geol. Soc. Am. Bull. 105, 715–737.

Coleman, R.G., 1971. Plate tectonic emplacement of upper mantle peridotites along continental edges. J. Geophys. Res. 76, 1212–1222.

Connolly, J.A.D., 2005. Computation of phase equilibria by linear programming: a tool for geodynamic modeling and its application to subduction zone decarbonation. Earth Planet. Sci. Lett. 236, 524–541.

Culling, W.E.H., 1960. Analytical theory of erosion. J. Geol. 68 (333–336).

Cundall, P.A., 1989. Numerical experiments on localization in frictional material. Ing. Arch. 59, 148–159.

Dahlen, F.A., 1990. Critical taper model of fold-and-thrust belts and accretionary wedges. Ann. Rev. Earth Planet. Sci. 18, 55–99.

Dahlen, F.A., Suppe, J., 1988. Mechanics, growth and erosion of mountain belts. Geol. Soc. Am. Spec. Pap. 218, 161–178.

Davies, J.H., 1999. Simple analytic model for subduction zone thermal structure. Geophys. J. Int. 139, 823–828.

Davis, D.M., Suppe, J., Dahlen, F.A., 1983. Mechanics of fold-and-thrust belts and accretionary wedges. J. Geophys. Res. 88 (B2), 1153–1172.

De Capitani, C., 1994. Gleichgewichts-Phasendiagramme: Theorie und Software. Beihefte zum European Journal of Mineralogy—Jahrestagung der Deutschen Mineralogischen Gesellschaft, p. 48.

DeCelles, P.G., Robinson, D.M., Zandt, G., 2002. Implications of shortening in the Himalayan fold–thrust belt for uplift of the Tibetan Plateau. Tectonics 21 (6), 1062. http://dx.doi.org/10.1029/2001TC001322.

Diez Fernández, R., Martínez Catalán, J.R., Arenas, R., Abati, J., 2012. The onset of the assembly of Pangaea in NW Iberia: constraints on the kinematics of continental subduction. Gondwana Res. 22, 20–25.

Doin, M.-P., Henry, P., 2001. Subduction initiation and continental crust recycling: the roles of rheology and eclogitization. Tectonophysics 342, 163–191.

Duretz, T., Gerya, T.V., May, D.A., 2011. Numerical modelling of spontaneous slab breakoff and subsequent topographic response. Tectonophysics 502, 244–256.

Duretz, T., Gerya, T.V., Kaus, B.J.P., Andersen, T.B., 2012. Thermomechanical modelling of slab eduction. J. Geophys. Res. 117. http://dx.doi.org/10.1029/2012JB009137.

Emerman, S.H., Turcotte, D.L., 1983. A fluid model for the shape of accretionary wedges. Earth Planet. Sci. Lett. 63, 379–384.

England, P.C., Houseman, G.A., 1989. Extension during continental convergence, with application to the Tibetan Plateau. J. Geophys. Res. 94, 17561–17579.

Ernst, W.G., 1973. Blueschist metamorphism and P–T regimes in active subduction zones. Tectonophysics 17, 255–272.

Ernst, W.G., 2001. Subduction, ultrahigh-pressure metamorphism, and regurgitation of buoyant crustal slices - implications for arcs and continental growth. Physics of the Earth and Planetary Interiors 127, 253–275.

Ernst, W.G., 2010. Subduction-zone metamorphism, calc-alkaline magmatism, convergent-margin crustal evolution. Gondwana Res. 18, 8–16.

Please cite this article as: Burov, E., et al., Rheological and geodynamic controls on the mechanisms of subduction and HP/UHP exhumation of crustal rocks during continental coll..., Tectonophysics (2014), http://dx.doi.org/10.1016/j.tecto.2014.04.033

Faccenda, M., Gerya, T.V., Chakraborty, S., 2008. Styles of post-subduction collisional orogeny: influence of convergence velocity, crustal rheology and radiogenic heat production. Lithos 103, 257–287.

Faccenda, M., Gerya, T.V., Burlini, L., 2009a. Deep slab hydration induced by bending related variations in tectonic pressure. Nat. Geosci. 2, 790–793.

Faccenda, M., Minelli, G., Gerya, T.V., 2009b. Coupled and decoupled regimes of continental collision: numerical modeling. Earth Planet. Sci. Lett. 278, 337–349.

Ford, M., Duchêne, S., Gasquet, D., Vanderhaeghe, O., 2006. Two-phase orogenic convergence in the external and internal SW Alps. J. Geol. Soc. Lond. 163, 1–12.

Francois, T., Burov, E., Agard, P., Meyer, B., 2012. Evaluating the effect of rheology on the evolution of continental collision: application to the Zagros orogen. Geophysical Research Abstracts, 14. EGU General Assembly (EGU2012-10283, 2012).

Francois, T., Burov, E., Agard, P., Meyer, B., 2014. Build-up of a dynamically supported orogenic plateau: numerical modelling of the Zagros/Central Iran case study. G3 (submitted for publication).

Gerya, T.V., Stöckhert, B., 2006. Two-dimensional numerical modeling of tectonic and metamorphic histories at active continental margins. Int. J. Earth Sci. 95, 250–274.

Gerya, T.V., Yuen, D.A., 2003. Rayleigh–Taylor instabilities from hydration and melting propel "cold plumes" at subduction zones. Earth Planet. Sci. Lett. 212, 47–62.

Gerya, T.V., Stöckhert, B., Perchuk, A.L., 2002. Exhumation of high-pressure metamorphic rocks in a subduction channel: a numerical simulation. Tectonics 26 (6), 1–15.

Gerya, T.V., Perchuk, L.L., Burg, J.-P., 2008. Transient hot channels: perpetrating and regurgitating ultrahigh-pressure, high temperature crust–mantle associations in collision belts. Lithos 103, 236–256.

Gleason, G.C., Tullis, J., 1995. A flow law for dislocation creep of quartz aggregates determined with the molten salt cell. Tectonophysics 247, 1–23.

Goetze, C., Evans, B., 1979. Stress and temperature in the bending lithosphere as constrained by experimental rock mechanics. Geophys. J. R. Astron. Soc. 59, 463–478.

Gorczyk, W., Gerya, T.V., Connolly, J.A.D., Yuen, D.A., Rudolph, M., 2006. Large-scale rigid-body rotation in the mantle wedge and its implications for seismic tomography. Geochem. Geophys. Geosyst. 7. http://dx.doi.org/10.1029/2005GC001075.

Gray, R., Pysklywec, R.N., 2010. Geodynamic models of Archean continental collision and the formation of mantle lithosphere keels. Geophys. Res. Lett. 37, L19301. http://dx.doi.org/10.1029/2010GL043965.

Gray, R., Pysklywec, R.N., 2012. Geodynamic models of mature continental collision: evolution of an orogen from lithospheric subduction to continental retreat/delamination. J. Geophys. Res. http://dx.doi.org/10.1029/2011JB008692.

Guillot, S., Hattori, K., de Sigoyer, J., 2000. Mantle wedge serpentinization and exhumation of eclogites: insights from eastern Ladakh, northwest Himalaya. Geology 28, 199–202.

Guillot, S., Hattori, K., de Sigoyer, J., Nägler, T., Auzende, A.L., 2001. Evidence of hydration of the mantle wedge and its role in the exhumation of eclogites. Earth Planet. Sci. Lett. 193, 115–127.

Guillot, S., Hattori, K., Agard, P., Schwartz, S., Vidal, O., 2009. Exhumation processes in oceanic and continental subduction contexts: a review. In: Lallemand, S., Funiciello, F. (Eds.), Subduction Zone Dynamics. Springer-Verlag, Berlin Heidelberg, pp. 175–204. http://dx.doi.org/10.1007/978-3-540-87974-9.

Hacker, B.R., Gerya, T.V., 2013. Paradigms, new and old, for ultrahigh-pressure tectonism. Tectonophysics 603, 79–88.

Hacker, B.R., Ratschbacher, L., Webb, L.E., McWilliams, M., Calvert, A., Dong, S., Wenk, H.-R., Chateigner, D., 2000. Exhumation of ultrahigh-pressure rocks in east-central China: Late Triassic–Early Jurassic tectonic unroofing. J. Geophys. Res. 105, 13339–13364.

Hacker, B.R., Calvert, A., Zhang, R.Y., Gary Ernst, W., Liou, J.G., 2003. Ultrarapid exhumation of ultrahigh-pressure diamond-bearing metasedimentary rocks of the Kokchetav Massif, Kazakhstan? Lithos 70, 61–75.

Hacker, B.R., Ratschbacher, L., Liou, J.G., 2004. Subduction, collision and exhumation in the ultrahigh-pressure Qinling–Dabie orogen. In: Malpas, J., Fletcher, C.J.N., Ali, J.R., Aitchison, J.C. (Eds.), Aspects of the Tectonic Evolution of Chiua. Geol. Soc. London, Spec. Pub, 226, pp. 157–175.

Hacker, B.R., McClelland, W.C., Liou, J.G., 2006. Ultrahigh-pressure Metamorphism: Deep Continental SubductionGeological Society of America (206 pp.).

Hacker, B.R., Andersen, T.B., Johnston, S., Kylander-Clark, A.R.C., Peterman, E.M., Walsh, E. O., Young, D., 2010. High-temperature deformation during continental-margin subduction & exhumation: the ultrahigh-pressure Western Gneiss Region of Norway. Tectonophysics 480 (1–4), 149–171.

Hacker, B.R., Kelemen, P.B., Behn, M.D., 2011. Differentiation of the continental crust by relamination. Earth Planet. Sci. Lett. 307, 501–516.

Handy, M.R., Schmid, S.M., Bousquet, R., Kissling, E., Bernoulli, D., 2010. Reconciling plate-tectonic reconstructions of Alpine Tethys with the geological–geophysical record of spreading and subduction in the Alps. Earth Sci. Rev. 102, 121–158.

Hassani, R., Jongmans, D., Chery, J., 1997. Study of plate deformation and stress in subduction processes using two-dimensional numerical models. J. Geophys. Res. 102 (B8), 17951–17965.

Hatzfeld, D., Molnar, P., 2010. Comparisons of the kinematics and deep structures of the Zagros and Himalaya and of the Iranian and Tibetan plateaus and geodynamic implications. Rev. Geophys. 48 (RG2005). http://dx.doi.org/10.1029/2009RG000304 (48 pp.).

Hermann, J., Müntener, O., Scambelluri, M., 2000. The importance of serpentinite mylonites for subduction and exhumation of oceanic crust. Tectonophysics 327, 225–238.

Hirth, G., Kohlstedt, D.L., 1996. Water in the oceanic upper mantle: implications for rheology, melt extraction and the evolution of the lithosphere. Earth Planet. Sci. Lett. 144, 93–108.

Houseman, C.A., Molnar, P., 1997. Gravitational (Rayleigh–Taylor) instability of a layer with nonlinear viscosity and convergence thinning of continental lithosphere. Geophys. J. Int. 128, 125–150.

Husson, L., Brun, J., Yamato, P., Faccenna, C., 2009. Episodic slab rollback fosters exhumation of HP-UHP rocks. Geophysical journal International 179, 1292–1300. http://dx.doi.org/10.1111/j.1365-246X.2009.04372.x.

Jolivet, L., Daniel, J.M., Truffert, C., Goffé, B., 1994. Exhumation of deep crustal metamorphic rocks and crustal extension in back-arc regions. Lithos 33, 3–30.

Jolivet, L., Raimbourg, H., Labrousse, L., Avigad, D., Leroy, Y., Austrheim, H., Andersen, T.B., 2005. Softening trigerred by eclogitization, the first step toward exhumation during continental subduction. Earth Planet. Sci. Lett. 237, 532–547.

Jolivet, L., Faccenna, C., Huet, B., Labrousse, L., Le Pourhiet, L., Lacombe, O., Lecomte, E., Burov, E., Denele, Y., Brun, J.-P., Philippon, M., Paul, A., Salaun, G., Karabulut, H., Piromallo, C., Monie, P., Gueydan, F., Okay, A.I., Oberhansli, R., Pourteau, A., Augier, R., Gadenne, L., Driussi, O., 2012. Aegean tectonics: Strain localisation, slab tearing and trench retreat. Tectonophysics 567, 2013. http://dx.doi.org/10.1016/j.tecto.2012.06.011 1-33.

Kylander-Clark, A.R.C., Hacker, B.R., Johnson, C.M., Beard, B.L., Mahlen, N.J., 2009. Slow subduction and rapid exhumation of a thick ultrahigh-pressure terrane. Tectonics 28, TC2003. http://dx.doi.org/10.1029/2007TC002251.

Kylander-Clark, A.R.C., Hacker, B.R., Mattinson, C.G., 2011. Size and exhumation rate of ultrahigh-pressure terranes linked to orogenic stage. Earth Planet. Sci. Lett. 321–322, 115–120.

Labrousse, L., Jolivet, L., Agard, P., Hebert, R., Andersen, T., 2002. Crustal-scale boudinage and migmatization of gneiss during their exhumation in the UHP Province of Western Norway. Terra Nova 14 (4), 263–270.

Lanari, P., Guillot, S., Schwartz, S., Vidal, O., Tricart, P., Riel, N., Beyssac, O., 2012. Diachronous evolution of the alpine continental subduction wedge: evidence from P–T estimates in the Briançonnais Zone houillère (France — Western Alps). J. Geodyn. http://dx.doi.org/10.1016/j.jog.2011.09.006.

Lavier, L., Steckler, M., 1997. The effect of sedimentary cover on the flexural strength of continental lithosphere. Nature 389, 476–479.

Le Pichon, X., Fournier, M., Jolivet, L., 1992. Kinematics, topography, shortening and extrusion in the India–Eurasia collision. Tectonics 11, 1085–1098.

Le Pourhiet, L., Burov, E., Moretti, I., 2004. Rifting through a stack of inhomogeneous thrusts (the dipping pie concept). Tectonics 23 (4), TC4005. http://dx.doi.org/10.1029/2003TC001584.

Li, Z., Gerya, T.V., 2009. Polyphase formation and exhumation of HP–UHP rocks in continental subduction zone: numerical modeling and application to the Sulu UHP terrane in eastern China. J. Geophys. Res. 114 (Article Number: B09406).

Li, Z.H., Gerya, T.V., Burg, J.-P., 2010. Influence of tectonic overpressure on P–T paths of HP–UHP rocks in continental collision zones: thermomechanical modeling. J. Metamorph. Geol. 28 (3), 227–247.

Li, Z.H., Xu, Z.Q., Gerya, T.V., 2011. Flat versus steep subduction: contrasting modes for the formation and exhumation of high- to ultrahigh-pressure rocks in continental collision zones. Earth Planet. Sci. Lett. 301, 65–77.

Li, Z.H., Xu, Z.Q., Gerya, T.V., et al., 2013. Collision of continental corner from 3-D numerical modeling. Earth Planet. Sci. Lett. 380, 98–111.

Liou, J.G., Ernst, W.G., Zhang, R.Y., Tsujimori, T., Jahn, J.G., 2009. Ultrahigh-pressure minerals and metamorphic terranes—the view from China. J. Asian Earth Sci. 35, 199–231.

Little, T.A., Hacker, B.R., Gordon, S.M., Baldwin, S.L., Fitzgerald, P.G., Ellis, S., Korchinski, M., 2011. Diapiric exhumation of Earth's youngest (UHP) eclogites in the gneiss domes of the D'Entrecasteaux Islands, Papua New Guinea. Tectonophysics 510, 39–68.

Mackwell, S.J., Zimmerman, M.E., Kohlstedt, D.L., 1998. High-temperature deformation of dry diabase with applications to tectonics on Venus. J. Geophys. Res. 103, 975–984.

Mancktelow, N., 1995. Nonlithostatic pressure during sediment subduction and the development and exhumation of high pressure metamorphic rocks. J. Geophys. Res. 100, 571–583.

Mancktelow, N.S., 2008. Tectonic pressure: theoretical concepts and modelled examples. Lithos 103 (1–2), 149–177.

Marschall, H.R., Schumacher, J.C., 2012. Arc magmas sourced from mélange diapirs in subduction zones. Nature Geoscience 5, 862–867.

Maruyama, Shigenori, Masago, H., Katayama, I., et al., 2010. A new perspective on metamorphism and metamorphic belts. Gondwana Res. 18, 106–137.

McAdoo, D.C., Martin, C.F., Poulouse, S., 1985. Seasat observations of flexure: evidence for strong lithosphere. Tectonophysics 116, 209–222.

Mouthereau, F., Watts, A.B, Burov, E., 2013. Collisional orogens, structural inheritance and the long-term strength of continental lithosphere. Nat. Geosci. 6 (9), 785–789.

Okay, A.I., Harris, N.B.W., Kelley, S., 1998. Exhumation of blueschists along a Tethyan suture in northwest Turkey. Tectonophysics 285, 275–299.

Parsons, B.E., Sclater, J.G., 1977. An analysis of the variation of ocean floor bathymetry and heat flow with age. J. Geophys. Res. 82, 803–827.

Patriat, P., Achache, J., 1984. India–Eurasia collision chronology has implications for crustal shortening and driving mechanism of plates. Nature 311, 615–621.

Patzelt, A., Li, H., Wang, J., Appel, E., 1996. Palaeomagnetism of Cretaceous to Tertiary sediments from southern Tibet: evidence for the extent of the northern margin of India prior to the collision with Eurasia. Tectonophysics 259, 259–284.

Pérez-Gussinyé, M., Watts, A.B., 2005. The long-term strength of Europe and its implications for plate-forming processes. Nature 436 (doi:10.1038).

Peterman, E.M., Hacker, B.R., Baxter, E.F., 2009. Phase transformations of continental crust during subduction and exhumation: Western Gneiss Region, Norway. Eur. J. Mineral. 21, 1097–1118.

Petrini, K., Podladchikov, Yu., 2000. Lithospheric pressure–depth relationship in compressive regions of thickened crust. J. Metamorph. Geol. 18, 67–78.

Platt, J.P., 1986. Dynamics of orogenic wedges and the uplift of high-pressure metamorphic rocks. Geol. Soc. Am. Bull. 97, 1037–1053.

Please cite this article as: Burov, E., et al., Rheological and geodynamic controls on the mechanisms of subduction and HP/UHP exhumation of crustal rocks during continental coll..., Tectonophysics (2014), http://dx.doi.org/10.1016/j.tecto.2014.04.033

Platt, J.P., 1993. Exhumation of high-pressure rocks: a review of concept and processes. Terra Nova 5, 119–133.
Plunder, A., Agard, P., Chopin, C., Okay, A., 2013. Geodynamics from the Tavsanli zone, western Turkey: insights into subduction/obduction processes. Tectonophysics. http://dx.doi.org/10.1016/j.tecto.2013.07.28,2013.
Poliakov, A.N.B., Podladchikov, Yu., Talbot, C., 1993. Initiation of salt diapirs with frictional overburden: numerical experiments. Tectonophysics 228, 199–210.
Ponziani, F., De Franco, R., Minelli, G., Biella, G., Federico, C., Pialli, G., 1995. Crustal shortening and duplication of the Moho in the Northern Apennines: a view from seismic refraction data. Tectonophysics 252, 391–418.
Pysklywec, R.N., 2006. Surface erosion control on the evolution of the deep lithosphere. Geology 34 (4), 225–228 (269).
Pysklywec, R., Beaumont, C., Fullsack, P., 2000. Modeling the behavior of the continental mantle lithosphere during plate convergence. Geology 28, 655–658.
Pysklywec, R.N., Beaumont, C., Fullsack, P., 2002. Lithospheric deformation during the early stages of continental collision: numerical experiments and comparison with South Island, New Zealand. J. Geophys. Res. 107 (B7). http://dx.doi.org/10.1029/2001JB000252.
Raimbourg, H., Jolivet, L., Leroy, Y., 2007. Consequences of progressive eclogitization on crustal exhumation, a mechanical study. Geophys. J. Int. 168, 379–401.
Ranalli, G., 1995. Rheology of the Earth2nd ed. Chapman and Hall, London (413 pp.).
Ranero, C.R., Phipps Morgan, J., McIntosh, K., Reichert, C., 2003. Bending-related faulting and mantle serpentinization at the Middle America trench. Nature 425, 367–373.
Ring, U., Will, T., Glodny, J., Kumerics, C., Gessner, K., Thomson, S., Gungor, T., Monie, P., Okrusch, M., Druppel, K., 2007. Early exhumation of high-pressure rocks in extrusion wedges: cycladic blueschist unit in the eastern Aegean, Greece, and Turkey. Tectonics 26 (2), TC2001. http://dx.doi.org/10.1029/2005tc001872.
Royden, L.H., 1993. The steady state thermal structure of eroding orogenic belts and accretionary prisms. J. Geophys. Res. 98 (B3), 4487–4507.
Sanzhong, Li, Kusk, Timothy M., Xiaochun, Liu, et al., 2009. Two-stage collision-related extrusion of the western Dabie HP–UHP metamorphic terranes, central China: evidence from quartz c-axis fabrics and structures. Gondwana Res. 16, 294–309.
Schmalholz, S.M., Podladchikov, Y.Y., 2013. Tectonic overpressure in weak crustal-scale shear zones and implications for the exhumation of high-pressure rocks. Geophys. Res. Lett. 40, 1984–1988.
Schmalholz, S.M., Podladchikov, Y.Y., Duretz, T., 2014. 2-D numerical modelling of nappe formation and pressure–temperature evolution in a shortening heterogeneous crust: implications for high and ultrahigh pressure tectonism. Tectonophysics (this volume).
Sizova, E., Gerya, T.V., Brown, M., 2012. Exhumation mechanisms of melt-bearing ultrahigh pressure crustal rocks during collision of spontaneously moving plates. J. Metamorph. Geol. 30, 927–955.
Smith, D., 1984. Coesite and pyroxene in Caledonides and its implications for geodynamics. Nature 310, 641–644.
Sobouti, F., Arkani-Hamed, J., 2002. Thermo-mechanical modeling of subduction of continental lithosphere. Phys. Earth Planet. Inter. 131, 185–203.
Spear, F.S., 1993. Metamorphic Phase Equilibria and Pressure–Temperature–Time PathsMineralogical Society of America (800 pp.).
Stöckhert, B., Gerya, T.V., 2005. Pre-collisional high pressure metamorphism and nappe tectonics at active continental margins: a numerical simulation. Terra Nova 17 (2), 102–110.
Tetsuzo, S., Rehman, H.U., 2011. When and why the continental crust is subducted: examples of Hindu Kush and Burma. Gondwana Res. 19, 327–333.
Thielmann, M., Kaus, B.J.P., 2012. Shear heating induced lithospheric localization: does it result in subduction? Earth Planet. Sci. Lett. 359–360, 1–13. http://dx.doi.org/10.1016/j.epsl.2012.10.002.
Thompson, A.B, Jezek, J., Schulmann, K., 1997. Extrusion tectonics and rapid elevation of lower crustal metamorphic rocks in convergent orogens. Geology 25, 491–494.
Tirel, C., Brun, J.-P., Burov, E., Wortel, M.J.R., Lebedev, S., 2013. A plate tectonics oddity: caterpillar-walk exhumation of subducted continental crust. Geology 41 (5), 555–558.
Toussaint, G., Burov, E., Jolivet, L., 2004a. Continental plate collision: unstable versus stable slab dynamics. Geology 32 (1), 33–36.
Toussaint, G., Burov, E., Avouac, J.-P., 2004b. Tectonic evolution of a continental collision zone: a thermo mechanical numerical model. Tectonics 23.
Turcotte, D.L., Schubert, G., 2002. GeodynamicsSecond edition. Cambridge University Press, Cambridge (456 pp.).
von Huene, R., Ranero, C.R., Vannucchi, P., 2004. Generic model of subduction erosion. Geology 32, 913–916.
Warren, C.J., Beaumont, C., Jamieson, R.A., 2008a. Formation and exhumation of ultra-high-pressure rocks during continental collision: role of detachment in the subduction channel. Geochem. Geophys. Geosyst. 9 (4). http://dx.doi.org/10.1029/2007GC001839.
Warren, C.J., Beaumont, C., Jamieson, R.A., 2008b. Modelling tectonic styles and ultra-high pressure (UHP) rock exhumation during the transition from oceanic subduction to continental collision. Earth Planet. Sci. Lett. 267 (1–2), 129–145.
Wassmann, S., Stockhert, S., 2013. Rheology of the plate interface — dissolution precipitation creep in high pressure metamorphic rocks. Tectonophysics 608, 1–29.
Watts, A.B., 2001. Isostasy and Flexure of the LithosphereCambridge University Press (458 pp.).
Weinberg, R.F., Podladchikov, Y., 1994. Diapiric ascent of magmas through power law crust and mantle. J. Geophys. Res. 99, 9543–9559.
Wenzel, F., 2002. Seismic experiments target earthquake-prone region in Romania. Eos Transactions, American Geophysical Union (83), 462–463.
Wilks, K.R., Carter, N.L., 1990. Rheology of some continental lower crustal rocks. Tectonophysics 182, 57–77.
Yamato, P., Agard, P., Burov, E., Le Pourhiet, L., Jolivet, L., Tiberi, C., 2007. Burial and exhumation in a subduction wedge: mutual constraints from thermo-mechanical modelling and natural P–T–t data (sch. Lustres, w. Alps). J. Geophys. Res. 112, B07410. http://dx.doi.org/10.1029/2006JB004441.
Yamato, P., Burov, E., Agard, P., Le Pourhiet, L., Jolivet, L., 2008. HP–UHP exhumation processes during continental subduction (W. Alps): when thermomechanical models reproduce P–T–t data. Earth Planet. Sci. Lett. 271, 63–75.
Yamato, P., Mouthereau, F., Burov, E., 2009. Taiwan mountain building: insights from 2D thermo-mechanical modelling of a rheologically-stratified lithosphere. Geophys. J. Int. 176, 307–326. http://dx.doi.org/10.1111/j.1365-246X.2008.03977.x.
Zhang, R.Y., Liou, J.G., Ernst, W.G., 2009. The Dabie–Sulu continental collision zone: a comprehensive review. Gondwana Res. 16, 1–26.
Zheng, Y.-F., 2012. Metamorphic chemical geodynamics in continental subduction zones. Chem. Geol. 328, 5–48.

Please cite this article as: Burov, E., et al., Rheological and geodynamic controls on the mechanisms of subduction and HP/UHP exhumation of crustal rocks during continental coll..., Tectonophysics (2014), http://dx.doi.org/10.1016/j.tecto.2014.04.033

Quantifying magma segregation in dykes

Yamato P.[1, 2,*], Duretz T.[3], May D.A.[2] and Tartèse R.[4]

[1]Géosciences Rennes, CNRS UMR 6118, Université de Rennes 1, 35042 Rennes Cedex, France

[2]Institute of Geophysics, Department of Earth Sciences, ETH-Zurich, Sonneggstrasse 5, CH-8092 Zurich, Switzerland

[3]Institute of Geology and Palaeontology, University of Lausanne, CH-1015 Lausanne, Switzerland

[4]Planetary and Space Sciences, The Open University, Walton Hall, Milton Keynes, MK7 6AA, United Kingdom

[*]Corresponding author: philippe.yamato@univ-rennes1.fr

Submission to: *Earth and Planetary Science Letters*

Abstract

The dynamics of magma flow is highly affected by the presence of a crystalline load. During magma ascent, it has been demonstrated that crystal-melt segregation constitutes a viable mechanism for magmatic differentiation. However, the influences of crystal volume fraction, geometry, size and density on crystal melt segregation are still not well constrained. In order to address these issues, we performed a parametric study using 2D direct numerical simulations, which model the ascension of crystal-bearing magma in a vertical dyke. Using these models, we have characterised the amount of segregation as a function of different quantities including: the crystal fraction (φ), the density contrast between crystals and melt ($\Delta\rho$), the size of the crystals (A_c) and their aspect ratio (R). Results show that crystal aspect ratio does not affect the segregation if R is small enough (long axis smaller than ~1/6 of the dyke width, W_d). Inertia within the system was also found not to influence crystal-melt segregation. The degree of segregation was however found to be highly dependent upon other parameters. Segregation is highest when $\Delta\rho$ and A_c are large, and lowest for large pressure gradient (P_d) and/or large values of W_d. These four parameters can be combined into a single one, the S_{number}, which can be used to quantify the segregation. Based on systematic numerical modelling and dimensional analysis, we provide a first order scaling law which allows quantification of the segregation for an arbitrary S_{number} and φ, encompassing a wide range of typical parameters encountered in terrestrial magmatic systems.

Keywords: Segregation; Magma differentiation; Dyke; Crystal-melt behaviour; Numerical modelling

1. Introduction

1.1. Background

Magmatic differentiation constitutes one of the major mechanisms that shapes internal structures and chemical compositions of planetary bodies. Addressing this process thus has broad applications including: understanding the behaviour of magma chambers underneath volcanoes; unravelling the petrogenesis of layered igneous intrusions and understanding planetary formation through crystallisation of magma oceans. One of the processes governing magmatic differentiation involves the physical separation of crystals carried by a melt phase, the so-called fractional crystallisation process. It can occur for example by crystal settling, or floating in a pool of magma, and is due to buoyancy contrasts between the crystals and the surrounding melt phase. One of the most emblematic examples of such a process is the differentiation of a lunar magma ocean into a mantle comprising heavy mafic minerals and a crust composed of light anorthositic plagioclase (e.g. Smith et al., 1970; Wood et al., 1970; Helmke et al., 1972; Philpotts et al., 1972).

The continental crust on Earth also differentiated through magmatic processes, deep partial melting producing enriched magmas, which subsequently ascended through the crust and were emplaced at different depths. Amongst the processes governing the upward travel of magma through the continental crust, dyking constitutes a key mechanism, especially for ascent through the continental crust (e.g. Nicolas, 1986; Clemens and Mawer, 1992; Petford et al., 2000; Vigneresse and Clemens, 2000). Mineralogical and geochemical observations are powerful tools to identify suites of cogenetic rocks, somehow related to each other, and which have been variably affected by differentiation processes. They allow us to decipher past petrogenetic processes, and are most of the time the only data available to infer processes happening at depth before magma emplacement. As differentiation trends are frequent and as it is inferred that magma ascent through the continental crust in dykes is a common process, fractionation at depth of crystals from ascending magmas has been proposed as a viable mechanism to account for magmatic differentiation for rock types

ranging from basaltic to granitic (e.g. Philpotts et al, 1988; Tartèse and Boulvais, 2010; Fourmentraux et al., 2012; Morfin et al., 2014).

However the underlying physical mechanisms inducing magmatic differentiation during magma ascent remains unclear (Marsh, 2013). In addition to a thorough study of the effects of the different physical processes involved during differentiation, precise quantification of the crystal-melt segregation during magma ascent in dykes requires further investigation. Indeed, despite the fact that geochemical and modelling studies highlight the viability of such a mechanism, even for highly viscous granitic magmas (Yamato et al., 2012), quantification of the mechanical crystal-melt segregation during magma ascent has not yet been provided.

1.2. Crystal-melt segregation processes

Mechanical segregation refers to the process by which melt can separate from the surrounding crystals. Processes inducing magma segregation in emplaced intrusions and deforming partially molten aggregates have been subjected to extensive studies (e.g. Fountain et al., 1989; Vigneresse et al., 1996; Suckale et al., 2012a, 2012b). In such models, melt segregation are induced by compaction and shear deformation of partially molten rocks (e.g., McKenzie, 1984; Brown et al. 1995; Rabinowicz and Vigneresse, 2004; Katz et al., 2006). In dykes, segregation may also occur when the rising magma carries a negatively buoyant crystalline load (Yamato et al., 2012), or when obstacles affect the flow (e.g. wall roughness). The segregation is considered equal to zero if the fraction of crystals φ does not change during magma ascent (i.e. the composition of the magma is not modified during its ascent). Conversely 100% of segregation corresponds to the cases where the melt phase only is extracted from the mush upward.

1.3. Two-phase flow regimes

Magmas, in the simplest form, can be described as a dispersed two-phase fluid (solid-liquid or crystal-melt). The dynamics of such systems is highly dependent on the volume fraction occupied by each phase. In the context we consider here (i.e. crystal suspended in magma), we summarise three different two-phase flow regimes. A dilute flow is one in which the volume fraction of the solid phase (φ) is small and the particle motion is purely determined by the fluid motion which give rise to surface and body forces acting on each particle (one-way coupled). With increasing volume fraction of the solid phase, feedbacks between the motion of the solid and the fluid occur due to hydrodynamical interactions (two-way coupled). When φ tends towards 1, dense flow ensues in which particle interactions (e.g. collisions) provide the dominant mechanism in defining the particle motion (four-way coupled).

Specific numerical methods are devised to study the dynamics of dispersed two-phase systems within a given regime. To understand segregation processes within dykes, we are primarily concerned by the systems undergoing a transition from being two-way coupled to being four-way coupled. In this context, the four-way coupled end-member would represent the deformation of a partially molten host rock possessing a small fraction of melt. In such a situation, the deformation of the solid phase dominates the deformation of the melt. This end member can be efficiently modelled using a "two-fluid" or "two-phase" model where volume averaged properties of the solid and melt phase are represented and evolved through time (McKenzie, 1985; Scott and Stevenson, 1986; Dufek and Bergantz, 2005; Keller et al., 2013). Two-phase models do not explicitly represent the finite size and geometry of individual solids. Consequently, such methods cannot be used to accurately model the dynamics of two-way coupled systems which require that the hydrodynamical interactions and coupling between the fluid motion and particle motion has to be resolved.

1.4. Aim of this study

In this paper, we present two dimensional (2D) numerical models of crystal-bearing magma ascending in a vertical conduit simulating a dyke. We quantify the amount of crystal-melt segregation and its dependency on both the magma properties and the dyke parameters through a parametric study. Based on the results

obtained from this systematic study, we develop a scaling law which allows us to predict the amount of segregation for all the influent parameters governing magma ascending in dyke.

2. Methods

2.1. Numerical Model

To study segregation processes within ascending crystal-bearing magma columns for dynamically regimes spanning both dilute and dense flows, we utilise in this work a 2D direct numerical simulation (DNS) methodology. In the following we outline the methodology and highlight some of its advantages.

In this work, we consider the dynamics of the multi-phase flow to be governed via incompressible Stokes flow (Yamato et al., 2012). In our DNS formulation, we explicitly represent finite sized, arbitrary shape crystals as prismatic inclusions with viscosity η_c and density ρ_c. The melt phase is described as a low viscosity fluid, $\eta_m << \eta_c$, with density $\rho_m < \rho_c$. In this study, we consider non-deforming crystals. For this, we enforce that the strain-rate tensor within each crystal domain vanishes by defining a crystalline viscosity of $\eta_c = 10^6\ \eta_m$, thereby effectively ensuring each crystal behaves as a rigid body.

The Stokes equations are discretised over a rectangular model domain using a finite difference staggered grid. The spatial discretisation of the material properties (viscosity and density) are provided via Lagrangian markers (Gerya and Yuen, 2003). No distinction is made between the markers used to define the crystals and the melt, other than in the definition of their material properties. Material properties defined on the markers are interpolated to the nodes in the finite difference mesh using a distance-dependent interpolation (1-Cell). All markers are evolved forward in time using a 4^{th} order (in space) Runge-Kutta scheme using the velocity field obtained from solving the Stokes problem. Further details concerning the accuracy of this method for fluid-solid interactions are available in Duretz et al., 2011 and Yamato et al., 2012.

We note that the velocity field obtained from solving the Stokes flow problem is continuous and defined over the whole model domain (i.e. inside both the melt and the crystal domains), which consistently couples both the melt and crystal phases. An immediate benefit of such an approach is that it avoids the requirement to impose special rules (i) to describe the updated position and orientation of the crystal at each time step (e.g. by imposing Newton's laws of rigid-body motion), and (ii) to avoid crystal interpenetration (e.g. Suckale et al, 2012a). As a result, in our model, all inter-particle interactions (collisions, viscous drag coupling) develop naturally.

2.2. Model description

The model domain is defined as a 1 m width (W) and 7.75 m height (L) box (Fig. 1a). The bottom of the domain consists of a 2.5 m height magma reservoir constituted by both crystal and melt. A conduit of 0.5 m width (W_d) and 5 m height (L_d) representing the dyke is directly located above the reservoir. Rigid blocks are located on both sides of the conduit and an additional crystal-free reservoir is located above the dyke. The positions of the crystals within the reservoir are randomly generated. Such an approach allows producing initial crystal configurations for different initial crystal fraction (φ, up to 45%), size (A_c), or aspect ratio (R). The melt viscosity is set to 10^4 Pa.s whereas the crystals are considered as rigid ($\eta_c = 10^{10}$ Pa.s). The density of the melt (ρ_m) is set to 2400 kg.m^{-3} whereas the density of the crystals (ρ_c) constitutes one of the parameter investigated in this study. Both buoyancy and a prescribed pressure gradient are responsible for driving the flow within the model domain. The negative buoyancy force is generated by the density difference between the crystals and the melt ($\Delta\rho$). The pressure gradient (P_d) results from the motion of the rigid blocks ($\eta_b = 10^{11}$ Pa.s) located on each lateral side of the dyke and indenting the magmatic mush with a constant velocity U_z defined as:

$$U_z = -\frac{P_d W_d^2}{24\eta_m}. \quad (1)$$

The value of the imposed pressure gradient therefore corresponds to the pressure gradient obtained in the crystal-free case (see Appendix A in Yamato et al., 2012). In our simulations, a pressure gradient of 24 $Pa.m^{-1}$ is used. This value ensures the onset of segregation for the considered experimental conditions (Yamato et al., 2012). A grid resolution of 401 by1551 nodes (i.e. producing a spatial resolution of dx = 2.5 mm and dz = 5 mm) was used for the numerical calculations, and ~5 000 to 20 000 time steps were usually performed during each simulation. Boundary conditions are set to free slip on all sides except along the rigid blocks where $U_x = 0$ and U_z is imposed following the Eq. 1. The experiments were carried out under the acceleration of gravity (g =10 $m.s^{-2}$). In the following, we will investigate the effect of the crystal fraction, density, size, and aspect ratio on the process of mechanical segregation of crystals from the melt during magma ascent in dyke.

3. Results

3.1. Reference model

In the reference model, the magma reservoir initially contains a crystal fraction of 15% (200 crystals) randomly distributed in space. The density difference between the crystals and the melt $\Delta\rho$ is set to 300 $kg.m^{-3}$ (i.e. ρ_c = 2700 $kg.m^{-3}$). Each crystal has a size A_c of 0.025 × 0.075 m^2 and an aspect ratio R of 3, corresponding to the ratio between its long and short axis. Compression of the reservoir due to the downward motion of the rigid blocks induces flow within the dyke conduit (Fig. 1b). However, as the crystals are denser than the melt ($\Delta\rho > 0$), convection may occur during the magma ascent leading to the extraction of the liquid phase above the crystals. This type of mechanical segregation results from the competition between the pressure driving the flow through the conduit and the negative buoyancy of the crystalline load which acts in the opposite direction.

3.2. Segregation definition

In this study, we define the amount of crystal-melt segregation from the magma as follows:

$$Seg = \frac{V_m - V_t}{V - V_t}, \quad (2)$$

where V and V_m correspond to the total volume of material (crystal and melt) and to the volume of melt only located within the dyke (i.e. material above the base of the rigid blocks, see Fig. 2 for illustration). V_t corresponds to the theoretical volume of melt that would be obtained considering no segregation and can be calculated for any crystal fraction (φ) as:

$$V_t = V(1 - \varphi). \quad (3)$$

V can be also obtained through time t, analytically, by considering a crystal-free case (Fig. 2a) by using the following equation (See Appendix in Yamato et al., 2012 for further details):

$$V = \frac{2P_d W_c^3 t}{24\eta_m}. \quad (4)$$

Segregation in the model can therefore be computed from the volume of melt measured within the dyke. Fig. 2c shows the evolution of V, V_m, V_m+V_c and V_t for the reference model through time. The corresponding segregation values are plotted in Fig. 2d. This figure shows that crystal-melt segregation stabilises after an initial transient stage. Values of segregation for each time-step between 20 000 s and 40 000 s were averaged to ensure that they are representative of steady-state segregation for each model. This also permits to avoid any possible perturbation, caused for example by injection of a large volume of material, originally resting at the bottom of the reservoir, which then locally contains a higher crystal fraction. Segregation (*Seg*) thus refers to a segregation amount, in contrast with the segregation rate (volume of extracted melt with time), which in our case (between 20 000 s and 40 000 s) is almost constant.

3.3. Parametric study

3.3.1. Initial crystal distribution

To study the impact of the initial crystal distribution in our simulations, we ran two end-member series of simulations with crystals initially oriented either horizontally or vertically (Fig. 3a). Results after 40 000 s of experiment are presented in Fig. 3b for a volume fraction φ of crystal of 15%. Altogether, these results show that the initial distribution of the crystals in the magma has a limited impact on the flow dynamics inside the conduit. Fig. 3c illustrates the dependency of the amount of segregation in the dyke to the initial crystal fraction for vertically-, horizontally- and randomly- initially distributed crystals where only small fluctuations were obtained over the crystallinity range. This shows that discrepancy in the segregation values occurs between φ = 15% and φ = 30% while never exceeding ±10%. The initial crystal distribution therefore does not influence whether segregation will occur or not.

3.3.2. Crystal aspect ratio

Previous studies focused on magma rheology have shown that crystal aspect ratio plays an important role on the effective magma viscosity (e.g. Cimarelli et al., 2011, Mueller et al., 2010, Mueller et al., 2011). In order to study the impact of crystal aspect ratio R on the segregation, we designed several experiments in which R varies while keeping the crystal areas A_c fixed (which ensure a constant mass for crystals). Results for φ = 15% are presented in Fig. 4 for R = 1, 2, 3, 4, 5 and 10. R can affect the behaviour of the magma within the dyke (hence the segregation) when the long axis (L_c) of the crystals is larger than ~1/6 of the dyke width. In the other experiments ($L_c < 1/6\ W_d$), the effect of R on the segregation process appears limited.

3.3.3. Crystal fraction

Crystal fraction constitutes one of the most influential parameters on the behaviour of magma (e.g. Vigneresse et al., 1996; Caricchi et al., 2007). Experiments have been carried out for φ varying from 5% (67 crystals) to φ = 45% (600 crystals). The results obtained after 40 000 s of experiment are presented in Fig. 5. They show that increasing the crystal fraction dramatically influences the magma behaviour in the dyke. When the crystal fraction increases, magma flow evolves from a typical Poiseuille-type, to an apparent Bingham-type flow, in agreement with previous studies (e.g. Petford and Koenders, 1998; Petford, 2003; Yamato et al., 2012). This transition takes place for φ > 15-35% and corresponds to the transition between ~90% and ~10% of segregation (Fig. 3c). Segregation amount decreases with increasing φ and follows a cumulative normal distribution law (Fig. 3c). At high crystal fractions (Fig. 5 at φ = 35% and 45%), melt extraction occurs differently. When the average crystal spacing is small, melt extraction (and hence segregation) is hindered. The liquid phase is collected in "melt pockets" located between crystal aggregates. The growth of melt pockets causes melt depletion and thus crystal aggregation in adjacent regions. The extraction of melt pockets may occur once their buoyancy overcomes the resistance of the surrounding crystalline mush. As a result, extraction of pockets occurs in pulses causing transient variations of the segregation.

3.3.4. Crystal-melt density difference

As segregation results from the competing effects of negative crystal buoyancy and upward pressure gradient, the effect of the crystal-melt density difference ($\Delta\rho$) naturally controls the amount of segregation. Fig. 6a shows how small variations of $\Delta\rho$ dramatically influence the segregation amount: the higher the density contrast, the larger the segregation. Fig. 6b illustrates how the cumulative normal distribution of segregation (which is a function of φ, see section 3.3.3. above) changes with the crystal-melt density difference. When $\Delta\rho$ increases, the mean of the cumulative normal distribution (i.e. the volume fraction of crystals φ needed to obtain 50% of segregation) increases and the standard deviation of this curve decreases (i.e. the slope of the curve increase). This means that the transition from 100% to 0% of segregation occurs for a small range of φ as $\Delta\rho$ increases.

3.3.5. Crystal size

The crystalline load affects the segregation process; however the above-described experiments only consider a fixed total volume of crystals (at a given φ) and do not investigate the impact of the mass of each crystal (for a fixed $\Delta\rho$). We ran several experiments considering the same crystal fraction but changing the size of each crystal (A_c) while ensuring a fixed total crystalline mass. The results show that the bigger the crystals, the larger the segregation for a fixed φ (Fig. 7). The crystal size hence needs to be considered as an important parameter controlling the amount of segregation.

3.4. First order scaling for predicting the amount of segregation

As presented above, the dominant parameters which control magma segregation during magma ascent are (1) the crystal-melt density difference, (2) the crystal size, (3) the initial reservoir crystal fraction, and (4) the applied pressure gradient (Yamato et al, 2012). In order to combine these parameters, we propose a non-dimensional number, S_{number}, expressed as:

$$S_{number} = \frac{\Delta\rho g A_c}{P_d W_d^2}, \qquad (5)$$

This number does not directly correspond to the segregation amount because the crystal fraction is not included; however the S_{number} is suitable to describe the flow behaviour observed in the different experiments. Indeed, at a given crystal fraction, it encompasses the fact that segregation is facilitated when $\Delta\rho$ and A_c are high and that segregation is limited for high pressure gradient and/or large dyke width (Yamato et al., 2012).

The value of P_d can not be directly estimated from field observations and/or petrological studies. However, bound values for the ascending magma maximum velocity (U_{am}) can sometimes be approached. Hence, it is convenient to express Eq. 5 in term of U_{am} using the pressure gradient formula (see Appendix A in Yamato et al., 2012) which yields:

$$S_{number} \propto \frac{\Delta\rho g A_c}{\eta_{am} U_{am}}, \quad (6)$$

where η_{am} corresponds to the effective viscosity of the ascending magma. Under this form, the S_{number} corresponds to the inverse of the prediction of Koyaguchi and Blake (1989) for mixing during the rise of a magma batch. As an example, a typical S_{number} value for an ascending granitic magma considering A_c = 1×1 cm^2, $\Delta\rho$ = 250 kg.m^{-3}, U_{am} = 10^{-2} m.s^{-1} and η_m=10^5 Pa.s yields $S_{number} \sim 10^{-4}$. A similar calculation for basaltic material, with A_c = 1×1 cm^2, $\Delta\rho$ = 500 kg.m^{-3}, U_{am} = 10^{-2} m.s^{-1} and η_m = 10^2 Pa.s, yields $S_{number} \sim 10^{-2}$. If ascent rates are 100 times lower (i.e. U_{am} = 10^{-4} m.s^{-1}), the S_{number} becomes on the order of 10^{-2} and 1 for the granitic and basaltic magmas, respectively.

Figure 8 shows experiments realised with different input parameters but with the same S_{number} value. The results exhibit similar general behaviour for a given crystal fraction. From this we conclude that the parameters related to the ascending flow (i.e. pressure gradient and dyke width) and the competing effect induced by the buoyancy of the crystal mass (combination of $\Delta\rho$ and A_c) can be included in a single expression.

The dominant parameters controlling the amount of segregation during magma ascent are the crystal fraction φ and the S_{number}. This is well illustrated in Fig. 6b which shows (i) that the amount of segregation highly depends on φ ("S" shape presented in section 3.3. following a cumulative normal distribution) and (ii) that this dependency varies with different values of $\Delta\rho$ (i.e. different S_{number}). Moreover, Fig. 6b shows that with

increasing S_{number}, the mean value of the cumulative distribution increases and the standard deviation decreases.

A normal distribution law as described in section 3.3. (see also Fig. 3c and Fig. 6b) could thus approximate the amount of segregation in the dyke (*Seg**). Such a law can then be expressed as follow:

$$Seg = Seg^* = 1 - \frac{1}{2}\left(1 + erf\left(\frac{\varphi - \mu}{\sqrt{2\sigma^2}}\right)\right), \quad (7)$$

where μ and σ are the mean and the standard deviation of the cumulative normal distribution, respectively. The amount of segregation (*Seg**) depends on the S_{number} and the crystal fraction (φ). For a given S_{number}, it is thus possible to fit the segregation values obtained from our numerical experiments and to obtain the corresponding values of μ and σ (Fig. 9a). A statistical fit was obtained using experiments described by different S_{number} presented in Fig. 6b and additional simulations for a S_{number} = 5 ($\Delta\rho$ = 1600 kg.m^{-3}). The obtained results are plotted in Fig. 9b for μ and in Fig. 9c for σ as a function of the S_{number}. The dependency of μ to the S_{number} follows a linear function in the semi-log space and can thus be described by the following equation:

$$\mu = A_\mu \log_{10}\left(S_{number}\right) + B_\mu, \quad (8)$$

which depends on two constants: A_μ and B_μ. The best fit of the experimental data gives A_μ = 22.8 and B_μ = 21.3 (R-square = 0.9791). The dependency of σ to the S_{number} was obtained using a similar approach (Fig. 9c). The experimental data were fitted using an exponential function:

$$\sigma = A_\sigma \exp\left(B_\sigma \cdot S_{number}\right), \quad (9)$$

which also depends on two constants: A_σ and B_σ. The best fit of the experimental data yields A_σ = 9.799 and

B_σ = -0.3339 (R-square = 0.9723).

To summarise, it is thus possible to propose a prediction law for the amount of segregation occurring in a magma ascending in a dyke for a given crystal fraction and a given S_{number}, which is:

$$Seg^* = 1 - \frac{1}{2}\left(1 + erf\left(\frac{\varphi - \left(A_\mu \log_{10}\left(S_{number}\right) + B_\mu\right)}{\sqrt{2}A_\sigma \exp\left(B_\sigma S_{number}\right)}\right)\right), \qquad (10)$$

Fig. 9d displays the segregation as a function of φ and S_{number}, with an extended part shown in Fig. 9e focusing on values of S_{number} between 0 and 3. For S_{number} = 0 (e.g. $P_d \rightarrow \infty$, $W_d \rightarrow \infty$, $\Delta\rho = 0$, or $A_c = 0$), no segregation takes place. At a low S_{number} (0-5), the transition between 100% and 0% of segregation occurs over a wide range of crystal fraction (up to 45%). The range of crystallinity over which this transition takes place decreases with increasing S_{number}. Finally, for large S_{number} (e.g. $P_d \rightarrow 0$, high $\Delta\rho$ or A_c), segregation occurs mainly by sedimentation (or mush compaction) in the reservoir, that could represent a deep-seated magma chamber alimenting a dyke, and may occur at larger crystallinity. This prediction is however derived for low values of S_{number}, which we regard as representative for dykes (see above).

4. Discussion

At large S_{number} (> 5), it is difficult to accurately predict the amount of segregation (Fig. 9d). For such parameters (large $\Delta\rho$ or A_c), the transition between 0 and 100% segregation becomes very sharp and small deviations between the amount of segregation obtained in the numerical models and the scaling prediction are observed. These deviations can reach up to 10% and may be explained by the "chaotic nature" of our experiments. The amount of segregation in the numerical models is calculated at a quasi-transient stage (Fig. 2d). The aggregation and disaggregation of crystals however causes transient fluctuations during the

segregation process (e.g. melt pockets formation at high crystal fraction), which probably affects our estimation of the amount of segregation.

Our prediction does not take into account the aspect ratio of the crystals. However, the segregation amount can vary when crystal long axis are larger than ~1/6 of the dyke width (Fig. 4). Under this condition, initially randomly oriented crystals may obstruct the conduit, which reduces the final amount of segregation.

Maximum packing fraction (i.e. the maximum fraction of crystals contained in the magmatic mush) is generally found to be different in 2D and in 3D. For example, in our 2D calculations the segregation mechanism is viable up to crystal fractions of about 40-45%. We thus expect that this limit should be different considering 3D prismatic crystals. Moreover, crystal size may vary (dissolution or crystal growth) during magma ascent (Nicholis and Rutherford, 2004), hence dynamically modifying the effective crystal fraction. Such effects cannot be taken into account in our simple mechanical models and the resulting predictions.

Although the Reynolds number corresponding to our reference experiment is low ($Re = 10^{-6}$ i.e. viscous forces dominate the inertial forces), thereby justifying the use of Stokes equations, we tested the impact of inertial effects on our results in Appendix A1. The results suggest that inertia does not significantly affect the segregation during magma ascent.

Our results indicate that crystal-melt segregation is likely to occur for crystallinities lower than 40 to 45% during magma ascent in dyke. When such high values of crystal fraction are reached, aggregation and close packing of crystals cause the magmatic mush to move coherently through the conduit, considerably lowering the amount of segregation. This result contrasts with that of Dufek and Bachman (2010), which predicted an optimal segregation window at high crystal fraction (50-70%). However, their prediction is related to compaction of a magmatic mush in a crystallising sill setting and cannot be directly compared to our magma ascent models.

5 - Conclusions

This study presents a wealth of 2D numerical models simulating crystal-melt segregation during ascent of magma in a vertical dyke. The extensive parametric study we have carried out shows that only a limited number of parameters control the amount of segregation:

(1) Experiments showed that initial crystal distribution in the reservoir as well as crystal aspect ratio does not noticeably affect the behaviour of magma flow, hence segregation. The aspect ratio might become important if the long axis is larger than 1/6 of the dyke width. This parameter consequently weakly influences the amount of segregation.

(2) Inertial forces (up to $Re \sim 10$) do not significantly influence the segregation process. Only small deviations due to inertia can occur at low melt viscosity (~10 Pa.s).

(3) The amount of segregation is controlled by the crystal fraction (φ) and the segregation number (S_{number}). The amount of segregation decreases when the crystal fraction increases following a cumulative normal distribution law ("S" shape curve). The segregation number S_{number} depends on the density contrast between the crystals and the carrying melt, the crystal size, the dyke width and the applied pressure gradient.

The first order scaling law derived from our parametric study allows to directly predict crystal-melt segregation from a magmatic mush, and is accurate (± 10%) for $S_{number} < 10$, which encompasses the common physical parameters related to ascent of granitic to basaltic magmas in dykes through the Earth's continental crust.

Acknowledgments

The authors wish to thank C. Luisier, E. Tornare, O. Reubi and S. Pilet for numerous stimulating discussions. P.Y. also thanks K. Gallagher for discussions on fitting method. Simulations were run on the ETH Brutus computational resource.

References

Brown, M., Averkin, Y.A., McLellan, E.L., Sawyer, E.W., 1995. Melt segregation in migmatites. Journal of Geophysical Research: Solid Earth 100, 15655–15679. doi:10.1029/95JB00517

Caricchi, L., Burlini, L., Ulmer, P., Gerya, T., Vassalli, M., Papale, P., 2007. Non-Newtonian rheology of crystal-bearing magmas and implications for magma ascent dynamics. Earth and Planetary Science Letters 264, 402–419. doi:10.1016/j.epsl.2007.09.032

Cimarelli, C., Costa, A., Mueller, S., Mader, H.M., 2011. Rheology of magmas with bimodal crystal size and shape distributions: Insights from analog experiments, Geochemistry, Geophysics, Geosystems 12, Q07024, doi:10.1029/2011GC003606

Clemens, J.D., Mawer, C.K., 1992. Granitic magma transport by fracture propagation. Tectonophysics 204, 339 – 360. doi:http://dx.doi.org/10.1016/0040-1951(92)90316-X

Dufek, J., Bachmann, O., 2010. Quantum magmatism: Magmatic compositional gaps generated by melt-crystal dynamics. Geology 38, 687–690. doi:10.1130/G30831.1

Dufek, J., Bergantz, G.W., 2005. Transient two-dimensional dynamics in the upper conduit of a rhyolitic eruption: A comparison of closure models for the granular stress. Journal of Volcanology and Geothermal Research 143, 113–132. doi:10.1016/j.jvolgeores.2004.09.013

Duretz, T., May, D.A., Gerya, T.V., Tackley, P.J., 2011. Discretization errors and free surface stabilization in the finite difference and marker-in-cell method for applied geodynamics: A numerical study. Geochemistry, Geophysics, Geosystems 12, Q07004, doi:10.1029/2011GC003567

Fountain, J.C., Hodge, D.S., Shaw, R.P., 1989. Melt segregation in anatectic granites: A thermo-mechanical model. Journal of volcanology and geothermal research 39, 279–296.

Fourmentraux, C., Métrich, N., Bertagnini, A., Rosi, M., 2012. Crystal fractionation, magma step ascent, and syn-eruptive mingling: the Averno 2 eruption (Phlegraean Fields, Italy). Contributions to Mineralogy and Petrology 163, 1121–1137.

Gerya, T.V., Yuen, D.A., 2003. Characteristics-based marker-in-cell method with conservative finite-differences schemes for modeling geological flows with strongly variable transport properties. Physics of the Earth and Planetary Interiors 140, 293–318. doi:10.1016/j.pepi.2003.09.006

Helmke, P., Haskin, L., Korotev, R., Ziege, K., 1972. Rare earths and other trace elements in Apollo 14 samples. Proceedings of the 3rd Lunar Science Conference, Geochimica et Cosmochimica Acta (supplement 3), 1275–1292.

Katz, R.F., Spiegelman, M., Holtzman, B., 2006. The dynamics of melt and shear localization in partially molten aggregates. Nature 442, 676–679. doi:10.1038/nature05039

Keller, T., May, D.A., Kaus, B.J.P., 2013. Numerical modelling of magma dynamics coupled to tectonic deformation of lithosphere and crust. Geophysical Journal International 195, 1406–1442. doi:10.1093/gji/ggt306

Koyaguchi, T., Blake, S., 1989. The dynamics of magma mixing in a rising magma batch. Bulletin of volcanology 52, 127–137.

Marsh, B.D., 2013. On some fundamentals of igneous petrology. Contributions to Mineralogy and Petrology 166, 665–690. doi:10.1007/s00410-013-0892-3

McKenzie, D., 1984. The generation and compaction of partially molten rock. Journal of Petrology 25, 713–765.

McKenzie, D., 1985. The extraction of magma from the crust and mantle. Earth and Planetary Science Letters 74, 81 – 91. doi:http://dx.doi.org/10.1016/0012-821X(85)90168-2

Morfin, S., Sawyer, E.W., Bandyayer, D., 2014. The geochemical signature of a felsic injection complex in the continental crust: Opinaca Subprovince, Quebec. Lithos 196–197, 339–355.

Mueller, S., Llewellin, E.W., Mader, H.M., 2010. The rheology of suspensions of solid particles. Proceedings of the Royal Society A: Mathematical, Physical and Engineering Sciences 466, 1201–1228. doi:10.1098/rspa.2009.0445

Mueller, S., Llewellin, E.W., Mader, H.M., 2011. The effect of particle shape on suspension viscosity and implications for magmatic flows: PARTICLE SHAPE AND SUSPENSION VISCOSITY. Geophysical Research Letters 38, n/a–n/a. doi:10.1029/2011GL047167

Nicholis, M.G., Rutherford, M.J., 2004. Experimental constraints on magma ascent rate for the Crater Flat volcanic zone hawaiite. Geology 32, 489–492.

Nicolas, A., 1986. A melt extraction model based on structural studies in mantle peridotites. Journal of Petrology 27, 999–1022.

Philpotts, J., Schnetzler, C., Nava, D., Bottino, M., Fullagar, P., Thomas, H., Schuhmann, S., Kouns, C., 1972. Apollo 14: Some geochemical aspects. Proceedings of the 3rd Lunar Science Conference, Geochimica et Cosmochimica Acta (supplement 3), 1293–1305.

Philpotts, A.R., Shi, J., Brustman, C., 1998. Role of plagioclase crystal chains in the differentiation of partly crystallized basaltic magma. Nature, 395, 343–346.

Petford, N., 2003. Rheology of granitic magma during ascent and emplacement. Annual Review of Earth and Planetary Sciences 31, 399–427, doi: 10.1146/annurev.earth.31.100901.141352.

Petford, N., Koenders, M.A., 1998. Granular flow and viscous fluctuations in low Bagnold number granitic magmas. Journal of the Geological Society 155, 873–881.

Petford, N., Cruden, A.R., McCaffrey, K.J.W., Vigneresse, J.L., 2000. Granite magma formation, transport and emplacement in the Earth's crust. Nature, 408, 669-673.

Rabinowicz, M., Vigneresse, J.L., 2004. Melt segregation under compaction and shear channeling: Application to granitic magma segregation in a continental crust. Journal of Geophysical Research 109. B04407, doi:10.1029/2002JB002372

Scott, D.R., Stevenson, D.J., 1986. Magma ascent by porous flow. Journal of Geophysical Research: Solid Earth 91, 9283–9296. doi:10.1029/JB091iB09p09283

Smith, J., Anderson, A., Newton, R., Olsen, E., Crewe, A., Isaacson, M., Johnson, D., Wyllie P., 1970. Petrologic history of the Moon inferred from petrography, mineralogy and petrogenesis of Apollo 11 rocks. Proceedings of the Apollo 11 Lunar Science Conference, Geochimica et Cosmochimica Acta, 1 (supplement), 897–925.

Suckale, J., Sethian, J.A., Yu, J., Elkins-Tanton, L.T., 2012a. Crystals stirred up: 1. Direct numerical simulations of crystal settling in nondilute magmatic suspensions. Journal of Geophysical Research 117. doi:10.1029/2012JE004066

Suckale, J., Elkins-Tanton, L.T., Sethian, J.A., 2012b. Crystals stirred up: 2. Numerical insights into the formation of the earliest crust on the Moon. Journal of Geophysical Research 117. doi:10.1029/2012JE004067

Tartèse, R., Boulvais, P., 2010. Differentiation of peraluminous leucogranites “en route” to the surface. Lithos 114, 353–368. doi:10.1016/j.lithos.2009.09.011

Vigneresse, J.L., Barbey, P., Cuney, M., 1996. Rheological transitions during partial melting and crystallization with application to felsic magma ségrégation and transfert. Journal of Petrology, 37, 6, 1579-1600.

Vigneresse, J.L., Clemens, J.D., 2000. Granitic magma ascent and emplacement: neither diapirism nor neutral buoyancy. Geological Society, London, Special Publications 174, 1–19. doi:10.1144/GSL.SP.1999.174.01.01

Wood, J.A., Dickey Jr., J.S., Marvin, U.B., Powell, B.N., 1970. Lunar anorthosites and a geophysical model of the Moon. Proceedings of the Apollo 11 Lunar Science Conference, Geochimica et Cosmochimica Acta, 1 (supplement), 965–988.

Yamato, P., Tartèse, R., Duretz, T., May, D.A., 2012. Numerical modelling of magma transport in dykes. Tectonophysics 526-529, 97–109. doi:10.1016/j.tecto.2011.05.015

Figure Captions

Figure 1. Model setup and reference experiment. **(a)** Rigid piston setup simulating an effective pressure gradient between the base and the top of a channel (representing a vertical dyke). The lateral rigid blocks compress the magmatic reservoir with a constant velocity U_z inducing a pressure gradient P_d along the conduit. The lengths L, L_d, W and W_d correspond to the length of the model, the length of the dyke, the width of the model and the width of the dyke, respectively. The grey and red melt layers correspond to passive markers highlighting the deformation of the fluid. η_c, ρ_c, η_m, and ρ_m correspond to the viscosity and the density of the crystals and of the melt, respectively. **(b)** Evolution of the reference experiment through time exhibiting crystal-melt segregation during magma ascent (Parameters used are: P_d = 24 Pa.m^{-1}, $\Delta\rho$ = 300 kg.m^{-3}, φ = 15%, $A_c = 0.025 \times 0.075$ m^2).

Figure 2. Segregation computation. **(a)** Model without any crystals. V is the volume of material (only melt here) extracted within the dyke (denoted via dotted white boundary) after 10 000 s of experiment, which fits the analytical solution for a Newtonian fluid in a Poiseuille flow (see Appendix A in Yamato et al., 2012,). **(b)** Same experiment with φ = 15%. V_m and V_c correspond to the volume of melt and of crystals extracted from the magmatic reservoir to the dyke, respectively ($V = V_m+V_c$). **(c)** Evolution of V, V_m, V_m+V_c and V_t through time for the reference experiment showed in Fig. 1b. V_t corresponds to the theoretical value of melt that would be extracted if the magma would not segregate. **(d)** Evolution of the amount of segregation (Seg) through time for the reference experiment (see text for details). σ stands for standard deviation.

Figure 3. Influence of the initial crystal distribution. **(a)** Left: random distribution (reference experiment), middle: horizontal distribution, right: vertical distribution. All other parameters are similar to those used in the reference simulation. **(b)** Results obtained after 40 000 s for these three experiments. The amount of segregation is indicated in the white ellipse. **(c)** Values of segregation obtained in these three configurations for different initial crystal fractions. Red line, squares and dots correspond to the initial random distribution

experiments, the initial horizontal distribution and the initial vertical distribution, respectively. Red shaded area corresponds to the variability of the segregation that could be obtained by changing the initial distribution of the crystals.

Figure 4. Influence of the crystals aspect ratio R. All parameters are identical to those used for the reference experiment except for the aspect ratio of each crystal. Volume of each crystal is also similar (i.e., the area A_c, and therefore the number of crystals, is the same in each experiment). We vary the ratio R that controls the ratio between the long (L_c) and short axis of the crystals. Computed segregation values are indicated in the white ellipses for each experiment. Results show that R does not significantly influence the amount of segregation value as long as L_c is small enough with respect to the width of the dyke W_d.

Figure 5. Influence of the crystal fraction φ. Other parameters are the same as those used for the reference experiment. This figure shows the results obtained after 40 000 s of experiment for φ = 5%, 15%, 25%, 35% and 45%, respectively. Computed segregation values are indicated in the white ellipses for each experiment.

Figure 6. Influence of the crystal-melt density difference $\Delta\rho$. In these experiments only the crystal density was varied, while keeping the melt density constant. **(a)** Results obtained after 40 000 s for $\Delta\rho$=100, 300, and 500 kg.m^{-3}, respectively. Computed segregation values are indicated in the white ellipses for each experiment. **(b)** Segregation values computed as a function of the crystal fraction φ for different $\Delta\rho$ values.

Figure 7. Influence of the crystal size. The crystal volumes A_c were varied, while the other parameters were kept consistent with those used for the reference experiment. Results are shown here after 40 000 s of experiment. A_{ref} corresponds to the crystal size of the reference experiment (i.e. 0.025 × 0.075 m^2). The crystal fraction is the same in the three experiments (i.e. the total mass of crystals is the same). The white ellipses indicate computed segregation amounts.

Figure 8. Model sensitivity to S_{number}. Experiments realised with the same S_{number} (but different input parameters) exhibit similar general behaviour. **(a)** Results obtained at 15% and 30% crystal fraction. A_{ref} and $\Delta\rho_{ref}$ correspond to the crystal size (i.e. 0.025×0.075 m^2) and to the density difference between crystals and melt (i.e., 300 kg.m^{-3}) of the reference experiment, respectively. **(b)** Results obtained also at 15% and 30% crystal fraction for different $\Delta\rho$ and A_c but keeping S_{number} constant.

Figure 9. Prediction of the segregation amount as a function of the crystal fraction (φ) and S_{number}. **(a)** Cumulative normal distribution fit (orange line) obtained from the segregation values computed in our numerical simulation for different crystal fractions (dots) at a given S_{number}. μ and σ corresponds to the mean and the standard deviation of the best fits of the data points, respectively. **(b)** μ vs. S_{number} fit. Black stars correspond to the mean values obtained (as in Fig. 9a) for different set of experiments at a given S_{number}. The red line corresponds to the law (equation in red) that can be used to predict μ for any given S_{number}. **(c)** σ vs. S_{number} fit. Black stars correspond to the standard deviation values obtained (as in Fig. 9a) for different set of experiments at a given S_{number}. The red line corresponds to the law (equation in red) that can be used to predict σ for any given S_{number}. **(d)** Diagram predicting the amount of segregation (Seg^*) as a function of the crystal fraction (φ) and S_{number}. **(e)** Zoom in the Segregation prediction (Seg^*) diagram for S_{number} ranging between 0 and 3. Values obtained in our numerical simulations are also indicated by colour dots.

Figure A1. (a) Vortex shedding test (Re = 100) in a 8 × 20 m box (N_x = 125, N_z = 250). The centre of a fixed cylinder (radius 0.5 m) is located at x = 4 m and z = 5 m. An inflow velocity of 10 m.s^{-1} is prescribed at the bottom side, zero normal stress is applied on the upper boundary and the lateral walls are free-slip. **(b)** Variations of kinetic energy with time. The onset of the vortex shedding instability ($t \sim 30$ s) yields to periodic fluctuations of kinetic energy (1.6 Hz).

Figure A2. Difference between models including or not inertia. Model parameters are similar to those employed in the reference model (Fig. 1). Simulations encompassing the same initial crystal distribution were computed with and without including inertial terms. The case $Re = 10^{-6}$ corresponds to the reference

1 experiment that leads to segregation. Final crystal positions can be affected but the macroscopic behaviour is
2 maintained. Simulations computed at higher Re ($10^{-3} < Re < 1$) are out of the segregation field ($10^{-3} > S_{number}$
3 $> 10^{-6}$).
4

Appendix

A1 - Influence of inertia on crystal bearing magma flow

In the numerical simulations, the Reynolds number *Re* can be computed using the relationship:

$$\mathrm{Re} = \frac{\rho_m U_{am} W_d}{\eta_m}, \qquad \text{(A1)}$$

Considering a constant melt density ρ_m (2400 kg.m^{-3}), a melt viscosity η_m of 10^4 Pa.s and a driving pressure of 24 Pa.m^{-1} yields a Reynolds number on the order of 10^{-6}. In order to evaluate the impact of inertia on our results, we have extended our viscous Stokes solver to account for fluid and solid acceleration. The Navier-Stokes equations are solved implicitly (backward Euler) and the non-linear convective acceleration term is treated by Picard iterations. The implementation was verified by running a vortex shedding experiment (e.g. Suckale et al., 2012a) with a Reynolds number of 100 (Fig. A1a). Our calculation delivers a vortex frequency of 1.6 Hz (Strouhal number of 0.16, Fig. A1b), which is in good agreement with other studies (Suckale et al., 2012a, and references therein). Subsequently, we have run our reference model (see section 3.1.) while taking inertia into account (Fig. A2). The obtained results indicate that inertial effects may affect the final position of crystals travelling in the conduit. However, under such experimental conditions, inertial effects do not produce notable variations on the amount of segregation, nor on the structures that develop during magma ascent.

Highlights

- We present 2D numerical models simulating the ascent of crystal-bearing magma in dyke
- We evaluate the role of magma and dyke parameters on crystal-melt segregation
- The crystal fraction and the segregation number control the amount of segregation
- Crystal aspect ratio does not noticeably affect magma flow, hence segregation
- We provide a first order scaling law to predict crystal-melt segregation in dykes

Figure 1

Click here to download Figure: Figure_1.eps

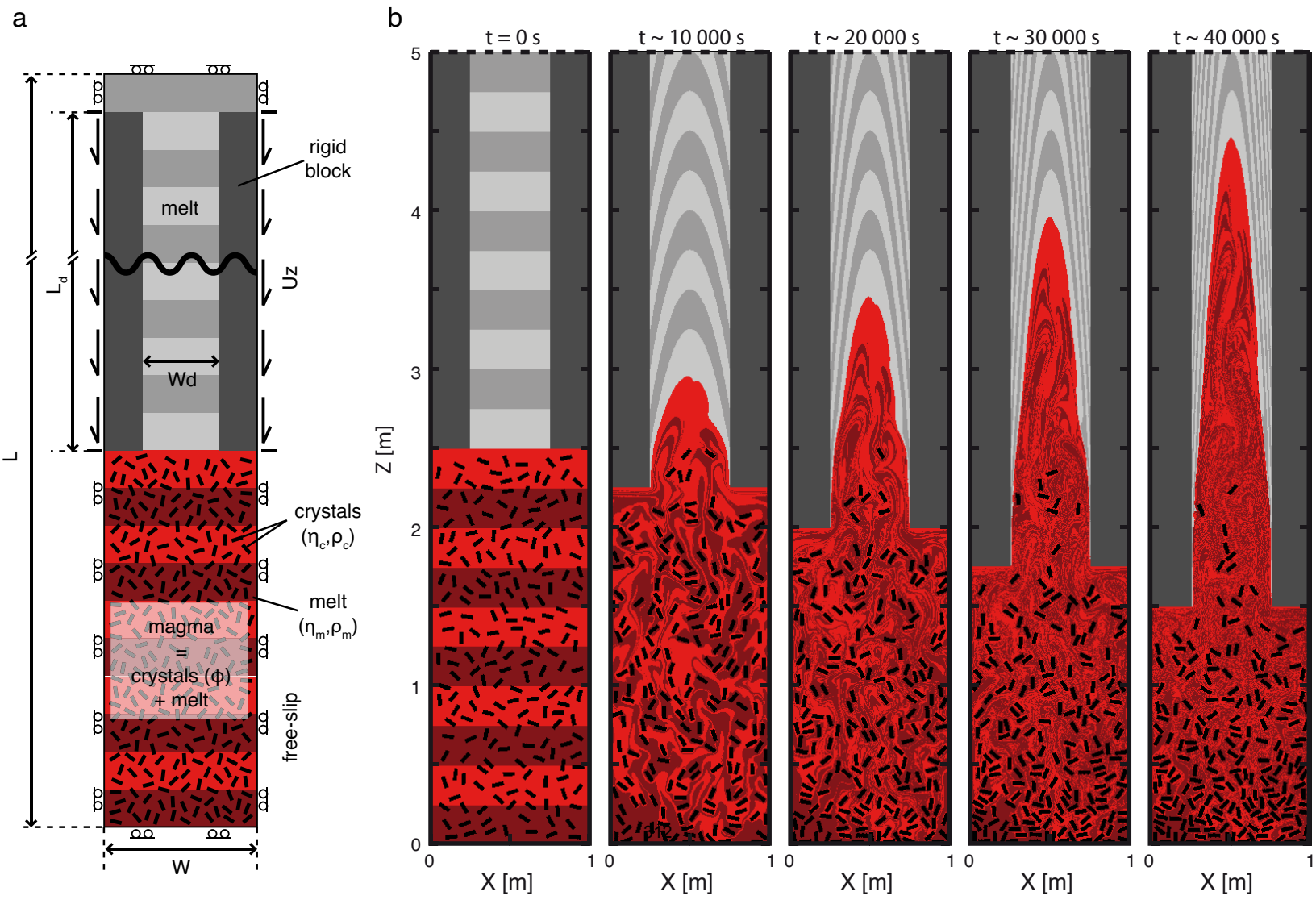

Figure 2

Click here to download Figure: Figure_2.eps

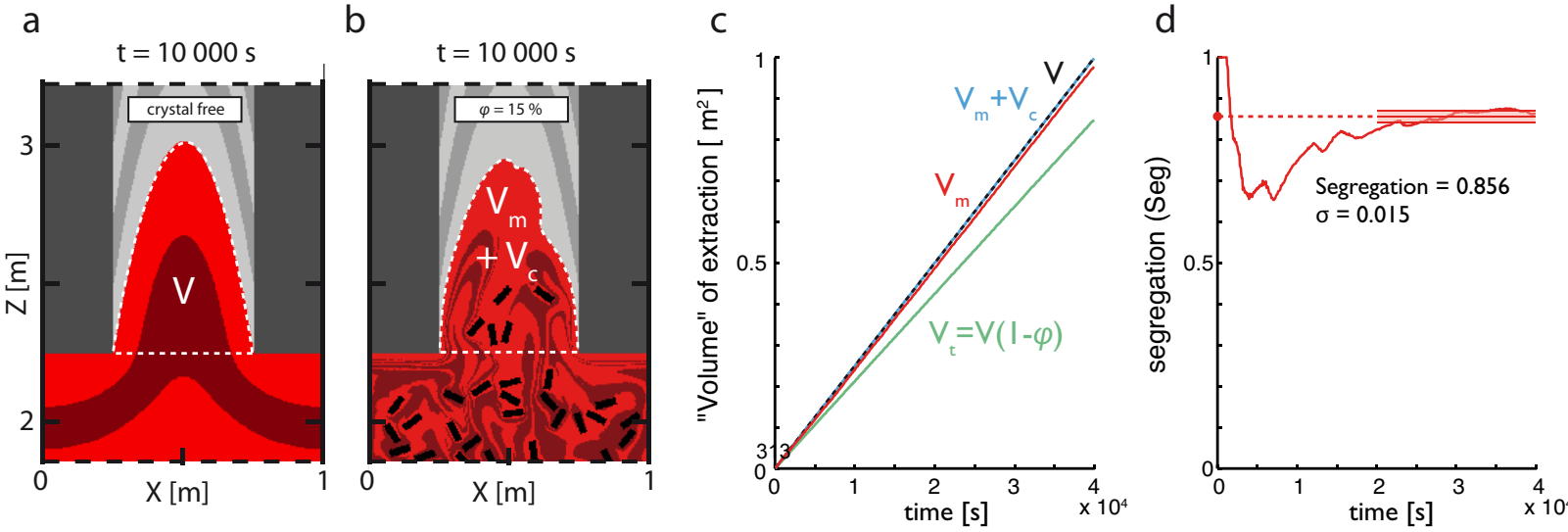

Figure 3

Click here to download Figure: Figure_3.eps

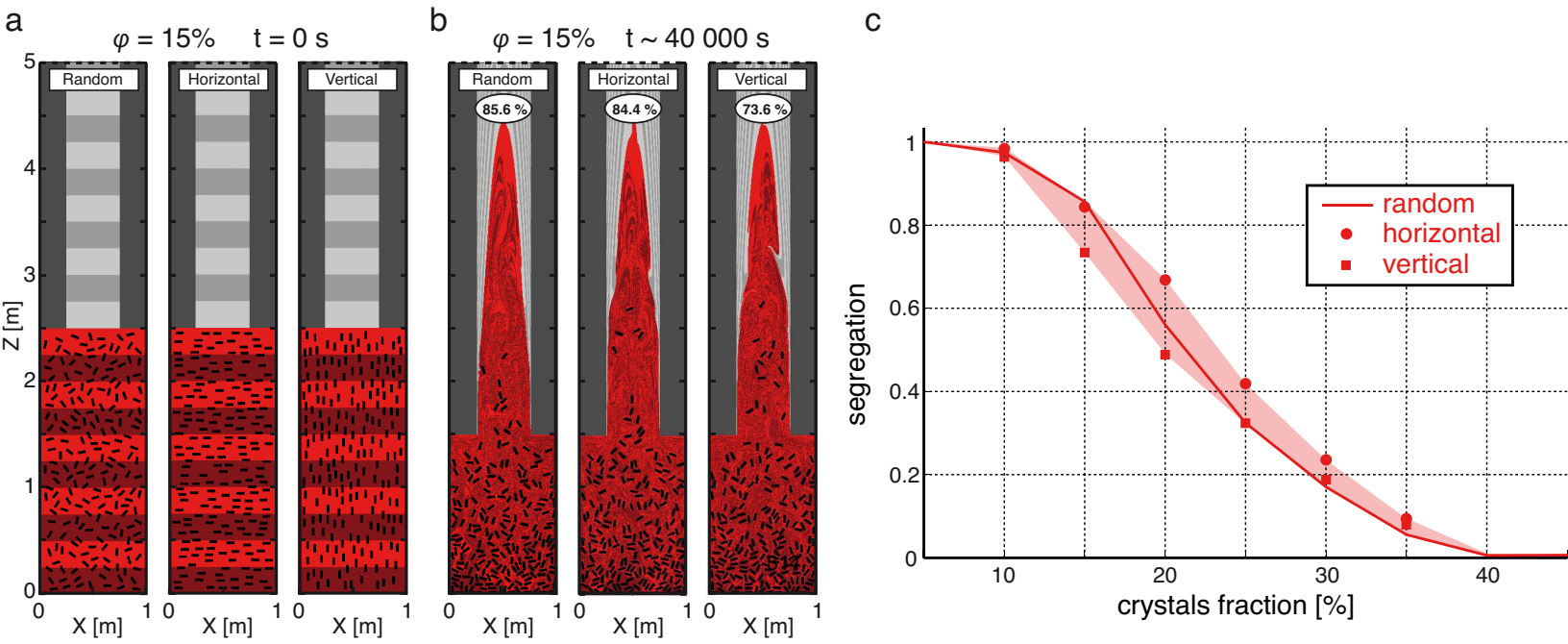

Figure 4

Click here to download Figure: Figure_4.eps

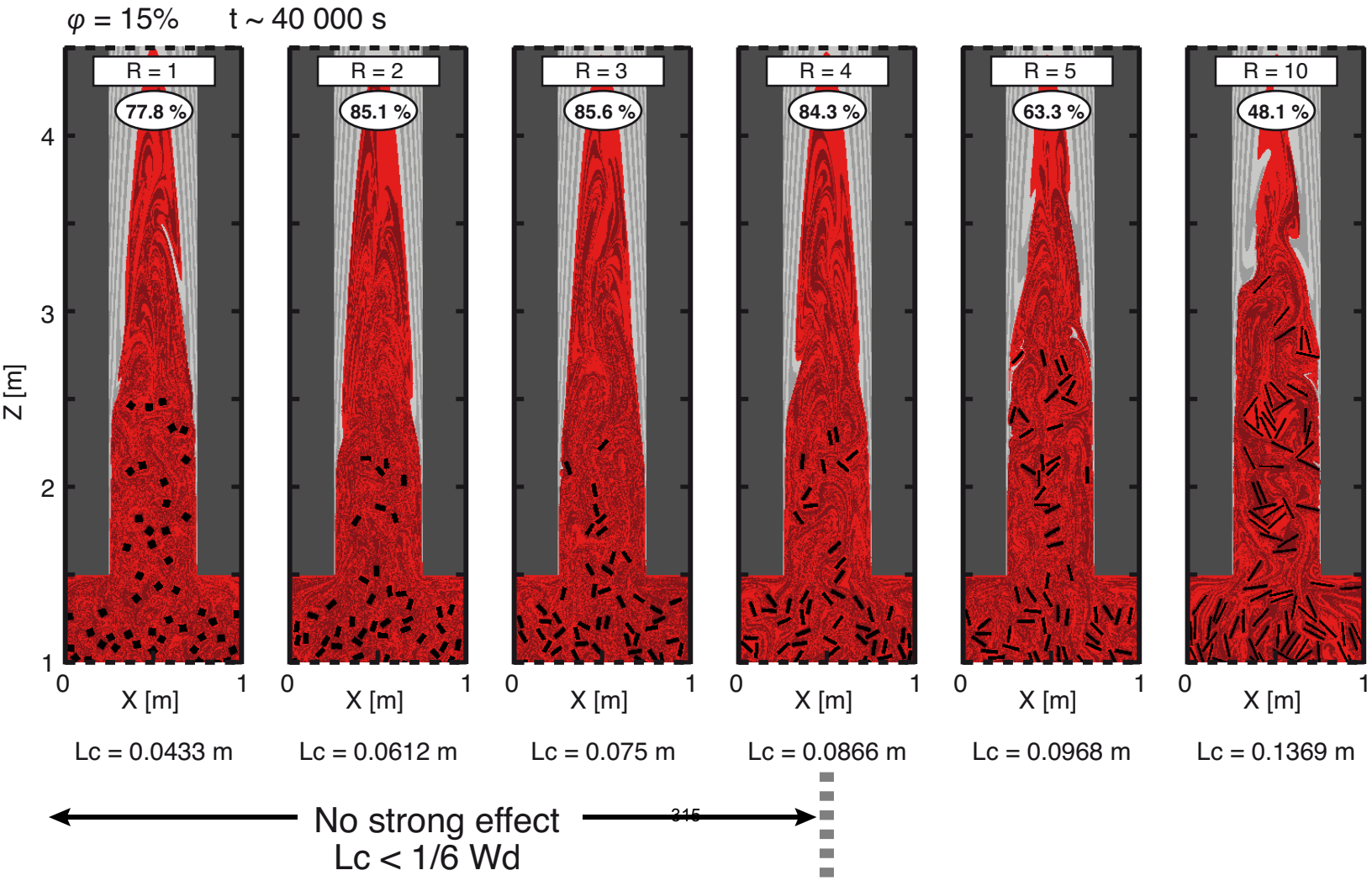

Figure 5
Click here to download Figure: Figure_5.eps

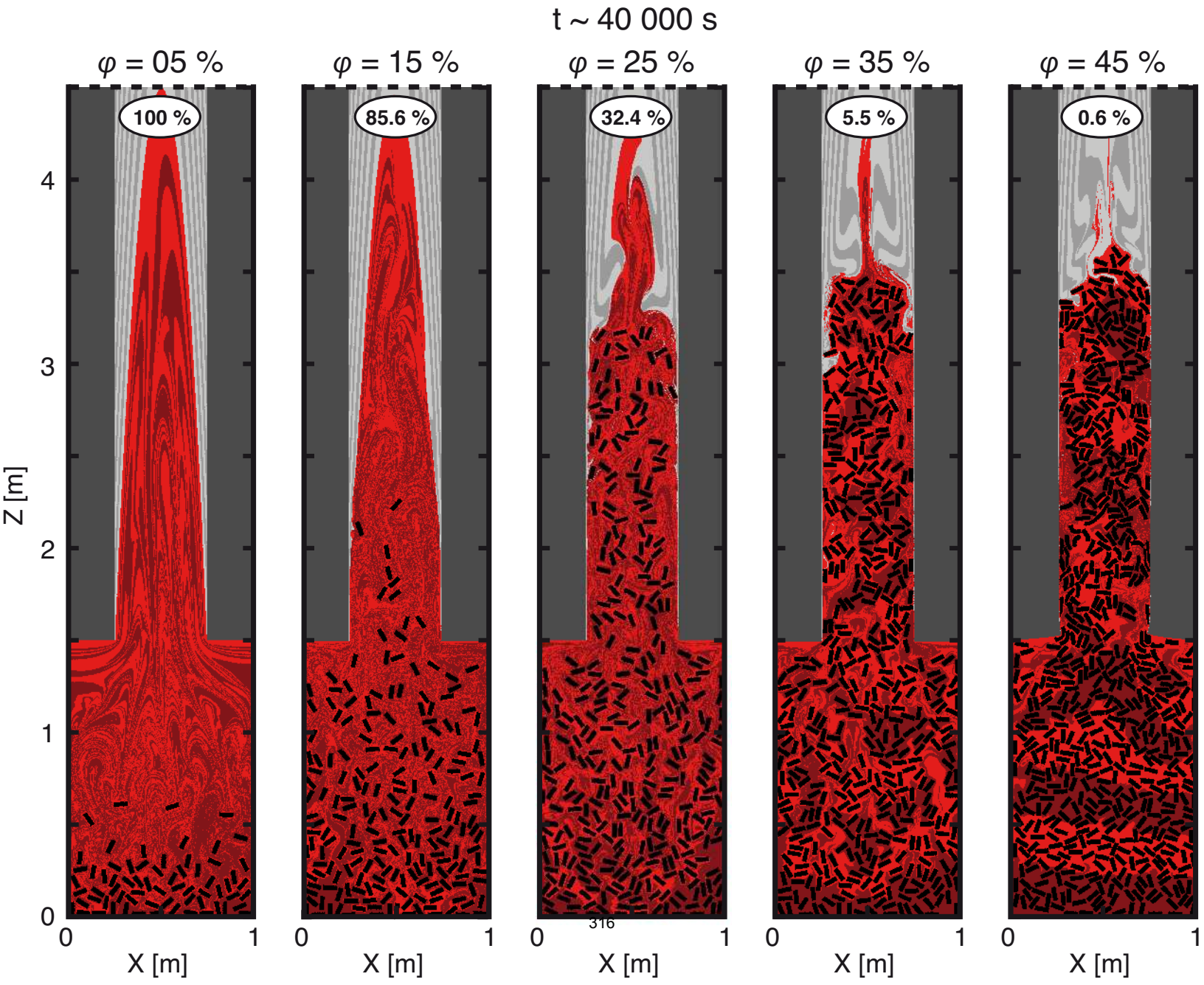

Figure 6
Click here to download Figure: Figure_6.eps

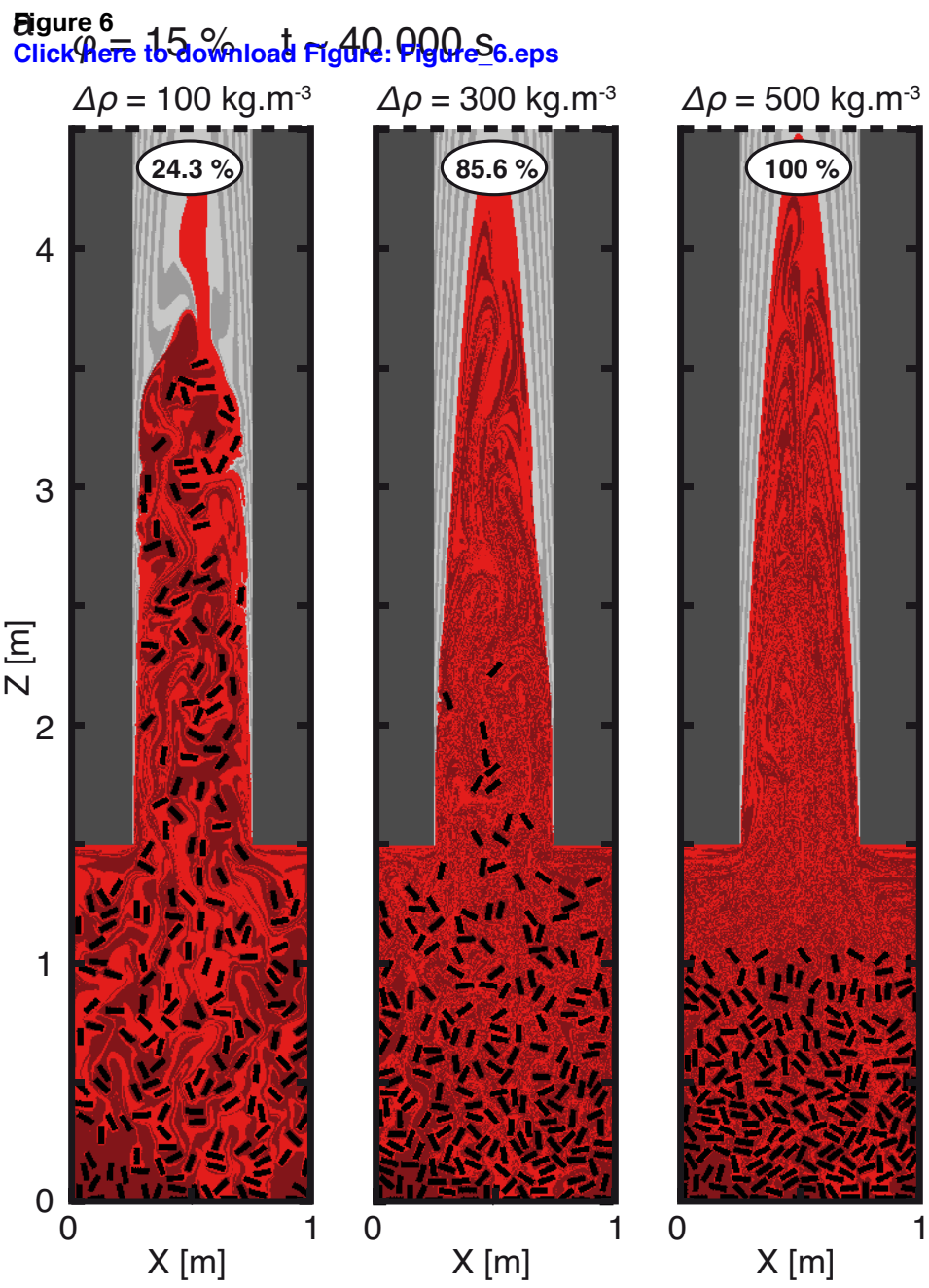

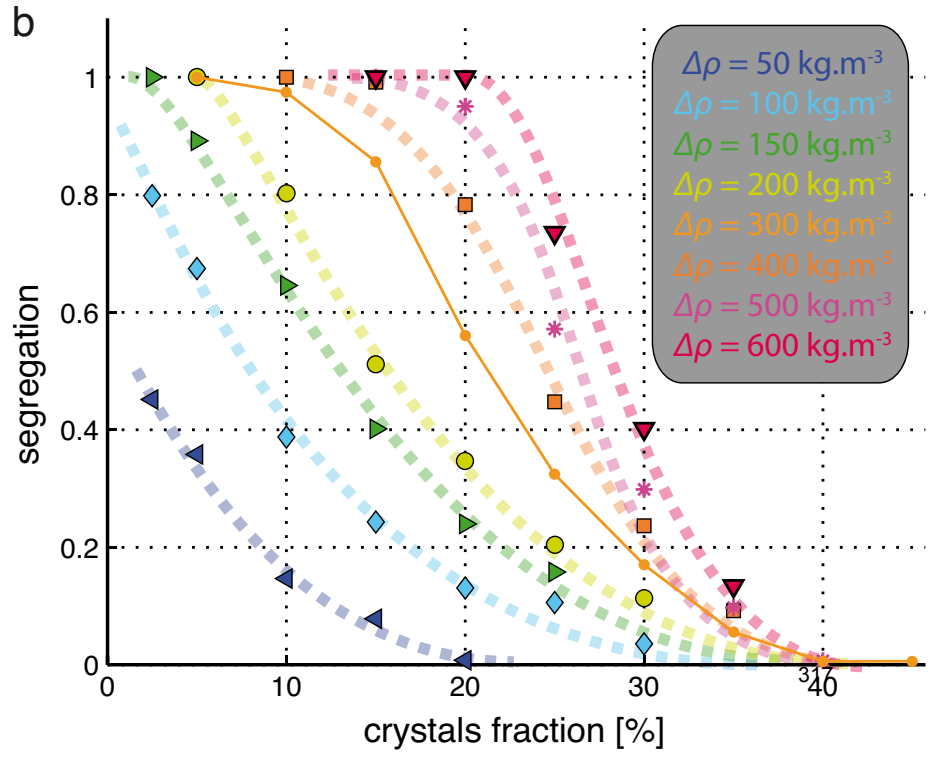

Figure 7
Click here to download Figure: Figure_7.eps

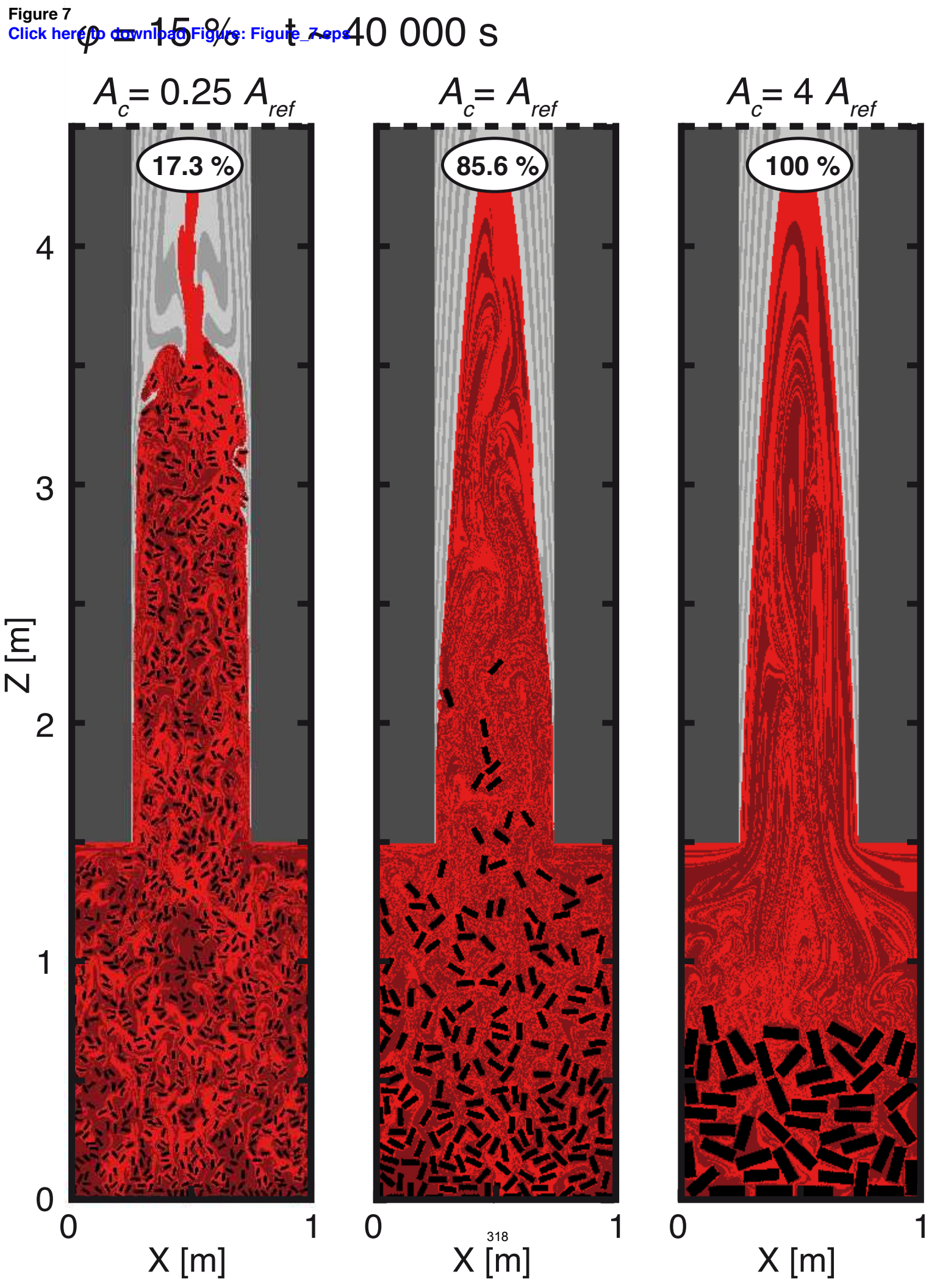

Figure 8
Click here to download Figure: Figure_8.eps

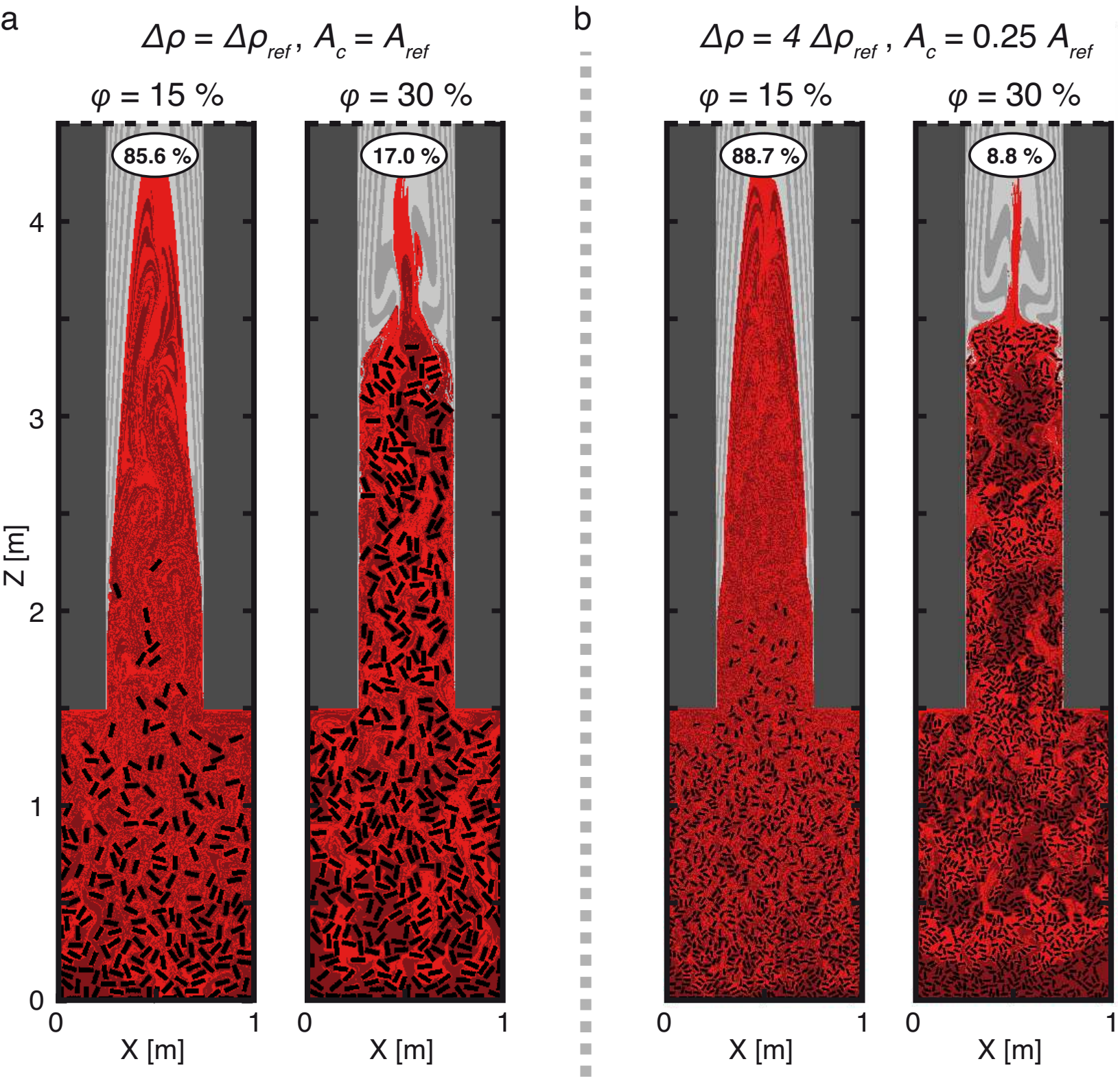

S_{number} = 0.9375

S_{number} = 0.9375

Figure 9

Click here to download Figure: Figure_9.eps

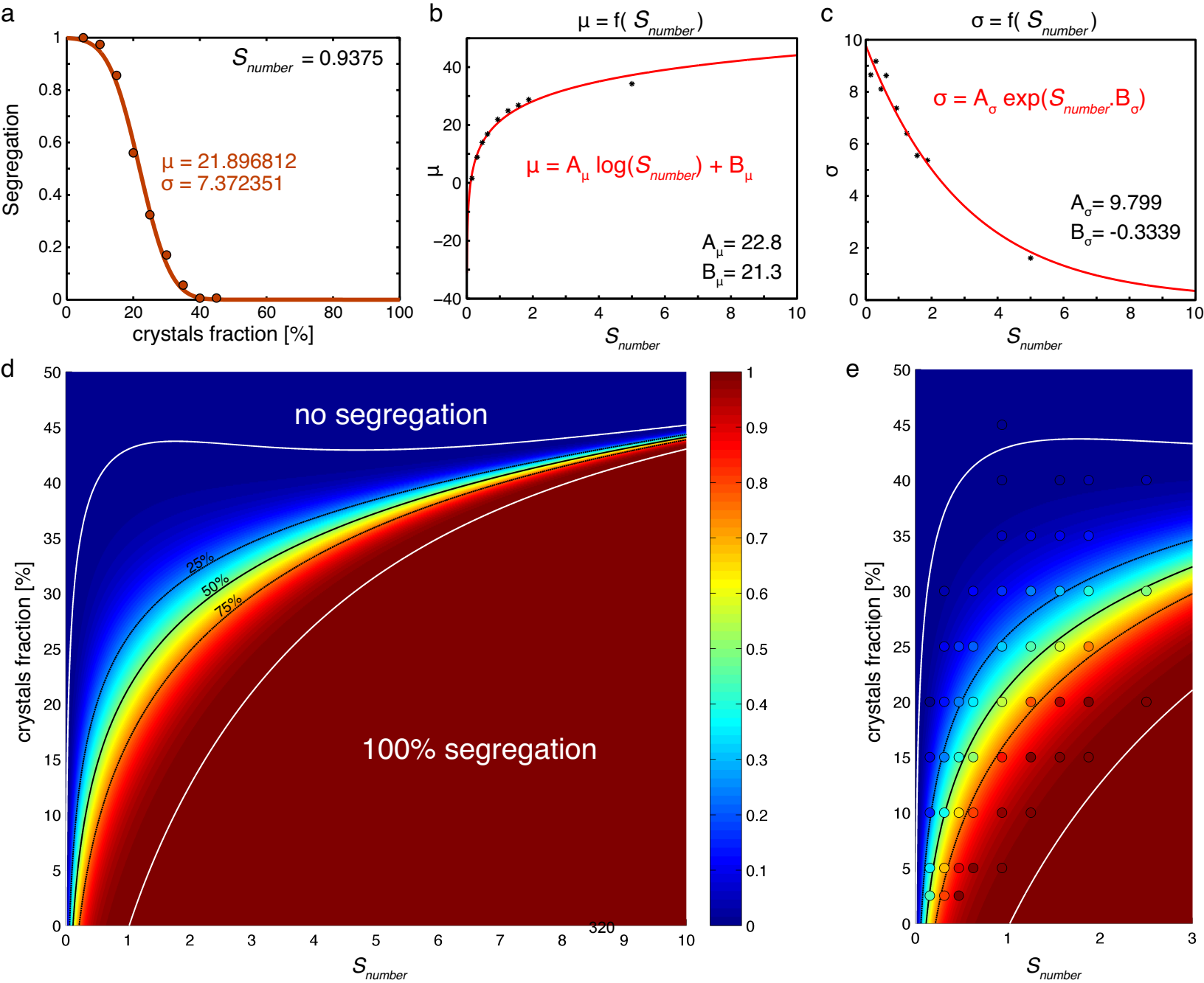

Figure Appendix A1
Click here to download Figure: Figure_A1.eps

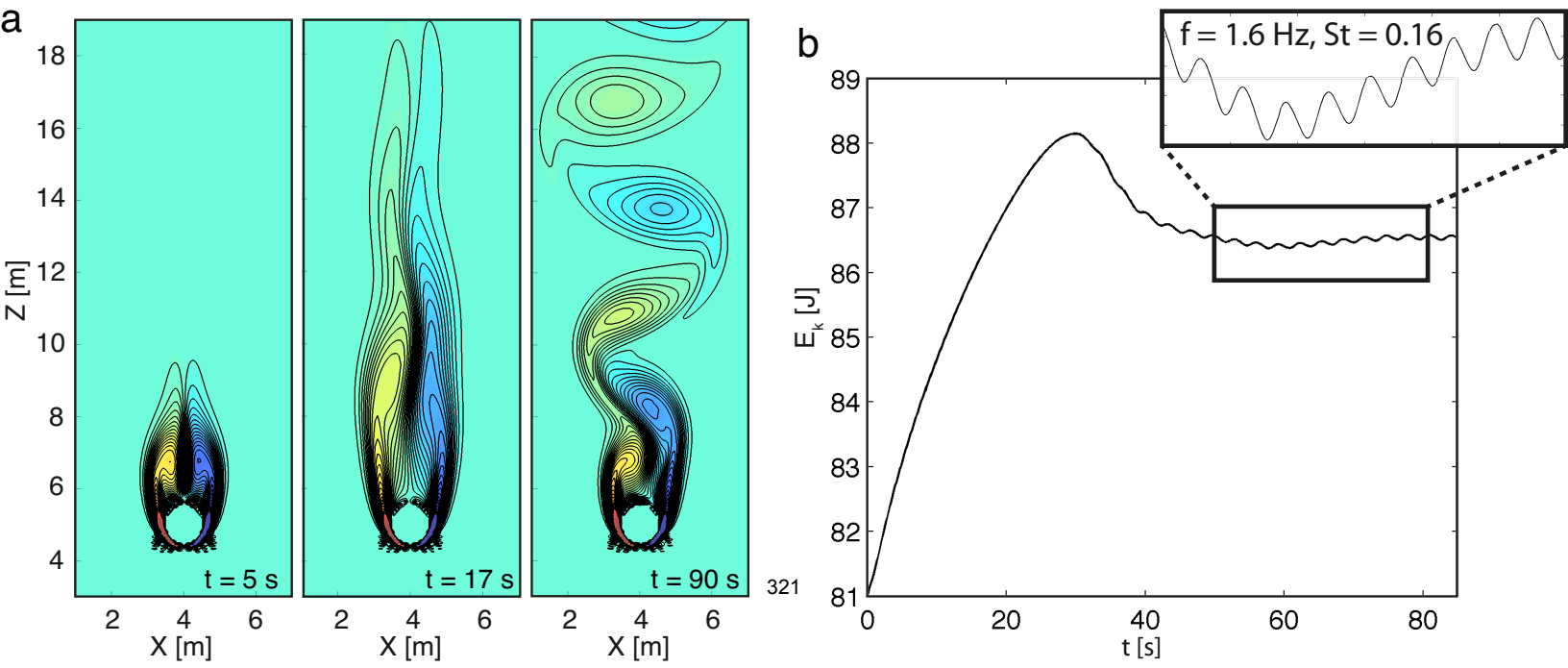

Figure Appendix A2

Click here to download Figure: Figure_A2.eps

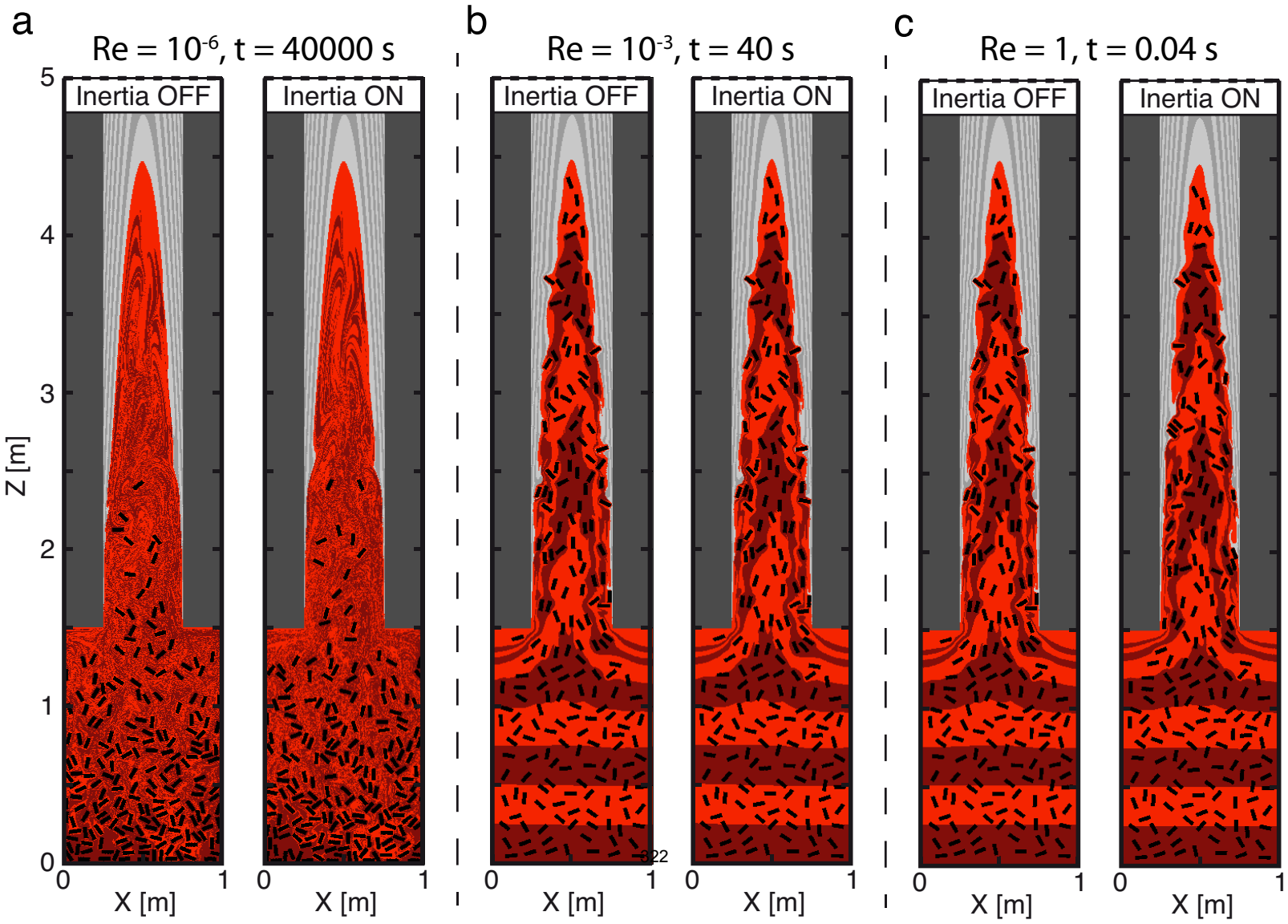

A dimensional analysis to quantify the thermal budget around lithospheric-scale shear zones

Sylvia Duprat-Oualid[1,2,*], Philippe Yamato[1,2,3], and Stefan M. Schmalholz[4]

[1]Université de Rennes 1, Géosciences Rennes, 35042 Rennes cedex, France

[2]CNRS, UMR 6118, 35042 Rennes cedex, France

[3]GFD group, Institute of Geophysics, Department of Geosciences, ETH-Zurich, CH-8093 Zurich, Switzerland

[4]Institute of Earth Sciences, University of Lausanne, CH-1015 Lausanne, Switzerland

[*]Corresponding author: sylvia.duprat-oualid@univ-rennes1.fr

tel: (+33)2 23 23 67 83

fax: (+33)2 23 23 60 97

Short title: Thermal budget around lithospheric-scale shear zones

Submission to: Terra Nova

Abstract

The thermal evolution around shear zones is controlled by three major thermal processes: diffusion, advection and shear heating. We present a dimensional analysis to quantify, at first-order, the relative contributions of these three processes to the thermal evolution around lithospheric-scale shear zones. We consider eleven parameters that control the kinematics, the three-dimensional (3-D) geometry, the initial thermal structure and the average strength of the shear zone. Three dimensionless parameters are presented to quantify the relative contributions of the three thermal processes. We validate the dimensional analysis with 2-D thermo-kinematic numerical models. The applicability of the dimensional analysis to any kind of shear zone (thrust, detachment and strike-slip) makes it a useful tool complementary to previous numerical and analytical studies. The particular thrust-type shear zones are finally used to illustrate how the three thermal processes control the thermal evolution.

Keywords

dimensional analysis; thermal processes; shear zone; shear heating.

1. Introduction

The displacements at tectonic plate boundaries occur mainly along kilometer-scale shear zones (e.g., Kreemer *et al.*, 2003). These zones of high strain and velocity (up to several $cm.yr^{-1}$) cross-cutting the lithosphere can undergo significant thermal perturbations related to the balance between three major thermal processes: the diffusion, the advection and the internal production of heat. While heat diffusion tends to smooth the thermal gradients over time, both advection,

45 related to the motion of blocks with different temperature fields, and localized heating due to
46 dissipative mechanical work can modify thermal gradients.

47 The structural development of shear zones over time is usually constrained by
48 geochronological and thermobarometric data. However, the same data often leads to different
49 interpretations and contrasting models in which the relative contribution of the different thermal
50 processes is often not quantified. Particularly, the role of shear heating (i.e., mechanical energy
51 converted into heat) constitutes a controversial issue in the general understanding of lithospheric-
52 scale shear zones; whether they are compressional, extensional or strike-slip (e.g., Lachenbruch
53 and Sass, 1980; Scholz, 1980; Brewer, 1981; Molnar and England, 1990; England and Molnar,
54 1993; Kincaid and Silver, 1996; Leloup *et al.*, 1999; Burg and Gerya, 2005; Burg and
55 Schmalholz, 2008; Nabelek *et al.*, 2010; Duprat-Oualid *et al.*, 2013; Kidder *et al.*, 2013; Souche
56 *et al.*, 2013; Duretz *et al.*, 2014). The controversy of the shear heating issue principally lies in the
57 lack of accurate rheological constraints at depth, that is, magnitudes of stress and strain rate
58 around shear zones. Indeed, the mechanical behaviour of rocks is described with empirical laws
59 and material parameters determined from laboratory rock deformation experiments (e.g., Ranalli
60 and Murphy, 1987; Bürgmann and Dresen, 2008). However, the predicted stress magnitudes for
61 given strain rates and temperatures can vary several orders of magnitude, depending for example
62 on the assumed amount of water in the rock. Since the amount of shear heating depends on the
63 product of stress times strain rate, shear heating can be significant or not depending on the
64 assumed rheological model.

65 In this study, we investigate the thermal budget around lithospheric-scale shear zones
66 (Fig. 1a) with a simple dimensional analysis. We consider eleven parameters defining any shear
67 zone scenario in terms of kinematics (i.e., relative velocity between the two blocks in contact, V,

dip angle, θ, pitch ψ and shear zone thickness, h), rheological strength (i.e., effective shear zone viscosity, η) and thermal characteristics (i.e., vertical mantle heat flux, Q, radiogenic heating depending on two parameters, the surface radiogenic heat production Hr_0 and a specific depth z_r, and the parameters controlling thermal diffusion, namely thermal conductivity, k, heat capacity, Cp and density, ρ). We cluster these eleven dimensional parameters into three dimensionless numbers to quantify the relative control of heat diffusion, advection and shear heating on the thermal evolution around shear zones. Predictions of the dimensional analysis are then validated with 2-D thermo-kinematic numerical modeling, and we especially investigate the analytical predictions for typical values and scenarios applicable to intra-continental thrusts. This study is in line with previous analytical studies (e.g., Brun and Cobbold, 1980; Brewer, 1981; Molnar and England, 1990; England and Molnar, 1993) which computed the thermal evolution around thrusts.

The main aim of our study is to provide a simple tool to easily quantify at first-order the relative contribution of heat diffusion, advection and shear heating to the thermal budget for any kind of lithospheric-scale shear zone.

2. Mathematical model

2.1. General heat equation and initial geotherm

The evolution of temperature (T) with time (t) is governed by the heat equation:

$$\frac{\partial T}{\partial t} = \kappa \nabla^2 T - \vec{V} \cdot \nabla T + \frac{Hr + Hs}{\rho\, Cp}, \qquad (1)$$

where κ is the thermal diffusivity, $\kappa = k/(\rho\, Cp)$. All thermal properties are considered constant and homogeneous. $\vec{V} \cdot \nabla T$ represents the advection of the temperature where $\vec{V}$ is the velocity

vector. *Hr* and *Hs* represent two different internal heat sources: the radiogenic heat production and the shear heating, respectively. Other possible internal energy conversions such as heat consumed or produced by metamorphic reactions are neglected.

The two heat sources, *Hr* and *Hs*, have a different impact on the thermal budget around shear zones. On the one hand, *Hr* partly constrains the initial thermal conditions and is continually produced in the radioactive domains. The initial distribution of *Hr* with depth *z* can be defined by the following equation (Turcotte and Schubert, 2002, p.141):

$$Hr(z) = Hr_0 \cdot \exp\left(\frac{-z}{z_r}\right), \quad (2)$$

where Hr_0 is the surface radiogenic heat production and z_r a characteristic depth controlling the decrease of *Hr* with depth. The initial steady state geotherm before the shear zone activity is (see SI#1 for more details):

$$T_0(z) = \frac{Q}{k} z + \frac{Hr_0 \, z_r^{\,2}}{k}\left(1 - \exp\left(\frac{-z}{z_r}\right)\right), \quad (3)$$

On the other hand, *Hs* is localized within the actively sheared domain. For a shear zone with thickness *h*, exhibiting a shear velocity *V* homogeneously distributed and an effective mean viscosity η (see Fig. SI.2), *Hs* can be expressed as:

$$Hs = \eta \frac{V^2}{h^2}. \quad (4)$$

Because shear heating generally dominates the heat production during shearing, radiogenic heat production is only considered for calculating the initial geotherm (see SI#1,2).

2.2. Advection in three dimensional shear zones

While pure thrust and detachment shear zones can be regarded as 2-D problems, a third dimension is required for cases with a strike-slip component (Fig. 1). The three components of the velocity vector then are:

$$\begin{cases} Vx = V \cdot \sin(\psi) \cdot \cos(\theta) \\ Vy = V \cdot \cos(\psi) \\ Vz = V \cdot \sin(\psi) \cdot \sin(\theta) \end{cases} . \quad (5)$$

ψ ranges between 0° and +90° and the sign of θ (between -90° and +90°) corresponds to the direction of the lower block. Hence, positive values of θ indicate thrusting whereas negative angles correspond to detachments.

For lithospheric-scale shear zones V is likely high and the thermal gradient is mostly a function of depth, such that horizontal thermal gradient can be neglected. For strike-slip zones, this assumption is always valid (Vz = 0, Eq. (5)). Consequently, the advective term of the heat equation can be expressed as:

$$-\vec{V} \cdot \nabla T = -Vz \frac{\partial T}{\partial z} = -V \cdot \sin(\psi) \cdot \sin(\theta) \frac{\partial T}{\partial z} . \quad (6)$$

Such a simplification is particularly relevant for thrusts or detachments with a high vertical component Vz that is higher than 0.5 mm.yr^{-1} (Ruppel and Hodges, 1994).

2.3. Dimensional analysis

To make the heat equation dimensionless, the variables z, T and t are associated to the following characteristic dimensions:

$$\begin{cases} z = h \cdot z^* \\ T = \dfrac{h}{z_f} \cdot T_0 \cdot T^* \\ t = t_0 \cdot t^* \end{cases} , \quad (7)$$

in which the stars mark the dimensionless variables. h is taken as the reference spatial scale. The temperature is normalized with the initial temperature T_0 at depth z_f (Eq. (3)) scaled with the shear zone thickness by the ratio h/z_f. This thus includes the influence of Q and Hr whose variability can highly affect the initial thermal profile (e.g., Artemieva and Mooney, 2001; Vilà *et al.*, 2010; Mareschal and Jaupart, 2013). The choice of t_0 for time-scale has no impact on the final result, and is described in SI#3. Using the expressions in Eq. (7), the heat equation (Eq. (1)) can be written as:

$$\frac{\partial T^*}{\partial t^*} = Dif \frac{\partial^2 T^*}{\partial z^{2*}} + Adv \frac{\partial T^*}{\partial z^*} + Pr, \quad (8)$$

where the three factors *Dif*, *Adv* and *Pr* (all dimensionless) represent terms controlling the impact of heat diffusion, advection and production, respectively:

$$\begin{cases} Dif = \dfrac{t_0 \kappa}{h^2} \\ Adv = -\dfrac{t_0 V \cdot \sin(\psi) \cdot \sin(\theta)}{h} \\ Pr = \dfrac{z_f \, t_0 \, \eta V^2}{T_0 \, \rho \, Cp \, h^3} \end{cases}. \quad (9)$$

Whereas *Dif* and *Pr* are systematically positive factors, *Adv* depends on the sign of θ revealing the vertical kinematic regime of the shear zone as described above. The total thermal budget for a specific shear zone at a given depth z_f can then be described by eleven parameters that define the initial thermal structure and the rock properties (Q, Hr_0, z_r, k, ρ, Cp), the kinematics (V, θ, ψ, h) and the mechanical strength of the shear zone (η).

To compare the relative importance of heat advection, diffusion and production, two positive dimensionless numbers are defined:

147
$$\begin{cases} Pe = \dfrac{|Adv|}{Dif} = \dfrac{h\,V \cdot \sin(\psi) \cdot \sin(|\theta|)}{\kappa} \\ Br = \dfrac{Pr}{Dif} = \dfrac{z_f\,\eta\,V^2}{h\,T_0\,k} \end{cases} . \quad (10)$$

148 These ratios use the absolute values of *Dif*, *Adv* and *Pr* as they are now considered as
149 representative of the intensity of each thermal process. Moreover, they are time-independent so
150 that the choice of the time scale used in the dimensionless development does not have any
151 consequence for the relative thermal contributions (see SI#3). The Peclet number *Pe* quantifies
152 the relative importance of heat advection and diffusion and the Brinkman number *Br* corresponds
153 to the ratio of viscous dissipation over heat diffusion (Fig. 2a). For a significant strike-slip
154 component ($\psi \approx 0°$), the *Pe* number tends to 0, and the *Br* number only has a physical meaning.
155 In order to quantify the relative contribution of diffusion, advection and shear heating on the
156 thermal budget in a simple way, three dimensionless numbers can thus be used:

157
$$\begin{cases} R_{Adv} = \dfrac{|Adv|}{|Adv| + Dif + Pr} = \dfrac{Pe}{Pe + 1 + Br} \\ R_{Dif} = \dfrac{Dif}{|Adv| + Dif + Pr} = \dfrac{1}{Pe + 1 + Br} \\ R_{Pr} = \dfrac{Pr}{|Adv| + Dif + Pr} = \dfrac{Br}{Pe + 1 + Br} \end{cases} . \quad (11)$$

158 Each dimensionless number quantifies the relative contribution of the corresponding thermal
159 process to the total thermal budget (Fig. 2b) and thus allow to quantify, in a comprehensive way,
160 the controlling thermal process for any given shear zone (Fig. 2c).

161

162 **3. Numerical modeling and dimensional analysis validation**

163 In order to validate our dimensional analysis, we used a 2-D thermo-kinematic numerical
164 model (Fig. 3a) where both kinematic and thermal computations are based on the finite

165 difference method on a regular Eulerian staggered grid (see Duprat-Oualid *et al.*, 2013, for a
166 detailed description of the code). The numerical model simulates a thrust-type shear zone (Fig.
167 3a).

168 When heat diffusion dominates, the thermal perturbation related to the thrust activity is
169 smoothed (Fig. 3b). When driven by the burial of cold material, the temperature field
170 progressively decreases so that low temperatures values are reached at the steady state. The low
171 η - high V domain, controlled by heat advection, also undergoes intense cooling (Fig. 3c). This
172 cooling rate is especially high if V is high. This thermal underthrusting can lead to a significant
173 transient thermal inversion whose spatial distribution straddles the shear zone. In contrast, a
174 shear heating controlled thermal evolution differs significantly from the other two thermal
175 evolutions (Fig. 3d). Because the internal heating efficiently balances both advection and
176 diffusion the temperatures within a several kilometers thick thrust progressively increase and
177 stabilize without any temperature decrease. The generated heat warms both sides of the shear
178 zone so that thermal inversion is restrained to the lower block. The respective thermal gradient
179 along the profile reaches and keeps intense inverse values in contrast to the advective thermal
180 behavior (Fig. 3c, d). The 2-D numerical results thus fully agree with the predictions of the
181 dimensional analysis.

182

183 **4. Thermal budget predictions**

184 For strike-slip zones, the advection term Adv is zero (Eq. (9), $\psi = 0°$). Consequently, the
185 thermal budget only depends on the balance between shear heating and diffusion. We thus
186 present here analytical results for the more complex cases assuming no strike component ($\psi =$
187 $90°$). Thrust-type shear zones are taken as example ($\theta > 0°$).

188 Variations of kinematic and rheological parameters are generally considered as more
189 important than the initial thermal conditions (e.g., England and Molnar, 1993; Duprat-Oualid *et*
190 *al.*, 2013). Therefore, we focus here only on variations of V, θ, h and η although other
191 parameters may also be presented.

192 For a wide range of realistic values of V and η, the three thermal processes of heat
193 diffusion, advection and shear heating can all be important for the thermal evolution (Fig. 2c).
194 When low viscosity material is involved in rapidly deforming zones ($\eta < 10^{20}$ Pa.s, $V > 3$ cm.yr^{-1}
195), as in oceanic subduction zones, heat advection controls the thermal evolution. Diffusion
196 dominates the thermal evolution for lower velocities ($V < 2$ cm.yr^{-1}), whereas for higher viscosity
197 ($\eta > 10^{20}$ Pa.s) shear heating is dominant. The presented dimensional analysis shows that
198 advection and shear heating processes can be of similar importance (R_{Adv} and $R_{Pr} > 0.25$) for a
199 wide range of realistic parameters (Fig. 2c, 4). Even if shear heating is not the dominating
200 thermal process, shear heating can still contribute significantly to the thermal evolution (e.g., R_{Pr}
201 > 0.25) and should therefore be considered in thermal calculations; also because shear heating
202 can favor shear localization (e.g., Brun and Cobbold, 1980; Duretz *et al.*, 2014). However, in
203 many numerical simulations of lithospheric deformation the relative contribution of thermal
204 processes is defined *a priori* and often shear heating is simply ignored (e.g., Ghazian and Buiter,
205 2013). For intra-continental thrusts, relative velocities are usually < 3 cm.yr^{-1} and viscosities are
206 10^{19}-10^{21} Pa.s (e.g., Hilley *et al.*, 2005; Burg and Gerya, 2005). For these parameter ranges the
207 dimensional analysis shows that all three thermal processes can be equally important (Fig. 4),
208 what demonstrates the difficulty to identify a single dominant process for the thermal evolution
209 around major shear zones. Heat diffusion controls the thermal evolution of low-angle, weak
210 thrust zones, and slightly of thin shear zones. Advection obviously becomes dominant when Vz

increases. Advection is also more dominant for thick thrusts due to the inverse dependence of *Pr* and *Dif* on *h*. In most scenarios the dominance of heat advection requires low viscosities. Shear heating is howeve the main thermal contribution for higher viscosities ($\eta > 10^{20}$ Pa.s), and particularly when shear zones exhibit high strain rates (Fig. 4, high *V* and small *h*).

5. Conclusion

Our dimensional analysis quantifies the relative contribution of the three major thermal processes of heat diffusion, advection and shear heating to the thermal evolution of lithospheric-scale shear zones. It involves eleven first-order parameters controlling the initial thermal conditions, the 3-D kinematic regime and the rheological strength averaged over the whole activity of the shear zone. This simple dimensional analysis constitues a powerful tool in addition to previous analytical solutions because it offers a simple and comprehensible quantification of the thermal budget for any kind of lithospheric-scale shear zone.

We show that for ranges of realistic parameters, each of the three thermal processes can control the thermal evolution around lithospheric-scale shear zones. This can explain why the geodynamic interpretation of thermal data around shear zones is often controversial (e.g., Huerta *et al.*, 1998; Jamieson *et al.*, 2004; Burg and Gerya, 2005; Bollinger *et al.*, 2006; Kidder *et al.*, 2013). In particular, the importance of shear heating is often debated (e.g., Duprat-Oualid *et al.*, 2013; Kidder *et al.*, 2013), but with such a dimensional analysis, its relative contribution can be quantified and compared in respect with heat diffusion and advection for different tectonic contexts (thrust, detachment and strike-slip).

Acknowledgments

We thank B. Huet and B. Grasemann for very helpful discussions. We also thank P. Tackley and D. May for the material support (2-D models of the parametric study were run on ETH Brutus cluster).

References

Artemieva, I.M. and Mooney, W.D., 2001. Thermal thickness and evolution of Precambrian lithosphere: A global study. *Journal of Geophysical Research: Solid Earth*, **106(B8)**, 16387–16414.

Bollinger, L., Henry, P. and Avouac, J.P., 2006. Mountain building in the Nepal Himalaya: Thermal and kinematical model. *Earth and Planetary Science Letters*, **244(1–2)**, 58–71.

Brewer, J., 1981. Thermal effects of thrust faulting. *Earth and Planetary Science Letters*, **56**, 233–244.

Brun, J.P. and Cobbold, P.R., 1980. Strain heating and thermal softening in continental shear zones: a review. *Journal of Structural Geology*, **2(1–2)**, 149–158.

Burg, J.P. and Gerya, T.V., 2005. The role of viscous heating in Barrovian metamorphism of collisional orogens: thermomechanical models and application to the Lepontine Dome in the Central Alps. *Journal of Metamorphic Geology*, **23(2)**, 75–95.

Burg, J.P. and Schmalholz, S.M., 2008. Viscous heating allows thrusting to overcome crustal-scale buckling: Numerical investigation with application to the Himalayan syntaxes. *Earth and Planetary Science Letters*, **274(1–2)**, 189–203.

Bürgmann, R. and Dresen, G., 2008. Rheology of the Lower Crust and Upper Mantle: Evidence from Rock Mechanics, Geodesy, and Field Observations. *Annual Review of Earth and Planetary Sciences*, **36(1)**, 531–567.

257 Duprat-Oualid, S., Yamato, P. and Pitra, P., 2013. Major role of shear heating in intra-
258 continental inverted metamorphism: Inference from a thermo-kinematic parametric study.
259 *Tectonophysics*, **608**, 812–831.
260 Duretz, T., Schmalholz, S.M., Podladchikov, Y.Y. and Yuen, D.A., 2014. Physics-controlled
261 thickness of shear zones caused by viscous heating: implications for crustal shear
262 localization. *Geophysical Research Letters*, doi: 10.1002/2014GL060438.
263 England, P. and Molnar, P., 1993. The interpretation of inverted metamorphic isograds using
264 simple physical calculations. *Tectonics*, **12(1)**, 145–157.
265 Ghazian, R.K. and Buiter, S.J.H., 2013. A numerical investigation of continental collision styles.
266 *Geophysical Journal International*, **193(3)**, 1133–1152.
267 Hilley, G.E., Bürgmann, R., Zhang, P.Z. and Molnar, P., 2005. Bayesian inference of
268 plastosphere viscosities near the Kunlun Fault, northerm Tibet. *Geophysical Research*
269 *Letters*, **32(1)**, L01302.
270 Huerta, A.D., Royden, L.H. and Hodges, K.V., 1998. The thermal structure of collisional
271 orogens as a response to accretion, erosion, and radiogenic heating. *Journal of Geophysical*
272 *Research: Solid Earth*, **103(B7)**, 15287–15302.
273 Jamieson, R.A., Beaumont, C., Medvedev, S. and Nguyen, M.H., 2004. Crustal channel flow: 2.
274 Numerical models with implications for metamorphism in the Himalayan-Tibetan orogen.
275 *Journal of Geophysical Research*, **109(B6)**, 1978–2012.
276 Kidder, S.B., Herman, F., Saleeby, J., Avouac, J.P., Ducea, M.N. and Chapman, A., 2013. Shear
277 heating not a cause of inverted metamorphism. *Geology*, **41(8)**, 899–902.
278 Kincaid, C. and Silver, P., 1996. The role of viscous dissipation in the orogenic process. *Earth*
279 *and Planetary Science Letters*, **142(3–4)**, 271–288.

Kreemer, C., Holt, W.E. and Haines, A.J., 2003. An integrated global model of present-day plate motions and plate boundary deformation. *Geophysical Journal International*, **154(1)**, 8–34.

Lachenbruch, A.H. and Sass, J.H., 1980. Heat Flow and Energetics of the San Andreas Fault Zone. *Journal of Geophysical Research*, **85(B11)**, 6185–6222.

Leloup, P.H., Ricard, Y., Battaglia, J. and Lacassin, R., 1999. Shear heating in continental strike-slip shear zones: models and field examples. *Geophysical Journal International*, **136(1)**, 19–40.

Mareschal, J.C. and Jaupart, C., 2013. Radiogenic heat poduction, thermal regime and evolution of continental crust. *Tectonophysics*, **609**, 524–534.

Molnar, P. and England, P., 1990. Temperatures, heat flux, and frictional stress near major thrust faults. *Journal of Geophysical Research*, **95(B4)**, 4833–4856.

Nabelek, P.I., Whittington, A.G. and Hofmeister, A.M., 2010. Strain heating as a mechanism for partial melting and ultrahigh temperature metamorphism in convergent orogens: Implications of temperature-dependent thermal diffusivity and rheology. *Journal of Geophysical Research*, **115(B12)**, B12417.

Ranalli, G. and Murphy, D.C., 1987. Rheological stratification of the lithosphere. *Tectonophysics*, **132(4)**, 281–295.

Ruppel, C. and Hodges, K.V., 1994. Role of horizontal thermal conduction and finite time thrust emplacement in simulation of pressure-time paths. *Earth and Planetary Science Letters*, **123(1–3)**, 49–60.

Scholz, C.H., 1980. Shear heating and the state of stress on faults. *Journal of Geophysical Research*, **85(B11)**, 6174–6184.

302 Souche, A., Medvedev S., Andersen, T.B. and Dabrowski, M., 2013. Shear heating in
303 extensional detachments: Implications for the thermal history of the Devonian basins of W
304 Norway. *Tectonophysics*, **608**, 1073–1085.
305 Turcotte, D.L. and Schubert, G., 2002. *Geodynamics*, 2nd edition. Cambridge University Press,
306 New York.
307 Vilà, M., Fernández, M. and Jiménez-Munt, I., 2010. Radiogenic heat production variability of
308 some common lithological groups and its significance to lithospheric thermal modeling.
309 *Tectonophysics*, **490(3–4)**, 152–164.
310

311 **Figure captions**

312 **Figure 1.** a) Sketch of three types of lithospheric-scale shear zones. b) Schematic 3-D geometry
313 of a shear zone defined according two specific angles: (i) the shear zone dip angle θ and (ii) the
314 pitch ψ of the shear direction in the shear zone plane. A Cartesian coordinate system (x, y, z) is
315 defined such that θ is set in the (x, z) plane. An additional z' axis is defined perpendicularly to
316 the shear zone plane, directed towards increasing z.

317 **Figure 2.** a) Phase diagram representing the three fields where the thermal budget around and
318 within a shear zone is dominated by either heat diffusion, heat advection or shear heating as a
319 function of the Peclet (*Pe*) and Brinkman (*Br*) numbers. b) Triangular diagram showing the three
320 poles of thermal contribution (heat diffusion (R_{Dif}), advection (R_{Adv}) and shear heating (R_{Pr})).
321 Diagrams a) and b), using the same colormap, constitute alternative dimensionless ways to
322 represent these different contributions. Bold white lines limit the three domains of thermal
323 dominance. Thin lines represent the proportions (every 10 %) of the different contributions
324 within their respective domain of dominance. Particularly, the white thin lines indicate the 50%

proportion of dominance of each thermal contribution. c) Dimensionless thermal contributions as a function of V and η, for a pure thrust zone ($\psi = 0°$) characterized by h = 2.5 km and $\theta = 30°$. Thermal parameters are kept constant: Q = 40 mW.m^{-2}, k = 3 W.m^{-1}.K^{-1}, ρ = 2800 kg.m^{-3}, Cp = 1000 J.kg^{-1}.K^{-1}, Hr_0 = 2 µW.m-3 and z_r = 15 km. The yellow, blue and red thin lines represent the 25% contributions of diffusion, advection and shear heating, respectively. Colored stars correspond to the [V, η] combinations in each domain for which the dominating thermal contribution represents 2/3 of the thermal budget and the secondary contributions are equal to 1/6 (see Fig. 3).

Figure 3. a) Lithospheric-scale numerical model configuration showing the velocity field V and highlighting the effective thrust viscosity η. All thermal, kinematic and rheological parameters are constant. Models simulate a pure thrust-type shear zone ($\psi = 0°$). The convergence is entirely controlled by the downgoing plate and the upper plate remains motionless. The small dash corresponds to the 10 km-long profile (perpendicular to the underthrusting direction and centered at 30 km depth across the thrust zone) for which the thermal evolutions are presented in b), c) and d). b), c), d): Thermal evolutions until the steady state (here after ~10 Myrs) along the profile. Results are from numerical models corresponding to the thermal budget dominated by heat production, diffusion and advection, respectively. The applied values of V and η correspond to colored stars from Fig. 2c. *z'* corresponds to the structural distance under the thrust (Fig. 1b). Colors represent the temperature field T and, particularly, black lines highlight the isotherms spaced with 50°C. Obtained results are in perfect agreement with the predictions made by our dimensional analysis.

Figure 4. Parametric study showing the dimensionless contributions of heat diffusion, advection and shear heating, R_{Dif}, R_{Adv} and R_{Pr}, respectively, on the thermal budget around an intra-

continental thrust zone. Results are presented as a function of V and η for different values of h and θ. Other parameters are set to the values established in Fig. 2c. As in Fig. 2c, the yellow, blue and red thin lines drawn in the central diagram represent the 25% contributions of diffusion, advection and shear heating, respectively. For reasons of clearness, such lines are not traced in other diagrams.

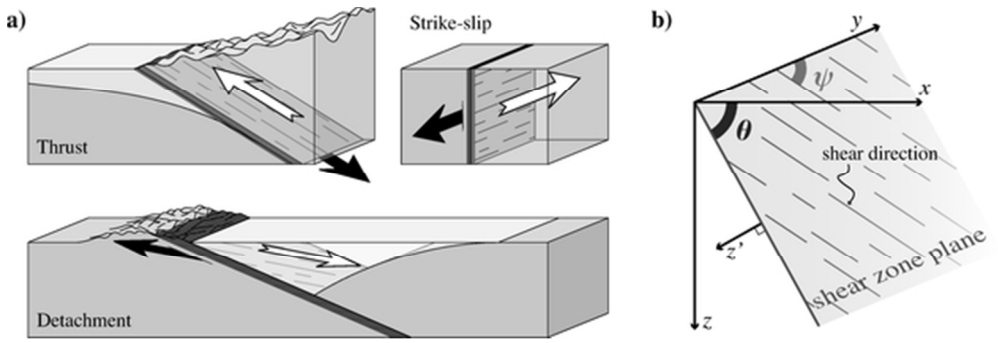

a) Sketch of three types of lithospheric-scale shear zones. b) Schematic 3-D geometry of a shear zone defined according two specific angles: (i) the shear zone dip angle θ and (ii) the pitch ψ of the shear direction in the shear zone plane. A Cartesian coordinate system (x, y, z) is defined such that θ is set in the (x, z) plane. An additional z' axis is defined perpendicularly to the shear zone plane, directed towards increasing z.
53x17mm (300 x 300 DPI)

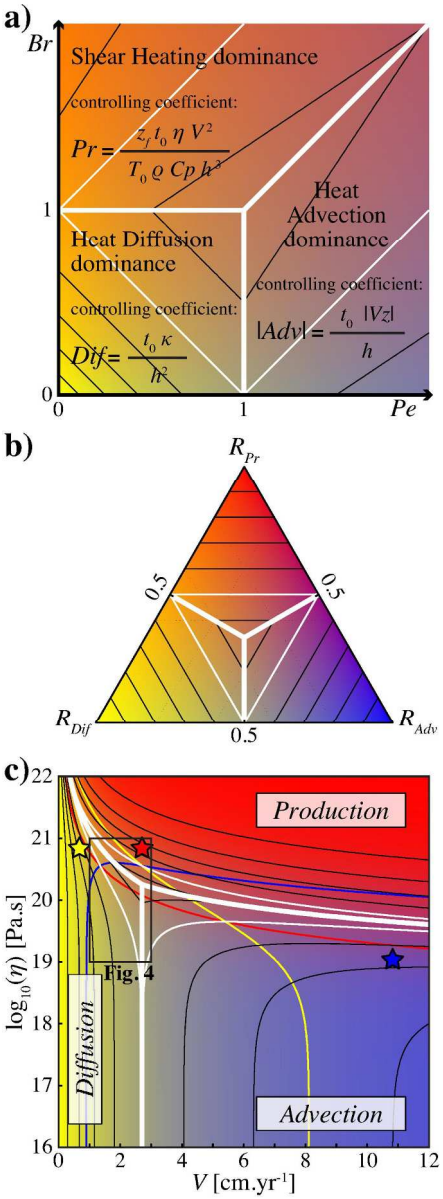

a) Phase diagram representing the three fields where the thermal budget around and within a shear zone is dominated by either heat diffusion, heat advection or shear heating as a function of the Peclet (Pe) and Brinkman (Br) numbers. b) Triangular diagram showing the three poles of thermal contribution (heat diffusion (RDif), advection (RAdv) and shear heating (RPr)). Diagrams a) and b), using the same colormap, constitute alternative dimensionless ways to represent these different contributions. Bold white lines limit the three domains of thermal dominance. Thin lines represent the proportions (every 10%) of the different contributions within their respective domain of dominance. Particularly, the white thin lines indicate the 50% proportion of dominance of each thermal contribution. c) Dimensionless thermal contributions as a function of V and η, for a pure thrust zone (ψ = 0°) characterized by h = 2.5 km and θ = 30°. Thermal parameters are kept constant: Q = 40 mW.m-2, k = 3 W.m-1.K-1, ρ = 2800 kg.m-3, Cp = 1000 J.kg-1.K-1, Hr0 = 2 μW.m-3 and zr = 15 km. The yellow, blue and red thin lines represent the 25% contributions of diffusion, advection and shear heating, respectively. Colored stars correspond to the [V, η] combinations in each domain for which the dominating thermal contribution represents 2/3 of the thermal budget and the

secondary contributions are equal to 1/6 (see Fig. 3).
139x383mm (300 x 300 DPI)

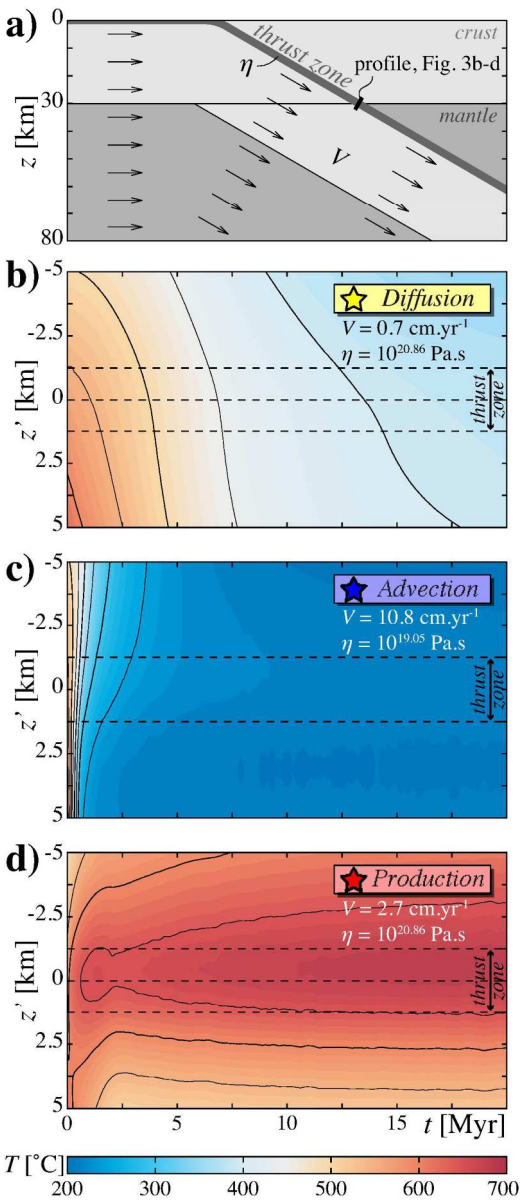

a) Lithospheric-scale numerical model configuration showing the velocity field V and highlighting the effective thrust viscosity η. All thermal, kinematic and rheological parameters are constant. Models simulate a pure thrust-type shear zone (ψ = 0°). The convergence is entirely controlled by the downgoing plate and the upper plate remains motionless. The small dash corresponds to the 10 km-long profile (perpendicular to the underthrusting direction and centered at 30 km depth across the thrust zone) for which the thermal evolutions are presented in b), c) and d). b), c), d): Thermal evolutions until the steady state (here after ~10 Myrs) along the profile. Results are from numerical models corresponding to the thermal budget dominated by heat production, diffusion and advection, respectively. The applied values of V and η correspond to colored stars from Fig. 2c. z' corresponds to the structural distance under the thrust (Fig. 1b). Colors represent the temperature field T and, particularly, black lines highlight the isotherms spaced with 50°C. Obtained results are in perfect agreement with the predictions made by our dimensional analysis.
118x276mm (300 x 300 DPI)

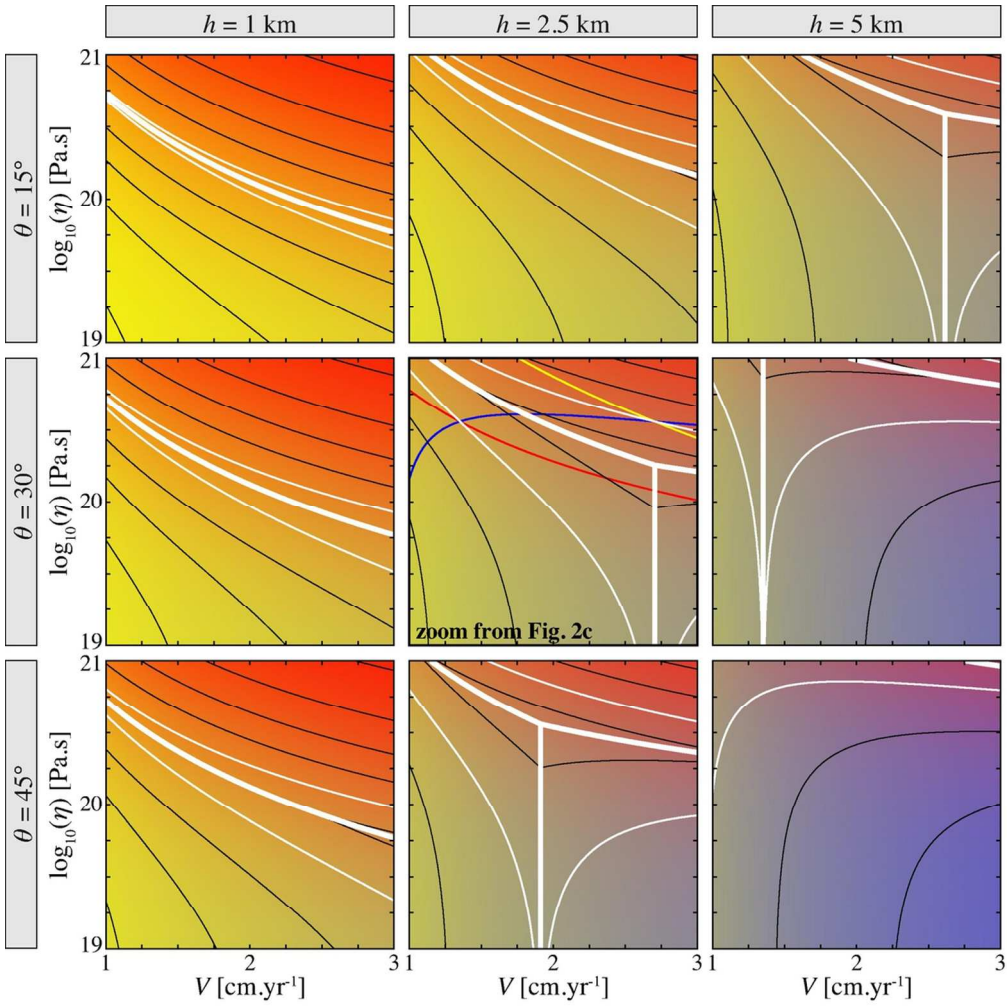

Parametric study showing the dimensionless contributions of heat diffusion, advection and shear heating, RDif, RAdv and RPr, respectively, on the thermal budget around an intra-continental thrust zone. Results are presented as a function of V and η for different values of h and θ. Other parameters are set to the values established in Fig. 2c. As in Fig. 2c, the yellow, blue and red thin lines drawn in the central diagram represent the 25% contributions of diffusion, advection and shear heating, respectively. For reasons of clearness, such lines are not traced in other diagrams.
107x107mm (300 x 300 DPI)

Supporting informations

Duprat-Oualid et al., "A dimensional analysis to quantify the thermal budget around lithospheric-scale shear zones"

Supporting information #1: Influence of radiogenic heat production on the initial thermal structure

Following Eq. (2) and Eq. (3) from Turcotte and Schubert (2002, p.141), the initial geothermal gradient is:

$$\frac{\partial T_0}{\partial z}(z) = \frac{Q}{k} + \frac{Hr_0 \cdot z_r}{k} \exp\left(\frac{-z}{z_r}\right). \quad \text{(SI.1)}$$

For crustal rocks, Hr values are commonly of the order of 1 $\mu W.m^{-3}$ (e.g., Jaupart and Mareschal, 2012). These low values may nevertheless impact on the initial thermal structure (Fig. SI.1). Moderate radioactive crust, i.e., $Hr_0 \sim 2\mu W.m^{-3}$ and a lower crust poorly radioactive ($z_r \sim 15$ km), can significantly increase the temperature in depth of more than 100°C compared to a geotherm only controlled by the Fourier's law of heat conduction from the mantle (Fig. SI.1a,b). Towards shallow depths, this increase becomes low whereas, due to the exponential rise of radiogenic heating, the thermal gradient undergoes a major change (Fig. SI.1c,d). Initial shallow geothermal gradient can be increased by ~ 10°C.km^{-1}, meaning a rise of the order of 100% compared to the Fourier gradient. In contrast, the impact on the vertical thermal gradient becomes insignificant in depth. Generally, radiogenic heating effects are significant for (i) the temperature field for which an increase takes place in depth and for (ii) the thermal gradient for which an important increase can occur in shallow domains.

When considering a thick highly radioactive crust, thermal effects become so intense that the deep geothermal gradient can even be doubled and the corresponding temperatures can increase by several hundreds of degrees (Fig. SI.1). The schematic law of Turcotte and Schubert (2002) remains a model, but it allows to approach, in a general way, the role of intensity and space distribution of radiogenic thermal increment by using only two parameters Hr_0 and z_r.

Figure SI.1. Initial radiogenic thermal contribution. a) Initial steady state temperature as a function of depth z, resulting from internal radioactivity according to the specific depth z_f and the surface radiogenic heat production Hr_0. Black lines represents absolute iso-values. The hatched domain at the surface plane exhibits the [z_r, Hr_0] combinations for which the mean radiogenic heating along a 30 km thick crust is higher than the common crustal value of 1 $\mu W.m^{-3}$ (e.g., Jaupart and Mareschal, 2012). b) Impact of radioactivity on the initial geotherm along z for the central [z_r, Hr_0] combination indicated in a). ① represents the absolute part due to radioactivity, ② the Fourrier part and ③ the total geotherm and its gradient, respectively. c) Part of the initial geothermal gradient due to Hr. Black lines represents absolute iso-values. White lines show the respective increment of thermal gradient relative to the constant gradient due to the Fourrier heat conduction of mantle heat. d) Impact of radioactivity on the initial gradient along z corresponding to the geotherm presented in b). ①, ② and ③ as for b).

Supporting information #2: Internal heat sources during the shear zone activity

In contrast to shear heating, radiogenic heating is active everywhere in the crustal domain, regardless of the distance to the shear zone. Moreover, comparatively, shear heating is often much more intense than radiogenic heat production (see Fig. SI.2). Consequently,

radiogenic heating during the shear zone activity is neglected and the production term *Pr* (Eq. (9)) corresponds to the shear heating only. Nevertheless, *Hr* is considered as an important contribution to the initial thermal structure.

Figure SI.2. Shear heating *Hs* as a function of the shear zone thickness *h*, its relative velocity *V*, and the mean effective viscosity η across the sheared domain. Values are considered for intracontinental shear zones. Whitened surface shows the 1 $\mu W.m^{-3}$ limit corresponding to the common mean crustal radiogenic heating.

Supporting information #3: Characteristic time scales

The characteristic time of advection t_{adv} (Molnar and England, 1990; England and Molnar, 1993) corresponds to the time required for a material initially at the front of the shear zone (belonging to the lower block for a thrust and to the upper block for a detachment) to reach the depth z_f along the fault:

$$t_{adv} = \frac{z_f}{Vz} = \frac{z_f}{V \cdot \sin(\psi) \cdot \sin(\theta)} \,. \qquad \text{(SI.2)}$$

Besides the advective time t_{adv}, a second characteristic time t_{dif} is defined for heat diffusion. Considering an instantaneous thermal perturbation at depth z_f, the time required to diffuse it evenly to the surface (whose temperature is constant) is defined as:

$$t_{dif} = \frac{z_f^{\,2}}{\pi^2 \kappa} \,. \qquad \text{(SI.3)}$$

According to Molnar and England (1990), the thermal steady state at the considered depth z_f along the shear zone is then roughly reached after a time t_{ss} corresponding to the sum of both advective and diffusive characteristic times:

$$t_{ss} = t_{adv} + t_{dif} = \frac{z_f}{V \cdot \sin(\psi) \cdot \sin(\theta)} + \frac{z_f^{\,2}}{\pi^2 \kappa} \,. \quad \text{(SI.4)}$$

For reasons of computations when at least one of the two angles ψ and θ is equal to 0°, the harmonic mean of t_{adv} and t_{dif} can be adopted to define t_0 to avoid a division by zero (Eq. (7)):

$$\frac{2}{t_0} = \frac{1}{t_{adv}} + \frac{1}{t_{dif}} = \frac{V \cdot \sin(\psi) \cdot \sin(\theta)}{z_f} + \frac{\pi^2 \kappa}{z_f^{\,2}} \,. \quad \text{(SI.5)}$$

However, the definition of t_0 does not matter if we are only interested to quantify the thermal contribution of each thermal process because t_0 disappears in Eqs. (10) and (11).

References

England, P. and Molnar, P., 1993. The interpretation of inverted metamorphic isograds using simple physical calculations. *Tectonics*, **12(1)**, 145–157.

Jaupart, C. and Mareschal, J.C., 2012. Constraints on crustal heat production from heat flow data. In: *Treatise on Geochemistry, 2nd edn. The Crust, vol. 3* (Rudnick, R.L., ed), Permagon, New-York, 65–84.

Molnar, P. and England, P., 1990. Temperatures, heat flux, and frictional stress near major thrust faults. *Journal of Geophysical Research*, **95(B4)**, 4833–4856.

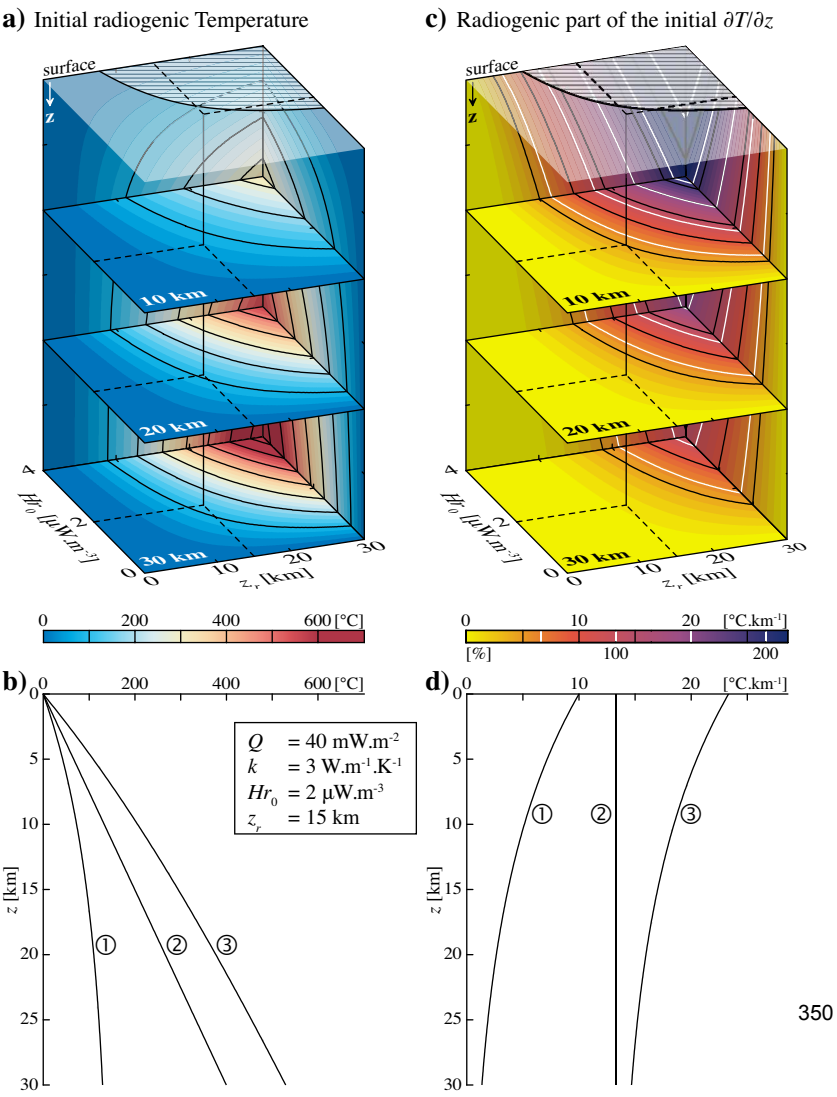
a) Initial radiogenic Temperature
surface
z
10 km
20 km
30 km
Hr_0 [µW.m^{-3}]
z_r [km]
0
200
400
600 [°C]
c) Radiogenic part of the initial ∂T/∂z
surface
z
10 km
20 km
30 km
Hr_0 [µW.m^{-3}]
z_r [km]
0
10
20
[°C.km^{-1}]
[%]
100
200
b)
Q = 40 mW.m^{-2}
k = 3 W.m^{-1}.K^{-1}
Hr_0 = 2 µW.m^{-3}
z_r = 15 km
①
②
③
z [km]
d)
①
②
③
z [km]

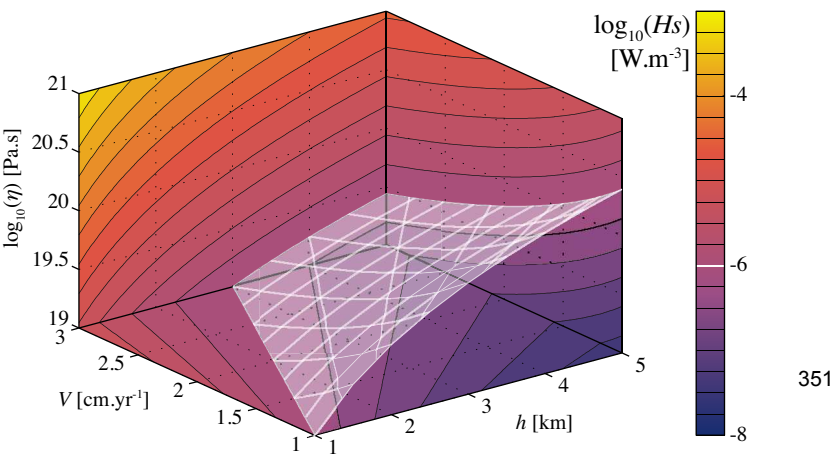
log10(Hs) [W.m-3]
-4
-6
-8
log10(η) [Pa.s]
21
20.5
20
19.5
19
V [cm.yr-1]
3
2.5
2
1.5
1
h [km]
1
2
3
4
5

Tectonophysics 484 (2010) 181–192

Contents lists available at ScienceDirect

Tectonophysics

journal homepage: www.elsevier.com/locate/tecto

Structural evolution of a three-dimensional, finite-width crustal wedge

Jean Braun *, Philippe Yamato [1]

Géosciences Rennes, Université de Rennes 1, CNRS, Rennes Cedex CS 35042, France

ARTICLE INFO

Article history:
Received 20 February 2009
Received in revised form 23 June 2009
Accepted 31 August 2009
Available online 10 September 2009

Keywords:
Wedge mechanics
Three-dimensional
Basal discontinuity
Structural geology
Surface processes
Numerical model

ABSTRACT

We present the results of three-dimensional numerical experiments designed to study the response of a layer of crustal material subjected to convergence through an imposed basal velocity discontinuity and to surface processes (erosion/sedimentation). We focus on the three-dimensional response of the system arising from the finite width of the imposed velocity discontinuity. In particular, we describe the complex structures that develop around the wedge and their interactions with the loading/unloading produced by the surface processes. We show that the pro- and retro-shear zones that develop in a doubly-vergent two-dimensional wedge curve around the end of the velocity line-discontinuity to merge into the strike-slip structure that naturally develop, i.e. as a consequence of the imposed boundary conditions, along the edge of the wedge. Along the retro-shear zone the stress orientation rotates along a vertical axis, which implies that the retro-shear zone is a pure thrust along all of its curved length, whereas, along the pro-shear zone stresses rotate along a horizontal axis, which, in turn, implies that the pro-shear zone progressively evolves towards an oblique thrust in its curved section. Furthermore, the outward motion (i.e. perpendicular to the direction of imposed shortening) along the curved section of the retro-shear zone is accommodated by oblique extension along a secondary, kinked structure antithetic to the retro-shear zone. We also show the complex evolution of the wedge when ductile flow and ductile strain softening is activated by increasing the imposed basal temperature. In this situation, the wedge is broader as structures develop at finite distances on either side of the line-discontinuity and its dynamics resembles more that of a 'vise-like' orogen. At the surface, a flat plateau forms that accumulates sediment from the surrounding actively deforming mountain ranges until a channel breaks through one of the sides and flushes the inward-draining basin of its sedimentary content. The complex numerical models provide a detailed insight into the geometry and complex three-dimensional structures within and at the margins of an orogen, and how they can be affected by erosional processes at the surface.

1. Introduction

Small orogens, such as the Southern Alps in New Zealand or Taiwan, are often regarded as doubly-vergent critical wedges that form above an imposed velocity discontinuity (or S-point) representing subduction of the underlying mantle lithosphere (Malavielle, 1984; Koons, 1990; Willett et al., 1993). As demonstrated in many analytical, analogue and numerical models, the behavior of a critical wedge is dictated by its internal rheological properties (i.e., internal and basal angles of friction and cohesion) as well as the nature and efficiency of the processes (erosion and deposition) acting on its surface (Dahlen, 1984; Willett et al., 1993). A wide variety of behaviors has been shown by varying the rheological and erosional parameters of wedge systems (Beaumont et al., 1992; Willett, 1999a,b; Whipple and Meade, 2004; Konstantinovskaia and Malavieille, 2005). However, and except for some very few exceptions (Braun, 1993; Koons, 1994; Braun and Beaumont, 1995; Gerbault et al., 2002), these efforts have been limited to two-dimensional studies, mostly due to the high computational cost of three-dimensional numerical models. None have explored the dynamics of a finite-width orogenic wedge. Here we present results from a new fully-coupled thermo-mechanical and surface process three-dimensional model describing the behavior of a frictional and viscous critical wedge driven by a finite-width (or *S-line*) velocity discontinuity along its base.

2. Numerical model description and experimental setup

A full description of the numerical methods used in the model, called DOUAR, can be found in Braun et al. (2008). Here, we will limit ourselves to the description of its main features. The model is centered on a finite element solution of the quasi-static force balance equations in three dimensions using an octree division of space that is dynamically adapted

* Corresponding author. Fax: +33 2 2323 6780.
E-mail address: Jean.Braun@univ-rennes1.fr (J. Braun).
[1] Now at the Geological Institute and Department of Earth Sciences, ETH-Zürich, Switzerland.

0040-1951/$ – see front matter © 2009 Elsevier B.V. All rights reserved.
doi:10.1016/j.tecto.2009.08.032

to the evolving solution. An octree division of the unit cube is an efficient, regular, yet non uniform way to define a finite element grid using 8 noded, tri-linear elements. It suffers however from nodal incompatibilities along the interfaces between adjacent elements of different sizes. These incompatibilities are solved by introducing linear constraints between the nodal degrees of freedom that belong to both elements and those which don't.

Rocks are assumed to behave like an incompressible visco-plastic fluid that obeys the Stokes flow law:

$$\begin{aligned} &\nabla\cdot\mu(\nabla v + \nabla v^T) - \nabla p = \rho g \\ &\nabla\cdot v = 0 \end{aligned} \tag{1}$$

where v is the velocity field, μ is the viscosity, p the pressure, g the acceleration due to gravity and ρ the density. During deformation, rocks are also assumed to obey Mohr–Coulomb failure criterion:

$$\tau = c_0 - \sigma_n \tan\phi \tag{2}$$

where τ is the magnitude of the shearing stress and σ_n is the normal stress, c_0 is cohesion and ϕ is the angle of friction, and to flow according to a power-law thermally-activated creep law:

$$\mu = \mu_0 \dot{\varepsilon}^{1/n-1} e^{Q/nRT} \tag{3}$$

where μ is the viscosity (in Pa s), μ_0 the intrinsic viscosity, $\dot{\varepsilon}$ the second invariant of the strain rate tensor, n the power-law exponent, Q the activation energy, R the gas constant and T the absolute temperature (values and units are presented in Table 1). We neglect the infinitesimal elastic contribution to the deformation.

Table 1
Numerical model parameters.

Parameter	Symbol	Value (units)	Reference
Model width	L	100 km	
Initial crustal layer height	h	10 km	
Imposed velocity	v_0	10 km Myr^{-1}	
Basal temperature (Exp.1 and 2)	T_0	250 °C	
Basal temperature (Exp.3)	T_0	400 °C	
Thermal diffusivity	$k/\rho c$	25 km^2 Myr^{-1}	
Heat production	H	0	
Cohesion	c_0	20 MPa	
Initial friction angle	ϕ_i	15°	
Reduced friction	ϕ_f	5°	
Frictional weakening strain range	$\Delta\varepsilon^{\phi}$	100%	
Activation energy	Q	223×10^3 J	Tullis (2002)
Power-law exponent	n	4	idem
Initial pre-exponential factor	$\mu_{0,i}$	2.92×10^6 Pa s$^{1/4}$	idem
Reduced pre-exponential factor	$\mu_{0,f}$	2.92×10^5 Pa s$^{1/4}$	
Viscous weakening critical strain	ε_i^{μ}	20%	
Viscous weakening strain range	$\Delta\varepsilon^{\mu}$	5%	
Rock density	ρ	2800 kg m^{-3}	
Tectonic time step length	Δt_t	10^4 yr	
Surface processes time step length	Δt_s	10 yr	
Hillslope diffusivity (Exp.1)	K_d	32×10^{-2} m^2 yr^{-1}	
Hillslope diffusivity (Exp.2)	K_d	0 m^2 yr^{-1}	
Hillslope diffusivity (Exp.3)	K_d	16×10^{-2} m^2 yr^{-1}	
Fluvial erosion/transport coefficient (Exp.1)	K_f	4×10^{-2} m yr^{-1}	
Fluvial erosion/transport coefficient (Exp.2)	K_f	8×10^{-2} m yr^{-1}	
Fluvial erosion/transport coefficient (Exp.3)	K_f	2×10^{-2} m yr^{-1}	
Bedrock erodibility length scale	l_{BR}	100 km	
Channel width	w_c	100 m	

Landscape evolution parameters are chosen within ranges used in other numerical studies: van der Beek and Braun (1998) and Kooi and Beaumont (1996). The exact value of these parameters is poorly constrained. It is the variation between the two first experiments that is of importance here.

In an elasto-plastic material, that undergoes an almost infinitesimal dilation during the early stages of (elastic) deformation, and as commonly observed in rocks, faults (brittle shear bands) form in a plane containing σ_2, the intermediary principal stress, and at $45°\pm(\phi/4+\psi/4)$ to the direction of σ_1, where ϕ is the angle of friction and ψ is the dilatancy angle, commonly assumed to be identical to the friction angle. Due to the incompressibility condition, in our model, shear bands that form in either of the two rheologies (brittle and viscous), form in a plane that is at 45° angle to the direction of σ_1. This difference between the model behavior and that of the natural system must be kept in mind during the interpretation of the results shown here.

Finite strain, ε is computed and stored on a three-dimensional cloud of points of self-adapting density and is used to include the effects of strain weakening which is parameterized here by progressive reduction in the internal angle of friction, ϕ, or in the intrinsic viscosity, μ_0, with deformation:

$$\phi = \phi_i + \frac{\varepsilon - \varepsilon_i^{\phi}}{\Delta\varepsilon^{\phi}}(\phi_f - \phi_i) \tag{4}$$

where ϕ_i and ϕ_f are the initial and final values for the angle of friction (i.e. before and after strain softening), respectively, and ε_i^{ϕ} and $\Delta\varepsilon^{\phi}$ are the deformation level at which brittle softening is initiated and the deformation increment over which brittle softening takes place, respectively, and:

$$\mu_0 = \mu_{0,i} + \left(0.5 + \arctan\left(\frac{\varepsilon - \varepsilon_i^{\mu}}{\Delta\varepsilon^{\mu}}\right) \Big/ \pi\right)(\mu_{0,f} - \mu_{0,i}) \tag{5}$$

where $\mu_{0,i}$ and $\mu_{0,f}$ are the initial and final values for the intrinsic viscosity (i.e. before and after strain softening), respectively, and ε_i^{μ} and $\Delta\varepsilon_i^{\mu}$ are the deformation level at which viscous softening is initiated and the deformation increment over which viscous softening takes place, respectively.

The temperature, T, is computed by including the effects of conduction and advection, according to:

$$\rho c\left(\frac{\partial T}{\partial t} + v\cdot\nabla T\right) = \nabla\cdot k\nabla T + \rho H \tag{6}$$

where k is the thermal conductivity, ρ is density, c is heat capacity and H is heat production per unit mass, and is used to compute the viscosity.

We track the free upper surface as well as internal interfaces defining regions of varying mechanical properties by advecting a self-adapting set of points and normals attached to each interface. At every time step, a Delaunay triangulation is computed among the points on each interface using a local metrics (or measure of distance) that takes into account the surface curvature. This triangulation is then used to compute a level set function on the nodes of the finite element mesh (the octree). The level set function is defined as the signed distance to the interface such that its zero iso-surface corresponds to the interface. The level set function is later used to localize any geometrical point, X, with respect to the interfaces by interpolation of the level set function from the node of the octree to X and inspecting its sign. For example, the use of level set functions provides an efficient way to determine the position of any integration point with respect to each of the potentially numerous material interfaces during the computation of the finite element matrix even in situation of complex intersections among the interfaces in a single element.

Like all other surfaces, the upper surface is advected by tectonic transport, i.e. using the velocity field derived from the solution of the Stokes equation (Eq. (2)).The advection of the surface nodes may lead to bow-tying of the Delaunay triangles used to define the level set

function. To prevent this undesirable result, we apply a small correction to the position of the nodes by moving each node towards the mean position (or center of mass) of its neighboring nodes (i.e. those to which it is connected by the Delaunay triangulation). We have tested that this slight perturbation of the nodes' position does not affect the solution because it perturbs the geometry of the surface by an amount that is almost negligible with respect to the perturbation brought upon by the surface processes.

At every time step, the geometry of the free upper surface is also subjected to a surface processes model (CASCADE, Braun and Sambridge (1997)) that includes the effects of fluvial and hillslope processes. In CASCADE, we assume that river channels have a carrying capacity (volume that can be carried per unit time), q_c, that is proportional to local slope, S, and drainage area, A, a proxy for local discharge (Kooi and Beaumont, 1994):

$$q_c = K_f S A. \tag{7}$$

K_f is a constant of proportionality (in m yr^{-1}) that is assumed to vary with climate, mostly with precipitation rate (higher K_f values corresponding to a higher precipitation rate). Where sediment load, q_s, obtained by integrating the volume of rock eroded from the upstream area, is smaller than the river capacity, erosion takes place, at a rate set by:

$$\frac{\partial h}{\partial t} = \frac{q_s - q_c}{w_c l_{BR}} \tag{8}$$

where l_{BR} is a length scale characterizing the erodibility of bedrock (Kooi and Beaumont, 1994) (higher l_{BR} values corresponding to more resistant rocks) and w_c is the set river channel width. Where sediment load exceeds capacity deposition takes place at a rate set by:

$$\frac{\partial h}{\partial t} = \frac{q_s - q_c}{\Omega} \tag{9}$$

where Ω is the surface area attached to each integration point and defined by the spatial discretization. Hillslope processes (landslides, soil creep, rainsplash, etc.) are represented by a simple diffusion equation that assumes that mass transport, q, is linearly proportional to slope, S (Kooi and Beaumont, 1994; Braun et al., 2001):

$$q = -K_d S. \tag{10}$$

K_d is a proportionality constant or diffusivity (in m^2 yr^{-1}) that is a measure of the efficiency of the hillslope transport processes and is mostly proportional to precipitation rate (higher values of K_d corresponding to wetter climates).

Here we present a series of numerical experiments in which shortening of an initially uniform crustal layer (thickness L and height h) is driven by an imposed basal velocity discontinuity (from v_0 to 0, Fig. 1). This discontinuity is meant to represent shortening of the underlying substratum in a subduction-like process (as used by Malavielle (1984) or Willett et al. (1993) in two dimensions) or across any mechanical or lithological discontinuity (as used in Braun and Sambridge (1994) for example). Here we are interested in generalizing the work done on doubly-vergent critical wedges to the third dimension by assuming that the discontinuity has a finite width (in the third dimension). As shown in Fig. 1, this discontinuity is imposed at $y = L/2$ but along one half of the model only (from $x = 0$ to $x = L/2$) giving to the experiment a three-dimensional character. The temperature is fixed at the base of the model ($T = T_0$) and the initial temperature structure is obtained by assuming conductive transport only. In the subsequent paragraphs, we present results of our computations for a small range of model parameters and discuss primarily the mechanical implications of considering the third dimension.

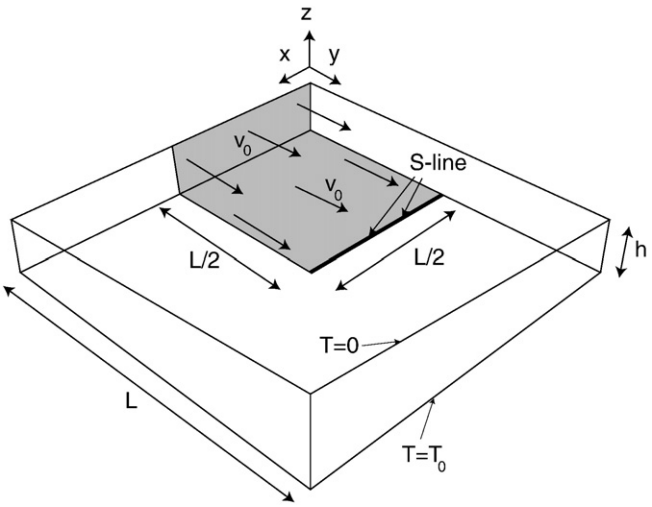

Fig. 1. Experimental setup and boundary conditions. On all sides of the model, all velocity components are set to zero, except along the grey shaded side boundary where the normal component (parallel to the y-axis) is set to v_0. Along the base of the model, the velocity is also set to zero, except along the grey shaded area where the velocity component parallel to the y-axis is set to v_0. The thick black line represents the location of the S-line velocity discontinuity, i.e. where the velocity changes from v_0 to 0.

The model general parameters and geometrical setup are shown in Fig. 1 and Table 1. Note that the thickness of the model, h, is relatively small, i.e. 10 km, because the base of the model being fixed, we cannot enforce the isostatic compensation. It is thus more appropriate to assume that the crustal layer being deformed is relatively thin such that the horizontal stress gradient created by its deformation and thickening can be sustained by the much thicker underlying lithosphere.

In a first step, we will show results from two separate model runs or experiments, differing by the assumed efficiency of surface processes. The value of the parameters characterizing the surface processes is arbitrary and has been selected such that the system is capable of reaching an approximate flux steady-state in a time that corresponds to shortening by an amount of the order of once to twice the model thickness. In the first of the two experiments, both fluvial and hillslope processes are activated. In the second experiment, fluvial efficiency is twice as large as in the first model, while hillslope processes (and thus the system's ability to erode drainage divide) have been turned off. In the last part of this paper, we will show results for a third, hotter model, i.e. one in which the basal temperature has been increased from 250 to 400 °C and the erosion parameters have been reduced by a factor 2 in comparison with the first experiment.

Strain softening is activated in all the experiments shown here. We have performed a few model experiments in which the strain softening was turned off; they show that the strain softening controls the width of the shear zones, but not their geometry (orientation).

3. Wedge development

The evolution of the system is shown in Fig. 2 for the two different model setups described above, the low erosional efficiency experiment on the left, and the high efficiency experiment on the right. For each experiment five snap shots are shown at the same times in the model evolution, i.e. for the same amount of convergence at $t = 1$, 2, 3, 4 and 5 Myr. We show the evolution of the surface topography, much larger in the first of the two experiments as expected if the surface processes efficiency is diminished, as well as the distribution of strain rate along a vertical cross-section parallel to the y-axis and located next to the axis of symmetry of the model (the $x = 0$ axis). In both cases, the model's response to basally-driven shortening is the formation of two oppositely-dipping shear zones accommodating reverse sense of shear. The resulting surface uplift is, at first, symmetrical, that is of equal width on

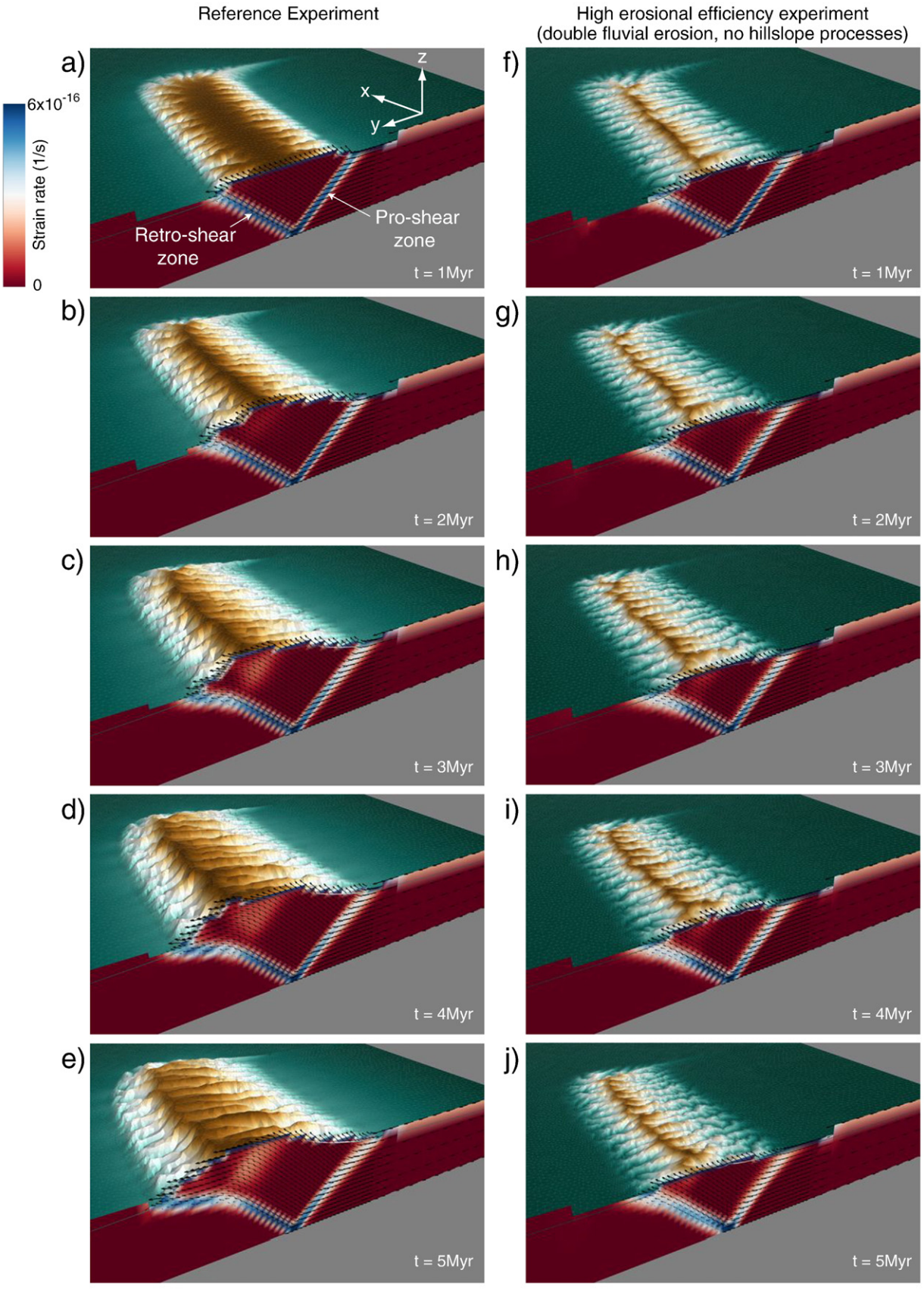
Reference Experiment
High erosional efficiency experiment
(double fluvial erosion, no hillslope processes)
a)
b)
c)
d)
e)
f)
g)
h)
i)
j)
6x10-16
Strain rate (1/s)
0
z
x
y
Retro-shear zone
Pro-shear zone
t = 1Myr
t = 2Myr
t = 3Myr
t = 4Myr
t = 5Myr

either side of the newly formed divide. As shortening proceeds, the system becomes asymmetrical with deformation accumulating along one of the two shear zones (the so-called retro-shear zone, (Willett et al., 1993)) while the other (the pro-shear zone) becomes a transient feature that is continuously advected through the V-shaped wedge that has developed between the two shear zones. This asymmetry is the result of the basal boundary condition, which imposes that the point where the velocity changes from v_0 to zero (the so-called discontinuity or "S-point") is attached to one of the two converging plate, here the one on the retro-side.

The surface topography simultaneously evolves into an asymmetrical shape with the divide being advected towards the retro-shear zone. The mean elevation is approximately 3 km and 1 km in the first and second experiments, respectively. This evolution is identical to that evidenced in many two-dimensional numerical (Willett et al., 1993; Batt and Braun, 1997) and analogic (Malavielle, 1984) experiments and this behavior is now well understood as that of a doubly-vergent, two-dimensional critical wedge, where rocks can be considered to be at or close to failure, according to Coulomb's criterion. This evolution leads to a steady-state situation where the tectonic flux is compensated by the surface erosion flux as postulated and observed in many orogenic settings (Jamieson and Beaumont, 1988; Bernet et al., 2001; Willett et al., 2001; Willett and Brandon, 2002; Whipple and Meade, 2004). The early evolution of the model is faster, and thus steady-state is reached more rapidly, in the second model experiment where surface processes are more efficient, in agreement with Whipple and Meade (2006) that it is the efficiency of surface processes that determines the rate at which an orogenic wedge goes back to steady-state conditions following a perturbation, whether it is climatic or tectonic in origin. Note, however, that although a flux steady-state is reached in both experiments, a geomorphic steady-state is never reached with the geometry of the surface continuing to evolve with time. Indeed, while, at flux steady-state, the mean elevation, the width of the mountain range, the spacing between the river channels and the mean position of the divide are all relatively stable, the shape of the surface is very dynamic, mostly in response to advection of the landforms by the horizontal component of the velocity. This important and characteristic feature of natural systems (Willett et al., 2001) is commonly neglected in quantitative models of the coupling between tectonics and landscape evolution, and can only be properly modeled in three dimensions.

The two experiments also differ in their structural evolution in that, in the case where surface processes are less efficient, the relatively large topographic gradient that has formed leads to a substantial perturbation of the stress state in the underlying crust. This perturbation leads to a local rotation of the direction of the principal stress axes along the x-axis which, in turn, causes a kink to develop in the retro-shear zone at mid-layer depth as well as a hinge structure to accommodate the bending of the wedge along that kink. To demonstrate this point, we show in Fig. 3 the orientation of the principal strain rate (and thus stress) axes as computed by the model in both experiments. In both experiments, the stress orientation is mostly determined by the horizontal compression resulting from the imposed basal shortening. As explained in the model description section, shear bands form at 45° to the direction of σ_1 which is horizontal and aligned with the y-axis in most of the deforming wedge. σ_3, the least compressive principal stress component is vertical and the intermediary stress, σ_2 is horizontal, in the x-direction. In Fig. 3, the retro- and pro-shear zones are labeled '1' and '2', respectively. In the first experiment (top panel), the topographic gradient that has developed in front of the retro-shear zone has led to a counter-clockwise rotation of the σ_1 and σ_3 axes around σ_2 which has led to the formation of a kink in the retro-shear zone. A secondary structure has developed (labeled '1a' in Fig. 3), originating at the kink in a direction parallel to the pro-shear zone and thus at 45° to the lower section of the retro-shear zone. In this shear band, the most compressive stress axis is vertical and the least compressive stress axis is horizontal. This structure accommodates extensional deformation. However, it is not *sensu strictu* a normal fault but a hinge structure because, although it corresponds to a discontinuity in the velocity field, velocity does not change in amplitude but only in direction. The formation of this structure is clearly related to the presence of the surface topographic gradient as it is not observed in the second, high erosional efficiency experiment.

4. Three-dimensional mechanical response

The three-dimensional nature of the experiment we propose here comes from the existence of a free edge (at $x=0.5$) between the deforming wedge and the adjacent 'intact' crust. To appreciate the complex nature and dynamics of this boundary, we show in Fig. 4 a horizontal cross-section, half-way through the thickness of the model, in which we have superimposed the principal stress orientations on a color map of the computed strain rate. The retro- and pro-shear zones (labeled '1' and '2' in Fig. 4) appear as two zones of intense deformation separated by the undeformed, yet uplifting plug. A third structure (labeled '4' in Fig. 4) accommodates the differential motion between the advancing crustal layer subjected to the imposed basal velocity and the neighboring, static crust. Along all of its length this structure is a pure strike-slip shear zone characterized by horizontal σ_1 and σ_3 axes both at 45° to the strike of the shear zone. The most compressive axis lies in the plane $x=y$. The retro-shear zone (labeled '1' in Fig. 4) does not connect in a simple manner with the strike-slip shear zone (labeled '4' in Fig. 4): it forms a curved arc along the outside corner of the model, above the termination point of the imposed basal discontinuity. Along this external section of the retro-shear zone (labeled '1b' in Fig. 4), the maximum compressive stress orientation rotates by almost 90° from parallel to the y-axis to sub-parallel to the x-axis, and remains perpendicular to the strike of the curved shear zone, indicating that all along its length, this shear zone '1'+'1b' is a pure thrust, i.e. it accommodates a pure reverse motion. The strike-slip deformation is entirely accommodated by the through-going strike-slip shear zone that runs parallel to the y-axis (labeled '4' in Fig. 4). This partitioning of the deformation between a pure thrust and a pure strike-slip shear zone is most visible in the first of the two experiments (Fig. 4a).

In contrast, the pro-shear zone (labeled '2' in Fig. 4) connects in a simpler manner to the strike-slip fault (labeled '4' in Fig. 4): away from the $x=0$ axis of symmetry and in the vicinity of the strike-slip shear zone, it also becomes curved, and more so in the first of the two experiments, but the direction of the most compressive stress remains parallel to the y-axis, implying that it is an oblique thrust, because the direction of the most compressive stress is not orthogonal to the strike of the shear zone. The deformation is not partitioned; there is only one structure (labeled '2b' in Fig. 4) accommodating the combined motions.

Fig. 2. Evolution of two model experiments differing by the efficiency of the surface processes (panels a to e correspond to low erosional efficiency and f to j to high efficiency). Surface color is proportional to the predicted height (or elevation); color range is dynamically adjusted to the range of elevation in each panel; colors on the vertical cross-section at $x=0$ represent the second invariant of the computed strain rate tensor; for ease of comparison, the color range is the same for all panels. The black arrows represent the computed velocity field. The two planes of high strain rate intensity correspond to major structures (the retro- and pro-shear zones) accommodating the shortening imposed by the basal velocity discontinuity. The two model experiments differ by the height of the predicted topography but also by the geometry of the retro-shear zone. Note that the axes given in panel a indicate the direction not the absolute position of the system of reference used to describe the solution. The high strain rate values shown along the top surface (i.e. at the interface between rock and atmosphere) in this figure and in Figs. 3, 5 and 7 are artifacts of the plotting package we have used.

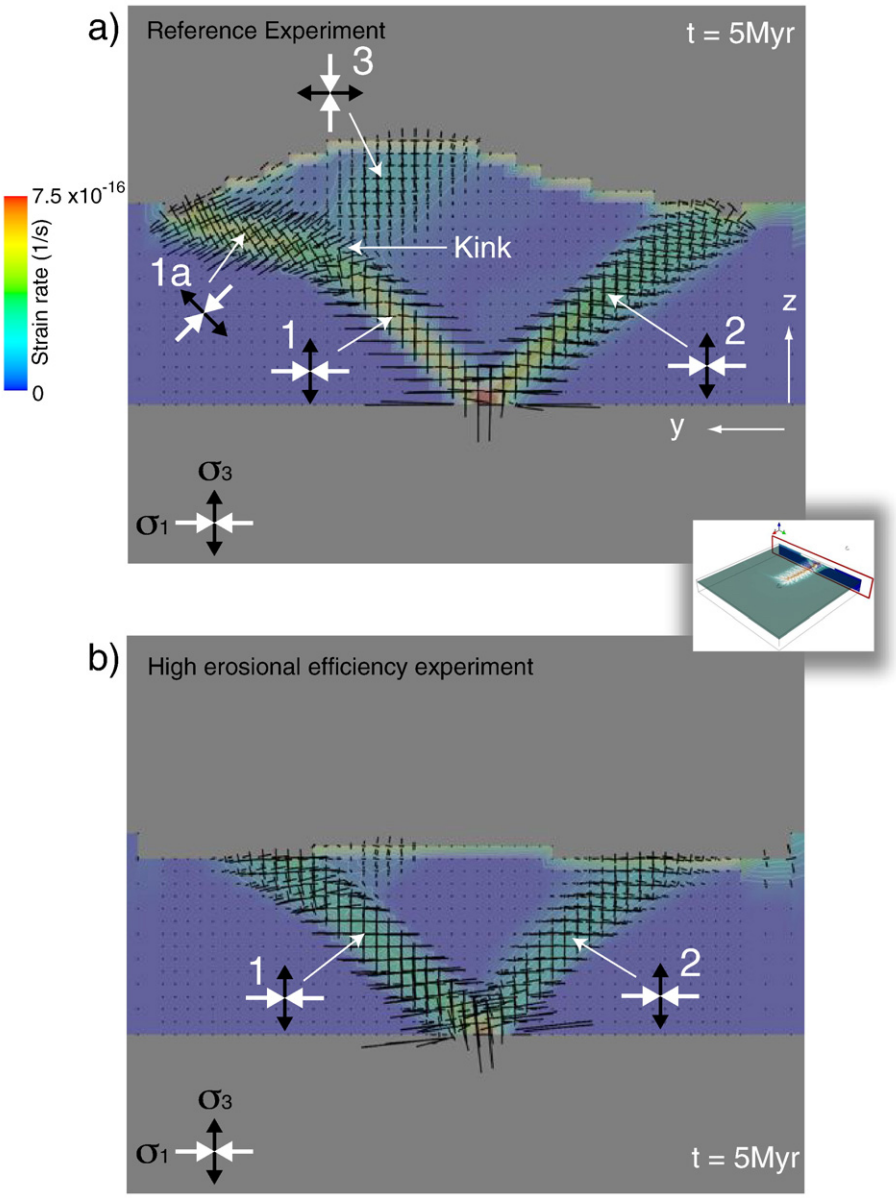

Fig. 3. Vertical cross-section in the $[y-z]$ plane at $x=0$ showing (in subdued colors) the computed strain rate and the orientation of the principal strain rate (and thus stress) axes for the two model experiments (a low and b high erosional efficiency). Labeled structures are: 1 = retro-shear zone; 2 = pro-shear zone; 1a = upper section of the retro-shear zone forming a kink with the lower section; and 3 = hinge. The double white arrow and double black arrow indicate the orientation of the most compressive principal stress (σ_1) and least compressive principal stress (σ_3), respectively.

Where the two shear zones ('2b' and '4') connect, the principal stress triad undergoes a complex rotation along both the vertical and *y*-axis such that both σ_1 and σ_3 lie in the horizontal plane.

Looking at the deformation in a plane perpendicular to the *y*-axis, half-way through the length of the model, i.e. along the basal velocity discontinuity (Fig. 5), one notices that thrusting along the curved thrust is accompanied by deformation along a secondary, oppositely-dipping shear zone (labeled '5' in Fig. 5) that is best seen in the first of the two experiments where surface processes are less efficient and substantial surface topography has developed (Fig. 5a). This structure is made of two sections: one, in the lower half of the model, that is nearly vertical and originates from the end of the basal velocity discontinuity, the other, in the upper half of the model, that is dipping at approximately 45° in a direction opposite to that of the main thrust plane (labeled '1b' in Fig. 5). Deformation on this structure is dominated by oblique normal movement in the upper part and strike-slip deformation in the lower part. To better understand how this structure connects to the others, we have plotted the strain rate along two cross-sections (Fig. 6), a vertical one passing through the velocity discontinuity and a horizontal one. Contrary to all other figures, we only show here results for the first of the two experiments. In the first of the two panels (Fig. 6a) the horizontal cross-section is placed half-way through the model, in the second panel (Fig. 6b), the horizontal section is closer to the surface. In the lower half of the model (Fig. 6a), the secondary structure (labeled '5') connects to the vertical, purely strike-slip shear zone (labeled '4' in Fig. 6a), parallel to the *y*-axis; in the upper half (Fig. 6b), the secondary structure (labeled '5') connects to the hinge structure (labeled '3' in Fig. 6b) that is antithetic to the main thrust (or retro-shear zone). Variations in the velocity field (not shown here for clarity) across this structure demonstrate that, in its lower section, it is a pure strike-slip shear zone while, in its upper section, it is a hinge that accommodates the change in velocity direction (not amplitude) from parallel to the *y*-axis to parallel to the *x*-axis. In other words it accommodates the

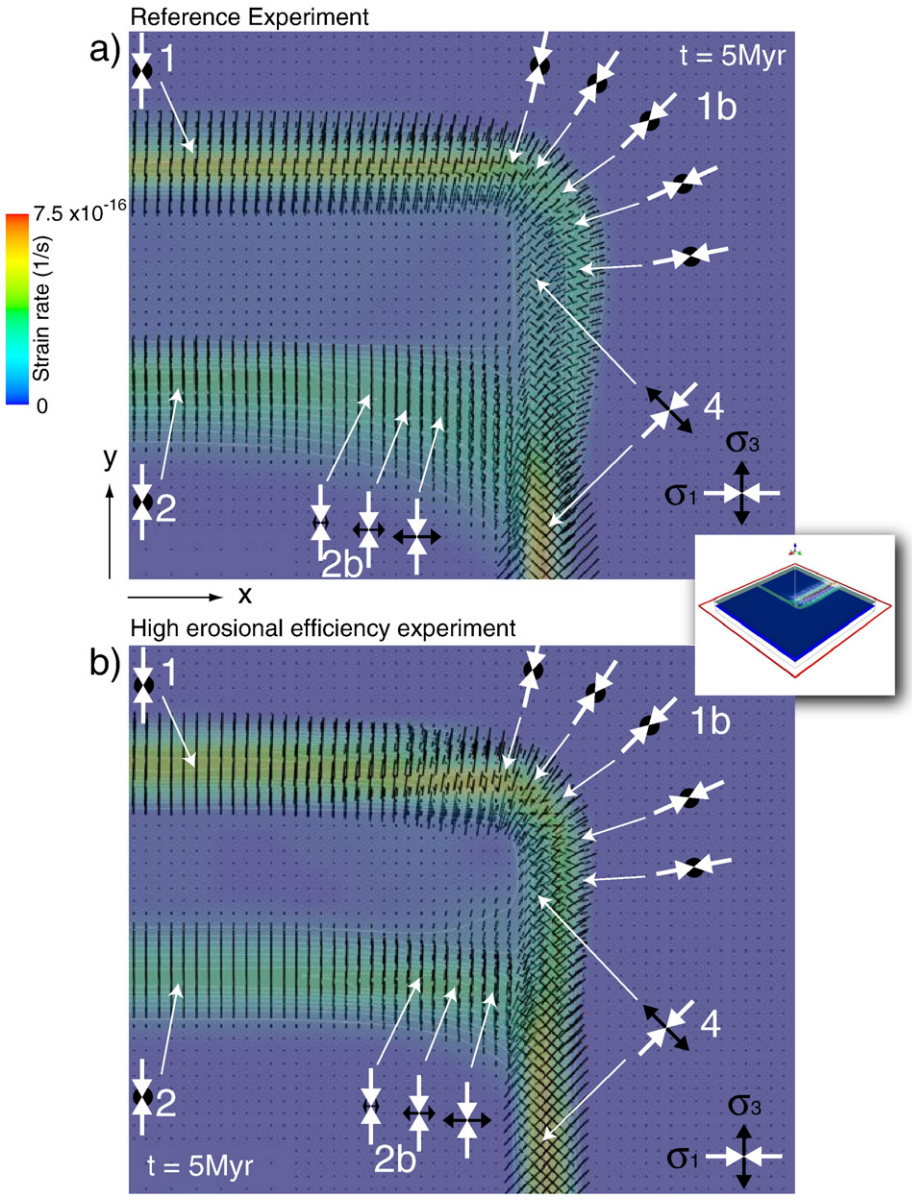

Fig. 4. Horizontal cross-section through the model half-way through the model thickness for the two model experiments (a low and b high erosional efficiency). Principal stress axes are superimposed on a color map of the second invariant of the computed strain rate. Labeled structures are: 1 = retro-shear zone; 2 = pro-shear zone; 1b = curved section of the retro-shear zone; 2b = curved section of the pro-shear zone; and 4 = strike-slip shear zone. The curved section of the retro-shear zone is a pure thrust while the curved section of the pro-shear zone is an oblique thrust.

change in velocity direction resulting from the 'lateral escape' motion accommodated by the curved section of the retro-shear zone.

5. Effect of basal viscous creep

Increasing the temperature at the base of the crustal layer from 250 to 400 °C leads to a very different mechanical and topographical response, with the formation of a thin decollement at the base of the crust, widening of the deforming region and uplift of a broad topographic plateau (Fig. 7). One may regard this imposed basal temperature as 'extreme' and difficult to justify at the base of a 10 km thick crustal layer; however, our purpose here is to demonstrate the importance of the mechanical behavior of the wedge material, from purely brittle to thermally-activated creep, on its three-dimensional response to basally-driven shortening. The model dimensions are thus kept identical for easy comparison with the previous two model runs. Surface erosion efficiency is twice as low as in experiment 1 (see Table 1 for the exact value of the erosional coefficient).

The 2D evolution is different to the one described above, but similar to that evidenced in other studies (Ellis et al., 1998; Beaumont et al., 2000) where a temperature increase has led to thermally-activated dislocation creep becoming the dominant deformation mechanism. In our simulation, the material is also subject to strain softening in the ductile regime. The system first evolves in a similar way to that of the pure brittle case, with the formation of oppositely-dipping crustal-scale shear zones (labeled '1' and '2' in Fig. 7a) that accommodate the basally-driven shortening and uplift of a triangular plug. However, with accumulating deformation and the growth of steep surface topography, a horizontal decollement (labeled '3' in Fig. 7) develops along the base of the model, first in the pro-direction (panels a, b and c in Fig. 7), then in the retro-direction (panels c and in Fig. 7). The development and evolution of this horizontal basal decollement is facilitated by the assumed strain softening component of the viscous rheology. When this decollement reaches the far-side ($y = 0$) boundary of the model, it cannot propagate any further, a thrust forms (labeled '5' in Fig. 7) and uplift takes place along the

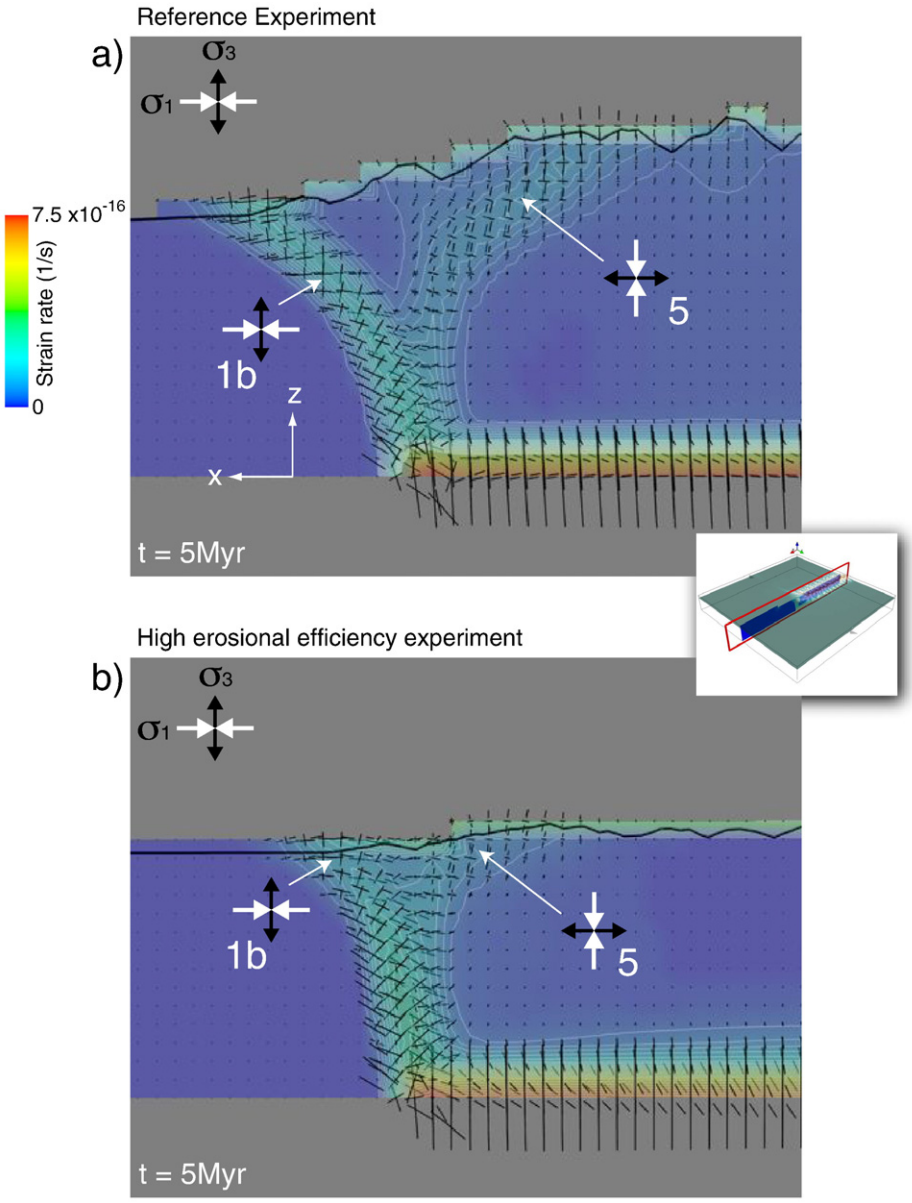

Fig. 5. Vertical cross-section through the model in a plane passing through the imposed basal discontinuity (i.e. at $y = 0.5$) for the two model experiments (a low and b high erosional efficiency). Principal stress axes are superimposed on a color map of the second invariant of the computed strain rate. Labeled structures are: 1b = curved section of the retro-shear zone; and 5 = oblique hinge. The oblique hinge is made up of two sections; the upper section dips at approximately 45° and the lower section is nearly vertical.

$y = 0$ far boundary. The location of this structure is thus imposed by the finite extent of the numerical experiment, and the interaction of the internal, mechanical response of the system with an artificially imposed boundary condition. In a natural system, such decollements propagate along distances that are dictated by the viscosity of the decollement, itself determined by the temperature and rheology at the base of the crustal layer, and the depth of the decollement (Braun and Beaumont, 1989; Vanbrabant et al., 2002). In many instances, horizontal heterogeneity in the crust will also dictate the distance over which such decollements propagate (Beaumont et al., 2000; Braun and Pauselli, 2004), with strong or cold inclusions inhibiting propagation and facilitating the nucleation of thrust faults.

Along the retro-side of the wedge, a secondary retro-shear zone develops (labeled '4' in Fig. 7) outboard of the initial wedge, that is connected to the imposed discontinuity (the 'S' point in Fig. 7) by the propagation of the basal decollement in the retro-direction. This propagation of the deformation in the retro-direction is likely to be the result of the inability of the system to propagate further in the other direction due to the finite length of the model. At this stage of its evolution, the wedge mechanics becomes disconnected from the line-discontinuity; its dynamics resembles more that of a side-driven or 'vise-type' compressional orogen (Ellis et al., 1998). Movement along the most external structures (4 and 5 in Fig. 7) leads to the formation of a broad, plateau-like surface that is composed of actively uplifting rugged mountain ranges along its boundaries and a very flat interior, that forms by sediment transport and deposition. Sediment accumulation lasts until a channel draining along the side of the plateau-like topographic feature is capable of breaking through the local drainage divide (between the plateau and the low-lying, underformed adjacent areas) and rapidly drains the thick sediment pile. This rapid unloading is concomitant with the formation of yet another structure (labeled '6' in Fig. 7), illustrating the complexity of interactions that one develops in a fully-coupled three-dimensional model of crustal deformation and surface processes.

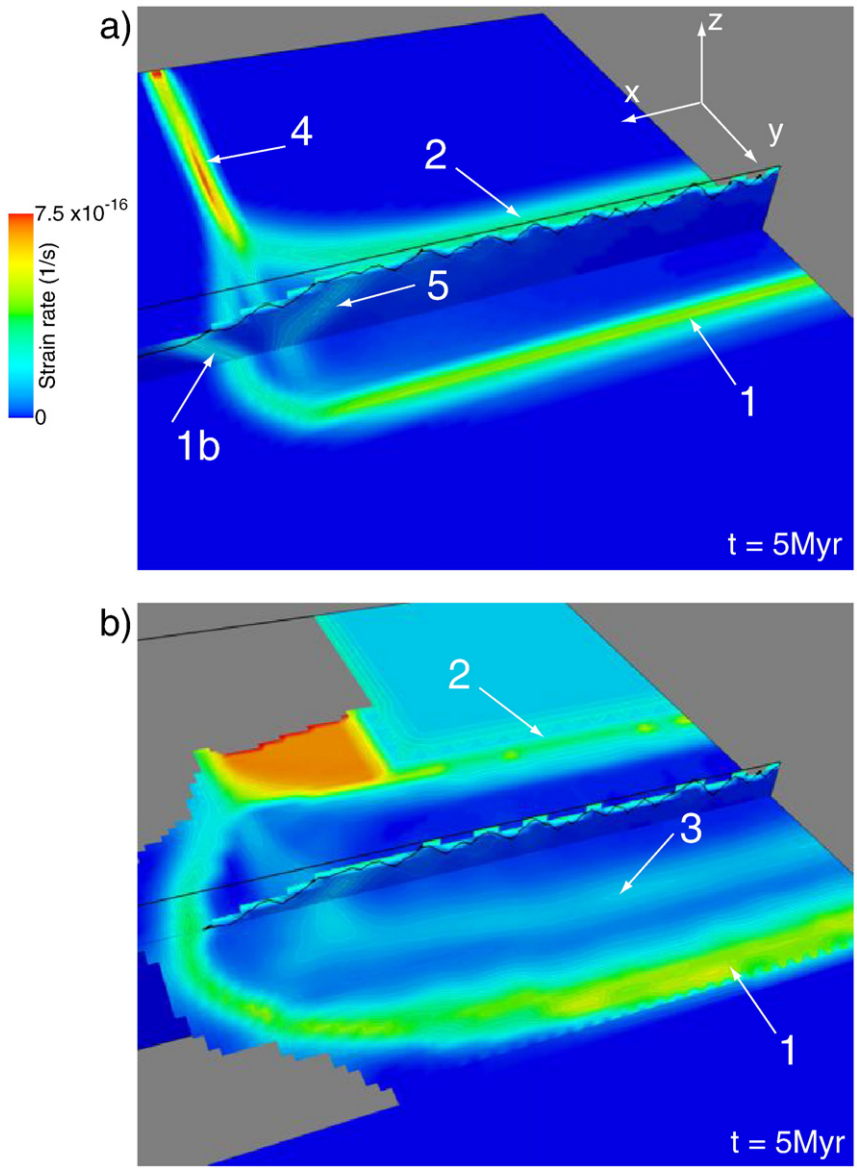

Fig. 6. Double cross-section through the model for the first of the two model experiments, i.e. the low erosional efficiency, high topography one. Vertical section is along a plane passing through the basal discontinuity (i.e. at $y=0.5$); the horizontal plane passes half-way through the model thickness in panel a and is closer to the surface (at $0.116\times h$, the model initial thickness, from the base of the model) in panel b. Labeled structures are: 1 = retro-shear zone; 2 = pro-shear zone; 1b = curved section of the retro-shear zone; 3 = hinge; 4 = strike-slip shear zone; and 5 = oblique hinge. Along its lower section the oblique hinge (labeled 5) connects to the strike-slip shear zone (labeled 4), while in its upper section, it connects to the hinge (labeled 3).

We complete this already dynamic evolution of the system by examining the three-dimensional nature of the solution (Fig. 8) and considering the evolution of the structures in a horizontal plane located near the surface (i.e. at $z=0.9$) with a special emphasis given to the external boundary of the deforming wedge (i.e. at $x=0.5$). In the initial stages of deformation (panel a in Fig. 8), the three-dimensional strain rate and its partitioning between pure thrust, pure strike-slip and oblique structures are similar to those of the purely brittle/frictional case shown above (Fig. 4). However, as deformation progresses, the pro-shear zone is abandoned and another structure (or secondary pro-shear zone) develops along the bottom part of the model (i.e. near the $y=0$ boundary in this top view of the model). This transfer is progressive (panels b to e in Fig. 8) and evolves from right to left, i.e. from the external boundary of the deforming wedge towards its interior. The reason for this progressive transfer is the preferential viscous strain weakening of the wedge material along its side boundary, in response to the accumulated strike-slip deformation. Note that this structure is, at all times, strongly controlled by, and thus pinned to, the edge of the model which is an artifact of the finite size of the experiment.

With further deformation, another or secondary retro-thrust develops outboard of the retro-shear zone which progressively accommodates thrusting. At the end of the model run (panel h), the thrusting is equally distributed among the two structures. Note that the outmost curved section of this secondary structure is, at all times in its evolution, a pure thrust, i.e. the most compressive stress component is everywhere perpendicular to the strike of the shear zone. On the contrary, the connection between the first retro-shear and the strike-slip shear zones on the right-hand side of the wedge (at $x=0.5$) is at first a curved pure thrust but evolves into an oblique structure. The strike-slip shear zone evolves through time too as it curves half-way through its length to connect the edge of the oblique retro-thrust with the imposed discontinuity in horizontal velocity along the bottom boundary (at $x=0.5$ and $y=0$).

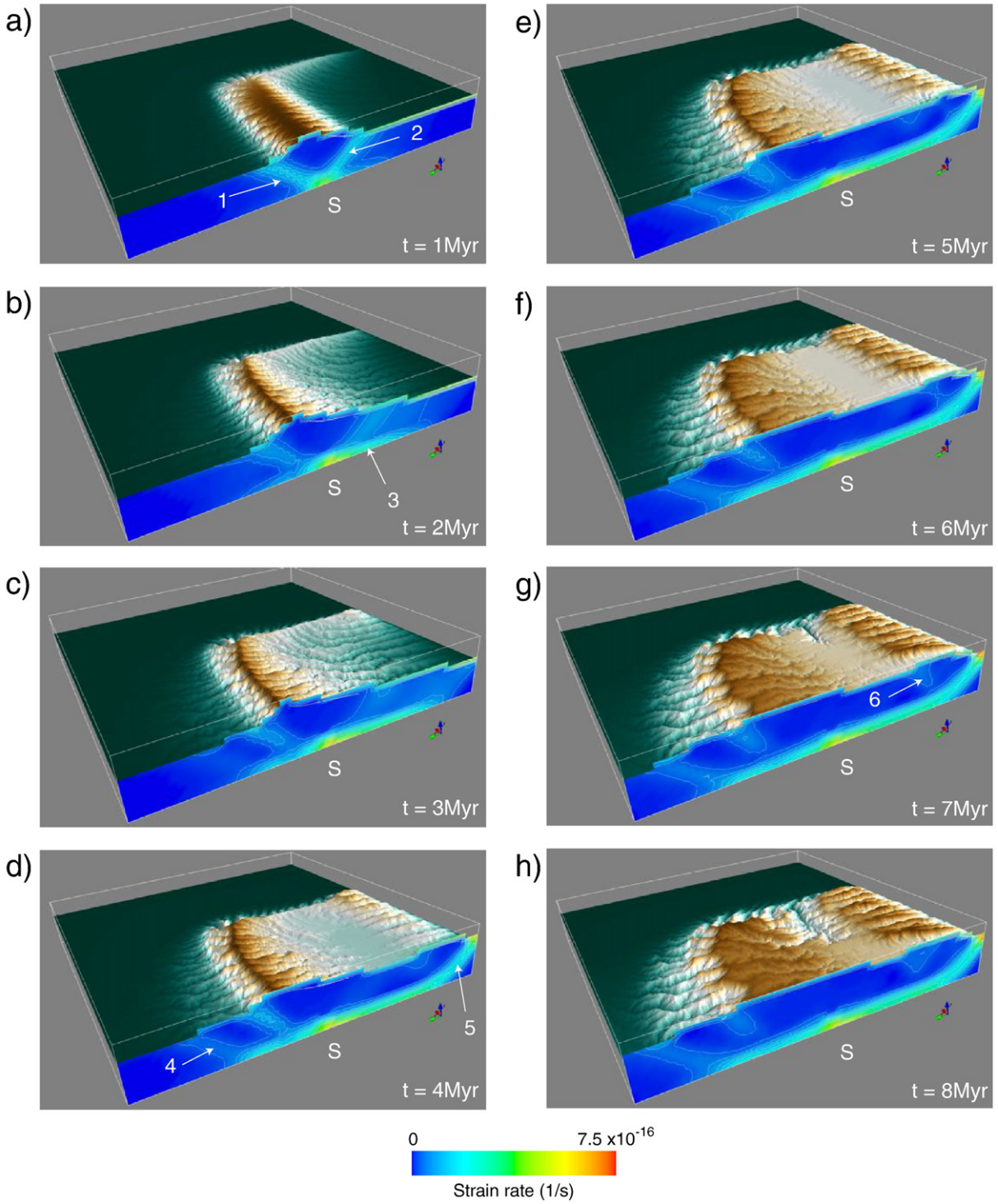

Fig. 7. Evolution of a model experiment characterized by a higher basal temperature and in which thermally-activated creep is thus activated. Surface color is proportional to the predicted height (or elevation); colors on the vertical cross-section at $x=0$ represent the second invariant of the computed strain rate tensor. White arrows and labels indicate structures discussed in the text. The 'S' label indicates the position of the imposed, fixed velocity discontinuity.

Finally, it is worth noting the formation of the final structure, antithetic to the secondary pro-thrust that developed earlier at the bottom ($y=0$) of the model (panels f to h). This structure evolves also from right to left, but it is not a 'fixed' structure like the bottom thrust; it is also progressively advected by the horizontal tectonic movement accommodated by thrusting along the two retro-shear zones near the top of the model. This explains its curved shape (panel h).

Fig. 8. Evolution of the model experiment shown in Fig. 7 but along a horizontal plane at $z=0.9$. Colors are proportional to the second invariant of the stain rate tensor and small black arrows show the direction and amplitude of the principal axis of the strain rate (and thus stress) tensor. Large white and black arrows indicate σ_1 and σ_3 directions, respectively.

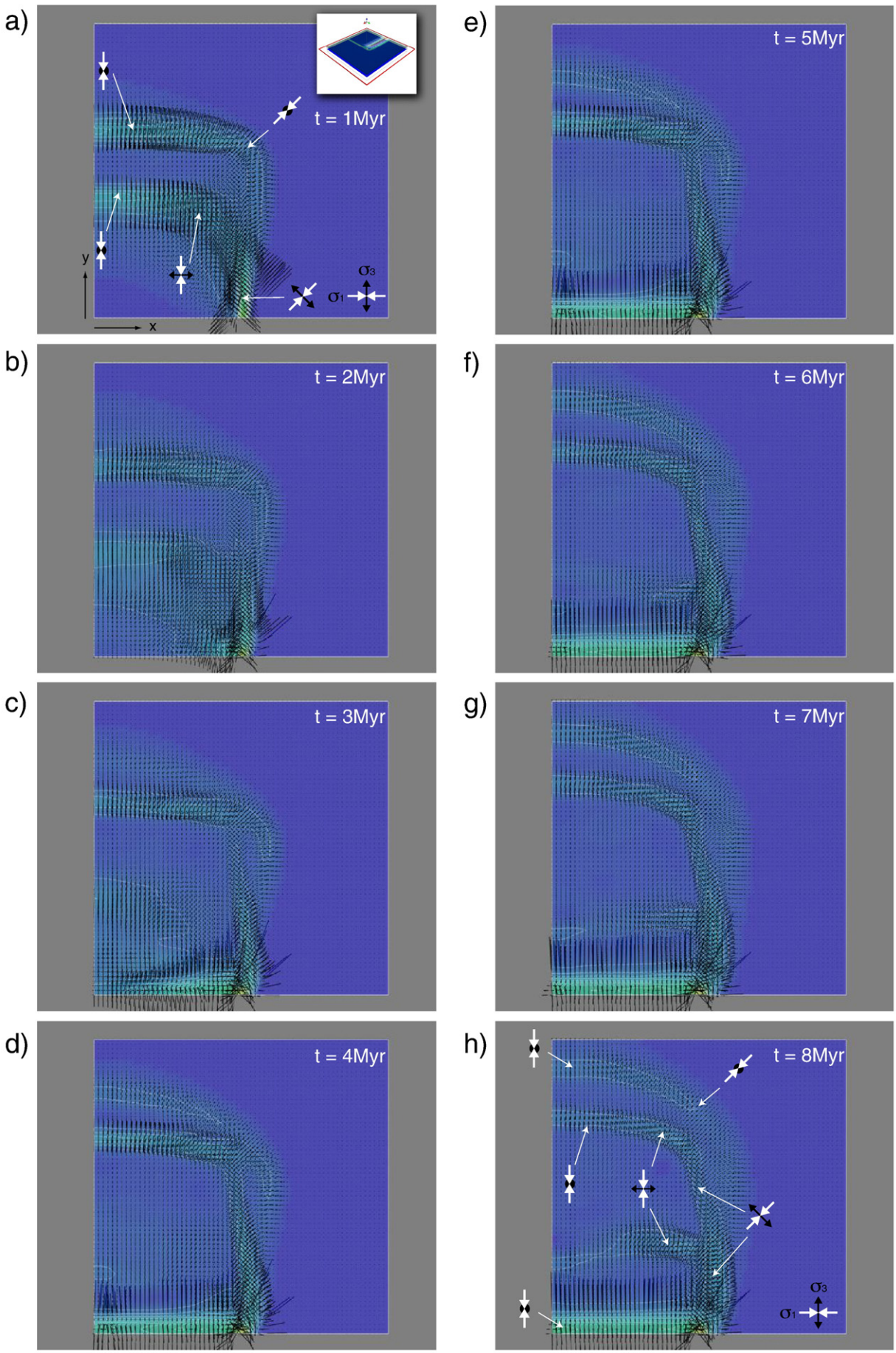
a)
t = 1Myr
y
x
σ3
σ1
b)
t = 2Myr
c)
t = 3Myr
d)
t = 4Myr
e)
t = 5Myr
f)
t = 6Myr
g)
t = 7Myr
h)
t = 8Myr
σ3
σ1

6. Conclusions

We have shown that three-dimensional effects arising from the finite width of an orogenic wedge are complex and certainly not intuitive. Most noticeable are two structures: (a) the curved section of the retro-shear zone around the edge of the imposed velocity discontinuity and (b), antithetic to it, the complex hinge structure that accommodates the change in velocity direction resulting from a kink in the retro-shear zone and the lateral escape of crustal material, which, in turn, are both the product of the finite amplitude topography that has developed in the model experiment characterized by low surface processes efficiency. The geometry and nature (sense of movement) of these structures could not be predicted from a simple stress balance argument as may be the case in a simple two-dimensional critical wedge. Our results therefore demonstrate the power of the numerical model we have used which provides unprecedented insight into the dynamics of orogenic systems. To be able to predict the formation and evolution of complex three-dimensional structures, to display their three-dimensional geometry, their interactions with each other and the free evolving surface and, finally, to compute and display the orientation of the stress or strain rate principal axes with accuracy is an exciting novel development. The theoretical insight that is gained complements what could be observed in the field or in an analogue experiment. Our numerical model, and the results of the computations made with it, should therefore be regarded as tools to help the structural geologist interpret observations in similar geological settings but in a broad range of environments and geometries/scales. Although some scaling issues regarding the balance between topographically generated gravitational stress gradients and the intrinsic strength of crustal rocks should be considered before applying our results to any given geological setting, one could consider using them to interpret the formation and evolution of complex three-dimensional structures at the scale of a small orogen down to that of a single sedimentary decollement.

We also note that major differences among model results originate in the assumed efficiency of the surface processes. Where surface processes are not efficient and relatively high topography develops at the surface of the model, the main thrust structures are kinked and antithetic hinge structures form. On the contrary, thrust faults are planar and no hinge develops when surface processes are efficient and the topography remains modest. Lowering the intrinsic strength of the crust by increasing the basal temperature and activating dislocation creep, makes the system more responsive to the loading/unloading effect of surface topography. In this situation, we have shown that the system rapidly evolves towards a widening of the region of active deformation with the formation of offset structures on either side of the original thrusts (the retro- and pro-shear zones). This, in turn, causes uplift over a wider area and the formation of a relatively flat inward-draining plateau surrounded by actively eroding mountain belts. Our computations do clearly show the strong couplings that exists between surface processes and crustal deformation, at least at the scale considered here, i.e. 10–100 km.

Acknowledgments

The work described in this paper has been supported by a Post-doctoral Fellowship (P. Y.) and a Chaire d'Excellence (J. B.) awarded by the Agence Nationale de la Recherche (ANR). We thank T. Yamasaki and S. Cox for very useful reviews of this manuscript.

References

Batt, G.E., Braun, J., 1997. On the thermomechanical evolution of compressional orogens. Geophys. J. Int. 128, 364–382.

Beaumont, C., Fullsack, P., Hamilton, J., 1992. Erosional control of active compressional orogens. In: McClay, K.R. (Ed.), Thrust Tectonics. Chapman, New York, pp. 1–18.

Beaumont, C., Munoz, J.A., Hamilton, J., Fullsack, P., 2000. Factors controlling the Alpine evolution of the central Pyrenees inferred from a comparison of observations and geodynamical models. J. Geophys. Res. 105, 8121–8145.

Bernet, M., Zattin, M., Garver, J.I., Brandon, M.T., Vance, J.A., 2001. Steady-state exhumation of the European Alps. Geology 29, 35–38.

Braun, J., 1993. Three-dimensional numerical modelling of compressional orogens: thrust geometry and oblique convergence. Geology 21, 153–156.

Braun, J., Beaumont, C., 1989. Dynamical models of the role of crustal shear zones in asymmetric continental extension. Earth Planet. Sci. Lett. 93, 405–423.

Braun, J., Beaumont, C., 1995. Three-dimensional numerical experiments of strain partitioning at oblique plate boundaries: implications for contrasting tectonic styles in the southern Coast Ranges, California and central South Island, New Zealand. J. Geophys. Res. 100, 18,059–18,074.

Braun, J., Sambridge, M., 1997. Modelling landscape evolution on geological time scales: a new method based on irregular spatial discretization. Basin Res. 9, 27–52.

Braun, J., Pauselli, C., 2004. Tectonic evolution of the Lachlan Fold Belt (Southeastern Australia): constraints from coupled numerical models of crustal deformation and surface erosion driven by subduction of the underlying mantle. Phys. Earth Planet. Inter. 141, 281–301.

Braun, J., Sambridge, M., 1994. Dynamical Lagrangian Remeshing (DLR): a new algorithm for solving large strain deformation problems and its application to fault-propagation folding. Earth Planet. Sci. Lett. 124, 211–220.

Braun, J., Heimsath, A.J., Chappell, J., 2001. Sediment transport mechanisms on soil-mantled hillslopes. Geology 29, 683–686.

Braun, J., Thieulot, C., Fullsack, P., Dekool, M., Beaumont, C., Huismans, R., 2008. DOUAR: a new three-dimensional creeping flow numerical model for the solution of geological problems. Phys. Earth Planet. Inter. 171, 76–91.

Dahlen, F.A., 1984. Noncohesive critical coulomb wedges: an exact solution. J. Geophys. Res. 89, 10,125–10,133.

Ellis, S., Beaumont, C., Jamieson, R.A., Quinlan, G., 1998. Continental collision including a weak zone: the vise model and its application to the Newfoundland Appalachians. Can. J. Earth Sci. 35, 1323–1346.

Gerbault, M., Davey, F., Henrys, S., 2002. Three dimensional lateral crustal thickening in continental oblique collision: an example from the Southern Alps, New Zealand. Geophys. J. Int. 150, 770–779.

Jamieson, R.A., Beaumont, C., 1988. Orogeny and metamorphism—a model for deformation and pressure–temperature–time paths with application to the Central and Southern Appalachians. Tectonics 7, 417–445.

Konstantinovskaia, E., Malavieille, J., 2005. Erosion and exhumation in accretionary orogens: experimental and geological approaches. Geochem. Geophys. Geosyst. 60 (2). doi:10.1029/2004GC000794.

Kooi, H., Beaumont, C., 1994. Escarpment evolution on high-elevation rifted margins: insights derived from a surface processes model that combines diffusion, advection and reaction. J. Geophys. Res. 99, 12,191–12,209.

Kooi, H., Beaumont, C., 1996. Large-scale geomorphology: classical concepts reconciled and integrated with contemporary ideas via a surface processes model. J. Geophys. Res. 101, 3361–3386.

Koons, P.O., 1990. Two-sided orogen: collision and erosion from the sandbox to the Southern Alps, New Zealand. Geology 18, 679–682.

Koons, P.O., 1994. Three-dimensional critical wedges: tectonics and topography in oblique collisional orogens. J. Geophys. Res. 99, 12,301–12,315.

Malavielle, J., 1984. Modélisation expérimentale des chevauchements imbriqués: application aux chaînes de montagnes. Bull. Soc. Geol. Fr. 26, 129–138.

Tullis, J., 2002. Deformation of granitic rocks: experimental studies and natural examples. In: Karato, S.-I., Wenk, H.-R. (Eds.), Plastic Deformation of Minerals and Rocks: Review in Mineralogy and Geochemistry, vol. 51, pp. 51–95.

Vanbrabant, Y., Braun, J., Yongmans, D., 2002. Models of passive margin inversion: implications for the Rhenohercynian fold-and-thrust belt, Belgium and Germany. Earth Planet. Sci. Lett. 202, 15–29.

van der Beek, P.A., Braun, J., 1998. Numerical modelling of landscape evolution on geological time scales: a parameter analysis and comparison with the southeastern highlands of Australia. Basin Res. 10, 49–68.

Whipple, K.X., Meade, B.J., 2004. Controls on the strength of coupling among climate, erosion, and deformation in two-sided, frictional orogenic wedges at steady state. J. Geophys. Res. 109, F01011. doi:10.1029/2003JF000019.

Whipple, K.X., Meade, B.J., 2006. Orogen response to changes in climatic and tectonic forcing. Earth Planet. Sci. Lett. 243, 218–228.

Willett, S.D., 1999a. Orogeny and orography: the effects of erosion on the structure of mountain belts. J. Geophys. Res. 104, 28,957–28,981.

Willett, S.D., 1999b. Rheological dependence of extension in wedge models of convergent orogens. Tectonophysics 305, 419–435.

Willett, S.D., Brandon, M.T., 2002. On steady states in mountain belts. Geology 30, 175–178.

Willett, S.D., Beaumont, C., Fullsack, P., 1993. Mechanical model for the tectonics of doubly-vergent compressional orogens. Geology 21, 371–374.

Willett, S.D., Slingerland, R., Hovius, N., 2001. Uplift, shortening, and steady state topography in active mountain belts. Am. J. Sci. 301, 455–485.

C. R. Geoscience 343 (2011) 443–453

Contents lists available at ScienceDirect

Comptes Rendus Geoscience

www.sciencedirect.com

Petrology, geochemistry

New U-Pb zircon and $^{40}Ar/^{39}Ar$ muscovite age constraints on the emplacement of the Lizio syn-tectonic granite (Armorican Massif, France)

Nouveaux âges U-Pb sur zircon et $^{40}Ar/^{39}Ar$ sur muscovite de mise en place du granite syn-tectonique de Lizio (Massif Armoricain, France)

Romain Tartèse [a,*], Marc Poujol [a], Gilles Ruffet [a,b], Philippe Boulvais [a], Philippe Yamato [a], Jan Košler [c]

[a] *UMR CNRS 6118 géosciences, université de Rennes 1, 35042 Rennes cedex, France*
[b] *CNRS (CNRS/INSU), UMR 6118, géosciences Rennes, 35042 Rennes cedex, France*
[c] *Department of Earth Science and Centre for Geobiology, University of Bergen, 5007 Bergen, Norway*

ARTICLE INFO

Article history:
Received 10 June 2011
Accepted after revision 18 July 2011
Available online 25 August 2011

Presented by Zdenek Johan

Keywords:
$^{40}Ar/^{39}Ar$ dating
Armorican Massif
Lizio granite
South Armorican Shear Zone
U-Pb dating
France

Mots clés :
Datation $^{40}Ar/^{39}Ar$
Massif Armoricain
Granite de Lizio
Cisaillement Sud-Armoricain
Datation U-Pb
France

ABSTRACT

LA-ICP-MS U-Pb analyses performed on zircon grains from the Lizio granite yielded an emplacement age of 316 ± 6 Ma. Typical S-C structures show that the Lizio granite was emplaced contemporaneously with dextral shearing along the northern branch of the South Armorican Shear Zone and that it was therefore active at that time. $^{40}Ar/^{39}Ar$ analyses performed on muscovite grains yielded plateau dates ranging between 311.5 and 308.2 Ma. Muscovite chemistry is typical of primary magmatic muscovite, which precludes a late fluids-induced resetting of the K-Ar isotopic system. $^{40}Ar/^{39}Ar$ dates thus likely correspond to the cooling ages below the argon closure temperature. Considering the uncertainties on the measured ages, we can propose that either the Lizio granite cooled down quickly in less than a million of years or that it remained in a hot environment for several millions of years after its emplacement. This latter scenario could have been sustained by shear heating during dextral shearing along the northern branch of the South Armorican Shear Zone.

RÉSUMÉ

Les analyses U-Pb réalisées sur des zircons du granite de Lizio par LA-ICP-MS ont livré un âge de mise en place de 316 ± 6 Ma. Des structures C-S caractéristiques démontrent que le granite de Lizio s'est mis en place pendant le cisaillement dextre le long de la branche nord du Cisaillement Sud Armoricain, qui était donc toujours actif à cette époque. Les analyses $^{40}Ar/^{39}Ar$ réalisées sur les muscovites ont donné des âges plateaux allant de 311,5 à 308,2 Ma. La chimie des muscovites est typique de celle d'une muscovite magmatique primaire, ce qui écarte une remise à zéro tardive, induite par des fluides, du système isotopique K-Ar. Ces dates $^{40}Ar/^{39}Ar$ correspondent donc probablement à des âges de refroidissement sous la température de fermeture de l'argon. En tenant compte des incertitudes sur les âges obtenus, cela implique, soit un refroidissement rapide du granite de Lizio en moins d'un million d'années, soit que le granite est resté dans un environnement chaud pendant plusieurs millions d'années après sa mise en place, grâce à la chaleur frictionnelle produite pendant le cisaillement dextre le long du Cisaillement Sud Armoricain.

* Corresponding author.
E-mail address: romain.tartese@univ-rennes1.fr (R. Tartèse).

1631-0713/$ – see front matter
doi:10.1016/j.crte.2011.07.005

1. Introduction

In the continental crust, granitic plutons emplace at different stages during the evolution of an orogen. In the Armorican Variscan belt, numerous peraluminous granites were emplaced during the Carboniferous (e.g. Bernard-Griffiths et al., 1985). Most of these granites are spatially associated with the dextral lithospheric-scale South Armorican Shear Zone (SASZ). Moreover, emplacement of these granites is often coeval with shearing as indicated by the S-C structures they display (Berthé et al., 1979; Gapais, 1989). The precise dating of these synkinematic granites and of their cooling history is therefore an essential tool to place time constraints on the different tectono-thermal events that occur during the life of the Variscan orogen.

So far, available geochronological data on the emplacement of these granites are solely provided by whole rock Rb-Sr isochron ages (Bernard-Griffiths et al., 1985; Peucat et al., 1979). Along the northern branch of the SASZ, three granitic massifs are assumed to have emplaced synkinematically around 344–337 ± 13–8 Ma, which implies that the shear zone was active during the Lower Visean. In order to better constrain dextral shearing along the northern branch of the SASZ, we have performed new zircon U-Pb and muscovite $^{40}Ar/^{39}Ar$ datings.

2. Geological framework

During Variscan times, the Armorican Massif has undergone deformation related to a major continental collision between Gondwana and Laurussia (e.g. Ballèvre et al., 2009). This episode was followed by the development of dextral shear zones that can be traced over a distance of a couple of hundred of kilometres, namely the North Armorican Shear Zone (NASZ) and the SASZ (Fig. 1a). The SASZ separates two distinct domains within the Armorican Massif that are characterized by contrasted metamorphic and structural histories. To the south, the South Armorican domain (SAD) is mainly composed of deep crustal units (medium to high-grade micaschists, migmatitic gneisses and anatectic granites) that have been exhumed during the extension associated with the chain collapse (e.g. Brown and Dallmeyer, 1996; Gapais et al., 1993; Turrillot et al., 2009). To the north, the central Armorican domain (CAD) is made of a Late Proterozoic–

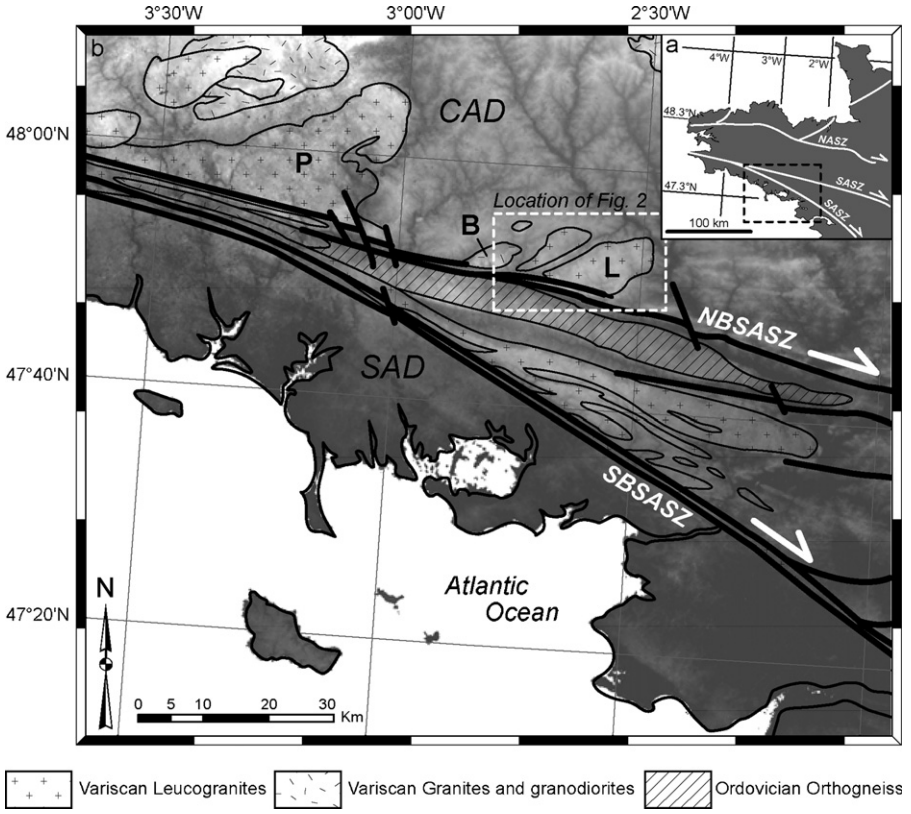

Fig. 1. (a) Location of the studied area in the Armorican Massif. NASZ: North Armorican Shear Zone; SASZ: South Armorican Shear Zone. (b) Simplified geological map of the studied area showing the plutonic intrusions. NBSASZ and SBSASZ are the northern and southern branches of the South Armorican Shear Zone, respectively. P, B and L are the Pontivy, Bignan and Lizio granites, respectively. CAD and SAD are the central and South Armorican domains, respectively.

Fig. 1. (a) Localisation de la zone d'étude dans le Massif Armoricain. NASZ: Cisaillement Nord-Armoricain; SASZ : Cisaillement Sud-Armoricain. (b) Carte géologique simplifiée de la zone d'étude représentant les intrusions plutoniques. NBSASZ et SBSASZ sont respectivement les branches nord et sud du Cisaillement Sud Armoricain. P, B et L sont les granites de Pontivy, Bignan et Lizio, respectivement. CAD et SAD sont respectivement les domaines centre et Sud Armoricain.

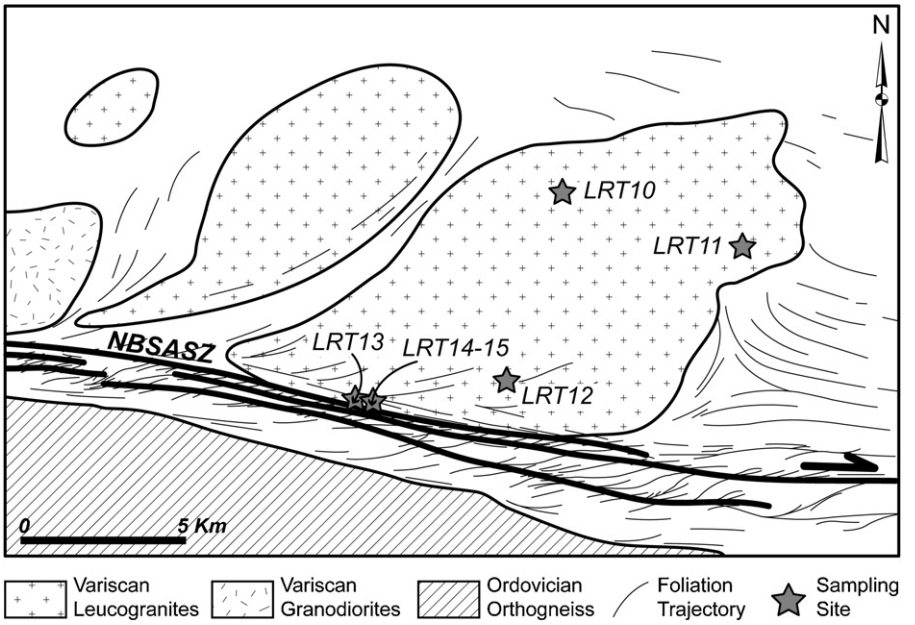

Fig. 2. Simplified geological map of the Lizio granite (after Berthé, 1980).

Fig. 2. Carte géologique simplifiée du granite de Lizio (d'après Berthé, 1980).

Early Palaeozoic sedimentary succession, which has been affected by low-grade metamorphism (e.g. Le Corre et al., 1991). In the CAD, both strain intensity (Gumiaux et al., 2004), metamorphic degree (Le Corre et al., 1991) and evidence of fluid flow (Gloaguen et al., 2007; Lemarchand et al., 2011) increase southward reaching a maximum on the SASZ itself.

The SASZ is geometrically defined by ca. 100–1000 m wide zone of highly strained mylonitic rocks (Jégouzo, 1980; Tartèse et al., 2011a). In details, the SASZ is divided into two main branches (Fig. 1a). In the southern branch network (SBSASZ), the mylonitic foliation bears a 5–10° eastward dipping stretching lineation. Along this branch, a dextral displacement of ca. 150 to 200 km has been proposed based on the width of the mylonitized rocks (Jégouzo and Rossello, 1988). The northern branch (NBSASZ) is sublinear and extends for about 300 km. It displays a subvertical mylonitic foliation also bearing a stretching lineation dipping at ca. 10° eastward. Along this branch, a 40 km minimal dextral offset has been estimated from geometrical reconstructions (Jégouzo and Rossello, 1988).

The Lizio two-mica granite was emplaced along the NBSASZ (Fig. 1b). This granitic massif is highly emblematic because it represents the *locus typicus* where S-C structures were first described as resulting from a single deformational event (Berthé et al., 1979). These structures indicate that the Lizio granite was emplaced during shearing along the NBSASZ. Indeed, "S-planes" correspond to shearing planes which localized the dextral deformation. These "S-planes" are vertical and their orientation mimics that of the NBSASZ. "C-planes" correspond to cleavage planes. These "C-planes" rotate during non-coaxial shearing. They define an angle of around 45° with "S-planes" in slightly deformed samples, angle which decreases with increasing strain until parallelisation of "S-planes" and "C-planes" in ultramylonitized samples (Berthé et al., 1979). According to Gapais (1989), these S-C structures developed during cooling of intrusives at temperatures around 550 °C. The synkinematic characteristics of the Lizio granite emplacement are also evidenced by the triple-point defined by the foliation around the intrusion (Fig. 2). This triple-point formed by the combination of the regional stress and the stress related to the granite emplacement.

Whole rock Rb-Sr data obtained on the Lizio granite define a 338 ± 13 Ma isochron age (2σ) interpreted as the granite emplacement age (Peucat et al., 1979). This age is similar within error to the 344 ± 8 Ma and 337 ± 13 Ma ages (2σ) obtained by these authors on the Pontivy and Bignan synkinematic massifs, both located a couple of kilometres westward and also rooted into the NBSASZ (Fig. 1b). More recently, a zircon U-Pb emplacement age of 316 +5/−3 Ma (ID-TIMS, Béchennec et al., 2001) has been obtained on the St-Thurien metagranite ca. 250 m south of the NBSASZ (3°40'23"W; 47°57'50"N). This St-Thurien metagranite is highly sheared and displays characteristic S-C structures, with subvertical "S-planes" and "C-planes" oriented N105-110° and ca. N080°, respectively (Béchennec et al., 2001). The St-Thurien metagranite is thus synkinematic with dextral shearing along the NBSASZ, which indicates that shearing continued after 330–325 Ma.

The geochemistry of the Lizio two-mica granite has been studied in details by Tartèse and Boulvais (2010). This study provided mineral and whole rock geochemical data as well as new Rb-Sr, Sm-Nd and O isotope data which are consistent with the few data published by Bernard-Griffiths et al. (1985). The Lizio granite is highly silicic, poor in ferromagnesian and was formed by partial melting of a metasedimentary source. Geochemical data show that

a subtle magmatic differentiation occurred by crystal fractionation from the melt (Tartèse and Boulvais, 2010). Finally the Lizio granite intruded Brioverian metapelites of the CAD. During its emplacement in the Brioverian metapellites, a syntectonic paragenesis of Bt + Ms + Chl + St + Grt ± And developed (Berthé, 1980; mineral abbreviations are after Whitney and Evans, 2010), corresponding to the facies 2b of Pattison and Tracy (1991) and to a pressure of around 4 kbar (Pattison et al., 1999).

3. Samples description

3.1. Petrography

A full petrographic description of the samples presented in this study, as well as mineral and whole-rock geochemical data, and oxygen isotope data are given in Tartèse and Boulvais (2010). To summarize, in the Lizio two-mica granite, quartz and feldspar (orthoclase, microcline and plagioclase) represent around 90% of the mineral assemblage (Fig. 3) while biotite and muscovite represent the remaining 10%, biotite being generally more abundant than muscovite. Accessory minerals are apatite, zircon and monazite.

In undeformed samples, quartz is large and often euhedral (Fig. 3a–b) whereas it is recrystallized in ribbons in deformed samples (Fig. 3c–d). Plagioclase is euhedral to subeuhedral and shows thin polysynthetic twinning. Alkali feldspar is generally subeuhedral. Microcline and orthoclase generally displays well-expressed tartan and Carlsbad twinning, respectively. Pleochroic biotite forms euhedral brown-reddish flakes (Fig. 3a–b) and hosts most of the accessory minerals (Fig. 3b). Muscovite usually forms large flakes, some of them having a fish-like habit due to shearing (Fig. 3c). In deformed samples, shear bands are usually localized in small biotite and muscovite grains aggregates (Fig. 3c–d).

3.2. Mineral chemistry

Analytical procedure for electron microprobe analysis of minerals are detailed in Pitra et al. (2008) and Tartèse and Boulvais (2010). K-feldspar is close to the orthose endmember (Or = 91–92 mol.%) and plagioclase is albite on average (Ab = 91 mol.%). Biotite composition is homogeneous in the investigated samples and typical of peraluminous granites (Tartèse and Boulvais, 2010). Concerning muscovite, complementary electron microprobe data have been acquired, compared to the dataset published in Tartèse and Boulvais (2010), as muscovite is the mineral chosen for $^{40}Ar/^{39}Ar$ dating in this study. Only data obtained on large muscovite phenocrysts are reported in Table 1 and displayed in Fig. 4. Muscovite grains have a homogeneous chemical composition with FeO = 1.1–1.4 wt.%, MgO = 0.8–0.9 wt.% and Na_2O = 0.5–0.7 wt.% (Table 1). They also have a high TiO_2 content (0.6–

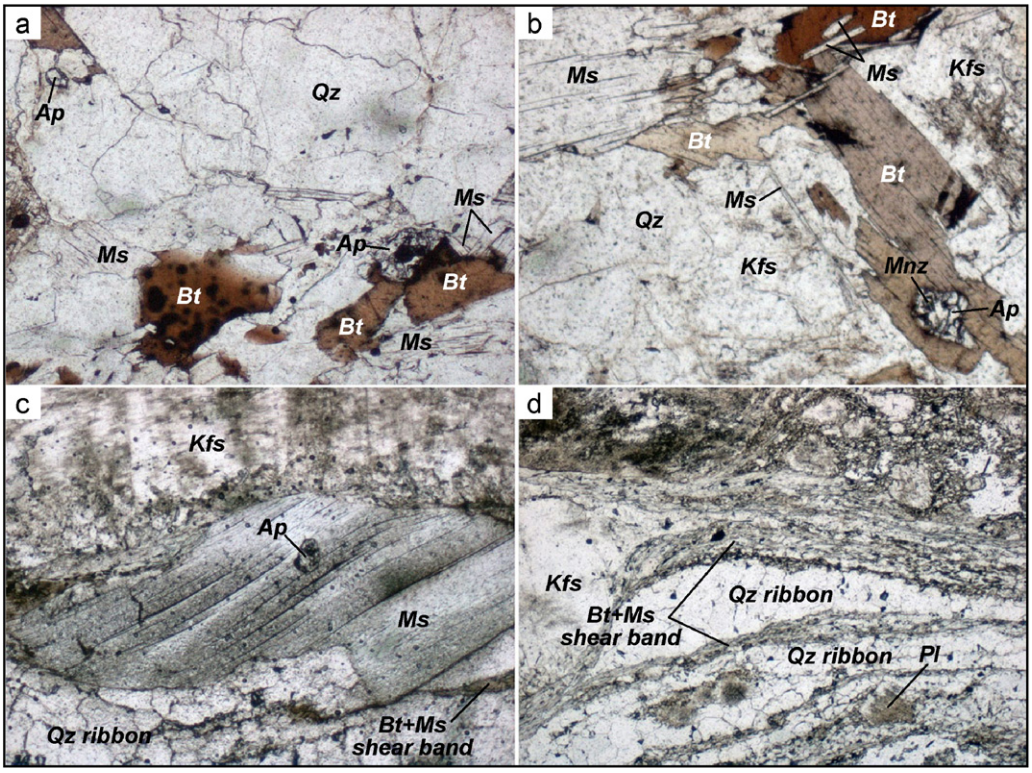

Fig. 3. Photomicrographs showing the typical structures of the Lizio granite samples, from undeformed (a and b) to mylonitized (c and d). Mineral abbreviations are after Whitney and Evans (2010).

Fig. 3. Microphotographies montrant les structures typiques des échantillons du granite de Lizio, depuis les échantillons non déformés (a et b) jusqu'aux échantillons mylonitisés (c et d). Les abréviations des minéraux sont celles de Whitney et Evans (2010).

Table 1
Average chemical compositions of muscovite.

Tableau 1
Compositions chimiques moyennes des muscovites.

	MUSCOVITE									
	LRT15 (n = 16)	sd	LRT10 (n = 19)	sd	LRT11 (n = 10)	sd	LRT12 (n = 14)	sd	LRT14 (n = 15)	sd
SiO_2	46.5	0.3	45.7	0.4	46.4	0.2	45.7	0.5	46.1	0.3
TiO_2	1.1	0.2	0.7	0.2	0.6	0.2	1.1	0.2	1.0	0.2
Al_2O_3	34.5	0.2	35.8	0.3	35.0	0.3	34.7	0.5	34.9	0.4
FeO	1.4	0.1	1.1	0.1	1.2	0.2	1.3	0.1	1.4	0.1
MgO	0.9	0.1	0.8	0.1	0.8	0.1	0.8	0.1	0.8	0.1
Na_2O	0.5	0.1	0.7	0.1	0.6	0.1	0.5	0.1	0.5	0.1
K_2O	11.0	0.2	10.8	0.2	10.7	0.6	11.2	0.3	11.1	0.2
SUM	95.8		95.6		95.3		95.4		95.8	
Structural formula based on 22 oxygen atoms										
Si	6.17	0.02	6.08	0.02	6.17	0.03	6.11	0.04	6.13	0.02
Ti	0.11	0.02	0.07	0.02	0.06	0.02	0.11	0.02	0.10	0.02
Al	5.40	0.03	5.61	0.03	5.49	0.03	5.48	0.06	5.47	0.05
Fe	0.16	0.01	0.13	0.01	0.14	0.02	0.15	0.01	0.15	0.01
Mg	0.18	0.01	0.15	0.01	0.15	0.02	0.16	0.02	0.17	0.02
Na	0.12	0.02	0.19	0.03	0.15	0.04	0.14	0.03	0.14	0.03
K	1.86	0.04	1.84	0.04	1.83	0.09	1.91	0.04	1.88	0.03
SUM	14.00		14.06		13.99		14.06		14.04	

Oxide contents in wt.% and cationic contents in apfu. sd: standard deviation.

1.1 wt.% on average, Table 1) and consistently fall in the primary magmatic muscovite field in the Mg-Ti-Na ternary diagram (Miller et al., 1981; Fig. 4a). In the Mg + Fe against Si plot (Fig. 4b), muscovite analyses are clustered showing that limited phengitic substitution occurred in the studied samples.

4. Geochronological results

4.1. Zircon U-Pb dating

Zircon U-Pb data were obtained in situ by laser ablation inductively coupled plasma mass spectrometry (LA-ICP-MS) performed at the Centre for Element and Isotope Analysis, University of Bergen, Norway. A classical mineral separation procedure has been followed to concentrate zircon grains suitable for U-Pb dating from samples LRT10, LRT12 and LRT15, these three samples representing undeformed, deformed and mylonitized end-members in the rock collection. Rocks were crushed and the powder fractions with a diameter $< 250\ \mu m$ have been isolated. Heavy minerals were successively concentrated by Wilfley table and heavy liquids procedures. Magnetic minerals were then removed with an isodynamic Frantz separator. Zircon grains were carefully examined under a binocular microscope, selected, and embedded in epoxy mounts. Then grains were hand-grounded and polished on a lap wheel with 6 μm and 1 μm diamond suspension successively. They were imaged in transmitted and reflected light, and their internal structure has been revealed using SEM BSE imaging at the LaSalle Institute, Beauvais, France.

Before analysis, grain mounts were cleaned using a weak HNO_3 solution and rinsed several times using Millipore water and ethanol in an ultrasonic bath. They

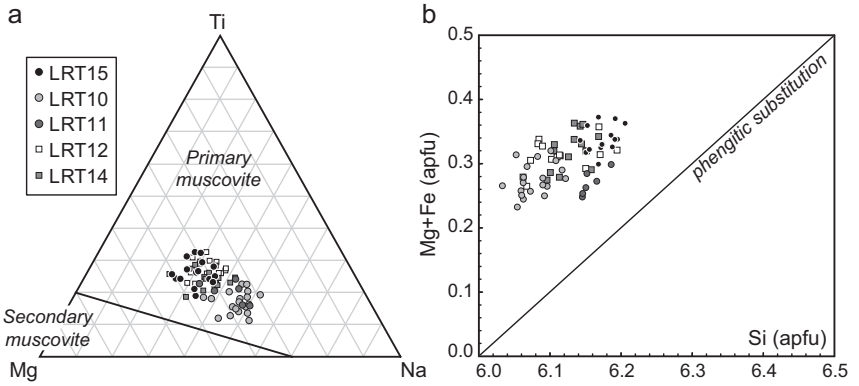

Fig. 4. (a) Muscovite chemical compositions plotted in the ternary Mg-Ti-Na diagram of Miller et al. (1981). (b) Mg + Fe (apfu) vs. Si (apfu) content of muscovite showing the extent of phengitic substitution.

Fig. 4. (a) Compositions chimiques des muscovites représentées dans le diagramme ternaire Mg-Ti-Na de Miller et al. (1981). (b) Teneurs Mg + Fe (apfu) vs. Si (apfu) des muscovites illustrant l'étendue de la substitution phengitique.

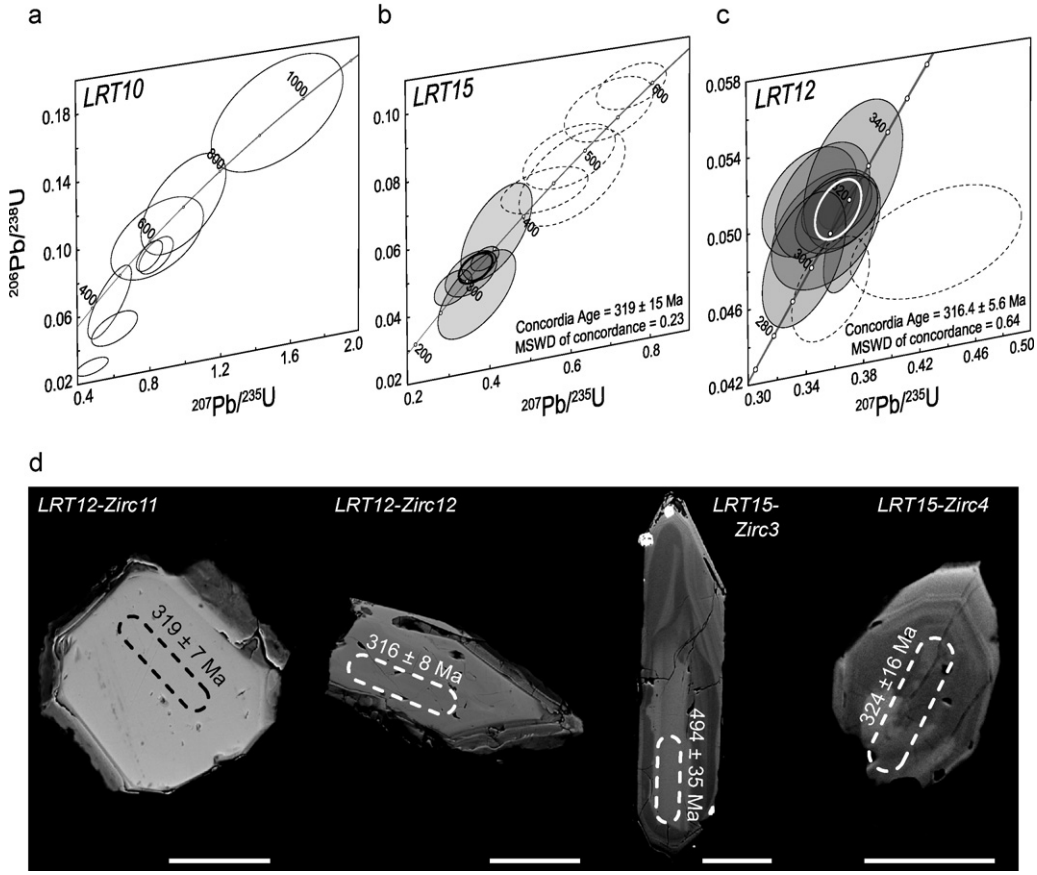

Fig. 5. (a) Wetherill concordia diagram for zircon data from the sample LRT10. (b) Wetherill concordia diagram for zircon data from the sample LRT15. (c) Wetherill concordia diagram for zircon data from the sample LRT12. In these diagrams, error ellipses are at 1σ. Concordia ages have been calculated with the ellipses in grey and include decay constants errors. (d) SEM BSE images of zircon grains from samples LRT12 and LRT15 with LA-ICP-MS analyzed rasters (dotted zones) and obtained $^{206}Pb/^{238}U$ dates. For all the grains, the scale bar represents 50 μm.

Fig. 5. (a) Diagramme concordia Wetherill pour les données des zircons de l'échantillon LRT10. (b) Diagramme concordia Wetherill pour les données des zircons de l'échantillon LRT15. (c) Diagramme concordia Wetherill pour les données des zircons de l'échantillon LRT12. Dans ces diagrammes, les ellipses d'incertitude sont à 1σ. Les âges concordia ont été calculés avec les ellipses en gris et incluent les incertitudes sur les constantes de désintégration. (d) Images MEB rétrodiffusées de grains de zircon des échantillons LRT12 et LRT15, avec les zones analysées (en pointillés) par LA-ICP-MS et les dates $^{206}Pb/^{238}U$ obtenues. L'échelle représente 50 μm pour tous les grains.

were then mounted in the laser ablation cell together with several standards for quality control. A 213 Nd-YAG laser (New Wave UP-213) was used coupled to a single-collector, double focusing magnetic sector ICP-MS system (Thermo Finnigan Element 2). Data have been plotted in Wetherill concordia diagrams using the software Isoplot/Ex (Ludwig, 2008). In Fig. 5, data are plotted with their uncertainties at 1σ. Results are reported in the Table 2 where uncertainties are listed at 1σ. When ages are calculated, all errors are reported at the 2σ confidence level.

Zircon grains were ablated using a laser beam of ca. 15 μm in diameter that was rastered over the sample surface to create a line of ca. 50 μm in length depending on the grain size. The laser energy was set at 5 $J.cm^{-2}$ with a repetition rate of 10 Hz. Together with the sample introduction, the system allowed the simultaneous nebulization of an internal standard tracer solution following the technique described by Košler et al. (2002) and Košler and Sylvester (2003). Zircon data were collected on unknown zircon grains and three zircon standards, 91500 (1065 Ma; Wiedenbeck et al., 1995), Plešovice (337 Ma; Sláma et al., 2008) and GJ-1 (609 Ma; Jackson et al., 2004). Typically 10–15 unknowns were collected for every 7 analyses of the standards. Analysing and treating the zircon standards as unknowns is a robust quality control procedure that allows assessment of the accuracy and precision of the technique during an analytical session. Analyses done on the Plešovice and GJ-1 zircon standards yielded concordant ages of 335 ± 4 Ma ($n = 12$; MSWD = 1.13) and 603 ± 11 Ma ($n = 9$; MSWD = 0.30). Raw data were processed offline using an Excel spreadsheet-based program (Lamdate; Košler et al., 2008).

BSE images of zircon grains from sample LRT12 revealed unzoned grey cores surrounded by thin darker rims, without evidence of inherited cores (Fig. 5d). In sample LRT15, zircon grains display a more pronounced oscillatory zoning where dark cores are surrounded by

Table 2
Zircon U-Pb isotopic data. All uncertainties are at 1σ.

Tableau 2
Données isotopiques U-Pb sur zircon. Les incertitudes sont à 1σ.

Sample, grain, spot	Isotopic ratios						Rho	Calculated ages (Ma)					
	$^{207}Pb/^{235}U$	±	$^{206}Pb/^{238}U$	±	$^{207}Pb/^{206}Pb$	±		$^{206}Pb/^{238}U$	±	$^{207}Pb/^{235}U$	±	$^{207}Pb/^{206}Pb$	±
LRT10 - Zircon													
Zirc1.2	0.8456	0.1709	0.0986	0.0150	0.0618	0.0063	0.38	606	88	622	94	667	220
Zirc2.1	1.5298	0.2502	0.1619	0.0217	0.0695	0.0065	0.41	967	120	942	100	915	192
Zirc3.1	0.8374	0.0634	0.0885	0.0067	0.0729	0.0084	0.50	547	40	618	35	1011	233
Zirc4.1	0.5790	0.0799	0.0656	0.0134	0.0634	0.0082	0.74	410	81	464	51	723	275
Zirc5.1	0.9942	0.1581	0.1165	0.0185	0.0581	0.0065	0.50	710	107	701	81	532	245
Zirc7.1	0.6049	0.0842	0.0494	0.0061	0.0891	0.0086	0.45	311	38	480	53	1406	184
Zirc7.2	0.8016	0.0485	0.0889	0.0057	0.0612	0.0031	0.53	549	33	598	27	645	107
Zirc8.1	0.4803	0.0583	0.0290	0.0031	0.1430	0.0120	0.44	184	19	398	40	2264	145
LRT12 - Zircon													
Zirc2.1	0.4324	0.0406	0.0478	0.0019	0.0664	0.0051	0.21	301	11	365	29	819	159
Zirc4.1	0.3640	0.0102	0.0509	0.0009	0.0507	0.0014	0.33	320	6	315	8	227	65
Zirc5.1	0.3711	0.0125	0.0490	0.0019	0.0538	0.0015	0.59	308	12	320	9	363	62
Zirc6.1	0.3542	0.0251	0.0495	0.0020	0.0528	0.0032	0.29	312	12	308	19	320	138
Zirc7.1	0.3429	0.0219	0.0511	0.0018	0.0501	0.0021	0.28	322	11	299	17	198	100
Zirc8.1	0.3519	0.0218	0.0511	0.0019	0.0503	0.0022	0.31	321	12	306	16	211	102
Zirc8.2	0.3734	0.0230	0.0522	0.0025	0.0527	0.0022	0.39	328	15	322	17	315	93
Zirc9.1	0.3571	0.0179	0.0463	0.0018	0.0562	0.0026	0.38	292	11	310	13	460	102
Zirc11.1	0.3618	0.0162	0.0507	0.0011	0.0524	0.0023	0.25	319	7	314	12	302	101
Zirc12.1	0.3616	0.0191	0.0502	0.0013	0.0540	0.0022	0.24	316	8	313	14	373	91
Zirc13.1	0.3387	0.0192	0.0481	0.0023	0.0524	0.0016	0.42	303	14	296	15	303	71
LRT15 - Zircon													
Zirc1.1	0.4161	0.0578	0.0607	0.0090	0.0516	0.0056	0.53	380	54	353	41	268	250
Zirc2.1	0.3675	0.0629	0.0431	0.0080	0.0608	0.0096	0.54	272	50	318	47	634	338
Zirc3.1	0.5965	0.0759	0.0796	0.0059	0.0548	0.0039	0.29	494	35	475	48	405	161
Zirc3.2	0.6041	0.0876	0.0732	0.0088	0.0598	0.0077	0.42	455	53	480	55	596	280
Zirc4.1	0.3682	0.0297	0.0515	0.0026	0.0515	0.0034	0.32	324	16	318	22	262	153
Zirc5.1	0.3531	0.0417	0.0496	0.0042	0.0524	0.0054	0.36	312	26	307	31	304	237
Zirc5.2	0.3871	0.0229	0.0533	0.0022	0.0537	0.0026	0.35	335	13	332	17	357	111
Zirc6.1	0.7527	0.0583	0.0977	0.0042	0.0589	0.0021	0.28	601	25	570	34	564	79
Zirc7.1	0.5352	0.0713	0.0707	0.0041	0.0581	0.0054	0.22	440	25	435	47	533	204
Zirc8.1	0.3093	0.0302	0.0464	0.0032	0.0502	0.0025	0.36	292	20	274	23	204	115
Zirc9.1	0.6964	0.0739	0.0918	0.0059	0.0555	0.0031	0.30	566	35	537	44	432	125

brighter rims (Fig. 5d). Some zircon grains also contain small monazite inclusions (for example in LRT15-Zirc3 in Fig. 5d). In sample LRT10, two analyses are largely discordant and yield therefore meaningless dates (Fig. 5a). From the remaining concordant analyses, one yields a date of ca. 950 Ma, and another five dates are grouped around 600–500 Ma (Fig. 5a). In sample LRT15, the complete dataset of 11 analyses plot in a concordant to subconcordant position (Fig. 5b). Among them, six define an imprecise concordia age of 319 ± 15 Ma (MSWD = 0.23). The five remaining datapoints define dates between ca. 600 and 450 Ma. Finally, in sample LRT12, eleven analyses have been performed (Table 2). When plotted in a Wetherill concordia diagram (Fig. 5c), nine datapoints define a concordia age of 316.4 ± 5.6 Ma (MSWD = 0.64), identical within error with the age recorded by sample LRT15 but more precise.

4.2. Muscovite $^{40}Ar/^{39}Ar$ dating

Euhedral to subeuhedral single grains of muscovite, with variably deformed shapes, were handpicked from the 0.25–1.50 mm fraction. Irradiation was performed at the McMaster reactor (Hamilton, Canada) and lasted 43.33 hr (total fluence of 2.6×10^{18} n.cm^{-2}). It was monitored with Taylor Creek Rhyolite (TCR-2) sanidine (28.34 Ma, Renne et al., 1998). Muscovite single grains were analyzed by step-heating with a $^{40}Ar/^{39}Ar$ laser probe, following the procedure described in Ruffet et al. (1991, 1995). Blanks were performed routinely each first or third step, and subtracted from subsequent sample gas fractions. A plateau age is obtained when apparent ages of at least three consecutive steps, representing a minimum of 70% of the ^{39}Ar released, agree within 2σ error bars with the integrated age of the plateau segment. The $^{40}Ar/^{39}Ar$ analytical data are portrayed as age spectra in Fig. 6. All reported uncertainties both in the Fig. 6 and in the text are at the 2σ confidence level.

Single muscovite grains have been analyzed in four samples from the Lizio granite (LRT10, LRT11, LRT13 and LRT15). These samples yielded plateau dates ranging between 311.5 ± 0.4 Ma down to 308.2 ± 0.6 Ma (Fig. 6). They display slight saddle-shaped $^{40}Ar/^{39}Ar$ age spectra that might reflect slight perturbations of the K-Ar isotopic system (e.g. Alexandrov et al., 2002; Cheilletz et al., 1999). An important point is that there is no relationship between the obtained dates and the shearing gradient observed throughout the Lizio granite.

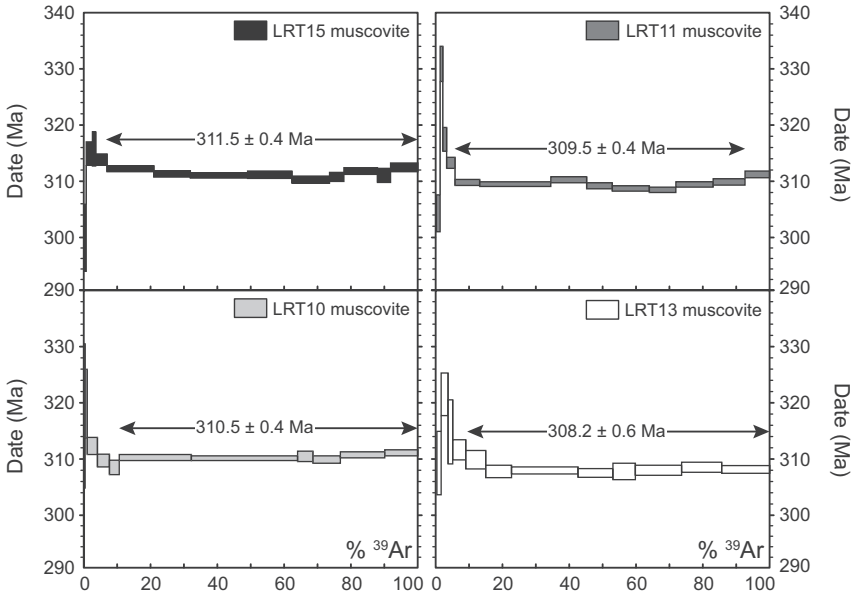

Fig. 6. $^{40}Ar/^{39}Ar$ age spectra of analyzed muscovites. The age error bars for each temperature steps are at the 1σ level. The errors in the J-values are not included. Plateau ages are given with a 2σ uncertainty.

Fig. 6. Spectres d'âges $^{40}Ar/^{39}Ar$ des muscovites analysées. Pour chaque étape de température, les barres d'erreur sur les âges sont à 1σ. Les incertitudes sur les facteurs-J ne sont pas incluses. Les âges plateaux sont donnés avec une incertitude à 2σ.

5. Interpretation and discussion

Considering the high closure temperature for the U-Pb radiogenic system in zircon in excess of 800 °C (Cherniak and Watson, 2001), we interpret the age of 316 ± 6 Ma obtained on sample LRT12 from the synkinematic Lizio granite as its emplacement age along the NBSASZ. The age of 319 ± 15 Ma obtained on sample LRT15 is imprecise but consistent with this emplacement age. Older dates obtained on zircon grains from samples LRT10 and LRT15 illustrate the classical phenomenon of inheritance which often characterizes granitic rocks (e.g. Bea et al., 2007; Harrison et al., 1987; Miller et al., 2003; Roddick and Bevier, 1995). Here, inherited dates mainly range between Neo-Proterozoic and Upper Ordovician times. Concerning the emplacement age of 316 ± 6 Ma, it is identical to the zircon U-Pb emplacement age of 316 +5/–3 Ma of the St-Thurien metagranite found by Béchennec et al. (2001) and contemporaneous with dextral shearing along the NBSASZ. It is also identical to the U-Pb zircon emplacement age obtained recently on the southward Questembert granite by Tartèse et al. (2011b), which is contemporaneous with dextral shearing along the SBSASZ. This new U-Pb emplacement age obtained on the Lizio granite thus indicates that both branches of the SASZ were active at the same time around 315–320 Ma. However, it is younger and does not overlap with the whole rock Rb-Sr isochron age of 337 ± 13 Ma (2σ), previously considered as the emplacement age of the granite (whole rock Rb-Sr isochron, recalculated from the six data of Peucat et al., 1979 and the three data of Tartèse and Boulvais, 2010). So far, all the available geochronological data imply that the NBSASZ has been active from ca. 344 Ma (whole rock Rb-Sr isochron age of the Pontivy granite, Peucat et al., 1979) down to ca. 315 Ma. However, it would be interesting to get new zircon U-Pb data on the other granitic massifs emplaced along the NBSASZ. Indeed, the existing Rb-Sr isochron ages may be too old for these granites. Such old inherited "isochrons" have been described for example by Roddick and Compston (1977) for the crustally-derived Murrumbidgee Batholith, Australia. Moreover, whole rock-mineral isochrons on two samples from the Pontivy granite (whole rock Rb-Sr isochron age of 344 ± 8 Ma) yielded ages identical within error at 311 ± 9 and 310 ± 9 Ma respectively (Peucat et al., 1979), ages that are consistent with a Late Carboniferous emplacement for the Pontivy granite. We thus believe that the ca. 340 Ma old emplacement ages obtained through whole rock Rb-Sr dating of synkinematic granites along the NBSASZ are actually not emplacement ages of these granites but rather represent inherited "isochrons" in the sense of Roddick and Compston (1977). In that case, initiation of dextral shearing along the NBSASZ may not be as old as the ca. 340 Ma age that has been considered so far. Indeed, our data on the Lizio granite give a maximum age of 322 Ma for the activity along the NBSASZ.

$^{40}Ar/^{39}Ar$ dates obtained on muscovite grains from four samples of the Lizio granite range between 311.5 and 308.2 Ma. The two oldest dates are identical within error with the zircon U-Pb emplacement age of 316 ± 6 Ma and involve a subinstantaneous cooling of the intrusion, and the two other dates are slightly younger, considering the uncertainties associated with both techniques. This implies that either the younger muscovite grains have been affected by fluid-induced recrystallization processes after their magmatic isotopic closure (e.g. Villa, 2010) which would have reset the $^{40}Ar/^{39}Ar$ dates, or that the Lizio granite remained sufficiently warm during 2–3 Ma after its emplacement, above the argon closure temperature of muscovite. The muscovite chemistry

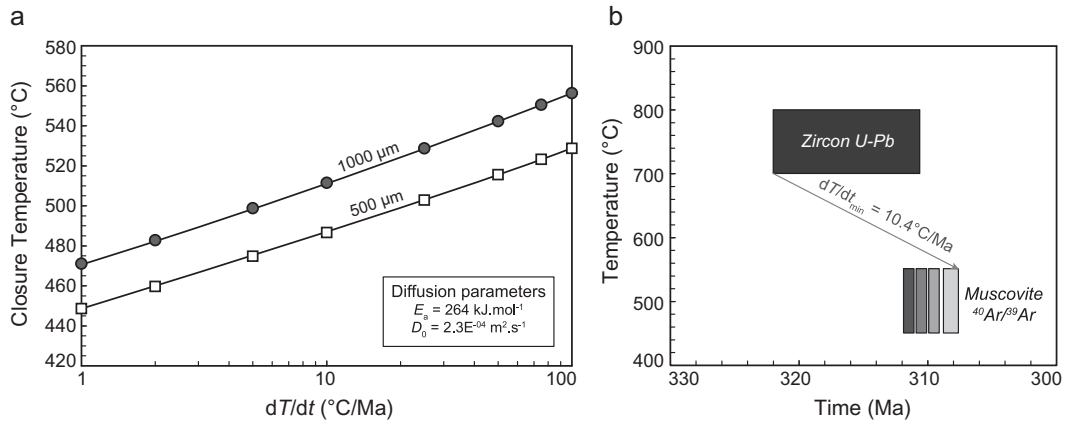

Fig. 7. (a) Computation of muscovite closure temperature (°C) for Ar diffusion against the cooling rate (°C/Ma) for diffusion radius of 0.5 and 1 mm. Parameters used are those of Harrison et al. (2009). (b) Temperature–Time plot for the Lizio granite.

Fig. 7. (a) Calcul de la température de fermeture (°C) pour la diffusion de l'Ar dans la muscovite en fonction du taux de refroidissement (°C/Ma), pour des domaines de diffusion de 0,5 et 1 mm. Les paramètres utilisés sont ceux de Harrison et al. (2009). b) Diagramme Température–Temps pour le granite de Lizio.

shows that all the muscovite grains have a typical primary magmatic composition, which likely precludes the first hypothesis of a fluids-induced recrystallization and resetting process. The closure temperature for argon in muscovite has for a long time been considered to be around 350 °C based in part on calibration of obtained ages vs. metamorphic grade (e.g. Purdy and Jäger, 1976). However, Harrison et al. (2009) recently published the first experimental study of argon diffusion in muscovite and showed that Ar retentivity in muscovite is greater than previously assumed. Based on their diffusion parameters (E_a = 264 kJ.mol^{-1}; D_0 = 2.3 E^{-04} m^2 s^{-1}), and taking 500 and 1000 µm for the diffusion radius, we have computed the different closure temperature as a function of cooling rates (Fig. 7a): the closure temperature ranges between ca. 450 and 550 °C, for the diffusion dimensions and cooling rates investigated. In a Temperature–Time diagram (Fig. 7b), the minimum cooling rate calculated considering U-Pb and ^{40}Ar/^{39}Ar ages and their associated uncertainties is 10.4 °C/Ma.

Taking the minimum zircon U-Pb age and the oldest muscovite dates corresponds to a subinstantaneous cooling of the granitic body. A simple 2D thermal numerical model (details in Appendix A) shows that a Lizio-type granitic pluton emplaced at mid-crustal depths cools down in less than 1 Ma (Fig. 8), consistently with this scenario. Conversely, a slow cooling rate of ca. 10 °C/Ma would imply that the Lizio granite remained at a temperature above ca. 480–500 °C for a long time after its emplacement. The Lizio granite was emplaced around 4 kbar, which corresponds to a depth of 15 km considering only the lithostatic pressure and a granite density of 2.7. At this depth, temperatures of around 550 °C can be reached and maintained along continental strike-slip shear zones due to heat production by shear heating (Leloup et al., 1999). The cooling below the closure temperature of ca. 500 °C for such a slow cooling rate would have occurred when heat advection due to shear heating and therefore shearing along the NBSASZ had stopped. Moreover, one cannot totally rule out the influence of some fluid-rock interactions which would have disturbed ^{40}Ar/^{39}Ar age spectra without being recorded by the whole rock and muscovite chemistry. Indeed, the analyzed muscovite grains display subtle saddle-shaped ^{40}Ar/^{39}Ar age spectra that may indicate fluid-induced disturbance (e.g. Alexandrov et al., 2002; Cheilletz et al., 1999). Finally, to a first order, our new data are consistent with a simple cooling of the intrusion, with possible, but limited, influence of shear heating and fluid-rock interaction. A surprising result is the absence of consistency between the muscovite ^{40}Ar/^{39}Ar dates and the shearing gradients observes throughout the Lizio granite. This could result from the choice we made to

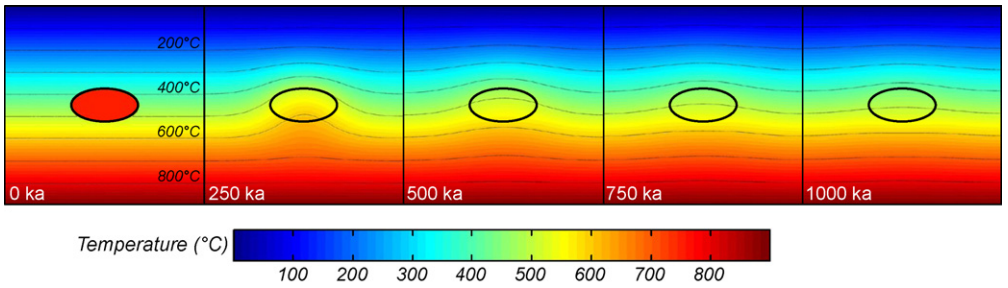

Fig. 8. 2D thermal modelling of the cooling of the Lizio granite during 1 Ma (see details in Appendix A).

Fig. 8. Modèle thermique 2D du refroidissement du granite de Lizio pendant 1 Ma (voir les détails dans l'Annexe A).

date large muscovite phenocrysts in all the samples. It would deserve further studies, notably dating increasingly deformed micas toward the NBSASZ to better evaluate if potential postemplacement events have affected the K-Ar system in micas.

6. Conclusion

Zircon U-Pb dating carried out on the Lizio granite yielded an age of 316 ± 6 Ma that is interpreted as the emplacement age of the granite, and therefore also of dextral shearing along the northern branch of the SASZ. This is significantly younger than the previous ca. 340 Ma whole rock Rb-Sr age interpreted as dating the emplacement of the Lizio granite. The significance of this older age is not yet well understood and it should therefore be treated with caution. $^{40}Ar/^{39}Ar$ analyses performed on various muscovite grains from the Lizio granite yielded dates of 311.5–308.2 Ma. As geochemical evidence precludes late fluids-induced large perturbations of the K-Ar isotopic system in muscovite, these dates likely reflect cooling ages below the argon closure temperature. Two extreme scenarios may explain the obtained ages, either a subinstantaneous cooling of the granite, or conversely, a very slow cooling which lasted several millions of years. This last scenario requires that the Lizio granite remained in a hot environment for a long time after its emplacement. This could have been caused by shear heating due to dextral shearing along the northern branch of the SASZ.

Acknowledgments

We are grateful to J. Tudri and O. Pourret (LaSalle Insitute, Beauvais, France) for providing us access to the secondary electron microprobe and to M. Bohn (IFREMER, Brest, France) for his assistance during electron microprobe analyses. This work was funded by grants from the CNRS-INSU ("3F" and "Action incitative" programs).

Appendix A. Appendix A: 2D thermal numerical model

The 2D thermal code used in this study solves the heat diffusion equation (A.1):

$$\rho C_p \frac{\partial T}{\partial t} = k \nabla^2 T + Hr \qquad \text{(A.1)}$$

where ρ, C_p and k are material density, specific heat capacity and thermal conductivity, respectively and Hr corresponds to the radiogenic heat production. This equation is solved numerically in the implicit formulation using the finite difference method. In this study, the heat production (Hr) is set to zero. Indeed, preliminary tests have been done with values from 1 to 5 $\mu W.m^{-3}$ and the results show that results are not significantly different after 1 Myr of experiment. The initial setup is displayed in the Fig. A1. The granitic intrusion is modelled as an ellipse (5 km high and 10 km long) located at 15 km depth in a host rocks medium with a linear thermal gradient of 30 °C km^{-1}. The resolution used is 151×151 nodes (i.e., 200 m).

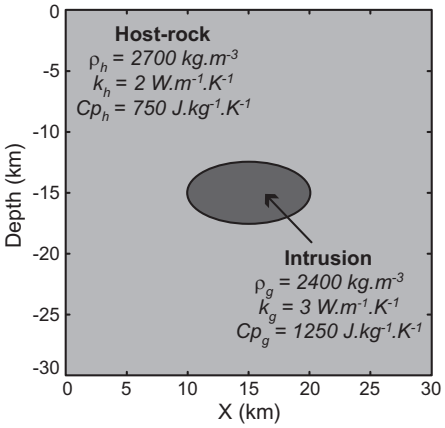

Fig. A1. Initial setup used for the 2D thermal modelling.

Fig. A1. Configuration initiale utilisée pour le modèle thermique 2D.

References

Alexandrov, P., Ruffet, G., Cheilletz, A., 2002. Muscovite recrystallization and saddle-shaped $^{40}Ar/^{39}Ar$ age spectra: Example from the Blond granite (Massif Central, France). Geochim. Cosmochim. Acta 66, 1793–1807.

Ballèvre, M., Bosse, V., Ducassou, C., Pitra, P., 2009. Palaeozoic history of the Armorican Massif: Models for the tectonic evolution of the suture zones. C. R. Geoscience 341, 174–201.

Bea, F., Montero, P., González-Lodeiro, F., Talavera, C., 2007. Zircon inheritance reveals exceptionally fast crustal magma generation processes in Central Iberia during the Cambro-Ordocvician. J. Petrol. 48, 2327–2339.

Béchennec, F., Hallégouët, B., Thiéblemont, D., 2001. Rosporden 1/50000 geological map manual (347). BRGM, Orléans, France.

Bernard-Griffiths, J., Peucat, J.J., Sheppard, S., Vidal, P., 1985. Petrogenesis of Hercynian leucogranites from the southern Armorican Massif: contribution of REE and isotopic (Sr, Nd, Pb and O) geochemical data to the study of source rock characteristics and ages. Earth Planet. Sci. Lett. 74, 235–250.

Berthé, D., 1980. Le Cisaillement Sud Armoricain dans la région de St. Jean Brévelay (Morbihan). Analyse de la déformation cisaillante. Unpublished Ph.D. Thesis, University of Rennes 1, France.

Berthé, D., Choukroune, P., Jégouzo, P., 1979. Orthogneiss, mylonite and non coaxial deformation of granites - Example of the South Armorican Shear Zone. J. Struct. Geol. 1, 31–42.

Brown, M., Dallmeyer, R.D., 1996. Rapid Variscan exhumation and the role of magma in core complex formation: southern Brittany metamorphic belt, France. J. Metamorph. Geol. 14, 361–379.

Cheilletz, A., Ruffet, G., Marignac, C., Kolli, O., Gasquet, D., Féraud, G., Bouillin, J.P., 1999. $^{40}Ar/^{39}Ar$ dating of shear zones in the Variscan basement of the Greater Kabylia (Algeria). Evidence of an Eo-Alpine event at 128 Ma (Hauterivian–Barremian boundary): geodynamic consequences. Tectonophysics 306, 97–116.

Cherniak, D.J., Watson, E.B., 2001. Pb diffusion in zircon. Chem. Geol. 172, 5–24.

Gapais, D., 1989. Shear structures within deformed granites: mechanical and thermal indicators. Geology 17, 1144–1147.

Gapais, D., Lagarde, J.L., Le Corre, C., Audren, C., Jégouzo, P., Casas Sainz, A., Van Den Driessche, J., 1993. La zone de cisaillement de Quiberon : témoin d'extension de la chaîne varisque en Bretagne méridionale au Carbonifère. C. R. Acad. Sci. Paris. Ser. IIa 316, 1123–1129.

Gloaguen, E., Branquet, Y., Boulvais, P., Moëlo, Y., Chauvel, J.J., Chiappero, P.J., Marcoux, E., 2007. Palaeozoic oolitic ironstone of the French Armorican Massif: a chemical and structural trap for orogenic base metal-As-Sb-Au mineralisation during Hercynian strike-slip deformation. Miner. Deposita 42, 399–422.

Gumiaux, C., Gapais, D., Brun, J.P., Chantraine, J., Ruffet, G., 2004. Tectonic history of the Hercynian Armorican Shear belt (Brittany. France). Geodin. Acta 17, 289–307.

Harrison, T.M., Aleinikoff, J.N., Compston, W., 1987. Observations and controls on the occurrence of inherited zircon in Concord-type granitoids. New Hampshire. Geochim. Cosmochim. Acta 51, 2549–2558.
Harrison, T.M., Célérier, J., Aikman, A.B., Hermann, J., Heizler, M.T., 2009. Diffusion of ^{40}Ar in muscovite. Geochim. Cosmochim. Acta 73, 1039–1051.
Jackson, S.E., Pearson, N.J., Griffin, W.L., Belousova, E.A., 2004. The application of laser ablation-inductively coupled plasma-mass spectrometry to in situ U-Pb zircon geochronology. Chem. Geol. 211, 47–69.
Jégouzo, P., 1980. The South Armorican Shear Zone. J. Struct. Geol. 2, 39–47.
Jégouzo, P., Rossello, E.A., 1988. La Branche Nord du Cisaillement Sud–Armoricain (France) : un essai d'évaluation du déplacement par l'analyse des mylonites. C. R. Acad. Sci. Paris, Ser. IIa 307, 1825–1831.
Košler, J., Sylvester, P.J., 2003. Present trends and the future of zircon in geochronology: laser ablation ICPMS. In: Hanchar, J.M., Hoskin, P.W.O. (Eds.), Zircon. Rev. Mineral. Geochem. 53, 243–275.
Košler, J., Fonneland, H., Sylvester, P., Tubrett, M., Pedersen, R.B., 2002. U-Pb dating of detrital zircons for sediments provenance studies–a comparison of laser ablation ICPMS and SIMS techniques. Chem. Geol. 182, 605–618.
Košler, J., Forst, L., Sláma, J., 2008. Lamdate and Lamtool: spreadsheet-based data reduction for laser ablation ICP-MS. In: Sylvester, P. (Ed.), Laser Ablation ICP-MS in the Earth Sciences: Current Practices and Outstanding Issues. Mineralogical Association of Canada, Short Course Series, 40. pp. 315–317.
Le Corre, C., Auvray, B., Ballèvre, M., Robardet, M., 1991. Le Massif Armoricain. Sciences Géologiques 44, 31–103.
Leloup, P.H., Ricard, Y., Battaglia, J., Lacassin, R., 1999. Shear heating in continental strike-slip shear zones: model and field examples. Geophys. J. Int. 136, 19–40.
Lemarchand, J., Boulvais, P., Gaboriau, M., Boiron, M.C., Tartèse, R., Cokkinos, M., Bonnet, S., Jégouzo, P., 2011. Giant quartz vein formation and high elevation meteoric fluid infiltration into the South Armorican Shear Zone: geological, fluid inclusion and stable isotope evidence. J. Geol. Soc. London, in press. doi:10.1144/0016-76492010-186.
Ludwig, K.R., 2008. Isoplot/Ex version 3.70: A geochronological toolkit for Microsoft Excel. Berkeley Geochronology Center, Special Publication 4, 73 p.
Miller, C.F., Stoddard, E.F., Bradfish, L.J., Dollase, W.A., 1981. Composition of plutonic muscovite; genetic implications. Can. Mineral. 19, 25–34.
Miller, C.F., McDowell, S.M., Mapes, R.W., 2003. Hot and cold granites? Implications of zircon saturation temperatures and preservation of inheritance. Geology 31, 529–532.
Pattison, D.R.M., Tracy, R.J., 1991. Phase equilibria and thermobarometry of metapelites. In: Kerrich, D.M. (Ed.), Contact Metamorphism. Rev. Mineral. Geochem., 26. pp. 105–206.
Pattison, D.R.M., Spear, F.S., Cheney, J.T., 1999. Polymetamorphic origin of muscovite + cordierite + staurolite + biotite assemblages: implications for the metapelitic petrogenetic grid and for P-T paths. J. Metamorph. Geol. 17, 685–703.
Peucat, J.J., Charlot, R., Mifdal, A., Chantraine, J., Autran, A., 1979. Définition géochronologique de la phase bretonne en Bretagne centrale. Étude Rb/Sr de granites du domaine Centre-Armoricain. Bull. B. R. G. M. 4, 349–356.
Pitra, P., Boulvais, P., Antonoff, V., Diot, H., 2008. Wagnerite in a cordierite-gedrite gneiss: witness of long-term fluid-rock interaction in the continental crust (Ile d'Yeu, Armorican Massif, France). Am. Mineral. 93, 315–326.
Purdy, J.W., Jäger, E., 1976. K-Ar ages on rock-forming minerals from the Central Alps. Mem. Inst. Geol. Min. Univ. Padova 30 .
Renne, P.R., Swisher, C.C., Deino, A.L., Karner, D.B., Owens, T.L., DePaolo, D.J., 1998. Intercalibration of standards, absolute ages and uncertainties in ^{40}Ar/^{39}Ar dating. Chem. Geol. 145, 117–152.
Roddick, J.C., Bevier, M.L., 1995. U-Pb dating of granites with inherited zircon: Conventional and ion microprobe results from two Paleozoic plutons, Canadian Appalachians. Chem. Geol. 119, 307–329.
Roddick, J.C., Compston, W., 1977. Strontium isotopic equilibration: a solution to a paradox. Earth Planet. Sci. Lett. 34, 238–246.
Ruffet, G., Féraud, G., Amouric, M., 1991. Comparison of ^{40}Ar/^{39}Ar conventional and laser dating of biotites from the North Tregor batholiths. Geochim. Cosmochim. Acta 55, 1675–1688.
Ruffet, G., Féraud, G., Ballèvre, M., Kienast, J.R., 1995. Plateau ages and excess argon in phengites - An Ar-40-Ar-39 laser probe study of alpine micas (Sesia zone, Western Alps, northern Italy). Chem. Geol. 121, 327–343.
Sláma, J., Košler, J., Condon, D.J., Crowley, J.L., Gerdes, A., Hanchar, J.M., Horstwood, M.S.A., Morris, G.A., Nasdala, L., Norberg, N., Schaltegger, U., Schoene, B., Tubrett, M.N., Whitehouse, M.J., 2008. Plešovice zircon - a new natural reference material for U-Pb and Hf isotopic microanalysis. Chem. Geol. 249, 1–35.
Tartèse, R., Boulvais, P., 2010. Differentiation of peraluminous leucogranites "en route" to the surface. Lithos 114, 353–368.
Tartèse, R., Boulvais, P., Poujol, M., Chevalier, T., Paquette, J.L., Ireland, T.R., Deloule, E., 2011a. Mylonites of the South Armorican Shear Zone: Insights for crustal-scale fluid flow and water–rock interaction processes. J. Geodyn., in press. doi:10.1016/j.jog.2011.05.003.
Tartèse, R., Boulvais, P., Poujol, M., Gloaguen, E., 2011b. The Late Carboniferous Variscan evolution of the Armorican Massif (France): magmatism, hydrothermalism and metallogenic consequences. Geophys. Res. Abstr. 13, 2422.
Turrillot, P., Augier, R., Faure, M., 2009. The top-to-the-southeast Sarzeau shear zone and its place in the late-orogenic extensional tectonics of southern Armorica. Bull. Soc. Geol. France 180, 247–261.
Villa, I.M., 2010. Disequilibrium textures versus equilibrium modelling: geochronology at the crossroads. In: Spalla, M.I., Marotta, A.M., Grosso, G. (Eds.), Advances in Interpretation of Geological Processes: Refinement of Multi-scale Data and Integration in Numerical Modelling. Geol. Soc. London Spec. Pub., 332. pp. 1–15.
Wiedenbeck, M., Alle, P., Corfu, F., Griffin, W.L., Meier, M., Oberli, F., von Quadt, A., Roddick, J.C., Spiegel, W., 1995. Three natural zircon standards for U-Th-Pb, Lu-Hf, trace element and REE analyses. Geostandard. Newslett. 19, 1–23.
Whitney, D.L., Evans, B.W., 2010. Abbreviations for names of rock-forming minerals. Am. Mineral. 95, 185–187.

Geomorphology 191 (2013) 71–79

Contents lists available at SciVerse ScienceDirect

Geomorphology

journal homepage: www.elsevier.com/locate/geomorph

The influence of surface slope on the shape of river basins: Comparison between nature and numerical landscape simulations

Sébastien Castelltort [a,b,*], Philippe Yamato [a,c]

[a] Earth Surface Dynamics, Geological Institute, Department of Earth Sciences, ETH Zürich, Sonneggstrasse 5, 8092 Zürich, Switzerland
[b] Section of Earth and Environmental Sciences, Rue des Maraîchers 14, 1205 Geneva, Switzerland
[c] Géosciences Rennes, UMR 6118, Université de Rennes 1, CNRS, Rennes, France

ARTICLE INFO

Article history:
Received 21 October 2010
Received in revised form 13 March 2013
Accepted 25 March 2013
Available online 29 March 2013

Keywords:
Landscape evolution model
River basin
Basin aspect ratio
Basin shape
Drainage network

ABSTRACT

We investigate the influence of initial conditions of slope and surface roughness on the shape (length to width aspect ratio) of incipient drainage basins in numerical experiments of simple tilted surfaces using the CASCADE code of landscape evolution. Comparison with data on the shape of river basins in nature shows that simple rules of the steepest-descent routing of water are sufficient to account for a natural range of incipient drainage basin shape, independently of the erosion processes at work. To produce numerical basins that respect the main aspect ratio of natural drainage basins, one must use very low initial regional surface slopes of less than 1° at the scale of the entire drainage basins, and a local roughness slope of less than 3° at the scale of local surface irregularities. Numerical studies addressing real study cases may take advantage of the relation between local roughness and regional slope in order to produce catchment aspect ratios similar to the natural studied cases.

1. Introduction

In the last three decades, many questions have been addressed about the possible couplings between deep (mantle) and shallow (crustal) tectonics and superficial climate-controlled erosion (e.g., Molnar and England, 1990; Willett, 1999). These led to a considerable improvement in the mathematical modeling of surface processes, in particular with the advent of numerical models of landscape evolution, and with the quantitative analysis of increasingly available high-resolution datasets of the Earth's topography. While the approaches on these topics have followed different paths, the main studies have focused on numerical modeling of the development and evolution of fluvial landscapes, i.e. landscapes composed of channels and hillslopes, because their structure constitutes a fundamental control on relief in tectonically active areas.

While numerical models of erosion usually produce fluvial landscapes that look similar to nature, how to objectively assess this similarity remains an outstanding problem. As summarized in the review by Tucker and Hancock (2010), questions like what are the essential characteristics of a catchment or a landscape, and how can we quantitatively assess landscape differences (Hancock, 2003) are still challenging. Until now, models have been tested against data obtained with the slope–area relationship or with catchment hypsometry (Hancock et al., 2002; Willgoose et al., 2003) but these measures are often insufficient to discriminate between landscapes that seem visually different (Tucker and Hancock, 2010). Braun and Sambridge (1997) provided a quantitative assessment of the similarity between their model's results and natural landscapes by showing that the numerically produced dendritic river patterns respected the main laws of network composition and topographic surfaces that have similar scaling behavior as natural landscapes. They noted, however, that most possible networks, either natural or not, inevitably obey Horton's and Schumm's laws of network composition, as pointed out by Kirchner (1993), and thus these laws may not be used readily to validate models.

One consistent output from model–data comparison tests is the sensitivity of models to initial conditions. Testing the SIBERIA landscape evolution model (Willgoose et al., 1991a,b,c) against common geomorphological statistics (e.g., Horton's and Tokunaga's ratios, non-dimensional drainage density, magnitude, mean relief, and mean stream relief), Ijjasz-Vasquez et al (1992) concluded that the large variability observed in their numerical dendritic networks is not random and is instead directly related to differences in the initial conditions. A subsequent test of the SIBERIA model by Hancock (2003) also concluded that, for a good match between simulated and field descriptors such as the hypsometric curve, area–slope relationship, width function and cumulative area, all that is needed is a catchment with an aspect ratio matching that of the field data, thus similarly emphasizing the role of initial conditions.

Recently, Castelltort et al. (2009) presented new measures of the shape (length to width aspect ratio) of large-scale (10^1–10^3 km^2)

* Corresponding author at: Section of Earth and Environmental Sciences, Rue des Maraîchers 14, 1205 Geneva, Switzerland. Tel.: +41 22 379 66 16, +41 76 490 37 65; fax: +41 44 632 14 22.
E-mail address: sebastien.castelltort@unige.ch (S. Castelltort).

0169-555X/$ – see front matter © 2013 Elsevier B.V. All rights reserved.
http://dx.doi.org/10.1016/j.geomorph.2013.03.022

incipient drainage basins formed on uniformly tilted surfaces. These data highlight the influence of regional surface slope versus surface roughness on the aspect ratio of incipient drainage basins. Steep and smooth slopes develop longer and narrower catchments than comparatively gently dipping and rougher surfaces.

In this brief report we use Castelltort et al.'s (2009) dataset to test the ability of the CASCADE landscape evolution model (Braun and Sambridge, 1997) to accurately reproduce drainage basin shape. The algorithm of routing water downstream used in the CASCADE is generic in essence (steepest slope) and is sufficient to reproduce the observations of natural basin shape. By tuning the ratio between regional slope and amplitude of the initial surface roughness, the initial drainage basin shape can be predicted. Numerical landscape evolution studies can thus choose the adequate initial conditions in order to generate drainage basins whose aspect ratios respect those commonly encountered in nature.

2. Incipient river basins on tilted surfaces

To measure the aspect ratio of a drainage basin, several methods can be used that depend on the choice of a dominant basin length (e.g. the longest channel length and length along the main valley axis to the drainage divide), basin area and basin orientation, and produce non-unique results. The method of computing the convergence angle of river basins as defined in Castelltort et al. (2009) leads to a unique measure of drainage basin shape independent of such choices. Considering a simplified rectangular basin of length L_b and width W_b, with $L_b > W_b$, the convergence angle is defined as the angle α that determines the aspect ratio of a basin:

$$\tan\alpha = \frac{1}{2}\cdot\frac{W_b}{L_b}. \quad (1)$$

Instead of enclosing a natural basin within a synthetic rectangle of dimensions L_b and W_b, the convergence angle method is based on calculating source–outlet vectors (Fig. 1). A source–outlet vector is defined as the vector between the current pixel and the basin outlet. After extracting the river network in order to define the catchment boundary, every pixel in the basin is linked with the outlet pixel in order to define the population of source–outlet vectors. The convergence angle is such that half of the source–outlet vectors possesses an azimuth comprised between $+\alpha$ and $-\alpha$ of the main median basin azimuth, and is thus found by taking half of the angular difference between the first and third quartiles of the azimuths of all source–outlet vectors (Castelltort

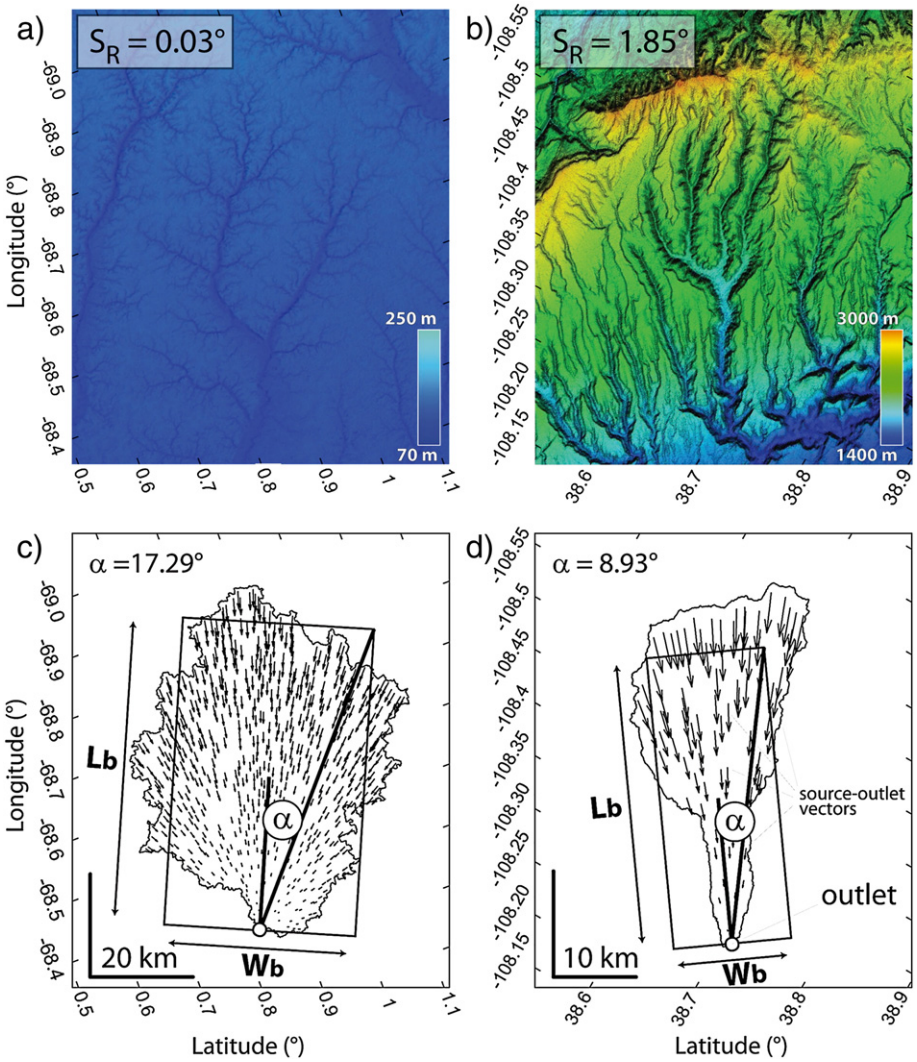

Fig. 1. Definition of the convergence angle α of river basins and influence of surface slope (S_R) in nature. a) and b) Digital elevation models (DEMs) of two examples of river basins in (a) South America and (b) North America (basin codes respectively SA5_4 and S6_3 in Castelltort et al., 2009). c) and d) Obtained convergence angles for the two basins. The steeper surface of basin S6_3 (d) displays a narrower basin and a smaller convergence angle than the gently dipping surface of basin SA5_4 (c). The synthetic rectangular basins of length L_b and width W_b are unique and obtained from the computed convergence angle (which sets the ratio between length and width) and a given drainage area of the considered basin.

et al., 2009). Large or small convergence angles correspond to relatively wide or narrow basins respectively.

Using the SRTM1 (~30 m horizontal resolution) digital topography for North America and the SRTM3 (~90 m) topography for South America, Castelltort et al. (2009) studied basins ranging in size from 8 to 12,500 km^2. They assumed that the considered basins were close to their initial state of evolution, i.e. were little dissected as witnessed by the presence of flat-top interfluves and the limited local relief of 3 to 368 m with an average of 80 m. The regional slope S_R of the surfaces on which these basins were formed ranges from 0.0085° to 6.98°. The obtained convergence angles are plotted in Fig. 2 and labeled by the region of provenance. These data show that basins having surface slopes of 1.5° generally display convergence angles of less than 8°, whereas basins on slopes of less than 1° display a large variety of convergence angles from ~5° to ~24°. Surface slope thus exerts an important control on the shape of river basins at their initiation. This result corroborates the initial assumptions of Zernitz (1932) on the influence of surface slope on catchment shape and the subsequent experimental results of Parker (1977) and Phillips and Schumm (1987).

This relationship between regional slope and basin shape results from the interaction between regional and local slopes (S_R and S_l). The analytical relation proposed in Castelltort and Simpson (2006a) describes α of a rectangular drainage basin as the characteristic deviation of water flowing orthogonally to topographic contour lines as a result of superimposed local roughness and regional slope:

$$\alpha = \frac{1}{2}\cdot \arctan \Phi, \tag{2}$$

where Φ is called the relative surface roughness corresponding to the ratio S_l/S_R, reflecting a simple surface roughness of wavelength λ_l, and amplitude A_l ($S_l = 2A_l / \lambda_l$) on a tilted surface (see Fig. 3).

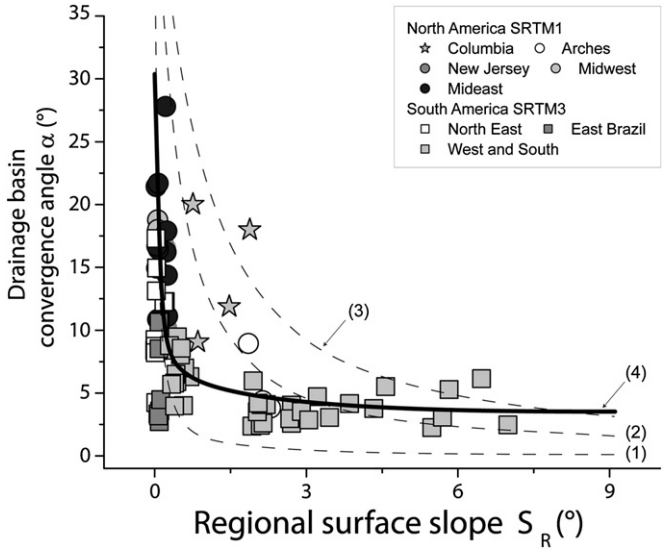

Fig. 2. Convergence angle α of river basins studied in Castelltort et al. (2009) versus their regional surface slope S_R. Steeper surfaces develop narrower basins with smaller α. The data are labeled according to their geographical location. Curves (1), (2) and (3) are model curves based on the theoretical relationship between S_R and α [$= 0.5\text{atan}(S_l/S_R)$] for different values of local surface roughness S_l of 0.05°, 0.5° and 1° respectively (Eq. (2) in the text). Curve (4) is an empirical fit to the data following $\alpha = 0.5\text{atan}(0.2067 S_R^{-0.2342})$. The control of the incipient drainage basin aspect ratio by topographic slope is related to the nature of surface water flow over tilted surfaces. Water flow is robustly focused downslope (small convergence angle) for steep and smooth surfaces whereas it is strongly defected (large convergence angle) relative to the downslope direction for gently tilted or relatively rough surfaces.

3. Numerical experiments

The aim of this study is to test the influence of slope and roughness on the shape of incipient river basins in a numerical model of landscape evolution. To reach that goal, we use the widely distributed CASCADE code (Braun and Sambridge, 1997; Braun and Yamato, 2010) because it computes water paths according to a generic steepest descent algorithm similar to that used in most other landscape evolution models.

3.1. Model setup

In our study, the model box is constituted by an inclined square surface of 100 × 100 km (Fig. 3) with S_R being defined by the ratio between maximum elevation at the top side (h) and the side length of the model (L):

$$S_R = \arctan\left(\frac{h}{L}\right). \tag{3}$$

The resolution of the model (r) is 1 km, i.e., 101 nodes both in the x and y directions.

The initial meshing is irregular, with 250 m of noisy displacement in both x and y directions.

The value of h changed according to the desired S_R value imposed to the experiment. The surface roughness is simulated by a simple uniform white noise topography of amplitude R, equivalent to S_l, applied at the beginning of the experiments (Fig. 3). Using a Gaussian white noise rather than uniform noise does not significantly modify the results. Although it is beyond the scope of this study, a more complete investigation of the role of different spectra of noise on α of river basins would be valuable. S_l is thus defined as:

$$S_l = \arctan\left(\frac{R}{2r}\right), \tag{4}$$

where r corresponds to the resolution shown in Fig. 3. S_l and S_R are then systematically varied to study their respective influence on α.

In the CASCADE, both fluvial and hillslope processes are taken into account. For fluvial processes, erosion is simulated by the difference between the river channels carrying capacity q_c and the sediment load q_s scaled on the bedrock erodibility (bedrock erodibility length scale l_{BR}) and the river channel width (w_c) such as:

$$\frac{\partial h}{\partial t} = \frac{q_s - q_c}{w_c \cdot l_{BR}} \tag{5}$$

where $\frac{\partial h}{\partial t}$ corresponds to the variation of topography through time due to fluvial erosion. q_s is obtained by integrating the volume of rocks eroded from the upstream area and q_c corresponds to the volume that can be carried by water per unit time. q_c is thus obtained by the stream-power-law proportional to the local river slope S and the drainage area A (Kooi and Beaumont, 1994):

$$q_c = K_f \cdot S^n \cdot A^m \tag{6}$$

where K_f is the fluvial erosion/transport coefficient (in m yr^{-1}) varying essentially with precipitation rate, and n and m are power-law exponents. Tests of the influence of varying the m/n ratio are presented in Section 3.2. If q_s is smaller than q_c, erosion takes place. At the opposite, when q_s exceeds q_c, deposition takes place at a rate of:

$$\frac{\partial h}{\partial t} = \frac{q_s - q_c}{\Omega} \tag{7}$$

where Ω is the surface area linked to each integration point and defined by the spatial discretization.

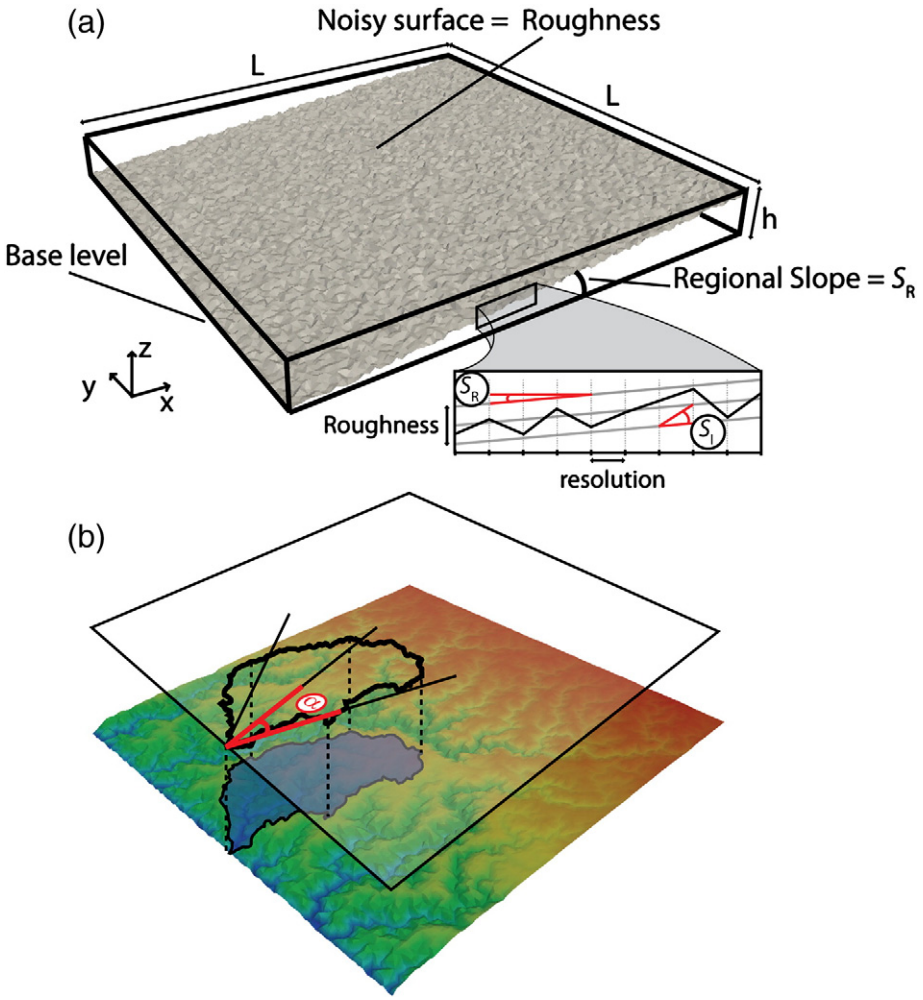

Fig. 3. Model setup. (a) Initial morphology of simulations corresponding to a simple tilted plane characterized by its regional slope S_R and the local slope S_l reflecting local roughness. (b) Topography after 500 ky in one experiment. Catchments are extracted and the convergence angle α is computed for each catchment.

For the hillslope processes, a diffusion equation is used to simulate the mass transport q linearly proportional to the river slope (Kooi and Beaumont, 1994; Braun et al., 2001)

$$q = -K_d \cdot S \tag{8}$$

where K_d is a diffusivity coefficient (in $m^2\ yr^{-1}$) corresponding to the efficiency of the hillslope transport processes.

3.2. Influence of model parameters

The values of the different parameters used are shown in Table 1. We here present their influences and discuss our choices of parameters for the study of the effect of slope and roughness.

Table 1
Numerical model constants used in our experiments. *Parameter tested that demonstrated no significant influence on the value of the convergence angle α (see text and Figs. 4 and 6 for details).

Parameter	Symbol	Value
Model width	L	100 km
time step	Dt	20 yr
Hillslope diffusivity	K_d^*	0 $m^2\ yr^{-1}$
Fluvial erosion/transport coefficient	K_f^*	5 $\times 10^{-6}$ m yr^{-1}
Uplift rate	V_z	5 $\times 10^{-3}$ m yr^{-1}
Bedrock erodibility length scale	l_{BR}^*	1 m
Channel width length scale	W_c^*	1 m

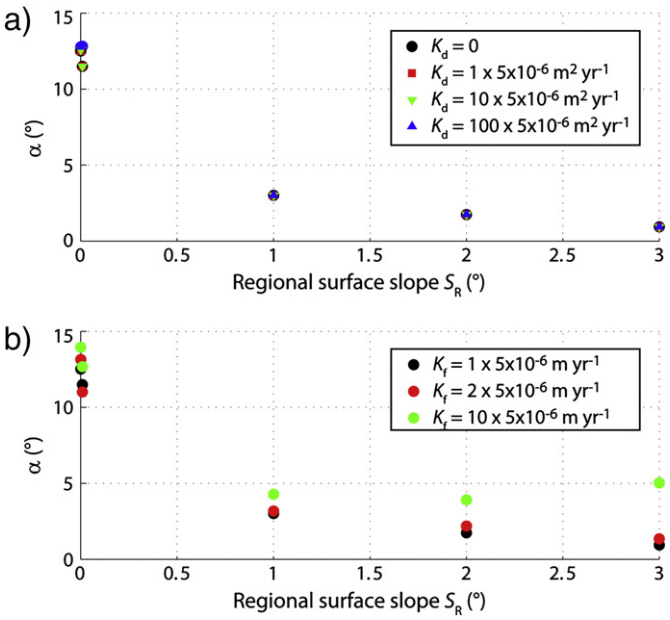

Fig. 4. Influence of the erosional parameters on the drainage basin convergence angle α. (a) Effect of diffusion (K_d). α is computed for a roughness R of 10 m for five different regional slopes (0.0001°, 0.001°, 1°, 2° and 3°). (b) Effect of fluvial coefficient (K_f). As in (a), α is computed for a roughness R of 10 m for five different regional slopes (0.0001°, 0.001°, 1°, 2° and 3°).

Diffusion leads to a "smoothing" of surface topography which does not produce changes in the final morphology of the river network. Tests presented in Fig. 4a show differences of 1° to 2° in α when K_d is varied by four orders of magnitude over a very small regional slope. When the regional slope is increased to 1°, 2° and 3°, K_d has no influence on the convergence angle. We thus neglect diffusion in other experiments ($K_d = 0$). Note that we have not tested the effect of using a non-linear slope-dependent transport law on hillslopes (e.g., Roering et al., 1999). Such a transport mode is essential in areas with high uplift and/or landslide-dominated incision. Our results are not relevant to such landscapes but rather to the initial stages of incision in areas undergoing topographic growth.

The effect of K_f was tested by varying it by factors of 2 and 10 (Fig. 4b). Because it is a constant of proportionality, varying K_f influences the rate of landscape evolution; given the other parameters used, if K_f is increased by more than 10, the landscape erodes instantaneously. However, the obtained α values for the same regional slope differ only by 4° or less (Fig. 4b). We thus decided to keep a K_f set to 5×10^{-6} m yr^{-1} throughout our study.

It is important to emphasize that with no diffusion and a constant coefficient of fluvial erosion, our experiments are designed for studying the influence of slope and roughness at the scale of dendritic convergent networks larger than incipient first-order streams. Indeed, the spacing of first-order channels has been demonstrated to be essentially controlled by the competition between advective and diffusive processes both under transport-limited (e.g., Simpson and Schlunegger, 2003) or detachment-limited (Perron et al., 2008) conditions.

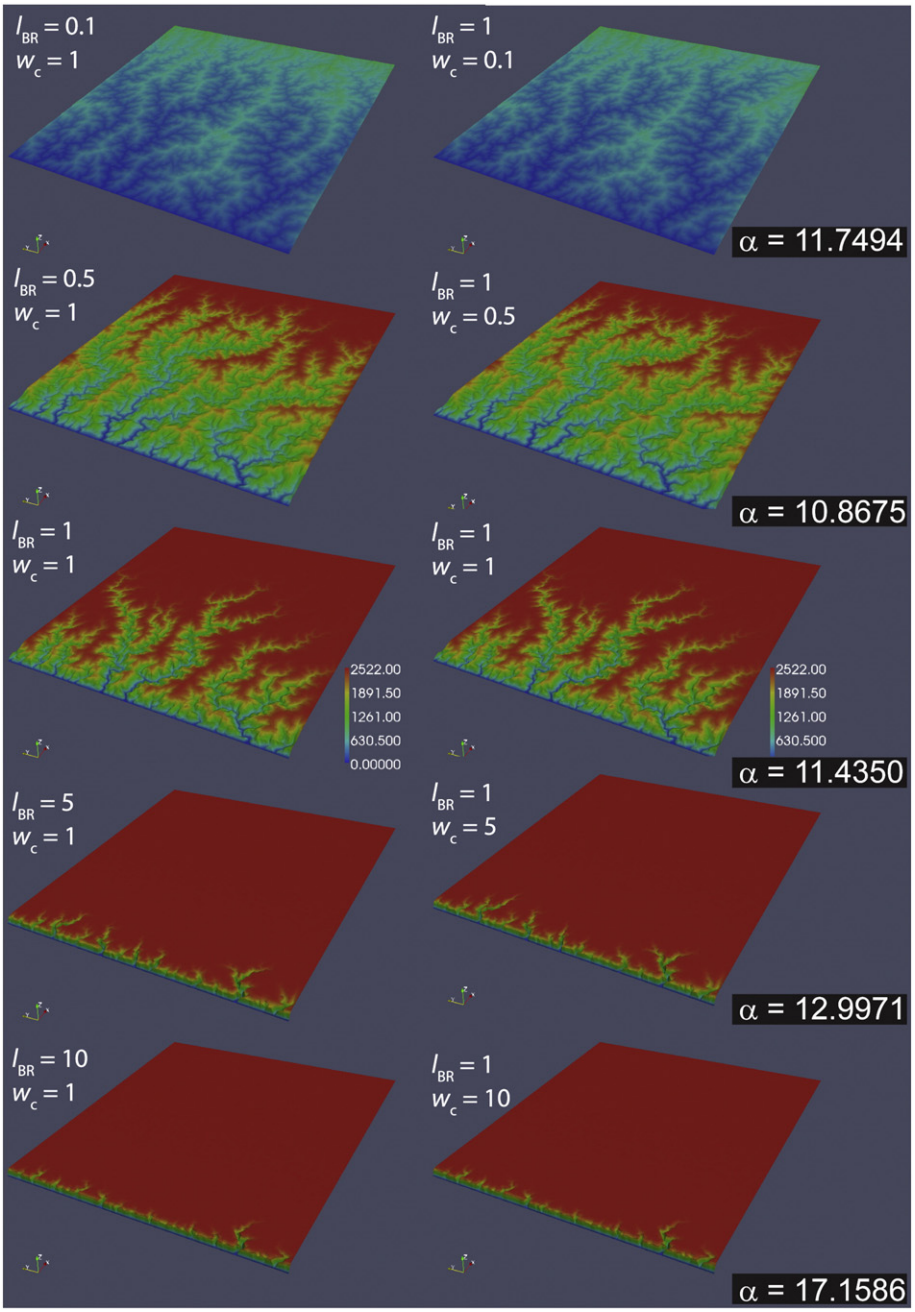

Fig. 5. Influence of bedrock erodibility (erodibility length scale l_{BR}, left column) and channel width (w_c, right column). The parameter values are $K_f = 5 \times 10^{-6}$ m yr^{-1}, $R = 10$ m and $S_R = 0.01°$. Results demonstrate that these two parameters act in the same way and do not affect the convergence angle α.

Because l_{Br} and w_c both come as proportionality factors into the erosion law used in this study (Eq. (5)), we have performed tests to confirm that they have similar influence on the simulations (Fig. 5). Results show that these parameters also affect the rate of landscape incision but modify α only by less than 5°. We thus set both l_{Br} and w_c to an intermediate value of 1.

In order to study the influence of m and n on α, we performed experiments using typical values of m/n, i.e. varying from 0.3 to 0.7 (Whipple and Tucker, 1999). Results are presented in Fig. 6 and show that varying the m/n ratio influences only the rate of erosion of the landscape but modifies α only within a range of 9.78° to 12.68°, i.e. not significantly. In the experiments focusing on the influence of slope and roughness on α, we have thus set m/n to a conservative value of 0.5 with n = 1, as commonly used in the literature (e.g., Whipple and Tucker, 1999).

It is important to highlight that, since the numerical parameters such as K_f, K_d, l_{BR}, w_c, m and n are not well constrained from natural data, the insight gained from the experiments emanates more from the qualitative differences of network shape obtained with different local and regional slopes rather than from the absolute values.

3.3. Simulations results

Fig. 7 displays the fluvial landscapes obtained after 25,000 time steps (equivalent to 500 ka) for different values of local roughness (0.1, 1, 10, 100 and 1000 m) and regional slopes (0.0001°, 0.01°, 1°, 3° and 5°). α is computed according to the method outlined above, for all basins with areas of 20 km^2 at least, and we then display the average α value for each experiment. Supplementary tests have been done for different values of minimum catchments and present almost the same results. In all experiments the water path over the surface is established quasi-instantaneously and the erosion wave that then propagates upstream tends to follow this pre-existing path. The role of dissection is limited to emphasizing the catchment form established early by water routing over the rough topography. The erosion processes are thus of limited importance in setting the landscape geometry, as also highlighted by the negligible impact of erosion parameters on α as explained in Section 3.2. In the experiments of Fig. 7, we have also investigated the evolution of α with time and the effect of the numerical grid resolution. Observation of drainage network evolution with time shows that reorganization is minimal and limited to nodes close to the divides in first-order basins. This is expressed by the evolution of α within a limited range of 1° to 3° for each experiment shown in Fig. 8. The spatial resolution of the numerical grid also does not affect α considerably (Fig. 9). Therefore, in these experiments, the combination of initial roughness and regional slope determines the final basin aspect ratio (α) almost entirely.

The obtained fluvial landscapes display dendritic networks that are visually different as a function of Φ. As intuitively expected and analytically predicted (Castelltort and Simpson, 2006b), the fluvial networks are more straight and narrow when S_R increases relative

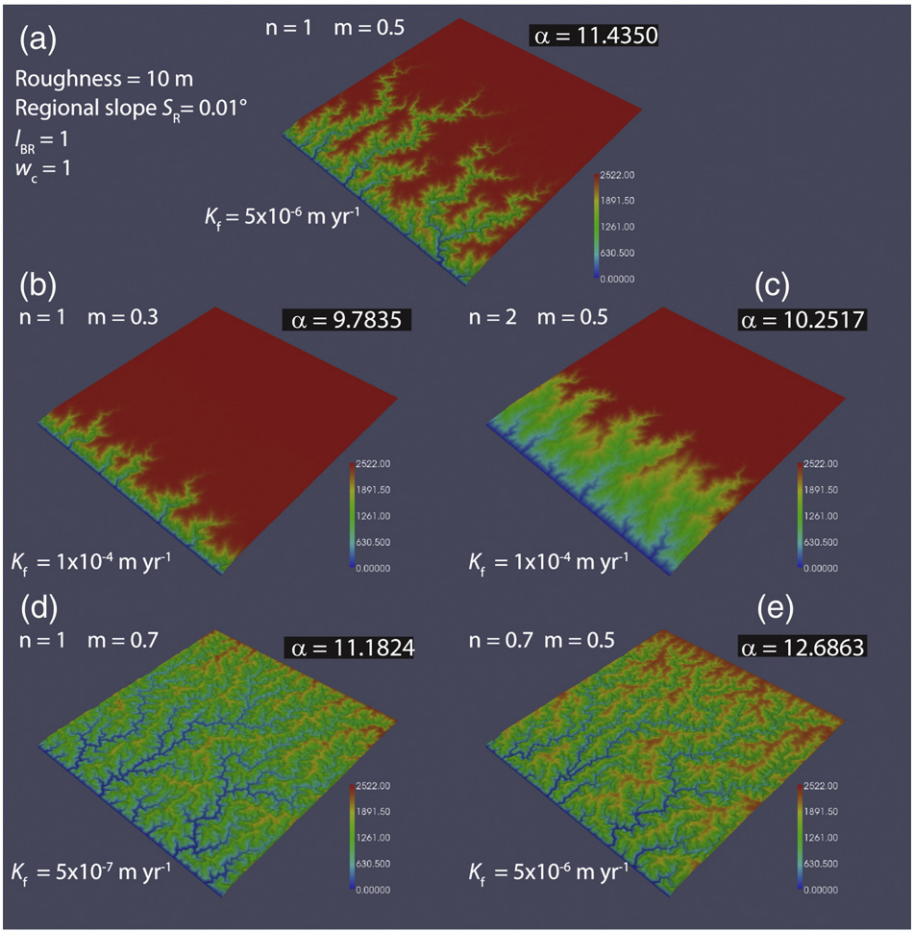

Fig. 6. Influence of the power-law exponents (m and n) for given roughness, regional slope, bedrock erodibility length scale and channel width. Since the fluvial erosion coefficient K_f does not influence the results of the computed convergence angle, this parameter was tuned here in order to produce incised river network after the 500-ka duration of experiments. a) Reference experiment where the m/n ratio is set to 0.5. b) and c) Two experiments with same parameters as in (a) but with m/n = 0.3 and 0.25, respectively. d) and e) Two experiments with same parameters as in (a) but with m/n = 0.7 and 0.71, respectively. Although the river networks appear visually different, the obtained convergence angles are very close. The influence of the m/n ratio is thus essentially restricted to changing the rate of landscape incision (and thus the amount of incision over a given duration), without significantly modifying the river network aspect ratio.

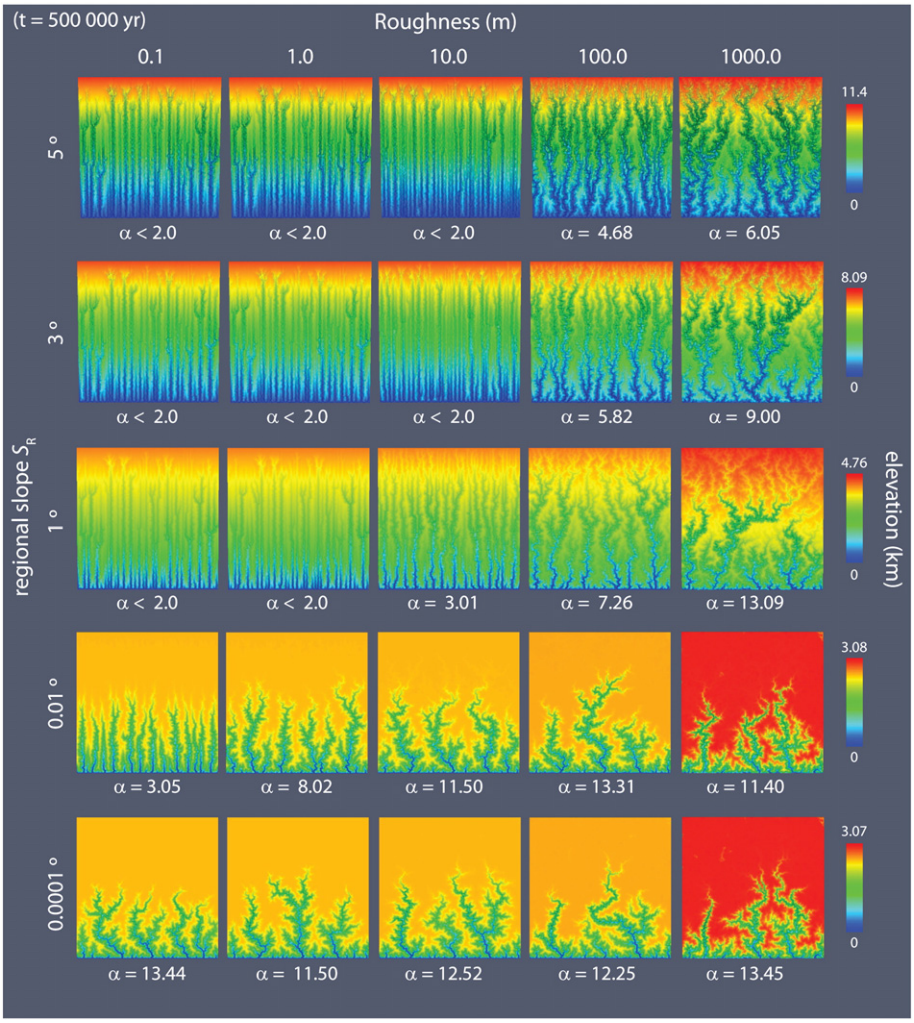

Fig. 7. Influence of initial regional surface slope and roughness on incipient river networks after 25,000 time steps (500 ky). The convergence angle does not evolve further with time. The amplitude R of the roughness is given in meters. The equivalent local slope S_l is obtained using Eq. (4); $R = 0.1$ corresponds to $S_l = 0.0029°$, $R = 1$ to $S_l = 0.0286°$, $R = 10$ to $S_l = 0.2865°$, $R = 100$ to $S_l = 2.8624°$, and $R = 1000$ to $S_l = 26.5651°$.

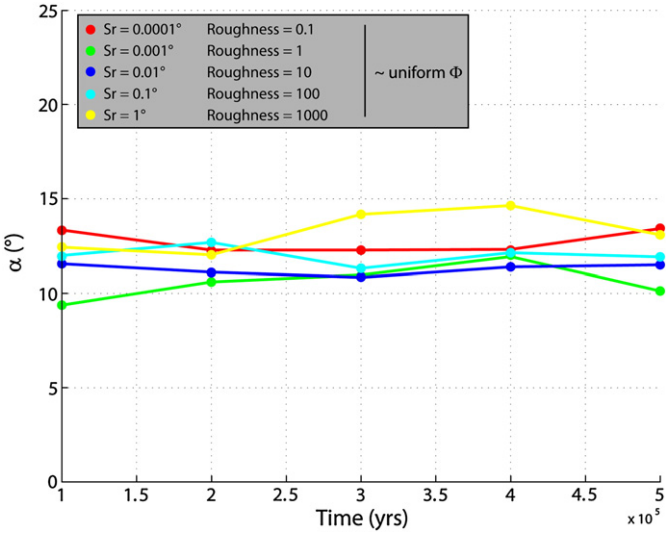

Fig. 8. Evolution of the convergence angle α with time. All the experiments here present approximately the same relative surface roughness Φ. The convergence angle α is set early in the simulated landscapes and shows little evolution with time.

to S_l (top left of Fig. 7), and are more dendritic and wide when local roughness dominates over S_R (bottom right of Fig. 7). For a constant slope (each row of Fig. 7), α of simulated networks increases with increasing roughness (from left to right). Similarly, for a constant roughness (each column of Fig. 7), α decreases with increasing S_R (from bottom to top).

Fig. 10a shows the comparison of α for simulated drainage networks and natural ones as a function of S_R. The values obtained in the numerical experiments are similar to those of drainage networks established on surfaces found in nature. For constant roughness (each colored dotted line represents a constant value of roughness), α decreases with increasing S_R as analytically predicted. The natural data (white dots and best fit black curve) are best matched by numerical experiments with local roughness of 100 m, i.e. S_L of 2.8624° (Fig. 10b). Although local roughness of less than 100 m produces very small α values on large S_R compared to natural data (Fig. 10b), it fits some of the lower bound on natural data (Fig. 10a). Local roughness of more than 100 m yields α values that are too large compared to natural values for networks on steep pristine slopes (Fig. 10b).

4. Discussion

The experiments conducted in this study show that the shape of catchments is extremely sensitive to the initial conditions of surface

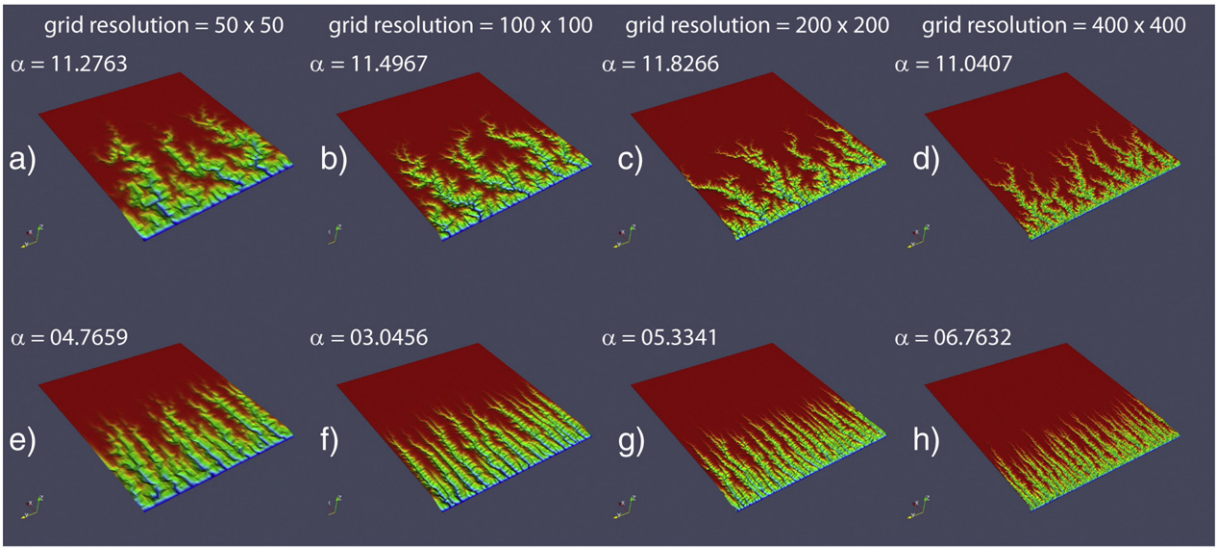

Fig. 9. Influence of the spatial grid resolution on the shape (convergence angle α) of simulated river networks. (a to d) Series of experiments with $S_R = 0.01$ and roughness = 10 m. (e to h) Series of experiments with $S_R = 0.01$ and roughness = 0.1 m. The grid resolution has a negligible influence on the convergence angle of river basins.

slope and roughness. The routing of water flow down the steepest slope in the CASCADE numerical model produces results that correspond well to analytical predictions and fit well to the observation of incipient drainage basin formation on large-scale tilted surfaces. In this case, the physical processes of erosion play only a minor role in structuring the drainage basin geometry which is rather controlled by the initial conditions of surface slope and roughness. It is thus possible to set up the initial roughness and slope of numerical experiments in order to obtain the desired catchment geometry needed for specific case studies. This can be particularly useful in studies that seek to invert a landscape's history, by choosing the appropriate initial conditions.

Basin length-to-width ratios in nature vary over a wide range of values around central values of 2 to 3 (Montgomery and Dietrich, 1992; Hovius, 1996), i.e. α between 9°and 14°. To produce fluvial landscapes with such a classical natural geometry on a simple tilted plane, it is clear from our experiments that the initial slope has to be significantly lower than 1° and be characterized by a "reasonable" amplitude of local roughness less than 100 m over 2 km, i.e. less than ~3° (Fig. 10). The experiments never produce basins with large α values (wide basins) as sometimes observed in nature. Such wide natural basins may result from structural control, tectonic or lithological, active or inherited, acting as an oriented roughness. This is the case for example at the front of the Himalayas, where large-scale orogeny-parallel anticlines divert the incipient fluvial systems and produce anomalously wide drainage basins (Hovius, 1996). Such a structural control can be input in numerical experiments in order to obtain wider basins. Beyond structural controls, however, one could introduce a different type of random noise on initial experiments in order to produce larger basins. In particular one could test the influence of having a spectrum of noise, i.e. different amplitudes at different wavelengths. However, a major drawback to constraining the input roughness comes from the absence of data on the roughness of natural surfaces at large scale in their pre-incision configuration. A third possible reason of never obtaining large α values in our experiments could be due to the water flowing algorithm which may force the water too straight down the regional slope. While the irregular mesh used in the CASCADE breaks the symmetry found on regular

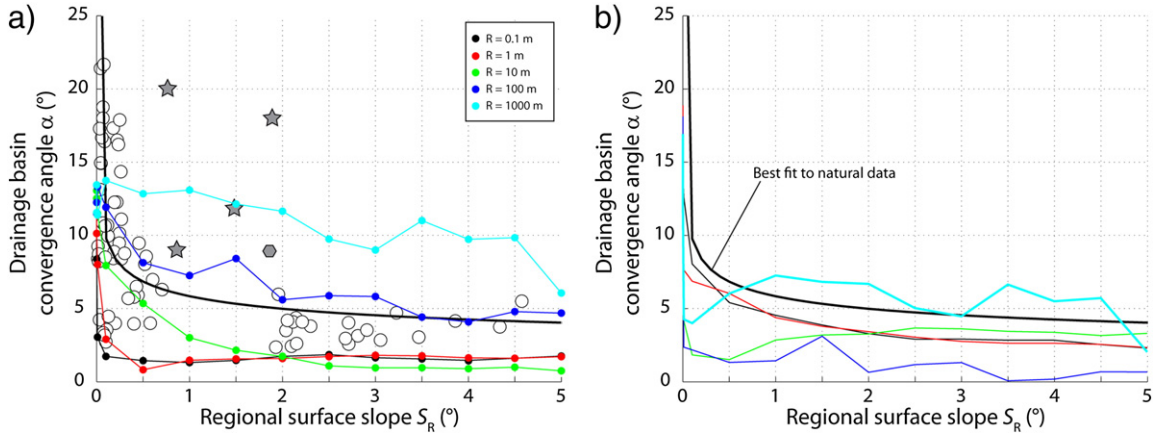

Fig. 10. Regional surface slope S_R and convergence angle α. a) α from the simulations performed (colored dots and lines) and natural α of incipient river networks on tilted surfaces (open dots) from Castelltort et al. (2009) versus S_R. Each colored line represents a set of experiments (each point is one experiment) with a constant roughness value. The black curve is an empirical non-linear fit to natural data as in Fig. 2. b) Absolute values of residuals between simulated networks and the best fit to natural data. Colors of plotted curves refer to the various tested local roughness values as in (a). Cyan colored line (roughness of 1000 m) displays values above the best fit to natural data and is thus rejected as being a good fit. Black, red and green lines also display relatively large misfits, but the corresponding curves in (a) remain within the domain of natural data (white dots). The lowest misfit is obtained for a local roughness of 100 m.

grids and therefore introduces a variety of flow directions, this may not be sufficiently close to the natural flow variation found in nature on very low slopes. Introducing some stochasticity in the flow directions like in other landscape evolution models (Murray and Paola, 1994) or using different flow algorithms such as the D-Infinity fluvial landscape evolution models (Pelletier, 2004, 2010) could be explored.

A major remaining research problem is the non-uniqueness of the results: while the initial conditions seem to be appropriate, this is not sufficient to exclude the importance of erosion processes in nature which may lead to the same results. This outlines the need for future research in producing landscape evolution models considering more internal dynamics.

5. Conclusions

In this study we have explored the influence of initial conditions of slope and roughness on the shape of drainage basins in numerical experiments of simple tilted surfaces using the CASCADE code of landscape evolution. We show that simple rules of routing water downstream according to the steepest path are sufficient to account for a natural range of the incipient drainage basin aspect ratio, independently of the erosion processes at work. To produce numerical basins that respect the main aspect ratio of natural drainage basins, one must use very low slopes of less than 1° and local roughness slope of less than ~3°. Numerical studies addressing real study cases may take advantage of the relation between local roughness and regional slope in order to produce catchment aspect ratios similar to the natural studied cases. Our simulations suggest that the maximum local slope that seems to account well for the natural observation is 10% (~3°). This value is a potential upper bound on the roughness of un-dissected surfaces in nature, for the first time obtained from a numerical model of landscape evolution as far as we know, within the limits of the model used. Accordingly, our results suggest that natural basins presenting anomalously large convergence angle (large width-to-length ratio) may either be controlled by anomalous roughness (structural or lithological), or have been strained tectonically. This study highlights the need for future research on natural observations of fluvial network changes and deformations, and on numerical implementation of better algorithms to reproduce river captures and drainage network reorganization that could also lead to wider drainage basins.

Acknowledgments

We are grateful to Gregory Hancock, Jon Pelletier and an anonymous reviewer whose thorough reviews have significantly improved the manuscript and to Geomorphology Editor Takashi Oguchi for editorial handling and his substantial input that sharpened the text. Guy Simpson is thanked for multiple discussions and Frédéric Herman for sharing his CASCADE expertise. ETH-Zürich funded Yamato's research (Sean Willett's and Paul Tackley's groups). Castelltort was funded by the Swiss National Science Foundation (grant numbers 20001-119841 and 200020-131890).

References

Braun, J., Sambridge, M., 1997. Modelling landscape evolution on geological time scales: a new method based on irregular spatial discretization. Basin Research 9, 27–52.
Braun, J., Yamato, P., 2010. Structural evolution of a three-dimensional, finite-width crustal wedge. Tectonophysics 484, 181–192.
Braun, J., Heimsath, A.M., Chappell, J., 2001. Sediment transport mechanisms on soil-mantled hillslopes. Geology 29, 683–686.
Castelltort, S., Simpson, G., 2006a. River spacing and drainage network growth in widening mountain ranges. Basin Research 18, 267–276.
Castelltort, S., Simpson, G., 2006b. Growing mountain ranges and quenched river networks. Comptes Rendus Geoscience 338, 1184–1193.
Castelltort, S., Simpson, G., Darrioulat, A., 2009. Slope-control on the aspect ratio of river basins. Terra Nova 21, 265–270.
Hancock, G.R., 2003. The effect of catchment aspect ratio on geomorphological descriptors. In: Wilcock, P.R., Iverson, R.M. (Eds.), Prediction in geomorphology. Geophysical Monograph Series. American Geophysical Union, Washington DC, pp. 217–230.
Hancock, G.R., Willgoose, G.R., Evans, K.G., 2002. Testing of the SIBERIA landscape evolution model using the tin camp creek, Northern Territory, Australia, field catchment. Earth Surface Processes and Landforms 27, 125–143.
Hovius, N., 1996. Regular spacing of drainage outlets from linear mountain belts. Basin Research 8, 29–44.
Ijjasz-Vasquez, E.J., Bras, R.L., Moglen, G.E., 1992. Sensitivity of a basin evolution model to the nature of runoff production and to initial conditions. Water Resources Research 28, 2733–2741.
Kirchner, J.W., 1993. Statistical inevitability of Horton's laws and the apparent randomness of stream channel networks. Geology 21, 591–594.
Kooi, H., Beaumont, C., 1994. Escarpment evolution on high-elevation rifted margins: insights derived from a surface processes model that combines diffusion, advection, and reaction. Journal of Geophysical Research 99, 12,191–12,209.
Molnar, P., England, P., 1990. Late Cenozoic uplift of mountain ranges and global climate change: chicken or egg? Nature 346, 29–34.
Montgomery, D.R., Dietrich, W.E., 1992. Channel initiation and the problem of landscape scale. Science 255, 826–830.
Murray, A.B., Paola, C., 1994. A cellular model of braided rivers. Nature 371, 54–57.
Parker, R.S., 1977. Experimental study of drainage basin evolution and its hydrologic implications. Colorado State University Hydrology Papers 90, 1–58.
Pelletier, J.D., 2004. Persistent drainage migration in a numerical landscape evolution model. Geophysical Research Letters 31. http://dx.doi.org/10.1029/2004GL020802.
Pelletier, J.D., 2010. Minimizing the grid-resolution dependence of flow-routing algorithms for geomorphic applications. Geomorphology 122, 91–98.
Perron, J.T., Dietrich, W.E., Kirchner, J.W., 2008. Controls on the spacing of first-order valleys. Journal of Geophysical Research 113, F04016. http://dx.doi.org/10.1029/2007JF000977.
Phillips, L.F., Schumm, S.A., 1987. Effect of regional slope on drainage networks. Geology 15, 813–816.
Roering, J.J., Kirchner, J.W., Dietrich, W.E., 1999. Evidence for nonlinear, diffusive sediment transport on hillslopes and implications for landscape morphology. Water Resources Research 35, 853–870.
Simpson, G., Schlunegger, F., 2003. Topographic evolution and morphology of surfaces evolving in response to coupled fluvial and hillslope sediment transport. Journal of Geophysical Research 108, F02300. http://dx.doi.org/10.1029/2002JB002162.
Tucker, G.E., Hancock, G.R., 2010. Modelling landscape evolution. Earth Surface Processes and Landforms 35, 28–50.
Whipple, K.X., Tucker, G.E., 1999. Dynamics of the stream-power river incision model: implications for height limits of mountain ranges, landscape response timescales, and research needs. Journal of Geophysical Research 104 (B8), 17661–17674.
Willett, S.D., 1999. Orogeny and orography: the effect of erosion on the structure of mountain belts. Journal of Geophysical Research 104, 28957–28981.
Willgoose, G., Bras, R.L., Rodriguez-Iturbe, I., 1991a. Results from a new model of river basin evolution. Earth Surface Processes and Landforms 16, 237–254.
Willgoose, G.R., Bras, R.L., Rodriguez-Iturbe, I., 1991b. A coupled channel network and hillslope evolution model: 1. Theory. Water Resources Research 27, 1671–1684.
Willgoose, G.R., Bras, R.L., Rodriguez-Iturbe, I., 1991c. A coupled channel network and hillslope evolution model: 2. Nondimensionalization and applications. Water Resources Research 27, 1685–1696.
Willgoose, G.R., Hancock, G.R., Kuczera, G., 2003. Variability of catchment statistics. In: Wilcock, P.R., Iverson, R.M. (Eds.), Prediction in geomorphology. Geophysical Monograph Series. American Geophysical Union, Washington DC, pp. 195–217.
Zernitz, E.R., 1932. Drainage patterns and their significance. Journal of Geology 40, 498–521.

Earth and Planetary Science Letters 385 (2014) 162–171

Contents lists available at ScienceDirect

Earth and Planetary Science Letters

www.elsevier.com/locate/epsl

Thermal structure of a major crustal shear zone, the basal thrust in the Scandinavian Caledonides

J. Fauconnier [a,b,*], L. Labrousse [a,b], T.B. Andersen [c], O. Beyssac [d], S. Duprat-Oualid [e], P. Yamato [e]

[a] UPMC Univ. Paris 06, UMR 7193, ISTeP, F-75005 Paris, France
[b] CNRS, UMR 7193, ISTeP, F-75005 Paris, France
[c] Center for Earth Evolution and Dynamics (CEED), Univ. of Oslo, Postbox 1047, Blindern, N-0316 Oslo, Norway
[d] Institut de Minéralogie et de Physique des Milieux Condensés (IMPMC), UMR CNRS-UPMC, Campus Jussieu, Case Courrier 115, 4 place Jussieu, F-75005 Paris, France
[e] Géosciences Rennes, CNRS UMR 6118, Université de Rennes 1, F-35042 Rennes, France

ARTICLE INFO

Article history:
Received 23 March 2013
Received in revised form 11 September 2013
Accepted 21 October 2013
Available online xxxx
Editor: Y. Ricard

Keywords:
RAMAN thermometry
thrust zones
Caledonides
thermo-kinematic modelling

ABSTRACT

Crustal-scale thrust zones accommodate most of the horizontal shortening at the front of orogenic wedges. Their thermal state is a key feature of collision zones, depending on critical parameters such as thrust rate or initial thermal properties of involved lithosphere units. We present here the first direct imaging of the thermal envelope of such a thrust zone: the Jotun Basal Thrust (JBT) in the Scandinavian Caledonides, through Raman Spectroscopy of Carbonaceous Material in the alum shales, an organic carbon-rich unit of Cambro-Ordovician age along which the basal decollement of the JBT developed. Maximum temperature mapping within this unit shows isotherms grading from ~320 °C in the south–east to ~500 °C in the north–west in the trailing end of the nappe stack. Based on bt + chl + grt + ph equilibrium, we estimate that the trailing end reached a temperature of 500 °C at 1.2 ± 0.1 GPa pressure. 2-D thermo-kinematic modelling constrained with these new natural data and timing considerations for the Scandian collision indicates that (1) peak temperature mainly reflects maximum burial stage, (2) thrust rate and dip angle must have been low for the JBT and (3) the Scandinavian Caledonides represent a relatively cold orogenic wedge compared to other orogens.

1. Introduction

In continental collision, most of the convergence between the facing plates is accommodated on a major thrust system at crustal to lithospheric scale. Our understanding of such crustal scale thrusts essentially comes from the well-studied and active Himalayan system (i.e. Main Frontal, Main Boundary and Main Central Thrusts) as well as the ancient equivalents such as the fold-and-thrust systems in the central and southern Appalachians (Boyer and Elliott, 1982). Numerical and analytical models on the thermal evolution of the MCT and the underthrusted Lesser Himalaya have been constrained by pressure–temperature paths or maximum temperature patterns across the MCT (Bollinger et al., 2004; Henry et al., 1997). Geometry at depth deduced from reflection and refraction seismic coupled with gravity measurements (Hetényi et al., 2006; Nábělek et al., 2009; Zhao et al., 1993) show that all thrusts branch from a shallowly dipping reverse ductile shear zone, the Main Himalayan Thrust (MHT), in which temperatures are only indirectly known.

The Scandinavian Caledonides, have many similarities to the Himalayas in both tectonostratigraphy and structure (Andersen et al., 2002; Labrousse et al., 2010) and therefore provide a unique opportunity to study the deeper parts of a crustal-scale thrust that compares with the MHT in size and offset. The Jotun Basal Thrust (JBT) accommodated a significant portion of the relative motion between the Caledonian nappe stack and *in-situ* basement and cover of Baltica during the Scandian collision and its later collapse (Andersen, 1998; Fossen and Dunlap, 1998). The late Proterozoic to lower Palaeozoic cover of the Baltic Shield, and most notably the graphitic black alum shale of late Cambrian to early Ordovician age, served as a decollement horizon for the thrusting. This carbon-rich black shale thus recorded the complete thermal evolution of the JBT. The thermometer based of Raman Spectrometry on Carbonaceous Material (RSCM, Beyssac et al., 2002) applied to the alum shales has enabled us to measure and map the peak temperatures along the thrust plane. Conventional thermobarometry and time-constraints from the Scandian orogeny sequence are used in the set-up of thermo-kinematic models for the JBT. The effect of convergence rate, thrust plane geometry, and duration of extensional reactivation are also evaluated. Synthetic thermal profiles from the

* Corresponding author.

0012-821X/$ – see front matter
http://dx.doi.org/10.1016/j.epsl.2013.10.038

numerical models are then discussed in the light of our new natural data.

2. Geological setting

2.1. Caledonian tectonics

The basal thrust of the Scandinavian Caledonides developed as a crustal scale shear zone when the mountain belt was assembled during the collision between Baltica and Laurentia, known as the Scandian Orogeny (Gee, 1975). The resulting Scandian nappe-pile contains four main Allochthons (Lower, Middle, Upper and Uppermost) that can be traced along the exposed length (~ 1800 km) of the orogen (Roberts and Gee, 1985). The Upper and Uppermost Allochthons are interpreted to be outboard oceanic terranes and portions of the overriding Laurentian plate, respectively (e.g. Roberts, 2003). The Middle- and Lower Allochthons are considered as the shortened pre-Caledonian passive to hyperextended margin of Baltica, but the Middle Allochthon may also contain some outboard exotic elements emplaced by large-scale strike-slip prior to the final collision (Nystuen et al., 2008; Andersen et al., 2012; Corfu et al., 2011; Kirkland et al., 2008).

In southern Scandinavia, the Middle Allochthon including the Jotun nappe is dominated by very large crystalline nappes of Proterozoic rocks, partly with meta-sedimentary cover (e.g. Lundmark and Corfu, 2007; Nystuen et al., 2008). In addition, an allochthonous melange unit with numerous mantle peridotites representing the remnants of deep basin(s) formed by hyperextension in the pre-Caledonian continental margin of Baltica, sits between the continental Lower Allochthon dominated by meta-sediments and the large Middle Allochthon nappes (see above and Andersen et al., 2012). The Jotun nappe is described as an association of Precambrian metamorphic basement thrust together with silico-clastic cover units ("Valdres Sparagmites") on top of the lower allochthon phyllites (Bryhni and Sturt, 1985).

The main thrusting of nappes onto Baltica started after the Middle Silurian Iapetus Ocean had closed in the Middle Silurian (~ 430 Ma, e.g., Corfu et al., 2006; Torsvik and Cocks, 2005). Several Pre-Scandian events affected distal parts of the margin of Baltica prior to the final closure, at 482, 450 and 446 Ma (e.g. Andersen et al., 1998; Brueckner and van Roermund, 2004; Roberts, 2003; Root and Corfu, 2012). The onset of collision is dated at ~ 430 Ma by: (i) cessation of subduction-related magmatism (e.g. Corfu et al., 2006), (ii) obduction of marginal basin/island-arc ophiolites in the Middle Silurian (Andersen and Jamtveit, 1990; Furnes et al., 1990) and (iii) the onset of the high-pressure metamorphism in the basement of Baltica (e.g. Glodny et al., 2008; Jolivet et al., 2005) as well as onset of molasses-type sedimentation in the foreland (Bockelie and Nystuen, 1985). The Scandian collision, crustal thickening and emplacement of the growing nappe-pile onto Baltica continued for ~ 25 Myr during the early Devonian. The basement rocks of the Western Gneiss Region (WGR) in the footwall of the Caledonian floor thrust reached high- and ultra-high pressure metamorphic conditions at ~ 410 to 400 Ma (e.g. Hacker et al., 2010; Kylander-Clark et al., 2008; Krogh et al., 2011). At this stage the Caledonian mountain belt in Scandinavia and East-Greenland reached dimensions similar to those of the present-day Himalaya (Labrousse et al., 2010).

The extensional phase that follows convergence can be divided in two stages (Fossen, 1992; Andersen, 1998). The early phase (Mode-I in Fossen, 1992) was induced by crustal collapse and results in reactivation of the JBT as a detachment. Late extension (Mode-II) produced crustal-scale extensional shear zones such as the Hardanger–Lærdal–Gjende Fault Zone (HLGFZ), which cross-cuts the entire nappe pile (Fossen and Hurich, 2005).

2.2. The alum shales

The black shales of the JBT, here subject to RSCM study, are located immediately above a thin discontinuous sedimentary cover to the allochthonous basement of Baltica (Fig. 1a). The basal decollement is more specifically located in the mechanically weak, organic-rich alum shales of Late Cambrian to Early Ordovician age (e.g. Bruton et al., 2010). In the field the alum shales are commonly 1 to 100 m thick and very rich in carbonaceous material (CM), with a Total Organic Carbon (TOC) up to 15% (Gautneb and Saether, 2009). The floor thrust is underlain by a thin and discontinuous (para)autochthonous cover of shale, quartzite and dispersed pockets of mostly thin basal conglomerate (e.g. Bruton et al., 1989). The floor-thrust known as the 'Osen-Røa Detachment' in the foreland of SE Norway (e.g. Nystuen, 1981; Bruton et al., 2010), can be traced westward below the Allochthons, across south-central Norway and continues into the JBT (Fig. 1). The JBT and the underlying autochthon reappear within the line of prominent basement windows formed by post-Caledonian (Permo–Triassic and younger) faulting accompanied by footwall uplift along the HLGFZ (Fig. 1) in central south Norway and beyond (Andersen et al., 1990; Fossen, 2010). The primary basement-cover relationships with local preservation of depositional contacts have also been identified below the basal thrust zone and nappes along the SE-margin of the WGR between the Bergen Arcs and Lom (Lutro and Tveten, 1998; Milnes et al., 1997). The basal thrust of the Caledonian mountain belt in South Norway can consequently be traced almost continuously across the strike from the down-faulted pin-point in the foreland south–east of Oslo within the Oslo Rift, between the deformed series at Holmstrand and the flat-lying Cambro-Silurian at Langesund (Oftedahl, 1943 in Morley, 1986; Bruton et al., 2010), to the hinterland cover on the WGR, over a distance of approximately 250 km. Our sampling profiles were collected away from areas where local thermal effect of the large Permo-Carboniferous magmatic rocks of the Oslo Rift were identified from conodont colour alteration index (Aldridge, 1984), and hence cover only 150 km of the observable across-strike section 180 km away from the fossil front (Fig. 1).

Samples collected in this study (Table 1, Fig. 1) show penetrative ductile stretching (Fig. 1a) with lineations trend from 100° to 135°. The foliation is parallel to the JBT, dipping toward the SE or NW defining the limbs of a large-scale synform in South Norway. Shear bands, drag folds, asymmetric boudinage within the alum shales systematically indicate top to NW to W shear-senses (Fig. 2), except for 2 sampling sites preserving top to SE shear sense indicators (Fig. 1a). Most of the structures within the alum shale layer therefore reveal extension along the former JBT dip direction related to north-westward extensional reactivation of the JBT (Fossen, 1992; Andersen, 1998).

The age of deformation along the decollement post-dates deposition of the Late-Silurian molasse-type fluvial deposits in the foreland as well as Lower Devonian (408 Ma) thrust-related growth of muscovite dated by $^{40}Ar/^{39}Ar$ method near the extensional break-away of the Valdres area (Fossen and Dunlap, 1998). In the central part of the orogen the basal decollement as well as the meta-sedimentary thrust wedge were strongly affected by late- to post-orogenic NW-directed extension, which was partly contemporaneous with thrusting in the foreland (e.g. Andersen, 1998; Fossen, 2010). The latest ages on syn-kinematic muscovites in the Jotun nappe and the shallowest levels of the WGR below the JBT indicate a north-westward reactivation until 400 to 395 Ma (Fossen and Dunlap, 1998; Hacker, 2007). JBT therefore underwent some stretching during late Caledonian extension as well as normal offset along cross cutting extensional (Fossen and Hurich, 2005).

The JBT can therefore be considered as a crustal-scale structure that first accommodated thrusting of outer Baltican continental

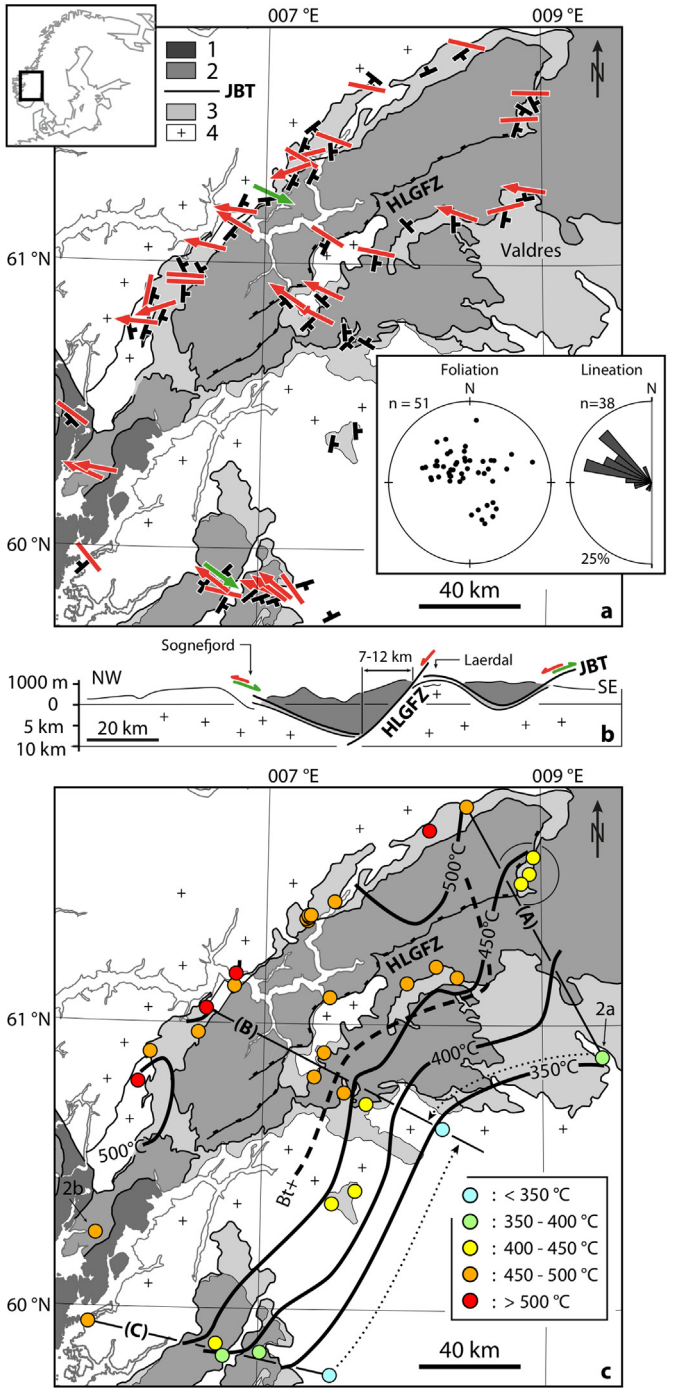

Fig. 1. (a) Location of sampling sites, foliation and lineation strike and dip. Arrows indicate sense of shear. Green arrows indicate syn-collisional thrust movements on JBT, red arrows indicate late top-to-northwest extension. Rose diagram shows lineations and stereoplot shows poles to foliation. 1. Upper Allochthon, 2. Middle Allochthon (i.e. Jotun nappe), 3. Lower Allochthon and Baltica cover, 4. Baltica basement. HLGFZ Hardanger–Lærdal–Gjende Fault Zone, JBT Jotun Basal Thrust. (b) Schematic cross-section through the southern Caledonides along profile B in Fig. 1c. Offset on the HLGFZ deduced from Lutro and Tveten (1998). (c) Maximum temperature estimates from RSCM on alum shales. A, B and C profiles refer to Fig. 3. Dashed arrows indicate the projection of profiles A and C on B for Fig. 3. Circled points are 46, 47, 48 discussed in the text. bt+ dashed line is biotite isograd.

margin as well as outboard terranes onto Baltica during Scandian collision for 25 Myr from 430 to 405 Ma (green arrows on Fig. 1a & b), which brought the westernmost WGR to UHP at 3.4 GPa (Hacker et al., 2010). Thereafter, it was reactivated as a top-to-west extensional detachment (red arrows on Fig. 1a & b) for 5 to 10 Myr (from 405 to 400–395 Ma). In the studied section of southern Norway, the alum shale is a nearly continuous lithology within the decollement, recording its complete thermal evolution down-dip for 150 km parallel to its displacement direction.

3. RSCM temperature envelope of the JBT and constraints on its geometry

3.1. Method

Organic matter trapped in sediments gradually changes its chemistry and structure under the effect of heating, burial and subsequent metamorphism (Beyssac et al., 2002). The RSCM thermometry is based on the quantitative determination of the degree of graphitisation of CM which is a reliable indicator of metamorphic temperature. Because graphitisation of CM is irreversible, the structural modification recorded by Raman spectrometry is insensitive to retrogression and therefore records the maximum temperature experienced by the rocks during a PT-time loop (Beyssac et al., 2002). Temperature can be determined with absolute confidence of ±50 °C in the range 330–650 °C. Within-sample and relative uncertainties between samples are, however, much smaller, in the 10–15 °C range (Beyssac et al., 2004). More recent work on lower-grade rocks have shown that CM Raman spectra also can be correlated with the metamorphic temperature in the range at 200–330 °C and a systematic correlation of the Raman spectra and temperature expands the total range from 200 to 650 °C (Lahfid et al., 2010). The absolute error of the method is ±50 °C, but we also estimate a standard deviation for each sample ($\sigma/\sqrt{n}$) which gives an insight on within-sample heterogeneity (detailed description of method and errors in Beyssac et al., 2002 and 2004). In this study Raman spectra were obtained using a Renishaw InVIA Reflex microspectrometer (IMPMC, Paris). We used a 514 nm Laser Physics argon laser in circular polarisation, and followed closely the analytical and fitting procedures described in Beyssac et al., (2002 and 2003). Measurements were done on polished thin sections and CM was systematically analysed below a transparent adjacent mineral, generally quartz. 586 spectra were recorded on 40 samples (Table 1) in extended scanning mode (700–2000 cm^{-1}, Fig. 2e) for lower T samples or restrained scanning mode (1200–1700 cm^{-1}, Fig. 2f) for higher T samples, with acquisition times from 30 to 60 seconds. Spectra were then processed using the software Peakfit (Beyssac et al., 2003).

3.2. Results

Temperatures were derived from 10 to 25 spectra in each sample. Only spectra disturbed by fluorescence of the adjacent mineral, and those measured in detrital graphite were not considered. Temperature estimates vary from 314 °C to 515 °C with a standard error between 2 and 7 (Table 1). Average scatter was ±25 °C with maximum value of ±35 °C. The low-T calibration values were preferred for 3 sites (1, 61 and 64), high-T calibration giving the same T values with larger scatters. In order to estimate the outcrop scale variations of maximum temperatures recorded by the alum shales, several outcrops were repeatedly sampled. Series 1a to 1d, or 9a and 9b coming from two outcrops yielded the same T_{max} value (Table 1) within the measurement uncertainties. Samples 92, 93 and 94 also come from the same outcrop. Differences in T_{max} are below 25 °C, meaning local variations in carbonaceous material maturation are within uncertainties. It is therefore possible to interpret the 40T_{max} estimates at the scale of the southern Caledonian nappes stack, as a mapping of the maximum temperatures reached by the alum shales along the footwall of the JBT during the Scandian collision (Fig. 1c). Along three profiles oriented perpendicular to the present-day thrust front, temperatures

Table 1
Samples, outcrop coordinates, mineral assemblages, number of spectra recorded for RSCM, R2 (*RA1) ratios calculated, average temperature and the standard deviation $\sigma/\sqrt{n}$.

Sample	Latitude	Longitude	Minerals	Raman			
				n spectra	R2 or RA1	*T* mean [°C]	$\sigma/\sqrt{n}$
1a	59.7570	7.5137	ph + pl	24	0.627*	314	3
1c				14	0.636*	325	2
1d				15	0.658*	353	2
4	59.8334	7.0139	chl + ph	16	0.584	381	2
6b	59.8176	6.7531	chl + ph + pl + tur	25	0.570	387	2
9a	59.8606	6.7008	ph + pl	15	0.504	417	2
9b				12	0.486	425	4
10b	59.9254	5.7898	cb + ph + pl	14	0.342	489	4
11	60.2419	5.8138	cb + chl + grt + ph + pl	15	0.355	483	4
16	60.7869	6.0705	bt + ph + pl	13	0.283	515	4
18	60.8942	6.1501	bt + cb + ph + pl + tur	15	0.386	469	4
20	61.0564	6.5500	bt + cb + chl + ph	13	0.284	515	5
21	61.1380	6.7509	bt + cb + ph	12	0.375	474	6
22	61.1819	6.7595	cb + chl + ph + pl	14	0.314	501	4
32	60.9693	6.4970	chl + ph	13	0.358	481	4
35	61.3760	7.2798	BT + chl + ph + pl	13	0.330	494	3
36	61.3831	7.2705	bt + chl + ph + pl	11	0.341	489	5
37	61.3886	7.2899	cb + ph + pl	18	0.349	485	4
38	61.3950	7.2843	bt + cb + ph	15	0.384	470	4
39	61.3964	7.3025	bt + ph + pl + tur	15	0.400	463	4
41	61.4459	7.4764	cb + chl + grt + ph	12	0.339	490	7
43	61.7041	8.1740	ph	14	0.242	534	4
44	61.7908	8.4500	chl + ph	15	0.329	495	4
46	61.6114	8.9519	ph	15	0.439	445	3
47	61.5518	8.9225	ph	13	0.464	435	3
48	61.5171	8.8619	chl + ph + tur	18	0.461	436	3
51	61.1808	8.3907	bt + cb + chl + ep + ph + pl	10	0.401	463	4
52	61.1581	8.0216	ph	15	0.366	478	5
54	61.1036	7.4560	bt + cb + chl + ph	15	0.343	488	4
56	60.9067	7.4221	bt + chl + ph + pl	13	0.366	478	6
57	60.8199	7.3539	bt + cb + chl + ph	15	0.412	458	3
58	60.7653	7.5740	ph	14	0.411	458	6
60	60.7259	7.7358	ph	16	0.458	437	3
61	60.6406	8.2944	ph	16	0.646*	338	3
62	60.3687	7.5015	chl + ph	14	0.431	449	3
63	60.4154	7.6679	ph + pl	14	0.460	436	7
64	60.8970	9.4593	–	13	0.658*	352	2
92	61.2186	8.2354	cb + chl + ph	14	0.418	455	2
93				14	0.382	471	3
94				14	0.361	480	4

rise from 314 to 352 °C in the SE end up to 483 to 534 °C at the NW termination (Fig. 3). The three profiles describe a regional increase in temperature with isotherms following the average strike of the Caledonian nappe-stack (Fig. 1c). When projected on a single profile (Fig. 3), our data show that temperature increase is roughly linear for the first 70 km from 320 °C to 500 °C. Temperature values for samples 46, 47 and 48 appear slightly out of trend on a temperature–distance diagram (circled in Figs. 1c and 3) possibly due to non-cylindricity of the regional tectonics toward the North. Alternatively it is also possible that these samples are from a structurally higher level, basement not being exposed near these sampling sites. Value points derived from samples in the hanging-wall of the HLGFZ have been restored in their initial position, considering horizontal offsets of 7 to 12 km on the HLGFZ according to cross-sections (Lutro and Tveten, 1998; Andersen et al., 1999), shaded boxes in Fig. 1b). Despite the offset on the HLGFZ, the samples in its hanging-wall do not show any changes in the global temperature trend. At regional scale, RSCM temperature pattern eventually draw a 130 km long subplanar envelope with lowest values of 320 °C at the present-day frontal hanging-wall cut off and 500 °C at the trailing end the JBT.

Corresponding with the maximum temperature increase, the alum shales also show a change in textural mode, from preserved detrital grains (micas, quartz and clay minerals) on the south–east (Fig. 2c), to chl + ph + pl + qz + CM ± cb paragenesis in the central area, and bt + ph + pl + qz + CM ± grt (Fig. 2d) in the trailing end near the WGR. The crystallization of biotite from chlorite can be traced as an isograd trending parallel to the nappe-stack regional strike between samples with comparable chemistries (Fig. 1c), close to the 450 °C RSCM isotherm.

Constraints on the maximum depth recorded by the alum shales were deduced from the peak metamorphic paragenesis bt + chl + grt + ph developed in the samples with highest RSCM temperatures. Within the paragenesis stability field in a pseudo-section derived from whole-rock composition of alum shales and thermodynamic modelling (supplemental material, Holland and Powell, 1998), Si content in phengites, reaching 3.2 Si p.f.u. and almandine rich ($X_{Alm} = 0.7$) overgrowth on garnet yield narrow PT conditions of 500–550 °C and 1.1–1.3 GPa pressures for peak equilibration, in agreement with the maximum temperature estimates from RSCM. Considering that this pressure corresponds a lithostatic pressure and assuming a density of 2700 kg/m^3 in average for the crust, this PT estimate yields a 45 ± 4 km depth for the maximum burial of the north-westernmost studied shales/schists.

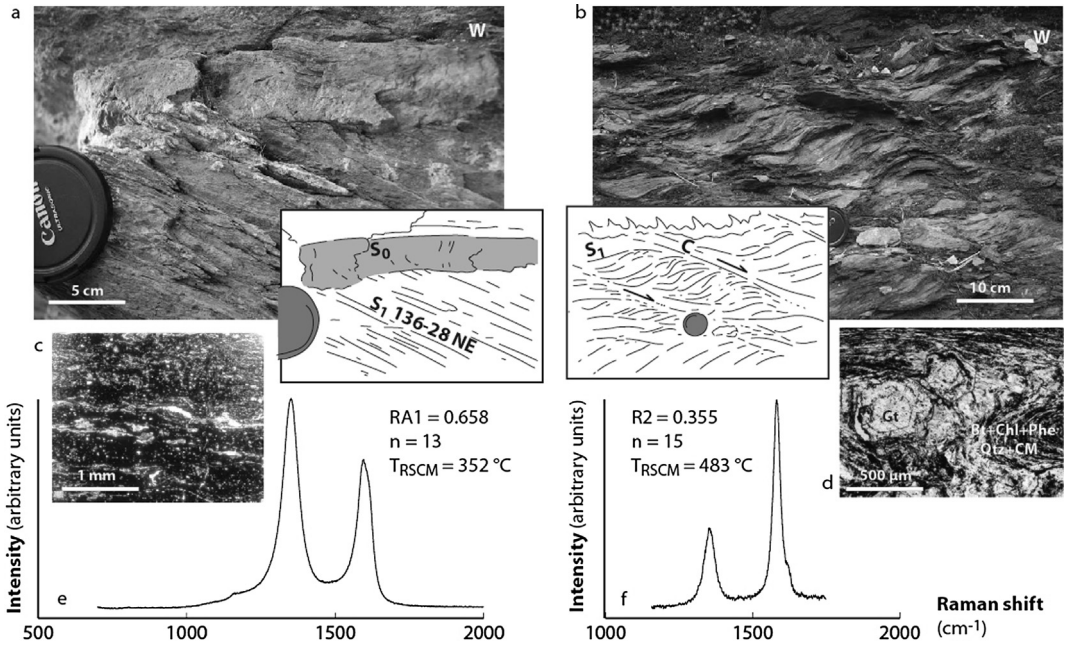

Fig. 2. Field photos, thin sections and representative Raman spectra for carbonaceous material from samples 64 (a, c, e) and 11 (b, d, f) (located 2a and 2b in Fig. 1) respectively on the southeastern and northwestern ends of profiles in Fig. 3. RA1 and R2 are parameters derived from curve fitting for low (Lahfid et al., 2010) and high (Beyssac et al., 2002) temperature calibrations.

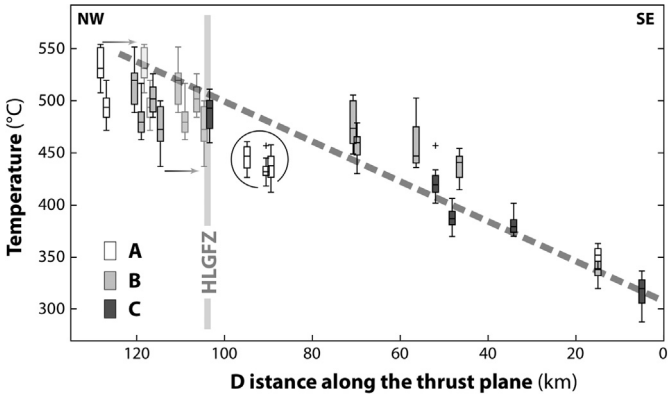

Fig. 3. RSCM temperatures profiles along lines A, B and C in Fig. 1. Segments represent maximum and minimum values, box plot represent 25%, 75% and median is shown within the box plots for each samples. Isolated cross stand for outliers. Shaded box-plots represent data points located in the hanging wall of the HLGFZ after restoration. Encircled points 46, 47, 48 are discussed in the text.

4. Thermo-kinematic modelling: the effect of convergence rate, dip and thermal heritage

The thermal profile along the JBT as deduced from RSCM data (Fig. 3) can be used as a constraint to model the thermal behaviour of a crustal scale thrust zone. The geodynamic significance of the maximum temperature profile remains unclear: is it representative of a synchronous stage in the JBT evolution or does it represent a diachronous envelope of its entire history? Once its significance is assessed, it can be used as a reference to evaluate the first order parameters governing the thermal profile shape of such a thrust zone. 2-D numerical modelling of temperature evolution along a thrust, both during collision and subsequent extensional reactivation, allowed us to test the influence of geometry, velocity and extensional reactivation on the maximal temperature distribution along the thrust, here considered as cylindrical (Fig. 1c).

4.1. Numerical code and experimental set-up

Relevant analytical computations of their thermal structure have been proposed for superficial wedge structures (e.g. Royden, 1993), as well as for lithospheric-scale thrust systems (Huw Davies and Stevenson, 1992). Nevertheless, integration of these partial analytical solutions would require interpolation (e.g. Huw Davies, 1999) for a full 2-D coverage of a complete orogenic wedge. For this reason, we privileged a numerical approach here, by using the thermo-kinematic model designed by Duprat-Oualid et al. (in press), to focus on the thermal evolution above and below crustal scale thrust systems. This code is an implicit finite difference code solving the heat equation (including diffusion, advection and heat production). The velocity field around the thrust is computed independently and the marker-in-cell method (Gerya, 2010) is used to advect temperature and rock properties through time. All the details about the numerical methods used in this study and comparisons with analytical solutions validating this code can be found in Duprat-Oualid et al. (in press).

Present-day topography in Western Norway, resulting of cumulated effects of N-Atlantic rifting (Redfield et al., 2005) and post-glacial uplift and erosion (Nielsen et al., 2009), is only poorly related to Caledonian tectonics. Estimates of climax Caledonian topography are based on comparison with Himalayas (Gabrielsen et al., 2005) or estimates of maximum crustal thickness (Andersen et al., 1998). Since no exact data is available for topography and erosion rates during the Caledonian collision, isostasy and erosion are not considered in this study. Shear heating, which in other studies have been shown to be important (e.g. Souche et al., 2013) is not included in the heat equation, since its implementation requires strong *a priori* hypothesis on parameters such as the effective viscosity of the shear zone, or the thickness on which strain is distributed. Furthermore the alum shale localizing the strain along the JBT has a very low shear strength and it is therefore unlikely that deformation produced significant heat (Souche et al., 2013).

Models are composed of three different horizontal layers as presented in Fig. 4: air (2 km), a 30 km thick continental crust, and a lithospheric mantle (Table 2) in a 150 km high model box.

Table 2
Parameters used for thermo-kinematic modelling of the JBT constant in every models presented.

Parameter	Meaning	Value
dx and dz	Vertical and horizontal mesh resolution	2 km
H	Model height	150 km
H_c	Crust thickness	30 km
T_{surf}	Surface temperature	20 °C
Q_m	Basal heat flux	25×10^{-3} W m^{-2}
A	Surface radiogenic heat production	3×10^{-6} W m^{-3}
Z_r	Thickness of the radiogenic layer	10 km
ρ_c	Crust density	2700 kg m^{-3}
ρ_m	Mantle density	3300 kg m^{-3}
k	Thermal conductivity	3 W m^{-1} K^{-1}
Cp	Heat capacity	1000 J kg^{-1} K^{-1}

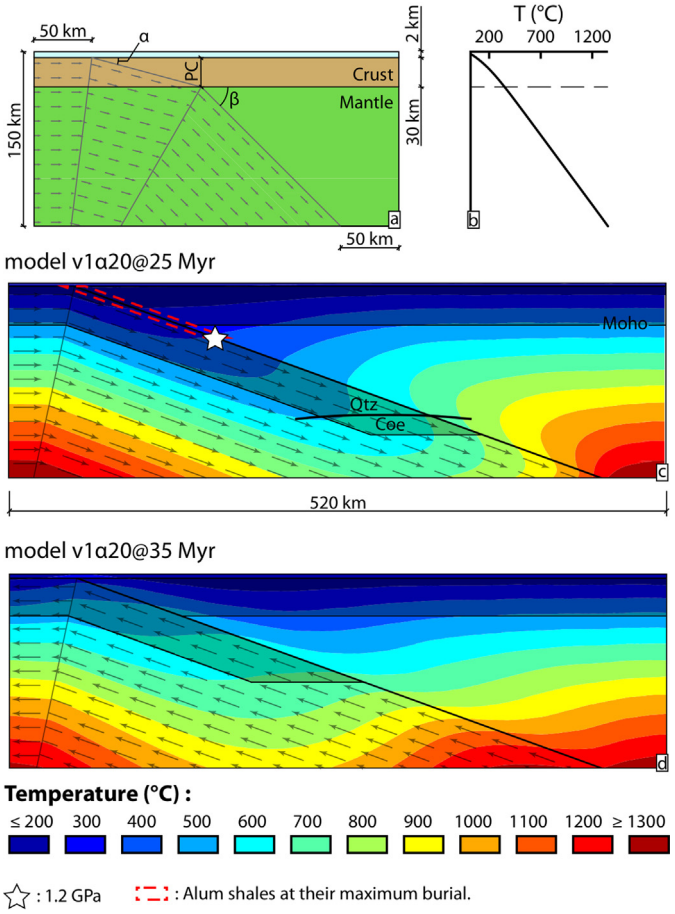

Fig. 4. Geometrical and velocity model setup (a). Geotherm used for the initial temperature field (b). Numerical model $v1\alpha20$ (i.e. 1 cm yr^{-1} convergence rate and 20° dipping thrust plane) geometry and isotherms pattern at maximum burial (c), and after 10 Myr divergence (d). White star pins depth where 1.2 GPa pressure is reached by the top of the subduction slab.

The width is adjusted so that 50 km remain on each side of the thrust whatever its dip to avoid side effects (Table 3 and Fig. 4). The spacial grid resolution is 2×2 km. Parameters such as density, thermal conductivity and heat capacity are not varied and are presented in Table 2. Radiogenic heat production is considered as exponential in the upper crust (10 km). Equivalent average radiogenic heat production for the upper crust would be 1.89 μW m^{-3} what compares with acknowledged average values for the continental crust (Rudnick and Gao, 2003). Thermal boundary conditions are set with constant surface temperature, constant basal heat flux (25 mW m^{-3}) and insulating boundary conditions (i.e. no heat flux) for the both lateral sides of the box. The initial geotherm is computed with a zero velocity field using the parameters described previously (i.e. constant surface temperature, constant heat flux, no heat flux on the side walls) until it reaches thermal equilibrium (i.e. a temperature change between two successive time-steps lower than 0.1 °C).

The duration of the thrusting is set to 25 Myr according to Scandian orogeny calendar (Section 2.1). Subduction dip angle and convergence rate are bound in order to bring the median continental crust to Ultra High Pressure (UHP) domain (100 km) at the end of continental subduction. In all models, subduction is followed by exhumation due to extension, with velocity equal to convergence rate.

Reference model ($v1\alpha20$) exhibits a 20° constant dip thrust with 1 cm yr^{-1} velocity (Table 3). Geometry effects have been explored by changing dip to 10° and velocity to 2 cm yr^{-1} in the experiment $v2\alpha10$. The effect of dip change within the mantle is evaluated in experiment $v1\alpha10\beta45$, with 10° superficial dip and 45° below 30 km, representing change from crustal to mantle lithologies and mechanical behaviour. The exhumation stage duration has been set to 10 Myr in the 3 configurations above, according to Scandian orogeny calendar. One experiment with 5 Myr lasting divergence ($v2\alpha10S$) evaluates the influence of a shorter extensional reactivation of the JBT, while $v2\alpha10L$ experiment represents a longer (20 Myr) extension scenario.

4.2. Results

All models show a deflection of isotherms (Fig. 4) during subduction stage, with temperature profile along the thrust zone flattening progressively from top to bottom with time. During divergence, profile turns convex upward, with inflexion point migrating from surface to depth with time (Fig. 5). The envelope profile resulting from this thermal evolution is therefore defined by the divergence stage at shallow depth and initial thermal conditions in the deeper part. This diachronous thermal envelope, representing the maximum temperature reached by markers at the top of the subducting slab, will later be compared with RSCM temperature estimates, considered as inherited from peak conditions (Fig. 6, Beyssac et al., 2002).

Thermal envelopes deduced from models, compare with peak thermal profiles computed for equivalent thrust zones (Fig. 7), Reference model $v1\alpha20$ is close to peak thermal profiles with equivalent set-up (model 1 in Henry et al., 1997, with no ero-

Table 3
Varying parameters for the different models. $v2\alpha10S$ and $v2\alpha10L$ are for short (5 Myr) and long-lasting (20 Myr) extensional reactivation.

Model	Convergence rate, v [cm yr^{-1}]	First subduction angle, α [°]	Second subduction angle, β [°]	Dip changement depth, PC [km]	Exhumation duration, t [Myr]	Model width, W [km]
$v1\alpha20$	1	20			10	520
$v2\alpha10$	2	10			10	950
$v2\alpha10S$	2	10			5	950
$v2\alpha10L$	2	10			20	950
$v1\alpha10\beta45$	1	10	45	30	10	390

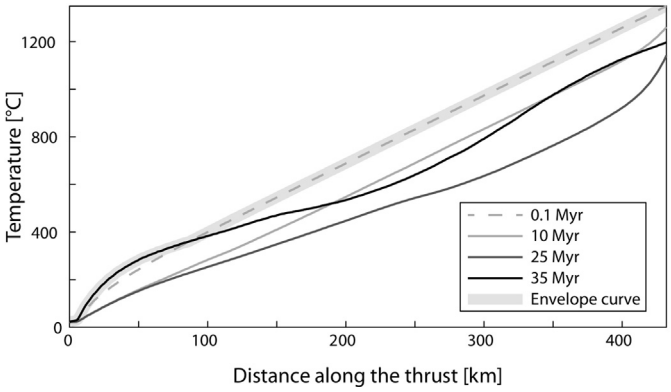

Fig. 5. Temperature profile along the thrust plane at 0.1, 10, 25, and 35 Myr for reference model $v1\alpha20$. Envelope curve of the instantaneous temperature profiles is used for comparison with RSCM data.

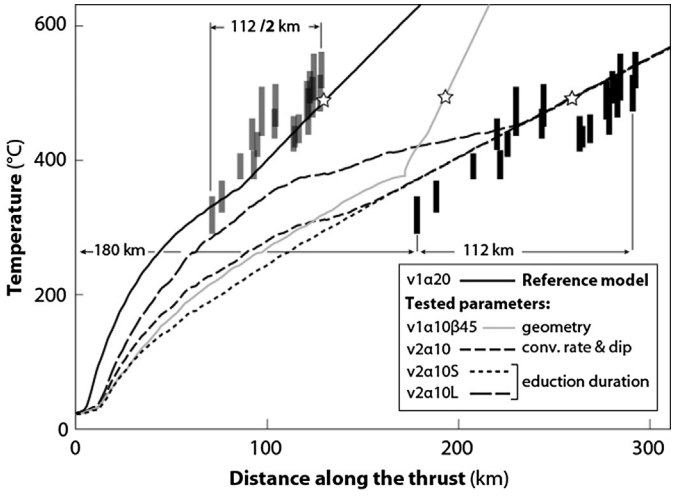

Fig. 6. Temperature profiles from numerical models and natural data. $v1$ series refer to models with 1 cm yr^{-1} convergence rate, $v2$ series to 2 cm yr^{-1}. α is the dip in degrees of the thrust at the surface, β is the second dip angle for slab with changing dip. S and L refer to models with shorter and longer extensional reactivation stages (5 and 20 Myr resp.). Natural data with their present-day position are shown with black rectangles. Grey rectangles show the same data with distances shortened by 50%. Stars represent the point along profiles where 1.2 GPa pressure was reached at maximum burial.

sion considered, mantle heat flux 28.5 mW m^{-2}, convergence rate 1.5 mm yr^{-1} and implementation of friction on fault). More sophisticated modelling with crustal layering, erosion and shear heating (Bollinger et al., 2006) also give similar results for a 20 Myr lasting activation. We therefore consider that our simplistic approach, even if not accounting for all processes occurring at depth, succeeds to reproduce first order thermal behaviour of subducting continental lithosphere. Along the reference profile for $v1\alpha20$ model, the 1.2 GPa pressure is reached at 130 km along the thrust. Convex shape is observed for the 100 shallower kilometers.

Change in dip and velocity from $v1\alpha20$ to $v2\alpha10$ causes a flattening of the temperature–distance profile along the thrust. 1.2 GPa pressure is reached at 250 km distance (Fig. 6). Thermal effect of divergence is observed for the 130 first kilometers. From reference model $v1\alpha20$ to $v1\alpha10\beta45$, the shape change induces a concave upward temperature profile, and 1.2 GPa pressure is reached at 190 km along the thrust. The effect of divergence is limited and restricted to the low temperature portion. Model $v2\alpha10S$ explores the effect of limited extensional stage. The resulting profile shows no convex portion in the first kilometers. Model $v2\alpha10L$ shows a wider (200 km long) convex portion with a maximum retrograde heating about 100 °C in comparison with model $v2\alpha10$.

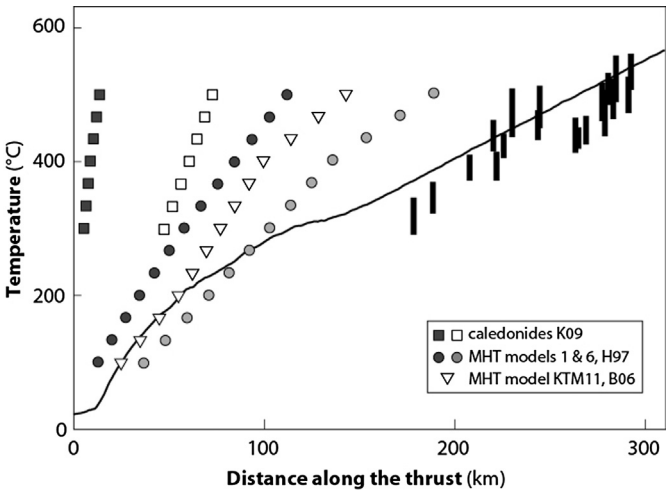

Fig. 7. Natural (black rectangles) and preferred synthetic profile (black line) from this study ($v2\alpha10$) compared to temperature profiles modelled for: the Caledonides (Kylander-Clark et al., 2009) at maximum burial (filled squares) and after 5 Myr exhumation of the upper lithosphere (open squares). Circles and triangles refer to the peak thermal state of the MHT in different thermo-kinematic models published by Henry et al. (1997) and Bollinger et al. (2006).

Diachronicity is therefore sensible only for long reactivation scenarios.

5. Discussion

The RSCM temperature estimates in the alum shales of the JBT throughout the Southern Scandinavian Caledonides yield a diachronous envelope for the thermal state of the shear zone during thrust and later extensional reactivation. Thermobarometry on the trailing end of the nappes allows to pin the now outcropping high T (500–520 °C) end of the alum shales unit at 1.2 GPa pressure, depth converted to a burial of 45 km. Assuming a cylindrical pattern for the RSCM temperature envelope, this can be rendered as a single profile to be compared with 2-D thermo-kinematic models for a crustal scale thrust zone. Rocks at the present-day hanging-wall cut-off (or eroded front), underwent temperature as high as 300–320 °C. The position of the thrust front in Caledonian times located about 180 km further SE near Oslo (Fig. 1) can be used as reference for the comparison of synthetic profiles with natural data (Fig. 6).

The models proposed here focus on the effect of initial geometry and convergence rate as well as duration of extensional reactivation (Table 3).

The comparison of synthetic profiles computed in this study with the natural RSCM temperature profile allows us to constrain the most probable geometry and history for the JBT, and to discuss implications for the behaviour of crustal scale thrust zones. If the present-day down-dip length of the JBT is considered as representative for its active stage, i.e. no stretching occurred during exhumation, then the reference model $v1\alpha20$, reaching 45 km and 500 °C at 130 km along dip from front, yield a too steep thermal envelope to reproduce the natural data (Fig. 6). Profile deduced from $v1\alpha10\beta45$ yield a less steep profile and the pinning depth at 45 km is reached at 500 °C but its length remains too short to fit natural data. Models with a higher velocity (i.e. 2 cm yr^{-1}) and lower dip value (10°) better reproduce the natural data. Extensional reactivation modifies the thermal envelope only in the shallowest levels, so that no natural data can be used to discriminate between 5 or 10 Myr extension scenarios. Longer extension duration (as in $v2\alpha10L$) would have had an impact on the sampled portion of the JBT, and seem therefore unlikely.

If exhumation of the alum shale is associated with thinning and stretching along the JBT, then the present-day length of the profile can be restored to a shorter length. It can be superimposed to the reference model $v1\alpha20$ if reduced to half its length, i.e. if stretching factor during exhumation was equal to 2 (Fig. 6). Assuming such a stretching implies that the distance between the front and the thrust segment sampled in this study was also shorter (i.e. data must be shifted horizontally in Fig. 6), which is unlikely since Caledonian extension was not recorded in basement units between the Caledonian thrust front and the present-day hanging wall cut-off, the limited extensional features being locally related to Permian rifting (Sundvoll and Larsen, 1994). Even if stretching may have occurred in the JBT footwall during late Caledonian extension, it must have remained limited; $v2\alpha10$ model therefore remains our preferred simulation.

Estimate of denudation for a 10° dip thrust yields 25 km above the present-day hanging-wall cut off, which encompasses both tectonic thinning during late Caledonian extension and subsequent erosion. In the $v2\alpha10$ model only 10 km are related to extensional reactivation and 15 km have to be accommodated by post-Caledonian erosion. Independent estimates of erosion by isostatic considerations (Nielsen et al., 2009) give a 10–20 km erosion for the reduction of an initial 3500 m topography. Even if this value is more relevant for the axial domain of the mountain range, it gives a compatible upper bound for the denudation aplomb to present-day hanging-wall cut-off.

The best-fit model convergence rate value (2 cm yr^{-1}) remains low regard to the 8–10 cm yr^{-1} latitudinal relative movement deduced from palaeomagnetism for Laurentia and Baltica (Torsvik et al., 1996). A higher convergence rate, not tested in our models, would imply a shallower dip and be geometrically impossible along dip length for the JBT. The apparent discrepancy between palaeomagnetic studies and the present conclusions can be explained by (1) a possible partition of convergence on different horizontal shortening structures, the JBT being one of them, and/or (2) an actually low orthogonal convergence rate between Laurentia and Baltica, due to oblique relative motion. Rotation data from palaeomagnetism indeed indicate that Laurentia and Baltica margins trended N–S when facing each other on the equator in Silurian times (Torsvik et al., 1996), the 8–10 cm yr^{-1} latitudinal relative motion being then the strike-slip component of their bulk relative velocity. A third possibility not accounted for in the averaged convergence data based on palaeomagnetic data is that the convergence rate drastically retarded after continent–continent collision started in the Middle to Late Silurian.

Comparison of our results with other thermo-kinematic models for the Caledonides (Kylander-Clark et al., 2009, Fig. 7) show drastic discrepancy, mainly due to the higher dip (45°) used in their models. Designed to reproduce the thermal field at depth, those models did not intend to reproduce a realistic wedge structure for the upper levels, and yield unrealistic high thermal profiles for the first kilometers of the thrust interface.

Comparison with other models for thrust zones with similar size and offset to the JBT, allow a discussion of the thermal behaviour of the Scandian thrust wedge with regard to present-day analogues. JBT indeed compares in geometry and thermal state with what is inferred from PT history of the exhumed Lesser Himalayas (Beyssac et al., 2004) or what indirect imaging assess for the present-day MHT. The anisotropic interface interpreted as the MHT in P-wave amplitude tomography (Schulte-Pelkum et al., 2005) indeed flattens at 42–45 km depth 230 km north to the MBT. Hi-Climb profile (Nábělek et al., 2009) also reveals flattening of the MHT at 40 km depth 200 km north to the MFT. Thermo-kinematic modelling of temperature field in the orogenic wedge constrained by gravity data (Hetényi et al., 2007) yield a MHT reaching 520 °C at 42 km depth 190 km north to the MBT.

The best-fit thermo-kinematic model for the MHT (model 1, Henry et al., 1997) compares with the $v1\alpha20$ model for the JBT, only valid for an unlikely and considerable stretching of the alum shales. The natural data from the JBT present-day front are still about 100 °C colder (Fig. 7) than the coldest model considered in Henry et al. (1997), with moderate erosion and friction on fault implemented. Equivalent models could also be proposed for the JBT with *ad hoc* erosion rate counterbalanced by significant shear heating on fault plane. RSCM data from Devonian supra-detachment basins in the WGR, above the western continuation of the JBT: the Nordfjord Sogn Detachment, shows that a temperature anomaly of 50 to 100 °C at the base of the basins could be due to shear heating on the detachment fault system during extensional reactivation (Souche et al., 2012). Whatever the combination of competing processes, such as erosion and shear heating, Scandian orogenic wedge must have remained relatively cold throughout the complete activation sequence of the JBT, compared to MHT for instance, implying that the Caledonides would plot out of the small/cold–large/hot trend inferred from worldwide considerations on orogens (Beaumont et al., 2006). First order control of the thermal gradient along the thrust being the initial geotherm within the thrust hanging-wall combined with thrust rate, this implies or (1) that the basement units involved in the Middle Allochthon nappe sequence were relatively cold at the onset of thrusting or (2) that the JBT had a significantly higher thrust rate than the present-day MHT. This second deduction is not supported by scatter of radiochronological data from WGR eclogites buried to UHP during the same event implying a slow rate for the coeval continental subduction (Kylander-Clark et al., 2009).

6. Conclusion

The RSCM data presented here constitute the first down-dip temperature mapping across a significant part (150 km) of a crustal-scale collisional thrust zone. The JBT, that compares in size, structural position and offset with the Himalayan MHT (Labrousse et al., 2010) is developed within the Cambro-Ordovician carbon-rich alum shale, which recorded the thermal evolution of the JBT throughout the Scandian thrusting and the subsequent extensional reactivation. Peak temperature estimates in the alum shale yield peak isotherms roughly parallel to the Caledonian nappe front grading from 320 °C on its leading edge to 500 °C on its trailing edge. Based on independent estimate of maximum burial depth recorded in the alum shales (45 km see above), time constraints on the Scandian collision, and compatible convergence rates, thermo-kinematic modelling of the JBT allows us to assess its most probable geometry while active. A 10° dip toward the NW and 2 cm yr^{-1} thrust rate is the best fit with a dynamic model for the JBT, however, without considering erosion and shear heating. The preferred geometry and thrust rate are compatible with independent constraints for the Caledonian orogenic wedge and reveal cold thermal regime for the Scandian collision when compared to the Himalayan collision. This is also supported by the lack of syn-collision granites similar to the Himalayan leucogranites on the Scandinavian side of the Caledonides. The thrust rate is considerably lower than relative plate-motion velocity between Baltica and Laurentia deduced from palaeomagnetic data (Torsvik et al., 1996), implying that the JBT only accommodated part of the horizontal shortening, alternatively that the plate convergence slowed down after continent–continent collision took place. The fully thermo-mechanical modelling of the Scandian continental collision now thermally exceptionally well constrained from near the top (250 °C) to bottom (800 °C in the UHP cores of the WGR, Hacker et al., 2010), would allow to precise whether this collision remained cool due to the implication of initially cold continental margins or due to high convergence rate compared to present-day equivalents.

Appendix A. Supplementary material

Supplementary material related to this article can be found online at http://dx.doi.org/10.1016/j.epsl.2013.10.038.

References

Aldridge, A.J., 1984. Thermal metamorphism of the Silurian strata of the Oslo region, assessed by conodont colour. Geol. Mag. 121, 347–349.

Andersen, T.B., 1998. Extensional tectonics in the Caledonides of southern Norway, an overview. Tectonophysics 285, 333–351.

Andersen, T.B., Berry IV, H.N, Lux, D.R., Andresen, A., 1998. The tectonic significance of pre-Scandian $^{40}Ar/^{39}Ar$ phengite cooling ages in the Caledonides of western Norway. J. Geol. Soc. (Lond.) 155, 297–309.

Andersen, T.B., Corfu, F., Labrousse, L., Osmundsen, P.T., 2012. Evidence for hyperextension along the pre-Caledonian margin of Baltica. J. Geol. Soc. 169, 601–612.

Andersen, T.B., Hartz, E., Torsvik, T.H., Osmundsen, P.T., Andresen, A., Eide, E.A., Braathen, A., 2002. The aftermath of the Caledonian continental collision in the North Atlantic Region: A structural template for later events?. In: Abstracts and Proceedings of the Norwegian Geological Society, vol. 2, pp. 12–14.

Andersen, T.B., Jamtveit, B., 1990. Uplift of deep crust during orogenic extensional collapse: a model based on field studies in the Sogn-Sunnfjord region of Western Norway. Tectonics 9, 1097–1111.

Andersen, T.B., Skjerlie, K.P., Furnes, H., 1990. The Sunnfjord Melange, evidence of Silurian ophiolite accretion in the West Norwegian Caledonides. J. Geol. Soc. 147, 59–68.

Andersen, T.B., Torsvik, T.H., Eide, E.A., Osmundsen, P.T., Faleide, J.I., 1999. Permian and Mesozoic faulting in central south Norway. J. Geol. Soc. 156, 1073–1080.

Beaumont, C., Nguyen, M.H., Jamieson, R.A., 2006. Crustal flow modes in large hot orogens. Geol. Soc. (London), Spec. Publ. 268, 91–145.

Beyssac, O., Bollinger, L., Avouac, J.-P., Goffé, B., 2004. Thermal metamorphism in the Lesser Himalaya of Nepal determined from Raman spectroscopy of carbonaceous material. Earth Planet. Sci. Lett. 225, 233–241.

Beyssac, O., Goffé, B., Chopin, C., Rouzaud, J.N., 2002. Raman spectra of carbonaceous material in metasediments: a new geothermometer. J. Metamorph. Geol. 20, 859–871.

Beyssac, O., Goffé, B., Petitet, J.P., Froigneux, E., Moreau, M., Rouzaud, J.N., 2003. On the characterization of disordered and heterogeneous carbonaceous materials using Raman spectroscopy. Spectrochim. Acta 59, 2267–2276.

Bockelie, J.F., Nystuen, J.P., 1985. The southeastern part of the Scandinavian Caledonides. In: Gee, D.G., Sturt, B.A. (Eds.), The Caledonide Orogen: Scandinavia and Related Areas, vol. 1. Wiley & Sons, pp. 69–88.

Bollinger, L., Avouac, J.-P., Beyssac, O., Catlos, E.J., Harrison, T.M., Grove, M., Goffé, B., Sapkota, S., 2004. Thermal structure and exhumation history of the Lesser Himalaya in central Nepal. Tectonics 23.

Bollinger, L., Henry, P., Avouac, J.-P., 2006. Mountain building in the Nepal Himalaya: Thermal and kinematic model. Earth Planet. Sci. Lett. 244, 58–71.

Boyer, S.E., Elliott, D., 1982. Thrust systems. Am. Assoc. Pet. Geol. Bull. 66, 1196–1230.

Brueckner, H.K., van Roermund, H., 2004. Dunk tectonics: A multiple subduction/eduction model for the evolution Scandinavian Caledonides. Tectonics 23.

Bruton, D.L., Gabrielsen, R.H., Larsen, B.T., 2010. The Caledonides of the Oslo Region, Norway: stratigraphy and structural elements. Norwegian J. Geol. 90.

Bruton, D.L., Harper, D.A.T., Repetski, J.E., 1989. Stratigraphy and fauna of the Parautochthon and Lower Allochthon of southern Norway. In: Gayer, R.A. (Ed.), The Caledonian Geology of Scandinavia. Graham & Tretman, London, pp. 231–241.

Bryhni, I., Sturt, B.A., 1985. Caledonides of southeastern Norway. In: Gee, D.G., Sturt, B.A. (Eds.), The Caledonide Orogen: Scandinavia and Related Areas, vol. 1. J. Wiley and Sons, pp. 89–107.

Corfu, F., Gerber, M., Andersen, T.B., Torsvik, T.H., Ashwal, L.D., 2011. Age and significance of Grenvillian and Silurian orogenic events in the Finnmarkian Caledonides, northern Norway. Can. J. Earth Sci. 48, 419–440.

Corfu, F., Torsvik, T.H., Andersen, T.B., Ashwal, L.D., Ramsay, D.M., Roberts, R.J., 2006. Early Silurian mafic–ultramafic and granitic plutonism in contemporaneous flysch, Magerøy, northern Norway: U–Pb ages and regional significance. J. Geol. Soc. (Lond.) 163, 291–301.

Duprat-Oualid, S., Yamato, P., Pitra, P., in press. Major role of shear heating in intracontinental inverted metamorphism: Inference from a thermo-kinematic parametric study. Tectonophysics, http://dx.doi.org/10.1016/j.tecto.2013.07.037.

Fossen, H., 1992. The role of extensional tectonics in the Caledonides of South Norway. J. Struct. Geol. 14, 1033–1046.

Fossen, H., 2010. Extensional tectonics in the North Atlantic Caledonides: a regional view. Geol. Soc. (London), Spec. Publ. 335, 767–793.

Fossen, H., Dunlap, W.J., 1998. Timing and kinematics of Caledonian thrusting and extensional collapse, southern Norway: Evidence from $^{40}Ar/^{39}Ar$ thermochronology. J. Struct. Geol. 20.

Fossen, H., Hurich, C., 2005. The Hardangerfjord Shear Zone in SW Norway and the North Sea: a large-scale low-angle shear zone in the Caledonian crust. J. Geol. Soc. (Lond.) 162, 675–687.

Furnes, H., Skjerlie, K.P., Pedersen, R.B., Andersen, T.B., Stillman, C.J., Suthren, R.J., Tysseland, M., Garmann, L., 1990. The Solund-Stavfjord Ophiolite Complex and associated rocks, west Norwegian Caledonides – geology, geochemistry and tectonic environment. Geol. Mag. 127, 209–224.

Gabrielsen, R.H., Braathen, A., Olesen, O., Faleide, J.I., Kyrkjebø, R., Redfield, T.F., 2005. Vertical movements in south-western Fennoscandia: a discussion of regions and processes from the Present to the Devonian. In: Wandas, B. (Ed.), Onshore-Offshore Relationships on the North Atlantic Margin. In: NPF Spec. Publ., vol. 12. Elsevier, Amsterdam.

Gautneb, H., Saether, O.M., 2009. A compilation of previously published geochemical data on the lower Cambro-Silurian sedimentary sequence, including the alum shales in the Oslo region. Report No. 2009.053, Trondheim, p. 25.

Gee, D.G., 1975. A tectonic model for the central part of the Scandinavian Caledonides. Am. J. Sci. 275A, 468–515.

Gerya, T., 2010. Introduction to Numerical Geodynamic Modelling. Cambridge University Press. 358 pp.

Glodny, J., Kuhn, A., Austrheim, H., 2008. Geochronology of fluid-induced eclogite and amphibolite metamorphic reactions in a subduction–collision system, Bergen Arcs, Norway. Contrib. Mineral. Petrol. 156, 27–48.

Hacker, B.R., 2007. Ascent of the ultrahigh-pressure Western Gneiss region, Norway. In: Cloos, M., Carlson, W.D., Gilbert, M.C., Liou, J.G., Sorensen, S.S. (Eds.), Convergent Margin Terranes and Associated Regions: A Tribute to W.G. Ernst. In: Spec. Pap., Geol. Soc. Am., vol. 419. Geological Society of America.

Hacker, B.R., Andersen, T.B., Johnston, S., Kylander-Clark, A.R.D., Peterman, E.M., Walsh, E.O., Young, D., 2010. High-temperature deformation during continental-margin subduction & exhumation: The ultrahigh-pressure Western Gneiss Region of Norway. Tectonophysics 480, 149–171.

Henry, P., Le Pichon, X., Goffé, B., 1997. Kinematic, thermal and petrological model of the Himalayas: constraints related to metamorphism within the underthrust Indian crust and topographic elevation. Tectonophysics 273, 31–56.

Hetényi, G., Cattin, R., Brunet, F., Bollinger, L., Vergne, J., Nábělek, J.L., Diament, M., 2007. Density distribution of the India plate beneath the Tibetan plateau: Geophysical and petrological constraints on the kinetics of lower-crustal eclogitization. Earth Planet. Sci. Lett. 264, 226–244.

Hetényi, G., Cattin, R., Vergne, J., Nábělek, J.L., 2006. The effective elastic thickness of the India Plate from receiver function imaging, gravity anomalies and thermomechanical modelling. Geophys. J. Int. 167, 1106–1118.

Holland, T.J.B., Powell, R., 1998. An internally consistent thermodynamic data set for phases of petrological interest. J. Metamorph. Geol. 16, 309–343.

Huw Davies, J., 1999. Simple analytic model for subduction zone thermal structure. Geophys. J. Int. 139, 823–828.

Huw Davies, J., Stevenson, D.J., 1992. Physical model of source region of subduction zone volcanics. J. Geophys. Res. 97, 2037, http://dx.doi.org/10.1029/91JB02571.

Jolivet, L., Raimbourg, H., Labrousse, L., Avigad, D., Leroy, Y., Austrheim, H., Andersen, T.B., 2005. Softening triggered by eclogitization, the first step toward exhumation during continental subduction. Earth Planet. Sci. Lett. 237, 532–547.

Kirkland, C.L., Daly, J.S., Whitehouse, M.J., 2008. Basement-cover relationships of the Kalak Nappe Complex, Arctic Norwegian Caledonides and constraints on Neoproterozoic terrane assembly in the North Atlantic Region. Precambrian Res. 160, 245–276.

Krogh, T.E., Kamo, S.L., Robinson, P., Terry, M.P., Kwok, K., 2011. U–Pb zircon geochronology of eclogites from the Scandian Orogen, northern Western Gneiss Region, Norway: 14–20 million years between eclogite crystallization and return to amphibolite-facies conditions. Can. J. Earth Sci. 48, 441–472.

Kylander-Clark, A.R.D., Hacker, B.R., Johnson, C.M., Beard, B.L., Mahlen, N.J., 2009. Slow subduction of a thick ultrahigh-pressure terrane. Tectonics 28, http://dx.doi.org/10.1029/2007TC002251.

Kylander-Clark, A.R.D., Hacker, B.R., Mattinson, J.M., 2008. Slow exhumation of UHP terranes: Titanite and rutile ages of the Western Gneiss Region, Norway. Earth Planet. Sci. Lett. 272, 531–540.

Labrousse, L., Hetényi, G., Raimbourg, H., Jolivet, L., Andersen, T.B., 2010. Initiation of crustal-scale thrusts triggered by metamorphic reactions at depth: insights from a comparison between the Himalayas and Scandinavian Caledonides. Tectonics 29, http://dx.doi.org/10.1029/2009TC002602.

Lahfid, A., Beyssac, O., Deville, E., Negro, F., Chopin, C., Goffé, B., 2010. Evolution of the Raman spectrum of carbonaceous material in low-grade sediments of the Glarus Alps (Switzerland). Terra Nova 22, 354–360.

Lundmark, A.M., Corfu, F., 2007. Age and origin of the Ardal dike complex, SW Norway: False isochrons, incomplete mixing and the origin of Caledonian granites in basement nappes. Tectonics TC2007.

Lutro, O., Tveten, E., 1998. Geologisk kart over Noreg. Årdal, Norges geologiske undersøking.

Milnes, A.G., Wennberg, O.P., Skår, Ø., Koestler, A.G., 1997. Contraction, extension and timing in the South Norwegian Caledonides: the Sognefjord transect. In: Burg, J.-P., Ford, M. (Eds.), Orogeny Through Time. In: Geol. Soc. Spec. Publ., vol. 121, pp. 123–148.

Morley, C.K., 1986. The Caledonian thrust front and palinspastic restorations in the southern Norwegian Caledonides. J. Struct. Geol. 8, 753–765.

Nábělek, J.L., Hetényi, G., Vergne, J., Sapkota, S., Kafle, B., Jiang, M., Su, H., Chen, J., Huang, B.S., 2009. Underplating in the Himalaya? Tibet collision zone revealed by the Hi-CLIMB experiment. Science 325, 1371–1374.

Nielsen, S.B., Gallagher, K., Leighton, C., Balling, N., Svenningsen, L., Holm Jacobsen, B., Thomsen, E., Nielsen, O.B., Heilman-Clausen, C., Egholm, D.L., Summerfield, M.A., Clausen, O.R., Piotrowski, J.A., Thorsen, M.R., Huuse, M., Abrahamsen, N., King, C., Lykke-Andersen, H., 2009. The evolution of western Scandinavian topography: A review of Neogene uplift versus the ICE (isostasy-climate-erosion) hypothesis. J. Geodyn. 47, 72–95.

Nystuen, J.P., 1981. The Late Precambrian Sparagmites of Southern-Norway – a Major Caledonian Allochthon – the Osen-Roa Nappe complex. Am. J. Sci. 481, 69–94.

Nystuen, J.P., Andresen, A., Kumpulainen, R.A., Siedlecka, A., 2008. Neoproterozoic basin evolution in Fennoscandia, East Greenland and Svalbard. Episodes 31, 35–43.

Oftedahl, C., 1943. Overskyvninger i den norsk fjellkjede. Naturen (Osio) 5, 243–250.

Redfield, T.F., Osmundsen, P.T., Hendriks, B.W.H., 2005. The role of fault reactivation and growth in the uplift of western Fennoscandia. J. Geol. Soc. 162, 1013–1030.

Roberts, D., 2003. The Scandinavian Caledonides: event chronology, palaeogeographic settings and likely modern analogues. Tectonophysics 365, 283–299.

Roberts, D., Gee, D.G., 1985. An introduction to the structure of the Scandinavian Caledonides. In: Gee, D.G., Sturt, B.A. (Eds.), The Caledonide Orogen: Scandinavia and Related Areas, vol. 1. J. Wiley, Chichester, pp. 55–68.

Root, D., Corfu, F., 2012. U–Pb geochronology of two discrete Ordovician high-pressure metamorphic events in the Seve Nappe Complex, Scandinavian Caledonides. Contrib. Mineral. Petrol. 163, 769–788.

Royden, L., 1993. The steady-state thermal structure of eroding orogenic belts and accretionary prisms. J. Geophys. Res. 98, 4487–4507.

Rudnick, R.L., Gao, S., 2003. The composition of the continental crust. In: Rudnick, R.L. (Ed.), The Crust. In: Treatise Geochem., vol. 3. Elsevier–Pergamon, Oxford, pp. 1–64.

Schulte-Pelkum, V., Monsalve, G., Sheehan, A., Pandey, M.R., Sapkota, S., Bilham, R., 2005. Imaging the Indian subcontinent beneath the Himalayas. Nature 435, 1222–1225.

Souche, A., Beyssac, O., Andersen, T.B., 2012. Thermal structure of supra-detachment basins: a case study of the Devonian basins of western Norway. J. Geol. Soc. 169, 427–434.

Souche, A., Medvedev, S., Andersen, T.B., Dabrowski, M., 2013. Shear heating in extensional detachments: implications for the thermal history of the Devonian basins of W Norway. Tectonophysics 365, 283–299.

Sundvoll, B., Larsen, B.T., 1994. Architecture and early evolution of the Oslo Rift. Tectonophysics 240, 173–189.

Torsvik, T.H., Cocks, L.R.M., 2005. Norway in space and time: A Centennial cavalcade. Norwegian J. Geol. 85, 73–86.

Torsvik, T.H., Smethurst, M.A., Meert, J.G., van der Voo, R., McKerrow, W.S., Brasier, M.D., Sturt, B.A., Walderhaug, H.J., 1996. Continental break-up and collision in the Neoproterozoic and Palaeozoic – A tale of Baltica and Laurentia. Earth-Sci. Rev. 40, 229–258.

Zhao, W., Nelson, K.D., Team, P.I., 1993. Deep seismic reflection evidence for continental underthrusting beneath southern Tibet. Nature 366, 557–559.

Bull. Soc. géol. France, 2014, t. 185, n° 3, pp. 147-168

Advances and challenges in geotectonic modelling

EVGENE BUROV[1,2], THOMAS FRANCOIS[1,2], PHILIPPE YAMATO[3] & SYLVIE WOLF[1,2]

Key-words. – Numerical modelling, Rifting, Passive margins, Subduction, Orogeny, Metamorphism, Rheology

Abstract. – Thermo-mechanical numerical modelling becomes a universal tool for studying short- and long-term lithosphere processes, validating and verifying geodynamic and geological concepts and putting stronger constraints on the observational data. State-of-the-art models account for rheological and mineralogical structure of the lithosphere, implement high resolution calculations, and their outputs can be directly matched with the geological and geophysical observations. Challenges of these models are vast including understanding of the behavior of complex geological systems and processes, parameterization of rheological parameters and other rock properties for geological conditions, not forgetting a large number of future methodological breakthroughs such as the development of ultra-high resolution 3D models coupled with thermodynamic processes, fluid circulation and surface processes. We here discuss both geological and geodynamic applications of the models, their principles, and the results of regional modelling studies focused on rifting, convergent and transform plate boundaries.

Modélisation géotectonique : avancées et challenges

Mots-clés. – Modélisation numérique, Rifting, Marges passives, Subduction, Orogenèse, Métamorphisme, Rhéologie

Résumé. – La modélisation numérique thermo-mécanique devient un outil universel pour étudier les processus lithosphériques court-terme et long-terme, pour valider les concepts géologiques et géodynamiques et pour apporter des contraintes plus importantes sures, et guider, les observations. Les modèles rendent compte de la structure rhéologique et minéralogique de la lithosphère, complètent les calculs à haute résolution et leurs « outputs » peuvent être directement confrontés et ajustés aux observations géologiques et géophysiques. Les défis de ces modèles sont étendus, incluant notamment la compréhension du fonctionnement des systèmes et processus géologiques complexes, la paramétrisation des variables rhéologiques et des autres propriétés des roches selon les conditions géologiques, sans oublier bon nombre d'avancées méthodologiques futures comme le développement de modèles 3D à très haute résolution couplés aux processus thermodynamiques, aux circulations de fluides et aux processus de surface. Nous discutons dans cet article à la fois des applications géologiques et géodynamiques des modèles, de leurs principes et des résultats de modélisations plus thématiques focalisées sur le rifting et les limites de plaques convergentes et transformantes.

INTRODUCTION

Physical models (fig. 1) replace real objects when direct study presents significant complications. In many cases direct study is simply impossible due to extreme spatial and time scales, inaccessibility or complex non-linear character of the underlying phenomena. In other cases it presents substantial risks and/or technical difficulties requiring important investments in terms of time, manpower and equipment. All of these conditions apply to geodynamic and tectonic processes that occur at temporal and spatial scales largely exceeding human time scales, refer to strongly non-linear complex processes while their study often requires significant financial investments and manpower.

The history of tectonic modelling is Earth Sciences comes back to the 19 century when Sir J. Hall has designed his first analogue models explaining folding of sedimentary layers. Even if not properly scaled, these models have played an essential role in sedimentary and structural geology providing new understanding of the evolution and mechanics of the stratified lithologies. This has been very soon recognized by contemporary geologists, e.g. by one of the fathers of modern geology, Charles Lyell, in his famous "Principles of Geology" [1865, first published in 1830] and "Elements of Geology" [1872]. The first analog mechanical models correctly scaled to nature [Cadell, 1890] have appeared at the end of 19th century. Since that, mechanical models were widely used and largely contributed to our understanding of the mechanics and physics of geological and tectonic processes such as formation of rifted basins [e.g., Allemand and Brun, 1991; Brun, 1999], oceanic spreading, mantle convection, lithosphere folding, subduction and collision [e.g., Davy and Cobbold, 1980; Chemenda *et al.*, 1996]. Analog models have a number of important

1. Sorbonne Universités, UPMC Univ Paris 06, UMR 7193, Institut des Sciences de la Terre Paris (iSTeP), F-75005 Paris, France
2. CNRS, UMR 7193, Institut des Sciences de la Terre Paris (iSTeP), F-75005 Paris, France
3. Geosciences Rennes, University of Rennes 2, France
Manuscript received on October 18, 2013; accepted on January 22, 2014

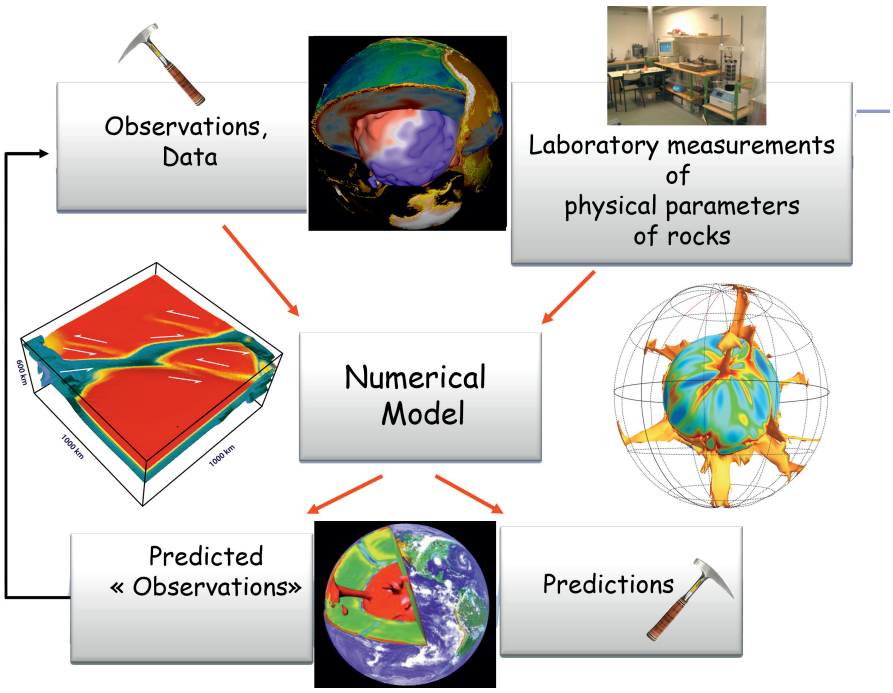

FIG. 1. – A flow chart of a typical research study in Earth Sciences. Models play a specific role since the observations generally cannot be entirely trusted nor directly interpreted in terms of large spatial and time scale evolution. The models serve not only for prediction and reconstruction of the geological or geodynamic evolution and understanding of the governing mechanisms of the geodynamic processes but also for integration and validation of the observational data, for example, by showing that some of these data imply inconsistent evolution of the targeted process. Model predictions next serve to target new field observations.

advantages, for example, being naturally three-dimensional and efficient, in terms of time needed to fulfill series of similar 3D experiments once the experimental procedure is established (though one should mention that any new type of an analog experiment often requires building a specific experimental setting, tuning and validation of an experimental procedure that may take several months). However, growing understanding of the importance of complex rheological properties and of thermo-mechanical interactions that are difficult to implement in analog models with sufficient respect of scaling laws, has put forward numerical models (fig. 2), that, with further increase of the computing power, progressively become a dominant modelling tool. An important feature of the numerical models is also their portability, i.e. same model can be run on standard computers at different places, while analog laboratories need heavy custom equipment. Nevertheless, as well pointed out by Gerya [2011], the numerical geodynamic modelling is still a very young developing domain, if one recalls that the first numerical modelling study has been published only in 1970 by Minear and Toksöz [1970].

In the early 70ties of 20th century it has become evident (see historical overview in, e.g, Burov [2011]) that the geological "substratum" has very specific properties being able to be both viscous (fluid-like, irreversible strain without localization), elastic (i.e. reversible strain) and brittle (localized irreversible strain) depending on pressure, temperature and timescale of deformation. For example, the Earth's mantle is elastic at human timescales but is viscous on geological timescales (> 10 000 years, post-glacial rebound) and can be strongly irreversibly deformed due to solid state creep.

Understanding such multi-scale interlinked processes requires integral approach. For these reasons, geodynamic numeric modelling, which has the power of combining different inter-independent physical processes, has been developing very rapidly since the past 30 years both, in terms of the number of various applications, and in terms of the numerical techniques. Geodynamic modelling stands now as one of the most dynamic and advanced fields of the Earth Sciences [Gerya, 2011].

The role of models in Earth Sciences is more versatile than in "human-scale" sciences such as engineering or biology, not only because of the impossibility of direct experiments, but also because in the Earth Sciences, the models have a wide spectra of specific functions such as verification and validation of the observational and experimental data (fig. 1). Indeed, geological observations are subject to large uncertainties being often extrapolations from local and small-time scale observations to larger spatial and temporal scales [Burov and Watts, 2006; Burov, 2011]. In difference from data of, for example, physical experiments, these observations cannot be always fully trusted since the raw data undergo important modifications and extrapolations before their application to geological problems. One of the typical examples of such modifications refers to the data of experimental rock mechanics, because the rocks are deformed under laboratory conditions that are highly different from natural conditions. Their applicability to geological conditions hence needs validation, and this function is largely fulfilled by geodynamic models that can test whether the inferred mechanical properties yield geologically-consistent behaviors at large time and temporal scales [Burov *et al.*, 1999; Burov, 2011]. It is also noteworthy that

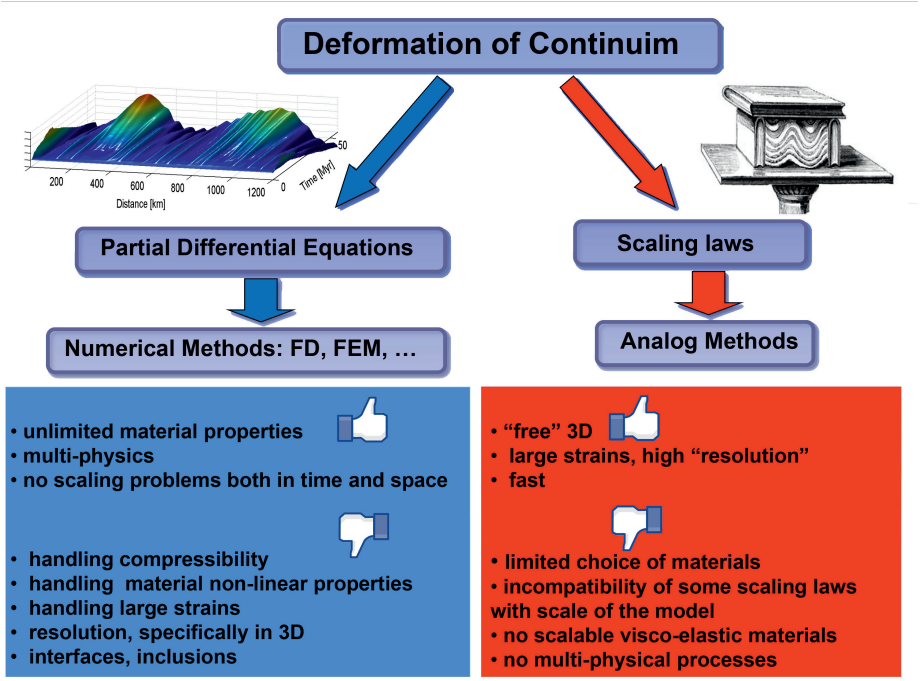

FIG. 2. – Comparison of analog and numerical mechanical models (courtesy of L. Le Pourhiet, modified). Both approaches are complementary and have their respective up- and down-sides. Since recent time, numerical models have been put forward due they better match for the crucial task of incorporation of multi-physical processes (thermo-mechanical coupling in the first run) and complex material properties.

due to the complexity and multi-process dependencies in geodynamic systems, simple "intuitive" hypothesis about their functioning often do not hold. One of the recent examples refers to new understanding of the mechanisms of formation of oceanic transform faults that stemos from the results of the numerical modelling [Gerya, 2010]. Despite common ideas, the numerical modelling experiments show that transform faults represent actively developing growth structures resulting from the mechanical instabilities at spreading centers, and not conventional faults, i.e. "passive" mechanical ruptures of the lithosphere. Earlier Cloetingh *et al.* [1999] have shown, on the base of self-consistent numerical models, and against common intuition, that lithospheric faulting does not prevent but enhances lithospheric folding, and vice-versa. Another contra-intuitive finding based on model-derived knowledge refers to later commonly accepted idea that fluids play a key role in the initialization of oceanic subduction and are responsible for subduction asymmetry [Faccenda *et al.*, 2009]. None of these fundamental geodynamic findings could be done solely on the basis of observations or analytical considerations. The list of fundamental geodynamic and tectonic discoveries that could not be even envisaged without thermo-mechanical modelling is long and continues growing, as the models start to account more and more accurately for physical processes and multi-disciplinary observational data.

The role of modern geodynamic models is therefore is multifold-fold: (1) understanding complex processes that cannot be assessed through analytical considerations, (2) validation, via refutation, of geological and geodynamic hypothesis, (3) validation of extrapolations from observations and experimental data, (4) orienting data acquisition, new laboratory and field research through demonstrating potential sensitivities of complex processes to particular observations.

In the next sections we discuss the main features of the numerical thermo-mechanical models used in geotectonic modelling. We will then confer applications of the geodynamic models to:

– convergent processes such as subduction (simple shear), lithosphere folding and pure-shear collision (fig. 3),

– extensional processes such as active and passive rifting (fig. 3),

– lithospheric flexure and regional isostasy,

– mantle-lithosphere interactions,

– surface-tectonics interactions.

NUMERICAL MODELS OF GEOTECTONIC PROCESSES: BASIC PROCESSES

Numerical models of geological processes are based on discrete presentation of physical laws controlling the geological phenomena (fig. 4). Therefore they treat problems of tectonic and geological deformation as that of deformation of the mechanical continuum where the basic physical laws such as conservation of momentum, mass and energy are observed. These basic laws are combined with laws that describe physical properties of the system, in the first order with the constitutive equations that describe rheological properties of the rocks, with the state equations that describe changes in physical properties of rocks as function of pressure and temperature, and with the equations describing surface processes, i.e. re-distribution of surface loads due to erosion and sedimentation. Additional physical processes

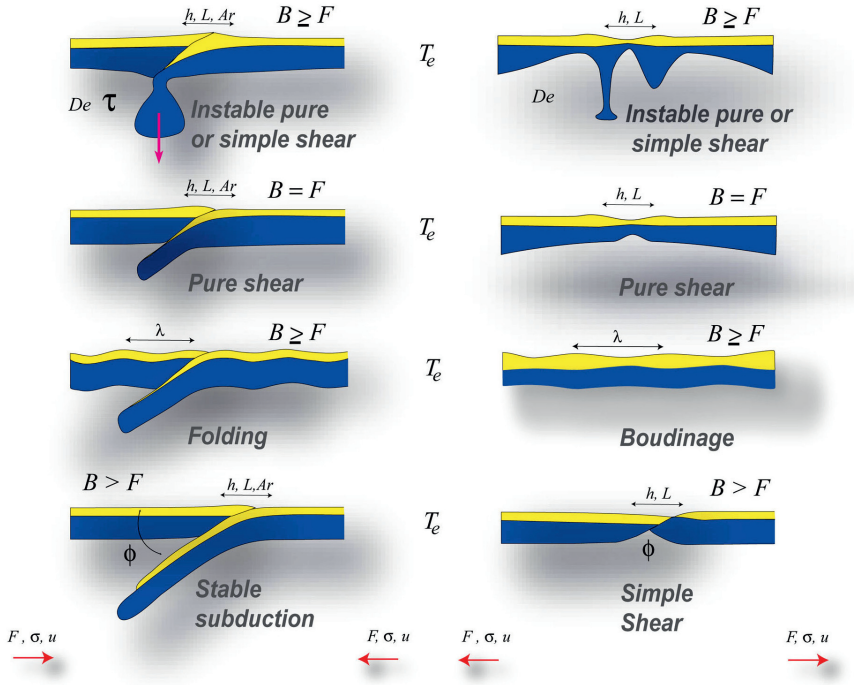

FIG. 3. – Possible collision and extension scenarios where horizontal shortening or extension is accommodated or largely influenced by: (A) removal of hot mantle lithosphere by Rayleigh-Taylor gravitational instability at the bottom of mantle lithosphere, combined with pure or simple shear deformation in the crust; (B) stable pure shear accommodation (stable collision without subduction or McKenzie's [1978] rifting concept); (C) unstable mode due to tensional or compressional instabilities (folding or boudinage); (D) stable uniform simple shear mode (subduction or rifting according to Wernicke's [1985] concept). Related large-scale parameters characterising collision style, lithospheric strength and rheology: T_e, F, σ, u, De, τ_m, h, L, λ, φ, T_e is equivalent elastic thickness. F, σ, u are respectively the horizontal force, stress and convergence/extension velocity, that are linked to the lithospheric strength and possible deformation styles. *De* and τ_m are respectively Deborah number and relaxation time related to viscosity contrasts in the lithosphere. λ is the characteristic wavelength of unstable deformation related to the thickness of the competent layers in the lithosphere. h, L are respectively the vertical and horizontal scale for process-induced topography supported by lithospheric strength, Argand number Ar = $\rho ghL/F$. φ is subduction or major thrust fault angle that is indicative of the brittle properties and of the overall plate strength.

are also often plugged-in such as fluid flow and melting [e.g., Faccenda *et al.*, 2009; Angiboust *et al.*, 2012].

The momentum equation corresponds to the Newton's second law of motion and describes the *conservation of momentum* for a continuous medium in the presence of gravity forces:

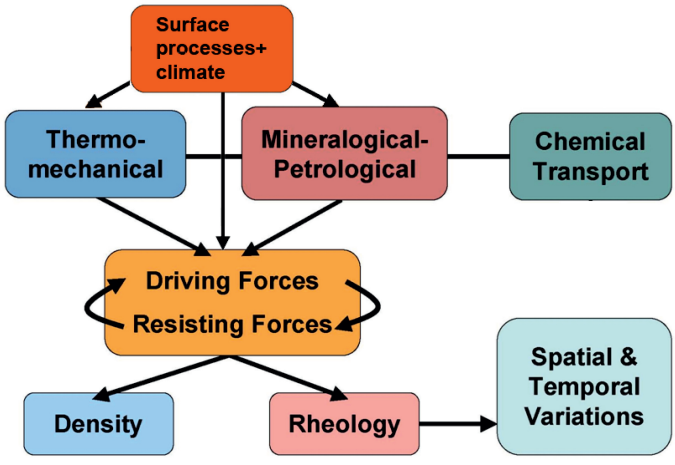

FIG. 4. – Flow chart of multi-physical processes considered in the numerical models (modified after courtesy of M. Billen) .

$$\frac{D\dot{u}_i}{Dt} = \frac{1}{\rho}\frac{\partial \sigma_{ij}}{\partial x_j} + g_i \qquad (1)$$

where D/Dt corresponds to objective derivative (in the Lagrangean framework), u is displacement, $\dot{u}_i$ are velocity components (i.e., time derivatives of displacement), ρ is density, σ_i is stress tensor components, x_j are coordinate components and g_i are acceleration due to gravity components.

Stresses are related to strains $\varepsilon(=\int \dot{u}dt)$ and strain rates $\dot{\varepsilon}(=\nabla\dot{u})$ via constitutive equations that may take various forms depending on rock rheology:

$$\frac{D\sigma}{Dt} = F(\varepsilon, \dot{\varepsilon}, \sigma, T, \ldots) = F(\dot{u}, \nabla\dot{u}, \sigma, T, \ldots) \qquad (2)$$

where T is temperature that contributes to buoyancy and plays essential role in case of ductile rheologies, as well as in case of rheological changes due to metamorphic reactions. Due to the temperature dependence of body forces and rheological properties, and, hence, of stresses, as well as due to the fact that constraining the thermal evolution of the system is important by itself, (1) and (2) have to be coupled with the heat transfer equation:

$$\frac{DT}{Dt} = \frac{1}{\rho C_p}\nabla(kT) + \sum_{i=1}^{n} H_i \qquad (3)$$

where k, C_p, T, H_i designate respectively thermal conductivity, specific heat, and internal heat production per

unit volume coming from different sources (*i* designates head-producing source, e.g. radiogenic heating or frictional heating).

Equations (1-3) constitute a starting base of all present-day mechanical numerical models of geodynamic and geological processes. In simplest case, only single rheology type is taken into account (eq. 2), for example viscous, plastic or elastic. In most advanced models, constitutive equations (2) account for complex viscous-elastic-plastic rheologies that characterize real rocks [e.g., Burov and Yamato, 2008; Gerya, 2010]. Depending on the degree of the realism of the models, heat transfer equation (3) may take into account different kinds of internal heat sources such as radiogenic heat production, frictional heating, latent heating, and so on.

Since density affects body forces and heat transfer, its variations must be also taken into account, which is reflected with different degrees of sophistication by state equations:

$$\rho = f(P, T) \quad (4)$$

The simplest form of these equations accounts only for thermal expansion (called simple Boussinesq approximation). More advanced approaches consider density and rheological variations associated with phase transforms on the basis of thermodynamic petrology models such as the program set Perple_X [Conolly, 2005]. This directly links the equation (4) with the equation (2). In continental domain, surface topography is actively modified by surface processes, whose rates in actively deforming zones are nearly the same as the rock uplift rates [e.g., Avouac and Burov, 1996]. Hence, surface processes models need to be also included, which is generally done in the following form [Culling, 1960]:

$$\frac{Dh}{Dt} = f(h, \nabla h, \nabla h, k_{err}, \ldots) \quad (5)$$

Where h is surface topography elevation, k_{err} is surface erosion coefficient, and the other parameters (not shown here) may include river discharge and dip, geometrical characteristics of the fluvial network, precipitation, climate conditions and so on [e.g., Willet, 1999]. In most simple cases, simple diffusion of topography with coefficient k_{err} is used to simulate surface processes [e.g., Avouac and Burov, 1996; Burov and Toussaint, 2007].

Finally, it has recently become clear that fluids may play a very important role in localization of deformation in various geodynamic contexts. For example, it has been shown that they may play a major role in subduction processes [Faccenda *et al*., 2009; Angiboust *et al*., 2012]. Hence, fluid circulation and partial melting have to be taken into account with different degree of physical and observational consistency in most cases [Gerya, 2011]. The simplest models [Arcay *et al*., 2007] impose fluid migration in predefined (basically vertical) direction, more realistic models implement Darcy's porous flow or even more complete bi-phase flow formulations [e.g. Mezri *et al*., 2013].

CONVERGENT PROCESSES

There is no surprise that the first numerical geodynamic models addressed mechanisms of oceanic subduction [Minear and Toksoz, 1970] and of mantle convection [Torrance and Turcotte, 1971], as two key processes behind – that time newly-born – plate tectonics theory. In both cases the role of thermal advection is essential and could not be consistently handled by analog models justifying numerical approach. The models of continental collision have followed the oceanic subduction models few years later [Daignières *et al*., 1978; Bird, 1978]. Since that, numerical models have been widely used for understanding various aspects of the convergent processes. A large number of studies have been focused on the oceanic subduction and have demonstrated that simple analytical models of sea-floor spreading and even numerical convection models that treat the lithosphere in simplified way, fail to explain some key observations associated with subduction. According to the plate tectonics theory, plates sink into the mantle when they become old and cold and hence negatively buoyant. Despite the elegant simplicity of this idea, it has met a number of major consistency problems when flexural observations and model have shown [Cloetingh *et al*., 1982; Watts, 2001] that plate strength grows with age so that old plates are so strong that they cannot bent down and hence cannot subduct. Furthermore, it has been also demonstrated that friction in the subduction channel would also strongly prevent subduction processes unless some mechanism of lubrication is not activated [Hassani *et al*., 1997]. The other enigmatic problem refers to the fact that the oceanic subduction is one-sided, while, from general point of view, both colliding plates should subduct symmetrically together. 30 years of numerical thermo-mechanical modelling has been required to show that plate flexure, or bending, initiates localized weakening of the brittle-elastic-ductile lithosphere [e.g., Burov and Diament, 1995; Burov, 2010] (fig. 5) and that fluids penetrating into the fractures networks created by flexural yielding result in further weakening of the plate enabling oceanic subduction [Faccenda *et al*., 2009] (fig. 6, 7). This mechanism also explains the mechanism of one-sided subduction, e.g. why only one of the converging oceanic plates subducts below the other. The next contra-intuitive problem related to oceanic subduction and successfully assessed by numerical modelling refers to the processes leading to slab-break-off and to the impact of slab breakoff on the surface evolution and on the following subduction history, including continental collision. It has been shown [Duretz *et al*., 2011] (fig. 8) that timing and depth of the slab-break-off are conditioned by multiple factors and that topographic impact of the slab-break off is a strong function of the slab-break-off depth, subduction rate, plate rheology and thermal age. 3D modelling studies of subduction processes made significantly evolve our vision of subduction dynamics by showing that subduction can be strongly affected by out-of plane flow so that slab-break-off can be initialized as a progressive out-of-plane tear of the slab (fig. 9) [Burkett and Billen, 2010; Stegman *et al*., 2010]. Hence, simple initial ideas on the mechanisms of oceanic subduction are conditioned by very complex processes, which at the end provide new elements for explanation of the uniqueness of the terrestrial plate tectonics.

While subduction is a predominant mechanism to accommodate plate convergence in the oceanic realm, except few zones of oceanic folding in Indian Ocean [e.g. Gerbault *et al*., 1999], in continents it is only the one of four possible ways of accommodation of shortening (fig. 3): pure-shear (i.e. volumetric thickening); stable subduction (or underplating), which is simple shear sliding of one plate below

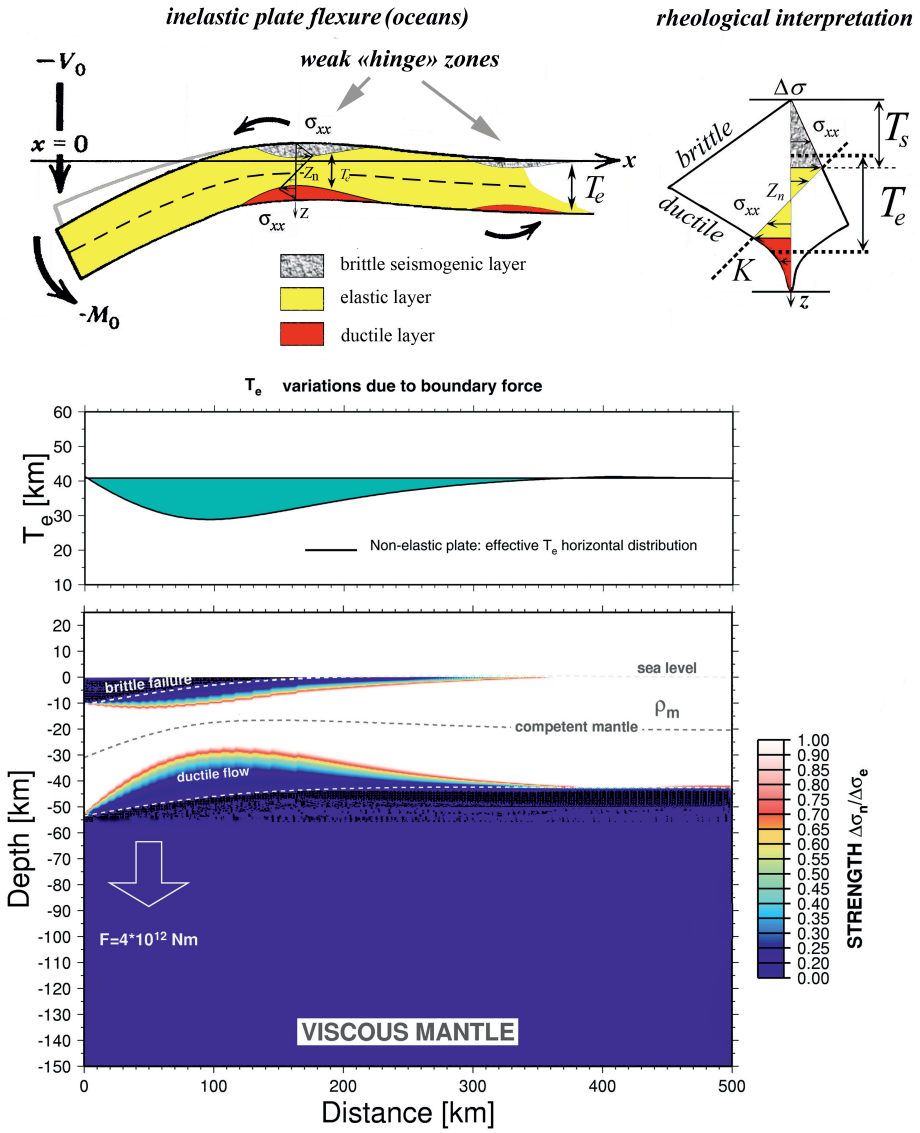

FIG. 5. – Models [Burov and Diament, 1995] predicted that flexural weakening is one of the primary mechanisms explaining bending of strong cold plates prior to subduction. Flexural strain are proportional to local plate curvature and increase with the distance from the neutral plane. Hence, the associated brittle and ductile stresses may locally reach yield limits resulting in localized weakening due to faulting at the surface and ductile weakening at the base of the plate.

the other; folding [Burg and Podladchikov, 2000; Cloetingh *et al.*, 1999]; instable pure or simple shear shortening, also dubbed "unstable subduction" and related to the development of gravitational Raleigh-Taylor instabilities in thickened, negatively buoyant lithosphere [e.g., Houseman and Molnar, 1997]. All these scenarios can be superimposed in nature. For instance, "megabuckles" created by lithospheric folding [Burg and Podladchikov, 2000] may (at least in principle) localize and evolve into subduction-like thrust zones or result in the development of Rayleigh-Taylor instabilities. On the other hand, RT and boudinage instabilities may occur in subducting slab leading in its break-off when it loses initial mechanical strength due to conductive heating from the surrounding mantle [Pysklywec *et al.*, 2000]. This complexity and diversity of convergence mechanisms in continental domain has been well demonstrated by the numerical experiments [e.g., Toussaint *et al.*, 2004; Burov and Yamato, 2008; Sizova *et al.*, 2010]. Indeed, due to overall positive buoyancy of the continental lithosphere, some very special conditions must be created to enable continental subduction [e.g., Cloos, 1993; Afonso and Zlotnik, 2011], otherwise the lithosphere would accommodate shortening in a different way. Nevertheless, the presence of exhumed UHP rocks, seismic tomography, structural and mass balance studies indicate that continental subduction should take place in a number of cases such is European Alps or Himalayan collision [e.g., Burov *et al.*, 2001; Toussaint *et al.*, 2004a, 2004b; Ford *et al.*, 2006; Yamato *et al.*, 2008; Zhang *et al.*, 2009; Handy *et al.*, 2010; Tetsuzo and Rehman, 2011]. Moreover, some of these studies show, on the basis of petrological evidence, that not only dense mantle and relatively dense lower crust but also an essential part of the upper crust and sediment can be buried to UHP depth during continental subduction. Therefore, a simple idea that

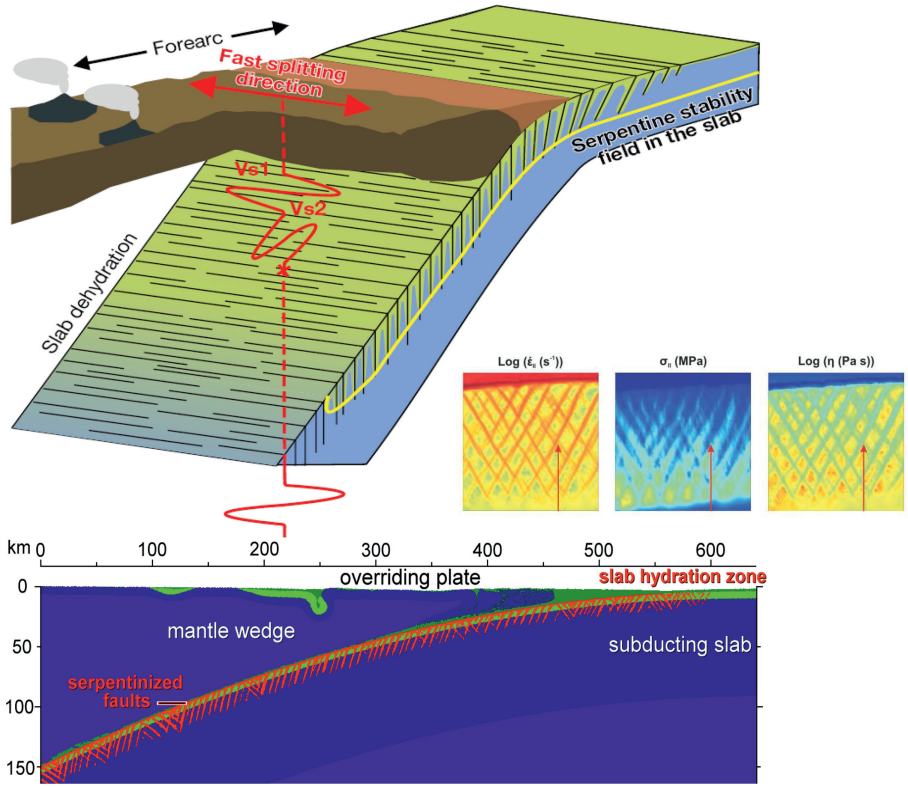

FIG. 6. – Fluids, as shown by the numerical models [after Faccenda *et al*., 2009] should play a major role in localized yielding of the lithosphere at the subduction sites. They also are responsible for the asymmetry of subduction. Fluids penetrate in normal faults initialized by flexural deformation (fig. 5) resulting both in pressure drop and serpentinization, hence, additional weakening of the plate at the inflexion point as well as in weakening of mantle-crustal interface. Flexurally induced normal faulting can also explain seismic anisotropy characterizing the subduction interface.

continental subduction can be made possible by skinning-off its low density upper crust is probably not universally valid. The driving mechanisms and plate-interface weakening processes that enable continental subduction are still not clear but the presence of thick, relatively weak and rheologically stratified crust as well as localized mechanical softening and density changes due to metamorphic transformations appear to play an important role [e.g., Burov *et al*., 2001; Yamato *et al*., 2008]. Preservation of slab integrity is a major problem for continental subduction, since continental convergence occurs at much slower rates than in oceans. Oceanic subduction typically takes place at rates of 5-15 cm.yr^{-1}, which implies relatively high (> 10) Peclet numbers (Peclet number is the ratio of the rate of heat advection to that of heat conduction). This practically means that cold oceanic slabs subduct so rapidly that they have no time to heat up (and hence reduce their strength) due to conductive heat exchanges with the surrounding asthenosphere before they reach significant depths (if the subduction dip is steep enough). As a consequence, steep-dip oceanic slabs break-off only by the moment when they have already sunk to great depths. In continents, convergence rates are much slower, sometimes not exceeding several mm.yr^{-1}. Under these conditions, the lithosphere may heat up, thermally weaken and break-off well before it reaches HP depths. It is therefore evident that the conditions for continental subduction cannot be assessed in a simple way and require a numerical modelling approach combining all of the key factors affecting the convergent processes. All of the above mentioned factors could not be treated within simple conceptual or analytical considerations, analog or conventional numerical models, and required major development of the numerical modelling techniques. For these reasons, thermo-mechanical models of continental subduction and exhumation are very recent (the first model of this kind was published in 2001 by Burov *et al*.). Since 2001 this domain has been addressed by a growing number of numerical studies (fig. 10) [Yamato *et al*., 2008; 2009; Gray and Pysklywec, 2012; Francois *et al*., 2013; Sizova *et al*., 2013] that demonstrated physical possibility of continental subduction – until recent doubted by many geologists – in various settings and helped defining the particular mechanisms behind this enigmatic process.

The new generation of observation-oriented models that have allowed for this major progress have among particular features the capacity of treating new multidisciplinary types of data and processes such as the data of metamorphic petrology and phase changes or denudation data and surface processes. For example, if one considers P-T conditions inferred for subduction zones, then UHP material should have been buried to depths of 100-150 km and brought back to the surface. The corresponding P-T and P-T-t paths not only demonstrate this possibility but also provide quantitative constraints, via P-T and P-T-t trends of the particular dynamics of the subduction (burial) and exhumation processes. Provided that the UHP depth estimates are correct

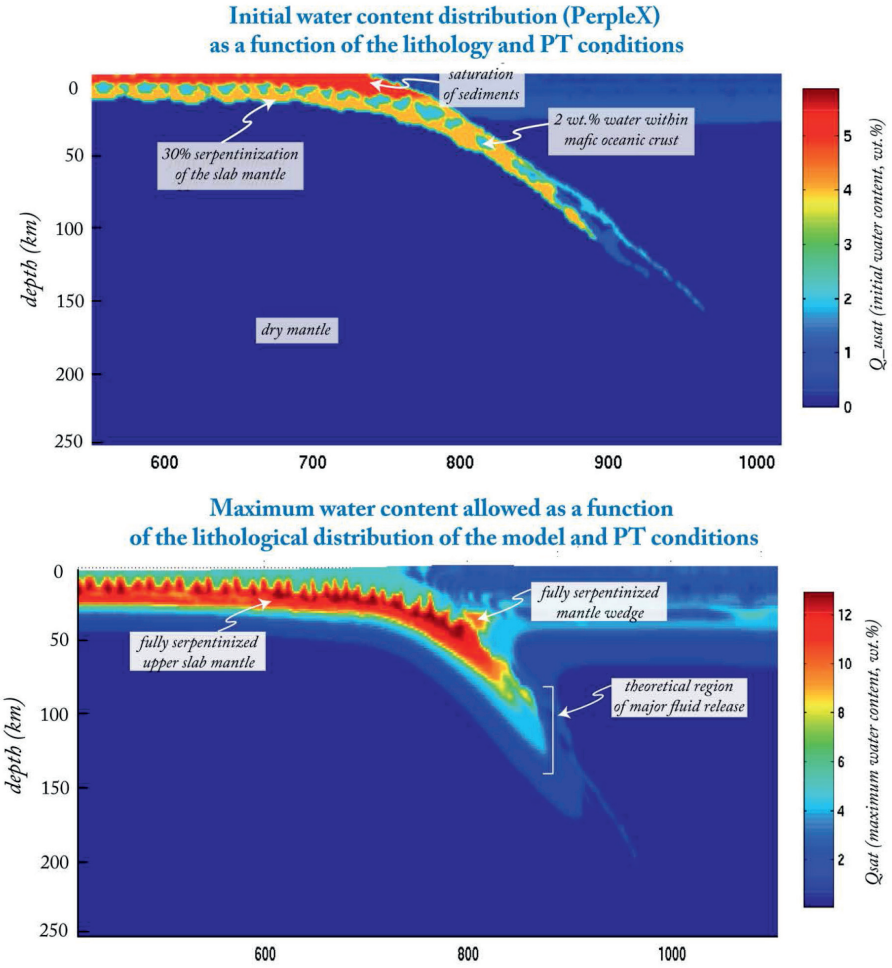

FIG. 7. – Fluids should also play a major role in exhumation of the metamorphic facies and lubrication of the subduction channel [Angiboust *et al.*, 2012]. The models show strong impact of fluids and metamorphic reactions on the dynamics on the subduction zone dynamics.

[e.g., Spear, 1993], the HP/UHP rocks can be regarded as direct markers of continental subduction and their P-T-t paths can be used for reconstruction of subduction dynamics and of the conditions at the subduction interface. Under these assumptions, detailed studies of HP/UHP rocks provide new direct constraints on thermo-mechanical processes in subduction zones [Coleman, 1971; Ernst, 1973; 2010]. These data can provide insights on the mechanisms of exhumation as well, since different processes and contexts would potentially result in different styles of deformation and hence in different P-T-t paths. In particular, based on the analysis of metamorphic data [Ernst, 2010], it has been suggested that two main types of continental convergence can be distinguished: fast "Pacific underflow", where continental subduction is preceded by that of thousands of kilometres of oceanic lithosphere, and slow "Alpine closure" of an intervening oceanic basin leading to short-lived continental subduction (simple shear) soon followed by lock-up of the subduction channel leading to switching to pure shear deformation mode (fig. 3). It has been also pointed out that the exhumed HP-UHP complexes display low-aggregate bulk densities [e.g., Ernst, 2010], while the exhumation rates in some cases largely exceed the convergence rates [e.g., Yamato *et al.*, 2008] (fig. 11), jointly suggesting a buoyancy-driven (Stokes flow) ascent mechanism, the idea that has been successfully tested in Burov *et al.* [2001] and Yamato *et al.* [2008]. By now, a large number of modelling studies have investigated various factors influencing subduction processes [e.g., Doin and Henry, 2001; Pysklywec *et al.*, 2000; Sobouti and Arkani-Hamed, 2002; Chemenda *et al.*, 1995; Gerya *et al.*, 2002; Yamato *et al.*, 2007, 2008; Warren *et al.*, 2008a,b; Sizova *et al.*, 2010; Gray and Pysklywec, 2010; 2012]. However, not all of the existing models fully match for the task. As mentioned, the analogue models are largely inadequate because of impossibility to incorporate phase changes, rheological simplifications and fairly scaled thermal coupling. The numerical models are often limited by simplified visco-plastic rheologies or by the rigid top/"sticky air" upper-boundary condition, often implemented in Eulerean codes instead of free-surface boundary condition. The use of rigid-top upper-boundary condition forces stable subduction [Doin and Henry, 2001; Sobouti and Arkani-Hamed, 2002], attenuates pure shear, cancels folding and does not allow for consistent prediction of topography evolution. Many models also do not incorporate surface processes, which are key forcing factors of continental collision [e.g., Avouac and Burov, 1996] and an integral part of the final stages of exhumation

[e.g., Yamato *et al.*, 2008]. Some studies also force a specific convergence mode, in particular, subduction, via prescription of favoring boundary conditions, for example, by putting an additional boundary condition (e.g., "S-point") inside the model [e.g., Beaumont *et al.*, 1996; Beaumont *et al.*, 2000]. Some models are also inadequate because they favor pure shear collision by including a weak zone in the plate shortened in the direction opposite to the pre-imposed mantle flow [Pysklywec *et al.*, 2002]. Finally, models operating in deviatoric stress formulation may also face specific difficulties with evaluation of total pressure needed correct account for brittle deformation and P-T-t conditions. Even though some earlier modelling studies [Burov *et al.*, 2001; Toussaint *et al.*, 2004a,b; Burg and Gerya, 2005; Gerya *et al.*, 2002] included simplified phase change algorithms, fully coupled models with progressive phase changes directly derived from thermodynamic relations have emerged only few years ago [Stöckhert and Gerya, 2005; Yamato *et al.*, 2007; Li and Gerya, 2009; Li *et al.*, 2010; 2011; Burov *et al.*, 2012; Francois *et al.*, 2013].

Summarizing the requirements to the numerical models of collision and exhumation, we can conclude that they should: (1) allow for all modes of deformation, (2) account for viscous-elastic-plastic rheology and thermal evolution, (3) be thermodynamically coupled, i.e. account for phase changes (and at best for fluid circulation), (4) account for surface processes and free-surface boundary condition (or at least incorporate "sticky air" approximation of the free surface), (5) provide an accurate solution for total pressure.

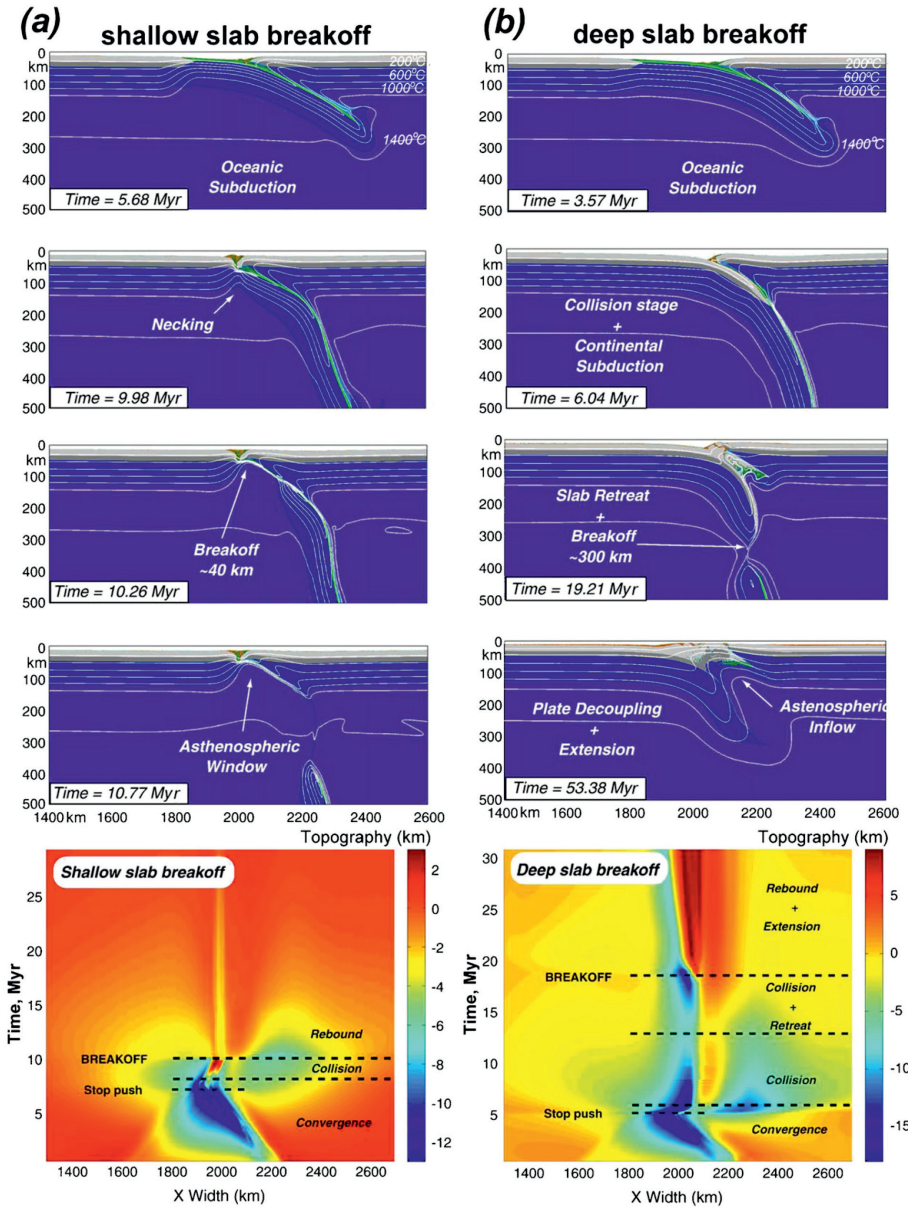

FIG. 8. – Examples of 2D numerical models of subduction resulting in spontaneous oceanic slab break-off during continental collision [Duretz *et al.*, 2011, see also Gerya, 2011]. (a) Four stages (top diagrams) of model evolution for the shallow slab break-off regime and associated surface topography development (bottom diagram). During slab necking and break-off, the subducted crust deforms in a brittle manner and the mantle lithosphere deforms viscously. (b) Four stages (top diagrams) of model evolution for the deep slab break-off regime and associated surface topography development (bottom diagram). During slab necking and break-off, the subducted crust deforms viscously and the mantle lithosphere deforms both viscously and by Peierls mechanism.

It is hence evident that a joint modelling approach considering collision processes in direct relation to exhumation, fluid circulation and formation of HP/UHP material is needed for understanding both the mechanisms of continental convergence and of UHP/HP exhumation.

By reproducing more and more sensible observations, the models allow us to understand the complexity and conditions of various factors involved in the oceanic and continental convergence. Due to the involvement of so many different factors, it is generally impossible to reduce these processes to simplified sketchy concepts

RIFTS AND MARGINS

Lithospheric extension is associated with tectonic deformation and/or magmatism governing formation of rifts and conjugate margins. Continental rifting begins with extensional stress applied to the lithosphere, laterally or from below, until it thins and eventually breaks apart, culminating in crustal rupture and creation of a new oceanic lithosphere accommodating the plates separation [see review by Ziegler and Cloetingh, 2004].

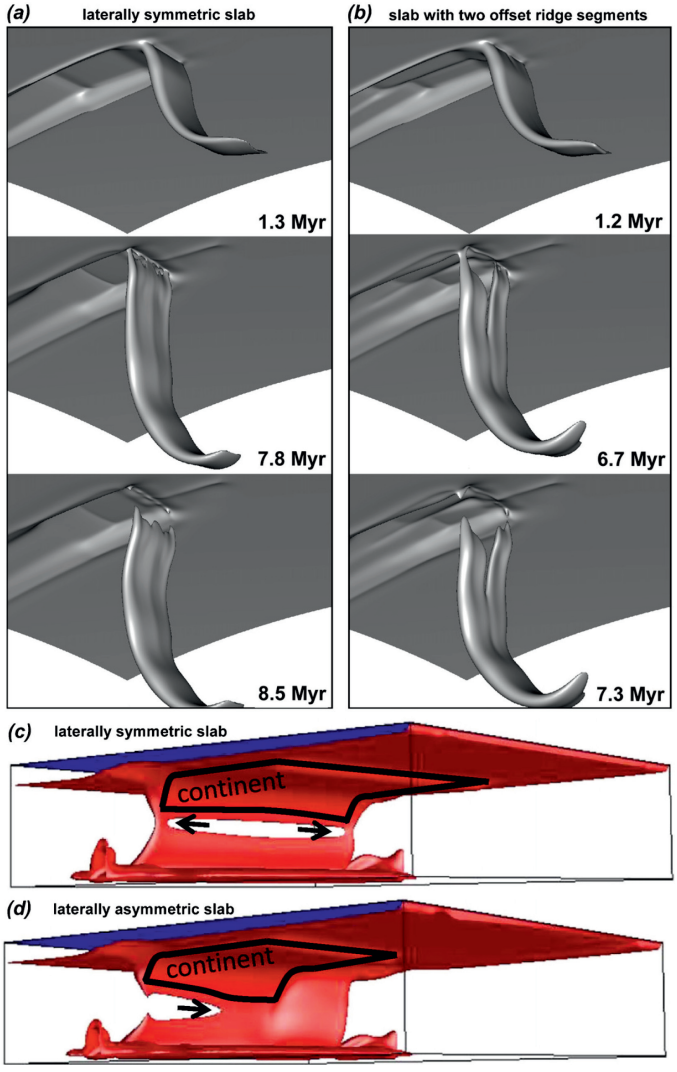

FIG. 9. – Example of 3D oceanic subduction [Burkett and Billen, 2010; van Hunen and Allen, 2011, see also Gerya, 2011]. 3D numerical models show the possibility of slab break-off due to ridge–trench collision (a, b) [Burkett and Billen, 2010] and continental collision (c, d) [van Hunen and Allen, 2011]. (a, c) Detachment of laterally symmetric slabs. (b, d) Detachment of laterally asymmetric slabs: (b) slab with two offset ridge segments separated by weak fracture zone, (d) only part of the slab has a continental block. Slab width is 300 km in (a, b) and 2,000 km in (c, d). The 1050°C isosurface is shown in (a, b) and 945°C in (c, d).

Due to their key role in geodynamics and their specific importance for mineral exploration, rifted basins and margins have been extensively studied by various observational methods as well as by analogue and numerical modelling. At the beginning, a very important contribution to understanding of syn-rift processes and of the importance of rheological stratification of the lithosphere has been made by analogue modelling [e.g., Brun, 1999]. In particular, the analogue modelling studies have shown that rift structure and rifting styles are largely controlled by the rheological properties and relative integrated strengths of crustal and mantle layers. The analogue models have also demonstrated that ductile flow in the lower crust should strongly affect rift evolution and, contra-intuitively, control localization and distribution of faults and tilted blocks at the surface [Brun, 1999]. Post-rift subsidence stages are, however, strongly affected by thermo-mechanical interactions as the large part of the post-rift subsidence is controlled by thermal cooling leading to density increase [McKenzie, 1978] and progressive mechanical strengthening of initially weakened lithosphere [Burov and Poliakov, 2001]. The numerical models have shown here that pure thermal subsidence due to cooling [McKenzie, 1978] is insufficient to explain post-rift evolution of rifted lithosphere since ductile strength recovery, gravitational instabilities and phase changes may largely interfere at this stage. For example, it has been demonstrated that at some stage, thinned lithosphere becomes stronger that it was before the rifting episode [Burov and Poliakov, 2001], which results in increasing flexural resistance and hence in eventually strong decrease of the amplitude of thermal subsidence (compared to McKenzie model). Since post-rift evolution of sedimentary basins is of particular interest for industrial exploration, the thermo-mechanical numerical models of post-rift subsidence have progressively taken an essential part in basin studies.

First models of formation of rifts and rifted margins predicted uniform thinning of the continental crust accommodated by tilted blocks that, in case of margins, are juxtaposed to the oceanic crust along a sharp boundary. Two end-member conceptual models have first been proposed for describing how the continental lithosphere deforms and extends: (1) the pure-shear model [McKenzie, 1978] where the same amount of extension occurs in the upper and lower crust, generally producing symmetric rifted margins; and (2) the simple-shear model [Lister *et al.*, 1986; Lister and Davis, 1989; Wernicke, 1985] where a low-angle shear zone extends through the entire lithosphere producing differential thinning of the crust and mantle lithosphere, and forming asymmetric rifts and margins. Combinations of these end-member mechanisms produce different styles of rift structures [e.g. Lister and Davis, 1989; Buck, 1991; Kusznir *et al.*, 1991; Bassi *et al.*, 1993]. Then, it has been shown that lithosphere necking can proceed to the break-up phase with or without lower crustal flow, affecting crustal thinning profiles [Braun and Beaumont, 1989; Hopper and Buck, 1996].

Thermo-mechanical modelling has been widely used not only to study the mechanisms of lithosphere extension but also for better constraining of the parameters governing the morphology of rifted structures [e.g. Dunbar and Sawyer, 1988; Bassi *et al.*, 1993; Burov and Cloetingh, 1997; Chéry *et al.*, 1989; Huismans *et al.*, 2001; Lavier *et al.*, 2000; Burov and Poliakov, 2001; Huismans and Beaumont, 2011; Tirel *et al.*, 2008; 2013; Watremez *et al.*, 2013].

Dynamic thermo-mechanical models have demonstrated their advantages (compared to analog models) not only for the analysis of the impact of thermal conditions but also for that of boundary conditions, such as extension velocity and surface erosion (fig. 12 and 13). In difference from most analog models, the numerical models have demonstrated that extension velocity is a key parameter governing the focusing of deformation and lithosphere breakup (fig. 14); [Huismans *et al.*, 2005]. In addition, they have shown that there, important implications of the lithosphere rheology with respect to extension, in particular, the relationship of viscous flow power-law exponent and development of necking [Fletcher, 1974; Schmalholz *et al.*, 2008] and Moho geometry [e.g., Tirel *et al.*, 2008]. The influence of melting-related weakening and other strain localization processes such as

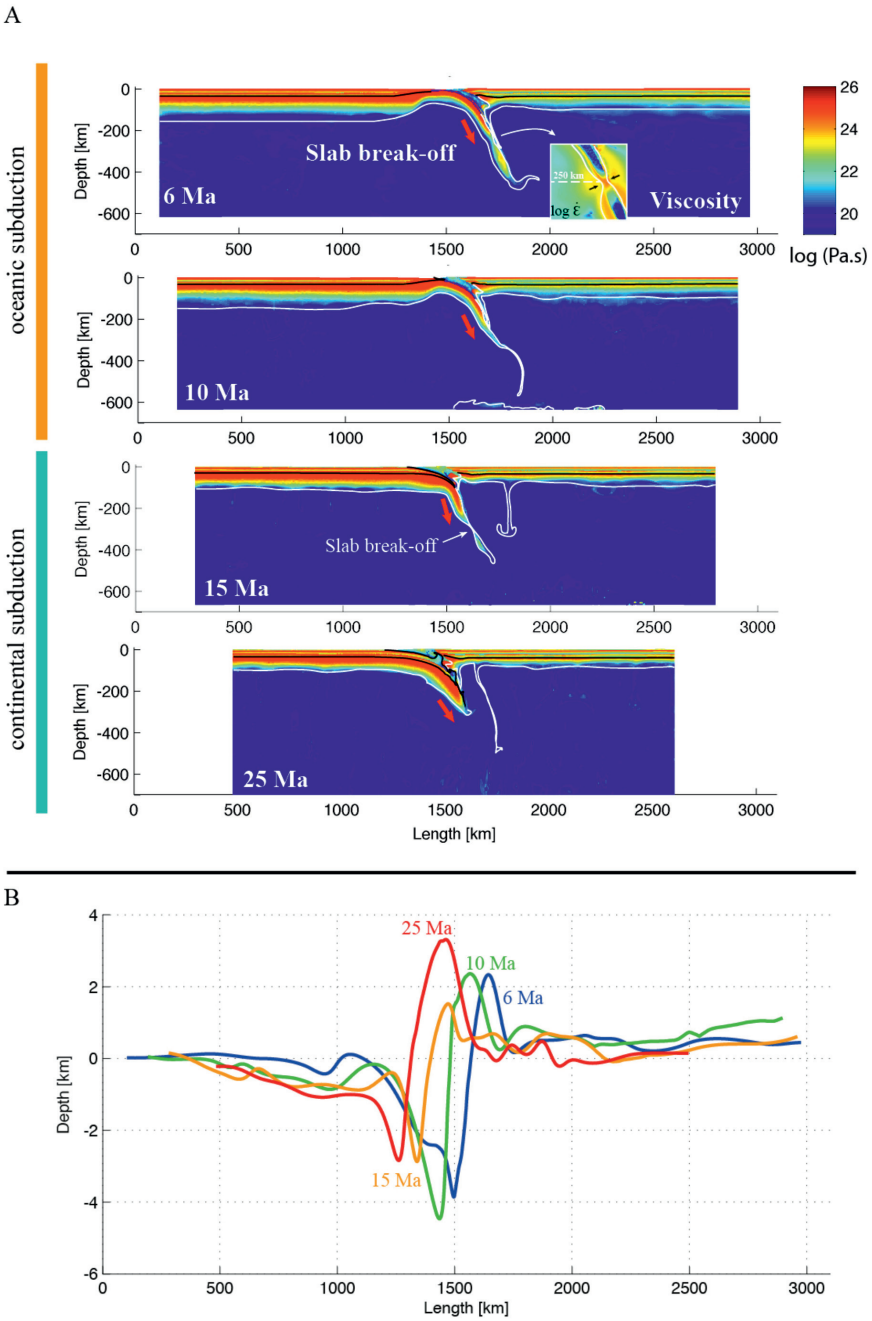

FIG. 10. – Example of continental subduction models [Francois *et al.*, 2013] showing initiation of a continental slab detachment some time past the oceanic slab break-off.

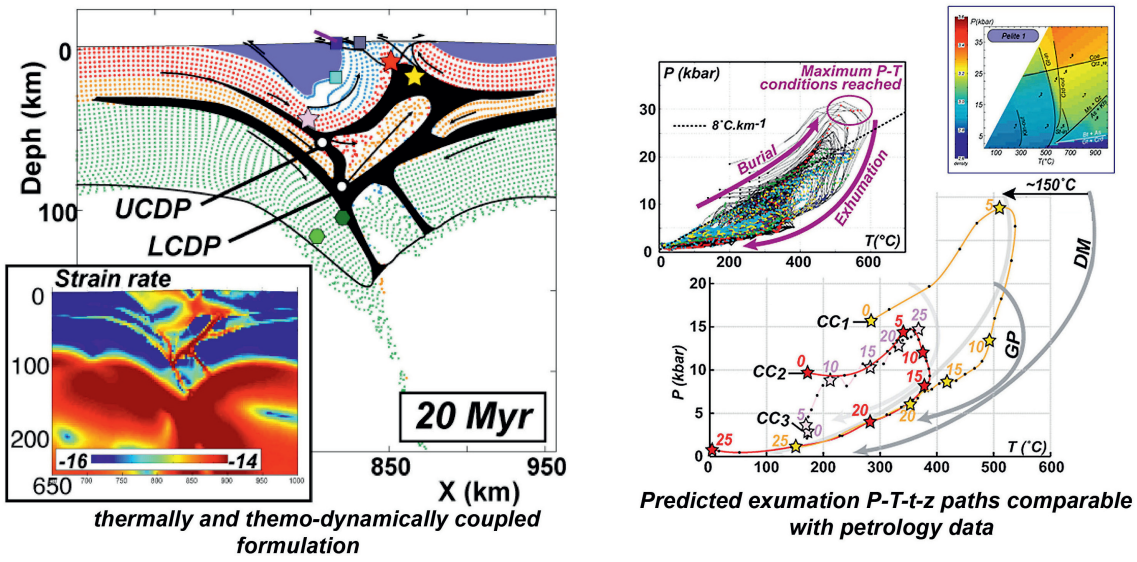

FIG. 11. – Example of continental subduction models [Yamato *et al.*, 2008] applied to slow Alpine collision. The model uses P-T-t data for better constraining of the subduction zone dynamics, and for explanation of UHP exhumation to the surfcae. The right part of the figure shows the match between the observed UHP data and the predicted P-T paths.

inherited tectonic heterogeneities [e.g., Le Pourhiet *et al.*, 2004] have been also shown to be considerable. For instance, Huismans and Beaumont [2003; 2007] and Huismans *et al.* [2005] have demonstrated that localization of deformation and rift mode selection during extension may be closely related to dynamic weakening; some recent publications emphasize several physical mechanisms to explain this weakening such as shear heating [Kaus and Podladchikov, 2006; Crameri and Kaus, 2010], damage evolution [Karrech *et al.*, 2011], grain size reduction [Braun *et al.*, 1999], lattice preferred orientation [Tomassi *et al.*, 2009] and some other mechanisms such as fluid-induced metamorphic reactions at different crustal levels [Mohn *et al.*, 2011].

Understanding the mechanisms of formation of the continental margins presents a particular challenge for geodynamic models. Application of the numerical models to the data of field observations has already provided an improved knowledge of the process leading to the formation of rifted margins [e.g. Brun and Beslier, 1996; Lavier and Manatschal, 2006; Huismans and Beaumont, 2011]. One can mention here the important contribution of the numerical models to understanding of the dependence of the rifting style and margin morphology on the extension rate. This dependence has been first established from direct observations of the morphology of oceanic spreading centres where slow spreading centres (e.g. Antlantic ridge) exhibit strong structural differences (localized rifting) from the fast spreading

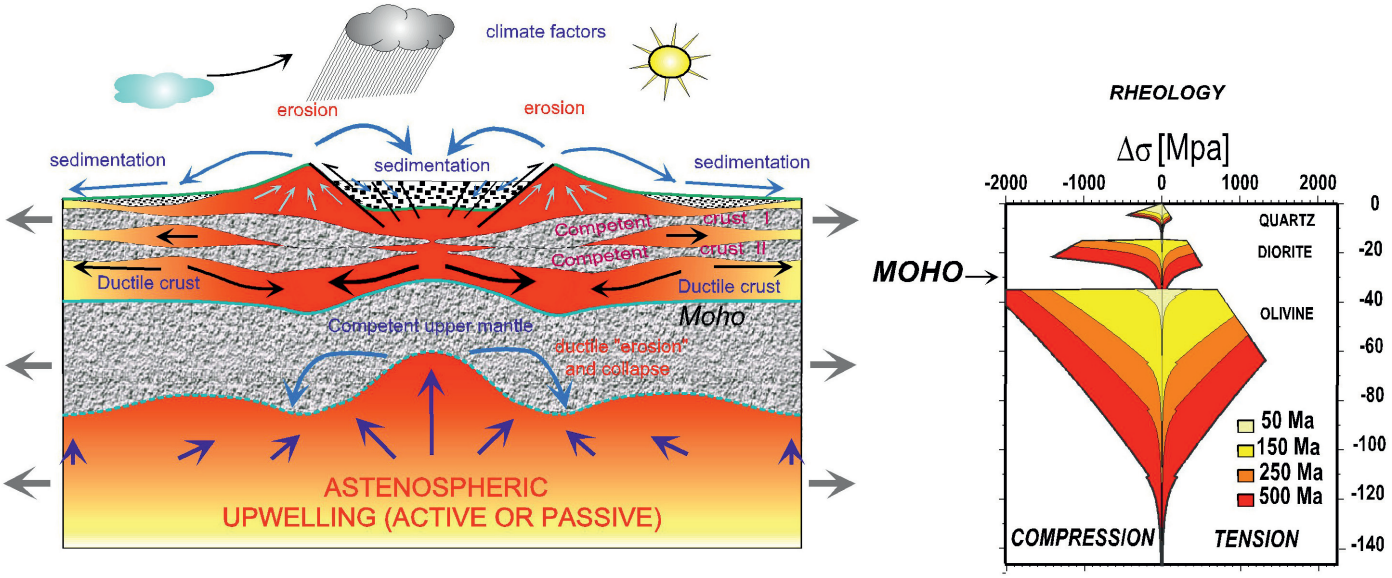

FIG. 12. – Extensional models: general conceptual setup. State of the art models account for elastic-brittle-ductile rheological structure of the lithosphere and surface processes (erosion and sedimentation).

centres (Pacific ridge, distributed rifting). However, the dependence of rifting style on the extension rate, well established for the oceans, has been long ignored for continental rifting and breakup (preceding formation of the continental margins). Salvenson's [1978] classification of rift morphology as a single function of the amount of crustal thinning (characterized by stretching factor β) has dominated for a prolonged period of time, until the thermally-coupled numerical models [Huismans and Beaumont, 2007; Burov, 2007] have shown that rifting styles and evolution of margins must be as strongly dependent on the extension rate as the oceanic rifts. It has been shown, for example, that slow extension (fig. 15) promotes development of strong gravitational instabilities that result in highly asymmetric rifting style, while fast extension promotes rift symmetry. Similarly, in difference from R. Buck [1991] hypothesis on predominate importance of the initial thermo-rheological profile on rifting style, it has been later demonstrated [Huismans and Beaumont, 2007] that the extension rate and mechanical softening may induce style variations comparable of the same order as the effect of the initial rheological stratification.

Based on thermo-mechanically-coupled numerical experiments, Burov [2007] suggested that slow extension may be associated with the development of gravitational instabilities in the lower lithospheric mantle along the margins of the area of mantle lithosphere thinning, resulting in its sinking into the asthenosphere, and, hence, in strong additional "gravitational" thinning of the lithosphere by mantle lithosphere delamination (fig. 15). These instabilities develop because the mantle lithosphere is colder and thus denser than the hot asthenosphere (1330ºC), which upwells to replace it in the zones of mantle lithosphere thinning, so that at each moment the degree of assimilation of the mantle lithosphere by the asthenosphere and the density contrast with them is limited by the ratio of thermal advection rate to thermal diffusion rate (Peclet number). If the extension rate is low enough, the characteristic time scale of growth of basal mantle-lithosphere gravitational instabilities becomes comparable or even smaller than the characteristic time scale of the syn-rift phase. These instabilities may eventually grow even at higher rates than the rate of lithospheric thinning by pure or simple shear.

Hence, the Rayleigh-Taylor instabilities interplay with rifting processes, potentially resulting in asymmetric rifting and/or in increased amount of thinning, specifically in the mantle part of the lithosphere. Mantle lithosphere delamination may also eventually lead to additional partial melting resulting from the ascent of the asthenospheric material to sub-moho depths (< 50 km). It can be further suggested that such delamination-caused partial melting can be generated even under non-volcanic margins. One of the other consequences of the mantle lithosphere instabilities

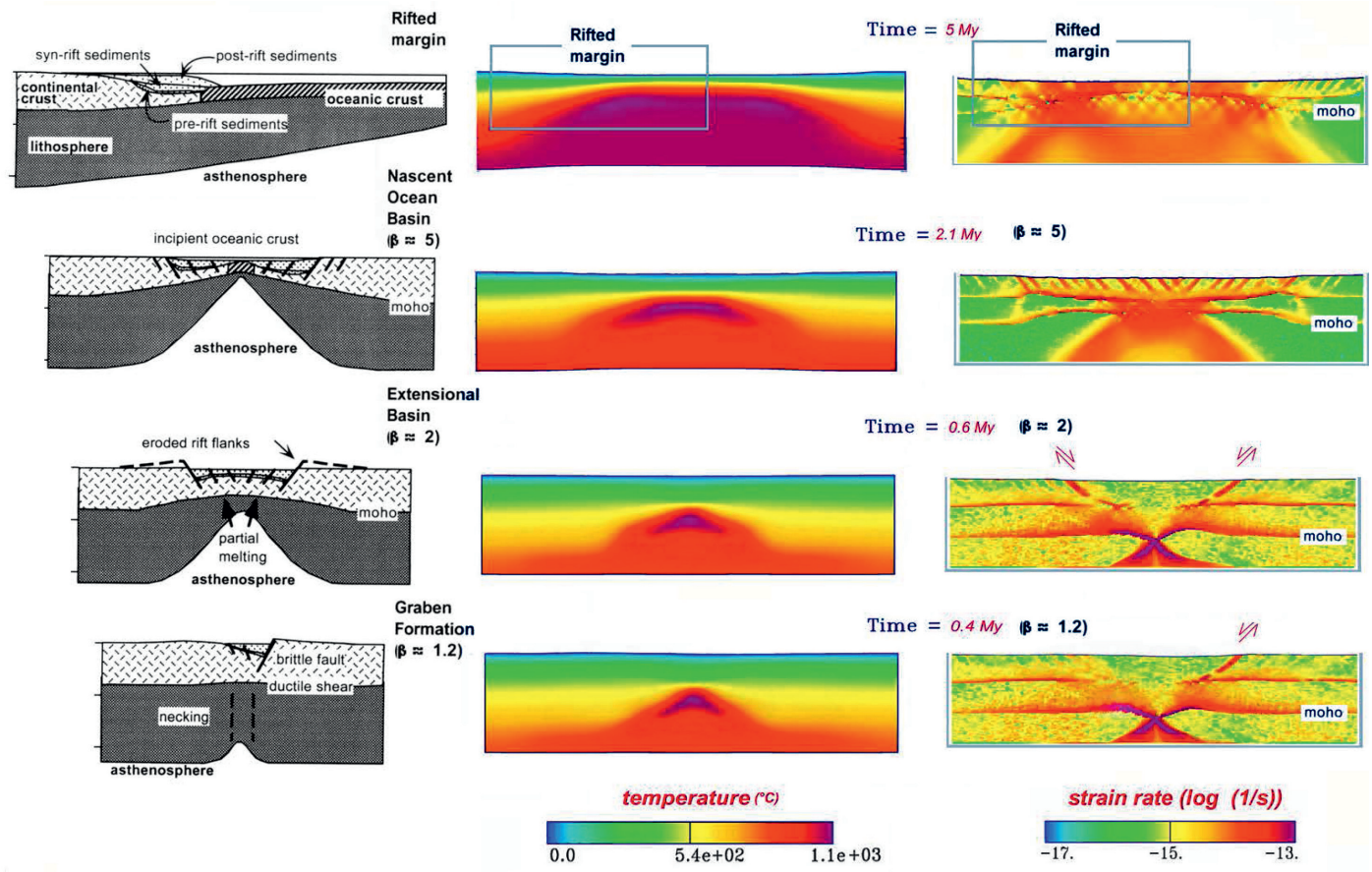

FIG. 13a. – Example of numerical experiments on extension [Burov and Polyakov, 2001]: reproducing basin morphology as function of the amount of crustal thickening (coefficient of extension β). The left part shows observationally constrained rift structures as function of β [Salvenson, 1978].

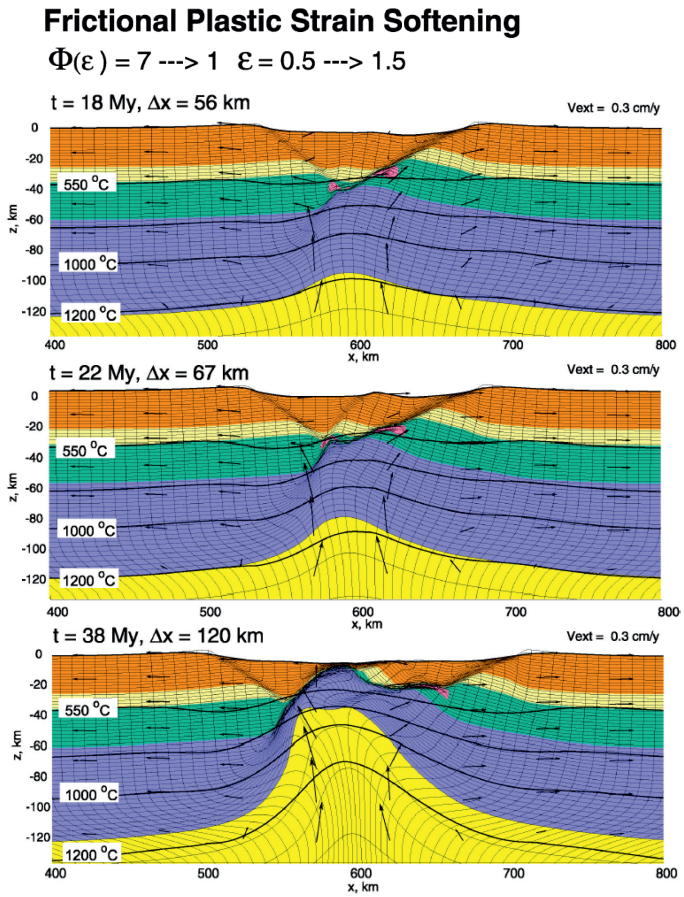

FIG. 13b. – Example of numerical simulation of rift basin formation in slow extensional context, assuming strong strain-softening of the material [Huismans and Beaumont, 2007].

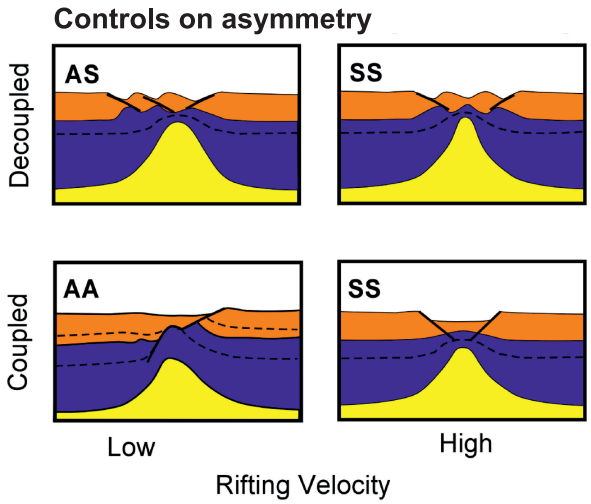

FIG. 14. – Dependence of rifting style on the extension rate [after Huismans and Beaumont, 2007]. Thermomechanical models have demonstrated that rifting style and morphology largely depends on the rheological structure and extension rate, and not only on the stretching factor β the amount of extensional thinning). "Coupled / Decoupled" means, respectively, rheological coupling and decoupling between crust and mantle.

predicted by the numerical experiments is the development of series of periodic changes in subsidence associated with delamination of dense mantle. To characterize the relative role of the gravitational instabilities during rifting, Burov [2007] introduced a special parameter, the "rift Deborah number":

$$De_r = 13.04\ \mu_{eff}\ u_x\ /\ (\Delta\rho g d\ L)$$

where μ_{eff} is effective viscosity. Assuming a ductile flow law:

$$De_r = 13.04\ \mu_0\ exp(H/nRT)\ u_x\ /\ ((\Delta\rho_c + \alpha\Delta\rho_0\Delta T) g d\ L)$$

with $\mu_0 = e^{d}{}_{II}{}^{(1-n)/n}\ (A^*)^{-1/n}$, $e^{d}{}_{II} = (\mathrm{Inv}_{II}\ (e_{ij}))^{1/2}$ is the effective strain-rate and $A^* = 1/2A\cdot 3^{(n+1)/2}$ is the material constant, H is the activation enthalpy, R is the gas constant, n is the power law exponent. L is the final width of the rift and u_x is the extension rate, $\Delta\rho_c + \alpha\rho_0\Delta T = \Delta\rho$, $\Delta\rho_c$ is the compositional density contrast, α is the coefficient of thermal expansion, ρ_0 is the density at reference temperature and ΔT is the temperature change in respect to the reference temperature. Based on the results of modelling and analytical analysis, Burov [2007] has shown that gravitational instabilities play an important role for $De_r < 10$, specifically for $De_r < 1.5$. It is also noteworthy that Moho depth and geometry are largely controlled by extension and the evolution of mantle-lithospheric gravitational instabilities. In particular, slow extension may result in subsidence of the Moho during the syn-rift phase. Figure 15b shows the experiment where extension occurs at extension rate (10 mm/yr) corresponding to subcritical value of De_r ($De_r \sim 1$) below which, inclusively, rifting can be treated as "slow" in terms of the impact of gravitational instabilities, so that Moho boundary remains almost flat or goes down instead of rising up. This experiment shows that, contrary to common assumptions, in case of deep lithospheric necking level, under low extension rates, the Moho may remain stable or even subside in response to lower mantle-lithosphere gravitational instabilities. Upon detachment of significant volumes of lithospheric mantle, the lithosphere may rebound and the graben flanks can be uplifted, even in the absence of further extension. The mantle detachment may occur in pace with thermal re-equilibration of the lithosphere so that the density contrast between the latter and the underlying mantle can be quite small at the moment when the detachment finally takes place. The models also show that the detachment may laterally migrate in the direction of the extension at rates exceeding extension rate. Hence, for relatively high extension rates, partial mantle delamination may occur at some distance from the rift flanks resulting in uplift of rift borders.

Rifted margins present another important challenge for the contemporary numerical models [e.g., Huismans and Beaumont, 2011] as their formation is associated with extreme deformation and intensive mantle-lithosphere interactions, after the lithosphere has been thinned by a factor higher than 5 [Salvenson, 1978]. Numerical models have been successfully used to address the most pertinent questions concerning evolution of rifted margin even though a number of questions such as impact of magmatic processes or formation of hyper-extended crusts still remains an open question.

Passive margins are usually separated into two large classes: volcanic or non-volcanic margins depending on whether magmatism have occurred during rifting or on later stages. Even if this classification is contested in terms of

both the underlying mechanisms and observations [Huismans and Beaumont, 2011; Geoffroy, 2005], it still can be retained in terms of morphological structures. Non-volcanic rifted margins usually show tectonized features (tilted blocks) and a transitional zone between the continental crust and the oceanic crust called Ocean-Continent transition (OCT) [e.g. Lavier and Manatschal, 2006]. The nature of the OCT is fairly known and seems to vary from one non-volcanic margin to the other. This OCT usually exhibits (1) a zone of exhumed continental mantle (ZECM) [e.g. Manatschal, 2004]; or (2) a deeper mantle serpentinized by percolation of the seawater into the sediments and the faulted crust; or (3) a highly tectonized oceanic crust formed by ultra-slow spreading. Non-volcanic margins can

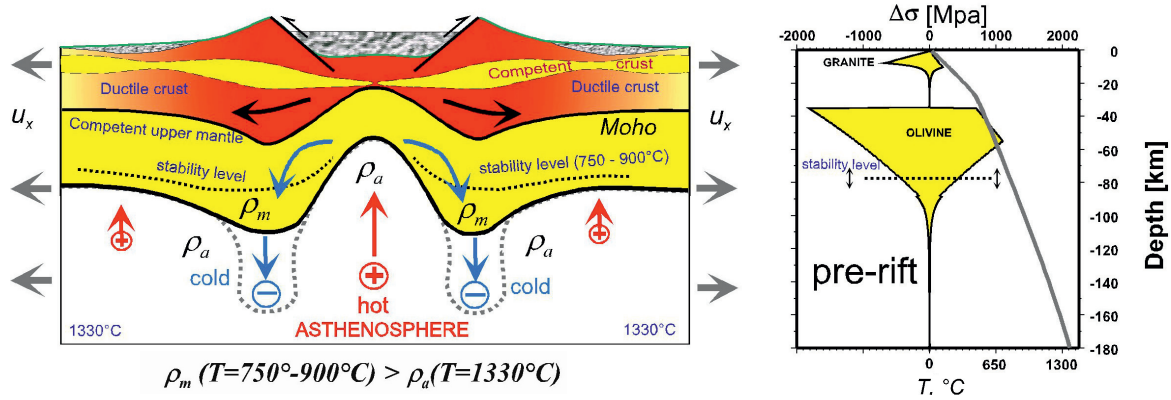

FIG. 15a. – Example of formation of a slow continental margin [Burov, 2007]: a conceptual model. The thermo-mechanical experiments suggest that slow rifting may be strongly influenced by competition between the advective and diffusive processes. If heat diffusion has same or faster characteristic time scales as heat advection, then gravitation instabilities develop, leading to gravitational removal of a large amount of mantle lithosphere, with strong consequences for surface evolution (e.g. enhanced thinning, uplift) and rift morphology.

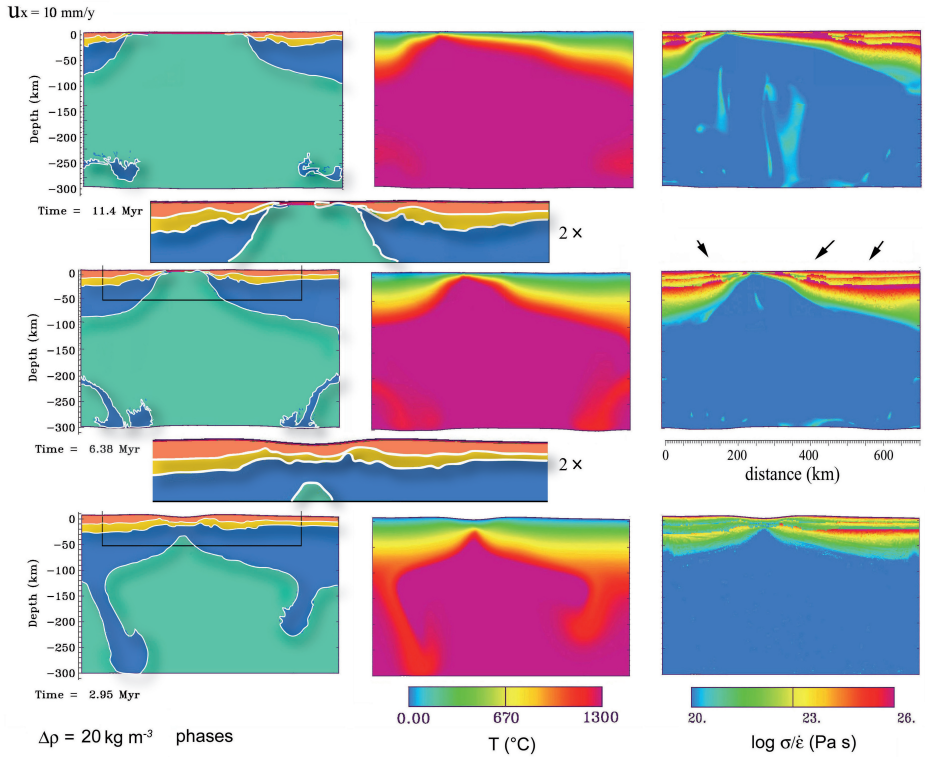

FIG. 15b. – Example of a numerical study reproducing formation of a slow margin [Burov, 2007]: a numerical experiment exploring gravitational instability of the mantle lithosphere during extension. Left panel: blue color corresponds to the mantle lithosphere, yellow – to the lower crust, orange – to the upper crust, purple is the new oceanic crust and sediment, green is the asthenosphere (Colours refer to the PDF version).

also show a limited magmatism attributed to decompressional melting during crustal thinning or post-rift thermal anomaly. Volcanic rifted margins are characterized by large amounts of magmatism (basalt flows, volcanoes, mafic underplating) produced during the rifting process [e.g. Geoffroy, 2006], and an ocean-continent boundary or a very narrow OCT. Volcanic margins are commonly associated with high thermal anomalies in the mantle, allowing for formation of significant amounts of melt under extension [e.g. White and McKenzie, 1989]. Most of the above problems present a challenge for next generations of numerical models. In particular, the interplay between extension and magmatism during continental breakup is still debated and recent numerical modelling studies suggest that the volumes of melts extruded at volcanic margins may also be generated by 'standard' thermal conditions, provided high extension rates can be implied [Huismans and Beaumont, 2011]. The numerical models under development would necessarily need an account for melting and other fluid-rock interactions during the extensional processes, through development of bi-phase flow approach addressing hydration-dehydration reactions and porous flow in the extended crust [Mezri *et al.*, 2013]. Since rock porosity appears to be pressure, temperature and strain-rate dependent [Angiboust *et al.*, 2012 and references therein] while metamorphic reactions also require presence of fluids, which have also strong impact on the brittle and ductile rock strength, one can suggest that there may be a strong coupling between tectonic and fluid circulation mechanisms in the extensional context.

Many fundamental questions remain unsolved and require further modelling efforts concerning the evolution of volcanic and non-volcanic margins. In particular, it is still not clear how the properties of the mantle lithosphere – except its thermal state and ductile strength – affect rift evolution. For example, the idea that common plastic failure criterion [Byerlee/Mohr-Coulomb, Byerlee, 1978] may not be applicable to the mantle lithosphere has been widely discussed in the recent literature [e.g. Burov, 2011; Precigout *et al.*, 2007; Watts and Burov, 2003]. It is suggested that this criterion may largely overestimate the mechanical strength of the lithosphere [e.g., Precigout *et al.*, 2007], leading to incorrect prediction of such key features as timing of continental break-up and margin geometry.

INTERPLAY BETWEEN LITHOSPHERE DYNAMICS AND SURFACE PROCESSES

Surface processes may play a significant role during both in subduction/collision processes [e.g., Dahlen and Suppe, 1988; Avouac and Burov, 1996; Beaumont *et al.*, 2000; Pysklywec, 2006; Burov, 2010] syn-rift and post-rift evolution [e.g., Burov and Cloetingh, 1997; Burov and Poliakov, 2001], not only in terms of the effect of sediments on thermal blanketing causing temperature rise in sedimentary basins [e.g., Lavier and Steckler, 1997], or due to their lubricating effect on the subduction channel, but first of all due to the straightforward effect of lateral distribution of important surface loads carried out by erosion and sedimentation processes (fig. 16). In zones of fast tectonic deformation (i.e., horizontal convergence/extension rates > ~1 cm/y), surface processes modify topography at rates comparable with the rates of the tectonic uplift/subsidence (a few 0.1 mm/yr), leading, in some cases, to erosion of thousands meters of topography from mountains or from rift flanks and deposition of the equivalent amounts of sedimentary infill [e.g., Avouac and Burov, 1996; Burov and Cloetingh, 1997]. The associated dynamic loading and unloading exerted on the supporting crust and lithosphere is on the same order as tectonic loading, suggesting possible strong feedbacks between the surface and tectonic processes. In particular, an increase of sedimentary loading may lead to localised yielding and deflection of the supporting lithosphere. At the same time, erosional unloading of orogenic belts or on rift shoulders leads to their flexural or isostatic uplift and strengthening. Of specific importance, according to some models, is also the "localizing" effect of erosion on faulting [e.g., Burov and Poliakov, 2001]. Surface processes, potentially resulting in acceleration of orogenic processes in collisional contexts or in enhanced subsidence and extension of rifted basins and uplift of the rift shoulders, create pressure gradients sufficient to drive ductile flow in the low-viscosity lower crust (fig. 16) [Burov and Cloetingh, 1997]. It must be noted, however, that the feedbacks between tectonics and surface process are most important in regions characterized by high rates of tectonic uplift or subsidence (such as India-Asia collision). Numerical models have shown that in slowly evolving regions such

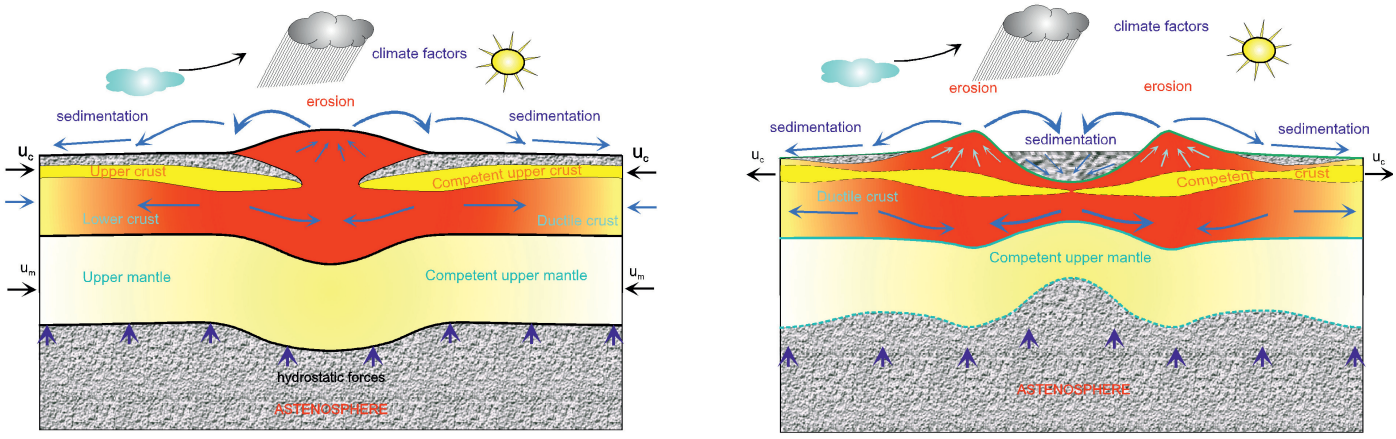

FIG. 16. – Interplay between surface and subsurface processes: concept illustrating possible feedbacks between surface processes and subsurface response through ductile flow in the crust and mechanical response of the lithosphere to loading/unloading.

as western Alpes, the "tectonic" impact of surface processes is rather insignificant [e.g., Yamato *et al*., 2008].

The complex interplays between surface processes, climate and tectonic deformation can be only assessed through physically consistent thermo-mechanical modelling. Models have shown the importance of isostatic effects associated with variations in surface loading caused by surface processes. They have demonstrated as well that crustal ductile flow may indeed occur until the ductile channel thickness is greater than a few km [Burov and Cloetingh, 1997] thus allowing for dynamic feedback between surface loading and subsurface deformation. This flow is also largely gravity driven, due to lateral Moho gradients associated with crustal thinning. In case of rifting, for example, the flow rate first progressively increases as the crust thins, and then decreases when there is no more ductile crustal material below the rift zone. This flow, directed outward from the centre of the basin may facilitate uplift of the rift shoulders (figs 16-17) [Burov and Poliakov, 2001]. It may even drive some post-rift "extension" [Burov and Poliakov, 2001]. In the limiting case of slow erosion and sedimentation rates, gravitational stresses can reverse the flow, resulting in retardation of basin subsidence rate, homogenisation of the crustal thickness, accelerated collapse of the shoulders and in some post-rift "compression". These effects may significantly change predictions of basin evolution inferred from the conventional stretching models.

Similarly, models of continental collision have revealed a strong potential dependence of the collision style on the intensity of surface processes and the degree of their interaction with the subsurface deformation. It has been shown that [Burov and Toussaint, 2007] in case of fast convergence rates (> 3 cm/y), there should be a very strong coupling between surface and subsurface processes so that not only the topography growth rates but also deep processes such as the amount of subduction are strongly affected by surface erosion. In particular, it has been demonstrated that in ''Himalayan context", coupling between surface and subsurface processes controls as much as 50% of the total amount of the subducted continental lithosphere [Toussaint *et al*., 2004b]. It has been even proposed, based on ductile crustal flow models [Beaumont *et al*., 2001], that the erosion is strong enough to drive the exhumation of the ductile crust of Tibet in the Himalayas, although these former ideas seemingly do not find sufficient confirmation from recent field observations [Searle *et al*., 2011; Searle, 2013]. However, as mentioned, in case of slow convergence rate [Yamato *et al*., 2008] the role of surface processes is far less significant.

MANTLE-LITHOSPHERE INTERACTIONS

Mantle convection and plumes are thought to constitute "engines" of plate tectonics. The problem of mantle-lithosphere interactions has been largely addressed by thermo-mechanical models due the principal difficulty to obtain any direct information about deep processes. The geophysical methods such as seismic tomography or gravity show only current, generally ambiguous snapshots of the Earth interiors while the interpretations of the impact of mantle dynamics on surface and tectonic deformation records are also subject of strong assumptions. Numerical models thus have played an essential role in the improvement of our understanding of the potential features of surface and tectonic response to mantle flow, in particular, dynamic topography and deformation fields produced by mantle plumes. Based on these models, it has been only recently shown that dynamic topography (i.e. surface undulations created by mantle upwellings and downwellings) may exhibit contre-intuitive features being strongly impacted by the rheological properties of the lithosphere. Burov and Guillou-Frottier [2005], for

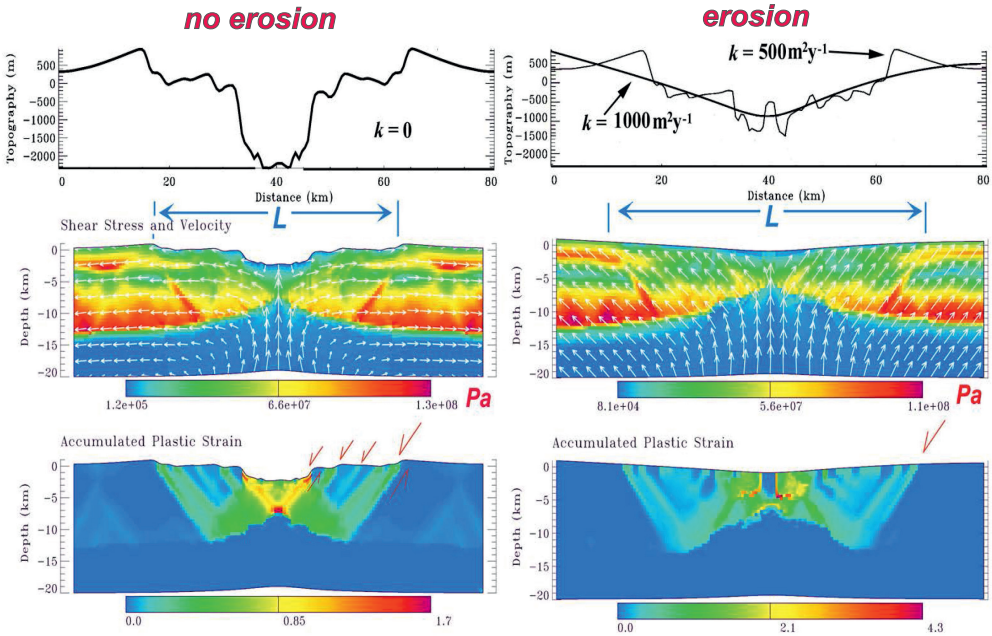

FIG. 17. – Interplay between surface and subsurface processes: example of a viscous-elastic-ductile numerical model of extension of a young lithosphere [Burov and Poliakov, 2001]. The left panel: extension of the lithosphere in the absence of extension. Right panel: extension of the lithosphere in presence of syn-rift erosion with erosion coefficient k of 1000 m^2/yr. For comparison, topography profile for k = 500 m^2/yr is also shown.

example, have shown that in contrast to usual expectation of long-wavelength surface deformation, the dynamic topography may in reality mainly present short-wavelength features (fig. 18). The resulting thermo-mechanical consequences for surface geodynamics and geology appear to be largely dependent not only on the characteristics on the mantle upwelling, but also on the thermo-rheological and density structure of the lithosphere [d'Acremont *et al.*, 2003; Burov

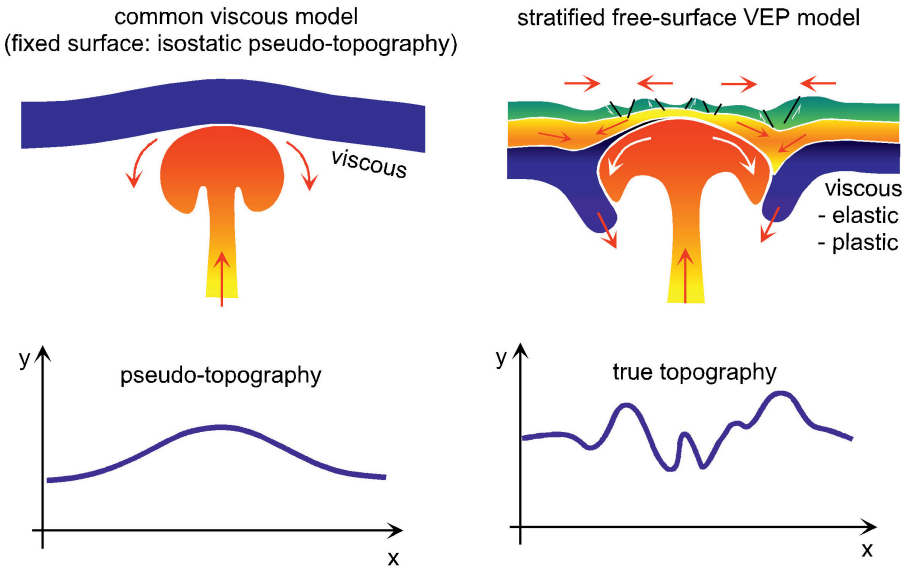

FIG. 18. – Dynamic topography over continents as revealed by thermo-mechanical models accounting for rheological stratification of the lithosphere [Burov and Cloetingh, 2010]: general concept. Left panel shows common intuitive assumption about dynamic topography in which the lithosphere is considered as a stagnant lid passively transmitting mantle motions to the surface. Right: a concept accounting for rheological stratification and free surface of the lithosphere suggesting that dynamic topography can be largely accommodated within the ductile crust, and overall modulated by crustal and lithosphere mantle deformation. In this case the long-wavelength will be attenuated and tensional/compressional instabilities in lithospheric layers may generate short wavelengths overprinting the long-wavelength signal.

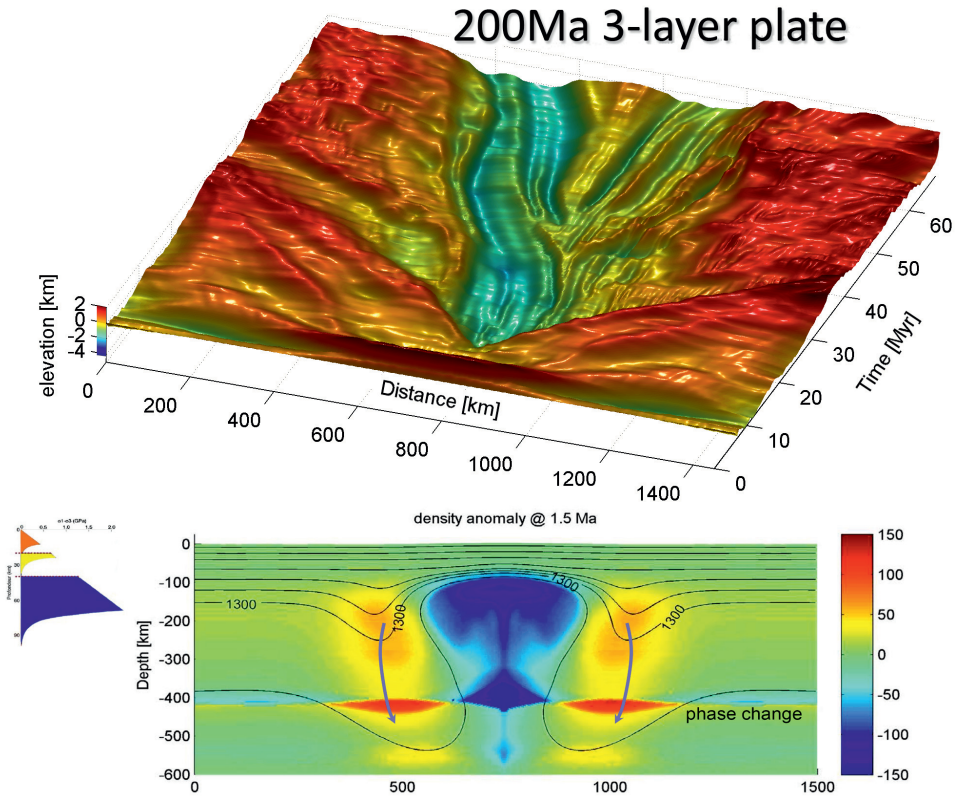

FIG. 19. – Dynamic topography evolution predicted by a numerical model [Burov and Gerya, 2014], in which mantle plume interacts with stratified viscous-elastic-ductile lithosphere. The lower panel shows density anomaly field associated with plume-mantle-lithosphere interaction. The upper panel shows induced topography evolution.

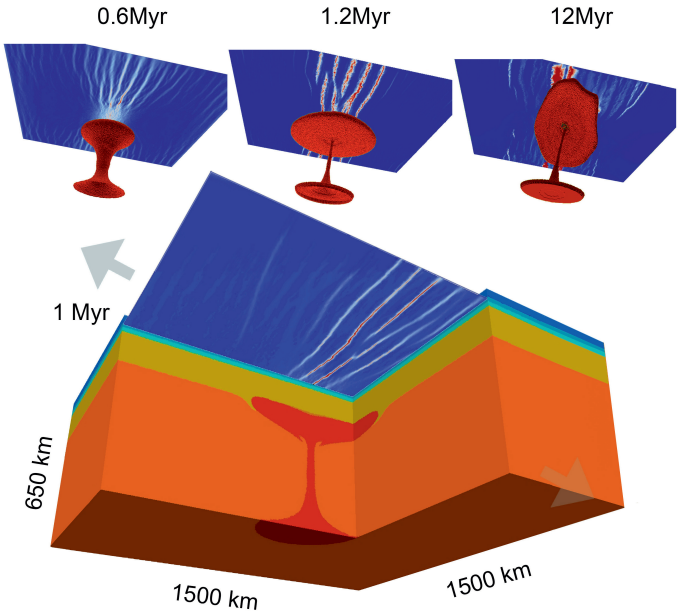

FIG. 20. – Example of a high-resolution 3D numerical model of evolution of crustal rifting patterns and plume geometry during plume-lithosphere interaction in presence of far-field tectonic stress (which direction in shown with grey arrows) applied to the lithosphere. The figure represents combined shear strain rate patterns (near surface horizontal sections) and material phase distribution [after Burov and Gerya, 2014; Burov *et al.*, 2014].

and Guillou-Frottier, 2005; Burov *et al.*, 2007; Burov and Cloetingh, 2009; 2010]. The models have demonstrated that both the thermo-tectonic age and rheological stratification of the lithosphere have a strong impact on the effect on mantle-lithosphere interactions [Burov and Guillou-Frottier, 2005]. As a result, the presence of low-viscosity ductile lower crust leads to essential damping of the long-wavelength dynamic topography and appearance of short-wavelength tectonic-scale features, associated with tensional and compressional instabilities in the crustal layers (figs 19 and 20). Certainly, the common assumption of a horizontally uniform lithosphere at the site of future lithosphere break-up caused by uprising asthenosphere is probably not realistic, in a view of the abundant evidence from the geological record that incipient rifts and rifted margins are usually localized at suture zones separating stronger lithosphere. Examples include the Caledonides suture of Laurentia-Greenland and Baltica, localizing Late Carboniferous and Permo-Triassic rifting and subsequent continental break-up around 65 Ma in the Arctic-northern Atlantic and the rift systems created at the edges of the African cratonic lithosphere [Corti *et al.*, 2004; Corti, 2005; Janssen *et al.*, 1995]. It should be noted also some natural examples do not always fit these assumptions. For instance, the Labrador Sea opened orthogonally to the basement grain, whereas the North Sea rift cuts obliquely across the Caledonian basement grain [Ziegler, 1988]. Plume impingement may also occur at the onset of the post-rift phase or even later. In this case the rifted margin lithosphere has been thermally reset to very young thermo-mechanical ages for the thinned continental lithosphere and the adjacent oceanic lithosphere. Hence, further model developments, in 2D and 3D, are needed to take into account the impact of tectonic heritage and spatially variable plate structure on the consequences of mantle-lithosphere interactions.

CONCLUSIONS

Observation-driven hypothesis can be verified indirectly through eliminating those that prove to be incompatible with the predictions of physically and observationally consistent models. On the other hand, model-driven hypothesis can orient field and laboratory research towards the acquisition of new data that may either confirm or dismiss model predictions.

The numerical models allow us to evaluate the relative importance of different processes involved in geological evolution and serve as power tools for interpretation of the geological, geophysical, petrological and other observations. The numerical thermo-mechanical models play an essential role allowing one to understand the phenomena, which spatial and temporal scales go beyond the scale of human-scale observations. They play a particular role in validation [e.g., Burov *et al.*, 1999; Burov, 2011], or more precisely, refutation

TABLE Ia. – Summary of thermal and mechanical parameters used in model calculations [e.g., Turcotte and Schubert, 2002].

Type	Definition	Units
Thermal	Surface temperature (0 km depth)	0°C
	Temperature at the base of thermal lithosphere	1330°C
	Temperature at the base of upper mantle (650 km)	1700° ±100°C
	Thermal conductivity of crust	2.5 Wm^{-1} $°C^{-1}$
	Thermal conductivity of mantle	3.5 Wm^{-1} $°C^{-1}$
	Thermal diffusivity of mantle	10^{-6} $m^2.s^{-1}$
	Radiogenic heat production at surface	9.5×10^{-10} W kg^{-1}
	Radiogenic heat production decay length	10 km
	Thermo-tectonic age of the lithosphere	50 to 600 Myr
Mechanical	Density of the upper crust*	2700 kg m^{-3}
	Density of lower crust*	2900 kg m^{-3}
	Density of oceanic crust*	2900 kg m^{-3}
	Density of sediment*	2600 kg m^{-3}
	Density of undepleted mantle*	3330 kg m^{-3}
	Density of asthenosphere*	3310 kg m^{-3}
	Lamé elastic constants λ , G (Here, $\lambda = G$)	30 GPa
	Byerlee's law – Friction angle	30°
	Byerlee's law – Cohesion	20 MPa

* We here provide average densities, in thermo-dynamically coupled models densities are derived directly from the assumed mineralogical composition as function of pressure and temperature conditions

TABLE Ib. – Example of ductile flow parameters assumed in model calculations. Compilation of Mackwell *et al.* [1998] based on data from Gleason and Tullis [1995], Hirth and Kohlstedt [1996], Chopra and Patterson [1981]. More recent data [see compilation in Bürgmann and Dresen, 2008] predict slightly different values for ductile flow parameters. However, on practice these differences are negated by adjusting geotherms or thicknesses of the rheological layers in a way that the integral strength of the lithosphere matches the observed T_e values.

Layer	Composition	Pre-exponential stress constant A MPa^{-n} s^{-1}	Power law exponent n	Activation energy, Q KJ mol^{-1}
Upper Crust	Wet Quartzite	1.1×10^{-4}	4	223
Lower Crust	Dry Maryland Diabase	8±4	4.7±0.6	485±30
	Undried Pikwitonei granulite	1.4×10^{4}	4.2	445
Mantle or Oceanic lithosphere	Dry Olivine	4.85×10^{4}	3.5	535
	Wet Olivine	417	4.48	498
	Diffusion creep	1.92×10^{-4}	1	3.0×10^{2}
	Peierls law	$10^{7.8} \times 10^{-12}$	Peierls stress= 5GPa	5.35×10^{2}

of geodynamic and geological hypotheses and for interpretation of various kinds of observations. The models serve also for validation, calibration and integration of different types of multidisciplinary data allowing one to elucidate the inconsistency in the data and validate extrapolations of these data to geological time and spatial scales. In particular, the data of rock-mechanics obtained at short and small laboratory scales can be tested through geodynamic models that can show at which extent the extrapolation of these data is valid. For example, seismic tomography images can be tested in terms of their compatibility with gravitational and mechanical stability of the mantle. The models serve also for directing field and laboratory research by showing sensibilities of studied processes to particular kinds of data thus suggesting which type of data needs to be acquired or sampled with improved accuracy.

The current challenges in the geodynamic modelling include further development of multi-process physically consistent models based on realistic viscous-plastic-rheologies. In particular, incorporation of thermodynamic processes such as phase changes and fluid percolation (porous flow) is on the neck of the art. Integration of surface processes is also an important challenge, especially in 3D, while expanding the geotectonic models down to the bottom of the upper mantle to take into account mantle lithosphere interactions is another paramount requirement. There is also a growing demand in terms of better spatial resolution of the models that should progressively reach that of field observations. In particular, tectonic scale models would ideally have spatial resolutions on the order of 100-1,000 m for grid resolutions on the order of 1,000-10,000 elements in single direction. Such resolution is a big algorithmic and methodological challenge in case of 3D models since it requires enormous computing resources and hence enormous code optimization efforts. Actually most advanced matrix inversion algorithms developed in the applied mathematics are limited to 1000^3 implying that accessing higher resolutions would need strong cooperation between geodynamic modellers and specialists in applied mathematics.

It is finally important to remind that geotectonic models are naturally simpler than the objects (in other sciences such as engineering, computer models can be as complex as their targets). They are also based on potentially erroneous knowledge of model parameters since the geological and geophysical data used for their construction are "blurred" due to numerous uncertainties. This has to be retained while interpreting results of numerical modelling.

Acknowledgements. – We thank both reviewers, J.-P. Brun and S. Cloetingh for their highly constructive comments. Different parts of the manuscript have also benefited from discussions with L. Le Pourhiet. This publication was supported by the advanced ERC grant RHEOLITH.
SGF editor: Olivier Lacombe

References

AFONSO J. C. & ZLOTNIK S. (2011). – The subductability of continental lithosphere: The before and after story, arc-continent collision. – *Frontiers in Earth Sciences*, *Part 1*, 53-86, doi: 10.1007/978-3-540-88558-0_3.

ALLEMAND P. & BRUN J.-P. (1991). – Width of continental rifts and rheological layering of the lithosphere. – *Tectonophysics*, **188**, 1-2, 63-69.

ANGIBOUST S., WOLF S., BUROV E., AGARD P. & YAMATO P. (2012). – Fluid circulation at the subduction interface: Insights from thermo-mechanical numerical modelling. – *Earth Planet. Sci. Lett.*, **357**, 238-248.

ARCAY D., DOIN M.-P., TRIC E. & BOUSQUET R. (2007). – Influence of the precollisional stage on subduction dynamics and the buried crust thermal state: Insights from numerical simulations. – *Tectonophysics,* **441**, 1-4, 27-45.

AVOUAC J.-P. & BUROV E.B. (1996). – Erosion as a driving mechanism of intracontinental mountain growth. – *J. Geophys. Res.-Solid Earth*, **101** (B8), 17747-17769.

BASSI G., KEEN C.E. & POTTER P. (1993). – Contrasting styles of rifting: Models and examples from the eastern Canadian margin. – *Tectonics*, **12**, 639-655.

BEAUMONT C., KAMP P.J.J., HAMILTON J. & FULLSACK P. (1996). – The continental collision zone, South Island, New Zealand: Comparison of geodynamical models and observations. – *J. Geophys. Res.*, **101**, 3333-3359.

BEAUMONT C., MUÑOZ J.A., HAMILTON J. & FULLSACK P. (2000). – Factors controlling the Alpine evolution of the central Pyrenees inferred from a comparison of observations and geodynamical models. – *J. Geophys. Res.*, **105**(B4), 8121-8146.

BEAUMONT C., JAMIESON R.A., NGUYEN M.H. & LEE B. (2001). – Himalayan tectonics explained by extrusion of a low-viscosity crustal channel coupled to focused surface denudation. – *Nature*, **414**, 738-742, doi: 10.1038/414738a.

BIRD P. (1978). – Finite elements modelling of lithosphere deformation: The Zagros collision orogeny. – *Tectonophysics*, **50**, 307-336.

BRAUN J. & BEAUMONT C. (1989). – A physical explanation of the relation between flank uplifts and the breakup unconformity at rifted continental margins. – *Geology*, **17**, 760-765.

BRAUN J., CHÉRY J., POLIAKOV A., MAINPRICE D., VAUCHEZ A., TOMASSI A. & DAIGNIÈRES M. (1999). – A simple parameterization of strain localization in the ductile regime. – *J. Geophys. Res.*, (B), **104**, 25167-25181.

BRUN J.-P. (1999). – Narrow rifts versus wide rifts: inferences for the mechanics of rifting from laboratory experiments. – *Phil. Trans. Royal Soc. A-Math. Phys. Eng. Sci.*, **357**, 1753, 695-710.

BRUN J.-P. & BESLIER M. (1996). – Mantle exhumation at passive margins. – *Earth Planet. Sci. Lett.,* **142**, 161-173.

BUCK W.R. (1991). – Modes of continental lithospheric extension. – *J. Geophys. Res.*, **96**, 20161-20178.

BURG J.-P. & GERYA T.V. (2005). – Viscous heating and thermal doming in orogenic metamorphism: numerical modelling and geological implications. – *J. Met. Geol.*, **23**, 75-95.

BURG J.-P. & PODLADCHIKOV Y. (2000). – From buckling to asymmetric folding of the continental lithosphere: Numerical modelling and application to the Himalayan syntaxes. *In*: M.A. KHAN *et al.*, Eds, Tectonics of the Nanga Parbat syntaxis and the western Himalaya. – *Geol. Soc. London Spec. Publ.*, **170**, 219-236.

BÜRGMANN R. & DRESEN G. (2008). – Rheology of the lower crust and upper mantle: evidence from rock mechanics, geodesy, and field observations. – *Annual Rev. Earth Planet. Sci.*, **36**, 531-567, doi: 10.1146/annurev.earth.36.031207.124326.

BURKETT E.R. & BILLEN M.I. (2010). – Three-dimensionality of slab detachment due to ridge-trench collision: laterally simultaneous boudinage versus tear propagation. – *Geochem., Geophys., Geosyst*., **11**, Q11012.

BUROV E. (2007). – Part 1: Surficial and deep processes in thrust belts, Chapter 1: Coupled lithosphere-surface processes in collision context. *In*: O. LACOMBE, J. LAVÉ, F. ROURE and J. VERGÈS, Eds, Thrust belts and foreland basins: From fold kinematics to hydrocarbon systems, Springer-Verlag, Berlin Heidelberg, series "Frontiers in Earth Sciences", 1-40, ISBN-13: 978-3-540-69425-0.

BUROV E. (2010a). – The equivalent elastic thickness (Te), seismicity and the long-term rheology of continental lithosphere: Time to burn-out "crème brûlée"? Insights from large-scale geodynamic modelling. – *Tectonophysics*, doi: 10.1016/ j.tecto.2009.06.013.

BUROV E. (2010b). – Thermo-mechanical models for coupled lithosphere-surface processes: Applications to continental convergence and mountain building processes. *In*: S. CLOETINGH and J. NEGENDANK, Eds, New frontiers in integrated solid Earth sciences. International Year of Planet Earth. – *Springer Science + Business Media*, 103-143, doi: 10.1007/ 978-90-481-2737-5_4.

BUROV E. (2011). – Rheology and strength of the lithosphere. – *Mar. Petrol. Geol.*, **28-8**, 1402-1443, doi: 10.1016/j.marpetgeo. 2011.05.008.

BUROV E.B. & CLOETINGH S. (1997). – Erosion and rift dynamics: new thermomechanical aspects of post-rift evolution of extensional basins. – *Earth Planet. Sci. Lett.*, **150**, 7-26.

BUROV E. & CLOETINGH S. (2009). – Controls of mantle plumes and lithospheric folding on modes of intraplate continental tectonics: differences and similarities. – *Geophys. J. Int*., **178**, 3, 1691-1722

BUROV E. & CLOETINGH S. (2010). – Plume-like upper mantle instabilities drive subduction initiation. – *Geophys. Res. Lett.*, doi: 10.1029/ 2009GL041535.

BUROV E.B. & DIAMENT M. (1995). – Effective elastic thickness of the continental lithosphere – what does it really mean? – *J. Geophys. Res.*, **100**, 3905-3927.

BUROV E. & GERYA T. (2014). – Rheology of continents and counterintuitive 3D features of the dynamic topography. – *Nature (submitted)*.

BUROV E. & GUILLOU-FROTTIER L. (2005). – The plume head-lithosphere interaction using a tectonically realistic formulation for the lithosphere. – *Geoph. J. Int.*, **161**, 469-490.

BUROV E. & POLIAKOV A. (2001). – Erosion and rheology controls on syn- and post-rift evolution: verifying old and new ideas using a fully coupled numerical model. – *J. Geophys. Res.*, **106**, 16461-16481.

BUROV E. & TOUSSAINT G. (2007). – Surface processes and tectonics: forcing of continental subduction and deep processes. – *Global Planet. Change, Spec. vol. on Topography of Europe*, **58**, 141-164.

BUROV E. & WATTS A.B. (2006). – The long-term strength of continental lithosphere: "jelly-sandwich" or "crème-brûlé"? – *GSA Today* (Geological Society of America), **16**, 1, doi: 10.1130/1052-5173 (2006)016:TLTSOC,.

BUROV E. & YAMATO PH. (2008). – Continental plate collision, P-T-t-z conditions and unstable vs. stable plate dynamics: Insights from thermo-mechanical modelling. – *Lithos*, **103**, 178-204.

BUROV E.B., PODLADCHIKOV Y., GRANDJEAN G. & BURG J.-P. (1999). – Validation of multidisciplinary data using thermo-mechanical modelling: application to the western and northern Alps. – *Terra Nova*, **11**, 124-131.

BUROV E.B., JOLIVET L., LE POURHIET L. & POLIAKOV A. (2001). – A thermo-mechanical model of exhumation of HP and UHP metamorphic rocks in Alpine mountain belts. – *Tectonophysics*, **342**, 113-136.

BUROV E., GUILLOU-FROTTIER L., D'ACREMONT E., LE POURHIET L. & CLOETINGH S. (2007). – Plume head-lithosphere interactions near intra-continental plate boundaries. – *Tectonophysics*, **434**, 1-4, 15-38, doi: 10.1016/ j.tecto.2007.01.002.

BUROV E., FRANCOIS T., YAMATO P. & WOLF S. (2012). – Mechanisms of continental subduction and exhumation of HP and UHP rocks. – *Gondwana Res*., doi: 10.1016/j.gr.2012.09.010,

BUROV E., GERYA T. & KOPTEV A. (2014). – Impact of lithosphere rheology on the dynamic topography, 27 April – 02 May 2014. – *EGU Assembly Vienna* 2014

BYERLEE J.D. (1978). – Friction of rocks. – *Pure Appl. Geophys.*, **116**, 615-629.

CADELL H.M. (1890). – Experimental researches in mountain building. – *Trans. Roy. Soc. Edinburgh*, **35**, 337p.

CHEMENDA A.L., MATTAUER M., MALAVIEILLE J. & BOKUN A.N. (1995). – A mechanism for syn-collisional deep rock exhumation and associated normal faulting: Results from physical modelling. – *Earth Planet. Sci. Lett.*, **132**, 225-232.

CHEMENDA A.I., MATTAUER M. & BOKUN A.N. (1996). – Continental subduction and a mechanism for exhumation of high pressure metamorphic rocks: New modelling and field data from Oman. – *Earth Planet. Sci. Lett.,* **143**, 173–182.

CHÉRY J., LUCAZEAU F., DAIGNIERES M. & VILOTTE J.-P. (1992). – Large uplift of rift flanks: A genetic link with lithospheric rigidity? – *Earth Planet. Sci. Lett*., **112**, 195-211.

CHERY J., DAIGNIERES M., LUCAZEAU F. & VILOTTE J.-P. (1989). – Strain localization in rift zones (case of a thermally softened lithosphere) - a finite-element approach. – *Bull. Soc. Géol. Fr.*, 8, **V**,3, 437-443

CHOPRA P.N. & PATERSON M.S. (1981). – The experimental deformation of dunite. – *Tectonophysics*, **78**, 453-473.

CLOETINGH S.A.P.L., WORTEL M.J.R. & VLAAR N.J. (1982). – Evolution of passive continental margins and initiation of subduction zones. – *Nature*, **297**, 139-142.

CLOETINGH S., BUROV E. & POLIAKOV A. (1999). – Lithosphere folding: Primary response to compression? (from central Asia to Paris Basin). – *Tectonics*, **18**, 1064-1083.

CLOETINGH S. & ZIEGLER P. (2004). – Dynamic processes controlling evolution of rifted basins. – *Earth-Sci. Rev.*, **64**, 1-50.

CLOOS M. (1993). – Lithospheric buoyancy and collisional orogenesis: Subduction of oceanic plateaus, continental margins, island arcs, spreading ridges and seamounts. – *Geol. Soc. Amer. Bull.*, **105**, 715-737.

COLEMAN R.G. (1971). – Plate tectonic emplacement of upper mantle peridotites along continental edges. – *J. Geophy. Res.*, **76**, 1212-1222.

CONNOLLY J.A.D. (2005). – Computation of phase equilibria by linear programming: A tool for geodynamic modelling and its application to subduction zone decarbonation. – *Earth Planet. Sci. Lett.*, **236**, 524-541.

CORTI G., BONINI M., SOKOUTIS D., INNOCENTI F., MANETTI P., CLOETINGH S. & MULUGETA G. (2004). – Continental rift architecture and patterns of magma migration: A dynamic analysis based on centrifuge models. – *Tectonics*, **23**, TC2012, doi: 10.1029/ 2003TC001561.

CORTI G. (2005). – Dynamics of periodic instabilities during stretching of the continental lithosphere: View from centrifuge models and comparison with natural examples. – *Tectonics*, **24**, TC2008.

CRAMERI F. & KAUS B. (2010). – Parameters that control lithospheric-scale thermal localization on terrestrial planets. – *Geophys. Res. Lett*., **37**.

CULLING W.E.H. (1960). – Analytical theory of erosion. – *J. Geol.,* **68** (333-336).

D'ACREMONT E., LEROY S. & BUROV E. (2003). – Numerical modelling of a mantle plume: the plume head-lithosphere interaction in the formation of an oceanic large igneous province. – *Earth Planet. Sci. Lett*., **206**, 3-4, 379-396.

DAIGNIERES M., FREMOND M. & FRIAA A. (1978). – Modèle de type Norton-Hoff généralisé pour l'étude des déformations lithosphériques (exemple: la collision himalayenne). – *C. R. Hebd. Séances Acad. Sci*., **268B**, 371-374.

DAHLEN F.A. & SUPPE J. (1988). – Mechanics, growth and erosion of mountain belts. – *Geol. Soc. Amer. Spec. Pap.,* **218**, 161-178.

DAVY P. & COBBOLD P. (1980). – Experiments on shortening of a 4-layer model of the continental lithosphere. – *Tectonophysics*, **188**, 1-2, 1-25.

DOIN M.-P. & HENRY P. (2001). – Subduction initiation and continental crust recycling: The roles of rheology and eclogitization. – *Tectonophysics*, **342**, 163-191.

DUNBAR J.A. & SAWYER D.S. (1988). – Continental rifting at pre-existing lithospheric weakness. – *Nature*, **333**, 450-452.

DURETZ T., GERYA T.V. & MAY D.A. (2011). – Numerical modelling of spontaneous slab breakoff and subsequent topographic response. – *Tectonophysics*, **502**, 244-256.

ERNST W.G. (1973). – Blueschist metamorphism and P-T regimes in active subduction zones. – *Tectonophysics*, **17**, 255-272.

ERNST W.G. (2010). – Subduction-zone metamorphism, calc-alkaline magmatism, convergent-margin crustal evolution. – *Gondw. Res.*, **18**, 8-16.

FACCENDA M., GERYA T.V. & BURLINI L. (2009). – Deep slab hydration induced by bending related variations in tectonic pressure. – *Nature, Geoscience*, **2**, 790-793.

FLETCHER R.C. (1974). – Wavelength selection in the folding of a single layer with power-law rheology. – *Am. J. Sci.*, **274**, 1029-1043.

FORD M., DUCHÊNE S., GASQUET D. & VANDERHAEGHE O. (2006). – Two-phase orogenic convergence in the external and internal SW Alps. – *J. Geol. Soc.,* London, **163**, 815–826.

FRANCOIS T., BUROV E., AGARD P. & MEYER B. (2013). – Build-up of a dynamically supported orogenic plateau: numerical modelling of the Zagros/Central Iran case study. – *Geophys. Geoecol. Geochem.* (in press).

GEOFFROY L. (2005). – Volcanic passive margins. – *C. R. Géoscience*, **337**, 1395-1408.

GERYA T. (2011). – Future directions in subduction modelling. – *J. Geodyn.*, **52**, 344-378.

GERYA T. (2010). – Dynamical instability produces transform faults at mid-ocean ridges. – *Science*, **329**, 1047-1050.

GERYA T.V., STÖCKHERT B. & PERCHUK A.L. (2002). – Exhumation of high-pressure metamorphic rocks in a subduction channel: A numerical simulation. – *Tectonics*, **26 (6)**, 1-15.

GERBAULT M., BUROV E.B., POLIAKOV A. & DAIGNIERES M. (1999). – Do faults trigger folding in the lithosphere? – *Geophys. Res. Lett*., **26**, 2, 271-274.

GRAY R. & PYSKLYWEC R.N. (2010). – Geodynamic models of Archean continental collision and the formation of mantle lithosphere keels. – *Geophys. Res. Lett.*, **37**, L19301, doi: 10.1029/2010GL043965.

GRAY R. & PYSKLYWEC R.N. (2012). – Geodynamic models of mature continental collision: Evolution of an orogen from lithospheric subduction to continental retreat/delamination. – *J. Geophys. Res*., doi: 10.1029/2011JB008692.

GLEASON G.C. & TULLIS J. (1995). – A flow law for dislocation creep of quartz aggregates determined with the molten salt cell. – *Tectonophysics*, **247**, 1-23.

HANDY M.R., SCHMID S.M., BOUSQUET R., KISSLING E. & BERNOULLI D. (2010). – Reconciling plate-tectonic reconstructions of Alpine Tethys with the geological-geophysical record of spreading and subduction in the Alps. – *Earth-Science Rev.*, **102**, 121-158.

HASSANI R., JONGMANS D. & CHERY J. (1997). – Study of plate deformation and stress in subduction processes using two-dimensional numerical models. – *J. Geophys. Res*., **102 (B8)**, 17951-17965.

HIRTH G. & KOHLSTEDT D.L. (1996). – Water in the oceanic upper mantle: Implications for rheology, melt extraction and the evolution of the lithosphere. – *Earth Planet. Sci. Lett.*, **144**, 93-108.

HOPPER J.R. & BUCK W.R. (1996). – The effect of lower crustal flow on continental extension and passive margin formation. – *J. Geophys. Res*., **101**, 20-20.

HOUSEMAN C.A. & MOLNAR P. (1997). – Gravitational (Rayleigh-Taylor) instability of a layer with nonlinear viscosity and convergence thinning of continental lithosphere. – *Geophys. J. Int.*, **128**, 125-150.

HUISMANS R.S. & BEAUMONT C. (2003). – Symmetric and asymmetric lithospheric extension: Relative effects of frictional-plastic and viscous strain softening. – *J. Geophys. Res.* **108**, 2496, doi: 10.1029/2002JB002026.

HUISMANS R.S. & BEAUMONT C. (2007). – Roles of lithospheric strain softening and heterogeneity in determining the geometry of rifts and continental margins. *In*: G.D. KARNER, G. MANATSCHAL & L.M. PINHIERO, Eds, Imaging, mapping and modelling continental lithosphere extension and breakup. – *Geol. Soc. London*, *Sp. Publ*., **282**, 107-134.

HUISMANS R.S. & BEAUMONT C. (2011). – Depth-dependent extension, two-stage breakup and cratonic underplating at rifted margins. – *Nature*, **473**, 74-78.

HUISMANS R.S., BUITER S. & BEAUMONT C. (2005). – Effect of plastic-viscous layering and strain softening on mode selection during lithospheric extension. – *J. Geophys. Res*., **110**, B2, B02406, doi: 10.1029/2004JB003114.

HUISMANS R.S., CLOETINGH S. & PODLADCHIKOV Y.Y. (2001). – Transition from passive to active rifting: relative importance of asthenospheric doming and passive extension of the lithosphere. – *J. Geophys. Res*., **106**, 11271-11291.

JANSSEN M.E., STEPHENSON R.A. & CLOETINGH S. (1995). – Temporal and spatial correlations between changes in plate motions and the evolution of rifted basins in Africa. – *Geol. Soc. Amer. Bull*., **107**, 1317-1332.

KAUS B.J.P. & PODLADCHIKOV Y.Y. (2006). – Initiation of localized shear zones in viscoelastoplastic rocks. – *J. Geophys. Res.-Solid Earth*, **111**, B04412, doi: 10.1029/2005JB003652.

KARRECH A., REGENAUER-LIEB K. & POULET T. (2011). – Continuum damage mechanics for the lithosphere. – *J. Geophys. Res*., **116**, B04205.

KUSZNIR N., MARSDEN G. & EGAN S. (1991). – A flexural-cantilever simple-shear/pure-shear model of continental lithosphere extension: applications to the Jeanne d'Arc basin, Grand Banks and Viking graben, North Sea. – *Geol. Soc. London Spec. Publ.*, **56**, 41.

LAVIER L. & STECKLER M. (1997). – The effect of sedimentary cover on the flexural strength of continental lithosphere. – *Nature*, **389**, 476-479.

LAVIER L. & MANATSCHAL G. (2006). – A mechanism to thin the continental lithosphere at magma-poor margins. – *Nature*, **440**, 324-328.

LAVIER L.L., BUCK W.R. & POLIAKOV A.N.B. (2000). – Factors controlling normal fault offset in an ideal brittle layer. – *J. Geophys. Res.* **105**, 431-423.

LE POURHIET L., BUROV E. & MORETTI I. (2004). – Rifting through a stack of inhomogeneous thrusts (the dipping pie concept). – *Tectonics*, **23** (4), TC4005, doi: 10.1029/2003TC001584.

LI Z. & GERYA T.V. (2009). – Polyphase formation and exhumation of HP-UHP rocks in continental subduction zone: Numerical modelling and application to the Sulu UHP terrane in eastern China. – *J. Geophys. Res*., **114**, B09406.

LI Z.H., GERYA T.V. & BURG J.-P. (2010). – Influence of tectonic overpressure on P-T paths of HP-UHP rocks in continental collision zones: thermomechanical modelling. – *J. Metam. Geol*., **28**(3), 227-247.

LI Z.H., XU Z.Q. & GERYA T.V. (2011). – Flat versus steep subduction: contrasting modes for the formation and exhumation of high- to ultrahigh-pressure rocks in continental collision zones. – *Earth Planet. Sci. Lett*., **301**, 65-77.

LISTER G., ETHERIDGE M. & SYMONDS P. (1986). – Detachment faulting and the evolution of passive continental margins. – *Geology* , **14**, 246-250.

LISTER G.S. & DAVIS G.A. (1989). – The origin of metamorphic core complexes and detachment faults formed during Tertiary continental extension in the northern Colorado river region, USA. – *J. Struct. Geol.,* **11**, 65-94.

LYELL C. (1865). – Elements of geology, 6th edition. – *John Murray*, London.

LYELL C. (1872). – Principles of geology, being an attempt to explain the former changes of the Earth's surface, by reference to causes now in operation, 11th edition. – *John Murray*, London.

MANATSCHAL G. (2004). – New models for evolution of magma-poor rifted margins based on a review of data and concepts from West Iberia and the Alps. – *Int. J. Earth Sci.*, **93**, 432-466.

MCKENZIE D. (1978). – Some remarks on the development of sedimentary basins. – *Earth Planet. Sci. Lett*., **40**, 25-32.

MACKWELL S.J., ZIMMERMAN M.E. & KOHLSTEDT D.L. (1998). – High-temperature deformation of dry diabase with applications to tectonics on Venus. – *J. Geophys. Res*., **103**, 975-984.

MEZRI L., WOLF S., LE POURHIET L. & BUROV E. (2013). – Impact of fluid-rock interactions and metamorphic reactions on rheological evolution and style of rifting during extension. – *Proceedings of XIII International Workshop on Modelling of Mantle and Lithosphere Dynamics* August 31-September 5, 2013, Hønefoss, p. 74.

MINEAR J.W. & TOKSÖZ M.N. (1970). – Thermal regime of a downgoing slab and new global tectonics. – *J. Geophys. Res*., **75**, 1397-1419.

MOHN G, MANATSCHAL G. & MASINI E. (2011). – Rift-related inheritance in orogens: a case study from the Austroalpine nappes in Central Alps (SE-Switzerland, N-Italy). – *Int. J. Earth Sciences*, **100**, (5), 937-961.

FACCENDA M., GERYA T.V. & BURLINI L. (2009). – Deep slab hydration induced by bending related variations in tectonic pressure. – *Nature*, Geosciences, **2**, 790-793.

POLIAKOV A.N.B., PODLADCHIKOV YU. & TALBOT C. (1993). – Initiation of salt diapirs with frictional overburden: numerical experiments. – *Tectonophysics*, **228**, 199-210.

PRECIGOUT J., GUEYDAN F., GAPAIS D., GARRIDO C. & ESSAIFI A. (2007). – Strain localisation in the subcontinental mantle: a ductile alternative to the brittle mantle. – *Tectonophysics*, **445**, 318-336.

PYSKLYWEC R.N. (2006). – Surface erosion control on the evolution of the deep lithosphere. – *Geology*, **269**, 34(4), 225-228.

PYSKLYWEC R., BEAUMONT C. & FULLSACK P. (2000). – modelling the behavior of the continental mantle lithosphere during plate convergence. – *Geology*, **28**, 655-658.

PYSKLYWEC R. N., BEAUMONT C. & FULLSACK P. (2002). – Lithospheric deformation during the early stages of continental collision: Numerical experiments and comparison with South Island, New Zealand. – *J. Geophys. Res*., **107** (B7), doi: 10.1029/2001JB000252.

SALVENSON J.O. (1978). – Variations in the geology of rift basins; a tectonic model. – *Conference Proceedings Los Alamos Scientific Laboratory*, **7487**, 82-86.

SCHMALHOLTZ S.M. (2008). – 3D numerical modelling of forward folding and reverse unfolding of a viscous single-layer: Implications for the formation of folds and fold patterns. – *Tectonophysics*, **446**, 31-41.

SEARLE M. (2013). – Crustal melting, ductile flow and deformation in mountain belts: Cause and effect relationships. – *Lithosphere*, doi: 10.1130/RF.L006.1

SEARLE M.P., ELLIOTT J.R., PHILLIPS R.J. & CHUNG S.L. (2011). – Crustal-lithospheric structure and continental extrusion of Tibet. – *J. Geol. Soc*., **168**, 633-672, doi: 10.1144/0016-76492010-139

SIZOVA E., GERYA T., BROWN M. & PERCHUK L.L. (2010). – Subduction styles in the Precambrian: Insight from numerical experiments. – *Lithos*, **116**, 209-229.

SIZOVA E., GERYA T. & BROW M. (2013). – Exhumation mechanisms of melt-bearing ultrahigh pressure crustal rocks during collision of spontaneously moving plates. – *J. Metam. Geol*., **30**, 9, 927-955.

SOBOUTI F. & ARKANI-HAMED J. (2002). – Thermo-mechanical modelling of subduction of continental lithosphere. – *Physics of the Earth and Planet. Interiors*, **131**, 185-203.

SPEAR F.S. (1993). – Metamorphic phase equilibria and pressure-temperature-time paths. – Mineralogical Society of America, 800 pp.

STEGMAN D.R., FARRINGTON R., CAPITANIO F.A. & SCHELLART W.P. (2010). – A regime diagram for subduction styles from 3D numerical models of free subduction. – *Tectonophysics*, **483**, 29-45.

STÖCKHERT B. & GERYA T.V. (2005). – Pre-collisional high-pressure metamorphism and nappe tectonics at active continental margins: a numerical simulation. – *Terra Nova*, **17** (2), 102-110.

TETSUZO S. & REHMAN H.U. (2011). – When and why the continental crust is subducted: Examples of Hindu Kush and Burma. – *Gondw. Res.*, **19**, 327-333.

TIREL C., BRUN J.-P. & BUROV E. (2008). – Dynamics and structural development of metamorphic core complexes. – *J. Geophys. Res*., **113**, doi: 10.1029/2005JB003694, 2008

TIREL C., BRUN J.-P., BUROV E. & LEBEDEV S. (2013). – Mechanics of continental accretion, slab rollback and high-pressure rock exhumation. – *Geology*, **41**, 5, 555-558.

TOMMASI A., KNOLL M., VAUCHEZ A., SIGNORELLI J.W., THORAVAL C. & LOGÉ R. (2009). – Structural reactivation in plate tectonics controlled by olivine crystal anisotropy. – *Nature*, Geoscience, **2**, doi: 10.1038/NGEO528

TORRANCE KE. & TURCOTTE D.L. (1971). – Thermal convection with large viscosity variations. – *J. Fluid Mechanics*, **47**, 113-125.

TOUSSAINT G., BUROV E. & JOLIVET L. (2004a). – Continental plate collision: unstable versus stable slab dynamics. – *Geology*, **32** (1), 33-36.

TOUSSAINT G., BUROV E. & AVOUAC J.-P. (2004b). – Tectonic evolution of a continental collision zone: a thermo mechanical numerical model. – *Tectonics*, **23**, TC6003, doi: 10.1029/2003TC001604

TURCOTTE D.L. & SCHUBERT G. (2002). – Geodynamics, applications of continuum physics to geological problems. – Cambridge Univ. Press, second ed., 456 pp.

VAN HUNEN J. & ALLEN M. (2011). – Continental collision and slab break-off: A comparison of 3-D numerical models with observations. – *Earth Planet. Sci. Lett.,* **302**, 1-2, 27-37.

WARREN C.J., BEAUMONT C. & JAMIESON R.A. (2008). – Modelling tectonic styles and ultra-high pressure (UHP) rock exhumation during the transition from oceanic subduction to continental collision. – *Earth Planet. Sci. Lett*., **267**, 129–145.

WATREMEZ L., BUROV E., D'ACREMONT E., LEROY S., HUET B., LE POURHIET L. & BELLAHSEN N. (2013). – Localising properties and buoyancy of cratonised mantle lithosphere: insights from thermo-mechanical models of the eastern Gulf of Aden. – *Geochem., Geophys., Geosyst.*, 10.1002/ggge.20179, ISSN: 15252027.

WATTS A.B. (2001). – Isostasy and flexure of the lithosphere. – Cambridge University Press, 458pp.

WATTS A.B. & BUROV E.B. (2003). – Lithospheric strength and its relationship to the elastic and seismogenic layer thickness. – *Earth Planet. Sci. Lett*., **213**, 113-131.

WHITE N.J. & MCKENZIE D.P. (1988). – Formation of the "steer's head" geometry of sedimentary basins by differential stretching of the crust and mantle. – *Geology*, **16**, 250-253.

WHITE R. & MCKENZIE D. (1989). – Magmatism at rift zones - the generation of volcanic continental margins and flood basalts. – *J. Geophys. Res.,* **94**, B6, 7685-7729

WILLETT S. (1999). – Orogeny and orography: The effects of erosion on the structure of mountain belts. – *J. Geophys. Res*., **104**, B12, 28957-28981.

WERNICKE B. (1985). – Uniform-sense normal simple shear of the continental lithosphere. – *Can. J. Earth Sci.*, **22**, 108-125.

YAMATO P., AGARD P., BUROV E., LE POURHIET L., JOLIVET L. & TIBERI C. (2007). – Burial and exhumation in a subduction wedge: Mutual constraints from thermo-mechanical modelling and natural p-t-t data (sch. Lustrés, W. Alps). – *J. Geophys. Res.*, **112**, B07410, doi: 10.1029/2006JB004441.

YAMATO P., BUROV E., AGARD P., LE POURHIET L. & JOLIVET L. (2008). – HP-UHP exhumation processes during continental subduction (W. Alps): when thermomechanical models reproduce P-T-t data. – *Earth Planet. Sci. Lett*., **271**, 63-75.

YAMATO P., MOUTHEREAU F. & BUROV E. (2009). – Taiwan mountain building: insights from 2D thermo-mechanical modelling of a rheologically-stratified lithosphere. – *Geophys. J. Int*., **176**, 307-326, doi: 10.1111/j.1365-246X.2008.03977.x.

ZHANG R.Y., LIOU J.G. & ERNST W.G. (2009). – The Dabie-Sulu continental collision zone: A comprehensive review. – *Gondwana Res.,* **16**, 1-26.

ZIEGLER P.A. (1988). – Evolution of the Arctic-North Atlantic and the western Tethys. – *Am. Assoc. Pet. Geol.* , **43**, 198 pp.

ZIEGLER P.A. & CLOETINGH S. (2004). – Dynamic processes controlling evolution of rifted basins. – *Earth-Sci. Rev.* , **64**, 1-50.

Tectonic record, magmatic history and hydrothermal alteration in the Hercynian Guérande leucogranite, Armorican Massif, France.

Ballouard C. *[1], Boulvais P. [1], Poujol M. [1], Gapais D. [1], Yamato P. [1], Tartèse R.[2], Cuney M.[3]

[1] UMR CNRS 6118, Géosciences Rennes, OSUR, Université, Rennes 1, 35042 Rennes Cedex, France
[2] Planetary and Space Sciences, The Open University, Walton Hall - Milton Keynes, MK7 6AA, UK
[3] GeoRessources UMR 7359, CREGU, Campus Sciences-Aiguillettes BP 70239, 54506 Vandoeuvre-lès-Nancy, France

*corresponding author. Tel : +33 223 23 30 81.
E mail adress: christophe.ballouard@univ-rennes1.fr

Key words: leucogranite petrogenesis, geochemistry, geochronology, structure, Hercynian, Armorican Massif

Abstract

The Guérande peraluminous leucogranite was emplaced in an extensive tectonic regime at the end of the Carboniferous in the southern part of the Armorican Massif. At the scale of the intrusion, this granite displays both petrographic and structural heterogeneities: the southern part, interpreted as the feeding zone, is characterized by a Ms-Bt bearing paragenesis, the presence of restites and migmatites enclaves, a low abundance of quartz veins compared to pegmatites and a weak deformation. In contrast, the northwestern part, interpreted as the apical zone of the intrusion, is characterized by Ms-Turm bearing paragenesis, evidence of albitization and gresenization, a larger amount of quartz veins and the occurrence of S/C and mylonitic fabrics.

During its emplacement, the syntectonic Guérande granite has probably experienced some partitioning of the deformation as shown by the occurrence of synchronous N-S and E-W stretching features both within the granite and in the country rocks. U-Th-Pb dating on zircon and monazite

revealed that the Guérande granite was emplaced 309.7 ± 1.9 Ma ago and that a late magmatic activity synchronous with hydrothermal circulation occurred ca. 304 Ma. Sr and Nd isotope compositions suggest that the granite was formed by the partial melting of metasedimentary formations. The magmatic history of the Guérande granite is controlled by fractional crystallization. The differentiation from the less to the more evolved samples can be explained by ~15 wt.% fractionation of an assemblage made of potassic feldspar, plagioclase, biotite and the accessory minerals found within it such as apatite, zircon, monazite and Fe-Ti oxide.

In addition to the localized hydrothermal activity recorded by quartz and pegmatite veins crosscutting the massif, the apex of the Guérande granite underwent a pervasive hydrothermal alteration revealed by a high enrichment in incompatible elements such as Cs, Sn, the decrease of geochemical ratios such as K/Rb, Nb/Ta and evidences of secondary muscovitization.

1. Introduction

Peraluminous leucogranites are widespread throughout orogenic belts especially those associated with continental collision (Barbarin, 1999). They formed mostly by partial melting of metasedimentary rocks buried at low crustal depths (Lefort et al., 1987; Puziewicz and Johannes, 1988; Patiño Douce and Johnston, 1991; Patiño Douce, 1999), while their exhumation within the crust is generally favored by crustal-scale faults or shear zones (Hutton, 1988; D'lemos et al., 1992; Collins and Sawyer, 1996; Searle, 1999). Peraluminous leucogranite or more generally S type granites (Chappell and White, 1974) can display geochemical heterogeneities from the sample scale to that of the magmatic chamber. These variations can reflect primary magmatic processes such as progressive partial melting, partial melting of heterogeneous metasedimentary sources (Deniel et al., 1987; Brown and Pressley, 1999), variable degree of entrainment of peritectic assemblage (Stevens et al., 2007; Clemens and Stevens, 2012), entrainment of unmelted restite (Chappell et al., 1987) or secondary processes such as magma mixing (Słaby and Martin, 2008), wall rock assimilation (Ugidos and Recio, 1993) and fractional crystallization (e.g. Tartèse and Boulvais, 2010).

During magma ascent and final crystallization at the emplacement site, magmatic fluids may exsolve from the melt and give rise to numerous pegmatite and quartz veins. Alteration induced by the

58 pervasive circulation of orthoderived fluids in the late stage of leucogranites evolution can induced
59 consequent element mobility (Dostal and Chatterjee, 1995; Förster et al., 1999; Tartèse and Boulvais,
60 2010).

61 In the Hercynian belt, peraluminous leucogranites are mostly Carboniferous in age (Bernard-Griffiths
62 et al., 1985; Lagarde et al., 1992). They are present throughout the belt in the Bohemian Massif (Förster
63 et al., 1999), in Cornwall (Willis-Richards and Jackson, 1989; Chen et al., 1993), in the Iberian Massif
64 (Capdevila et al., 1973) as well as in the French Armorican and Central Massifs (Lameyre et al., 1980; La
65 Roche et al., 1980; Bernard-Griffiths et al., 1985).

66 In the Armorican Massif, the peraluminous leucogranites are syntectonic (Cogné, 1966; Jégouzo,
67 1980) and mostly located in its southern part. They are closely associated with either strike slip
68 litospheric shear zones, the two branches of the South Armorican Shear Zone (Berthé et al., 1979;
69 Strong and Hanmer, 1981; Tartèse and Boulvais, 2010) or with extensional shear zones (Gapais, et al.,
70 1993 ; Turrillot et al., 2009).

71 The Guérande granite is one of these leucogranites and was emplaced during the Carboniferous
72 synconvergence extension of the internal zone of the Hercynian belt (Gapais et al, 1993). Because it is
73 well exposed along the coast, the Guérande granite represents a remarkable object that allows studying
74 the petrological and geochemical evolutions of a pluton from the roots to its apical zone where
75 numerous quartz veins occur, some of which being mineralized in Sn (Audren et al., 1975). The
76 Guérande granite thus offers a unique opportunity to characterize the internal differentiation of a
77 granitic pluton, and to study the relationships between crustal magmatism and (i) regional tectonics and
78 (ii) fluid driven alteration, in the heart of the Hercynian belt. The purpose of this paper is therefore to
79 address these different issues, based on new field descriptions and new petrological, geochemical and
80 geochronological data. These data are the first obtained on this strategic intrusion for the last thirty
81 years (Bouchez et al., 1981; Ouddou, 1984).

82

83 ## 2. Geological setting

84 ### *2.1. The South Armorican Massif*

85 The southern part of the Armorican Massif (Fig. 1) belongs to the internal zone of the Hercynian
86 orogenic belt of Western Europe. It is bounded to the north by the South Armorican Shear Zone (SASZ),
87 a lithospheric dextral strike-slip shear zone divided in two branches (Gumiaux et al., 2004). From top to
88 bottom, three main tectono-metamorphic units can be distinguished in the South Armorican domain
89 (Fig. 1):

90 - High Pressure-Low Temperature units, represented at the top by the blueschist klippes of the
91 Groix island and the Bois-de-Cené (1.4-1.8 GPa, 500-550°C, Bosse et al., 2002) and at the bottom
92 by the Vendée Porphyroid Nappe made of metamorphosed metavolcanics and black shales (0.8
93 Gpa, 350-400°C; Le Hébel et al., 2002). Ductile deformations, metamorphism and exhumation of
94 these units relate to early tectonic events, around 360 Ma (Le Hébel, 2002; Bosse et al., 2005).
95 - Intermediate units mostly made of micaschists affected by a Barrovian metamorphism from
96 greenschist to amphibolite facies conditions (Bossière, 1988; Triboulet and Audren, 1988;
97 Goujou, 1992)
98 - Lower units constituted by high grade metamorphic rocks comprising gneiss, granitoids and a
99 large amount of migmatites (0.8 Gpa, 700-750°C; Jones and Brown, 1990).

100 The Barrovian metamorphism developed during a major crustal thinning and extensional shearing
101 event that occurred during Upper Carboniferous, around 310 Ma (Gapais, et al., 1993; Burg et al., 1994;
102 Cagnard et al., 2004). Crustal extension was accompanied by exhumation and rapid cooling of
103 migmatites (Jones and Brown, 1990; Gapais et al., 1993). At a regional scale, the structural pattern can
104 be described as lower crustal, migmatites bearing, extensional domes, covered by micaschist units and
105 overlying HP-LT units that belonged to the upper brittle crust during upper Carboniferous extension.

106 Several leucogranites (Quiberon, Sarzeau, Guérande) are structurally located within the micaschists,
107 above migmatite bearing units and below the contact with the porphyroids (Fig. 1). These granites were
108 emplaced during the Upper Carboniferous extension (Gapais et al., 1993; Turrillot et al., 2009).

109 Several leucogranite intrusions are also found along the SASZ (Berthé et al., 1979) and present S/C
110 structures that indicate syn-cooling shearing (Gapais, 1989). Among them, the Questembert and Lizio
111 granites (Fig. 1), that have been dated at 316 ± 3 Ma (Tartèse et al., 2011b) and 316 ± 6 Ma (Tartèse et

al., 2011a) respectively, were formed by the partial melting of Upper Proterozoic metasediments, and shared a similar magmatic history, marked by the fractionation of feldspar and biotite together with the zircon and monazite grains included in biotite (Tartèse and Boulvais, 2010).

Some giant quartz veins are also located along the SASZ, in a network of vertical fractures orientated N160°. They have been interpreted as giant tension gashes and attest for crustal-scale fluid circulations during the exhumation of the lower crust and the concomitant regional strike slip deformation. These fluids originated from both lower crust exhumation and from downward meteoric circulation (Lemarchand et al., 2012).

2.2. Previous study on the Guérande granite

The Guérande leucogranite (Fig. 2 and 3), a ca. 1 km thick blade shaped structure dipping slightly northward (Vigneresse, 1983; Bouchez et al., 1981), was emplaced along an extensional deformation zone (Gapais et al., 1993). To the north, the granite presents an abrupt contact with micaschists and metavolcanics that recorded a contact metamorphism as demonstrated by the presence of staurolite and garnet (Valois, 1975). To the south, the contact is different and presents a progressive evolution with the Saint-Nazaire migmatites, which may represent the source of the Guérande granite (Bouchez et al., 1981). Several enclaves of micaschists are found within the granite and an anatectic isotropic sub-facies crosscuts its southwestern edge (Fig. 2 and 3). Within the granite, the fabric is generally weak, mostly magmatic, dips generally 20-30° northward and bears lineations of dip-slip type (Fig. 2). The southern part of the intrusion is also characterized by magmatic or migmatitic like fabrics. In contrast, S/C fabrics affect its northern edge (Bouchez et al., 1981). The occurrence of migmatites to the south, below the intrusion, and of micaschists to the north above it, underlines that the southern part corresponds to the base of the granite and the northern part to its roof (Bouchez et al., 1981). A fluid-inclusion study performed on quartz veins found near the roof of the Guérande granite reveals that it was probably emplaced at shallow depth (around 3 km; Le Hébel et al., 2007). The northwestern part of the granite is affected by an extensional graben (the so-called “Piriac synform”; Valois, 1975), where

138 rocks from the HP-LT upper unit (Vendée porphyroid unit) crop out (Fig. 3). This structure has been
139 interpreted as resulting from the collapse of the roof of the intrusion (Valois, 1975; Cathelineau, 1981).
140 Although its age is not well constrained yet, the Guérande granite was emplaced during the Upper
141 Carboniferous as demonstrated by two whole-rock Rb-Sr ages of 314 ± 5 Ma and 322 ± 5 Ma
142 (Cathelineau, pers. com.). In addition, muscovite $^{40}Ar/^{39}Ar$ data yielded younger dates of 307 ± 0.3 Ma
143 on an undeformed sample that could be interpreted as a cooling age and 304 ± 0.6 Ma on a mylonitized
144 sample which could represent the age of the deformation (Le Hébel, 2002). Le Hébel (2002) also
145 reported $^{40}Ar/^{39}Ar$ dates of 303.3 ± 0.5 Ma for a quartz vein intrusive within the Guérande granite and
146 303.6 ± 0.5 Ma for a sheared granite sample.
147
148 **3. Field description and sampling**
149 Since the Guérande granite is mainly covered by salt marsh (Fig. 2), the outcrops are limited to only
150 few inland quarries and to the available outcrops along the coastline. Overall, these coastal outcrops are
151 of good quality and are therefore suitable for the establishment of cross sections from the southern to
152 the northern parts of the intrusion.
153
154 *3.1. Petrographic zonation within the Guérande granite*
155 At the scale of the intrusion, the Guérande granite displays petrographic heterogeneities with
156 variable proportions of muscovite, biotite and tourmaline (Fig. 2). The southwestern part of the pluton is
157 characterized by a muscovite-biotite paragenesis (Fig. 4a) while the northwestern part is characterized
158 by a muscovite-tourmaline paragenesis (Fig. 4b). Moreover, numerous metric intrusions of isotropic
159 granite (I granite in Fig. 4c), as well as enclaves of restites and migmatites are present in the
160 southwestern part of the granite, while greisens and albitized rocks can be observed in the
161 northwestern part (Fig. 2). These observations are consistent with the zonation of the pluton, the
162 southern part corresponding to the feeding zone of the granite while the northwestern part
163 corresponds to the apical zone which typically concentrates the hydrothermal activity.
164 *3.2. Structures and dykes*

The central and southern parts of the intrusion display magmatic fabrics or roughly defined foliations (Fig. 4a and d) whereas S/C structures and mylonites (Fig. 4e) occur along the northern edge. This shows that strain localization occurred to the north, at the roof of the pluton.

A large amount of pegmatitic dykes (Fig. 4c) together with a few aplitic dykes and quartz veins (Fig. 4f) crosscut the Guérande granite. To the north, pegmatites are biotite-free and contain muscovite ± tourmaline while, to the south, the pegmatites are biotite-bearing. These differences in the pegmatite compositions mimic the petrographic heterogeneities previously described for the pluton (i.e., biotite is absent to the north and present to the south while tourmaline appears only in the northwestern part of the intrusion). The strike directions for these dykes and veins have been measured in three distinct areas. These measurements (180 in total) are reported in rose diagrams presented in Figure 5. In the northernmost area (Piriac) located close to the roof of the intrusion and associated, in part, with the mylonitized granite (Fig. 4e), the pegmatites contain Qtz-Fsp-Ms. The number of quartz veins is significant but lower than the number of pegmatites (Fig. 5a). The strike of the dykes and veins in this zone is mostly oriented N110°-N140° and is nearly perpendicular to the lineation recorded in the granite. Further to the south, close to La Turballe, pegmatitic dykes contain a Qtz-Fsp-Ms±Turm assemblage. The proportion of pegmatites dykes over quartz veins (Fig. 5b) is comparable to that in Piriac. In this area, dykes are mainly orientated N160°-N170° and are slightly oblique to the granite lineation. In the southernmost area (Le Croisic), pegmatites dykes contain Qtz-Fsp-Ms±Bt and appear in a greater proportion than quartz veins (Fig. 5c). Dykes in this zone strike dominantly N000°-N020°, i.e. roughly parallel to the granite lineation. In most parts of the intrusion, the dykes and veins record an E-W stretching, which is different from that recorded by the granite itself, although a significant scattering of the lineations is observed (Fig. 2).

This rather puzzling kinematic pattern is further recorded by other features. Along the coast, at the roof of the granite, dip-slip type lineations (Fig. 5d) associated with top to the north S/C fabrics are observed. However, the adjacent country-rocks also show evidence of E-W stretching, with outcrop-scale tilted blocks and rocks affected by contact metamorphism bearing E-W elongated patches of retrogressed cordierite (Fig. 5e).

From the local occurrence of S/C fabrics and contact metamorphism indicators attesting for potentially coeval N-S and E-W motions, we must consider the possibility that extension in the area resulted in subhorizontal flattening strains, with local partitioning of dominant extension directions. At a more regional scale, Gapais et al. (1993) showed that the extension direction was variable to the north of the Guérande area, from E-W to N-S, according to the local orientation of the foliation, the stretching lineations associated with the extension tending to show dominant dip-slip attitudes. Field evidences do not support successive deformation events for these variable local kinematics. It has been previously argued that extension in south Brittany was coeval with dextral wrenching along the South Armorican Shear Zone (Gumiaux et al., 2004). A combination of regional EW extension and WNW-SSE strike-slip shearing might have contributed to the observed local scattering of extension directions (Gapais et al., submitted). Another additionnal working hypothesis could be a tendency of the brittle upper crust to record chocolate-tablet type strains (Ramsay and Huber, 1983) induced by a regional vertical shortening, which could constrain the partitioning of the kinematics in the underlying ductile middle crust (Gapais et al. submitted). Further arguments would require a detailed analysis of brittle strain patterns within the upper HP-LT units.

3.3. Sampling and samples

A sampling strategy was developed in order to take into account the petrographic variability observed in the field at the scale of the intrusion. For this purpose, we targeted all the inland ancient quarries in addition to the outcrops available along the coast. A total of 21 samples were collected.

All the samples contain a Qtz-Kfs-Pl-Ms assemblage (Fig. 6a) with a variable amount of Bt and Turm. Quartz is usually anhedral, frequently forms polycrystalline cluster (Fig. 6b) and often displays undulose extinction characteristic of intracrystalline deformation. The alkali feldspar is generally anhedral and sometimes displays Carlsbad twining and rare string-shaped sodic perthitic exsolutions. The plagioclase is anhedral to sub-euhedral, shows polysynthetic twinning and is sometimes associated with myrmekites. Muscovite is generally euhedral, flake shaped and is also found with a fish-like habit (Ms I in Fig. 6c). Fine-grained secondary muscovite can be abundant in some facies. It developed as sericite

219 inclusion in feldspar, as small grains around coarse primary muscovite or within foliation planes (Ms II in
220 Fig. 6c). Biotite is brown, sub-euhedral to euhedral and often appears as intergrowth within muscovite
221 flakes (Fig. 6b). Biotite hosts most of the accessory minerals such as apatite, Fe-Ti oxide, zircon and
222 monazite (Fig. 6a).

223 The 21 samples have been divided into five different groups, based on their respective petrographic
224 characteristics (see Table 1, and sample location on Fig. 2):

225 (1) The root facies is characteristic of the southwestern part of the pluton (root zone) and includes
226 both highly evolved diatexites marked by a roughly defined foliation (Fig. 4a and d) and
227 intrusions of isotropic granites (Fig. 4c). The grain size is fine to medium (1-3mm) and
228 muscovite is usually more abundant than biotite. The root facies contains numerous accessory
229 minerals (Fe-Ti oxide, apatite, zircon and monazite) (Fig. 6a). Small garnet grains have been
230 observed in the sample GUE-17 (Table 1).

231 (2) The Ms-Bt coarse to medium grained granite (3-5 mm) represents the most common facies in
232 the massif. The muscovite is usually coarse (> 1 mm) and is more abundant than biotite (<1
233 mm, Fig. 6b). Fine secondary muscovite (< 1 mm) is sometimes observed inside the foliation.

234 (3) The Ms-Turm coarse to medium grained granite (3-5 mm) is only found in the northwestern
235 part of the intrusion (apex, Fig. 2). Tourmaline (<5%) is usually plurimillimetric, green brown in
236 color, presents coarse cracks and hosts inclusions of quartz and feldspar. Fine secondary
237 muscovite (<1mm) is abundant in this facies (Fig. 6c) where it occurs inside fabric planes or
238 around coarse primary muscovite flakes (>1mm). Biotite is rare and, most of the time, appears
239 as inclusions inside primary muscovite crystals (Fig. 6c).

240 (4) The Ms-Bt fine grained granite (0.5-2 mm) has been mainly observed locally near La Turballe
241 and in the northeastern extremity of the intrusion. Ouddou (1984) has reported some
242 occurrences of this facies in the eastern and the southwestern parts. Bouchez et al (1981)
243 interpreted this facies as kilometer thick dykes (Fig. 3), but the existence of mingling features at
244 the contact between this fine grained facies and the coarse to medium grain granites suggest

245 that they are contemporaneous (Ouddou, 1984). In this granite, perthitic orthoclase is common
246 and muscovite is more abundant than biotite. This facies contains numerous monazite grains.
247 (5) Granitic meter-thick dykes have been sampled in different locations within the intrusion. They
248 usually show similar mineralogical and textural features, and often display an aplitic texture
249 (Table 1).
250
251 Chloritization, albitization and greisenization have been observed at different locations in the
252 Guérande massif (Table 1 and Fig. 2). Chloritization of biotite is visible at the microscopic scale and is
253 localized in the northern central part of the granite (Fig. 2). The chlorite often hosts small (< 50 μm)
254 highly pleochroic anhedral grains, likely anatase. Albitization is linked to shear zones and results in a
255 greater proportion of albite relative to quartz and micas. Garnet is present in the albitized sample GUE-
256 19a (Table 1). Meter-scale greisenization has been observed and both albitization and greisenization are
257 restricted to the northwestern part of the Guérande granite (Fig. 2).
258
259 **4. Analytical techniques**
260 *4.1. Mineral compositions*
261 Mineral compositions were measured using a Cameca SX-100 electron microprobe at IFREMER,
262 Plouzané, France. Operating conditions were a 15 kV acceleration voltage, a beam current of 20 nA and
263 a beam diameter of 5 μm. Counting times were approximately 13–14 s. For a complete description of
264 the analytical procedure and the list of the standards used, see Pitra et al. (2008).
265 *4.2. Major and trace elements analyses*
266 Large samples (5 to 10 kg) were crushed following a standard protocol to obtain adequate powder
267 fractions using agate mortars. Chemical analyses were performed by the Service d'Analyse des Roches
268 et des Minéraux (SARM; CRPG-CNRS, Nancy, France) using ICP-AES for major elements and ICP-MS for
269 trace elements following the techniques described in Carignan et al. (2001)
270 *4.3. Isotopic analyses*

Sm-Nd and Sr isotopic values were determined on crushed whole rock samples. All the analyses were carried out at the Géosciences Rennes Laboratory using a 7 collectors Finnigan MAT-262 mass spectrometer. Samples were spiked with a ^{149}Sm-^{150}Nd and ^{84}Sr mixed solution and dissolved in HF-HNO_3. They were then dried and taken up with concentrated HCl. In each analytical session, the unknowns were analyzed together with the Ames Nd-1 Nd or the NBS-987 Sr standards, which during the course of this study yielded an average of 0.511956 (± 5) and 0.710275 (± 10) respectively. All the analyses of the unknowns have been adjusted to the long-term value of $^{143}Nd/^{144}Nd$ value of 0.511963 for Ames Nd-1 and reported $^{87}Sr/^{86}Sr$ values were normalized to the reference value of 0.710250 for NBS-987. Mass fractionation was monitored and corrected using the value $^{146}Nd/^{144}Nd = 0.7219$ and $^{88}Sr/^{86}Sr = 8.3752$. Procedural blanks analyses yielded values of 400 pg for Sr and 50 pg for Nd and are considered to be negligible.

4.4. U-Th-Pb

A classic mineral separation procedure has been applied to concentrate minerals suitable for U-Th-Pb dating using the facilities available at Géosciences Rennes. Rocks were crushed and only the powder fraction with a diameter < 250 µm has been kept. Heavy minerals were successively concentrated by Wilfley table and heavy liquids. Magnetic minerals were then removed with an isodynamic Frantz separator. Zircon and monazite grains were carefully handpicked under a binocular microscope and embedded in epoxy mounts. The grains were then hand-grounded and polished on a lap wheel with a 6 µm and 1 µm diamond suspension successively. Zircon grains were imaged by cathodoluminescence (CL) using a Reliotron CL system equipped with a digital color camera available in Géosciences Rennes, while monazite grains were imaged using the EPMA facility in IFREMER, Brest.

U-Th-Pb geochronology of zircon and monazite was conducted by in-situ laser ablation inductively coupled plasma mass spectrometry (LA-ICPMS) at Géosciences Rennes using a ESI NWR193UC excimer laser coupled to a quadripole Agilent 7700x ICP-MS equipped with a dual pumping system to enhance sensitivity. The instrumental conditions are reported in Table 2.

The ablated material is carried into helium, and then mixed with nitrogen and argon, before injection into the plasma source. The alignment of the instrument and mass calibration was performed

298 before each analytical session using the NIST SRM 612 reference glass, by inspecting the ^{238}U signal and
299 by minimizing the ThO+/Th+ ratio (<0.5%). During the course of an analysis, the signals of ^{204}(Pb+Hg),
300 ^{206}Pb, ^{207}Pb, ^{208}Pb and ^{238}U masses are acquired. The occurrence of common Pb in the sample can be
301 monitored by the evolution of the ^{204}(Pb+Hg) signal intensity, but no common Pb correction was applied
302 owing to the large isobaric interference with Hg. The ^{235}U signal is calculated from ^{238}U on the basis of
303 the ratio $^{238}U/^{235}U$=137.88. Single analyses consisted of 20 s of background integration followed by 60 s
304 integration with the laser firing and then a 30 s delay to wash out the previous sample. Ablation spot
305 diameters of 26-44 µm and 20 µm with repetition rates of 3-5 Hz and 1-2 Hz were used for zircon and
306 monazite, respectively. Data were corrected for U–Pb and Th–Pb fractionation and for the mass bias by
307 standard bracketing with repeated measurements of the GJ-1 zircon (Jackson et al., 2004) or the Moacir
308 monazite standards (Gasquet et al., 2010). Repeated analyses of 91500 (1061 ± 3 Ma (n=20);
309 (Wiedenbeck et al., 1995) or Manangoutry monazite (554 ± 3 Ma (n=20); Paquette and Tiepolo, 2007)
310 standards treated as unknowns were used to control the reproducibility and accuracy of the corrections.
311 Data reduction was carried out with the GLITTER® software package developed by the Macquarie
312 Research Ltd. (Jackson et al., 2004). Concordia ages and diagrams were generated using Isoplot/Ex
313 (Ludwig, 2001). All errors given in Supplementary Table 1 and 2 are listed at one sigma, but where data
314 are combined for regression analysis or to calculate weighted means, the final results are provided with
315 95% confidence limits.

316 ## 5. Mineralogical composition

317 Five samples from the Guérande granite representative of the different petrographic varieties have
318 been selected for chemical analyses on feldspar, biotite and muscovite. These are two Ms-Bt coarse to
319 medium grained granite (GUE-3 and GUE-8), one Ms-Turm coarse to medium grained granite (GUE-1),
320 one Ms-Bt fine grained granite (GUE-4) and one granitic dyke (GUE-5).

321

322 ### *5.1. Feldspar and biotite (Supplementary Table 3)*

323 Plagioclase chemical compositions display a well-defined trend in the Ab-An-Or ternary diagram (Fig.
324 7a). The calcium content of plagioclase decreases from the Ms-Bt fine-grained granite (GUE-4; An = 0.09)

to the Ms-Turm coarse to medium grained granite (GUE-1; An = 0.02), while the Ms-Bt coarse to medium grained granites and the dyke display intermediate contents (An = 0.07-0.05). In alkali feldspar, the potassium content slightly increases from the Ms-Bt fine grained granite (GUE-4; Or = 0.90) to the Ms-Turm coarse to medium grained granite (GUE-1; Or = 0.93). Again, the Ms-Bt coarse to medium grained granites and the dyke show intermediate composition (Or=0.91-0.93).

Biotite displays typical chemical composition for peraluminous granites with an elevated content in Al (Al_{TOT}>3.5 pfu; Nachit et al., 1985) and X_{Mg} = 0.27 - 0.28. GUE-3 displays a lower Mg content (X_{Mg} = 0.22).

5.2. Muscovite (Supplementary Table 4)

Muscovite grains in the Ms-Bt fine grained granite (GUE-4) and the granitic dyke (GUE-5) fall in the primary muscovite field defined by Miller et al. (1981) and display homogenous Mg content (Fig. 7b). The Mg content of the muscovite grains increases in the other samples and the secondary affinity of muscovite tends to increase from the Ms-Bt coarse to medium grained granites (GUE-3 and 8) to the Ms-Turm coarse to medium grained granite (GUE-1, Fig. 7b). In these samples, several grains of coarse muscovite display heterogeneous Mg contents: the cores are poorer in Mg and belong to the primary muscovite field while their rims are richer in Mg and fall in the secondary muscovite field (Fig. 7b). Regarding the small muscovite grains present in the magmatic foliation, they all plot in the secondary field, revealing a hydrothermal affinity comparable to the rims of the coarse muscovite grains. This is consistent with the petrographic descriptions where these two types of muscovite have already been identified (Fig. 6c).

6. Whole rock geochemistry

6.1. Major elements (Table 3)

The chemical diagram of Hughes (1973) is useful to identify magmatic rocks that have undergone metasomatism, which may have been responsible for the loss of their initial igneous composition. In this

352 diagram (Fig. 8a), three samples fall outside or at the limit of the field for igneous rocks. These are the
353 two samples from the aplite dyke GUE-19a and GUE-19b and a Ms-Turm coarse to medium grained
354 granite (sample GUE-21). The chemical mineralogical Q-P diagram (Debon and Le Fort, 1988) is useful to
355 evidence the mineralogical changes linked to chemical composition modification in igneous rocks
356 because it is sensible to the proportion of quartz (Q parameter) and to the proportion of alkali feldspar
357 relative to plagioclase (P parameter). In this diagram (Fig. 8b), samples GUE-19a and GUE-19b display a
358 trend characteristic of an albitic alteration where albitization and dequartzification are associated with
359 the neoformation of albite. Samples GUE-2 and 20 display a weak albitization. Concerning the GUE-21
360 sample, it displays dequartzification associated with the neoformation of alkaline feldspar. These results
361 are consistent with field and petrographic descriptions, which indicate that albitization affected samples
362 GUE-19 and GUE-2 while greisens were observed in the vicinity of sample GUE-21 (Fig. 2 and Table 1).
363 According to the Hughes and Q-P diagram (Fig. 8 a and b), the Guérande granite samples can be
364 separated into two groups: the unaltered samples, which display igneous compositions and the altered
365 samples GUE-19 and GUE-21 showing evidences of hydrothermal alteration.

366 Similarly to some neighboring granites such as the Questembert and Lizio granites (Tartèse and
367 Boulvais, 2010), all the unaltered samples from the Guérande granite display a peraluminous affinity in
368 the A/NK vs A/CNK diagram (Fig. 8c). However, the altered sample GUE-19a shows A/CNK and A/NK
369 values close to 1, which is typical for an albitized granite (Boulvais et al., 2007) and reflects the
370 disappearance of muscovite during albitization.

371 As shown in Figure 9a, unaltered samples display high SiO_2 contents ranging from 71.6 wt.% (GUE-
372 15) to 75.3 wt.% (GUE-20). The altered sample GUE-21 yields a low SiO_2 content of 69.8 wt.% while
373 albitized samples show high SiO_2 contents of 73.5 to 74.4 wt.%. Most of the major elements for the
374 unaltered samples display fairly well defined evolution trends with increasing SiO_2, i.e., K_2O, CaO and
375 Fe_2O_3+MgO+TiO_2 contents decreasing whereas Na_2O content increases. Conversely, the altered samples
376 rarely follow these trends (Fig. 9a).

377 *6.2. Trace elements (Table 3)*

While some incompatible trace elements such as Rb, Cs, W, U or Sn are not correlated with SiO_2, several other trace elements from the unaltered samples display well-defined evolution trends and show large variations against SiO_2. Sr and Ba mimic the trends defined by K_2O, CaO and Fe_2O_3+MgO+TiO_2: their contents decrease while the SiO_2 content increases, suggesting alkali feldspar, plagioclase and biotite fractionation either as restite in the source during partial melting or as crystallization products removed from the melts (Fig. 9a). Zr, Th and La are also inversely correlated with SiO_2 and they decrease respectively from 81 to 13 ppm, 9.2 to 0.3 ppm and 19.1 to 1.3 ppm (Fig. 9a). Zr correlates well with Fe_2O_3+TiO_2+MgO while a very good correlation exists between Zr, Th and La (Fig. 9b) suggesting a similar magmatic history involving zircon, monazite and biotite. This is consistent with petrographic descriptions as zircon and monazite were mainly observed as inclusions within biotite. Among altered samples, GUE-21 does not follow the general trend provided by the unaltered samples in the Harker diagrams reported in function of SiO_2 (Fig. 9a). Nevertheless, sample GUE-21 is indistinguishable from unaltered samples in the diagrams involving Zr, La and Th (Fig. 9b). Samples GUE-19a and GUE-19b plot at the lower extremity of these trends (Fig. 9b). GUE-19a, 19b and 20 are highly enriched in Be compare to the other samples (Be>120ppm).

The REE patterns obtained on the unaltered samples are somewhat variable (Fig. 10), show high fractionation ($(La/Lu)_N$ =10.8-28) and display either positive or negative Eu anomalies (Eu/Eu*=0.7-1.2), the largest positive anomaly being recorded by dyke sample GUE-5. These spectra are similar to those obtained for the other Armorican Massif leucogranites (Bernard-Griffiths et al., 1985; Tartèse and Boulvais, 2010). The aplite dyke GUE-20 is remarkable because of its large depletion in REE. Concerning the altered samples, GUE-19a and GUE-19b show REE patterns similar to the ones from the aplite dyke GUE-20. Sample GUE-21 displays a REE spectrum comparable with the other unaltered samples suggesting that the REE distribution in this sample was not affected during fluid-rock interaction.

The evolution of some of the geochemical tracers sensible to the interaction with fluids is reported in Figure 11a with respect to the distance to the northwestern edge of the Guerande granite, identified as the apical zone of the intrusion. In the apical zone, the Cs and Sn contents increase by about one order of magnitude, from around 10 ppm to 100 ppm for both elements. This behavior is the same for

Rb, which increases from 200 to 450 ppm. Also, samples from the Guérande granite display fractionation of the Nb/Ta ratios from about 6-8 down to about 2-4 in the apical zone, similarly to the hydrothermal alteration trends identified in the nearby Questembert granite (Tartèse and Boulvais, 2010). Taking the Cs content as a qualitative tracer for increasing fluid-rock alteration (Fig. 11b), the Sn contents show a very well-correlated evolution, while the Nb/Ta ratios are rather anti-correlated with the Cs contents. Both trends are defined by unaltered and altered samples.

7. Radiogenic isotopes: Rb-Sr and Sm-Nd.

Sr and Sm-Nd isotope analyses for some of the samples from the Guérande granite are reported in Table 4 and Figure 12. Initial $^{87}Sr/^{86}Sr$ (I_{Sr}) and εNd(T) values have been recalculated for an age of 310 Ma (see part 8). I_{Sr} values are high and vary from 0.7148 to 0.7197 while εNd(T) varies from -7.8 to -9.0. T_{DM} values are old (1642-1736 Ma) and reflect an important crustal recycling. In the εNd(T) vs I_{Sr} diagram (Fig. 12), a regional trend is defined by the Rostrenen, Pontivy, Lizio, Questembert and Guérande peraluminous granites: εNd(T) values decrease while I_{Sr} increases. This evolution may indicate an increase of crustal recycling going southward in the southern part of the Armorican Massif as already noticed by Bernard-Griffiths et al. (1985).

8. Geochronology

Sample GUE-3, a Ms-Bt coarse to medium grain granite collected in the northwestern part of the intrusion (Fig. 2), provided both zircon and monazite grains. Nineteen zircon grains with a total of 36 analyses were measured (Supplementary Table 1). The zircon population was characterized by translucent colorless euhedral to sub-euhedral grains. Cathodoluminescence imaging reveals the presence of inherited cores surrounded by zoned rims for most of the grains (Fig. 13a). They plot in a concordant to discordant position (Fig. 14a). As expected from the CL imaging, they yield apparent $^{207}Pb/^{206}Pb$ ages ranging from 2604 ± 18 Ma down to 307 ± 27 Ma demonstrating the presence of heterogeneous inherited material. Because most of the data are not concordant, it is impossible to discuss individual group of ages but basically two main periods of inheritance can be seen with a few

Late Archean-Proterozoic and numerous Paleozoic cores (youngest apparent $^{207}Pb/^{206}Pb$ age of 341 ± 27 Ma). This spread of ages is well known in the leucogranites from the Armorican Massif (see for example Tartese et al., 2011 a) and is in a good agreement with the proposed metasedimentary source for this granite. A group of nine concordant to sub-concordant analyses allow to calculate a mean $^{206}Pb/^{238}U$ date of 309 ± 2.6 Ma (MSWD=1.0). The remaining 5 data (dashed line on Fig. 14a) plot in a sub-concordant to discordant position and can be best explained by the presence of initial common Pb together with a complex Pb loss.

Sixteen monazite grains have been analyzed (Supplementary Table 2). In a $^{206}Pb/^{238}U$ vs. $^{208}Pb/^{232}Th$ concordia diagram, they plot in a concordant to sub-concordant position (Fig 14b). All sixteen analyses yield a mean $^{206}Pb/^{238}U$ date of 311.3 ± 2.2 Ma (MSWD=0.5) while the fifteen most concordant analyses allow to calculate an equivalent (within error) concordia date of 309.7 ± 1.9 Ma (MSWD=3.1).

Within the same facies (ie. Ms-Bt coarse to medium grain granite), a large zircon grain found in sample GUE-8 was analyzed. It displays well-defined magmatic zoning without any evidence of inherited core (Fig. 13b). Eight analyses were performed and allow to calculate a poorly constrained concordia date of 309.3 ± 6.1 Ma (MSWD=11) for the 6 most concordant points (not shown in this paper).

All these dates (309 ± 2.6 Ma: Zrn GUE-3; 309.3 ± 6.1 Ma: Zrn GUE-8; 309.7 ± 1.9 Ma: Mnz GUE-3) are equivalent within error. Therefore, we conclude that this granite was emplaced 309.7 ± 1.9 Ma ago.

The third sample, GUE-4, is a Ms-Bt fine grain granite that was collected within the La Turballe quarry (Fig. 2). This sample also provided zircon and monazite grains. All the zircon grains were characterized by the presence of core and rim. Unfortunately, all the analyses performed on the zircon rims were perturbated by a large amount of common Pb together with variable degrees of Pb loss. Furthermore these zircon grains yielded uranium contents up to 20,000 ppm. Therefore, no ages could be calculated from these zircon grains.

Forty-one analyses out of 12 monazite grains were performed. The monazite grains are rather large (up to 300 micrometer), euhedral, and characterized by a Th distribution from heterogeneous (patchy) to nicely zoned (Fig. 13c) with a systematic Th enrichment around the edges of the grains. Independently from where the spot analyses were located, all the acquired data are fairly consistent

458 and plot in a concordant to sub-concordant position in a $^{206}Pb/^{238}U$ vs. $^{208}Pb/^{232}Th$ concordia diagram
459 (Fig. 14c). Thirty-two concordant analyses allow to calculate a concordia date of 309.7 ± 1.3 Ma
460 (MSWD=13) which is equivalent within error with a mean $^{206}Pb/^{238}U$ date of 310.9 ± 1.4 Ma (n=37;
461 MSWD=0.5). We interpret this date of 310.9 ± 1.4 Ma as the emplacement age for this fine grain granite.
462 This age is therefore identical, within error, to the age of 309.7 ± 1.9 Ma found for the coarse to medium
463 grain granites (see above) and is consistent with the field observation of Ouddou (1984) which revealed
464 mingling features at the contact between these two facies attesting for their synchronous emplacement
465 Finally, sample GUE-5 corresponds to a dyke intrusive into GUE-4. It provided abundant zircon and
466 monazite grains. Here again, all the zircon grains display cores and rims and all of them but one were
467 common-Pb rich and affected by variable degree of Pb loss. The only zircon that was not common-Pb
468 rich (Fig. 13d) yields a concordia date of 299.6 ± 5.4 Ma (MSWD =0.79) for the two analyses performed
469 in the rim.
470 Twenty-three analyses out of sixteen grains were realized.They all plot in a concordant to sub-
471 concordant position in $^{206}Pb/^{238}U$ vs. $^{208}Pb/^{232}Th$ concordia diagram (Fig. 14d). The 18 most concordant
472 points yield a concordia date of 302.5 ± 1.6 Ma (MSWD=3.5), equivalent within error with a mean
473 $^{206}Pb/^{238}U$ date of 303.7 ± 1.7 Ma (MSWD=0.9) computed for all the analyses. These dates of 302.5 ± 1.6
474 and 303.7 ± 1.7 Ma are equivalent within error with the concordia date obtained on the zircon grain at
475 299.6 ± 5.4 Ma. We therefore conclude that this dyke was emplaced 303.7 ± 1.7 Ma ago.
476 To conclude, our data show two separate events, although they are close in time. First, the
477 Guérande leucogranite was emplaced ca. 310 Ma (309.7 ± 1.9 Ma: GUE-3; 310.9 ± 1.4 Ma: GUE-4). As
478 the Guérande granite displays S/C and mylonitic structures in the northern part of the intrusion, this age
479 of ca. 310 Ma also constrain the age of the extensive tectonic event. This age compares well to one the
480 two Rb/Sr whole-rock age of 314 ± 5 Ma but is younger than the other at 322 ± 5 Ma (Cathelineau, pers.
481 com). It is indeed quite frequent that the Rb/Sr ages obtained on the Armorican Massif leucogranites are
482 older than the real emplacement ages (see Tartese et al., 2011a and references therein).

Le Hébel (2002) published an Ar-Ar age of 307 ± 0.3 Ma on muscovite for the undeformed granite. This Ar-Ar age is slightly younger than our younger U-Pb age and could therefore be interpreted as a cooling age.

The second event corresponds to the emplacement age of the dyke GUE-5 at 303.7 ± 1.7 Ma. This age is directly comparable to the muscovite Ar-Ar age of 303.3 ± 0.5 Ma obtained for an intrusive quartz vein (Le Hébel, 2002). This demonstrates that magmatism and hydrothermal activity were synchronous ca 304 Ma ago. But this age of ca. 304 Ma is also identical within error with muscovite Ar-Ar ages of 303.6 ± 0.5 Ma obtained on sheared granite and 304 ± 0.5 Ma on a mylonitic granite (Le Hébel, 2002). At this stage, two hypotheses can be proposed: (1) a second phase of deformation took place ca. 304 Ma ago or (2) fluids responsible for the quarz veins emplacement circulated in these then permeable deformed zones and lead to recrystallization or neocrystallization of muscovite. This second hypothesis is conceivable because secondary muscovitisation process seem important in the Guérande massif (Fig. 7). Yet, we do not know where these samples were collected exactly nor the composition of the muscovite grains analyzed by Le Hébel (2002). This is why it is impossible at this stage to choose between these two hypotheses.

9. Discussion

9.1. Magmatism

9.1.1. Source

The high peraluminous index (Fig. 8c), the high I_{Sr} ratio the low εNd(T) values (Fig. 12) of the samples, together with the presence of inherited cores, with variable apparent ages, within the dated zircon grains (Fig. 13 and 14) suggest a metasedimentary source for the Guérande granite. The value of I_{Sr} and εNd(T) plot at the transition between the fields defined for the Brioverian and the Paleozoic sediments (Michard et al., 1985; Dabard et al., 1996; Fig. 12). This observation as well as the presence of inherited cores within the zircon grains with apparent ages ranging from the Archean-Proterozoic to the Paleozoic suggest that both Brioverian and Paleozoic sedimentary formations may have been sampled during partial melting.

Along a transect roughly perpendicular to the South Armorican Shear Zone, the Guérande granite together with the others, mostly contemporaneous, syntectonic granites yield a peculiar evolution in the I_{Sr} vs εNd(T) diagram (Fig. 1 and 12). Indeed, from roughly north to south, the I_{Sr} values increase while the εNd(T) decrease from the Rostrenen (316 ± 3 Ma, U-Pb zircon; Euzen, 1993), Pontivy (344 ± 8 Ma, Rb-Sr whole rock isochron; Bernard-Griffiths et al., 1985; 311 ± 2 Ma, $^{40}Ar/^{39}Ar$ muscovite; Cosca et al., 2011), Lizio (316 ± 6 Ma, U-Pb zircon; Tartèse et al., 2011a), Questembert (316 ± 3 Ma, U-Pb zircon; Tartèse et al., 2011b) to the Guérande granite (309.7 ± 1.9 Ma, U-Pb zircon and monazite; this study). We can propose three hypotheses at two different spatial scales to account for this trend:

(1) The Lizio, Questembert and Guérande granites have a pure metasedimentary source (Fig. 12). Consequently, the N-S trend displayed by these three granites in Figure 12 could be explained by a mixing between two metasedimentary end-members. To the north, the source of the peraluminous granites is almost exclusively constituted by the Brioverian sediments while, going south, the proportion of Paleozoic sediments, characterized by older model ages, increases. This would be consistent with the fact that, the further south the granites are located, the further away they are from the Cadomian domain, i.e. from the source for the Brioverian sediments (Dabard et al., 1996), that are well expressed in the northern part of the Armorican Massif.

(2) Comparing the Rostrenen-Pontivy granites to the Lizio-Questembert-Guérande granites in Figure 12, the εNd(T) and I_{Sr} values of some of the samples from the Rostrenen and Pontivy granites suggest a mantellic contribution (two points with positive εNd(T) values). This hypothesis is supported by the fact that granitoids of mantellic affinity have been described in the Rostrenen massif (Plélauff monzodiorite; Euzen, 1993). We could tentatively link the mantle influence in the Rostrenen and Pontivy granites to the thickness of the continental crust, which decreased from south to north at the end of the Carboniferous in Southern Brittany: the crust was very thick below the Guérande and the Questembert massifs because these granites were emplaced close to the core of the Hercynian belt while the crust was thinner below the Lizio-Pontivy granites and almost not thickened at all below the Rostrenen massif (Ballèvre et al., 2009). To the south of the South Armorican Shear Zone, the important thickness of the crust

could have prevented a mantellic underplated magma to reach the upper crustal level, while such a process might have been possible to the north.

(3) Another hypothesis to explain the low I_{Sr} and the high εNd(T) found for the northernmost granites (Peucat et al., 1988) could be the contribution of juvenile components from the St-Georges-sur-Loire synclinorium, located a few tens of kilometers to the east of the Questembert region, and interpreted by some authors as the trace of an early Devonian back-arc basin (Ballèvre et al., 2009 and references therein).

These three hypotheses are not individually exclusive and could have all contributed to the southward evolution of the granitic sources during the Carboniferous evolution of the Hercynian belt in the region.

9.1.2. Differentiation process

In the Harker diagrams (Fig. 9), several major and trace elements display well defined correlations when plotted against SiO_2. These chemical variations could reflect a number of processes such as the melting of heterogeneous sources combined with variable entrainment of peritectic assemblages and accessory minerals in the melt (Stevens et al., 2007; Clemens and Stevens, 2012), a variable degree of partial melting, a variation in the amount of mineral-melt segregation during differentiation (Tartèse and Boulvais, 2010; Yamato et al., 2012) or a coalescence of several magma batches issued from different sources followed by differentiation of these melts (Deniel et al., 1987; Le Fort et al., 1987). For the Guérande granite, we think that a process of fractional crystallization implying the segregation of feldspar and biotite hosting accessory minerals is the main process behind the observed chemical variations. First, despite the fact that we cannot exclude source heterogeneities, the similar εNd and the low variation of I_{Sr} for the samples (Fig. 12) suggest a derivation from a relatively homogeneous melt. Second, the Guérande leucogranite samples display geochemical characteristics comparable to that of the liquids produced during experimental melting of metasediments (Vielzeuf and Holloway, 1988; Patiño Douce and Johnston, 1991; Montel and Vielzeuf, 1997), with low content of ferromagnesian and CaO (Fe_2O_3+MgO+TiO_2 < 2%; CaO < 1%), suggesting that they are close to anatectic melts (Patiño Douce,

1999) and that the amount of peritectic or restitic minerals entrained from the source is negligeable. Moreover, the K_2O content of the Guérande samples is correlated with the sum Fe_2O_3+MgO+TiO_2, as both parameters decrease with SiO_2 (Fig. 9a), which is the opposite behavior expected for a process of entrainment of peritectic garnet (Stevens et al., 2007; Clemens and Stevens, 2012). Third, two main observations based on trace elements behavior are in favor of a fractional crystallization process:

(1) The Ba and Sr contents, two elements compatible in biotite and feldspar, decrease largely with SiO_2 (Fig. 9a). Such variations in compatible elements (212 to 75 ppm for Sr and 411 to 133 ppm for Ba from GUE-15 to GUE-1) are very difficult to explain with a simple partial melting process. In fact, by modeling the process of "partial or batch melting" (details in Janoušek et al., 1997) using $D(Sr)^{res/liq}$= 4.4 for a pure plagioclase and $D(Ba)^{res/liq}$= 6.36 for a pure biotite (Hanson, 1978), unrealistic variation of rates of melting from 0 to about 80% are required to match the measured contents in Ba and Sr. On the other hand, such important variations in compatible elements can be easily explained by a fractional crystallization process involving a few tenths of a percent of mineral fractionation (Hanson, 1978).

(2) In Figure 9b, the excellent correlation between Zr and La reveals a common process between zircon (which hosts Zr) and monazite (which hosts La), while the good correlation between Zr and Fe_2O_3+Mgo+TiO_2, which both display the same overall range of variation (factor of 4 between 80 and 20ppm for Zr and factor 4 between 1.6 and 0.4 wt.% for Fe_2O_3+Mgo+TiO_2), indicates that zircon and biotite shared a common magmatic history. In thin sections, zircon and monazite are mostly observed as inclusions within biotite, which suggests that the common magmatic process which controls the distribution of Zr and La is the fractional crystallization of zircon and monazite-bearing biotite.

9.1.3. Fractional crystallization modeling

The inverse correlation between Fe_2O_3+MgO+TiO_2 and SiO_2 is consistent with the fractionation of biotite, while the depletions in CaO and K_2O in the SiO_2-rich samples are consistent with the fractionation of plagioclase and potassic feldspar respectively (Fig. 9). Here, we propose a quantification

591 of the amount of minerals that were segregated from the melt during the process of fractional
592 crystallization, first by using major elements and then by using trace elements hosted by the main rock
593 forming minerals. The aplitic sample GUE-20 has been removed from these calculations because it
594 displays a much more evolved composition than the other samples, which is difficult to model solely by
595 fractional crystallization processes. Some of the characteristics of this sample may indeed be attributed
596 to the interaction with a fluid phase (discrete albitization as seen in the Q-P diagram (Fig. 8b) and
597 enrichment in Be (Table 3).
598
599 *9.1.3.1. Major elements*
600 In Figures 15a and 15b, the whole rock compositions of the unaltered samples from the Guérande
601 granite are plotted in Harker diagrams together with the theoretical composition of an An20 plagioclase
602 and the average composition of biotite and potassic feldspar from the most primitive sample (GUE-4)
603 out of all the samples where chemical analyses of minerals have been carried out. In these diagrams, the
604 prolongation of the trends displayed by the granite samples allows to calculate the mineralogical
605 composition of the segregate assemblage (see Tartèse and Boulvais, 2010 for details about the
606 calculation), which yield an assemblage composed by 40-55 wt.% Kfs + 20-40 wt.% Bt + 5-40 wt.% An20.
607 Independently, we used the "inverse major" plugin included in the GCD Kit software (Janoušek et al.,
608 2006) to calculate the amount and the mineralogical composition of the segregated cumulate required
609 to produce the chemical composition of the more evolved sample GUE-12 from the composition of the
610 less evolved sample GUE-15. The results obtained with this modeling (Table 5) are consistent with those
611 obtained with the first method and the differences between the calculated and the actual compositions
612 are small as indicated by a ΣR^2 (sum of the squared residuals) of 0.16. This modeling also implies that
613 apatite had a non-negligible contribution to the fractionating assemblage, as shown by the modal
614 composition of the calculated segregate assemblage that contains 45 wt.% Kfs + 21 wt.% Bt + 31 wt.%
615 An20 + 4 wt.% Ap. Such amount of apatite is rather high but it allows for a good reproduction of the CaO
616 behavior. The P_2O_5 behavior is not well reproduced, as already noticed by Tartèse and Boulvais (2010),
617 and could perhaps be attributed to the mobility of P_2O_5 in deuteric systems (Kontak et al., 1996). The

618 calculated amount of fractional crystallization in this model is 13 wt.%. These results are similar to those
619 obtained for the Lizio and Questembert granites by Tartèse and Boulvais (2010), who estimated that the
620 high SiO_2 samples from the Questembert granite could have derived from magmas similar to the low
621 SiO_2 samples of the Lizio granite if a fractionation of 16 wt.% of an assemblage composed of 51 wt.% Kfs
622 + 22 wt.% Bt + 27 wt.% Pl occurred.
623
624 *9.1.3.2. Trace elements*
625 Ba is a compatible element in biotite and potassic feldspar while Sr is compatible in plagioclase and
626 apatite. In Figure 15c, the whole rock composition of the unaltered Guérande granite samples are
627 plotted in a Ba versus Sr diagram, with two theoretical models of evolution for the Ba and Sr contents
628 for a variable amount of fractional crystallization of the assemblage 0.45 Kfs + 0.21 Bt + 0.31 Pl + 0.04
629 Ap. The two models have been calculated using the Rayleigh distillation-type fractional crystallization for
630 two different ranges of Kd displayed in the table in Figure 15c. The two calculated trends reproduce
631 quite well the trend defined by the Guérande granite samples and the calculated amount of
632 crystallization between 10 and 30% is consistent with the previous amount of fractionate (13 wt.%)
633 calculated using the major elements. Sample GUE-2 displays higher degrees of mineral-melt
634 segregation, but as noticed previously, this sample underwent a weak albitization (Table 1). Therefore,
635 its Sr and Ba contents could have been modified during this hydrothermal process. Regarding other
636 trace elements whose behavior are controlled by accessory minerals (Th, Zr, REE), an example of
637 modeling developed by Tartèse and Boulvais (2010) showed that even a minute fraction of mineral
638 fractionation can account for the content variations actually measured in the rocks. Such a modeling is
639 not reproduced here and the interested readers are invited to refer to these authors.
640
641 *9.2. Hydrothermal history*
642 Several evidences for fluid -rock interactions have been observed in the Guérande granite:

643 (1) Numerous pegmatitic and quartz veins crosscut the granite. These veins recorded localized
644 magmato-hydrothermal activity contemporaneous with the deformation recorded in the
645 intrusion, and therefore with its emplacement.
646 (2) The presence of tourmaline in the samples localized near the apical zone of the intrusion (Fig. 2
647 and 4b) indicates that they crystallized from a magma highly enriched in volatiles, either through
648 magmatic differentiation or by interaction with the enclosing micaschists.
649 (3) Greisens and albitized rocks have been described in the northwestern part of this intrusion (Fig.
650 2 and 8b). Greisenization generally occurs during the interaction with hot magmatic fluids (400-
651 600°C; Jébrak and Marcoux, 2008) while albitization can be related to the interaction with fluids
652 of variable origins, either magmatic (Lee and Parsons, 1997) or post-magmatic (Boulvais et al.,
653 2007). Here, the facts that these albitized rocks are concentrated near the apical zone of the
654 intrusion and are spatially associated with greisenization, (i.e., a magmato-hydrothermal
655 process where albitization is complementary; Schwartz and Surjono, 1990), suggest that both
656 alterations resulted from the interaction with high temperature fluids of magmatic origin at the
657 apex of the Guérande granitic body. Figure 8a allows to discriminate samples which have lost
658 their igneous compositions during such a hydrothermal alteration. Among them, the albitized
659 dyke samples GUE-19a and GUE-19b (Fig. 8b) display textural similarities with the aplitic dyke
660 GUE-20 (Table 1) suggesting that they share the same aplitic origin. This hypothesis is supported
661 by the fact that samples GUE-20, GUE-19a and 19b display similar REE patterns (Fig. 10). Also,
662 these three samples are enriched in Be, an independent feature related to the interaction with a
663 fluid phase.
664 (4) In Figure 11a, some samples (mostly the Ms-Turm bearing ones) display a strong increase in
665 their Cs and Sn contents, up to one order of magnitude, towards the apical zone of the granite
666 where cassiterite (SnO_2) occurs in quartz veins (Audren et al., 1975). In Figure 11b, Cs and Sn are
667 very well correlated; this trend could be interpreted as reflecting the magmatic behavior of Sn
668 and Cs, two highly incompatible elements, during fractional crystallization. Nevertheless, the
669 increase in the Cs content from 5 (GUE-17) to 77 ppm (GUE-1), for example, would imply an

unrealistic amount of fractional crystallization (more than 90 %) even if we consider that Cs displays a purely incompatible behavior. The high Cs and Sn contents therefore rather reflect an enrichment in samples that interacted with magmatic fluids where Sn and Cs were strongly concentrated (e.g., Förster et al., 1999).

(5) K/Rb values for the Guérande granite samples range from 243 down to 71, with values for the Ms-Turm bearing samples always below 150. Such values below 150 are characteristic of the pegmatite-hydrothermal evolution of Shaw (1968).

(6) The ratios of twin elements like Nb/Ta may be fractionated during magmato-hydrothermal processes either by muscovite and biotite fractionation (Stepanov et al., 2014) or by fluid-rock interaction (Dostal and Chatterjee, 2000). Here, the Nb/Ta ratio decreases below a value of 5 toward the apical zone (Fig. 11a) and is anti-correlated with Cs (Fig. 11b), likely indicating that the decrease of the Nb/Ta ratios marks the interaction with late magmatic fluids, as noticed by Tartèse and Boulvais (2010) for the most evolved samples from the Questembert granite.

(7) Chemical analyses of muscovite grains (Fig. 7b) reveal that a secondary muscovitization process occurred in the Guérande granite. This phenomenon increases from the Ms-Bt to the Ms-Turm bearing samples and seems to be correlated with the decrease of the Nb/Ta ratios and the increase of the Cs and Sn contents. These observations suggest that secondary muscovitization could also be related to an interaction with late magmatic fluids.

To sum up, the Guérande granite experienced both localized and pervasive magmato-hydrothermal activity. Localized fluid circulation is recorded at the scale of the intrusion by the presence of numerous quartz and pegmatitic veins while the pervasive hydrothermal interaction was prevalent at the apical zone of the pluton. Hydrothermal activity occurred at the time of pluton emplacement at ca. 310 Ma but also later as revealed by the muscovite Ar-Ar age at 303.3 ± 0.5 Ma obtained on an intrusive quartz vein (le Hébel, 2002).

10. Conclusion

696 This study provides new constraints on the tectonic and magmatic history of the Guérande
697 peraluminous leucogranite and allows to shed some light on the mobility of elements during
698 hydrothermal activity. These new structural and petro-geochemical data lead to the following
699 conclusions:

700 (1) Structural and petrographic observations throughout the intrusion indicate that the southern
701 part of the Guérande granite represent the feeding zone while its northwestern part
702 corresponds to the apical zone.

703 (2) The Guérande granite was emplaced in an extensive tectonic regime and probably underwent a
704 partitioning of the deformation during its cooling. Indeed, the strike of quartz veins and
705 pegmatitic dykes and the lineations directions measured within the massif suggest that both N-S
706 and E-W stretching occurred synchronously in this area.

707 (3) U-Th-Pb dating on zircon and monazite reveal that the Guérande granite was emplaced 309.7 ±
708 1.9 Ma ago and that a late magmatic activity synchronous with hydrothermal circulation
709 occurred ca. 304 Ma ago.

710 (4) Sr and Nd isotope data suggest that the Guérande granite formed by the partial melting of
711 metasedimentary formations. When compared to others syntectonic peraluminous granites
712 from both the central and southern part of the Armorican Massif, from north to south, the
713 increase of I_{Sr} and the decrease of εNd could be explained by sedimentary sources becoming
714 gradually dominated by Paleozoic sediments relative to Brioverian sediments, combined with a
715 mantellic contribution limited to the central Armorican Massif.

716 (5) The magmatic history of the Guérande granite is controlled by fractional crystallization where an
717 amount of ~15% of fractionation of an assemblage composed of Kfs + Pl + Bt (±Ap ± Zrn ± Mnz ±
718 Fe-Ti oxyde) can explain the chemical variations observed between the samples.

719 (6) The apex of the Guérande leucogranite experienced pervasive hydrothermal alteration which
720 induced an enrichment in incompatible elements such as Sn and Cs, secondary muscovitisation
721 and the decrease of geochemical ratio such as K/Rb and Nb/Ta in the samples. The fluid-rock
722 interaction documented here likely provides some key information on the U and Sn

mineralization geometrically associated with the Guérande intrusion. Actually, a specific study on this subject is timely and could now be undertaken provided that our knowledge of the magmatic and hydrothermal history of the Guérande granite is improved.

Acknowledgements

This study is based on the work carried out by C. Ballouard for his Master's degree and was supported by the 2012 and 2013 NEEDS-CNRS (AREVA - CEA) grants to M. Poujol. Rémi Sarrazin helped during field work. The authors want to thank D. Vilbert (Géosciences Rennes) and J. Langlade (IFREMER, Brest) for their contributions during the radiogenic isotopes and the electron microprobe analyses respectively.

References

Audren, C., Jegouzo, P., Barbaroux, L., Bouysse, P., 1975. La Roche-Bernard, 449. Bureau de Recherches Géologiques et Minières.

Ballèvre, M., Bosse, V., Ducassou, C., Pitra, P., 2009. Palaeozoic history of the Armorican Massif: Models for the tectonic evolution of the suture zones. Comptes Rendus Geosci. 341, 174–201.

Barbarin, B., 1999. A review of the relationships between granitoid types, their origins and their geodynamic environments. Lithos 46, 605–626.

Bernard-Griffiths, J., Peucat, J.J., Sheppard, S., Vidal, P., 1985. Petrogenesis of Hercynian leucogranites from the southern Armorican Massif: contribution of REE and isotopic (Sr, Nd, Pb and O) geochemical data to the study of source rock characteristics and ages. Earth Planet. Sci. Lett. 74, 235–250.

Berthé, D., Choukroune, P., Jegouzo, P., 1979. Orthogneiss, mylonite and non coaxial deformation of granites: the example of the South Armorican Shear Zone. J. Struct. Geol. 1, 31–42.

Bosse, V., Ballevre, M., Vidal, O., 2002. Ductile Thrusting Recorded by the Garnet Isograd from Blueschist-Facies Metapelites of the Ile de Groix, Armorican Massif, France. J. Petrol. 43, 485–510.

Bosse, V., Féraud, G., Ballèvre, M., Peucat, J.-J., Corsini, M., 2005. Rb–Sr and $^{40}Ar/^{39}Ar$ ages in blueschists from the Ile de Groix (Armorican Massif, France): Implications for closure mechanisms in isotopic systems. Chem. Geol. 220, 21–45.

Bossière, G., 1988. Evolutions chimico-minéralogiques du grenat et de la muscovite au voisinage de l'isograde biotite-staurotide dans un métamorphisme prograde de type barrovien: un exemple en Vendée littorale (Massif Armoricain). C.R. Acad. Sc., Paris, série II, 306 , 135-140.

Bouchez, J., Guillet, P., Chevalier, F., 1981. Structures d'écoulement liées à la mise en place du granite de Guérande (Loire-Atlantique, France). Bull. Soc. Géol. France, XXIII-4 , 387-399.

Boulvais, P., Ruffet, G., Cornichet, J., Mermet, M., 2007. Cretaceous albitization and dequartzification of Hercynian peraluminous granite in the Salvezines Massif (French Pyrénées). Lithos 93, 89–106.

Brown, M., Pressley, R.A., 1999. Crustal melting in nature: Prosecuting source processes. Phys. Chem. Earth Part Solid Earth Geod. 24, 305–316.

Burg, J.P., Van Den Driessche, J., Brun, J.P., 1994. Syn-to post thickening extension in the Variscan Belt of western Europe: modes and structural consequences. Géol. Fr. 3, 33–51.

Cagnard, F., Gapais, D., Brun, J.P., Gumiaux, C., Van den Driessche, J., 2004. Late pervasive crustal-scale extension in the south Armorican Hercynian belt (Vendée, France). J. Struct. Geol. 26, 435–449.

Capdevila, R., Corretgé, G., Floor, P., 1973. Les granitoides Varisques de la Meseta Ibérique. Bull. de la Soc. Géol. France, XV-3-4 , 209-228.

766 Carignan, J., Hild, P., Mevelle, G., Morel, J., Yeghicheyan, D., 2001. Routine Analyses of Trace Elements in
767 Geological Samples using Flow Injection and Low Pressure On-Line Liquid Chromatography Coupled to
768 ICP-MS: A Study of Geochemical Reference Materials BR, DR-N, UB-N, AN-G and GH. Geostand. Newsl. 25,
769 187–198.
770 Cathelineau, M., 1981. Les Gisements Uraniferes de la Presqu'ile Guerandaise (Sud Bretagne); Approche
771 Structurale et Metallogenique. Miner. Deposita 16, 227–240.
772 Chantraine, J., Autran, A., Cavelier, C., 2003. Carte géologique de la france à l'échelle du millionième, 6ème édition.
773 Bureau de Recherches Géologiques et Minières.
774 Chappell, B., and White, A., 1974. Two contrasting granite types. Pac. Geol. 8 , 173-174.
775 Chappell, B.W., White, A.J.R., Wyborn, D., 1987. The Importance of Residual Source Material (Restite) in Granite
776 Petrogenesis. J. Petrol. 28, 1111–1138.
777 Chen, Y., Clark, A.H., Farrar, E., Wasteneys, H.A.H.P., Hodgson, M.J., Bromley, A.V., 1993. Diachronous and
778 independent histories of plutonism and mineralization in the Cornubian Batholith, southwest England. J.
779 Geol. Soc. 150, 1183–1191.
780 Clemens, J.D., Stevens, G., 2012. What controls chemical variation in granitic magmas? Lithos 134–135, 317–329.
781 Cogné, J., 1966. Les grands cisaillement hercyniens dans le Massif Armoricain et les phénomènes de granitisation.
782 Etages tectoniques. Ed. de la Braconière , 179-192.
783 Collins, W.J., Sawyer, E.W., 1996. Pervasive granitoid magma transfer through the lower–middle crust during non-
784 coaxial compressional deformation. J. Metamorph. Geol. 14, 565–579.
785 Cosca, M., Stunitz, H., Bourgeix, A.L., Lee, J.P., 2011. 40Ar* loss in experimentally deformed muscovite and biotite
786 with implications for $^{40}Ar/^{39}Ar$ geochronology of naturally deformed rocks. Geochim. Cosmochim. Acta 75,
787 7759–7778.
788 Dabard, M.P., Loi, A., Peucat, J.J., 1996. Zircon typology combined with Sm-Nd whole-rock isotope analysis to study
789 Brioverian sediments from the Armorican Massif. Sediment. Geol. 101, 243–260.
790 Debon, F., Le Fort, P., 1988. A cationic classification of common plutonic rocks and their magmatic associations:
791 principles, method, applications. Bull. minéralogie, vol. 111, n°5 , 493-510.
792 Deniel, C., Vidal, P., Fernandez, A., Fort, P.L., Peucat, J.J., 1987. Isotopic study of the Manaslu granite (Himalaya,
793 Nepal): inferences on the age and source of Himalayan leucogranites. Contrib. Mineral. Petrol. 96, 78–92.
794 D'lemos, R.S., Brown, M., Strachan, R.A., 1992. Granite magma generation, ascent and emplacement within a
795 transpressional orogen. J. Geol. Soc. 149, 487–490.
796 Dostal, J., Chatterjee, A.K., 1995. Origin of topaz-bearing and related peraluminous granites of the Late Devonian
797 Davis Lake pluton, Nova Scotia, Canada: crystal versus fluid fractionation. Chem. Geol. 123, 67–88.
798 Dostal, J., Chatterjee, A.K., 2000. Contrasting behaviour of Nb/Ta and Zr/Hf ratios in a peraluminous granitic pluton
799 (Nova Scotia, Canada). Chem. Geol. 163, 207–218.
800 Euzen, T., 1993. Pétrogenèse des granites de collision post-épaississement. Le cas des granites crustaux et
801 mantelliques du complexe de Pontivy-Rostrenen (Massif Armoricain, France). Memoires Géosciences
802 Rennes, 51 , 360p.
803 Evensen, N.M., Hamilton, P.J., O'Nions, R.K., 1978. Rare-earth abundances in chondritic meteorites. Geochim.
804 Cosmochim. Acta 42, 1199–1212.
805 Förster, H.-J., Tischendorf, G., Trumbull, R.B., Gottesmann, B., 1999. Late-Collisional Granites in the Variscan.
806 Erzgebirge, Germany. J. Petrol. 40, 1613–1645.
807 Gasquet, D., Bertrand, J.-M., Paquette, J.-L., Lehmann, J., Ratzov, G., Guedes, R.D.A., Tiepolo, M., Boullier, A.-M.,
808 Scaillet, S., Nomade, S., 2010. Miocene to Messinian deformation and hydrothermal activity in a pre-
809 Alpine basement massif of the French western Alps: new U-Th-Pb and argon ages from the Lauzière
810 massif. Bull. Soc. Geol. Fr. 181, 227–241.
811 Gapais, D., 1989. Shear structures within deformed granites: Mechanical and thermal indicators. Geology 17,
812 1144–1147.
813 Gapais, D., Lagarde, J.L., Le Corre, C., Audren, C., Jegouzo P., Casas Sainz, A., Van Den Driessche, J., 1993. La zone
814 de cisaillement de Quiberon: témoin d'extension de la chaine varisque en Bretagne méridionale au
815 Carbonifère. C.R. Acad. Sc., Paris, série II, 316, 1123-1129.
816 Gapais, D., Brun, J.P., Gumiaux, C., Cagnard, F., Ruffet, G., Le Carlier de Veslud, C. Extensional tectonics in the
817 Hercynian Armorican belt (France). An overview. Bull. Soc. Geol. Fr. submitted.
818 Goujou, J.C., 1992. Analyse pétro-structurale dans un avant-pays métamorphique: influence du plutonisme tardi-
819 orogénique varisque sur l'encaissant épi à mésozonal de Vendée. Document du Bureau de Recherche
820 Géologique et Minière, 216.
821 Gumiaux, C., 2003. Modelisation du cisaillement hercynien de Bretagne Centrale: deformation crustale et
822 implications litosphériques. Thèse, Université de Rennes 1, 266p.

Gumiaux, C., Gapais, D., Brun, J.P., Chantraine, J., Ruffet, G., 2004. Tectonic history of the Hercynian Armorican Shear belt (Brittany, France). Geodin. Acta 17, 289–307.
Hanson, G.N., 1978. The application of trace elements to the petrogenesis of igneous rocks of granitic composition. Earth Planet. Sci. Lett. 38, 26–43.
Hassenforder, B., Cogné, J., Barbaroux, L., Ottman, F., Berthois, L., 1973. Saint-Nazaire, 479. Bureau de Recherches Géologiques et Minières.
Hughes, C.J., 1973. Spilites, keratophyres, and the igneous spectrum. Geol. Mag. 109, 513–527.
Hutton, D.H.W., 1988. Granite emplacement mechanisms and tectonic controls: inferences from deformation studies. Earth Environ. Sci. Trans. R. Soc. Edinb. 79, 245–255.
Icenhower, J., London, D., 1995. An experimental study of element partitioning among biotite, muscovite, and coexisting peraluminous silicic melt at 200 MPa (H_2O). Am. Mineral. 80, 1229–1251.
Icenhower, J., London, D., 1996. Experimental partitioning of Rb, Cs, Sr, and Ba between alkali feldspar and peraluminous melt. Am. Mineral. 81, 719–734.
Jackson, N.J., Willis-Richards, J., Manning, D.A.C., Sams, M.S., 1989. Evolution of the Cornubian ore field, Southwest England; Part II, Mineral deposits and ore-forming processes. Econ. Geol. 84, 1101–1133.
Jackson, S.E., Pearson, N.J., Griffin, W.L., Belousova, E.A., 2004. The application of laser ablation-inductively coupled plasma-mass spectrometry to in situ U–Pb zircon geochronology. Chem. Geol. 211, 47–69.
Janoušek, V., Rogers, G., Bowes, D.R., Vaòková, V., 1997. Cryptic trace-element variation as an indicator of reverse zoning in a granitic pluton: the Ricany granite, Czech Republic. J. Geol. Soc. 154, 807–815.
Janoušek, V., Farrow, C.M., Erban, V., 2006. Interpretation of Whole-rock Geochemical Data in Igneous Geochemistry: Introducing Geochemical Data Toolkit (GCDkit). J. Petrol. 47, 1255–1259.
Jébrak, M., Marcoux, É., 2008. Géologie des Ressources Minérales. Ministère des ressources naturelles et de la faune.
Jégouzo, P., 1980. The South Armorican Shear Zone. J. Struct. Geol. 2, 39–47.
Jones, K.A., Brown, M., 1990. High-temperature “clockwise”P-T paths and melting in the development of regional migmatites: an example from southern Brittany, France. J. Metamorph. Geol. 8, 551–578.
Kontak, D.J., Martin, R.F., Richard, L., 1996. Patterns of phosphorus enrichment in alkali feldspar, South Mountain Batholith, Nova Scotia, Canada. Eur. J. Mineral. 8, 805–824.
Kretz, R., 1983. Symbols for rock-forming minerals. Am. Mineral. 68, 277–279.
Lagarde, J.L., Capdevila, R., Fourcade, S., 1992. Granites et collision continentale; l’exemple des granitoides carboniferes dans la chaine hercynienne ouest-europeenne. Bull. Soc. Géol. France 163, 597–610.
Lameyre, J., 1980. Les magmas granitiques: leurs comportements, leurs associations et leurs sources. Mém. hors-série Soc. Géol. France 10, 51–62.
La Roche, H., Sussi, J., Chauris, L., 1980. Les granites à deux micas hercyniens français. Sciences de la Terre, 24 , 5-121.
Lee, M.R., Parsons, I., 1997. Dislocation formation and albitization in alkali feldspars from the Shap Granite. Am. Mineral. 82, 557–570.
Le Fort P., Cuney M., Deniel C., France-Lanord C., Shepard S.M.F., Upreti B.N., Vidal P., 1987. Crustal generation of the Himalayan leucogranites. Tectonophysics, 134, 39-57.
Le Hébel, F., 2002. Déformation continentale et histoire des fluides au cours d'un cycle subduction, exhumation, extension. Exemple des porphyroïdes Sud-Armoricains. Thèse, Université de Rennes 1, 218p.
Le Hébel, F., Vidal, O., Kienast, J.-R., Gapais, D., 2002. Les « Porphyroïdes » de Bretagne méridionale : une unité de HP–BT dans la chaîne hercynienne. Comptes Rendus Geosci. 334, 205–211.
Le Hébel, F., Fourcade, S., Boiron, M.-C., Cathelineau, M., Capdevila, R., Gapais, D., 2007. Fluid history during deep burial and exhumation of oil-bearing volcanics, Hercynian Belt of southern Brittany, France. Am. J. Sci. 307, 1096–1125.
Lemarchand, J., Boulvais, P., Gaboriau, M., Boiron, M.-C., Tartèse, R., Cokkinos, M., Bonnet, S., Jégouzo, P., 2012. Giant quartz vein formation and high-elevation meteoric fluid infiltration into the South Armorican Shear Zone: geological, fluid inclusion and stable isotope evidence. J. Geol. Soc. 169, 17–27.
Liew, T.C., Hofmann, A.W., 1988. Precambrian crustal components, plutonic associations, plate environment of the Hercynian Fold Belt of central Europe: Indications from a Nd and Sr isotopic study. Contrib. Mineral. Petrol. 98, 129–138.
Ludwig, K. R., 2001. Isoplot/Ex version 2.49. A geochronological toolkit for Microsoft Excel. Berkeley Geochronology Center, Special Publication 1a , 1-55.
Michard, A., Gurriet, P., Soudant, M., Albarede, F., 1985. Nd isotopes in French Phanerozoic shales: external vs. internal aspects of crustal evolution. Geochim. Cosmochim. Acta 49, 601–610.
Miller, C.F., Stoddard, E.F., Bradfish, L.J., Dollase, W.A., 1981. Composition of plutonic muscovite; genetic implications. Can. Mineral. 19, 25–34.

Montel, J.-M., Vielzeuf, D., 1997. Partial melting of metagreywackes, Part II. Compositions of minerals and melts. Contrib. Mineral. Petrol. 128, 176–196.
Nachit, H., Razafimahefa, N., J.M., S., Carron, J., 1985. Composition chimique des biotites et typologie magmatique des granitoïdes. C.R. Acad. Sc., Paris, série II, 301, 813-818.
Ouddou, D., 1984. Le Massif de Guérande-Le Croisic (Loire-Atlantique): Caractérisation géochimique et minéralogique de l'évolution magmatique. Comportement de l'uranium. Thèse, INPL-CREGU Nancy, 309p.
Paquette, J.L., Tiepolo, M., 2007. High resolution (5 µm) U–Th–Pb isotope dating of monazite with excimer laser ablation (ELA)-ICPMS. Chem. Geol. 240, 222–237.
Patiño Douce, A.E., Johnston, A.D., 1991. Phase equilibria and melt productivity in the pelitic system: implications for the origin of peraluminous granitoids and aluminous granulites. Contrib. Mineral. Petrol. 107, 202–218.
Patiño Douce, A.E., 1999. What do experiments tell us about the relative contributions of crust and mantle to the origin of granitic magmas? Geol. Soc. Lond. Spec. Publ. 168, 55–75.
Peucat, J., Charlot, R., Mifdal, A., J., C., Autran, A., 1979. Définition géochronologique de la phase bretonne en Bretagne centrale, étude Rb-Sr de granites en domaine Centre-Armoricain. Bull. BRGM (2) I4 , 349-356.
Peucat, J.J., Jegouzo, P., Vidal, P., Bernard-Griffiths, J., 1988. Continental crust formation seen through the Sr and Nd isotope systematics of S-type granites in the Hercynian belt of western France. Earth Planet. Sci. Lett. 88, 60–68.
Pitra, P., Boulvais, P., Antonoff, V., Diot, H., 2008. Wagnerite in a cordierite-gedrite gneiss: Witness of long-term fluid-rock interaction in the continental crust (Ile d'Yeu, Armorican Massif, France). Am. Mineral. 93, 315–326.
Proust, J., Guennoc, P., Thinon, I., Menier, D., 2009. Carte géologique de la France à 1/250 000 de la marge continentale : Lorient, Bretagne Sud. Bureau de Recherches Géologiques et Minières; Centre National de La Recherche Scientifique.
Prowatke, S., Klemme, S., 2006. Trace element partitioning between apatite and silicate melts. Geochim. Cosmochim. Acta 70, 4513–4527.
Puziewicz, J., Johannes, W., 1988. Phase equilibria and compositions of Fe-Mg-Al minerals and melts in water-saturated peraluminous granitic systems. Contrib. Mineral. Petrol. 100, 156–168.
Ramsay, J. G., Huber, M. I., 1983. Strain analysis, The techniques of modern structural geology, Vol. 1. Strain Analysis (London: Academic Press).
Ren, M., Parker, D.F., White, J.C., 2003. Partitioning of Sr, Ba, Rb, Y, and LREE between plagioclase and peraluminous silicic magma. Am. Mineral. 88, 1091–1103.
Schwartz, M.O., Surjono, 1990. Greisenization and albitization at the Tikus tin-tungsten deposit, Belitung, Indonesia. Econ. Geol. 85, 691–713.
Searle, M.P., 1999. Emplacement of Himalayan leucogranites by magma injection along giant sill complexes: examples from the Cho Oyu, Gyachung Kang and Everest leucogranites (Nepal Himalaya). J. Asian Earth Sci. 17, 773–783.
Shand, S., 1943. Eruptive rocks. Their genesis, composition, classification, and their relations to ore-deposits. Wiley, New York, 2, 444.
Shaw, D., 1968. A review of K-Rb fractionation trends by covariance analysis. Geochim. Cosmochim. Acta 32, 573–601.
Słaby, E., Martin, H., 2008. Mafic and Felsic Magma Interaction in Granites: the Hercynian Karkonosze Pluton (Sudetes, Bohemian Massif). J. Petrol. 49, 353–391.
Stepanov, A., Mavrogenes, J.A., Meffre, S., Davidson, P., 2014. The key role of mica during igneous concentration of tantalum. Contrib. Mineral. Petrol. 167, 1–8.
Stevens, G., Villaros, A., Moyen, J.-F., 2007. Selective peritectic garnet entrainment as the origin of geochemical diversity in S-type granites. Geology 35, 9–12.
Strong, D.F., Hanmer, S.K., 1981. The leucogranites of southern Brittany; origin by faulting, frictional heating, fluid flux and fractional melting. Can. Mineral. 19, 163–176.
Tartèse, R., Boulvais, P., 2010. Differentiation of peraluminous leucogranites "en route" to the surface. Lithos 114, 353–368.
Tartèse, R., Poujol, M., Ruffet, G., Boulvais, P., Yamato, P., Košler, J., 2011a. New U-Pb zircon and 40Ar/39Ar muscovite age constraints on the emplacement of the Lizio syn-tectonic granite (Armorican Massif, France). Comptes Rendus Geosci. 343, 443–453.
Tartèse, R., Ruffet, G., Poujol, M., Boulvais, P., Ireland, T.R., 2011b. Simultaneous resetting of the muscovite K-Ar and monazite U-Pb geochronometers: a story of fluids. Terra Nova 23, 390–398.

937 Triboulet, C., Audren, C., 1988. Controls on P–T–t deformation path from amphibole zonation during progressive
938 metamorphism of basic rocks (estuary of the River Vilaine, South Brittany, France). J. Metamorph. Geol.,
939 6, 117–133.
940 Turrillot, P., Augier, R., Faure, M., 2009. The top-to-the-southeast Sarzeau shear zone and its place in the late-
941 orogenic extensional tectonics of southern Armorica. Bull. Soc. Geol. Fr. 180, 247–261.
942 Ugidos, J.M., Recio, C., 1993. Origin of cordierite-bearing granites by assimilation in the Central Iberian Massif
943 (CIM), Spain. Chem. Geol. 103, 27–43.
944 Valois, J., 1975. Les formations métamorphiques de Pénaran (presqu'île de Guérande, Loire Atlantique) et leur
945 minéralisation uranifère. Thèse 3e cycle, Nancy, 136p.
946 Vielzeuf, D., Holloway, J.R., 1988. Experimental determination of the fluid-absent melting relations in the pelitic
947 system. Contrib. Mineral. Petrol. 98, 257–276.
948 Vigneresse, J., 1983. Enracinement des granites armoricains estimé d'après la gravimétrie. Bulletin de la societé
949 Géologique et minéralogique de Bretagne, vol. (C), 15 (1), 1-15.
950 Watson, E.B., Green, T.H., 1981. Apatite/liquid partition coefficients for the rare earth elements and strontium.
951 Earth Planet. Sci. Lett. 56, 405–421.
952 Willis-Richards, J., Jackson, N.J., 1989. Evolution of the Cornubian ore field, Southwest England; Part I, Batholith
953 modeling and ore distribution. Econ. Geol. 84, 1078–1100.
954 Wiedenbeck, M., Allé, P., Corfu, F., Griffin, W. l., Meier, M., Oberli, F., Quadt, A.V., Roddick, J. c., Spiegel, W., 1995.
955 Three Natural Zircon Standards for U-Th-Pb, Lu-Hf, Trace Element and Ree Analyses. Geostand. Newsl. 19,
956 1–23.
957 Yamato, P., Tartèse, R., Duretz, T., May, D.A., 2012. Numerical modelling of magma transport in dykes.
958 Tectonophysics 526–529, 97–109.
959

960

961 Table Caption

962 Table 1: GPS coordinates and simplified petrographic description of the Guérande granite samples.
963 Ms-Bt: Ms-Bt coarse to medium grain granite; Ms-Turm: Ms-Turm coarse to medium grain granite; Fine: Ms-Bt
964 fine grain granite; Root: root facies; Ch: chloritisation; Ab: albitization; G: greisenization.
965
966 Table 2: Operating conditions for the LA-ICP-MS equipment.
967
968 Table 3: Whole rock chemical compositions of the Guérande granite samples.
969 Root: Root facies; Ms-Bt: Ms-Bt coarse to medium grain granite; Ms-Turm: Ms-Turm coarse to medium grain
970 granite; fine: Ms-Bt fine grain granite.
971
972 Table 4: Rb-Sr and Sm-Nd whole rock data for the Guérande granite. Rb concentrations have been obtained by
973 ICP-MS, other concentrations by isotopic dilution.
974 **Two stages T_{DM} calculated using the equation of Liew and Hofmann (1988) for an age of 310 Ma.*
975
976 Table 5: Result of fractional crystallization modeling between the less differentiated sample GUE-15 and more
977 differentiated sample GUE-12.
978
979
980
981
982
983
984
985
986
987
988

989 Figure caption

990

991 Figure 1: Structural map of the southern part of the Armorican Massif showing the localization of the Guérande
992 granite. Modified from Gapais et al. (1993), Gumiaux (2003), the 1/1000000 geological map of France (Chantraine
993 et al., 2003) and the 1/250000 geological map of Lorient (Proust et al., 2009). NBSASZ: Northern Branch of the
994 South Armorican Shear Zone; SBSASZ: Southern Branch of the South Armorican Shear Zone.

995 Figure 2 : Geological map of the Guérande granite modified after the 1/50000 geological maps of La Roche Bernard
996 (Audren et al., 1975) and St-Nazaire (Hassenforder et al., 1973). The different petrographic facies and the alteration
997 types are reported. Sampling sites with sample numbers are also indicated. Structural data are modified from
998 Bouchez et al. (1981). Mineral abbreviations are from Kretz (1983).

999

1000 Figure 3: Simplified cross section of the Guérande granite. The localization of the cross section is on Figure 1.
1001 Modified after Bouchez et al. (1981).

1002

1003 Figure 4: Representative pictures from the Southern part (a, c, d) and the northwestern part (b, e, f) of the Guérande
1004 granite. a) Ms-Bt bearing root facies (sample GUE-13). The roughly defined foliation (S) is marked by muscovite
1005 and biotite stretching. b) Ms-Turm coarse grained granite (sample GUE-18). c) Root facies. The granite with a
1006 roughly defined foliation (F Granite) is cross cut by an isotropic granite intrusion (I Granite) and by a pegmatite
1007 dyke. d) Typical outcrop of the root facies with a roughly defined foliation (S). e) Mylonitic granite (sample GUE-
1008 9). f) Large quartz vein cross cutting Ms-Turm coarse grained granite near the contact with the micaschists and
1009 metavolcanics.

1010

1011 Figure 5: a-b-c) Rose diagram displaying the strikes of pegmatites, aplite dykes and quartz veins of three strategic
1012 areas from the south to the north of the Guérande granite. The numbers inside the diagrams (horizontal and vertical
1013 axes) represent the amount of measured dykes displaying a range of strike. The light grey areas represent the main
1014 strike of lineation (most of the lineation data are from Bouchez et al., 1981). n: number of measured dykes. d-e)
1015 Pictures of stretching lineation (SL) in the Guérande massif: d) N030° stretching lineation in the mylonitic sample

GUE-9, e) E-W stretching lineation marked by contact metamorphism minerals in the micaschists localized at the contact with the Guérande granite. Both pictures are localized on the map.

Figure 6 : Thin section photomicrographs showing the different petrographic facies of the Guérande granite. a) Root facies (Bt>Ms), b) Ms-Bt coarse to medium grain granite (Ms>Bt) and c) Ms-Turm coarse to medium grain with two generation of Ms (MsI: primary muscovite; MsII: secondary muscovite). Mineral abbreviation from Kretz (1983).

Figure 7: Chemical compositions of plagioclase and muscovite from the Guérande granite. a) Triangular classification of plagioclase. b) Ternary Ti-Na-Mg diagram for muscovite and chemical map of Mg distribution in muscovite for the Ms-Turm granite sample GUE-1 and the Ms-Bt granite dyke GUE-5. The primary and secondary fields of muscovite are from Miller et al. (1981). In figure the inset "cleavage" refers to small muscovite grains located within foliation planes.

Figure 8 : a) Chemical (after Hughes, 1973) and b) chemical-mineralogical (after Debon and Le Fort, 1988) diagrams for the Guérande granite samples. Samples GUE-19a, 19b and 21 show evidences of alteration. In diagram b), the crosses indicate the location of common igneous rock: **gr** = granite, **ad** = adamellite, **gd** = granodiorite, **to** = tonalite, **sq** = quartz syenite, **mzq** =quartz monzonite, **mzdq** = quartz monzodiorite, **s** =syenite, **mz** = monzonite, **mzgo** = monzogabbro. Q and P parameters are expressed in molar proportion multiplied by 1000. c) Shand (1943) diagram (A/CNK = $Al_2O_3/(CaO+Na_2O+K_2O)$; A/NK = (Al_2O_3/Na_2O+CaO) ; molar proportions) where unaltered and altered samples are distinghuished on the basis of figures a) and b). Lizio and Questembert granite samples are shown for comparison (Tartèse and Boulvais, 2010).

Figure 9 : Harker diagrams of selected major and trace elements reported as a function of a) SiO_2 and b) Zr and Th for the Guérande granite.

Figure 10: Chondrite normalized REE patterns of the Guérande granite samples. Normalization values from Evensen et al. (1978).

1044

1045 Figure 11 : a) Evolution of some geochemical tracers sensible to the interaction with fluids as a function of the
1046 distance to the NW edge of the Guérande granite. b) Evolution of chosen tracers as a function of the concentration
1047 of Cs.

1048

1049 Figure 12 : Sr and Nd isotopic compositions of the Guérande granite compared with the Lizio, Questembert (Tartèse
1050 and Boulvais, 2010), Pontivy and Rostrenen granite (Peucat et al., 1979 ; Euzen, 1993). εNd and I_{Sr} are calculated
1051 for an age of 310 Ma. The vertical bars representing εNd(T) composition of the Brioverian and Paleozoic sediments
1052 from Central Brittany are calculated from Michard et al. (1985) and Dabard et al. (1996). The exceptionally high
1053 εNd(T) value of 0.5 measured in the Paleozoic sediments (Michard et al., 1985) is not reported in the figure.

1054

1055 Figure 13 : selected images of zircon and monazite grains. a-b-d) cathodoluminescence images of zircons from the
1056 sample GUE-3, GUE-5 and GUE-8. c) Th chemical map of monazite from the sample GUE-4. Dashed circles
1057 represent the location of LA-ICP-MS analyses with the corresponding $^{206}Pb/^{238}U$ ages in Ma.

1058

1059 Figure 14 : a) Tera-Wasserburg diagram displaying the analyses made on zircon of the sample GUE-3. The Grey
1060 ellipses represent the inherited zircons and the dashed ellipses represent zircon submitted to a lost or a gain in
1061 common lead. #: $^{207}Pb/^{206}Pb$ ages at 1 σ. b-c-d) $^{206}Pb/^{238}U$ vs $^{208}Pb/^{232}Th$ concordia diagram for monazite of the
1062 sample GUE-3, GUE-4 and GUE-5. The dashed ellipses represent the analyses not used for the calculation of
1063 Concordia ages. In the diagrams error ellipses are plotted at 1σ.

1064

1065 Figure 15 : a-b) Harker diagrams displaying the whole rock compositions of the unaltered samples from the
1066 Guérande granite. The black stars represent the average compositions of potassic feldspar and biotite from the
1067 sample GUE-4 and the composition of a theoretical plagioclase (An20). The grey areas represent the magmatic
1068 trends defined by the whole rock data including the errors. The intersection of this trend with the assemblage
1069 Bt+Pl+Kfs encompasses the mineralogical composition of the segregate. c) Ba vs Sr diagram displaying the whole
1070 rock compositions of the unaltered samples from the Guérande granite. The two lines represent two different models

of evolution of Ba and Sr compositions in a liquid during the fractional crystallization of an assemblage made of 0.45Kfs+0.31Pl+0.21Bt+0.04Ap. The numbers under the line indicate the amount of the assemblage fractionated from the melt in Wt.%. The primitive composition of the liquid used to model fractional crystallization is the composition of sample GUE-15. Kd used and presented in the table in inset in the diagram are from a. Hanson, (1978); b. Icenhower and London, (1996); c. Ren et al., (2003); d. Icenhower and London, (1995); e. Watson and Green, (1981); f. Prowatke and Klemme, (2006).

Figure
Click here to download high resolution image

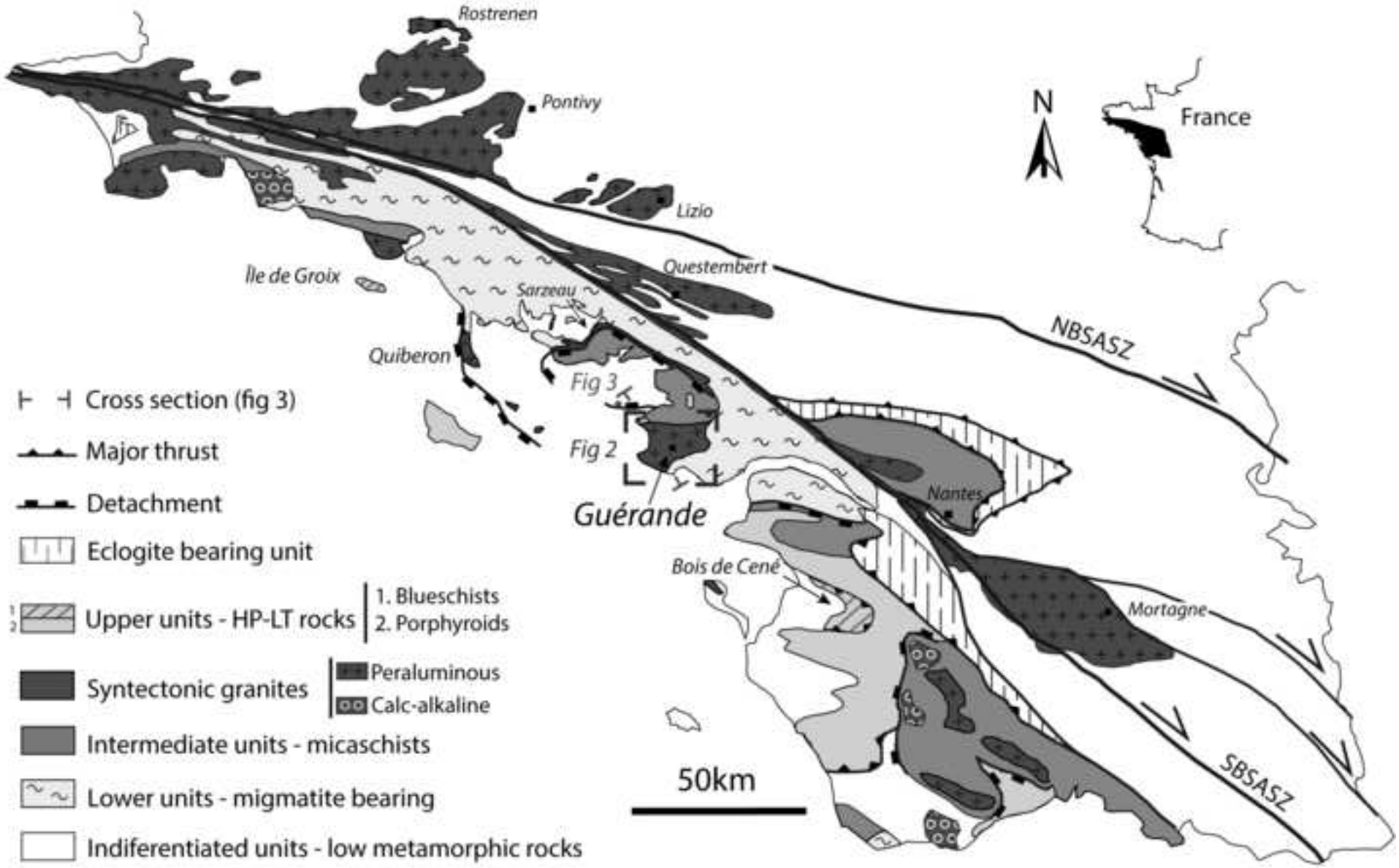

458

Figure

Click here to download high resolution image

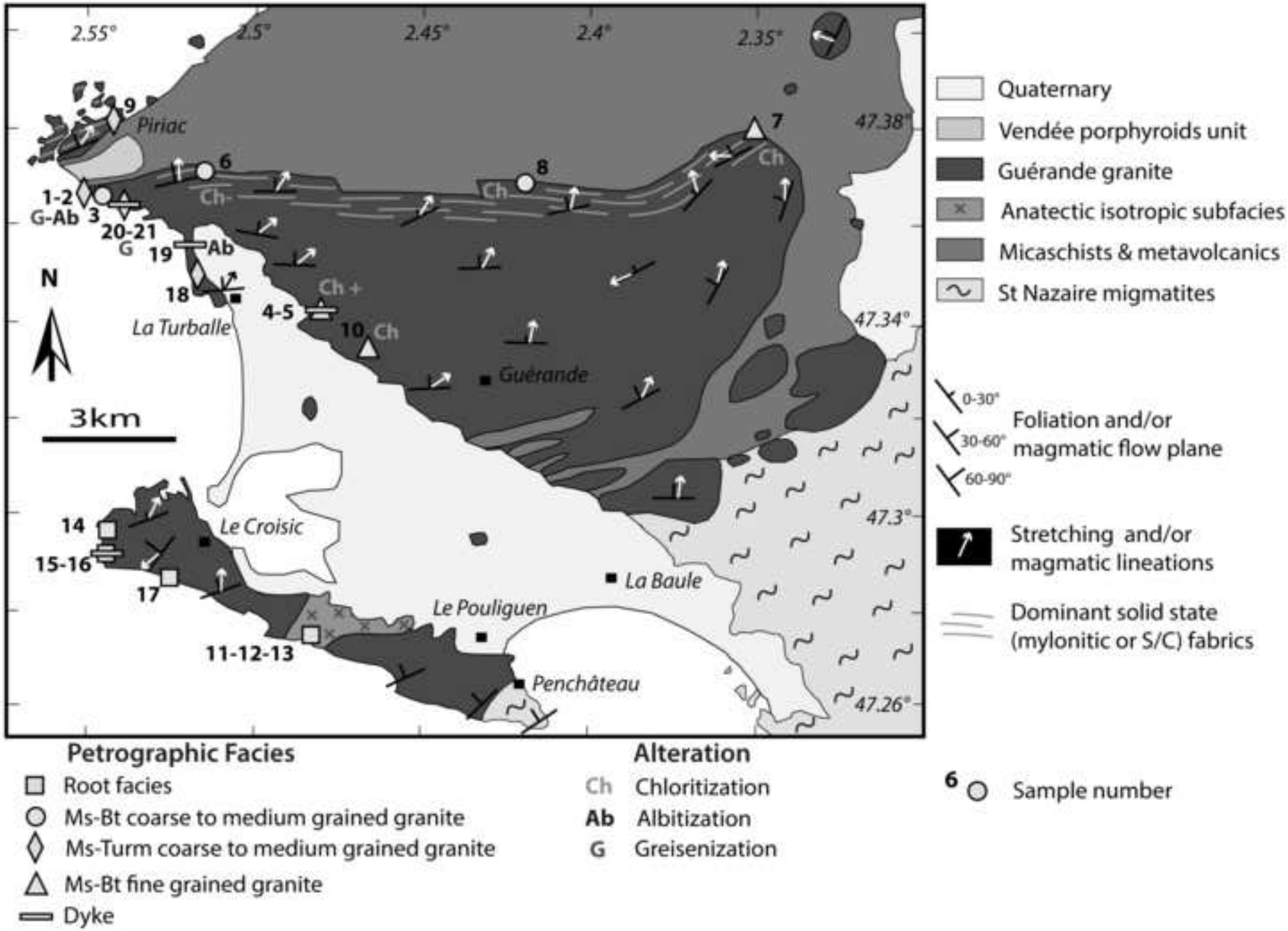

Figure

Click here to download high resolution image

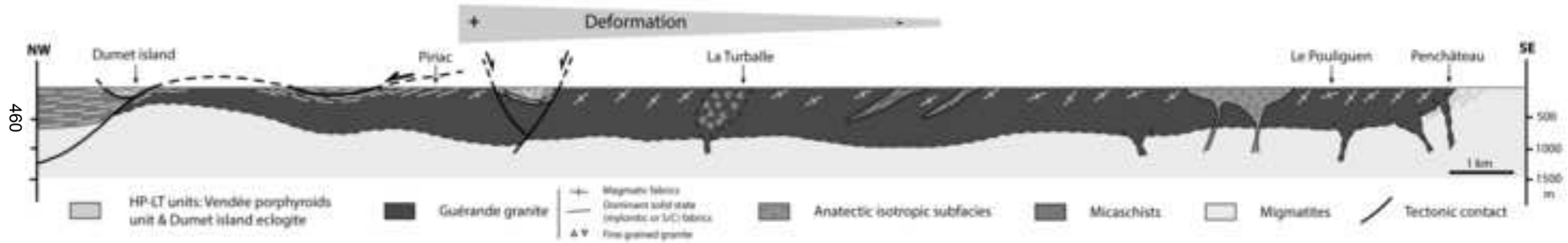

Figure
Click here to download high resolution image

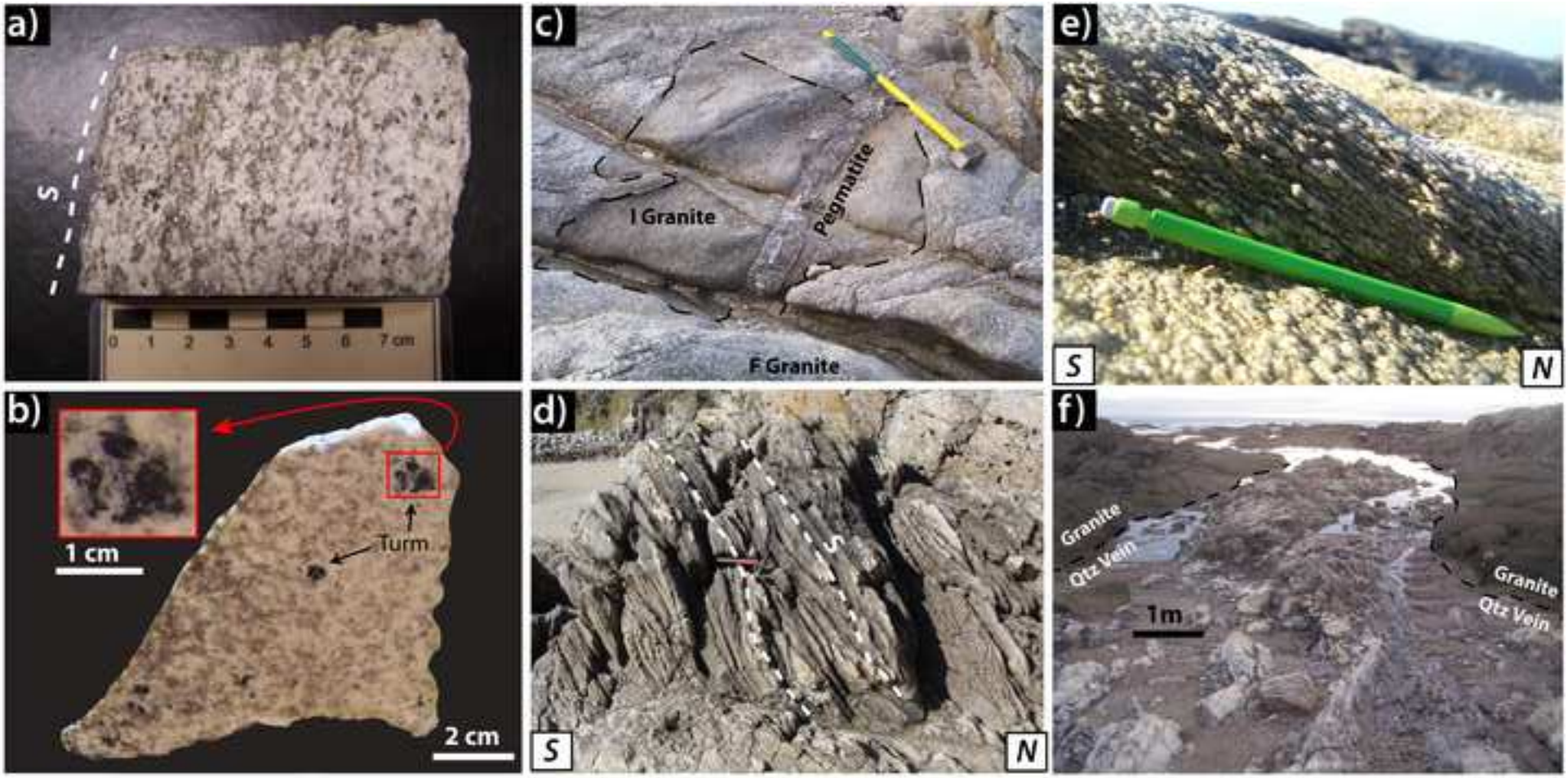

461

Figure
Click here to download high resolution image

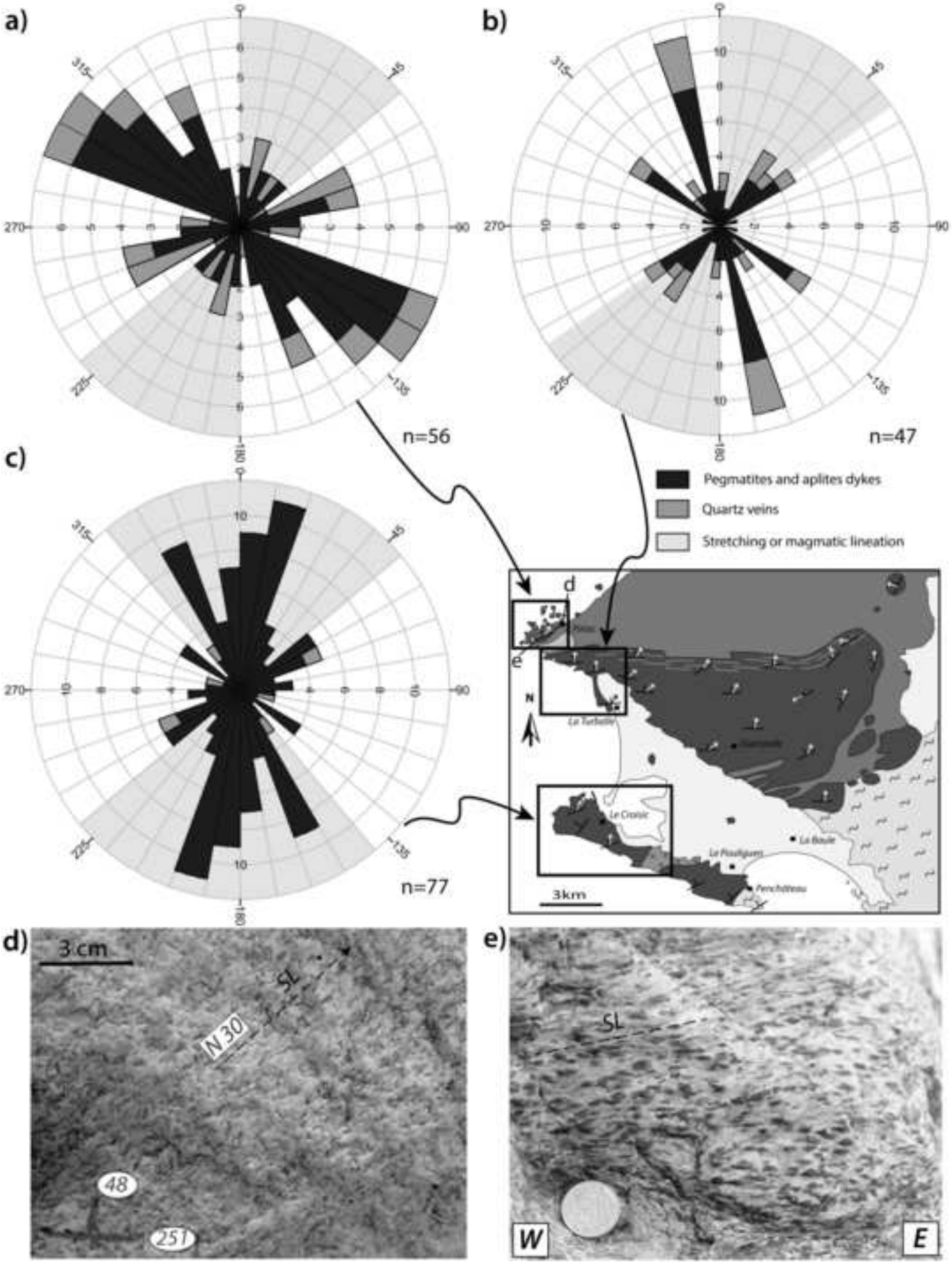

Figure
Click here to download high resolution image

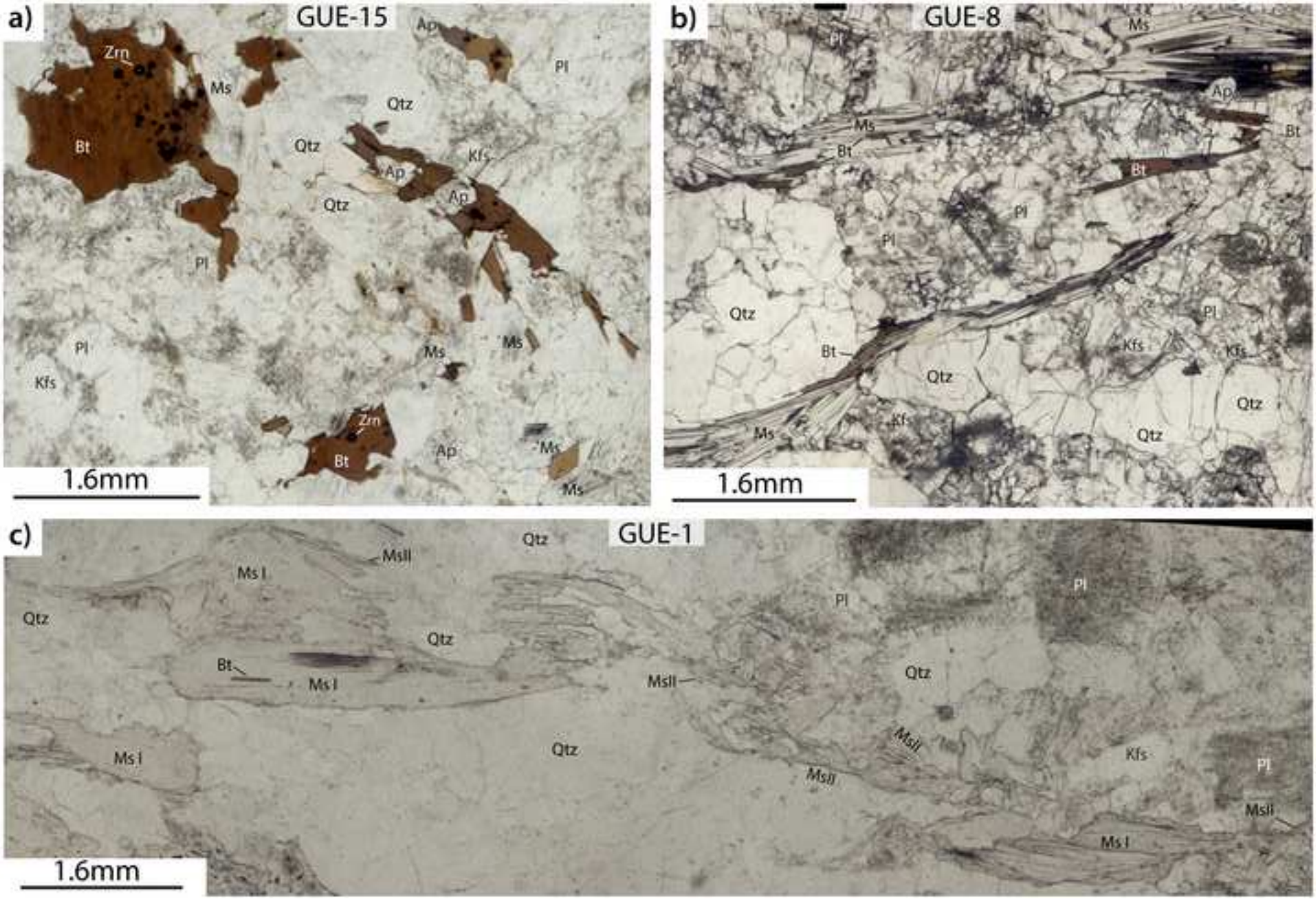

Figure
Click here to download high resolution image

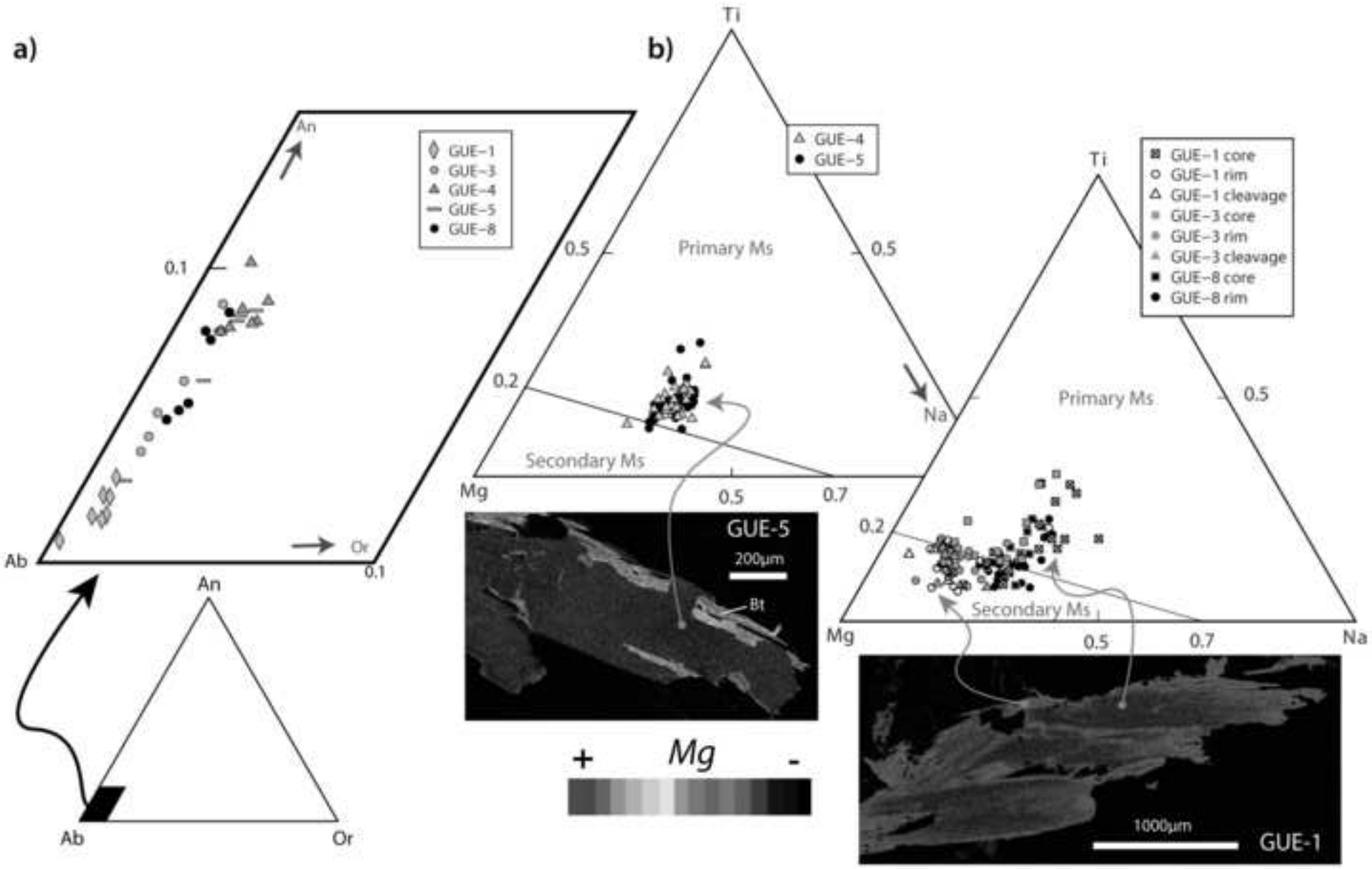

Figure

Click here to download high resolution image

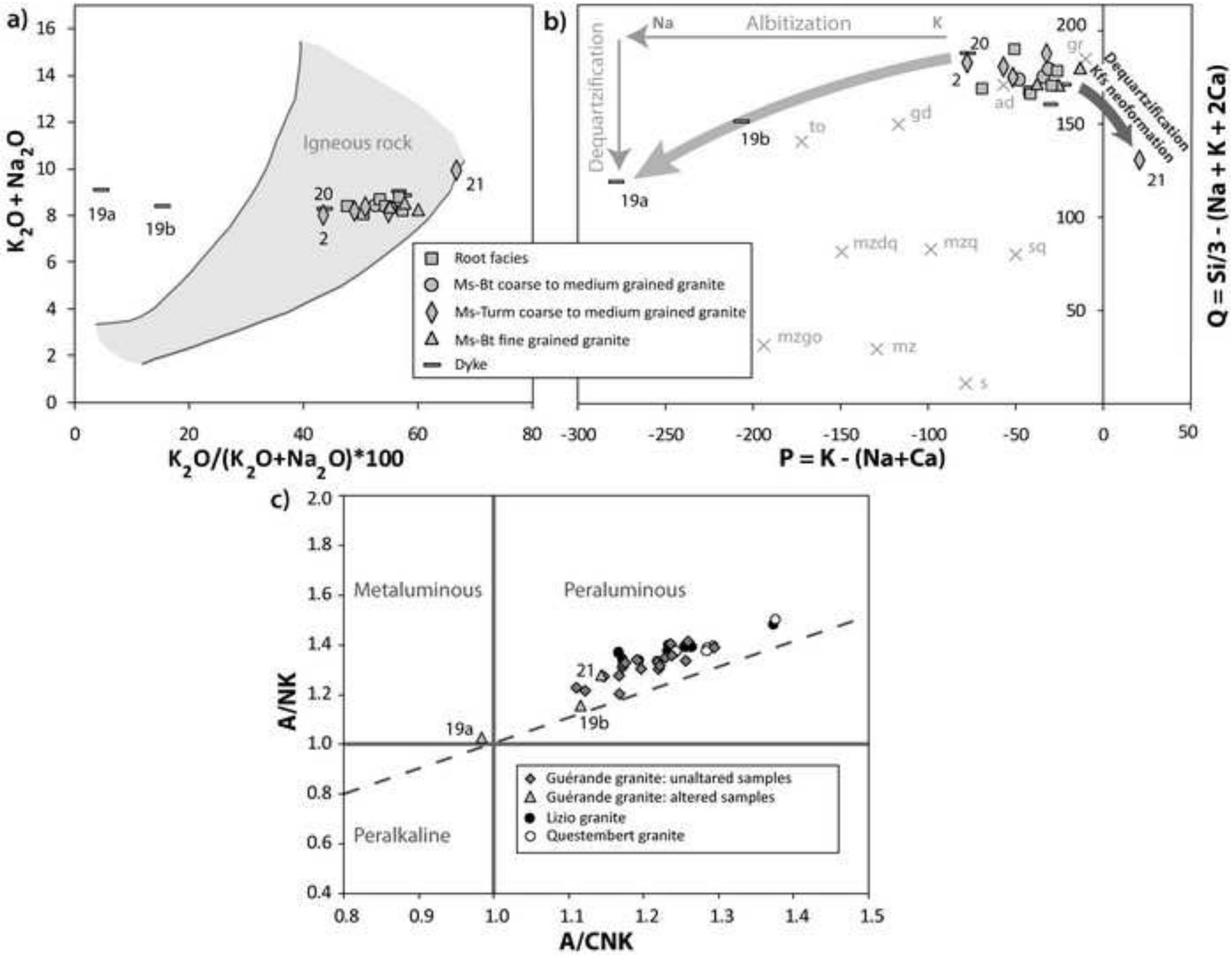

Figure
Click here to download high resolution image

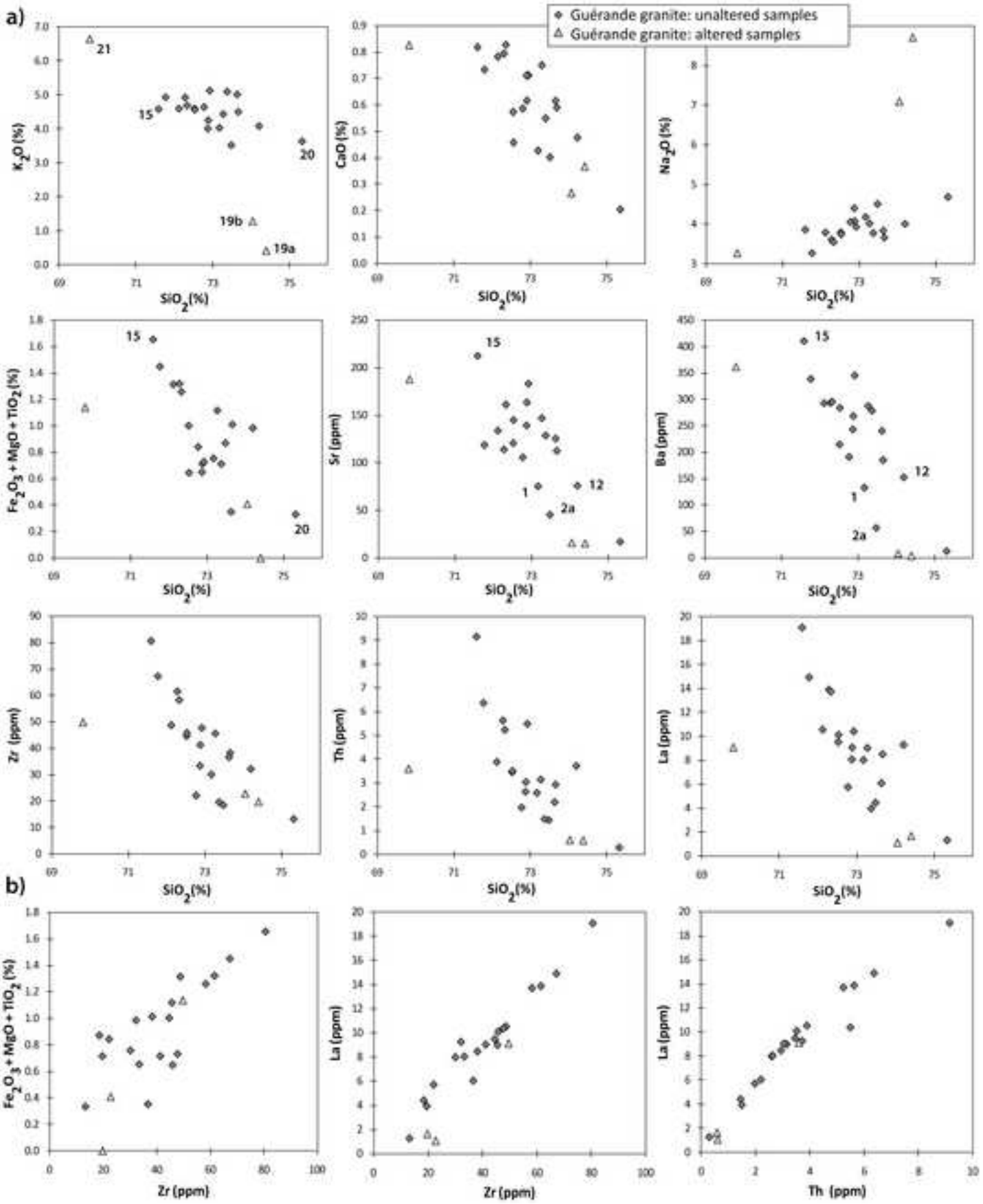

Figure
Click here to download high resolution image

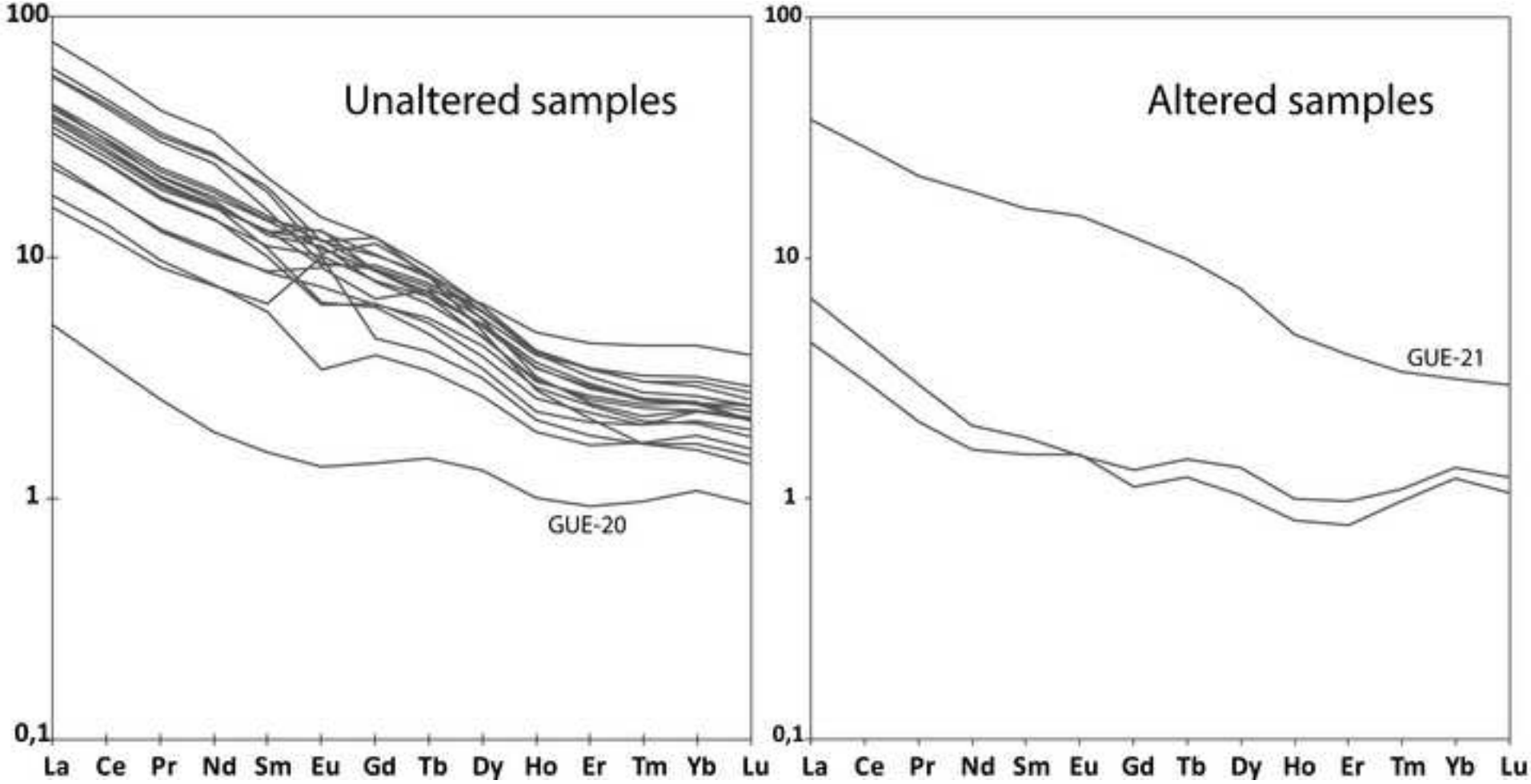

Figure

Click here to download high resolution image

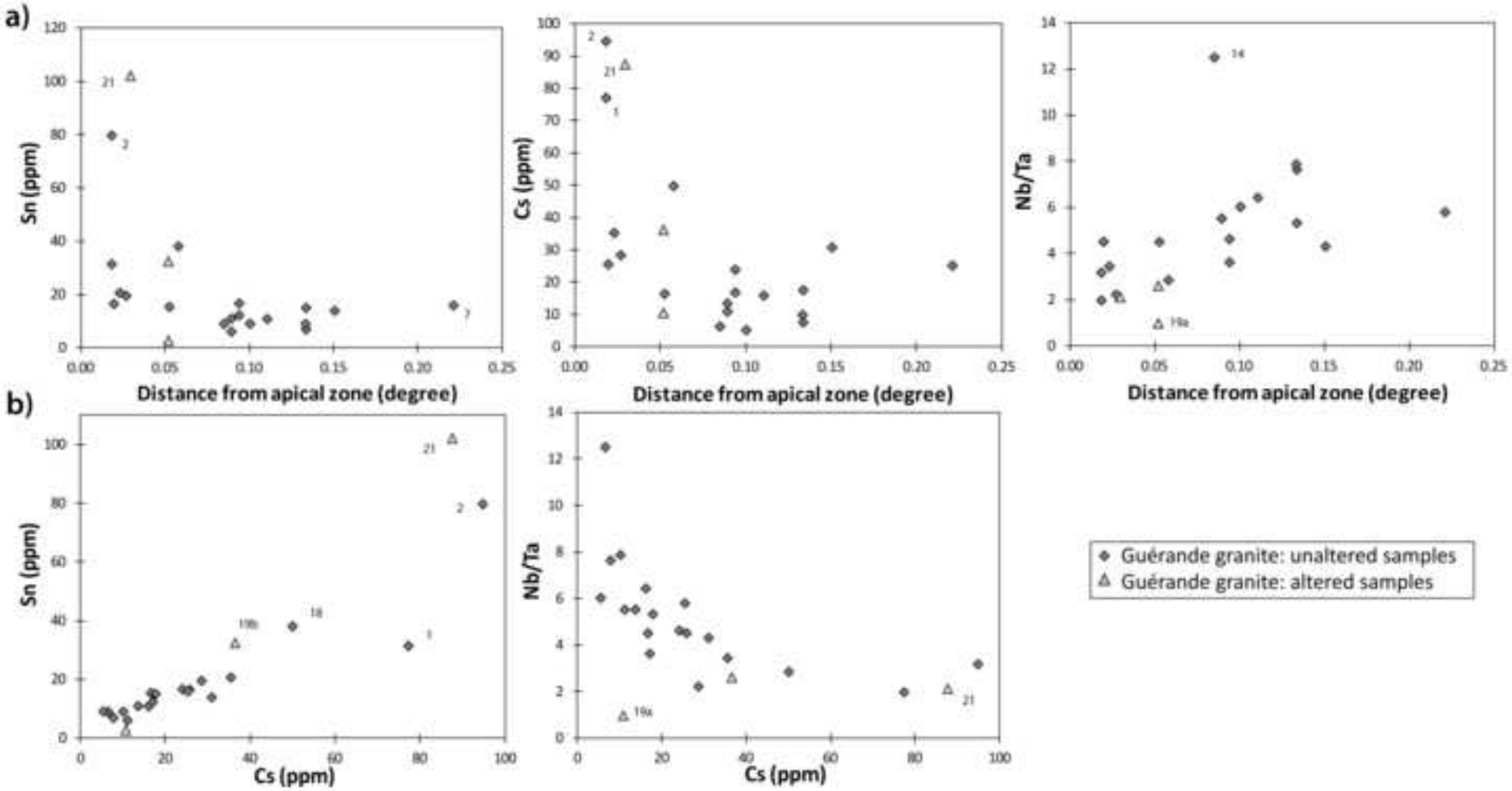

Figure
Click here to download high resolution image

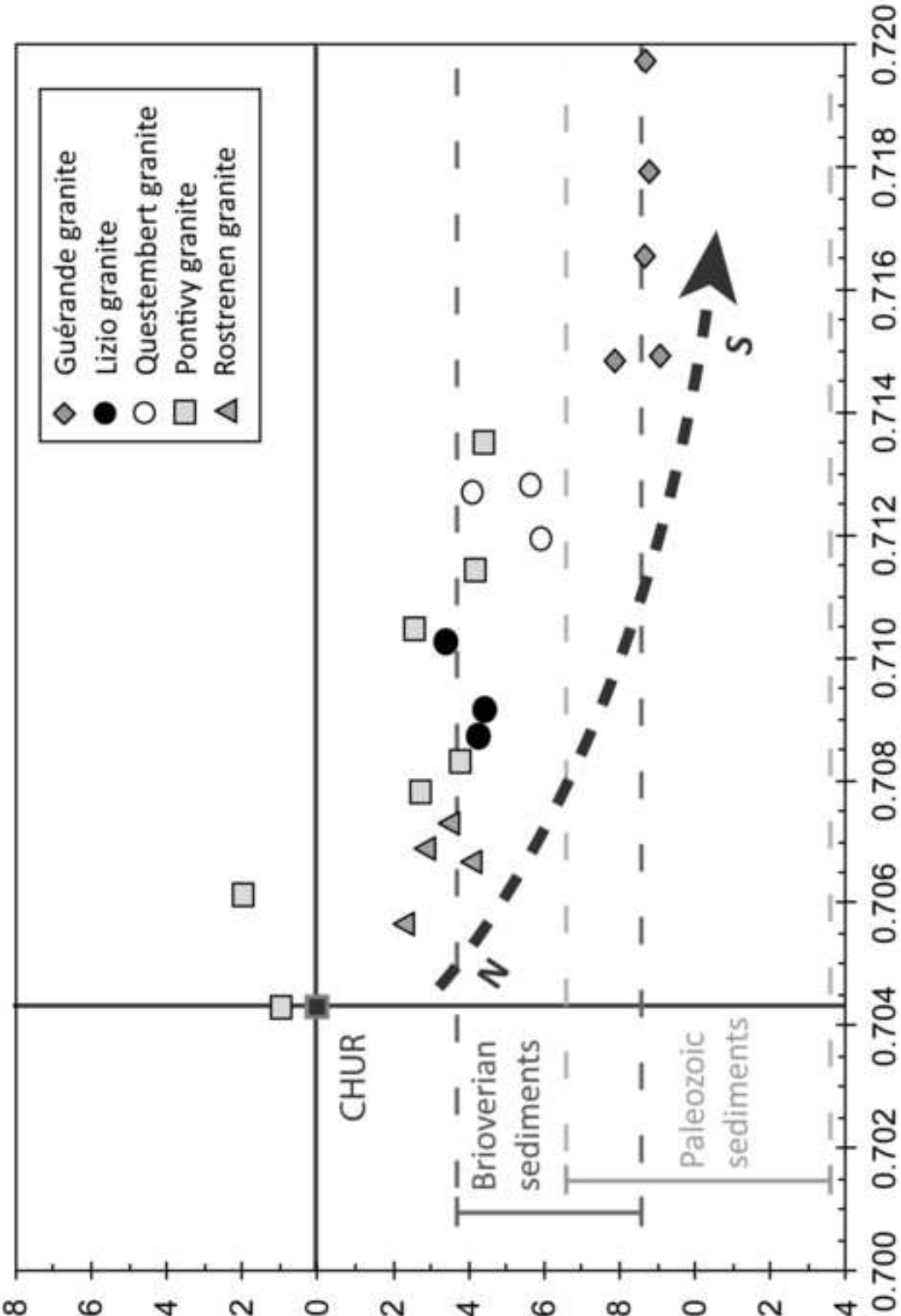

Figure

Click here to download high resolution image

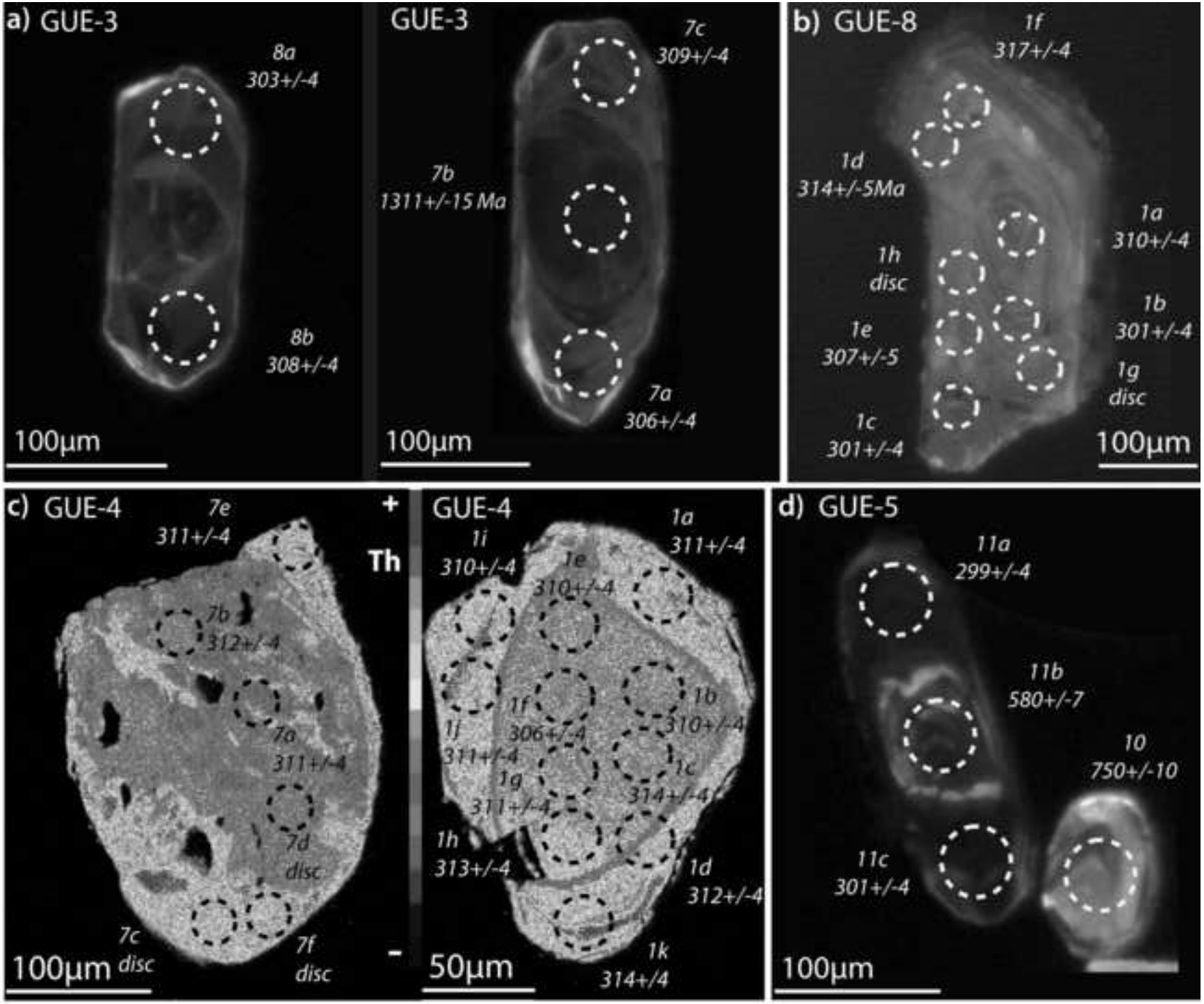

Figure

Click here to download high resolution image

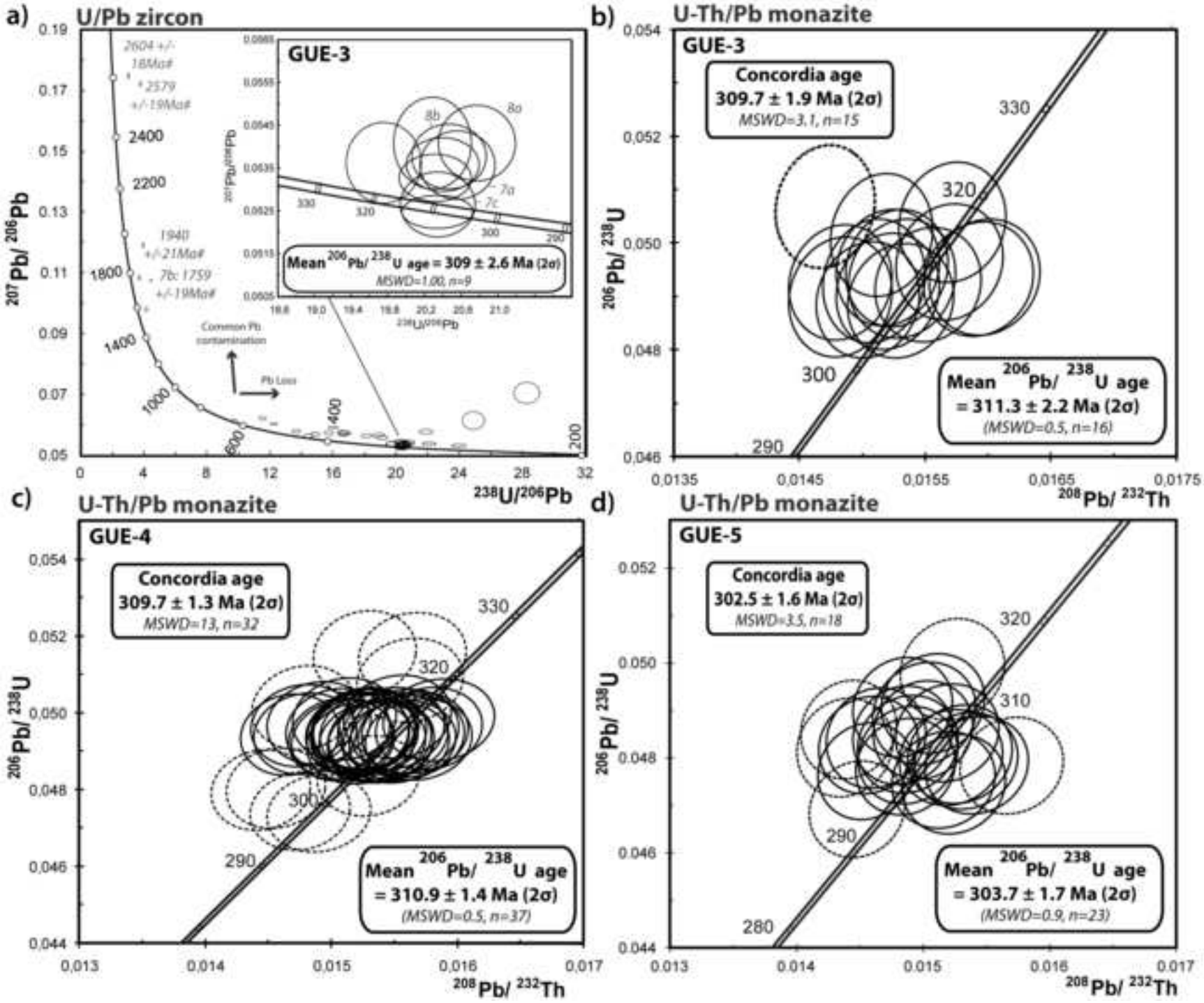

Figure

Click here to download high resolution image

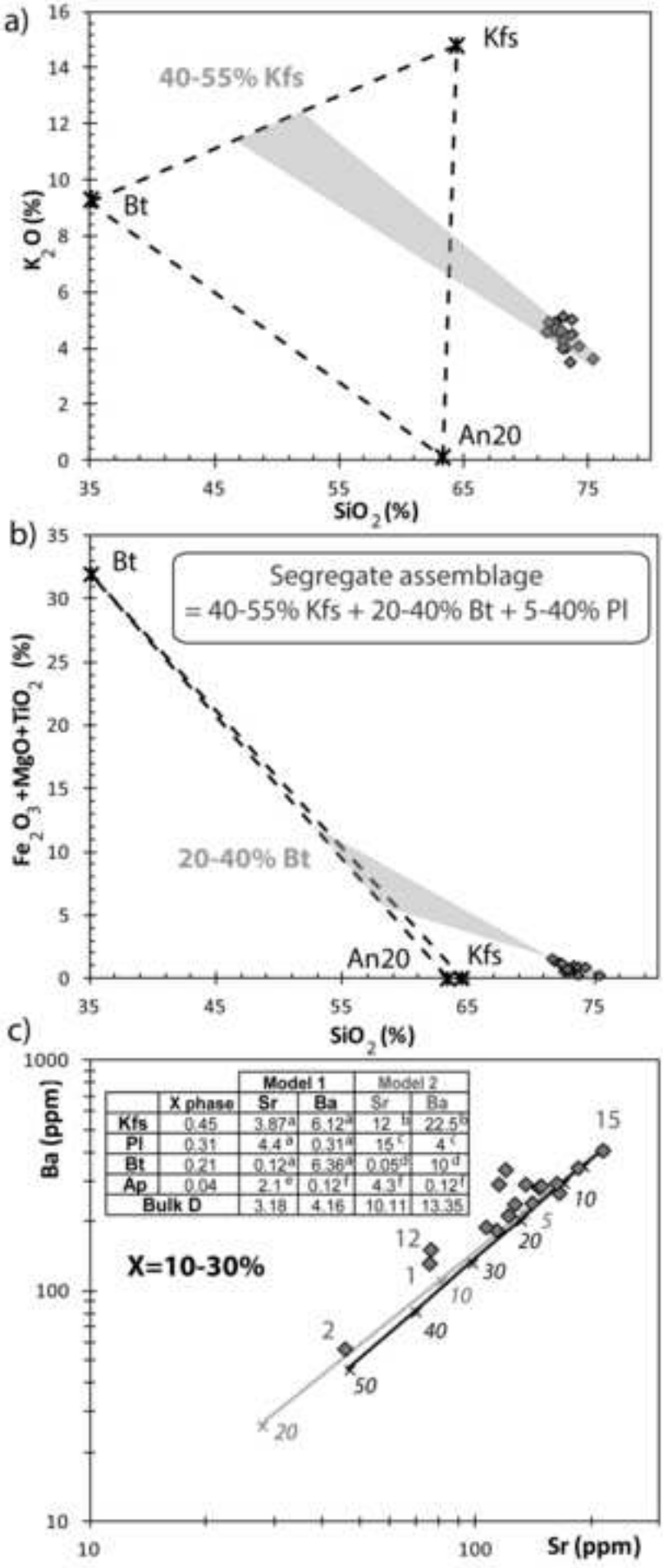

Table

Click here to download Table: Table_1_Ballouardetal.docx

Sample	Longitude (°)	Latitude (°)	Facies	Texture	Strain	Mineralogy	Alteration
GUE-11	-2.484200	47.274183	Root	Medium grain (2mm), roughly defined foliation	+	Ms>>Bt	
GUE-12	-2.484200	47.274183	Root	Fine to medium grain (1-3mm), isotropic		Ms>Bt	
GUE-13	-2.484533	47.274367	Root	Medium grain (2-3mm), roughly defined foliation	+	Ms>>Bt	
GUE-14	-2.546383	47.296217	Root	Fine grain (1mm), isotropic		Ms>Bt	
GUE-15	-2.546417	47.291733	Root	Medium grain (2-3mm), roughly defined foliation		Bt>Ms	
GUE-17	-2.526550	47.286967	Root	Fine grain (1-2mm), solid state fabric	+	Ms>>Bt>Grt	
GUE-3	-2.547297	47.368122	Ms-Bt	Medium to coarse grain (2-4mm), magmatic fabric	+	Ms>Bt	
GUE-6	-2.515918	47.370945	Ms-Bt	Medium to fine grain (1-3mm), S/C fabric	++	Ms>Bt	
GUE-8	-2.417652	47.368925	Ms-Bt	Coarse grain (3-5mm), isotropic		Ms>Bt	Ch-
GUE-1	-2.552081	47.369195	Ms-Turm	Coarse grain (3-5mm), magmatic fabric	+	Ms>>Turm> Bt	
GUE-2	-2.552081	47.369195	Ms-Turm	Coarse grain (3-4mm), shear zone	++	Ms >> Turm	Ab-
GUE-9	-2.548596	47.381192	Ms-Turm	Fine to medium grain (<0.5-2mm) , S/C mylonite	+++	Ms>>Turm	
GUE-18	-2.517417	47.350167	Ms-Turm	Medium to coarse grain (2-3mm), isotropic		Ms>>Bt>Turm	
GUE-21	-2.541317	47.365750	Ms-Turm	Coarse grain (3-5mm), magmatic fabric	+	Ms>>Turm	G?
GUE-4	-2.481191	47.342346	Fine	Fine grain (0.5-2mm), isotropic		Ms>Bt	
GUE-7	-2.346883	47.380000	Fine	Fine grain (0.5-2mm), solid state fabric	+	Ms>Bt	Ch
GUE-10	-2.466283	47.334767	Fine	Fine grain (1-2mm), isotropic		Ms>Bt	Ch
GUE-5	-2.481191	47.342346	Dyke	Medium grain (2mm), isotropic		Ms>>Bt	Ch+
GUE-16	-2.546417	47.291733	Dyke	Fine grain (1-2mm), isotropic		Ms=Bt	
GUE-19a	-2.520933	47.356367	Dyke	Aplitic texture (0.5-1mm), shear zone	++	Ms>Turm>Grt	Ab+
GUE-19b	-2.520933	47.356367	Dyke	Aplitic texture (0.5-1mm), shear zone	++	Ms>Bt >Turm	Ab
GUE-20	-2.544000	47.366067	Dyke	Aplitic texture (0.5-1mm), isotropic		Ms	Ab-?

Table

Click here to download Table: Table_2_Ballouardetal.docx

Laser-ablation system ESI NWR193UC	
Laser type/wavelength	Excimer 193 nm
Pulse duration	< 5 ns
Energy density on target	~ 7 J/cm^2
ThO^+/Th^+	< 0.5%
He gas flow	~ 800 ml/min
N_2 gas flow	4 ml/min
Laser repetition rate	3-5 Hz (zircon);1-2 Hz (monazite)
Laser spot size	26-44 µm (zircon); 20µm (monazite)
ICP-MS Agilent 7700x	
RF power	1350 W
Sampling depth	5.0-5.5 mm (optimised daily)
Carrier gas flow (Ar)	~ 0.85 l/min (optimized daily)
Coolant gas flow	16 l/min
Data acquisition protocol	Time-resolved analysis
Scanning mode	Peak hopping, one point per peak
Detector mode	Pulse counting, dead time correction applied, and analog mode when signal intensity > ~ 10^6 cps
Isotopes determined	^{204}(Hg + Pb), ^{206}Pb, ^{207}Pb, ^{208}Pb, ^{232}Th, ^{238}U
Dwell time per isotope	10 ms (30 ms for ^{207}Pb)
Sampler, skimmer cones	Ni
Extraction lenses	X type

Table

Click here to download Table: Table_3_Ballouardetal.docx

Sample		GUE-11	GUE-12	GUE-13	GUE-14	GUE-15	GUE-17	GUE-3	GUE-6	GUE-8	GUE-1	GUE-2	GUE-9	GUE-18	GUE-21	GUE-4	GUE-7	GUE-10	GUE-5	GUE-16	GUE-20	GUE-19a	GUE-19b
Facies		Root	Root	Root	Root	Root	Root	Ms-Bt	Ms-Bt	Ms-Bt	Ms-Turm	Ms-Turm	Ms-Turm	Ms-Turm	Ms-Turm	fine	fine	fine	dyke	dyke	dyke	dyke	dyke
SiO_2	wt.%	72.9	74.2	72.8	72.3	71.6	73.6	72.5	72.5	73.3	73.2	73.5	72.9	73.7	69.8	72.1	72.3	71.8	73.4	72.9	75.3	74.4	74.1
Al_2O_3	wt.%	14.76	14.50	15.27	15.34	15.04	15.01	14.95	15.43	14.97	14.66	15.01	15.27	14.81	16.11	15.04	14.92	15.18	14.28	14.79	14.01	15.20	15.14
Fe_2O_3	Wt.%	0.45	0.73	0.59	0.87	1.16	0.22	0.68	0.38	0.78	0.52	0.67	0.45	0.71	0.81	0.96	0.92	0.99	0.53	0.51	0.26	bdl	0.36
MnO	Wt.%	0.01	0.02	0.01	0.01	0.01	0.01	0.01	0.01	0.01	0.01	0.02	0.01	0.02	0.01	0.01	0.01	0.01	0.01	0.01	0.01	0.01	0.03
MgO	Wt.%	0.14	0.16	0.16	0.24	0.32	0.07	0.20	0.15	0.24	0.16	0.15	0.16	0.21	0.22	0.24	0.26	0.30	0.12	0.14	0.06	bdl	0.05
CaO	Wt.%	0.71	0.48	0.59	0.83	0.82	0.62	0.57	0.46	0.75	0.43	0.40	0.62	0.59	0.83	0.78	0.80	0.73	0.55	0.71	0.21	0.37	0.27
Na_2O	Wt.%	4.40	4.00	4.05	3.54	3.85	3.83	3.79	3.73	4.01	4.18	4.51	4.07	3.66	3.28	3.78	3.61	3.26	3.77	3.93	4.68	8.71	7.10
K_2O	Wt.%	4.01	4.08	4.65	4.70	4.59	5.03	4.61	4.57	4.44	4.03	3.51	4.26	4.51	6.64	4.61	4.93	4.94	5.11	5.14	3.63	0.42	1.29
TiO_2	Wt.%	0.07	0.09	0.09	0.15	0.18	0.06	0.12	0.12	0.10	0.08	0.06	0.11	0.10	0.11	0.12	0.15	0.16	0.06	0.08	0.02	bdl	bdl
P_2O_5	Wt.%	0.16	0.25	0.14	0.25	0.23	0.22	0.23	0.23	0.23	0.24	0.29	0.21	0.35	0.59	0.25	0.22	0.23	0.18	0.25	0.14	0.23	0.19
LOI	Wt.%	0.94	0.95	0.79	1.00	0.89	0.05	1.14	1.54	0.98	1.10	1.09	1.19	1.25	1.09	1.04	0.74	1.34	0.63	0.67	0.84	0.39	0.80
Total	Wt.%	98.51	99.47	99.11	99.27	98.69	98.75	98.83	99.15	99.79	98.57	99.19	99.23	99.86	99.49	98.95	98.83	98.93	98.63	99.16	99.18	99.72	99.27
Cs	ppm	8	18	10	6	14	5	35	16	31	77	95	26	50	88	24	25	16	17	11	28	11	36
Rb	ppm	202	271	223	195	230	218	353	239	251	357	365	244	384	459	245	293	252	266	222	325	14	150
Sr	ppm	139	76	106	161	212	125	121	145	147	75	46	163	113	187	134	114	119	129	183	17	15	16
Ba	ppm	243	153	191	296	411	241	215	284	288	133	57	269	185	362	293	294	339	279	346	13	4	8
Be	ppm	5.7	11.0	7.0	3.9	9.2	9.2	18.4	11.3	13.7	18.7	12.9	15.0	34.5	6.0	15.4	9.8	9.2	24.0	12.6	131.3	129.3	158.5
Y	ppm	6.7	4.5	5.5	7.6	7.7	9.7	5.9	7.2	6.6	5.1	3.8	6.3	7.7	9.1	7.6	5.1	6.0	4.1	5.9	2.2	2.4	1.8
Zr	ppm	33	32	22	58	81	37	45	46	46	30	19	41	38	50	49	61	67	20	48	13	20	23
Hf	ppm	1.19	1.10	0.77	1.77	2.46	1.37	1.54	1.54	1.53	1.26	0.96	1.44	1.41	1.78	1.65	2.00	2.03	0.73	1.70	1.10	1.30	1.46
Nb	ppm	4.68	7.75	6.34	7.96	8.61	10.64	6.39	6.70	5.70	6.81	10.57	6.51	11.39	11.09	8.03	5.67	6.66	4.95	7.02	8.63	1.59	11.14
Ta	ppm	0.61	1.45	0.80	0.64	1.55	1.76	1.85	1.48	1.32	3.41	3.31	1.44	3.97	5.19	1.73	0.97	1.03	1.36	1.27	3.85	1.59	4.23
Th	ppm	2.64	3.72	1.97	5.24	9.15	2.20	3.46	3.52	3.14	2.59	1.44	3.04	2.94	3.59	3.89	5.63	6.36	1.49	5.49	0.29	0.59	0.61
U	ppm	2.35	3.99	2.74	2.44	4.75	4.02	3.35	4.24	6.42	2.90	1.71	2.41	3.09	4.05	5.98	7.24	3.78	6.21	3.64	1.63	1.96	1.87
Pb	ppm	73	41	74	68	77	83	54	68	65	61	41	73	66	92	55	44	52	76	85	42	15	15
V	ppm	1.9	1.7	2.8	4.2	8.2	1.0	3.9	4.3	3.5	2.2	1.4	3.8	4.5	3.7	4.0	3.5	5.0	1.1	2.2	bdl	bdl	bdl
Ni	ppm	bdl	bdl	bdl	bdl	bdl	bdl	bdl	bdl	bdl	bdl	bdl	10.0	bdl	bdl	bdl	bdl	bdl	bdl	bdl	bdl	bdl	bdl
Cr	ppm	4.6	12.2	9.0	6.3	17.2	bdl	9.9	11.0	15.9	10.3	5.7	25.7	10.7	13.9	14.9	16.7	5.5	36.3	5.3	5.1	4.1	bdl
Co	ppm	0.5	0.4	0.6	0.6	1.4	bdl	0.8	1.3	0.8	bdl	bdl	0.5	0.8	0.9	0.8	0.8	1.1	0.4	bdl	bdl	bdl	bdl
Cu	ppm	bdl	bdl	bdl	bdl	bdl	bdl	bdl	bdl	bdl	bdl	bdl	bdl	bdl	bdl	bdl	bdl	bdl	bdl	bdl	bdl	bdl	bdl
Zn	ppm	24	45	33	35	52	14	48	27	48	31	57	25	44	52	54	69	56	30	23	23	bdl	32
Ga	ppm	22.4	22.4	24.9	23.4	26.9	21.8	26.2	25.9	24.0	25.1	30.8	25.8	25.8	31.7	26.6	29.1	25.7	21.5	20.0	23.7	18.8	25.4
Sn	ppm	7.1	15.2	9.2	9.2	11.1	9.2	20.8	15.5	14.1	31.6	79.9	16.7	38.3	102.3	16.8	16.1	11.0	12.4	6.3	19.7	2.9	32.6
W	ppm	0.85	2.10	0.98	3.17	2.47	1.65	1.12	1.18	1.09	1.69	1.92	1.00	1.57	2.87	1.77	0.86	1.82	1.03	1.96	0.51	bdl	0.44
Bi	ppm	1.7	0.7	1.9	0.1	0.6	2.7	1.7	1.6	1.6	2.3	1.7	1.7	1.8	0.5	1.9	0.9	1.2	3.5	1.0	0.4	0.6	0.7
Cd	ppm	0.1	bdl	bdl	0.7	0.1	0.4	bdl	bdl	0.1	bdl	0.2	bdl	0.3	0.2	0.1	bdl	0.1	0.4	0.3	0.2	0.3	0.2
Ge	ppm	1.2	1.6	1.2	1.2	1.4	1.5	1.6	1.3	1.4	1.8	2.2	1.4	1.9	2.0	1.3	1.2	1.2	1.5	1.5	2.4	2.7	2.6
La	ppm	8.04	9.26	5.73	13.71	19.08	6.06	9.50	10.10	9.00	8.00	4.43	9.04	8.48	9.10	10.54	13.88	14.91	3.94	10.39	1.28	1.65	1.08
Ce	ppm	15.55	17.96	11.33	26.65	36.36	11.52	18.84	19.86	17.42	15.58	8.74	17.51	16.61	18.23	20.55	27.54	28.75	7.82	19.49	2.34	2.86	1.95
Pr	ppm	1.69	1.98	1.26	2.90	3.93	1.23	2.09	2.19	1.95	1.71	0.94	1.92	1.83	2.08	2.27	3.06	3.18	0.88	2.06	0.25	0.28	0.20
Nd	ppm	6.85	7.77	5.08	11.58	15.65	4.93	8.50	8.85	7.92	6.89	3.66	7.75	7.65	8.81	9.15	12.42	12.80	3.60	8.19	0.89	0.95	0.76
Sm	ppm	1.73	1.68	1.34	2.42	3.31	1.35	2.19	2.23	1.97	1.55	0.92	1.97	1.99	2.46	2.30	3.01	2.88	0.99	1.90	0.24	0.27	0.24
Eu	ppm	0.60	0.38	0.44	0.55	0.85	0.53	0.63	0.74	0.68	0.37	0.20	0.75	0.54	0.86	0.67	0.68	0.61	0.58	0.65	0.08	0.09	0.09
Gd	ppm	1.65	1.27	1.30	1.82	2.46	1.38	1.80	2.12	1.81	1.32	0.81	1.80	1.89	2.46	2.08	2.47	2.32	0.95	1.62	0.29	0.27	0.23
Tb	ppm	0.26	0.18	0.21	0.28	0.34	0.27	0.26	0.31	0.27	0.20	0.13	0.27	0.29	0.37	0.32	0.31	0.32	0.15	0.24	0.06	0.05	0.05
Dy	ppm	1.35	0.88	1.09	1.43	1.59	1.64	1.19	1.54	1.31	0.99	0.68	1.34	1.51	1.87	1.59	1.26	1.41	0.81	1.21	0.33	0.34	0.26
Ho	ppm	0.21	0.13	0.16	0.22	0.23	0.28	0.18	0.23	0.20	0.15	0.11	0.20	0.23	0.27	0.23	0.16	0.18	0.12	0.17	0.06	0.06	0.05
Er	ppm	0.50	0.35	0.40	0.58	0.58	0.74	0.43	0.53	0.48	0.38	0.28	0.47	0.56	0.65	0.53	0.35	0.41	0.30	0.45	0.15	0.16	0.13
Tm	ppm	0.07	0.05	0.05	0.08	0.08	0.11	0.06	0.07	0.07	0.05	0.04	0.07	0.08	0.09	0.07	0.04	0.06	0.04	0.06	0.03	0.03	0.03
Yb	ppm	0.42	0.38	0.34	0.53	0.51	0.71	0.39	0.44	0.41	0.35	0.30	0.41	0.48	0.52	0.44	0.26	0.38	0.28	0.41	0.18	0.22	0.20
Lu	ppm	0.05	0.05	0.05	0.07	0.07	0.10	0.05	0.06	0.06	0.05	0.04	0.05	0.07	0.08	0.06	0.04	0.06	0.04	0.06	0.02	0.03	0.03

Table

Click here to download Table: Table_4_ballouardetal.docx

Sample	Rb (ppm)	Sr (ppm)	$^{87}Rb/^{86}Sr$	$^{87}Sr/^{86}Sr$	±	$(^{87}Sr/^{86}Sr)$ 310 Ma	Sm (ppm)	Nd (ppm)	$^{147}Sm/^{144}Nd$	$^{143}Nd/^{144}Nd$	±	εNd (310 Ma)	T_{DM}*
GUE-3	353	101	10.2	0.759868	11	0.7149	2.0	8.1	0.149821	0.512081	5	-9.0	1736
GUE-4	245	131	5.4	0.741854	11	0.7179	2.3	9.3	0.147638	0.512088	6	-8.8	1718
GUE-5	266	121	6.4	0.744704	12	0.7165	0.9	3.5	0.163489	0.512128	6	-8.6	1707
GUE-8	251	147	5.0	0.741599	11	0.7197	2.1	8.5	0.149165	0.512099	5	-8.6	1707
GUE-15	230	197	3.4	0.729724	10	0.7148	3.1	15.3	0.123199	0.512089	5	-7.8	1642

Table

Click here to download Table: Table_5_ballouardetal.docx

	Less differentiated GUE-15 sample	More differentiated GUE-12 sample			Segregate composition
		Measured	Computed	Difference	
SiO_2	71.60	74.21	74.07	0.140	55.52
Al_2O_3	15.04	14.50	14.35	0.151	19.54
Fe_2O_3	1.16	0.73	0.53	0.195	5.23
MgO	0.32	0.16	0.21	-0.054	1.01
CaO	0.82	0.48	0.42	0.058	3.41
Na_2O	3.85	4.00	3.92	0.080	3.40
K_2O	4.59	4.08	3.98	0.097	8.54
TiO_2	0.18	0.09	0.13	-0.040	0.51
P_2O_5	0.23	0.25	0.02	0.232	1.61
Segregating minerals, Wt.%		Kfs	44.5		
		Bt	21.1		
		An20	30.7		
		Ap	3.7		
Amount of solid segregate removed, wt.%			13.3		
Sum residuals squared ΣR^2			0.16		